

Ramesh Bansal *Editor*

Handbook of Distributed Generation

Electric Power Technologies, Economics
and Environmental Impacts

 Springer

Handbook of Distributed Generation

Ramesh Bansal
Editor

Handbook of Distributed Generation

Electric Power Technologies, Economics
and Environmental Impacts

 Springer

Editor

Ramesh Bansal
Department of Electrical, Electronics &
Computer Engineering
University of Pretoria
Pretoria
South Africa

ISBN 978-3-319-51342-3 ISBN 978-3-319-51343-0 (eBook)
DOI 10.1007/978-3-319-51343-0

Library of Congress Control Number: 2016961659

© Springer International Publishing AG 2017

This work is subject to copyright. All rights are reserved by the Publisher, whether the whole or part of the material is concerned, specifically the rights of translation, reprinting, reuse of illustrations, recitation, broadcasting, reproduction on microfilms or in any other physical way, and transmission or information storage and retrieval, electronic adaptation, computer software, or by similar or dissimilar methodology now known or hereafter developed.

The use of general descriptive names, registered names, trademarks, service marks, etc. in this publication does not imply, even in the absence of a specific statement, that such names are exempt from the relevant protective laws and regulations and therefore free for general use.

The publisher, the authors and the editors are safe to assume that the advice and information in this book are believed to be true and accurate at the date of publication. Neither the publisher nor the authors or the editors give a warranty, express or implied, with respect to the material contained herein or for any errors or omissions that may have been made. The publisher remains neutral with regard to jurisdictional claims in published maps and institutional affiliations.

Printed on acid-free paper

This Springer imprint is published by Springer Nature
The registered company is Springer International Publishing AG
The registered company address is: Gewerbestrasse 11, 6330 Cham, Switzerland

Preface

Worldwide, the effects of environmental, economic, social, political, and technical factors have led to the rapid deployment of various sources of renewable energy-based power generation. The incorporation of these generation technologies has led to the development of a broad array of new methods and tools to integrate this new form of generation into the power system networks. This book, arranged into six parts, gives a comprehensive discussion on various renewable energy-based distributed generation (DG) technologies as follows:

Part I provides a detailed overview of the distributed generation (DG) technologies, where the classification of DG units based on renewable and non-renewable energy technologies is discussed. In this part, Chap. 1 discusses the fundamentals of distributed renewable energy technologies with emphasizes on their modeling approaches. More specifically, wind turbines, solar PV system, and biomass technologies are briefly presented. The discussion of non-renewable energy technologies is provided in Chap. 2 with detailed discussion focused on gas turbines, diesel generators, small hydro, and fuel cells.

Part II is devoted to wind power systems. The part provides (i.e., Chaps. 3 through 8) a concrete discussion on wind turbine configuration, operation, and technical aspects of interconnection requirements from small-scale to large-scale deployment. Chapter 3 is devoted to large-scale development of wind turbine in the existing power networks with the case study of Mexican power grid. Load flow analysis of power system with wind farm is presented in Chap. 4 while Chap. 5 discusses the sensorless estimation of rotor position for DFIG-based wind turbine. Wind turbine standards and certification with respect to Indian prospective are presented in Chap. 6. The operating and interconnection requirements of wind farms with a case study of Egyptian grid code are discussed in Chap. 7 while the potential configuration for off-shore wind farm interlinked with HVDC collection grid is presented in Chap. 8.

Part III focuses on solar PV systems. Chapter 9 presents the steady-state analysis of unbalanced distribution networks with high penetration of photovoltaic generation. Also, the impact of PV system on voltage and stability is discussed in Chap. 10. The techno-economic evaluation of grid-connected solar PV system for rural

banks is analyzed in Chap. 11. The application of indirect matrix converter for DG units with experimental implementation approach is discussed in Chap. 12 while zeta buck-boost converter for PV system application is presented in Chap. 13.

Part IV is based on the modeling, design, control, and protection. Chapter 14 focuses on key points on modeling, design, and control of smart DC microgrid for integration of various nanoconventional DG units. The effects of DG operating power factor on its location and size using genetic algorithm (GA) are described in Chap. 15. In recent times, protection of DG has been a very critical issue and therefore Chaps. 16–18 are devoted to protection of DG systems. The distributed generation control and protection is presented in Chap. 16, and more details on protection systems in distribution system with DG units are explained in Chap. 17 with some typical examples. In the case of microgrid and multi-microgrid system protection, Chap. 18 has extensively discussed both islanded and grid-connected microgrid protection system.

Part V is devoted to the miscellaneous topics, i.e., power electronic applications, reliability, economic aspect, energy storage, and management for renewable distributed generation (DG) and renewable energy integration in current and future energy markets. In Chap. 19, the applications of power electronic in DG units, grid codes, power quality issues, and participation of DG in the current and future electricity markets are described. This chapter extends the mathematical modeling for DG with power converters, energy resources, and control strategy and summarizes the approaches used to obtain the lifecycle cost of a project. Chapter 20 reviews the energy efficiency of the DG units with energy storage systems and conventional energy system. The methods for reliability evaluation and enhancement of microgrid incorporating the effects of DG units are presented in Chap. 21. Chapter 22 describes the economic aspect of DG units. At the end, Chap. 23 presents with an overview of intelligent energy management strategy (IEMS) in future power distribution networks. It presents the roles of IEMS in power distribution networks with nanogrid, microgrid, and VPPs in which renewable energy resources are integrated.

I am very grateful to a number of individuals who have directly (or indirectly) made contributions to this book. In particular, we would like to appreciate all the authors for their contributions, and the reviewers for reviewing the book chapters, thus improving the quality of this handbook. I would like to thank Dr. Jackson J. Justo for providing continued support throughout this book. We would also like to thank the authorities and staff members of Springer Publishing for being very generous and helpful in maintaining a cordial atmosphere and for leasing us the facilities required during the publication of this handbook.

Lastly, I would like to express my gratitude and sincere regards to my family members who have provided me great support during the preparation of this handbook.

Contents

Part I DG Technologies

- 1 **Distributed Renewable Energy Technologies** 3
Henerica Tazvinga, Miriam Thopil, Papy B. Numbi
and Temitope Adefarati
- 2 **Non-renewable Distributed Generation Technologies:
A Review** 69
Temitope Adefarati, Numbi Bubele Papy, Miriam Thopil
and Henerica Tazvinga

Part II Wind Power Systems

- 3 **Large-Scale Wind Generation Development in the Mexican
Power Grid: Impact Studies** 109
Arturo R. Messina, Rafael Castellanos, Claudia M. Castro,
Emilio Barocio and Armando Jiménez Zavala
- 4 **Load Flow Analysis with Wind Farms** 149
Pradeep Kumar and Asheesh K. Singh
- 5 **Sensor-Less Estimation of Rotor Position in a Doubly
Fed Induction Machine** 171
G. Saravana Ilango, C. Nagamani, M.A. Asha Rani,
M. Jaya Bharata Reddy and A. Karthikeyan
- 6 **Wind Turbine Standards and Certification:
Indian Perspective** 205
Rajiv Singh, Asheesh Kumar Singh and Padmanabh Thakur
- 7 **Egyptian Grid Code of Wind Farms and Power Quality** 227
Shady H.E. Abdel Aleem, Almoataz Y. Abdelaziz
and Ahmed F. Zobaa

8	Integrating an Offshore Wind Farm to an Existing Utility Power Network via an HVDC Collection Grid: Alternative Topology	247
	Kabeya Musasa, Michael Njoroge Gitau and Ramesh Bansal	
Part III PV Systems		
9	Steady-State Analysis of Unbalanced Distribution Networks with High Penetration of Photovoltaic Generation	285
	Kalpesh Joshi and Naran Pindoriya	
10	Distributed Solar-PV Generation: Impact on Voltage Control and Stability	317
	Lasantha Meegahapola and Tim Littler	
11	Techno-economic Evaluation of Grid-connected Solar Photovoltaic Power Plant for Rural Banks	343
	Rajashekar P. Mandi	
12	Indirect Matrix Converter for Distributed Generation Application: An Experimental Study	375
	Rahul Kumar Garg, Kavita Yadav, Vinod Kumar and Monika Vardia	
13	An Experimental Study on Zeta Buck–Boost Converter for Application in PV System	393
	Neeraj Priyadarshi, Kavita Yadav, Vinod Kumar and Monika Vardia	
Part IV DG Modelling, Operation, Control, Protection		
14	Modelling, Design, and Control of Smart DC Microgrid for Integration of Various Non-conventional Distributed Generators	409
	Mahesh Kumar and S.N. Singh	
15	Effects of DG Operating Power Factor on Its Location and Size by Using GA in Distribution Systems	459
	Bindeshwar Singh, R.P. Payasi and Janmejaya Sharma	
16	Protection Issues in Microgrids and Multi-microgrids	503
	Sachit Gopalan, Victor Sreeram, Yateendra Mishra and Herbert Iu	
17	Power Management and Protection of Distribution Systems with Distributed Generations	549
	Yuan Liao	
18	Protection of Distribution Systems Integrated with Distributed Generation	583
	Adeyemi Charles Adewole, Raynitchka Tzoneva and Alexander Apostolov	

Part V Miscellaneous: Power Electronics, Reliability, Economic Aspects, Energy Storage and Management

19 Power Electronic Applications, Grid Codes, Power Quality Issues, and Electricity Markets for Distributed Generation 631
 Akshay Kumar Rathore and Prasanna Udupi Rajagopal

20 Reliability Evaluation and Enhancement of Microgrid Incorporating the Effect of Distributed Generation 685
 Debomita Ghosh, Sanchari Deb and Dusmanta Kumar Mohanta

21 Economic Aspects of Distributed Generation 731
 Ponnaganti Pavani and Sri Niwas Singh

22 Solar PV System with Energy Storage and Diesel Generator 749
 Rajashekar P. Mandi

23 Intelligent Energy Management Strategy Considering Power Distribution Networks with Nanogrids, Microgrids, and VPP Concepts. 791
 Jackson J. Justo

Index 817

Part I
DG Technologies

Chapter 1

Distributed Renewable Energy Technologies

**Henerica Tazvinga, Miriam Thopil, Papy B. Numbi
and Temitope Adefarati**

1.1 Introduction

In order to reduce the dependency on producing electric energy from fossil fuel, distributed renewable energy technologies are becoming increasingly important in the energy supply systems of many countries. Distributed renewable energy incorporates various technologies, such as solar power, wind turbines, fuel cells, small hydro, biomass, geothermal and ocean (waves and tidal) energy systems. Solar photovoltaic (PV) as opposed to solar thermal is the most important solar technology for distributed generation, hence its consideration in this chapter. These energy technologies can be used to meet cooling, heating, remote power, backup power, baseload power, peaking power and power quality requirements. They also have the potential to reduce the impact of electricity price fluctuations, strengthen energy security, mitigate congestion in transmission lines, provide greater stability to the electricity grid and reduce the gas emission.

H. Tazvinga (✉)
Energy Centre, Council for Scientific and Industrial Research,
P.O. Box 395, Pretoria 0001, South Africa
e-mail: HTazvinga@csir.co.za

M. Thopil · T. Adefarati
Department of Electrical/Electronic and Computer Engineering,
University of Pretoria, Pretoria, South Africa
e-mail: MiriamThopil@tuks.co.za

T. Adefarati
e-mail: u14459109@tuks.co.za

P.B. Numbi
Department of Electrical Engineering, Centre for the Development
of Green Technologies, Mangosuthu University of Technology,
P.O. Box 12363 Jacobs, Durban 4026, South Africa
e-mail: numbib@mut.ac.za

The term distributed generation herein refers to small-to-medium power plants located at or near electricity users such as in off-grid or rural or periurban locations. In this context, distributed resources also include distributed generation technologies, located within the distribution system or on the customer side of the meter, and demand-side resources, such as load management systems, to shift electricity use from peak to off-peak periods, and energy efficiency options, e.g. to reduce peak electricity demand, to increase the efficiency of buildings or drives for industrial applications or to reduce the overall electricity demand. In this chapter, different distributed renewable energy technologies together with their advantages and disadvantages are explored.

1.2 Solar Photovoltaic Technology

The photovoltaic effect demonstrated by semiconductor materials, wherein electric charge is generated when in contact with solar radiation, can be successfully applied to generate electricity. A brief historical timeline of the development of photovoltaic technology for electricity generation is summarized in Table 1.1.

From an economic standpoint, the use of photovoltaic technology for electricity generation has been limited by high investment costs, but these costs have been decreasing over the years. The first-generation solar cells were first used for space applications, and hence, a certain quality had to be maintained. From around the mid-1970s, the technology has been used on the earth as a viable method for generating electricity, and it is increasingly becoming attractive owing to the decreasing cost of producing PV modules in recent years. With the advancements made to improve the efficiency of the first-generation solar cells, their demand rose, hence making large-scale manufacturing possible and further reducing investment costs. The cost and pricing trends of PV technology have been studied extensively in [5, 6]. Table 1.2 [6] demonstrates the differences in a PV module production costs and impacts during the years 1975 and 2001.

Table 1.1 Brief historical timelines of the development of photovoltaic technology [1–4]

Year	Event
1839	Discovery of photovoltaic effect by Alexandre-Edmund Becquerel
1876	Demonstration of photovoltaic effect on selenium bar by William Grylls Adams and Richard Evans Day
1883	Construction of the first solar cell by using the semiconductor selenium with gold by Charles Fritts
1941	Patent for p-n junction solar cell using semiconductor silicon was applied by Russel Shoemaker Ohl for Bell Telephone Laboratories
1954	First practical silicon solar cell with an efficiency of 6% was constructed by Daryl M. Chapin, Calvin S. Fuller and Gerald L. Pearson for Bell Laboratories

Table 1.2 PV module production costs and impacts in the years 1975 and 2001 [6]

Parameter	1975	2001	Change to module cost
Module efficiency	6.3%	13.5%	-17.97
Size of PV plants	76 kW/year	14 MW/year	-13.54
Cost of silicon	300 USD/kg	25 USD/kg	-7.74
Consumption of silicon	30 g/W	18 g/W	-1.06
Wafer size	45 cm ²	180 cm ²	-0.67

Semiconductor materials have various physical properties such as light emission and thermal energy conversion that makes them a good candidate for a wide range of applications. They can be doped to create p-type and n-type semiconductors, which when merged together from a p–n junction, the very basic constituent of all semiconductor-based electronic devices, including the solar cell. The solar cell is formed by exploiting the photoelectric property of semiconductors, wherein electrons and holes are created in the semiconductor material when high-energy photons from a source of light hit its surface. The movement of electrons creates a flow of electric charge, which can be collected in the form of direct current (DC) electricity.

The most commonly used semiconductor, silicon, belongs to group IV of the periodic table. Semiconductors can belong exclusively to group IV or group VI (such as selenium) or can exist in the form of compounds belonging to groups II–VI, groups III–V, groups III–VI and groups IV–VI. There are other forms of semiconductors too, such as organic semiconductors that can be used to construct a solar cell; however, the most prevalent form of solar cell is silicon-based. The type of semiconductor used depends on the generation level of the solar cell in question. The various technologies used for the practical application of photovoltaic effect to generate electricity can be classified as first-, second- and third-generation technologies.

The first-generation solar cells are essentially silicon-based solar cells and are largely used for residential rooftop applications. They are very expensive to produce and have low efficiency; however, they are very robust. Each silicon cell can produce a maximum of 0.6 V in the presence of sunlight, and under standard conditions of 25 °C and 1000 W/m² of solar irradiance, it can have a module efficiency of up to 15%.

The second-generation solar cell makes use of thin-film technology, thereby reducing the high costs involved in the production of first-generation solar cells. They do not have an improved efficiency over the first-generation model and often make use of cadmium telluride (CdTe), copper–indium–gallium–diselenide (CIGS) or hydrogenated amorphous thin-film silicon. Due to its thin structure, it is widely used for building-integrated photovoltaic (BIPV) applications and in photovoltaic power stations. CdTe and CIGS have lower module efficiencies than silicon; however, they are cheap and have long-term stability.

A lot of research is ongoing on third-generation solar cells, and these are by far the type of solar cells with the highest efficiency, but they are quite expensive and make use of a variety of materials such as nanotubes and silicon wires. Copper–zinc–tin–sulphide solar cell, perovskite solar cell and quantum dot solar cell are a few examples of third-generation solar cells. Ongoing researches at various laboratories aim to make third-generation solar cells more cost-friendly.

1.2.1 Solar Cell Working Principle

The basic working principle of a solar cell is demonstrated in the form of a flow chart and schematic diagram in Figs. 1.1 and 1.2. It is observed that the amount of energy required by the photon to cause the dislodgement of electrons from the semiconductor depends on the bandgap of the semiconductor element. The photon energy must overcome the bandgap potential to dislodge electrons. For example, silicon has a bandgap of 1.17 eV [7].

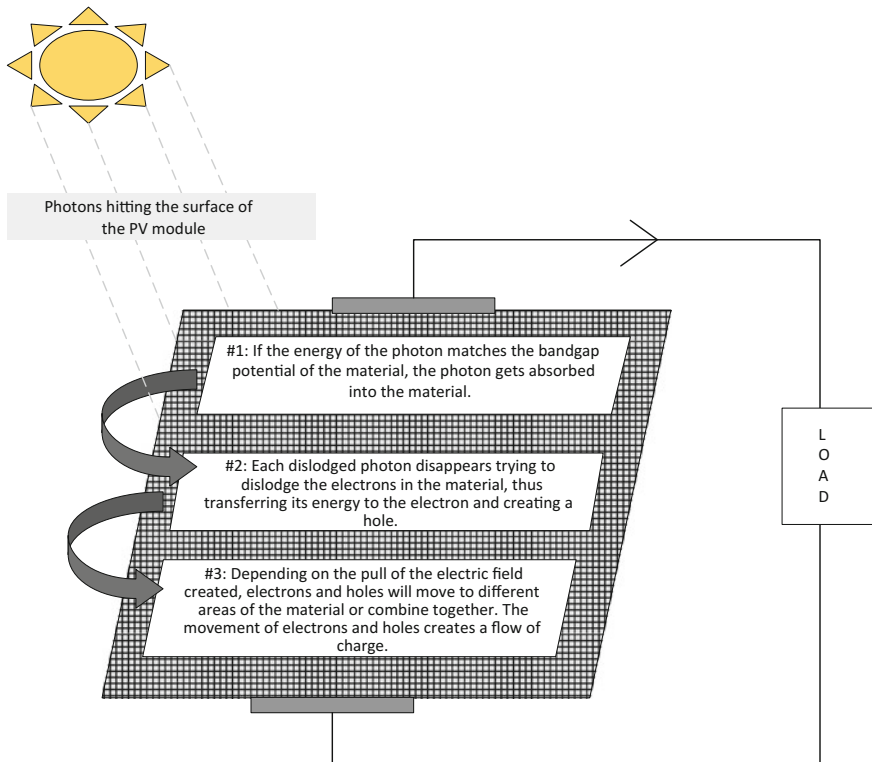


Fig. 1.1 Flow chart demonstrating the working principle of a photovoltaic or solar cell

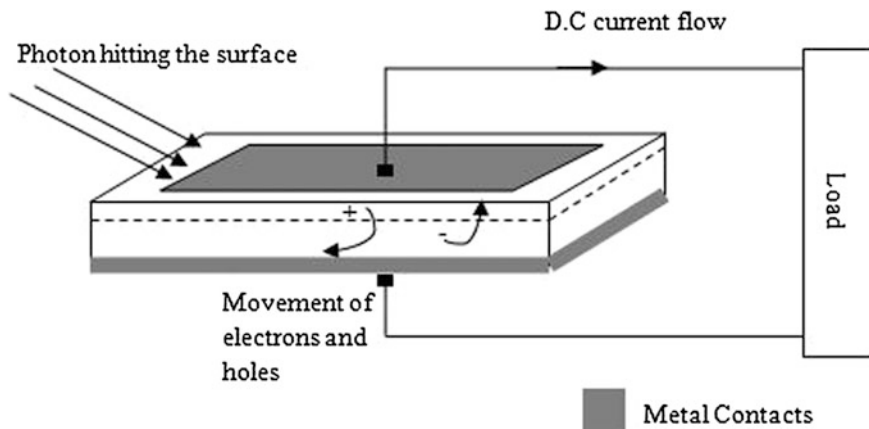


Fig. 1.2 Schematic diagram showing the working of a photovoltaic or solar cell

Photons that reach the interior of the cells with an amount of energy equal to or greater than the bandgap are absorbed in the bulk of the semiconductor generating electron–hole pairs that can act as carriers of current. The electric field or potential difference (p.d.) produced by the p–n junction is responsible for the separation of carriers before any recombination has taken place. This results in a p.d. and a current in the external circuit that includes the load as shown in Fig. 1.1. The p.d. across the device produces phenomena of injection and recombination of the electron–hole pairs. In a solar cell, these create losses whose extent depends on the p.d. When a load is connected to an illuminated solar cell, the current that flows is due to two counteracting current components, the photogenerated current and the diode current.

The energy of a single photon is transferred to the semiconductor material of a solar cell to form electric energy. This energy can be represented mathematically as shown in Eq. (1.1).

$$E_p = h\nu, \tag{1.1}$$

where

h 6.625×10^{-34} J s (Planck’s constant)

E_p Energy in a photon (J)

ν Frequency (s^{-1})

and

$$\nu = c/\lambda, \tag{1.2}$$

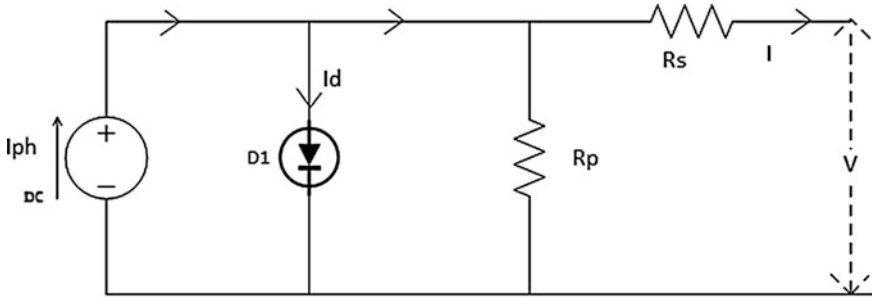


Fig. 1.3 Equivalent circuit diagram of a PV cell [8]

where

c 3×10^8 m/s (speed of light)

λ Wavelength (m)

This E_p is converted into I_{ph} (current produced by photon) in the semiconductor. The equivalent electric circuit of a PV cell is shown in Fig. 1.3. A solar cell is represented using a current source (I_{ph}), diode (due to the p–n junction of the semiconductor) and series and parallel resistances (representing the cell's resistance and diode's internal resistance, respectively). The current I that reaches the load is the difference between I_{ph} and I_d (diode current which flows when there is no solar radiation present and the diode is forward-biased). The voltage across the load resistance will be the DC output voltage of the solar or PV cell [8].

1.2.2 Solar Cell Electrical Characteristics

The current flowing through each cell can be expressed mathematically as shown in Eq. (1.3). The value of the dark saturation current is dependent on the cell temperature and it increases with increase in temperature. For a circuit consisting of an ideal current and an ideal diode the characteristic I – V curve is obtained as follows:

$$I = I_{ph} - I_d = I_{ph} - I_o \left[\exp \left\{ \frac{eV}{kT_c} \right\} - 1 \right], \quad (1.3)$$

where

e $1.6021765 \times 10^{-19}$ C (electron charge)

V Voltage across the cell in Volts

K $1.38064852 \times 10^{-23}$ J/K

T_c Absolute cell temperature (K)

I_o Dark saturation current (A)

In a real solar cell, there are other effects that are not considered in the above expression and these affect the output or external behaviour of the particular solar cell. These intrinsic effects include series resistances (R_s) and parallel resistances (R_p) and are distributed throughout the device; hence, they cannot always be represented by a resistance of constant value. In practice, they are represented by lumped resistances as shown in Fig. 1.3.

Parallel resistance has its greatest effect when the voltage is lowest, that is, when the current passing through the circuit diode is very small. This resistance may originate from leakages around the edge of the cells, diffusions along grain boundaries (if present) or small metallic short circuits. In many practical cases such as in silicon solar cells, parallel resistance has very little significance under normal operating conditions. Series resistance may be due to resistance of the metal contacts within the semiconductor, layers of the semiconductor or metallic fingers which make up the front grid of the cells.

The current–voltage (I – V) and power–voltage (P – V) characteristics of a PV cell are well documented in various texts [8]. When the PV cell is short-circuited, the current through the cell is at its peak and the voltage across the cell is zero and the current at that point is called I_{SC} . Similarly, when the PV cell is open-circuited, the voltage is at a maximum value, whereas the current through the cell is zero and the voltage at that point is V_{OC} .

The knee point of the I – V curve (refer to Fig. 1.6) represents the optimal operating point of a PV cell. At that point, the slope of the curve will give the conductance or $1/R_{optimal}$ of the load and $R_{optimal}$ represents the optimal resistance value. With increase or decrease in load resistance value, the operating point will shift to the left or to the right of the curve, respectively. By multiplying I and V , it is possible to obtain the value of the corresponding power (P). These values can be with respect to V to get the P – V curve as shown in Fig. 1.4. The knee point of the P – V curve indicates the maximum power point or the ideal operating point of the PV cell. Trackers called maximum power point trackers (MPPTs) can be installed to keep the PV cell function at this point. The maximum power point or the optimal

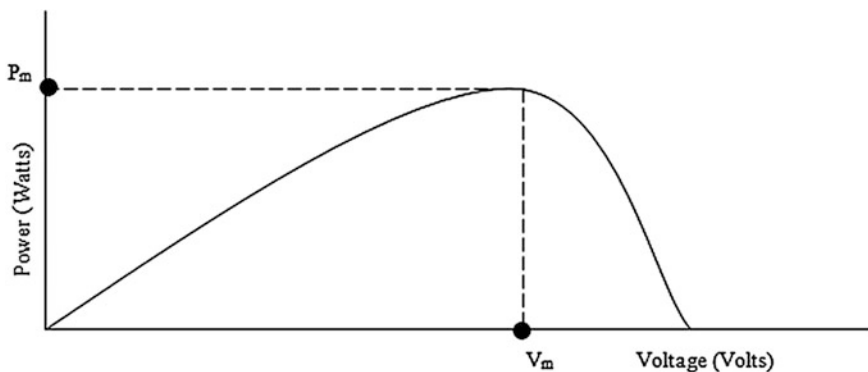


Fig. 1.4 P – V curve of a PV cell from [8]

power point can be expressed mathematically as shown in Eq. (1.4). Another parameter referred to as the fill factor [8] is introduced as a measure of the quality of the PV cell operation and is mathematically expressed in Eq. (1.5). The value of the fill factor decreases with increase in temperature.

$$P_{\max} = I_m \times V_m \quad (1.4)$$

$$P_{\max} = I_{sc} \times V_{oc} \times \text{Fillfactor} \quad (1.5)$$

The efficiency of a PV cell can also be expressed in terms of its power output and power input in the form of power from solar energy as shown in Eq. (1.6) [8].

$$\eta = \frac{P_{\max}}{P_{\text{input}}} = \frac{I_{\max} V_{\max}}{AG_T}, \quad (1.6)$$

where

- P_{input} Input power from solar energy in Watts
- A Area of the cell in square metre
- G_T Solar irradiance in Watts per square metre
- η Efficiency of a PV cell

1.2.3 Photovoltaic Systems for Distributed Generation

Since the maximum possible potential difference across a monocrystalline silicon-based solar cell is only around 0.6 V, it is necessary to modify its construction and design for practical use. Many solar cells are connected together, along with other protective components, to form a PV module. Many such modules can be arranged in rows to form an array to further increase the power output. PV cells can be connected in series or parallel or series-parallel depending on the specific application. Parallel connections increase the current output, and series connections increase the voltage output. A schematic representation of $N_{PM} = 5$ (number of parallel-connected PV modules) and $N_{SM} = 3$ (number of series-connected PV modules) is shown in Fig. 1.5. The total current generated by all these modules is represented as I_M and the DC output voltage across the entire array as V_M .

The functioning of PV technology would be non-existent without the presence of solar energy, and it is for this reason that it is important to further understand its impact on the power output from a PV module. The I - V curve of a first-generation silicon solar cell under varying levels of solar irradiation is shown in Fig. 1.6. The relationship of solar irradiation levels falling on the cell on the power output of the cell is seen to be directly proportional.

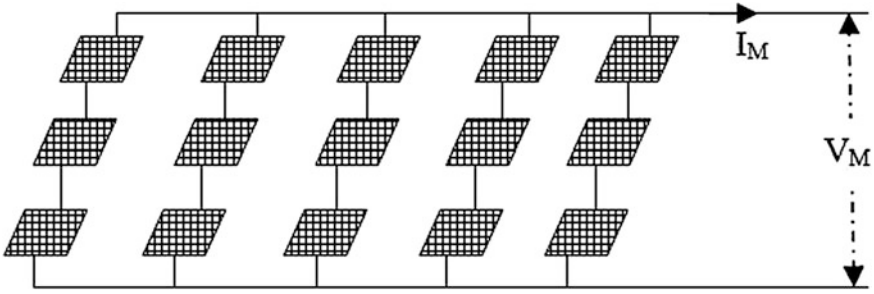


Fig. 1.5 Arrangement of a PV array with 5 parallel modules and 3 series modules

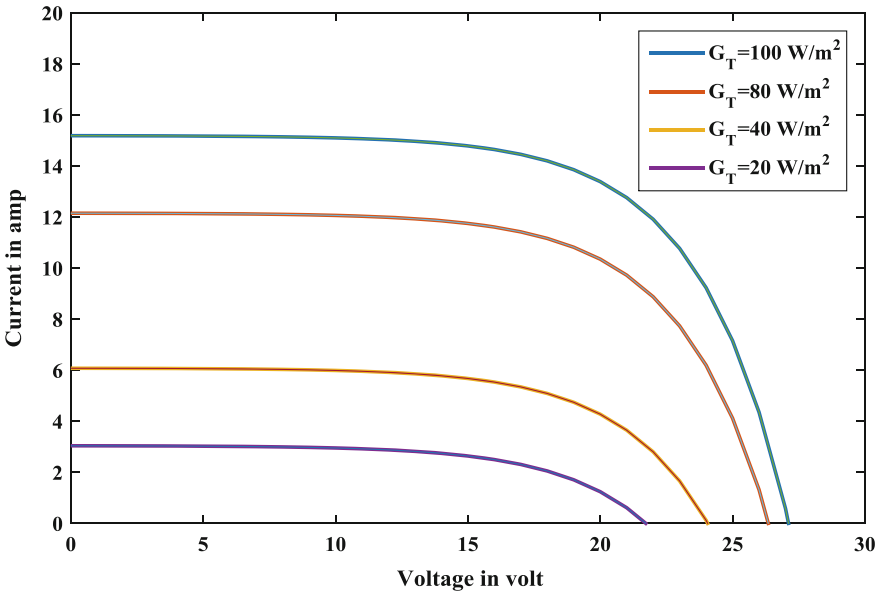


Fig. 1.6 Variation in I - V curve when solar irradiance (G_T) value changes [9]

There are various other factors besides solar irradiance that affect the operation of a PV cell, and these are summarized in Table 1.3. All of these factors must be taken into consideration when designing a PV module arrangement in order to maximize the efficiency of the modules.

Once PV modules are designed, it is necessary to test them before operation. The standard testing conditions for PV cells are $G_T = 1000 \text{ W/m}^2$ and cell temperature $T_C = 25^\circ\text{C}$. However, under normal operating conditions, $G_T = 800 \text{ W/m}^2$ and ambient temperature, $T_{AC} = 20^\circ\text{C}$ at a wind speed of 1 m/s. Some of the various tests that are undertaken to ensure maximum quality of these modules are: thermal cycling sequence to track any drawbacks in the design which ensures that

Table 1.3 Impact of various parameters on PV module performance [10]

Parameter	Impact on PV cell performance
Ambient temperature	High ambient temperatures do not always indicate high power output, as even at ideal operating point, only 10–15% of solar radiation is converted to electricity; the rest is converted into thermal energy
Moisture interference	Moisture can seep into the modules through the deterioration of protective layers due to the usage of low-quality materials, rough handling and harsh temperature conditions. It causes degradation of the PV module
Presence of reflective materials	The presence of any reflective materials on the surface of the module is counterproductive to the process of converting solar energy to electricity, as a portion of light energy will be lost through reflection. For this reason, antireflective coatings are mandatory in PV modules
Quality of the materials used	Low-quality materials would lead to quick deterioration of the PV cell since PV technology is employed in places receiving very high levels of solar radiation and hence is prone to rough weather conditions. Since the modules are left uncovered, the materials must be able to withstand hail, lightning and other natural hazards
Size of the PV module	The area of a PV module has an impact on the solar power produced; however, larger sizes imply higher capital costs
Operating point	If the operating point of the PV cell is maintained close to the optimal operating point, then it can work efficiently. Trackers must be employed to ensure that the modules are working as close to the optimal operating point as possible
Tilt angle of the module	The tilt angle is defined as the angle the module makes with the horizontal surface on which it is placed. Tilt angle, when adjusted depending on the seasons, will help the modules yield higher power output. Tracking systems, though expensive, can result in even higher energy yields

the modules can withstand the effect of thermal expansion, damp heating test where the modules are exposed to extremely harsh conditions not usually seen in the practical scenarios for testing quality of the module materials, mechanical load test, hail test, and exclusive tests by laboratories for certification purposes. Each of these tests is performed under conditions that vary depending on the purpose of the test. In most countries, it is essential to obtain a certification from laboratories before the modules can be used, particularly for distributed generation applications as it will be connected to the main grid [9, 11].

Although PV cells are the basic building blocks of a PV system, it is necessary to use other components in order for the system to find practical applications. A block diagram of all the components that go into the making of a complete PV unit is shown in Fig. 1.7.

Since the output of a PV module is always DC voltage, inverters are used to transform this into AC voltage so that it can be used to satisfy the AC load demand. In grid-connected PV systems, the AC output of the inverter is connected to the distribution network through circuit breakers and energy meters. The efficiency of

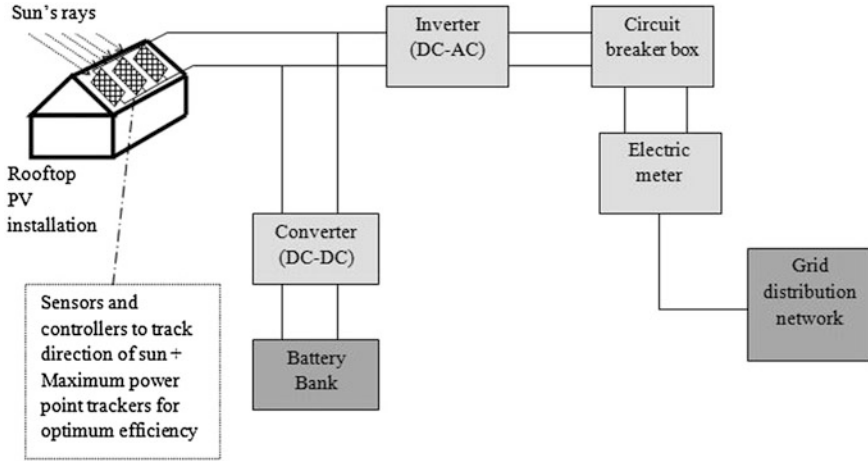


Fig. 1.7 A simple block diagram representing the various elements of a grid-connected photovoltaic system with battery backup [12]

an inverter plays an important role in the overall efficiency of the system. The total energy delivered to the grid is represented as shown in Eq. (1.7) [8].

$$E_{del} = E_{avail} \eta_{ab} \eta_{dist}, \tag{1.7}$$

$$E_{avail} = \eta_{inv} E_{PV}, \tag{1.8}$$

where

- E_{del} Energy delivered to the grid
- E_{avail} Energy available to the grid
- η_{ab} Absorption rate of the grid
- η_{dist} Efficiency of the distribution system
- η_{inv} Efficiency of the inverter
- E_{PV} Energy output from the PV arrays

In countries where feed-in tariffs are in use, wherein the consumer gets paid by the utility for supplying electricity, bidirectional electricity meters will have to be installed. When the grid undergoes a fault or during load shedding, the circuit breakers will be tripped and the PV system is disconnected from the grid, thus reducing probable hazards to workers repairing the fault. Batteries are used to store excess electricity that is produced by the PV arrays and can be used to supply electricity to the load when there is no supply from the grid. They are charged with the help of converters that will protect the battery from overcharging due to high-voltage penetration from the PV array. Many batteries can be connected in parallel to increase the capacity, thus forming a battery bank. The most commonly used battery is the lead–acid type; however, other battery types such as nickel–cadmium and lithium batteries can also be used.

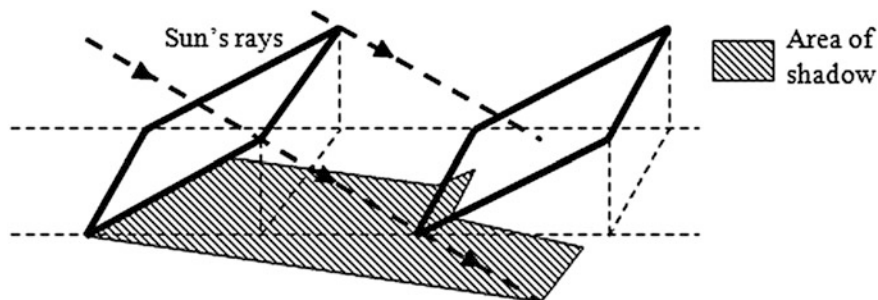


Fig. 1.8 Shading of a PV module caused due to its placement behind another PV module [13]

Tracking systems help change the position of the modules with respect to the sun, in order to maximize the solar radiation falling on the PV module surface. These systems can be single-axis (moving up and down) or double-axis trackers (moving up and down, and left to right), with the latter having the capability to improve the system efficiency to a larger value than the former. The use of a tracking system allows for 20–50% improvement on efficiency compared to a fixed mount system [12]. Maximum power point tracker is yet another element that can be incorporated into the PV system in order to improve its efficiency. The arrangement can be made such that there is one MPPT for the entire PV array, or there is one for each PV module in the array in order to improve the efficiency of each module. These trackers employ control systems and logic to ensure that each PV module or array is function at its maximum power point on the I - V curve [8]. The spacing of the modules plays a vital role in the yield of a PV system. When modules are placed in rows on a flat surface, it is possible that the shadow of one row of modules can fall on the row behind it, as shown in Fig. 1.8.

Shading can also be caused by the presence of a tree, or a building, or even temporary shading by a bird flying above the PV panel. When shading occurs, all the cells on which the shadow falls yield zero current as there is no photoelectric effect taking place in those cells. In cases where these cells are connected in series, the current and hence the power output of the entire string of cells will go to zero. In large modules with large levels of voltage across, inverse voltage will be applied to the defunct cells causing it to heat up and eventually damage the module. This can be overcome by placing a diode referred to as bypass diode, such that it is parallel to a smaller group of cells, thereby stopping the defunct cell from receiving large values of inverse voltage and causing damage [9]. In the case of shading caused by a row of module on another row, blocking diodes can be used to block out the entire shaded row, thus preventing it from causing damage to other rows of modules [9]. It is also possible to optimize the distance between two module rows during its design and before installation so that shading will be minimized. The connection of blocking diodes and bypass diodes in a PV system is shown in Fig. 1.9.

Besides the use of PV modules and arrays in the form of tilted panels as shown in Figs. 1.5, 1.7, 1.8 and 1.9, it is also possible to integrate these modules with the

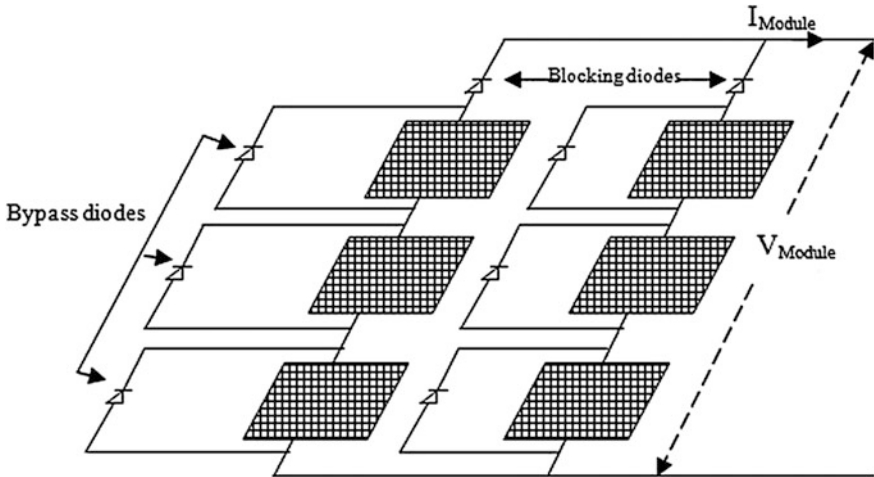


Fig. 1.9 Connection of bypass diodes and blocking diodes to the PV modules

outer surface (façade) of a building structure to form what is referred to as building-integrated photovoltaic (BIPV) system. Since BIPV systems are incorporated into the design of a building, they are not as expensive or space-consuming as rooftop installations. The size of the BIPV system is designed based on the electrical, water and space-heating needs of the building it is going to be integrated with. These panels can be connected to the grid, thus reducing the dependency of the building on the utility grid. Besides the above-mentioned benefits provided by BIPV systems, they also contribute to the architectural design by providing shade and allowing natural daylight to enter. It can also be designed to allow natural ventilation of the building, thus helping to cool down spaces on a hot day and also reducing the temperatures of the panel surface as overheating of the panels will cause a reduce in efficiency and can also damage the material used [14].

Distributed generation is undoubtedly the way forward considering the deregulated electric energy model being adopted by most countries. It is practical, has long-term cost benefits and also encourages the incorporation renewable sources into the energy mix. One such source of renewable energy that can be used is the photovoltaic technology discussed in detail in the previous subsections. Photovoltaic technology makes use of light energy from the sun, a resource that is widely available in most parts of the world. It is not as unpredictable as wind or tidal energy and does not require frequent maintenance as other renewable technologies do. The photovoltaic panels are robust and are tested extensively before use to ensure it can withstand harsh climatic conditions. It must also be noted that photovoltaic technology is one of the few forms of renewable energy technology that can be easily installed in residential and office buildings.

Photovoltaic technology has matured in terms of its cost-effectiveness and efficiency and is becoming highly competitive with other supply sources owing to

the continuously decreasing costs. The effect of shading, even by a small bird flying past the panels, can cause its power output to plummet, thus causing technical issues such as voltage fluctuations to the grid. Solar energy is a variable energy resource, which means it may not be available when required and this impacts negatively on its reliability as a secure source of energy. The second-generation thin-film PV cells are also used for distributed generation, but they possess very low efficiencies of below 20%. Ongoing research to develop the third-generation PV cells into a cheaper technology will help the PV technology to gain more popularity as an efficient and cheap way to produce electricity. Research in the field of building-integrated PV systems can also help alter the architecture of buildings.

1.3 Wind Technology

In this section, a review on how wind energy is converted from kinetic energy in the wind to the electrical energy is presented. A theory on wind energy conversion is described followed by a discussion of wind turbine structures. The power flow model of the fixed-speed wind turbine based on squirrel cage induction generator (SCIG) is reviewed. On the other hand, the maximum power point tracking control of variable-speed wind turbines is reviewed. Lastly, the advantages and disadvantages of wind energy systems are discussed.

1.3.1 Wind Energy Conversion

Before obtaining electrical power from the electrical generator of the wind turbine, the airflow or kinetic energy available in moving air is extracted from the swept area of the blades and converted to mechanical energy by the wind turbine rotor. From this stage, the conversion of mechanical to electrical energy is done by means of the stator of the electrical generator. Therefore, the aerodynamic conversion that consists of kineto-mechanical conversion is the first most important step in wind power conversion. The portion of airflow power available at the swept area of the wind turbine rotor is given by [15]:

$$P_{\text{air-flow}} = \frac{1}{2} \rho A v^3, \quad (1.9)$$

where ρ (approximately 1.225 kg/m^3) is the air density, A (m^2) is the swept area of the turbine rotor and v (m/s) is the upwind free wind speed (at the hub height).

The mechanical power is obtained from Eq. (1.9), through the aerodynamic or power coefficient, $C_P(\lambda, \beta)$ of the wind turbine rotor. This mechanical power is given as follows:

$$P_{WT} = \frac{1}{2} \rho A C_P(\lambda, \beta) v^3, \quad (1.10)$$

where β ($^\circ$) is the blade pitch angle of the wind turbine rotor and λ is the tip speed ratio which is the quotient of the speed of a blade tip (which is the same as the peripheral wind speed) v_{tip} (m/s) to the undisturbed wind speed (upwind free wind speed). This tip speed ratio is therefore expressed as follows:

$$\lambda = \frac{v_{tip}}{v} = \frac{\omega_{WT} R}{v}, \quad (1.11)$$

where ω_{WT} (rad/s) is the rotational speed of the turbine rotor and R (m) is the radius to tip of the turbine rotor.

Taking β as a parameter, the so-called $C_P - \lambda$ performance characteristic can be either determined from field data or approximated by nonlinear analytical functions [16]. The theoretical maximum value of C_P is defined by the Betz limit, which states that a turbine can never extract more than 59.3% of the power from the airstream [15, 16]. However, in reality, the maximum values of C_P are in the range of 25–45% [15].

In [17] for instance, the aerodynamic coefficient is approximated by the nonlinear function given as follows:

$$C_P(\lambda, \beta) = 0.73 \left(\frac{151}{\lambda_i} - 0.58\beta - 0.002\beta^{2.14} - 13.2 \right) \exp\left(\frac{-18.4}{\lambda_i} \right), \quad (1.12)$$

where

$$\lambda_i = \left[\left(\frac{1}{\lambda - 0.02\beta} \right) - \left(\frac{-0.003}{\beta^3 + 1} \right) \right]^{-1}. \quad (1.13)$$

Figure 1.10 shows the performance characteristic $C_P - \lambda$ of a wind turbine with the blade pitch angle β equal to zero.

Fig. 1.10 Performance characteristic curve of a wind turbine (with $\beta = 0^\circ$)

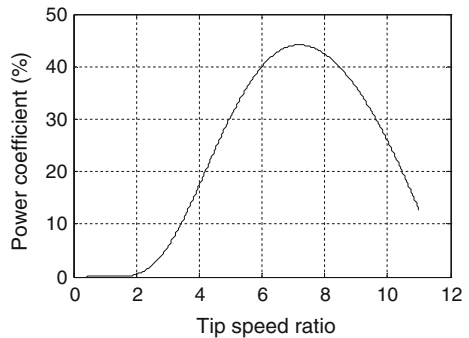
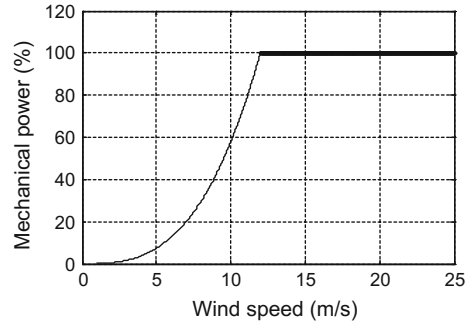


Fig. 1.11 Mechanical power curve of the wind turbine at its hub height



From Fig. 1.10, it can be seen that since $C_p - \lambda$ is concave, the maximum power coefficient can be obtained at a unique optimal value of the tip speed ratio ($\lambda \cong 7$). Maintaining this tip speed ratio at its optimal value requires a continuous linear variation of the rotational speed of the turbine rotor in terms of the wind speed while satisfying Eq. (1.13). Therefore, one of the motivations of operating a wind turbine at variable rotational speed is to allow it to operate at a maximum C_p over a range of wind speeds. This implies that at every wind speed, there is an optimum turbine rotational speed at which the power extracted from the wind resource is maximized [18].

In Fig. 1.11, three specific wind speeds can be noticed:

- Cut-in wind speed (about 2.5 m/s for the given curve): the minimum wind speed at which the wind turbine can deliver useful power. Below this wind speed, the wind turbine remains shut down.
- Rated wind speed (12 m/s for the given curve): the wind speed at which the rated power output of the electrical generator is obtained. Above the rated wind speed, the mechanical power extracted from the wind speed is kept constant in order to reduce the mechanical loads on the drive train.
- Cut-out wind speed (25 m/s for the given curve): the maximum wind speed at which the turbine is allowed to deliver the mechanical power. Above this wind speed, the wind turbine is shut down.

1.3.2 Wind Energy Technologies

Wind energy technology can be classified depending on whether the wind turbine operates at fixed (actually with a speed variation of about 1%) or variable speed [19]. Each of these two wind turbine technologies has its own advantages and drawbacks. In some countries, fixed-speed wind farm based on SCIG is more attractive due to its robust construction, low cost, low maintenance, long life (more than 50 years), low power-to-weight ratio and ease of integration [20, 21]. In China for instance, fixed-speed wind turbine based on SCIG is widely used [22].

However, the big amount of reactive power demand of a large wind farm based on SCIG may not be satisfied by the grid. Therefore, the deficiency of reactive power would lead to some voltage problems as well as increased energy losses within the electrical network [22, 23]. In order to meet the reactive power demand of the wind farm based on SCIG, capacitors or static var compensators (SVCs) are usually employed [23]. On the other hand, the main advantage of the variable speed is its capacity to extract the maximum active power from the wind resource, but also to support the grid voltage control through its reactive power control capability, independently from the active power generation process [24]. According to [15, 19, 24, 25], variable-speed wind turbine based on doubly fed induction generator (DFIG) is the most used for the recently built wind farms [24–26], but also by the wind turbine industry for larger wind turbines (3–5 MW) [19]. However, the complexity of the variable-speed wind turbine makes it to be relatively more costly.

1.3.3 Fixed-Speed Wind Turbine

The generator of the fixed-speed wind turbine is connected directly to the electrical grid as shown in Fig. 1.12. A multiplier gearbox is connected between the turbine shaft and the generator shaft in order to increase the rotational speed of the turbine to the level of the nominal rotational speed of the electrical generator. This technology consists mainly of a squirrel cage induction generator (SCIG). Hence, a power factor correction capacitor is connected to the terminal for compensation of the reactive power consumed by the SCIG [15]. Since the rotational speed is almost constant to the grid frequency, and not controllable, the wind speed turbulence cannot be stored in the form of rotational energy. This would therefore lead to a fluctuation power output of the fixed-speed wind turbine and thus to a poor power quality of grid [19].

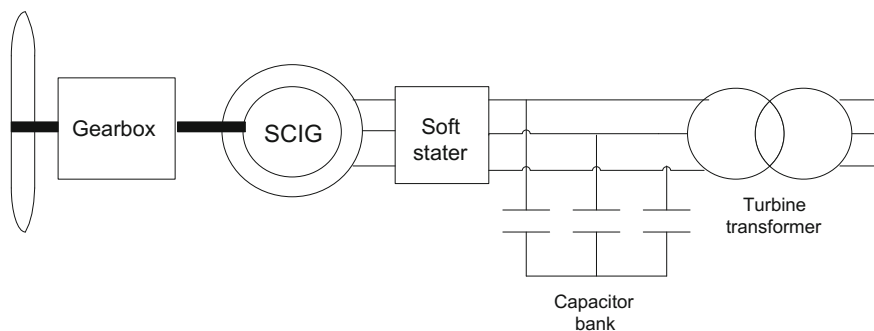


Fig. 1.12 Fixed-speed wind turbine based on squirrel cage induction generator (SCIG)

1.3.4 Variable-Speed Wind Turbine

In a variable-speed wind turbine, the generator is controlled by a variable-frequency power converter (VFPC) before feeding the electrical grid [19]. The VFPC is made up of two AC/DC voltage source converters (VSCs), linked by a DC bus. This scheme allows the ability of the wind farm to comply with grid requirements and the reduction in mechanical loads [15]. The grid code implies that when a wind farm is connected to the national grid, it should supply not only active power but also reactive power (grid voltage control) at a constant grid frequency [27–30]. The use of power electronic converter isolates the variation of the generator speed from the grid frequency. This permits the wind turbine generator to operate at variable rotational speed for maximum power tracking (MPT) scheme while feeding the AC grid at the system frequency [15, 24, 31]. Unlike in fixed-speed wind turbines, the fluctuations of the power output caused by wind turbulence are more or less absorbed in variable-speed wind turbines because of the rotor speed variability [19]. The most common variable-speed wind farm configurations used are the fully rated converter (FRC) wind farm and the doubly fed induction generator (DFIG) [15].

1.3.5 Fully Rated Converter (FRC) Wind Turbine

This structure, presented in Fig. 1.13, consists of a wind turbine where the VFPC is connected to the stator, transferring the full power to the grid. Hence, the designation of FRC wind turbine is due to the fact that all the power generated by the wind turbine goes through the power converter to feed the grid. The converter connected to the stator side is called machine-side converter (MSC) or stator-side converter (SSC), while the one connected to the grid is called grid-side converter (GSC). Many types of electrical generators may be used in this structure. This includes induction generator (IG), wound rotor synchronous generator (SG) and permanent magnet SG [15, 19]. Generally, a gearbox is employed to match the rotational speed of the turbine shaft and that of the electrical generator shaft.

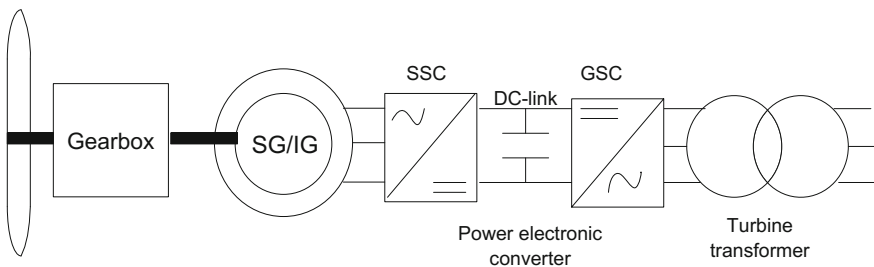


Fig. 1.13 Variable-speed wind turbine based on FRC with induction generator (IG) or synchronous generator (SG)

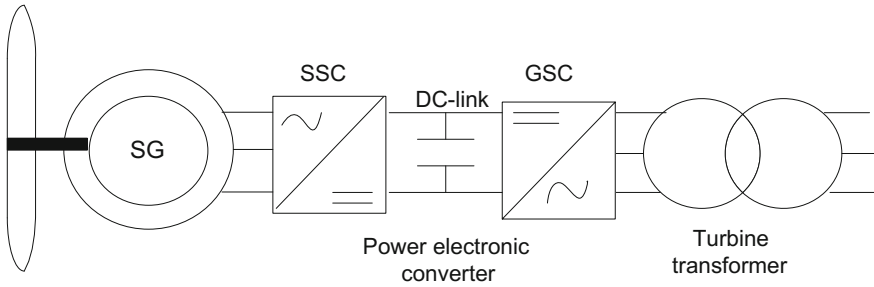


Fig. 1.14 A gearbox-less variable-speed wind turbine based on FRC with synchronous generator (SG)

However, in some cases where a wound rotor SG or permanent magnet SG is designed with multiple poles, the FRC wind turbine is gearbox-less [19]. This is shown in Fig. 1.14.

1.3.6 Doubly Fed Induction Generator (DFIG) Wind Turbine

This structure, shown in Fig. 1.15, consists of a wound rotor induction generator whose stator is directly connected to the grid, whereas the rotor winding is fed by a VFPC via slip rings. A gearbox links the turbine shaft to the generator shaft. The converter connected to the rotor side is called rotor-side converter (RSC), whereas the one connected to the grid is called grid-side converter (GSC). The double connection of the generator makes it possible for the DFIG system to deliver power to the grid through both stator and rotor. However, in subsynchronous speed, the rotor absorbs active power, while in supersynchronous speed this active power is delivered by the rotor. In contrast to FRC wind turbine, at full load, the power converter of DFIG wind turbine only handles (delivers or absorbs) a maximum of 25–30% of the total active power generated according to [26], 20–30% according to [19] and 25% according to [30], while the operating slip range for nominal power between 1.5 and 6 MW is $\pm 35\%$ [30]. However, mechanical and other restrictions limit the maximum slip, and practical speed range may be between 0.7 p.u. and 1.2 p.u. [15]. This corresponds to a slip range of -30 to 20% .

Since the converter has to handle only about a quarter ($1/4$) of the total active power with DFIG wind turbine technology, the energy losses in this power electronic converter will be less than the losses in FRC wind turbine where the power electronic converter has to handle the total power. This also leads to the cost reduction of the converter. These advantages have made DFIG wind turbine to be the most employed structure in newly installed wind power generations [19, 24–26].

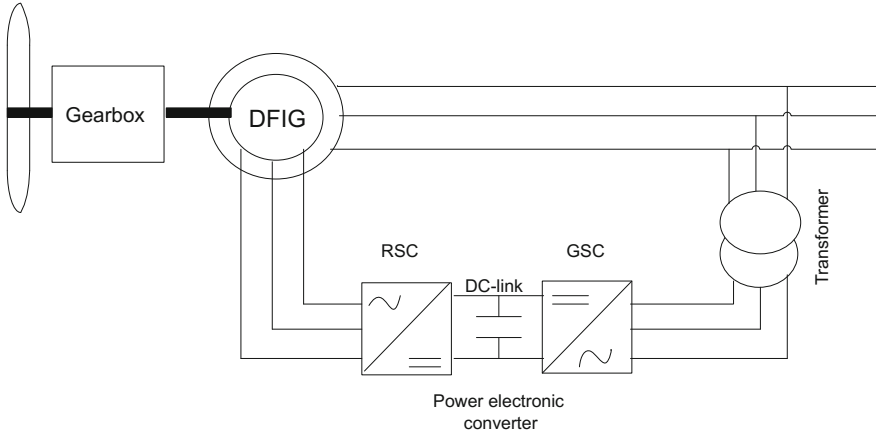


Fig. 1.15 Variable-speed wind turbine based on DFIG

For this reason, in this work, DFIG wind turbine is considered from variable-speed wind turbines.

1.3.7 Model for SCIG Power Flow Calculation

Since the power output of the wind farm based on SCIG will interact with the grid, the power flow model of SCIG therefore needs to be known. The conventional PQ bus model being the most used, the active and reactive powers of SCIG should have constant values [32]. To get the active power constant, the daily active power output curve is discretized as a steplike function by time [22, 23]. The reactive power consumed by the wind farm is therefore expressed as a function of active power output and terminal voltage for power flow calculation [21, 22]. However, in this work, a more detailed power flow of SCIG wind turbine is given. Figure 1.16 shows the steady-state simplified equivalent circuit of the SCIG with all quantities in this circuit referred to the stator. X_{lS} is the stator leakage reactance, X_{lr} is the rotor leakage reactance, R_r is the rotor resistance, X_m is the magnetizing reactance, i_s is the stator current and s is the slip. The terminal voltage, v_s , wind turbine active power output, P_{WT} , and reactive power consumed, Q_{WT} , are the per-phase RMS quantities. In this circuit, the stator resistance and the magnetizing resistance current are ignored.

From Fig. 1.16, the active power injected by the wind turbine based on SCIG to the electrical grid is expressed as follows [21, 22]:

$$P_{WT} = \frac{-v_s^2 \frac{R_r}{s}}{\left(\frac{R_r}{s}\right)^2 + X^2} \quad (1.14)$$

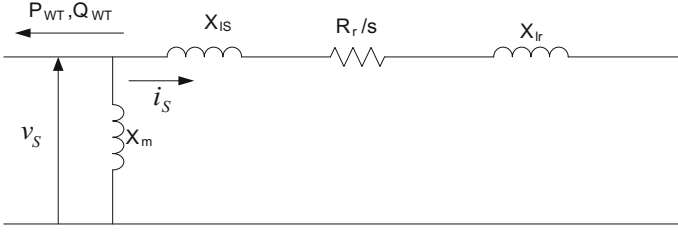


Fig. 1.16 The simplified equivalent circuit of SCIG wind turbine

where $X = X_{IS} + X_{lr}$.

Equation (1.14) can be rearranged as a second-order equation where s is the variable, as given below:

$$P_{WT}X^2s^2 + v_s^2R_r s + P_{WT}R_r^2 = 0 \quad (1.15)$$

The acceptable solution (slip which is within the range of the SCIG speeds) of Eq. (1.16) is as follows:

$$s = \frac{-v_s^2R_r + \sqrt{v_s^4R_r^2 - 4P_{WT}^2X^2R_r^2}}{2P_{WT}X^2} \quad (1.16)$$

From Fig. 1.16, it can be seen that the impedances jX_m and $\frac{R_r}{s} + jX$ are in parallel. Therefore, the equivalent impedance can be expressed as given below:

$$Z_{eq} = \frac{-X_mX + jX_m\frac{R_r}{s}}{\frac{R_r}{s} + j(X + X_m)} \quad (1.17)$$

After multiplying the denominator and numerator of Eq. (1.17) by the conjugate of its denominator, the equivalent impedance can also be rewritten as follows:

$$Z_{eq} = \frac{\frac{R_rX_m^2}{s} + jX_m\left[X(X + X_m) + \left(\frac{R_r}{s}\right)^2\right]}{\left(\frac{R_r}{s}\right)^2 + (X + X_m)^2} \quad (1.18)$$

The tangent of the power factor angle of SCIG represents the ratio given by the imaginary part Z_{eq} over its real part. After mathematical simplification, this ratio is given as follows:

$$\tan \varphi = \frac{s^2X(X + X_m) + R_r^2}{sX_mR_r} \quad (1.19)$$

Therefore, the reactive power absorbed by the SCIG wind turbine will be expressed as follows:

$$Q_{WT} = P_{WT} \tan \varphi = \frac{s^2 X(X + X_m) + R_r^2}{sX_m R_r} P_{WT} \quad (1.20)$$

Substituting Eq. (1.16) in Eq. (1.20) yields the reactive power which is a function of the terminal voltage and the active power output of the wind turbine. This is given by:

$$Q_{WT} = - \frac{\left[4P_{WT}^2 X^3 R_r^2 + (X + X_m) \left(\sqrt{R_r^2 v_s^4 - 4P_{WT}^2 R_r^2 X^2} - R_r v_s^2 \right)^2 \right] \left(\sqrt{R_r^2 v_s^4 - 4P_{WT}^2 R_r^2 X^2} + R_r v_s^2 \right)}{8P_{WT}^2 X^3 R_r^3 X_m} \quad (1.21)$$

Equation (1.21) can be approximated by a second-order equation by means of MacLaurin polynomial. In this polynomial, the terminal voltage v_s is assumed to be constant and the variable is the wind farm active power output P_{WT} . Hence, the constant term in the approximated equation will express the no-load reactive power and the remaining term will express the load-dependent reactive power.

In this work, the small variation of v_s around its rated value is ignored during the wind speed change. Therefore, the reactive power absorbed by the wind turbine is calculated at rated SCIG voltage. With this simplification, the error is not significant [32].

1.3.8 Maximum Power Point Tracking for Variable-Speed Wind Turbines

As the power output of the wind turbine varies in a nonlinear relationship with regard to the wind speed, the aim of maximum power point tracking (MPPT) control is to continually adjust the wind turbine rotor speed in such a way to extract maximum power from the wind resource for each wind speed [26]. Hence, in this control scheme, the wind speed is taken as a parameter, while the rotor speed of the turbine or generator is a variable. The MPPT scheme is achieved by first substituting the tip speed ratio given by Eq. (1.11) into the power coefficient given by Eq. (1.12). With the blade pitch angle, β , set to zero, the power coefficient now becomes a function of turbine rotor speed, ω_{WT} , and wind speed, v , which can be written as follows:

$$C_p = C_p \left(\frac{\omega_{WT} R}{v} \right) \quad (1.22)$$

Taking into account the gearbox ratio noted by n , Eq. (1.22) can be rewritten and given by the function below:

$$C_P = C_P \left(\frac{\omega_r R}{nv} \right) \tag{1.23}$$

where

$$n = \left(\frac{\omega_r}{\omega_{WT}} \right) \tag{1.24}$$

In (1.23), ω_r (rad/s) is the generator rotor speed.

Therefore, the new expression of the wind turbine power is obtained by substituting Eq. (1.23) into the previous wind power expression, given by Eq. (1.10). This yields:

$$P_{WT} = \frac{1}{2} \rho A C_P \left(\frac{\omega_r R}{nv} \right) v^3 = \frac{1}{2} \rho A C_P \left(\frac{2\pi N_r R}{60nv} \right) v^3 \tag{1.25}$$

The wind turbine power expressed by Eq. (1.25) is a parametric function where the wind speed, v , is a parameter and the generator rotor speed, ω_r (rad/s) or N_r (rpm), is the variable. One should note that the expression in bracket in Eq. (1.25) refers to the function and not multiplication. This means that the power coefficient C_P is a function of the term in bracket. Figure 1.17 shows the MPPT characteristic of a 2-MW wind turbine based on DFIG.

It can be seen from Fig. 1.17 that the maximum or optimum power represented by the curve P_{opt} can be extracted from the wind resource at each wind speed by varying

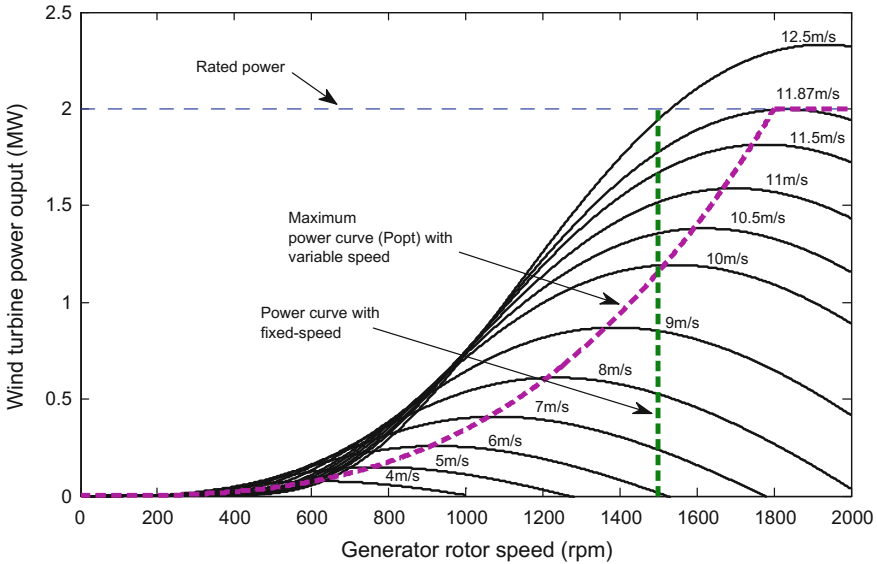


Fig. 1.17 MPPT characteristic of a wind turbine based on variable speed

the rotor speed of the generator. On the other hand, the power curve with fixed speed shows that a maximum power can be extracted from the wind resource at a specific wind speed (about 10 m/s for this case), and for other wind speeds, the efficiency of the fixed-speed wind turbine is less than that of variable-speed wind turbine.

This MPT characteristic P_{opt} can be directly plotted if the optimal (maximum) point of the power coefficient C_p curve is known in advance. If this optimal point is taken as $(C_{p_{\text{opt}}}, \lambda_{\text{opt}})$, the MPT curve is obtained by substituting the tip ratio expression directly in the power expression in such a way that the rotor speed is the only variable in the new power expression. Hence, we have:

$$P_{\text{opt}} = \frac{1}{2} \rho A C_{p_{\text{opt}}} \left(\frac{R \omega_{\text{WT}}}{\lambda_{\text{opt}}} \right)^3 \quad (1.26)$$

Referring to the generator shaft (by using the gearbox ratio, n), and expressing the generator rotor speed in rpm, Eq. (1.26) becomes:

$$P_{\text{opt}} = \frac{1}{2} \rho A C_{p_{\text{opt}}} \left(\frac{2\pi R N_r}{60 n \lambda_{\text{opt}}} \right)^3 = \frac{1}{2} \rho A C_{p_{\text{opt}}} \left(\frac{2\pi R}{60 n \lambda_{\text{opt}}} \right)^3 N_G^3 \quad (1.27)$$

$C_{p_{\text{opt}}}$ and λ_{opt} being constant, Eq. (1.27) can be condensed using the following expression:

$$P_{\text{opt}} = K_{\text{opt}} N_r^3 \quad (1.28)$$

where

$$K_{\text{opt}} = \frac{1}{2} \rho A C_{p_{\text{opt}}} \left(\frac{2\pi R}{60 n \lambda_{\text{opt}}} \right)^3 \quad (1.29)$$

For instance, with the approximated power coefficient, C_p , given by Eq. (1.12) and plotted in Fig. 1.10, the optimal point is $(C_{p_{\text{opt}}} = 0.427, \lambda_{\text{opt}} = 7)$ at a pitch angle, $\beta = 0$. With the air density, $\rho = 1.225 \text{ kg/m}^3$, $K_{\text{opt}} = 0.000341655$ for the MPT characteristic of the DFIG plotted in Fig. 1.17.

1.3.9 Advantages of Wind Power

Some of the advantages of wind power are given as follows:

- Renewable and sustainable:
Wind is widely distributed and is caused by the heating of atmosphere by the sun, earth's irregularity and its rotation. This means that as long as the sun will shine and the wind blows, energy from wind source will always be produced.

- **Clean technology:**
Wind power does not pollute the air like conventional power plants based on fossil fuels, such as coal and natural gases. During operation, no greenhouse gas emissions are produced.
- **Efficient technology:**
As compared to other renewable technologies, such as solar, wind energy system has higher energy conversion efficiency, as well as little space requirement.
- **Modularity:**
Wind energy system can be built to any size, provided that the space allows. When the system starts generating profit or more energy is required, the wind farm can be extended by adding more wind turbines.
- **Job creation:**
Because its relatively high technology level and maintenance cost, more people are required during both manufacturing and operation of wind energy systems.

1.3.10 Disadvantages of Wind Power

They are also some challenges associated with the use of wind energy systems, therefore hindering their use and applications.

- **Cost-effectiveness:**
Wind power will depend on the wind strength of the site. Another challenge is that good wind sites are generally found in the remote locations. This means that the installations of wind farms on sites with poor wind resources will lead to a less competitive energy system compared to conventional energy sources. Also, the construction of additional transmission lines to transport power from remote location to places where it is consumed will lead to high energy cost.
- **Low reliability:**
Wind energy is not predictable and hence patchable due to its stochastic nature. The power output of the wind turbine is dictated by the wind strength at a particular time, which is weather dependent.
- **Noise disturbance:**
As the turbine blades extract kinetic energy from the airflow through rotation movement, the air pressure around the turbine varies, which leads to noise disturbance. This is one of the constraints that make wind farms to be erected far away from the electricity consumers.
- **Wildlife threat:**
Since wind farms are usually constructed in remote areas, this would lead wildlife disturbances. Furthermore, during turbine rotation, flying animals, such as birds, will incur the risk of being drawn towards the blades and killed.

- Visual impact:
Although some people are attracted by the beauty of wind turbines, the majority of them feel unsafe. Many people are scared only by seeing these huge wind blades rotating.
- Safety issues:
Nowadays, many countries in the world have been experiencing natural calamities, such as storms. With this, storms may lead to the damage of wind turbines, which in this case will be considered as hazard to the workers in the wind farms as well as animals.

1.4 Biomass/Biogas Technology

Decentralized biogas technology is one of the most promising technologies of biomass and bioenergy that addresses the current global issues on climate change and energy poverty. Naturally produced biogas has been known to exist since the seventeenth century, while studies date back to mid-nineteenth century. Biogas production has got a wide feedstock base, and the combustible gas can be used in various applications including cooking, lighting, electricity and heat production as well as many other applications. Besides its contribution towards the improvement of the energy balance, biogas also plays an important role in the preservation of natural resources and environmental protection [33, 34]. The biomass resources that can be grouped as follows [35]:

- (i) Industrial and municipal wastes, such as municipal solid waste (MSW), sewage sludge and industry waste.
- (ii) Energy crops, including industrial crops, agricultural crops, aquatic crops, herbaceous energy crops as well as woody energy crops.
- (iii) Agricultural residues and waste, such as crop and animal wastes.
- (iv) Forestry residues and waste, such as logging residues, trees, shrub residues and mill wood waste.

Energy production processes from biomass are generally grouped into biological and thermochemical processes. The biological processes are photofermentation, dark fermentation, direct bio-photolysis, indirect bio-photolysis and biological water–gas shift reaction. The thermochemical processes mainly include combustion, pyrolysis, liquefaction and gasification. Combustion processes involve direct burning of biomass in air, thereby converting the biomass chemical energy into heat, mechanical power or electricity through the use of equipment such as stoves, furnaces, boilers or steam turbines, respectively. For combustion, the energy efficiency is low (10–30%) and the by-products are associated with pollutant emissions, making the process unsuitable for hydrogen production for sustainable development. In biomass liquefaction, biomass is heated to a temperature range of 525–600 K in water in the absence of air and under a pressure range of 5–20 MPa

[35]. Catalysts or solvents can be added in the liquefaction process. It is, however, difficult to achieve the above operating conditions, and hydrogen production is low, making this method unfavourable for hydrogen production. Other thermochemical processes such as gasification and pyrolysis and biological processes such as biological water gas shift reaction, bio-photolysis and fermentation are feasible and receiving a lot of attention in the hydrogen production research communities [35].

1.4.1 Biomass Estimation

There are wide variations in biomass usage in different parts of the world owing to the differences in fuel use, energy requirements, biomass cost and the relative availability of the biomass resource in different regions. It is therefore difficult to estimate the quantity of biomass used per annum in a particular country or region because of factors such as:

- Regional differences in climate and geography,
- Seasonal availability of the resource, and
- Differences in income groups of the users.

The statistical data are not readily available making it difficult to quantify the amount of biomass used and also the supply sector is not always defined.

1.4.2 Biomass Combustion

Biomass combustion is a chemical reaction in which a substance (fuel) reacts with oxygen to produce heat energy. The main products include water, carbon dioxide (CO_2), nitrogenous oxides and sulphurous oxides depending on the chemical composition of the fuel. Biomass combustion is affected by both chemical and physical properties of the substances involved. Chemical properties include the chemical composition of the fuel, while physical properties include the ash content, moisture content and bulk density.

The ash content is the fraction of the mass of ash of the total mass which can be expressed in wet basis, in dry basis and in dry ash-free basis. Ash is made up of elements such as potassium, silica, calcium and phosphorous and does not play a vital role in heat transfer. The quantities of these inorganic compounds or elements vary among the various biomass species. Moisture content affects the net amount of heat and is expressed in wet basis and in dry ash-free basis. It is normally expressed as a percentage, and the higher the moisture content, the lower the energy value. In the biomass combustion process, some of the heat produced is used to heat up the water to its evaporation point, thus reducing the combustion efficiency. The amount of energy released is reduced by an amount required to evaporate the water.

Biomass can be oven-dried or air-dried. Bulk density refers to the mass per unit volume of the biomass. The volume in this case is composed of solid volume, pore volume and void volume. Bulk density depends on the degree of compaction and is expressed either on oven dry basis or on wet basis depending on the packing conditions. It is mostly used when dealing with biomass that is in particulate form such as potato peels, rice husks and saw dust. Density influences the energy density of materials, transport and energy costs and design of the combustion system and gives an indication of whether or not retreatment is required to improve combustion.

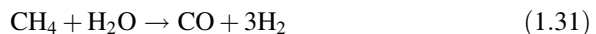
The biomass system typically consists of the furnace where the fuel is burnt and the heat exchanger. Air or water can act as a heat transfer medium, and a combination of the furnace and heat exchanger is known as a boiler. Furnace types include the great, suspended and fluidized bed furnaces. Good airflow is necessary to ensure complete combustion. Too little air results in incomplete combustion, while too much air would also lower combustion temperatures, hence reducing the efficiency of the burner. Proper airflow control is therefore vital. Poor mixing of volatiles with air and poor residence time of the volatiles in the combustion chamber can cause incomplete combustion. Good combustion chamber design and secondary airflow control are therefore crucial in order to overcome the above problems. Feedstock also has to be suited to the combustion chamber design.

1.4.3 Hydrogen Production from Biomass

Pyrolysis is a thermochemical process in which the biomass is heated to temperatures of 650–800 K at pressures of 0.1–0.5 MPa in the absence of air to convert biomass into solid charcoal, liquid oils and gaseous compounds. It can be divided into slow pyrolysis and fast pyrolysis. Slow pyrolysis is not suitable for sustainable hydrogen production because its main product is charcoal, while products of fast pyrolysis can be liquid, solid or gaseous states [36]. Although most pyrolysis processes are designed for biofuel production, if high temperature and sufficient volatile phase residence time are allowed, hydrogen can be produced directly through fast or flash pyrolysis as follows [35, 37]:



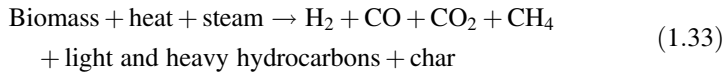
Methane and other hydrocarbon vapours are produced as below through reforming of steam to increase the production of hydrogen:



Water–gas shift reaction can be applied as follows in order to increase the hydrogen production:



The biomass gasification process occurs in the absence of oxygen at temperatures above 1000 K, and the particles go through partial oxidation resulting in the production of gas and charcoal. The charcoal is then reduced to form H_2 (hydrogen), CO (carbon monoxide), CO_2 and CH_4 (methane). The gases produced during this process can be steam-reformed to produce hydrogen and can be further improved by water–gas shift reactions as above. The gasification process can be applied to biomass that has moisture content less than 35% [38]. The reaction can be given by:



Biological hydrogen production is still being investigated in many research communities, and all biological processes are controlled by the hydrogen-producing enzymes, including nitrogenase and hydrogenase [39].

1.4.4 *Biogas Technology*

Biogas is a product of the fermentation of biodegradable waste materials owing to bacterial activity in the absence of oxygen. This process known as anaerobic digestion (AD), and the biogas produced is a renewable energy source. Feedstocks for biogas production include animal wastes and sewage, the organic fraction of the waste from households and industry, residues of crop production (i.e. straw) and energy crops such as maize. Biogas is important in the production of electricity, heat and transportation fuels. It is used for direct combustion in stoves in household and gas lamps and also for power generation in an effort to reduce the carbon footprint. For overall efficiency of utilization of the gas, combined heat and power (CHP) plants are now common technologies especially in developed countries. In a CHP plant, a portion of the heat is used to maintain the reactor temperature and also for heat treatment of materials in the pretreatment process of the biogas production process chain.

It is crucial to know the biogas yield of feedstocks in order to estimate the amount of biogas produced. For a CHP, the productions of electrical and thermal energy depend on the amount of biogas used, the gas turbine efficiency and the calorific value of the biogas. The amount of biogas produced depends on the biogas yield of the particular feedstock which in turn depends on the substrate composition including content of lipids, carbohydrates and proteins. The amount of biogas produced can be obtained by [40]:

$$B = B_y \cdot D_m \quad (1.34)$$

where B (m^3) is the amount of biogas produced, B_y (m^3/ton) the biogas yield and D_m (ton) the biogas yield.

The potential energy output can be obtained by:

$$B_{PE} = B \cdot B_{CV} \quad (1.35)$$

where B_{PE} is the potential energy output (kWh) and B_{CV} is the calorific value depending on the CH_4 content in the biogas.

1.4.5 Biogas Composition

Biogas is composed primarily of methane and carbon dioxide. There are also some small amounts of nitrogen or hydrogen. Contaminants found in biogas include sulphur or siloxanes, depending on the digester feedstock. The amounts of methane and carbon dioxide in the biogas are influenced by a number of factors including the dilution factor in the digester and the ratio of carbohydrates, proteins and fats in the feedstock. Biogas consists of 50–75% CH_4 , 25–45% carbon dioxide CO_2 , 2–8% water vapour (H_2O) and traces of oxygen (O_2), nitrogen (N_2), ammonia (NH_3), H_2 and hydrogen sulphide (H_2S). The energy content of biogas depends mainly on its methane content. The higher the methane content, the higher the energy value. The average calorific value of biogas is in the range of 21–23.5 MJ/m^3 , such that 1 m^3 of biogas corresponds to 0.5–0.6 L of diesel fuel or about 6 kWh [41].

Biogas production is achieved through various types of digester including the floating-drum plant (KVIC model) consisting of a cylindrical digester, fixed-dome plant (Janata model) composed of a brick-reinforced moulded dome, floating-drum plant (Pragati model) consisting of a hemispherical digester, fixed-dome plant (Deenbandhu model) with a hemispherical digester, floating-drum plant (Ganesh model) composed of angular steel and plastic foil, floating-drum plant composed of prefabricated reinforced concrete compound units and floating-drum plant consisting of fibreglass-reinforced polyester [42, 43]. There are also many types of anaerobic digesters for large-scale applications for sewage treatment and biogas generation, and these are well documented in various literatures [44–46].

1.4.6 Operating Parameters

AD has several operating parameters which influence the amount of biogas produced. These include total solids (TS) content which is categorized into low solids AD systems containing less than 10% TS, medium solids ranging from 15 to 12%

and high solid systems ranging from 22 to 40% [46]. At the design stage, by increasing TS content, the digester volume is reduced owing to lower water requirements. Another important factor is temperature; AD can take place under two main temperature conditions, namely mesophilic ranging between 20 and 45 °C with an average of 35 °C and thermophilic ranging between 50 and 65 °C with an average of 55 °C [46]. The optimum operating temperature may vary depending on the composition of the feedstock and digester type but should generally be remain constant to sustain the production of the gas. In terms of loading rate, retention time and gas production, thermophilic digesters are more efficient than mesophilic digesters; however, they require higher heat input and are more sensitive to operating and environmental variables, making them more complex in operation [46]. The amount of time necessary for complete degradation of the organic matter is called the retention time. This depends on the parameters of the process such as waste composition and temperatures involved in the particular process. For wastes treated in mesophilic digesters, the retention time is in the range of 15–30 days, and for thermophilic digesters, it is in the range of 12–14 days [46]. The pH values are also very important in the digestion process and are different for acidogenesis and methanogenesis stages. The pH values fall during acidogenesis owing to the formation of lactic, acetic and propionic acids. The low pH values can hinder acidogenesis, and pH values lower than 6.4 can be toxic in methanogenesis stage.

The carbon-to-nitrogen ratio (C/N) is another important parameter representing the proportions of carbon and nitrogen in the organic matter. In AD digesters, the optimal ratios are in the range of 20–30:1 with a high ratio indicating rapid consumption of nitrogen by the methanogens resulting in lower gas production, while lower ratios result in the accumulation of ammonia and pH values higher than 8.5 which are toxic to methanogenic bacteria [46]. Digester mixing is also crucial as it improves contact between the substrate and the micro-organisms, hence increasing the ability of the bacterial population to obtain nutrients. It also prevents the development of temperature gradients and formation of scum in the digester. Excessive mixing tends to disturb the micro-organisms, and as such, care must be taken when mixing; hence, slow mixing is usually preferred. Organic loading rate (OLR) is an important factor which is defined as a measure of the AD system's biological conversion capacity. It is a vital parameter particularly in continuous systems, and loading the system above normal can result in reduced biogas yield as a result of fatty acid accumulation leading to failure if the accumulation rate is not reduced [46].

1.4.7 Anaerobic Digestion Overview

The production of biogas through anaerobic digestion is achieved through closely related process steps, which involve the continuous breakdown of the initial feedstock into smaller units. In each of the steps, particular groups of micro-organisms are involved and they also decompose the products of the previous

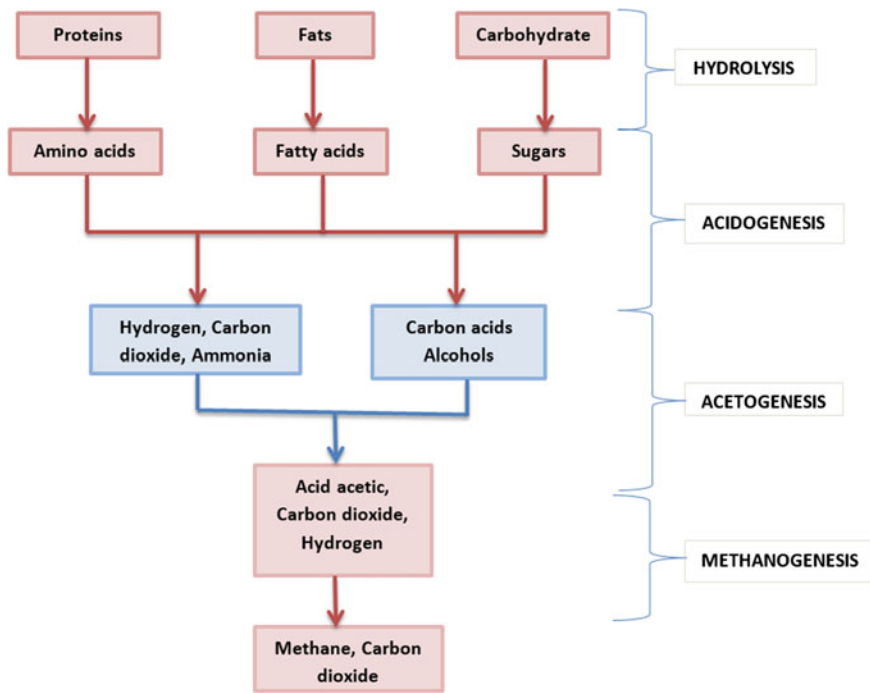


Fig. 1.18 Anaerobic digestion processes

steps successively. The four main processes of the AD process are hydrolysis, acidogenesis, acetogenesis, and methanogenesis. These are shown in the simplified diagram in Fig. 1.18.

The hydrolysis stage involves the decomposition of complex organic matter (polymers) into smaller units (mono- and oligomers), and polymers such as carbohydrates, proteins, lipids and nucleic acids are converted into glucose, pyridines, glycerol and purines. Hydrolytic enzymes are excreted by hydrolytic microorganisms resulting in the conversion of biopolymers into simpler and soluble compounds. In the acidogenesis stage, acidogenic (fermentative) bacteria convert the products of hydrolysis into methanogenic substrates. The degradation of simple sugars, amino acids and fatty acids into acetate, carbon dioxide, hydrogen (70%), volatile fatty acids (VFA) and alcohols (30%) occurs during acidogenesis [34].

Some products of the acidogenesis process that cannot be converted directly to methane by methanogenic bacteria are converted into methanogenic substrates during the acetogenesis process. VFA and alcohols are oxidized resulting in methanogenic substrates such as acetate, hydrogen and carbon dioxide, while VFA, which have longer carbon chains (greater than two units) and alcohols that have longer carbon chains (more than one unit), are oxidized to form acetate and hydrogen. The hydrogen production increases the hydrogen partial pressure.

The conversion of hydrogen into methane takes place during the methanogenesis stage. There is a symbiotic relationship between organisms involved in the acetogenesis and methanogenesis processes, and these processes usually run parallel. Methanogenic bacteria are responsible for the production of methane and carbon dioxide from intermediate products and 70% of the formed methane comes from acetate, while the remainder (30%) is from the conversion of hydrogen and carbon dioxide. This stage is very crucial in the digestion process and is also affected by operating conditions including feedstock composition, pH, feeding rate and temperature. Digester overloading, temperature changes or entry of large quantities of oxygen can terminate methane production [34].

1.4.8 Advantages and Disadvantages of Biogas Technology

Biogas produced from anaerobic digestion of biodegradable wastes has got many advantages including environmental and socioeconomic benefits for societies as well as contributing to the alleviation of energy poverty.

Biogas is a renewable energy source; therefore, it cannot be exhausted. It is an environment-friendly gas; hence, it reduced greenhouse gas emissions and mitigates global warming. The carbon cycle of biogas is closed within a very short time of between one and several years. The greenhouse gas potential of methane is 23 times higher when compared to that of carbon dioxide and 296 times more than that of nitrous oxide. Therefore, the use of biogas as opposed to fossil fuels in energy production and transport mitigates global warming through the reduced emissions of CO₂, CH₄ and N₂O [34]. Development and utilization of biogas technology have great potential in terms of increasing security of national energy supply and reducing dependency on imported and fossil-based fuels. Biogas production contributes towards waste reduction by using the waste as feedstock to obtain a valuable energy resource. Many countries and municipalities have many problems associated with excess production of organic wastes from agriculture, industry and households as well as high costs associated with waste disposal, and these can be solved through implementation of biogas technology. Recycling of waste reduces pollution and spread of diseases. An attractive feature of AD is that it inactivates pathogens and parasites and can effectively reduce the occurrence of waterborne diseases.

Another important potential advantage of biogas technology for many nations is employment creation both at community and commercial levels. Manpower is required for collection and transportation of feedstock, in the production of biogas, power and/or heat, manufacture of technical equipment, construction, operation and maintenance of biogas plants. Biogas is also used for different applications such as direct use for cooking and lighting and for CHP, and in some cases, it is upgraded and fed into natural gas grids. It is also used as vehicle fuel and in fuel cells. The digested substrate (also called digestate) which is a by-product of the AD biogas production system is an excellent fertilizer as it is rich in nitrogen, phosphorus,

potassium and micronutrients. It has higher homogeneity and nutrient value, better C/N ratio and significantly reduced odours when compared to raw animal manure.

Biogas technology is very flexible in that it utilizes various types of feedstock for biogas production such as organic wastes from municipal solid wastes, food industries and households, crop residues, energy crops, wastewater sludge and many other organic wastes. In some cases, biogas is produced from codigestion of various feedstocks. On a small scale, biogas systems are easy to build and little capital investment is required; therefore, many farms or households or communities can become self-sufficient through the utilization biogas plants and waste materials produced by their livestock on a daily basis and/or agricultural wastes and crops. It has been reported that a one cow can provide enough waste material per day to power a light bulb for a whole day [43, 47].

There are, however, some drawbacks associated with biogas technology such as lower biogas yields owing to the dilute nature of substrates used. Another issue is that on a large industrial scale, the production process is not very attractive economically when compared to other biofuels. It contains some corrosive gas impurities that can damage metal parts of internal combustion engines, and the need to remove these gases makes the production process expensive.

1.4.9 Biogas Technology Applications

Biogas is a particularly important renewable source of energy because of its use in internal combustion engines in the transport sector and also in the power generation sector. When the gas been cleaned of carbon dioxide, a fairly homogeneous fuel results with up to 80% of methane with over 25 MJ/m³ calorific capacities. Methane is the most important component of biogas that is involved in the combustion process.

Thermodynamic properties of CH₄ at 273 K and 101,325 Pa are as follows [33, 34]:

- Specific heat, $C_p = 2.165 \text{ kJ/kg K}$
- Molar mass, $M = 16.04 \text{ kg/kmol}$
- Density, $\rho = 0.72 \text{ kg/m}^3$
- Individual gas constant, $R = 0.518 \text{ kJ/kg K}$
- Lower calorific value, $C_L = 50,000 \text{ kJ/kg}$, $C_{L,n} = 36,000 \text{ kJ/m}^3\text{n}$

The actual calorific value of biogas is the function of the CH₄ percentage, the temperature and the absolute pressure, which are different and case specific.

To calculate the actual calorific value of biogas which is an important parameter for engine performance, the following relation is used:

$$C_{L,\text{actual}} = V_{\text{CH}_4} / V_{\text{total}} * \rho_{\text{CH}_4,\text{actual}} * C_{L,n} \quad (1.36)$$

For an IC engine that uses biogas, the fuel consumption is usually specified in m^3/h or m^3/kWh , where m^3 is the standard cubic metre [i.e. volume of 1 cubic metre of gas under standard conditions (273 K and 10,132 Pa)]. The biogas consumption in actual volume will be different from these data depending on the actual conditions of biogas fed into the engine with respect to temperature, pressure and CH_4 content.

Biogas production in a digester or plant is a continuous process, but the demand for power is often not continuous and this warrants the need for storage. When compared to liquid fuels, biogas can be stored in larger quantities either in large, low-pressure storage tanks or in a compressed form requiring special efforts. The storage systems are costly, so there is need to ensure balanced production and consumption to minimize the storage capacity and cost. Continuous fuel consumption by way of using a smaller capacity of engine (lower cost) in a continuous engine operation mode and shifting of loads can equalize the demand profile.

1.4.10 Biogas for Mobility

Biogas is also useful in the mobility sector as it can be used as fuel for natural gas vehicles. Biomethane if used in vehicles can contribute to the reduction of greenhouse gas emissions. The power-to-liquid concept is another interesting area in research communities aimed at increasing the production of synthetic fuels using hydrogen produced from water electrolysis using renewable energy sources. The proportion of biomethane in natural gas that has been used as fuel is reported to have risen by 18% in the years 2010–2013, and many natural gas-filling stations have been established in Germany [48].

1.4.11 Generation of Electricity and Heat (CHP)

Biogas plays an important role in stationary applications such as in combined heat and power plants for generating electrical and thermal with a high degree of efficiency. The power produced can be fed into the grid network or can be for off-grid applications by autonomously supplying power to commercial and industrial areas, or by providing power to rural settlements or areas where it is difficult or financially not economic to connect to the national electricity grid. In a CHP, the waste heat can be used in downstream systems for heating, drying, refrigeration and additional power generation, hence improving the overall system efficiency.

1.4.12 Biogas for the Natural Gas Grid

Biogas can also be fed into the natural gas grid if it is adequately processed to the right quality; for instance, it can be purified to form biomethane which has high methane content (up to 98%). Biogas therefore has great potential in the energy balance as the natural gas grid can play a vital role as a long-term storage option for renewable energy. Currently, a lot of research is going on with regard to whether or not the “hydrogen economy” is the way to go in near future. The power-to-gas concept is gaining a lot of interest whereby renewable produced hydrogen combined with biogas (biomethane) is fed into the natural gas grid. This solves the issue of renewable energy fluctuation by providing storage of energy for seasonal applications, hence promoting the use of greener technologies.

1.5 Small Hydroelectric Power Plants for Distributed Generation

The gravitational force of water falling from a raised level to ground level can be efficiently converted to electric energy. This form of electricity generated from hydropower is called as hydroelectricity. Hydropower is a source of renewable energy, and its small-scale applications can be used for distributed generations. This form of electricity generation has been implemented since the nineteenth century. William George Armstrong developed the very first practical hydroelectric system in 1878 in England, and in 1881, the Schoellkopf Power Station started operation in the Niagara Falls [49].

Over the span of decades, large-scale hydroelectric power stations quickly became major contributors to the energy mix in various countries across the globe. There are different methods of harnessing the energy stored in water; however, the most common and conventional method is by collecting water with the help of a dam or reservoir and letting it flow downwards through a pipe onto a turbine which then runs a generator, thus converting potential energy of the water stored in the dam, into kinetic energy of the water flowing through the pipe, to the mechanical energy produced by the turbine and finally into electricity obtained through the generator.

1.5.1 Overview

The implementation of a hydroelectric power station is restricted by the availability of water bodies. In order to generate significant amounts of electricity, a large river is often required. However, there are many smaller water bodies present in the form of river distributaries, backwaters and lakes that are usually nearby communities.

They can be used for small-scale generation of hydroelectricity which can then be supplied to these local residential and commercial load centres, thus making it a viable option for distributed generation.

Besides tapping into the natural flow of water from small water bodies as mentioned above, the downward flow of water from any existing dams or reservoirs, renovation of old hydropower stations and water treatment plants can also be exploited in order to set up a small hydro system. In order to classify a hydroelectric power station as a small hydro power station, it is necessary that it generates a maximum power output in the range of 10–50 MW, depending on the cut-off adopted by different countries. An outline of the locations where small hydroelectric power stations can be set up in the case of water falling from a high head is shown in Fig. 1.19. The first location is next to the dam, thus receiving direct water flow from the dam to its turbines without the loss of much head. The next location can be nearby water treatment plants, where the flow of water from a sufficiently high head can be used for small hydroelectric power generation [50].

The water from these treatment plants is stored in reservoirs or tanks before being supplied to nearby residential or industrial areas. The head at which water is stored can be tapped into in order to generate electricity, albeit a small amount. Very close to the load centres, i.e. residential and industrial areas, it is possible to make use of the water at pressure-reducing stations where water from the reservoirs is sent in order to reduce the water pressure so that it can safely be used by residential and industrial pipe systems. This water before entering the station will be at very high pressure and has the potential to provide sufficient electrical energy, often enough for use by local loads such as office buildings or residential complexes.

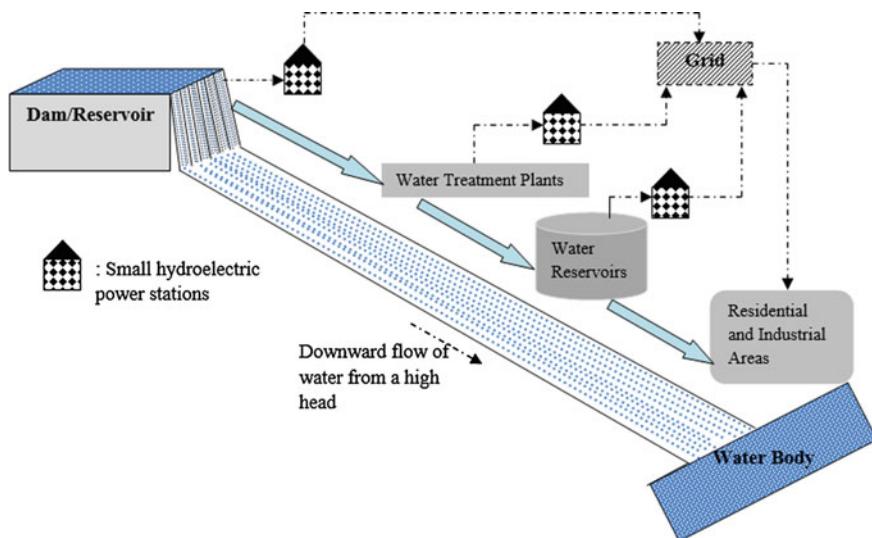


Fig. 1.19 Schematic representation of a small hydroelectric power station when there is a downward flow of water from a high head [50]

In the case of water flowing from a small head, i.e. where there is not enough pressure present, small hydroelectric power stations can still be installed. In the example of the dam shown in Fig. 1.19, this can be the water from the other end of the dam where there is no or little head present.

In such cases, the small hydro stations will be similar to run of river type of power stations. It is common for the areas supplied by dam outflow to be used for farming; the water from the irrigation systems can be used for electricity generation. Besides this, water flowing from industries and wastewater treatment plants can be used to generate electricity. While there can be ample locations for the setting up of a small hydroelectric power station, the pressure and flow of the water in these areas must be measured before proceeding with any installation. The economic viability of such a project must be considered, along with all possible social implications including environmental impacts [50].

1.5.2 Components of a Small Hydropower System

The main components of a small hydroelectric power station are the turbine, generator and transformer. Complimentary components such as voltage regulator, gearbox, turbine controller, switchgear, sensors, substation and backup power supply will help improve the quality of electricity produced. The different types of turbines that can be used for small hydroelectric generation are summarized in Table 1.4. Turbines function through the conversion of potential energy of the

Table 1.4 Types of turbines for small hydro applications [50]

Type of turbine	Description	Type of head (m)	Efficiency (%)
Cross-flow turbine	Employs curved blades fixed onto a rotor, the top of which the water hits and enters the rotor. The water then hits another blade from the inside of the rotor and makes an exit towards the tailrace	2–200	86
Pelton turbine	Jets of water are sprayed tangentially through nozzles onto split-curved buckets placed on the rim of a wheel, thus causing it to turn	50–1300	90
Turgo turbine	Jets of water are sprayed at an angle and hit on many split-cured buckets at once	50–250	85
Kaplan turbines	Rotor is placed axially against the flow of water, which when hits the rotor will turn its blades	2–40	91
Francis turbine	Rotor is placed in a radial position against the flow of water and will let the water enter inside in order to turn the blades and leaves the rotor axially. It can also allow water to flow into the rotor in an axial position, in which case the turbine is called a mixed-flow Francis turbine	25–350	94

water in a head into kinetic energy of the water flowing through a penstock and nozzle if present, thus hitting a set of blades or curved buckets which are placed on a rotor (any rotating part of a machine) with a shaft or prime mover attached to its centre. The water hitting the blades with a force representative of the kinetic energy of the water causes it to rotate and thus is enabling the shaft to rotate as well and yielding rotational mechanical energy. The torque and power of a turbine are defined by the formulation expressed in Eqs. (1.37) and (1.38).

$$T = \rho Q(R_{in} V_{in} - R_{out} V_{out}) \quad (1.37)$$

$$P = \omega T \quad (1.38)$$

where

- T Torque of the turbine (Nm)
- P Power output of the turbine (W)
- Q Flow rate of the fluid (m^3/s)
- R Radius of the turbine (m)
- V Velocity of the fluid hitting the blades tangentially (m/s)
- ρ Density of the fluid (kg/m^3)
- ω Rotational speed of the turbine (rad/s)

The shaft of the turbine is connected to an AC generator or alternator, which can be of either synchronous or asynchronous type. The former always operates at its synchronous speed which depends on the number of poles of permanent magnets used and the frequency of the AC electricity at the grid (usually 50 Hz). Squirrel cage induction machines can be used as asynchronous generators and supply electricity when the rotor is made to rotate at a speed higher than the synchronous speed. Regardless of the type of generator used, the basic operating principle is the same; when a moving conductor is placed in a stationary magnetic field or when a stationary conductor is placed in a rotating magnetic field, there will be voltage induced on the conductor [51].

Voltage regulators used can be either electronic or electromechanical. The former makes use of a simple resistor and diode connected in series, with a feedback provision made to negate any error or difference in voltage levels. In the latter type, an electromagnet defined by the voltage of the electricity generated is used and it moves depending on the strength of the magnetic field. The magnet is connected to a switch which opens or closes depending on the rise or fall in voltage. To control the speed of the turbines, speed governors that control the flow of water and load governors that maintain full load levels are employed. Switchgear and protection play a very important role for the smooth connection of the electricity generated through a small hydropower source to the grid. Breakers are used to disconnect the system from the grid during faults and irregularities, and current and voltage transformers are used to manage current and voltage levels, respectively; in the case of induction generators, reverse power relay is used to prevent it from working in motor mode. Relays and switches are used for the transformer to protect it from

faults. A meter is also an essential component through which the energy sold to the grid can be measured.

1.5.3 System Parameters

The optimal sizing of the turbine generator system is an important topic of research that can lead to minimizing the costs and technical issues and maximizing energy production and efficiency of small hydroelectric technology [52]. Once operation has begun, it is possible to optimize the operating conditions to maximize practical efficiency and the profitability of the system. Optimization can also be performed for designing the layout of a hydropower scheme and designing the blades of the turbine runner [53].

The performance of a small hydroelectric power system, particularly the turbine used, depends on the type of flow and height of head present in the area where it is to be installed. The only technique to test such a system before its implementation was to make a prototype of the turbine model and test it at the location or rely on past data and adapt it to the situation. Research in the field of computational flow dynamics has helped engineers use simulation and hence evade the expensive method of model testing and also improve the performance of the turbine [52]. Since the turbine forms a vital component of a small hydropower project, research to improve the design and characteristics of the existing models by studying the effects of erosion of the turbine, choosing the right turbines for different levels of head, speed control and variation of the turbine propellers, is performed. Speed control is also a topic of study in the case of generators used in small hydropower schemes, as it gives flexibility during changes in flow or head. The behaviours of different generators can be studied and observed for different operating scenarios such as grid-connected projects and rural electrification and during natural calamities such as floods and landslides.

Small hydroelectric technology remains an efficient source of energy in the renewable energy mix that can be used successfully for distributed generations. By using existing water reservoirs and dams, water treatment plants, pressure-reducing centres, irrigation canals and wastewater treatment plants, it is possible to make the most of the present system with minimal investment cost and set up a small hydroelectric station. However, if dams or reservoirs have to be built from scratch, then the impact of such a construction to the environment, local population, marine life and the high investment costs incurred must be considered. From the perspective of the policy design adopted by different countries, there must be absolute clarity. The geographical area and its climatic conditions must be considered during the design and construction of the plant, along with choosing the right turbine generator set for the function. Regular maintenance must be performed to ensure the smooth operation of the plant, especially before and after turbulent weather such as heavy rain and storm.

Small hydroelectric power systems make use of a reliable and available energy resource that does not cause any emissions or pollutants during its operation. They are efficient and often provide support to grid instability issues due to its ability to cater to varying load. However, more studies must be performed to analyse its financial and economic impacts, effect on the biosystem near the site, consequence on rural populations from a social perspective, improving the design of electromechanical equipment and intensive research into the multidisciplinary field of science that forms the basic operating principle of a small hydropower system.

1.6 Fuel Cells

Fuel cell technology was first observed and studied as a viable form of generation of electrical energy in the nineteenth century by Sir William Grove and Christian Friedrich Schonbein [54, 55]; however, it was around the turn of the century that fuel cells began to gain popularity. The first fuel cell was constructed by Francis Thomas Bacon in 1939 and could generate a power output of 5 kW. Fuel cells have since been used for space travel applications, fuel cell-powered automobiles, portable fuel cells for electronic devices and stationary power applications [56, 57]. Fuel cells have high energy efficiency, do not release harmful emissions while generating electricity unlike typical conventional sources and have very low number of moving parts, hence reducing operation and maintenance costs and thus making it a viable contender for the role of a reliable distributed generation technology [58].

1.6.1 Basic Structure

The fuel cell is essentially a device that facilitates the conversion of chemical energy into electrical energy. The chemical energy available for energy conversion is derived from the free energy produced as a result of chemical reactions within the cell. In order to explain the working principle of a fuel cell, the example of a hydrogen–oxygen (H_2 – O_2) fuel cell is considered. A schematic representation of such a cell is shown in Fig. 1.20.

Like any other electrochemical cell, the fuel cell consists of two electrodes that function as an anode and cathode and an electrolyte placed in between them. In the case of this example, H_2 is the fuel, along with O_2 as the oxidant, supplied to the cell through vents on either side as shown in Fig. 1.20. The electrodes are designed to be porous so that they will readily absorb these gases. For every H_2 molecule that enters, the anode oxidizes it and forms two H^+ atoms and two free electrons. These positive H^+ ions move towards the cathode, where it combines with O^{2-} ions created due to the reduction of O_2 with the cathode and form H_2O . The free energy

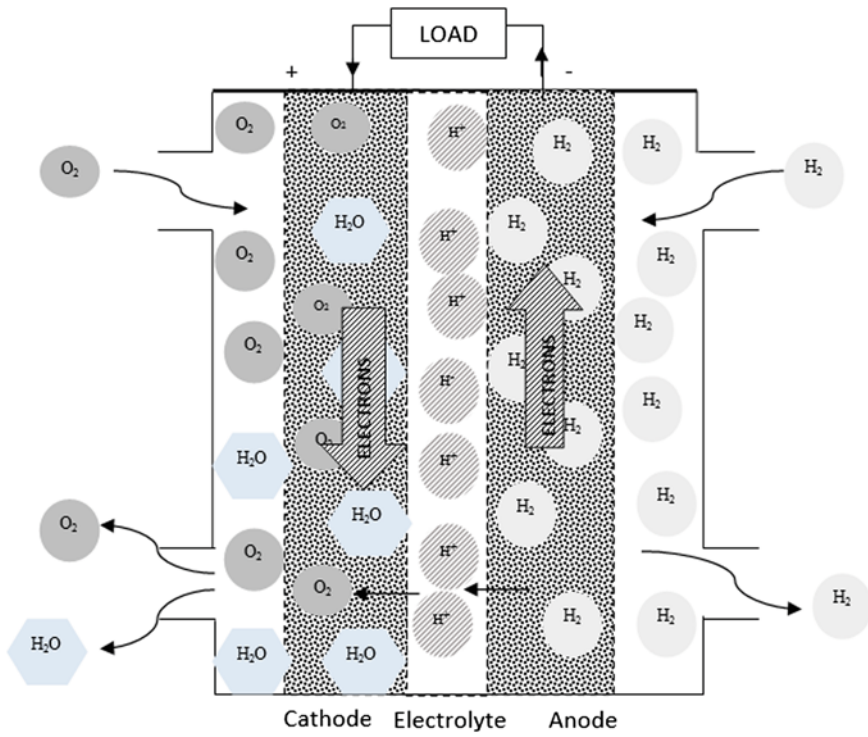


Fig. 1.20 Schematic representation of a H₂-O₂ fuel cell, from [59]

formed during this reaction of 2H⁺ ions and one O²⁻ ion is defined by the Gibbs free energy, shown in Eq. (1.39).

$$\Delta G = -nF\Delta U_0 \tag{1.39}$$

where

- ΔG Gibbs free energy (kJ/mol)
- n Number of electrons released during the chemical reaction
- F Faraday's constant (96,485.33 C/mol)
- ΔU_0 Voltage of the cell to sustain thermodynamic equilibrium when there is no current flow through the cell (V = J/C).

The Gibbs free energy change for the H₂O chemical reaction is -237 kJ/mol, and it indicates the amount of energy per mol of H₂ that will be converted to electricity, which is used to supply a load connected to the cell. The theoretical output voltage of a fuel cell is calculated to be approximately 1.2 V; however, in reality, it can only be achieved during open-circuit conditions. This effect is called as polarization and is represented by the electrical characteristic curve also called as the static polarization curve as shown in Fig. 1.21. The y-axis represents the cell

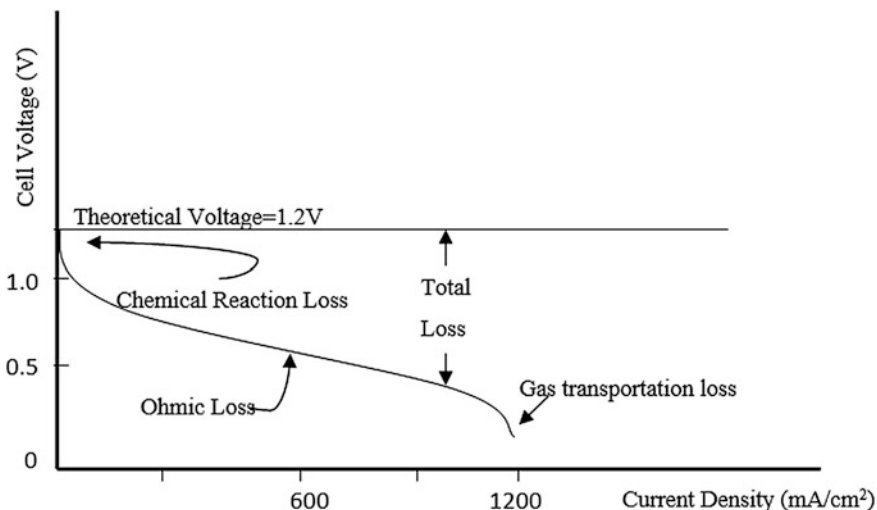


Fig. 1.21 Polarization curve of a fuel cell [58]

voltage in V, and the x -axis represents the current density in mA/cm^2 . The polarization is caused due to chemical and physical losses occurring to a fuel cell. Fuel cells work best when it only undergoes ohmic losses. It can be observed that the cell voltage drops with increase in current density.

1.6.2 Types of Fuel Cells

The H_2 - O_2 fuel cell is an example of a simple and basic fuel cell. There are various other types of fuel cells [60] that differ from each other based on their characteristics, fuel type and electrolyte used and are summarized in Tables 1.5 and 1.6.

The solid polymer membrane of a PEM fuel cell allows the smooth conduction of protons. The electrodes are saturated with platinum, which acts as a catalyst to increase the speed of chemical reactions, but without interfering with the reactants or by-products. H_2 acts as the fuel, which releases electrons during oxidization at the anode. The overall reaction releases water as the by-product. This fast-acting fuel cell is used commonly in electric vehicles, as its power output can be changed quickly. In some cases, hydrocarbons may be present in the fuel mix, in which case CO may be formed as a by-product before reacting with H_2O to form H_2 and CO_2 . The presence of CO must be managed as it can interfere with the working of platinum as catalysts. In direct methanol fuel cells, a type of PEM fuel cell, a polymer membrane is used as an electrolyte as well. However, as the name suggests, the fuel injected is methanol. They have low noise and can function in low temperatures, thus making it an effective candidate for consumer goods and military

Table 1.5 Characteristics of various fuel cells [58, 60, 61]

Parameters	Proton exchange membrane (PEM)	Direct methanol fuel cell	Phosphoric acid fuel cell
Electrolyte	Solid polymer membrane (Nafion)	Solid polymer membrane (Nafion)	Liquid phosphoric acid (H ₃ PO ₄) in silicon carbide
Fuel	Pure H ₂ (allows CO ₂)	Methanol in water solution	Pure H ₂ (allows CO ₂ and 1% CO)
Catalyst	Platinum	Platinum	Carbon-supported platinum
Operating temperatures (°C)	60–80	Up to 110	160–220
Electrical efficiency (%)	40–60	≤ 40	36–42
Principle chemical reaction	H ₂ + 1/2O ₂ → H ₂ O	CH ₃ OH + 3/2O ₂ → 2H ₂ O + CO ₂	2H ₂ + O ₂ → 2H ₂ O

Table 1.6 Characteristics of various fuel cells [58, 60, 61]

Parameters	Solid oxide fuel cell	Alkaline fuel cell	Molten carbonate fuel cell
Electrolyte	Solid ceramic or metal oxide	Potassium hydroxide in water solution	Alkali carbonates
Fuel	H ₂ and other hydrocarbons (allows CO ₂)	Pure H ₂	H ₂ and other hydrocarbons (allows CO ₂)
Catalyst	Non-platinum group catalysts	Non-precious metal crystals	Non-platinum group catalysts
Operating temperatures (°C)	800–1000	Up to 230	600–700
Electrical efficiency (%)	50–60	60–70	50–60
Principle chemical reaction	H ₂ + 1/2O ₂ → H ₂ O	H ₂ + 1/2O ₂ → H ₂ O	H ₂ + 1/2O ₂ + CO ₂ → H ₂ O + CO ₂

applications. The alkaline fuel cell is one of the oldest types of fuel cells and was used for spacecraft applications. However, they are easily affected by the presence of any CO₂ and hence best suited for applications in a controlled environment.

Phosphoric acid fuel cells operate at higher temperatures compared to PEM fuel cells, as high temperatures are necessary for the efficient working of phosphoric acid as a conductive electrolyte. The fuel used is ideally pure H₂, but due to its high operating temperatures, it is more tolerant of other substances such as hydrocarbons which can release CO and CO₂. Since large amounts of heat will be generated, this type of fuel cells can be used to heat water and spaces and hence commonly used

for high-energy applications. Solid oxide fuel cells and molten carbonate fuel cells work at an even higher operating temperature and are best suited for large stationary power applications. Both these types of fuel cells generate a lot of heat, which can then be diverted and used for heating purposes, thus enabling cogeneration. They can also use a mix of H_2 and hydrocarbons as the fuel mix; however, any presence of sulphur (greater than 0.1 ppmV) as a by-product must be eliminated. They differ from each other based on the materials used for the electrolyte, anode and cathode.

MCFC uses a mixture of alkali carbonates as the electrolyte, and these are contained in a matrix made of ceramic. The anode and cathode are made of nickel and nickel oxide, respectively. As the name suggests, SOFC uses a solid non-porous oxide as the electrolyte. This is usually a metal oxide such as zirconium dioxide. The anode is porous and made of a ceramide material such as yttria-stabilized zirconia, while the cathode is usually made of lanthanum strontium manganite [60].

1.6.3 Applications

Current research works on fuel cells indicate the scope for a new variety called microbial fuel cells that are organic in nature. They use any organic matter as the fuel and allow microbes to consume it. Electric energy is generated as a by-product of the digestive process. These cells are miniature in size and can be used effectively for medical applications. There are other types of fuel cells such as zinc air and regenerative fuel cells as well. The former generates electricity through the combination of zinc with air and an alkaline electrolyte in the presence of non-noble metal oxide as a catalyst, while the latter is a fuel cell that uses the regenerative process of electrolysis wherein H_2O by-product is made to undergo electrolysis to generate H_2 and thus maintain a continuous supply of fuel.

The storage of the essential fuel H_2 is implemented by extracting it from alcohols such as methanol, hydrocarbons such as methane and other compounds such as ammonia [59]. These carrier compounds are easier to transport, are readily available, and have many applications in existing, deep-rooted technologies. A schematic diagram explaining two common methods of extraction of H_2 from these carrier compounds is shown in Fig. 1.22. There are other forms of extracting H_2 too, such as autothermal reforming and membrane reactors (applicable to both alcohols and hydrocarbons), and propane cracking and gasification of coal (applicable for hydrocarbons).

A complete fuel cell system consists of a fuel extractor which supplies H_2 to the fuel cell, which in turn supplies DC power which goes through a power-conditioning unit before being used for AC load applications. The excess heat generated is sent to a heat and power recovery system for cogeneration. SOFC and MCFC types of fuel cells are observed to be best for large stationary power applications due to the high efficiency, scope for cogeneration and lack of reforming of the fuel. For medium and small stationary power plants, PEM fuel cells and

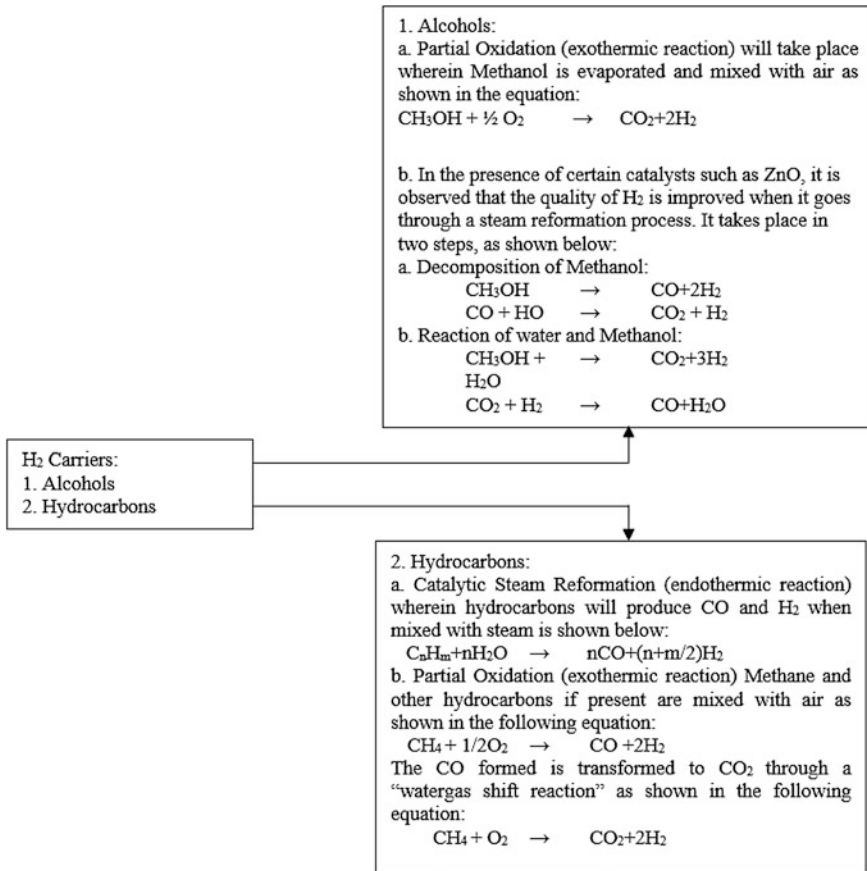


Fig. 1.22 Extraction of H₂ from alcohols and hydrocarbons [59]

direct methanol fuel cells are an excellent option due to their high energy and compact size. PEM can be used for cogeneration applications, albeit to supply low residential loads. A block diagram representing a basic stationary fuel cell system connected to the grid is shown in Fig. 1.23.

The fuel passes through a processor where the carrier compounds are processed to extract pure H₂ gas, which is then supplied to the fuel cell. For large-scale applications, fuel cells are designed to generate a power output from 300 kW to 20 MW, for medium-scale applications, it generates a power output from 10 to 300 kW, and for small-scale applications, it generates a power output up to 10 kW. The power output from a fuel cell is DC in nature and hence goes through several processes to convert it into good-quality AC supply. The DC booster will boost the output voltage of the fuel cell, and the DC-DC controller (two-loop current-controlled mode) will help to maintain the output voltage at a constant level. The voltage source inverter (VSI) will convert this DC voltage to AC voltage

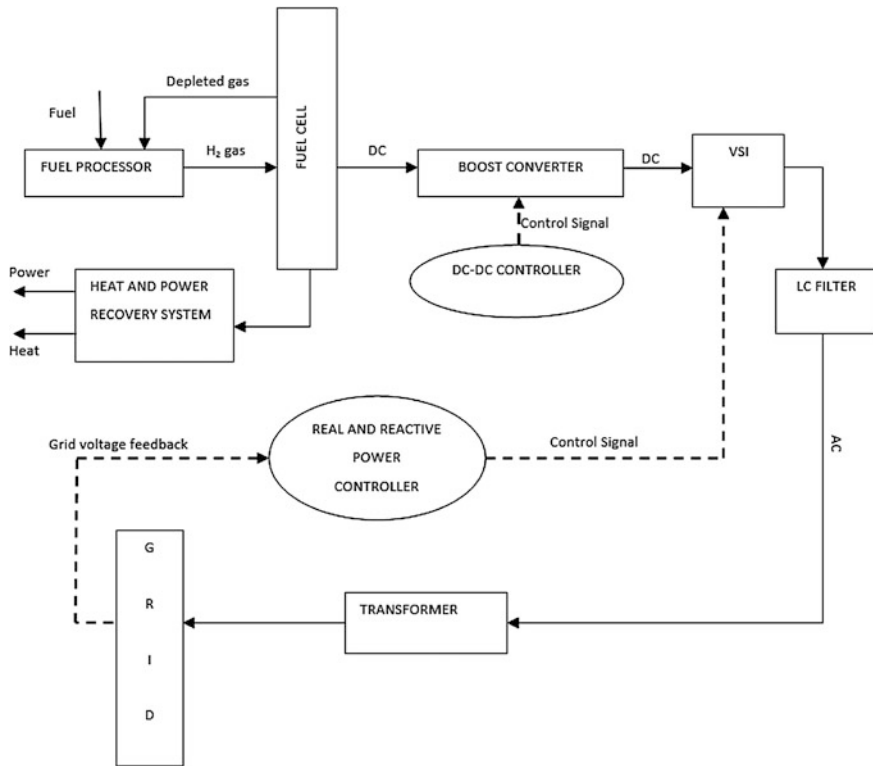


Fig. 1.23 Block diagram of a grid-connected fuel cell system for distributed generation [58, 62]

and is passed through an LC filter for reducing harmonics and maintaining the frequency. The AC voltage is then supplied to the grid via a transformer, and a portion of this AC voltage can be given as a feedback to an active and reactive power controller which will maintain the quality of the electricity supplied to the grid [62, 63]. The components introduced between the fuel cell and the grid form the power-conditioning unit of a grid-connected fuel cell system.

While choosing a distributed generation technology, it is vital to consider whether it is dependable, cheap (especially for long-term use) and robust. Fuel cell technology has come a long way through the decades to prove that it is dependable and robust; however, the jury is still out on whether it is a cheap technology as the capital cost of a fuel cell is very high, due to high costs of the materials used to produce a good-quality fuel cell. Therefore, while fuel cells have a high efficiency, do not emit any pollutants, and can withstand many start-and-stop cycles, it is not a popular choice for distributed generation. The lack of data concerning the practical applications of a fuel cell contributes to the lack of research to mitigate high costs. Some studies indicate that high costs can be combated by large volumes of production, a strategy that seemed to have worked for photovoltaic technology.

Minimizing the cost of the materials used and hence minimizing the overall cost of the system can be considered as a potential topic for future research work. While doing so, it would be best to factor in the payback period of installing such a system so as to figure out the true cost of installing fuel cells for distributed generation by taking into account its future value. Fuel cells have found many applications as a good source of portable energy and for transportation such as electric vehicles; however, it still has a long way to go to become a cheap source of stationary power.

1.7 Geothermal Technology

There has been tremendous emphasis on the utilization of renewable energy resources due to detrimental effects of using fossil fuels for different applications. With the public awareness of using environment-friendly energy resources and government policies to harness geothermal resources, utilization of geothermal energy for direct use and production of electricity and heat pumps has increased significantly in the last three decades. The installed capacity of geothermal power plants has grown from 6832 MW in 1995 to 12,635 MW in 2015. The electrical energy from geothermal power plants also increased from 38,038 GWh in 1995 to 73,549 GWh in 2015 [64]. This shows that geothermal technologies have been embraced by the utilities and power regulatory agencies due to its environment-friendliness, reliability, high efficiency, low maintenance, low operating costs, economic benefits and non-reliance on the weather conditions. The estimated potential of the geothermal resources for power generation is 210 GW [65]. This tremendous hidden resource is 50,000 times the energy of fossil fuel resources in the world [66]. Geothermal plays a significant role in countries where geothermal resources are being utilized. However, only 6% of the geothermal resource has been utilized for different applications using the current technologies.

Geothermal energy is the heat from a few metres beneath the earth's surface due to the radiogenic isotopes of uranium, potassium and thorium. Geothermal energy is used for electrical power generation, space heating, greenhouse applications, industrial applications, combined heat and power cogeneration applications and heat pump applications. It is a clean and sustainable energy resource when compared with the conventional sources of power generation as it contributes to the reduction of greenhouse gas (GHG) emissions and fossil fuel costs. The installed capacity of geothermal power plant stands at 12.6 GW with annual electricity generation of 73,549 GWh in 2015. The total electrical energy from geothermal energy represents 0.3% of the global electrical energy. The global investment in the geothermal technologies in 2015 was estimated to be about \$4 billion. This figure represents a 48% investment increase from the previous year. The statistical data show that the global installed capacity and electrical generation of geothermal have increased by 15.95 and 9.373%, respectively, since 2010. The cost of generating 1 kWh of electricity by using geothermal technologies is between 2 and 10 US cents/kWh.

A comparative analysis of the energy supply resources has shown that the total electricity power generation from different sources worldwide in 2014 was 4892 TWh. Of this total, 77.2% was from fossil fuels and nuclear, while 22.8% was from renewable energy resources. Out of the total electricity produced from the renewable resources in 2014, 16.6% came from geothermal and ocean, 3.1% from wind, 0.9% from solar and 16.6% from hydropower [64]. The cost of direct heat production from the geothermal energy is another added advantage for utilizing this resource at a commercial level. The cost of direct heat from biomass is 1–5 US cent/kWh, geothermal 0.5–5 US cent/kWh and solar heating 3–20 US cent/kWh. Geothermal energy utilization can make a substantial influence towards reducing global greenhouse gas emissions. Moreover, global energy has been projected to reach 20 GW by 2030 by a number of international organizations. To meet this global development target, the future energy requirements must be based on the economic growth and environmental protection. This can be achieved by harnessing geothermal energy based on its great potential when compared with other renewable resources.

1.7.1 Current Status of the Geothermal Potential in the World

According to the GEA statistics, over 160 geothermal power plants have been added across the globe since 2005. With this record, it shows that 4 GW has been added to the electricity grids worldwide. In addition to this milestone, 21 new power plants with a total installed capacity of 6400 MW were commissioned in 2014 and tied to the electricity grids in Turkey, Kenya, Indonesia, and the Philippines [67]. The present installed capacity of geothermal power plant across 24 countries in the world is presented in Table 1.7, while the top 12 countries with the largest amounts of geothermal electricity-generating capacity in the world are presented in Fig. 1.24. The global geothermal industry is expected to reach between 14.5 and 17.6 GW by 2020 based on the annual growth of 3.6% [68]. Only 6.5% of the total potential of the global geothermal energy has been used due to the technical and financial constraints. The World Bank has estimated that over 40 countries could meet their power demand from geothermal power resource if it is

Table 1.7 Total global installed capacity of geothermal energy from 1995 to 2020

Year	Installed capacity (MW)	Energy produced (GWh)
1995	6832	38,035
2000	7972	49,261
2005	8933	55,709
2010	10,897	67,246
2015	12,800	73,549
2020	21,443	84,767

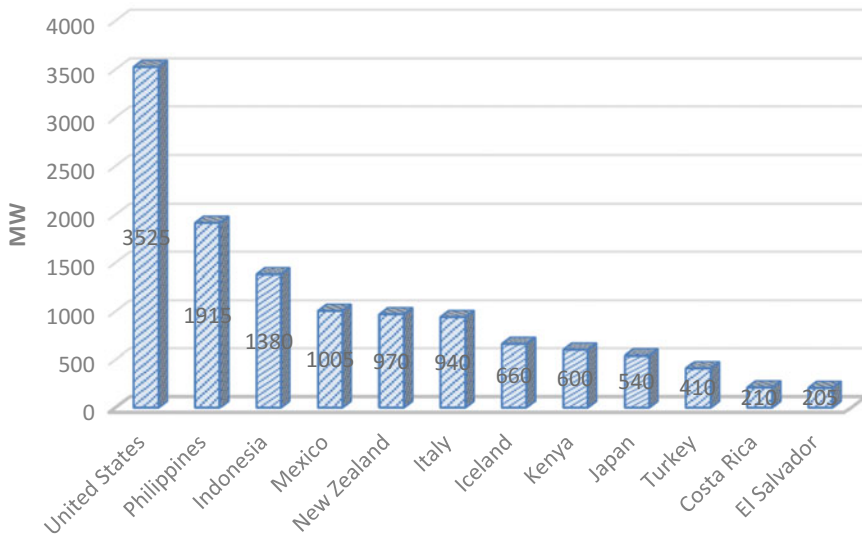


Fig. 1.24 Geothermal power installed capacity per country (MW)

properly harnessed. To achieve this landmark, the World Bank has deployed over \$235 million towards investment in geothermal energy globally. The total installed capacity of geothermal power plants for some countries is shown to have increased in 2014. Turkey increased its capacity by 107 MW, Kenya increased its capacity by 358 MW, Indonesia improved its geothermal power capacity by about 5%, and the Philippines raised its geothermal capacity to 1.9 GW by adding 49.9 MW, while the USA and Japan also added a 2 MW to the existing geothermal capacity of their countries [64, 69, 70].

1.7.2 The Technical, Economic and Environmental Benefits of Geothermal Energy

Geothermal energy has been harnessed for over a century, mostly for power and direct-use applications. The economic, technical and environmental benefits of using geothermal energy for several applications are presented in Table 1.8.

Table 1.8 Technical, economic and benefits of geothermal energy [70–73]

Technical benefits			Economic benefits	Environmental benefits
Reliability improvement	Security enhancement	Operational advantages	1. Reduced O & M costs	1. Environmentally friendly
1. Improved power system reliability	1. Enhanced security of the critical loads	1. Increased productivity	2. No fuel cost	2. Reduction in greenhouse gas emissions
2. Reduced capacity	2. No intermittent energy resources	2. Easy O & M	3. Low installation cost	3. Sustainable energy source
3. Improved generation diversity	3. Improved power utilities security	3. Improved total efficiency	4. Job creation	
	4. Long lifespan	4. Small size of land	5. Moderate capital costs	
		5. Simple operation	6. Reduced ancillary costs	

1.7.3 Comparison of Geothermal Energy with Other Renewable Energy Resources

Renewable energy resources including geothermal resources have great potential for power generation and other applications. Some key performance indicators (KPIs) are used in Table 1.9 to compare geothermal, solar, wind and small/mini/micro hydro power generation systems, while the advantages and disadvantages of geothermal energy are presented in Table 1.10.

1.7.4 Geothermal Technology Applications

Geothermal power plants make use of the geothermal resources from the interior part of the earth to produce steam for power generation and hot water for direct-use applications. Unlike the conventional power plants whose operations are based on the fossil fuels such as coal, oil, oil shale, bitumen, natural gas and peat, geothermal plants utilize renewable energy resources. This natural heat from the molten magma heats up the water accumulated in the geothermal reservoir until it becomes a superheated fluid. Production wells are drilled to bring the superheated fluid to the earth’s surface where it will be used for a number of applications. The superheated fluid is turned to steam with the aid of a crystallizer reactor clarifier technology, which also removes many solid wastes from the superheated fluid. The steam can be used to spin the turbine blades for power generation. After the steam has been utilized for power generation, the steam will pass through a condenser that will turn it back to a fluid. The minerals in the fluid will be recovered before being injected

Table 1.9 Comparison of geothermal with solar and wind power generation systems [74–77]

Renewable DG technologies				
DG technologies	Geothermal	PV	Wind	Small/mini/micro hydro
Capacity range	>30 kW	1–20 kW	0.2–3 MW	Small: 100 kW–100 MW, Micro: 25 kW–1 MW
Efficiency (%)	10–17	8–35	35–45	60–90
Fuel	Nil	Sun	Wind	Water
CO ₂ emission, (g/kWh)	120	No direct emission	No direct emission	Small: 10–12 Micro: 16–20
SO ₂ emission, (g/kWh)	0.0031	No direct emission	No direct emission	Small: 0.024–0.029 Micro: 0.038–0.046
NO _x emission, (g/kWh)	0.01	No direct emission	No direct emission	Small: 0.046–0.056 Micro: 0.071–0.086
Installed capacity (GW)	12.635	177	370	1055
Energy production (TWh)	73.549	0.5	18	–
Installation cost/kW, (US\$/kW)	800–3000	1550–3830	900–1400	30–250
Energy cost (US cent/kWh)	2–10	25–125	5–13	2–10
Capital factor (%)	45–90	8–20	20–30	20–70
O & M cost (US\$/MWh)	10–30	1–4	10	0.045–0.09
Payback period (year)	5.7	1–2.7	0.4–1.4	11.8 (small) 0.5 (large)

Table 1.10 Advantages and disadvantages of geothermal energy [78–85]

Advantages	Disadvantages
<ul style="list-style-type: none"> ✓ Reliable ✓ Long-term resource potential ✓ Low emissions ✓ Low operating and maintenance costs ✓ Longer lifespans ✓ High availability ✓ Cost-effective and significant cost saving ✓ Modularity and diversity of use ✓ Reduced dependency on fossil fuels ✓ Does not occupy much space compared with oil and gas production ✓ Medium-to-high efficiency ✓ Not dependent on weather conditions ✓ No waste products ✓ High capacity factor 	<ul style="list-style-type: none"> ✓ Naturally occurring vents are not widely available and suitable in particular area ✓ Disturbance to animals and humans ✓ High installation costs ✓ Vegetation loss ✓ Low number of experts due to non-widespread of geothermal energy resources ✓ Impaired hearing ✓ Soil erosion and degradation ✓ Impact on watershed ✓ The total generation potential of geothermal energy is too small ✓ There is always a danger of eruption of volcano ✓ Long payback time ✓ Long construction time

back into the geothermal reservoir where it is reheated and send back to the earth's surface through a production well. The efficiency of geothermal technology for power generation is between 10 and 17% which is lower than the efficiencies of conventional power plants. Diesel-reciprocating engines have efficiencies of 36–43%, gas-reciprocating engines 28–42%, gas turbines 21–40% and micro turbines 25–30%. The lowest efficiency values of geothermal power plants when compared with the conventional power plants are due to the low temperature of the steam (200 °C).

The main applications of geothermal energy such as power generation, direct use and heat pumps depend on the temperature of the geothermal fluid and steam. The main temperature categories are as follows: high-temperature geothermal resources (200–350 °C), low-to-medium temperature geothermal resources (below 200 °C) and ground heat (10–20 °C). Geothermal energy plays significant roles in the countries where this natural resource is fully utilized. For example, over 15% of electricity comes from geothermal power plants in EL Salvador, 50% in Iceland, 21% in the Philippines, 6% in Kenya, 6% in Costa Rica and 15% in Nicaragua. This is also applicable to direct-use application of geothermal energy where China (6100 MWh), Turkey (2800 MWh), Japan (2100 MWh), Iceland (2000 MWh), India (1000 MWh), Hungary (900 MWh), Italy (800 MWh), and the USA (600 MWh) are leading the whole world with 80% of global capacity [64].

1.7.5 Direct-Use Applications

The direct use of geothermal energy involves using hot water from geothermal resources directly for heating of buildings, cooling, industrial processes, bathing, pasteurizing milk, washing, fish farms, microbreweries, fruit and vegetable drying, pulp and paper processing, lumber drying, greenhouses, aquaculture and other applications. The most common applications are domestic and industrial applications as well as power generation. Direct application of geothermal involves low- and high-temperature geothermal resources. The present installed capacity for geothermal energy in the world is 73,549 MW with direct-use energy of 53 TWh/a.

1.7.6 Heat Pumps

Geothermal heat pumps are efficient renewable energy technologies that utilized the properties of the geothermal energy beneath the earth's surface for the production of heat source in winter and a cooling source in summer. Geothermal heat pumps can support the domestic and industrial space-heating and cooling needs. In summer, water that has absorbed heat from a building is cooled as it circulates through a closed-loop system that contains an evaporator and a condenser. The cooled water is sent back into the building to absorb more heat and continue to cool the building.

The system is reversible in the winter where the cold water that is circulating within a building is heated by the earth and delivers warmth back to the building. The system is more efficient than using fossil fuel-based electricity to produce heat. The capital and installation costs of geothermal heat pumps are higher than those of conventional heating and cooling systems. This shortcoming can be compensated by using high-efficiency geothermal pumps. The rate of installation of these is estimated to be between 10,000 and 40,000 per year.

1.7.7 Geothermal Electricity Production

The geothermal power plant generates electrical energy by using the steam produced in geothermal reservoirs found beneath the earth's surface. Unlike fossil-based conventional steam power plants that use natural gas, coal or crude oil for power generation applications, geothermal power plants use the steam from the earth's surface to spin the turbine blades. The generated electricity as mentioned earlier is used for residential, industrial, commercial, government, institutional and agricultural applications. There are three geothermal power plant technologies that can convert geothermal steam from the geothermal reservoirs to electricity, i.e. dry steam, flash steam and binary cycle. This conversion depends on the temperature of the fluids and their states, i.e. steam and water. The total installed capacity of various geothermal power plant types is as follows: dry steam power plant (37%), flash steam power plant (59%) and binary cycle power plants (4%).

1.7.8 Direct Dry Steam

The direct dry steam power plant being the cheapest and simplest technology allows a continuous circulation of steam between the production and discharge wells. The dry steam power plant is used to generate power and has got pipes that carry steam directly from a geothermal reservoir through a production well to the earth surface where it can be utilized. Working steam leaves the geothermal reservoir through a production well and rejected back through a discharge well. It utilizes steam of high temperature to spin the turbine blades. The turbine turns a shaft that is coupled directly to an electrical generator. This activates the generator to produce electricity, and the condensed water from the condenser is injected back into the geothermal reservoir through the injection well. The steam eliminates the need for additional boilers and fossil fuels to run the turbine. These plants release little amounts of greenhouse gas emissions into the atmosphere. Dry steam power plants also eliminate the need for transportation and fuel storage facilities at the power plant. The mode of operation of direct dry steam power plant is presented in Fig. 1.25.

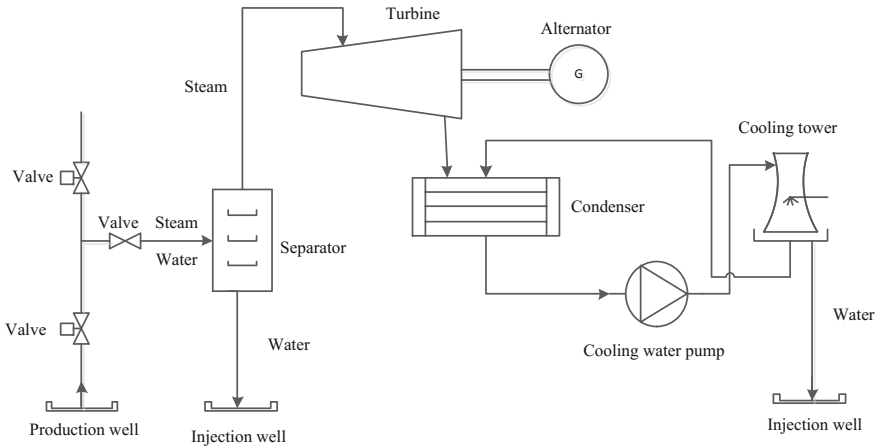


Fig. 1.25 Dry steam power plant [86]

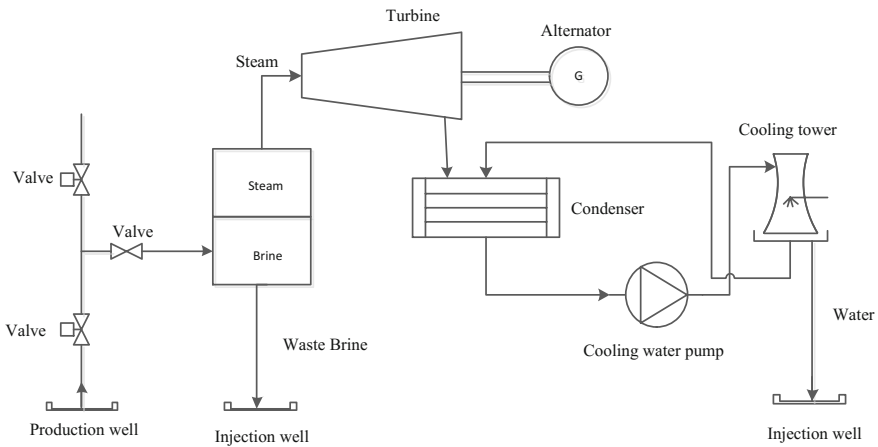


Fig. 1.26 Flash steam power plants [86]

1.7.9 Flash Steam Power Plants

Flash steam power plants are the most popular among the three types of geothermal power plants. Flash steam power plants use geothermal reservoir of water with high-temperature temperatures for their operations as shown in Fig. 1.26. The hot water flows through the production wells from the geothermal reservoir under its own pressure, and this pressure decreases when it reaches the earth surface causing a small portion of the fluid to flash into steam. The mixture of steam and super-heated fluid flows into a wet head separator where the steam is separated from the

water. The steam can then be used to spin the blades of turbine and generate electricity. If there is any geothermal fluid that is not flashed in the wellhead separator vessel, it can be flashed again in a second vessel called a standard pressure crystallizer to extract more energy. The fluid that is not flashed into the steam and the condensed water from the condenser are injected back into the geothermal reservoirs through injection well for reuse.

1.7.10 Binary Cycle Power Plants

The mode of operation of binary cycle geothermal power plants is different from the dry steam and flash steam power plants in the sense that the steam from the geothermal reservoir does not have a direct contact with the turbine units. The fluid extracted from the geothermal reservoir flows from the production well and pipelines to the heat exchanger. The heated geothermal fluid and a secondary fluid that has a lower boiling point pass through the heat exchanger where the secondary fluid is vaporized or flashed to steam. The steam is then used to spin the turbine blades as shown in Fig. 1.27. The condensed fluid from the system is recycled back into the heat exchanger where it is flashed to steam for further operation of the turbine. The cooled geothermal fluid will be re-injected into the geothermal reservoir for further reuse after passing through a cooling process. Based on the closed-loop configuration of the binary cycle power plant, there is no emission of greenhouse gas pollutants into the atmosphere except water vapour and some concentrated solid wastes. Nevertheless, binary power plant is the most cost-effective technology to convert low-temperature geothermal resources into electricity.

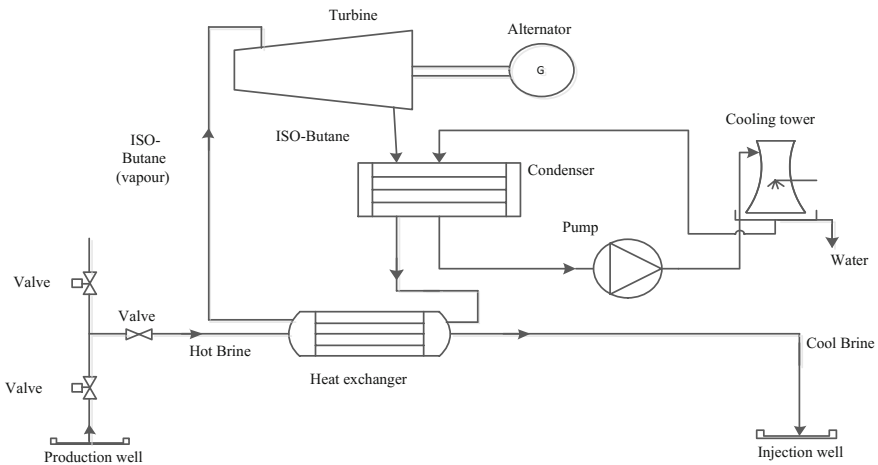


Fig. 1.27 Binary cycle power plants [86]

1.7.11 Levels of Emission from Different Types of Geothermal Energy Power Plants

Geothermal energy like other renewable energy sources is environment-friendly and is one of the renewable energy resources that emits small amount of greenhouse gases depending on the geological conditions of the geothermal resources and fields. Geothermal power plants use scrubber systems to remove the traces of greenhouse gas emissions from geothermal steam and hot water before they are injected back into the drill holes. The pollutants from the geothermal technology are not released into the atmosphere. However, the amount of CO₂ emissions from geothermal power plants is in the range of 13–130 g/kWh, whereas the CO₂ emissions from the conventional power plants are 1042 g/kWh for coal, 906 g/kWh for oil and 453 g/kWh. The amount of SO₂ emissions from the geothermal power is equivalent to 3% of the coal-fired electric power plants. Geothermal power plants do not emit nitrogen oxide, and this is contrary to fossil fuel-based conventional power plants that produce a large amount of these harmful pollutants. The reduction of greenhouse gas emissions has improved the position of some countries that utilize large percentages of geothermal technology for power generation in the global map with respect to atmospheric pollution. In addition to this, the waste products from the geothermal power plants can be converted to liquid fertilizer at a commercial level. The estimated emission levels for different types of geothermal plants are presented in Table 1.11.

1.7.12 Challenges of Geothermal Technologies

Geothermal power is lagging behind other renewable sources and conventional power plants in terms of installed capacity and annual growth rate due to high capital cost, long payback period, long construction duration, difficulty to access resource and difficulty to modularize. Non-availability of skilled manpower that can handle operation and maintenance of geothermal power plants across the world pose a serious challenge to adoption of geothermal energy. In addition to this, many incentives from financial institutions and government agencies for development of

Table 1.11 Estimated emission levels for various geothermal energy power plants [33, 87]

Emissions (lbs/MWh)	Dry steam	Flash	Binary
CO ₂	59.82	396.3	–
CH ₄	0.000	0.000	–
PM _{2.5}	–	–	–
PM ₁₀	–	–	–
SO ₂	0.0002	0.35	–
N ₂ O	0.000	0.000	–

geothermal energy technology have reduced recently. Also, the investment in geothermal energy resources has been discouraged by many organizations.

Therefore, geothermal energy can be described as sustainable energy that has more technical, economic and environmental benefits than the conventional energy resources. These benefits have increased the interest of the public to harness the heat energy for power generation, direct use and geothermal heat pumps. Geothermal energy has commercial advantage over conventional power plant due to price fluctuation of crude oil and constant power output when compared to variable renewable energy resources such as solar and wind. In view of many benefits and applications of geothermal energy and relevant policies, geothermal energy can play a significant role in the energy supply systems of many countries.

1.8 Ocean Thermal Energy Conversion

Ocean thermal energy conversion (OTEC) is an energy technology which utilizes the natural temperature gradient of the ocean to drive a turbine, which is linked to a generator. The idea was conceived in 1881, but the development delayed due to high initial capital cost associated with this technology until the early 1970s with the energy shortages of that period as the main driver. Many academic institutions and oceanic industries have been and are still carrying out research that has advanced this technology over the years [88]. Large ocean surfaces act as a solar energy reservoir which can be described as having a vertical temperature distribution composed of two major layers separated by an interface or thermocline. The top water surface layer is heated by the sun and is mixed by wave motion to depths of about 100 m, and the bottom layer is made up of deep colder water formed at higher latitudes resulting in an interface with a temperature range of 10–25 °C, with higher values being found in equatorial waters [89]. This creates two large reservoirs that can act as a heat source (warm top layer) and heat sink (bottom cold layer) required for a heat engine or turbine to convert mechanical or thermal energy into electrical energy. OTEC therefore generates electricity indirectly from solar energy as a result of the differences in temperature between the surface and thousand metre depth ranging between 10 and 253 °C. Larger temperature differences are found in equatorial and tropical waters.

Equatorial waters lie between 10°N and 10°S with the exception of areas around the west coast of South America, and also considerable enhancements of seasonal temperatures (e.g. with solar ponds) would be necessary for areas around the west coast of southern Africa. Deep-water temperatures along the east coast of Africa are warmer by about 2 °C. Tropical waters, on the other hand, extend from the equatorial region between 20°N and 20°S, with the exception of the west coasts of Southern Africa and South America. Considerable temperature enhancements are essential in the regions around the west coast of Northern Africa, Horn of Africa and off the Arabian Peninsula [89]. The best, land-based OTEC sites include island locations. The potential advantages of OTEC could only be achieved on a large

scale by developing floating plants, and a lot of research and experimentation are on-going. Tropical and subtropical island locations could benefit from OTEC technology and reduce independency on conventional fuels for the electricity production and for water desalination. OTEC thus finds markets in smaller or less industrialized islands, and industrialized nations and islands for energy production and water desalination.

1.8.1 Technology Types

The three main types of OTEC systems are the closed cycle, open cycle and hybrid cycle. The closed-cycle system utilizes a working fluid (e.g. ammonia) that is pumped around a closed loop composed of a pump, turbine and heat exchanger (evaporator and condenser). The warm sea water goes through the evaporator and converts the ammonia liquid into high-pressure ammonia vapour which is then fed into an expander where it goes through and turns a turbine that is connected to a generator. The low-pressure ammonia vapour coming from the turbine goes through a condenser, where it is cooled by the cold sea water back to liquid state. The open-cycle system consists of the same basic components and is almost similar to the closed-cycle system. It uses warm sea water as the working fluid, and this is converted into steam as it goes through the evaporator and the steam then drives the generator/turbine. The steam leaving the turbine is then cooled by the cold sea water to form desalinated water which can be used for both industrial and domestic purposes. The hybrid system, as the name implies, combines parts of both open-cycle and closed-cycle systems to generate electricity and desalinated water. Electricity is generated in the closed-cycle system, and the warm and cold sea water discharges go through the flash evaporator and condenser of the open-cycle system to produce freshwater. The operating principles of closed and open systems are shown in the simplified diagrams in Figs. 1.28 and 1.29, respectively.

The operation principles of these systems are based on thermodynamics principles, for instance, the basic relationship is given by:

$$\frac{PV}{T} = \text{constant}, \quad (1.40)$$

where P is the pressure, T the temperature and V the volume of a fluid. The relationship can be controlled by the manipulation of the other two variables. The difference in temperature of the fluid can be used to create an increase in pressure in another thereby generating mechanical energy. When considering a system that has an open-cycle heat engine and its environment, the Rankine cycle applies as the cycle is closed and cycle yields obtained are given by:

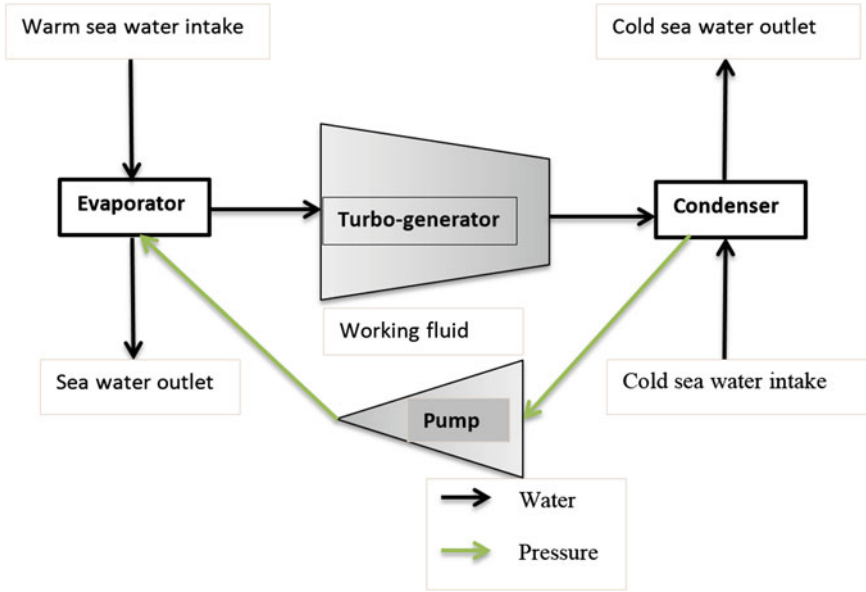


Fig. 1.28 Closed-cycle system

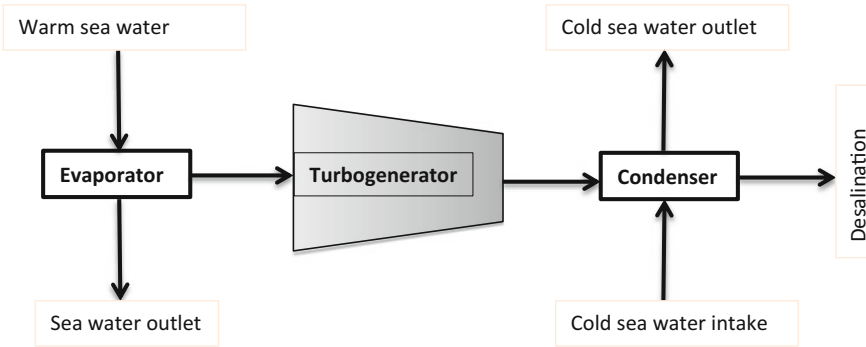


Fig. 1.29 Open-cycle system

$$\text{Heat absorbed from water [J/s], } Q_{wF} = \dot{m}_F C_p (T_{F1} - T_{F2}) \quad (1.41)$$

$$\text{Steam generation rate [kg/s], } \dot{m}_S = \frac{Q_w}{H_e} \quad (1.42)$$

$$\text{Work done by turbine [J/s], } W_T = \dot{m}_S \eta_T (h_3 - h_{5S}) \quad (1.43)$$

$$\text{Heat rejected into water [J/s]}, \quad Q_{\text{wC}} = \dot{m}_{\text{C}} C_{\text{p}} (T_{\text{C2}} - T_{\text{C1}}) \quad (1.44)$$

where the mass flow rate of warm water is represented by \dot{m}_{F} and the specific heat by C_{p} , while T_{F1} and T_{F2} , T_{C1} and T_{C2} are the sea water temperatures at the inlet and outlet of the heat exchanger (warm and cold sea water), respectively. H_{e} is the latent heat of evaporation, and h_3 and h_5 are the enthalpies at the indicated points with the subscript s referring to constant entropy, while η_{T} stands for the turbine isentropic efficiency. For the closed cycle that uses anhydrous ammonia as the working fluid, the saturated Rankine cycle is employed, based on a unit mass flow rate of ammonia vapour in the saturated cycle.

1.8.2 Advantages and Disadvantages of OTEC

OTEC systems have the potential to produce freshwater and electricity for island regions where freshwater availability is limited. Floating OTEC plants can generate power even at mid sea and can be used to provide power for offshore mining and processing of manganese nodules. The technology utilizes renewable, clean, natural resources; therefore, fossil-based fuels are replaced by warm surface sea water and cold water from deep sea in the production of electricity. Tropical and subtropical islands thus could be made free from fossil fuel pollution since OTEC plants unlike fossil fuel plants do not pollute the environment by releasing carbon dioxide emissions or other polluting substances. OTEC also helps reduce the country's dependence on imported fossil fuels. Unlike other forms of renewable energy such as wind and solar energy, the output of OTEC is continuous, showing very little daily or seasonal variation. It could be used to produce hydrogen and hence contribute to the hydrogen economy. It has the potential to help enrich fishing grounds owing to the nutrients extracted from the unproductive deep waters to the warmer surface waters.

The technology also has some disadvantages which include high capital investment coupled with maintenance cost making them uneconomical for small plants and is currently more costly than fossil fuels in electricity production. It is also argued that construction of OTEC plants and pipes in oceans may be harmful to onshore marine ecosystems and reefs. Discharging of cold and warm sea water needs to be carried out several metres away from the shore to avoid any impact on marine ecosystems. The plants have low efficiency, conversion efficiency about 3–4% owing to small temperature differences between the surface water and deep water. Technology maturity is another issue as this technology has been tested only in small-scale applications.

1.9 Conclusion

Distributed energy technologies are becoming increasingly important in the global energy supply systems. This chapter captured various renewable technologies such as solar power, wind, geothermal, biomass, hydro power and ocean thermal energy conversion systems. A brief historical timelines of the development of renewable energy technologies are also discussed. The use of renewable energy resources has witnessed a rapid growth recently due to public concerns on the environmental impacts of using conventional plant for power generation. The integration of renewable energy resources into a conventional power system has many advantages such as environmental and socio-economic benefits for societies as well as contributing to the alleviation of energy poverty. Renewable energy source cannot be exhausted, and it is an environment-friendly power-generating source that reduces greenhouse gas emissions and mitigates global warming. Renewable energy technologies in conjunction with the electric storage systems can be used for baseload power, peaking power, backup power, remote power as well as cooling and heating applications. Renewable energy distributed generator has the potential to be used by the power utilities to mitigate congestion in transmission lines, reduce the impact of electricity price fluctuations, strengthen energy security and provide greater stability to the electricity grid. In this work, different renewable energy distributed generation technologies are discussed with their advantages and disadvantages as well as the current status, updates and utilization of renewable energy technologies in the world. The renewable energy technologies are also compared based on the technical, economic and environmental benefits.

References

1. Adams WG, Day RE (1876) The action of light on selenium. *Proc R Soc Lond* 25:113–117
2. Siemens W (1885) On the electromotive action of illuminated selenium, discovered by Mr. Fritts, of New York. *J Franklin Inst* 119(6):IN6–456
3. Ohl R (1946) Light-sensitive electric device. United States Patent Office, New York
4. Chapin DM, Fuller CS, Pearson GL (1954) A new silicon p-n junction photocell for converting solar radiation into electrical power. *J Appl Phys* 25:676–677
5. Candellise C, Winkler M, Gross RJK (2013) The dynamics of solar PV costs and prices as a challenge for technology forecasting. *Renew Sustain Energy Rev* 26:96–107
6. Nemet GF (2006) Beyond the learning curve: factors influencing cost reductions in photovoltaics. *Energy Policy* 34(17):3218–3232
7. Balkanski M, Wallis RF (2012) Electronic energy bands: semiconductors. In: *Semiconductor physics and applications*. Oxford University Press, Oxford, pp 44–72
8. Kalogirou SA (2014) *Solar energy engineering—processes and systems* (2nd edn), Elsevier, Amsterdam
9. Labouret A, Viloz M (2010) *Solar photovoltaic energy*. Institution of Engineering and Technology
10. Blazev AS (2012) Crystalline silicon photovoltaic technologies. In: *Photovoltaics for commercial and utilities power generation*. Fairmont Press, Inc., pp 27–90

11. Osterwald CR (2003) Testing, monitoring and calibration. In: Practical handbook of photovoltaics—fundamentals and applications. Elsevier, Amsterdam, pp 794–809
12. Khaligh A, Onar OC (2011) Energy sources. In: Power electronics handbook—devices, circuits and application. Elsevier, Amsterdam, pp 1289–1324
13. Appelbaum J, Bany J (1979) Shadow effect of adjacent solar collectors in large scale systems. *Sol Energy* 23:497–507
14. Florensa RS, Cueva RL (2003) Photovoltaic systems: case studies. In: Practical handbook of photovoltaics—fundamentals and applications. Elsevier, Amsterdam, pp 726–747
15. Anaya-Lara O, Jenkins N, Ekanayake J, Cartwright P, Hughes M (2011) Wind energy generation: modelling and control. Wiley, NY
16. Heier SWR (2006) Grid integration of wind energy conversion systems. Wiley, Chichester
17. Kayikçi M, Milanović J (2008) Assessing transient response of DFIG-based wind plants—the influence of model simplifications and parameters. *IEEE Trans Power Syst* 23(2):545–554
18. Chowdhury B, Chellapilla S (2006) Double-fed induction generator control for variable speed wind power generation. *Electr Power Syst Res* 76(9):786–800
19. Petersson A (2005) Analysis, modeling and control of doubly-fed induction generators for wind turbines
20. El-Helw H, Tennakoon S (2008) Evaluation of the suitability of a fixed speed wind turbine for large scale wind farms considering the new UK grid code. *Renew Energy* 33(1):1–12
21. Wei X, Qliu X, Xu J, Li X (2010) Reactive power optimization in smart grid with wind power generator. In: Power and energy engineering conference (APPEEC), Asia-Pacific, 28–31 March 2010
22. Li L, Zeng Xiang J, Zhang P (2008) Wind farms reactive power optimization using genetic/tabu hybrid algorithm. In: International conference on intelligent computation technology and automation (ICICTA)
23. Li L, Zeng X, Zhang P, Xia Y, Liu G (2008) Optimization of reactive power compensation in wind farms using sensitivity analysis and tabu algorithm. In: Industry Applications Society annual meeting (IAS'08)
24. Zhao J, Li X, Hao J, Zhang C, Lu J (2009) Wind farm reactive power output optimization for loss reduction and voltage profile improvements. In: IEEE 6th international power electronics and motion control conference, 2009, IPEMC'09
25. Konopinski R, Vijayan P, Ajarapu V (2009) Extended reactive capability of DFIG wind parks for enhanced system performance. *IEEE Trans Power Syst* 24(3):1346–1355
26. Vijayan P (2010) Utilizing reactive capability of doubly fed induction generators to enhance system voltage performance and withstand wind variability
27. Erlich I, Wilch M, Feltes C (2007) Reactive power generation by DFIG based wind farms with AC grid connection. In: IEEE European conference on power electronics and applications
28. Pappala V, Wilch M, Singh S, Erlich I (2007) Reactive power management in offshore wind farms by adaptive PSO. In: IEEE international conference on intelligent systems applications to power systems
29. El-Helw H, Tennakoon S (2008) Evaluation of the suitability of a fixed speed wind turbine for large scale wind farms considering the new UK grid code. *Renew Energy* 33(1):1–12
30. Engelhardt S, Erlich I, Feltes C, Kretschmann J, Shewarega F (2011) Reactive power capability of wind turbines based on doubly fed induction generators. *IEEE Trans Energy Convers* 26(1):364–372
31. Lai L, Chan T (2008) Distributed generation: induction and permanent magnet generators. Wiley, New York
32. Feijoo AE, Cidras J (2000) Modeling of wind farms in the load flow analysis. *IEEE Trans Power Syst* 15(1):110–115
33. Mihic S (2004) Biogas fuel for internal combustion engines. *Annals of the Faculty of Engineering Hunedoara, Tome II. Fascicule 3, 2004*
34. Al Seadi T (2008) Biogas handbook, Syddansk Universitet

35. Ni M, Leung D, Leung M, Sumathy K (2006) An overview of hydrogen production from biomass. *Fuel Process Technol* 87(5):461–472
36. Demirbaş A (2001) Biomass resource facilities and biomass conversion processing for fuels and chemicals. *Energy Convers Manag* 42(11):1357–1378
37. Balat H, Kirtay E (2010) Hydrogen from biomass—present scenario and future prospects. *Int J Hydrogen Energy* 35(14):7416–7426
38. Demirbaş A (2002) Hydrogen production from biomass by the gasification process. *Energy Sources* 24(1):59–68
39. Levin D, Pitt L, Love M (2004) Biohydrogen production: prospects and limitations to practical application. *Int J Hydrogen Energy* 29(2):173–185
40. Varfolomejeva R, Sauhats A, Umbrasko I, Broka Z (2015) Biogas power plant operation considering limited biofuel resources. In: 2015 IEEE 15th international conference on environment and electrical engineering
41. Wang J (2014) Decentralized biogas technology of anaerobic digestion and farm ecosystem: opportunities and challenges. *Front Energy Res* 2:10
42. Bond T, Templeton M (2011) History and future of domestic biogas plants in the developing world. *Energy Sustain Dev* 15(4):347–354
43. Wellinger A, Murphy J, Baxter D (2013) *The biogas handbook: science, production and applications*. Elsevier, Amsterdam
44. Gunaseelan V (1997) Anaerobic digestion of biomass for methane production: a review. *Biomass Bioenergy* 13(1):83–114
45. Holm-Nielsen J, Al Seadi T, Oleskowicz-Popiel P (2009) The future of anaerobic digestion and biogas utilization. *Bioresour Technol* 100(22):5478–5484
46. Monnet F (2003) An introduction to anaerobic digestion of organic wastes
47. Balussou D, Kleyböcker A, McKenna R, Möst D, Fichtner W (2012) An economic analysis of three operational co-digestion biogas plants in Germany. *Waste Biomass Valoriz* 3(1):23–41
48. GE Agency (2013) Renewable energy solutions for off-grid applications
49. “Niagara Falls info,” [Online]. Available: http://www.niagarafallsinfo.com/history-item.php?entry_id=1435¤t_category_id=242. Accessed 28 March 2016
50. vanVuuren SJ, vanDijk M, Loots I, Barta B, Scharfetter BG (2014) *Conduit hydropower development guide*. Water Research Commission, Pretoria
51. Mishra S, Singal SK, Khatod DK (2012) A review on electromechanical equipment applicable to small hydropower plants. *Int J Energy Res* 36(5):553–571
52. Ardizzon G, Cavazzini G, Pavesi G (2014) A new generation of small hydro and pumped-hydro power plants: advances and future challenges. *Renew Sustain Energy Rev* 31:746–761
53. Ferro LMC, Gato LMC, Falcao AFO (2011) Design of the rotor blades of a mini hydraulic bulb-turbine. *Renew Energy* 36(9):2395–2403
54. Grove WR (1838) On a new voltaic combination. *Philos Mag J* 13(84):430–431
55. Schoenbein CF (1839) On the voltaic polarisation of certain solid and fluid substances. *Philos Mag J* 14(85):43–45
56. Bills GW (1964) Voltage and current control for spacecraft fuel cell systems. *IEEE Trans Aerosp* 2(2):478–482
57. Barnett BM, Teagen WP (1992) The role of fuel cells in our energy future. *J Power Sources* 37:15–31
58. Huang X, Zhang Z, Jiang J (2006) Fuel cell technology for distributed generation: an overview. In: *IEEE international symposium on industrial electronics (Volume: 2)*, Montreal
59. Carette L, Friedrich K, Stimming U (2001) Fuel cells- fundamentals and applications. *Fuel Cells* 1(1):5–39
60. “National Fuel Cell Research Center,” U.S. Department of Energy and the California Energy Commission [Online]. Available: <http://www.nfrcr.uci.edu/3/TUTORIALS/EnergyTutorial/fuelcell.html>. Accessed 20 March 2016
61. “Fuel Cells 2000,” Breakthrough Technologies Institute [Online]. Available: http://www.fuelcells.org/base.cgim?template=types_of_fuel_cells. Accessed 20 March 2016

62. Tomal MU, Gabbar HA (2015) Key performance assessment of fuel cell based distributed energy generation system in resilient micro energy grid. In: IEEE international conference on smart energy grid engineering, Oshawa
63. Candusso D, Valero L, Walter A, Bacha S (2002) Modelling, control and simulation of a fuel cell based power supply system with energy management. In: IEEE annual conference of the Industrial Engineering Society, Sevilla
64. REN21, Renewables 2015 global status report, 2015
65. World Energy Resources (2013) Geothermal World Energy Council 2013
66. WER Survey (2013) World Energy Council for sustainable energy
67. IEA (2014) Growth in final energy consumption for years 2007 through 2012, Paris
68. Ürge-Vorsatz D, Cabeza L, Serrano S, Barreneche C, Petrichenko K (2015) Heating and cooling energy trends and drivers in buildings. *Renew Sustain Energy Rev* 41:85–98
69. Walwyn D, Brent A (2015) Renewable energy gathers steam in South Africa. *Renew Sustain Energy Rev* 41:390–401
70. Chowdhury AA, Agarwal SK, Koval D (2013) Reliability modelling of distributed generation in conventional distribution systems planning and analysis. *IEEE Trans Ind Appl* 39(5):1493–1501
71. Gil HA, Joos G (2008) Models for quantifying the economic benefits of distributed generation. *IEEE Trans Power Syst* 23(2):327–335
72. Barker P, De Mello R (2000) Determining the impact of distributed generation on power systems. I. Radial distribution systems. *IEEE Power Eng Soc Summer Meet* 3:1645–1656
73. Jenkins N, Ekanayake JB, Strbac G (2010) Distributed generation. *IET Renew Energy Ser* 1, 1:1–20
74. Hung DQ, Mithulananthan N (2011) Handbook of renewable energy technology: DG allocation in primary distribution systems considering loss reduction. World Scientific Publishers, pp 587–628
75. Strachan N, Farrell A (2006) Emissions from distributed vs. centralized generation: the importance of system performance. *Energy Policy* 34(17):2677–2689
76. Borbely A, Kreider J (2001) Distributed generation: the power paradigm for the new millennium. CRC press, Boca Raton
77. Narbel P, Hansen J, Lien J (2014) Energy technologies and economics. Springer, Berlin
78. Gupta H, Roy S (2007) Worldwide status of geothermal resource utilization. *Geotherm Energy*, 199–229
79. Kose R (2007) Geothermal energy potential for power generation in Turkey: a case study in Simav, Kutahya. *Renew Sustain Energy Rev* 11(3):497–511
80. Kömürçü M, Akpınar A (2009) Importance of geothermal energy and its environmental effects in Turkey. *Renew Energy* 34(6):1611–1615
81. Fridleifsson I (2003) Status of geothermal energy amongst the world's energy sources. *Geothermics* 32(4):379–388
82. Lund J, Freeston D, Boyd T (2005) Direct application of geothermal energy: 2005 worldwide review. *Geothermics* 34(6):691–727
83. Chamorro C, Mondéjar M, Ramos R, Segovia J, Martín M, Villamañán M (2012) World geothermal power production status: energy, environmental and economic study of high enthalpy technologies. *Energy* 42(1):10–18
84. Glassley W (2014) Geothermal energy: renewable energy and the environment. CRC Press, Florida
85. Lund J, Freeston D, Boyd T (2011) Direct utilization of geothermal energy 2010 worldwide review. *Geothermics* 40(3):159–180
86. Renewable energy sources: an overview geothermal energy [Online]. Available: <https://people.uwec.edu/piercech/210webs/renewable/geothermal.htm>. Accessed 8 April 2016
87. EIA, Climate Registry 2012, EIA 2013e, EPA 2009, EPA 2011, NRC 2010
88. Vega L (1995) Ocean thermal energy conversion, encyclopaedia of energy technology and the environment. Wiley, New York
89. Vega LA (2002/2003) Ocean thermal energy conversion primer. PICHTR Honolulu, HI Marine Technol Soc J 6(4):25–35

Chapter 2

Non-renewable Distributed Generation Technologies: A Review

**Temitope Adefarati, Numbi Bubele Papy, Miriam Thopil
and Henerica Tazvinga**

2.1 Introduction

Distributed generation (DG) is an integration of small-scale renewable and non-renewable technologies into a conventional distribution system for the purpose of supplying electrical power at or near the consumer' load points. The DG technologies include diesel reciprocating engines, gas reciprocating engine, gas turbine, wind turbine, photovoltaic system, fuel cell, micro hydro and mini hydro can provide a grid-connected and a stand-alone power solution. The integration of the DG units in a power system offers a lot of technical, economic and environmental benefits. This section will only capture the reciprocating engine which is one of the common DG technologies in the world. The reciprocating engines are highly flexible and suitable for several applications, among which are electric power generation, combined heat and power generation (CHP) and mechanical prime

T. Adefarati · M. Thopil
Department of Electrical/Electronic and Computer Engineering,
University of Pretoria, Pretoria, South Africa
e-mail: u14459109@tuks.co.za

M. Thopil
e-mail: MiriamThopil@tuks.co.za

N.B. Papy (✉)
Department of Electrical Engineering, Centre for the Development
of Green Technologies, Mangosuthu University of Technology,
P.O. Box 12363 Jacobs, Durban 4026, South Africa
e-mail: numbib@mut.ac.za

H. Tazvinga
Energy Centre, Council for Scientific and Industrial Research,
P.O. Box 395, Pretoria 0001, South Africa
e-mail: HTazvinga@csir.co.za

movers for many equipment and propulsion. The reciprocating technologies can operate as a stand-alone to meet the power demands of consumers in remote locations or grid-connected power system, where it can feed the surplus to the grid having met the power requirements of the local consumers [1]. The reciprocating engines have been universally accepted by the power utilities as one of the DG units that can be effectively utilized to increase the reliability of a power system because they can be built, commissioned and become operational faster than other conventional DG technologies owing to their modular sizes and cost-effectiveness. The available statistical data have established that over \$170 billion was invested on the reciprocating engines and other DG technologies in 2015. In the same year, around 142 GW of the DG technologies for power generation were installed globally. The DG capacity for power generation is projected to increase to 200 GW in 2020 with the installation of additional 58 GW. This represents an annual growth rate of 4.4%. The total investment in the DG technologies is also expected to increase from \$170 to \$206 in 2020 while the global electricity consumption will also increase from 20.8 to 26.9 TWh with an annual growth rate of 3.3% [2]. This target can only be met by encouraging utilization of the reciprocating engines despite of their short comings. The commercial production of reciprocating engines has improved the economic activities of many countries.

The reciprocating engines have played many crucial roles in the major sectors of the economy due to their fuel economy, sturdiness, reliability and rigidity. The benefits of using the reciprocating engines have been limited owing to the greenhouse gas emission which is one of the sources of the global warming, acid rain and ozone depletion [3]. The power generation from the reciprocating power units represents about 10–15% of the world power demand and have the capacity to supply 22.8% of the global electricity demand. The global acceptance of the reciprocating engine for over a decade is due to its high efficiency, durability and reliability of the engines that have been improved by the introduction of several technologies [4]. This has made the reciprocating engines to offer a very-low capital cost and can run on multiple fuels, such as light fuel oil, heavy fuel oil, biofuels, natural gas and crude oil [5]. The reciprocating engines are piston-driven internal combustion engines that use a number of reciprocating pistons to convert pressure into a rotating motion. This will cause the crankshaft of the engine to be turned by moving the pistons up and down in a cylinder. The reciprocating engines can be classified into the spark-ignition (SI) engine and the compression-ignition (CI) engine based on the methods of ignition [6]. The SI engine uses the spark plug to initiate the combustion process and a CI engine utilizes the heat of compression to initiate ignition of the fuel that has been injected into the combustion chamber of the engine. The reciprocating engines are more efficient than other non-renewable DG technologies but are prone to production of harmful gas emissions and dirty particles that have been a source of concern by the public, i.e. nitrogen oxides (NO_x), sulphur dioxide (SO_2), carbon dioxide (CO_2), carbon monoxide (CO) and particulate matter (PM). The statistical data has shown that over 70% of

the global fuel consumed by the reciprocating engines is used for transportation. The quantity of gas emissions from the reciprocating engines will continue to increase if proper measures are not taking. The greenhouse gas emissions from the reciprocating engines can be reduced to legally acceptable levels with more effective environmental technologies and research activities [7, 8]. The efficiencies of the reciprocating engines can be improved to above 80% via CHP as well as the fuel consumption regulations. The maintenance costs of the reciprocating engines are higher than renewable DG technologies because of the complex nature of the engines and numerous parts of the engines [5].

In addition to this, the reciprocating engines are commercially available and widely used as prime movers for automobile and industrial equipment, combined heat and power (CHP) and power generation applications such as backup, peak shaving, standby/emergency and a grid support for critical power requirements of many organizations [4]. Due to the fuel flexibility and compact sizes of the reciprocating engines, they can be used to supply remote locations that are not connected to the grid or being used by the power utility as mobile emergency or standby power units. The utilization of the diesel engines should be encouraged in a situation where natural gas is not available or very expensive. The operations of diesel engines have been limited in some countries due to greenhouse gas emissions and the framework set up by some environmental protection regulatory bodies [4]. This section shall give a detailed description of the reciprocating engines and their operating characteristics such as technologies, efficiency, operation and maintenance costs, type of fuels and emissions.

2.1.1 Technology Description of the Reciprocating Engines

The reciprocating engines produce electrical and mechanical power for many domestic, commercial and industrial applications. The high efficiency and fuel flexibility coupled with an economic CHP option have made the reciprocating engines to be one of the widely used engines in the world. In addition to this, the reciprocation engine has the following performance characteristics, i.e. quick start-up, high availability, high reliability, low capital cost and low operating costs. The medium-speed, low-speed and high-speed reciprocating engines can be used as the grid support, base load and emergency power applications. They can also be used for the DG in some small towns and villages that are not tied to the utility power networks due to some technical and financial barriers [9]. They can be used as prime movers for automobiles, industrial equipment, ship propulsion and numerous machinery and equipment. The reciprocating engines are well-known technologies that have been accepted due to the characteristics presented in Table 2.1.

Table 2.1 Operation characteristics [4, 5]

Operation characteristics	Description
• Long life	Provided many years of optimal operations
• Quick start-up	Easy and quick to start-up for provision of electrical power for peaking and emergency power applications
• Availability	Reciprocating engines have excellent availability
• Reliable	Highly reliable
• Black-start capability	Reciprocating engines can start with battery in event of power outage
• Economical size range	Available in various sizes based on the power demand by consumers

Table 2.2 Technical, economic and benefits of the reciprocating engines [49–56]

Technical benefits			Economic benefits
Reliability	Security	Operational advantages	Low installation cost
Enhanced reliability of a power system. Minimized capacity release of a power system Enhanced generation diversity of a power system	Improved security of the critical loads in a power system No intermittent energy resource Improved security of the power supplied by the utilities. Long life span	Increased productivity Easy O&M Improved total efficiency Utilized small size of land for installation Simple operation High efficiency	Moderate capital costs Reduced ancillary costs Lower capital cost per kW of capacity

2.1.1.1 Comparative Analysis of the Reciprocating Engines

The reciprocating engines can be compared with other non-renewable energy by using some notable benchmarks that are applicable in the power systems. These characteristics are presented in Tables 2.2, 2.3 and 2.4.

2.1.1.2 Applications of the Reciprocating Engines

The reciprocating engines can be used for multiple applications such as power generation and prime movers to drive many industrial equipment and machinery.

Table 2.3 Comparative analysis of non-renewable technologies [23, 37, 57–59]

Non-renewable DG technologies				
DG technologies	Steam turbines	Reciprocating engines	Gas turbines	Microturbines
Capacity range	Any	Gas: 50 kW–5 MW Diesel: 20 kW–10 MW	1–20 MW	30–250 kW
Efficiency (%)	30–42	Gas: 28–42 Diesel: 36–43	21–40	25–30
Fuel	Coal, natural gas, oil and biogas	Diesel, gasoline, natural gas, LPG and biogas	Natural gas, heavy oil, LPG, LNG, crude oil, coal gas and ethanol	Natural gas, biogas, hydrogen, diesel, propane, LPG, kerosene, vegetable oil and CNG
Availability (%)	Near 100	Diesel: 90–95 Gas: 92–97	90–98	90–98
CO ₂ emission (g/kWh)		Diesel: 650 Gas: 500–620	580–680	720
CO emission (g/kWh)		Diesel: 2.8 Gas: 1.8	0.42	0.47
Life time (year)	25	20	20	10
SO ₂ emission (g/kWh)		Diesel: 0.032 Gas: 1.25	0.032	0.037
NO _x emission (g/kWh)	0.82	Diesel: 10 Gas: 0.2–1	0.3–0.5	0.1
Installation cost/kW (US\$/kW)	800–1000	Diesel: 125–300 Gas: 250–600	300–600	500–750
O&M cost (US\$/MWh)	4	Diesel: 5–10 Gas: 7–15	3–8	5–10

These engines are manufactured in the large quantity because of the following features: high start-up, highly reliable moderate fuel cost and moderate capital costs. The maintenance and operating costs, capital costs and fuel costs of reciprocating engines are very high when compared with the renewable DG technologies. The DG potential of the reciprocating engines in a conventional distribution power system includes peak shaving, standby and grid support. The reciprocating engines can also be used as prime movers for many equipment such as pumps, compressors, train, ship and vehicle. In addition to this, the waste heat from the reciprocating engines’ exhausts can be recovered and converted to hot water and steam through the heat exchanger [4, 5].

Table 2.4 Advantages and disadvantages of the reciprocating engines

Advantages	Disadvantages
<ul style="list-style-type: none"> • High reliability and more rugged • Longer life spans • Modularity • Diversity of use • It does not occupy much space • High efficiency • High capacity factor • High availability • Lower lead times to construct • Easier to install • Flexibility to upgrade the plant • Short start-up times • Black-start capability • Multi-fuel capability • Low investment cost 	<ul style="list-style-type: none"> • Long payback time • High emissions • High vibrations in reciprocating engines • Relatively high maintenance cost • Frequent maintenance intervals • Relatively dependency of fossil fuels • Cold start difficulty • Higher noise

Standby Power

The standby power generating unit is an independent electric power source that provides electric power supply to some loads in an event of power failure or outage from the utility so that consumers' facilities will continue to operate satisfactorily based on the specifications of the manufacturers [10]. The reciprocating engines are installed in a conventional distribution system to act as standby units, so that the power supply will be restored back into the power system automatically or manually in the event of power interruption from the utilities. The standby power units are installed in the public, commercial and residential buildings to provide an alternate source of power so that certain critical devices and equipment will be allowed to operate effectively during a power outage. The failure of these equipments would expose the health and safety of the personnel in the buildings or facilities to perpetual risk. The reciprocating engines are usually preferred because of quicker start-up, low capital cost and low installation costs. Due to a short duration of using reciprocating engines as standby units in a power system, some key performance indicators such as emissions, capital costs, efficiency and operation and maintenance costs are not likely to be prioritized. The reciprocating engines are the most popular choice for power generation due to the low cost of installation when compared to other types of DG technologies and short starting time. The reciprocating engines can also run on diesel as well as natural gas through a dual fuel configuration [4, 5].

Peak Shaving

The reciprocating engines are utilized by various consumers to supply electrical power into their facilities during the peak periods. The peak shaving generating

units are owned by the electricity consumers, rather than by the utility. The reciprocating engines can be used for peak shaving application because of portable size, low capital cost, modular size, quick start-up and high reliability characteristics. The integration of reciprocating engines into a conventional power system for peak shaving applications has a lot of benefits for the consumers that have poor load factors. The economic operation of the reciprocating engines for peak shaving is high, if they can be combined with other functions such as standby and CHP. The benefits are summarized as follows:

- deferred investment on generation, transmission and distribution facilities,
- increased reliability,
- improved power quality,
- avoided ancillary service costs and reduced load shedding, and
- reduce the operational cost of power generating units.

Grid Support

The grid support plants normally run when there is a high power demand that cannot be met by the existing power generating units. The power utilities use a number of the reciprocating engines at various substations and power plants to provide a grid support during the peak demand. This will balance the power shortage that arises from the generating units' outage in a power plant. The integration of the reciprocating engines into a power system as the grid support units will defer any investment on extension or upgrading of the transmission and distribution facilities, reduced load shedding, optimized operational costs, reduced economic cost that is associated with power outages and increase the peaking capacity of a power system. The diesel engines and SI engines can be strategically incorporated into the distribution system due their operational characteristics. The grid support generating units can be used to increase the output power of a power plant. This can be achieved once the grid support units have been synchronized to the grid in response to the generating units' outages in a power plant.

Combined Heat and Power

The reciprocating engines can be used for generation of power and production of heat simultaneously. The combined processes of generating power and heat concurrently is more energy efficient than the separate generation of electrical power and heat from different DG technologies [11]. The CHP technology reduces the total fuel consumption and greenhouse gas emissions of the reciprocating engines, since both electrical power and heat are from the same source of fuel. The heat recovered from the reciprocating engines can also be used for cooling applications. The CHP can provide electricity, mechanical power to drive compressor, pumps

and fan and heat energy that can be used for steam or hot water. The application of the reciprocating engines for production of heat and power separately has a combined heat efficiency of about 45%, while cogeneration system that combines heat and power generation processes can be up to 80% efficient [11]. The reciprocating engines have been widely accepted for CHP applications due to the following features: quick start-up, high efficiency, portability and flexibility of fuel. The reciprocating engines can offer the following benefits if they are used for the CHP applications:

- reduced GHG emissions,
- reduced economic losses due to power outage,
- reduced power lost in the transmission and distribution (T&D) systems,
- reduced congestion in the distribution system, and
- deferred investments in new T&D facilities.

2.1.2 Classes of Reciprocating Engines

The reciprocating engines can be classified into various categories by using the following criteria.

2.1.2.1 Methods of Igniting the Fuels

The reciprocating engines are classified into the CI/diesel engines and the SI engines based on the methods of igniting the fuels. The SI engines run on multiple fuels such as natural gas, propane, gasoline, *compressed natural gas (CNG)*, *methanol*, *ethanol*, bioethanol, liquefied petroleum gas (LPG) and hydrogen. The CI engines or diesel engines are designed by the original equipment manufacturers (OEMs) to operate with any available fuel. The diesel engines are designed with the modern technology to run on both natural gas and diesel through a dual fuel configuration. They are the most popular reciprocating engines due to some technical characteristics, but their operations have been limited to emergency and standby in some countries due to emission constraints set up by the environmental protection regulators. The natural gas-fired SI engine has become widely accepted owing to the public awareness of environmental hazard of carbon emissions and higher duty cycle. These engines are now available at a commercial level in various sizes. The natural gas-fired reciprocating engines offer the following benefits, i.e. high availability, quick start-up and high reliability. These benefits are subject to proper maintenance of the engines. The different types of the reciprocating engines and their characteristics are presented in Table 2.5.

Table 2.5 Types of the reciprocating engines and their characteristics [4, 5]

Reciprocating engines	Spark ignition	Diesel
Size range (kW)	30–5000	30–5000
Electrical efficiency (%)	31–42	26–43
Overall efficiency (%)	80–89	85–90
NO _x emissions (g/kWh)	0.7–42	6–22
CO emissions (g/kWh)	0.8–27	1–8
Packaged cost (\$/kW)	300–700	200–700
Installation cost (\$/kW)	150–600	150–600
Electricity cost (cents/kWh)	7.6–13.0	7.1–14.2
Applications	Continuous power, peak power and CHP	Continuous power, peaking power, premium power and CHP
Cogeneration cost (cents/kWh)	6.1–10.7	5.6–10.8
Availability (%)	90–97	90–97
Start-up time (s)	5–10	10
Planned schedule (h)	1000–2000	1000–2000
Time between overhauls (h)	10000–24000	10000–24000
Noise levels (dB)	80–100	67–92

2.1.1.2.2 Operation of a Diesel Engine

The diesel engine is one of the efficient engines that are available in the market owing to its simple operation and fuel economy. The diesel engine is an internal combustion engine that operates based on the principle of compressing the fresh air that is introduced into the engine cylinder during the intake stroke. The engine is designed in such a way that it will allow the motion of the intake valve to be controlled by the crankshaft, while the exhaust valve remains closed during the intake stroke operation. The compression ratio that has a range of 12:1–22:1 is used for compressing the air in the cylinder during the compression stroke. The fuel injector is utilized to inject fuel into the combustion chamber at the end of the compression stroke, this will initiate the combustion process in the engine. The air inside the cylinder is compressed so that it raises its temperature and pressure to match the auto ignition temperature of the diesel during the power stroke. The fuel will absorb heat from the hot air in the cylinder and vaporise, this will result in

Table 2.6 Characteristics of the compression-ignition or diesel engines [4, 5]

Advantages	Disadvantages
<ul style="list-style-type: none"> • Fuel economy • More efficient than spark-ignition engines • Produce very little amount of carbon dioxide • Produced little waste heat during cooling and exhaust processes • They are durable than spark-ignition engines • Diesel fuel is safer than petrol and natural gas engines • Diesel engines have advantage of higher torque • Diesel engines can run at a cooled temperature than spark-ignition engines • Lower running speeds • Diesel fuel is less flammable than petrol • Fumes from diesel engine are less toxic and polluting than petrol engines • Simple to design and operate • Portable and required little space • High quick start • Low initial start • Lower fuel consumption 	<ul style="list-style-type: none"> • Diesel engine must provide more torque to produce the same output power as spark-ignition engines • Noisier than spark-ignition engines • Required high compression ratios for ignition to take place in the cylinder • They are bigger and heavier than spark-ignition engines of the same power output • Starting is often difficult because it requires more starting torque • Produce black soot from their exhaust • Retrofitting is difficult in most of the cases • Friction loss due to many moving parts • Limited compression ratio lowers efficiency • High cost of maintenance • High cost of lubricants • Small power generation capacity compared with thermal power plants

combustion and subsequently generation of energy that can be used for different applications. The high efficiency of the diesel engine has been attributed to its high expansion ratio and intrinsic burn. The characteristics of the CI or diesel engines are presented in Table 2.6.

2.1.2.3 Operation of a Spark-Ignition Engine

The SI engine uses three basic components such as piston, connecting rod and crankshaft for its operation. The intake valve opens to allow the mixture of air and fuel to be injected into the cylinder during the intake stroke. The mixing of air and fuel process is achieved by using a can and follower mechanism. The exhaust valve remains closed during the intake stroke. The piston moves the mixture of fuel and air from the injector into the cylinder. The intake and exhaust valves are designed by the original equipment manufacturer to remain closed during this process so that the piston will be able to compress the mixture of air and fuel in the cylinder effectively. The mixture of air and fuel is compressed to a high pressure as a means to allow combustion to take place in the engine. A spark is produced by the spark plug located in the cylinder head after the compression has completed. The exhaust and the intake valve are closed during this stroke for optimal operation of the engine. The spark from the spark plug burns the mixture of air and fuel. This will

Table 2.7 Characteristics of the spark-ignition engines [4, 5]

Advantages	Disadvantages
<ul style="list-style-type: none"> • Lower capital costs • Lower maintenance costs • Can be easily retrofitted for alternative fuels • Light in weight and portable • Higher running speeds 	<ul style="list-style-type: none"> • Less overall fuel efficiency and economy • High service requirement • Not durable • Lower efficiency • More expensive fuel

result in combustion and generation of mechanical energy that can be used as a prime mover for many applications. During the exhaust stroke, the exhaust valve is opened by using a configuration that will allow the exhaust gasses to escape out of the cylinder. The efficiency of spark engines is lower than the CI engine because of the difference in the compression ratio. In addition to this, the poor oxidation of fuel in the SI engine also contributes to its low efficiency. The characteristics of SI engines are presented in Table 2.7.

2.1.2.4 Operating Cycle or Number of Strokes

The reciprocating engines are also classified based on the operating cycle it requires to complete a combustion cycle. A stroke is the full travel of the piston from the top of the cylinder to the bottom of the cylinder. The SI and CI engines are designed by the manufacturers to operate effectively on both two-stroke cycle and four-stroke cycle. A two-stroke reciprocating engine operates in such a way that it can complete its combustion cycle in one revolution of the crankshaft. The two-stroke engines are lighter, cost effective and simple to manufacture, because they do not have valves. A four-stroke reciprocating engine completes its combustion cycle in four strokes during two revolutions of the crankshaft. The four-stroke engines have been produced in a large quantity by different manufacturers because of their durability, fuel economy, low emissions, simple operation and high torque.

2.1.2.5 Speed

The reciprocating engines can be categorized based on the speed of the crankshaft. The speed of a reciprocating engine depends on its weight and capacity of the power output. The ranges of the reciprocating engines are presented as follows.

High Speed

The high-speed engines are designed to operate at the speed range of 1000–3600 rpm. The reciprocating engines can operate at 1500 rpm (50 Hz) for power generation applications. They have the lowest capital cost among the three classes of reciprocating engines based on their speed but have poor efficiency [4, 5].

Medium Speed

The medium-speed diesel reciprocating engines operate within the approximate speed range of 275–1000 rpm. The capital costs and efficiency of the medium-speed engines are more than high-speed engines and also have flexible operation on various fuels. They can be used as prime movers for the locomotive and marine engines. They can also be used for the grid support, emergency, base load and peak shaving power generation units [4, 5].

Low Speed

The low-speed diesel reciprocating engines are designed to operate within the speed range of 58–275 rpm. These engines are used for propulsion units of the ship because of the simplicity to couple them directly to the shaft and propeller. They operate effectively on lower grade fuels than medium- and high-speed engines. They are also more efficient and cost effective than medium- and high-speed engines. The low-speed engines can be utilized in a situation where the prices of natural gas and heavy oil are extremely expensive for the power utilities. They can also be used for different application wherever the natural gas and heavy oil are not available [4, 5].

Ratings

The reciprocating engines can be classified into three classes based on the power generation applications, i.e. continuous, prime or standby based on their mode of operations.

Standby Generators

The standby generators are designed to run only in a situation when there is an interruption of power supply from the utility grid. The need for standby unit arises whenever there is a short-term power disruption in an event of faults in the primary supply networks. This happens when the power supply from the main grid goes out due to some faults which can quickly be rectified by the utility so that power will be restored back to the systems. The standby reciprocating generating units have the following advantages over other non-renewable technologies that have been assigned to perform the same application:

- Standby reciprocating units can cool down naturally without using artificial cooling system such as fan, water cooling system and lube oil cooling system.
- Scheduled or breakdown maintenance activities are carried out by the assigned personnel without disrupting the power supply to the grid.

- These units do not need emission control units.
- Standby units do not need an elaborate cooling system.

Prime Generators

The prime generators are designed by the original equipment manufacturers to operate for long durations at variable loads. The prime generators can be used in the locations where there is no access to connect consumers to the distribution networks or national grid provided by the power utility [12]. The prime generators are subject to the applications that will cause a continuous flow of current in the alternator winding of the generator. This will lead to an enormous quantity of heat to be generated through the alternator's winding. This will increase the capital cost of the prime power plant due to the procurement of a large cooling system. The temperature build up in a prime generator can be reduced with the incorporation of a cooling system. This will subsequently improve the efficiency and optimal operation of the system.

Continues Generators

The continuous generator sets are designed by the original equipment manufacturer to operate continuously with a constant load without power interruption. The continuous generators are primarily used in remote locations where there is no access to tie their power systems to the grid due to some financial and technical constraints [12]. The continuous generating units can also be used when there is a limitation on the maximum amount of electric power that can be drawn from the utilities' distribution and transmission lines. The power limitation is imposed on some oil and gas companies by the regulators so that they can utilize the available resources (crude oil, natural gas and LPG) within their vicinity to generate power for their consumables. The continuous operation of the reciprocating generating unit does not allow the engine to be cooled down naturally. The water cooling system, lube oil cooling system and fan cooling system are incorporated into the continuous generating units as a measure to cool all the complicated parts of the engines. This will improve the optimal operation and efficiency of the generating units without exposing the consumers to the intermittent power interruption or load shedding.

2.1.3 Performance of Reciprocating Engines

The key performance indicators that are affecting the operations of the reciprocating engines are presented as follows:

- heat rate,
- efficiency,
- capacity factor and
- load factor.

2.1.3.1 Heat Rate

The heat rate is the quantity of energy that an electrical generator used to generate one kilowatt-hour of electricity. This is achieved as a result of the engine's energy conversion process. The reciprocating engines have been configured to be running at the optimal operating rate at the lower heat rate. The heat rate can be used by the power utilities as a standard to compare the performances of different generating units in the same plant or at different sites. The heat rate can be used to reduce the operating cost of a reciprocating power unit. Due to the fact that the cost of the heat rate is directly proportional to the fuel cost. As a result of power deregulation, the power utilities must operate their generating units at the lowest operating cost that will allow them to compete with other investors or competitors in the power sectors and at the same time maximize their profits. This can be achieved by monitoring the heat rate so that it will not deviate from the manufacturer's specifications. The heat rate of a reciprocating engine can be expressed mathematically as:

$$\text{Heat rate} = \frac{H}{E} (\text{kJ/kWh}), \quad (2.1)$$

where H is the thermal energy of the power plant (kJ) and E is the electrical energy output of the power plant (kWh).

2.1.3.2 Efficiency

The efficiency is a ratio of the output power of a power plant to the energy input of the system, and it increases with the engine's size. An optimal operation of the reciprocating engines is a serious challenge for the utilities because of fuel cost, operation and maintenance costs, reliability, emissions, etc. The operators of the reciprocating power plants derive a lot of benefit from running the engines at high efficiency. These benefits are not limited to fuel economy, optimization of greenhouse emissions and reduction of emission without installing emission control equipment. The efficiency of a reciprocating engine can be used as a long-term tool to reduce the greenhouse gas emissions that are associated with the reciprocating engines. The efficiency of a reciprocating engine can be estimated as follows:

$$\text{Efficiency} = \frac{\text{Output power (kW)}}{\text{Input energy (BTU/h)}} \quad (2.2)$$

2.1.3.3 Capacity Factor

The capacity factor of a reciprocating power plant is the ratio of the average value of the load to rated value of the generating unit for a period of time. This is an important measure to estimate the electric generator usage and how intensively a generating unit is running. It is used by the power utility to estimate how fully a unit's capacity is utilized. The base load generating units have high capacity factors, while the peak load generating units have low capacity factors based on their performance features and mode of operation. The stochastic renewable sources such as solar and wind also have lower capacity factors due to the intermittent characteristics of their local RER [13]. The capacity factor of a reciprocating power plant can be expressed mathematically as:

$$\text{Capacity Factor} = \frac{\text{AL}}{\text{RC}} * 100(\%), \quad (2.3)$$

where AL = average load (kW) and RC = rated capacity (kW).

2.1.3.4 Load Factor

The load factor for a reciprocating power plant is the ratio of average load demand to peak load. The greatest challenge for the power utilities is how to operate their reciprocating power generating units at a high load factor. The high load factor can be attained if the reciprocating power plants are operating at the lower fuel cost per unit with more output. At a high load factor and spark spread, it is mandatory for the power utilities to sell their electricity. The load factor can be used by the power plant operators to determine the load capacity of the reciprocating power plant. If all the reciprocating generating units in a power plant are running at 100% load factor, it shows that the power plant is operating at the optimum capacity, i.e. full load of the installed capacity. The performance of a reciprocating power plant is directly proportional to the load factor. One of the advantages of high load factor is that it can be used to reduce power plant forced outages. The load factor is the key indicator that can be used to estimate the performance of a reciprocating power plant. The load factor of a reciprocating power plant can be expressed as:

$$\text{LF} = \frac{\text{AL}}{\text{PL}} * 100\%, \quad (2.4)$$

where AL is the average load (kW); LF is load factor (%); and PL is the peak load (kW).

2.1.4 Emissions

The rapid increase in the global emission of greenhouse gas emissions has been attributed to the economic growth, coupled with the accelerated industrialization and urbanization. This has led to a sudden increase in the electric power demand that is difficult to meet in some countries. The electrical power demand can only be met by harnessing all the available energy resources, i.e. renewable and non-renewable energy resources. The total electric power generation from different sources worldwide was estimated in 2014 to be 4892 TWh. This statistical data showed that 77.2% of the global power demand came from fossil fuels and nuclear, while 22.8% came from RER [13]. The largest percentage of global greenhouse gas emission come from the fossil fuels fired conventional power plants. The reciprocating engine which is one of the notable conventional power plants emits some unburnt fuel particles and a number of pollutants such as CO, CO₂, SO₂ and NO_x [5]. The emissions from the fossil-based reciprocating plant have become a serious public concern due to the harmful effects on property, animals and human beings.

2.1.4.1 Sulphur Oxides Emissions

The Sulphur oxides (SO₂) are produced in the combustion chamber of a reciprocating engine through the oxidization process. The SO₂ will be formed whenever the oxidized sulphur enters the atmosphere and combined with water. The SO₂ will return to the earth's surface in the form of acid rain which has many adverse effects on human beings, animals, plants, environment and buildings. The SO₂ from the fossil fuels fired reciprocation power plant depends on the sulphur content of the fuels [14]. This is contrary to the CO₂ and NO₂ emissions that depend on design and operating conditions of the power plants. The SO₂ emission has become a serious issue because of the environmental effects such as acid rain, eye irritation and breathing difficulty [15].

2.1.4.2 NO_x Emissions

NO_x are formed when nitrogen and oxygen react with each other. The formation of NO_x is influenced by the concentration of oxygen and the flame temperature in the combustion chamber when fuel is burned. The NO_x emissions have become a great concern because emissions from the diesel engines are the highest among the DG technologies. The NO_x emissions depend on the fuel and combustion process as well as on the fuel to air ratio and fuel and air mixing pattern [16]. The diesel engines emit a large quantity of the NO_x emissions compared with the natural gas generators. The poor emissions profile of the diesel generators has discouraged the utilities to install them in some non-attainment locations [16].

2.1.4.3 CO₂ Emissions

The carbon dioxide (CO₂) emissions are produced from the combustion of fossil fuels for different applications. The quantity of CO₂ emitted from the reciprocating engines that used diesel or natural gas is a function of the carbon content of the fuel used and the efficiency of the engines [16, 17]. The CO₂ emissions have become a great challenge due to its contribution to climate change and adverse effects on human beings.

2.1.4.4 CO Emissions

The carbon monoxide is a result of incomplete combustion that takes place in the reciprocating engines owing to inadequate oxygen to complete the combustion process of the fuels. The CO emissions are a direct waste of fuel energy due to incomplete combustion of fossil fuels. The CO emission's costs constitute the greatest part of the power plant running costs [16]. The cooling of the combustion chamber is one of the factors that contribute to incomplete combustion and increase in CO emissions. carbon monoxide is a dangerous gas that can impair human's health. The concentration of CO in the atmosphere can cause depletion of the ozone layer. Some measures must be introduced to reduce the menace of CO emissions in the reciprocating power plants [17].

2.1.4.5 Emission Control

The CO₂, NO_x, CO and SO₂ emissions profile of the reciprocating engines have been reduced through the efforts made by the manufacturers in designing of better and optimally operated engines [16]. This peculiar landmark is achieved by the integration of emission reduction and controlling techniques such as catalyst reduction and air/fuel ratio control. Some modern techniques to control the combustion process were also embedded into the reciprocating engines. The methods of reducing these emissions of PM include the following: a bag house, selective catalytic reduction, oxidation catalysts, three-way catalyst systems, an electrostatic precipitator (ESP), cyclone collector and diesel particulate filter [17].

2.1.5 Plant Availability

The availability of a reciprocating engine power plant is the number of time that the power plant is able to generate electricity over a certain period of time [18]. It can also be defined as the number of time that the reciprocating power plant is in upstate to perform its functions [19]. This depends on the type of engine, speed of the engine, the quality of the fuel and proper maintenance. The reciprocating power

plant availability is associated with the proper management of the reciprocation power plants [20]. The reciprocating engines required a lot of maintenance that must be frequently carried out based on the schedule of the manufacturers or breakdown maintenance that is normally carried out during the power outages to restore back power supply to the system [16]. The availability of a power plant can be increased to 96% if the proper maintenance schedule is put in place and implemented.

2.1.6 Fuels

The reciprocating engines have an advantage to operate on various fuels such as diesel, natural gas liquids, gasoline and jet fuel, as well as alternative gas fuels such as LPG, propane, biogas, sour gas, industrial gas and synthetic gases. The reciprocating engines have been designed to use any available fuel that meets the specifications of the original equipment manufacturers. The CI engines can utilize both diesel and heavy fuel oil for their optimal operations. Also, the SI engine can operate with natural gas, petrol and alternative fuels [16]. The current state-of-the-art technology of the reciprocating engines with the modern features allows them to operate effectively on both natural gas and diesel through a dual fired configuration. The dual fuel reciprocating engines are designed by the original equipment manufacturers with the capability of running on liquid fuels, alternative fuels and gaseous fuels. The dual fuel reciprocating engines can use any available fuel that has been allocated as a backup by the power utility [16]. The fuel will be utilized to run the engine whenever there is an interruption of the main supply from the source. The flexible fuel operation of the dual fuel reciprocating engine allows easy conversion from one fuel to another while in operation. This benefit allows the power plant operators to switch to the more economically viable fuel among the available fuels. For the optimal operation of the reciprocating to be achieved, the low-cost fuel and the high-cost fuel can be used simultaneously to run a reciprocating plant based on the load schedule, i.e. peak load and base load [17]. The combination of low-fuel cost and high-fuel cost provides a number of benefits for the power utilities.

2.1.6.1 Liquid Fuels

The liquid fuels are combustible molecules that can be used to produce mechanical energy for power generation and automobile and industrial machinery. The liquid fuels are usually in liquid forms, i.e. diesel, gasoline, biodiesel and kerosene [16]. The high-speed diesel engines have been designed to operate with a good quality fuel with good combustion property. The fuels must meet the requirements of the manufacturer such as low sulphur content, combustible and good flashpoint. The poor quality fuel may damage the injection pump or the injector and results in total

Table 2.8 Major constituents of natural gases [16, 21]

Fuel component	Natural gas
Methane, CH ₄ (% vol.)	80–97
N ₂ (% vol.)	0–14
Higher C _x H _{2x+2} (% vol.)	0–0.2
CO ₂ (% vol.)	0–1.8
H ₂ (% vol.)	0–0.1
LHV (BTU/scf)	830–1075
Ethane, C ₂ H ₆ (% vol.)	3–15
Butane, C ₄ H ₁₀ (% vol.)	0–0.9
Propane, C ₃ H ₈ (% vol.)	0–3

failure of the reciprocating engines [16, 17]. The high-speed diesel engines are not designed by the manufacturers to operate with heavy oil, because it may have an adverse effect on the optimal operation of the engine. The medium-speed engines and low-speed reciprocating engines can run on both heavy oil and low-grade fuels.

2.1.6.2 Natural Gas

The natural gas is a hydrocarbon that is made up of compounds of hydrogen and carbon, and it can be found by itself or in association of the crude oil [16]. The major constituents of natural gas are presented in Table 2.8. The natural gas-fired reciprocating engines are used for power generation and industrial applications, i.e. compressors, pumps and ship propeller.

2.1.6.3 Alternative Gas Fuels

The reciprocating engines can operate on a number of alternative gaseous fuels such as LPG, sour gas, biogas, industrial waste gases and synthetic gases [21]. The optimal operation of the reciprocating engines on the alternative gaseous fuels depends on the following factors: volumetric heating value, auto ignition characteristics, detonation tendency, contaminants and hydrogen [16].

2.1.7 Fuel Cost

The fuel cost required to generate electrical power in a reciprocating power station depends on fuel price per unit of energy and the net power plant efficiency [16]. The profit margin of a power plant depends on the fuel cost which carries the largest percentage of the power plant operating cost. The fluctuation of fuel prices has a significant effect on the profit margin of the reciprocating power plant [21]. The fuel

cost function of a power generating unit can be expressed by a quadratic function of power output P_i as:

$$FC = H \left\{ \sum_{i=1}^n a + bP_i + cP_i^2 \right\} (\$/h), \quad (2.5)$$

where a , b and c are fuel cost coefficients of the generating unit; H is the fuel price (\$/L); n is the number of the generation unit; P_i is the active power of the i th generating unit (kW).

2.1.8 Cost of Electricity Production

The cost of electricity production for various reciprocating plants can be estimated by using the following parameters, i.e. capital cost, operations and maintenance, cost of fuel and initial investment. The levelized cost of electricity (LCOE) is the price at which electricity from various sources of energy must be sold in order to break even over the economic life of the power plant [22, 23]. The optimal operations of different reciprocating power plants can be compared based on their LCEOs, but this comparison depends on a number of main parameters such as fuel price and plant utilization rate. The LCOE of a reciprocating power plant can be estimated as [22, 23]:

$$LCOE = \frac{\sum_{t=1}^n \frac{I_t + M_t + F_t}{(1+r)^t}}{\sum_{t=1}^n \frac{E_t}{(1+r)^t}} (\$/kWh), \quad (2.6)$$

where I_t is the investment costs in the year t ; M_t is the O&M costs in the year t ; F_t is the fuel costs in the year t ; E_t is the electricity generation in the year t ; r is the discount rate; and n is the economic life of the system.

2.1.9 Maintenance

Maintenance is a periodic activity that is being carried out on a reciprocating generating unit in order to put the unit in a good working condition at all time. This includes breakdown maintenance, preventive maintenance, periodic maintenance, predictive maintenance and corrective maintenance. The reciprocating engines' maintenance is comprised of periodical inspections, replacements of parts and engine oil, coolant and spark plugs, servicing, greasing, retightening of loosed bolts and nuts and cleaning of the engines. The periodic maintenance is always carried on the reciprocating generating unit every 500–2000 h, this depends on the type and size of the engine [24]. The maintenance time interval for the reciprocating engines

based on the specifications of their manufactures is 12,000–15,000 h for minor overhaul and 24,000–30,000 h for a major overhaul [24]. The maintenance cost of the reciprocating engine is high due to the fact that it has many moving parts. The maintenance cost of the reciprocating power plant is \$10/MWh, which is very high when compared with the gas turbine that has a maintenance cost of \$4.5/MWh [16]. The low O&M costs of the reciprocating engines have increased the economic benefits of using the engines for different applications. The economic operating life span of the diesel generator can be increased with a proper maintenance program which must be scheduled based on the manufacturer's specifications. The economic operating life span of a reciprocating engine depends on the capacity of the engine, availability of spare parts and the maintenance culture of the reciprocating engines' operators [16].

2.2 Microturbines in Distributed Generation System

2.2.1 *Brief Descriptions*

DG system can be defined as a small-scale technology used to produce energy in the form of power or heat at or near the point of consumption. The system can be either operated as a stand-alone or connected to the main grid at the lower voltage distribution network and hence be a part of the microgrid. Various technologies including renewable energy, fossil fuel and energy storage can be used in DG system. DG units based on renewable energy technologies include, for instance, solar, wind, hydro, biomass and geothermal, while those based on fossil fuel include, mainly, reciprocating engines and microturbines (MTs). Energy storage systems such as batteries, fuel cells, flywheels, pumped hydro, supercapacitors, hydrogen production and storage form also part of the DG system. With DG systems, both economic and technical benefits are achieved. On the one hand, installing power generating units at the end-users means no transmission or distribution will be required by the utilities, thus leading to investment cost savings. On the other hand, this also means that no extra power loss will be incurred by the electrical grid, thus leading to the grid efficiency improvement.

Although DG systems based on renewable energy have gained much attention in the past, due to their environmental benefits, the lack of dispatchability of most of these technologies has limited their spread. On the other hand, with DG technologies based on MTs, the power output can be adjusted to meet the load consumption at any time. Another advantage of MTs is that they can be used as a cogeneration to produce both electrical power and heat, referred to as combined heat and power (CHP), with less pollution and noise [25, 26]. Because of the above reasons, MTs are considered as a relatively new DG technology, suitable for small industries and commercial buildings [26]. The main focus of this work is to give a review on different technologies used in MTs, energy model, economic analysis, systems optimization, advantages and limitations.

2.2.2 Technology Description

2.2.2.1 Working Principle

A MT is a small gas turbine-based power generation system whose capacity generally ranges between 20 and 500 kW [25–27] and usually used for applications, such as peak shaving, remote power control and cogeneration [28, 29]. The working principle of a MT is similar to that of the gas turbine, which is based on Bryton cycle, with about 30% thermal efficiency [26, 30]. The fossil fuel is burnt by the MT to create high rotation speed to an electrical generator shaft. Most MTs have single-stage centrifugal turbine and compressor, and radial flow [27].

2.2.2.2 Classification of Microturbines

MTs are generally classified based on the number of shafts as follows [26].

Single-Shaft Microturbine

The schematic of a single shaft is shown in Fig. 2.1. The single-shaft MT is simple, easy but expensive to build. Its simplicity and ease of manufacturing make this technology to be the most used [27]. The main components of a single-shaft MT are the compressor, recuperator, combustor, power turbine and electrical generator. The inlet ambient air is firstly compressed to a higher pressure by the compressor. The pressured air is then preheated in the recuperator using the exhaust. The pressured

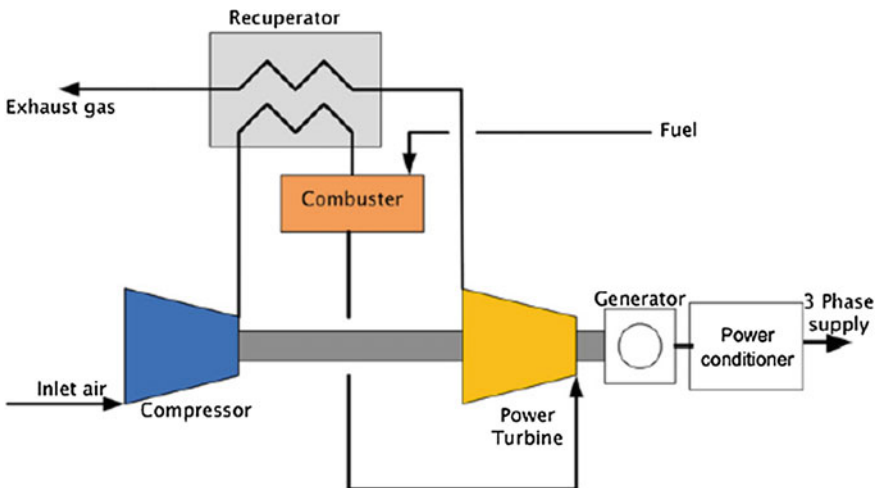


Fig. 2.1 Schematic diagram of a single-shaft microturbine [26]

and heated air is thereafter mixed with the fuel in the combustor. The resulting hot combustion gas expands through a power turbine by transforming gas pressure into turbine power. A 3-phase electrical generator is directly coupled to the power turbine in order to convert available mechanical power into electrical power. Single-shaft MTs rotate at high speed, between 50,000 and 120,000 rpm.

As shown in Fig. 2.1, only one shaft is used to transmit the mechanical power from the power turbine to the compressor and generator. This configuration will make the generator to also rotate at the same speed as the turbine, which is high. With this, the electrical frequency of the special high-speed AC generator used will range between 1500 and 4000 Hz, which will require the use of a power conditioner as an interface to synchronize the frequency with that of the utility grid (50 or 60 Hz). However, the use of a special high-speed AC generator and power conditioner justifies the high initial investment cost of the single-shaft MT. Since high-speed DC electrical generators are easily manufactured, these can also be used with a simple inverter to produce AC power.

Two-Shaft Microturbines

The configuration of a two-shaft MT, also called split-shaft MT is shown in Fig. 2.2. In contrast to the single-shaft MT, a two-shaft MT is a two-stage device where the compressor shaft is separated from the generator shaft by adding a second turbine and gearbox. In this configuration, the hot combustion gas expands through the first turbine coupled only to the compressor, while the exhaust gas from this turbine is used to expand through a second turbine (power turbine) connected to the electrical generator through a gearbox. The first shaft coupling the first turbine with the compressor will still rotate between 50,000 and 120,000 rpm as in the

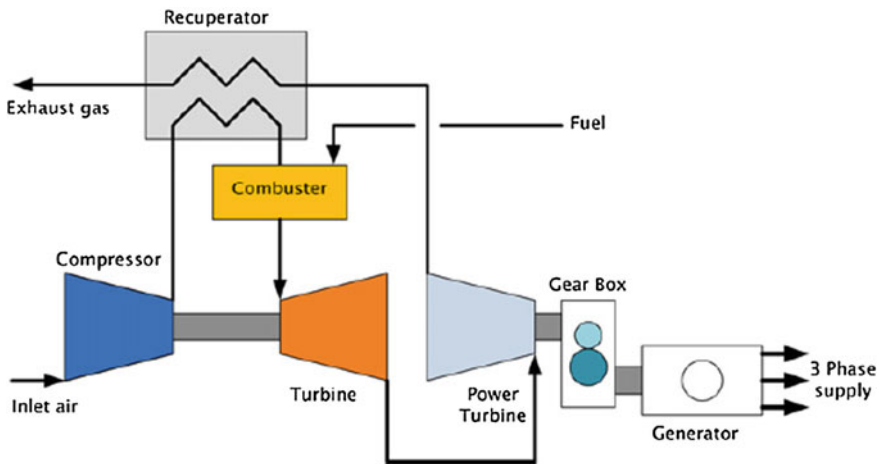


Fig. 2.2 Schematic of a two-shaft microturbine [26]

single-shaft configuration, while the second shaft coupling the power turbine with the gear box will rotate at a lower speed between 3000 and 3600 rpm. The addition of a gearbox will make the generator to rotate at low speed, hence a 3-phase induction or synchronous generator can be used, while avoiding the use of a power conditioner. However, although the two-stage MT configuration will generally lead to a lower initial investment cost due to the avoidance of using high-speed generator and power conditioner, additional moving parts, such as the second turbine and shaft, and gearbox will result in a higher maintenance cost.

2.2.2.3 Comparison Between Single and Two-Shaft Microturbines

Comparison between single-shaft and two-shaft MTs is given in Table 2.9 based on both technical and economic parameters.

Table 2.9 Comparison between single-shaft and two-shaft microturbines [26]

Parameter	Microturbine type	
	Single shaft	Two shaft
Power turbine speed (rpm)	50,000–120,000	3000–3600
Generator frequency (Hz)	1500–4000	50 or 60
Coupling	Direct coupling of power turbine and electrical generator	Indirect coupling: gearbox is used for coupling of power turbine with electrical generator
Power electronic interface	Needed to convert the high frequency from the generator to low frequency of the grid frequency (50 or 60 Hz)	Not needed
Type of generator	Usually permanent magnet synchronous generator, but DC generator can also be used	Usually induction generator, but permanent magnet synchronous generator can also be used
Maintenance level	Lower	Higher due to additional moving parts (second turbine and shaft, and gearbox)
Initial capital cost	Higher due to the use of special high-speed electrical generator and power electronic converter	Lower
Failure level	Higher probability due to the presence of power electronic converter	Lower probability due to the robustness of gearbox compared to power electronic converter
Dimension and weight	Lower	Higher due to the presence of additional moving parts (second turbine and shaft, and gearbox) and gearbox lubricating system

2.2.2.4 Combined Heat and Power

Because of the high temperature of the exhaust gas of MTs during power generation, the waste heat can be recovered and used in a heat exchanger for water or space heating. Since the energy is produced in form of both power and heat, the MT is referred to as combined heat and power (CHP) or cogeneration system. The configuration of a CHP system is depicted by Fig. 2.3, where it is shown that the gas product #6 from the recuperator (II) is used as a heat source to the heat water in a heat exchanger (III) instead of being dissipated in the atmosphere as the case with traditional MTs (see Figs. 2.1 and 2.2).

The aim of this technology is to improve the efficiency of the traditional MT from 30 to about 85–90% [30]. CHP or generation system is widely recognized as cleaner technology compared to the traditional centralized fossil fuel-based power plants. With CHP, multiple benefits are achieved. Some of these benefits are as follows:

- cost-effectiveness due to its high thermal efficiency, higher than 80%,
- lower CO₂ and SO_x emissions with the use of natural gas as fuel,
- increase security level of energy supply due to its stand-alone ability,
- energy savings by reducing the base load electricity and hot water,
- reduced investment cost of installing new boilers,
- energy cost savings due to energy savings,
- potential benefits from renewable heat Incentives, and
- reduced transmission losses from the grid since installed at the end-users.

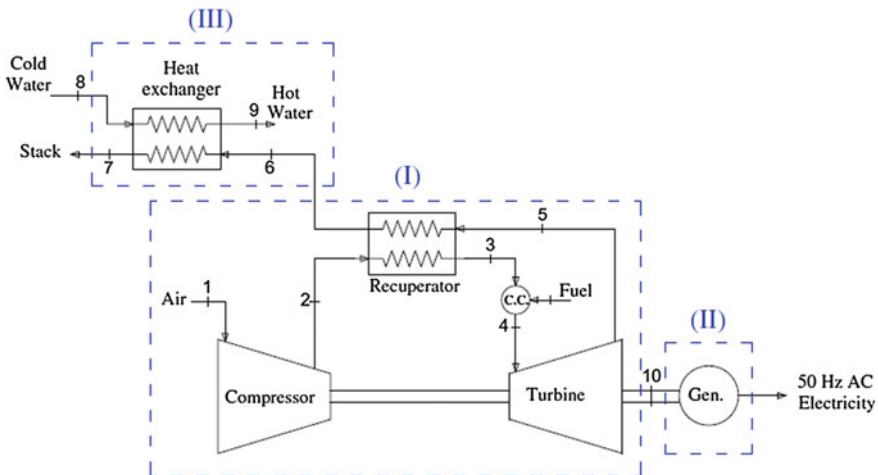


Fig. 2.3 Schematic diagram of a combined heat and power (CHP) system [30]

2.2.2.5 Fuels

One of the advantages of a MT is its flexibility in using a variety of fuels, such as natural gas, propane, diesel and light oil, as opposed to reciprocating engines when diesel is the most used fuel.

2.2.2.6 Thermal Modelling of a Microturbine

The objective of the MT thermal model is to estimate the generated electrical power energy. To achieve this, expressions of mass balance and energy balance need to be known. Since the MT is a CHP system with addition of heat exchanger, the thermal model of CHP will also include that of MTs.

Mass Balance

Based on the principle of conservation of fluid mass between the input and output of each component, the following equations are obtained:

Compressor:

$$q_{m1} = q_{m2} = q_{m12} \quad (2.7)$$

Turbine:

$$q_{m4} = q_{m10} = q_{m4-10} \quad (2.8)$$

Recuperator:

$$q_{m2} = q_{m3} = q_{m2-3} \quad (2.9)$$

$$q_{m5} = q_{m6} = q_{m5-6} \quad (2.10)$$

Heat exchanger: with assumption of negligible heat loss

$$q_{m6} = q_{m7} = q_{m6-7} \quad (2.11)$$

$$q_{m8} = q_{m9} = q_{m8-9} \quad (2.12)$$

Combustion:

$$Q_{m4} = q_{m3} + q_{mf} \quad (2.13)$$

In Eqs. (2.7)–(2.13), $q_{m1, \dots, 10}$ denote the mass flow rates of the gas or water (in kg/s) at different point of the cycle, and q_{mf} is the mass flow rate of the fuel (in kg/s).

Energy Balance

Based on thermodynamic analysis, the energy balance applied at different components of the CHP system depicted in Fig. 2.3 can be written as follows:

Turbine:

$$E_T = q_{m4-10} * (h_4 - h_{10}) \quad (2.14)$$

Compressor:

$$E_C = q_{m1-2} * (h_2 - h_1) \quad (2.15)$$

Recuperator: with assumption of negligible heat loss

$$q_{m2-3} * (h_3 - h_2) = q_{m5-6} * (h_5 - h_6) \quad (2.16)$$

Heat exchanger: with assumption of negligible heat loss

$$q_{m6-7} * (h_6 - h_7) = q_{m8-9} * (h_9 - h_8) \quad (2.17)$$

Generator:

$$E_G = \eta_G * E_T. \quad (2.18)$$

Combustor:

$$E_f = q_{mf} * LHV_f \quad (2.19)$$

In Eqs. (2.14)–(2.19), E_T is the output mechanical power of the macro-turbine (in kW); E_C is the input mechanical power of the compressor (in kW); E_G is the generated electrical power (in kW); E_f is the fuel energy (in kW); LHV_f is the lower heating value of the fuel (in kJ/kg); $h_{4,\dots,10}$ are the specific enthalpies of the gas or water at different point of the cycle (in kJ/kg); and η_G is the overall efficiency of the generator (in %).

2.2.3 Microturbines in Hybrid Energy Systems

MTs have proven their ability to be used in a hybrid energy system in combination with other small-scale power generation systems, such as solar, wind, hydro, fuel cell, tidal and battery storage. The use of MTs in a hybrid system where renewable energy systems, such as solar photovoltaic and wind are used will help to improve the grid stability (smooth power) by compensating the intermittency characteristics of these renewable energy systems.

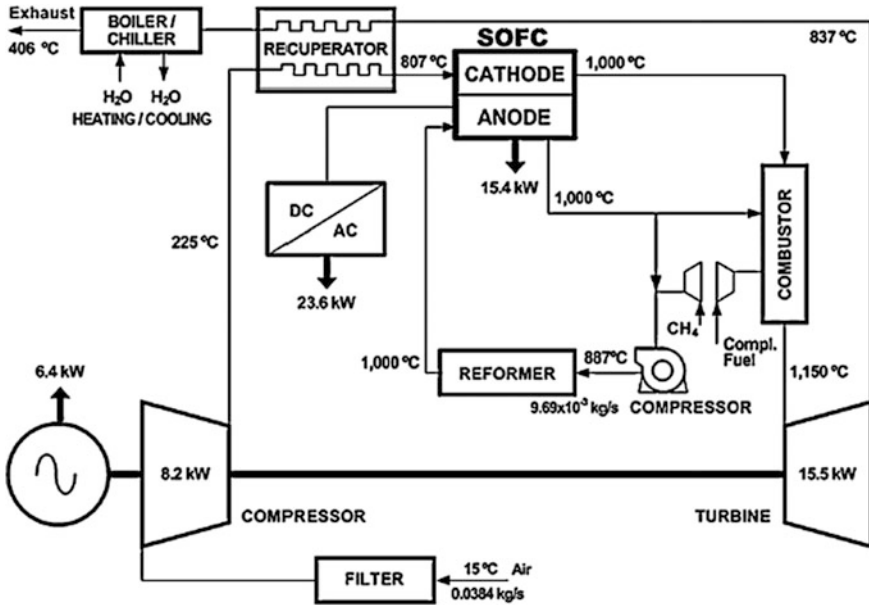


Fig. 2.4 Schematic diagram of a fuel cell/microturbine hybrid system [32]

2.2.3.1 Hybridization of Fuel Cell with Microturbine

Research studies conducted in Refs. [31–33] show that the hybridization of a solid oxide fuel cell with MT will improve the efficiency of both the MT and fuel cell systems, with a global efficiency up to 95.9% [32]. In fuel cell-microturbine hybrid system as shown in Fig. 2.4, the compressed air is preheated by both the recuperator and high temperature fuel cell in order to use less fuel in the combustor and produce more energy through the power turbine, hence improving the efficiency of the system.

2.2.3.2 Hybridization of Microturbine with Multiple Energy Sources

In Ref. [34], a microturbine is hybridized with a wind turbine, tidal turbine and battery storage system to supply an offshore load. The resulting hybrid system has shown the effectiveness of supplying isolated loads (Fig. 2.5).

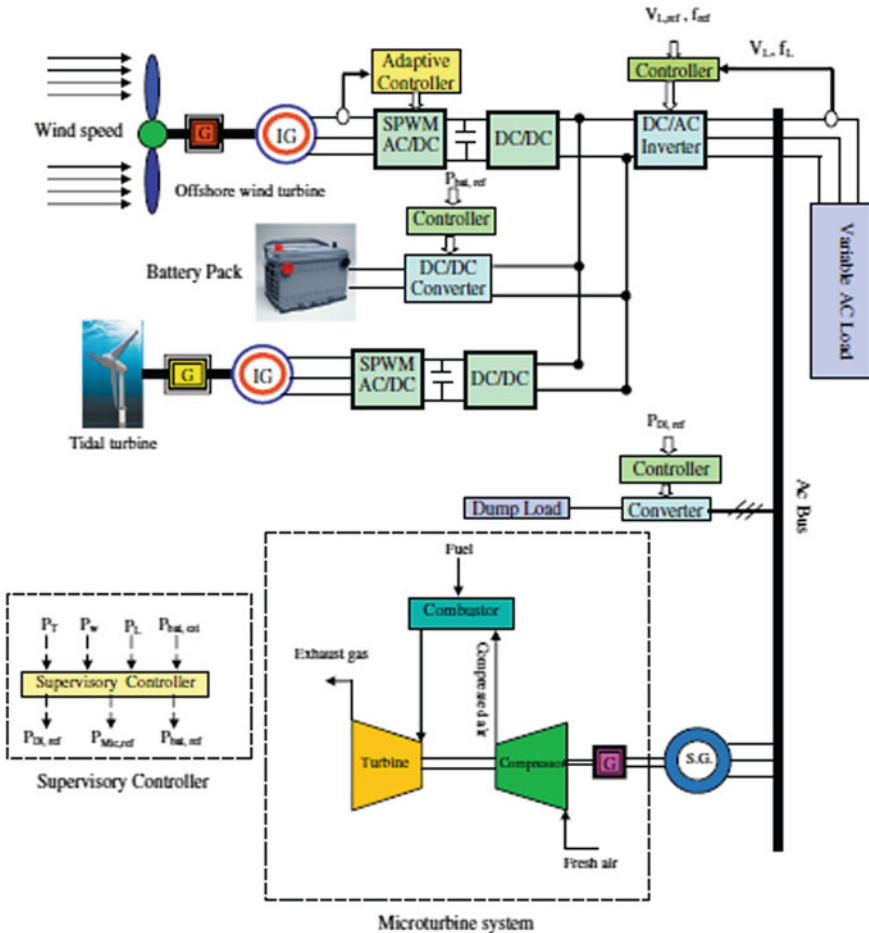


Fig. 2.5 Schematic diagram of a microturbine/renewable hybrid energy system [34]

2.2.3.3 Hybridization of Microturbine with Residential Rooftop Solar PV System

The application of grid-connected PV system has found more market in commercial and industrial sectors than residential sectors. For urban residential buildings, a grid-connected solar PV system might not be cost effective owing to the fact that most electricity usage will not be offset by the investment cost of the solar PV system. The reason is that unlike industrial and commercial customers, in urban residential buildings, more amount of electricity is needed during the evening than during the day, while the PV panels produce power only during the day. To solve this issue, several approaches are possible. The first one is to sell the excess power to the utility grid during the day when the residential load demand is insignificant.

However, selling a large amount of PV excess power to the distribution network will lead to a less cost-effective residential solar PV system because of the less attractive feed-in tariff (FIT) offered by many utility grids. The second solution is to use battery for storing the excess power during the day and use it later in the morning and evening when the load demand is high. However, the use of battery bank may not lead to a cost-effective residential rooftop solar PV project due to the high initial investment cost and low lifetime of the battery bank. Another solution is the use of a solar PV/CHP hybrid energy system [35]. Although the initial capital cost of a CHP maybe relatively high, the technology has shown to have an attractive payback period of between 4 and 10 years [30]. The reason is that CHP has a long lifetime (up to 20 years) and a relatively low maintenance cost.

2.2.4 Economic Analysis of a Microturbine

The cost-effectiveness of any system can be analyzed based on various economic performance indicators, such as payback period (PBP), net present value (NPV) or net present worth (NPW), internal rate of return (IRR), benefits/cost ratio (BCR) and life cycle cost (LCC), also called net present cost (NPC) [36]. However, the LCC is one of the most used methods due to the fact that it takes into account the total costs and revenues of the system components over the project lifetime. Another feature of LCC is that it helps to make choice between more than one alternative in order to have an optimal economic decision-making. For this reason, LCC is considered in this work. However, since the energy yield is another useful performance index for energy generation systems, a ratio between LCC and the energy yield, referred to as levelized cost of energy (LCOE) is usually used as the performance indicator for these systems.

2.2.4.1 Life Cycle of a Microturbine

The LCC or NPC condenses all the costs (positive) and revenues (negative) occurring within the MT lifetime project. In contrast to the NPV calculation, the cash outflows or costs in NPC are considered to be positive, and cash inflows or revenues are negative.

Costs/cash outflows of the MT include the following:

- Initial capital investment costs: include the purchase cost, installation labour and interconnection and permitting costs.
- Operation and maintenance (O&M) costs: the cost of operating the MT to maintain its performance efficiency over its lifetime. This cost therefore includes the maintenance labour and consumable and spare parts. The cost of continual personnel training may also be included. O&M costs may also include insurance and taxes, such as the one due to carbon emissions.

- Fuel costs.
- Replacement costs: are actual costs to replace the MT system at its current market value. This will occur if the MT system is not operated until the project lifetime due. This may happen if the project lifetime is longer than the MT lifetime or the MT is accidentally damaged before the end of its lifetime. Revenues/cash inflows include the MT:
- Income or energy cost savings: from selling power to the grid and/or thermal energy to the heat network,
- Salvage value: estimated resale value of MT at the end of the project lifetime.

Since all cash flows except the initial investment cost, occur at some future periods after installation, these are discounted at their present worth (PW) for the calculation of the LCC [36]. Hence, the LCC will consist of the MT initial capital investment of MT (C_0), PW of its O&M costs (C_{OM}), PW of its fuel costs (C_F), PW of its replacement costs (C_R), PW of its emission costs (C_E), PW of its energy cost savings (C_{ES}) and PW of its salvage value (S).

The LCC or NPC of a MT can be written as below:

$$LCC = C_0 + C_{OM} + C_F + C_R + C_E + C_{ES} + S \quad (2.20)$$

where C_0 is the initial capital investment; C_{OM} is the PV of the operation and maintenance cost; C_R is the PV of the replacement cost and is the salvage value. The formula that discounts future worth (FW) of C_{OM} , C_F , C_R , C_E , C_{ES} and S occurring at n th year, to their PW is given as follows [37]:

$$PW = FW * (1 + i)^{-n}, \quad (0 \leq n \leq N) \quad (2.21)$$

where n is the year at which the FW occurs; N is the project lifetime; $(1 + i)^{-n}$ is the present value factor or discount factor; and i is the interest or discount rate. Equation (2.21) shows that at year 0, $PW = FW$, which is the initial capital cost.

2.2.4.2 Levelized Cost of a Microturbine

After calculating the LCC, the LCOE of a MT can be obtained by dividing the annualized LCC, noted $(LCC)_A$ by the MT annual energy supplied as follows [38, 39]:

$$LCOE = \frac{(LCC)_A}{\sum_{m=1}^{12} N_d * L_m} = \frac{LCC * CRF}{\sum_{m=1}^{12} N_d * L_m} \quad (2.22)$$

where N_d is the number of days per month, L_m is the monthly daily total electrical and thermal energy supplied by the microturbine per month; CRF is the capital recovery cost, expressed as below:

$$\text{CRF} = \frac{i(1+i)^N}{(1+i)^N - 1}. \quad (2.23)$$

2.2.5 Systems Optimization

The overall efficiency of most energy systems can be improved on four different levels, namely technology (T), equipment (E), operation (O) and performance (P). This is referred to as POET concept [40]. While technology efficiency improvement occurs during the design phase by using efficient energy conversion methods, equipment and operation efficiency are achieved during operation of the system. Equipment efficiency is usually through retrofitting of old components of the energy conversion system by new and efficient components. However, this will often require high investment costs and long payback periods. The operation efficiency is achieved through optimal coordination of the system variables and working time. This, on the other hand, will require lower investment cost and shorter payback period. The well-known example of operation efficiency improvement on energy generation systems is the economical load dispatch (ELD), which consists of scheduling different fossil fuel generators to produce optimal powers in such a way to meet the system load consumption at the possible lowest fuel cost, while meeting the transmission network and generator operation constraints.

Systems optimization has also been widely applied to industrial processes as a supervisory control system, sitting at the upper control layer [41]. The aim of this is to optimally adjust in real time, the set points of the lower control layer, usually referred to as regulatory control system, in such a way to either minimize costs or maximize profits. Hence, depending on the performance indices, different control objective, such as minimization of energy consumption, energy cost [41–44], emissions and downtime, and maximization of total plant throughput and product quality can be considered.

ELD is also a kind of systems optimization that has shown great potential to be applied to microgrids composed of multi-area MT or CHP energy production where the cost of power production (for MT microgrid) or cost of both power and heat (for CHP microgrid) and sometime the cost of emission are minimized while satisfying the demand and operational limitations. References such as [45–48], the ELD problem is applied to a multi-area CHP system by using different optimization algorithms, such as linear programming, Cuckoo search, group search optimization, double benders decomposition to minimize the total cost associated with the production of power, heat and emissions.

The optimization problem of a multi-area CHP network can be generally formulated as a multi-objective optimization problem as follows [10, 49–51]:

$$\text{Min } C_P + C_H + C_E, \quad (2.24)$$

where C_P is the total power production cost from all CHPs; C_H is the total heat production cost from all CHPs; and C_E is the total emission production from all CHPs.

Subject to

- (a) power balance,
- (b) heat balance,
- (c) power generation limits and
- (d) heat generation limits.

2.2.6 Comparison with Reciprocating Engines

2.2.6.1 Advantages

Some of the advantages of MT systems are given as follows:

- high system reliability: the simple working principle of MT due to its pure rotation motion and smaller number of moving parts provides higher reliability compared to reciprocating engines.
- stability: the MT provides a shorter response time in terms of load variations. The steady-state frequency regulation is also much better compared to most generation systems.
- light weight and compact size: MTs are very light and can be installed in a reduced space when compared to reciprocating engines.
- higher power-to-weight ratio: for a given weight, MTs produce higher power when compared to reciprocating engines.
- fuel flexibility: MTs can use a wide range of fuels, such as natural gas, propane, diesel or light oil.
- higher efficiency in cogeneration: since the exhaust gas has high temperature in MTs, higher system efficiency can be achieved in large MT systems.
- lower emission: the combustion products are cleaner than that from reciprocating engines, especially when natural gas is used as fuel.
- lower maintenance cost: the service interval is higher compared to that reciprocating engines since foil bearings and air-cooling operating without lubricating oil, coolants or other hazardous material are used.
- Noise level: MTs provide a quieter operation than reciprocating engines.

2.2.6.2 Disadvantages

- high investment cost: MTs require a higher investment cost due to the high temperature materials used.

- higher skills: MTs require extremely skilful and knowledgeable workers due to the higher level technology involved.
- robustness: the efficiency of MTs is more sensitive to ambient conditions than reciprocating engines.
- low fuel to electricity efficiency: the fuel efficiency of MTs is lower than that a well-designed reciprocating engines.

2.3 Conclusion

DG is a small-scale technology used to produce energy in the form of power or both power and heat at or near the consumer load points. DG can be classified as renewable and non-renewable DG technologies. DG units based on renewable energy technologies include, for instance, solar, wind, hydro, biomass and geothermal, while those based on fossil fuel include, mainly, reciprocating engines and MTs. Non-DG technologies have gained a lot of popularity because of their economic and technical benefits such as fuel economy, quick start-up, high availability, high efficiency, reliability, rigidity, multiple fuels operation, durability, low capital cost, low operating cost, high efficiency, low cost of installation and utilization for multiple applications. These characteristics have made non-renewable DG technologies to be widely accepted for industrial, commercial and domestic applications. Currently, non-renewable DG technologies are being used as prime movers for automobiles, industrial equipment, ship propulsion and numerous machinery and equipment. They are also flexible and suitable for electrical power generation and CHP applications. Non-renewable DG technologies can be utilized by the utilities and consumers to offer power solutions through stand-alone, peak shaving, grid support, backup, CHP, standby or emergency, prime and continues applications.

References

1. Kaundinya DP, Balachandra P, Ravindranath NH (2009) Grid-connected versus stand-alone energy systems for decentralized power—a review of literature. *Renew Sustain Energy Rev* 13(8):2041–2050
2. Owens B (2014) The rise of distributed power. *Ecomagination*, pp 1–47
3. Bulent Koc A, Abdullah M (2013) Performance and NO_x emissions of a diesel engine fuelled with biodiesel–diesel–water nanoemulsions. *Fuel Proc Technol* 109:70–77
4. Kanoğlu M, Işık SK, Abuşoğlu A (2005) Performance characteristics of a diesel engine power plant. *Energy Convers Manag* 46(11–12):1692–1702
5. Gupta SB, Biruduganti M, Bihari B, Sekar R (2012) Natural gas fired reciprocating engines for power generation: concerns and recent advances. *Intech*, pp 211–234
6. Chollacoop N, Saisirirat P, Fukuda T, Fukuda A (2011) Scenario analyses of road transport energy demand: a case study of ethanol as a diesel substitute in Thailand. *Energies* 4:108–125

7. Dismukes DE, Kleit AN (1999) Cogeneration and electric power industry restructuring. *Resour Energy Econ* 1999(21):153–166
8. Hountala DT, Kouremenos AD (1999) Development and application of a fully automatic troubleshooting method for large marine diesel engines. *Appl Therm Eng* 19:299–324
9. Adefarati T, Bansal RC (2016) Integration of renewable distributed generators into the distribution system: a review. Available on line RPG IET, 2016
10. IEEE Std. 446-1995 (1995) IEEE recommended practice for emergency and standby power systems for industrial and commercial applications
11. Final Report for Assessment of Visibility and Control Options for Distributed Energy Resources. <http://www.caiso.com/Documents/FinalReport-Assessment-Visibility-ControlOptions-DistributedEnergyResources.pdf>. Assessed on 23 Apr 2016
12. Kaundinya DP, Balachandra P, Ravindranath NH (2009) Grid-connected versus stand-alone energy systems for decentralized power—a review of literature. *Renew sustain Rev* 8(8):2041–2050
13. Energy Information Administration. EIA data for 2010
14. Mittal ML (2012) Estimates of emissions from coal fired thermal power plants in India. In: 2012 international emission inventory conference, Florida, USA, 2012, pp 1–22
15. EPA AP-42. Natural gas fired reciprocating engines
16. National Renewable Energy Laboratory (2003) Gas fired distributed energy resource technology characterizations. <http://www.nrel.gov/docs/fy04osti/34783.pdf>. Accessed on 21 Apr 2016
17. Canova A, Chicco G, Genon G, Mancarella P (2008) Emission characterization and evaluation of natural gas-fuelled cogeneration microturbines and internal combustion engines. *Energy Convers Manag* 49(10):2900–2909
18. Moreira JML, Cesaretti MA, Carajilescov P, Maiorino JR (2015) Sustainability deterioration of electricity generation in Brazil. *Energy Policy* 87:334–346
19. Daim TU (2016) Hierarchical decision modelling. Springer International Publishing Switzerland
20. Govender T (2013) Energy supply challenges in South Africa. In: Proceedings of 13th African utility week, Cape town, South Africa, pp 1–25
21. SFA pacific, Inc. North America combustion handbook
22. Masters GM (2013) Renewable and efficient electric power systems, 2nd edn. Wiley, New York, pp 170–175
23. Borbely A, Kreider JF (2011) Distributed generation the power paradigm for the new millennium. CRC Press, Washington DC, pp 20–250
24. Review of combined heat and power technologies. Energy efficiency and renewable energy. <http://www.distributed-generation.com/Library/CHP.pdf>
25. Kiaee M, Tousi AM, Toudefallah M (2015) Performance adaptation of a 100 kW microturbine. *Appl Therm Eng* 87:234–250
26. Ismail MS, Moghavvemi M, Mahlia TMI (2013) Current utilization of microturbines as a part of a hybrid system in distributed generation technology. *Renew Sustain Energy Rev* 21: 142–152
27. Soares C (2008) Microturbines, fuel cells, and hybrid systems. In: Burlington MA (ed) Gas turbines. Butterworth-Heinemann, Oxford, pp 617–635
28. Alimardani A, Keshtkar H, Abdi B (2011) Optimization of fuel consumption in micro-turbines. *Energy Proc* 12:779–788
29. Keshtkar H, Alimardani A, Abdi B (2011) Optimization of rotor speed variations in microturbines. *Energy Proc* 12:789–798
30. Sanaye S, Ardali MR (2009) Estimating the power and number of microturbines in small-scale combined heat and power systems. *Appl Energy* 86:895–903
31. Komatsu Y, Kimijima S, Szymid JS (2010) Performance analysis for the part-load operation of a solid oxide fuel cell-micro gas turbine hybrid system. *Energy* 35:982–988
32. San Martín JJ, Zamora I, San Martín JJ, Aperribay V, Eguia P (2010) Hybrid fuel cells technologies for electrical microgrids. *Electric Power Syst Res* 80:993–1005

33. Rajashekara K (2005) Hybrid fuel-cell strategies for clean power generation. *IEEE Trans Ind Appl* 41:682–689
34. Mousavi SGM (2012) An autonomous hybrid energy system of wind/tidal/microturbine/battery storage. *Electric Power Energy Syst* 43:1144–1154
35. Pearce JM (2009) Expanding photovoltaic penetration with residential distributed generation from hybrid solar photovoltaic and combined heat and power systems. *Energy* 34:1947–1954
36. Capehart BL, Kennedy WJ, Turner WC (2008) Guide to energy management, 5 edn. Indian Trail, The Fairmont Press, Inc., USA
37. International renewable energy agency. Renewable power generation costs in 2014. http://www.irena.org/documentdownloads/publications/re_technologies_cost_analysis-hydropower.pdf. Accessed May 2015
38. Li C, Ge X, Zheng Y, Xu C, Ren Y, Song C (2013) Techno-economic feasibility study of autonomous hybrid wind/PV/battery power system for a household in Urumqi, China. *Energy* 55:263–272
39. Kolhe M, Kolhe S, Joshi JC (2012) Economic viability of stand-alone solar photovoltaic system in comparison with diesel-powered system for India. *Energy Econ* 24:155–165
40. Xia X, Zhang J, Cass W (2012) Energy management of commercial buildings—a case study from a POET perspective of energy efficiency. *J Energy South Afr* 23:23–31
41. Numbi BP, Xia X (2015) Systems optimization model for energy management of a parallel HPGR crushing process. *Appl Energy* 149:133–147
42. Numbi BP, Zhang J, Xia X (2014) Optimal energy management for a jaw crushing process in deep mines. *Energy* 68:337–348
43. Numbi BP, Xia X (2016) Optimal energy control of a crushing process based on vertical shaft impactor. *Appl Energy* 162:1653–1661
44. Numbi BP, Xia X, Zhang J (2014) Optimal energy control modelling of a vertical shaft impact crushing process. *Energy Proc* 61:560–563
45. Abdollahi E, Wang H, Lahdelma R (2016) An optimization method for multi-area combined heat and power production with power transmission network. *Appl Energy* 168:248–256
46. Sadeghian HR, Ardehali MM (2016) A novel approach for optimal economic dispatch scheduling of integrated combined heat and power systems for maximum economic profit and minimum environmental emissions based on Benders decomposition. *Energy* 102:10–23
47. Basu M (2016) Group search optimization for combined heat and power economic dispatch. *Int J Electr Power Energy Syst* 78:138–147
48. Nguyen TT, Vo DN, Dinh BH (2016) Cuckoo search algorithm for combined heat and power economic dispatch. *Int J Electr Power Energy Syst* 81:204–214
49. Momoh JA, Meliopoulos S, Saint R (2012) Centralized and distributed generated power systems—a comparison approach. In: Future grid initiative white paper, pp 1–10
50. The potential benefits of distributed generation and the rate related issues that may impede its expansion. Report Pursuant to Section 1817 of the Energy Policy Act of 2005. <http://energy.gov/oe/downloads/potential-benefits-distributed-generation-and-rate-related-issues-may-impede-its>. Accessed June 2015
51. Jenkins N, Ekanayake JB, Strbac G (2010) Distributed generation. *IET Renew Energy Ser* 1:1–20
52. Chowdhury AA, Agarwal SK, Koval DO (2013) Reliability modelling of distributed generation in conventional distribution systems planning and analysis. *IEEE Trans Ind Appl* 39(5):1493–1501
53. Balamurugana K, Srinivasan D, Reindl T (2012) Impact of distributed generation on power distribution systems. *Energy Proc* 25:93–100
54. Gil HA, Joos G (2008) Models for quantifying the economic benefits of distributed generation. *IEEE Trans Power Syst* 23(2):327–335
55. Delfino B (2002) Modelling of the integration of distributed generation into the electrical system. In: IEEE conference of power society summer meeting, Chicago, USA, 2002, pp 170–175

56. Barker PP, de Mello RW (2011) Determining the impact of distributed generation on power systems: part 1-radial distribution systems. In: IEEE PES summer meeting, Seattle, Washington, USA, 2011, vol 3, pp 1645–1656
57. Strachana N, Farrellb A (2006) Emissions from distributed vs. centralized generation: the importance of system performance. *Energy Policy* 34:2677–2689
58. Narbel P, Hansen JP, Lien JR (2014) *Energy technologies and economics*. Springer, London, pp 170–180
59. Hung DQ, Mithulananthan N (2011) DG allocation in primary distribution systems considering loss reduction. In: *Handbook of renewable energy technology*. World Scientific Publishers, Singapore, pp 587–628
60. REN21. *Renewables 2015 global status report*
61. Thermal Power Station Advice. *Reciprocating Engines Study Report for the Electricity Commission, PB Report for the Electricity Commission, 2013*. Available on line: <https://www.ea.govt.nz/dmsdocument/963>. Accessed on 10 Mar 2016

Part II
Wind Power Systems

Chapter 3

Large-Scale Wind Generation

Development in the Mexican Power Grid: Impact Studies

Arturo R. Messina, Rafael Castellanos, Claudia M. Castro,
Emilio Barocio and Armando Jiménez Zavala

3.1 Overview

Large-scale integration of wind energy in the Mexican interconnected system (MIS) requires a careful appraisal of system dynamic characteristics and expected operating conditions. Integrating large amounts of wind energy into the system is challenging because of the variability in the power flow patterns and a more complex active and reactive power dispatch.

In recent years, several wind farms (WFs) have been installed in the Mexican system, especially in the southeastern network of the system (2.2 GW) [1, 2] increasing the complexity of the system and its variability. Other significant wind generation projects are being planned or announced (3.9 GW) based upon the doubly fed induction generator (DFIG) technology [2].

The incorporation of new wind farm resources into the southeastern grid is expected to have a major impact on system frequency and voltage control, particularly as the amount of wind generation becomes a significant portion of the local hydrogeneration and WFs grow in size and complexity.

To address the interconnection impacts, detailed planning models of both WFs and the associated voltage and speed control systems are being developed or

A.R. Messina (✉) · C.M. Castro · A. Jiménez Zavala
The Center for Research and Advanced Studies,
CINVESTAV, Guadalajara, Mexico
e-mail: aroman@gdl.cinvestav.mx

R. Castellanos
Electrical Research Institute, Palmira, Mexico
e-mail: rcb@iie.mx

E. Barocio
The University of Guadalajara, Guadalajara, Mexico
e-mail: Emilio.barocio@cucei.udg.mx

updated. Using recent planning and operational data, dynamic simulation studies of several critical scenarios associated with a large percentage of electricity from wind are conducted on a realistic planning model of the MIS. Barriers and challenges for the penetration of wind energy into the system are identified, and the effects of added generation on major power flows, voltage profiles, and system frequency performance are evaluated under disturbance conditions. Advanced generation scheduling and control of hydroresources are also investigated to meet the continuously changing demand.

3.2 System Description and Scenario Definitions

The bulk MIS is constituted by the integrated operation of seven regional networks designated as northwestern (NW), northern (N), northeastern (NE), western (W), central (C), southeastern (SE), and the Peninsular (P) areas. The total peak-load demand for the system is currently about 38,000 MW.

A schematic diagram of this system is shown in Fig. 3.1 showing the location of key critical interfaces and wind generation sites. General characteristics of this system are described in [2, 3]. Due to its sparse structure, large system

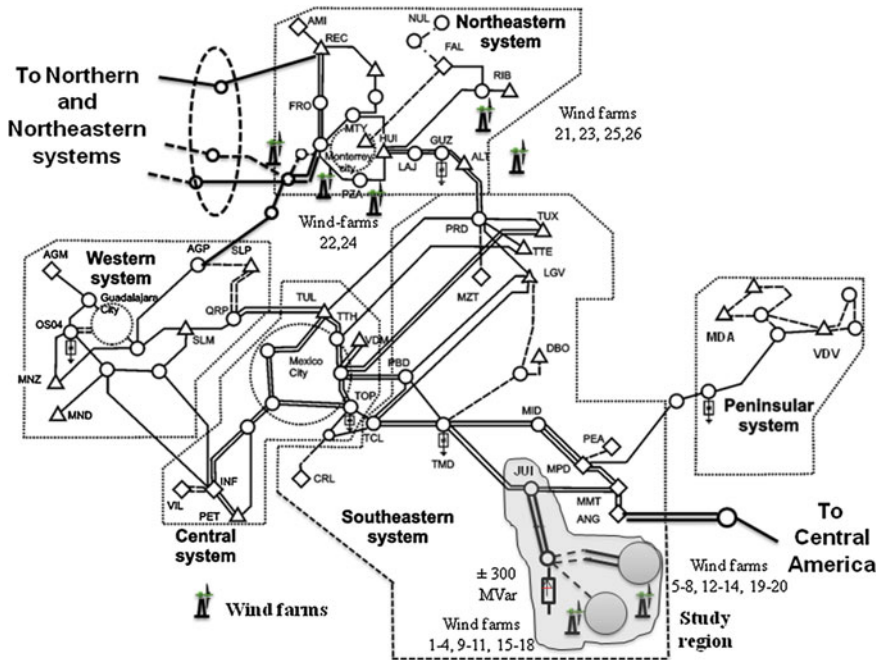


Fig. 3.1 Schematic diagram of the Mexican interconnected system indicating the approximate location of major wind farms and key interfaces in the system

Table 3.1 Total installed wind generation in the system

Area	No. of wind farms	Installed capacity (MW)	POI rated voltage (kV)
Southeastern	24	2250	400
Western	2	150	115
Northwestern	1	10	34.5
Northeastern	2	75	115/138/230
Northern	1	225	230

contingencies such as the loss of major generators or loads result in severe generation–load imbalances often leading to automatic under frequency load shedding (UFLS). To maintain system stability and satisfy design standards, extensive use has been made of special protection systems/remedial schemes including generation tripping and fast acting UFLS schemes [3].

The installed level of wind generation in the MIS has grown significantly over the last decade. Most of this generation is located at the southeastern and northern regions and must be transmitted over long distances to the major load centers in the central, western, and northeastern regions of the system.

Of particular interest, twenty WFs are installed in the SE system (shaded region in Fig. 3.1) and are the subjects of this study. A large SVC (± 300 MVar) provides voltage support to the 400-kV lines that connect the WFs to the bulk 400-kV network [4].

Table 3.1 summarizes the main characteristics of WFs installed in the system, showing the installed capacity and the point of interconnection (POI) voltages. At present, there is over 2250 MW of wind power installed in the SE system; by contrast, the total peak demand in the SE network is about 3200 MW.

3.2.1 *The SE Transmission System*

The SE network of the MIS consists, predominantly, of a longitudinal 400-kV transmission system characterized by long transmission lines, remote generation sources, and sparse load distribution. Capacitive series compensation and fast dynamic voltage support by means of several large SVCs allow for increased transient and small-signal stability margins and enhanced voltage regulation [3].

Local generation includes four large hydropower plants accounting for about 5 GW of installed capacity—see Table 3.2. This makes the power flow across the 400-kV SE network more variable and difficult to predict.

Operational experience shows that wind integration has a noticeable impact on the time frame associated with the system inertial response and primary regulation time frames. Specific concerns identified include the following:

(1) At high penetration levels of wind generation, a key concern is determining the (minimum) amount of dispatchable hydrogeneration to balance wind variability;

Table 3.2 Main generation in the SE system

Generating station	Type	Station capacity (MW)	AGC contribution	Supplementary control
Chicoasen (MMT)	Hydro	8 × 300	Yes	PSS
Malpaso (MPD)	Hydro	6 × 200	Yes	–
Angostura (ANG)	Hydro	5 × 190	Yes	–
Peñitas (PEA)	Hydro	4 × 100	Yes	–
Laguna Verde (LAV)	Nuclear	2 × 600	No	–

(2) large wind power ramping events, especially during the early morning hours and late afternoon hours, result in a more complex operation of the grid; and (3) wind power may affect the frequency nadirs and, therefore, the performance of UFLS scheme strategies in the system.

Within this framework, the following mechanisms have been identified to affect system dynamic behavior in the southeastern network of the MIS.

Power flow redistribution across the southeastern–central interface

- (i) *Displacement of hydrogeneration in the system:* Large-scale wind integration in the SE lowers system inertia. As a result, the rate of change of frequency increases and the minimum frequency decreases during disturbances. This, in turn, affects the operation of UFLS scheme strategies.
- (ii) *Modification of active and reactive power flow dispatch,* resulting in more complex operating strategies.
- (iii) *Voltage profile and reserve management:* Displacement of synchronous generators can affect voltage profiles and result in a complex strategy to provide dynamic reserves in both SVCs and synchronous generators.

These issues are discussed next. First, operational issues are identified.

3.2.2 Operational Challenges Presented by Wind Generation

Because of their location relative to the bulk 400-kV network and the relatively weak transmission systems, the integration of new wind generation in the SE system presents multiple technical challenges to system security and reliability that need to be addressed.

Several issues, in particular, make the integration of wind power (and other variable resources) difficult:

- (1) Wind power spatial distribution. A large amount of wind power is concentrated on a small geographical region making geographic diversity of wind power small (refer to Fig. 3.1).

- (2) Wind power intermittency. Wind power fluctuations ranging from 0 to about 100 MW within an hour are not uncommon, especially early in the morning or late in the afternoon. Further, wind generation is out of phase with load power demand, thus adding to system variability.
- (3) Relative size. The ratio of wind power relative to hydrogeneration in the southeastern system is high. As a result, the local AGC must correct the random fluctuations in both—wind generation and load demand.
- (4) Point of interconnection. WFs in the southeastern network are connected radially to the bulk 400-kV system. As a result, loss of SVC voltage support or major transmission lines may result in the loss of a large amount of wind generation.

At present, almost all of wind and hydrogeneration in the SE system is transmitted to the C system through a radial five-circuit 400-kV corridor (refer to Fig. 3.1) rendering the control of the interchange schedule difficult [1, 2]. The amount of power transfer through this interface and the lack of voltage support at key system locations have been shown to have a detrimental effect on system damping and transient stability [3].

Owing to its fast response, hydrogeneration in the southeastern system is especially well suited to balance wind variability providing the dynamic reserves needed for missed wind power and load forecasts. Integrating wind and hydro-power, however, presents unique challenges for current operating and reliability practices and can be affected by other technical, environmental, and economic issues as discussed below.

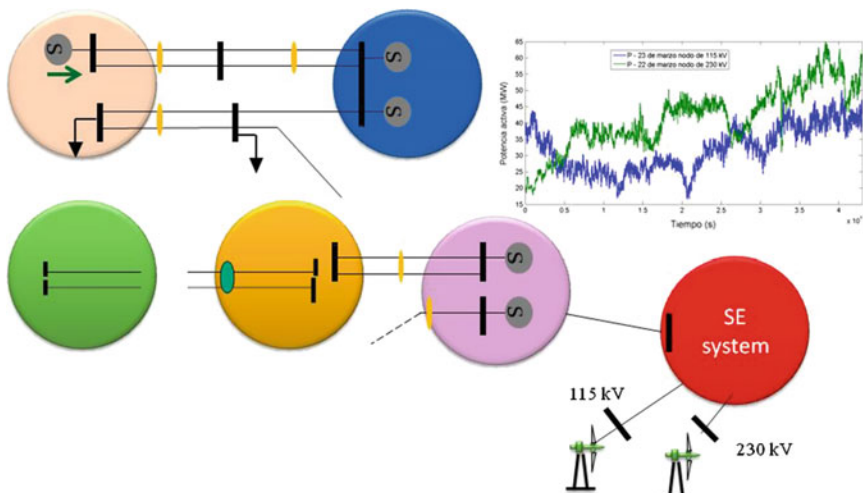
Figure 3.2a gives a pictorial representation of the Mexican power grid showing the location of major WFs; the inset shows representative SCADA recordings of wind generation output at the POI of two nearby WFs. Data were recorded every 4 s by the MIS SCADA system.

Figure 3.2b depicts one week of total power output of WFs showing typical wind power variability and sudden changes in wind power levels.

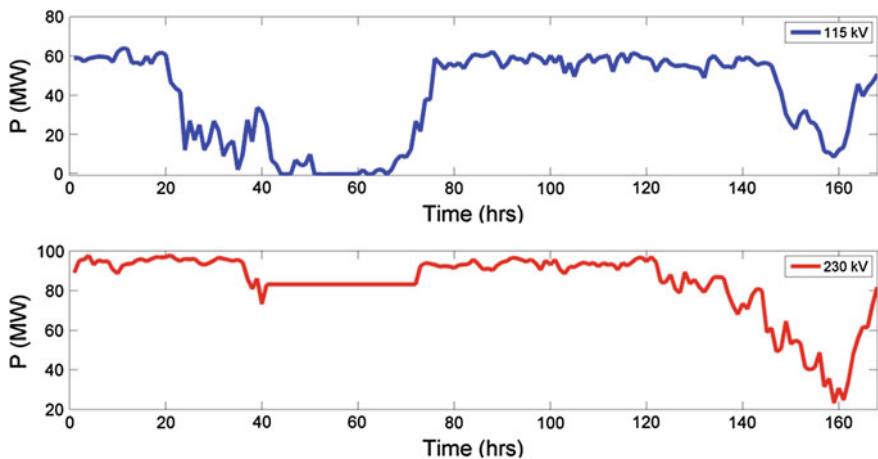
3.3 Short-Term Wind Generation Forecasting

Monitored wind power data provide a good indication for the order of magnitude and frequency of wind power output changes [5, 6]. Measured data may also be used to assess the impact of short-term output variations in WFs on system operation, as well as to determine the collective contribution of WFs to oscillatory response [7].

Owing to its stochastic nature, each wind power time series is represented by an unobserved component model of the form [8]:



(a) Schematic of the MIS showing one day of active power output from two wind farms.



(b) SCADA recordings. One week of total power output from wind farms in the SE system.

Fig. 3.2 Schematic of the MIS showing representative wind power measurements at two key system locations

$$x(t) = T(t) + S(t) + \varepsilon(t) \tag{3.1}$$

where $x(t)$ is the observed time series, t denotes time, $T(t)$ and $S(t)$ represent the trend and quasi-cyclical components, respectively, and ε is an irregular component normally distributed Gaussian sequence with zero-mean value and variance σ_ε^2 .

Early work suggested that time series can be separated into a time-varying mean and a nonstationary fluctuating component by virtue of advanced time series analysis techniques. These representations are of the form [9]:

$$x(t) = T(t) + \sum_{j=1}^p A_j(t) \cos \varphi_j(t) \quad (3.2)$$

where p is the number of relevant modes, and $A_j(t)$ and $\varphi_j(t)$ are the instantaneous amplitude and phase of the j th component, respectively.

In the problem considered here, the unobserved component model and (Eq. 3.1) the time-varying components $T(t)$, $S(t)$ are represented by a dynamic harmonic regression (DHR) model of the form [10]:

$$x(t) = T(t) + S(t) + \varepsilon(t) = \sum_{j=0}^R a_j(t) \cos(\omega_j t) + b_j(t) \sin(\omega_j t) + \varepsilon(t) \quad (3.3)$$

where the $\omega_j(t)$ are the fundamental and harmonic frequencies of the sinusoidal components associated with the j th DHR component.

In this representation, $a_j(t)$ and $b_j(t)$ are assumed to be stochastic, time-varying parameters that follow a Generalized Random Walk (GRW) process, and $\varepsilon(t)$ is used to represent noise in the observed time series; $a_0(t)$ is a slowly varying component or a trend $T(t) = S(\omega = 0) = a_0(t)$. Therefore, nonstationarity is allowed in the various components.

3.3.1 State-Space Modeling Framework

To account for the time-varying nature of the wind data, a random walk plus noise model in which the evolution of every $2R + 1$ parameters in Eq. 3.3 is characterized by two stochastic variables; the level or amplitude, $l_j(t)$, and the slope or drift, $d_j(t)$ [11], is proposed.

Let the stochastic state vector be defined as $\mathbf{x}_j(t) = [l_j(t) \quad d_j(t)]^T$. The state-space equation of Eq. 3.3 can be written as a Gaussian model of the form

$$\mathbf{x}_{j,t} = \mathbf{x}_j(t) = \mathbf{F}_j \mathbf{x}_j(t-1) + \mathbf{G}_j \boldsymbol{\eta}_j(t), \quad j = 0, 1, \dots, R \quad (3.4)$$

where $\boldsymbol{\eta}_j = [v_{j,t} \quad \xi_{j,t}]^T$, $\{v_{j,t}\} \sim w.n \quad N(0, \sigma_{v_j}^2)$, and $\{\xi_{j,t}\} \sim w.n \quad N(0, \sigma_{\xi_j}^2)$, with

$$\mathbf{F}_j = \begin{bmatrix} \alpha_j & \beta_j \\ 0 & \gamma_j \end{bmatrix}; \quad \mathbf{G}_j = \begin{bmatrix} \delta_j & 0 \\ 0 & 1 \end{bmatrix}$$

The overall state-space model can be constructed by combining the individual state representations in Eq. 3.4, and the DHR model in Eq. 3.3, and can be written as

$$\begin{cases} \mathbf{x}_t = \mathbf{F}_t \mathbf{x}_{t-1} \mathbf{G} \boldsymbol{\eta}_t \\ \mathbf{y}_t = \mathbf{H}_t \mathbf{x}_t + \boldsymbol{\xi}_t \end{cases} \quad (3.5)$$

Once the dynamic model has been expressed in state-space form, the Kalman filter can be used to estimate the states or time-varying parameters.

3.3.2 Smoothing Algorithms

To introduce the adopted model, consider the problem of estimating a state vector \mathbf{x} (k) associated with a stochastic dynamic system modeled by the simple Gauss–Markov process [12]:

$$\begin{aligned} \mathbf{x}_{j_i} &= \mathbf{F}_j \mathbf{x}_{j_i} + \mathbf{G}_j \boldsymbol{\eta}_{j_i} \\ \mathbf{y}_{j_i} &= \mathbf{H}_j \mathbf{x}_{j_i} + \boldsymbol{\xi}_{j_i} \end{aligned}$$

where \mathbf{y}_j is a $px1$ -dimensional vector of observations that are linearly related to the state vector \mathbf{x}_j by the matrix \mathbf{H}_j and $\boldsymbol{\eta}_{j_i}$ and $\boldsymbol{\xi}_{j_i}$ are zero-mean statistically independent white-noise disturbance vectors with possibly time-variable covariance matrices \mathbf{Q}_j and \mathbf{R}_j , respectively.

In conventional practice, estimation of the state \mathbf{x} relies on the application of the Kalman filter. Given a set of measurements, $x(t_0), \dots, x(t_N)$ the optimal estimate $\hat{x}(t+1)$ of $x(t+1)$ can be obtained by minimizing the expected value of the magnitude of the error $\min_{\hat{\mathbf{x}}} \left\{ \left[\|\mathbf{x}_t - \hat{\mathbf{x}}_{t|\tau}\|^2 \right] \right\}$ where the subscripts $t|\tau$ refer to an estimate at time t given information up to and including time τ .

Dynamic harmonic regression techniques estimate the time-varying parameters using a two-step (prediction-correction) Kalman filter, followed by a fixed interval smoothing algorithm.

The Kalman filter algorithm can be described by the following equations for each time period $t = 1, \dots, N$ [13]:

Prediction

$$\begin{aligned} \hat{\mathbf{x}}_{t|t-1} &= \mathbf{F} \hat{\mathbf{x}}_{t-1|t-1} \\ \mathbf{P}_{t|t-1} &= \mathbf{F} \mathbf{P}_{t-1|t-1} \mathbf{F}^T + \mathbf{G} \mathbf{Q} \mathbf{G}^T \end{aligned} \quad (3.6a)$$

Correction

$$\begin{aligned}
\Lambda_t &= \mathbf{y}_t - \mathbf{H}\hat{\mathbf{x}}_{t|t-1} \\
\mathbf{S}_t &= \mathbf{H}\mathbf{P}_{t|t-1}\mathbf{H}^T + \mathbf{R}_t \\
\mathbf{K}_t &= \mathbf{P}_{t|t-1}\mathbf{H}^T\mathbf{S}_t^{-1} \\
\hat{\mathbf{x}}_{t|t} &= \hat{\mathbf{x}}_{t|t-1} + \mathbf{K}_t\Lambda_t \\
\mathbf{P}_{t|t} &= (\mathbf{I} - \mathbf{K}_t\mathbf{H})\mathbf{P}_{t|t-1}
\end{aligned} \tag{3.6b}$$

where $\mathbf{Q} = \text{diag}[\sigma_v^2, \sigma_\xi^2]$, with initial conditions $\hat{\mathbf{x}}_0$ and \mathbf{P}_0 , and the notation $\hat{\mathbf{x}}_{t|t-1}$ is used to indicate the estimate of $\mathbf{x}(t)$ given the observations $x(0), \dots, x(t-1)$. Here, Λ_t is the one-step-ahead prediction error (innovation), \mathbf{S}_t is its variance, \mathbf{K}_t is the optimal Kalman gain, and $\hat{\mathbf{x}}_{t|t}$ and $\mathbf{P}_{t|t}$ represent the updated state estimate and the updated estimate covariance for the state vector, respectively.

During the prediction state, the optimal estimate of the state vector at time t becomes $\hat{\mathbf{x}}_{t|t-1} = \mathbf{F}\hat{\mathbf{x}}_{t-1|t-1}$, and the associated covariance matrix of the estimation error is $\mathbf{P}_{t|t-1} = \mathbf{F}\mathbf{P}_{t-1|t-1}\mathbf{F}^T + \mathbf{G}\mathbf{Q}\mathbf{G}^T$; the updating Eqs. 3.6a, b are then used to calculate a new estimate of the state as new observations arrive.

After the filtering stage, a fixed interval smoother is used to update (correct) the filter estimated state $\hat{\mathbf{x}}_{t|t}$. In this case, using the output of the Kalman filter, smoothing takes the form of a backward recursion for $t = N, \dots, 1$, operating from the end of the sample set to the beginning:

$$\begin{aligned}
\hat{\mathbf{x}}_{t+1|N} &= \hat{\mathbf{x}}_{t+1|t+1} - \mathbf{P}_{t+1}^* \mathbf{F}_{t+1}^T \lambda_{t+1} \\
\mathbf{P}_{t|N}^* &= \mathbf{P}_{t|t}^* + \mathbf{P}_t^* \mathbf{F}_t \mathbf{P}_{t+1|t}^*{}^{-1} [\mathbf{P}_{t+1|N}^* - \mathbf{P}_{t+1|t}^*] \mathbf{P}_{t+1|t}^*{}^{-1} \mathbf{F}_t^* \mathbf{P}_t^* \\
\lambda_t &= (\mathbf{I} - \mathbf{H}_{t+1}^T \mathbf{R}_{t+1}^T \mathbf{H}_{t+1} \mathbf{P}_{t+1|t+1}) \mathbf{F}_{t+1}^T \lambda_{t+1} \\
&\quad - \mathbf{H}_{t+1}^T \mathbf{R}_{t+1}^{-1} (\mathbf{y}_{t+1} - \mathbf{H}_{t+1} \hat{\mathbf{x}}_{t+1|t+1})
\end{aligned} \tag{3.7}$$

Smoothing allows estimating the state vector at a given time point (given all the available data) and hence, to interpolate missing observations in the observed time series and the associated mean-square error of the interpolated estimates.

Equations 3.6a, b–3.7 describe a recursive algorithm that runs backward in time from the last observation. In the first stage, the estimates $\hat{\mathbf{x}}_{t|t-1}$ and $\mathbf{P}_{t|t-1}$ are the one-step-ahead state estimates and the associated covariance matrix is obtained from Eqs. 3.6a, b.

3.3.3 Stochastic Trend Extraction

Approaches to the analytical characterization of the slow trend of wind power time series are of ongoing interest for model prediction and forecasting. In the adopted

formulation, the trend is modeled by a local linear trend model of the form 3.4, where $\mathbf{x}_{o_t} = [a_{o_t} \ \hat{a}_{o_t}]^T$, $\boldsymbol{\eta}_o = [v_{j_o} \ \xi_{j_o}]^T$. Therefore, estimation of the noise covariance matrices \mathbf{Q} , \mathbf{R} and the associated distributions $\sigma_{\varepsilon t}^2$ is central for practical implementation of this method. Following [3], let the signal–noise ratio (SNR) in \mathbf{Q}_t be defined as $\text{SNR} = \sigma_{\xi}^2 / \sigma_{\varepsilon}^2$. To initiate the algorithm, an estimate of the initial trend and the SNR matrix is needed, and the SNR must be estimated separately.

The SNRs are estimated in the frequency domain. The method is based on the fact that the pseudo-spectrum of the DHR model of the $R + 1$ different frequency components included in the model can be written as [8]:

$$f_y(\omega, \boldsymbol{\sigma}^2) = \frac{1}{8\pi} \sum_{j=0}^R \left[\frac{\sigma_{\omega_j}^2}{(1 - \cos(\omega + \omega_j))^2} + \frac{\sigma_{\omega_j}^2}{(1 - \cos(\omega - \omega_j))^2} \right] + \frac{\sigma^2}{2\pi} \quad (3.8)$$

where $\boldsymbol{\sigma}^2 = [\sigma^2 \ \sigma_{\omega_0}^2 \ \sigma_{\omega_1}^2 \ \dots \ \sigma_{\omega_R}^2]$; $\sigma_{\omega_0}^2$ is the variance associated with the zero frequency term, i.e., with the trend, and the terms $\sigma_{\omega_i}^2$ are the variances associated with the harmonic components, and σ^2 is the variance of $\varepsilon(t)$.

Under the assumption that each element $a_j(t)$ and $b_j(t)$ follows an autoregressive (AR) process, the time-varying parameters can be estimated by minimizing an appropriate functional.

The problem can be mathematically stated as follows:

$$J = \sum_{i=0}^R [f_y(\omega_i) - \hat{f}_y(\omega_i, \boldsymbol{\sigma}^2)]^2 \quad (3.9)$$

where $f_y(\omega_i)$ is the spectrum of $y(t)$.

First, the dominant harmonic frequencies $\omega_i, \forall i = 1, 2, \dots, R$ are extracted from the AR spectrum of the observed time series. Then, the unknown parameters are estimated from least-squares optimization of the functional 3.9. Once these parameters are estimated, the time-varying trends and harmonic components can be obtained using the Kalman filter approach discussed earlier.

In current approaches, the R oscillatory components $\omega_j, j = 1, 2, \dots, R$ are estimated separately using an AR model of the observed data.

Application to wind power time series forecasting is discussed below.

3.3.4 Short-Term Prediction of Wind Output

From Eq. 3.4, model prediction for wind power output at time t is given by

$$\mathbf{x}_j(t) = \mathbf{F}_j \mathbf{x}_j(t-1) \quad (3.10)$$

for $t = 1, \dots, T$. A short-term prediction technique based on the above model has been developed to estimate wind power output using a sliding window approach. A conceptual representation of this model is shown in Fig. 3.3a.

To provide efficient short-term prediction, the method is applied to short segments of data. In this case, a moving data window is used. First, the size of each window, N_s , and the forecasting horizon F_h are defined; then, the number of moving samples N_w is selected. The parameters k^i and p^i are used to indicate where the i th window starts and finishes. Formally, the model can be described as

$$\begin{aligned} k^i &= N_w(i - 1) + 1 \\ p^i &= N_s + N_w(i - 1), \quad i = 1, 2, \dots, N \end{aligned}$$

The sliding window approach starts from the left, attempting to begin with the oldest data. When a new sampling segment enters into the data window, the older sample is removed: Selection of an appropriate N_w allows for the use of a flexible moving window depending on the time that every new sample is recorded. This is illustrated in Fig. 3.3b that shows the definition of data-adaptive windows.

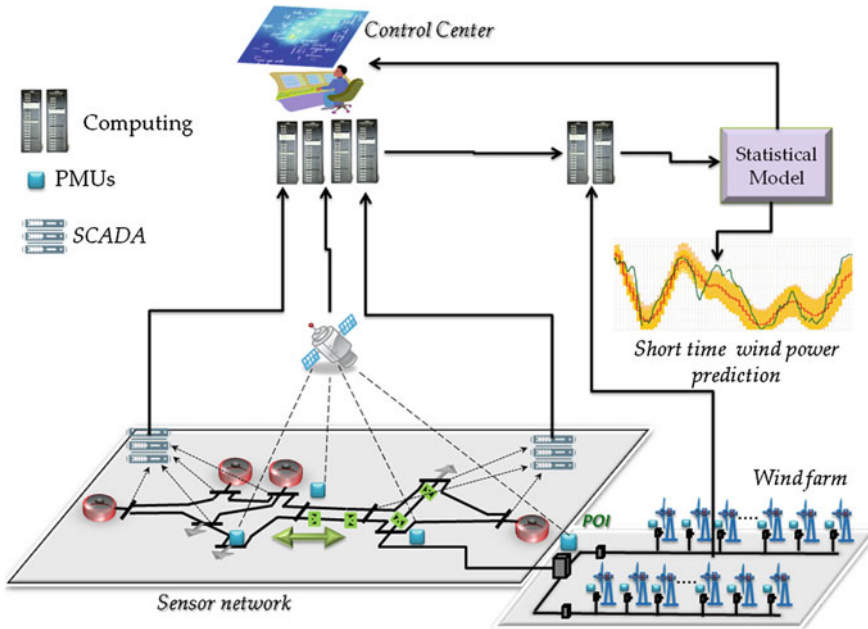
Extensions to this basic approach to allow a close-to-real-time implementation (e.g., $N_w = 1$) and typical sampling rates from 30 to 60 samples per second are being investigated. Note that, in this case, N_w and F_h are selected such that every new forecasting horizon starts where the previous ends.

Building upon these ideas, the forecasting ability of DHR was investigated. A 394-sample window, with a sampling period of 5 s, was used to obtain a 30-s forecast from each window, that is $N_w = 394$, $N_w = 6$; each of the windows was moved forward 6 samples every iteration so that $N_w = 6 = F_h = 6$.

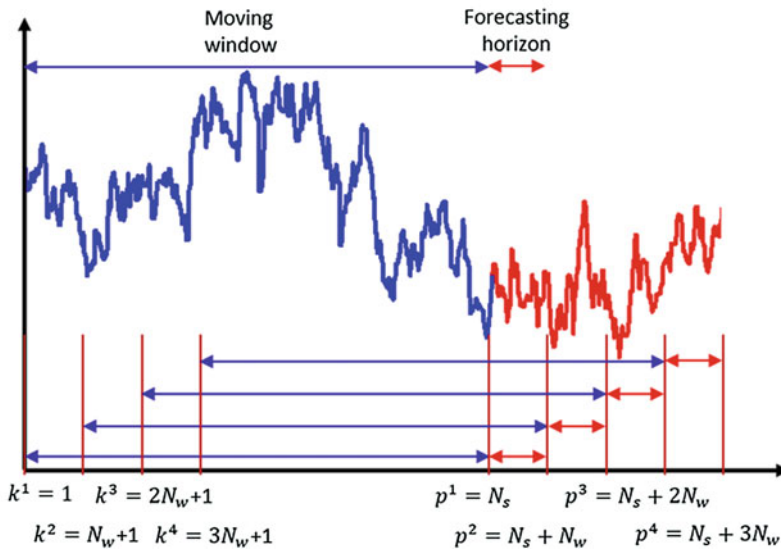
This case is represented schematically by Fig. 3.3b in which every time window is recorded so that each forecasting horizon is located after the last one. Figure 3.4 shows the application of this approach to actual measured data in Fig. 3.2a starting at $t = 1970$ s.

Results show that the proposed DHR approach is able to extract the time-varying components $T(t)$, $S(t)$ in Eqs. 3.1 and 3.3 as well as to predict wind generation output. Figure 1.4a shows the trend extracted using DHR, while Fig. 3.4b shows the detrended signal. Figure 3.4c, in turn, shows wind generation output estimates. Estimates are shown to be in good agreement with measurements as shown in the inset in Fig. 3.4c.

Comparing the complete original time series and forecasting results, the coefficient of determination indicates that the model explains 95.8% of the original data, with a mean-square forecast error, $NMSE = 1.92 \times 10^{-3}$. The cause of this high error may be explained by the use of $N_w = 6$.



(a) Schematic of the adopted approach.



(b) Sliding window DHR formulation.

Fig. 3.3 Schematic of the adopted forecasting technique

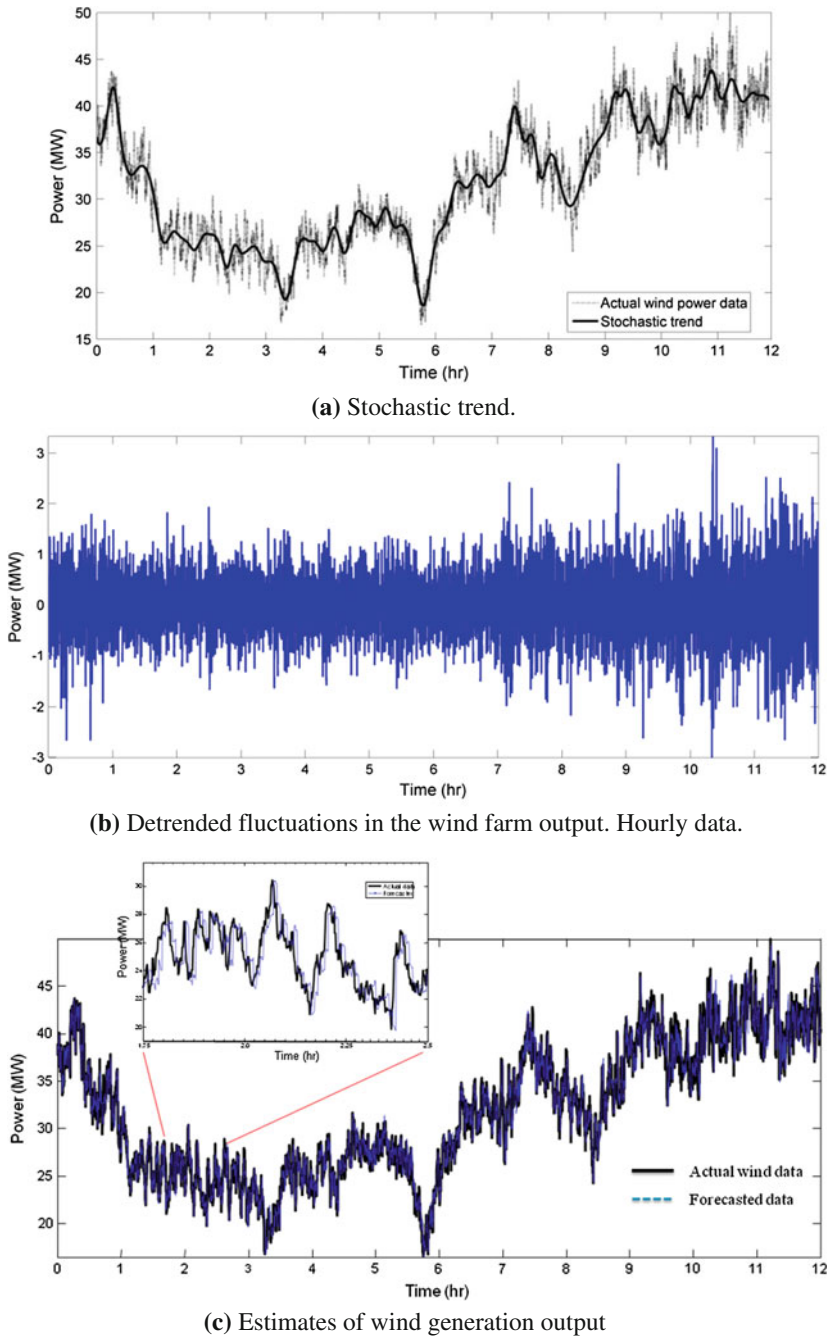


Fig. 3.4 Detrended fluctuations in the wind farm output. The regression (prediction–correction–smoothing) is shown only for the first 394 samples (the corresponding first moving window); each 30-second segment is a true forecast based on the last recorded window

3.4 Dynamic Impact of Wind Energy

WFs in the SE system have a strong influence on system behavior, including small and large system performance. Early studies indicate that WFs, especially in the SE network of the system, may affect system behavior by displacing hydrogenerators and affecting major power path flows [14, 15].

Integration issues associated with increased wind penetration are examined next.

3.4.1 Effect of Wind Generation on Oscillatory Stability

A detailed seven-area model of the Mexican power system has been developed to evaluate the effect of wind penetration on small-signal rotor angle stability. The complete system model used for dynamic simulations consists of 5449 buses, 635 generators, 5292 transmission lines, and 26 WFs. In this model, all governors on conventional generators (about 45% of generation capacity with active governor) are modeled in detail.

The seven-area MIS model includes representations of the NW, N, NE, W, C, SE, and P areas of the MIS; the study area is centered around the SE network which includes 20 large WFs (type-3 DFIG generators) connected to the 400-kV network via two 400-kV transmission lines and one large SVC.

In an initial step, small-signal stability analyzes were conducted to examine the impact of wind generation on modal stability. The seven-area MIS model has several inter-area modes that can be affected by increased wind energy penetration. Table 3.3 synthesizes the main characteristics of the slowest modes of the system, indicating the major areas participating in the oscillations.

Modes 1 and 2 are of special concern since they involve a significant participation of the 400-kV network of the SE system

Insight into the nature of oscillatory behavior can be gleaned from the analysis of the mode shapes of the two slowest inter-area modes in Fig. 3.5 obtained using small-signal analysis. Extensions to this model-based approach to include the effect of wind generation are discussed in Sect. 3.4.3.

Table 3.3 Slowest electromechanical modes of the MIS. Base-case condition

Mode	Frequency	Damping	Swing pattern
1	0.394	0.350	NW, NE systems versus SE and P systems
2	0.547	7.000	NE system versus P, NW and SE systems
3	0.653	8.620	NW systems versus P and N systems
4	0.696	7.470	NW versus W and P systems
5	0.730	1.580	C versus SE region

Two wind power flow scenarios were developed to assess the impact of increased wind penetration on system damping:

Scenario 1. A base case with 4% of expected wind energy generation based on the 2016 summer system conditions (this represents a penetration of about 8% of the hydrogeneration capacity at machines ANG, MPD, PEA, and MMT). This scenario is the base case used for comparisons.

Scenario 2. A 2016 revised case with about 15% wind energy penetration. In this case, synchronous spinning reserves are maximized to prevent large post-contingency frequency deviations and control voltage and reactive power flows at major SVCs

In addition, several further scenarios were developed considering various control strategies, i.e., hydromachines with/without power system stabilizers.

Since the SE power system is predominantly hydro, the effect of increasing wind generation in the southern portion of the SE system is examined by reducing generation at hydroplants in the SE system. In both cases, generation was redispatched and voltage profiles were optimized.

More general operating scenarios can be handled by considering operating constraints but this approach will serve for the purpose of explanation.

Detailed small-signal stability studies were performed to assess the impact of increased wind penetration on system oscillatory response. Table 3.4 shows the effect of wind generation on system damping. Examination of these exploratory simulation studies suggests that increased levels of wind penetration may have beneficial effects on the damping of inter-area modes 1 and 2, but the oscillatory phenomena are very complex and results may be affected by the assumptions used in the analysis and the accuracy of the simulation model.

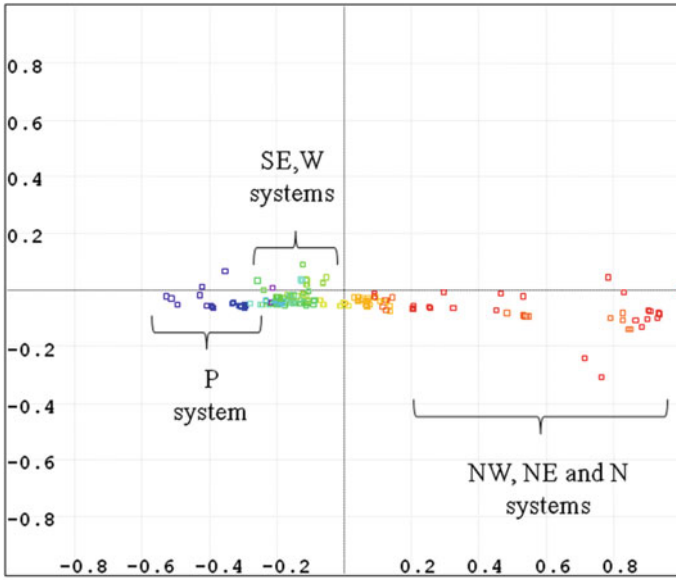
Further studies are needed since damping may be affected by several factors:

- Directly, by displacing hydrounits equipped with PSSs and fast-acting control systems in the SE system.
- Indirectly, by affecting system topology and behavior, and displacing conventional inertia.
- Indirectly, by affecting the generation pattern and power flows across the 400-kV network.

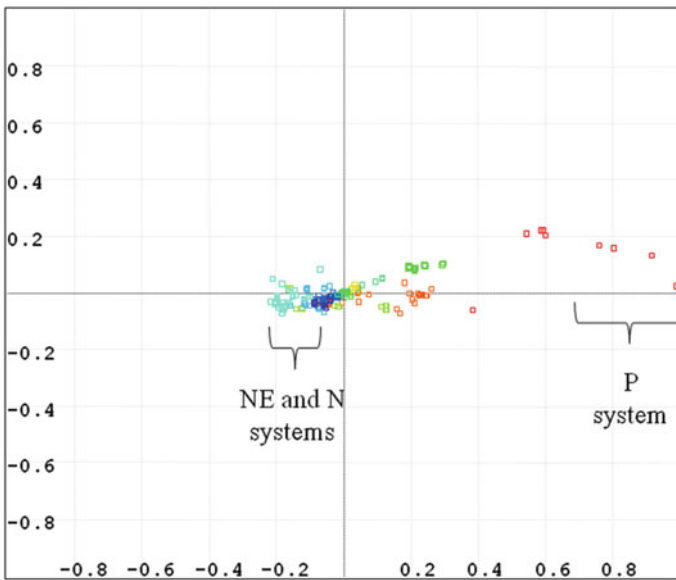
3.4.2 Large System Performance

Early transient stability studies carried out in the past have indicated that WFs in the SE and NE systems have a noticeable impact on rotor angle stability. To excite the slowest electromechanical modes and investigate the impact of wind generation on oscillatory stability, three-phase faults were applied at major 400-kV buses.

Selected simulation results are shown in Figs. 3.6 and 3.7.



(a) Inter-area mode 1



(b) Inter-area mode 2

Fig. 3.5 Normalized mode shape of inter-area modes 1 and 2

Table 3.4 Effect of wind generation on system damping for various power flow wind scenarios

Mode	Scenario 1	Scenario 2
	f (Hz) } ζ (%)	f (Hz) } ζ (%)
1	0.394 0.35	0.398 0.61
2	0.545 7.00	0.552 7.90
3	0.653 8.62	0.652 8.28
4	0.696 7.47	0.700 7.57
5	0.730 1.58	0.741 1.55

The signals of interest are bus frequency and power measurements at key system generators. For clarity of exposition, only 40 measurements from selected system generators are selected for study. These generators represent the largest unit from dominant plants participating in the oscillations.

Several issues emerge as the amount of wind generation becomes substantial in the SE system.

- WFs tend to form clusters of coherent machines for various contingency events examined. This behavior can be used to improve global (regional) wind forecasting as well as to design control and operating strategies for system mitigation. A similar behavior has been observed with the incorporation of other renewable energy sources
- WFs in the north and south systems tend to swing in opposition as shown in the lower panel in Figs. 3.6a and 3.7a. This suggests that WFs may have an impact on the energy exchange involving the north and south systems. The analysis of phase relationships cannot be studied using conventional small analysis techniques

Spectral analyses in Fig. 3.8 reveal that WFs in the SE, N, and NE systems have a dominant participation in the slowest inter-area mode at 0.41 Hz. Moreover, the spectra of machines in the SE system show relatively smaller peaks at 0.55 Hz associated with inter-area mode 2. Phase relationships associated with these spectra (not shown) provide further evidence of the underlying energy exchange process that drives system behavior.

The significant peaks in the power spectra in Figs. 3.8b, c indicate that WFs strongly participate in the slowest inter-area mode and to a lesser extent, in other high frequency modes, especially in the northern and northwestern systems.

The nature of this interaction is examined in more detail in the following sections

3.4.3 Advanced Monitoring of System Behavior

Advanced wide-area data-driven analysis techniques to extract modal behavior are being developed, which complement and extend traditional measurement-based monitoring approaches. These models may combine historical/measured data with

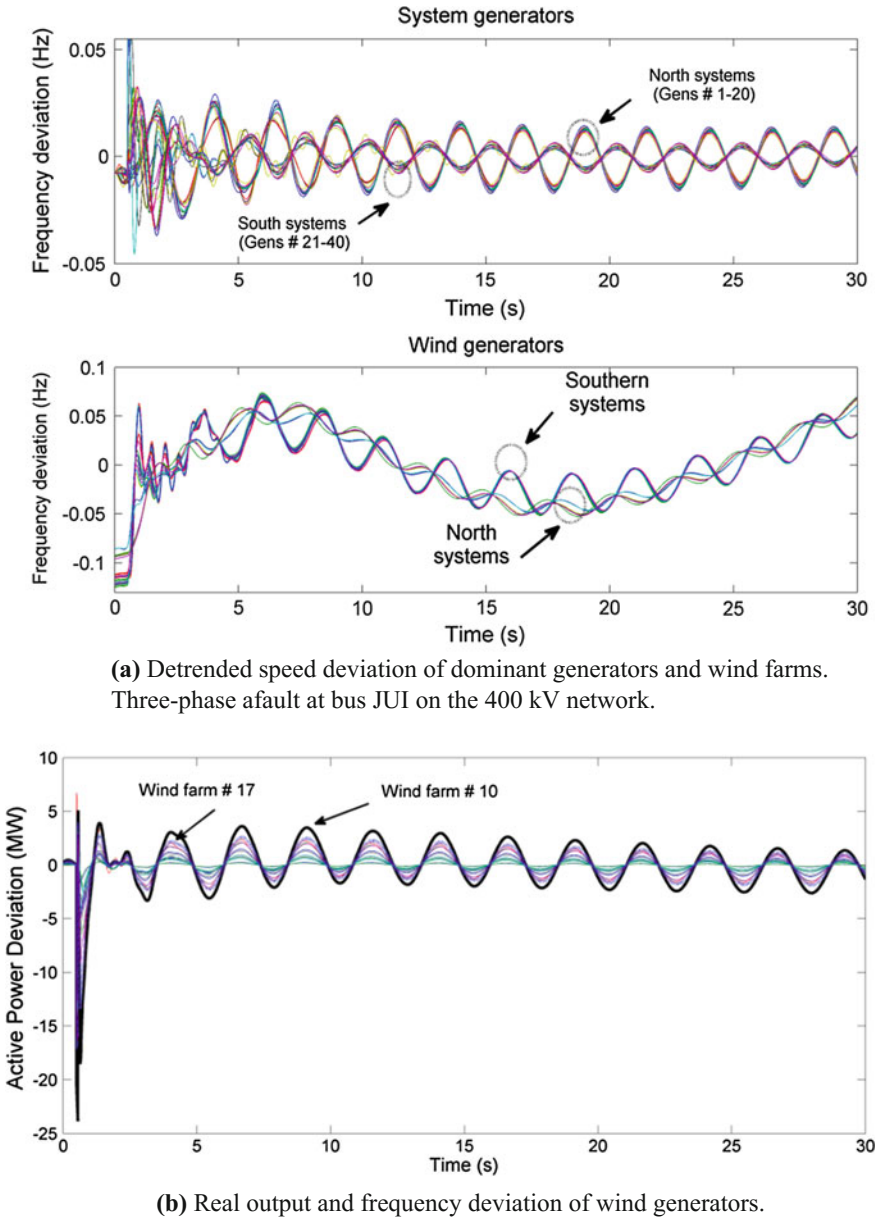


Fig. 3.6 Active power and frequency response to a three-phase fault at JUI

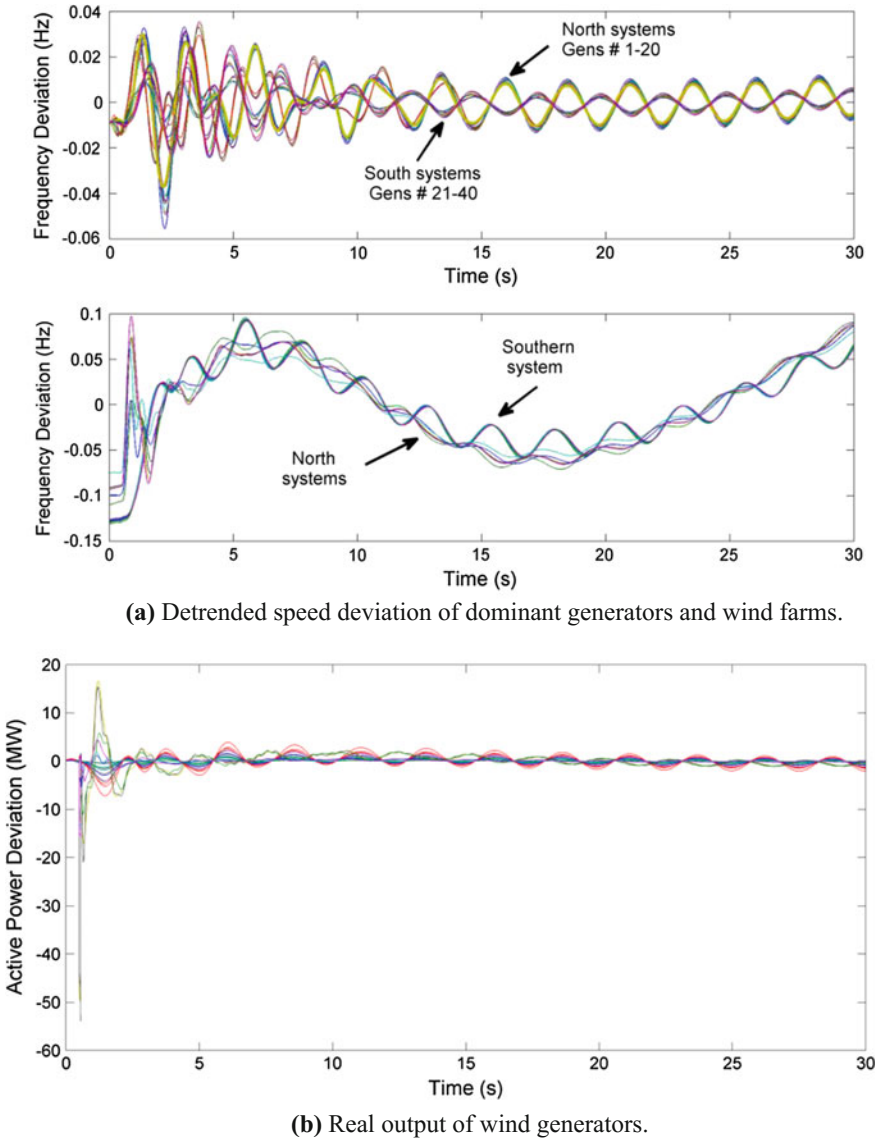


Fig. 3.7 Active power and frequency response to a three-phase fault at LAJ on the north–south interface

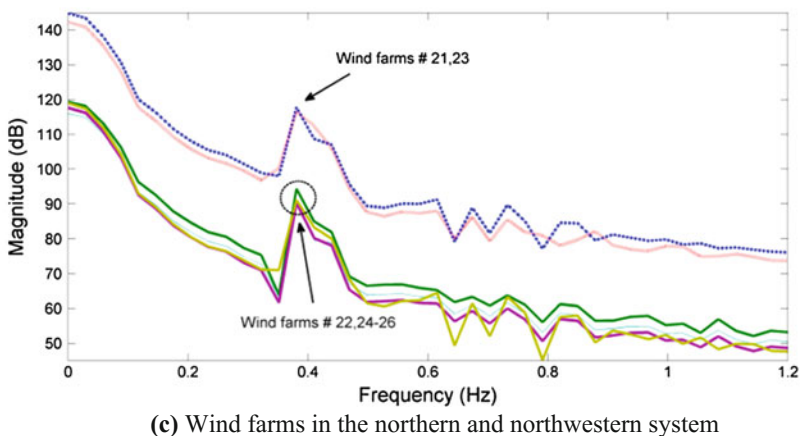
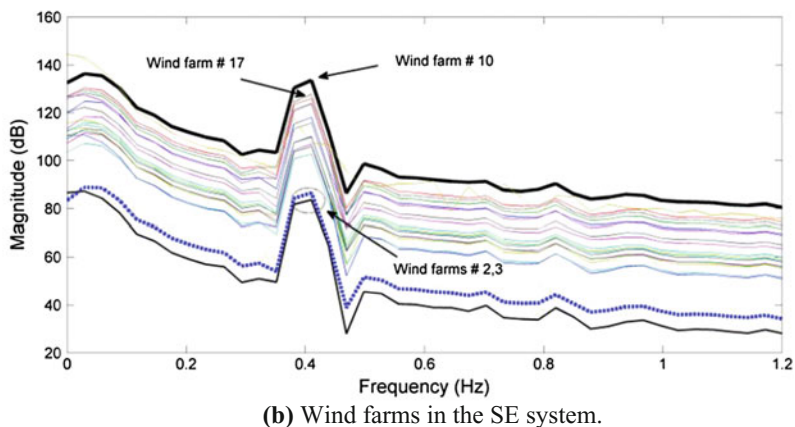
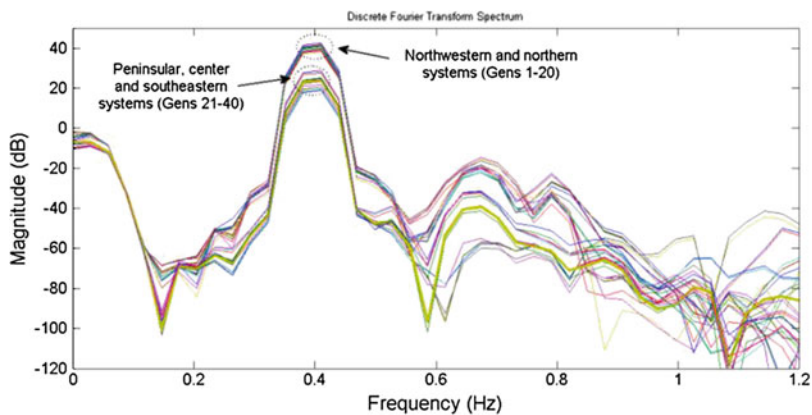


Fig. 3.8 Power spectrum of speed deviation of major system generators/wind farms

simulation data from transient stability simulations to study and better understand system behavior and can be used for automated wind data analysis.

The resulting coordinates can be correlated with the timescales of specific motion or be effectively used to extract spatiotemporal features of high-dimensional data.

The wide-area monitoring algorithm can be divided into three main steps:

- Step 1: Data collection and filtering,
- Step 2: Model reduction, and
- Step 3: Feature extraction and visualization.

The processing of massive high-dimensional sets coming from multiple sensors is posed as a data fusion problem. Assume that $\mathbf{x}_k(t_j)$ denotes a sequence of observations of a measured transient process or variables at locations (sensors) x_k , $k = 1, \dots, m$, and times t_j , $j = 1, \dots, N$. The measured variables may represent individual wind measurements or data measured at the POI of a wind farm.

The union of these data sets can be denoted as

$$\mathbf{X} = [\mathbf{X}_{\text{wind}_1} \quad \dots \quad \mathbf{X}_{\text{wind}_k} \quad \mathbf{X}_{k+1} \quad \dots \quad \mathbf{X}_m] \quad (3.11)$$

where $\mathbf{x}_j = [x_j(t_1) \ x_j(t_2) \ \dots \ x_j(t_N)]^T$, $j = k+1, \dots, m$.

The fundamental problem is the extraction of both, the dominant modes that characterize the collective motion from sparse and noisy observational data, and a reduced-order representation. A schematic of the adopted approach is shown in Fig. 3.9.

Based on this approach, several techniques to extract the dominant spatiotemporal patterns of variability from measured data have been developed. These approaches fall into the general category of multivariate estimation techniques and are briefly summarized below. The idea of these methods is to expand the data matrix \mathbf{X} as a linear combination of functions of space and time [15, 16] as:

$$\mathbf{X} = \sum_{j=1}^m \phi_j \lambda_j \mathbf{a}_j(t) = \underbrace{\sum_{j=1}^d \phi_j \lambda_j \mathbf{a}_j(t)}_{\text{Relevant system behavior}} + \underbrace{\sum_{j=1}^{d+1} \phi_j \lambda_j \mathbf{a}_j(t)}_{\text{Non-essential coordinates}} \quad (3.12)$$

where the first d components are expected to capture the system's slowest process (i.e., the slowest inter-area modes); the \mathbf{a}_j 's are the temporal modal amplitudes, the ϕ_j 's are the dynamic or spatial modes, and the λ_j 's are the associated frequencies. Examples include Dynamic Mode Decomposition (DMD) and Koopman Mode Decomposition (KMD) [16].

Two distinct problems are of interest here: (i) identifying measurements that best describe the observed system behavior, and (ii) extracting from these measurements a low-dimensional representation from which a physical, reduced-order model of the system can be obtained.

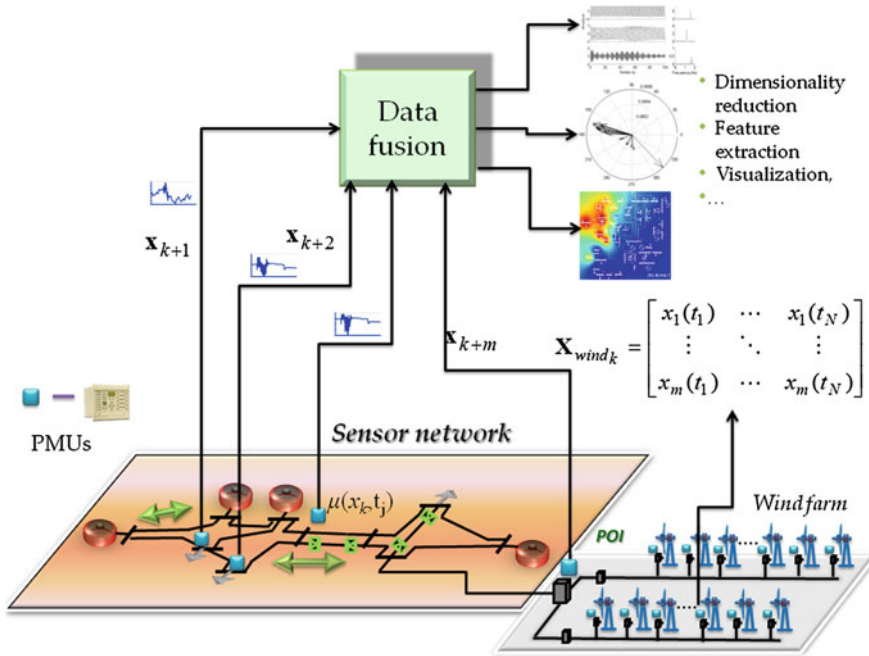


Fig. 3.9 Multivariate sensor fusion

Dimensionality reduction

Utility-scale wind integration studies are extremely challenging due in part to the dimensionality of the models and a more complex generation dispatch. However, many dynamical features of wind impact can be inferred from low-order models if the prominent structures of the data are properly represented.

In this subsection, a diffusion map (DM) framework to map high-dimensional data of the form 3.1 into a lower dimensional representation is developed that draws upon previous work.

With reference to (3.1), let the distance between two time trajectories $\mathbf{x}_i(t)$, $\mathbf{x}_j(t)$, up to time t_N , be defined as

$$k_{ij}(t) = k(\mathbf{x}_i, \mathbf{x}_j) = e^{-\|\mathbf{x}_i - \mathbf{x}_j\|^2 / \varepsilon}, \quad 1 \leq i, j \leq m,$$

where $\varepsilon > 0$ is the kernel scale [17, 18]. Note that $k_{ii} = 0$ if $\mathbf{x}_i = \mathbf{x}_j$, for all i, j , and $k_{ij} = \alpha$, otherwise. The thresholding operation has the effect of retaining only short pairwise distance.

The $m \times m$ -dimensional matrix of distances can now be defined as

$$\mathbf{K} = [k_{ij}] = \begin{bmatrix} k_{11} & \dots & k_{1m} \\ \vdots & \ddots & \vdots \\ k_{m1} & \dots & k_{mm} \end{bmatrix}$$

where the diagonal elements k_{ii} are zero by definition.

Matrix \mathbf{K} is symmetric and positivity preserving but is not positive semidefinite and can be interpreted as a weighted graph where the measurement points (sensors) are the graph nodes and the weight of the edge connecting node i to node j is the distance K_{ij} .

Once a meaningful affinity matrix is obtained, a Markov transition matrix can be defined as $\mathbf{M} = [m_{ij}] = \mathbf{D}^{-1}\mathbf{K}$, where $\mathbf{D} = [d_{ij}]$ is a diagonal matrix with elements $d_{ii} = k_{ij} / \sum_{j=1}^m k_{ij}$, $i, j = 1, \dots, m$. Spectral (eigenvalue) analysis of the locally scaled kernel provides a convenient way to extract the low-dimensional structure prevalent in the data. In pursuit of further generalization, the eigenvalue problem for the operator \mathbf{M} is expressed in terms of singular values, σ_j , as

$$\mathbf{M}\Psi_j = \sigma_j\Psi_j \quad (3.13)$$

with corresponding (nontrivial) singular vectors Ψ_j .

Since \mathbf{M} is a Markov matrix ($\sum_i m_{ij} = 1, \forall i$), the singular values σ_j are bounded in the range $[0,1]$; the eigenvectors associated with the largest singular values correspond to slow modes governing the long-time system evolution, such that

$$\underbrace{\sigma_1 \geq \sigma_2 \geq \dots \geq \sigma_d}_{\text{Slow motion}} > > \sigma_{d+1} \geq \dots \geq \sigma_m$$

It follows from the above definition that

$$\begin{aligned} \mathbf{M} &= \mathbf{D}^{-1}\mathbf{K} = \mathbf{D}^{-1/2}(\mathbf{D}^{-1/2}\mathbf{K}\mathbf{D}^{-1/2})\mathbf{D}^{1/2} \\ &= \mathbf{D}^{-1/2}\mathbf{M}_s\mathbf{D}^{1/2} \end{aligned} \quad (3.14)$$

where $\mathbf{M}_s = \mathbf{D}^{-1/2}\mathbf{K}\mathbf{D}^{-1/2} = \mathbf{D}^{1/2}\mathbf{M}\mathbf{D}^{-1/2}$.

The following properties can be easily verified. Matrix \mathbf{M}_s is symmetric (and therefore diagonalizable) and positive-definite with a decomposition $\mathbf{M}_s = \mathbf{U}\Lambda\mathbf{U}^T$, where $\Lambda = \text{diag}\{\sigma_1, \sigma_2, \dots, \sigma_m\}$ and has a complete set of singular vectors $\mathbf{U} = [\mathbf{u}_0, \mathbf{u}_1, \dots, \mathbf{u}_m]$, and $\mathbf{U}\mathbf{U}^T = \mathbf{U}^T\mathbf{U} = \mathbf{I}$ [17]. In terms of the Markov matrix defined above, it follows that the corresponding similar matrix, \mathbf{M}_s , can be written as

$$\begin{aligned} \mathbf{M}_s &= \mathbf{D}^{1/2}\mathbf{M}\mathbf{D}^{-1/2} = \mathbf{U}\Lambda\mathbf{U}^T \\ \mathbf{M} &= \mathbf{D}^{-1/2}\mathbf{U}\Lambda\mathbf{U}^T\mathbf{D}^{1/2} = \Psi\Lambda\Phi = \sum_{j=1}^m \sigma_j\Psi_j\Phi_j \end{aligned} \quad (3.15)$$

where $\Psi = \mathbf{D}^{-1/2}\mathbf{U}$, $\Phi = \mathbf{U}^T \mathbf{D}^{1/2}$, $\Psi = [\psi_0, \psi_1, \dots, \psi_{m-1}]$, $\Phi = [\phi_0, \phi_1, \dots, \phi_{m-1}]$.

Associated with the spectral model, the diffusion distance, \hat{d}_{ij} , can now be defined in terms of the forward probabilities \mathbf{M} , as

$$\left\{ \hat{d}_{ij} = \sum_{r=1}^m \frac{(M_{ir} - M_{jr})}{\Psi(x_r)}; \Psi(x_m) = \frac{\sum_{j=1}^m M_{jm}}{\sum_{k=1}^m \sum_{j=1}^m M_{jk}} \right. \quad (3.16)$$

As discussed below, diffusion distances can be used to identify spatial patterns associated with dynamic trajectories or measurements (clustering). The d -dimensional diffusion map is defined at time t , as the map $\Psi = [\lambda_1 \psi_1, \lambda_2 \psi_2, \dots, \lambda_d \psi_d]^T$ with $\psi_j^T \psi_k = 1$, if $j = k$, and $\psi_j^T \psi_k = 0$ if $j \neq k$. Figure 3.10 shows a schematic representation of the adopted procedure.

Here, the dynamic trajectories, \mathbf{x}_i , constitute the input to the DM dimensionality reduction framework; affinities from all pairs of trajectories can be computed sequentially, for a given time window, or globally for the whole data record.

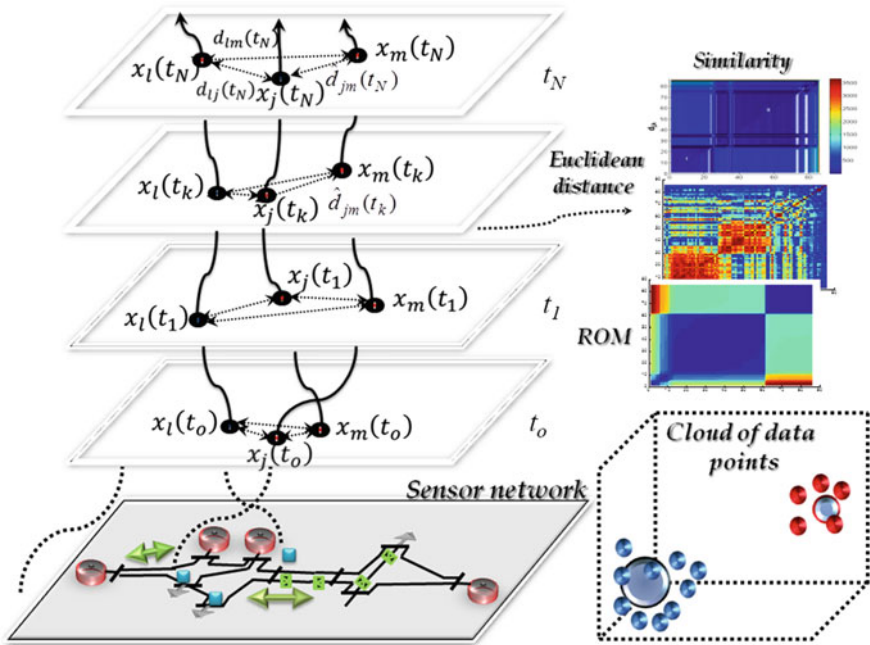


Fig. 3.10 Representation of the diffusion map-based approach

Cluster decomposition

Oscillatory phenomena in the MIS can be highly complex and involve the nonlinear interaction of major inter-area modes. Enhanced clustering techniques have been used to understand the role of wind generation on system dynamics as well as to develop dynamic equivalents.

In an initial step, the notion of diffusion distances was applied to the matrix of diffusion distances, $\hat{D} = [\hat{d}_{ij}]$, in Eq. 3.16. The k -means technique was then used to identify cluster decomposition associated with specific system behavior.

As illustrated in the schematic 3.10, the idea is to partition m trajectories in the diffusion distance matrix into k clusters. This is done using the k -means algorithm [10]. Figure 3.11 shows the identified clusters extracted using the k -means algorithm. As is shown in this plot, the technique essentially identifies two clusters: cluster # 1 that includes WFs # 1–4, 9–11 and 15–18. Cluster # 2 singles out WFs # 1–5–8, 12–14 and 19–20.

Detailed analysis of the time evolution of the speed deviation of WFs in Fig. 3.11 confirms the validity of this analysis.

Section 3.6 discusses the use of this approach to examine potential interactions between WFs and system controllers.

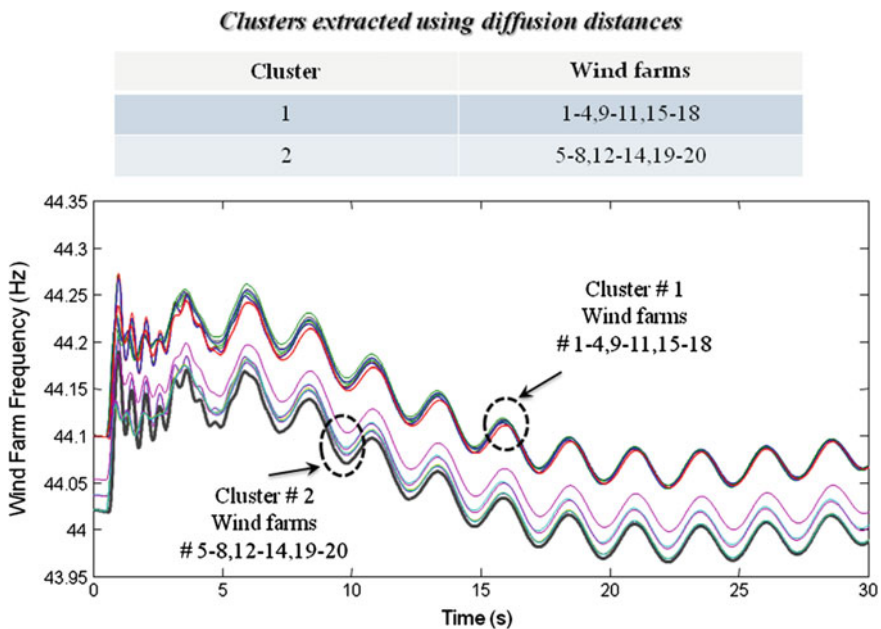


Fig. 3.11 Clusters extracted using the diffusion distances in (3.16). The upper panel shows the clusters of wind farms identified from (3.16). The lower panel shows a detail of wind farm frequencies in Fig. 3.6a

Time-domain decomposition of the data matrix

The diffusion coordinates provide an alternative decomposition of the data matrix \mathbf{X} into modal coordinates. In analogy with Eq. 3.12, the snapshot trajectories in Eq. 3.1 can be approximated by a linear combination of the first nontrivial coordinates as

$$\hat{\mathbf{X}} = \underbrace{\mathbf{a}_o(t)\boldsymbol{\Psi}_o^T + \cdots + \mathbf{a}_d(t)\boldsymbol{\Psi}_d^T}_{\text{Relevant system behavior}} + \underbrace{\sum_{j=d+1}^m \mathbf{a}_j(t)\boldsymbol{\Psi}_j^T}_{\text{non-essential coordinates}} \quad (3.17)$$

where $\mathbf{a}_j(t) = [a_j(t_1) \ a_j(t_2) \ \dots \ a_j(t_N)]^T$, with $\mathbf{a}_j(t) = \mathbf{X}\boldsymbol{\Psi}_j$, $j = 1, \dots, d$, and

$$\mathbf{X}_{ave} = \mathbf{X}_o = \mathbf{a}_o(t)\boldsymbol{\Psi}_o^T \quad (3.18)$$

This expression is analogous to the decomposition 3.12. The results can be interpreted in the following straightforward manner:

- \mathbf{X}_{ave} represents the average system behavior (an approximation to the signals' trend).
- \mathbf{a}_j represent the time coefficients of the dominant diffusion coordinates, $\boldsymbol{\Psi}_j$.

Essentially, the dynamic representation in Eq. 3.17 consists of two components —(i) the relevant, which represents the slow-mode dynamics, and (ii) the nonessential, which represents nonrelevant or unphysical coordinates.

Using Eq. 3.17, the mode shape analysis results can be directly compared to Koopman and Prony estimations. In the studies described below, the diffusion map was applied to extract the essential dynamic modes of simulation trajectories. Emphasis focuses on the extraction of spatial patterns (mode shapes) and the identification of clusters without the need for eigenvalue analyzes. Figure 3.12a, b depicts the extracted modal components and clusters of coherent machines from measured data in Fig. 3.5.

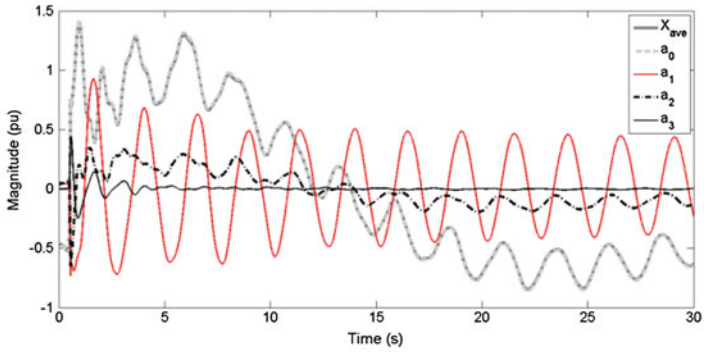
To make the comparison between these techniques more quantitative, the techniques were applied to the entire data window (30 s). Table 3.5 compares the results obtained by these approaches

In these studies, the observational data matrix, \mathbf{X} , in Eq. 3.11 is approximated as

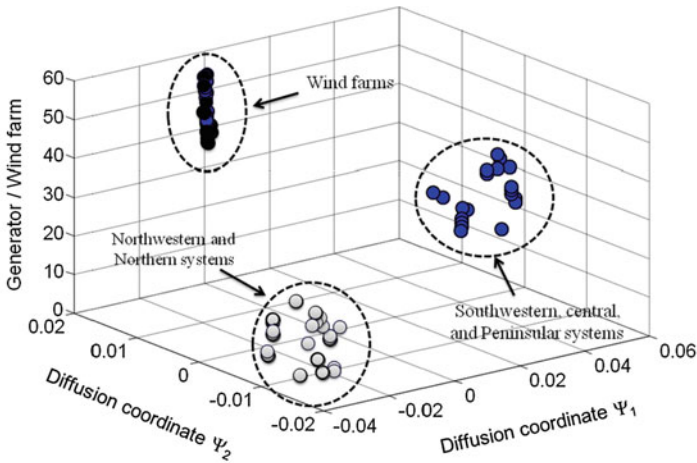
$$\tilde{\mathbf{X}} = \begin{bmatrix} a_o(t_1) & a_1(t_1) & \dots & a_p(t_1) \\ a_o(t_2) & a_1(t_2) & \dots & a_p(t_2) \\ \vdots & \vdots & \ddots & \vdots \\ a_o(t_N) & a_1(t_N) & \dots & a_p(t_N) \end{bmatrix}$$

Relevant modes in [17]

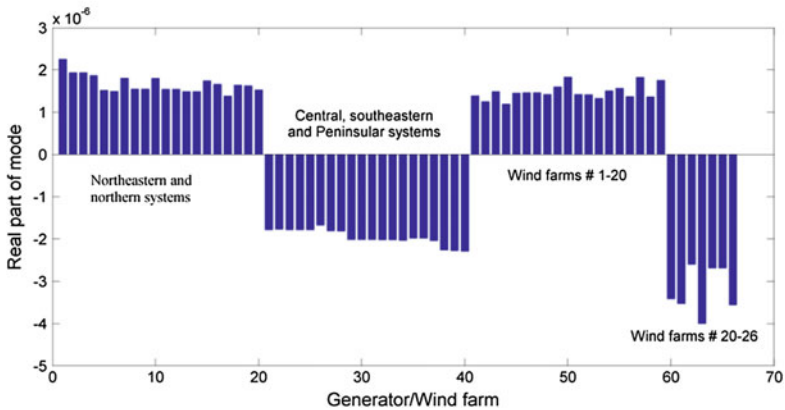
where p is the number of relevant modes.



(a) Time-dependent coefficients of diffusion coordinates.



(b) Three dimensional representation of diffusion coordinates



(c) Mode shape of the dominant coordinate a_0

Fig. 3.12 Spatiotemporal coordinates extracted using the diffusion map framework

Table 3.5 Comparison of modal estimates for the three slowest inter-area modes in the system

Mode	Prony analysis of raw signals in Fig. 1.5a f (Hz), ζ (%)	Koopman mode analysis of signals in Fig. 1.5a f (Hz), ζ (%)	DM analysis of signals a_0, a_1, a_2 ($p = 2$) f (Hz), ζ (%)
1	0.397 0.495	0.397 0.299	0.396 0.334
2	0.553 4.823	0.546 4.961	0.523 5.025
3	0.667 7.584	0.638 7.769	0.668 8.008

The subsequent analyzes examine the ability of model reduction techniques to extract relevant system behavior. The diffusion coordinates and associated spatial modes are then computed using the procedures developed in Sect. 3.4.3.

Figure 3.12a shows the extracted temporal coordinates, a_j , while Fig. 3.12b shows the mode shape associated with the dominant component a_0 in Fig. 3.12a. Also of interest, Fig. 3.12c shows the clusters of coherent generators identified using the temporal coefficients.

The identified clusters and mode shapes in Fig. 3.12 show an excellent agreement with mode shape information in Fig. 3.5, but with added wind information. To validate the quality of the extracted reduced-order models, results were compared with other multivariate analysis techniques, namely multivariate Prony analysis, KMD/DMD analysis, and diffusion maps.

In all cases, the existing algorithms and preprocessing techniques were modified to allow for a coupled analysis of both, wind and conventional generator dynamics. Comparisons of modal estimates in Table 3.5 indicate that data-driven techniques may accurately estimate modal behavior.

3.5 System Frequency Control

The MIS operates as a multi-area (control) system, in which the individual areas are interconnected by radial tie-lines (refer to Fig. 3.1). In the present scheme, the Energy Management System is hierarchically organized and includes several functions such as economic dispatch, interchange schedules, and automatic generation control (AGC).

The scheduled net interchange for each area, P_{net} , is evaluated every four seconds maintaining system frequency and the external system net interchange within the specified tolerance. Calculated values are then transmitted to the individual area control centers to act on generators operating under AGC [19].

In addition to continuous control, a sophisticated remedial action scheme based on a combination of UFLS, generator, and line tripping schemes is used to prevent frequency deviations outside the allowable frequency range of 60 ± 800 MHz (59.2–60.8 Hz) and maintaining interconnected network stability [20]. Because large (hydro) machines in the southeastern system are equipped with secondary

frequency control and hydromachines are very responsive to frequency deviations, frequency control at machines MPD, PEA, ANG, and MMT is of special interest here.

Integration of larger amounts of wind generation into the system is challenging due to the variability in power flow patterns and a more complex real and reactive power dispatch. Several mitigating and operating strategies are being investigated to maintain system performance at acceptable levels.

Exploratory alternatives covered in the following discussions include: (a) providing inertial emulation through modification of converter controls, (b) implementing advanced reactive power control for voltage support at major WFs and its coordination with nearby SVC voltage support, (c) developing advanced operating criteria to maintain regulating reserves, especially for frequency disturbance events, and (d) active power control. In this case, the active power injected by the wind turbine generator is made proportional to the local frequency deviation.

3.5.1 Frequency Control in the Southeastern System

Frequency control in the southeastern system plays a key role in the AGC implemented on the Mexican system. As indicated in the diagram in Fig. 3.1, the SE system is predominantly hydroelectric with four generating stations making up nearly 13% of the total system peak demand.

Due to its fast response and capacity, these hydropower stations are well suited to balance wind and load variations. The integration of new wind generation into the south systems presents multiple technical challenges to system security that need to be addressed.

Several issues, in particular, make the integration of wind power difficult:

- (1) Wind power spatial distribution. A large amount of wind power is concentrated on a small geographical region.
- (2) Wind variability. Wind power fluctuations ranging from 0 to about 100 MW within an hour are not uncommon, especially early in the morning and during off-peak hours. Further, wind generation is out of phase with load demand, thus adding to system variability.
- (3) Relative size. The ratio of wind power relative to hydrogeneration in the southeastern system is high. As a result, the local AGC must compensate fluctuations in wind power output and load variations. Existing WFs do not provide inertial or frequency control services to the system.
- (4) Point of interconnection. Wind parks are connected radially to the bulk 400-kV system. As a result, the loss of SVC voltage support or loss of major transmission lines may result in the loss of a large amount of wind generation. This also makes voltage control and reactive power management more complex.

- (5) Power flow variability. Power from hydroplants and wind generators is transmitted several hundred kilometers to serve load in central Mexico (about 9000 MW), making the total power flow across the southeastern–central interface highly variable.

Since the dynamic response of wind power plants is primarily determined by control functions, efforts are being directed to use active power control to support grid frequency stability.

Figure 3.13 illustrates the adopted southeastern load–frequency control area principle, which is used in this analysis. For the purposes of modeling and analysis, the mix of generation of resources in the area is divided into controllable and noncontrollable resources.

From the perspective of AGC in the system, controllable sources include fast-acting hydrounits with the ability to provide fast contingency reserve, and variable speed turbines with the ability to provide inertial support and frequency control services to the system. As noted above, at present local WFs do not participate in frequency regulation or AGC services.

Basic control characteristics being investigated include: (i) implementing primary control during frequency events, and (ii) active power control on wind plants following frequency events.

The incorporation of wind plants into the AGC system of the MIS is not considered.

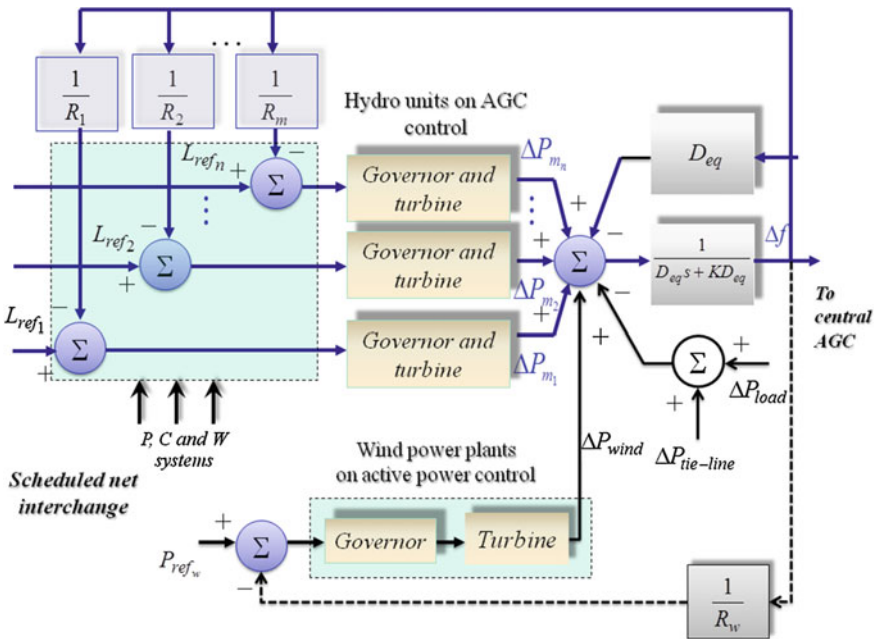


Fig. 3.13 Schematic showing the principle of area control in an integrated wind and hydrosystem

3.5.2 *Wind Integration Cases Studies*

The study evaluates three grid integration case studies and two basic control strategies:

- (1) Base case with no wind generation.
- (2) Case # 1. A case with wind power plants supplying 1000 MW.
- (3) Case # 2. A case with 2000 MW of wind generation.
- (4) Case # 3. A case with 3000 MW of wind generation.
- (5) Case # 4. Inertia emulation in WFs.
- (6) Case # 5. Active power control on wind generators.

These scenarios are designed to approximate the effect of wind generation on system operation. Starting from the base case, wind generation was increased and active and reactive power was rescheduled. To accommodate the added wind farm generation, generation schedules in the central and southeastern networks were reduced. Also, voltage profiles were optimized to meet system requirements.

Among the various contingency scenarios inspected, the loss of the largest generating unit is a critical factor to system security and can cause a significant frequency decrease. In addition, two-and-three loss-of-generation disturbances were selected to examine frequency response following large mismatches between generation and load.

The following three contingency scenarios have been studied:

- (1) **CS1.** Trip of the largest thermal/hydromachines in the system (250 MW).
- (2) **CS2.** Simultaneous trip of two hydro-/thermal units or an equivalent large nuclear unit (500 MW).
- (3) **CS3.** Simultaneous trip of three synchronous machines amounting to 750 MW.

3.5.3 *Performance Under High Levels of Wind Penetration*

The system model used for the dynamic analysis included the detailed representation of seven geographical regions, 635 generators, 25 SVCs, and 26 wind farm generators. All governors in conventional generators are modeled in detail.

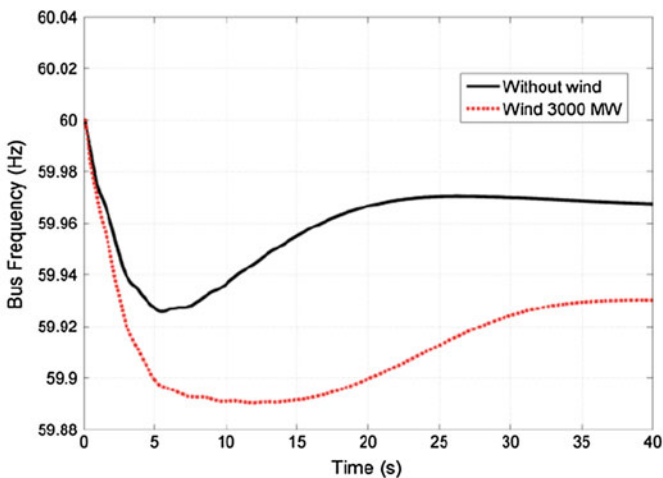
To evaluate the performance impact of WFs, user-written model of the WFs in the southeastern network was developed including active power control and inertial support—see [21].

The simulations include individual representations of the machines which participate in the actual AGC of the MIS and the existing UFLS scheme.

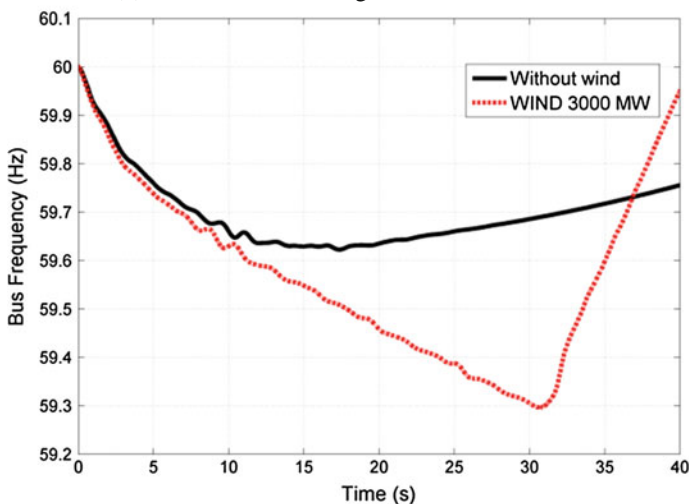
The studies described herein had two specific objectives, namely (1) to define limits of integration of wind energy in the SE system, and (2) to evaluate advance control actions to improve frequency regulation on the grid.

3.5.4 Impact of Wind Generation on Frequency Regulation

Figure 3.14 shows simulated frequency responses at a major transmission bus for contingency scenarios above. For case CS1 above, the frequency nadir in Fig. 3.14a is about 59.93 Hz above the first step of the under UFLS scheme in the system (59.3 Hz).



(a) Loss of 250 MW of generation. Scenario CS1.



(b) Loss of 750 MW of generation. Scenario CS3.

Fig. 3.14 Frequency response at a major 400-kV transmission bus to loss of generation

Simulation results for more stringent operating conditions indicate a stable frequency performance at high levels of wind generation; the system can reliably accommodate up to 3000 MW (5%) of wind penetration.

For scenarios involving double and triple contingencies, simulation results in Fig. 3.14b show a higher rate of change of frequency. Another concern with wind generation is that the system frequency does not recover to an acceptable level in a reasonable time (i.e., 30 s).

Results in Fig. 3.14b show that, as the amount of generation trip increases, the first stage of the UFLS is reached for cases with 3000 MW of wind generation, indicating a need to investigate the effect of control actions on system behavior.

For comparison, Figs. 3.15 and 3.16 show the frequency traces for two different generator events for the cases with no wind and a large wind penetration level (3000 MW). Of particular concern, simulation studies show the presence of frequency overshoot by as much as 10%. Since the frequency drops below the first UFLS set point, about 1549 MW of firm load are shed.

Higher levels of wind integration result in a faster rate of change of frequency and lower frequency nadirs following loss-of-generation frequency events. Results show that about 1000 MW of wind generation can be integrated into the SE system without an adverse impact on the operation and security of the grid.

Figure 3.17, in turn, illustrates the effect of loss-of-generation events on power system frequency for various operating conditions. As shown in this plot, integration of large amounts of wind power may result in both, under frequency and over frequency.

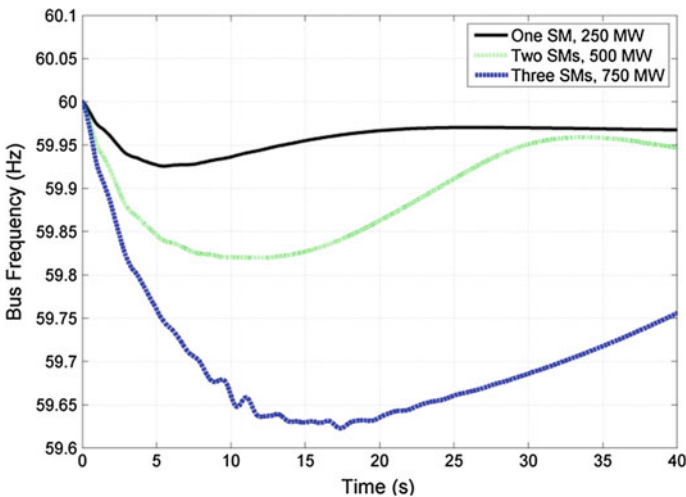


Fig. 3.15 Case without wind plants. Frequency behavior in a representative bus of the grid with several contingencies

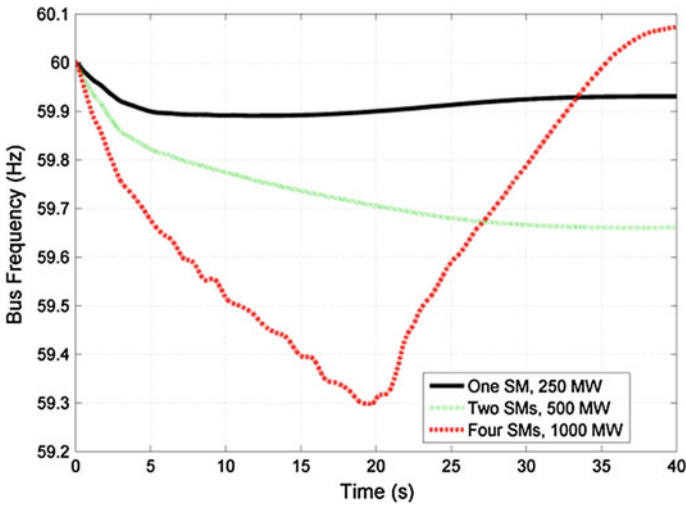


Fig. 3.16 Case with 3100 MW of wind generation. Frequency behavior in a representative bus of the grid with several contingencies

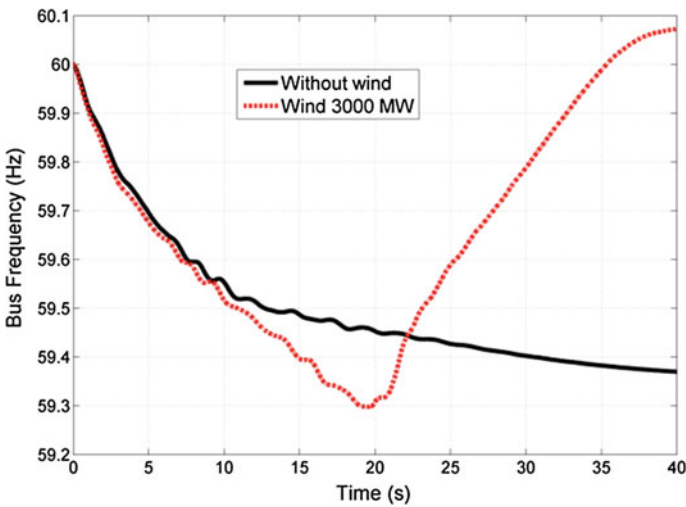


Fig. 3.17 System response to a three-phase fault at 400-kV bus. Simultaneous tripping of four synchronous machines (1200 MW)

Also apparent from Fig. 3.18 is that reduction of system inertia results in lower post-contingency voltages below the acceptable range of system behavior. Maintaining acceptable levels of system security requires higher levels of active (reactive) power reserves and an efficient integration of wind and hydroresources.

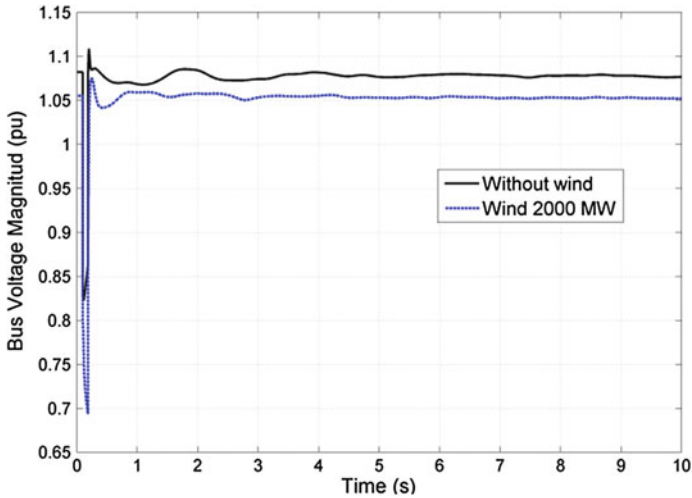


Fig. 3.18 Frequency response at a major 400-kV transmission bus following tripping of a 300 MW synchronous machine

3.5.5 Inertial Support and Active Power Control

Simulation results suggest that frequency behavior of the southeastern grid can be improved by providing inertial response and fast active power control during transient events. These issues have been investigated in recent research [22–24].

For the purposes of discussing potential benefits of both approaches, sensitivity studies were conducted using fast hydrounits in the SE systems operating at low output (synchronous condenser mode). Due to the longitudinal structure of the system, this strategy is commonly used to control voltage and reactive power output at nearby SVCs.

Figure 3.19 shows the system frequency response following the loss of three large generators for the case with and without 300 MW injection of active power to the power grid. Two levels of wind generation in the SE system are considered: 1000 and 2000 MW. In this case, the real power was added to the grid 1.5 s after the start of the contingency event.

The solid line in these plots shows the system response with no real power injection, while the dashed line is the simulation result with the proposed active control strategy included. This approach requires hydroplant to operate at lower output (10%) to provide inertial support (synchronous reserves). It is also important to note that hydrogeneration units would require improved design of the MIS special protection system in the system.

Preliminary simulation results in Fig. 3.19 demonstrate that active power control of fast hydroturbines improves frequency control; the best results were obtained for high penetration levels of wind power.

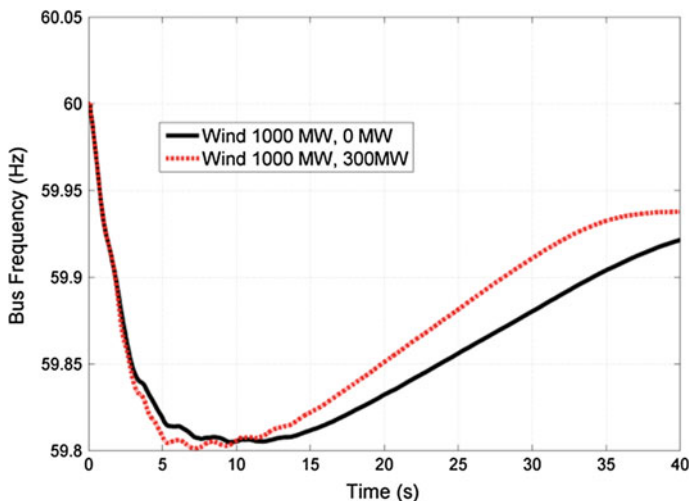


Fig. 3.19 Bus frequency (southeastern POI) behavior with active power control of hydrounits. Tripping of three synchronous machines, with 1000 MW of wind generation

3.6 Impact on Torsional Dynamics

Recent studies indicate that type-3 wind generators in the SE system could adversely interact with series-compensated circuits and fast-acting controls of nearby SVCs [18]. Based on the original 5449-bus model, a reduced-order model of the area where WFs # 1–20 are located was developed for the analysis of SSR and subsynchronous control interactions (SSTI) between wind turbine generators and series capacitors/SVCs. A diagram of the reduced system is shown in Fig. 3.20.

Using the diffusion maps' approach in Sect. 3.4.3, a three-machine detailed EMTP-type dynamic equivalent for the WFs in the SE region was developed. The model includes two DFIG equivalent generators representing Cluster # 1 (WFs 1–4, 9–11, 15–18) and Cluster # 2 (WFs 5–8, 12–14, 19–20) in Fig. 3.1, one large SVC and 3 series-compensated transmission lines. In addition, a small Type I wind generator was included in this representation representing the dynamics of the La Venta wind farm, one of the oldest WFs in the system.

In this representation, DFIG generators were represented using a detailed model, i.e., the electronic power converter and crowbar protection includes electronic devices, implemented with insulated gate bipolar transistors (IGBTs) and anti-parallel diodes; the control blocks for the reactive and active power at the POI are based on conventional vector control. Transmission lines are modeled as π -sections to represent mutually coupled three-phase lines.

The remaining of the interconnected Mexican bulk system is represented by its Thevenin equivalent at the 400-kV JUI substation.

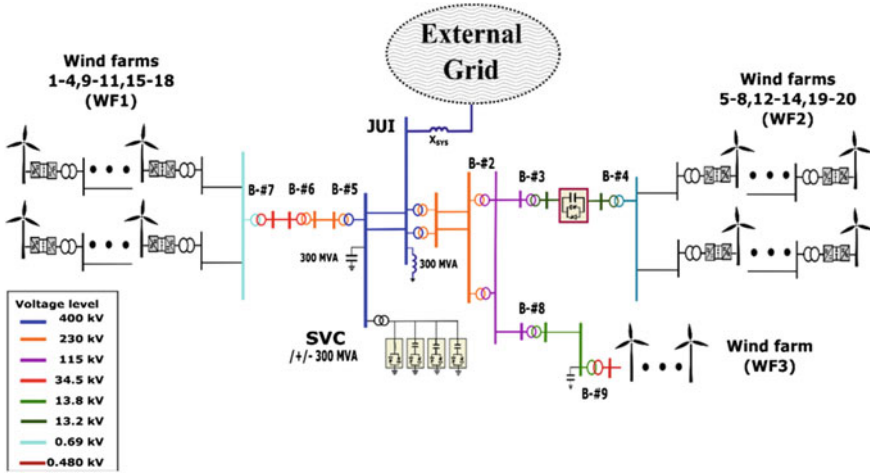


Fig. 3.20 Schematic of the study area for analysis of SSR and STI in Fig. 3.1

The study seeks to perform a coupled analysis of SSR response at La Venta system and SSTI of DFIG with SVC controls and nearby series-compensated transmission lines.

Figure 3.21 shows selected PSCAD simulations following a three-phase fault at bus JUI at 2.5 s, cleared at 3.5 s by removing one of the lines to bus B#2.

To identify the underlying contributions of each state to the torsional interactions, and the observables that best describe the observed phenomena, multivariate analysis techniques were applied to the whole sets of signals. These include the individual active and reactive power output and mechanical torques (\mathbf{X}_{FW1} , \mathbf{X}_{FW2} , \mathbf{X}_{FW3}) of the WFs, electric power and voltage (\mathbf{X}_V) at the POI of the WFs, tie-line powers (\mathbf{X}_P , \mathbf{X}_Q), bus voltage magnitudes, and SVC's output (\mathbf{X}_{SVC}).

The overall measurement matrix is defined as

$$\mathbf{X} \in \mathfrak{R}^{10000 \times 49} = [\mathbf{X}_P \quad \mathbf{X}_Q \quad \mathbf{X}_V \quad \mathbf{X}_{SVC} \quad \mathbf{X}_{WF1} \quad \mathbf{X}_{WF2} \quad \mathbf{X}_{WF3}] \quad (3.19)$$

where

$$\begin{aligned} \mathbf{X}_P &\in \mathfrak{R}^{10000 \times 9} = [P_{JUI}, P_{JUI-B\#2}, P_{B\#2-3}, P_{B\#3-4}, P_{B\#2-8}, P_{B\#8-9}, P_{JUI-B\#5}, P_{B\#5-6}, P_{B\#6-7}] \\ \mathbf{X}_Q &\in \mathfrak{R}^{10000 \times 9} = [Q_{JUI}, Q_{JUI-B\#2}, Q_{B\#2-3}, Q_{B\#3-4}, Q_{B\#2-8}, Q_{B\#8-9}, Q_{JUI-B\#5}, Q_{B\#5-6}, Q_{B\#6-7}] \\ \mathbf{X}_V &\in \mathfrak{R}^{10000 \times 9} = [V_{JUI}, V_{B\#2}, V_{B\#3}, V_{B\#4}, V_{B\#8}, V_{B\#9}, V_{B\#5}, V_{B\#6}, V_{B\#7}] \\ \mathbf{X}_{SVC} &\in \mathfrak{R}^{10000 \times 4} = [Q_{SVC}, V_{SVC}, B_{SVC}, \alpha_{SVC}] \\ \mathbf{X}_{WF1} &\in \mathfrak{R}^{10000 \times 6} = [T_{MT}, T_{MT-G}, P_{WF1}, Q_{WF1}, \omega_{WF1}, V_{DCap1}] \\ \mathbf{X}_{WF2} &\in \mathfrak{R}^{10000 \times 6} = [T_{MT}, T_{MT-G}, P_{WF2}, Q_{WF2}, \omega_{WF2}, V_{DCap2}] \\ \mathbf{X}_{WF3} &\in \mathfrak{R}^{10000 \times 6} = [T_{MT}, T_{MT-G}, P_{WF3}, Q_{WF3}, \omega_{WF3}] \end{aligned}$$

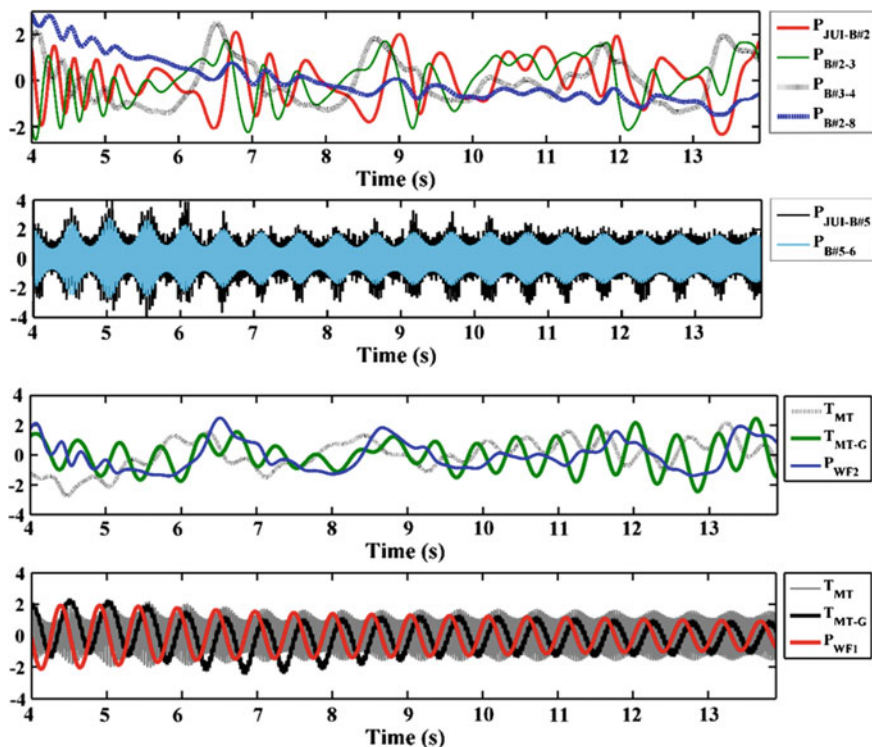


Fig. 3.21 Transient system response following a three-phase fault at bus JUI

Table 3.6 Estimated torsional modes

f (Hz)	ξ (%)
32.24	0.008
30.30	-0.062
28.377	-0.012
1.896	1.292
0.919	2.102
0.42	-0.007

Table 3.6 shows the frequency and damping obtained using the diffusion maps’ approach. Modal analysis results reveal two dominant, undamped modes at frequencies about 30.30, 28.37 Hz in close agreement with small-signal stability results (not shown). The performance is clearly unacceptable.

To identify the system parameters that best describe the SSR/SSTI phenomenon, Koopman mode analysis and the diffusion map approach were applied to the full sets of signals in Eq. (3.19). The mode shape information in Fig. 3.22 suggests that the SVC at the 400-kV JUI substation may strongly affect the observed oscillatory behavior in Fig. 3.21.

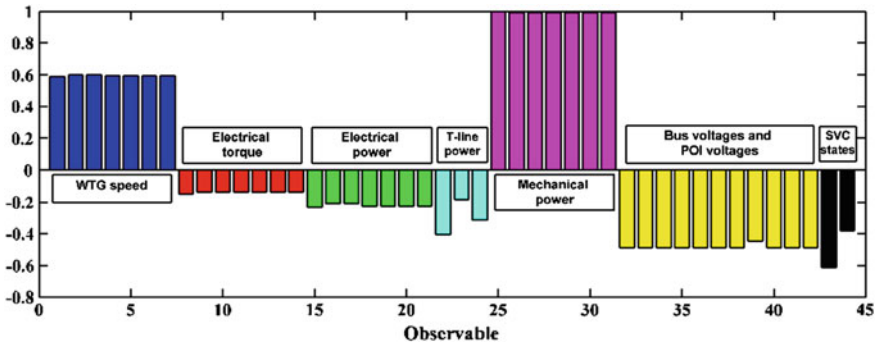


Fig. 3.22 Spatial shape extracted using diffusion maps

Additional studies are now being conducted to analyze the influence of control strategy and mode of operation of the SVC on the damping of subsynchronous modes as well as to prevent interaction with phenomena outside the desired control bandwidth.

References

1. Inda A, Villa G (2011) Operational impact evaluation of wind generation integration in the mexican electrical system. In: IEEE Trondheim Power Tech
2. Mexico Department of Energy, Development program of the national electric system, 2015–2029 (Spanish, Programa de desarrollo del Sistema Electrico Nacional, PRODESEN 2015-2029)
3. Gámiz JS, Aboytes F (1984) Operation and control of the Mexican interconnected system. In: IEEE transaction on power apparatus and systems, vol PAS-103, no 8, August 1984, pp 2081–2088
4. Luna E, Perez C, Fernandez E, Tequitalpa G (2014) Active power control of wind farms in Mexico to mitigate congestion energy problems and contribute to frequency regulation. IEEE-ROPEC 2014 special session on renewable energy, Mexico
5. Cadogan J, Milligan M, Wan Y, Kirby B (2000) Short-term output variations in wind farms—NREL 2000. In: Presented at the wind power for the 21st century conference Kassel, Germany September 26–28, 2000
6. Cigre Working Group 6.08, Grid integration of wind generation, February 2011
7. Cigre Working Group B4.39, Integration of large scale wind generation using HVDC and power electronics, February 2009
8. Young PC, Pedregal DJ, Tych W (1999) Dynamic harmonic regression. J Forecast 18:369–394
9. Zavala AJ, Messina AR (2014) A dynamic harmonic regression approach to power system modal identification and prediction. Electr Power Compon Syst 42(13):1474–1483
10. Messina AR (2015) Wide-area monitoring of interconnected power systems. IET Power and Energy Series 77, London, UK
11. Young PC (2011) Recursive estimation and time-series analysis: an introduction for the student and practitioner, 2nd edn. Springer, Berlin

12. Anderson BDO, Moore JB (1989) Forecasting structural time series models and the Kalman filter, 1st edn. Cambridge University Press, Cambridge
13. Norton JP (1986) An introduction to identification. Academic Press, New York
14. Vittal V (2013) Ayyanard, grid integration and dynamic impact of wind energy, power electronics and power systems. Springer, New York
15. Messina AR, Vittal V (2007) Extraction of dynamic patterns from wide-area measurements using empirical orthogonal functions. *IEEE Trans Power Syst* 22(2):682–692
16. Barocio E, Pal BC, Thornhill NF, Messina AR (2015) A dynamic mode decomposition framework for global power system oscillation analysis. *IEEE Trans Power Syst* 30(6):2902–2912
17. Coifman R, Lafon S, Lee AB, Maggioni M, Nadler B, Warner F, Zucker SW (2005) Geometric diffusion as a tool for harmonic analysis and structure definition of data: Diffusion maps. *Proc Natl Acad Sci* 102(21):7426–7431
18. Arvizu CMC, Messina AR (2016) Dimensionality reduction in transient simulations: a diffusion maps approach, To appear, *IEEE transaction on power delivery*
19. Skopp AR, Varadan S (2000) ABB information & energy management. *ABB Rev* 1:35–41
20. Mexico Department of Energy (2012) Interconnection rules to the national electric system (in Spanish, Reglas Generales de Interconexión al Sistema Eléctrico Nacional)
21. Brendan J (2004) Kirby, frequency regulation basic and trends, ORNL/TM-2004/291, December 2004
22. Clark K, Miller NW, Sanchez-Gasca JJ (2010) Modeling of GE wind turbine-generators for grid studies. General Electric International, 16 Apr 2010
23. Gautam D, Vittal V, Harbour T (2009) Impact of increased penetration of DFIG-based wind turbine generators on transient and small signal stability of power systems. *IEEE Trans Power Syst* 24(3):214–224
24. Miller NW, Shao M, Venkataraman S (2011) Frequency response study, report California ISO (CAISO), November 2011

Chapter 4

Load Flow Analysis with Wind Farms

Pradeep Kumar and Asheesh K. Singh

4.1 Introduction

The load flow analysis (LFA) is a powerful tool to analyze the power flow in the power system. It provides a solution to the nonlinear mathematical models of the line power flow, at steady-state operating conditions [1]. It requires a few iterations to provide an acceptable accuracy of the solution, which is in terms of voltage (V) and angles (δ) at the nodes/buses, active (P) and reactive power (Q) in the lines, and line losses [2].

The LFA involves modeling of the generators, lines, and loads. The LFA is performed for the transmission and distribution system, separately. The lines are modeled as circuit elements, resistance, inductance, and capacitance, while the loads are presented as P and Q . The generators are represented in terms of P and V . These nodes or buses are termed as, PQ bus, PV bus, and Slack bus. By performing LFA, V and δ are obtained at these buses [1]. Conventionally, LFA does not involve any detailed generator model. The conventional power generation, using synchronous generators is deterministic in nature, i.e., the power is generated at a specified voltage, as per requirement. However, with the development of renewable energy sources (RES) and their grid interconnection, modification in the LFA has become a necessity [3]. The RES are stochastic nature due to their dependence on weather condition, availability, and distribution of natural resources [3–6]. As a result, the calculation of power with changing operating conditions

P. Kumar (✉)

Department of Electrical Engineering, NIT Kurukshetra, Kurukshetra, India
e-mail: pradeepkumar@ieee.org

A.K. Singh

Department of Electrical Engineering, MNNIT Allahabad, Allahabad, India
e-mail: asheesh@mnnit.ac.in

becomes important. The inclusion of generator models of these RES assists in calculating the parameters P , Q , V , and δ from the specifications. To determining the operating condition, forecasting comes into aid and predicts the grid adequacy requirement.

Amongst the various RES, large-scale deployment of wind energy conversion systems (WECS) has taken place in the power system to supply the electric power [7], so they are considered here. Its inclusion in the LFA is the considered in this chapter. The wind generation faces fluctuations and intermittency, due to wind's intermittent nature. To analyze the performance of hybrid power system, i.e., conventional energy sources with wind energy sources, LFA is helpful to [8],

- assess the impact of wind turbines (WTs) on the grid's steady-state operation,
- lay foundation for theoretical studies, such as grid stability [9],
- identify technical constraints,
- identification and scheduling of the generation requirement,
- analyze the power fluctuations in the grid,
- perform contingency analysis, and
- technoeconomic studies to access the impact of commercial energy exchanges in the transmission network [10].

In this chapter, LFA is discussed for wound-rotor induction generators (WRIGs)-based WECS. The models of the WTs for LFA are either individual machines or the aggregate models [11]. They offer different parameters for the LFA, which affects their accuracy. Here, the different models of the WRIGs discussed are as follows:

- PQ model [3, 12],
- RX (resistance reactance) model [3, 13],
- Three-node model [8], and
- Probabilistic model [5, 14, 15].

The discussion is based on the LFA for a transmission system using the Newton–Raphson (NR) method [1].

The rest of the chapter is divided into following sections; in Sect. 4.2, the WECS and the principle of power generation using are discussed. In Sect. 4.3, the basics of LFA are discussed. Section 4.4 discusses the different models of the WTs and wind farms. Results using the LFA with different models of WECS are discussed in Sect. 4.5. Finally, the conclusions are drawn in Sect. 4.6.

4.2 Wind Energy Conversion Systems (WECS)

Wind energy is a clean form of energy and available across the globe. In recent year, large scale proliferation of the wind energy has been observed. A typical WECS power generation scheme is shown in Fig. 4.1 [16]. Here, the kinetic energy

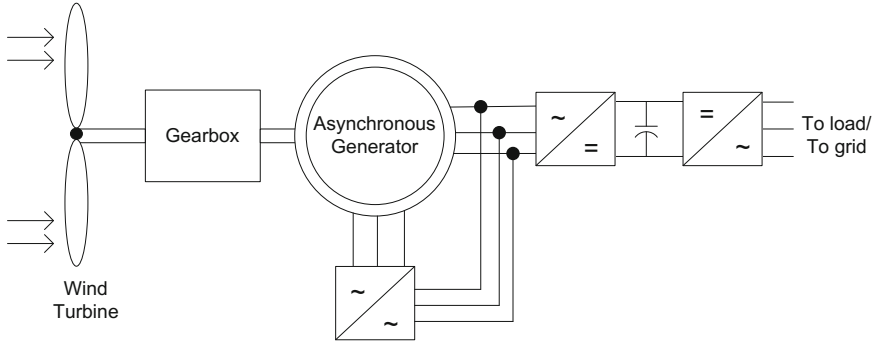


Fig. 4.1 Power generation scheme from the wind using asynchronous generator

is used to generate electricity. The wind rotates the WT, which in turn rotates the wing generator. The WT and wind generator (WG) are connected through a gearbox, which allows generation even at low speeds [7]. The output of the gearbox is connected to the generation scheme, which converts the mechanical energy to electrical energy. This is converted to AC/DC and DC/AC using the power electronic converters. The net power generated in a WECS is given as [7],

$$P = \frac{1}{2} \rho A U^3 c_p \quad (4.1)$$

Here, A is the rotor area, ρ is the density of air, U is the wind speed, and c_p is the power coefficient, relating the power to the tip speed using a polynomial as [7].

$$c_p = \sum_{i=1}^n a_i \lambda^i \quad (4.2)$$

where a_i are the constants. From (4.1) and (4.2), it can be seen that power generated depends on the speed of the WTs, U modeled as the interaction between the wind and WT blades, termed as tip speed; λ is given as,

$$\lambda = \frac{\omega R}{U} \quad (4.3)$$

Thus, it can be observed that the power generated using WTs depends on the

- Speed of WT and
- Interaction of WT with the wind.

The WTs converting the wind into rotatory motion are classified as fixed speed and variable speed WTs, broadly [16]. The fixed speed WT has small variations in speed, leading to reduced power generation, as shown in Fig. 4.2a. However, in case of the variable speed WTs, large power variations are possible due to large

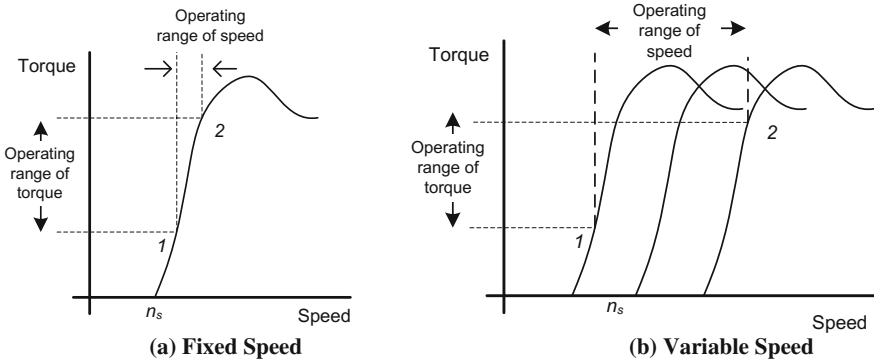


Fig. 4.2 Torque–speed characteristic of WTs

variations in operating speeds, as shown in Fig. 4.2b [16]. Thus, variable speed power WTs is more popular than the fixed speed WTs.

Moreover, the use of fixed speed and variable speed WTs creates variations in the power generated at the terminals. Therefore, the inclusion of generator models in the LFA becomes important. Since, the operating conditions of the WTs change rapidly, the LFA should be able to provide the performance of the power system for a full range of availability of wind speeds, different grid voltages at different power levels. Also, it should identify the modifications required in plant design, if any. The general LFA is discussed in the next section.

4.3 Load Flow Analysis

The basic LFA problem deals with the determination of system performance at a given loading condition, at an assumed generation level. The calculations provide a subsequent adjustment of generation levels and supply voltage to meet economic and security requirements. The major applications of LFA in power systems are given in Table 4.1 [2]. It is formulated using four variables per node— δ , V , P , and Q injections. Active power losses in the system are not known in advance as they depend on the active power injection pattern and voltage profile. Other variables are also interdependent, making the problem nonlinear. Mathematically, the LFA can be represented as a set of nonlinear equations as (4.4), which can be solved using numerical technique [17].

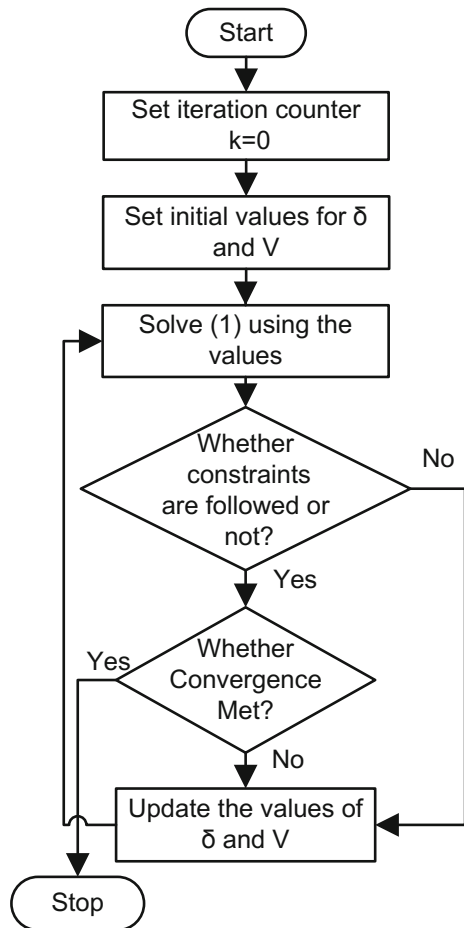
$$f(\delta, V) = 0 \text{ such that, } x_i \in [a_i, b_i], \quad (4.4)$$

where x_i is the system state variable, a and b are the lower and upper limits, respectively. The nonlinear models for LFA are often linearized and solved successively. The LFA can be either (i) AC or (ii) DC. The DC load flow is a simplification and linearization of a full AC load flow.

Table 4.1 Applications for LFA in power system

Application	Description
Transmission planning	Check for system overloads, voltage variations, and identify locations for network reinforcements
Contingency analysis	Test for effect line and/or generator outages
VAR/Voltage analysis	Evaluate effectiveness of VAR/voltage devices
Transfer capability analysis	Test for inter-utility power transfer limits
Online control and security enhancement	Analyze effectiveness of corrective measures to alleviate emergencies

Fig. 4.3 General algorithm for load flow calculations



For LFA with WECS, the generator specification can be based on power or impedance specifications of the generator. Depending upon the specifications and the relations of the WRIG the other LFA parameters are calculated. In comparison

to the conventional synchronous generator, the WRIG requires Q to maintain the voltage [13]. So, it is not modeled as a PV bus; rather other models are developed. These models are discussed in the next section. The load flow models considered in this study are solved using NR method. The general procedure for any LFA is shown in Fig. 4.3 [13].

4.4 Modeling of Wind Farms

The principle of power generation using wind is explained in Sect. 4.3, using the configuration as shown in Fig. 4.1. As the wind falls on the blade of the WT, it rotates the generator to generate electricity. To model the behavior of the WG in LFA, different models have been proposed in the literature. These methods can be either dependent on the generator design or the performance of the generator. The generator design dependent models use the relationship between the different power and voltage parameters of the generators to provide the parameter values. These models are machine specific, i.e., specific model for a specific machine. These models become a necessity in LFA, especially with the WRIG as they require Q to maintain the terminal voltages, which is based on the operating condition of the grid. These models include the PQ , RX , and the three-node model. The generator performance-based models use the probabilistic models, derived using the input-output relationship of the generators. These models are independent of the type of machine used for the generator. So, as a result, they are more general in the interpretation of the results. In the present chapter, the different models considered are as follows:

- PQ models of asynchronous WT [3] and its modification [12],
- RX model [3] and its modification [13],
- Three-node model [8], and
- Probabilistic model [5, 14, 15].

With asynchronous generation, the PQ and RX models are more popular [3]. However, the probabilistic models can be utilized, also. The detail of these models is described below.

4.4.1 Model-1: PQ Model of Asynchronous WT

In WECS, the asynchronous WG with short-circuited rotor works at a super-synchronous speed [3]. They generate P but require Q to maintain the terminal voltage, V , and δ at the generator bus. This increases the complexity of the model. Performing LFA is difficult, without having relationships between different quantities for the WRIG. So, different models of the WG are used for the analysis.

These models use different specifications given by the manufacturer to determine the relationships [12]. In PQ model, the active power, P is specified, while depending on the operating condition, the Q requirement to maintain the terminal voltage is calculated. From the power curves, provided by the manufacturers of these machines, these quantities can be obtained. The PQ model is of interest if the Q is adequately estimated. In this chapter, two PQ models are discussed, namely, (a) the conventional model [3], and (b) the modified model [12]. The details of these models are discussed below.

4.4.1.1 Conventional PQ Model

In this model, the circuit model of the induction machine is utilized. The conventional model of the induction machine is shown in Fig. 4.4. Here, subscript ‘1’ denotes the stator parameters and ‘2’ is for the rotor parameters, while ‘ m ’ represents the magnetizing branch, which is assumed to be operating in the linear region. The symbol P_m represents the mechanical power, i.e., the power converted into electrical power. Applying Boucherot’s theorem to conserve the complex power, the Q consumed (positive) by the machine is given as (4.5) [3], where P is the real power at voltage, V , X is the sum of X_1 and X_2 , X_c is the reactance of the capacitor bank, and R is the sum of R_1 and R_2 .

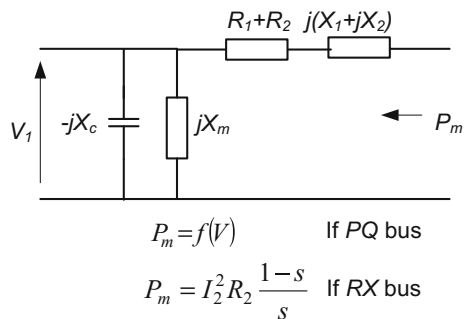
$$Q = V^2 \frac{X_c - X_m}{X_c X_m} + X \frac{V^2 + 2RP}{2(R^2 + X^2)} - X \frac{\sqrt{(V^2 + 2RP)^2 - 4P^2(R^2 + X^2)}}{2(R^2 + X^2)} \quad (4.5)$$

The reactive power, Q of the machine can be represented as a quadratic equation in terms of P , i.e., $Q = f(P)$ as,

$$Q = -Q_0 - Q_1 P - Q_2 P^2 \quad (4.6)$$

where Q_0 , Q_1 , and Q_2 are the coefficients determined experimentally. Using (4.1) and (4.5), Q can be obtained in simplified form as,

Fig. 4.4 Conventional steady-state model of the induction machine



$$Q \approx V^2 \frac{X_c - X_m}{X_c X_m} + \frac{X}{V^2} P^2 \quad (4.7)$$

So, with known P , the reactive power, Q is known, as $Q = f(P)$ using (4.6) [3]. Here, f represents a general quadratic function.

This relationship provides the conventional model for the calculation of Q from the P specifications. In performing the LFA, the P requirement is based on the electricity demand forecasting. So, for this particular value of P , the Q is calculated at a particular voltage, V . This constitutes the conventional PQ model. A modified PQ model [12] using the circuit transformations, which is found more accurate than the conventional model.

4.4.1.2 Modified PQ Model

In modified PQ model, the circuit model of the induction machine is transformed. The conventional induction machine model is represented as T two-port network as shown in Fig. 4.5. The elements of this model can be denoted as,

$$\left. \begin{aligned} Z_1 &= R_1 + jX_1 \\ Z_2 &= R_2 + jX_2 \\ Z_3 &= jX_3 \end{aligned} \right\} \quad (4.8)$$

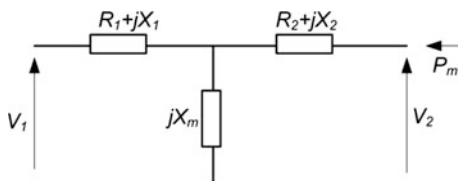
This equivalent T model can be converted into π model as depicted in Fig. 4.6 using the following relations,

$$Z_a = Z_2 + Z_3 + \frac{Z_2 Z_3}{Z_1} \quad (4.9)$$

$$Z_b = Z_1 + Z_3 + \frac{Z_1 Z_3}{Z_2} \quad (4.10)$$

$$Z_c = Z_1 + Z_2 + \frac{Z_1 Z_2}{Z_3} \quad (4.11)$$

Fig. 4.5 Equivalent representation of conventional induction machine as a T two-port network



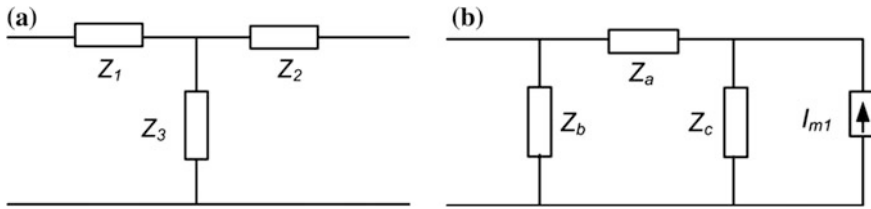


Fig. 4.6 Equivalent representation of T two-port network of induction machine converted as π model

The mechanical power, P_m , of the rotor is converted into the current source, I_{m1} , as,

$$I_{m1} = \frac{P_m}{V_2^*} \tag{4.12}$$

In the π circuit, the Z_b becomes the stator side impedance. This can be represented as admittance, $Y_b = 1/Z_b$ in the admittance matrix of the network.

The rest of the circuit is represented by Z_a and Z_c . This provides an advantage of the inclusion of machine parameters in LFA to provide more accurate performance of the model.

The complex power, S is given as,

$$S = \frac{V_1}{V_2} \left(\frac{Z_a}{Z_a + Z_c} \right) P_m \tag{4.13}$$

The voltages V_1 and V_2 at the stator and rotor ends are related as,

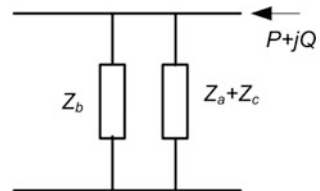
$$\frac{V_1}{V_2} = \frac{Z_a + Z_c}{Z_a} - \frac{Z_c P_m}{V^2} \tag{4.14}$$

On solving the complete circuit, the simplified circuit is shown in Fig. 4.7. The simplified model relating the complex power, in terms of the terminal voltage, is given as (4.14).

$$V_2 = V_1 - Z_c \left(- \left(\frac{S_{MAQ}}{V_1} \right) - \frac{V_1}{Z_b} \right) \tag{4.15}$$

where $S_{MAQ} = S - Y_{MAQ} V_1^2$ and $Y_{MAQ} = 1/Z_b + 1/(Z_a + Z_c)$.

Fig. 4.7 Simplified circuit model of the induction machine



Thus, it can be seen that the relations using the π model are more accurate than that with the conventional T model. The difference in the accuracy of the two models arises due to the approximation involved in the T model, which are eliminated in the π model.

In PQ model, the bus at which the WG is connected is represented as a PQ bus. A different form of representation is used, which is in terms of the machines resistance and reactance (RX) model. The details of the model are discussed below.

4.4.2 Model-2: RX Model

The operation of the asynchronous machine is dependent dynamics of the machine and its slip, s . So, in this model, the machine is modeled in terms of model parameters, as the RX bus. Since, the machine parameters are dependent on the slip. The model is concerned with the determination of slip, s , at a particular operating point. Depending on the model, it is either conventional [3] or modified [13]. The details of the model are presented below.

4.4.2.1 Conventional Model

In the conventional model, the steady-state model of the induction machine represented as, $\bar{Z} = R_1 + jX_1 + (jX_m || ((R_2/s) + jX_2))$ and a shunt capacitor with susceptance B_c . For a fixed value of mechanical power, P_m the slip, s can be calculated as,

$$s = \frac{-V^2 R_2 + \sqrt{V^4 R_2^2 - 4PR_2^2(PX^2 + V^2 R_2)}}{2(PX_2 + V^2 R_2)} \quad (4.16)$$

This equation is based on the steady-state model of the machine. It provides the slip, s , at a particular value of operating point. With the change in the operating conditions, the slip of the machine is calculated at using the algorithm given below.

1. Begin with $s = s_{\text{nom}}$ in each machine, s_{nom} being the rated slip. With this calculate the impedance \bar{Z} .
2. Using these values, model the WG as an RX bus including the admittance of the machine in the admittance matrix and terms of the Jacobian.
3. Perform LFA and obtain the bus voltages. Also, obtain the mechanical power of the machine is calculated as

$$P_m = -I_R^2 R_R ((1 - s)/s) \quad (4.17)$$

4. With the value of s , calculate λ and c_p , and the power extracted from the wind using (4.1–4.3).
5. Compare the calculated and actual power, if they are not equal, recalculate s by means of

$$s_k = s_{k-1} + \Delta s \quad (4.18)$$

where s_{k-1} and s_k are the present slip and the new slip and,

$$\Delta s = J^{-1} \Delta P_m \quad (4.19)$$

where ΔP_m is the difference between both powers. With the approximation $((1 - s)/s) = (1/s)$ is assumed in the proximity of the working point, J , calculated as:

$$J = R_2 \left(\frac{S'}{V} \right)^2 \frac{A + B}{s^2 \left(\left(\frac{R_2}{s} \right)^2 + (X_2 + X_m)^2 \right)} \quad (4.20)$$

an equation where $S' = \sqrt{P_g^2 + Q_c^2}$, and P_g and Q_c are the P generated and Q consumed by the induction machine. P_g and Q_c are given as $P_g = -\left(\frac{V^2}{Z^2}\right) \text{Re}(\bar{Z})$ $Q_c = \left(\frac{V^2}{Z^2}\right) \text{imag}(\bar{Z})$. The A and B are as follows:

$$A = -\frac{2X_m R_2}{s} \left(\frac{R_2}{s} + (X_2 + X_m)^2 \right) \quad (4.21)$$

$$B = -\left((X_m(X_2 + X_m))^2 + \left(\frac{X_m R_2}{s} \right) \right) \cdot \left(-\frac{R_2}{s} + \left(\left(\frac{R_2}{s} \right)^2 + (X_2 + X_m)^2 \right) \right)^2 \quad (4.22)$$

After this, go to step 2. If they are equal, the algorithm finishes.

With new values of s and J , the LFA is repeated, and the process finishes when the mechanical power P_m and the power taken out from the wind, P_k are equal, or the difference between both is acceptable. This error is calculated as $\sum_{i=1}^n (P_{mi} - P_i)^2$, where i is the number of machines in the wind farm.

The RX model derived in the section is based on the T model of the induction machine [3]. The model can be improved with the use of a π model, which is discussed in the next section. The model is more accurate and termed as $RX2$ [13]

4.4.2.2 Modified Model: $RX2$

In the conventional model, the inductive elements, X_1 and X_2 are connected in series, while rotor resistance, R_1 is neglected as shown in Fig. 4.8. The details of the model are discussed above in Sect. 4.2.1. A slight modification in this conventional model includes the actual circuit model without any assumption. It includes the stator resistance R_1 in the original configuration, as shown in Fig. 4.9. To solve the

Fig. 4.8 Conventional model of the induction machine with R_1 neglected

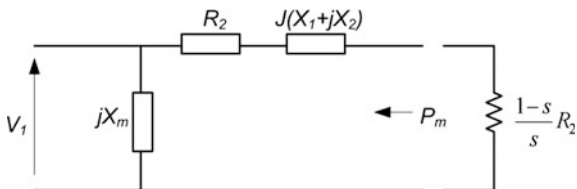


Fig. 4.9 Circuit model of the induction machine for $RX2$

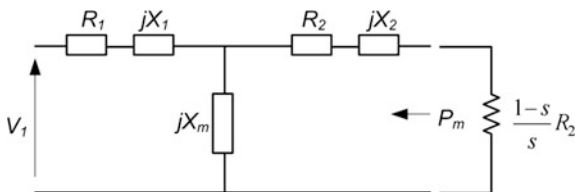
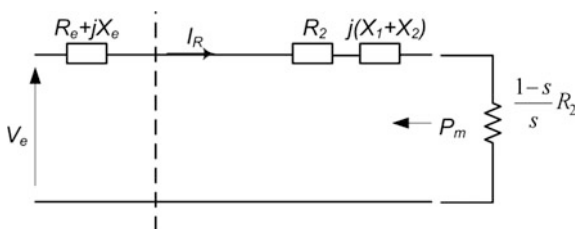


Fig. 4.10 Thevenin equivalent circuit model of the induction machine



circuit, its Thevenin equivalent circuit is drawn as shown in Fig. 4.10. For this circuit, the equivalent voltages and impedance, V_e and $R_e + jX_e$, respectively, is given as,

$$V_e = V_1 \frac{jX_m}{R_1 + j(X_1 + X_m)} \tag{4.23}$$

$$R_e + jX_e = \frac{(R_1 + jX_1)jX_m}{R_1 + j(X_1 + X_m)} \tag{4.24}$$

For the circuit shown in Fig. 4.9, the mechanical input power, P_m , of the WRIG calculated (4.17) becomes,

$$P_m = \frac{|V_e|^2 R_2 s^2 - R_2 |V_e|^2 s}{sR_e^2 + 2R_e R_2 s + R_2^2 + (sX_1 + sX_2)^2} \tag{4.25}$$

The procedure to obtain the slip remains same as discussed in Sect. 4.2.1. However, with the change in the active power, P is given as,

$$s_k = s_{k-1} + \Delta s = s_{k-1} + [J]^{-1} \Delta P_m \tag{4.26}$$

Thus, it can be seen that the *RX2* model includes the stator resistance. This makes the model more accurate, as it is not based on assumptions considered in *RX* model. This may add the computational burden on the LFA. However, the accuracy achieved is higher than the *RX* model. A slight modification of this to include the power calculations at all nodes of the model is presented in the next section.

4.4.3 Model-3: Three-Node Model

The model-1 and model-2 described above utilizes a simplified model of the induction machine. It includes stator and rotor, both in a single model. The three-node model is also a circuit-based model as shown in Fig. 4.11, but the circuit is not simplified, rather it adds three additional nodes, for each machine, in comparison to the existing power systems. The nodes included are *N1*, *N2*, and *N3*. *N1* is the node between the power system and stator; *N2* is the node connecting the stator, rotor, and the magnetizing component of the machine. *N3* is the node of the rotor at which the wind interacts with the rotor. The power available at *N3* is calculated using (4.17).

These models consider the dynamics of the individual machines. However, in case of a combination of different WGs, aggregate models and probabilistic model are used as discussed in the next section.

4.4.4 Model-3: Probabilistic Model

In configurations such as shown in Fig. 4.12, where a number of WTs are used to generate electricity. As the generators operate in a different manner, while maintaining the bus specifications, it is difficult to analyze the system. The models developed in earlier sections are based on individual asynchronous generator models. The performance of the farm at the bus is an aggregate of the generators

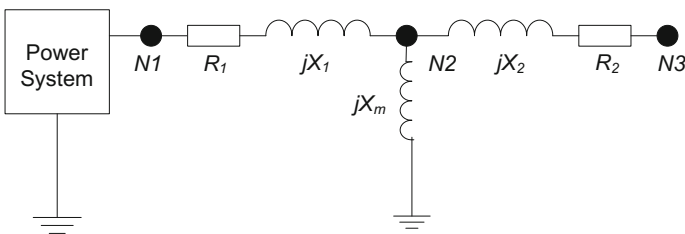
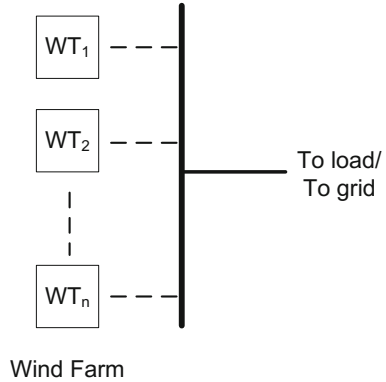


Fig. 4.11 Three-node model of the induction machine

Fig. 4.12 The general algorithm for load flow calculations



connected to the wind farm. In such situations, the generator is analyzed using the probabilistic model. The wind speed probability distribution is generally considered to follow a Weibull distribution. This function depends on three parameters (ξ_0 , α , and c), which are given by formula:

$$F(x) = 1 - \exp\left\{-\left(\frac{x - \xi_0}{\alpha}\right)^c\right\}, \quad x > \xi_0 \tag{4.27}$$

where

- x Wind speed
- α Scale parameter. The value of this parameter is related to the average wind speed at the location. If the wind speed probability distribution is given in m/s, then $\alpha \in [0.01, 20]$
- c Shape parameter, also known as slope, because the value of ‘ c .’ $c \in [0.25, 2.5]$
- ξ Location parameter. In this particular case, as the minimum wind speed is 0, $\xi_0 = 0$.

Therefore, it is easy to generate ‘pseudorandom’ observations using approaches such as

$$U = F(X; \xi_0, \alpha, c) = 1 - \exp\left\{-\left(\frac{X - \xi_0}{\alpha}\right)^c\right\} \tag{4.28}$$

while inverting the transformation produces

$$X = \xi_0 + \alpha(-\ln(1 - U))^{1/c} \tag{4.29}$$

After the generation of ‘pseudorandom’ observations U of a uniform distribution $(0, 1)$, the required observation of X of a Weibull distribution can be obtained from the previous expression for specific values of ξ_0 , α , and c .

The final mean power at a mean speed U_m is the probability density distribution $P(u)$ multiplied by the steady-state power $W(u)$ and summed (i.e., integrated) over all the range of wind speeds. Thus, the mean power P_m at a mean speed U is given by:

$$P_m = \int_0^{\infty} P(u) \cdot W(u) du \quad (4.30)$$

Using this, aggregate wind power of the wind farm is calculated, which can be used in the load flow analysis. Using these power models, the LFA is performed using WTs, which is discussed below.

4.5 Results Discussion

The LFA is a vital tool to perform a performance analysis of the power system with varying operating condition, along with different component. To compare the performance of the power system with different WGs models, Newton–Raphson-based LFA algorithm is considered. The results are discussed in three studies, namely

1. *Study-1*: The different PQ models are compared.
2. *Study-2*: The *RX* models and model-3 of the WGs are considered.
3. *Study-3*: Comparison of the accuracy of model-1 and model-2.

Finally, the probabilistic model-based LFA is discussed separately.

4.5.1 Study-1

In this study, the performance of different PQ models of the WECS in LFA is compared. To test the performance, the system shown in Fig. 4.13 is considered. Using NR, the LFA is performed with WGs with following parameters: $R_1 = 0.00571$ pu, $R_2 = 0.00612$ pu, $X_1 = 0.06390$, $X_2 = 0.1878$, and $X_m = 2.78000$. Using this turbine, the generator performance was observed at different wind speed conditions. The variation of power and voltage at the bus is shown in Figs. 4.13 and 4.14, respectively. Figure 4.13a shows that the active power, P determined by two methods remains same, nearly. However, the difference arises in the reactive power, Q , as shown in Fig. 4.13b, the requirement to maintain the terminal voltage, shown in Fig. 4.14.

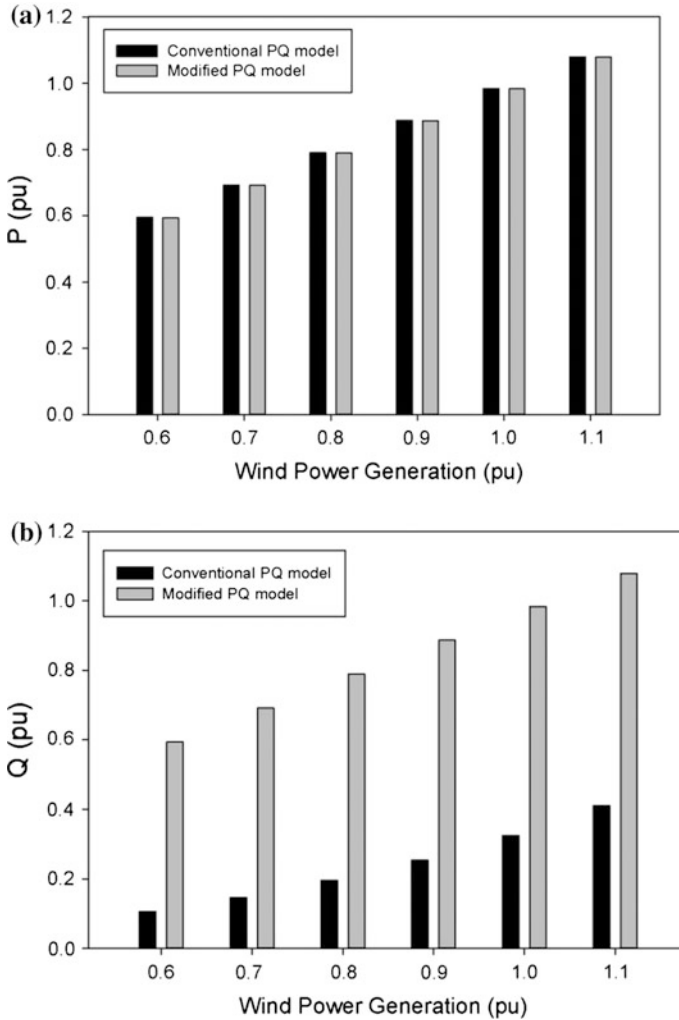


Fig. 4.13 P and Q obtained using conventional and modified PQ models

4.5.2 Study-2

To test the performance of the two RX models, i.e., RX and $RX2$, LFA was performed on IEEE-30 bus system [18]. To consider the wind in the bus system, a new bus, BUS 31 is added to the IEEE-30 bus system. This new bus is connected to the BUS 5. Twenty identical 660-kW wind-driven WRIGs are assumed to be connected to properly. Using the Steps discussed in Sect. 4.4.3, the LFA is performed. The

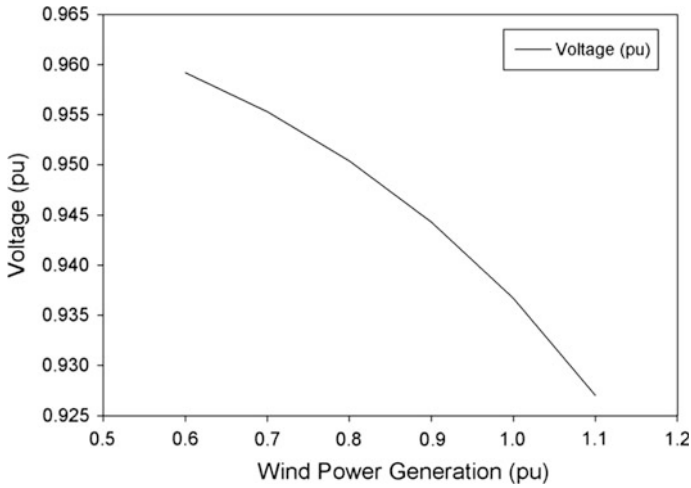


Fig. 4.14 Voltage variation at bus-bar

variations of the voltage and power are discussed and shown in Fig. 4.15 and Table 4.2 [13], respectively. It shows that slight variation is observed between the two models. With *RX2*, having no assumption is more accurate. Similar results are obtained with model-3, but with better convergence than model-1 and model-2 [8].

4.5.3 Study-3

The performance of the model-1 and model-2, in LFA is performed using a single WRIG. Using the WG with following specifications: $R_s = 0.00708 \Omega$, $X_1 = 0.07620 \Omega$, $X_m = 3.44979 \Omega$, $X_2 = 0.23289 \Omega$, and $R_R = 0.00759 \Omega$, *Rated Voltage* = 660 V, *Area swept by wind turbine* 531 m² and *rated power* = 330 kW, *wind speed variations* = 7–21 m s⁻¹ in steps of 2 m s⁻¹.

The power generated is calculated using WTs at wind speed varying from 7 to 21 m s⁻¹. For model-1, the power is calculated using (2); whereas, for model-2, it is calculated using the machine parameters. In both of these cases, the power generated depends on c_p , given by (2), is calculated using the constants given in Table 4.3 [3]. For these values, the power generated using the wind is calculated, and the LFA was performed using NR method, as shown in Table 4.4 [3]. The P depends on the wind speed; while Q requirement corresponds to the terminal voltage, as shown in the table. It shows that slight difference in the voltages between model-1 and model-2 is observed. This may be attributed to the difference in calculating the power generated. Figure 4.16 [3] shows the difference in

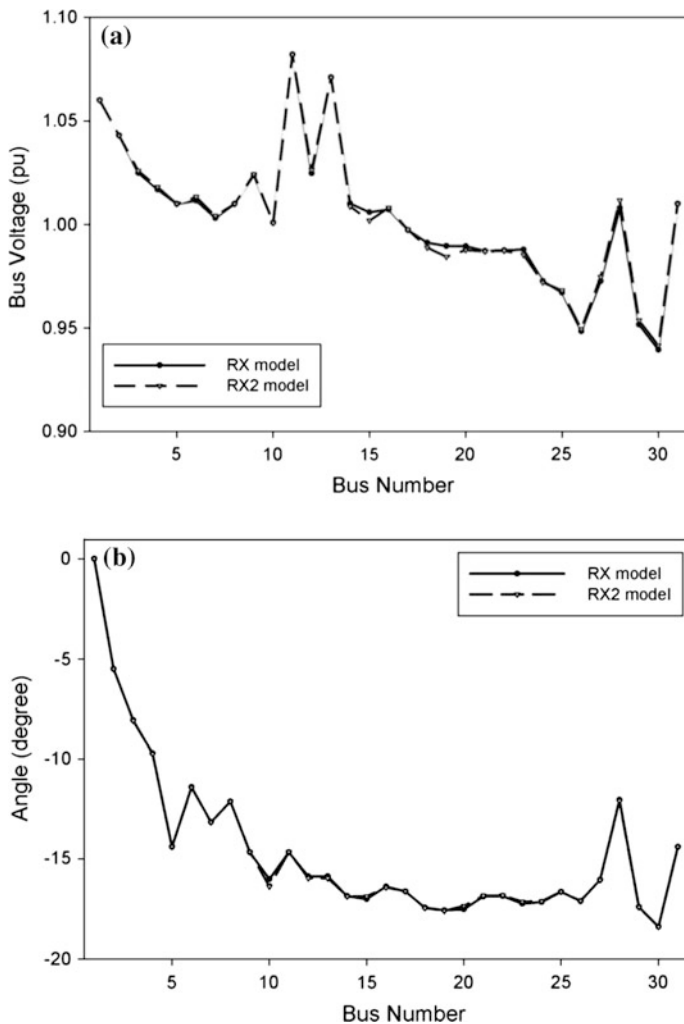


Fig. 4.15 Voltage and angle obtained using RX and RX2

calculating the power from the curve of the generator and WTs. From the curve, it is observed that RX model is more accurate model, as it lies near the operating point of the generator. Thus, RX models are more accurate for the inclusion of the wind in LFA.

Table 4.2 Comparative active and reactive power at the buses for the different *RX* models

S. No.	<i>RX</i>				<i>RX2</i>			
	P_g (pu)	P_l (pu)	Q_g (pu)	Q_l (pu)	P_g (pu)	P_l (pu)	Q_g (pu)	Q_l (pu)
1	261.3840	0.0000	-18.9510	0.0000	261.5840	0.0000	-19.5510	0.0000
2	0.0000	21.7000	46.7670	12.7000	0.0000	21.7000	44.9670	12.7000
3	0.0000	2.4000	0.0000	1.2000	0.0000	2.4000	0.0000	1.2000
4	0.0000	7.6000	0.0000	1.6000	0.0000	7.6000	0.0000	1.6000
5	0.0000	94.2000	36.2660	19.0000	0.0000	94.2000	35.3080	19.0000
6	0.0000	0.0000	0.0000	0.0000	0.0000	0.0000	0.0000	0.0000
7	0.0000	22.8000	0.0000	10.9000	0.0000	22.8000	0.0000	10.9000
8	0.0000	30.0000	33.4100	30.0000	0.0000	30.0000	27.2790	30.0000
9	0.0000	0.0000	0.0000	0.0000	0.0000	0.0000	0.0000	0.0000
10	0.0000	5.8000	0.0000	2.0000	0.0000	5.8000	0.0000	2.0000
11	0.0000	0.0000	30.3240	0.0000	0.0000	0.0000	30.0340	0.0000
12	0.0000	11.2000	0.0000	7.5000	0.0000	11.2000	0.0000	7.5000
13	0.0000	0.0000	35.4140	0.0000	0.0000	0.0000	34.1750	0.0000
14	0.0000	6.2000	0.0000	1.6000	0.0000	6.2000	0.0000	1.6000
15	0.0000	8.2000	0.0000	2.5000	0.0000	8.2000	0.0000	2.5000
16	0.0000	3.5000	0.0000	1.8000	0.0000	3.5000	0.0000	1.8000
17	0.0000	9.0000	0.0000	5.8000	0.0000	9.0000	0.0000	5.8000
18	0.0000	3.2000	0.0000	0.9000	0.0000	3.2000	0.0000	0.9000
19	0.0000	9.5000	0.0000	3.4000	0.0000	9.5000	0.0000	3.4000
20	0.0000	2.2000	0.0000	0.7000	0.0000	2.2000	0.0000	0.7000
21	0.0000	17.5000	0.0000	11.2000	0.0000	17.5000	0.0000	11.2000
22	0.0000	0.0000	0.0000	0.0000	0.0000	0.0000	0.0000	0.0000
23	0.0000	3.2000	0.0000	1.6000	0.0000	3.2000	0.0000	1.6000
24	0.0000	8.7000	0.0000	6.7000	0.0000	8.7000	0.0000	6.7000
25	0.0000	0.0000	0.0000	0.0000	0.0000	0.0000	0.0000	0.0000
26	0.0000	3.5000	0.0000	2.3000	0.0000	3.5000	0.0000	2.3000
27	0.0000	0.0000	0.0000	0.0000	0.0000	0.0000	0.0000	0.0000
28	0.0000	0.0000	0.0000	0.0000	0.0000	0.0000	0.0000	0.0000
29	0.0000	2.4000	0.0000	0.2000	0.0000	2.4000	0.0000	0.2000
30	0.0000	10.6000	0.0000	1.9000	0.0000	10.6000	0.0000	1.9000
31	0.0000	0.0000	0.0000	0.0000	0.0000	0.0000	0.0000	0.0000

4.5.4 LFA Using Model-3

The probabilistic model of the power generated through the WTs is more general as compared to the model-1 or model-2. The model relates the input and output of to provide the power generated, which is to be used for the LFA. As shown in Table 4.5 [14], the number of WTs operating (m) varies from 28 to 30 [14]. This allows considering the conditions of having some units generating power, only.

Table 4.3 Constant for power coefficient, c_p [3]

Constant	P_m (kW) = $f(U(\text{m s}^{-1}))$	$c_p = f(\lambda)$
a_0	-393.35	0.0699
a_1	468.91	-0.3765
a_2	-237.49	0.7400
a_3	65.71	-0.7216
a_4	-10.95	0.3892
a_5	1.16	-0.1214
a_6	-0.0804	0.0230
a_7	0.0035	-0.0027
a_8	9.49×10^{-9}	0.0001

Table 4.4 Real power (MW), reactive powers (MVar), and voltage (pu) obtained by means of Model-1 and Model-2 [3]

U (m s^{-1})	Real power		Reactive power		Voltage	
	PQ	RX	PQ	RX	PQ	RX
7	-3.132	-3.102	0.140	0.013	1.004	1.004
9	-6.807	-6.696	0.647	0.560	1.003	1.003
11	-11.366	11.036	1.837	1.785	1.000	1.000
13	-15.413	-14.843	3.395	3.449	0.995	0.995
15	-17.543	-16.640	4.182	4.467	0.992	0.992
19	-15.388	-14.929	3.377	3.494	0.995	0.995
21	-14.400	-13.550	2.957	3.211	0.996	0.997

Fig. 4.16 Curve for generator and wind turbine [3]

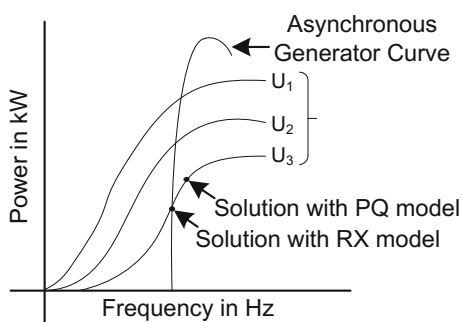


Table 4.5 Result for the simulation using Model-3

U (m s^{-1})	No. of wind speed (m)	Electric power generated (P)	Voltage (pu)
7	28	-5.34	1.004
9	28	-8.17	1.003
11	29	-10.97	1.000
13	30	-19.73	0.992
15	30	-27.86	0.980
17	28	-28.00	0.977

4.6 Conclusions

Renewable energy has provided an alternative to the utilities to have sustainable development. Wind energy has seen a large contribution in the power generation, worldwide. In these stochastic sources, it is difficult to obtain a particular value of power generated. This makes the operation and planning of the power system using the conventional techniques become difficult. The performance of the system becomes important to plan the capacities accordingly. LFA is a vital tool for this. However, stochastic nature of wind energy sources makes this analysis difficult, even with the load flow studies, which makes the inclusion of generator models in the LFA vital. This chapter shows the different methods for inclusion of wind energy sources in the LFA using different models. For this study, the models considered are (i) *PQ* model and its modification, (ii) *RX* model and its modification, (iii) three-node model, and (iv) probabilistic model. Based on these models, the load flow analysis is performed using *NR* method. To validate, these models developed are simulated using the MATLAB. The results show that *PQ* models offer large variation, as compared to the *RX* models. So, *RX* models are more suitable for LFA using individual machines. The three-node model improves the convergence of the *RX* models. However, probabilistic models are suitable for LFA in a wind farm.

References

1. Das JC (2011) Power system analysis: short-circuit load flow and harmonics, 2nd edn. CRC Press, Boca Raton
2. Debs AS (2008) Load flow analysis. In: Modern power systems analysis. Springer, US, pp 71–128
3. Feijoo AE, Cidras J (2000) Modeling of wind farms in the load flow analysis. IEEE Trans Power Syst 15(1):110–115
4. Herbert GMJ, Iniyan S, Sreevalsan E, Rajapandian S (2007) A review of wind energy technologies. Renew Sustain Energy Rev 11(6):1117–1145
5. Heras IS, Escrivá GE, Ortega MA (2011) Wind farm electrical power production model for load flow analysis. Renew Energy 36(3):1008–1013
6. Martinez JA, Mahseredjian J (2011) Load flow calculations in distribution systems with distributed resources. A review. In: 2011 IEEE Power and Energy Society general meeting, pp 1–8
7. El-Sharkawi MA (2015) Wind energy: an introduction. CRC Press, Boca Raton
8. Wang J, Huang C, Zobaa A (2016) Multiple-node models of asynchronous wind turbines in wind farm for load flow analysis. Electr Power Compon Syst 44(2):135–141
9. Muyeenname SM, Hasanien MH, Al-Durra A (2014) Transient stability enhancement of wind farms connected to a multi-machine power system using an adaptive ANN-controlled SMES. Energy Convers Manag 78(1):412–420
10. IEC 61400-21, Wind turbines (2008) Part 21: Measurement and assessment of power quality characteristics of grid connected wind turbines
11. Petru T, Thiringer T (2002) Modeling of wind turbines for power system studies. IEEE Trans Power Syst 17(4):1132–1139
12. Feijoo AE (2009) On *PQ* models for asynchronous wind turbines. IEEE Trans Power Deliv 24(4)

13. Wang L, Lin YH, Chen YT (2011) Load-flow analysis of a wind farm containing multiple wind-driven wound-rotor induction generators with dynamic slip control using RX models. *IEEE Trans Sustain Energy* 2(3):256–264
14. Divya KC, Nagendra Rao PS (2006) Models for wind turbine generating systems and their application in load flow studies. *Electr Power Syst Res* 76(9–10):844–856
15. Kabir MN, Mishra Y, Bansal RC (2016) Probabilistic load flow for distribution systems with uncertain PV generation. *Appl Energy* 163(1):343–351
16. Li H, Chen Z (2008) Overview of different wind generator systems and their comparisons. *IET Renew Power Gener* 2(2):123–138
17. Stott B (1974) Review of load-flow calculation methods. *Proc IEEE* 62(7):916–929
18. University of Washington, Electrical Engineering, “Power system test case archive,” available at: <http://www.ee.washington.edu/research/pstca/>

Chapter 5

Sensor-Less Estimation of Rotor Position in a Doubly Fed Induction Machine

G. Saravana Ilango, C. Nagamani, M.A. Asha Rani,
M. Jaya Bharata Reddy and A. Karthikeyan

Nomenclature

V	Instantaneous voltage
i	Instantaneous current
φ	Instantaneous flux
v_{dc}	DC link voltage
i_{ms}	Instantaneous stator magnetizing current
i_{dc}, i_L	DC side current for the front-end and the rotor-end converters, respectively
R	Resistance
L	Inductance
C	Capacitance
P	Real power
Q	Reactive power
ω_e	Angular frequency of stator flux
ω_r	Angular speed of rotor
ε	Phase shift between stator and rotor axis
μ	Phase shift between stationary axis and stator flux axis

G. Saravana Ilango · C. Nagamani · M.A. Asha Rani · M. Jaya Bharata Reddy (✉)
Department of Electrical and Electronics Engineering,
National Institute of Technology, Tiruchirappalli,
Tamil Nadu 620015, India
e-mail: jbreddy@nitt.edu

G. Saravana Ilango
e-mail: gsilango@nitt.edu

C. Nagamani
e-mail: cnmani@nitt.edu

M.A. Asha Rani
e-mail: asha_siju@yahoo.co.in

A. Karthikeyan
Department of Electrical and Electronics Engineering,
National Institute of Technology, Karnataka,
Surathkal, Mangalore, Karnataka 575025, India
e-mail: jakarthik@yahoo.com

θ_1	Phase shift between i_r and stator reference frame
θ_2	Phase shift between i_r and rotor reference frame
θ_s	Phase shift between V_s and stator reference frame

First Subscripts

s	Stator
r	Rotor
m	Mutual
fe	Front-end converter

Second Subscripts

a, b, c	Three phases
α, β	Stator reference frame
α_r, β_r	Rotor reference frame
d, q	Synchronous reference frame

Superscripts

*	Reference
---	-----------

5.1 Grid-Connected Doubly Fed Induction Machine

While the squirrel cage rotor induction machines are used mainly for a wide range of low- and medium-power applications, the wound rotor or slip ring induction machines are commonly used in medium- and large-power applications with limited range of operating speeds. The Doubly Fed Induction Machine (DFIM) is a system, where the stator of the slip ring induction machine is directly connected to the utility grid while the rotor terminals are interfaced to the grid via two back-to-back voltage source converters with a common DC link and a transformer. DFIMs are attractive due to the high performance and are used in high-power drives and also in the wind power generation systems. The rotor-side control implies that the power converters need to be only fractional rated. The increased cost of a slip ring machine is well adjusted by the reduced size and cost of power electronic converters in the rotor circuit. Variable speed operation, four-quadrant control, operation at unity power factor, and low-power losses are the other advantages [1]. Stator flux-oriented vector control or decoupled control is the preferred technique with a good dynamic and steady state response facilitating independent control of speed and torque when the machine is used as a motor. Alternatively, the stator active and reactive powers are controlled independently when the machine is used as a

generator which is popularly known as the Doubly Fed Induction Generator (DFIG) [2]. Considering the growing importance of distributed generation, the present emphasis is on the generating mode of operation of DFIM.

5.2 Basics of Decoupled Control

The schematic diagram of the DFIM is shown in Fig. 5.1.

The stator terminals are directly connected to the utility grid with nominal voltage and frequency while the rotor terminals are interfaced with the grid through a pair of back-to-back connected converters and a suitable transformer. Usually, this is a step-up transformer to match the voltage ratio between the stator and rotor in the machine.

Independent control of active and reactive powers is accomplished through current injection in the rotor circuit [3]. Appropriate switching control of rotor-side converter regulates the rotor-fed voltage, frequency, and phase, thus facilitating bidirectional flow of active power in the rotor. Also, the excitation requirement of the machine can be shared between the stator and rotor. Due to the bidirectional power control capability, the operating range in the torque–speed plane spreads out on either side of synchronous speed implying both sub-synchronous and super-synchronous modes of motoring or generating. Thus, four-quadrant operation is an attractive possibility. Likewise, the line-side converter facilitates unity power factor operation apart from regulating DC bus voltage. Flicker problems are limited as a result of variable speed operation of rotor.

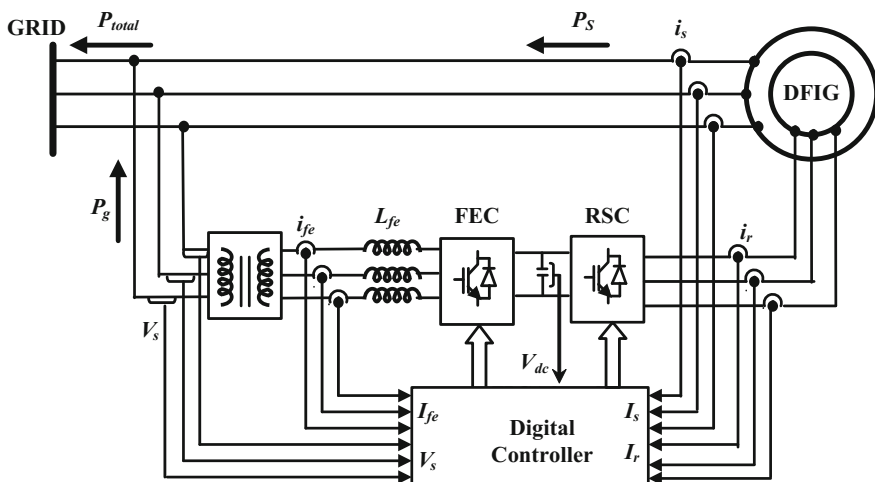


Fig. 5.1 Schematic diagram of the doubly fed induction generator

The mathematical model of a generalized machine [4, 5] is the basis for modeling the DFIM. The stator and rotor voltages in the synchronous reference frame can be expressed as

$$\begin{bmatrix} V_{sq} \\ V_{sd} \\ V_{rq} \\ V_{rd} \end{bmatrix} = \begin{bmatrix} R_s + sL_s & \omega_e L_s & sL_m & \omega_e L_m \\ -\omega_e L_s & R_s + sL_s & -\omega_e L_m & sL_m \\ sL_m & (\omega_e - \omega_r)L_m & R_r + sL_r & (\omega_e - \omega_r)L_r \\ -(\omega_e - \omega_r)L_m & sL_m & -(\omega_e - \omega_r)L_r & R_r + sL_r \end{bmatrix} \begin{bmatrix} i_{sq} \\ i_{sd} \\ i_{rq} \\ i_{rd} \end{bmatrix} \quad (5.1)$$

where s is the Laplace operator.

The stator and rotor flux linkages can be written in terms of currents as

$$\varphi_{sq} = L_s i_{sq} + L_m i_{rq}; \quad \varphi_{sd} = L_s i_{sd} + L_m i_{rd} \quad (5.2)$$

and

$$\varphi_{rq} = L_r i_{rq} + L_m i_{sq}; \quad \varphi_{rd} = L_r i_{rd} + L_m i_{sd} \quad (5.3)$$

The relationship between the speed ω_r and electromagnetic torque T_e is given by

$$T_e = T_L + J \frac{d\omega_m}{dt} + B\omega_m = T_L + \frac{2}{P} J \frac{d\omega_r}{dt} + \frac{2}{P} B\omega_r \quad (5.4)$$

where T_L is load torque, J is the combined moment of inertia of rotor and load, B is coefficient of friction, P is number of poles, ω_e is the angular frequency of stator flux, ω_m is the rotor angular velocity (mechanical rad/s), and ω_r is rotor angular velocity (electrical rad/s). In terms of currents, the electromagnetic torque T_e can be written as

$$T_e = \frac{3P}{2} L_m (i_{sq} i_{rd} - i_{sd} i_{rq}), \quad \text{while } \omega_r = \frac{d\varepsilon}{dt} \quad \text{and, } \omega_e = \frac{d\theta_s}{dt} \quad (5.5)$$

The rotor d - q voltages and currents need to be computed using the rotor position (ε) information whereas the stator flux position (θ_s) is obtained from a grid-side PLL.

5.2.1 Control of Rotor-Side Converter (RSC)

The space vector diagram depicting different variables under balanced grid conditions is shown in Fig. 5.2a, and the per phase steady state equivalent circuit of a doubly fed induction machine referred to the stator is shown in Fig. 5.2b.

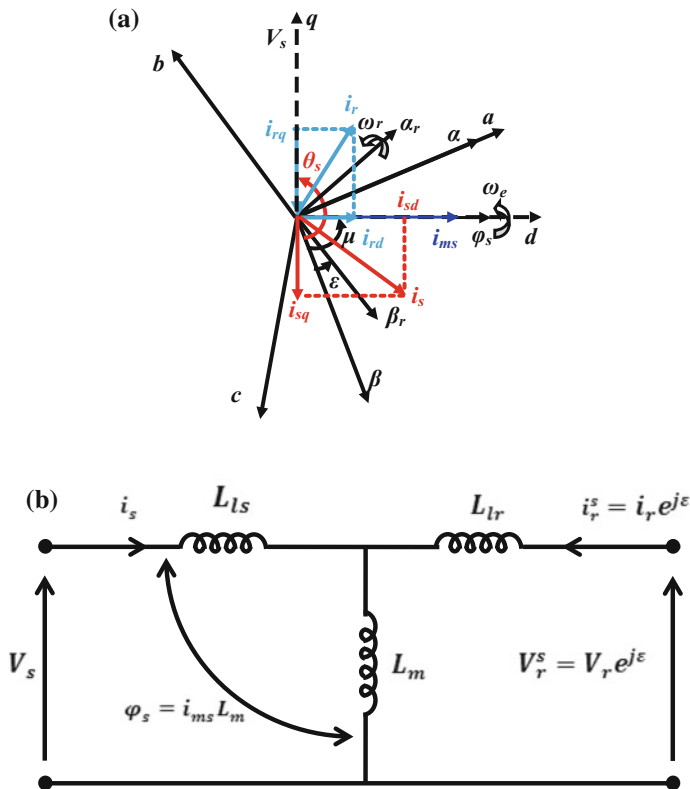


Fig. 5.2 a Space vector representation under balanced grid conditions. b Per phase steady state equivalent circuit of DFIM

The α -axis is oriented along stator a -phase axis whereas the β -axis leads the α -axis by 90° . The d - q reference frame rotates at synchronous speed ω_e with respect to the stationary α - β reference frame and makes an angle $\theta_s = \omega_e t = (90^\circ + \mu)$ with respect to α - β frame at time t .

The synchronously rotating d - q reference frame (Fig. 5.2a) is selected such that the direct or d -axis is oriented along the stator flux space vector (φ_s) and the quadrature or q -axis is oriented along the stator voltage space vector (V_s) facilitating a stator flux-oriented frame of reference. Such a selection enables the decoupling of active and reactive current loops. Also, the magnetizing current vector i_{ms} responsible for stator flux is aligned with φ_s . That is, only the forced flux, i.e., the positive sequence flux alone, revolves in the air gap with balanced grid voltages. Thus, the stator voltage component along d -axis and the stator flux/magnetizing current along q -axis are zero.

The stator d - q voltages under balanced grid conditions can be represented as

$$V_s = V_{sq} - jV_{sd} = V_{sq} \quad (5.6)$$

Similarly, the components of stator flux (5.2) and magnetizing current in the d - q frame are given by

$$\varphi_{sd} = L_s i_{sd} + L_m i_{rd}; \quad \varphi_{sq} = L_s i_{sq} + L_m i_{rq} = 0 \quad (5.7)$$

and

$$i_{ms} = i_{msd} = \frac{L_s}{L_m} i_{sd} + i_{rd}; \quad \frac{L_s}{L_m} i_{sq} + i_{rq} = i_{msq} = 0 \quad (5.8)$$

Along the d -axis, the stator and rotor currents i_{sd} and i_{rd} add to make up the magnetizing current (i_{ms}) of the machine. Thus, by controlling i_{rd} suitably, the magnitude of i_{sd} can be controlled automatically, thereby regulating the stator power factor.

Since the q -axis magnetizing current is zero, the magnitude of stator active current i_{sq} is equal to the magnitude of i_{rq} but opposite in polarity. Thus, by controlling i_{rq} , the magnitude of i_{sq} can be controlled and hence the stator active power can be controlled.

Thus, the stator active and reactive power of a DFIM in terms of d - q components of stator voltages and currents under balanced grid voltage are given by

$$P_s = \frac{3}{2} (V_{sq} i_{sq} + V_{sd} i_{sd}) \quad (5.9)$$

and

$$Q_s = \frac{3}{2} (V_{sq} i_{sd} - V_{sd} i_{sq}) \quad (5.10)$$

For the desired steady state active and reactive power references, the respective commands for stator d - q currents can be derived from (5.9) and (5.10) substituting $V_{sd} = 0$. Thus,

$$i_{sq(\text{ref})} = \frac{P_{\text{sref}}}{\frac{3}{2} V_{sq}} \quad (5.11)$$

and

$$i_{sd(\text{ref})} = \frac{Q_{\text{sref}}}{\frac{3}{2} V_{sd}} \quad (5.12)$$

Further, the references for rotor currents can be deduced from (5.11) to (5.12) using (5.8) as

$$i_{rq(\text{ref})} = -\frac{L_s}{L_m} i_{sq(\text{ref})} \quad (5.13)$$

and

$$i_{rd(\text{ref})} = i_{msd} - \frac{L_s}{L_m} i_{sd(\text{ref})} = \frac{V_{sq}}{\omega_e L_m} - \frac{L_s}{L_m} i_{sd(\text{ref})} \quad (5.14)$$

Equations (5.13) and (5.14) depict the feature of decoupled control of torque and flux, respectively in the DFIM (stator active and reactive powers in DFIG) through appropriate current injection in the rotor circuit at required magnitude, phase, and frequency. Further, the reference for the rotor d -axis current can be stipulated directly depending on the sharing of reactive power between the stator and rotor. The rotor d - q voltages required to drive the commanded currents can be obtained by subtracting the feed forward terms from the output of current controllers and can be expressed as

$$V_{rd} = R_r i_{rd} + L_r \frac{d}{dt} i_{rd} + L_m \frac{d}{dt} i_{sd} - (\omega_e - \omega_r)(L_r i_{rq} + L_m i_{sq}) \quad (5.15)$$

and

$$V_{rq} = R_r i_{rq} + L_r \frac{d}{dt} i_{rq} + L_m \frac{d}{dt} i_{sq} + (\omega_e - \omega_r)(L_r i_{rd} + L_m i_{sd}) \quad (5.16)$$

where all the rotor d - q voltages and currents are referred to the stator. The transformation of quantities in rotor reference frame to the synchronously rotating d - q reference frame or to the stator α - β reference frame and vice versa requires accurate information of rotor position for precise control.

5.2.2 Control of Front-End Converter (FEC)

The FEC can be controlled to regulate the DC link voltage and to maintain a desired power factor at the stator terminals. By regulating these, the total active and reactive powers can be controlled. The DC link voltage is regulated using a PI-based voltage controller such that the output of the controller can be considered as a reference for the FEC q -axis current.

The FEC active and reactive powers can be represented as

$$P_g = \frac{3}{2} (V_{sq} i_{feq} + V_{sd} i_{fed}) \quad (5.17)$$

$$Q_g = \frac{3}{2} (V_{sq} i_{fed} - V_{sd} i_{feq}) \quad (5.18)$$

Thus, the reference currents for FEC can be derived from (5.17) and (5.18) substituting $V_{sd} = 0$.

$$i_{\text{feq(ref)}} = \frac{P_{\text{feref}}}{\frac{3}{2} V_{\text{sq}}} \quad (5.19)$$

and

$$i_{\text{fed(ref)}} = \frac{Q_{\text{feref}}}{\frac{3}{2} V_{\text{sd}}} \quad (5.20)$$

The necessary voltages from the FEC are as follows:

$$V_{\text{fed}} = V_{\text{sd}} - R_{\text{fe}} i_{\text{fed}} - L_{\text{fe}} \frac{d}{dt} i_{\text{fed}} + \omega_e L_{\text{fe}} i_{\text{feq}} \quad (5.21)$$

and

$$V_{\text{feq}} = V_{\text{sq}} - R_{\text{fe}} i_{\text{feq}} - L_{\text{fe}} \frac{d}{dt} i_{\text{feq}} - \omega_e L_{\text{fe}} i_{\text{fed}} \quad (5.22)$$

The rate of change of the DC link voltage and the current i_L influences the q -axis reference current of FEC. That is,

$$C \frac{dV_c}{dt} = i_{\text{dc}} - i_L \quad (5.23)$$

Further, after compensating for the cross-coupling terms in (5.21) and (5.22), the d - q control voltages for FEC are obtained. Both RSC and FEC current controllers are generally chosen to be PI controllers designed in field coordinates as shown in Fig. 5.3. Thus, the control variables are DC quantities which result in zero steady state error under balanced grid voltage. Hence, magnitude and phase errors are absent and also design and implementation are simpler.

The voltage references for RSC and FEC in d - q coordinates are then transformed to the a - b - c frame of reference. Further, they are usually processed in a Pulse Width Modulation (PWM) block to generate the switching pulses for the power converters. The output voltages of the power converters (RSC and FEC) are thus commanded in closed loop to obtain the desired targets of torque and flux of DFIM (or active power and reactive power in DFIG).

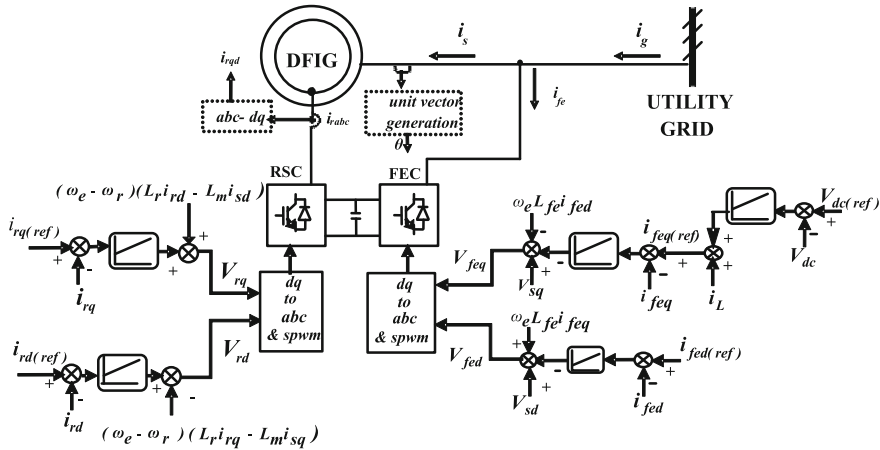


Fig. 5.3 Schematic diagram of DFIG control system

5.3 Significance of Rotor Position and Speed

Typically, the decoupled control of grid-connected DFIM involves maneuvering of the active and reactive components of rotor current as seen in the stator flux reference frame. Thus, by using the rotor-side control, the speed and torque (or stator active and reactive powers) can be independently controlled while the stator terminals are directly connected to the grid. Commonly, the grid flux-oriented reference frame is adopted [6] for the controller. Resolving the rotor current into components, one along the stator flux and the other along an axis perpendicular to it, is a complex process, wherein the dynamically varying position of the rotor (with respect to that of the stator flux) is an important input signal. In other words, the transformation of rotor quantities from the rotor reference frame to the synchronously rotating d - q reference frame for precise control requires accurate information of rotor position. The accuracy of the rotor position signal has a significant impact on the outcome of the decoupled control of the DFIM. Further, the actual rotor speed is one of the input parameters needed in the signal processing stage for the decoupled control.

Literature reveals several studies [7, 8] based on the hardwired sensors for extracting the rotor position and speed. Embedded flux (search) coils shaft-mounted encoders were some of the physically mounted devices to track the rotor position signal. However, the errors in the extracted signal, additional mounting and cabling, tedious maintenance, and added cost are the undesirable features of these hardwired sensors. Thus, an ideal sensor-less estimation technique or algorithm should facilitate starting on the fly and should provide a quick, accurate, and stable signal even under varying grid supply or load conditions, while requiring only a minimal set of real-time voltage and current as feedback signals. Conveniently, such voltage

and current sensors are commonly a part of the existing system hardware for power or speed control and also do not need any maintenance.

5.4 Brief Review of Sensor-Less Estimation Techniques

Sensor-less estimation of rotor position or speed has been widely investigated by several researchers. Typically, the schemes can be classified as two broad categories: closed loop and open loop. Generally, open loop schemes [9, 10] involve computations based on the mathematical model of machine while the closed loop schemes are based on Model Reference Adaptive System (MRAS) techniques or observer-based techniques. The open loop schemes are noninvasive and do not require any additional signals to be injected along with the machine input. These methods depend on measured currents and voltages to estimate the flux linkage in order to compute the rotor speed/position using the dynamic equations of the machine. Most open loop schemes involve estimation of stator flux space vector which generally is obtained by integrating the induced emf or stator voltage (neglecting the resistive voltage drop). However, these techniques are prone to inaccuracies due to parameter variations apart from errors due to the drift and saturation of integrator(s). Also, the differentiation of the position signal to get the speed signal causes high-frequency noise and glitches and calls for low-pass filtering. This in turn leads to time delays in the response. For the flux estimation, the open loop schemes either employ a voltage integrator [11, 12], or depend upon inverse trigonometric computations in real time [13], or employ recursive procedures [14, 3]. An improved stator flux position estimation scheme for rotor-side control of a Wound Rotor Induction Machine (WRIM) is presented in [15], where the phase and magnitude errors due to the low-pass filter are eliminated using an error-decaying mechanism in the estimator.

Among the closed loop schemes, the Model Reference Adaptive System (MRAS) technique is widely reported. The idea behind MRAS-based algorithms developed by Landau in the year 1979 was to minimize the difference between the reference model and an adaptive model using an adaptation mechanism. Generally, the reference model is based on a set of equations independent of the parameter to be estimated (rotor speed, say). A few of the variables are measured whereas one of the unmeasured state variables is considered as the tuning signal for forcing or maneuvering the adaptation mechanism. The error signal used to drive the adaptation mechanism is derived from either the current or flux in the rotor or stator. Further, the MRAS schemes also require an ideal integrator in the reference model. In addition, closed loop MRAS schemes use different reference variables such as rotor flux [16], measured stator current [17], rotor currents [18–21], reactive power [22, 23] or back emf error [24]. Adaptive sliding mode observer schemes report use of stator current [25] or magnetizing current [26] as the tuning variable for the sensor-less estimation of position and speed in an induction machine. Other techniques such as observer-based estimation, or methods employing recursive

approach or inverse trigonometric calculations present a daunting computational burden and also time delay. The product of voltage and current (X-MRAS scheme) as a reference input [27–29] facilitates operation at low speeds, while the sensitivity to machine parameter variations limits the efficacy of the scheme. Further, the need for speed information to compute the position of the stator flux vector and failure under shoot-through faults are the other drawbacks.

Schemes based on Artificial Neural Network (ANN) [30–32] and fuzzy logic [33] are computationally demanding and hence involve fast digital processors and large memory. Similarly, predictive [34] and other MRAS schemes with parallel PI control loops for torque and flux control include integration of stator voltage [35] for speed estimation. Estimation of rotor speed from the rotor position involves the measured stator currents and voltages [36, 37] and rotor currents [36]. However, adding a central frequency rather than the actual frequency to the PI controller for rotor position computation leads to slow dynamic response and hence a large settling time [36]. Inverse trigonometric computations are also used [37] for rotor flux position estimation. An angle tracking observer (ATO) scheme based on rotor position [38] and a rotor flux-based MRAS scheme [39] are proposed for speed estimation. However, the position of stator voltage vector can be computed essentially through use of inverse trigonometric computation [38] and rotor speed information [39].

5.5 Sensor-Less Estimation of Rotor Position

As mentioned earlier, most sensor-less estimation techniques can be classified as open loop or closed loop. This section presents the underlying theory and the mathematical formulation of the algorithms for both categories. Also, one of the recently reported techniques under each category is illustrated.

5.5.1 *Open Loop Techniques*

The rotor current space vector subtends an angle θ_1 with the stationary reference frame (alpha axis) whereas it makes an angle θ_2 with the rotor reference frame (α_r -axis). Evidently, the difference between these two angles gives the required rotor position [14]. Thus, the rotor position, ε , can be written as

$$\varepsilon = \theta_1 - \theta_2 \quad (5.24)$$

However, in a recently reported scheme which has several improvements over the predecessors, the computation of rotor currents in the stator reference frame involves estimation of magnetizing current [3] using a recursive approach (Fig. 5.4a). Further, the rotor speed is estimated by the differentiation of the rotor

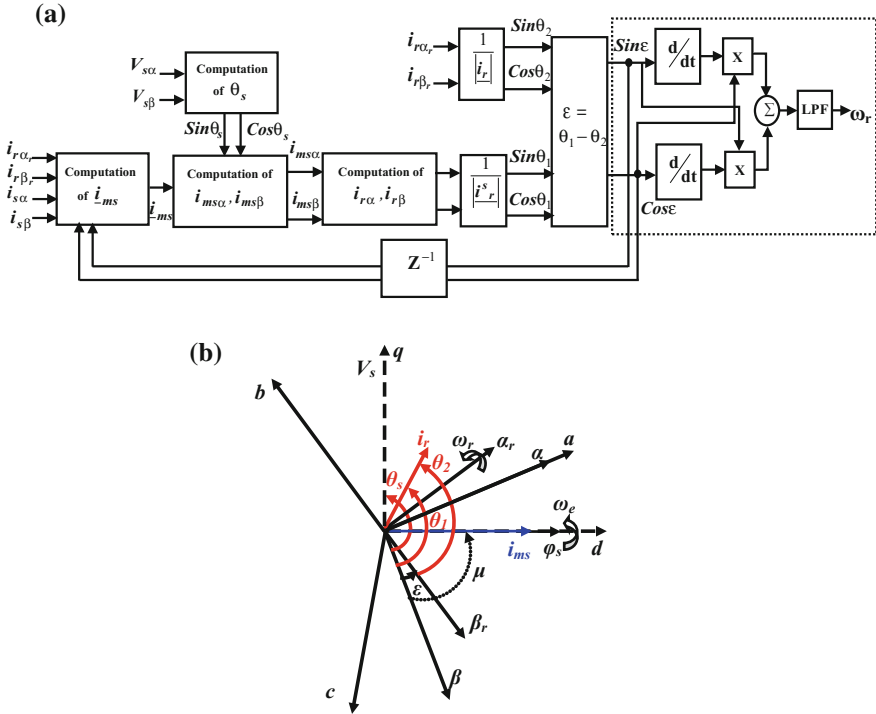


Fig. 5.4 **a** Block diagram of the rotor position computation scheme proposed in [3] and **b** Space vector diagram showing the angular relation between vectors in [3]

position signal which needs to be followed by trigonometric computations. The space vector diagram showing the angular relation between vectors in [3] is as shown in Fig. 5.4b.

Karthikeyan et al. [10] adopted the basic idea of the phase difference between the stationary and rotor reference frames while proposing a novel and significantly improved mechanism of computing the rotor position without actually computing or estimating the stator flux, especially under nominal grid voltage conditions. The main improvement comes from utilizing the resolved components of stator flux in the stationary reference frame to obtain the rotor current components in the same (stationary) reference frame.

5.5.1.1 Computing Rotor Position of a Grid-Connected DFIM

The rotor position is computed in a simple process, which is devoid of flux estimation or computation. The measured stator and rotor quantities along with known machine parameters are used to compute the components of stator flux in the stationary reference frame. The algorithm is slightly modified to accommodate the

case when the stator flux is not constant. The method does not include voltage integration. The direct computation of rotor position eliminates recursive or inverse trigonometric computations in real time. As a consequence of the above factors, the system response is spontaneous and exact, even while transiting through the synchronous speed. Further, the practical implementation can be done using a low-cost digital processor.

It is assumed that there is no saturation in the machine and the grid voltage is balanced. Two cases are considered: (a) the stator flux is constant and (b) the stator flux is fluctuating. Foregoing sections present the steps in rotor position computation, laboratory implementation, and test results.

5.5.1.2 Case of Constant Stator Flux

Figure 5.4a shows the space vectors of the stator voltage, flux, and the rotor current in the stationary and rotor reference frames. The α and β axes define the stationary reference frame whereas the rotor reference frame is defined by α_r and β_r axes. The β -axis of stator reference frame makes an angle θ_1 with i_r and with respect to the β_r -axis it makes an angle θ_2 . From this, it can be inferred that the rotor position ε is essentially the difference between θ_1 and θ_2 . The sequence of steps in computing the rotor position ε is given below.

Step 1A: Compute the unit vectors of μ and angular velocity ω_e of stator flux

Since the stator voltage is balanced and the stator flux is constant in the present case, the position and angular velocity of stator flux can be computed from the measured stator voltage V_s after transformation to the α - β reference frame.

$$\sin(\mu) = -\frac{V_{s\alpha}}{\sqrt{(V_{s\alpha}^2 + V_{s\beta}^2)}} \quad (5.25)$$

$$\cos(\mu) = \frac{V_{s\beta}}{\sqrt{(V_{s\alpha}^2 + V_{s\beta}^2)}} \quad (5.26)$$

From (5.25) and (5.26), the angular velocity of stator flux can be computed as

$$\omega_e = \cos(\mu) \frac{d}{dt} \sin(\mu) - \sin(\mu) \frac{d}{dt} \cos(\mu) \quad (5.27)$$

Step 2A: Compute the unit vectors of θ_2 and components of i_r in rotor reference frame ($i_{r\alpha_r}$ and $i_{r\beta_r}$).

Measured rotor winding currents are utilized to compute the components in the α_r - β_r reference frame. Further, from Fig. 5.4b,

$$\sin(\theta_2) = \frac{i_{r\alpha_r}}{\sqrt{(i_{r\alpha_r}^2 + i_{r\beta_r}^2)}} \quad (5.28)$$

$$\cos(\theta_2) = \frac{i_{r\beta_r}}{\sqrt{(i_{r\alpha_r}^2 + i_{r\beta_r}^2)}} \quad (5.29)$$

Step 3A: Compute the unit vectors of θ_1 and components of i_r in stator reference frame ($i_{r\alpha}$ and $i_{r\beta}$)

The rotor current coordinates in the stationary reference frame can be computed in a simple manner based on analytical substitutions for the resolved flux components in terms of measurable stator and rotor quantities. Thus, the scheme eliminates the need for estimation or computation of stator flux when it can be considered constant.

The components of stator flux in the α - β reference frame can be expressed as

$$\varphi_{s\alpha} = L_s i_{s\alpha} + L_m i_{r\alpha} \quad (5.30)$$

$$\varphi_{s\beta} = L_s i_{s\beta} + L_m i_{r\beta} \quad (5.31)$$

From (5.30) and (5.31), the rotor currents in the stationary reference frame can be written as

$$i_{r\alpha} = \frac{(\varphi_{s\alpha} - L_s i_{s\alpha})}{L_m} \quad (5.32)$$

$$i_{r\beta} = \frac{(\varphi_{s\beta} - L_s i_{s\beta})}{L_m} \quad (5.33)$$

If these currents can be expressed in terms of variables other than the flux through equivalent analytical substitutions, the procedure can be rendered significantly simpler. In the stationary reference frame, the stator voltage components are given by

$$V_{s\alpha} = R_s i_{s\alpha} + \frac{d}{dt} \varphi_{s\alpha} \quad (5.34)$$

$$V_{s\beta} = R_s i_{s\beta} + \frac{d}{dt} \varphi_{s\beta} \quad (5.35)$$

Also, the components of stator flux can be expressed as

$$\varphi_{s\alpha} = \left| \underline{\varphi}_s \right| \sin \mu \quad (5.36)$$

$$\varphi_{s\beta} = \left| \underline{\varphi}_s \right| \cos \mu \quad (5.37)$$

Upon differentiation of (5.36) and (5.37) with respect to time,

$$\frac{d}{dt} \varphi_{s\alpha} = \frac{d}{dt} (|\varphi_s| \sin \mu) = |\varphi_s| \cos \mu \frac{d\mu}{dt} + \sin \mu \frac{d|\varphi_s|}{dt} = \varphi_{s\beta} \omega_e + \sin \mu \frac{d|\varphi_s|}{dt} \quad (5.38)$$

and

$$\frac{d}{dt} \varphi_{s\beta} = \frac{d}{dt} (|\varphi_s| \cos \mu) = -|\varphi_s| \sin \mu \frac{d\mu}{dt} + \cos \mu \frac{d|\varphi_s|}{dt} = -\varphi_{s\alpha} \omega_e + \cos \mu \frac{d|\varphi_s|}{dt} \quad (5.39)$$

where the term $\frac{d}{dt}(\mu)$ can be readily observed to be the same as the angular velocity of the stator flux. Also, for the present case, the magnitude of stator flux is constant, and hence, the time derivative of the same in (5.38) and (5.39) can be ignored.

Using the result of (5.38) and (5.39) in (5.34) and (5.35) gives

$$V_{s\alpha} = R_s i_{s\alpha} + \omega_e \varphi_{s\beta} = R_s i_{s\alpha} + \omega_e (L_s i_{s\beta} + L_m i_{r\beta}) \quad (5.40)$$

and,

$$V_{s\beta} = R_s i_{s\beta} - \omega_e \varphi_{s\alpha} = R_s i_{s\beta} - \omega_e (L_s i_{s\alpha} + L_m i_{r\alpha}) \quad (5.41)$$

By rearranging the terms in (5.40) and (5.41), we get

$$i_{r\alpha} = \frac{R_s i_{s\beta} - (V_{s\beta} + \omega_e L_s i_{s\alpha})}{\omega_e L_m} \quad (5.42)$$

and

$$i_{r\beta} = \frac{V_{s\alpha} - (R_s i_{s\alpha} + \omega_e L_s i_{s\beta})}{\omega_e L_m} \quad (5.43)$$

As against (5.32) and (5.33), Eqs. (5.42) and (5.43) do not contain flux terms and contain only the measurable stator voltages and currents. Thus, $i_{r\alpha}$ and $i_{r\beta}$ are computed implicitly totally avoiding computation or estimation of the stator flux. Using (5.42) and (5.43), the unit vectors of angle θ_1 can be computed.

$$\sin(\theta_1) = \frac{i_{r\alpha}}{\sqrt{(i_{r\alpha}^2 + i_{r\beta}^2)}} \quad (5.44)$$

$$\cos(\theta_1) = \frac{i_{r\beta}}{\sqrt{(i_{r\alpha}^2 + i_{r\beta}^2)}} \quad (5.45)$$

Step 4A: Computation of rotor position [i.e., the angle $(\theta_1 - \theta_2)$]

Having obtained the values of $\sin(\theta_1), \cos(\theta_1), \sin(\theta_2),$ and $\cos(\theta_2)$, the unit vectors $\sin(\varepsilon)$ and $\cos(\varepsilon)$ can be computed using

$$\sin(\varepsilon) = \sin(\theta_1) \cos(\theta_2) - \cos(\theta_1) \sin(\theta_2) \tag{5.46}$$

$$\cos(\varepsilon) = \cos(\theta_1) \cos(\theta_2) + \sin(\theta_1) \sin(\theta_2) \tag{5.47}$$

Finally, the rotor speed is given by [3]

$$\omega_{r(\text{computed})} = \cos(\varepsilon) \frac{d}{dt} \sin(\varepsilon) - \sin(\varepsilon) \frac{d}{dt} \cos(\varepsilon) \tag{5.48}$$

A first-order low-pass filter is used to filter the undesirable noise due to signal differentiation.

The procedure outlined through Steps 1A–4A brings forth the uniqueness of this technique wherein the rotor position and speed are directly computed. It is notable that in the particular case of constant stator flux, there is no need to compute the flux. This is one singular feature much different from several other methods reported earlier [12, 13, 18, 25]. Thus, the method facilitates to compute the rotor position without the explicit estimation or computation of stator flux, when it is constant in particular. Figure 5.5 shows the schematic of the rotor position computation algorithm for the case of constant stator flux.

5.5.1.3 Case of Fluctuating Stator Flux

Similar to the case of constant stator flux, the basic assumptions of balanced grid voltage and no magnetic saturation are considered here also. However, the stator flux is assumed constant for the initialization alone. Further, as in the previous case,

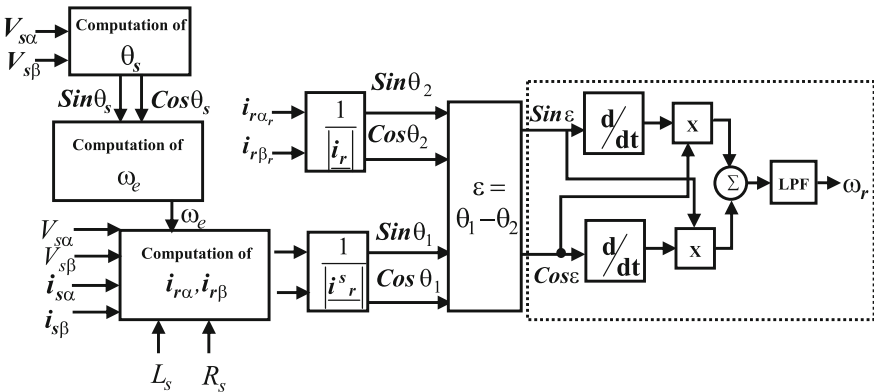


Fig. 5.5 Rotor position computation under constant stator flux

the computation of position μ and angular velocity ω_e of stator flux is based (5.25)–(5.27) using the stator voltage components just for the initial sampling cycle alone. However, after the initial sampling cycle, the magnitude of stator flux, position μ , and also angular velocity ω_e is computed explicitly in every sampling cycle. Except for this minor modification, the algorithm for rotor position computation remains largely the same. This is illustrated below.

Step 1B: Compute the position vectors of μ and angular velocity ω_e of stator flux.

With the balanced grid voltages and constant stator flux (assumed) initially, the position and angular velocity of stator flux can be computed from the measured stator voltage V_s after transformation to the α - β reference frame (as in Step 1A).

Step 2B: Compute the position vectors of θ_2 and components of i_r in rotor reference frame. This is the same as Step 2A. Thus, $\sin(\theta_2)$ and $\cos(\theta_2)$ can be computed.

Step 3B: Compute the position vectors of θ_1 and components of i_r in stator reference frame.

The rotor current coordinates in the stationary reference frame can be computed in a slightly different procedure to account for the fluctuations in stator flux. In this case, the time rate of change of stator flux vector in the stationary reference frame needs to be computed explicitly. Thus, there is only a minor addition in this step as compared to Step 3A.

As explained in Step 3A, the stator flux components $\phi_{s\alpha}$ and $\phi_{s\beta}$ are computed from (5.30) to (5.37) using the initial value for position μ and angular velocity of stator flux ω_e . For the initial sampling cycle alone, the time derivatives of these flux components are assumed to be negligible. However, subsequently, these can be computed using the known, previous samples of $\phi_{s\alpha}$ and $\phi_{s\beta}$. That is, the terms $\frac{d}{dt}|\phi_s|$ appearing in (5.38) and (5.39) can be expressed as

$$\left[\frac{d}{dt} |\phi_s| \right] = \frac{d}{dt} \left| \sqrt{(\phi_{s\alpha}^2 + \phi_{s\beta}^2)} \right|$$

5.48 In other words, using discrete samples,

$$\left[\Delta |\phi_s|_y \right] = \left[\left| \sqrt{(\phi_{s\alpha}^2 + \phi_{s\beta}^2)} \right|_y - \left| \sqrt{(\phi_{s\alpha}^2 + \phi_{s\beta}^2)} \right|_{y-1} \right] \quad (5.49)$$

where the suffixes ‘y’ and ‘y – 1’ denote the present and previous samples, respectively. The fluctuations in the angular velocity ω_e of the stator flux can also be precisely tracked now in terms of the individual components as follows:

$$\sin(\mu) = \frac{\phi_{s\alpha}}{\sqrt{(\phi_{s\alpha}^2 + \phi_{s\beta}^2)}} \quad (5.50)$$

$$\cos(\mu) = \frac{\phi_{s\beta}}{\sqrt{(\phi_{s\alpha}^2 + \phi_{s\beta}^2)}} \quad (5.51)$$

Having computed the stator flux components [from (5.30) to (5.37)], the time rate of change of stator flux from (5.49), and the position of stator flux [from (5.50) and (5.51)], the rotor current components in the stationary reference frame, $i_{r\alpha}$ and $i_{r\beta}$, can be readily computed using the fully expanded form of (5.42) and (5.43) as follows:

$$i_{r\alpha} = \frac{R_s i_{s\beta} - (V_{s\beta} + \omega_e L_s i_{s\alpha}) + \cos \mu \frac{d|\varphi_s|}{dt}}{\omega_e L_m} \quad (5.52)$$

and

$$i_{r\beta} = \frac{V_{s\alpha} - (R_s i_{s\alpha} + \omega_e L_s i_{s\beta} + \sin \mu \frac{d|\varphi_s|}{dt})}{\omega_e L_m} \quad (5.53)$$

Subsequently, the angle position θ_1 can be computed using (5.44) and (5.45).

Step 4B: Computation of rotor position [i.e., the angle ($\theta_1 - \theta_2$)].

This step is identical to Step 4A in the previous case (constant stator flux).

Through minor modifications in Steps 3 and 4, the rotor position can be computed in a simple manner even under fluctuations in the grid voltage/stator flux. Figure 5.6 shows the flowchart for the rotor position computation algorithm with fluctuating stator flux.

5.5.1.4 Results and Discussion

Figure 5.1 shows the test setup used for verifying the proposed computation algorithm. To verify the efficacy of the Rotor Position Computation Algorithm (RPCA), it is implemented on a laboratory test bench with a 3-hp DFIM (grid-connected) system using a FPGA-based digital controller. Details of the experimental setup are given in the Appendix.

Verification of RPCA

Four different cases viz. sub-synchronous speed, super-synchronous speed, transition through synchronous speed, and symmetrical dip in the grid voltage are considered.

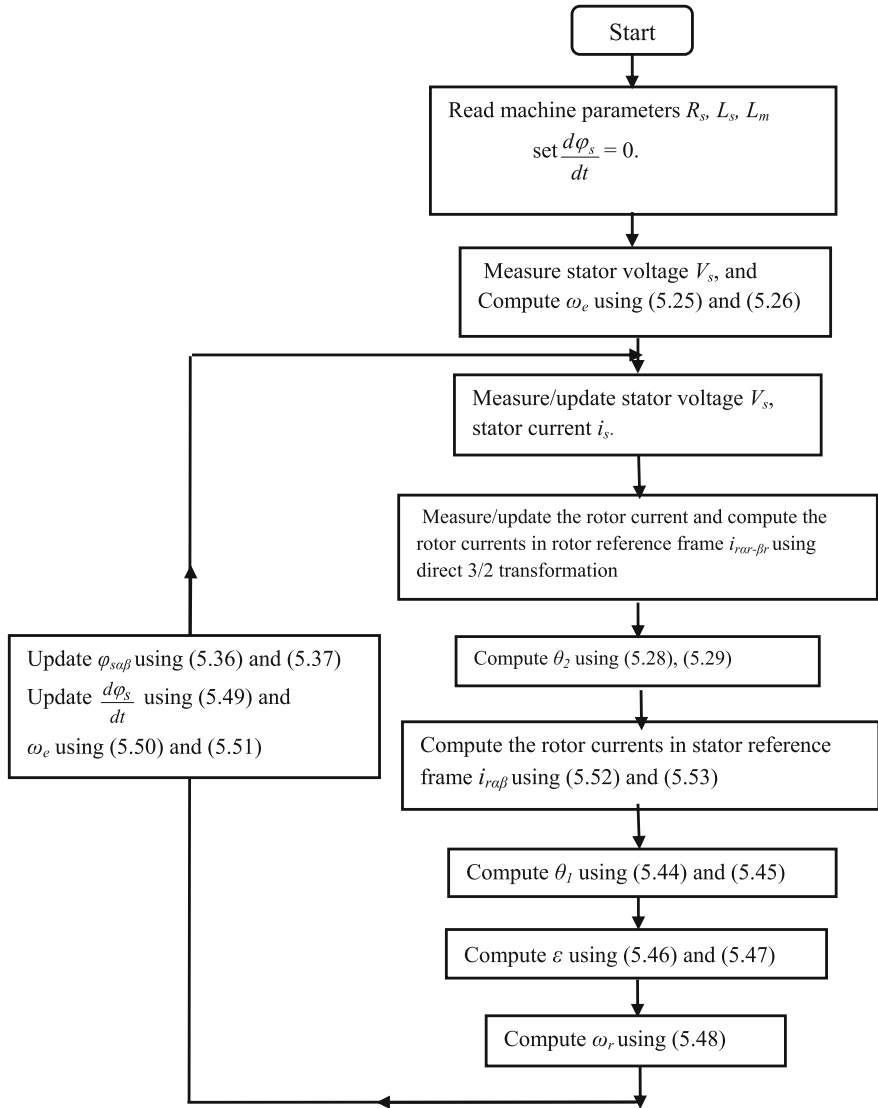


Fig. 5.6 Flowchart of the rotor position computation algorithm with fluctuating stator flux

Case 1: Sub-synchronous Speed

The test oscillograms of the measured and computed rotor position (ϵ_m —mechanical radians) at 1350 rpm (sub-synchronous) are shown in Fig. 5.7a. At 1350 rpm, the error between the measured and computed rotor position is found to be 3.3° (shown as Δx) and the corresponding DC value for the error is also shown in Fig. 5.7b.

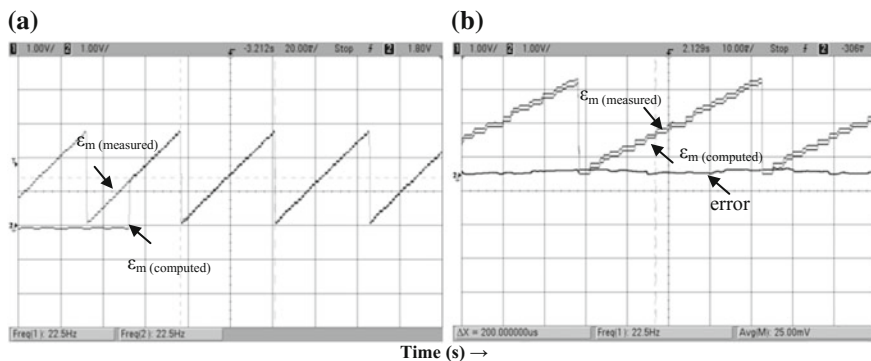


Fig. 5.7 Performance of position computation algorithm at sub-synchronous speed. **a** Actual and computed rotor position (ϵ_m —mechanical angle) at 1350 rpm. **b** Magnified graph of rotor position with error at 1350 rpm

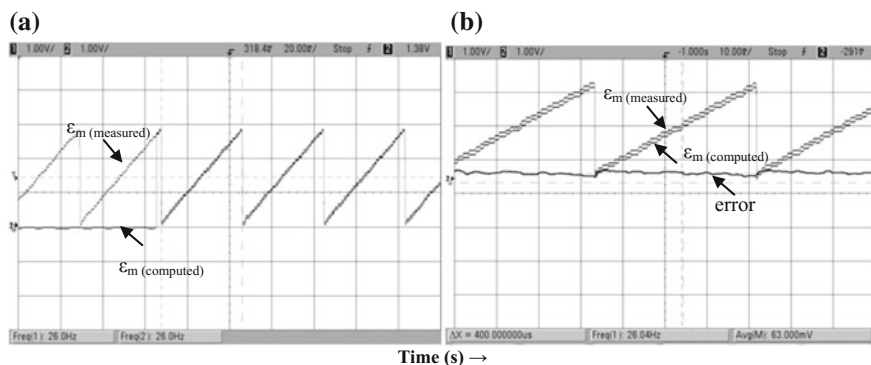


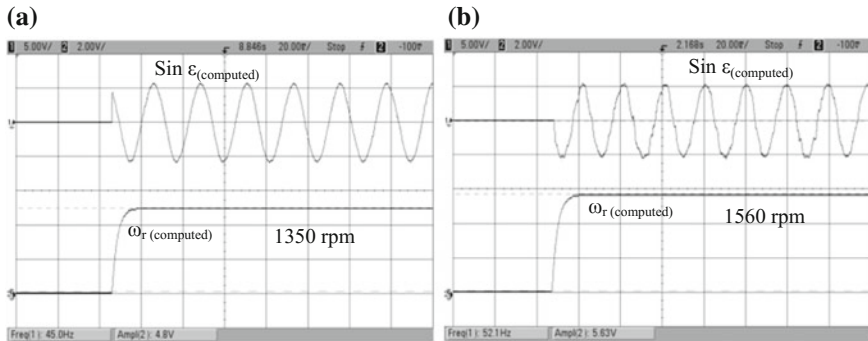
Fig. 5.8 Performance of position computation algorithm at super-synchronous speed. **a** Actual and computed rotor position (ϵ_m —mechanical angle) at 1560 rpm; **b** magnified graph of rotor position with error at 1560 rpm

Case 2: Super-synchronous Speed

The test oscillograms of the measured and computed rotor position (ϵ_m —mechanical radians) at 1560 rpm (super-synchronous) are shown in Fig. 5.8a. For 1560 rpm, the error is about 7.5° as shown in Fig. 5.8b. Instantaneous tracking of the position and speed signals and accurate steady state computation at both the sub-synchronous and super-synchronous speed can be observed in Fig. 5.9a, b, respectively.

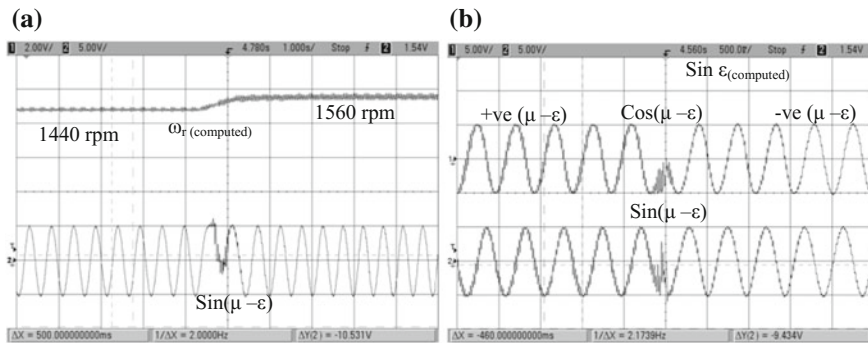
Case 3: Transition through Synchronous Speed

The rotor speed and the unit vector $\sin(\mu - \epsilon)$ through the synchronous speed are shown in Fig. 5.10a. The polarity of unit vector $\sin(\mu - \epsilon)$ changes from positive to negative when the speed changes from sub-synchronous to super-synchronous.



Time (s) →

Fig. 5.9 Performance of position computation algorithm computed rotor position unit vector ($\sin \epsilon$ —electrical angle) and speed (612 rpm/div) at **a** 1350 rpm and **b** 1560 rpm



Time (s) →

Fig. 5.10 Performance of position computation algorithm during transition through synchronous speed **a** computed rotor speed (330 rpm/div) and unit vector $\sin(\mu - \epsilon)_{\text{computed}}$; **b** computed $\sin(\mu - \epsilon)$ and $\cos(\mu - \epsilon)$ through synchronous speed

Also, the plots of $\sin(\mu - \epsilon)$ and $\cos(\mu - \epsilon)$ are shown in Fig. 5.10b. The phase reversal of $\sin(\mu - \epsilon)$ while transiting through synchronous speed is notable.

Case 4: Symmetrical dip in grid voltage

The case of 20% symmetrical dip in the grid voltage at 1350 rpm is illustrated in Fig. 5.11. The position error in this case is approximately 5.2° whereas with the nominal grid voltage the error is 3.3° . The increase in error is negligible. Thus, even with the stator voltage dip, the computation of the rotor position is largely accurate.

5.5.2 Closed Loop Techniques

MRAS techniques and observer-based techniques make use of the idea of computing speed/position by minimizing the error between the reference model and adaptive model with the help of an adaptation mechanism as shown in Fig. 5.12. The reference variable is selected from among relevant state variables such as rotor or stator current, reactive power, back emf, and product of voltage and current (X-MRAS scheme).

Generally, the error signal used to drive the adaptation mechanism is derived from either the current or flux in the rotor or stator. These algorithms require an ideal integrator in the reference model.

Fig. 5.11 Actual and computed rotor position (ϵ_m —mechanical angle) with a 20% dip in the grid voltage (332 V/div)

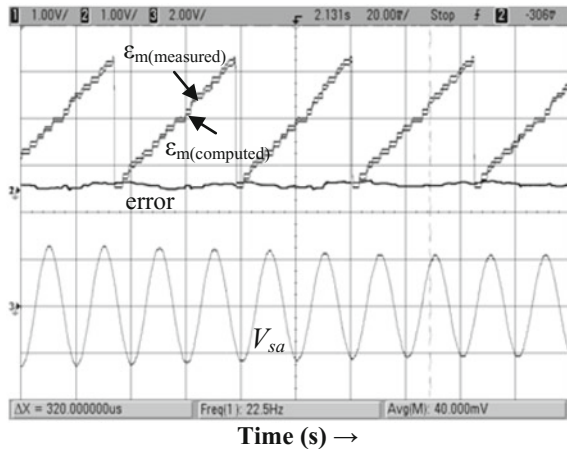
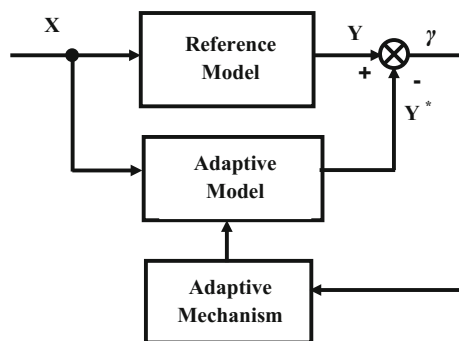


Fig. 5.12 Basic block schematic of a MRAS-based scheme



5.5.2.1 Closed Loop Rotor Position Computation

Literature reveals that the speed is computed either by differentiating the computed rotor position which involves trigonometric computations or by using mathematical calculations based on the measured stator and rotor currents, voltages, and rotor position. However, the differentiated speed signal calls for filtering and this leads to transient errors. Whereas inverse trigonometric computations and voltage integration in speed/position computation lead to signal attenuation, computational delay, noise, etc.

Rotor-Side Phase-Locked Loop (R-PLL) for the Computation of Rotor Position of a DFIM

A novel method for computing the rotor position of a DFIM with a balanced grid voltage [40] is described. The rotor position is computed in closed loop using a feedforward rotor-side PLL. The salient features include the use of a Feedforward phase-locked loop (FPLL) [41] on the grid side to obtain the position and angular frequency of grid/stator flux. The computed rotor speed signal is used as a feedforward input to rotor-side R-PLL. This feedforward input to R-PLL enables low steady state error, fast dynamic response, and hence reduced locking time.

The method includes the following steps:

1. Computation of position and angular frequency of stator flux ω_e .
2. Computation of rotor currents using the measured stator voltages and currents.
3. Computation of angular speed of rotor ω_r using the computed ω_e and stator and rotor currents in the synchronous reference frame.
4. Computation of rotor position ε using a feedforward phase-locked loop (PLL) with the computed ω_r as feedforward input and q -axis stator flux as reference input.

Step 1C: Computation of position and angular frequency of stator flux ω_e

The position μ and angular frequency ω_e of grid/stator flux are computed using a PLL. Here, a Feedforward phase-locked loop (FPLL) [41] is used for computing the position of stator voltage vector θ_s since it should be a dependable solution even under varying grid conditions. The computed angular frequency of stator flux ω_e is fed forward while the positive sequence stator d -axis voltage V_{sd+} (set to zero) serves as the reference input signal to the phase detector. Here, the positive sequence term of d -axis stator voltage as reference signal to FPLL enables accurate estimation of θ_s even with unbalanced grid voltage. Knowing the position vectors of θ_s , those of μ can be computed since

$$\mu = (\theta_s - \pi/2) \text{ as shown in Fig. 5.4b.}$$

The angular frequency of stator flux ω_e can be computed [3] from the position of stator voltage vector θ_s as

$$\omega_{e(\text{comp})} = \sin \theta_s \frac{d}{dt} \cos \theta_s - \cos \theta_s \frac{d}{dt} \sin \theta_s \quad (5.54)$$

Thus, ω_e can be computed in real time without using voltage integration or inverse trigonometric computations. Since the reference input signal to the phase detector V_{sd+} is extracted from V_{sd} using a LPF, the PI controller parameters are to be designed appropriately taking into account of the filter transfer function in order to compensate for the delay in the FPLL response and for the stable operation of FPLL.

Step 2C: Computation of rotor currents

For the case of constant flux, the rotor currents referred to the stator α - β reference frame can be computed implicitly using the measured stator voltages and currents as in (5.42) and (5.43) without computing the stator flux. Reproducing these for convenience,

$$i_{r\alpha} = \frac{R_s i_{s\beta} - (V_{s\beta} + \omega_e L_s i_{s\alpha})}{\omega_e L_m} \quad (5.55)$$

and

$$i_{r\beta} = \frac{V_{s\alpha} - (R_s i_{s\alpha} + \omega_e L_s i_{s\beta})}{\omega_e L_m} \quad (5.56)$$

{Note: When the stator flux is varying, the α - β components of rotor current can be computed as indicated in Step 3B of Sect. 5.5.1.3, using Eqs. (5.52)–(5.53) with the computed θ_s information from grid-side FPLL}. Further, the rotor d - q currents can be computed using frame transformation. Thus,

$$i_{rd} = i_{r\alpha} \sin \mu + i_{r\beta} \cos \mu \quad (5.57)$$

$$i_{rq} = i_{r\alpha} \cos \mu - i_{r\beta} \sin \mu \quad (5.58)$$

where

$$\cos \theta_s = -\sin \mu; \quad \sin \theta_s = \cos \mu \quad (5.59)$$

It is notable that there is no need for rotor current measurements or for rotor position particularly when the stator flux is constant.

Step 3C: Computation of Rotor Speed ω_r

The block diagram of the proposed R-PLL algorithm with the rotor speed computation is shown in Fig. 5.13. The angular speed of rotor can be computed using the rotor q -axis voltage with the computed ω_e and rotor currents as follows:

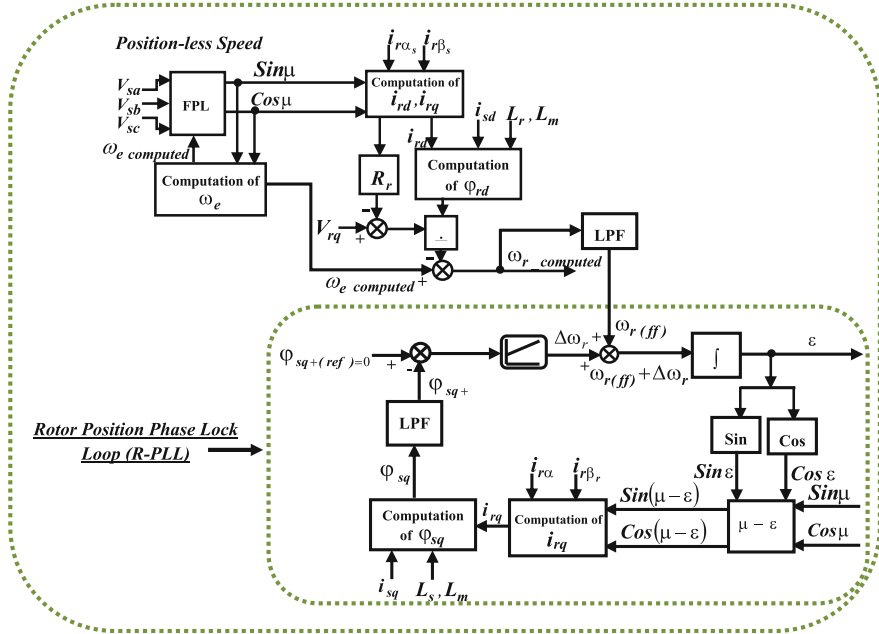


Fig. 5.13 Block diagram of the proposed feedforward R-PLL with the computed rotor speed

The rotor q -axis voltage can be represented as

$$V_{rq} = R_r i_{rq} + \frac{d}{dt} \varphi_{rq} + (\omega_e - \omega_r) \varphi_{rd} \quad (5.60)$$

where ω_r is the angular speed of rotor and φ_{rd} and φ_{rq} are the rotor flux linkages in the d - q reference frame. The speed of rotor (ω_r) is derived from (5.60) by neglecting the rate of change of rotor q -axis flux as it is zero under balanced grid condition. Thus, the angular speed of the DFIM rotor can be computed using the computed ω_e and computed rotor currents in d - q frame as

$$\omega_{r(\text{computed})} = \omega_{e(\text{comp})} - \frac{V_{rq} - R_r i_{rq}}{\varphi_{rd}} = \omega_{e(\text{comp})} - \frac{V_{rq} - R_r i_{rq}}{L_r i_{rd} + L_m i_{sd}} \quad (5.61)$$

Step 4C: Computation of Rotor Position—Rotor-side PLL (R-PLL)

This part of the scheme is analogous to a FPLL for grid synchronization. In the stator flux-oriented frame of reference, with a balanced grid voltage, stator d -axis voltage, V_{sd} , and stator q -axis flux, φ_{sq} , are zero. However, under grid voltage unbalance, both V_{sd} and φ_{sq} will not be zero but contain negative sequence components. Hence, only the positive sequence stator voltage V_{sd+} is used as the reference input signal to FPLL. Thus, even with distorted grid voltage information, a

grid-side PLL (FPLL) can be used to determine the appropriate grid frequency and stator flux position. This has led to the investigation of a rotor-side phase-locked loop (R-PLL) for rotor position computation.

Similar to the manner in which a FPLL tracks the position of the stator voltage vector θ_s , R-PLL is designed to track the exact rotor position ε , using the positive sequence stator q -axis flux φ_{sq+} as the reference input set to zero. Further, the reference input, $\varphi_{sq+(\text{ref})}$, is compared with the actual signal, $\varphi_{sq+(\text{actual})}$, and the error output of the phase detector is fed to a PI controller as shown in Fig. 5.13. The PI controller output ($\Delta\omega_r$) is added to the feedforward computed speed signal (ω_{rff}), and the time integral of this signal gives the rotor position (ε). Since the feedforward signal is the computed angular frequency of rotor which is independent of rotor position and is updated each instant, the frequency error can be quickly eliminated. This enables fast settling and since there is no need of a wide change in $\Delta\omega_r$ to adjust to the actual frequency, the steady state error can be eliminated.

Since the positive sequence stator q -axis flux φ_{sq+} is extracted from the total stator q -axis flux, φ_{sq} using a LPF, the R-PLL response may have a time delay. In order to compensate for this delay, the PI controller parameters are to be designed appropriately taking into account of the filter transfer function.

5.5.3 Results and Discussion

Simulations are carried out in PSCAD/EMTDC software, and further experiments are carried out on the laboratory DFIG setup. Typical results are presented. The schematic diagram of the setup is shown in Fig. 5.1.

R-PLL scheme is validated through experiments on a grid-connected DFIG test setup under three different cases viz. (i) Case A: Sub-synchronous speed, (ii) Case B: Transition through synchronous speed, and (iii) Case C: Dynamic load variations.

Case A: Sub-synchronous speed

The oscillograms of the computed rotor speed (rad/s) and rotor position with a balanced grid voltage for different sub-synchronous speed conditions are shown in Figs. 5.14 and 5.15.

Figure 5.14a, b shows the computed speed signal during starting the machine in motoring mode and with linear speed variation, respectively. Figure 5.14c shows the operation at near synchronous speed and Fig. 5.14d shows the transition from motoring to generating mode of operation and vice versa between 1426–1126 rpm and 1126–1426 rpm. Excellent tracking of speed is notable.

Also, it is evident that R-PLL facilitates tracking of rotor position with near zero steady state error (Fig. 5.15b–d) and with a worst-case transient error of less than $+2^\circ$ under speed transitions (Fig. 5.15d), respectively.

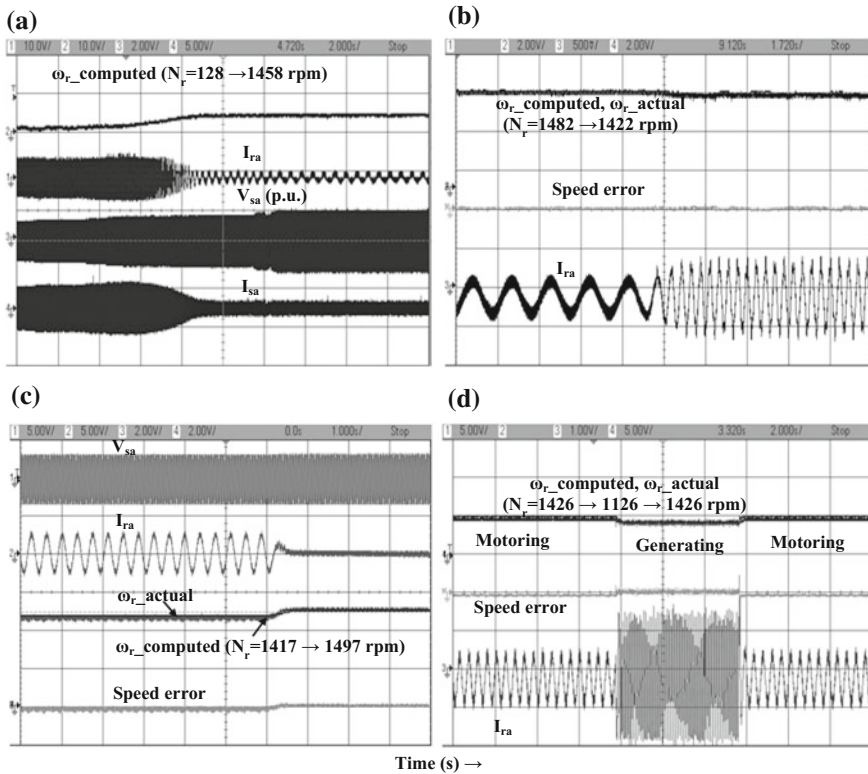


Fig. 5.14 Experimental results of R-PLL for case A **a** computed rotor speed, ω_r (rad/s) (3000 rpm/div), phase-*a* grid voltage, V_{sa} (p.u), phase-*a* rotor current (I_{ra}) (20A/div), and stator current (I_{sa}) (10A/div) (A) during starting, **b**, **c** actual and computed ω_r (rad/s) (600 rpm/div), error between actual and computed ω_r and I_{ra} (A) [(1A/div) and (10A/div), respectively], and **d** actual and computed ω_r (rad/s) (1500 rpm/div) (for DFIG in generating mode), I_{ra} (A) (2A/div), and error between actual and computed ω_r (2 V/div; 5 V = 100%)

Case B: Transition through Synchronous speed

The transition of rotor speed through synchronous speed (i.e., transition from motoring to generating and vice versa) along with the computed rotor position (ϵ) is shown in Figs. 5.16 and 5.17.

The computed rotor speed follows the actual machine speed from sub-synchronous to super-synchronous speed and vice versa through synchronous speed (Fig. 5.16b) while tracking the rotor position even through the synchronous speed (Fig. 5.17).

Case C: Load Variation

Tests are carried out under dynamic load variations by loading the DFIM using a DC shunt generator (coupled to it) with balanced supply voltage. A resistive load of

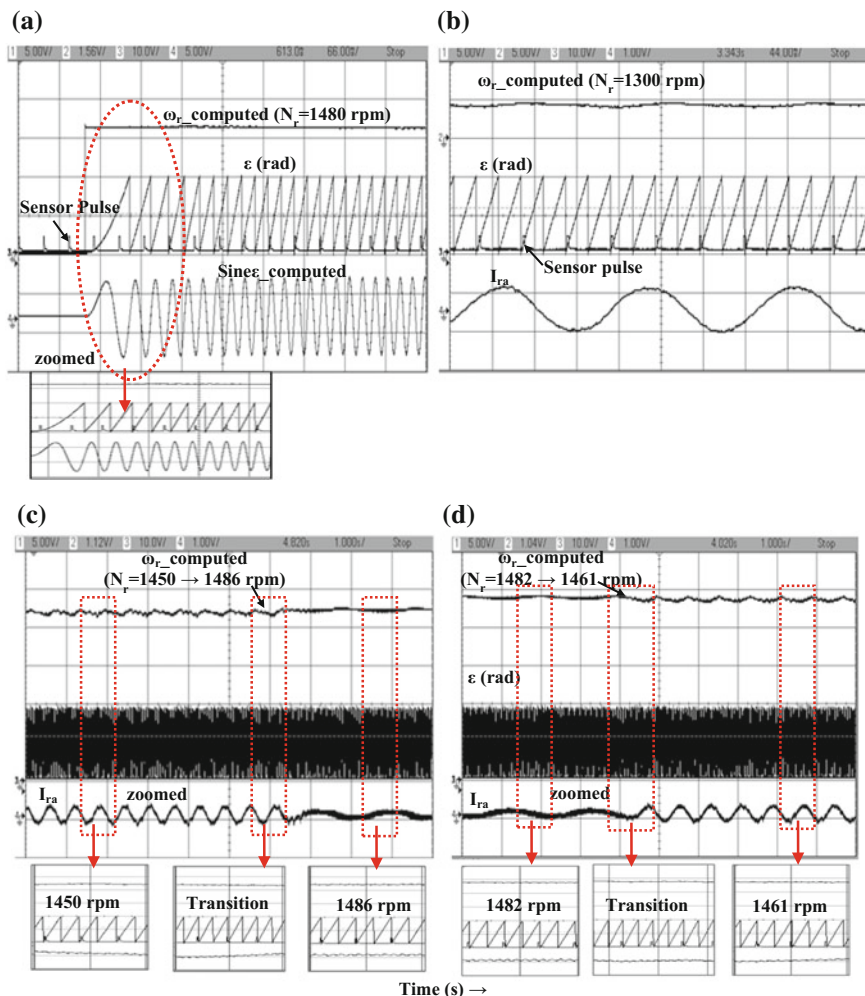


Fig. 5.15 Experimental results of R-PLL for case A **a** computed ω_r (rad/s) (300 rpm/div), computed rotor position ε (rad) (11 rad/div), sensor output, and computed $\text{Sine } \varepsilon$ showing start on the fly capability, **b** I_{ra} (p.u.) (2A/div), sensor output, ε (rad) (11 rad/div) from R-PLL, and ω_r (rad/s) (1500 rpm/div) and **c, d** phase- a rotor current (A) (2A/div), sensor output, computed ω_r (rad/s) (300 rpm/div) and rotor position ε (rad) (11 rad/div) from R-PLL for different sub-synchronous speeds including speed transition

460 W is applied at a speed of 1484 rpm which leads to a speed reduction (to 1439 rpm) as shown in Fig. 5.18a. Similarly under sudden removal of load at a speed of 1440 rpm, an increase of 40 rpm in speed is observed (Fig. 5.18b). The computed rotor speed tracks the actual signal along with accurate computation of ε (Fig. 5.19) even under dynamic load variations.

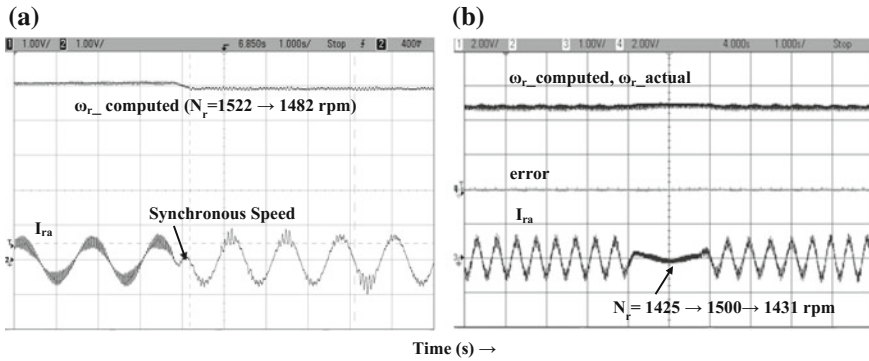


Fig. 5.16 Experimental results for case B **a, b** computed ω_r (rad/s) (300 and 600 rpm/div resp.) and phase-*a* rotor current (A) (2A/div) and **b** actual ω_r and error between actual and computed ω_r (2 V/div; 5 V = 100%) for super-synchronous to sub-synchronous speed transition and through synchronous speed, respectively

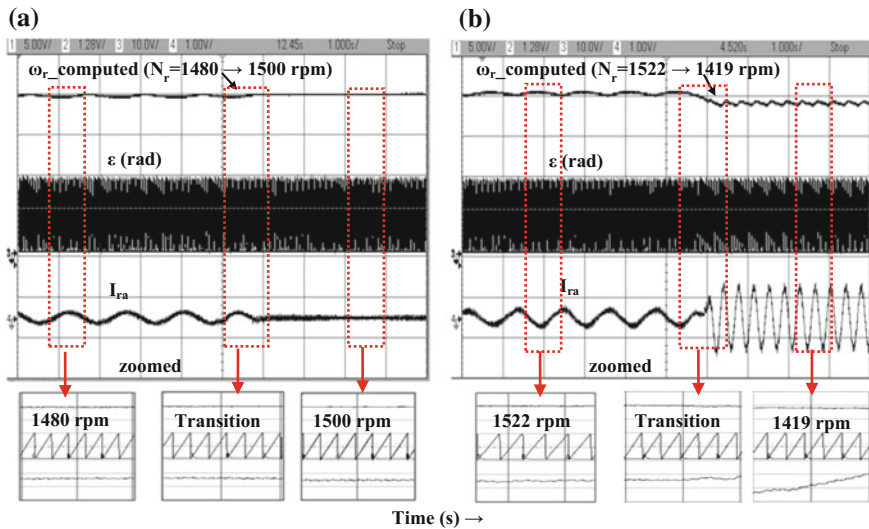


Fig. 5.17 Experimental results for case B **a, b** computed ω_r (rad/s) (300 rpm/div), phase-*a* rotor current (A) (2A/div), sensor output and computed ε (rad) ($1I_{ra}$ rad/div) from R-PLL for speed transitions from sub-synchronous to synchronous and super-synchronous to sub-synchronous speeds

The worst-case error in computed speed and computed rotor position ε with balanced grid voltage is given in Tables 5.1 and 5.2, respectively. The R-PLL scheme has a reduced error under steady state as well as under transient conditions including near synchronous speed. The rotor speed is computed with worst-case

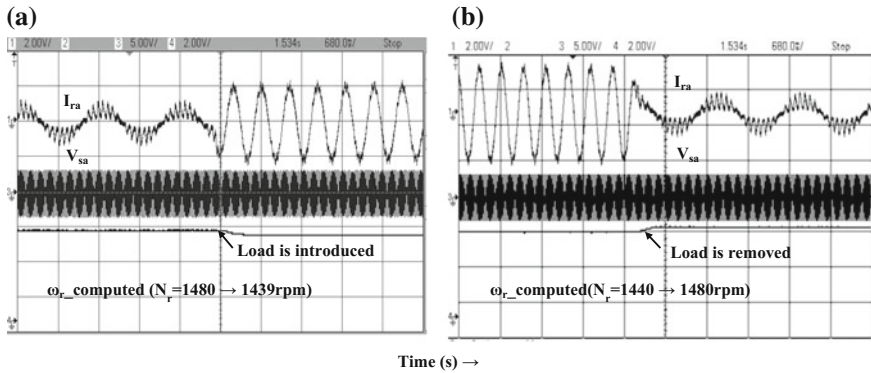
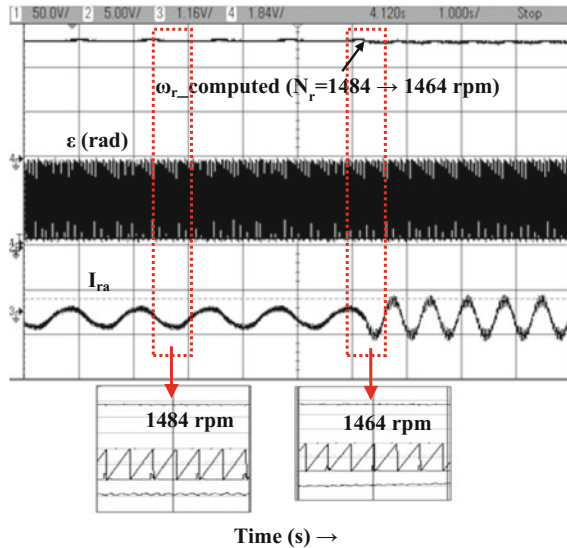


Fig. 5.18 Experimental results **a** Phase-*a* stator voltage (p.u.), computed ω_r (rad/s) (600 rpm/div), and rotor current (A) (4A/div) under load variation

Fig. 5.19 Experimental results for case C-phase-*a* rotor current (p.u.) (2A/div), sensor output, computed rotor position ε (rad) (11 rad/div), and ω_r (rad/s) (300 rpm/div) with a resistive load of 460 W at 1484 rpm



steady state and transient errors less than 0.2 and 1%, respectively, under balanced grid condition (including load variations). Moreover, the settling time of the computed speed signal is observed to be less than 0.1 s.

Also, the RPLL scheme has smaller position error (worst-case error is $+0.15^\circ$ less than that in [10, 20], respectively) under steady state and transient conditions including near synchronous speed.

Table 5.1 Comparison of worst-case steady state and transient error in rotor speed

Scheme	Balanced grid condition		
	Steady state error (%)		Transient error (%)
	Sub-synchronous Speed	Super-synchronous Speed	Load variations and near synchronous speed (1400–1540 rpm)
Rotor current-based MRAS scheme [20]	+0.88	+0.88	+0.95
ANN-based MRAS scheme [32]	+0.2	–	+1.6
Open loop scheme [10]	–3.84	–4	±4.8
Rotor current-based MRAS scheme [38]	–	–	–
ATO-based scheme [38]	+1.27	–	+7.96
Rotor flux-based MRAS scheme [39]	±5	±5	–8
R-PLL scheme	+0.12	+0.12	±0.6

Table 5.2 Comparison of worst-case steady state and transient error in rotor position

Scheme	Balanced grid condition			
	Steady state error (%)			Transient error (%)
	Sub-synchronous speed	Super-synchronous speed	Synchronous speed	Load variations
Open loop scheme [10]	+3.3°	+7.5°	–	–
MRAS scheme [20]	+0.2°	–	±0.5°	–
R-PLL scheme	+0.05°	+0.05°	+0.1°	+2°

‘–’ indicates not mentioned in the reported manuscript

5.6 Conclusions

This chapter presents a review of sensor-less estimation techniques for obtaining the rotor position and speed of a DFIM. Both open loop and closed loop categories are considered, and two case studies are demonstrated in detail.

In the RPCA scheme, the rotor speed and position of wound rotor induction machine are computed in a straightforward manner without the need for estimating the flux. Although it is an open loop technique, it does not involve voltage integration or inverse trigonometric computations in real time.

A Rotor-Side Phase-Locked Loop (R-PLL) for the computation of rotor speed and position of DFIM in the synchronous reference frame is discussed. The rotor position of DFIM is computed in closed loop with the computed rotor speed signal as feedforward input. This feedforward input to R-PLL enables fast dynamic response and hence reduced locking time with low steady state error. In addition, R-PLL scheme also facilitates the absence of signal attenuation, noise, need for filtering, etc.

The other salient features of both the schemes include start on the fly and accurate computation near and through the synchronous speed.

Appendix

Machine parameters

Parameters of DFIM	Value in SI units
R_s	3.68 Ω
R_r	5.26 Ω
L_s	0.307 H
L_r	0.307 H
L_m	0.282 H
J	0.012 kg m ²
B	0.033 kg m ² /s

Doubly fed induction machine:	DC machine: (Separately excited)
3 HP, 50 Hz, 4-Pole	5 HP, 1500 rpm
Stator: 415 V, 4.7A, Y-connected	Armature: 220 V, 19 A
Rotor: 185 V, 7.5A, Y-connected	Field: 220 V, 1 A

References

1. Tazil M, Kumar V, Bansal RC, Kong S, Dong ZY, Freitas W, Mathur HD (2010) Three phase doubly fed induction generators: an overview. IET Electr Power Appl 4:75–89
2. Pena R, Clare JC, Asher GM (1996) A doubly fed induction generator using back-to-back PWM converters supplying an isolated load from a variable speed wind turbine. Proc Inst Elect Eng Elect Power Appl 143:380–387
3. Datta R, Ranganathan VT (2001) A Simple position-sensorless algorithm for rotor-side field-oriented control of wound-rotor induction machine. IEEE Trans Ind Electron 48:786–793

4. Krause PC, Wasynczuk O, Sudhoff SD (2002) Analysis of electric machinery and drive systems. Wiley-Interscience, USA
5. Abad G, Lopez J, Rodriguez MA, Marroyo L, Iwanski G, Doubly fed induction machine modeling and control for wind energy generation. IEEE Press Power Eng Series 459
6. Petersson A, Thiringer TO, Harnefors L, Petru TA (2005) Modeling and experimental verification of grid interaction of a DFIG wind turbine. IEEE Trans Energy Convers 20: 878–886
7. El-helw HM, Tennakoon SB (2008) Vector control of a doubly fed induction generator for standalone wind energy application. In: Wind power to the grid-EPE wind energy chapter, 1st seminar, EPE-WECS, pp 1–6
8. Ben-Brahim L, Yokohama, Kawamura A (1992) A fully digital control of a field oriented induction motor drive using flux observer with and without speed sensor-600 Hz switching frequency case. IEEE Trans Ind Electron 39:241–249
9. Poddar G, Ranganathan VT (2006) Sensorless double-inverter-fed wound-rotor induction-machine drive. IEEE Trans Ind Electron 53:86–95
10. Karthikeyan A, Nagamani C, Ray Chaudhury AB, Ilango GS (2012) Implicit position and speed estimation algorithm without the flux computation for the rotor side control of doubly fed induction motor drive. IET Electr Power Appl 6:243–252
11. Hopfensperger B, Atkinson DJ, Lakin RA (2000) Stator-Flux oriented control of a doubly-fed induction machine with and without position encoder. IEE Proc Elect Power Appl 147:241–250
12. Xu L, Cheng W (1995) Torque and reactive power control of a doubly fed induction machine by position sensorless scheme. IEEE Trans Ind Appl 31:636–642
13. Morel L, Godfroid H, Mirzaian A, Kauffmann JM (1998) Double-fed induction machine: converter optimisation and field oriented control without position sensor. IEE Proc Elect Power Appl 145:360–368
14. Abolhassani MT, Enjeti P, Toliyat H (2008) Integrated doubly fed electric alternator/active filter (IDEA), a viable power quality solution, for wind energy conversion systems. IEEE Trans Energy Convers 23:642–650
15. Bhattacharya T, Umanand L (2009) Rotorposition estimator for stator flux-oriented sensorless control of slip ring induction machine. IET Electric Power App 3:67–76
16. Ohyama K, Asher GM, Sumner M (2006) Comparative analysis of experimental performance and stability of sensorless induction motor drives. IEEE Trans Ind Electron 53:178–186
17. Orłowska-Kowalska T, Dybkowski M (2010) Stator-current-based MRAS estimator for a wide range speed-sensorless induction-motor drive. IEEE Trans. Ind. Electron. 57:1296–1308
18. Cardenas R, Pena R, Clare JC, Asher GM, Proboste J (2008) MRAS observers for sensorless control of doubly-fed induction generators. IEEE Trans Power Electron 23:1075–1084
19. Carmeli MS, Castelli-Dezza F, Iacchetti M, Perini R (2010) Effects of mismatched parameters in MRAS sensorless doubly fed induction machine drives. IEEE Trans Power Electron 24:2842–2851
20. Pena R, Cardenas R, Proboste J, Asher G, Clare J (2008) Sensorless control of doubly-fed induction generators using a rotor-current-based MRAS observer. IEEE Trans Energy Convers 55:330–339
21. Cardenas R, Pena R, Proboste J, Asher G, Clare J (2005) MRAS observer for sensorless control of standalone doubly fed induction generators. IEEE Trans Energy Convers 20: 710–718
22. Maiti S, Chakraborty C, Hori Y, Ta CM (2008) Model reference adaptive controller-based rotor resistance and speed estimation techniques for vector controlled induction motor drive utilizing reactive power. IEEE Trans. Ind. Electron. 55:594–601
23. Monalisa Pattnaik; Debaprasad Kastha (2012) Adaptive Speed Observer for a Stand-Alone Doubly Fed Induction Generator Feeding Nonlinear and Unbalanced Loads. IEEE Trans Energy Convers 27:1018–1102

24. Kumar R, Das S, Syam P, Chattopadhyay AK (2015) Review on model reference adaptive system for sensorless vector control of induction motor drives. *IET Electr Power Appl* 9: 496–511
25. Comanescu M (2009) An induction-motor speed estimator based on integral sliding-mode current control. *IEEE Trans Ind Electron* 56:3414–3423
26. Vieira RP, Cauduro Gastaldini C, Azzolin RZ, Gründling HA (2014) Sensorless sliding-mode rotor speed observer of induction machines based on magnetizing current estimation. *IEEE Trans Ind Electron* 61:4573–4582
27. Verma V, Chakraborty C, Maiti S, Hori Y (2013) Speed sensorless vector controlled induction motor drive using single current sensor. *IEEE Trans Energy Convers* 28:938–950
28. Ravi Teja AV, Chakraborty C, Maiti S, Hori Y (2012) A new model reference adaptive controller for four quadrant vector controlled induction motor drives. *IEEE Trans Ind Electron* 59:3757–3767
29. Chakraborty C, Verma V (2015) Speed and Current sensor fault detection and isolation technique for induction motor drive using axes transformation. *IEEE Trans Ind Electron* 62:1943–1954
30. Karanayil B, Fazlur Rahman M, Grantham C (2007) Online stator and rotor resistance estimation scheme using artificial neural networks for vector controlled speed sensorless induction motor drive. *IEEE Trans Ind Electron* 54:167–176
31. Gadoue SM, Giaouris D, Finch JW (2009) Sensorless control of induction motor drives at very low and zero speeds using neural network flux observers. *IEEE Trans Ind Electron* 56:3029–3039
32. Maiti S, Verma V, Chakraborty C, Hori Y (2012) An adaptive speed sensorless induction motor drive with artificial neural network for stability enhancement. *IEEE Trans Ind Inf* 8:757–766
33. Liu P, Hung C-Y, Chiu CS, Lian KY (2011) Sensorless linear induction motor speed tracking using fuzzy observers. *IET Electr Power Appl* 5:325–334
34. Guzinski J, Abu-Rub H (2013) Speed sensorless induction motor drive with predictive current controller. *IEEE Trans Ind Electron* 60:699–709
35. Benlaloui I, Drid S, Chrifi-Alaoui L, Ouriagli M (2015) Implementation of a new MRAS speed sensorless vector control of induction machine. *IEEE Trans Energy Convers* 30: 588–595
36. Shen B, Mwinyiwiwa B, Zhang Y, Ooi B-T (2009) Sensorless maximum power point tracking of wind by DFIG using rotor position phase lock loop (PLL). *IEEE Trans Power Electron* 24:942–951
37. Stojic D, Milinkovic M, Veinovic S, Klasnic I (2015) Improved stator flux estimator for speed sensorless induction motor drives. *IEEE Trans Power Electron* 30:2363–2371
38. Abdellatif M, Debbou M, Slama-Belkhdja I, Pietrzak-David M (2014) Simple low-speed sensorless dual DTC for double fed induction machine drive. *IEEE Trans Ind Electron* 61:3915–3922
39. Marcetic DP, Vukosavic SN (2007) Speed-sensorless AC drives with the rotor time constant parameter update. *IEEE Trans Ind Electron* 54:2618–2625
40. Asha Rani MA, Nagamani C, Saravana Ilango G (2017) An improved rotor PLL (R-PLL) for enhanced operation of doubly fed induction machine. *IEEE Trans Sustain Energy* 8:117–125
41. Indu Rani B, Aravind CK, Saravana Ilango G, Nagamani C (2011) A three phase PLL with a dynamic feed forward frequency estimator for synchronisation of grid connected converters under wide frequency variations. *Int J Electr Power Energy Syst* 41:221–231

Chapter 6

Wind Turbine Standards and Certification: Indian Perspective

Rajiv Singh, Asheesh Kumar Singh and Padmanabh Thakur

6.1 Introduction

Recent rapid developments in wind power technology, its proven reliability, and cost competitiveness have made it a very attractive option for the power generation companies and utilities, thereby providing protection against the fluctuating fossil fuel prices. Wind industry also helps in mitigating the causes of climate change and providing other benefits such as energy security, stability of power costs, and employment to the people [1]. The key drivers of wind power growth had been the growing demand of clean, affordable, reliable, and easily installable sources of power generation. Significant developments were observed in wind power across the globe in 2014 after a minor slump in the previous years with new capacity additions of 51,473 MW. Consequently, 44% annual market growth was recorded leading the total installed capacity to 3,69,597 MW in the end of 2014 [2]. The increasing wind penetration requires reliable and safe operation of wind generators dispersed uniformly over a geographical area constituting a wind farm. It is normally desired that a wind generator should keep operating continuously without major repair and maintenance for at least 20 years. Hence, the wind farm operators must ensure reliability, quality, and safety of the wind generators besides economic operation throughout their lifetime. The WT testing according to prescribed stan-

R. Singh (✉)

Department of Electrical Engineering, G.B. Pant University
of Agriculture & Technology, Pantnagar, India
e-mail: rajiv77singh@gmail.com

A.K. Singh

Department of Electrical Engineering, Motilal Nehru National
Institute of Technology, Allahabad, India

P. Thakur

Department of Electrical Engineering, Graphic Era University,
Dehradun, Uttarakhand, India

dards and their certification is an established approach adopted by the wind industry to ensure safe and reliable operation of the wind farms. The certification is mainly required for establishing confidence among various stakeholders such as turbine manufacturers, wind farm developers, and financing agencies about the quality of turbine design. It also provides quality assessment of the various WT designs provided by different manufacturers. *Type certification* of WT is a formal statement of compliance by a competent third party (*certification agency*) that WT design is meeting the well-defined standards [3]. The chapter discusses elaborately about the WT certification procedures followed in India in light of IEC 61400 standards and is organized as follows: In Sect. 6.2, a brief history and current scenario of standards adopted in wind industry is presented followed by an illustration about the various aspects of international IEC 61400-1 standards and the Indian *Type Approval Provisional Scheme* (TAPS-2000) for certification developed by National Institute for Wind Energy (NIWE) in Sects. 6.3 and 6.4, respectively. Finally, conclusions are drawn in Sect. 6.5 by considering the various external environmental conditions applicable for certification of WTs for sites in India, thereby highlighting the need for adopting uniform certification process and testing standards across the globe.

6.2 History and Contemporary Scenario of WT Standards and Certification

A few stalwarts in the field of wind energy such as Denmark, the Netherlands, USA, Canada, and Germany initiated the process of WT testing and certification in the early 1980s involving rather simpler rules and parameters. But, these certification strategies involving only a few modules such as power performance and acoustic noise tests were confined locally to the above countries and more truly to the research facilities for the benefits of native industries and laboratories [3, 4]. Later on, with the exchange of information among various stakeholders a formal testing and certification procedure comprising testing modules such as power performance testing, acoustics assessment, and power quality measurement was evolved under the aegis of International Energy Agency (IEA). The benefits of American and European efforts in developing harmonized certification and testing procedures were reaped by International Electrotechnical (IEC) Commission by evolving a credible and widely acceptable series of wind energy standards called IEC 61400. The IEC standards were more comprehensive than their previous counterparts and covered almost every aspect of WT design, testing, and certification. In spite of every effort made by the technical committee TC88 to incorporate all the issues related to testing and certification of a WT in standards IEC 61400, a few of them were left unattended and insufficiently covered. These aspects were further considered by the European WT standards project (EWTS) giving completeness to the standards and certification procedures in wind power domain [3, 4].

Table 6.1 lists a few prominent type certification agencies and year of adoption of certification standards by them.

6.3 An Overview of Standards IEC 61400 for WT

IEC 61400 is a globally accepted WT standard for testing and certification of WTs published by International Electrotechnical Commission. For reliable operation of a WT, it is required to ensure satisfactory operation of every structural, mechanical, electrical, and control components. The series of 61400 standards are the most elaborate documents providing benchmarks for standardization and certification of WT components, thereby corroborating the reliability of turbine operation [5, 6]. The efforts initiated in 1995 by the technical committee (TC 88) on formulations of WT standards culminated in the year 2001, when the first module in IEC standard series appeared. A few modules like general design requirements in these standards were amended in order to accommodate the contemporary turbine designs. IEC 61400 standards are classified into several parts on the basis of their use and relevance for a WT component [6]. The broad classifications and subcategories are summarized in Table 6.2, and their prominent features are discussed in subsequent sections.

Table 6.1 Chronology of a few type certification agencies for WT [4]

S. no	Certifying agency	Country	Nomenclature	Inception year
1.	Center for Wind Energy technology (http://niwe.res.in/)	India	TAPS-2000	2003 Amended)
2.	Der Norske Veritas (www.detnorskeveritas.com/)	Denmark	DNV GL Renewable Certification	–
3.	TUV NORD CERT GmbH (www.tuev-nord.de/en/company)	Germany	TUV NORD Certification	2009
4.	Center for renewable Energy Sources & Saving (http://www.cres.gr/kape/index_eng.htm)	Greece	CRES	–
5.	American Wind Energy Association (www.awea.org/)	USA	AWEA 9.1	2009
6.	China General Certification Center (http://www.cgc.org.cn/)	China	CGC	2008
7.	(www.csagroup.org/)	Canada	CAN/CSA	2008

Table 6.2 A brief summary of various parts in WT standard IEC 61400 [6]

Design requirements	Power performance requirements	Mechanical and structural aspects	Communication and control	Miscellaneous
<p>IEC 61400-1 Design requirements for WTs in general</p> <p>IEC 61400-2 Design requirements for small WTs</p> <p>IEC 61400-3 Design requirements for offshore WTs</p> <p>IEC 61400-4 Design requirements for WT gearboxes</p>	<p>IEC 61400 12-1 Power performance measurements of electricity producing WTs</p> <p>IEC 61400 12-2 Power performance measurement of electricity producing WTs based on nacelle anemometry</p> <p>IEC TS 61400-14 Declaration of apparent sound power level and tonality values</p>	<p>IEC TS 61400-13 Measurement of mechanical loads</p> <p>IEC 61400-23 Full-scale structural testing of rotor blades</p>	<p>IEC 61400-25-1 Communications for monitoring and control of wind power plants—Descriptions of principles and models</p> <p>IEC 61400-25-2 Communications for monitoring and control of wind power plants—Information models</p> <p>IEC 61400-25-3 RLV communications for monitoring and control of wind power plants—Information exchange models</p> <p>IEC 61400-25-4 Communications for monitoring and control of wind power plants—mapping to communication profile</p> <p>IEC 61400-25-5 Communications for monitoring and control of wind power plants—Conformance testing</p> <p>IEC 61400-25-4 Communications for monitoring and control of wind power plants—Logical node classes and data classes for condition monitoring</p>	<p>IEC 61400-11 Acoustic noise measurement techniques</p> <p>IEC 61400-21 Measurement and assessment of power quality characteristics of grid-connected WTs</p> <p>IEC 61400-24 Lightning protection</p> <p>IEC TS 61400-26-1 Time-based availability of WT generating systems</p> <p>IEC TS 61400-26-2 Production-based availability of WTs</p> <p>IEC 61400-27-1 Electrical simulation model WTs</p>

6.3.1 IEC 61400-1 Design Requirements

Part 1, which specifies the essential design requirements applicable to almost all the categories of WT, deals with every subsystem such as control and protection mechanism, electrical and mechanical system, and support structure. The applicability of design requirements is to ensure the integrity of turbines by providing appropriate level of protection against wear and tear and any other damages during its maximum operational life of 20 years. The third edition of design requirements published in 2005 is mainly focused on the horizontal-axis machines excluding the small WTs with rotor swept area of 200 m² or less to be covered in IEC 61400-2 [5, 6]. These requirements are broadly divided into nine headings constituting various aspects of WT design as listed in Table 6.3 and discussed in subsequent sections.

6.3.1.1 Principal Elements

This section in IEC 61400-1 standards illustrates the *design methods* which emphasizes on the prediction of design loads using structural dynamics models for different wind conditions taking into account the wind turbulences mentioned in section *External conditions* of Table 6.3. Under the *safety classes* section, the safety issues regarding the WT design are classified into two categories (a) *normal safety class* constituting social, economic outcomes, and personal hazards due to failures in the turbine (b) *special safety class* applicable for *class S turbines* constituting safety requirements governed by the local regulations or those requirements as mutually agreed between the manufacturer and customer. Also, *quality assurance* of every WT component is essential for design, procurement, manufacture, installation, operation, and maintenance in accordance with ISO 9001 [6, 7]. It is also required that the *WT markings* displaying some important information such as *manufacturer name and country, serial number, rated power, and IEC turbine class* regarding the turbine must be marked clearly on the nameplate [6, 7].

6.3.1.2 External Conditions

It is essential to consider the *external conditions* involving *environmental factors* like wind and other parameters, *electrical conditions* like capacity of power networks, and *soil parameters* relevant to the design of turbine foundation, during the design and commissioning of WT, thereby ensuring its reliable operation. Broadly, these parameters can be categorized as *normal conditions* constituting the regularly appearing loading conditions and *extreme conditions* appearing casually during turbine operation. Based on the tolerance limits of the wind speed and turbulences, the turbines are divided into several classes providing an insight into its robustness and structural integrity [3, 6, 7]. Class I_A, II_A, and III_A turbines can tolerate 10-min average reference wind speeds (V_{ref}) up to 50, 42.5, and 37.5 m/sec, respectively,

Table 6.3 A brief summary of design aspects for WT standard IEC 61400-1 [6, 7]

Principal element	External conditions	Structural design	Control and protection system	Mechanical systems	Electrical system	WT site-specific condition assessment	Assembly, installation and erection	Commissioning, operation, and maintenance
(a) Design methods (b) Safety classes (c) Quality assurance (d) WT markings	(a) WT classes (b) Wind conditions (c) Environmental conditions (d) Power network conditions	(a) Design methodology (b) Loads (c) Design situations and load cases (d) Load calculations (e) Ultimate limit state analysis	(a) Control functions (b) Protection functions (c) Braking system	(a) Hydraulic or pneumatic systems (b) Main gearbox (c) Yaw system (d) Pitch system (e) Protection function (f) Mechanical brakes (g) Rolling bearings	(a) General requirements for electrical systems (b) Protective devices (c) Disconnect devices (d) Earth systems (e) Lightning protection (f) Electrical cables (g) Self-excitation (h) Protection against lightning (i) Impulse (j) Power quality (k) Electromagnetic compatibility	(a) Topographical complexity of site (b) Wind conditions for assessment (c) Wake affect from neighboring turbines (d) Other environmental conditions (e) Earthquake (f) Electrical network conditions (g) Soil conditions (h) Structural integrity with reference to wind data (i) Structural integrity by load calculations	(a) Planning (b) Installation conditions (c) Site access (d) Environmental conditions (e) Documentation (f) Receiving, handling, and storage (g) Foundation/anchor systems (h) Assembly of WT (i) Erection of WT (j) Fasteners and attachment (k) Cranes, hoists, and lifting equipments	(a) Requirements for safe operation, inspection, and maintenance (b) Commissioning instructions (c) Energization (d) Commissioning tests (e) Records (f) Post-commissioning activities (g) Operator's instruction manual

and high-intensity turbulence effects of 0.16 measured at 15 m/sec wind speeds. While, the classes of turbines represented by (I, II, III)_B and (I, II, III)_C can operate safely at V_{ref} same as class A turbines but are designed for sustaining medium and low turbulence intensities of 0.14 and 0.15. However, Class S WTs can sustain all the wind speeds and turbulence intensities as above or as specified by the customer/designer [5–7]. The *wind conditions* occurring frequently are classified as *normal conditions* and those appearing rarely in 1–50-year period are classified as *extreme conditions*. The wind components considered are constant average components (v_{av}), varying deterministic gust component (v_{gst}) and randomly varying turbulence component (v_{tur}). The wind turbulence components are classified as longitudinal component (σ_1 flowing along v_{av}), lateral component (σ_2 flowing normal to longitudinal component), and upward component (σ_3 flowing in quadrature with both the above components). The standard deviations of σ_2 and σ_3 are given by (6.1) and (6.2), respectively, while the turbulence scale parameter A_1 for σ_1 at hub height z is given by (6.3) as follows:

$$\sigma_2 \geq 0.7\sigma_1 \quad (6.1)$$

$$\sigma_3 \geq 0.5\sigma_1 \quad (6.2)$$

$$A_1 = \left. \begin{array}{ll} 0.7z & z \leq 60 \text{ m} \\ 42z & z \geq 60 \text{ m} \end{array} \right\} \quad (6.3)$$

The section *wind conditions* cover comprehensively several wind scenarios and extreme environmental conditions such as operating temperature range (–20–50 °C), ice conditions, and earthquakes during the turbine design [7]. However, due to space limitations it is difficult to cover all of them.

6.3.1.3 Structural Design

The structural integrity of WT load carrying components can be assessed through calculations and by using model or prototype tests based on ISO 2394 for ensuring the desired safety standards. Sufficient documentation should be made available for describing the methods of calculation and tests [5, 6]. The appropriate *design methodology* should be adopted such that the safety load limits of static and dynamic loads are not exceeded in the turbine design. Several *loads* such as *gravitational and inertial loads* (due to gravity, rotation, vibration, and seismic activity), *aerodynamic loads* (created due to interaction of blowing air with turbine components), *actuation loads* (appearing due to torque, pitch, yaw control, and mechanical braking), and *other loads* (due to sudden impact, ice and wake loading) are considered for appropriate design calculations [6–8]. A WT is supposed to experience several significant load conditions in its lifetime. These conditions are represented by many *design situations and load cases*. Several *design situations and load cases* are estimated for testing the structural efficacy of a WT using the

normal design situations and a few extreme external conditions together with fault design situations, transportation, installation and maintenance design situations, etc. A *design load situation* is considered to be valid if a relationship can be established between a fault condition and extreme external conditions resulting in several load conditions for every design situations. A few design load conditions are summarized in Table 6.4. Moreover, the *WT load calculations* are performed using dynamic simulations involving structural dynamic models. Ultimate load analysis under the category *ultimate limit state analysis* is represented in terms of partial safety factors giving information about changes and uncertainties in loads, materials, and analysis methods [6, 8].

6.3.1.4 Control and Protection System

It is required to protect the settings of control and protection systems from any unauthorized interference. The application of control is to maintain the turbine functions within the satisfactory operational limits. A control selector is used for deciding the control mode of the turbine. The current selected mode will override the previous one depending on the position of selector except in the situations of emergency stop conditions [6, 8, 9]. The *protection system* will operate after the failure of control components or any other internal and external failure during hazardous events. It is always desired that the settings of protection systems be within the design limits of the WT in order to ensure its safety and reliability. The *braking system* functioning should not be hampered under any circumstance not even during the failure of external power supply. Also, the turbine should be brought to complete halt from running conditions with the help of braking system in minimum time depending on the turbine design parameters. Moreover, for a given wind speed, the *braking system* must be capable of maintaining the full halt situation of the turbine rotor for at least one hour after the application of brake [6, 8, 9].

6.3.1.5 Mechanical Systems

The *mechanical systems* in a WT consist of the motion transmitters involving drive train components such as gearboxes, shafts, couplings, and auxiliary components such as brakes, pitch, and yaw control mechanisms as depicted in Fig. 6.1.

ISO 6336-1 to ISO 6336-3 are the guiding standards for gearbox design while ISO 6336-5 provides the solution for material choice in the design. In *yaw system*, there should be appropriate means (hydraulic brakes) to maintain fixed yaw rotation, change yaw orientations (motors, gearboxes and pinions), and mechanisms for guiding its rotation (bearing). The motors used for any of the above purposes in yaw system should follow clause 10 of the document for standards. The *pitch system* should also contain appropriate mechanisms for adjusting the blade pitch angle and systems for rotation guidance [5–7]. The *mechanical brakes* performing the *protection functions* should use hydraulic or spring pressure to generate friction.

Table 6.4 Design load situations in a WT [6–8]

S. no.	Broad design category	Design load case (DLC)	Description
1.	Power production	DLC 1.1–1.2	Loads due to atmospheric turbulences during normal operation (NTM) in lifetime
2.		DLC 1.3	Ultimate loading due to extreme turbulence conditions
3.		DLC 1.4–1.5	Few transient cases specified as critical events in wind turbine's life
4.	Power production plus occurrence of fault or loss of electrical connection	DLC 2.1	Faults related to control function or loss of network connection to be considered as normal events
5.		DLC 2.2	Occasional situations including faults related to protection functions or internal electrical systems to be considered as normal
6.		DLC 2.3	Events of gusts combined with internal or external electrical faults are considered as abnormal events
7.		DLC 2.4	Electrical network connection failure not causing sudden shutdown resulting in significant damage in normal turbulence conditions
8.	Start-up	DLC 3.1–3.3	Involves all the situations leading to loading of turbine for transition from idling situation to power production
9.			
10.			
11.	Normal shutdown	DLC 4.1–4.2	Just vice versa of the previous start-up situations
12.	Emergency shutdown	DLC 5.1	Involves loading on the turbine due to its emergency closure
13.	Parked (standstill or idling)	DLC 6.1–6.3	Loading conditions on the turbine during extreme wind conditions when standstill or idling
14.		DLC 6.4	Normal turbulence wind condition during parked state
15.	Parked plus fault condition	DLC 7.1	Involves deviations from the normal behavior of a turbine due to power network faults when parked
16.	Transport, assembly, maintenance, and repair	DLC 8.1–8.2	All the wind conditions and design situations for transport, assembly, maintenance, and repair of the turbine which continues for 1 week

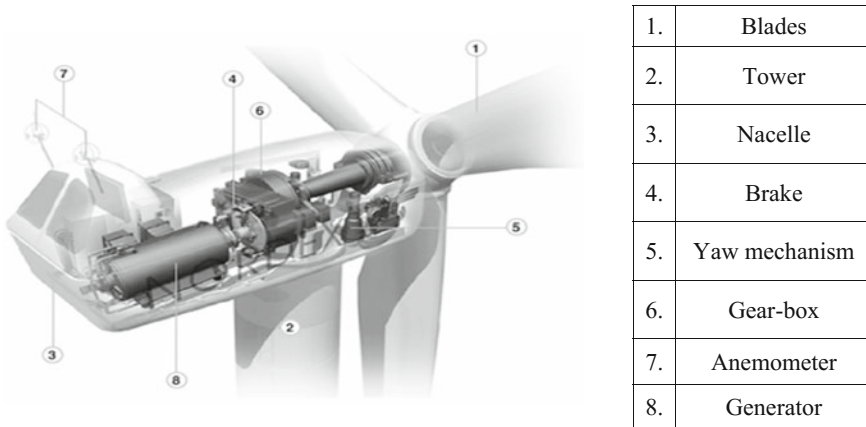


Fig. 6.1 Wind generator components

The period of rotor slip in braking mode with minimum braking effort during turbulent wind conditions should be minimum to avoid overheating and fire which may cause impairments of braking system. The design of *rolling bearings* in main shaft and gearbox should be according to ISO 76 and ISO 281 such that it can sustain for 20 years of lifetime. As per ISO 76, the ratio of static rating to design load should be unity and also the load distribution due to flexibility in the materials should be carefully taken into account [6–8].

6.3.1.6 Electrical System

According to the *general requirements of the electrical system*, design IEC 60204-1 guidelines should be followed for designing all the electrical equipments and components. For the turbines having components operating at voltages greater than 1 kV ac or 1.5 kV dc, the electrical system design should follow IEC 60204-11, and the fixed installations shall comply with the requirements of IEC 60364 [6, 8, 9]. Also the fluctuating nature of output power from the WTs should be considered while designing the electrical system. The turbines should be equipped with *protective devices* to avoid its mal-operation and faults in external electrical circuits hampering the overall safety of personnel and equipment. Maintenance and testing issues require the disconnection of electrical system of a WT with the help of *disconnect devices* generally comprising of semiconductor switches and other auxiliary circuits to be used, respectively, during normal conditions and extreme conditions like lightning. IEC 60364 involving appropriate operation of electrical installations in a WT and IEC 61024-1 involving lightning protection should be complied with by the WT designs with the help of a local earth electrode system [6, 7, 9]. The equipments of earthing arrangements (electrodes, conductors, earthing terminals, and bars) should be selected in accordance with IEC 60364-5-54.

Appropriate provisions for earthing during maintenance must be done for electrical systems operating above 1 kV ac and 1.5 kV dc. The *lightning protection* provisions must be designed according to IEC 61024-1, and the inclusion and exclusion of components to be protected is governed according to IEC 61400-24. According to the provisions for *electrical cables*, armors or conduit protection should be provided for protection from rodents and other animals in overground cables while the underground cables must be buried at appropriate depths to avoid damages. Self-excitation equipments in the wind generators like capacitor banks used for power factor correction shall be disconnected in the events of network power failure to avoid self-excitation of wind generators. The *power quality* norms should be in accordance with IEC 61400-21 while the issues of *electromagnetic compatibility* like emissions due to radiated disturbances shall abide by the requirements of IEC 61400-6-4 and immunity to radiated disturbances shall be in accordance with IEC 61000-6-1 or IEC 61000-6-2 [6, 9].

6.3.1.7 Assessment of a WT for Site-Specific Conditions

Assessment of a site before WT installation is an important step for deciding its design in order to avoid structural hazards during normal operation. The *topographical complexity of the site* is assessed according to the variations in the site topography in reference to a plane. The values of a few terrain complexity indicators such as *fitted plane slope*, *terrain variation from the fitted plane*, and *distance range from the WT* are used for assessing the site characteristics. *Wind conditions assessment* for a site can be carried out by estimating the factors such as *wind flow inclination*, *wind shear*, and *air density*. For the sites where the data on air density are not available, the values can be assumed according to ISO 2533:1975 by considering appropriate corrections for the annual average temperature [6, 9, 10]. The *wake effect* involves the increase in loading due to the effect on wind flow through the neighboring turbines. Hence, the effect of deterministic turbulent flow as a result of wake effect due to single or more upwind turbines for all ambient wind speeds and directions must be considered. Effect of other *environmental factors* such as operating temperature range, ice, hail and snow, humidity, lightning, solar irradiance, and salinity is assessed at the site in comparison with the range of values considered during turbine design [9, 10]. Assessment of *earthquake conditions* for a site is required for determining the structural integrity of a turbine for the locations where loading due to seismic activity may be critical. The compatibility with electrical design conditions can be evaluated on the basis of *electrical network conditions* at the generator terminals for a particular site. However, the evaluation of soil conditions can be performed by a professional geotechnical engineer in consonance with the local building codes. The *structural integrity* of the WTs can be assessed on the basis of the following: (a) difference between the wind

parameters at the installation site and values considered for turbine design and (b) calculation of load on the turbine due to specific site conditions in reference to the load calculations considered for the turbine design [8–10].

6.3.1.8 Assembly, Installation, and Erection

It is mandatory for every turbine manufacturer to provide installation manual for the turbine structures and equipments and also depute trained personnel for carrying out installation-related activities according to the prescribed instructions. *Planning* of installation procedures is essential for performing the erection tasks in consonance with the local and national regulations. The planning constitutes several tasks such as (a) formulating rules for safe evacuation of personnel from site, (b) illustrative drawings depicting work specifications and inspection plans, (c) planning safe blasting, and (d) tower and anchor installation plans. The *installation conditions* require that the site shall be properly maintained so as to avoid the safety risks and also the *site access* during installation should be made safe by considering the features such as (a) traffic, (b) road surface, (c) road width, and (d) clearance [7, 11]. Factors like *environmental conditions* specified by the manufacturers shall be considered during installation and erection. The site-specific conditions such as *wind speed, ice, blowing sand, visibility, and rain* must be assessed in reference with their values considered for design. The *fastening and attachment* issues require threaded fasteners and other attachment devices to be installed as per the manufacturer guidelines for torque and other specifications. Moreover, it is necessary to test all other equipments such as slings and hooks for ascertaining their load safety limits through appropriate certification [9–11].

6.3.1.9 Commissioning, Operation, and Maintenance

Facilities for safe access and maintenance of WT components should be incorporated in the turbine design. *Safe operation, maintenance, and inspection* norms require that the normal operation of WT can be achieved by personnel at ground level. Also there should be provisions for overriding manual control over the automatic control. Besides these, the manufacturer should also include initial excitation (*energization*) procedures for the electrical system of the turbine. *Commissioning tests* such as (a) safe start-up, (b) safe shutdown, (c) safe emergency shutdown, and (d) protection system functioning should be performed after the turbine installation in order to ascertain the safe operation of various devices and controls [7, 9, 10]. The turbine model must be accompanied with a proper maintenance manual illustrating the various regular and emergency maintenance procedures specified by the manufacturer. The operator's maintenance manual should also contain criteria for the replacement of parts affected by wear and tear along with the required *post-commissioning* activities [10, 11].

6.4 Description of Type Approval Provisional Scheme (TAPS-2000)

The Indian wind power sector has witnessed significant growth over the past decade bringing the country at 5th place in terms of wind power installed capacity. As a sequel of recent developments in wind energy sector, the formulation of appropriate standards and certification process was felt necessary. The standards and certification unit of national institute of wind energy (NIWE) in collaboration with RISO national laboratories, Denmark, developed the Indian standards and certification scheme TAPS-2000 for type certification of WTs. The provisional type testing and provisional type certification system may be used by the wind energy sector in India till any other final scheme of type approval and certification is formalized [12]. TAPS-2000 document which is applicable for inland grid-connected horizontal-axis WTs having rotor swept area of 40 m² comprises 4 chapters, references, and 6 annexures. The first chapter provides an *introduction* about the document, the second chapter consists of ‘*approval and organization*,’ and the third and fourth chapters deal with *definitions and type approval certification*, respectively. *References* contain the *list of acts, standards, and guidelines* applicable in TAPS while the supporting information for meaningful interpretation of TAPS is given in annexures [12].

The scope of TAPS can be enumerated as following:

- The whole WT including the wind terminals and its connection to the grid is covered in TAPS.
- All the aspects of WT including design, manufacturing, and installation are included in TAPS.
- Type approval for a turbine is based on the verification of document provided by the manufacturer with the help of tests, calculations, surveillance, and inspections.
- The quality management system (QMS) of manufacturer should be reviewed to check its compliance with ISO 9001: 2000, for ensuring the manufacturing and installation quality of WTs [12, 13].

The S&C unit of NIWE is the implementation agency for TAPS which provides the type certificate usually for a year; however, this duration may vary from case to case.

6.4.1 Provisional Type Certification (PTC)

Chapter 4 of the TAPS document which contains the issues related to *PTC* of WTs defines the various categories of certification, methodology of issuing provisional type certificate, and the requirements to be followed by the suppliers. As documented in Chap. 4, the *PTC* is classified into three categories. In *category I*, *PTC* for the WTs already possessing type certificate or approval is given while in *category II*, *PTC* for WT already possessing type certificate or approval with minor

modifications/changes including provisional type testing/measurements at the test site of C-WET/field is provided and *category III* contains, PTC issues for new or significantly modified WTs including provisional type testing/measurements at the test site of C-WET/field. The major issues of these classifications are illustrated in the subsequent sections [13]. Also, the PTC is issued after the verification of supplier documentation as per the TAPS prepared in accordance with the IEC WT-01 and IEC 61400-1 with few modifications in later for incorporating the local Indian conditions as presented in Annexure 2.

6.4.1.1 PTC: Category I

A WT already possessing type certification from recognized certification agencies is placed under this category for certification according to TAPS. Here, if any changes in the turbine design is recommended it should follow the load safety constraints of the previous design and must be represented appropriately in the documentation provided by the manufacturer. However, any such changes should not alter the approved load safety requirements as per the previous design [13]. In category I, the required PTC modules are presented in Fig. 6.2, and relevant descriptions of the modules are presented in subsequent sections.

Partial Design Evaluation/Review of Type Certificate

Annexure 1 contains the list of type certification and approvals recognized by TAPS such as in Denmark and the Netherland, Germanischer Lloyd and the IEC. A WT

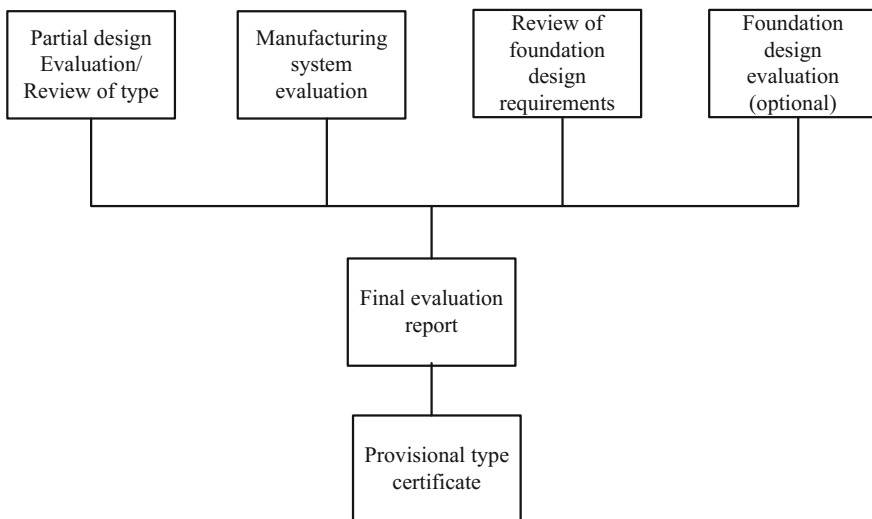


Fig. 6.2 PTC working modules for category I [13]

certified by any agency other than the above four can be considered for certification under TAPS provided the manufacturer provides the complete details of the previous certification system. PTC based on TAPS in category I can be provided to such turbines after thorough review of the previous certificate and the evaluation of its conformity to local Indian conditions stated in Annexure 2. On-the-spot checking of wind farm for verification of safety norms and other specifications will be performed before or after the issue of PTC [5, 7, 13].

Manufacturing System Evaluation

The second module in category I involves *manufacturing system evaluation* to assess the compliance of WT manufacturing and design according to the design documentation provided by the manufacturer.

This module includes two components:

- (a) Quality system evaluation on the basis of ISO 9001: 2000 standards, performed by an accredited body operating according to ISO/IEC guide 17062 [12, 13].
- (b) Manufacturing system evaluation shall be based on requirements mentioned in Sect. 8.4 of IEC WT 01.

However, if the system quality certification for a WT design is not available, the same should be obtained by an authorized certification body according to the guidelines of clause 8.4 of IEC WT 01 which can be placed before the type certification body for evaluation and assessment.

Review of Foundation Design Requirements

The *foundation design requirements* mentioned in Annexure 5 shall be evaluated as per IEC WT 01. It generally involves a comparison of loads at the bottom of the tower mentioned in the design documentation with loads considered during the foundation design. Besides above, a foundation designer requires a few more additional information regarding the soil conditions such as (a) site-specific local codes; (b) earthquake information; and (c) requirements for flatness, level, bolt patterns, and tolerances [13, 14].

Foundation Design Evaluation

This optional module provides the flexibility to manufacturers for choosing among one or more types of foundation designs for PTC in conformity with the requirements of IEC WT 01. The design chosen by the manufacturer shall be evaluated by the type certification body as per the requirements in IEC WT 01, thereby issuing a conformity statement to corroborate a satisfactory foundation design.

Final Evaluation Report

In this module, the type certification body prepares the *final evaluation report* in the form of a document after satisfactorily evaluating all the elements of PTC for a particular type of WT design [13].

Provisional Type Certificate

In this module, PTC will be issued by S&C unit of NIWE, for a WT design type based on the satisfactory evaluation report. The certificate is valid generally for a specified time period in the format presented in Annexure 6.

6.4.1.2 PTC: Category II

PTC category II certification scheme is applicable for the WT types covered in category I; hence, it includes all the conditions for certification as required in category I. Out of the total eight working modules required for evaluation in category II as depicted in Fig. 6.3, four modules, namely (a) partial design evaluation/review of type certificate, (b) manufacturing system evaluation, (c) review of foundation design requirements, (d) foundation design evaluation, (e) final evaluation report, and (f) provisional type certificate, are same as category I. The newly included modules in this category are illustrated in sections below [10, 13, 15].

Provisional Type Test

The provisional type tests are required to generate those test data which cannot be obtained through analysis but are essential for verifying the power performance and

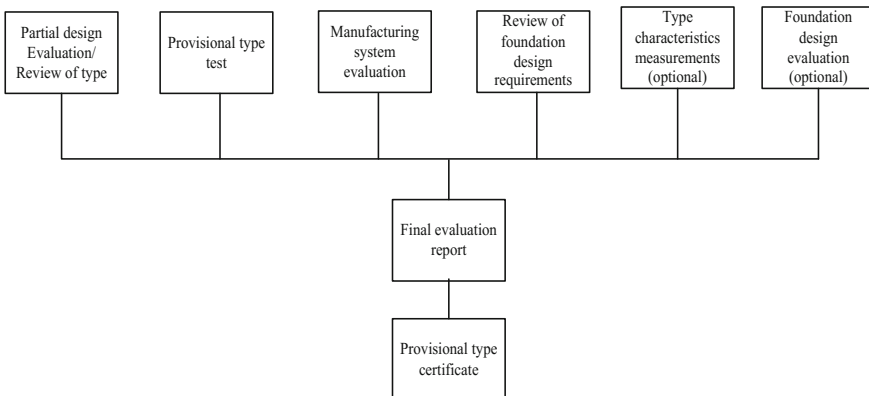


Fig. 6.3 PTC working modules for category II [13, 15]

safety analysis of the WTs. These tests are performed as per IEC requirements modified according to the local Indian conditions and reviewed by the certification body [10, 13]. The tests in this module include (a) safety and function test, (b) power performance measurement, and (c) yaw efficiency measurement. The first test shall be observed by the type certification body while the power performance measurement is performed in accordance with IEC 61400-12 changed to suit the Indian conditions. The tests in this module shall be performed by an accredited laboratory or the S&C unit of NIWE, if the accreditation is pending. A thorough evaluation of test reports prepared by the certification body according to the requirements of ISO/IEC 17025 is necessary to ensure the test quality and appropriateness of the test documents followed by a conformity statement after satisfactory evaluation [13, 15].

Type Characteristic Measurement

This module includes *power quality measurement* involving reactive power assessment for a WT according to IEC 61400-21 along with the turbine power measurement. The 10-min average reactive power values should be specified in tabular form as function of 10-min average value of active power for 0, 10, ..., 90 and 100% of rated active power output [13, 15, 16].

6.4.1.3 Provisional Type Certification: Category III

Newly adopted WT designs or the designs undergone through major modifications come under PTC category III and are certified in accordance with the requirements of IEC WT 01. The working modules involved in this category are presented in Fig. 6.4. It can be observed that almost all the modules except the first one

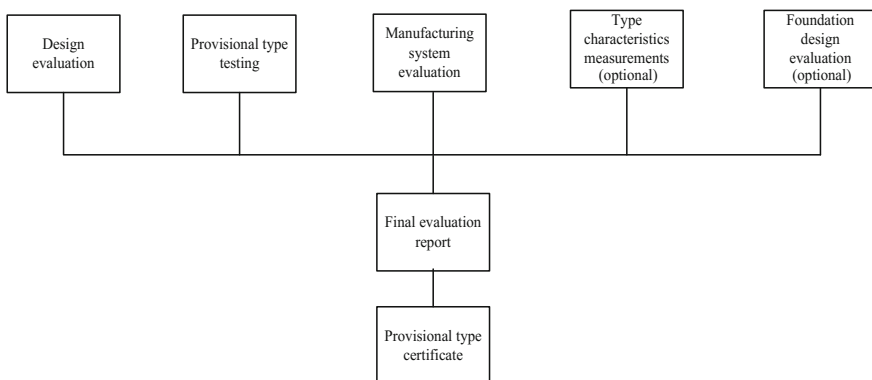


Fig. 6.4 PTC working modules for category III [13, 15]

Table 6.5 Elements of design evaluation module [13, 15]

Control and protection system evaluation	Load and load cases evaluation	Structural, mechanical and electrical component evaluation	Foundation design requirements evaluation	Control design evaluation	Manufacturing, installation and maintenance plans	Personnel safety evaluation	Design evaluation conformity statement
<p>(i) Control and protection system must comply with IEC 61400-1</p>	<p>(i) Loads considered for evaluation are as follows: (a) inertial and gravitational loads (b) aerodynamic loads (c) operational loads (d) wake and impact loads (ii) Loads and load cases must be evaluated according to IEC 61400-1 (iii) Load calculation for stall regulated WT's less than 31 mts. diameter given in Annexure 4</p>	<p>(i) All the structural, mechanical and electrical components should follow the requirements of IEC 61400-1 (ii) Structural analysis and design should also be carried out as per ISO 2394 (iii) The requirements of capacitors are: (a) capacitor design should follow IEC 60831-1 and 60931-1 except voltage level, current limits harmonics and temperature requirements (b) able to sustain short-term overvoltages during <i>routine tests</i> described in clause 9 IEC 60831-1 (c) capable of sustaining short-term overvoltages during <i>type tests</i> mentioned in clause 9.2 IEC 60831-1 (c) current and temperature limits in clause 21 IEC 60831-1 and harmonics in clause 37.2.1 IEC 60831-1</p>	<p>This module is illustrated in Annexure 5. Few important issues are: (i) design evaluations are based on IEC WT 01 (ii) besides load calculations the soil conditions and geometric interface information are also required for appropriate evaluation</p>	<p>(i) Control design should comply with ISO 9001:2000 subclause 4.4</p>	<p>(i) The installation and maintenance plans must be submitted to the certification body (ii) The quality system certification body shall evaluate these plans according to IEC WT 01</p>	<p>(i) Personnel safety aspects in design documentation should be evaluated according to IEC 61400-1</p>	<p>After satisfactory assessment of the design evaluation report a conformity statement shall be issued regarding: (a) WT type identification (b) applicant identification (c) list of IEC 61400 series used (d) external conditions in reference with WT class (e) reference to evaluation reports</p>

(*design evaluation*) are similar as PTC in category II; hence, the tests and evaluation procedures in these modules must be carried out in accordance with the requirements of the modules in category II [13, 15, 16]. The prominent issues of *design evaluation* module are presented in Table 6.5.

6.4.1.4 Relevant External Environmental Conditions in India for TAPS

The environmental conditions specific to Indian sites should be taken into consideration while evaluating a WT design considered for PTC under TAPS. The conditions, as listed in Table 6.6, may vary at various sites in the country, and hence, site-specific assessment of the WT design must be ensured before providing it a valid certificate. The difference in certification procedures between IEC 61400 and TAPS-2000 mainly depends on these external environmental conditions [13, 15, 16].

Table 6.6 External environmental conditions in India for TAPS [13, 15]

Wind conditions	Other climatic conditions	Site conditions	Operational conditions
Normal wind conditions are assessed in reference with 61400-1 Extreme wind conditions are assessed in reference with IS 875 (part 3) 1987	Conditions of lightning, hail and ice formation are not considered. Temperature range for design is between -5 and 60 °C Up to 99% humidity is considered in design. Minimum air density is 1.20 kg/m^3	Terrain conditions, hill slope considerations, and wind disturbances due to objects are considered according to IS: 875 (part 3)-1987 The special requirements of park effect should not be considered Local earthquake parameters should be considered for a site Salt, sand, dust and chemical effects should also be considered Solar radiation intensity of 1500 W/m^2 should be considered	Cutout wind speed should be specified Extreme yaw error as defined in IEC 61400-1 should be considered 20 years of lifetime according to IEC 61400-1 Operating temperature range $0-50$ °C Voltage transition limit is $\pm 10\% V_{\text{nom}}$ Voltage unbalance should not exceed 2% Electrical network outages should be at 350 times/year Maximum outage duration should be 1 week

6.5 Conclusions

With the recent significant leap in the Indian wind power market, the demand of reliable operational approaches for testing and evaluating the WT designs has become apparent. In sequel, the S&C unit of NIWE has developed a provisional type certification scheme (TAPS-2000), for evaluating and certifying the WT generators in India. This provisional scheme was amended in 2003 and shall remain applicable for all the WTs in India till the issue of a final type approval scheme. The *ad hoc* TAPS has evolved mostly from the IEC 61400 standards tailored to include a few changes commensurate with the local Indian conditions. In this chapter, the basic features of IEC 61400-1 standard and TAPS-2000 scheme have been elaborated. The external environmental conditions specific to the sites in India are also discussed in order to bring forth the basic differences between IEC 61400-1 and TAPS-2000. The TAPS-2000 scheme still in its infancy has to mature itself in the form of a permanent certification procedure like IEC 61400 in order to cater the future challenges associated with offshore and new WT designs. Introduction of new features in TAPS would provide it appropriate directions for improving the quality of WT certification, thereby ensuring safety and reliability of the newly inducted designs in the wind industry. In spite of the fact that most of the testing and certification procedures have been developed in reference with IEC standards, of course with a few local or site-specific requirements, the necessity of harmonizing and bringing uniformity in these procedures is required to ensure smooth acceptance of WT technology and designs across the globe.

References

1. Kaldellis JK, Apostolou D, Kapsali M, Kondili E (2016) Environmental and social footprint of offshore wind energy. Comparison with onshore counterpart. *Renewable Energy* 92 (2):543–556
2. Global wind report, Annual market update-2014
3. Hulle FV (2012) Testing standardization certification in wind energy. *Compr Renew Energy* 2 (5):371–389
4. Booma J, Priyanka K, Dhaneraja A, Revency J (2014) A review on type certification schemes of wind turbine. *Int J Eng Res Technol* 3(1):1414–1419
5. Byrene R et al (2011) Recommended practices for wind turbine testing and evaluation: part 12-consumer label for small wind turbines. International Energy Agency
6. International standard, IEC 61400-1. www.iec.ch
7. Burton T, Sharpe D, Jenkins N (2004) *Wind energy handbook*. Wiley, New York
8. *Wind Turbines: Pt 1: design requirements (2005) (IEC 61400-1:2005(EQV). Part 1, NASAI*
9. Gasch R, Twele J (2012) *Wind power plants: fundamentals, design, construction and operation*. Springer, Berlin. ISBN 978-3-642-22937-4
10. Heier S (2014) *Grid integration of wind energy: on shore and offshore conversion systems*. Wiley, New York
11. Ernst B, Seume JR (2012) Investigation of site specific wind field parameters and their effects on loads of offshore wind turbines. *Energies* 5(3):3835–3855

12. www.mnre.gov.in/file-manager/akshay-urja/September-october.../Focus.pdf
13. www.iie.org.mx/proyectoMEM/docpdf/TAPS-2000-India.pdf
14. Indian wind power, Volume 1, Issue 2, June–July, 2014. Available on: http://www.indianwindpower.com/pdf/IWTMA_magazine_v1_issue2.pdf
15. www.niwe.res.in
16. 19th National Training course on wind energy technology, CWET Chennai, March 14–18, 2016, Available on: http://niwe.res.in/national_19.php

Chapter 7

Egyptian Grid Code of Wind Farms and Power Quality

Shady H.E. Abdel Aleem, Almoataz Y. Abdelaziz and Ahmed F. Zobaa

7.1 Introduction

Currently, unpredictable fuel costs, global warming, pollution, fossil fuel shortages, and aging infrastructure have forced all stakeholders, supply sources, the grid, and customers, to focus more on renewable energies such as solar energy, wind energy, and biofuels as environmentally friendly sources of energy. Nowadays, the main challenge is to press on all the power system structures all over the world to move for the realization of smart grids with a low-carbon economy [1]. However, this cannot be achieved by one structure. All should interact with each other to achieve this goal. In order to do this, establishing or updating of standards and codes that determine and organize rights and responsibilities of each stakeholder should be taken into account. In general, grid code is a set of technical boundaries established by the authorizations for stakeholders regarding grid integration. These regulations guarantee smooth and stable operation of all the structures integrated with the grid and of course, the grid itself [2, 3]. Also, this implies the components that will be connected to the grid in the future.

S.H.E. Abdel Aleem
Mathematical, Physical and Engineering Sciences Department,
15th of May Higher Institute of Engineering, Helwan, Cairo 11731, Egypt
e-mail: engyshady@ieee.org

A.Y. Abdelaziz (✉)
Faculty of Engineering, Ain Shams University, Abbassia 11517, Egypt
e-mail: almoatazabdelaziz@hotmail.com

A.F. Zobaa
College of Engineering, Design and Physical Sciences,
Brunel University London, Uxbridge, Middlesex UB8 3PH, UK
e-mail: azobaa@ieee.org

In its broadest scene, each energy source has unique requirements and benefits. In addition to their technical benefits, almost all of them have little to no global warming emissions [4]. However, among all the renewable energy resources, wind power is a promising green source of energy. Wind energy releases about 0.04 lb of CO₂ equivalent for each 1 kWh (CO₂E/kWh). This is about 20% of the corresponding natural gas emissions of CO₂E/kWh [5]. Hence, they improve the environmental quality and public health. Based on [6], it is expected to attain about 2000 GW global installed capacity of wind energy by 2030, i.e., supply 19% of the global electricity. On the other hand, the increase in penetration of wind energy in different countries has led to some technical challenges which may affect the reliability and quality of performance of the entire power system. In the past, the grid-interconnected wind farms (WFs) were weaker to cause a significant disturbance in the system. However, this situation has been totally changed keeping in mind that Denmark made a new world record in 2015 by producing 42% of its electricity from wind turbines [7].

In the few recent years, a lot of standards, drafts, and codes had been published in the countries that have substantial wind generation, such as USA, Germany, Spain, Denmark, China, and Ireland [3, 8]. The fundamental goal of these standards is to ensure that the power networks operate in a safe, secure, and economic manner. However, one of the barriers in this context is the diversity, ambiguity, consecutive drafts, and the different sets of connection requirements of the international codes, especially in the developing countries that try to follow these codes. The two ways to overcome these obstacles are the continuous training of the technicians, engineers, designers, and operators to ensure they gained the required skills to deal with such codes and certifying the WFs that succeeded to follow the requirements while giving a limited opportunity for the others to follow the code requirements. Otherwise, the power system operator is authorized to take the suitable action depending on the case.

Among all the published codes, providing the WFs with static and dynamic profiles similar to the operational characteristics of the conventional centralized power plants can be achieved through manipulations of the technical requirements for grid-connected WFs. The most common requirements include voltage and frequency variation limits, conditions of connection and disconnection from the grid, power quality (PQ) issues such as harmonics, flickers, and voltage imbalance, active power modes of control, characteristic control of the power factor with the active power and grid voltage variations, single and multi-rules for voltage dips and fault ride-through (FRT) capabilities, dynamic capability of reactive power, grid protection, and real-time control [9]. However, PQ issues need more attention among all of these requirements because of the today's advance of the power electronic equipment and nonlinear loads that may worsen the quality of power of the system. Additionally, wind turbines are proposed in proper windy places in which the wind speeds are sufficient to be utilized in electric power generation. In many cases, these WFs are possibly connected to weak grids. Hence, PQ aspects such as harmonics, voltage fluctuations, voltage flickers, and low-power factors are expected when the penetration is low. With high penetration, the overall power

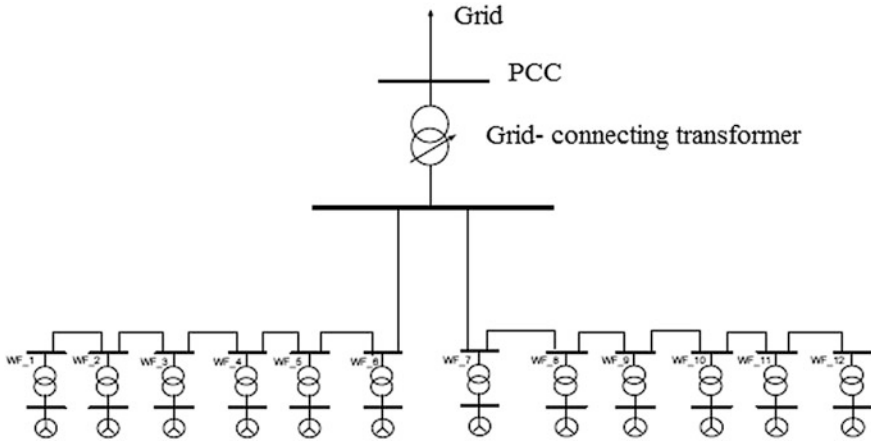


Fig. 7.1 Illustration of the point of common coupling (PCC) for a grid-connected wind farm

system gets affected. Therefore, a real-time control should be implemented to allow the grid operators to assess the wind turbine generator's performance by measuring different PQ indices such as voltage, current, frequency, active and reactive power at the point of common coupling (PCC). Basically, the PCC is the common interface between the wind farm (WF) and the transmission system, or the point where the wind turbine generators interconnect to the grid, as shown in Fig. 7.1.

Other indices can be measured such as wind speed, temperature, and grid-connected transformer tap position. Consequently, the grid operator determines the quality of the generated power with respect to the code, and in case that the WF operator is not complying with the code regulations, the grid operator is authorized to disconnect it from the grid [10, 11].

In what follows, the general requirements for WFs-grid interconnection, authorities, and responsibilities of the grid operators, conditions of the connection, reconnection and disconnection of farms, and active and reactive power control will be introduced and discussed in detail. Additionally, the various requirements concerning quality of power (especially in weak grids), such as harmonics, flickers, imbalance, and voltage fluctuations are presented and discussed.

7.2 Conditions of Connection and Disconnection of Wind Farms

According to [12], conditions of the soft starting up of the WFs, connecting and reconnecting of disconnected farms, and disconnecting of WFs are given below.

7.2.1 Start-Up of Wind Farm Conditions

In the case of starting up a WF, the rate of increasing the active power (P) should not go beyond 10% of the rated power (P_{Rated}) of this farm per minute, where P_{Rated} is the maximum output active power at normal operating conditions.

7.2.2 Reconnection of Disconnected Wind Farm Conditions

The WFs can only connect to the grid, if the grid frequency (f) and the PCC voltage (U_{PCC}) are within the following limits:

Frequency condition: $48 \text{ Hz} \leq f \leq 50.2 \text{ Hz}$, and
 PCC voltage range: $95\% \leq U_{PCC} \leq 105\%$ of the nominal voltage.

7.2.3 Disconnection Conditions

The grid-connected WFs must operate continuously and deliver its available active power, according to wind conditions, whenever U_{PCC} is within the range of 0.85–1.1 p.u., and the grid frequency f is between 47.5 and 51.5 Hz. Moreover, any automatic disconnection of the WF from the grid will be restricted and prohibited by the operator.

Figure 7.2 gives the regions and the period requirements (in minutes) of the WF's output power during variations of f and U_{PCC} [12]. When the deviations are significant and exceed the permissible values, output power reduction may be allowed for certain time [3, 9, 12]. According to the German and Egyptian codes, a decrease in the active power (P) with a definite rate of 40% of P_{actual} per hertz, in the over-frequency range (50.2–51.5 Hz), will be requested [13].

Fig. 7.2 Regions and time regulations of the output power of the wind farm during variations of f and U_{PCC} [12]

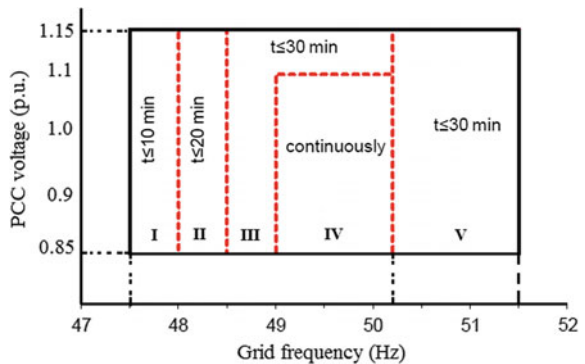


Fig. 7.3 Output active power of the wind farm during frequency variation [12]

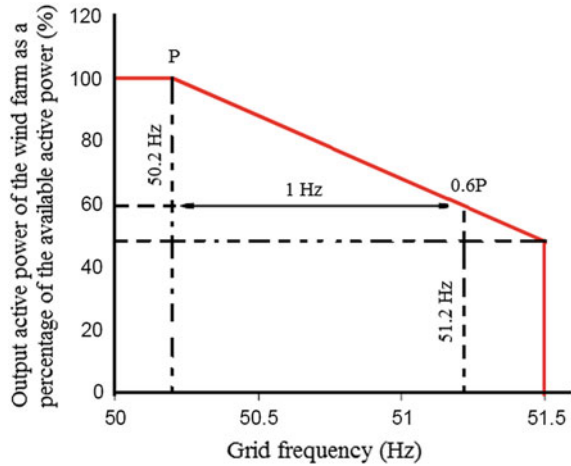


Figure 7.3 shows a characteristic curve that illustrates the reduction of active power with the positive deviation of frequency above 50.2 Hz. Besides, an increase in the delivered power by the WFs may be requested in the case of negative deviations of the frequency (under frequency); however, this will depend on the spinning reserve of the WFs [3, 9].

To meet the requirements of change of the output active power at the interface to the transmission system, the WFs operator shall have an input signal from the grid operator for a set-point value at the PCC.

The WF operator should follow this signal within a definite time, which is stated as 1 min in [12]. For example, the WF operator must be capable of reduction of the output active power with a definite step (10% P_{Rated} of the WF) with a rate of 20% of P_{Rated} per minute. Other codes require the operators of WFs to be capable of reduction of the active power using different ramp rates. By instance, a ramp rate of 1–30 MW per minute is demanded by the Irish code, and the Danish grid code requires a ramp rate of 10–100% P_{Rated} per minute [3, 14, 15]. In addition, according to the initial agreement between the power system and the WF operators, the grid operator may request a reduction in the active power within certain rates in other cases such as maintenance, islanding, overloading, and grid safety or stability issues.

Islanding occurs if a portion of the grid becomes disconnected from the main grid due to any abnormal events such as emergency, short-circuits, or lightning strikes. It may lead to PQ problems for customers, WFs, and power system operators. During such cases, the supply frequency and the PCC voltage may drift outside the limits, particularly because of the synchronization problems that occur upon re-establishment of the connection to the main grid. Therefore, the WF has to be disconnected automatically from the grid (based on the agreements between the grid and the WF operators) to avoid the current surges that will flow in both grid

and wind turbine generators [10, 12]. Based on the European practice, if a fault causes islanding, the ramp-down rate is at least 40% of the nominal P_{Rated} within one second [3].

The requirements concerning active power regulations and control modes for the WFs will be presented in Sect. 7.3, for the sake of completeness of active power control functions.

7.3 Active Power Regulations Modes for the Wind Farms

The grid operator should adjust production of the WFs based on the system needs through submitting control signals to the WF control system. Consequently, the WF operator has to follow the grid operator's instructions and to decide which precise actions or mode of control shall be taken to achieve the desired power values at the PCC. Different active power regulation modes are required in WFs. The most common modes of control (delta control, specific power limit, and balanced control) are demonstrated in Fig. 7.4, respectively [3, 9]. Figure 7.4a shows the first method of control which is called the delta control. In this mode, the WF produces less power than the available power (at any wind condition) by a reserve margin "Delta". This means the WF has to maintain a certain reserve of the available power. This mode enables the operator to have a chance to increase the system generation when needed. Figure 7.4b illustrates the second method of control which is called the maximum power limit. In this mode, the output power is constrained to a specific value; thus, the surplus in the generated power in the grid power generation is prevented. Figure 7.4c shows the third method of control which is called the balance control or real-time control. In this mode, the output power is regulated by the grid operator by submitting control signals to the wind farm control system. Besides, up and down rates are possible for an output active power increase or decrease.

It should be mentioned that following the ramp rates is not simple with wind turbines, particularly with the aging wind turbines because the speed of ramping depends on different factors such as the generator and turbine inertia, pitch angle, and wobbling limits of the blades [9].

7.4 Power Quality

Despite the term "PQ" is common nowadays, it has no standard definition. It may have different meanings for people in various electric working groups. For example, some use PQ to express the quality of voltage, some use it for the quality of current, and some use it to define the service reliability. Furthermore, PQ can be classified according to the AC electricity delivery stage where it corresponds to the reliability

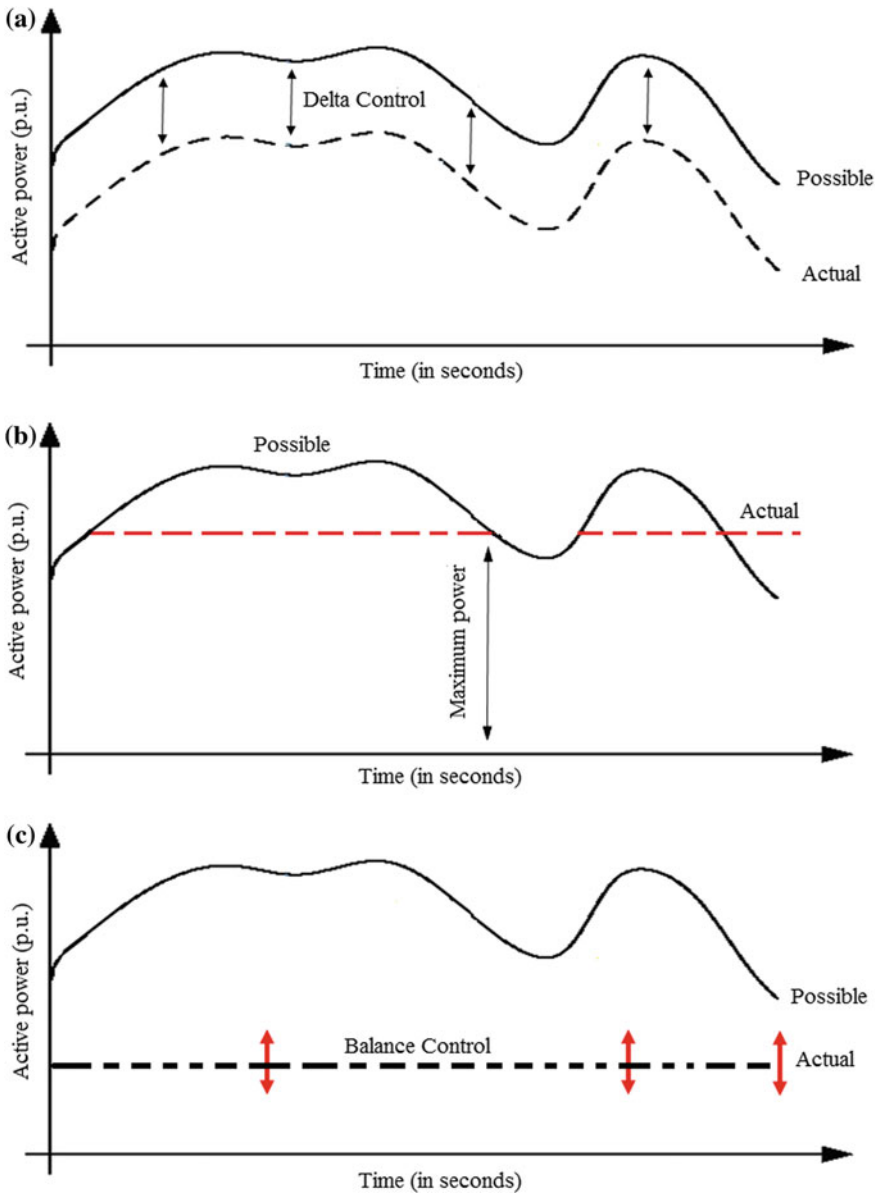


Fig. 7.4 Common modes of power production control. a Delta control, b maximum power control, and c balance control

in power generation stations, voltage quality in transmission systems, current and voltage quality in distribution systems. Additionally, it can be used to express the electricity quality in the electrical energy markets.

In this chapter, the PQ is defined as an agreement between the stakeholders as a “joint responsibility” to follow and honor definite sets of electrical boundaries that allow the grid and its connected components to operate securely and safely in the most economic intended manner without loss of performance [16–19].

Particularly, harmonics, flickers, voltage imbalance, and voltage fluctuations are the significant PQ issues which should be considered with wind turbines to maintain reasonable voltage waveform quality at the PCC.

7.4.1 Harmonics

The 50 or 60 Hz is the fundamental design frequency for all power system networks. Harmonics are multiples of this fundamental frequency [20]. Different sources can contribute to harmonic distortion such as variable speed wind turbines that use power converters, nonlinear loads as computers, furnaces, DC and AC drives loads, and the various types of FACTS devices (STATCOMs, SVCs) [21]. Also, another risk can occur which is the resonance between the shunt capacitor banks that may exist with the induction generators and the system inductive reactance [22]. Moreover, another form of resonance may occur at low frequencies between the AC submarine cables and the power system [23].

The electrical grid plays a significant role in the determination of the percent of the voltage harmonic distortion at the PCC by the variations that may occur in the grid impedance. According to the common practice, the worst case of the grid impedance has to be considered while specifying WF responsibility in the harmonic pollution. Also, a weak interconnection of WFs to the electrical grid may worsen the case with the increased severity of resonance hazards.

Harmonic voltages and currents must be limited to their allowable levels at the PCC, which is the agreed location of measurements. It should be noted that the contribution of each source to the voltage total harmonic distortion (VTHD) may be determined independently as given in IEEE Standard 519 [24]. However, it should not be arithmetically added because of the different phase angles of the measured voltage or current waveforms. Hence, the summation laws of the IEC 61400-21 can be used in this case for an accurate determination of the total harmonic distortion [25]. Consequently, passive, active, or hybrid filters can be employed for reactive power compensation, voltage support, power factor improvement, resonance dampen, and harmonics mitigation [21].

For measuring the distortion of a nonsinusoidal waveform, the total harmonic distortion (THD), the individual harmonic distortion (IHD), and the total demand distortion (TDD) are usually used. All of them are suitable for either voltage or current. The total and IHD of the PCC voltage are illustrated in Eqs. (7.1) and (7.2), respectively. Also, the total demand distortion of the current, measured at the PCC, is defined in Eq. (7.3), where U_1 is the root-mean-square (rms) value of the fundamental voltage, n is the harmonic order, I_n is the n th harmonic current, and I_L is the maximum demand current at normal operating conditions.

$$\text{VTHD} = \frac{\sqrt{\sum_{n \geq 2} U_n^2}}{U_1} \quad (7.1)$$

$$\text{VIHD} = \frac{U_n}{U_1} \quad (7.2)$$

$$\text{TDD} = \frac{\sqrt{\sum_{n \geq 2} I_n^2}}{I_L} \quad (7.3)$$

In Egypt, India, Turkey, and other developing countries, the IEEE 519 is the standard that is used to define the quality of power recommendations at the PCC. Details of allowable harmonic currents and inter-harmonic current distortions at different frequency ranges, and the allowable levels of individual and total voltage harmonic distortion can be found in [12, 24]. One or more harmonic filter can be added at the WF location to reduce the harmonic distortion below the permissible level [21].

7.4.2 Voltage Flickers

Voltage flicker is an important PQ issue in the wind systems that occur because of voltage fluctuation, particularly for WFs connected to the distribution networks. Some loads such as induction and arc furnaces cause considerable variation in the distribution bus voltage which has a spectral characteristic lie between a fraction of a hertz and about 10 Hz and may lead to apparent differences in light output [11, 23]. For transmission grid-connected WFs, flickers are not a critical issue. However, if it exceeds its permissible values, it may constrain the maximum wind power production. The main reason which causes voltage flicker in the WFs' continuous operation mode is the variable output power of the turbine generators because of the changes in the wind speed, pitching angle, wind shear, and tower shadows [23]. In the switching mode of operation, flickers occur by power fluctuations at the start or the stop operations of the wind turbines. In addition, some parameters of the electrical grid itself affect the flicker, such as the short-circuit ratio (SCR), and phase angle of the grid impedance. Furthermore, large wind turbines produce lower voltage flicker compared to small wind turbines.

Flicker is not a primary concern for variable speed wind turbines compared with the fixed ones. According to IEC 61000-4-15 [26], the flicker takes statistical measurements at 10-min intervals. The short-term flicker (P_{st}) severity is calculated every 10 min, while the long-term flicker (P_{lt}) severity, given in Eq. (7.4), is calculated over 120 min; thus, the P_{lt} severity is a combination of 12 P_{st} values. As a border limit, a value of 1 for P_{st} represents a visible disturbance, or by definition, a level of visual severity at which 50% of people might notice a flicker in a 60-W incandescent bulb.

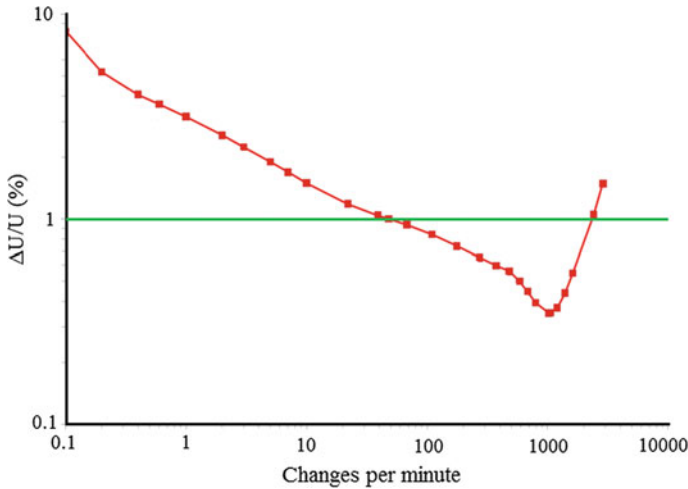


Fig. 7.5 A typical flicker curve for a 120 V, 60-watt bulb, with P_{st} equals 1: borderline of irritation [27]

Figure 7.5 illustrates a typical flicker meter curve that was taken with a regular rectangular voltage change for a 120 V, 60-W bulb with P_{st} equals 1 [27].

$$P_{lt} = \frac{1}{S_K} \sqrt{\sum_{i=1}^N (C_i(v_a, \psi_k) \cdot S_{R,i})^2} \quad (7.4)$$

where S_K is the short-circuit apparent power at the grid connection interface, C_i represents the flicker coefficient for wind turbine “ i ”. It can be calculated from the wind speed’s Rayleigh distribution. N represents the turbines’ number in a particular park, v_a represents the annual average wind speed, ψ_k represents the grid impedance phase angle, and $S_{R,i}$ is the i th rated power of a turbine.

According to the Egyptian code, and based on the IEC 61000-3-7 [28] for voltage flicker limits, values of P_{st} and P_{lt} must be below 0.35 and 0.25 in the emission levels, respectively [12]. It should be mentioned that the Danish code gives more restrictive regulations for the flicker limits, which are 0.30 and 0.20 for the P_{st} and P_{lt} values, respectively [23].

7.4.3 Voltage Imbalance

Voltage imbalance is specified by the ratio of the deviation between the highest and lowest line voltages and the average line voltage of the three line voltages [23]. It is another important PQ issue of grid-integrated WFs because of the negative

sequence currents that may flow in the generator rotors and alter their performance. The line voltage unbalance rate (LVUR) is defined as [29]

$$\text{LVUR} = \frac{\text{Maximum } (U_d)}{U_{\text{avg}}} \quad (7.5)$$

where U_d represents the deviation of the line voltage from the average voltage (U_{avg}). NEMA gave this definition in [29]. However, another precise unbalanced voltage factor (VUF) using symmetrical components is defined as follows [30]:

$$\text{VUF} = \frac{U_-}{U_+} \times 100 \quad (7.6)$$

where U_- and U_+ are the magnitudes of the fundamental harmonic negative and positive sequence voltages at the PCC. According to [12], WFs shall be able to withstand voltage unbalance that is not exceeding 2%.

7.4.4 Voltage Fluctuations

The voltage at the PCC may fluctuate because of the switching operations of the WF such as starting or stopping a wind turbine generator, inrush currents, and capacitor banks switching. According to the Egyptian code, the voltage at the PCC has not to change more than $\pm 5\%$ of its nominal value [12].

7.5 Power Factor and Reactive Power Control

Requirements for the reactive power are employed using different control modes such as the set-point and characteristic controls. The set-point controls include controlling parameters such as the reactive power (Q) or power factor (PF). The characteristic controls include PF versus the wind turbine's active power, $\text{PF} = f(P)$, or Q versus the PCC voltage, $Q = f(U_{\text{PCC}})$ [23].

The grid operator determines the suitable mode of operation of the reactive power control by providing the set-point signal. Consequently, the WF operator should follow this set-point signal within 60 s [12].

The regulation of the PF defines the Q capability of the WFs. In Egypt, the WF operator is requested to handle the reactive power at the PCC by operating at the rated output power within acceptable limits ranging between 0.95 lagging to 0.95 leading PF, as demonstrated in Fig. 7.6 for the continuous Q capability. A permissive reactive power range is allowed at low output power range, precisely for $P < 0.2$ p.u.

Figure 7.7 illustrates a typical characteristic curve of the PF variation with the PCC voltage, while, Fig. 7.8 demonstrates different reactive power capability PQ charts for different grid operators in Europe [31].

Future updates to these regulations include taking the advantages of the Spanish code in providing a bonus (incentive) for the WFs that sustain the permissible power factor limits at the PCC and penalizing the WFs that do not honor these boundaries [23]. However, an updated policy will be needed to trigger this trend.

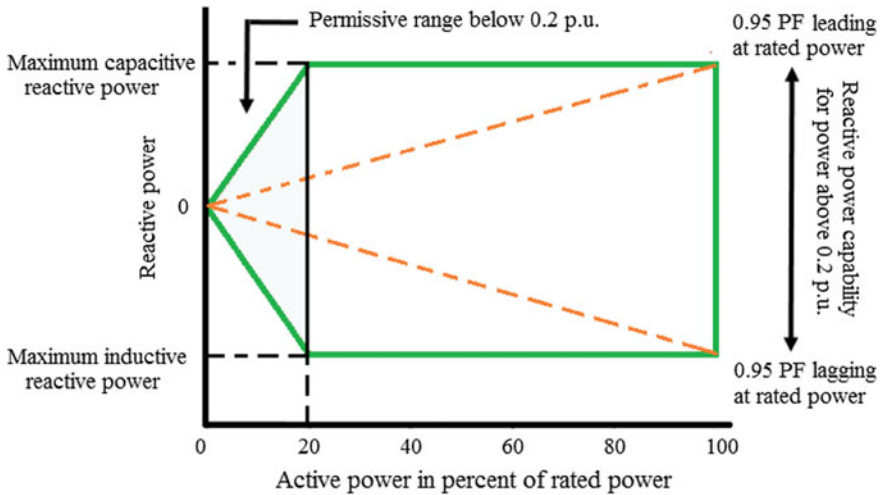
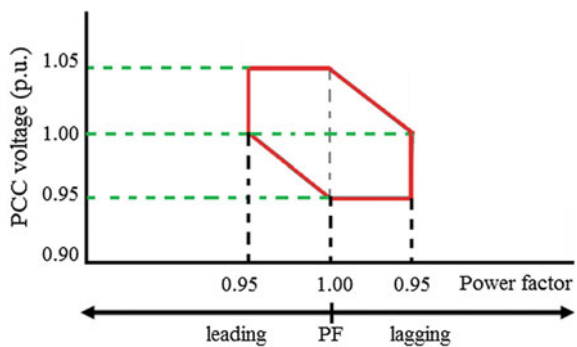


Fig. 7.6 Reactive power capability chart of the Egyptian grid operator: the PQ operating range [12]

Fig. 7.7 PF variation with the PCC voltage



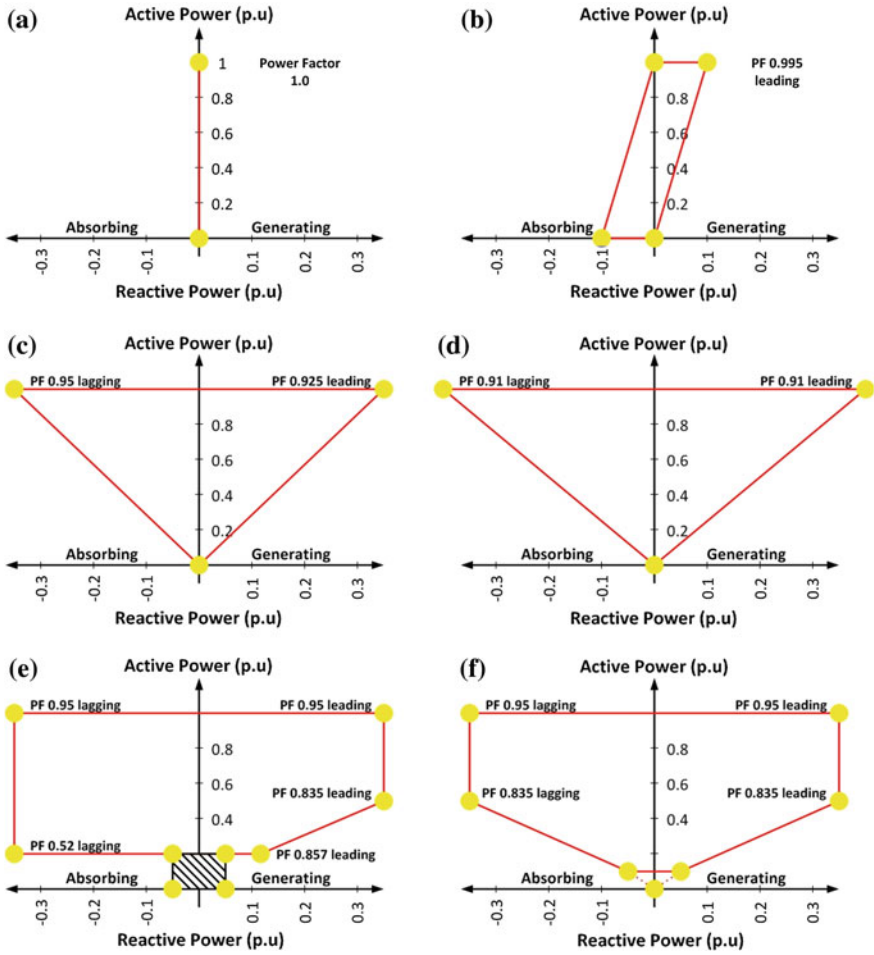


Fig. 7.8 Different reactive power capability PQ charts for different grid operators in Europe. **a** The Sweden Svenska Kraftnät (SVK), **b** the Danish national transmission system operator (Energinet), **c** the German network operator (E.ON), **d** the Norwegian transmission system operator (Statnett), **e** the national grid electricity transmission in Great Britain (NGET), **f** the Irish network operator (ESBNG) [31]

7.6 Voltage Disturbances

Reliability of the grid-connected wind systems may be significantly affected by system disturbances due to asymmetrical or symmetrical grid faults. As the grid operators are liable to sustain a reasonable performance of the operated system even with the involved wind systems, they demand strict regulations for the disconnection of the wind power plants under these events. Accordingly, these wind

plants should have the ability to endure these temporary voltage sags, follow the active and reactive power requirements to support the network during these events, and conduct a fast transition to the pre-fault steady-state operation after voltage restoration.

7.6.1 Single and Multi Low-Voltage Ride-Through Capabilities

The power system operators necessitate the WF operators to maintain their service, according to specific voltage–time limits profiles during these voltage disturbances. These voltage–time profiles are commonly recognized as FRT, or low-voltage ride-through (LVRT) [9]. Figure 7.9 illustrates the FRT profile of the Egyptian grid-interconnected WFs.

As demonstrated in Fig. 7.9, the WFs are obliged to remain connected to the grid after a fault on any or all phases for faults duration of 150 ms (7.5 cycles). The minimum voltage level (% of the rated voltage), during the fault, is 0%, whereas the maximum voltage sag duration is 3 s. However, disconnection of wind turbines is permitted if the fault remained longer than the standard clearing time. Additionally, Table 7.1 gives the LVRT characteristics in other different international grid codes [3, 9, 15, 23].

Line reclosing actions and multiple disturbances may occasionally occur in power systems. Hence, the wind turbine generators can be impacted by multiple faults. According to [12], for temporary voltage drops due to a nonsuccessful reclosing action, multiple fault-multiple LVRT capabilities should be applied as shown in Fig. 7.10, where each fault is treated as a different event with a new LVRT profile.

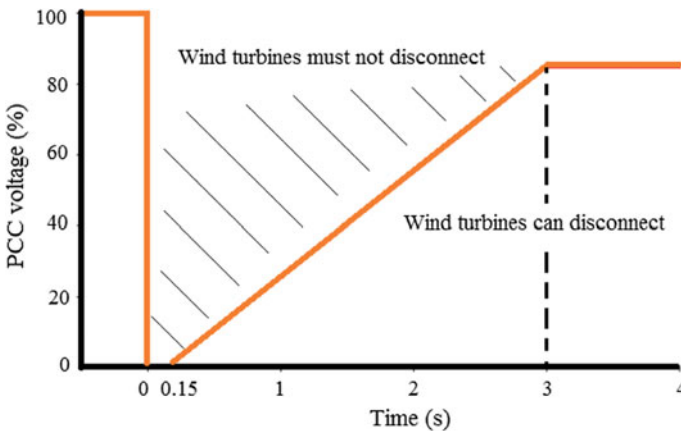


Fig. 7.9 FRT profile of the Egyptian grid-interconnected wind farms [12]

Table 7.1 LVRT characteristic in different international codes

Code/Country	Duration of fault (ms)	Minimum PCC voltage (%)	Time to restore voltage (s)
Canadian AESO ^a	625	15	3
Canadian HQ ^b	150	0	1
Energinet (<100 kV) ^c	140	25	0.75
Energinet (>100 kV) ^c	100	0	10
German E.ON.	150	0	1.5
Egypt	150	0	3
Ireland	625	15	3
Italy	500	20	0.8
Spain	500	20	1
UK	140	0	1.2
USA	625	15	3

^aAESO stands for Alberta Electric System Operator

^bHQ stands for Hydro-Québec

^cDanish grid code

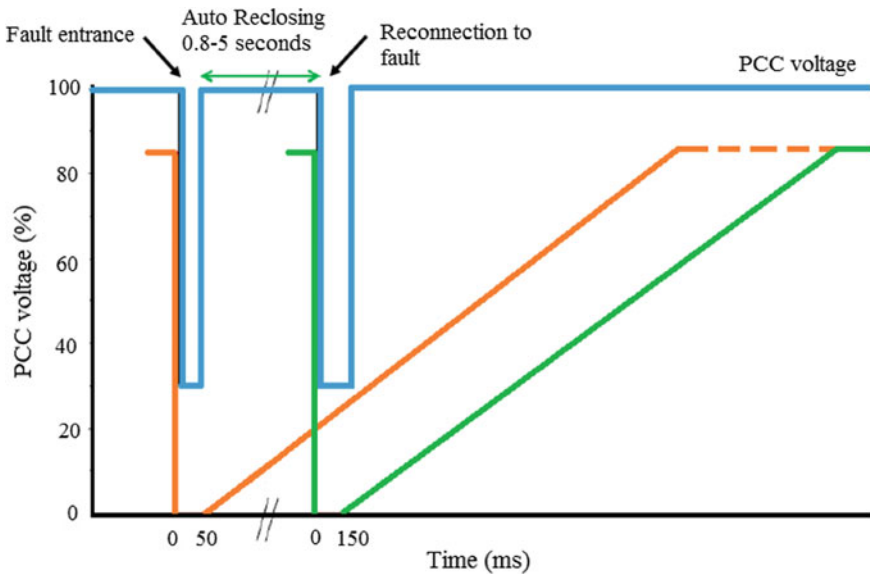


Fig. 7.10 Two successive temporary voltage drops due to a nonsuccessful reclosing action [12]

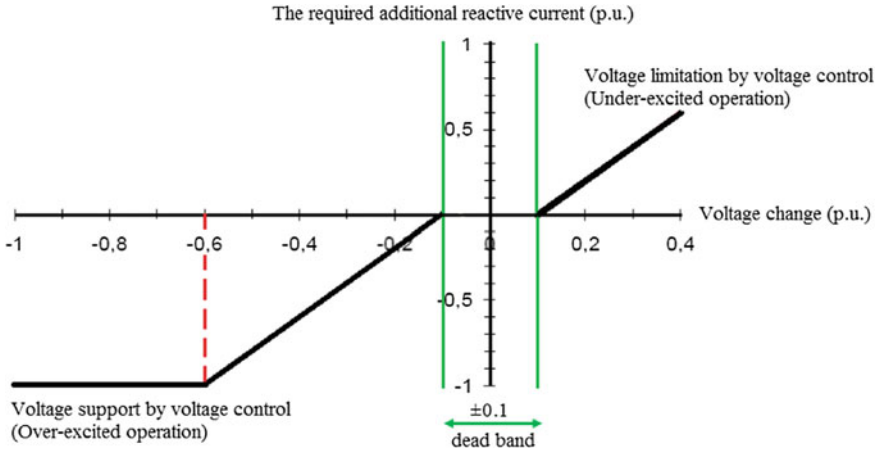


Fig. 7.11 Dynamic regulations during disturbances [12]

7.6.2 Dynamic Regulations During Faults

Along with the LVRT requirements, the Egyptian grid code, as well as other transmission grid codes, demands an injection of capacitive current to enhance the PCC voltage during faults according to the characteristic shown in Fig. 7.11. For 3-phase faults, between 10 and 60% voltage drop and after the origin of the voltage dip with 150 ms (7.5 cycles), the wind turbine generators must supply a capacitive reactive current with a particular rate of the rated current for each 1% drop in the grid voltage. The rate of the injection is adjustable between 2% (as the German code, by instant) and 4% (as per the Australian code) of the rated current for each 1% drop in the grid voltage.

Other countries such as Spain and UK demand maximum reactive current injection during the faults. For 2-phase and 1-phase faults, a reactive power consumption of maximum 40% of the rated power may be allowed after the fault entrance by a 150 ms period. Furthermore, active power consumption should not exceed 30% of the wind turbine generators' rated power in each grid cycle (20 ms) [3, 9, 23, 31].

7.6.3 Dynamic Regulations After Faults

Another important technical requirement in the grid codes is the restoration rate of the active power after faults. According to the Egyptian grid code, it is required to restore the generators' active power to the pre-fault one within 10 s after the clearance of the fault. Also, reactive power absorption should be equal or less than the pre-fault consumption value.

Table 7.2 Recommended settings of the grid protection devices [12]

Function	Range	Recommended settings	
		Level	Settling time (ms)
Under voltage <	0.1-1 $U_{nominal}$	0.8 $U_{nominal}$	3000
Under voltage <<	0.1-1 $U_{nominal}$	0.3 $U_{nominal}$	300–1000
Over voltage <<	1-1.3 $U_{nominal}$	1.2 $U_{nominal}$	≤3000
Over frequency	50–52 Hz	51.5 Hz	≤100
Under frequency	47.5–50 Hz	47.5 Hz	≤500

7.7 Grid Protection

Protection system requirements must ensure safe and reliable operation of both the grid and wind turbine generators. In this context, Table 7.2 gives the functions and the recommended settings of the protection devices that have to be utilized according to the transmission grid code. Additionally, phasor measurement units with a GPS source should be installed at the PCC for real-time control, measuring, monitoring, and recording the different concerned quantities [12].

7.8 Summary

Compliance with interconnection requirements is mandatory for grid-interconnected WFs. In this chapter, the recent regulations and technical requirements concerning the grid-connected WFs are introduced. Also, rights and responsibilities of the grid and WF operators, conditions of connection, reconnection and disconnection of farms, active power control modes, power factor requirements, and reactive power regulations are presented and discussed. Besides, the various requirements concerning the quality of power, such as flickers, harmonics, imbalance, and voltage fluctuations are discussed in detail.

Generally, the technical requirements are general rules that employed to ensure that the grid and its connected equipment are operating in a reliable, stable, and technoeconomic manner. However, some barriers to integrating substantial WFs can exist, especially in the developing countries. Thus, continuous developing and adapting of the grid codes, and identifying the new ways for energy balance and stability issues while developing schemes to avoid them, should be regularly discussed and updated as newer solutions can regularly exist because of the rapid advances in technology.

Finally, the stochastic nature of the wind and the predictable requirements should be taken into account when designating standardized transmission grid codes, as the forecasting of wind speed or solar intensity is still highly inaccurate.

Acknowledgements The authors gratefully acknowledge and thank Chris Mullins, VP of Engineering, Power Monitors, Inc. for his support and information he freely provided during the preparation of this work.

References

1. Abdel Aleem SHE, Zobaa AF, Abdel Mageed HM (2015) Assessment of energy credits for the enhancement of the Egyptian Green Pyramid Rating System. *Energy Policy* 87:407–416
2. Bansal RC, Zobaa AF, Saket RK (2005) Some issue related to power generation using wind energy conversion system: an overview. *Int J Emerg Electr Power Syst* 3:1–14
3. Tsili M, Papathanassiou S (2009) A review of grid code technical requirements for wind farms. *IET Renew Power Gener* 3:308–332
4. Salameh Z (2014) *Renewable energy system design*. Academic Press, Elsevier, London, UK
5. IPCC (2011) IPCC special report on renewable energy sources and climate change mitigation. Working Group III of the Intergovernmental Panel on Climate Change
6. Font V (2016) Wind energy setting records, growing still: the wind energy outlook for 2016
7. Neslen A (2016) Wind power. Denmark broke world record for wind power in 2015. <http://www.theguardian.com/environment/2016/jan/18/denmark-broke-world-record-for-wind-power-in-2015>
8. Smith JC, Milligan MR, DeMeo EA (2007) Utility wind integration and operating impact state of the art. *IEEE Trans Energy Convers* 22:900–907
9. El-Sharkawi MA (2015) *Wind energy: an introduction*. CRC Press, Taylor and Francis Group
10. Danish Wind Industry Association (2003) http://www.motiva.fi/myllarin_tuulivoima/windpower%20web/en/tour/grid/rein.htm
11. Mohod SW, Aware MV (2013) Power quality and grid code issues in wind energy conversion system. In: Lu D (ed) *An update on power quality*. InTech, Croatia, European Union
12. ETGC (2014) Wind farm grid connection code in addition to the Egyptian transmission grid code. Revised Draft
13. Erlich I, Winter W, Dittrich A (2006) Advanced grid requirements for the integration of wind turbines into the German transmission system. In: *Proceedings of IEEE power engineering society general meeting, Montreal, Que*
14. Porter K, Yen-Nakafuji D, Morgenstern B (2007) A review of the international experience with integrating wind energy generation. *Electron J* 20:48–59
15. Thomas A (2005) *Wind power in power systems*. Wiley, Hoboken
16. Abdel Aleem SHE, Zobaa AF, Abdel Aziz MM (2012) Optimal C-type passive filter based on minimization of the voltage harmonic distortion for nonlinear loads. *IEEE Trans Ind Electron* 59:281–289
17. Bollen MHJ, Gu IYH (2006) *Signal processing of power quality disturbances*. IEEE
18. Dixit JB, Amit Y (2010) *Electrical power quality*. Laxmi Publications Ltd.
19. Abdel Aleem SHE, Balci ME, Zobaa AF, Sakr S (2014) Optimal passive filter design for effective utilization of cables and transformers under non-sinusoidal conditions. In: *Proceedings of 16th international conference harmonics and quality of power, ICHQP'14, Bucharest, Romania, 25–28 May*, pp 626–630
20. Zobaa AF, Abdel Aziz MM, Abdel Aleem SHE (2010) Comparison of shunt-passive and series-passive filters for DC drive loads. *Electr Power Compon Syst* 38:275–291
21. Heetun ZK, Abdel Aleem SHE, Zobaa AF (2016) Voltage stability analysis of grid-connected wind farms with FACTS: static and dynamic analysis. *Energy Policy Res* 3:1–12
22. Abdel Aleem SHE, Ibrahim AM, Zobaa AF (2016) Harmonic assessment-based adjusted current total harmonic distortion. *IET J Eng*. doi:10.1049/joe.2016.0002
23. A review of interconnection rules for large-scale renewable power generation: principal technical issues in grid interconnection (2015) <http://machineryequipmentonline.com/>

[electrical-power-generation/a-review-of-interconnection-rules-for-large-scale-renewable-power-generation/principal-technical-issues-in-grid-interconnection/](#)

24. IEEE Standard 519 (2014) IEEE recommended practice and requirements for harmonic control in electrical power systems
25. IEC 61400-21 (2008) Wind turbines—part 21: measurement and assessment of power quality characteristics of grid connected wind turbines
26. IEC 61000-4-15 (2010) Electromagnetic compatibility (EMC)—part 4–15: testing and measurement techniques—flickermeter—functional and design specifications
27. Andrus C (2013) Understanding IEEE flicker, Ifl, Pst, Plt. <http://images.powermonitors.com/white-papers/WP104.pdf>
28. IEC 61000-3-7 (2008) Electromagnetic compatibility (EMC)—part 3–7: limits—assessment of emission limits for the connection of fluctuating installations to MV, HV and EHV power systems
29. Pillay P, Manyage M (2001) Definitions of voltage unbalance. IEEE Power Eng Rev Mag 5:50–51
30. Balci ME, Abdel Aleem SHE, Zobia AF, Sakr S (2014) An Algorithm for optimal sizing of the capacitor banks under non-sinusoidal and unbalanced conditions. Recent Adv Electr Electron Eng 7:116–122
31. Sandia NL (2012) reactive power interconnection requirements for PV and wind plants (SAND2012-1098). <http://energy.sandia.gov/wp/wp-content/gallery/uploads/Reactive-Power-Requirements-for-PV-and-Wind-SAND2012-1098.pdf>
32. Heier S (2006) Grid integration of wind energy conversion systems. Wiley

Chapter 8

Integrating an Offshore Wind Farm to an Existing Utility Power Network via an HVDC Collection Grid: Alternative Topology

Kabeya Musasa, Michael Njoroge Gitau and Ramesh Bansal

8.1 Introduction

Electricity production from fossil fuels has been widely adopted in the world because of diverse reasons, such as higher energy density in relatively large quantity, cheaper and well-known technology. However, it is estimated that if the energy from fossil fuels continues to be consumed at the present rate, it will not last long. Furthermore, electricity generation from coal is no longer a good choice due to several environmental concerns [1]. The global warming experienced due to the use of coal- and oil-fired-based power plants has motivated the use of renewable energy solutions, such as photovoltaic (PV), energy storage source (ESS) and wind. In fact, a large percentage of installed renewable energy sources generate DC power output. This output needs to be converted appropriately for supplying the AC loads.

On the other hand, there is also large numbers of devices using DC power for their operation. The DC loads can be directly supplied by the DC power output from renewable energy sources, which is actually not the case. However, there are large numbers of power converters (e.g. rectifiers) being used in the conventional AC power network to feed the DC loads. It is true that the power converters are the main sources of voltage/current harmonic distortion [2]; these significantly affect the power quality of the conventional AC power network. The power converters

K. Musasa (✉) · M.N. Gitau · R. Bansal
Department of Electrical, Electronics and Computer Engineering,
University of Pretoria, Pretoria, South Africa
e-mail: kabeyamusasa@gmail.com

M.N. Gitau
e-mail: njoroge.gitau@up.ac.za

R. Bansal
e-mail: rcbansal@ieee.org

also generate high power losses, thus reducing the efficiency of the AC power network. Wide number of researches has focussed on the design of high-efficiency power converters; for example, the line-commutated converters (LCCs) are proven more efficient than the voltage source converter (VSC) in terms of power losses due to the low switching frequency operation, but these generate high current harmonic distortion [3–5]. The VSCs generate low harmonic distortion but high power losses due to the high switching frequency operation [5]. High-efficiency power converter topologies require more complicated circuits because of the large number of components employed, which may reduce the system reliability and greatly increases cost.

There is actually high interest in the development of DC grids. A large number of small-scale DC grids are being installed for telecommunications, automobile industries and households, such as the use of solar geysers and power backup system using PV and batteries storage system (BSS). Furthermore, extensive published works have already addressed the issues of integrating renewable energy sources into existing electrical power networks by means of DC power collection systems [5, 6]. Generally, the use of DC power collection grids is less selected as opposed to the AC power collection systems because of the lack of economically realisable protection devices for the DC collection system. However, efficient and cost-effective protection devices for DC grids are actually being designed [7–9].

For the control strategy of DC power collection grids, the VSC with pulse width modulation (VSC-PWM) control scheme can be a good choice because of the fast dynamic performance. In contrast, the LCC system is cheaper and robust, but it may not be a good option for wind farms. The LCC system employs thyristors as switches in the power electronic converters, and the commutation of thyristors depends on the AC signal output of the wind turbine generator. Because of the strong perturbation of wind signals at sea, the AC signals are probably weak, and consequently, the control of voltage/current signal can be highly affected at most instants.

8.1.1 Wind Farm with Output AC Power Collector

Conventional offshore wind farms are constructed with the aggregation of AC wind energy conversion units (WECUs); each WECU includes a wind turbine with mechanical parts (wind turbine blades, shaft and gearbox), a generator (DFIG, PMSG and SCIG), and a huge 50- or 60-Hz power transformer. The large number of magnetic components employed in the power transformer makes the WECUs less compact and not strong enough to withstand the high wind speeds. A typical arrangement of an offshore wind farm with an internal AC collection grid can be found in [6, 10–12]; the layouts consist of series, parallel, series–parallel, star, ring or radial interconnections of WECUs. The total power output of the wind farm is collected via a short AC cable and sent to a high-voltage (HV) AC offshore platform, which also includes a huge 50- or 60-Hz power transformer. The HVAC

platform boosts the medium output voltage of the wind farm to HVAC for transmission to onshore grid.

Offshore wind farm sites are not necessarily located close to onshore grids or loads. Increasingly, sites are being located far from the loads for maximum wind energy tracking and some other environmental issues, such as minimising the visual and audible impacts on nearby residences. Because of higher charging currents associated with AC cables for a long transmission line, the HVDC transmission system may be a preferable option. Other advantages of choosing the HVDC transmission system are low number of DC cables needed, no charging current and skin effect exist in the DC cables, power factor is close to unity, and there are less corona loss and radio interference [13, 14]. If the HVDC system is selected for power transmission, another offshore platform or power converter station is needed to convert the HVAC signal to HVDC. This makes the structure of offshore wind farm with an AC power collection system very complex and less compact.

The state-of-the-art technological concept for various WECUs employed in the AC power collection grids is presented in [15–19]. Pitchable blades are integrated into the WECUs to control the input power to the wind turbines. The active stall concept is an alternative pitch strategy to control the input power to the wind turbine. The use of asynchronous machines embedded with power electronic converter has led to the control concept named “variable speed wind turbine”. The power electronic converter provides the control flexibility of active and reactive powers, frequency, voltage and torque. The use of variable speed WECU concepts such as DFIG- or PMSG-based WECU is motivated by a number of reasons; these include reduction of the mechanical stress of the drive trains (internal elements of the gearbox), enabling tracking of the maximum wind energy and providing control of frequency and voltage, which is very important for satisfactory integration of offshore wind farms with the onshore grid [20–22].

Fixed or constant speed WECU, such as SCIG-based WECU, is another control concept that does not integrate power electronic circuits into the WECUs. The control of voltage and frequency is coordinated by a regulator, e.g. a static compensator (STATCOM) installed at the onshore grid side. The principle of operating a fixed speed-based WECU is that the speed of the wind turbine blade is boosted, via a gearbox, up to generator–rotor synchronous speed. The difference between the generator electrical angular frequency imposed by the onshore grid and the generator–rotor mechanical speed produces a positive slip, thus enabling power flow enhancement. The constant speed-based WECU results in non-optimum operation of the wind turbine over a wide range of wind speeds.

8.1.2 Wind Farm with Output DC Power Collector

The use of AC power collection grids for wind farms, instead of the DC collection grids, is mainly motivated by the availability of control and protection devices. Efficient and cost-effective control and protection devices for DC collection grids

have already been addressed [7–9], and this may not be a problem anymore. For a wind farm with DC power collection grid, the power transformer in each WECU is replaced by the power converter [23–26]. Technically, the power converter uses lower quantity of magnetic components compared to the power transformer of a similar power rating, thus reducing the size and weight of the WECUs and hence reducing the offshore wind farm structure.

The layouts of wind farms with internal DC collection grids are usually the series or series–parallel interconnection of WECUs [6, 23, 24]. The series connection of WECUs enables building of a voltage high enough for the HVDC collection grid. Parallel branches are added in order to increase the current rating and hence achieve a high enough power capacity. A typical arrangement of the DC collection grid can be found in [8, 27]; this includes a series-connected WECU and an HVDC platform. The HVDC platform includes a boost DC–DC converter, which steps up the voltage of the DC bus (or DC collector) to HVDC and also limits the voltage variation of the DC bus. There are no operational high-voltage DC–DC converters yet (e.g. above 100 kV) [28], but research is still being conducted to develop such converter topologies. For example, the author of [29] has recently developed a boost DC–DC converter for high-power DC grid application, which consists of an interconnection of multiple modular DC–DC converters.

Consequently, the use of an HVDC platform at the output of a wind farm may not be a good option at the moment. The HVDC platform can be replaced by an HVDC collection system, which consists of the series connection of WECUs as adopted in [23, 25]. The control of DC voltage at the output of wind farm can be achieved by using the power inverter installed at the onshore grid side. Currently, there are no operational wind farms with output DC power collector; only theoretical and small-scale prototypes are being investigated worldwide. Therefore, a suitable configuration of the DC power collector for wind farm, which has been practically verified, is not available yet.

The configurations of the DC power collector for wind farms can be differentiated based on the adopted topology of power converters in the WECUs. Most of the published works on the design of DC power collector for offshore wind farms employ “the conventional three-phase full-bridge active rectifier” as the power converter topology in the WECUs [8, 9, 30–32]. Some studies also combine the conventional three-phase full-bridge active rectifier with an isolated boost DC–DC converter, which consists of an active bridge inverter, an AC link consisting of a high- or medium-frequency transformer and a passive diode rectifier [25, 33–35]. These power converters perform well the power filtering and power conditioning; however, large numbers of high switching frequency controlled switches and complex control circuits are needed, which considerably increase the cost. The power loss generated by these converters is high because of the high switching frequency operation.

The topology of power converter for WECU employed in [36] consists of a three-level neutral point-clamped converter cascaded with an isolated full-bridge three-level DC–DC converter, including chopper resistors installed at the output of NPC for overvoltage protection. Large numbers of components and a complex

control structure are employed in the circuit. Another topology of power converter employed for the WECU by the author in [28] consists of a three-phase LCC rectifier cascaded with a DC–DC resonant converter. However, the LCC system uses thyristors as switches in the power converter, where the commutation of the thyristor depends on the AC signal characteristics (i.e. input signal to the power converter). Because of strong perturbations of wind in the sea, the AC network is most probably weak, and hence, the control of active and reactive power is badly affected at most times.

Other simplified topologies of the power converter in WECUs are proposed in [23, 26, 37–39]; a three-phase diode bridge rectifier cascaded with a single-controlled switch DC–DC converter is presented in [23, 26, 37, 38], while the half-bridge VSC in [39] is proposed for low-power application. This reduces the power losses, control circuits, cost, size and weight of the WECUs.

8.1.3 Aim of Study and Contribution

The use of large number of converters in the conventional AC power network to feed DC loads causes high current/voltage harmonic distortion and high power losses. This study intends to explore an alternative topology for interconnecting an AC power network with a DC network. The proposed topology will limit the use of large number of power converters in the conventional AC power network and therefore mitigates the voltage/current harmonic distortion, reduces the power losses and also improves the efficiency of the AC power network.

Indeed, a separate AC and DC grids are considered in the study. The AC grid consists of a single equivalent feeder (i.e. three-phase synchronous generator) with AC loads installed into five buses. The DC grid consists of the following feeders: wind farm, PV and BSS with connected HVDC transmission line and low-voltage DC loads. The tie between the AC and DC power networks is facilitated by a bidirectional VSC, which coordinates the interchange of power between AC and DC grids. The link between high-voltage DC node and low-voltage DC loads is enabled through an automatic adapter. The technical concept of an automatic adapter is introduced in this study. The BSS and PV system are needed in the DC network for counteracting the intermittent power generation from offshore wind farm.

The output of offshore wind farm consists of a DC collector, which is realised by means of the series connection of WECUs. Based on the conducted review in the introduction on the layout of WECUs, three topologies of WECUs are analysed. This includes a WECU integrated with the conventional three-phase full-bridge active rectifier, a WECU integrated with the single-controlled switch active rectifier and a WECU integrated with the interleaved single-switch boost converter. Details of operation and control principle of the proposed topology are discussed further.

8.2 Proposed Distributed Power System Description

Figure 8.1 shows the overall structure of the proposed distributed power network, which includes an AC power network with five buses and seven lines, an offshore wind farm with output DC power collector, BSS and a PV system including power electronic converters. The offshore wind farm consists of k number of WECUs connected in series. The series-connected WECUs enable building up a voltage V_{DC} across the output of wind farm or DC collector, as given by Eq. (8.1), where V_{dc} is the voltage across each WECU output terminal.

$$V_{DC} = \sum_{k=1}^k V_{dc(k)} \tag{8.1}$$

The series connection of WECUs is the simplest and most cost-effective topology of wind farms with output DC power collection system [40]. However, if a single WECU through the series-connected branch fails to operate, that can affect the entire wind farm or other fault-free units. A solution to bypass the faulty unit without affecting the other fault-free units is briefly presented in this study. In [24], the use of an auxiliary path was adopted as a means to bypass the defective branch.

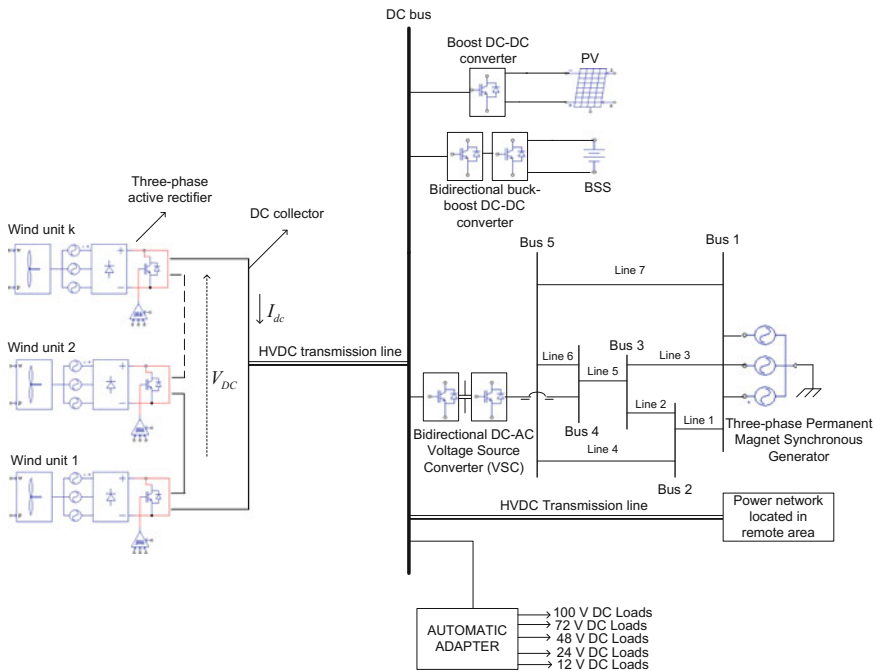


Fig. 8.1 Proposed distributed power system with separated AC and DC power networks

Each WECU on wind farm includes a wind turbine with mechanical parts (i.e. wind turbine blades, shaft and gearbox), a generator such as a doubly-fed induction generator (DFIG), permanent magnet synchronous generator (PMSG) or squirrel cage induction generator (SCIG) and a three-phase active rectifier.

The AC power network includes an equivalent three-phase synchronous machine, which feeds power to AC loads installed in five Buses. On the other side, the DC power network is composed of a DC collector at the output of wind farm, an HVDC transmission line and a high-voltage DC-bus feeding power to both DC loads and a remote area. Mainly, the DC appliances in telecommunication, automobile industries and households work on the voltage levels of 100, 72, 48, 24 and 12 V. Therefore, an automatic adapter is used to enable connection between the low-voltage loads and HVDC bus. The interchange of power between the AC and DC power networks is coordinated by means of a bidirectional DC/AC VSC. The control and operating principle of the VSC is analysed in this chapter. Under the normal operation, the offshore wind farm, PV and BSS feed power to DC loads and remote area, and if there is a surplus of energy, then it sent to AC power network. In the case of energy deficit on the DC network side, the AC power network through DC/AC VSC will compensate the gap, but when there is an excess of power at both the side and batteries are fully charged, then the wind farm will reduce its power through wind turbine blade control strategy.

The main requirement for integrating a DC grid with AC power network is to maintain the DC-bus voltage within a limited variation band, i.e. 0.95–1.05 p.u. [41]. An abnormal variation of V_{DC} , given by Eq. (8.1), can disrupt the normal operation or even cause the whole DC grid to collapse. The use of BSS [42, 43] and PV systems can offer greater flexibility in enabling effective protection and control of the overall DC grid. These handle the power fluctuations and provide necessary DC-bus voltage regulation. The BSS can consist of a series or series–parallel interconnection of chemical batteries or any supercapacitors [44].

8.3 AC Power Network

For AC power network, generally the generators are widely distributed in the network and it is always necessary to include their effects in the analysis. However, in this study, a simplified network is considered, which includes a three-phase synchronous generator capable of feeding power to AC loads installed in five buses, as shown in Fig. 8.1. In the context of load-flow problem, generally the real power (P) and reactive power (Q) requirements for each bus are specified. From Fig. 8.1, Bus 4 is a controlled point of the AC power network capable of balancing the required quantity of active and reactive powers. The amount of reactive power injected through Bus 4 depends on the angle of the synchronous generator excitation for any particular level of real power output. Indeed, the real power and voltage magnitude at Bus 4 are predefined to fixed values, while the reactive power

and voltage angle are free to vary. The reactive power at Bus 4 cannot in practice exceed certain limits, which lie between maximum and minimum values.

8.3.1 Active and Reactive Power Control Methods at Bus 4 of Fig. 8.1

Under the normal operation, one can assume that the three-phase synchronous generator supplies an infinite bus at which the voltage is fixed as shown in Fig. 8.2, where I_a is the generator stator current, $V_t < 0^\circ$ is the voltage of the infinite buses or reference voltage, X_d is the generator synchronous reactance, V_g is the generator voltage excitation and δ is the generator excitation angle or power angle.

The total apparent power delivered to the infinite buses is derived in Eq. (8.2) as

$$S = V_t I_a^* = |V_t| \left[\frac{|V_g| \sin \delta + j(|V_g| \cos \delta - |V_t|)}{X_d} \right] \quad (8.2)$$

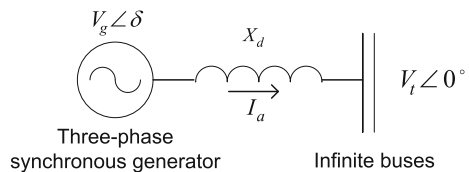
The active and reactive powers are deduced from Eq. (8.2) as in Eqs. (8.3) and (8.4), respectively [45],

$$P = \frac{|V_t| |V_g| \sin \delta}{X_d} \quad (8.3)$$

$$Q = \frac{|V_t| (|V_g| \cos \delta - |V_t|)}{X_d} \quad (8.4)$$

From Eq. (8.3), the maximum power that the synchronous generator can supply to the infinite buses occurs at $\delta = 90^\circ$. If this theoretical limit is exceeded, then the power output to the generator will fall below the mechanical power input and the machine will speed up and fall out of step with the network to which it is connected. In order to preserve the stability of the AC power network when δ limit is exceeded, reactive power is injected through Bus 4 from the DC power network, which balances the power deficit and thus regulates $|V_t|$ and δ . In practice, the value of Q at the controlled point (i.e. Bus 4) cannot exceed some specified limit and this requires adjusting the voltage magnitude $|V_t|$ through Bus 4 of Fig. 8.1.

Fig. 8.2 Steady-state representation of a three-phase synchronous generator supplying power to infinite buses



To understand the operation of the bidirectional AC/DC VSC shown in Fig. 8.1, which connects the DC power network to the controlled point of the AC power network, and its ability to regulate the voltage magnitude or Q at Bus 4, as well as the power angle δ , refer to Fig. 8.3. The AC-side voltage signal inputs to the three-phase VSC are given in Eqs. (8.5)–(8.7) [46], where $\theta(t)$ is a variable frequency function defined as in Eq. (8.8); $V_a(t)$, $V_b(t)$ and $V_c(t)$ are the three-phase voltage signal output of Bus 4 or the input voltage signals to the VSC; $|\hat{V}_t| = |\hat{V}_4|$ is the peak amplitude of the voltage at the controlled point or Bus 4; θ_o is the initial voltage phase angle; and δ is the power angle. It should be noted that the power angle is the difference between the synchronous generator excitation angle and the voltage angle of the controlled point. The dual-active bridge converter of Fig. 8.3 enables to step up/step down the voltage in the AC/DC junction and also to facilitate the bidirectional power flow.

$$V_a(t) = |\hat{V}_t| \cos[\theta(t)] \tag{8.5}$$

$$V_b(t) = |\hat{V}_t| \cos[\theta(t) - 120^\circ] \tag{8.6}$$

$$V_c(t) = |\hat{V}_t| \cos[\theta(t) - 240^\circ] \tag{8.7}$$

$$\theta(t) = \theta_o + \int_0^t \delta(\tau) dt \tag{8.8}$$

Equations (8.5)–(8.7) can be described using the space vector form as in Eq. (8.9).

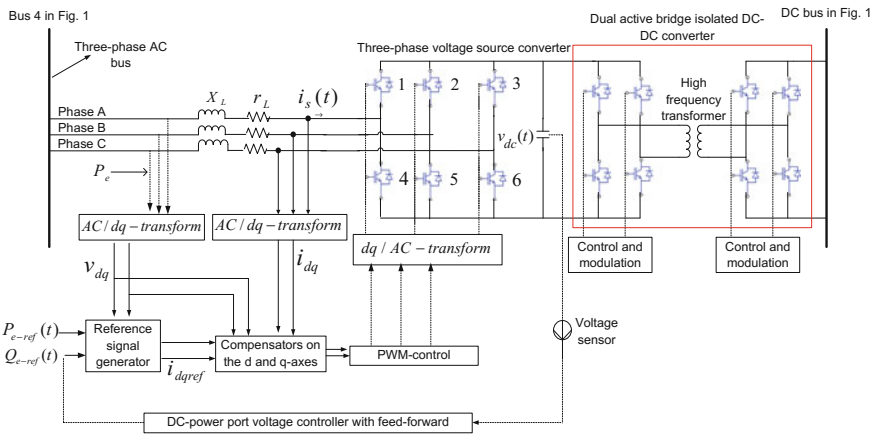


Fig. 8.3 Bidirectional AC–DC voltage source converter connecting the DC grid to the controlled point of the AC power network or bus 4

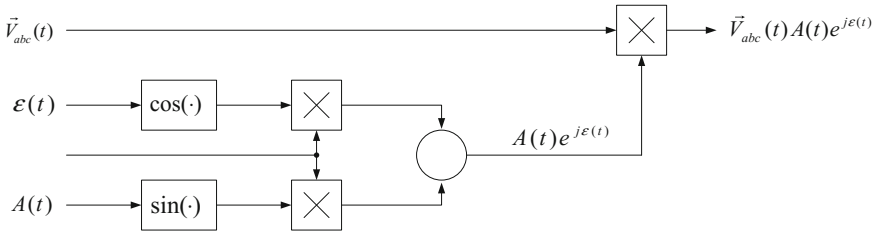


Fig. 8.4 Control block diagram illustrating the phase shift and amplitude-scale techniques provided by the VSC

$$\vec{V}_{abc}(t) = |\hat{V}_t(t)|e^{j\theta(t)} \tag{8.9}$$

Based on Eqs. (8.3) and (8.4), a small variation in $\delta(t)$ and $|V_t|$ will result, respectively, in a high fluctuation of P and Q ; therefore, the VSC of Fig. 8.3 will control δ and $|V_t|$ to operate around the steady-state point. Consider, for example, that a small variation of amplitude $|\epsilon|$ occurs in $\delta(t)$, and thus, $\theta(t)$ in Eq. (8.9) changes as to become $\theta_s(t) = \theta(t) + |\epsilon|$. For $\delta(t)$ in Eq. (8.8) to remain operating around the steady-state point, a small phase shift of same amplitude (with opposite sign) as $|\epsilon|$ needs to be added to $\theta(t)$, such that the actual power angle in Eq. (8.8) becomes $\delta_{shift} = \delta + |\epsilon|$.

On the other hand, when a variation occurs in $|V_t|$, in order to preserve the system stability, the vector $\vec{V}_{abc}(t)$ in Eq. (8.9) will be scaled or adjusted by an amplitude $A(t)$. The control technique that describes the phase shift and amplitude-scale method is presented by means of Fig. 8.4 [46]. The voltage signal output of the VSC when $\vec{V}_{abc}(t)$ in Eq. (8.9) is subjected to variations is obtained as in Eq. (8.10). The control system is incorporated in Fig. 8.3 using the direct (d) and quadrature (q) frame representation.

$$\vec{V}_{abc(s)}(t) = \vec{V}_{abc}(t) \times A(t) \times e^{j\epsilon(t)} \tag{8.10}$$

8.3.2 AC Power Network Solution Using Load-Flow Analysis Method

To illustrate the control technique achieved at Bus 4 of Fig. 8.1, consider an AC power network composed of five buses, seven lines and a single generator, as shown in Fig. 8.1; Bus 1 is the slack bus, for which the voltage is selected as 1.0 p.u.; Buses 2, 3 and 5 are load buses, for which both active and reactive powers are predefined; and Bus 4 is the controlled point of the AC network, for which the reactive power limits are specified. The loading conditions are shown in

Table 8.1 Bus loading conditions for the AC power network of Fig. 8.1 with centralised control point at bus 4 [41]

Bus	P (MW)	Q (MVar)	V_4	Q_{\max} (MVar)	Q_{\min} (MVar)
Bus 1 (slack)	–	–	–	–	–
Bus 2 (P, Q)	40	20	–	–	–
Bus 3 (P, Q)	25	15	–	–	–
Bus 4 (P, V)	30	–	1.0	20	–15
Bus 5 (P, Q)	50	20	–	–	–

Table 8.2 AC power network line parameters [41]

From bus	To bus	R (p.u.)	X (p.u.)	B (p.u.)
1	2	0.05	0.11	0.02
1	3	0.05	0.11	0.02
1	5	0.03	0.08	0.02
2	3	0.04	0.09	0.02
2	5	0.04	0.09	0.02
3	4	0.06	0.13	0.03
4	5	0.04	0.09	0.02

Tables 8.1 and 8.2 gives the interconnecting line series impedance and shunt admittance data [41]. The system base quantities are apparent power $S_{\text{base}} = 100 \text{ MVA}$ and $V_{\text{base}} = 132 \text{ kV}$.

The AC power network of Fig. 8.1 can be solved using the Newton–Raphson method, which solution is based on Eqs. (8.11) and (8.12)

$$P_m = |V_m| \sum_{n=1}^l |Y_{mn}| |V_n| \cos(\delta_m - \delta_n - \phi_{mn}) \quad (8.11)$$

$$Q_m = |V_m| \sum_{n=1}^l |Y_{mn}| |V_n| \sin(\delta_m - \delta_n - \phi_{mn}) \quad (8.12)$$

where V_m is the voltage magnitude at Bus m , V_n is the voltage magnitude at Bus n , Y_{mn} is the line admittance between Buses m and n , δ_m is the voltage phase angle at Bus m , δ_n is the voltage phase angle at Bus n , and ϕ_{mn} is the line admittance phase angle.

The voltage of the controlled point is nominally 1.0 p.u., and the load-flow solution of the AC power network of Fig. 8.1 produces at Bus 4: $Q_4 = 0.0226360 \text{ p.u.}$ and $V_4 = 1.004616 + j0.01021 \text{ p.u.}$ The value of Q_4 lies within the specified range for reactive power of $+0.2$ to -0.15 p.u. However, the value of $|V_4| = 1.0047$ must be scaled by the VSC to meet the voltage magnitude specification of 1.0 p.u. at Bus 4. This is generally achieved in load-flow analysis using a simple scaling approach based on Eqs. (8.13) and (8.14) [41]

Table 8.3 Bus voltages of AC power network in Fig. 8.1 with centralised control point at bus 4

Bus 2 voltage	Bus 3 voltage	Bus 4		Bus 5 voltage
		Q	V_4	
0.974707	0.981296	0.193505	0.999916	0.980726
$-j0.026648$	$-j0.021173$		$-j0.012996$	$-j0.025049$

$$\Re[V_4]_{\text{reg}} = \Re[V_4]_{\text{actual}} \times \frac{|V_4|_{\text{spec}}}{|V_4|_{\text{actual}}} \quad (8.13)$$

$$\Im[V_4]_{\text{reg}} = \Im[V_4]_{\text{actual}} \times \frac{|V_4|_{\text{spec}}}{|V_4|_{\text{actual}}} \quad (8.14)$$

where \Re_e and \Im_m represent, respectively, the real and imaginary parts of V_4 , $[V_4]_{\text{reg}}$ is the adjusted or regulated value of V_4 , $[V_4]_{\text{actual}}$ is the actual measured value of V_4 , and $[V_4]_{\text{spec}}$ is the specified value of V_4 . In the load-flow iteration process, if $Q_4 > Q_{\text{max(spec)}}$, then the VSC will regulate Q_4 to $Q_{\text{max(spec)}} = 0.2$ p.u. using the voltage amplitude-scale method; but if $Q_4 < Q_{\text{min(spec)}}$, then Q_4 will be adjusted to $Q_{\text{min(spec)}} = -0.15$ p.u. Table 8.3 presents the final result after a complete computation of the AC power network.

8.4 DC Power Network Analysis

Referring to Fig. 8.1, the DC power network is composed of a DC power collector at the output of offshore wind farm, an HVDC transmission line and a DC-bus feeding power to low-voltage DC loads and a remote area. It should be noted that the main requirement for integrating a DC grid into the AC power network is to maintain the DC voltage to oscillate within acceptable band. Use of state-of-the-art programmable solid-state protective devices, BSS and PV system including power electronic converters can offer greater flexibility in enabling effective protection and control of the DC power network. Based on Fig. 8.1, the AC power network connects to DC grid through a power electronic converter, which controls the voltage in the AC/DC junction. The WECUs on the offshore wind farm interface with the DC grid through active rectifiers, which regulate the voltage/current signal output of generators (i.e. PMSG). The PV system and BSS are also interconnected with DC grid via the power electronic converters, which control the voltage at DC bus.

8.4.1 Protective Device

The key design criteria for any protective device include reliability, i.e. predictability of the protective device response to faults, speed, i.e. fast clearance of faults and rapid restoration of the normal condition, economics, i.e. low cost and simplicity and less complexity [47, 48]. Based on the state-of-the-art technology of protective devices, fuses are not a good option for DC grid protection because of the reliability and speed problems [47]. The use of DC circuit breakers as protective devices may be economical for DC grids with DC link voltage less than 600 V [49], but this device generally costs more. The response of the DC circuit breaker to faults is also limited which may affect the DC grid's performance to some extent. The solid-state switches or active current-limiting switches have the advantage of being able to stop current within a microsecond [47]; however, the size, weight and cost are significant. More details on DC circuit breakers for high-power DC applications can be found in [50, 51].

8.4.2 BSS and PV System

The BSS and PV power sources handle the power fluctuations from offshore wind farm and provide necessary DC grid voltage regulation, by sustaining the power exchange between AC and DC power networks. If $P_{dc(w)} = \sum_{k=1}^k P_{u(k)}$ is the total active power generated by the offshore wind farm, with P_u being the total active power output of each WECU, and also, if $P_{dc(g)}$ is the total active power interchanged with the AC network, consumed by the DC loads and sent to a remote area, then the output voltage of offshore wind farm, i.e. V_{DC} given in Eq. (8.1), will tend to increase or decrease when $P_{dc(w)}$ or $P_{dc(g)}$ fluctuates. The voltage V_{DC} is related to the DC-bus voltage by Eq. (8.15), where R_{dc} is the HVDC transmission line resistance, I_{dc} is the HVDC transmission line current and $V_{dc(R)}$ is the DC-bus voltage.

$$P_{dc(w)} = V_{DC} I_{dc} = V_{dc(R)} I_{dc} + R_{dc} I_{dc}^2 = P_{dc(g)} + R_{dc} I_{dc}^2 \quad (8.15)$$

For maintaining the stability of the DC grid, one must ensure at all times that $P_{dc(w)} \cong P_{dc(g)}$ (neglecting the transmission power loss). Under the normal operation (i.e. when $P_{dc(w)} \cong P_{dc(g)}$), the BSS and PV can simply remain in standby mode. However, during abnormal conditions, the ESS operates in charging or discharging mode to provide the necessary DC grid voltage regulation. For example, under conditions of low wind (i.e. small $P_{dc(w)}$) and high demands (i.e. large $P_{dc(g)}$), the BSS and PV must switch from standby mode to powering mode to provide the necessary power balancing. On the other hand, during conditions of

high wind (i.e. large $P_{dc(w)}$) and light loads (i.e. small $P_{dc(g)}$), the BSS must switch from standby mode to charging mode.

On the other hand, when $P_{dc(w)}$ is very large and $P_{dc(g)}$ is very low, the BSS will accommodate the surplus of $P_{dc(w)}$. However, this could also exceed the power (or energy charges) rating required by the BSS. This condition can be solved by reducing P_u or $P_{dc(w)}$, through wind turbine pitch angle control technique. The wind turbine blade control (or pitch angle control) is coordinated by the active rectifiers installed in the WECUs.

8.5 DC Collection Grid: Power Control Techniques

8.5.1 BSS Output Power Control Using Buck–Boost DC–DC Converter

As depicted in Fig. 8.1, the bidirectional buck–boost DC–DC converter enables bidirectional power flow interchanges between BSS and DC grid. A typical circuit diagram of a bidirectional buck–boost DC–DC converter for high-power application is shown in Fig. 8.5a [44, 52]. It consists of the dual-active bridge DC–DC converter (i.e. two active full-bridge converters), which are interfaced through a

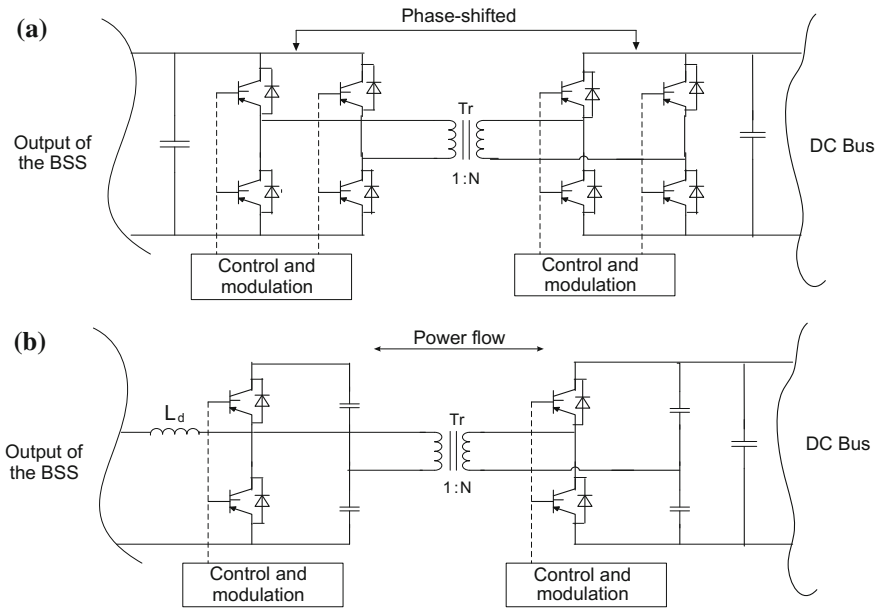


Fig. 8.5 Bidirectional buck–boost DC–DC converter. **a** Dual-active full-bridge converter. **b** Dual-active half-bridge converter

high-frequency transformer and are phase-shifted from each other to regulate the amount of power that flows from the BSS to the DC grid. Figure 8.5b shows a simplified circuit diagram of the dual-active bridge DC–DC converter [53], which includes a dual half-bridge converter instead of the dual full-bridge converter configuration. The number of controlled switches is reduced, thus simplifying the control circuits of the DC–DC converter. The dual-active bridge DC–DC converter works in voltage-scale mode to power the high-voltage side (or DC grid side); otherwise, it works in buck mode to recharge the BSS.

8.5.2 PV Output Power Control Using Boost DC–DC Converter

Based on Fig. 8.1, the PV system is connected to the DC bus through a boost DC–DC converter capable of tracking maximum power point. The output power induced in the PV panel depends on the temperature of the solar cells and solar radiation. The efficiency of the PV system is maximised by tracking the maximum power point of the solar radiation (i.e. input source). The equivalent circuit of a PV array is shown in Fig. 8.6 [54], with I_{sc} is the input source (i.e. the light-generated current which depends on the solar radiation), V and I are, respectively, the voltage and current outputs of the PV array, and R_s and R_{sh} are, respectively, the series and shunt equivalent resistances of the cells.

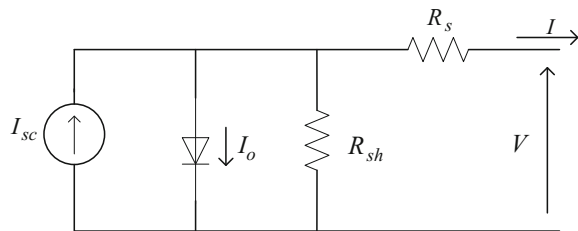
The output current to the PV array can be defined by means of a nonlinear function, as shown in Eq. (8.16) [54]

$$I = I_{sc} - I_o \left\{ \exp \left[\frac{q(V + R_s I)}{nkT} \right] - 1 \right\} - \frac{V + R_s I}{R_{sh}} \quad (8.16)$$

where q is the electronic charge, k is the Boltzman constant, T is the temperature in Kelvin, I_o is the reverse saturation current, and n is a dimensionless factor. Equation (8.16) clearly shows that the output power of a PV panel, i.e. $P_{pv} = VI$, depends on the solar radiation (I_{sc}) and temperature.

Consequently, to enable the maximum power point tracking (MPPT), a boost DC–DC converter is inserted to the output of the PV panel, as shown in Fig. 8.7.

Fig. 8.6 Equivalent circuit diagram of a PV array [54]



The active switch (e.g. IGBT or MOSFET) coordinated by a control and modulation circuit (or a pulse width modulation scheme) is responsible for modulating the power transfer from the input source to the DC grid through the variation of the duty cycle. In fact, the MPPT is the automatic regulation of the load current, $I_{Load}(t)$, to achieve a maximum possible power output. This regulation process is achieved based on Eq. (8.17), where $d(t) = t_{on}/T_s$ is the duty ratio, t_{on} represents the turn-on interval time for the switch, T_s is the switching period, and V_{do} is the voltage output of the boost DC–DC converter.

$$\frac{V_{do}}{V} = \frac{I}{I_{Load}} = \frac{1}{1 - d(t)} \tag{8.17}$$

8.5.3 Offshore Wind Farm Output Power Control Using Active Rectifiers

The offshore wind farm is realised by means of a series connection of WECUs as shown in Fig. 8.1. Each WECU consists of a wind turbine, a PMSG and a three-phase active rectifier. For maximising the efficiency of the wind farm, each WECU on wind farm has to operate under the MPPT. The active rectifier installed in each WECU enables the MPPT through the wind turbine blade control strategy.

A. Wind turbine blade control technique

The total input power to the wind turbine can be described by means of Eq. (8.18) [55, 56]

$$P_t = 0.5\rho AV_w^3 C_p(\lambda, \beta) \tag{8.18}$$

where ρ is the air density (kg/m^3), $A = \pi r^2$ is the blade impact area (m^2), r is the blade radius (m), V_w is the wind speed (m/s), $C_p(\lambda, \beta)$ is the power coefficient or

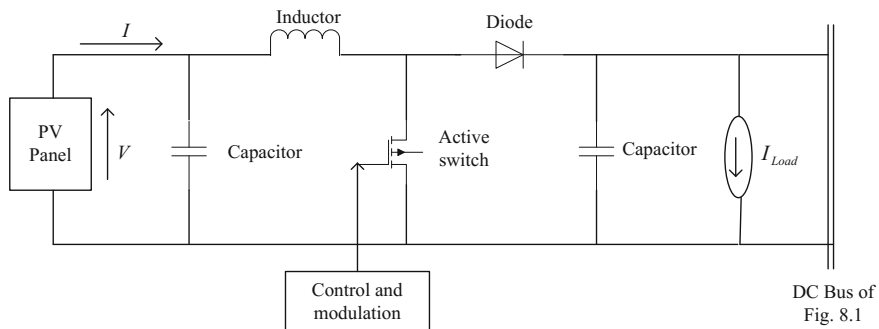


Fig. 8.7 PV panel integrated with a boost DC–DC converter capable of MPPT

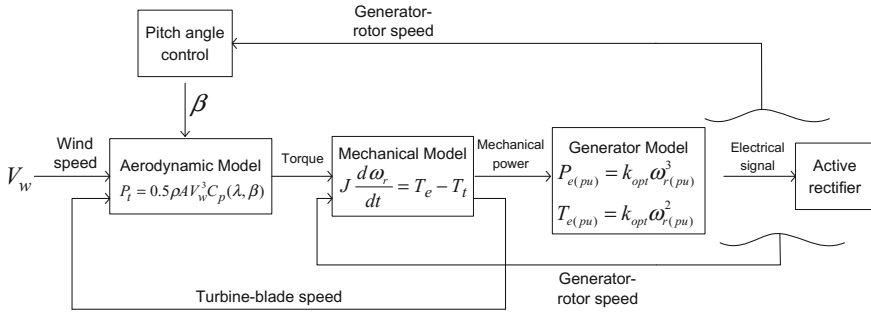


Fig. 8.8 Diagram describing the wind turbine blade control mechanism provided by the active rectifier installed in WECU

performance coefficient, λ is the tip-speed ratio given in Eq. (8.19) with ω_t being the blade angular velocity, and β is the blade pitch angle.

$$\lambda = \frac{r\omega_t}{V_w} \tag{8.19}$$

The term $\rho A V_w^3$ in Eq. (8.18) cannot be controlled; it changes unexpectedly, and only the term $C_p(\lambda, \beta)$ can be controlled through the regulation of λ and β . The adjustment of λ is done via the control of ω_t in Eq. (8.19). The performance coefficient is approximated by a nonlinear function given in Eq. (8.20) [56]:

$$C_p(\lambda, \beta) = \frac{1}{2} \left(\frac{1}{\lambda} - 0.022\beta^2 - 5.6 \right) \exp^{-\frac{0.17}{\lambda}} \tag{8.20}$$

Based on Eq. (8.18), to track the maximum wind power, $C_p(\lambda, \beta)$ must be regulated at its maximum value, and such that, if $C_p(\lambda, \beta)$ is the maximum, P_t is also the maximum. Therefore, the optimal value of λ (i.e. λ_{opt}) has to correspond at every operating instant with the maximum value of $C_p(\lambda, \beta)$ (i.e. C_{p-max}) in Eq. (8.20) by controlling ω_t in Eq. (8.19) to operate around the optimal point (i.e. ω_{t-opt}). This process can be explicitly described by means of Eq. (8.21) and Fig. 8.8. Equation (8.21) is obtained by substituting Eq. (8.19) into (8.18).

$$P_{t-max} = \left(\frac{0.5 \rho A r^3 C_{p-max}}{\lambda_{opt}^3} \right) \times \omega_{t-opt}^3 \tag{8.21}$$

The various component models in Fig. 8.8 are derived as follows: the optimal wind turbine torque is given in Eq. (8.22). The wind turbine blade speed is expressed in terms of the generator-rotor angular speed as $\omega_r = N\omega_t$, with N is the gearbox ratio. The generator electrical torque T_e is also related to ω_r based on Eq. (8.23) [46], where J is the moment of inertia. Equations (8.21) and (8.22) are

given in per unit as in Eqs. (8.24) and (8.25), respectively, where k_{opt} is derived in Eq. (8.26), P_{eb} is the active power output of the generator base value, and ω_{tb} is the generator-rotor angular speed base value; T_{eb} is the electrical torque base value given in $T_{\text{eb}} = P_{\text{eb}}/\omega_{\text{tb}}$; and $\omega_{\text{tb}} = \omega_{\text{rb}}/N$ is the turbine angular speed base value.

$$T_{\text{t-opt}} = \frac{P_{\text{t-max}}}{\omega_{\text{t-opt}}} = \left(\frac{0.5\rho A r^3 C_{\text{p-max}}}{\lambda_{\text{opt}}^3} \right) \times \omega_{\text{t-opt}}^2 \quad (8.22)$$

$$J \frac{d\omega_r}{dt} = T_e - T_t \quad (8.23)$$

$$P_{\text{t-max}}(\text{pu}) = k_{\text{opt}} \times \omega_{\text{t-opt}}^3(\text{pu}) \quad (8.24)$$

$$T_{\text{t-opt}}(\text{pu}) = k_{\text{opt}} \times \omega_{\text{t-opt}}^3(\text{pu}) \quad (8.25)$$

$$k_{\text{opt}} = \frac{0.5\rho A r^3 \omega_{\text{tb}}^3 C_{\text{p-max}}}{N^3 P_{\text{eb}} \lambda_{\text{opt}}^3} \quad (8.26)$$

B. Control mechanism provided by active rectifiers

A sample structure of a PMSG-based WECU integrated with a three-phase active rectifier is shown in Fig. 8.9. The active rectifier is the key component that facilitates the entire control process; the voltage, current and frequency signal outputs of the PMSG are actively regulated by varying the converter switch duty cycle. The frequency of a PMSG, i.e. ω_e , can be expressed in terms of the wind turbine blade angular speed or generator-rotor angular speed as $\omega_e = 0.5pN\omega_t = 0.5p\omega_r$ [23], where p being the total number of poles. The voltage induced in the PMSG is also proportional to the rotational speed, given in $V_{\text{s rms}} = k_{\text{PM}}\omega_r$, with k_{PM} is the stator field constant. Thus, the control of ω_e or $V_{\text{s rms}}$ by the three-phase active

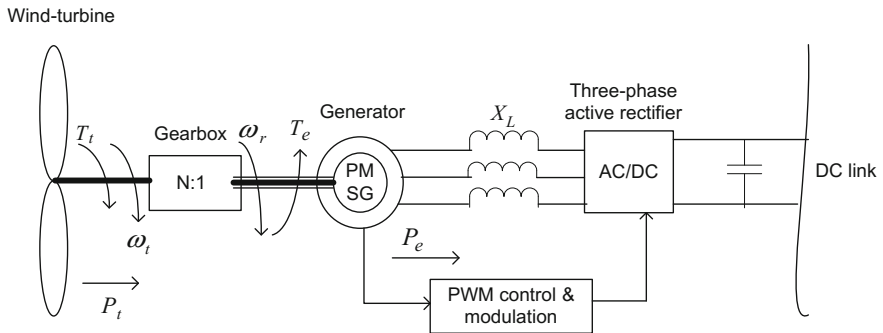


Fig. 8.9 Structure of a PMSG-based WECU integrated with a three-phase active rectifier

rectifier results in the control of ω_t and ω_r . Consequently, λ in Eq. (8.19) and $C_p(\lambda, \beta)$ in Eq. (8.20) are regulated as a result, and P_t in Eq. (8.18) is controlled at its maximum value.

The control of ω_e involves the regulation of active power or PF according to Eq. (8.27) [23, 57].

$$P_e = T_e \omega_e = 3V_{s(\text{rms})}I_{s1(\text{rms})}\text{PF} \quad (8.27)$$

where PF is the input total power factor expressed as in Eq. (8.28), $V_{s(\text{rms})} \approx I_{s1(\text{rms})}$ is the stator rms line-to-neutral voltage, $I_{s1(\text{rms})}$ is the fundamental rms line current, THD_I is the AC-side current total harmonic distortion, THD_V is the AC-side voltage total harmonic distortion, S_e is the total apparent power, $\text{DPF} = \cos \phi$ is the displacement power factor, and ϕ is the displacement angle or the phase difference between voltage and current signals.

$$\text{PF} = \frac{\text{DPF}}{\sqrt{1 + \text{THD}_I^2} \sqrt{1 + \text{THD}_V^2}} = \frac{P_e}{S_e} \quad (8.28)$$

To ensure the tracking of maximum wind energy by the active rectifier, the PF in Eq. (8.28) has to be maintained close or about unity, and thus, $\text{DPF} = \cos \phi \approx 1$, $\text{THD}_I \approx 0\%$, and $\text{THD}_V \approx 0\%$.

8.6 DC Power Collection Grid Analysis

The DC-bus voltage of Fig. 8.1 must satisfy the following criteria: $V_{\text{dc}(\text{R})} \geq 2 \times \hat{V}_4$ [46] when integrating with the AC power network to ensure proper control of active and reactive powers, where $\hat{V}_4 \approx \sqrt{2} \times V_{\text{base}(\text{L-N})}$ is the peak value of the line-to-neutral voltage at Bus 4 of Fig. 8.1, and $V_{\text{base}(\text{L-N})}$ is the line-to-neutral voltage base quantity of the AC network. The line-to-line voltage base quantity of the AC power network is given in Sect. 8.3.2 as $V_{\text{base}(\text{L-N})} = 132 \text{ kV}$; thus, the DC-bus voltage is deduced from $V_{\text{dc}(\text{R})} = 215 \text{ kV}$. The voltage output of the wind farm of Fig. 8.1 is expressed in terms of the DC-bus voltage $V_{\text{dc}(\text{R})}$ as in Eq. (8.29).

$$V_{\text{DC}} = \sum_{k=1}^k V_{\text{dc}(k)} = V_{\text{dc}(\text{R})} + R_{\text{dc}}I_{\text{dc}} \quad (8.29)$$

By assuming a lossless HVDC transmission line, $R_{\text{dc}} \approx 0 \Omega$ and thus $V_{\text{DC}} \approx V_{\text{dc}(\text{R})} = 215 \text{ kV}$. Consider that the offshore wind farm is realised by means of 80 series-connected WECUs, and then, the average voltage output of each WECU is about $V_{\text{dc}} = 2.7 \text{ kV}$ according to Eq. (8.1). If the offshore wind farm of Fig. 8.1 produces a total apparent power of $S_{\text{base}} = 30 \text{ MVA}$, then it is practical to

assume that each WECU generates an apparent power of about $S_u = 375$ kVA. The total real power that the offshore wind farm generates is obtained using Eq. (8.30).

$$P_{dc(W)} = \sum_k P_{u(k)} = V_{DC} I_u \tag{8.30}$$

where P_u is the real power output of each WECU and $I_u = I_{dc}$ is the current output of each WECU.

8.6.1 Effect of Input Power Factor on Maximum Active Power Tracking

A. PMSG-based WECU integrated with conventional active rectifier

Figure 8.10 shows an example of a PMSG-based WECU topology integrated with the conventional three-phase full-bridge active rectifier or VSC. The control scheme for VSC is usually implemented in the direct-quadrature (dq) reference frame. The reason is that if the controller is implemented in the AC reference frame, in order to track the sinusoidal AC commands, then the compensator transfer function must be of higher order and bandwidth. However, in the dq reference frame, a simple control scheme is needed. Also, the problem of tracking a sinusoidal command is transformed to an equivalent problem of tracking a DC command with about zero steady-state error. The time-varying inductances of the AC source are converted to DC command, thus enabling the use of simple and available linear compensators such as the proportional-integral (PI) or proportional-integral derivative (PID).

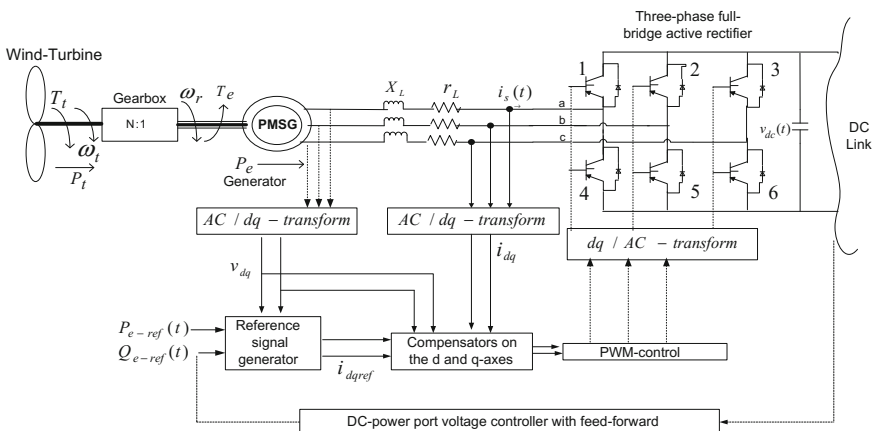


Fig. 8.10 PMSG-based WECU integrated with a conventional three-phase full-bridge active rectifier

The characteristics of voltage signal output and current signal output of PMSG or inputs to the VSC are shown in Fig. 8.11; the total apparent power is obtained from Fig. 8.11a, b and Eq. (8.31) as $S_e = 372 \text{ kVA}$, where $V_{dc(R)} = 1000 \text{ V}$ is the line-to-neutral voltage peak value measured from Fig. 3.11a, and $I_{s(\text{peak})} = 248 \text{ A}$ is the line current peak value measured from Fig. 3.11b.

$$S_e = 3V_{s(\text{rms})}I_{s(\text{rms})} = \frac{3}{2}V_{s(\text{peak})}I_{s(\text{peak})} \tag{8.31}$$

The total input power factor is obtained as $\text{PF} = P_e/S_e$ with $S_e = 372 \text{ kVA}$. If neglecting the converter power losses, one can assume that $P_e \approx P_u = V_{dc}I_{dc}$ with $V_{dc} = 2.7 \text{ kV}$. A resistive load $R_L = 20 \Omega$ is connected to the output side of Fig. 8.10, and thus, the average current output of the WECU is obtained as $I_{dc} = 135 \text{ A}$. Based on Eq. (8.28), the PF expression includes two terms, which are the distortion power factor and displacement power factor. The distortion power factor term is deduced from Eq. (8.28) as $\text{DF} = 1/\left(\sqrt{(1 + \text{THD}_I^2)(1 + \text{THD}_V^2)}\right)$

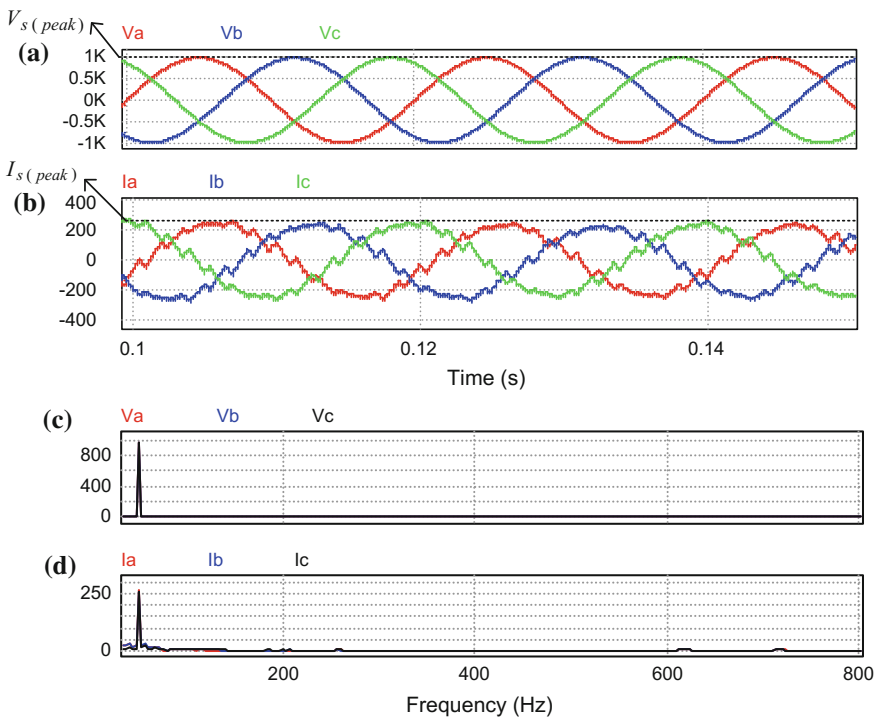


Fig. 8.11 **a** Characteristics of the voltage signal input to the VSC showing peak amplitude. **b** Characteristics of the current signal input to the VSC showing peak amplitude. **c** Voltage harmonic spectrum indicating the magnitude of voltage harmonic components. **d** Current harmonic spectrum indicating the magnitude of current harmonic components

with THD_V and THD_I are obtained from the voltage and current spectrums plotted in Fig. 8.11c, d. No high-frequency harmonic component exists in the voltage signal, and thus, $THD_V = 0$ in Fig. 8.10c. However, very small amplitudes of high-frequency harmonic components exist in the current signal, as a result of $THD_I \approx 5\%$ in Fig. 8.10d. Therefore, using Eq. (8.28), a distortion power factor of about zero is obtained, and thus, $PF \approx DPF = 96.5\%$. The total input power factor of 96.6% is a result of very low distortion power factor (about zero) and slightly high DPF. The system presents a good performance in terms of tracking the maximum active power points because of a good PF that is close to unity with voltage and current signal maintained almost in phase.

B. PMSG-based WECU integrated with single-controlled switch active rectifier

The topology of a WECU integrated with the three-phase single-controlled switch active rectifier is shown in Fig. 8.12a. This includes wind turbine blades, gearbox, PMSG and a cascade connection of a three-phase diode bridge rectifier and a single-switch DC–DC boost converter. Only a single-controlled switch, for example IGBT cells, is installed across the DC–DC converter. In practice, the IGBT cells are grouped in series or parallel and incorporated in a composite box named a valve which handles certain required voltage or current. Because of the switching stresses and power-handling capability issues of the single-phase DC–DC boost converter controlled switch, the interleaved single-switch boost DC–DC converter presented in Fig. 8.12b is an improved topology of the single-switch active rectifier. The layout of an interleaved single-switch boost converter is similar to paralleling two single-switch boost converters. However, the gating signals to the interleaved

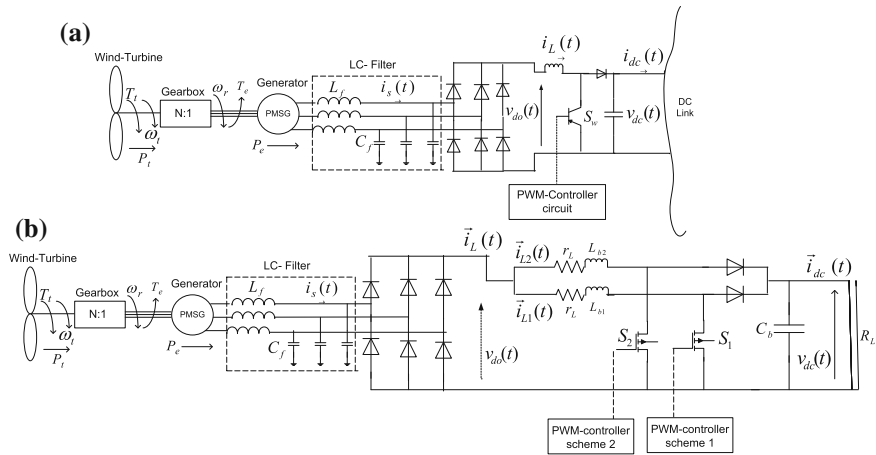


Fig. 8.12 PMSG-based WECUs topology. **a** Integrated with a single-controlled switch active rectifier. **b** Integrated with an interleaved single-switch boost converter

phases are generated in such a manner as to allow equal current sharing among the phases and also to ensure ripple cancellation.

Figure 8.13 plots the dynamic characteristics of the voltage and current signals at the AC power port side of the three-phase diode bridge rectifier for Fig. 8.12a, b

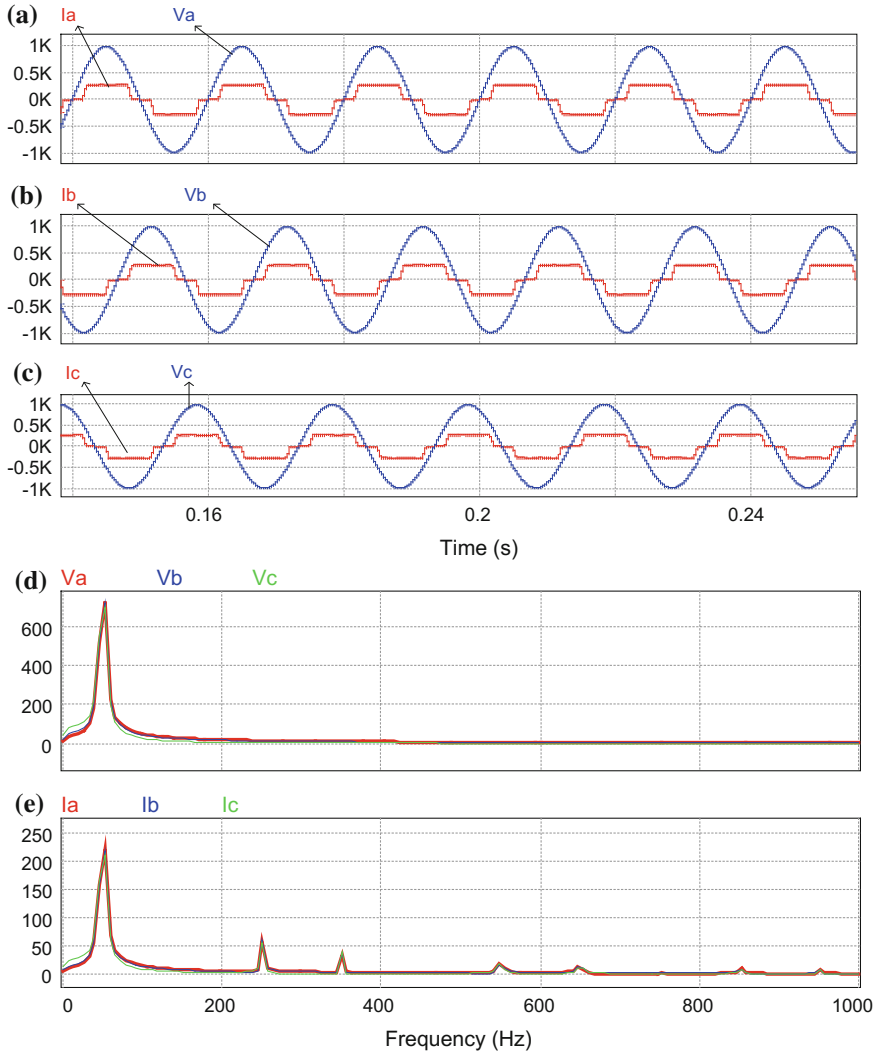


Fig. 8.13 **a** Phase A voltage/current signal input to the diode rectifier showing peak amplitudes. **b** Phase B voltage/current signal input to the diode rectifier showing peak amplitudes. **c** Phase C voltage/current signal input to the diode rectifier showing peak amplitudes. **d** Voltage harmonic spectrum indicating the magnitude of the voltage harmonic components. **e** Current harmonic spectrum indicating the magnitude of the current harmonic components

with no installed LC filter. The total apparent power is obtained as $S_e = 372$ kVA based on Eq. (8.31); the real power injected by the source is measured as about $P_e = 349$ kW; and the total input power factor is obtained as $PF = P_e/S_e = 93.8\%$. Based on Eq. (8.28), the distortion power factor term is $DF = 1/\left(\sqrt{(1 + THD_I^2)(1 + THD_V^2)}\right)$, with THD_V and THD_I are defined in Eqs. (8.32) and (8.33) [2].

$$THD_V = \frac{1}{V_{s1}} \sqrt{\sum_{h=2}^{\infty} V_h^2} \quad (8.32)$$

$$THD_I = \frac{1}{V_{s1}} \sqrt{\sum_{h=2}^{\infty} I_h^2} \quad (8.33)$$

The current and voltage harmonic components are measured from the signal spectrums plotted in Fig. 8.13d as $\sum_{h=2}^{\infty} V_h = 0$ and in Fig. 8.13e as $\sum_{h=2}^{\infty} I_h \neq 0$. Thus, $THD_V = 0$ and $THD_I \approx 27\%$. The current harmonic components are $I_5 = 49$ A at 250 Hz, $I_7 = 40$ A at 350 Hz, $I_{11} = 21$ A at 550 Hz, and $I_{13} = 17$ A at 650 Hz. Through the substitution of (8.32) and (8.33) into (8.28), one obtains a distortion power factor of about 96% and a displacement power factor of about 97.7%. Thus, the total input power factor is 93.8%, which is the result of 97.7% displacement power factor and 96% distortion power factor. The system presents a good performance in terms of tracking the maximum active power points.

However, the total current harmonic distortion has to be maintained as required by the standard; for example, IEEE standard 519 “IEEE Recommended Practices and Requirements for Harmonic Control in Electric Power Systems” [42] limits the voltage total harmonic distortion to 2.5% and total current harmonic distortion to $THD_I = 5\%$. Therefore, a T-type LC harmonic filter is installed at the input side of the three-phase diode bridge rectifier as depicted in Fig. 8.12. For example, with an LC filter consisting of $L_f = 10$ mH \times 3 and $C_f = 10$ μ F \times 3, the THD_I is improved to about 5% and $PF \approx DPF = 97.7\%$.

8.6.2 Equivalent Circuit Diagram of DC Power Collection Grid

The DC power collection grid of Fig. 8.1 is presented by means of the equivalent diagram shown in Fig. 8.14, where $V_{DC} = \sum_k V_{dc(k)} = 215$ kV is the voltage output of the offshore wind farm; $I_{dc} = 135$ A is the current output of the wind farm; $V_{dc/ac} \approx V_{dc(R)} = 215$ kV is the voltage at the DC/AC junction; $R_L + R_{HV}$ is the equivalent DC load resistance; R_{ac} is the equivalent AC-side load resistance; $R_b \approx 0$ is the DC-bus resistance; V_{pv} is the voltage output of the PV panel; V_{bss} is

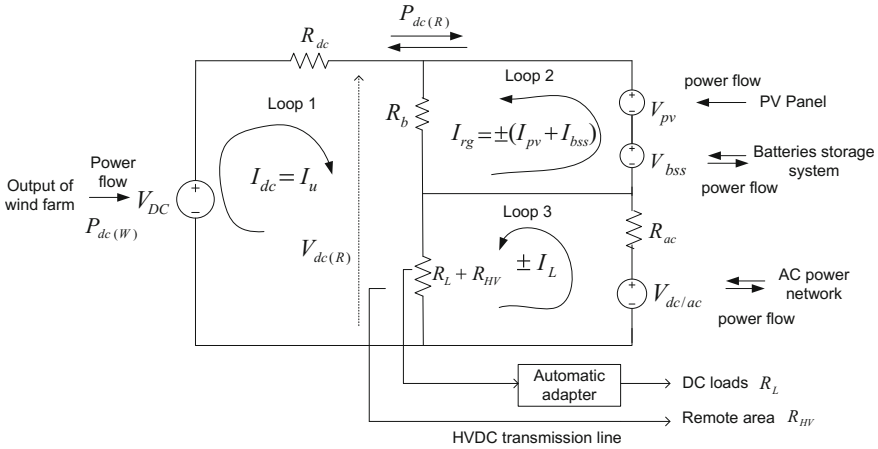


Fig. 8.14 Equivalent circuit diagram of the DC power collection system of Fig. 8.1

the voltage output of the BSS; I_L is the current that flows between AC and DC network; and $I_{rg} = I_{pv} + I_{bss}$ is the total current output of the PV panel and BSS (i.e. regulator current). If the demand is greater than the capacity of the wind farm, then power will be supplemented from Loop 2 (i.e. the regulator loop) by the BSS and PV system to limit the power fluctuations on the DC power network.

A. Power fluctuation control analysis

Based on the equivalent model shown in Fig. 8.14, which is derived from the DC power collection grid of Fig. 8.1, let $P_{dc(W)}$ be the total power produced by the offshore wind farm and $P_{dc(R)}$ be the total power received by the AC network and DC loads and sent to a remote area. The power flow becomes unbalanced when the equality (or equivalence) in Eq. (8.34) is not satisfied. The sending power $P_{dc(W)}$ is given in Eq. (8.30).

$$P_{dc(W)} \cong P_{dc(R)} \tag{8.34}$$

In the case where $P_{dc(W)}$ is much higher than $P_{dc(R)}$, the voltage V_{DC} across the DC collector will tend to increase. This condition can occur, for example, when there is a fault or load disconnection on the receiving end side (or load side). On the other hand, if $P_{dc(W)}$ is much lower than $P_{dc(R)}$, the voltage across the DC collector will tend to decrease. This condition occurs when the offshore wind farm supplies less power than what it is expected by the loads, as a result, for example, of a disconnection of a WECU on the wind farm or low wind speed.

There are existing methods that have already been proposed to deal with the issues of power flow imbalances, for example the use of chopper resistance in the power electronic converter circuit to sustain the grid when $P_{dc(W)} > P_{dc(R)}$ (e.g. low power demand and high wind energy). The chopper resistance circuit absorbs the

excess power and prevents the DC voltage from increasing [58]. However, the size of the chopper resistance circuit may not sustain a high level of power flow imbalance. The chopper resistance also dissipates the absorbed energy in the form of heat and contributes to power losses. The alternative solution consists of using the BSS and PV system [59–61], as presented in Figs. 8.1 and 8.14 Loop 2. The BSS stores excess energy and supplements deficits of energy to sustain the DC power collection grid during power fluctuations or power imbalances, while the PV system sustains the grid against the energy deficits. This approach is efficient, but may increase the overall cost of the distributed power system.

In the series-connected WECU topology shown in Fig. 8.1, a voltage $V_{DC} = k \times V_{dc}$ is built up across the DC collector, where k is the total number of WECUs in the series branch and V_{dc} is the voltage output of each WECU. If $|\hat{V}_{dc}|$ represents the excess or the deficit voltage magnitude when the power grid becomes imbalanced, the actual voltage across the DC collector becomes $V_{DC(a)} = (k \times V_{dc}) + |\hat{V}_{dc}|$. The voltage $|\hat{V}_{dc}|$ is distributed evenly as additional input to the k units in the series branch. The actual voltage across each unit in the series branch is then derived in Eq. (8.35) as

$$V_{dc(a)} = V_{dc} + \frac{|\hat{V}_{dc}|}{k} \quad (8.35)$$

where $V_{dc(a)}$ is the actual voltage across each unit in the series branch, and $|\hat{V}_{dc}|$ is the extra or deficit voltage magnitude across the DC collector due to power flow imbalances. $|\hat{V}_{dc}| > 0$ when $P_{dc(W)} > P_{dc(R)}$; and $|\hat{V}_{dc}| < 0$ when $P_{dc(W)} < P_{dc(R)}$.

The actual voltage output of the wind farm is expressed as in Eq. (8.36)

$$V_{DC(a)} = k \times V_{dc(a)} = k \left(V_{dc} + \frac{|\hat{V}_{dc}|}{k} \right) \quad (8.36)$$

The voltage noise amplitude $|\hat{V}_{dc}|$ in Eqs. (8.35) and (8.36) is supplemented or extracted by the BSS and PV system through the regulator Loop 2 in Fig. 8.14, which maintains $V_{dc(a)} \approx V_{dc}$ and $V_{DC(a)} \approx V_{DC}$.

B. Unit breakdown analysis

A fault condition can result in a complete disconnection of WECUs from the DC collector of Fig. 8.1. It should be noted that if the pitch control option is adopted for the wind turbine blade control, β in Eq. (8.20) is actively regulated to limit P_t in Eq. (8.18). Usually, β is set to 0° for maximum wind energy tracking, or to 90° for stopping wind power generation. If, for example, one unit in the series branch of Fig. 8.1 is being bypassed because of a fault ($\beta = 90^\circ$), the voltage across that unit at the branch becomes zero, and thus, the voltage across the faulted node can be viewed as $V_{dc} + |\hat{V}_f|$, where $|\hat{V}_f| < 0$ and $V_{dc} = |\hat{V}_f|$. The voltage $|\hat{V}_f|$ will evenly

share out across the fault-free units in the series branch. Thus, the actual voltage across each of the remaining fault-free units becomes $V_{dc} = [|\hat{V}_f|/(k-1)]$.

It is also possible for more than one unit to break down simultaneously in a series branch of Fig. 8.1. Consider two units, for example, failing at the same time; the voltage across each of the two faulty units is $V_{dc} + |\hat{V}_f|$. The voltage $2 \times |\hat{V}_f|$ is evenly spread across the $k-2$ fault-free units in the series branch. The actual voltage across each of the fault-free units in the series branch becomes $V_{dc} + [2 \times |\hat{V}_f|/k-2]$. To generalise, consider n units failing simultaneously in a series branch; the actual voltage across fault-free units in the series branch is expressed in Eq. (8.37) as

$$V_{dc(a)} = V_{dc} + \left(\frac{n \times |\hat{V}_f|}{k-n} \right) \quad (8.37)$$

where n is the total number of simultaneously failing units; $|\hat{V}_f| \approx V_{dc}$ is the voltage noise amplitude resulting from a breakdown of single unit in the series-connected branch.

The actual voltage output of the wind farm when n units break down or fail to operate is given in Eq. (8.38),

$$V_{DC(a)} = (k-n) \times V_{dc} = (k-n) \times \left[V_{dc} + \left(\frac{n \times |\hat{V}_f|}{k-n} \right) \right] \quad (8.38)$$

The voltage noise amplitude $|\hat{V}_f|$ in Eqs. (8.37) and (8.38) is supplemented by the BSS and PV system through the regulator Loop 2 in Fig. 8.14, which maintains $V_{DC(a)} \approx V_{DC}$.

8.6.3 Automatic Adapter Layout

As depicted in Fig. 8.1, the automatic adapter is responsible for monitoring the low and/or medium DC link voltages. It facilitates the power interchange between high-voltage DC link and low- or medium-voltage DC loads. The structure of an automatic adapter is shown in Fig. 8.15; the input voltage to the automatic adapter is about $V_{dc(R)} \approx 215$ kV, the input current is obtained as $I_{b2} = I_b - I_{b1}$ with I_{b1} is the current flowing on HVDC transmission line to a remote area, and I_b is the DC load current. The magnitude of I_{b2} can change depending on the magnitude of the DC loads at the output of the automatic adapter, but the DC-bus voltage magnitude is always maintained within acceptable oscillating band, i.e. 0.9–0.1 p.u., regardless of the variations in DC loads. The internal configuration of the automatic adapter consists of a bench of interconnected buck DC–DC converters, which enables

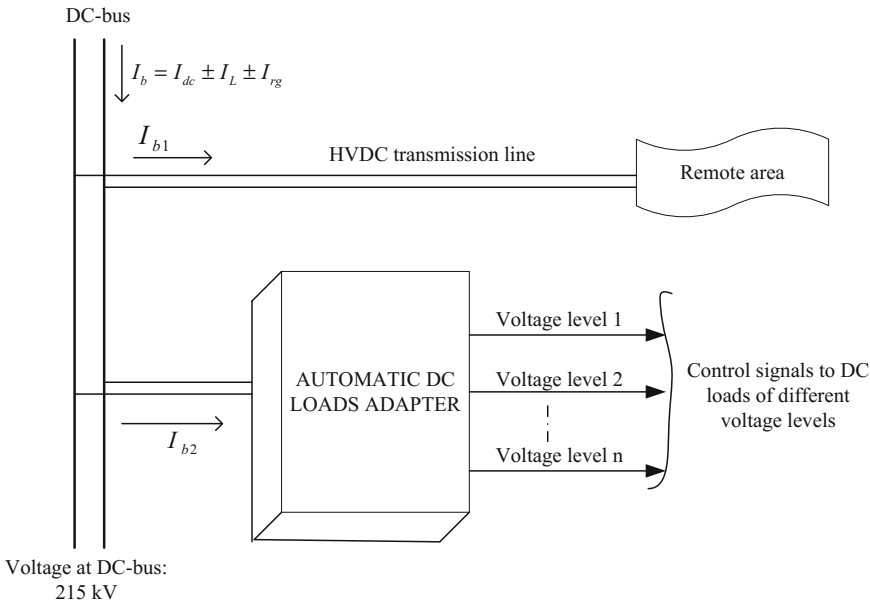


Fig. 8.15 External structure of an automatic adapter

stepping down the high input voltage $V_{dc(R)} \approx 215 \text{ kV}$ to low voltages, e.g. 120, 100 and 48 V for using in houses, automobiles industries, telecommunications, etc.

8.7 DC Collection Grid: Voltage and Current Dynamics

8.7.1 Voltage/Current Output Characteristics of WECU

Each WECU on the offshore wind farm of Fig. 8.1 is designed with the ability to achieve a total output power of 364 kW/372 kVA; the steady-state voltage and current output of each WECU are given as $V_{dc} = 2.7 \text{ kV}$ and $I_{dc} = I_u = 135 \text{ A}$. Figure 8.16a, b plots, respectively, the dynamic of voltage and current output of the WECU depicted in Fig. 8.10 (i.e. PMSG-based WECU integrated with the conventional three-phase full-bridge active rectifier), and Fig. 8.17a, b plots, respectively, the dynamic of voltage and current output of the WECU depicted in Fig. 8.12 (i.e. PMSG-based WECU integrated with the three-phase single-controlled switch active rectifier).

By comparison with Figs. 8.16 and 8.17, it can be noted that in addition to the low-current total harmonic distortion for the WECU topology depicted in Fig. 8.10, another advantage is the low percentage overshoot in the dynamic of voltage and current signals, as shown in Fig. 8.16a, b, and a very small % overshoot is observed

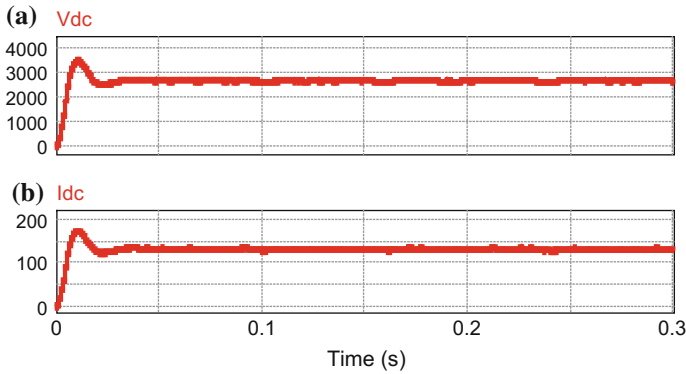


Fig. 8.16 **a** Dynamic of voltage output of WECU depicted in Fig. 8.10 showing an overshoot of about 28% and a steady-state voltage of about 2.7 kV. **b** Dynamic of current output of WECU depicted in Fig. 8.10 showing an overshoot of about 28% and a steady-state current of about 135 A

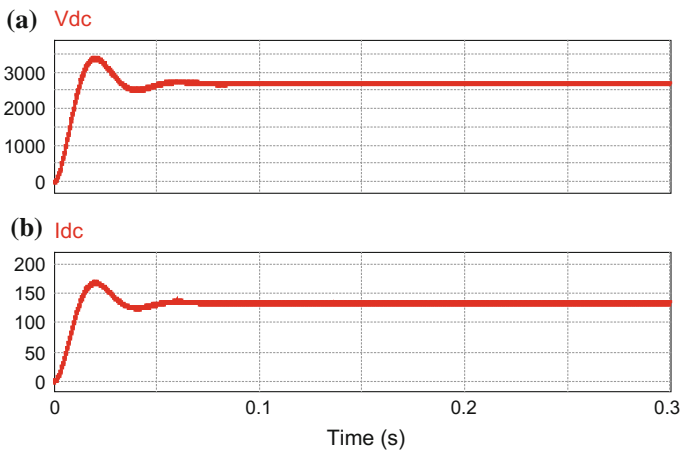


Fig. 8.17 **a** Dynamic of voltage output of WECU depicted in Fig. 8.12 showing an overshoot of about 26% and a steady-state voltage of about 2.7 kV. **b** Dynamic of current output of WECU depicted in Fig. 8.12 showing an overshoot of about 26% and a steady-state current of about 135 A

at $t = 0.04$ s, although the shape at the steady-state operating interval is slightly oscillating. For the WECU topology depicted in Fig. 8.12, in addition to the high-current total harmonic distortion (i.e. $\text{THD}_I = 27\%$ with no LC filter), another drawback is the high percentage overshoot, which is about 26% in Fig. 8.17a, b; however, the shape at the steady-state operating interval looks uniform and stable.

8.7.2 Voltage/Current Characteristics Across DC Collector

The dynamic of the voltage and current signal output of the offshore wind farm of Fig. 8.1 when 80 units are connected in series is shown in Fig. 8.18. The average voltage output of each unit is $V_{dc} = 2.7$ kV; thus, in steady state, a total average voltage of $V_{DC} = 215$ kV is obtained across the DC collector or output of wind farm according to Eq. (8.1), as shown in Fig. 8.18a. The steady-state average DC current at the output of the wind farm is also obtained as $I_{dc} = 135$ A, as shown in Fig. 8.18b.

A. Power flow imbalances analysis

Based on Fig. 8.1 with $k = 80$ (i.e. the total number of series-connected units), the power flow imbalances may occur, for example, when the offshore wind farm supplies less power than what it is expected by the demand due to a deficit of wind energy and/or an increase of loads. Under the steady-state condition, the offshore wind farm generates an output current (i.e. proportional to the output power) of about $I_{dc} \approx I_L = 135$ A; under this condition, the regulator Loop 2 of Fig. 8.14 can operate in standby mode. During the period of wind energy deficit and/or high demand, the current output of the wind farm decreases, from steady-state point to about $I_{dc(f)} = 37$ A at $t_f = 0.2$ s, as shown in Fig. 8.19a. Figure 8.19b shows the effect of current (or power) deficit on the dynamic of voltage output of the wind farm. A small % overshoot is noted at $t_f = 0.2$ s in Fig. 8.19b, and then, the voltage kept oscillating within about 10% band. It is observed that the voltage variation is

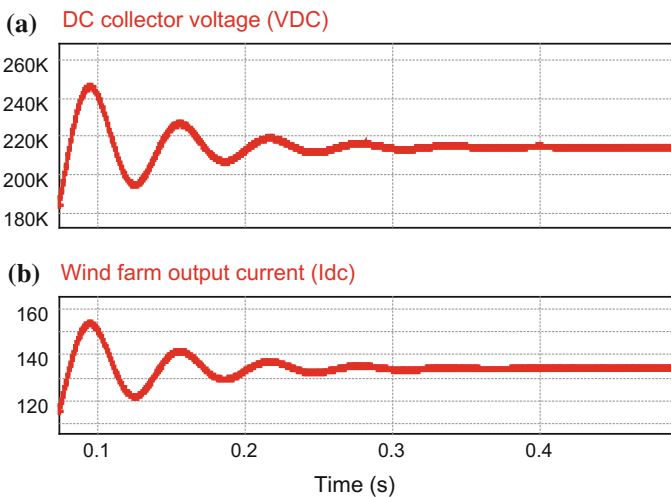


Fig. 8.18 **a** Characteristic of voltage output of the wind farm of Fig. 8.1 with 80 series-connected WECUs showing the total average steady-state voltage of $V_{DC} = 215$ kV obtained from Eq. (8.1). **b** Characteristic of current output of the wind farm of Fig. 8.1 with 80 series-connected WECUs showing the average steady-state voltage of $I_{dc} = 135$ A

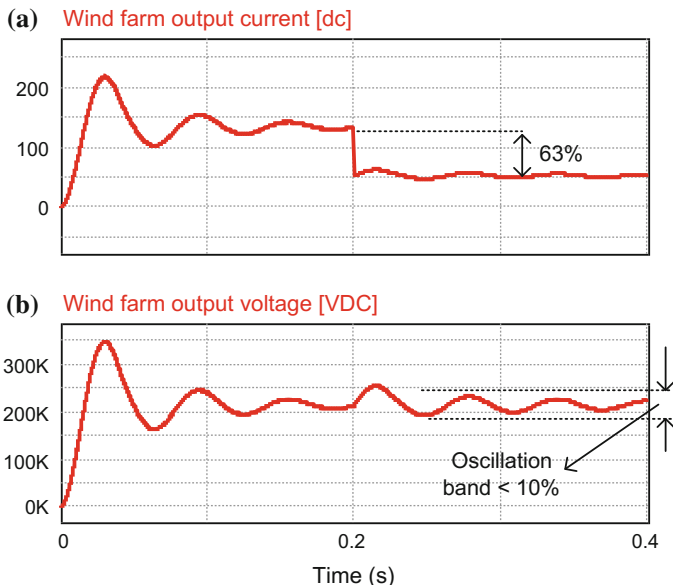


Fig. 8.19 **a** Characteristic of the current output of wind farm showing a decrease in current at $t_f = 0.2$ s due to the deficit in wind energy. **b** Dynamic of voltage output of the wind farm showing a small % overshoot at $t_f = 0.2$ s and then a voltage oscillation of less than 10%

maintained within an acceptable oscillating band by the BSS and PV system through the regulator Loop 2 of Fig. 8.14 whatever the drop in the current (or power) signal is.

B. Unit breakdown analysis

In the case where a group of 8 units from the 80 series-connected units on the wind farm is momentarily disconnected (or breaks down), for example when a sudden cut-off of the supply voltage of 8 units occurs at time $t_f = 0.2$ s due to a fault condition, β is set to 90° in those units, and thus, the dynamic of voltage output of faulty units is shown in Fig. 8.20a. It can be observed from Fig. 8.20a that before the fault, the steady-state average voltage output of 8 series-connected units is $V_{dc(8u)} = 21.6$ kV, and during the fault period, $V_{dc(8u)}$ becomes zero. Figure 8.20b plots the dynamic of the actual voltage output of the remaining fault-free units (i.e. 72 units); it can be observed that the actual voltage signal is not significantly affected by the disconnection of 8 units; a small % overshoot is noted at $t_f = 0.2$ s and then oscillating within 10% band. The current (or power) signal output of the wind farm slightly decreases at $t_f = 0.2$ s due to the cut-off of the supply voltage of 8 units, as shown in Fig. 8.20c. The power deficit is supplemented by the BSS and PV system through the regulator Loop 2 of Fig. 8.14.

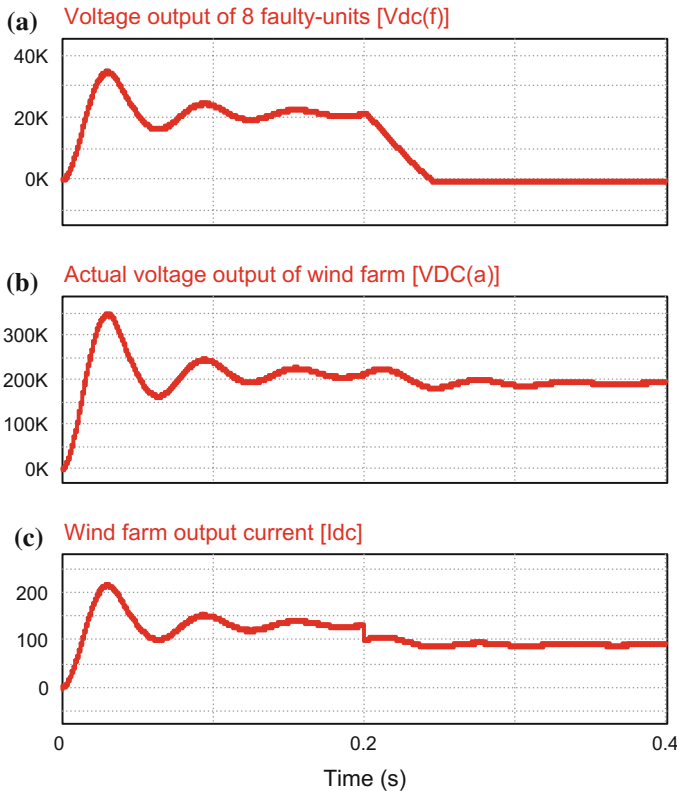


Fig. 8.20 Cut-off of the supply voltage of 8 units from 80 series-connected unit at $t_f = 0.2$ s (β is set to 90°). **a** Dynamic of the voltage output of 8 units showing $V_{dc(8u)}$ steps down at $t_f = 0.2$ s to zero from 21.6 kV (i.e. steady-state voltage) to about 0 V. **b** Dynamic of voltage output of the wind farm, showing a very small % overshoot at $t_f = 0.2$ s and then oscillating within 10% band. **c** Dynamic of the current output of the wind farm, showing a small decrease in current (or power) magnitude at $t_f = 0.2$ s due to break down of 8 units

8.8 Conclusion

In this chapter, an alternative topology of a distributed electrical power network is proposed, which is capable of interconnecting large AC and low-voltage DC networks. For the analysis and discussion, one considered a distributed power network, which consists of an AC network of five buses and a DC network supplying power to a remote area and to low-voltage DC loads. The proposed distributed power network topology is designed to work with renewable power sources such as wind farm, PV and BSS. The following systems are the considered power sources: a three-phase synchronous machine on the AC network side, PMSG-based WECUs integrated with three-phase active rectifiers capable of tracking maximum wind

energy on the wind farm, a PV panel with MPPT and a BSS. The BSS and PV system handle the power fluctuations from the offshore wind farm.

The main advantages for selecting the proposed distributed power network topology include the reduction of the multi-conversion process, which is often taking place in the conventional AC power network and the uses of large number of passive or active rectifiers to feed DC loads, thus causing power losses and affecting the AC power quality. With the proposed distributed power grid topology, the voltage/current harmonic distortion and ripple generated by the power converters are reduced, and the efficiency and power quality on the AC power network are improved. The equivalent circuit model of the DC power collection grid is also presented.

Furthermore, the dynamic performance of the DC power collection grid is investigated when exposed to power flow imbalances and unit disconnection. The BSS and PV system handle properly the variations by maintaining the DC voltage oscillation within acceptable band. The operating principle of various components employed in the proposed distributed power network is mathematically described, such as the principle of MPPT using the boost DC–DC converter and active rectifiers. The low-voltage DC loads are connected to the DC bus through an automatic adapter; the concept of an automatic adapter to monitor low-voltage DC loads is presented, which introduces a great degree of autonomy of the DC networks.

References

1. Greenpeace (2005) “The environmental impacts of coal” climate, New Zealand. www.greenpeace.org/new-zealand
2. Wakileh GJ (2001) Power systems harmonics fundamental, analysis and filter design. Springer, New York
3. Andersen BR, Xu L (2004) Hybrid HVDC system for power transmission to island networks. *IEEE Trans Power Deliv* 19(4):1884–1890
4. Chen X, Sun H, Wen J, Lee W-J, Yuan X, Li N, Yao L (2011) Integrating wind farm to the grid using hybrid multi-terminal HVDC technology. *IEEE Trans Ind Appl* 47(2):965–972
5. Mogstad AB, Molinas M (2008) Power collection and integration on the electric grid from offshore wind parks. Nordic workshop on power and industrial electronics (NORPIE), 9–11 June 2008
6. De Prada MG, Dominguez-Garcia JL, Diaz-Gonzalez F, Aragues-Peñalba M, Gomis-Bellmunt O (2015) Feasibility analysis of offshore wind power plants with DC collection grid. *Renew Energy* 78:467–477
7. Xiang W, Hua Y, Wen J, Yao M, Li N (2014) Research on fast solid state DC breaker based on a natural current zero-crossing point. *J Mod Power Syst Clean Energy* 2(1):30–38
8. Yang J, Fletcher JE, O’Reilly J (2010) Multiterminal DC wind farm collection grid internal fault analysis and protection design. *IEEE Trans Power Deliv* 25(4):2308–2318
9. Tang L, Ooi B-T (2007) Locating and isolating DC faults in multi terminal DC systems. *IEEE Trans Power Deliv* 22(3):1877–1884

10. Wu YK, Lee CY, Shu GH (2011) Taiwan's first large-scale offshore wind farm connection—a real project case study with a comparison of wind turbine. *IEEE Trans Ind Appl* 47(3):1461–1469
11. Berenguel D, de Prada M, Bellmunt OG, Martins M (2013) Electrical interconnection options analysis for offshore wind farms. In: Europe's premier wind energy event, EWEA, Vienna, Austria, 2013
12. Varela GQ, Ault GW, Lara OA, McDonald JR (2007) Electrical collector system options for large offshore wind farms. *IET Renew Power Gener* 1(2):107–114
13. Chou CJ, Wu YK, Han GY, Lee CY (2012) Comparative evaluation of the HVDC and HVAC links integrated in a large offshore wind farm—an actual case study in Taiwan. *IEEE Trans Ind Appl* 48(5):1639–1648
14. Meah K, Ula S (2007) Comparative evaluation of HVDC and HVAC transmission systems. In: Power engineering society general meeting, 2007
15. Hansen L, Blaabjerg F, Christensen H, Lindhard U, Eskildsen K, Madsen P (2001) Generators and power electronics technology for wind turbines. In: 27th annual conference of the IEEE industrial electronics society, IECON, 2001
16. Chen Z, Guerrero JM, Blaabjerg F (2009) A review of the state of the art of power electronics for wind turbines. *IEEE Trans Power Electron* 24(8):1859–1875
17. Yaramasu V, Wu B, Sen PC, Kouro S, Narimani M (2015) High-power wind energy conversion systems: state-of-the-art and emerging technologies. *Proc IEEE* 103(5)
18. Li H, Chen Z (2008) Overview of different wind generator systems and their comparisons. *IET Renew Power Gener* 2(21):123–138
19. Hansen LH, Helle L, Blaabjerg F, Ritchie E, Munk-Nielsen S, Bindner H, Sorensen P, Bak-Jensen B (2001) Conceptual survey of generators and power electronics for wind turbines. Riso National Laboratory, Roskilde, Denmark
20. Giddani OA, Adam GP, Anaya-Lara O, Burt G, Lon KL (2010) Control strategies of VSC-HVDC transmission system for wind power integration to meet GB grid code requirements. In: International symposium on power electronics electrical drives, automation and motion SPEEDAM, 2010
21. Erlich I, Brakelmann H (2007) Integration of wind power into the German high voltage transmission grid. In: Power engineering society general meeting, 2007
22. Erlich I, Winter W, Dittrich A (2006) Advanced grid requirements for the integration of wind turbines into the German transmission system. In: Power engineering society general meeting, 2006
23. Veilleux E, Lehn PW (2014) Interconnection of direct-drive wind turbines using a series-connected DC grid. *IEEE Trans Sustain Energy* 5(1):139–147
24. Chuangpishit S, Tabesh A, Moradi-Shahrabak Z, Saedifard M (2014) Topology design for collector systems of offshore wind farms with pure DC power systems. *IEEE Trans Ind Electron* 61(1):320–328
25. Holtsmark N, Bahirat HJ, Molinas M, Mork BA, Hoidalén HK (2013) An all-DC offshore wind farm with series-connected turbines: an alternative to the classical parallel AC model. *IEEE Trans Ind Electron* 60(6):2420–2428
26. Musasa K, Gitau MN, Bansal RC (2015) Dynamic analysis of DC-DC converter internal to an offshore wind farm. *IET Renew Power Gener* 9(6):542–548
27. Chen W, Huang AQ, Li C, Wang G, Gu W (2013) Analysis and comparison of medium voltage high power DC/DC converters for offshore wind energy systems. *IEEE Trans Power Electron* 28(4):2014–2023
28. Robinson J, Jovicic D, Joos G (2010) Analysis and design of an offshore wind farm using a MV DC grid. *IEEE Trans Power Deliv* 25(4):2164–2173
29. Yiqing L, Grain PA, Derrick H, Stephen JF (2016) Medium-voltage DC/DC converter for offshore wind collection grid. *IET Renew Power Gener* 10(5):651–660
30. Lu W, Ooi B-T (2005) Premium quality power park based on multi-terminal HVDC. *IEEE Trans Power Deliv* 20(2):978–983

31. Lu W, Ooi BT (2003) Optimal acquisition and aggregation of offshore wind power by multiterminal voltage source HVDC. *IEEE Trans Power Deliv* 18(1):201–206
32. Guo C, Zhao C (2010) Supply of an entirely passive AC network through a double-infeed HVDC system. *IEEE Trans Power Electron* 24(11):2835–2841
33. Meyer C, Hoing M, Peterson A, Donckeri RWD (2007) Control and design of DC grids for offshore wind farms. *IEEE Trans Ind Appl* 6(43):1475–1481
34. Max L (2009) Design and control of a DC collection grid for a wind farm. Thesis for the degree of doctor of philosophy, Chalmers University of Technology, 2009, pp 1–157
35. Deng F, Chen Z (2011) An offshore wind farm with DC grid connection and its performance under power system transients. In: *IEEE power and energy conference*, San Diego, USA, 2011, pp 1–8
36. Deng F, Chen Z (2013) Operation and control of a DC-grid offshore wind farm under DC transmission system faults. *IEEE Trans Power Deliv* 28(3):1356–1363
37. Musasa K, Gitau MN, Bansal RC (2015) Analysis of a DC collector-based power converter topology for an offshore wind farm. *Electric Power Compon Syst* 43(8–10):1113–1121
38. Musasa K, Gitau MN, Bansal RC (2015) Performance analysis of power converter based active rectifier for an offshore wind park. *Electric Power Compon Syst* 43(8–10):1089–1099
39. Guan M, Xu Z (2014) A novel concept of offshore wind-power collection and transmission system based on cascaded converter topology. *Int Trans Electr Energy Syst* 24(3):363–367
40. Flourentzou N, Agelidis VG, Demetriades GD (2009) VSC-based HVDC power transmission systems: an overview. *IEEE Trans Power Electron* 24(3):592–602
41. Powell L (2004) Power system load flow analysis. McGraw-Hill, New York
42. Puran R, Patrick JN, Steven DA, Stuart JG, Graeme MB (2016) Evaluation of the impact of high-bandwidth energy-storage systems on DC protection. *IEEE Trans Power Deliv* 31(2):586–594
43. Lie X, Dong C (2011) Control and operation of a DC microgrid with variable generation and energy storage. *IEEE Trans Power Deliv* 26(4):2513–2522
44. Jalbrzykowski S, Citko T (2009) A bidirectional DC-DC converter for renewable energy systems. *Bull Pol Acad Sci Tech Sci* 57(4)
45. Arrillaga J, Liu YH, Watson NR (2007) Flexible power transmission: the HVDC options. Wiley, Hoboken
46. Yazdani A, Iravani R (2010) Voltage-sourced converters in power systems: modelling, control, and applications. Wiley, New Jersey
47. Cuzner RM, Venkataraman G (2008) The status of DC micro-grid protection. In: *IEEE industry applications society annual meeting*, Edmonton, Alta, 5–9 Oct 2008
48. Stamatiou G, Srivastava K, Reza M, Zanchetta P (2011) Economics of DC wind collection grid as affected by cost of key components. In: *World renewable energy congress*, Linköping, Sweden, 8–13 May 2011
49. Salomonson D, Sannino A (2007) Low-voltage DC distribution system for commercial power system with sensitive electronic loads. *IEEE Trans Power Deliv* 22(3):1620–1627
50. Krstic S, Wellner E, Bendre A, Semenov B (2007) Circuit breaker technologies for advanced ship power system. In: *IEEE electric ship technology symposium*, 2007
51. Meyer C, Kowal M, Doncker RW (2005) Circuit breaker concepts for future high-power DC-applications. In: *IEEE-IAS conference record*, 2–6 Oct 2005, pp 860–866
52. Kheraluwala MH, Gascoigne RW, Divan DM, Bauman ED (1992) Performance characterization of high power dual active bridge DC-to-DC converter. *IEEE Trans Ind Appl* 28(6):1294–1301
53. Li H, Peng FZ, Lawler IS (2003) A natural ZVS medium-power-bidirectional DC-DC converter with minimum number of devices. *IEEE Trans Ind Appl* 39(2):525–535
54. Attou A, Massoum A, Saidi M (2014) Photovoltaic power control using MPPT and boost converter. *Balkan J Electr Comput Eng* 2(1):23–27
55. Slootweg JG, Polinder H, Kling WL (2003) Representing wind turbine electrical generating systems in fundamental frequency simulations. *IEEE Trans Energy Conv* 18(4):516–524

56. Anderson PM, Associates PM, Bose A (1983) Stability simulation of wind turbine systems. *IEEE Trans Power App Syst* 102(12):3791–3795
57. Moham N, Undeland TM, Robbins WP (2003) *Power electronics: converters, applications, and design*. Wiley, Hoboken
58. Ramtharan G, Arulampalam A, Ekanayake J, Hughes F, Jenkins N (2009) Fault ride through of fully rated converter wind turbines with AC and DC transmission systems. *IET Renew Power Gener* 3(4):426–438
59. Zhao H, Wu Q, Hu S, Xu H, Rasmussen CN (2015) Review of energy storage system for wind power integration support. *Appl Energy* 137(4):545–553
60. Zhang L, Wang Y, Li H (2012) Coordinated control of MTDC-based microgrid with wind turbines. In: *IEEE 7th international power electronics and motion control conference, ECCE Asia, 2012*
61. Swierczynski M, Teodorescu R, Rasmussen CN, Rodriguez P, Vikelgaard H (2010) Overview of the energy storage systems for wind power integration enhancement. In: *IEEE international symposium, industrial electronics (ISIE), 2010*, pp 3749–3756

Part III
PV Systems

Chapter 9

Steady-State Analysis of Unbalanced Distribution Networks with High Penetration of Photovoltaic Generation

Kalpesh Joshi and Naran Pindoriya

Nomenclature

Transformer and Voltage Regulator Modelling

CT_P, CT_S	Respectively, primary and secondary side current rating (A) of Current Transformer (CT);
I_{An}, I_{Bn}, I_{Cn}	Phase currents (A) on primary side of Voltage Regulator (VR) in phase a, b and c , respectively;
I_{an}, I_{bn}, I_{cn}	Phase currents (A) on secondary side of VR in phase a, b and c , respectively;
N_1, N_2	Number of turns in shunt and series winding, respectively, in VR;
N_{PT}	Turns ratio of potential transformer;
$R_{comp-\Omega}, X_{comp-\Omega}$	Resistance and reactance (Ω) obtained for VR setting;
$R_{line-\Omega}, X_{line-\Omega}$	Resistance and reactance (Ω) for line to be compensated;
R_{pu}, X_{pu}	Resistance and reactance in per unit for VR setting;
R'_{pu}, X'_{pu}	Resistance and reactance (V) for VR setting;
V_{An}, V_{Bn}, V_{Cn}	Phase to neutral voltage (V) on primary side of VR for phase a, b and c , respectively;
V_L, I_L	Load side voltage (V) and current (A), respectively, in VR;
V_{LN}	Line to neutral voltage (V) in VR;
V_{an}, V_{bn}, V_{cn}	Phase to neutral voltage (V) on secondary side of VR for phase a, b and c , respectively;
a_r, a_R	Voltage regulator ratio and effective voltage regulator ratio, respectively;
a_{ra}, a_{rb}, a_{rc}	VR ratio in phase a, b and c , respectively.

K. Joshi (✉) · N. Pindoriya
 IIT Gandhinagar, Palaj, Gandhinagar, Gujarat, India
 e-mail: kalpeshjoshi@iitgn.ac.in

PV Array Modelling

Δ_T	Difference in module temperature with respect to Standard Temperature Conditions (STC) in Kelvin
G_n	Global irradiance under STC (W/m^2)
$I_{0,n}$	Diode saturation current (A) under STC
I_0	Diode saturation current (A) under normal temperature
I_{mp}	Module current (A) when PV module operates at MPP
I_{pv}	PV Module current (A) due to photovoltaic effect
$I_{sc,n}$	PV module short circuit current (A) under STC
K_I	Coefficient of temperature for current in $\%/K$
K_V	Coefficient of temperature for voltage in $\%/K$
N_s	Number of PV cells connected in series in a PV module
$P_{\max,e}$	Maximum power (W) produced by module under STC
PV_{area}	Gross area of photovoltaic modules receiving solar insolation, m^2
R_p	Equivalent parallel resistance in Ω
R_s	Equivalent series resistance in Ω
V_{mp}	PV Module voltage (V) operating at maximum power point
$V_{oc,n}$	PV module open circuit voltage (V) under STC
V_t	Thermal voltage (V) of PV module at temperature T
G	Global irradiance in W/m^2
I	PV Module current (A) at given temperature and irradiance
T	Temperature of PN junction in Kelvin
V	PV module voltage (V) at given temperature and irradiance
a, k	Diode ideality factor, Boltzmann's constant
q	Electron charge
η	Overall gross efficiency of photovoltaic plant

9.1 Introduction

Electric power system is undoubtedly one of the most complex systems. It needs to maintain a very precise balance between production and consumption of electricity as it is difficult to store. Since the bulk power generation plants are normally situated away from the load centres, the entire power system is geographically spread over a vast area. Therefore, the power system itself is in general conceptualized as comprising of three major subsystems, namely the generation, transmission and distribution systems.

Typically, distribution systems require a significant capital investment and careful planning. Security and reliability of the electric power supply system has gained increasing attention due to critical and stringent requirements of consumers and increasing penetration of Distributed Generation (DG) based on Renewable

Energy Sources (RES). In order to meet these new demands, it is felt that the distribution systems need to be automated. Automation of the distribution systems increases efficiency, reliability and security of the system. Power flow simulation is the basic building block for analyzing the behaviour and response of distribution networks to the increasing penetration of RES-based DGs. Such an analysis can then be used to formulate complex control strategies to improve system efficiency and reliability. This chapter is therefore focused on modelling and analysis of unbalanced distribution networks with DGs including phase-domain modelling and sequential time simulations (STS).

9.2 Need for Detailed Modelling of Unbalanced Distribution Networks

Historically, use of single-line equivalent networks for distribution systems has been prevalent. However, detailed phase-domain modelling techniques have also been developed and recommended for unbalanced distribution networks [1]. Depending on the extent of unbalance, phase-wise control of voltage regulating equipment including on-line tap changers (OLTC), Line Drop Compensators (LDC) and Shunt Capacitors (SC) is very much commonly employed. Apart from these, the fact that the effect of unbalance in load is most severely perceived in distribution networks necessitates detailed phase-domain modelling for analysis. Also, increasing penetration of household single-phase DGs in multi-phase distribution networks needs phase-wise treatment of analysis. The inherent unbalance in network topology such as unavailability of one or more phases in a section of a feeder or absence of load in a particular phase needs to be modelled accurately. These factors need to be considered and accounted for in management of day-to-day operations of distribution networks as well as in planning stages for effective control strategies. Next section describes the phase-domain modelling of major components in distribution networks.

9.3 Phase-Domain Modelling

Unlike the transmission system studies, the distribution networks are inherently unbalanced based on topological phase unbalance, load unbalance due to consumer behaviour as well as inadequate transposition in short distribution lines. Apart from these requirements, various configurations of distribution transformers, large single-phase loads, phase-unbalanced shunt compensation etc. make it inevitable to consider phase-domain detailed modelling to reflect actual scenario faithfully in power flow simulations. It also requires the power flow algorithm to be modified or replaced by special 3-phase power flow algorithms such as forward-backward

sweep algorithm. These algorithms accept phase-domain modelling of all major components in the form of 3×3 (or larger) matrices. As an example, modelling of VR is discussed in the following Sect. (9.3.1). It is based on [1], in which modelling details of all major components of distribution networks (except PVDG) can be found.

9.3.1 Voltage Regulators

A step-voltage regulator consists of an autotransformer and a load tap changing mechanism. The voltage change is obtained by changing the taps of the series winding of the autotransformer. The position of the tap is determined by a control circuit (LDC). Standard step regulators contain a reversing switch enabling a $\pm 10\%$ regulator range, usually in 32 steps. This amounts to a $5/8\%$ change per step, or 0.75 V change per step, on a 120 V base. Step regulators can be connected in a Type A or Type B connection according to the ANSI/IEEE C57.15-1986 standard. Some important definitions for voltage regulators are as under:

1. Voltage Level: the desired voltage (on a 120 V base) to be held at the load centre. The load centre may be the output terminal of the regulator or a remote node on the feeder.
2. Bandwidth: the allowed variance of the load centre voltage from the set voltage level. The voltage held at the load centre will be \pm one half of the bandwidth.
3. Time-Delay: length of time that raises or lowers operation is called for before the actual execution of the command. This prevents tap changing during transients or short time change in current.
4. Line Drop Compensator: set to compensate for the voltage drop (line drop) between the regulator and the load centre. The settings consist of R and X settings in Volts corresponding to the equivalent impedance between the regulator and the load centre.

The defining voltage and current equations for the regulator in the raise position are as follows:

$$V_s = \left(1 - \frac{N_2}{N_1}\right)V_L \quad \text{and} \quad I_L = \left(1 - \frac{N_2}{N_1}\right)I_s \quad (9.1)$$

$$a_r = 1 - \frac{N_2}{N_1}$$

V_s and I_s are secondary side (low voltage side) voltage and current, whereas V_L and I_L are load side voltage and current, respectively.

In lower position, the regulator ratio will change to: $a_r = 1 + \frac{N_2}{N_1}$

The actual turns-ratio of the winding is not known; however, the particular tap position will be known. Each tap changes the voltage by $5/8\%$ or 0.00625 per unit.

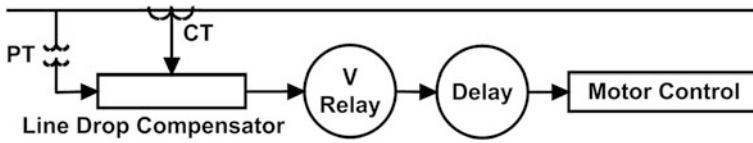


Fig. 9.1 Step-voltage regulator control circuit [1]

Table 9.1 Important relationships

Base	Line circuit	Compensator circuit
Voltage	V_{LN}	$\frac{V_{LN}}{N_{PT}}$
Current	CT_P	CT_S
Impedance	$Z_{base-line} = \frac{V_{LN}}{CT_P}$	$Z_{base-comp} = \frac{V_{LN}}{N_{PT}CT_P}$

Therefore, the effective regulator ratio can be given by: $a_r = 1 \mp 0.00625 \bullet \text{Tap}$ (negative sign applies for the raise position).

The changing of taps on a regulator is controlled by the LDC as shown in Fig. 9.1. The purpose of the regulator is to model the voltage drop of the distribution line from the regulator to the load centre. The compensator is an analogue circuit that is a scale model of the line circuit. The compensator input voltage is typically 120 V, and therefore, a PT is used to step down the line voltage to this level. The CT ratio is according to the line current of the feeder. The most critical setting is that of the R and X calibrated in Volts. These values must represent the equivalent impedance from the regulator to the load centre. The basic requirement is to force the per-unit line impedance to be equal to the per-unit compensator impedance. A consistent set of base values need be developed wherein the per-unit voltages and currents in the line and compensator are equal. These values are given in Table 9.1.

The per-unit values and R and X should be same in line and in compensator. These are computed from Eqs. (9.2–9.4) as given below:

$$R_{pu} + jX_{pu} = (R_{line-\Omega} + jX_{line-\Omega}) \frac{CT_P}{V_{LN}} \tag{9.2}$$

$$R_{comp-\Omega} + jX_{comp-\Omega} = (R_{line-\Omega} + jX_{line-\Omega}) \cdot \frac{CT_P}{N_{PT} \cdot CT_S} \tag{9.3}$$

$$\therefore R'_{pu} + jX'_{pu} = (R_{line-\Omega} + jX_{line-\Omega}) \cdot \frac{CT_P}{N_{PT} \cdot CT_S} \cdot CT_S \text{ V} \tag{9.4}$$

Equation (9.4) gives the values of R and X in terms of voltage (p.u.) directly. Hence, knowing the equivalent impedance of the line in ohms, the R and X settings can be obtained in volts by using the above equation. The three-phase regulators also can be similarly modelled using matrix representation. The wye-connected

three-phase regulators found in IEEE-13 node and IEEE-34 node test feeders can be implemented using following voltage and current relationships:

$$\begin{bmatrix} V_{An} \\ V_{Bn} \\ V_{Cn} \end{bmatrix} = \begin{bmatrix} a_{ra} & 0 & 0 \\ 0 & a_{rb} & 0 \\ 0 & 0 & a_{rc} \end{bmatrix} \begin{bmatrix} V_{an} \\ V_{bn} \\ V_{cn} \end{bmatrix} \quad (9.5)$$

$$\begin{bmatrix} I_A \\ I_B \\ I_C \end{bmatrix} = \begin{bmatrix} 1/a_{ra} & 0 & 0 \\ 0 & 1/a_{rb} & 0 \\ 0 & 0 & 1/a_{rc} \end{bmatrix} \begin{bmatrix} I_a \\ I_b \\ I_c \end{bmatrix} \quad (9.6)$$

where a_{ra} , a_{rb} and a_{rc} are the effective turns-ratios in the respective phase regulators.

9.3.2 Photovoltaic Generators and Power Electronic Converters

A very basic and simple model for photovoltaic generator is often used in the form of an equation that crudely replicates a photovoltaic array. For example, GridLAB-D [2], uses (9.7) to approximate the maximum power generated from a set of Mono-Crystalline PV modules. This results in a gross modelling with considerable errors. A comparison of approximate modelling based on (9.7) is presented in Fig. 9.2 with actual measurements. Error to the tune of $\pm 15\%$ is easily incurred even after taking an actual efficiency value from recorded measurements. The simplified model completely ignores the effect of ambient temperature which actually shifts the generation curve slightly on left side of the solar insolation curve. This amounts to significantly high error when time-integral studies are carried out with such a gross model.

$$P_{\max,e} = G \cdot \eta \cdot PV_{\text{area}} \quad (9.7)$$

In order to represent the effect of ambient temperature, wind speed and effective insolation normal to the PV modules elaborate modelling exercise should be carried out. A 2-stage approach for comprehensive model of a PV plant considering all above factors is shown in Fig. 9.3. The first stage uses a Faiman model [3], to obtain module temperature from measured ambient temperature and wind speed at given location. Another stage uses a single diode equivalent model for PV cells integrated over a number of cells in a PV module and further integrated over many such modules to represent a full PV plant as a single PV generator [4]. This comprehensive PV generator model uses the module temperature given by first stage and produces PV generator output with high accuracy. Key equations and their use in iterative algorithm are described in brief below:

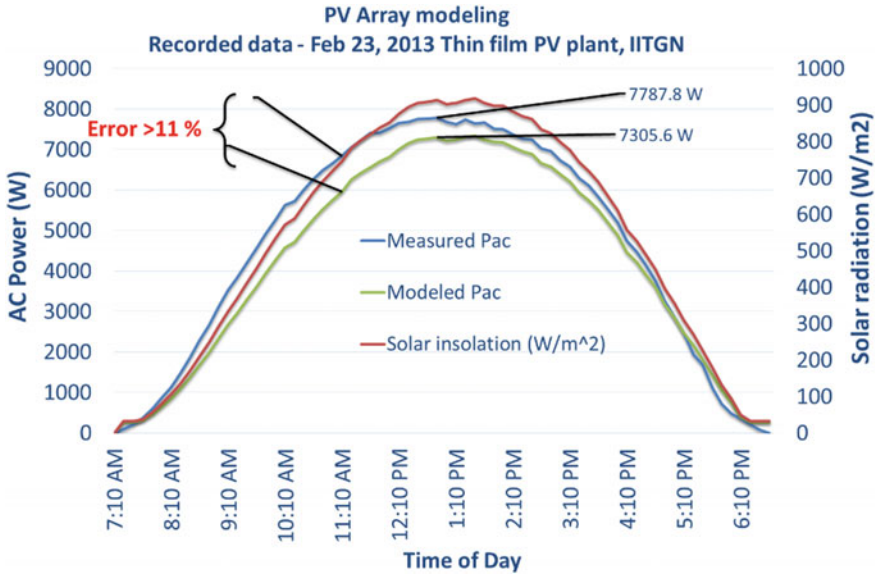


Fig. 9.2 Comparison of approximate model of PV plant with recorded measurements

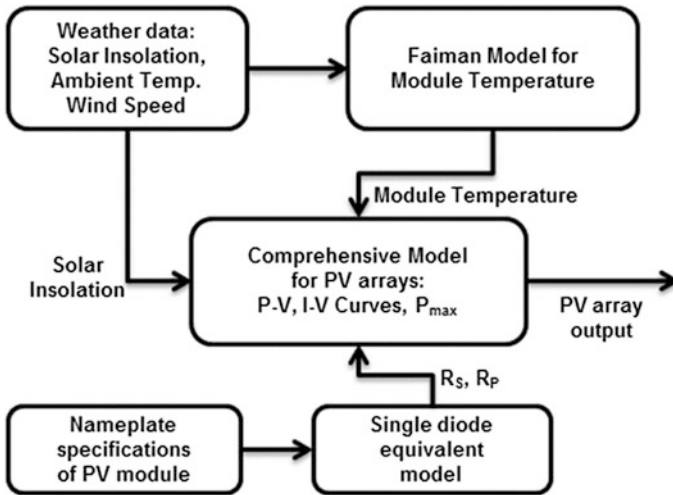


Fig. 9.3 PV generator modelling using Faiman model for module temperature [3] and comprehensive model for PV arrays [4]

With value of I_0 from (9.9), R_p and R_s are obtained by iterating for range of values for R_s in (9.8) till the maximum power obtained from the modelled values of R_p and R_s becomes equal to the one provided in data sheet of the module at STC.

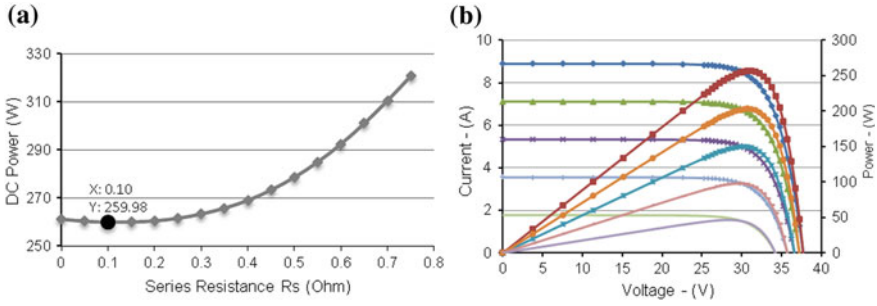


Fig. 9.4 **a** Values of series resistance R_s obtained iteratively. **b** P - I - V curves for a multi-crystalline PV module

Sample results of the iterative algorithm for determining R_s are shown in a $P_{max} \rightarrow R_s$ curve in Fig. 9.4a.

$$R_p = \frac{V_{mp}(V_{mp} + I_{mp}R_s)}{\left\{ V_{mp}I_{pv} - V_{mp}I_0 \exp\left[\frac{V_{mp} + R_s I_{mp}}{aN_s} \frac{q}{kT}\right] + V_{mp}I_0 - P_{max,e} \right\}} \tag{9.8}$$

$$I_0 = (I_{sc,n} + K_I \Delta T) \left\{ \exp\left(\frac{V_{oc,n} + K_V \Delta T}{aV_i}\right) - 1 \right\}^{-1} \tag{9.9}$$

Once determined, the values of R_p and R_s can then be used in (9.10) & (9.11) for the range of operating voltage from $[0 \ V_{oc,n}]$ to obtain I . The set of values for V and I obtained from (9.10) are used to get $I \rightarrow V$ and $P \rightarrow V$ characteristics at different module temperature and solar irradiation. The $P \rightarrow V, I \rightarrow V$ and $P_{max} \rightarrow R_s$ characteristic curves are provided in Fig. 9.4b. The array output is then scaled up with a de-rating factor and loss factor to allow for losses.

$$I = I_{pv} - I_0 \left[\exp\left(\frac{V + R_s I}{V_i a}\right) - 1 \right] - \frac{V + R_s I}{R_p} \tag{9.10}$$

$$I_{pv} = (I_{pv,n} + K_I \Delta T) G(G_n)^{-1} \tag{9.11}$$

9.4 Sequential Time Simulations

Integration of RES-based DG to the power delivery networks affects the operations of distribution network by introducing unpredictability and intermittency of local generation. Several operational issues with increasing penetration of RES in distribution grid are elaborated in [5]. Apart from concerns for protection issues, abnormal operations under islanding and system restoration, steady-state operational issues such as voltage regulation in the presence of DG, interaction of DG

with capacitor operations and impact on VR switching are also of major concern. Impact of a rooftop PV system on unbalance 3-phase operations of a spot network in India was investigated in [6] with detailed 3-phase modelling of all network components. But, the conventional worst-case analysis based on snapshot power flow studies cannot reflect the variations that a typical distribution network with DG has to manage. It is apparent that the active distribution networks (ADNs) operating in smart-grid environment will need to respond to continuous variations in generation by incorporating flexible and adaptive control and dispatch strategies for real and reactive power sources [7]. In this context, STS can play a decisive role in characterizing variability in distribution system operations and validation of strategies to improve operational efficiency [8, 9]. However, the implementation of any intelligent technique for improving operational efficiency of ADNs should necessarily be weighed against the involved costs and expected benefits as pointed out in [5]. Report by Sandia National Laboratory [10, 11] demonstrates the applicability of Time-Series Power Flow (TSPF) analysis in a distribution network with photovoltaic (PV) generation. It also proposes the use of TSPF analysis in analyzing the steady-state effect of PV variability on feeder voltage profile and power factor which in turn can help in designing the control strategies for capacitor switching and altering the operating power factor of PV inverters. A simple but unique early application of TSPF analysis can be found in [12]. Impact of distributed micro-PV generation (typically $2.16 \text{ kW}_{\text{peak}}$) along with domestic scale-combined heat and power (micro-CHP) systems is investigated for a representative day in each season—winter and summer. Hourly analysis is applied in this work with LV secondary network operating at 400/230 V to estimate voltage rise due to DGs. More rigorous hourly analysis over a period of one year in a distribution network at 33 kV has been presented in [13] to assess the capacity of the existing power delivery network to accommodate new wind generation installations. Feeder voltage profile, cable loading and power exchange between load and generating centres at different load power factor are among the major criteria in this work [13] for evaluating performance of distribution network with increasing wind penetration. Similar exercise is taken up in [14] with optimal power flow for time-series data of onshore and offshore wind, wave and tidal resources to estimate the required curtailment of real power injections by RES in order to ensure network operations within acceptable voltage limits. TSPF analysis is also used in [15] to assess the effect of high wind penetration on voltage stability limits in transmission systems. STS are also used at half-hourly intervals to assess the risk of unintentional islanding in a spot network due to a rooftop PV system [16].

9.4.1 Inadequacy of Extreme Value Analysis

Extreme value analysis is historically used for large networks spread over several hundreds of kilometres including long transmission networks. It is used for scheduling and coordination of different types of bulk electricity generators. It is

also used in studying the security, reliability, protection and control aspects at systems level. However, effects of variation in load demand are most perceived in low-voltage networks. Also, penetration of RES-based non-dispatchable generation adds to the uncertainty and intermittency in main network variables such as node voltages, branch currents and power flows. It should be noted that the variations are cyclical and have typical diurnal as well as seasonal occurrences. In order to optimize the daily operations of low-voltage networks, these cyclical variations need to be reflected in the analysis which cannot be achieved by several extreme value analyses [9]. The power flow simulations need to be performed over a long duration (typically annual period is considered) with moderate selection of resolution of data sets (e.g. 15 min interval for annual analysis). Hourly annual analysis is common for STS, but nowadays, quasi-static simulations use 1 min of sub-minute intervals for annual analysis. This necessitates huge amount of data and exhaustive analysis to capture trends among the results.

9.4.2 Data Requirements and Time Resolution

Apart from system data that is needed for detailed phase-domain modelling of all major components in distribution networks, as discussed in preceding sections, exhaustive time-series data sets of load profiles are also required to perform STS. These data sets are huge as they need to capture the seasonal as well as diurnal variations in demand and generation (e.g. PV generators or Wind generators). Resolution of the load profiles and generation from DGs can be anywhere from one minute to one hour. Normally, the variation in demand is considered slow and a 15-min resolution is considered sufficient, whereas DG data should have a resolution of one minute or even less if required by the nature of analysis. Quasi-static sequential simulations can use data with resolution of one to several seconds [9]. Daily load profiles also vary in their shapes for industrial, commercial and residential consumers which can be easily observed in Fig. 9.5. Industrial load profiles remain more or less constant throughout the day whereas commercial and residential load profiles show greater variations. The daily load profiles shown in Fig. 9.5 are produced by using publically available data sets in [17]. Out of more than 120 customer groups' annual load profiles, typical load profiles as shown in Fig. 9.5 are integrated at different nodes in a distribution network to produce a scaled version of annual load profile at each node in a network. This leads to a realistic scenario of variation in demand over a period of one year. Whereas, solar insolation data along with weather data, available in [18], can be used to produce time-series data for PV generators using PV models discussed earlier. These two data sets combined together can be used to generate near-real annual scenarios of demand and generation for a given location in a selected feeder. This kind of data

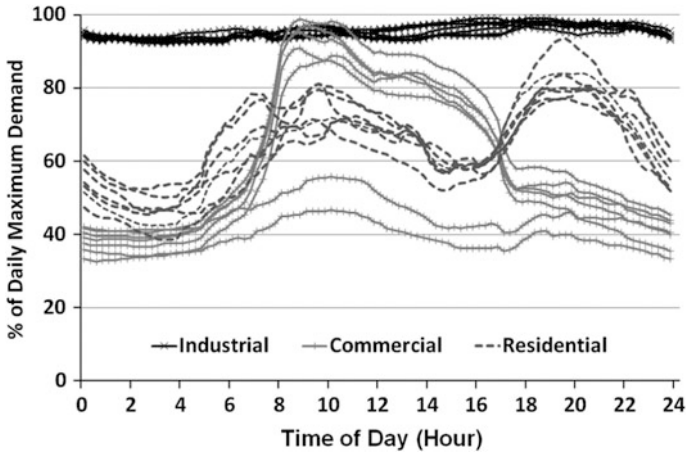


Fig. 9.5 Load profiles for industrial, commercial and residential user groups

sets is used in case studies which are presented later in this chapter with IEEE test feeders and an actual operating distribution network in India.

9.5 Feeder Response Characteristics

Feeder's response—in terms of feeder voltage profile, power and energy losses, active and reactive power flows, daily maximum demand and performance of voltage regulating equipment including SCs—to the seasonal and diurnal variations in generation and demand can be obtained by annual STS. Response of different feeders is expectedly different. But this case-specificity is emphasized particularly in [19] where uniqueness of feeder response characteristics is presented as an important criteria in the planning exercises of distribution systems. It also states that the feeder response characteristics should be used in grouping the feeders so as to design different management strategies in daily operations management of feeders.

In this section, a broad discussion of factors affecting the feeder response characteristics is presented including the effect of feeder-specific factors that lead to case specificity in response characteristics. It should be noted here that the effect of factors such as size, type and location of DGs in distribution networks are well researched and documented as a part of investigation of DG influence on distribution network operations, whereas feeder-specific factors such as geo-electric size and spread of networks, load unbalance and inherent topological unbalance in networks and load density are mostly ignored. These feeder-specific factors are well attended and investigated in the next section as a part of case studies.

9.5.1 Effect of Size, Type and Location of Photovoltaic Generators

Few other attempts are specifically aimed at analyzing the impact of PV generation in distribution systems. Authors in [20] have demonstrated the effect of increasing PV penetration in a set of 16 feeders with consideration for location (near or far from source node) and type of PV integration (central or distributed), whereas effectiveness of various control strategies at utility level are evaluated in [21] for high PV penetration in LV networks in Germany. To minimize the influence of PV generation on number of tap changer operations (TCOs) of VR and to avoid run-away conditions, STS approach is used in [22] on hourly bases with optimal power flow having an objective of minimizing TCOs by coordinating the reactive sources available in the network.

9.5.2 Effect of Network-Specific Factors on Feeder Response Characteristics

It is well known that distribution networks are rich in diversity and have many factors that determine their unique response to changes in operational parameters. However, this fact is not given its due consideration while proposing novel algorithms and strategies for optimizing the daily operations of these networks. For example, the optimization approach itself can be based on worst-case scenarios that do not represent the variability and its associate complexities. The benefits that are ripped over a long period of time should not be based on worst-case scenarios as these happen seldom in distribution networks. These benefits may otherwise not be available during normal operations. Another major flaw in the algorithms can be plain negligence of network-specific factors that dominate its response to variabilities, e.g. inherent phase unbalance in network topology, the load unbalance, the uneven distribution of connected load spatially. These factors change the response of network to an extent that it becomes purely a unique problem to be optimized. Also, the cyclical load variations and intermittency of DGs form a unique set of data points for optimum daily operations. It implies that the approach used for optimizing daily operations of unbalanced distribution networks should necessarily be based on STS and detailed phase-domain modelling of these networks.

Taking into account the above considerations, several case studies based on different feeders are presented in the following sections elaborating the effect of increasing PV penetration on unbalanced distribution networks. All these studies show sample results derived from annual STS at 15-min interval with full 3-phase modelling of all components in the feeders. These results collectively give insight into the high degree of uniqueness in feeder response characteristics, and it emphasizes that the generic algorithm may propose inferior solutions without considering the effect of network-specific factors.

9.6 Case Studies

In order to evaluate the effect of network-specific factors such as geo-electric size, load density and phase-unbalancing, annual sequential simulations are performed on three IEEE test feeders—IEEE 13 node, 34 node and 37 node test feeders—and one actual operating network in India—IITGN-VGEC network. Exhaustive results are analyzed and summarized in this section to understand the effect of increasing PV penetration in low-voltage unbalanced distribution networks. The feeder response is analyzed for feeder voltage profile, power and energy losses, real and reactive power demand, power factor and performance of VR and SCs. When collectively considered, these factors can very well provide indicators for daily operations management. In order to validate the power flow algorithm, base-case power flow results were obtained and found in close agreement with the published results in [23]. Sequential simulations are then performed for all the networks. For the sake of uniformity for fair comparison, results are obtained for increasing PV penetration from 0 to 100% (of the respective network's peak demand) in steps of 20%. However, considering the available current carrying capacity of the network cables, PV penetration is increased up to 80% for IITGN-VGEC network.

9.6.1 Analysis of IEEE Standard Test Feeders

Two modifications in the IEEE 13 node standard test feeder are applied. The distributed load between nodes 632 and 671 is considered lumped at node 671. Node 680 is selected for integrating the PV plant with varying size from 0 to 3.5 MW. The trunk of this network from source node 650 to 680 is the one having conductors with maximum current carrying capacity—enough to carry load current for nearly 3.5 MW with marginal overloads. Node 680 has no local load connected, and the PV inverter integrates the DG at 4.16 kV voltage level. A 3- Φ detailed diagram with the modifications is given in Fig. 9.6 for this network. The inherent phase unbalancing is quite apparent from Fig. 9.6. Apart from unbalancing caused by varying load demand, the topological unbalance with non-availability of phases in many line sections can be observed in Fig. 9.6. At node 646, an additional SC is connected in order to balance the reactive power compensation among phases. This is discussed in Sect. 9.10.

IEEE 34 node feeder, Fig. 9.7a represents a long, sparsely loaded rural feeder, an actual feeder located in Arizona, USA, with all overhead lines [23]. Its base-case configuration shows little higher than 2 MW demand at substation node. Two modifications to the standard IEEE 34 node test feeder are done similar to those done in IEEE 13 node feeder. The distributed loads are considered as spot loads and a PV plant same as the one simulated for IEEE 13 node feeder is connected at node 890 working at 4.16 kV. PV penetration is raised from 0 to 2 MW—close to 100% of maximum demand for this network.

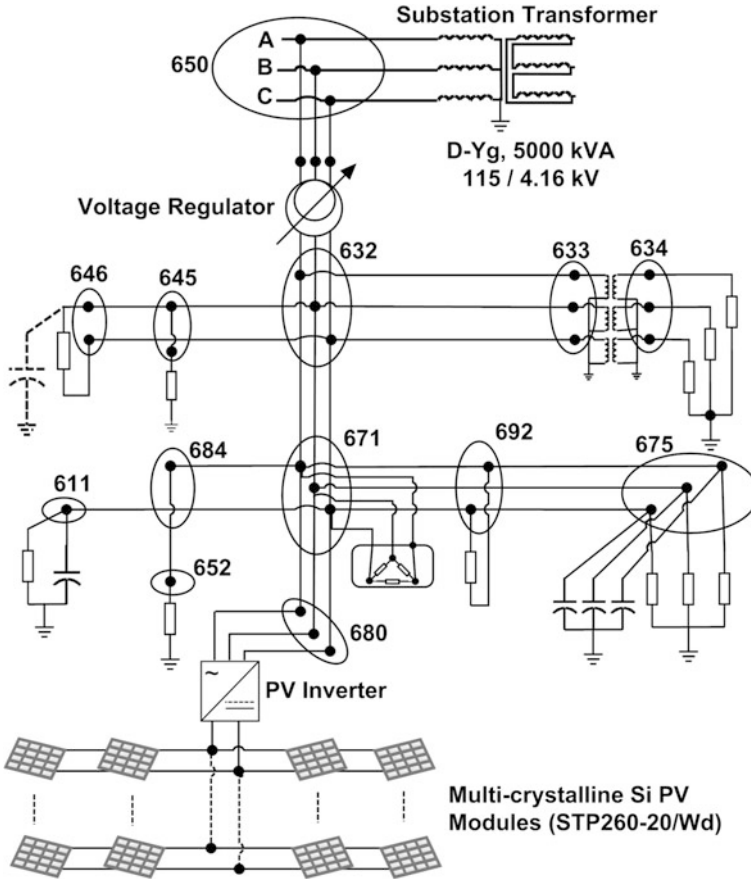


Fig. 9.6 3-phase diagram of modified IEEE 13 node test feeder, note the extra capacitor at node 646

IEEE 37 node feeder represents an urban, highly unbalanced, underground cable-fed distribution network, an actual feeder located in California, USA [23]. It has a fairly good base-case voltage profile without any reactive power support. But the voltage profile is maintained by an open delta-connected VR at substation node. The feeder is modified by a PV plant at node 775.

Each node in IEEE test feeders is populated with an annual load profile scaled to the maximum connected node specified in [23] for each node in all these feeders. Any one or combination of annual load profiles are used for each node from the data sets available in [17]. Based on the connected loads, either industrial, commercial, residential or combination of any of these is used to attach a time-series load profile data to each node. It should be noted that the maximum demand produced by such a scaled set of load profiles never exceeds the specified demand at substation node. Also, the inherent topological phase unbalancing as well as

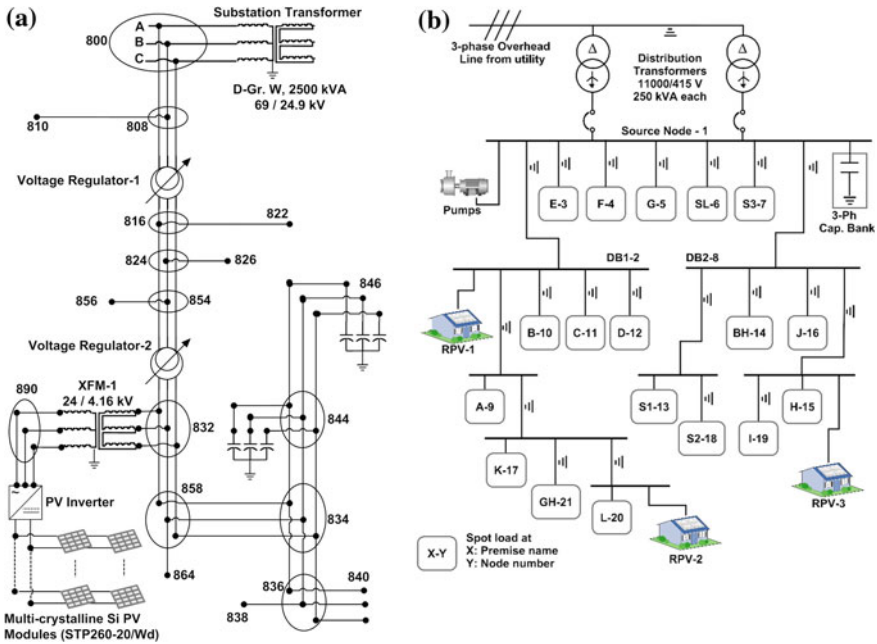


Fig. 9.7 a IEEE 34 node network with modifications. b IITGN-VGEC network with 3 rooftop PV plants

proportional load unbalance—both are preserved while attaching the time-series data. It is worth noting that the ratio of real to reactive power is also maintained to avoid unrealistic power factor values at any node at any time. The PV generation data is selected based on the location of the corresponding feeder. The weather data and insolation data is obtained from [18].

9.6.2 Analysis of an Actual Distribution Network

IITGN-VGEC feeder is an actual operating network in India with three rooftop PV plants and a capacitor bank to regulate the power factor at substation node. As shown in Fig. 9.7b, the underground cable-fed network serves as an academic institute including some residential blocks. The rooftop PV plants have data loggers that continuously measure 11 variables including ambient temperature, solar insolation and power (AC and DC) at 5-min interval. These recorded measurements are directly used for STS along with the substation node demand data which is made available by the local utility [24]. The load composition at each node was surveyed and more details of this network can be found in [6].

9.7 Feeder Voltage Profile with Photovoltaic Generation

Feeder voltage profile is assessed in terms of maximum and minimum node voltage limit violations. The feeder voltage range specified in ANSI C84.1 [25] is used as the benchmark for enumerating maximum and minimum node voltage violations in the IEEE test feeders. The range-A in ANSI C84.1 specifies the feeder voltage range as $\pm 5\%$ of nominal voltage to be maintained by utility supplying the electricity. Apart from the fact that distribution system operator (DSO) is obliged to respect this voltage range, the effect of increasing PV penetration on node voltage limit violations is also important in estimating feeders' hosting capacity for DGs. If the node voltage limits are frequently violated due to increased PV injection, the feeder is supposed to have reached its hosting capacity for DGs. Feeder-specific factors also cause voltage limit violations such as phase unbalance and change in load density. It is observed that the feeder acts like a trampoline. If one of the ends is under more tension, then the resulting thrust also changes its direction. Likewise, if the feeder has highly unbalanced distribution of connected load, the increasing PV penetration can result in both minimum and maximum node voltage limits. The same network with evenly distributed load (geo-electrically i.e. electrically phase-wise and geographically spatial even distribution) can support high PV injections without exceeding the voltage limits.

Results are summarized and discussed based on minimum and maximum voltages observed in a feeder for each time-interval (15 min) throughout the one year time frame. Number of violations indicates whether the feeder supports given penetration of PV injection. Effect of SCs is also analyzed in feeder's voltage profile. It is observed that capacitor switching needs to be coordinated with diurnal variation of PV generators when maximum node voltage limits are increasingly violated.

9.7.1 Minimum and Maximum Node Voltages

From the results of feeder voltage profile analysis for IITGN-VGEC network, it is observed that the maximum node voltage limit violations are very rare. However, 209 occurrences of maximum node voltage limit violations are observed with 80% PV penetration. IEEE 13 node network is the best-behaved network so far as feeder voltage profile is concerned with no minimum node voltage violations and few maximum node voltage violations. The minimum and maximum feeder voltages are shown in Fig. 9.8 (top) for IEEE 13 node feeder. Among all the nodes in IEEE 13 node feeder, minimum and maximum node voltages are selected and plotted against time axis with 100% penetration of PVDG. Maximum node voltage violations with 100% PV penetration are found to be 28. No minimum node voltage limit violations are observed. However, maximum feeder voltage profile with SC frequently violates the limit of 1.05 p.u. It is

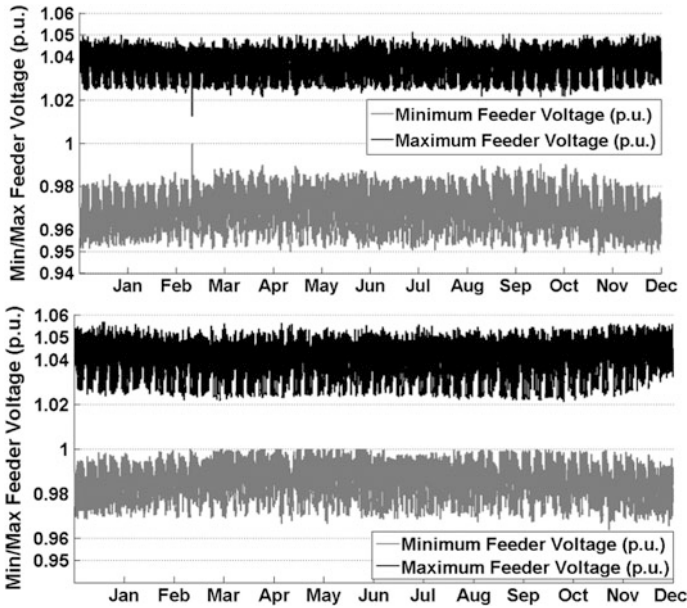


Fig. 9.8 Feeder voltage profile for IEEE 13 node network—without SC (*top*) and with SC (*bottom*)

clearly observable in Fig. 9.8 (bottom). It should also be observed by comparison of two sets (top and bottom) of feeder voltage profiles in Fig. 9.8 that presence of SC considerably improves the minimum feeder voltage profile while worsening the situation for maximum feeder voltage profile. It implies that correction in reactive power compensation is warranted with increasing penetration of PVDG.

The feeder voltage profile of IEEE 34 node network responds with many maximum node voltage violations as the PV penetration increases. The voltage rise due to increasing PV penetration downstream the node 632 remains unchecked. It is worth noting here that the base-case voltages at nodes 844 and 848 with capacitors (without PV penetration) are in the range of 1.03–1.032 p.u. Minimum node voltage violations are not observed in any of the feeders.

Among all the feeders, IEEE 37 node feeder is observed to have no node voltage limit violations with increasing PV penetration. It should be noted that most of the feeder’s cable section are underutilized with regard to their current carrying capacity. IITGN-VGEC network is also a small network served by underground cable network. Its voltage profile also remains unaffected. However, the current carrying capacity of cables is not sufficient to support 100% PV penetration, and therefore, maximum PV penetration is restricted to 80% in this network.

9.7.2 Voltage Fluctuations and Voltage Flickers

Feeder voltages are affected by variations in real power injection from PV generators in two ways—change in voltages for a relatively longer duration with increasing value of PV generation and a short duration change in voltage as a result of sudden change in PV generation caused by, for example, cloud movement. The change in voltage for short duration is referred as voltage flickers [11]. A high-resolution time-series data—with resolution of one to several seconds—is required for estimating voltage flickers with quasi-static time-series simulations. However, the present analysis is based on a resolution of 15-min interval which is insufficient to capture flickers in node voltages. But it should be noted that the same analysis can be performed with high-resolution data.

9.8 Power and Energy Losses

In distribution networks, not only power losses but also energy losses are important. With increasing PV penetration, it is imperative to have an estimate of change in power and energy losses. If the network is small and highly dense with loads, the available local generation will not have much effect on losses of the network, whereas in a sparse and large network, the availability of local generation can significantly change the power and energy losses. Again, it is the load density in vicinity of the local generation that plays a critical role. If the remote load is fed by the local DG, power and energy losses significantly reduce as power is not fed from the remote substation. However, if the DG has to feed a remote load, significant change in losses may not be observed. On the other hand, increased PV penetration can also increase losses significantly if local generation exceeds all local demand resulting in reverse power flow from a DG towards substation. Some of these cases are clearly observed in the results discussed in this section.

9.8.1 Losses with Increasing Penetration of Photovoltaic Generation

The base-case power loss in IEEE 13 node network stands at 111 kW—approximately 3.1% of its active power demand, whereas the same is over 13% of its active power demand in IEEE 34 node network as reported in [23]. The geo-electric size and spread of the network when considered with load density explains the difference in active power losses for the two networks. The IITGN-VGEC spot network has its active power losses close to 1.5%. In IEEE 13 node network, energy losses decrease almost linearly with linear increase in PV penetration—with and without reactive support, Fig. 9.9a. However, IEEE 34 node network has no linear trend.

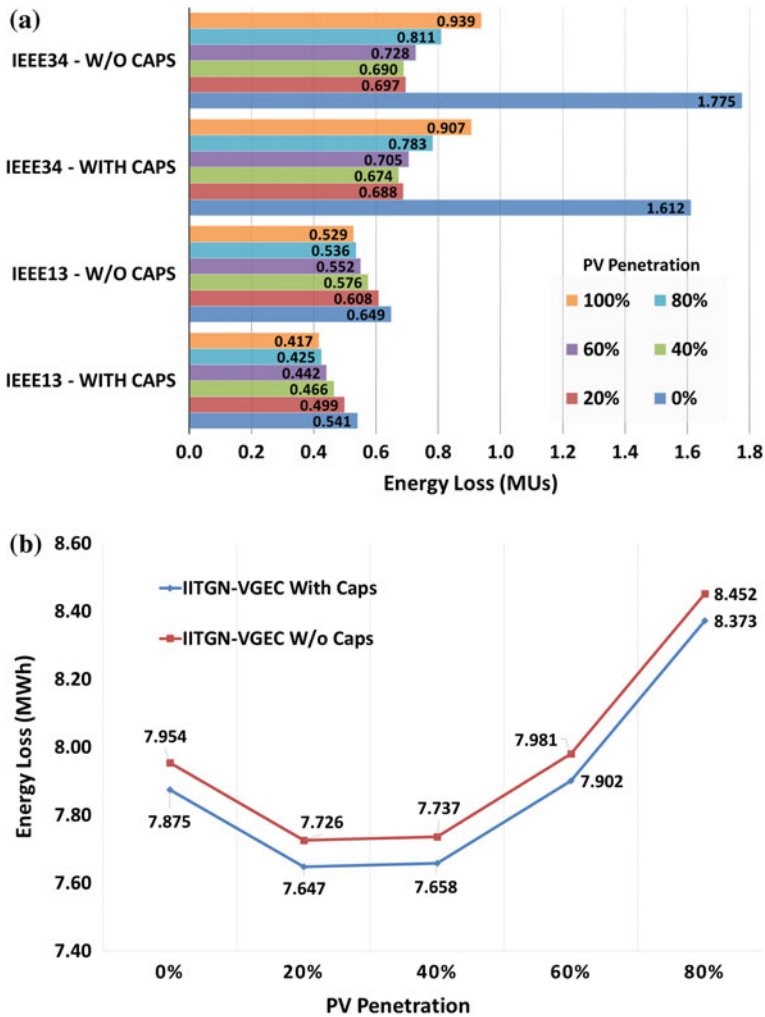


Fig. 9.9 Energy loss with increasing penetration in **a** IEEE 13 node and IEEE 34 node network **b** IITGN-VGEC network

Energy losses are highest without PV generation (at 1.612 MUs—with caps) and sharply reduce to 0.674 MUs with 40% PV penetration.

This is followed by increasing energy losses for increasing PV penetration—unlike the consistently decreasing trend in IEEE 13 node network. Similar observation also holds for the IITGN-VGEC network; wherein, the energy losses attain a minimum value at 20% PV penetration—as shown in Fig. 9.9b—followed by increasing losses.

The effect of capacitors is quite significant on the annual energy losses—as the energy loss reduces noticeably with capacitors, as shown in Fig. 9.9a, b in all the

Table 9.2 Energy drawn from source node (in MUs)

PV penetration (%)	IEEE 13 node		IEEE 34 node		IITGN-VGEC	
	With caps	W/o caps	With caps	W/o caps	With caps	W/o caps
0	23.08	22.91	14.20	13.48	0.53	0.53
20	22.02	21.86	9.55	8.91	0.50	0.50
40	20.97	20.82	8.94	8.32	0.47	0.47
60	19.91	19.77	8.33	7.73	0.43	0.43
80	18.86	18.73	7.72	7.14	0.40	0.40
100	17.82	17.70	7.11	6.55	–	–

networks. However, a reverse trend is observed in annual energy drawn in the presence of capacitors. A marginal increase in annual energy drawn is consistently observable in Table 9.2 with capacitors for two IEEE test feeders. But the same is not true for the IITGN-VGEC network as there is no measurable change in energy drawn. In case of IEEE test feeders, presence of capacitors measurably improves the feeder voltage profile. This also results in increased power consumption of voltage sensitive loads. Whereas, in case of IITGN-VGEC network, the overall voltage profile may not get affected with reactive support leading to no noticeable change in energy drawn, refer to Table 9.2. It should be noted here that the role of shunt compensation is different in these networks.

9.8.2 Reverse Power Flow

Reverse power flow is often observed due to a local DG capable of producing power in excess of local demand. For example, in IITGN-VGEC network, it is noted that the reverse power flow is observed for 80% PV penetration. Significant amount of real power flows back towards substation node for longer periods resulting in increased energy losses, Fig. 9.9b. Whereas, reverse power flow is observed in some parts of IEEE test networks but that does not significantly increase the energy losses.

The aggregate energy losses exhibit opposing trends with increasing PV penetration in IEEE test feeders. As discussed earlier, the reason for this opposite trends is attributed to the network topology and load density. Availability of balanced high power consumers in vicinity of the PV plant at far end of the network in IEEE 34 node feeder causes sharp fall in energy losses with increasing PV penetration up to 40%. However, energy losses tend to increase as the local generation starts feeding the load centres away from its location causing reverse power flow in a significant portion of the feeder. With fairly uniform load density on either side of the trunk feeder in IEEE 13 node network, energy losses exhibit a linear fall with increasing penetration and reverse power flow—even if caused—does not amount to increase in losses.

9.9 Real and Reactive Power Demand and Power Factor

It is obvious to expect reduction in real power demand at substation node with local PV generators. Normally, the daytime real power demand is expected to reduce based on the amount of PV penetration in a given distribution network. This also means that the daytime peak demand is also expected to reduce. However, as shown in the following sub-sections, the daytime peak reduction may not be observed in all the cases with increasing PV penetration. Similarly, reactive power demand as such may not be affected by real power injection from PV plants unless the PV inverter is set to operate at non-unity power factor. But in either case, if the real power injection is sufficient to raise the voltage profile of the downstream feeder, it can affect the reactive power demand significantly as it is squarely proportional to voltage magnitude. Some cases show non-negligible drop in substation power factor due to high PV penetration. Diverging and contradicting observations are made in the test cases explained below.

9.9.1 Real Power Demand at Substation Node

It is obvious to expect fall in daily peak demand at substation node with sizable local PV generation. However, no significant reduction in real power demand is observed in any of the three IEEE test feeders. The reason being the fact that the peak demand is observed to occur during evening hours when the PV generation drops rapidly to zero. Whereas in case of IITGN-VGEC network, significant reduction in maximum demand is observed as shown in Fig. 9.10. It should be noted here that IITGN-VGEC network serves an institutional load which peaks twice during daytime and has low demand after working hours. Therefore, the local generation helps in meeting the local demand and effectively reduces the maximum demand.

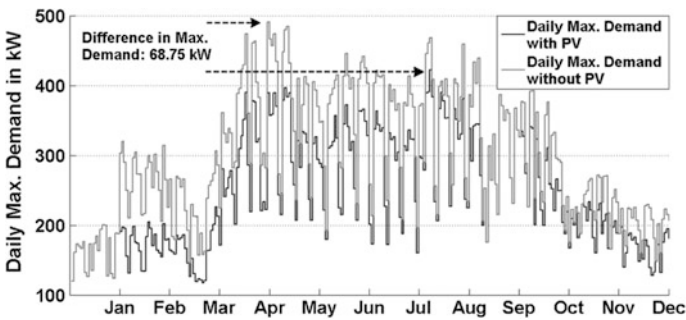


Fig. 9.10 Effect of local PV generation on daily maximum demand—reduced by 68.75 kW for the year 2012

9.9.2 Reactive Power Flow and Reactive Power Demand

While real power flow can substantially reduce due to local PV generators, the reactive power flow remains more or less unchanged unless the inverter of PV generators is configured to provide part reactive power. Figure 9.11a shows variation of real and reactive power demand affected by local real power injection from PV generator. With reduced real power demand and unchanged reactive power demand, power factor at substation node significantly reduces. This is also apparent in monthly average power factor which is discussed in next section.

Reactive power flow can even increase in the presence of local PV generation which is observed in IEEE 34 node network. This is due to the fact that the local generators can improve the voltage profile in close proximity of its location resulting in increased node voltages. The increased node voltages then in turn results in high reactive power injection from fixed capacitors if found nearby the local PV generators. This is precisely the case with IEEE 34 node network; wherein, the improved downstream voltages in remote end of feeder with a local PV generator results in high reactive power injection from nearby capacitors which further supports the increased node voltages. However, this effect is not cumulative as the real power injection from PV generators does not change with node voltages.

9.9.3 Power Factor at Substation Node

For maintaining a healthy power factor at source node, the ratio of reactive to active power needs to be kept under 0.5. It is an obligation of the bulk power consumers in many countries to maintain the power factor within a stipulated range. Figure 9.12a, b shows monthly average power factor for the IITGN-VGEC network and IEEE 13 node network, respectively. A dip in power factor is clearly visible in the months from February to April in IITGN-VGEC network. Low power consumption

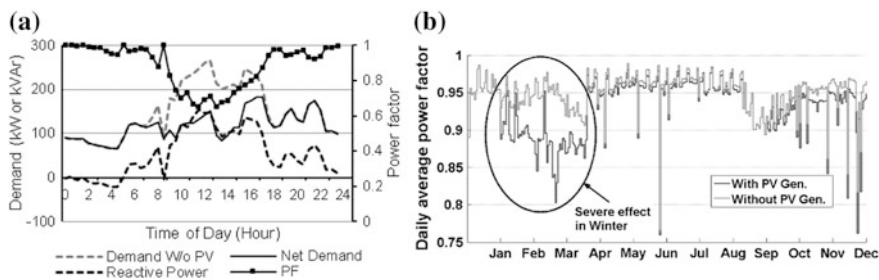


Fig. 9.11 a A typical diurnal variation in power factor on 27 February, 2012, along with real and reactive power demand and b Daily average power factor—effect of local PV generation is significant during winter days when local demand is substantially less

coupled with maximum PV generation (as negative effect of ambient temperature on PV modules is minimum in winter) causes a sharp dip in active power demand during sunshine hours. With reactive power demand unchanged, the ratio of reactive to active power goes well above 1.0 at peak PV generation and remains close to 0.75 on average during sunshine hours. This results in poor power factor at source end—with shunt compensation as shown in Fig. 9.12a.

In case of IEEE 13 node network, the average power factor without PV penetration and with capacitors remains close to 0.92. The power factor can further be improved with an additional capacitor (refer to Fig. 9.6, node 646) to 0.95 without PV penetration. This value remains fairly constant throughout without any DG in the network. However, the active power injection with 40% PV penetration causes average power factor to go well below 0.9 in the months from February to October—with capacitors. This can be explained as follows: the base-case reactive power demand of the network is close to 2000 kVAr with 700 kVAr provided by SCs placed at two nodes in the network. Thus, an average reactive power demand of 1.3 MVar is sourced from the substation end. With the active power injection to the tune of 40% (at peak) from PV plant, active power demand dips with reactive power demand unchanged. This leads to poor power factor during sunshine hours—more so with longer sunshine days of the year—resulting in lower average power factor.

IEEE 34 node feeder has a base-case demand of 1044 kVAr against its maximum active power demand of around 1800 kW. The network has reactive support of 750 kVAr in the form of SCs at two nodes (844 and 848, refer to Fig. 9.7a). It can be seen in Fig. 9.12c that the monthly average power factor is maintained very close to unity without any PV penetration with the given reactive support. It is also observed from the base-case voltage profile of the network that the node voltages remain within 1.02 to 1.05 p.u (where the capacitors are connected) which makes sure that the reactive support in excess of 1.04 p.u is supplied to the network. With active power injection from PV plant at node 890, the node voltages downstream of node 632 start increasing, refer to Fig. 9.7a. This leads to increased voltages at nodes 844 and 848 during sunshine hours resulting in increased reactive power injection from the 3-phase capacitor banks. It therefore turns out that the power factor with 40% PV penetration becomes leading at source end.

In order to avoid reactive component of current to flow in long feeders like IEEE 34 node network, balanced 3- Φ capacitor banks are provided towards the far end of the feeder, close to major loads. This arrangement works well without PV penetration. But with increasing PV penetration, further rise in node voltages at the far end of the feeder causes capacitors to provide excessive reactive power which flows back towards the source end—making the power factor leading at source node. This also contributes to increasing energy losses with PV penetration beyond 40%. IEEE 13 node feeder being small and having less reactive support does not respond with leading power factor with increasing PV penetration. However, like IITGN-VGEC network, it experiences low average power factor with increasing PV penetration. It can be seen that the geo-electric size and spread of the network complemented with

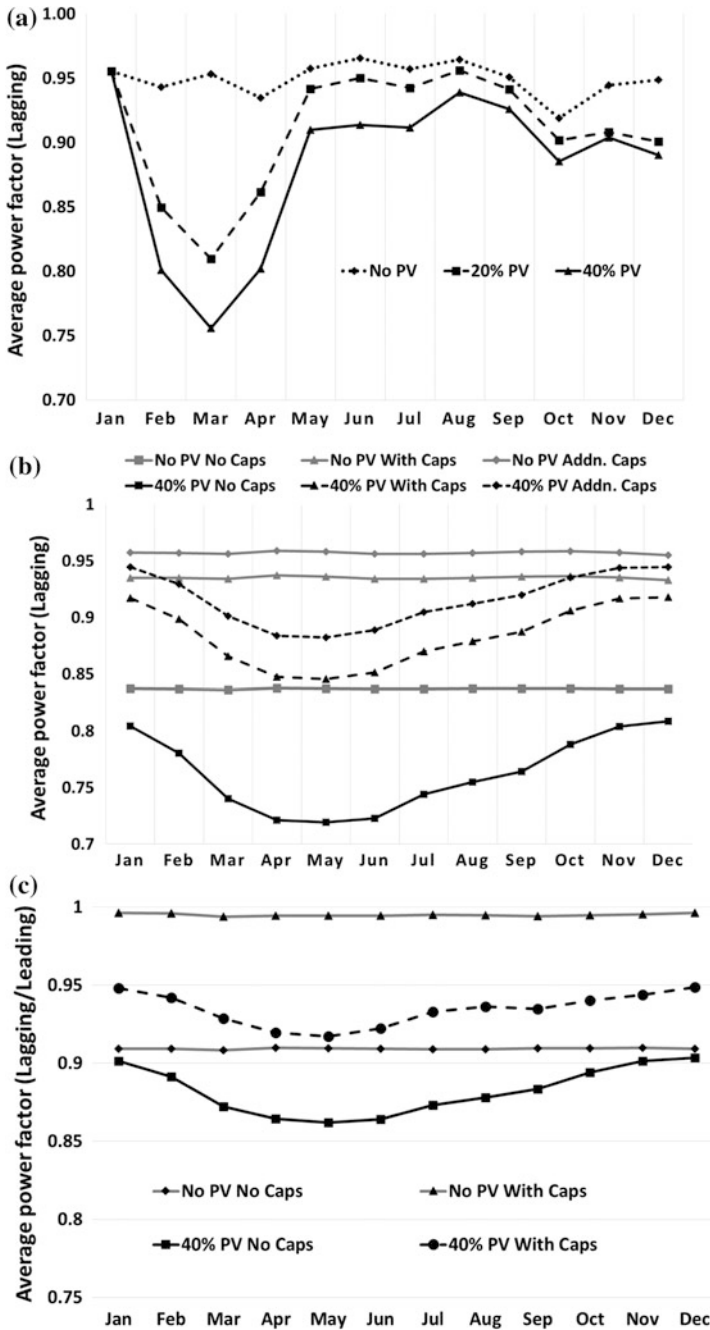


Fig. 9.12 Monthly average power factor at source node in **a** IITGN-VGEC network and **b** IEEE 13 node network, **c** IEEE 34 node network—40% PV with caps marked by *dark circles* represents a leading power factor, all other values refer to lagging power factor

the location and amount of reactive support determines power factor at source node in response to increasing PV penetration.

9.9.4 PV Inverter Power Factor and Its Control

As discussed in the preceding sub-sections, real power injection from local PV generators can lead to poor power factor at substation nodes. This can be corrected by making sure that the PV inverters are set to operate at non-unity power factor. Ability of PV inverters to deliver reactive power can be utilized as an advantage for improved power factor. However, this comes at the cost of curtailing some equivalent real power from the PV generator. Since, the revenue generated by PV generators is normally only for the real power they provide, the DG owners would not want to set the PV inverter at non-unity power factor. Nowadays, regulatory authorities and DSO therefore argue in favour of making it obligatory for the DG owners to make provision for reactive power while supplying real power from DGs. This way, the substation power factor can well be controlled without any extra effort from DSO with an added benefit of avoiding any extraneous flow of reactive power in the network over a considerable length of feeder. With ability to control the power factor setting continuously online in real time, such an obligation is not difficult to implement.

9.10 Performance of Voltage Regulators and Shunt Capacitors

9.10.1 Tap Change Operations of Automatic Voltage Regulators

Number of TCOs of VR determines the maintenance schedule and its lifespan. Here, the effect of PV penetration on TCOs of VR is analyzed in the presence/absence of capacitors. It is observed that the total number of TCOs increase almost linearly with increasing PV penetration from 0 to 3.5 MW (100% penetration of maximum demand). Inclusion of capacitors in the network also increases the TCOs. This is evident from Fig. 9.13a.

However, a close look at the Figures in Table 9.3 reveals that TCOs decrease in phase *A* and *C* in the presence of capacitors as against without capacitors for a given PV penetration. It is the phase *B* which shows the opposite trend, and its effect is dominant among the three phases leading to overall rise of TCOs due to inclusion of capacitors.

A single-line equivalent network analysis will erroneously lead to a conclusion that capacitors may increase the number of TCOs and that the situation may become

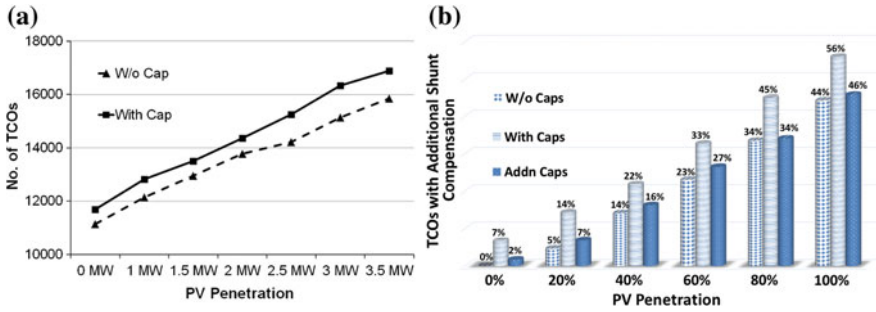


Fig. 9.13 a Effect of PV penetration and capacitors on total no. of TCOs—increasing trend and b TCOs of VR—effect of PV penetration and extra capacitor

Table 9.3 Phase-wise tap changing operations of VR

Case		VR tap changing operations				
Caps	PV (MW)	Ph A	Ph B	Ph C	Total	% Change
No	0	4101	2613	4425	11,139	—
Yes	0	4093	3199	4393	11,685	5
No	1	4571	2813	4757	12,141	9
Yes	1	4305	3761	4751	12,817	15
No	1.5	4881	3081	4993	12,955	16
Yes	1.5	4619	3953	4929	13,501	21
No	2	5173	3377	5225	13,775	24
Yes	2	4869	4339	5147	14,355	29
No	2.5	5363	3433	5411	14,207	28
Yes	2.5	5177	4671	5399	15,247	37
No	3.0	5695	3801	5643	15,139	36
Yes	3.0	5573	5053	5711	16,337	47
No	3.5	5937	4009	5897	15,843	42
Yes	3.5	5825	5163	5905	16,893	52

worse with increasing PV penetration. SCs provided in this feeder are at two nodes—node 675 and 611—as shown in Fig. 9.6. Node 675 has a balanced source of reactive power of 200 kVAR from each phase. But node 611 has a 100 kVAR of reactive power source in phase C only. It is observed that the reactive power requirement at source node from phase A is a minimum among three phases.

Thus, it is phase B with high loads at 645 and 646 that lacks compensation resulting in the increase in number of TCOs. After adding a capacitor as a 100 kVAR source in phase B at node 646—shown with dashed line in Fig. 9.6—number of TCOs is observed to be consistently less as compared to earlier capacitor connections. Not only this, the TCOs are also consistently less than that without capacitors. Detailed comparison of TCOs is depicted in Fig. 9.13b showing change

Table 9.4 TCOs of VR-1 in IEEE 34 node network

PV penetration (%)	VR-1: with caps			VR-1: without caps		
	Ph A	Ph B	Ph C	Ph A	Ph B	Ph C
0	9597	6597	7055	9643	8264	8022
20	8759	6349	5763	9387	4975	7864
40	9679	8591	8117	11,569	5773	7794
60	11,243	10,861	10,759	13,523	7861	9924
80	13,735	13,103	13,547	14,977	10,411	12562
100	16,509	15,705	16,359	17,221	12,831	15,356

Table 9.5 TCOs of VR-2 in IEEE 34 node network

PV penetration (%)	VR-2: with caps			VR-2: without caps		
	Ph A	Ph B	Ph C	Ph A	Ph B	Ph C
0	13,043	13,135	12,964	11,248	11,473	14,131
20	12,453	11,479	13,490	11,885	10,444	11,011
40	14,875	13,155	14,658	13,627	13,074	14,393
60	17,351	14,451	15,800	15,903	15,124	17,357
80	18,033	14,601	16,042	18,527	16,988	18,915
100	19,825	15,477	17,378	19,959	17,734	19,539

in number of TCOs as a percentage of TCOs without capacitors and without PV generation.

Phase-wise TCOs—aggregated over a year—to the increasing PV penetration reveals the effect of unbalance on each VRs in IEEE 34 node network as detailed in Tables 9.4 and 9.5. Following observations can be made from these results: (1) VR-1 and VR-2 has predictable rise in number of TCOs in each phase with increasing PV penetration. (2) Phase B and C in VR-1 respond with more TCOs in the presence of capacitors—collectively dominant over the reduction in phase A’s TCOs. This leads to overall increase in number of TCOs with capacitors. (3) Exactly opposite trend—as compared to phase-wise trends in VR-1—is exhibited by each phase in VR-2, i.e. phase B and C has reduced number of TCOs with capacitors. It should be noted here that the IITGN-VGEC network has no VRs, and hence no corresponding results are included.

The results for VR tap changing operations have multiple implications: (1) size, phase and placement of capacitors need to be reconsidered when a DG is integrated into the network (2) effect of capacitors on TCOs is based also on number of other factors such as the inherent phase unbalancing in the network, load density and topology of the network, and daily load profile (3) single-phase equivalent analysis of unbalance networks for control of capacitors and VR switching may not succeed in equal measure with actual unbalance scenarios. Results have shown that the capacitors can cause positive as well as negative impact on VR switching.

9.10.2 Switching of Shunt Capacitors in the Presence of PV Generators

Preceding sub-sections have demonstrated the effect of increasing PV penetration on TCOs of voltage regulators in the presence and absence of fixed capacitors. It is also observed that the fixed SCs can also give rise to leading power factor in the presence of increasing PV penetration due to improved node voltages. In these circumstances, it is prudent to opt for a switching sequence in coordination with PV Generators so as to minimize the voltage limit violations and also power and energy losses. One specific attempt in unbalanced distribution networks with PV generators is made in [26]; wherein, a strategy to design a switching sequence for manually switched capacitors is proposed for working and non-working days of different seasons.

Identifying the need for flexible dispatch of reactive power support in the DG integrated secondary distribution networks, the STS approach is applied to perform a selective search from the available dispatch options for SCs. In order to account for the seasonal and diurnal variations in demand to propose a switching sequence for SCs, data pre-processing exercise is performed, and characterized daily load profiles (CDLPs) are obtained for working and non-working days of three seasons—winter, summer and transition season. DPF simulations are then performed for the selected reactive power support options and best among them are chosen on hourly basis to derive the switching sequences. In essence, the proposed strategy in [26] starts with characterizing daily load profiles of different seasons to represent seasonal and diurnal variations in demand at substation node. This is followed by an exhaustive search among all possible switching options to find out optimum benefits with respect to losses and voltage profile for different seasons. The proposed switching sequences are shown in Fig. 9.14a, b for working and non-working days, respectively—all seasons. Level of reactive power support is shown hourly for three seasons.

9.10.3 Coordination of Voltage Regulators and Shunt Capacitors

In smart-grid environment where real-time communication between major components of distribution networks is feasible, coordination among voltage regulating equipment such as voltage regulators, OLTCs, LDCs and SCs can become an important tool in implementing dynamic solutions for optimizing daily operations of distribution networks. Voltage and temperature set-points have long been used for automatic switching of SCs. However, with coordination with DGs, voltage regulators and other major controlled equipment, a complex decision-making system can be utilized with remote switching abilities.

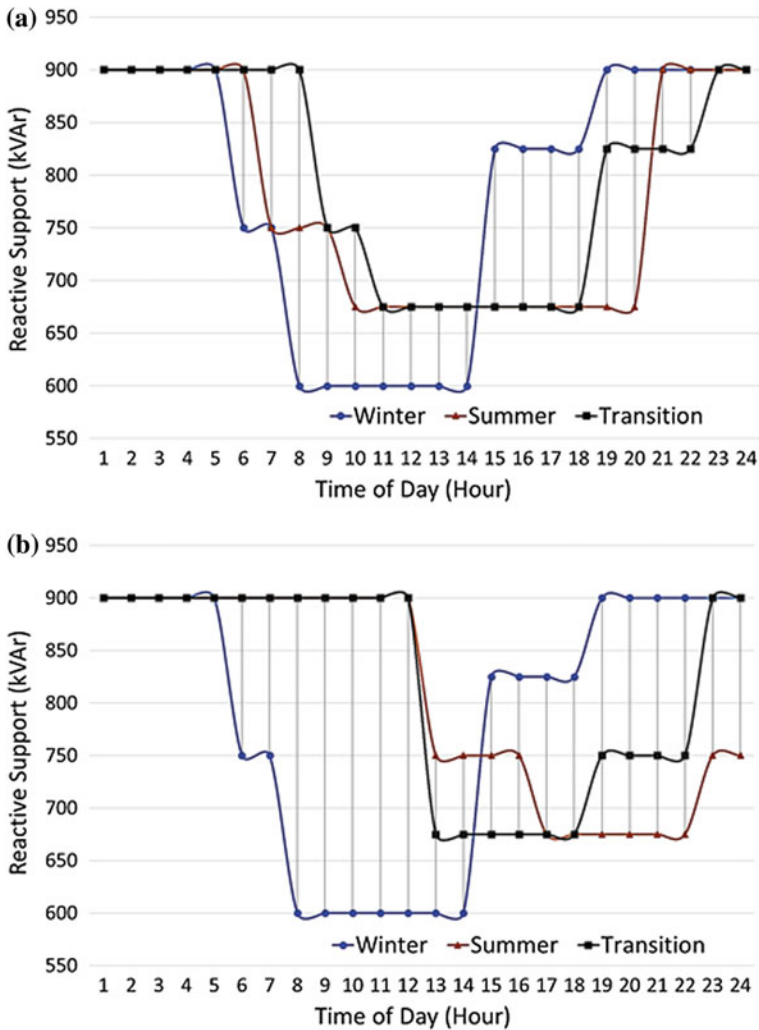


Fig. 9.14 Switching sequence for characterized DLPs of a working days and b non-working days

9.11 Role of Energy Storage Systems with PVDGs

Balancing of production and consumption of electricity at a medium to small scale is becoming an important area of active research with increasing thrust on green energy production and promotion of self-reliant microgrids. As pointed out in [27], the role of new energy storage systems is undergoing a change from static emergency back-up system to dynamic and fast-acting local resource in order to effectively harness the intermittent generation from DGs based on renewable energy resources. Apart from peak load shaving [28], and load levelling [29] in

low-voltage networks with a centralized electrical energy storage (EES), the benefits of EES are also explored for improved voltage controls schemes by considering multiple EES in different locations and phases in an unbalance distribution network [30]. In the presence of DGs such as PV generators, the sizing of EES needs to be revisited, as is done in [31]; whereas, the unwanted effects of voltage unbalance by local generation can also be mitigated by employing EES with proper control strategies as proposed in [32, 33]. More profound utilization of ESS is proposed in [34] with multi-objective battery energy storage system (BESS) integration for residential grids with PV generation.

A phase-wise dispatch strategy for BESS in low-voltage unbalance distribution networks is proposed in [35] by harnessing the unbalance among phases as an advantage to gain better peak load shaving and improved load levelling. In a two-stage exercise, the CDLPs are first obtained based on quantifying the ‘similarity’ in daily load profiles. The CDLPs are then used in the scheduling algorithm to estimate phase-wise potential available for discharging and recharging in every time slot. It is followed by arriving at a collective three-phase potential over an entire day with a consideration to balance of charge. The scheduling algorithm attempts to preserve the charge over a day and ensures conservation of charge weekly presuming that the variations in load profile would remain within estimated range provided by CDLP. Reduction in annual maximum demand and improved PAR show the potential of this approach in unbalance distribution networks.

9.12 Conclusion

Present day emphasis on RES-based DG has led to increased penetration of PVDG in low-voltage networks also. Size, type and location of DG affect the daily operations of these feeders. However, many other factors such as uncertainty in demand and generation, topological phase unbalancing, load density and geo-electric size of feeder play critical role in determining distribution feeders’ response to increasing penetration of PVDG. While effect of size, type and location of PVDG on performance of distribution networks are well researched, the feeder-specific factors such as its size, load density and phase unbalancing have gained little attention. Based on (a) detailed phase-domain modelling of all major components and (b) STS of three IEEE test feeders and one actual operating network in India, this chapter has presented results with several realistic case study scenarios to analyze the effect of high penetration of PVDG on operational parameters such as losses, feeder voltage profile, TCOs of VRs, power factor and peak demand at source node. It is demonstrated that size, location and phasing of shunt compensation need to be carefully revised with high penetration of PVDG, as it can adversely affect the feeder voltage profile and reactive power flows. It is also shown that the interaction of VR and shunt compensation can lead to very high number of TCOs in the presence of PVDG.

While the steady-state analysis of unbalanced distribution networks with high penetration of PVDG is presented in this chapter, it also hints towards the possible ways of mitigating the undesired effects of DG on daily operations of distribution networks. Switching sequences for SCs and use of grid-connected energy storage systems are presented as examples to improve network operations in the presence of PVDG.

References

1. Kersting WH (2012) Distribution system modeling and analysis, 3rd edn. CRC Press, Boca Raton
2. DoE and PNNL, “GridLAB-D.” 2014
3. Faiman D (2008) Assessing the outdoor operating temperature of photovoltaic modules. *Prog Photovolt Res Appl* 16:307–315
4. Villalva MG, Gazoli JR, Filho ER (2009) Comprehensive approach to modeling and simulation of photovoltaic arrays. *IEEE Trans Power Electron* 24(5):1198–1208
5. Walling RA, Saint R, Dugan RC, Burke J, Kojovic LA (2008) Summary of distributed resources impact on power delivery systems. *IEEE Trans Power Deliv* 23(3):1636–1644
6. Joshi KA, Pindoriya NM (2012) Impact investigation of rooftop solar PV system: a case study in India. In: 3rd IEEE PES international conference and exhibition on innovative smart grid technologies (ISGT Europe), pp 1–8
7. Arritt RF, Dugan RC (2011) Distribution system analysis and the future smart grid. *IEEE Trans Ind Appl* 47(6):2343–2350
8. Arritt RF, Dugan RC (2014) Value of sequential-time simulations in distribution planning. *IEEE Trans Ind Appl* 50(6):4216–4220
9. Dugan RC (2012) The value of quasi-static time series simulation. In: Distribution system modeling workshop
10. Ortmeyer T, Dugan R, Crudele D, Key T, Barker P (2008) Renewable systems interconnection study: utility models, analysis, and simulation tools. Sandia National Laboratory [Online, Accessed: 20 Sep 2015]
11. Broderick RJ, Quiroz JE, Reno MJ, Ellis A, Smith J, Dugan R (2013) Time series power flow analysis for distribution connected PV generation. Sandia National Laboratory [Online, Accessed: 18 Sep 2015]
12. Thomson M, Infield DG (2007) Network power-flow analysis for a high penetration of distributed generation. *IEEE Trans Power Syst* 22(3):1157–1162
13. Boehme T, Wallace AR, Harrison GP (2007) Applying time series to power flow analysis in networks with high wind penetration. *IEEE Trans Power Syst* 22(3):951–957
14. Boehme T, Harrison GP, Wallace AR (2010) Assessment of distribution network limits for non-firm connection of renewable generation. *IET Renew Power Gener* 4(1):64–74
15. Vittal E, O’Malley M, Keane A (2010) A steady-state voltage stability analysis of power systems with high penetrations of wind. In: IEEE PES general meeting, 2010, pp 1–8
16. Joshi KA, Pindoriya NM (2013) Risk assessment of unintentional islanding in a spot network with roof-top photovoltaic system—a case study in India. In: 2013 IEEE innovative smart grid technologies-Asia (ISGT Asia), pp 1–6
17. Electric Reliability Council of Texas, Inc.—Annual Load Profiles (2014) [Online]. Available: <http://www.ercot.com/mktinfo/loadprofile>
18. National Renewable Energy Laboratory—Data Resource (2014) [Online]. Available: <http://www.nrel.gov/gis/data.html>. Accessed: 20 Apr 2004

19. Smith J, Rylander M, Rogers L, Dugan R (2015) It's all in the plans: maximizing the benefits and minimizing the impacts of DERs in an integrated grid. *IEEE Power Energy Mag* 13 (2):20–29
20. Hoke A, Butler R, Hambrick J, Kroposki B (2013) Steady-state analysis of maximum photovoltaic penetration levels on typical distribution feeders. *IEEE Trans Sustain Energy* 4 (2):350–357
21. Stetz T, Marten F, Braun M (2013) Improved low voltage grid-integration of photovoltaic systems in Germany. *IEEE Trans Sustain Energy* 4(2):534–542
22. Agalgaonkar YP, Pal BC, Jabr RA (2014) Distribution voltage control considering the impact of PV generation on tap changers and autonomous regulators. *IEEE Trans Power Syst* 29 (1):182–192
23. Kersting WH (1991) Radial distribution test feeders. *IEEE Trans Power Syst* 6(3):975–985
24. "Torrent Power Ltd., Gujarat, India." Ahmedabad, 2014
25. American National Standard for Electric Power Systems and Equipment—Voltage Ratings (60 Hertz) ANSI C84.1-2011, 2011
26. Joshi KA, Pindoriya NM (2014) Reactive resource reallocation in DG integrated secondary distribution networks with time-series distribution power flow. In: 2014 IEEE international conference on power electronics, drives and energy systems (PEDES), pp 1–6
27. Roberts BP, Sandberg C (2011) The role of energy storage in development of smart grids. *Proc IEEE* 99(6):1139–1144
28. Rowe M, Yunusov T, Haben S, Singleton C, Holderbaum W, Potter B (2014) A peak reduction scheduling algorithm for storage devices on the low voltage network. *IEEE Trans Smart Grid* 5(4):2115–2124
29. Jung KH, Kim H, Rho D (1996) Determination of the installation site and optimal capacity of the battery energy storage system for load leveling. *IEEE Trans Energy Convers* 11(1):162–167
30. Wang P, Liang DH, Yi J, Lyons PF, Davison PJ, Taylor PC (2014) Integrating electrical energy storage into coordinated voltage control schemes for distribution networks. *IEEE Trans. Smart Grid* 5(2):1018–1032
31. Yang Y, Li H, Aichhorn A, Zheng J, Greenleaf M (2014) Sizing strategy of distributed battery storage system with high penetration of photovoltaic for voltage regulation and peak load shaving. *IEEE Trans Smart Grid* 5(2):982–991
32. Chua KH, Lim YS, Taylor P, Morris S, Wong J (2012) Energy storage system for mitigating voltage unbalance on low-voltage networks with photovoltaic systems. *IEEE Trans Power Deliv* 27(4):1783–1790
33. Alam MJE, Muttaqi KM, Sutanto D (2013) Mitigation of rooftop solar PV impacts and evening peak support by managing available capacity of distributed energy storage systems. *IEEE Trans Power Syst* 28(4):3874–3884
34. Tant J, Geth F, Six D, Tant P, Driesen J (2013) Multiobjective battery storage to improve PV integration in residential distribution grids. *IEEE Trans Sustain Energy* 4(1):182–191
35. Joshi KA, Pindoriya NM (2015) Day-ahead dispatch of battery energy storage system for peak load shaving and load leveling in low voltage unbalance distribution networks. In: IEEE PES general meeting, pp 1–5

Chapter 10

Distributed Solar-PV Generation: Impact on Voltage Control and Stability

Lasantha Meegahapola and Tim Littler

10.1 Introduction

Solar-PV generation has gained significant momentum over the past two decades as one of the most viable renewable power generation options and has contributed significantly to achieve sustainable energy targets in many power networks across the world. Consequently, electricity network operators have been required to solve various planning, operational, and control issues with the increasing penetration of distributed solar-PV generation [1, 2]. These issues include intermittency and volatility, voltage control and regulation, stability, and line congestion.

Unlike other renewable power generation technologies, the majority of solar-PV generators are connected to power distribution feeders. This paradigm shift has resulted in bidirectional power flow in distribution feeders, requiring utilities to manage potential voltage rise issues as solar-PV penetration levels increase [3]: in particular, voltage rise can affect consumer equipment protection and transformer lifetime. Therefore, distribution utilities must develop innovative methods to regulate distribution feeder voltage profile within stipulated limits defined by standards.

The preservation of voltage stability is one of the major challenges faced by the power network operators. Typically, synchronous generators provide a significant portion of network reactive power; however, as solar-PV penetration levels

L. Meegahapola (✉)
Electrical and Computer Engineering,
RMIT University, Melbourne 3000, Australia
e-mail: lasantha.meegahapola@rmit.edu.au

T. Littler
School of Electronics, Electrical Engineering & Computer Science,
the Queen's University Belfast, Co. Antrim,
BT9 5AH Belfast, Northern Ireland, UK
e-mail: t.littler@qub.ac.uk

increase, conventional synchronous generating units are displaced. Subsequently, network reactive power levels decrease as solar-PV generators are not capable of providing sufficient reactive power to replace large-scale reactive power levels provided by synchronous units [1, 2]. Therefore, careful management of voltage stability is required to sustain higher penetration of solar-PV generation.

This chapter investigates the distribution feeder voltage control and voltage stability issues resulting from greater penetration of solar-PV generation in electricity networks. Voltage stability is investigated using static and dynamic methods. This chapter also critically evaluates various strategies that can be used for distribution feeder voltage regulation and voltage stability improvement in the context of high penetration of solar-PV generation.

10.2 Modelling of Solar-PV Systems

A solar-PV system is comprised of a number of different components: a solar-PV panel, DC-DC boost converter, voltage source inverter (VSI), inverter controller and maximum power point tracking (MPPT) system, and an LCL filter. It is essential to model each component of the solar-PV system in detail to accurately represent the behaviour of the solar-PV system for dynamic simulations. A discussion of the dynamic simulation model of the solar-PV system is based on an actual 5 kW single-phase solar-PV system. The schematic diagram of the dynamic simulation model for a single-phase solar-PV system is shown in Fig. 10.1.

The 5 kW solar-PV array is comprised of two parallel rows, and each row contains ten series-connected PV panels. The parameters of an actual solar-PV panel [4] are shown in Table 10.1.

Using the parameters in Table 10.1, and by following the methodology outlined in [5], I-V and P-V curves were produced for the 5 kW PV array. It is assumed that the solar-PV array is exposed to an ambient temperature of 25 °C (Fig. 10.2).

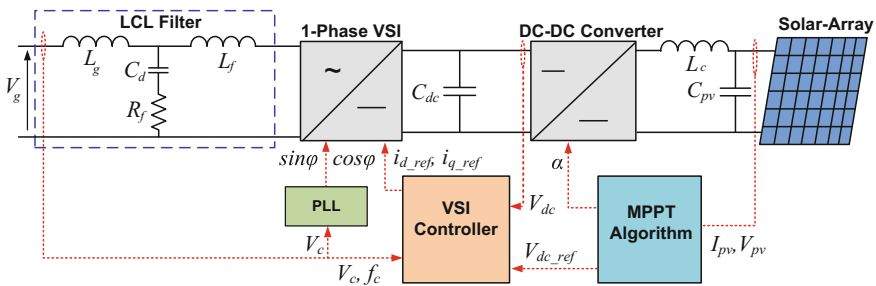
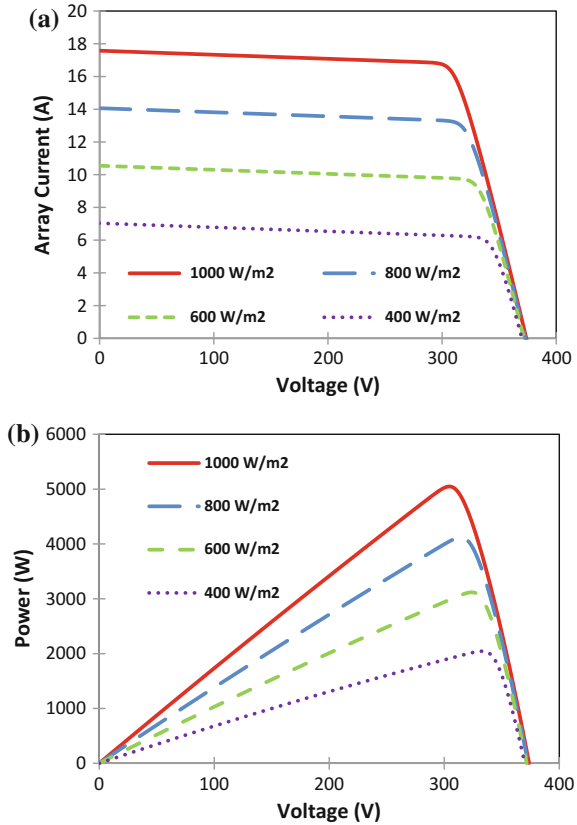


Fig. 10.1 Dynamic simulation model of a single-phase solar-PV system

Table 10.1 Solar-PV panel parameters

Parameter	Value
Nominal power— P_{MP} (Wp)	250
Nominal power voltage— V_{MPP} (V)	30.2
Nominal power current— I_{MPP} (A)	8.30
Open-circuit voltage— V_{OC} (V)	37.4
Short-circuit current— I_{SC} (A)	8.86
Module efficiency (%)	15.1
Temperature coefficient of P_{MPP} (%/°C)	-0.40
Temperature coefficient of V_{OC} (%/°C)	-0.27
Temperature coefficient of I_{SC} (%/°C)	0.024

Fig. 10.2 5 kW solar-PV array’s characteristics: **a** I-V curve and **b** P-V curve



The dynamic simulation model of the solar-PV system has the capability to respond variable solar irradiation and ambient temperature conditions. The MPPT system is based on the incremental conductance (IC) algorithm [6], since this algorithm performs well under rapid variations in solar irradiance. The VSI is rated

at 5.5 kVA and represented by an average converter model. The LCL filter parameters (L_g, C_d, L_f) are selected based on the methodology outlined in [7]. The DC link capacitor (C_d), input filter capacitor (C_{pv}), and DC coupling inductor (L_c) sizes were determined based on [8]. The solar-PV system was designed with the capability to control voltage at the point of common coupling (PCC) of solar-PV system. The solar-PV system active and reactive power control schemes are shown in Fig. 10.3.

Active power reference (P_{ref}) is determined by taking the difference between the actual (V_{dc}) and reference DC link (V_{dc_ref}) voltages, and then, by feeding the active power reference through a PI controller, the d -axis current reference (I_{d_ref}) is determined. A further control loop is established in the active power control loop in order to decrease active power generation during over-frequency events. The reactive power reference is determined by calculating the difference between the actual (V_{ac}) and reference (V_{ac_ref}) AC voltages at the solar-PV system PCC; then, the reactive power reference is feed through a PI controller to determine the q -axis current reference (I_{q_ref}). The current limiter d -axis current reference receives priority, while the q -axis current reference will be limited by the current rating of the inverter.

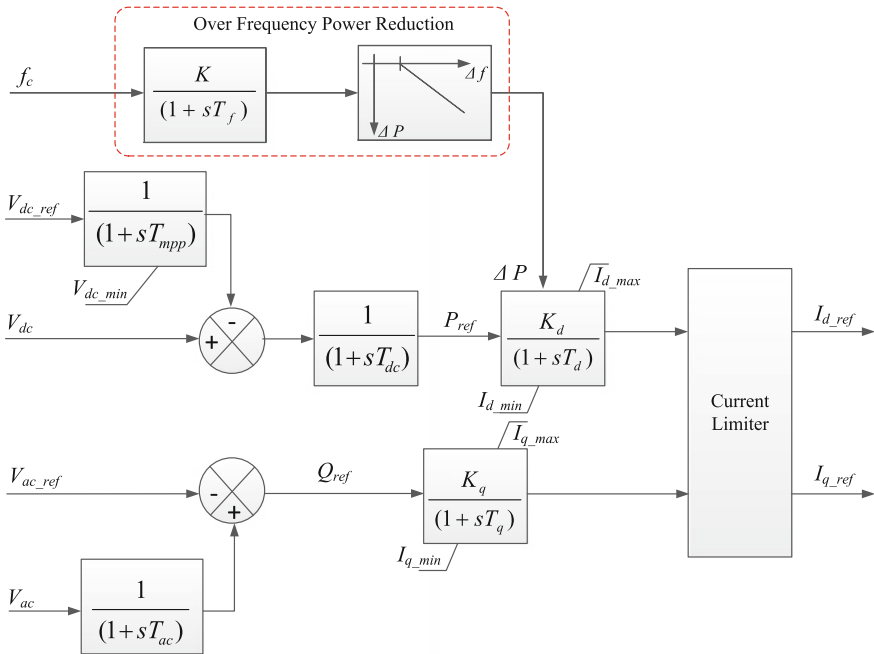
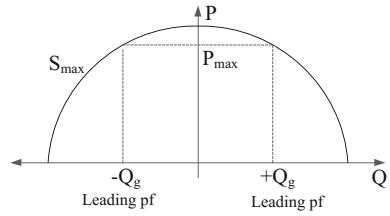


Fig. 10.3 Solar-PV model active and reactive power control scheme

Fig. 10.4 Solar-PV system capability curve



10.2.1 Active and Reactive Power Characteristics

The active and reactive power characteristics of the solar-PV system depend on the rating of the inverter. Typical inverters are rated with 10% more than the active power rating; hence, they can still produce some reactive power at the full active power output. The active and reactive power characteristics of a typical solar-PV system are shown in Fig. 10.4.

10.3 Voltage Regulation in Distribution Feeders

In conventional power distribution feeders, power flow is unidirectional; hence, the voltage decreases from the LV side of the distribution transformer towards the end of the feeder. This voltage drop can be easily understood by considering a distribution feeder with a line impedance of $R + jX$ and upstream source V_s , as in Fig. 10.5.

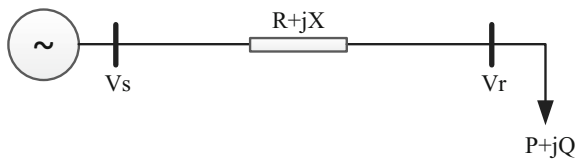
A $P + jQ$ load is connected at the receiving end; hence, the sending-end voltage (V_s) can be approximated by:

$$\begin{aligned}
 V_s = V_r &= (R + jX)I \quad \text{where } I = \frac{(P - jQ)}{V_r^*} \\
 \Rightarrow V_s &= \left[V_r + \frac{RP + XQ}{V_r} \right] + j \left[\frac{XP - PQ}{V_r} \right]
 \end{aligned}
 \tag{10.1}$$

The sending-end voltage given in (10.1) can be presented in the following form:

$$V_s = V_r + \Delta V_m + j\Delta V_p
 \tag{10.2}$$

Fig. 10.5 LV distribution feeder model



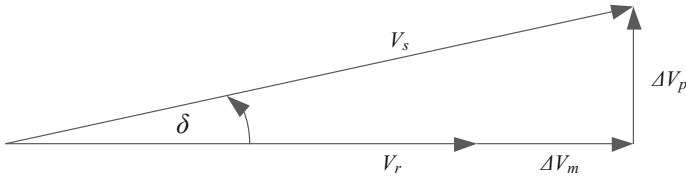


Fig. 10.6 Phasor diagram representation for voltage drop along a feeder

Magnitude change: $\Delta V_p = \frac{XP-RQ}{V_r}$ Phase change: $\Delta V_m = \frac{RP+XQ}{V_r}$.

This can be represented by a phasor diagram as follows (Fig. 10.6):

The phase angle δ is too small for distribution networks, and hence,

$$\Delta V_p \ll V_r + \Delta V_m \quad (10.3)$$

Therefore, the sending-end voltage can be approximated as follows:

$$V_s = V_r + \frac{RP + XQ}{V_r} \quad (10.4)$$

The voltage drop in the distribution feeder can be approximated as follows:

$$V_s - V_r = \Delta V = \frac{RP + XQ}{V_r} \quad (10.5)$$

The voltage drop in the distribution feeder depends on the power factor of the connected load and the impedance of the distribution feeder. The voltage drop in a distribution feeder is typically treated as voltage regulation. Voltage regulation is strongly influenced by the load power factor and is largest for a lagging power factor and smallest—or even negative—for a leading power factor. Voltage regulation is defined as follows:

$$\begin{aligned} \text{Voltage Regulation (VR)} &= (V_{nl} - V_{fl}) / V_{fl} = (V_s - V_r) / V_r \\ \Rightarrow \text{Voltage Regulation (VR)} &= \frac{(RP + XQ)}{V_r^2} \end{aligned} \quad (10.6)$$

where V_{fl} and V_{nl} are defined as voltage at full load and voltage at no load, respectively. When distribution feeder is considered, V_{fl} can be considered as voltage at the source, and V_{nl} can be considered as the voltage at the load end (receiving end).

Line losses are given by:

$$\begin{aligned} \text{Line Losses} &= I^2 R = \left[\frac{(P - jQ)}{V_r^*} \right]^2 R \\ \Rightarrow \text{Line Losses} &= \left[\frac{(P^2 + Q^2)}{V_r^2} \right] R \end{aligned} \tag{10.7}$$

According to Eq. (10.7), both active and reactive power contribute to line losses, and hence, reactive power flow in the distribution line must be minimised in order to decrease the line losses.

Illustration An 11 kV 15-km distribution feeder delivers power to a 150 kW load. The distribution feeder has a per-length impedance of $0.3 + j0.031 \Omega/\text{km}$. The load power factor is changed from 0.8 lagging to 0.8 leading while maintaining the receiving-end voltage at 11 kV. The distribution feeder voltage drop and line losses are shown in Fig. 10.7.

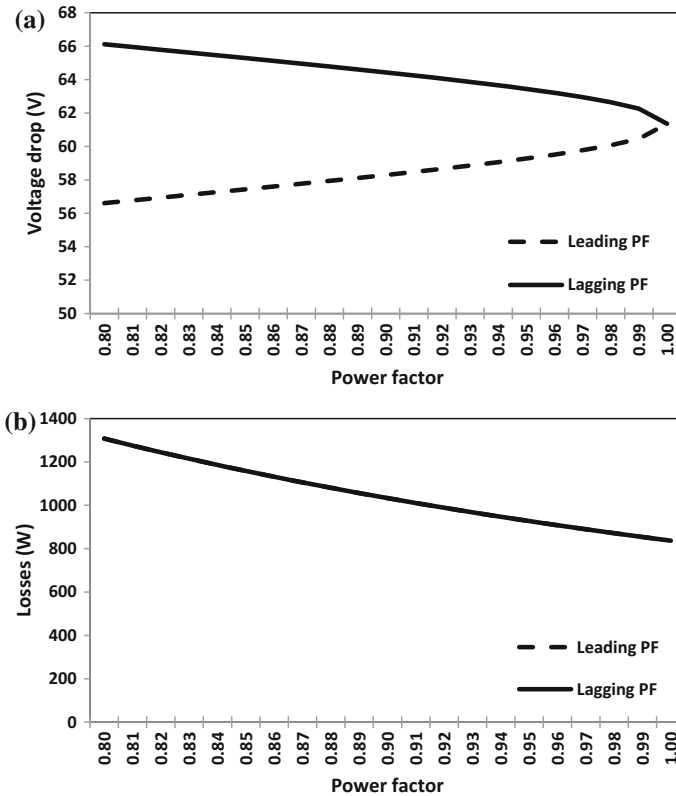


Fig. 10.7 Distribution feeder performance: **a** voltage drop variation with power factor and **b** line loss variation with power factor

According to Fig. 10.7a, when the leading power factor of the load is increased from 0.80 to 0.99, the voltage drop increased from 56.61 to 60.46 V. Conversely, a lagging power factor of the load increased from 0.80 to 0.99 and the voltage drop decreased from 66.12 to 62.26 V. However, irrespective of the load operating as either a leading or a lagging power factor, system losses are decreased with an improved load power factor. Therefore, a large reactive power has resulted in greater losses in the network.

10.3.1 Voltage Regulation Standards

Typically, utilities follow the voltage regulation standards stipulated by various standard bodies, such as IEC. The IEC 60038 is one of the commonly adopted standards in many countries for voltage regulation. The stipulated LV/MV voltage ranges in IEC 60038 are given in Table 10.2.

According to Table 10.2, the voltage regulation limits for different voltage levels are defined in three different time frames and peak impulse voltage is defined separately. The steady-state voltage is the main focus of this chapter; hence, according to the IEC 60038 for a residential distribution feeder, the allowable voltage range is 216.2–253 V. Typically, the voltage varies along the feeder based on the connected load; hence, distribution utilities apply various strategies to maintain the voltage within these limits.

10.3.2 Methods to Improve Distribution Feeder Voltage Regulation

Aforementioned, distribution utilities use various methods to regulate the feeder voltage profile and maintain the voltage within limits stipulated by standards. The following approaches are commonly used in distribution feeders to regulate the feeder voltage profile:

Table 10.2 Voltage standards specified in IEC 60038

Voltage level (kV)	Timescale			Peak impulse voltage (kV)
	Steady state	<1 min.	<10 s	
<1	+10% to -6%	+14% to -10%	+50% to 100% (L-E) +20% to 100% (L-L)	6
1 to 6.6	±6% (± 10% rural)	±10%	+80% to 100% (L-E) +20% to 100% (L-L)	60
11				95
22				150
66	±10%	±15%	+50% to 100% (L-E) +20% to 100% (L-L)	325

- Tap-changing transformers,
- Shunt capacitors and reactors,
- Line voltage regulators,
- Static VAR systems, and
- Static synchronous compensators (STATCOMs).

- Tap-Changing Transformers.

Tap-changing transformers can be divided into two types: (i) offload and (ii) on-load transformers. Typically, offload transformers are used in LV distribution feeders, while on-load units are used for primary distribution feeders. Offload transformers are typically *fixed tap*, and their tap settings are typically changed during summer and winter periods.

It is assumed that two tap-changing transformers are installed at both the sending- and receiving-end of the feeder as shown in Fig. 10.8.

Then, by considering a single-phase equivalent circuit of a radial distribution feeder with two tap-changing transformers (as shown in Fig. 10.8), the voltage drop of the feeder can be calculated as given in Eq. (10.8), [9],

$$\Delta V = V_1(t_s/t_r) - V_2 \approx \frac{RP + XQ}{t_r^2 V_2} \tag{10.8}$$

The product of t_r , t_s is maintained at unity; this ensures that the overall voltage level remains in the same order.

In certain cases, voltage control of the transformer includes a measurement of current through the transformer. This is known as line-drop compensation (LDC) and allows the voltage to be controlled at a remote point of the distribution feeder, as shown in Fig. 10.9. The LDC is incorporated with the measured voltage as follows:

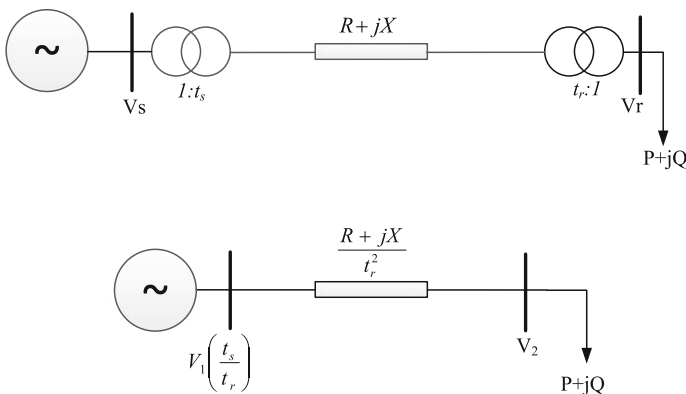


Fig. 10.8 Distribution feeder with tap-changing transformers

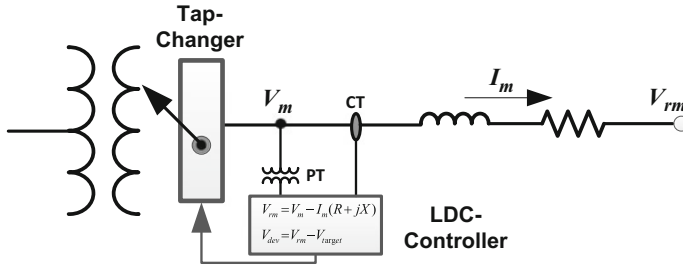


Fig. 10.9 Line-drop compensation (LDC) scheme of the transformer [10]

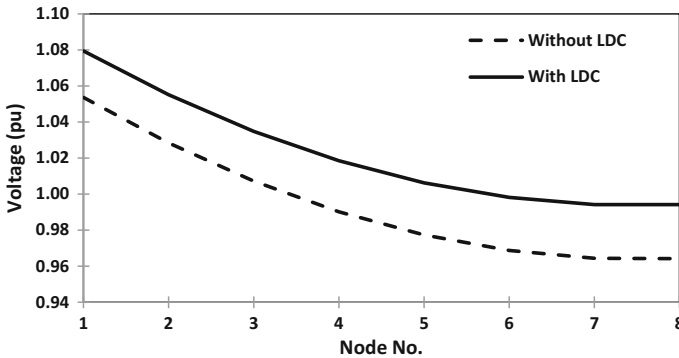


Fig. 10.10 Comparison of feeder voltage profile with and without LDC

$$V_{rm} = V_m - I_m(R + jX)$$

$V_{dev} = V_{rm} - V_{target}$ where V_m , I_m , and V_{rm} are the measured voltage, measured current, and effective voltage at the remote location of the feeder. Then, the voltage deviation (V_{dev}) from the target voltage (V_{target}) is calculated to determine the tap position.

Figure 10.10 illustrates the voltage profile of an MV distribution feeder with and without LDC.

It must be noted that transformer is located at the node 1, while the LDC is applied to control the voltage at node 8 to arrest the voltage at 1 pu (with a lower bound of 0.99 pu and an upper bound of 1.01 pu). According to Fig. 10.10, once the LDC is applied for node 8, transformer tap position is adjusted to arrest the node 8 voltage within the bounds despite the voltage rise at node 1.

- Shunt Capacitors and Reactors

Shunt capacitors are used to compensate lagging power factor loads, while the reactors are used for feeders which generate reactive power on lightly loaded

cables. Shunt capacitors are directly connected to the busbar and tertiary winding of transformers. In certain conditions, capacitors are installed along a distribution feeder to compensate for losses and any voltage drop. The reactive power dispatch from a capacitor or a reactor is given by:

$$Q = \frac{V^2}{X}, \quad X_c = \frac{1}{\omega C} \quad \text{or} \quad X_L = \omega L \quad (10.9)$$

The reactance X can be either capacitive (X_C) or inductive (X_L). However, if the voltage decreases, the reactive power produced by the shunt capacitors and reactors will decrease in proportion to the square of the voltage.

- Line Voltage Regulators

Voltage regulators are autotransformers with automatically adjusting taps. Commonly, regulators provide a range from -10 to $+10\%$ with 32 steps. A single-phase regulator has three terminals: the source (S), the load (L), and the source-load (SL). The series winding is between S and L. The line current is measured at the load terminal (L) using a current transformer (CT), while the voltage is measured between the load (L) and source-load (SL) terminals using a potential transformer (PT). A regulator controller uses the measured current and voltage values to determine the required tap setting for regulation. Tap changing is normally performed by a relay mechanism with three settings: (i) *Set Voltage*—the desired output voltage of the regulator; (ii) *Bandwidth*—parameter used to initiate tap operation when the difference between the set voltage and measured voltage exceeds half of the bandwidth; and (iii) *Time Delay*—the waiting time between the time when the voltage goes out of band and when the controller initiates a tap [11]. If the voltage is still out of bounds after a tap change, the controller makes additional tap changes until the voltage is brought within bounds. A schematic diagram of the regulator windings is shown in Fig. 10.11.

- Static VAr Compensator (SVC) Systems

An SVC is a combination of thyristor-switched capacitor banks and thyristor-controlled inductors. SVCs are capable of delivering both capacitive and inductive reactive power based on the terminal voltage of the SVC. However, as the capacitors and inductors of the SVC are directly exposed to the terminal voltage, reactive power capability is affected by the magnitude of the terminal voltage. Therefore, an SVC performs well only when the terminal voltage is >0.9 pu, and its reactive power capability linearly decreases with reduction in terminal voltage [12]. Therefore, SVCs are not effective under large system contingencies, such as short-circuit faults as they fail to deliver adequate reactive power to compensate a voltage drop in the network.

- Static Synchronous Compensators (STATCOMs)

A STATCOM is comprised of a voltage source convertor (VSC), a capacitor, and a coupling transformer. If the terminal voltage magnitude is less than the preset

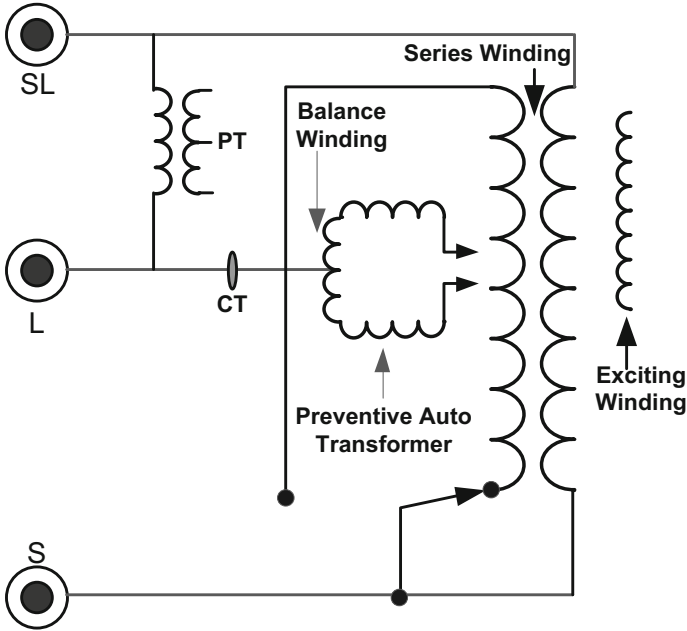


Fig. 10.11 Configuration of the line voltage regulator

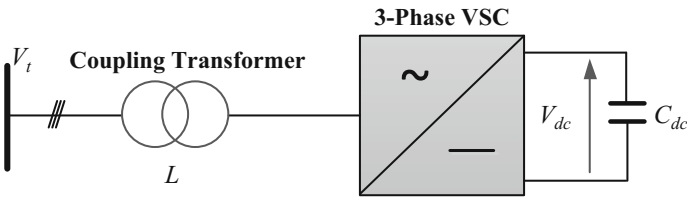


Fig. 10.12 A schematic of a STATCOM

voltage, then the STATCOM will generate capacitive reactive power, whereas if the terminal voltage is higher than the preset voltage, the STATCOM will render inductive reactive power. During normal operation, the STATCOM voltage lags the network voltage by a small angle in order to maintain capacitor charge. The main advantage of the STATCOM is its superior dynamic performance even at very low voltage levels [12]. Typically, a STATCOM is capable of delivering the rated capacitive reactive power even at very low voltage levels such as 0.2 pu (Fig. 10.12).

10.4 Impact of Solar-PV Generation on Feeder Voltage Regulation

Renewable power penetration has significantly increased during the last decade due to improvements in power electronic converter technologies and government directives to reduce greenhouse gas emissions (GHGs). The majority of renewable generation has been integrated at medium-voltage (MV) and low-voltage (LV) distribution feeders; generation sources of this type are commonly known as distributed generators (DGs). Conventional distribution networks are designed for power flow in one direction; however, with the integration of DGs, power flow is potentially bidirectional, resulting in variation (with possible violation) of voltage standards [13]. In particular, during high DG penetration levels, the upper voltage limit can be exceeded. The penetration level is defined as the ratio of power generated by the DG to the total connected load to the feeder, in percentage at any given time. If the penetration level is over 50%, then it could be considered as high penetration.

Consider the distribution feeder shown in Fig. 10.13, which contains a distributed generator connected at the load end of the feeder. The distributed generator generates $P_G + jQ_G$.

With the distributed generator installed at the end of the feeder, the voltage at the receiving end depends on the net power at the receiving-end busbar. Therefore, Eq. (10.4) can be modified based on the net power flow at the load end of the distribution feeder,

$$V_s - V_r = \Delta V = \frac{RP_{\text{net}} + XQ_{\text{net}}}{V_r} \quad (10.10)$$

where $P_{\text{net}} = P_L - P_G$ $Q_{\text{net}} = Q_L - Q_G$.

Therefore, if P_{net} is negative ($P_G > P_L$), then the distribution feeder voltage will increase and voltage limits may be violated at the end of the feeder.

Example A 20-km-long 11-kV distribution feeder provides power to a 450 kW, 140 kVA load. The distribution feeder has 0.3 Ω /km resistance and 0.031 Ω /km reactance. A 750 kVA distributed generator is installed at the load end of the feeder. Calculate the voltage rise in the feeder when it generates 650 kW active

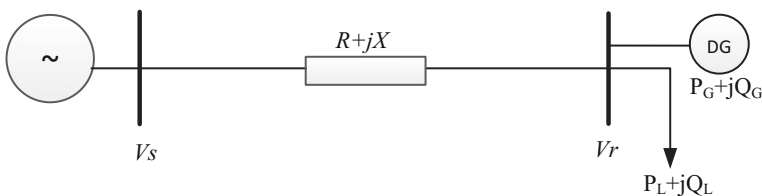


Fig. 10.13 Distribution feeder with a distributed generator

power at 0.9 leading power factor. Assume that the receiving-end voltage is 11 kV when the distributed generator is connected to the network.

$$\text{Voltage Rise } (\Delta V) = \frac{RP_{\text{net}} + XQ_{\text{net}}}{V_r}$$

$$\Delta V = \frac{(0.3 \times 20) \cdot (450 - 650) \times 10^3 + (0.031 \times 20) \cdot (140 - 314.81) \times 10^3}{11 \times 10^3}$$

$$\Delta V = -119 \text{ V}$$

The distribution feeder voltage will, therefore, increase by 119 V due to DG.

10.4.1 Voltage Rise Issues with Solar-PV Generation

In order to demonstrate the potential for voltage rise in distribution feeders with solar-PV generation, a simulation was carried out in DIGSILENT Power Factory for a LV distribution feeder (see Fig. 10.16). The LV distribution feeder was modelled with three separate single-phase feeder segments, and each phase contains 8 domestic households separated by 43.05 m. The distribution line has an impedance of $0.315 + j0.259 \Omega/\text{km}$. Also, it is assumed that every household has a 3.3 kVA solar-PV system. The simulation scenarios are shown in Table 10.3.

Figure 10.14 illustrates the voltage profiles observed for phase A of the distribution feeder for all three scenarios.

As illustrated in Fig. 10.14, for scenario 1 (midday scenario) voltage limits have not been violated at any of the distribution feeder nodes. However, the lower voltage limit has been violated by scenario 2 due to the high-load demand of the domestic households during the evening peak. Therefore, distribution transformer tap position is raised to an upper value (optimised position) in order to maintain the feeder voltage within stipulated voltage limits at all conditions, and this is depicted in scenario 3. It must be noted that the optimised tap position for scenarios 3 and 4 is position 4, and the additional voltage per tap is 2.5%. According to Fig. 10.14, in scenario 3, the feeder voltage is now maintained within the stipulated voltage limits at all nodes of the distribution feeder. As the distribution transformers are typically fixed-tap transformers, this will be fixed for an entire season. Therefore, when solar-PV is added to the network, it is likely that the feeder voltage increases

Table 10.3 Solar-PV scenarios for each household

Scenario	Load	Solar-PV	Description
1	2.4 kW, 0.95 pf lag	0	Midday, zero tap
2	12 kW, 0.95 pf lag	0	Evening peak, zero tap
3	12 kW, 0.95 pf lag	0	Evening peak, optimised tap
4	2.4 kW, 0.95 pf lag	3 kW	Midday with solar, optimised tap

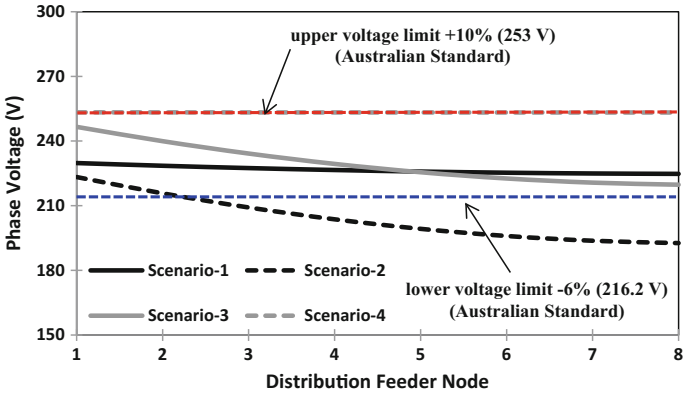


Fig. 10.14 Distribution feeder voltage variation

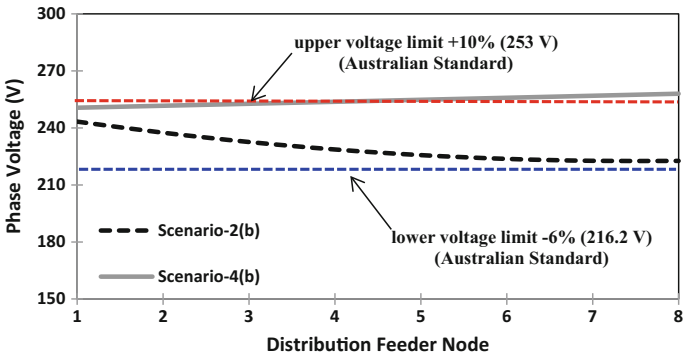


Fig. 10.15 Distribution feeder voltage variation with capacitor banks

beyond stipulated limits during low-load, midday conditions. This is evident from scenario 4 which depicts voltage increase due to the solar-PV generation.

Furthermore, it must be noted that increasing the tap position to improve the network voltage profile during high-load conditions would not be effective for long-distribution feeders as it may excessively increase the voltage at the start of the feeder. Therefore, for long-distribution feeders, capacitor banks are employed at the middle or near end of the distribution feeders in order to improve the voltage profile during high-load conditions, while maintaining the tap position at a low value. In order to demonstrate the deployment of capacitor banks in distribution feeders, an additional scenario was simulated considering load generation data given for scenario 2 and scenario 4 in Table 10.3. It is noted that the tap position is maintained at 3, while a capacitor bank rated at 20 kVAr per phase is now connected to the end of the feeder. Distribution feeder voltage profiles are shown in Fig. 10.15.

According to Fig. 10.15, when both the transformer tap operation and capacitor banks are used at the distribution feeder (scenario 2(b)), a much flatter voltage profile can be achieved in comparison with an optimised transformer tap position (scenario 2). For example, when an optimised transformer tap position is used, the distribution feeder voltage varies from 246.6 to 219.7 V, while for scenario 2(b) where both transformer tap operation and capacitor banks are used, the distribution feeder voltage profile varies only between 243 and 223 V. However, once the solar-PV generation is added to the distribution feeder (scenario 4(b)) with the same configuration (i.e. with fixed-transformer tap and capacitor banks), the distribution feeder voltage profile violates the stipulated limits at a much higher magnitude than scenario 4. Thus, voltage rise issue becomes much aggravated with solar-PV generation when transformer taps and capacitor banks are used in distribution feeders.

10.4.2 Voltage Regulation Methods with Distributed Solar-PV Generation

In order to mitigate the voltage rise in distribution feeders with solar-PV generation, the following methods are proposed by researchers, some of which are already applied to power distribution networks:

- Reactive power compensation by solar-PV inverter [3, 14],
 - Energy storage systems (ESSs) [15], and
 - Electronic tap-changing transformers [3].
- Reactive Power Compensation by solar-PV inverter.

As shown in Fig. 10.4, a solar-PV inverter has considerable reactive power capability, and that could be used to improve the voltage profile of the distribution feeder. Theoretically, reactive power compensation through solar-PV generation can be explained as follows:

Let us assume that both the sending-end voltage (V_s) and receiving-end voltage (V_r) are maintained at the same value by reactive power compensation at the receiving end of the feeder. Then, the voltage drop of the feeder becomes zero ($\Delta V = 0$). Therefore, Eq. (10.10) becomes:

$$\Delta V = \frac{RP_{\text{net}} + XQ_{\text{net}}}{V_r} = 0 \Rightarrow Q_{\text{net}} = -\frac{RP_{\text{net}}}{X} \quad (10.11)$$

Thus, in order to compensate for the voltage variation due to the change in P_{net} , Q_{net} must be maintained at $(-RP_{\text{net}}/X)$. Hence, the distributed generator must provide reactive power given by Eq. (10.12):

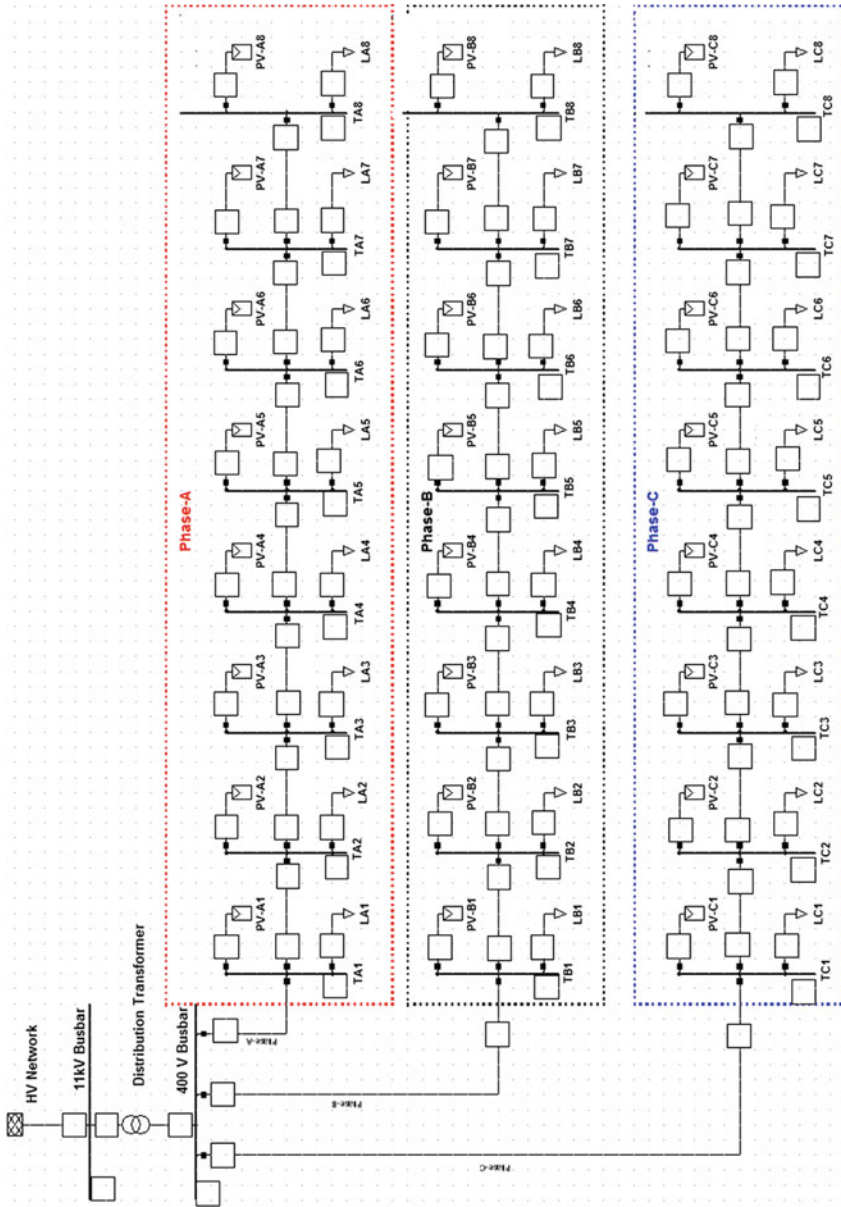


Fig. 10.16 Distribution feeder model

$$Q_G = \frac{RP_{\text{net}}}{X} + Q_L \quad (10.12)$$

Based on the installed load in the distribution feeder and generation level of the solar-PV generator, the actual reactive power capability available from the solar-PV generation would be insufficient to mitigate the voltage increase in the distribution feeder; hence, some other methods must be used for distribution feeder voltage management.

- Energy Storage Systems

Energy storage systems (ESSs) can be used to overcome the voltage rise in distribution feeders. ESSs can be installed either at an individual household as single-phase units, or at a large scale as three-phase units on the distribution network. A schematic of an ESS is shown in Fig. 10.17.

ESSs are typically comprised of a VSI, line filter, coupling transformer, DC link and DC-DC converter, and energy source. Different types of energy sources are used, and this includes battery banks (e.g. Li-Ion), flywheels, supercapacitors, and superconducting magnetic storage. ESSs are capable of both delivering and absorbing active and reactive power to maintain the voltage at a given or set value.

- Electronic Tap-changing Transformers

Conventional distribution transformers are fixed-tap transformers; hence, tap positions are set manually, once every season. Therefore, distribution utilities do not have any control over tap position; thus, the control capability of the feeder voltage is fixed. Electronic tap-changing transformers offer flexibility at low cost in comparison with mechanical on-load tap-changing transformers. In electronic units, tap changing is performed by semiconductor switches, using either back-to-back thyristors or insulated gate bipolar transistors (IGBTs) [16]. The ability to move from one tap to any other tap repeatedly at half-cycle intervals enables high-speed voltage regulation in the distribution feeder, while it also helps manage the distribution feeder voltage profile with installed solar-PV generation to overcome cloud cover effects [3].

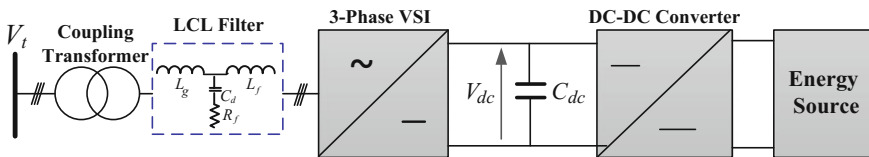


Fig. 10.17 Schematic diagram of an energy storage system

10.4.3 Case Study—Mitigation of Voltage Rise in Distribution Feeders with Solar-PV Generation

This section presents a case study to demonstrate the methods used for distribution feeder voltage regulation with installed solar-PV generation. The network presented in Fig. 10.16 and scenario 4 (presented in Table 10.3) has been used to demonstrate the capability of voltage regulation. In fact, two voltage regulation methods have been investigated separately: (i) solar-PV inverter reactive power capability (each solar-PV inverter absorbs 1.4 kVAr) and (ii) 50 kVA ESS installed at the end of the feeder. The ESS is configured to maintain the voltage at the end of the feeder at a predefined value. It is noted that the simulation was completed with the tap position set at 2 (2.5% change in each tap) and a 20 kVAr capacitor bank at each phase of the distribution feeder.

From Fig. 10.18, it is apparent that the distribution feeder voltage profile has substantially improved by using the reactive power capability of the inverter. It is also noted that 1.4 kVAr is the maximum reactive power output of the solar-PV inverter as it generates 3 kW (inverter rating 3.3 kVA). However, this reactive power capability is insufficient to maintain voltage levels below the stipulated maximum limit (in the Australian standard) at all nodes in the distribution feeder. Therefore, after node 6, the distribution feeder voltage exceeds stipulated limits. However, by employing a 50 kVA ESS, the distribution feeder voltage profile is maintained within stipulated limits.

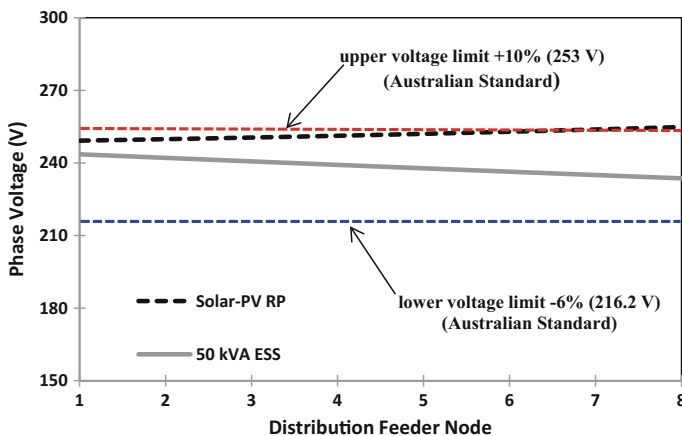


Fig. 10.18 Voltage regulation techniques with solar-PV generation

10.5 Voltage Stability with Solar-PV Generation

10.5.1 Voltage Stability Definition

Voltage stability is defined as the ability of a power network to maintain steady-state voltage levels across all nodes of the power network following a contingency in the network [17]. Voltage stability is strongly correlated with network reactive power capability, and conventional synchronous generators contribute significantly to network reactive power reserve. When renewable power penetration levels increase, synchronous generation is withdrawn from the energy portfolio; hence, reactive power reserves decrease as the renewable sources are incapable of providing the equivalent level of necessary reactive power reserve. If a significant solar-PV generation is installed in the distribution grid, the reactive power capability is limited due to inverter constraints and by the distribution transformer installed upstream of the distribution feeder [3].

Voltage stability can be evaluated using dynamic and static methods. In dynamic methods, a credible contingency is created in the network, and subsequently, voltage profiles are evaluated in the time domain to verify the network capacity to recover from a voltage dip created during the contingency [18]. Static voltage stability methods are developed based on load flow analysis, and commonly used static methods are P-V curve, Q-V curve, and modal analysis [18]. P-V curve analysis is mainly used to evaluate the impact of network load increase on voltage instability. The Q-V curve was used in previous studies to evaluate the voltage stability with renewable power generation as the renewable power generators are more likely to affect the reactive power reserve of the system [19]. Since distributed solar-PV generation also affects the network reactive power reserves, Q-V curve analysis is used in this chapter to evaluate the static voltage stability of the network.

The Q-V curve is generated by varying the reactive power at a given busbar and then determining the voltage at the same busbar by solving load flow for the network. Therefore, the Q-V curve method determines busbar voltage sensitivity to reactive power. Figure 10.19 illustrates the Q-V curve for a network busbar.

At steady state, the busbar voltage is maintained at V_{ss} , while the reactive power at the steady state is Q_{ss} . When the reactive power is progressively increased, the bus voltage will decrease progressively until it reaches $dQ/dV = 0$. After this point, busbar voltage will further decrease even though the reactive power is decreased further.

10.5.2 Static Voltage Stability with Solar-PV Generation

The static voltage stability with solar-PV generation is evaluated using Q-V curve analysis for the model IEEE-14 bus network with solar-PV generation added to the LV network of the IEEE model. It is noted that solar-PV generation is added to the

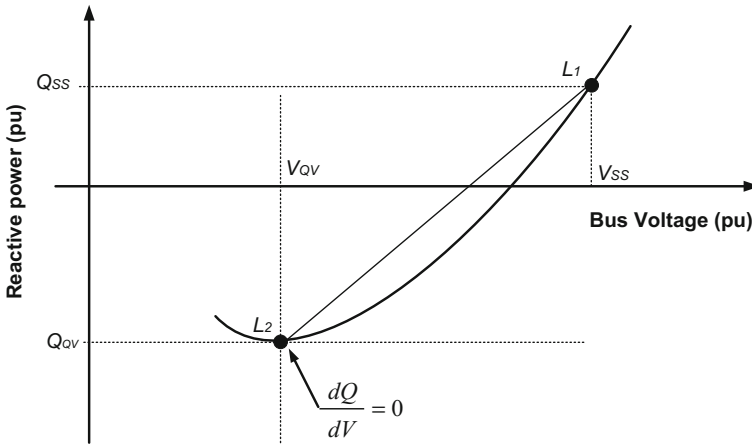


Fig. 10.19 Q-V curve method

Table 10.4 Generation portfolio for solar-PV scenarios

Scenario	Active power dispatch (MW)					
	Bus 1 (SG)	Bus 2 (SG)	Bus 11 (solar-PV)	Bus 12 (solar-PV)	Bus 13 (solar-PV)	Bus 14 (solar-PV)
1	232.9	40	0	0	0	0
2	210.2	40	5	5	5	5
3	188.0	20	15	15	15	15
4	168.3	0	25	25	25	25
5	128.1	0	35	35	35	35

network as aggregated three-phase solar-PV units, and synchronous generators are progressively withdrawn from the generation mix as the solar-PV levels increase. Solar-PV generation was added to buses 11, 12, 13, and 14, and solar-PV levels at each busbar were increased from 5 to 35 MW with 10 MW steps; subsequently, a Q-V curve was generated for each busbar. Also, note that the solar-PV generation was operated at unity power factor. The generation portfolio for each solar-PV scenario is shown in Table 10.4. It is noted that the synchronous machines at busbars 3, 6, and 8 are operated in synchronous condenser mode.

Figure 10.20 illustrates the V-Q curves generated for bus 3 and bus 12.

As illustrated in Fig. 10.21, integration of solar-PV generation with the distribution network rendered impacts in two ways. In terms of the high-voltage network, bus voltage stability decreased with solar-PV generation inclusion. For example, the voltage instability point reached -232 VAr consumption (with no solar-PV generation), while with a 140 MW solar-PV contribution (i.e. scenario 5) the instability point reached -181 VAr. Conversely, for the LV network, the V-Q instability point improved with the inclusion of solar-PV generation. Moreover, the voltage

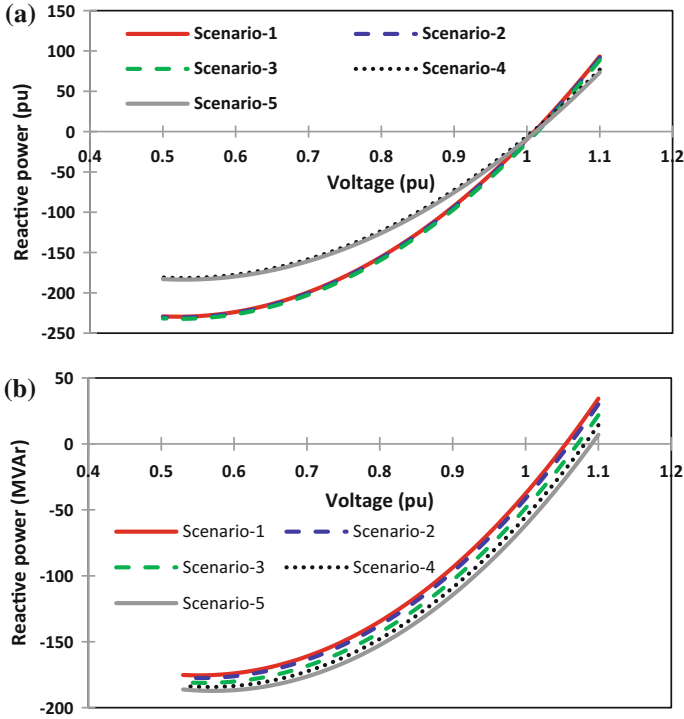


Fig. 10.20 V-Q curves: **a** bus 3 and **b** bus 12

instability point reached -177.5 VAr consumption (with no solar-PV generation), whereas with 140 MW solar-PV contribution, the instability point reached -187 VAr. Therefore, by integrating distributed solar-PV generation, the static voltage stability effectively improved in the HV network, while for the LV network, voltage stability deteriorated.

10.5.3 Dynamic Voltage Stability with Solar-PV Generation

The dynamic voltage stability was evaluated by creating a 150-ms three-phase, short-circuit fault at an HV node (bus 3) and on the LV network (bus 13). The scenarios 1 and 5 outlined in Table 10.4 have been analysed for dynamic voltage stability. For scenario 5, two additional scenarios were considered: (a) solar-PV with no dynamic voltage support and (b) solar-PV with dynamic voltage support. A dynamic three-phase solar-PV model outlined in [20] was used for simulations. The bus voltage variations following the short-circuit faults for scenarios 1 and 5 are shown in Fig. 10.22a and b, respectively.

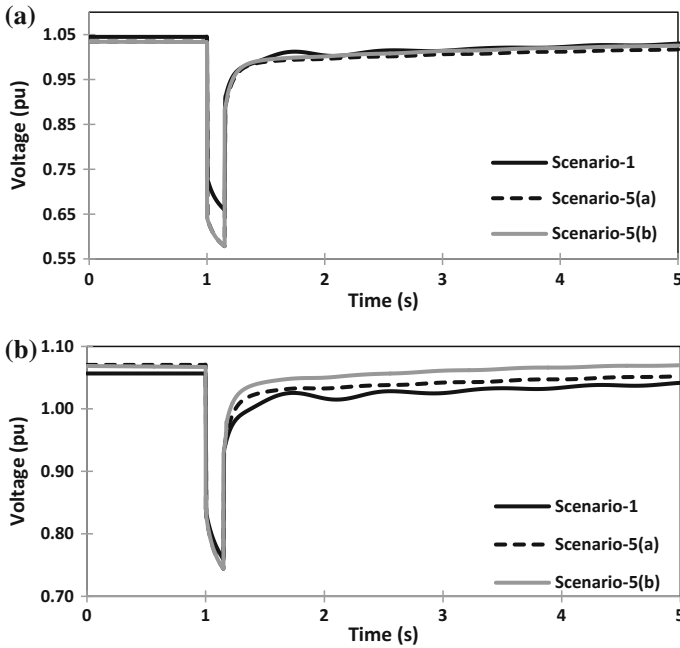


Fig. 10.21 Fault in the HV busbar (bus 3): **a** voltage variation at bus 2 and **b** voltage variation at bus 11

From Fig. 10.22, when a fault occurs at the HV busbar, it adversely affects the HV network for the scenario which includes solar-PV generation. Without solar-PV contribution, the HV network bus 2 voltage decreased to 0.65 pu, whereas with solar-PV inclusion, the bus voltage decreased to 0.56 pu. This occurred as a consequence of the removal of the conventional generation when the distributed solar-PV generation was added to the network. However, when the distributed generation is equipped with dynamic voltage support, this supports rapid HV bus voltage recovery—faster than with dynamic reactive power support.

In terms of the LV network buses, addition of distributed solar-PV generation significantly contributes to the recovery process of the LV bus voltage (i.e. bus 11) following the disturbance in the HV network. In particular, when the solar-PV generation is equipped with dynamic voltage support (scenario 5(b)), significant improvement in voltage recovery following the HV network fault is evident.

Similar observations are apparent when a fault occurs in the LV network (see Fig. 10.22), except that the LV network voltages decrease substantially compared to the HV network buses due to the close proximity to the fault.

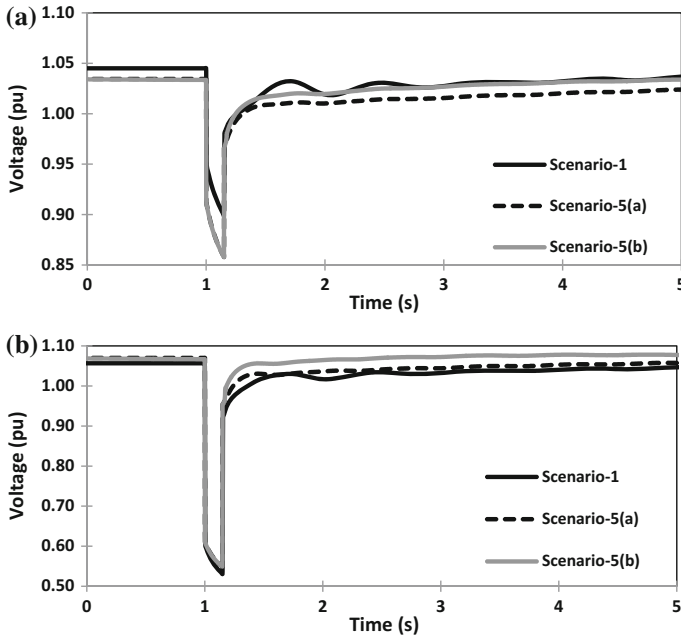


Fig. 10.22 Fault in the LV busbar (bus 13): **a** voltage variation at bus 2 and **b** voltage variation at bus 11

10.6 Discussion and Conclusions

This chapter has investigated feeder voltage control and voltage stability issues arising from high penetration of solar-PV generation in distribution networks. Voltage regulation methods have been investigated for conventional distribution feeders. This chapter has demonstrated that conventional voltage regulation approaches are broadly inadequate in managing distribution feeder voltage profiles when solar-PV generation is installed as voltage profiles can exceed stipulated limits imposed by relevant standards. Therefore, innovative methods that use power electronics technologies for voltage regulation, such as electronic tap-changing transformers, STATCOM, and ESS, have been presented to solve associated problems. This chapter has used several case studies to demonstrate the applicability of presented methods to manage distribution networks governed by stipulated standards and limits in voltage profile regulation. The results have further shown that multiple strategies may be required to regulate the feeder voltage profile under very high solar-PV penetration.

In addition, this chapter has investigated the impact of a high penetration of PV-solar generation on voltage stability using static and dynamic methods. The V-Q curve method, which analyses static voltage stability, demonstrates that solar-PV generation has an impact on HV and LV networks: as solar-PV generation

is added to an LV network, it adversely affects the voltage stability of the HV network, while the LV network benefits from improvements in voltage stability with the integration of solar-PV units. Furthermore, observations from dynamic voltage stability analyses indicate that while solar-PV generation can potentially weaken an HV network, integration can, however, strengthen LV distribution networks.

References

1. AEMO (2014) Renewable energy integration in South Australia. Available via <http://www.aemo.com.au/Electricity/Planning/Integrating-Renewable-Energy>. Accessed 4 Apr 2015
2. Fraunhofer ISE (2015) Recent facts about photovoltaics in Germany. Available via <https://www.ise.fraunhofer.de/en/publications>. Accessed 12 Mar 2015
3. Kabiri R, Holmes G, McGrath B, Meegahapola L (2015) LV grid voltage regulation using transformer electronic tap changing, with PV inverter reactive power injection. *IEEE J Emerg Sel Top Power Electron* 3(4):1182–1192
4. REC Peak Energy Series (2015) High performance solar modules. Available via <http://www.recgroup.com/en>. Accessed 17 Dec 2015
5. Villalva MG, Gazoli JR, Filho ER (2009) Comprehensive approach to modelling and simulation of photovoltaic arrays. *IEEE Trans Power Electron* 24(5):1198–1208
6. Hussein KH, Mota I (1995) Maximum photovoltaic power tracking: An algorithm for rapidly changing atmospheric conditions. *IEE Proc Gener Transm Distrib* 142(1):59–64
7. Liserre M, Blaabjerg F, Hansen S (2005) Design and control of an LCL-filter-based three-phase active rectifier. *IEEE Trans Ind Appl* 41(5):1281–1291
8. Feng G, Ding L, Loh PC, Tang Y, Wang P (2009) Indirect dc-link voltage control of two-stage single-phase PV inverter. In: *IEEE Energy Conversion Congress and Exposition (ECCE 2009)*, Sep 2009
9. Weedy BM, Cory BJ, Jenkins N, Ekanayake JB, Strbac G (2012) *Electric power systems*, 5th edn. Wiley, London
10. Short TA (2005) *Electric power distribution equipment and systems*. CRC Press (Taylor and Francis), New York
11. Siemens (2008) JFR-instruction-manual. Available via: <http://www.energy.siemens.com/us/pool/us/power-distribution/voltage-regulators>. Accessed 2 Apr 2016
12. Kundur P (2014) *Power system stability and control*. McGraw-Hill, New York
13. Steffel SJ, Caroselli PR, Dinkel AM, Liu JQ, Sackey RN, Vadhar NR (2012) Integrating solar generation on the electric distribution grid. *IEEE Trans Smart Grid* 3(2):878–886
14. Alam MJE, Muttaqi KM, Sutanto D (2015) A Multi-mode control strategy for VAR support by solar PV inverters in distribution networks. *IEEE Trans Power Syst* 30(3):1316–1326
15. Alam MJE, Muttaqi KM, Sutanto D (2012) Distributed energy storage for mitigation of voltage-rise impact caused by rooftop solar PV. In: *IEEE Power and Energy Society General Meeting*, San Diego, CA, USA
16. Faiz J, Siahkollah B (2011) *Electronic tap-changer for distribution transformers*. Springer, Charm, Switzerland
17. Kundur P et al (2004) Definition and classification of power system stability IEE/CIGRE joint task force on stability terms and definitions. *IEEE Trans Power Syst* 19(3):1387–1401
18. Cutsem TV, Vournas C (1998) *Voltage stability of electric power systems*. Springer, Switzerland

19. Amarasekara HWKM, Meegahapola L, Agalgaonkar AP, Perera S (2013) Impact of renewable power integration on VQ stability margin. In: Power Engineering Conference (AUPEC). Hobart, Tasmania
20. Meegahapola L, Robinson D (2016) Dynamic modelling, simulation and control of a commercial building microgrid In: Smart Power Systems and Renewable Energy Systems Integration, Springer, Cham, Switzerland

Chapter 11

Techno-economic Evaluation of Grid-connected Solar Photovoltaic Power Plant for Rural Banks

Rajashekar P. Mandi

11.1 Introduction

Electrical energy is the most essential part of all processes and human being due to its simplicity in usage at end use [1]. In order to achieve the sustainable energy growth of the country with the increased population and energy demand and to provide more energy to the rural population, the non-conventional and renewable energy sources need to be installed and used. Due to the wider gap between power supply and demand, the electrical distribution companies have implemented power cuts to rural areas to balance the power supply and demand. To overcome the shortage of electrical power in rural areas, the renewable energy systems need to be used in large [2]. Because of acute shortage of power in rural grids, the distribution companies are switching off the power supply for a period of 8–10 h in a day. The rural banks generally operate from 09:00 h to 17:00 h on all working days (experience of about 4–5 h power cut daily). At present in all the rural branches, two of 3 kVA UPS are installed to provide the uninterrupted power supply (UPS) (refer Fig. 11.1). Out of two UPS, one will be in service continuously and other will be in standby (redundancy) mode. As soon as the main UPS fails, other UPS will take over the total load through static switch. These UPS are designed to provide energy autonomy for a period of four hours continuously. If the power failure is more than four hours, 5 kVA diesel generator (DG) set is installed to provide the power supply through UPS in each branch.

Because of heavy power cut, the load on UPS is increasing. Due to the poor maintenance of batteries and UPS, these UPS are not providing the required power for the computers all the time. The DG sets are being operated to compensate the power. The average cost of supply for utility power is \$0.06–0.10 per kWh and the

R.P. Mandi (✉)
School of Electrical and Electronics Engineering, REVA University,
Bangalore, India
e-mail: rajashekarmandi@yahoo.com

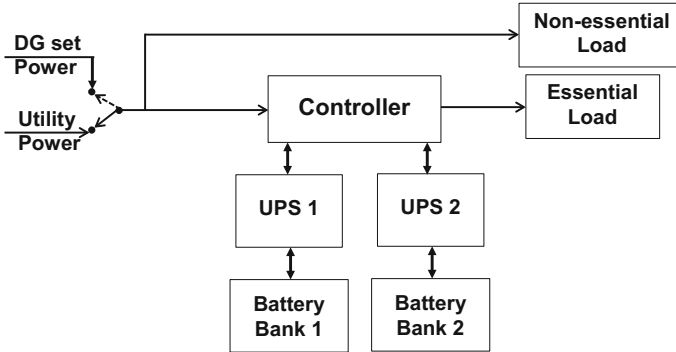


Fig. 11.1 Schematic of UPS supply to load

cost of power generation from DG sets is in the range of \$0.32–0.40 per kWh. The cost of power generation through DG set is almost 4–6 times of the power from utility.

11.2 Power Crisis

In order to evaluate the power crisis and critically view the performance of UPS systems in rural banks, the study is carried out in 10 branches of rural banks in Karnataka. In one of the rural bank branches, 3 kVA UPS was installed with 9 numbers of 75 Ah, 12 V batteries. The batteries are arranged 3 in series with 3 parallel circuit to provide 36 V and 675 Ah to provide the autonomy of 4 h minimum. Figure 11.2 gives the variation in battery discharge voltage with load. The open-circuit voltage was 40 V DC across battery terminals before applying load (open-circuit voltage). As soon as the load was applied (load was varying between 0.85 and 1.05 kW), the voltage drops down to 37.7 V which is slightly higher than the design battery voltage (rated voltage: 36 V). The voltage gradually drops down to 35.5 V in a time period of 15 min and the “battery low” hooter started and the voltage of battery further drops down to 34.1 V in a time period of 33 min and finally the UPS was tripped. The UPS supported the load for period of 33 min which is very low compared to design autonomy of 4 h. The batteries are not getting charged because of prolonged power cut from utility supply. The life of batteries is also reduced due to improper charge–discharge cycle and improper maintenance of UPS and batteries.

In another branch office, there are two 3 kVA UPS (operated in parallel redundancy mode). One main UPS will be in service during normal operation, and in case of problem with the main UPS, the static switch will change over to other UPS. Each UPS is provided with 8 numbers of 12 V, 75 Ah sealed maintenance

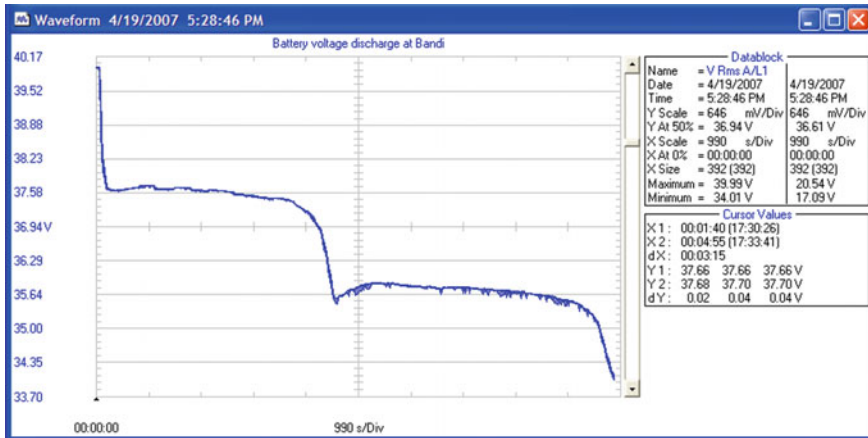


Fig. 11.2 Battery voltage discharge with load

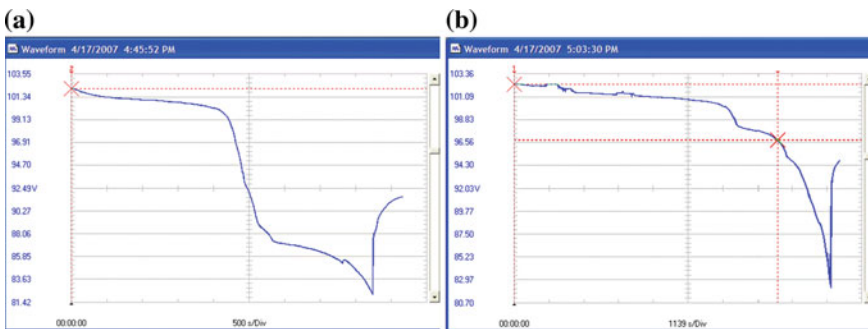


Fig. 11.3 Battery voltage discharge with load at a UPS 1 and b UPS 2

free (SMF) batteries. All 8 batteries are connected in series to get the design voltage of 96 V. Figure 11.3a, b gives the variation in battery discharge voltage with load at UPS 1 and 2, respectively. The open-circuit voltage at UPS 1 was 102.18 V DC across battery terminals. As soon as the load was applied (load varying between 0.78 and 1.09 kW), the voltage drops gradually down to 82.2 V after 16 min 30 s for UPS 1. The static switch transferred automatically to UPS 2. The open-circuit voltage at UPS 2 was 102.4 V DC across battery terminals. Then, the voltage of UPS 2 drops gradually down to 82.1 after 34 min 38 s. The total backup time was 51 min. As per the specification of the battery, cutoff voltage is 84 V but the battery was cutoff at 82.2V for UPS 1 and 82.1 V for UPS 2. These batteries are getting deep discharge.

Therefore, in many of the rural bank branch offices, the UPS is not providing the required power backup and DG sets are being operated to provide the backup power immediately after the utility power failure.

Fig. 11.5 Variation of monthly daily average solar irradiance

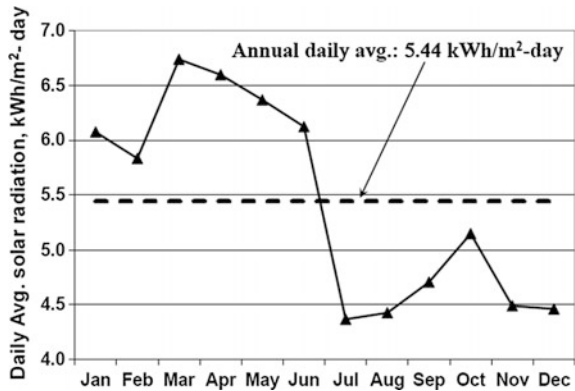


Fig. 11.6 Variation of monthwise hourly ambient temperature

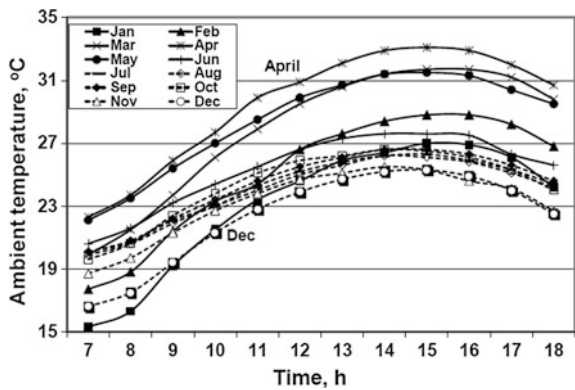


Figure 11.6 gives the variation in monthwise hourly ambient temperature for a typical one year for that particular site. The ambient temperature is maximum during the month of April which is 33.1 °C at 15:00 h and is minimum during the month of January which is 15.3 °C at 07:00 h.

The solar intensity will be high during the month of March to May. The solar energy is available from 07:00 to 18:00 h and will not be there during evening and night hours from 18:00 to 07:00 h.

The daily average solar insolation (W/m²) falling at a typical site is computed and fitted with polynomial curve fit as follows:

$$P_i = A_0 + A_1 \times h + A_2 \times h^2 + A_3 \times h^3 + A_4 \times h^4 + A_5 \times h^5 + A_6 \times h^6 \quad (11.1)$$

where A_0, A_1, \dots, A_6 are constants given in Table 11.1 for different months for a typical site.

The use of solar PV alone may not provide the firm and steady power required by the load, and in order to enhance the capacity factor of solar PV system, it must

Table 11.1 Coefficients of solar insolation

Month	A_0	A_1	A_2	A_3	A_4	A_5	A_6
January	21.918	-11.089	2.189	-0.2191	0.012	-0.0004	5E-06
February	23.916	-12.660	2.654	-0.2867	0.173	-0.0006	8E-06
March	36.662	-19.257	4.017	-0.4304	0.025	-0.0008	1E-05
April	38.105	-20.555	4.422	-0.4908	0.030	-0.001	1E-05
May	19.739	-10.452	2.174	-0.2309	0.014	-0.0004	6E-06
June	22.145	-11.532	2.361	-0.2458	0.014	-0.0004	5E-06
July	31.264	-17.54	3.946	-0.4589	0.029	-0.001	1E-05
August	-13.38	16.858	-1.473	0.1674	-0.010	0.0003	-4E-06
September	29.705	-15.725	3.326	-0.3634	0.022	-0.0007	9E-06
October	9.7745	-5.0679	1.014	-0.1038	0.006	-0.0002	3E-06
November	23.245	-11.455	2.225	-0.2208	0.012	-0.0004	4E-06
December	4.6776	-1.9922	0.268	-0.0102	-0.0003	3E-05	-5E-07
Average	20.647	-10.872	2.2607	-2.2417	0.0143	-0.0005	6E-06
Maximum	41.27	-21.438	4.4469	-0.4756	0.0282	-0.0009	1E-05
Minimum	60.727	-32.871	7.1883	-0.817	0.0513	-0.0017	2E-05

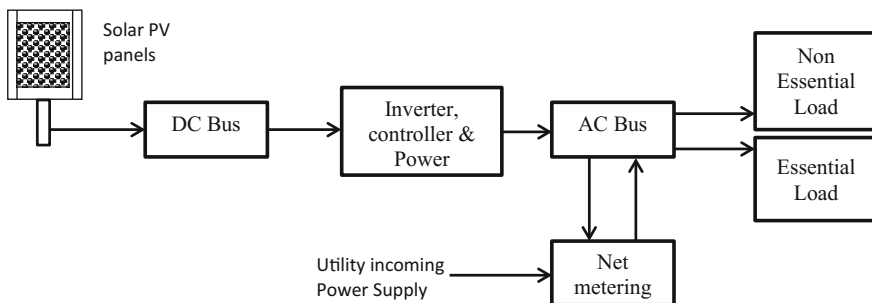


Fig. 11.7 Schematic of solar PV power plant

be integrated with either energy storage system or conventional generators such as DG set or grid. Integration or hybridization is an important way of increasing the utilization, energetic and exegetic efficiencies of energy conversion systems [7]. Energy systems are integrated through sources or tasks, spatially or timewise, to increase their overall energy utilization factor, enhance the security of energy supply, and reduce capital and running costs of equipment [8].

The proposed schematic of the PV system with grid backup and direct grid supply to provide reliable power supply to all the rural bank branches is given in Fig. 11.7.

The broad overall scheme for providing power supply to the load is as follows:

- (i) Continuous AC power will be fed from the solar PV system whenever the solar energy is available.
- (ii) When there is no solar power, direct grid AC power will be fed through controller without any processing.
- (iii) When the solar power is more than the load requirement, excess power will be sent to grid.
- (iv) When the solar power is less than the load requirement, the deficit power is fed from grid along with solar power.

11.4 Load Pattern

A typical medium sized rural banks in India will have the load requirements of three computers (one server), two printers, two fans, and two 40 W fluorescent lamps. These loads have to be supported by uninterrupted power supply (UPS). One split air conditioner, two 40 W fluorescent lamps, and two comfort fans are fed from raw power supply. The total load of each branch is given in Tables 11.2 and 11.3. As per the Bank's requirements, uninterrupted power supply is required at all the branches.

The rural banks operate between 09:00 and 17:00 h in normal working days. Figure 11.8 gives the variation in power input at UPS for a typical day. The UPS power used for essential load is varying between 0.21 and 1.15 kW. The utility power was not available for 4 h (between 10:00 and 12:00 noon and 14:40–16:40 h), and the DG set supported the power during utility power cut. The power during after office hour is about 0.21–0.34 kW. Figure 11.9 gives the variation in raw power used for nonessential load for a typical day. The raw power used for nonessential load such as split air conditioner and fluorescent lamps is varying between 0.1 and 1.45 kW. The total UPS energy required for a typical day is

Table 11.2 Load pattern on UPS of each branch

Sl. No.	Type of load	Power, W	Quantity, Nos.	Total power, W
01	Computers	200	3	600
02	Printers	150	2	300
03	Ceiling fans	50	2	100
04	Fluorescent lamps	55	2	110
Total UPS max. output power				1110
Diversity factor at 80%				890
Design margin for transients at 10%				89
Measured current THD on UPS output side 83.3% at 30%				267
Loss in UPS (average UPS efficiency at 90%)				138
Total UPS max. input power required				1384

Daily average energy required: 14 kWh/day

Table 11.3 Load pattern of raw power of each branch

Sl. No.	Type of load	Power, W	Quantity, Nos.	Total power, W
01	Fluorescent lamps	55	2	110
02	Ceiling fans	50	2	100
03	Split air conditioner 1TR	1250	1	1250
Total raw power				1460
Diversity factor at 80%				1168
Design margin for transients, presence of harmonics, etc. at 10%				117
Total power required				1285

Daily average energy required: 13.5 kWh/day

Fig. 11.8 Variation of power input at UPS input

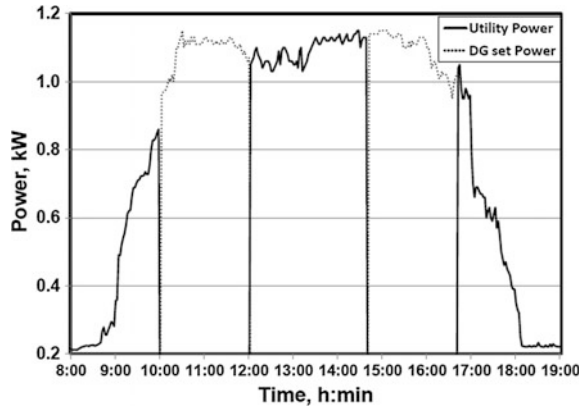
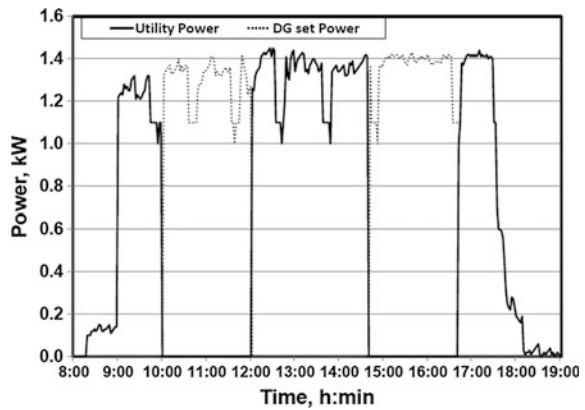
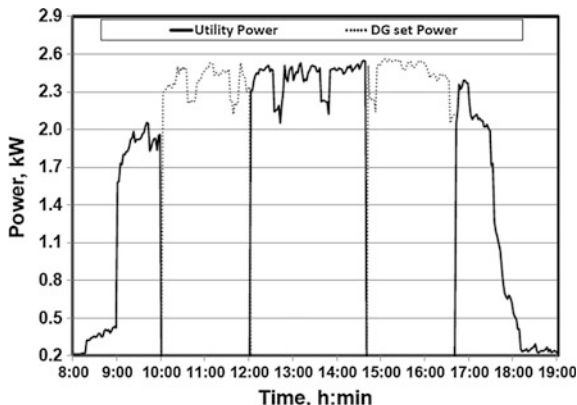


Fig. 11.9 Variation of raw power used for nonessential load



14 kWh/day, and the energy for nonessential load is 13.5 kWh/day. Figure 11.10 gives the variation in total raw power at input. It is shown in the Fig. 11.10 that the power is varying between 0.31 and 2.51 kW and the total energy required is 27.5 kWh/day.

Fig. 11.10 Variation of total power at input



The total power including essential and raw power is 2.67 kW, and total energy requirement is about 27.5 kWh/day.

The solar power system operates in tandem with grid, and whenever grid power is not available, it has to work as a stand-alone system. During the stand-alone operation, the solar PV system should be capable of withstanding the transients generated by the start-up loads. Some of the loads are nonlinear loads (i.e., computers).

11.5 System Sizing

The efficiency and performance indices considered while designing the solar PV power plant are given in Table 11.4.

The solar power output depends on the availability of solar irradiance throughout the year. The solar power generation starts at 7:00 h and gradually increases to its maximum value near to 1000 W/m² at about 12:00–13:00 h at standard test condition (STC) at 25 °C. The solar intensity or solar specific energy generation (SSEG) of 1000 W/m² at STC is called one sun hour. The sun hours varies with season and climatic conditions. The sun hour is high during summer and is less during winter in India. The sun hour varies between 3 and 7 h in India.

Figure 11.11 shows the variation in monthly average of daily SSEG at a typical site. The radiation is varying in the range of 4.366 kWh/m²-day and 6.739 kWh/m²-day (deviation maximum to minimum value is 43.6%).

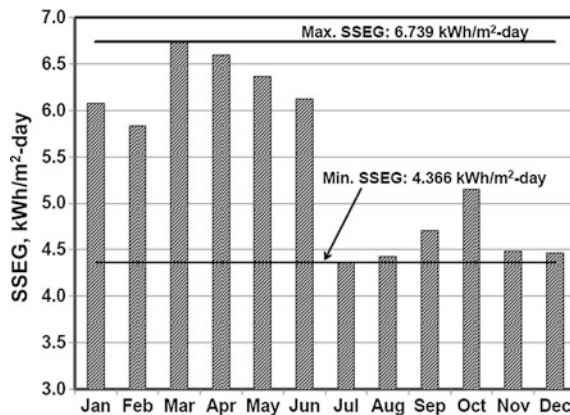
The sizing of solar PV system may be based on optimum SSEG. The energy requirement for rural bank branch is 27.5 kWh/day, and the peak power requirement is 2.67 kW.

If the sizing is based on minimum SSEG of 4.366 kWh/m²-day, the PV panel size (m²) is computed as

Table 11.4 Efficiency and performance indices

Sl. No.	Variable	Unit	Value
01	Overall cell efficiency (max.) at solar radiation of 1000 W/m ² at 25 °C	%	16
02	Fill factor of solar PV panel	%	90
03	Overall module efficiency	%	14.4
04	Inverter efficiency	%	90
05	Circuitry loss	%	0.7
06	Overall SPV to AC load efficiency (η_{SPV})	%	12.25
07	Battery charger efficiency	%	85
08	Maximum depth of discharge of battery banks	%	70

Fig. 11.11 Monthly average daily SSEG



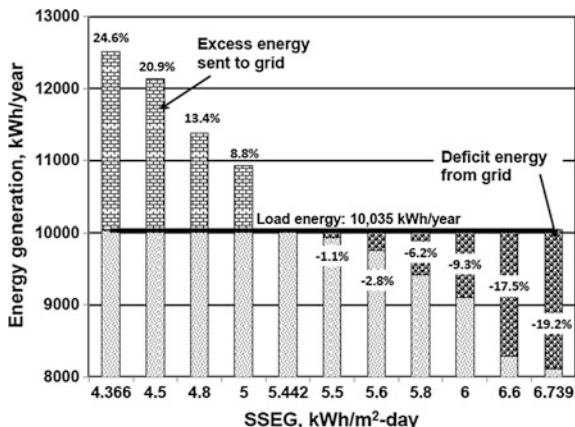
$$PV_s = \frac{E_d}{SSEG} \times \frac{100}{\eta_{SPV}} = \frac{27.5 \times 100}{4.366 \times 12.25} = 51.4 \tag{11.2}$$

where E_d is the total energy required by load per day (kWh/day), SSEG is specific solar energy generation (kWh/m²-day), and η_{SPV} is the solar PV power plant efficiency (%).

Figure 11.12 gives the variation in energy generation by solar PV power plant with SSEG. At minimum SSEG of 4.366 kWh/m²-day, the size of SPV plant is maximum and the energy generation by solar PV power plant is high, i.e., excess generation which need to be exported into grid.

- At 4.366 kWh/m²-day: 12,504 kWh/month (excess energy generation of 24.6%),
- At SSEG of 4.8 kWh/m²-day: 20.9%,
- At SSEG of 5.0 kWh/m²-day: 13.4%, and
- At SSEG of 5.0 kWh/m²-day: 8.8%.

Fig. 11.12 Total energy generated by SPV plant with minimum SSEG



For the SSEG above optimum value, the energy generation by solar PV power plant is less than the load requirement which needs to be supported by grid.

- At SSEG of 5.5 kWh/m²-day, the energy deficit will be -1.1%,
- At SSEG of 5.6 kWh/m²-day: -2.8%,
- At SSEG of 5.8 kWh/m²-day: -6.2%,
- At SSEG of 6.0 kWh/m²-day: -9.3%,
- At SSEG of 6.6 kWh/m²-day: -17.5%, and
- At SSEG of 6.739 kWh/m²-day: -19.2% (i.e., the maximum SSEG).

11.5.1 Minimum SSEG

For the minimum SSEG (solar hours), the solar PV power plant size will be maximum for meeting the total energy required during the month of minimum solar radiation, i.e., July month. Energy generation during other months will be excess. During the month of March, the excess energy generation is 54.5%, April is 51.1%, May is 45.9%, June is 40.2%, January is 39.1%, February is 33.5%, and remaining months it is less (refer Fig. 11.13).

If the sizing is based on maximum SSEG of 6.739 kWh/m²-day, the PV panel size (m²) is computed as

$$PV_s = \frac{E_d}{SSEG} \times \frac{100}{\eta_{SPV}} = \frac{27.5 \times 100}{6.739 \times 12.25} = 33.3 \tag{11.3}$$

The total energy generated by solar PV power plant is 8101 kWh/year for considering maximum SSEG of 6.739 kWh/m²-day (refer Fig. 11.14) and the average energy consumption of bank is 10,035 kWh/year. There will be a deficit of energy generation of about 1934 kWh/year (19.3% of total energy required) from solar PV power plant which is to be imported from the grid.

Fig. 11.13 Total energy generated by SPV plant with minimum SSEG

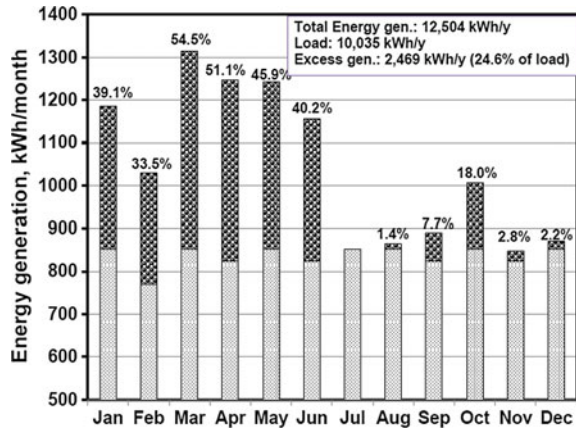
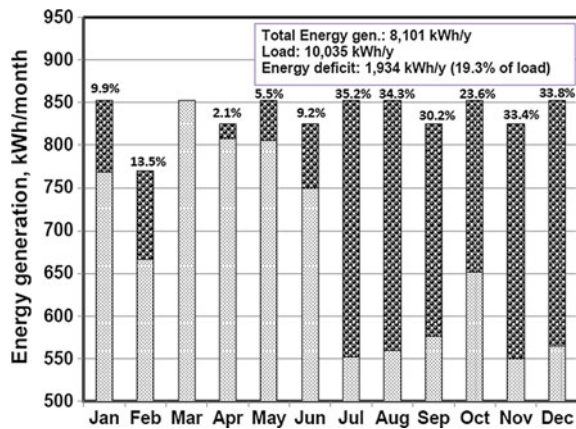


Fig. 11.14 Total energy generated by SPV plant with maximum SSEG



11.5.2 Maximum SSEG

For the maximum SSEG, the solar PV power plant size will be minimum for meeting the total energy required during the month of maximum solar radiation, i.e., March month. Energy generation during other months will be less than the energy required to meet the load, and the grid is to support the load, i.e., dependence on the grid power will increase. During power cut, again DG set needs to be operated or energy storage elements like batteries need to be installed. During the month of July, the energy deficit is 35.2%, August is 34.3%, December is 33.8%, November is 33.4%, September is 30.2%, October is 23.6%, and remaining months it is less.

11.5.3 Optimum SSEG

The optimization study is carried out by using HOMER software considering the energy generation by solar PV power plant equal to the energy required to meet the load [9]. In India, at present to promote solar PV rooftop power plants, electricity distribution companies are allowing solar PV power plant producers to operate grid-connected solar PV power plants. This scheme will allow the solar PV power producers to pump the excess power generation to the grid during day hours, and whenever the customer needs power especially during night hours, they can draw the power from the grid. The distribution companies are installing the net metering system. The energy charges will depend on the net energy import from grid or export to the grid. The distribution companies will compute net energy for every month. If the energy export to grid is more than the energy import to the load, distribution companies will pay \$0.10 per kWh to customer. If the energy import is more than the energy export during the particular month, the additional energy import will be charged at the commercial rate fixed by the distribution companies, i.e., \$0.10 per kWh.

The energy required to meet the load is 10,035 kWh/y and the panel size (m²) is computed as

$$PV_s = \frac{E_y \times 100}{SSEG \times 365 \times \eta_{SPV}} \quad (11.4)$$

where E_y is the total energy required by load per year (kWh/y), i.e., 10,035 kWh/y. The efficiency of solar PV power plant is considered as 12.25%. The solar PV power panel size and SSEG are unknown parameters. These parameters are computed by using the HOMER software through optimization technique, i.e., minimization criteria was the difference between energy export to grid and energy import from grid must be near to zero.

$$\sum_{i=1}^{i=365} (E_{SPVd} - E_d)_i = 0 \quad (11.5)$$

where E_{SPVd} is the energy generation by solar PV power plant (kWh/day) and i is the number of days from 1 to 365 days/year.

The optimum value of SSEG obtained is 5.442 kWh/m²-day, and the area of solar PV power plant is 41.24 m² (refer Fig. 11.15).

Figure 11.16 gives the variation in solar PV panel size with SSEG. As the SSEG increases, the solar PV panel size (m²) decreases and the variation is curve fitted to

$$PV_s = 224.4898 \times SSEG^{-1} \quad (11.6)$$

Fig. 11.15 Monthly average daily optimum SSEG

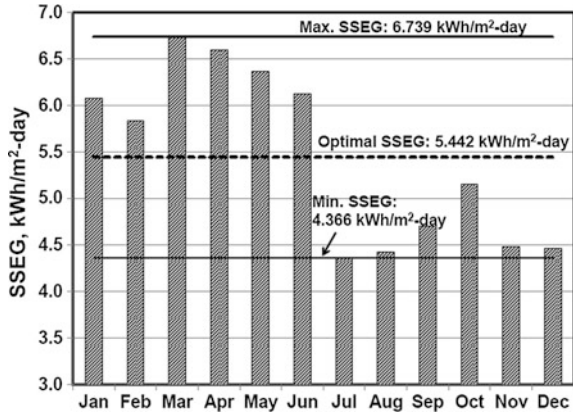
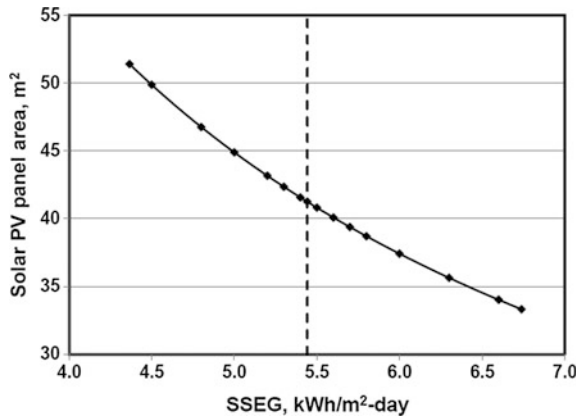


Fig. 11.16 Solar PV panel size with SSEG



The solar PV power rating (kW) is estimated by considering the solar cell efficiency of 16%, fill factor of 90%, and solar PV power plant overall efficiency of 12.25%, and specific solar PV panel area is assumed as 7 m²/kW.

$$PV_r = \frac{PV_s}{7} = 5.89 \tag{11.7}$$

The solar PV power plant size varies between 4.8 kW at SSEG of 6.739 kWh/m²-day and 7.3 kW at SSEG of 4.366 kWh/m²-day (refer Fig. 11.17). The size of the solar PV power plant at optimum SSEG of 5.442 kWh/m²-day is 5.9 kW. The size of the solar PV power plant (kW) is curve fitted to

$$PV_r = 32.07 \times SSEG^{-1} \tag{11.8}$$

Fig. 11.17 Solar PV power plant size with SSEG

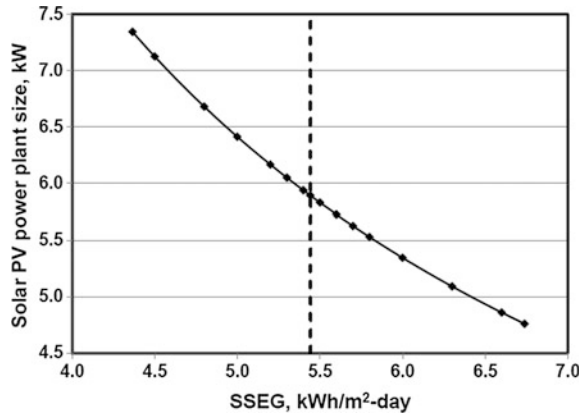
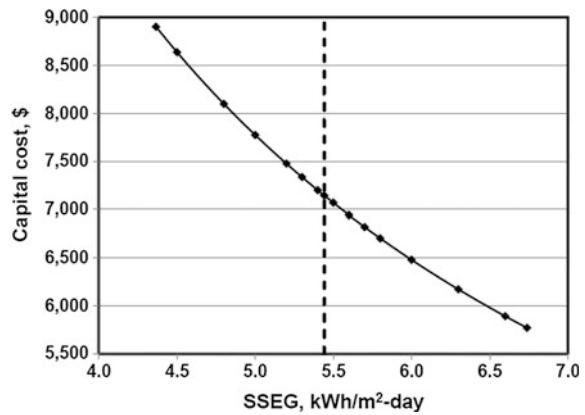


Fig. 11.18 Capital cost for installation of SPV plant with SSEG



11.5.4 Economics

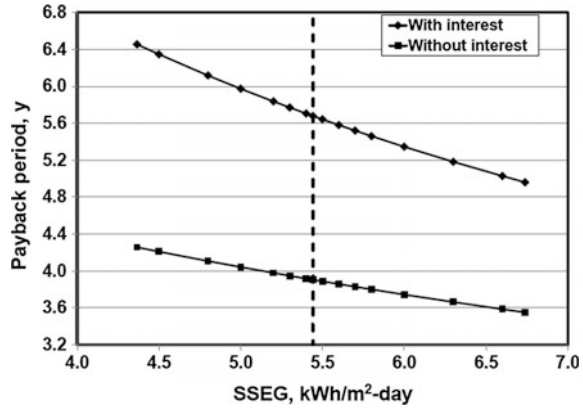
The capital cost (\$) for installing the solar PV power plant is varying between \$5769 and \$8904 (refer Fig. 11.18) and is curve fitted to

$$CC = 38872.69 \times SSEG^{-1} \tag{11.9}$$

The capital cost for the optimized solar PV power plant of 5.9 kW size is \$7143. The payback period (y) for the investment for solar PV power plant is calculated for the SSEG varying between 4.366 and 6.739 kWh/m²-day and is computed as

$$PP = \frac{CC}{(E_{SPV_y} - E_{DG}) \times EC_G + E_{DG} \times EC_{DG} - ((CC \times \frac{i}{100}) + MC)} \tag{11.10}$$

Fig. 11.19 Variation of payback period with SSEG



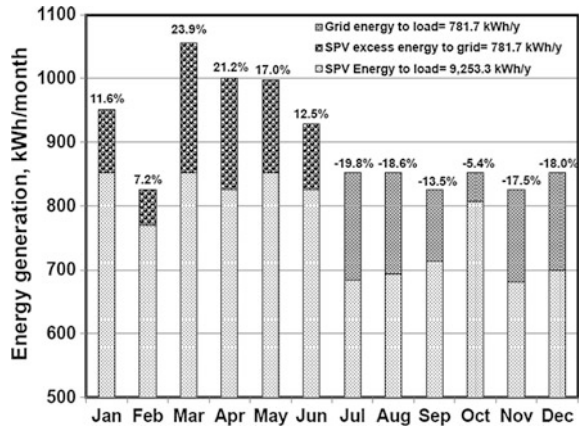
where E_{SPV_y} is the total energy generated by solar PV power plant (kWh/y), E_{DG} is the energy generated by DG set during power cut (kWh/y), i.e., average value taken as 4280 kWh/y, E_{SPV_G} is the average excess energy export to grid after meeting the load (kWh/year), EC_{DG} is energy generation cost by DG (\$/kWh), i.e., the present value is taken as \$0.32 per kWh, i is the interest rate (%) and is considered as 8%, and MC is the operation & maintenance (O&M) cost (\$) (i.e., 2% of total investment).

The payback period is varying between 5.0 and 6.5 years for considering the interest on the capital cost, and if the interest on investment is not considered, the payback period will be 3.6–4.4 years (refer Fig. 11.19). The payback period for optimum sizing of solar PV power plant to meet the load requirement is 5.7 years.

11.5.5 Energy Generation

Figure 11.20 gives the variation in energy generated by solar PV power plant, excess energy export to grid, and deficit energy imported from grid to meet the load. The total energy generation by solar PV power plant is varying between 683.9 and 1055.6 kWh/month. During the months between January and June, the solar radiation is high and the energy generation by solar PV power plant is excess of load requirement. The excess energy is exported to grid. The net energy export to grid during the months of January to June is varying between 55.5 and 203.4 kWh/month (7.2 and 23.9% of load requirement). During the months between July and December, the energy generation by solar PV power plant is not sufficient to meet the load requirement and the deficit of energy is met from the grid. During these months, the net energy imported from the grid is varying between 45.5 and 168.3 kWh/month (−5.4 to −19.8% of load requirement).

Fig. 11.20 Energy generation by SPV plant, excess generation, and energy from grid



The energy requirement by load, energy supplied by solar PV power plant, excess energy export to grid, and deficit energy import from grid are computed by using HOMER software as well as MATLAB/Simulink program [10]. Figure 11.21a–l gives the share of energy supplied by solar PV power plant, energy export to grid, and energy import from grid to meet the load for daily average load requirement for 12 months. The following observations are drawn from the Fig. 11.21a–l and Table 11.5:

- (1) The load during night hours from 19:00 to 07:00 h is fed from grid. From 7:00 h onwards, solar PV power plant provides the power to meet the load requirement and excess energy generation by SPV is exported to grid.
- (2) Whenever the power generation by SPV power plant is less than the load requirement, the excess power requirement by load is met from the grid.
- (3) The peak power generation by SPV power plant is maximum during the month of March, i.e., 4.84 kW which is 82.0% of design capacity, and minimum during the month of July, i.e., 2.90 kW (49.2% of design capacity).
- (4) The energy generation by SPV power plant is maximum during the month of March, i.e., 1055.6 kWh/month and is minimum during the month of July, i.e., 683.9 kWh/month.
- (5) The energy supplied by SPV power plant directly to load is varying between 606.3 kWh/month (November) and 699.6 kWh/month (March).
- (6) The excess energy generation by SPV power plant after meeting the load during sun hours is varying between 57.9 kWh/month (July) and 356.0 kWh/month (March). During the months between January and June (28.0–41.8% of load), the energy export to grid is higher compared to other months between July and December (6.8–19.5%).
- (7) The energy import from grid during non-solar hours (during night hours) to meet the load requirement is varying between 145.6 kWh/month (June) and 231.6 kWh/month (December). During the months between January and June

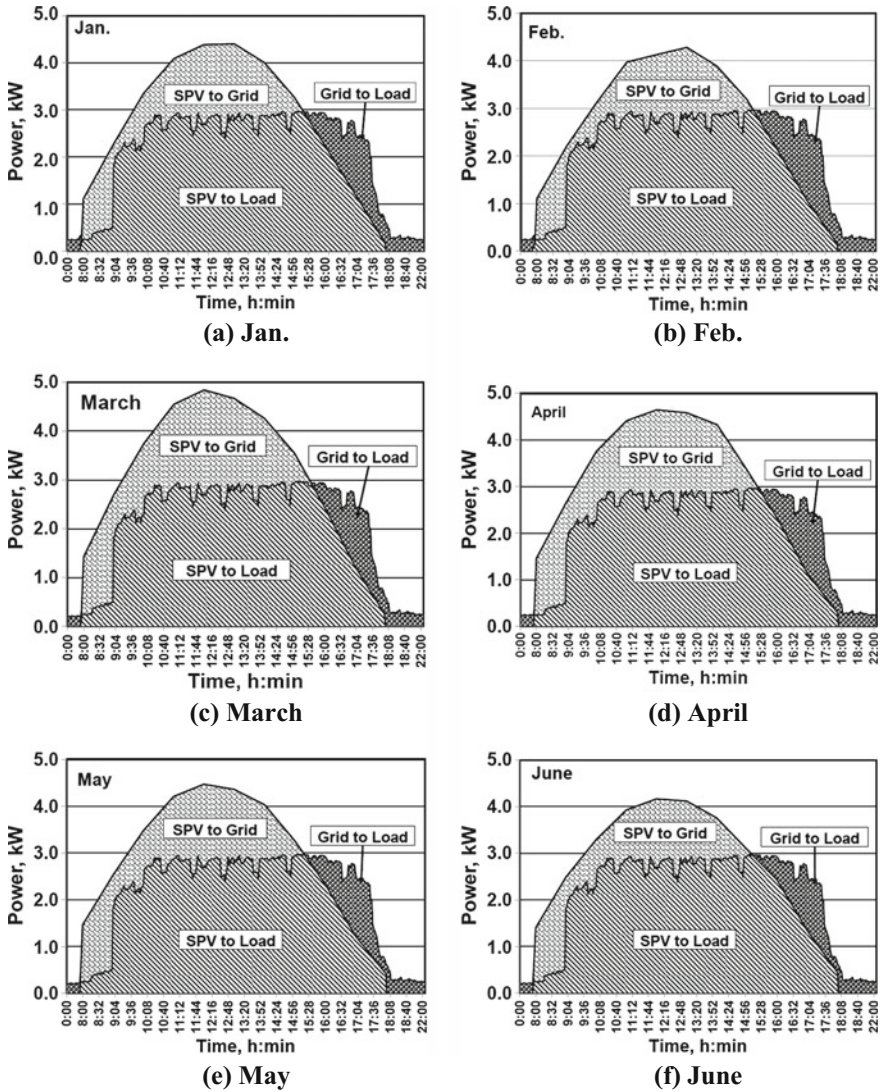


Fig. 11.21 a–f Energy generation by SPV, energy export and import from grid

(17.7–20.8% of load), the energy import from grid is less compared to other months between July and December (24.8–27.2%).

- (8) The monthly net energy export to grid is happening during the sunny months of January to June and is varying between 55.2 kWh/month, i.e., 7.2% of load (February) and 203.1 kWh/month, i.e., 23.9% of load (March).

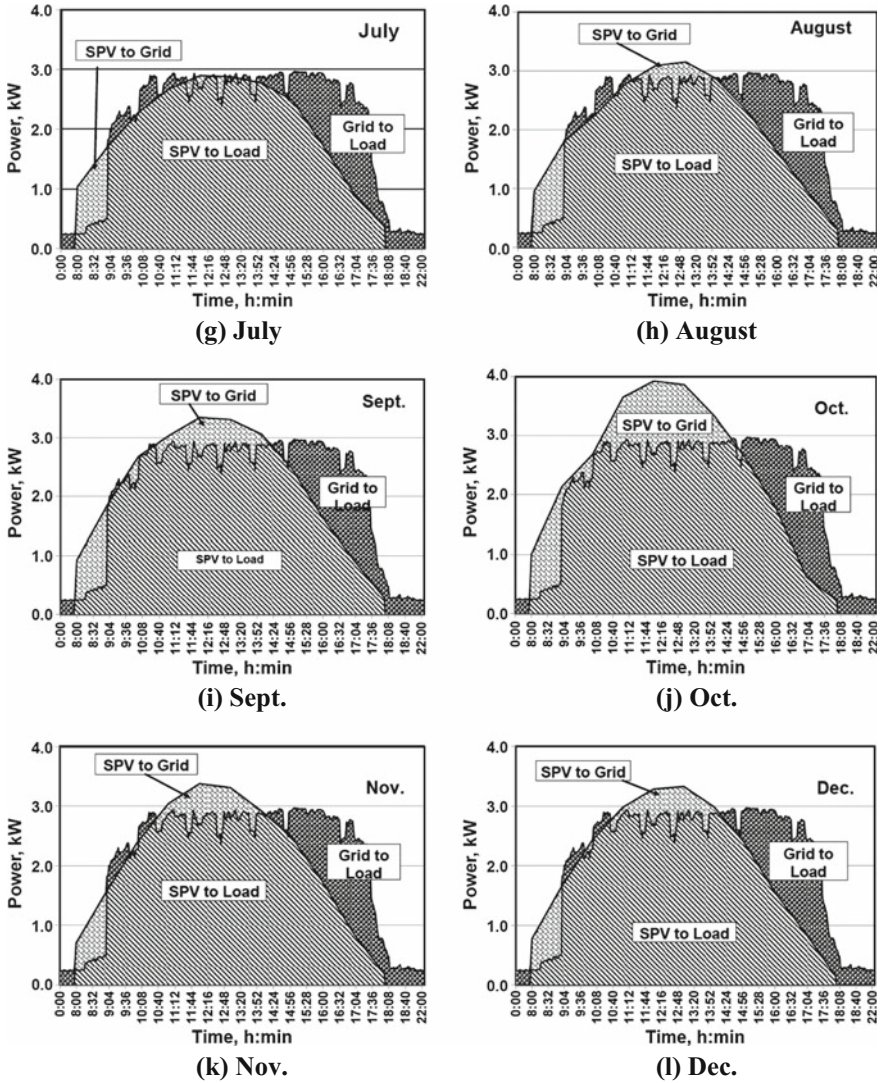


Fig. 11.21 (continued)

- (9) The monthly net energy import from grid during the months (more cloudy months) of July to December is varying between -45.7 kWh/month, i.e., 5.4% of load (October) and -168.6 kWh/month, i.e., 19.8% of load (July).
- (10) The peak power supplied by solar PV power plant is varying between 2.90 and 4.84 kW (49.2–82.0%) during noon hours (refer Fig. 11.22). It can be seen from Fig. 11.23 that as the peak power increases, the energy generation (kWh/y) by solar PV power plant increases and is curve fitted to

Table 11.5 Power and energy parameters of SPV power plant

Month	Peak power (kW)	SPV energy generation (kWh/month)	SPV energy directly to load (kWh/month) (%)	Excess energy export to grid (kWh/month) (%)	Import energy from grid (kWh/month) (%)	Net energy export to grid/import from grid (kWh/month) (%)
January	4.40	951.5	682.9 (80.1%)	268.6 (31.5%)	169.6 (19.9%)	+99.0 (11.6%)
February	4.28	825.5	609.3 (79.2%)	215.9 (28.0%)	160.7 (20.8%)	+55.2 (7.2%)
March	4.84	1055.6	699.6 (82.1%)	356.0 (41.8%)	152.9 (17.9%)	+203.1 (23.9%)
April	4.65	1000.2	662.8 (80.3%)	337.4 (40.9%)	162.2 (19.7%)	+175.2 (21.2%)
May	4.47	997.5	696.6 (81.7%)	300.9 (35.3%)	155.9 (18.3%)	+145.0 (17.0%)
June	4.16	928.2	679.4 (82.3%)	248.9 (30.2%)	145.6 (17.7%)	+103.3 (12.5%)
July	2.90	683.9	626.0 (73.4%)	57.9 (6.8%)	226.5 (26.6%)	-168.6 (19.8%)
August	3.15	693.3	621.1 (72.9%)	72.2 (8.5%)	231.4 (27.1%)	-159.2 (18.6%)
September	3.35	713.4	620.6 (75.2%)	92.8 (11.3%)	204.4 (24.8%)	-111.6 (13.5%)
October	3.92	806.7	640.6 (75.1%)	166.2 (19.5%)	211.9 (24.9%)	-45.7 (5.4%)
November	3.38	680.5	606.3 (73.5%)	74.2 (9.0%)	218.7 (26.5%)	-144.5 (17.5%)
December	3.33	698.8	620.9 (72.8%)	77.9 (9.2%)	231.6 (27.2%)	-153.7 (18.0%)

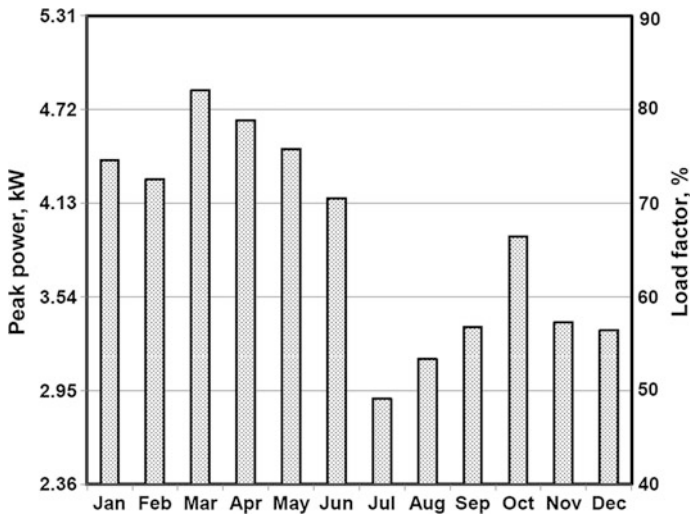
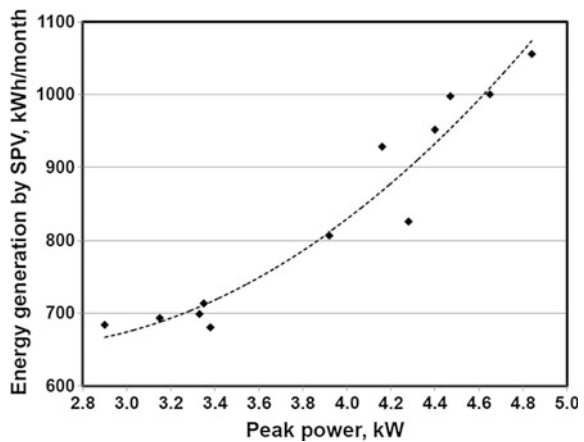


Fig. 11.22 Variation of peak power

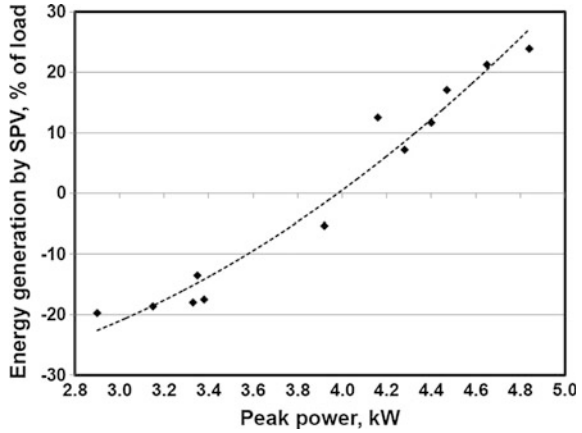
Fig. 11.23 Variation of energy generation with peak power



$$PV_s = 1.103.74 - 366.71 \times P_{\text{peak}} + 74.491 \times P_{\text{peak}}^2 \quad (11.11)$$

- (11) Figure 11.24 gives the variation in energy generation by solar PV power plant as a percentage of load requirement with peak power. As the peak power of solar PV power plant increases above 4.0 kW, energy generation by solar PV power plant will be excess which needs to be exported to the grid whereas below 4.0 kW, the energy is to be imported from grid to meet the load

Fig. 11.24 Variation of energy generation as a % of load with peak power



requirement. The variation in energy generation by solar PV power plant as a percentage of load (%) is curve fitted to

$$PV_{sp} = -19.7557 - 16.9502 \times P_{peak} + 5.5032 \times P_{peak}^2 \tag{11.12}$$

11.6 Economics of the Project

The anticipated investment for installation of optimum-sized solar PV power plant of 5.9 kW is \$7143, and the payback period is 5.7 years.

In order to calculate the simple levelized cost of energy, only capital cost and recovery cost are considered for replacement of equipment at the end of life for each equipment, i.e., life for PV panels is considered as 25 years and 10 years for electronic components.

(a) **Annualized capital cost:** The annualized capital cost (ACC) (\$/y) is computed by

$$ACC = CC \times CRF(i, L_{proj}) \tag{11.13}$$

where CC is initial capital cost (\$) and CRF is capital recovery factor and is given by

$$CRF(i, L_{proj}) = \frac{i(1+i)^{L_{proj}}}{(1+i)^{L_{proj}} - 1} \tag{11.14}$$

where i is interest rate (%) and L_{proj} is life of the project (y).

ACC is computed as \$670 by considering the interest rate of 8% and life of project as 25 years and capital cost of \$7143.

- (b) **Annualized replacement cost:** The annualized replacement cost (ARC) (\$/y) is calculated by

$$ARC = CRC \times \left[f_{\text{rep}} \times \text{SFF}(i, L_{\text{comp}}) - \left(\frac{L_{\text{rem}}}{L_{\text{comp}}} \right) \times \text{SFF}(i, L_{\text{proj}}) \right] \quad (11.15)$$

where CRC is capital recovery cost at the end of life of component (\$) and f_{rep} is replacement factor and is given by

$$f_{\text{rep}} = \begin{cases} \frac{\text{CRF}(i, L_{\text{proj}})}{\text{CRF}(i, L_{\text{rep}})} & \text{for } L_{\text{rep}} > 0 \\ 0 & \text{for } L_{\text{rep}} = 0 \end{cases} \quad (11.16)$$

where L_{rep} is replacement cost duration (y) and is given by

$$L_{\text{rep}} = L_{\text{comp}} \times \text{INT} \left(\frac{L_{\text{proj}}}{L_{\text{comp}}} \right) \quad (11.17)$$

where L_{comp} is lifetime of the individual components (y), L_{rem} is remaining life of component (y), and SFF is sinking fund factor and is given by

$$\text{SFF}(i, L_{\text{proj}}) = \frac{i}{(1+i)^{L_{\text{proj}}} - 1} \quad (11.18)$$

Since the life of project is considered as 25 years, the life of solar PV panels is 25 years and the life of electronic component is considered as 10 years. Hence, it is required to compute the annualized replacement cost for electronic components and is computed as \$24.6.

- (c) **Annual maintenance cost (AMC):** Since grid-tied solar PV power plant is planned with any storage elements like batteries which need more maintenance, the annual maintenance cost for maintaining solar PV power plant is considered as 2% of capital cost, i.e., \$143 per year.
- (d) **Annual fuel cost (AFC):** The energy supply during night hours is imported from grid, and no DG set operation is planned under the scheme during normal operation of plant.

Total annualized cost of energy (\$/y) is given by

$$TAC = ACC + ARC + AMC + AFC = 670 + 24.6 + 143 + 0 = 837.6 \quad (11.19)$$

Levelized cost of energy (COE) (\$/kWh) is calculated by

$$\text{COE} = \frac{\text{TAC}}{E} = \frac{837.6}{10035} = 0.083 \quad (11.20)$$

The levelized cost of energy for the project is \$0.083 per kWh which is much cheaper than the cost of energy from utility, i.e., \$0.10 per kWh and also cheaper than energy generation by DG set of \$0.32 per kWh.

The lifetime gain considering the life of 25 years for solar PV panels and life of 10 years for electronic components is \$19,970.

11.7 Results and Discussions

The solar PV power plant of 5.9 kW is installed in one of the banks situated at rural part in Karnataka. Figure 11.25 shows the solar PV power plant installed at rural bank. The total load is supplied through grid-connected solar rooftop PV power plant. Generally, the load will be met from solar PV power plant during day hours, and during night hours, the energy will be met from the grid. The excess energy generation by solar PV power plant after meeting the load will be pumped into the grid. The net metering system is installed at the main incomer. The net energy consumption will be calculated for each month. If the net energy is excess, the utility will adjust the excess energy consumption during the next month, and if the net energy is deficit, i.e., energy import from grid is higher than the energy export to grid, the charges for deficit energy drawn from grid are to be paid by the customer to utility.

Figure 11.26a–l gives the variation in design load, actual measured monthwise half hourly average load, design power generation by SPV plant, and actual measured energy generation by solar PV power plant. The performance results are given in Table 11.6. The observations from the study are as follows:

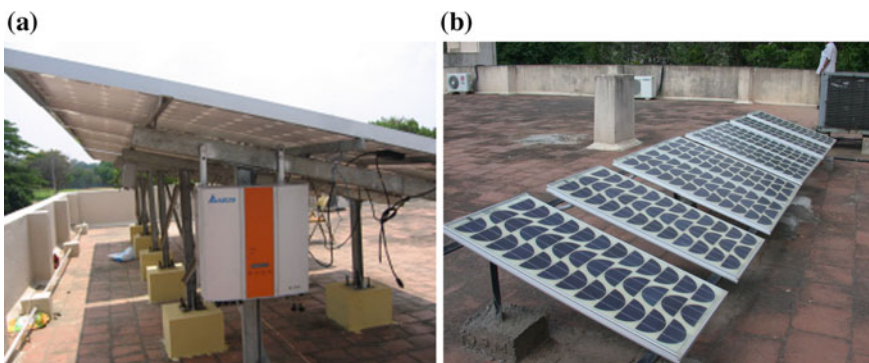


Fig. 11.25 a Inverter and controls of SPV plant and b PV panels

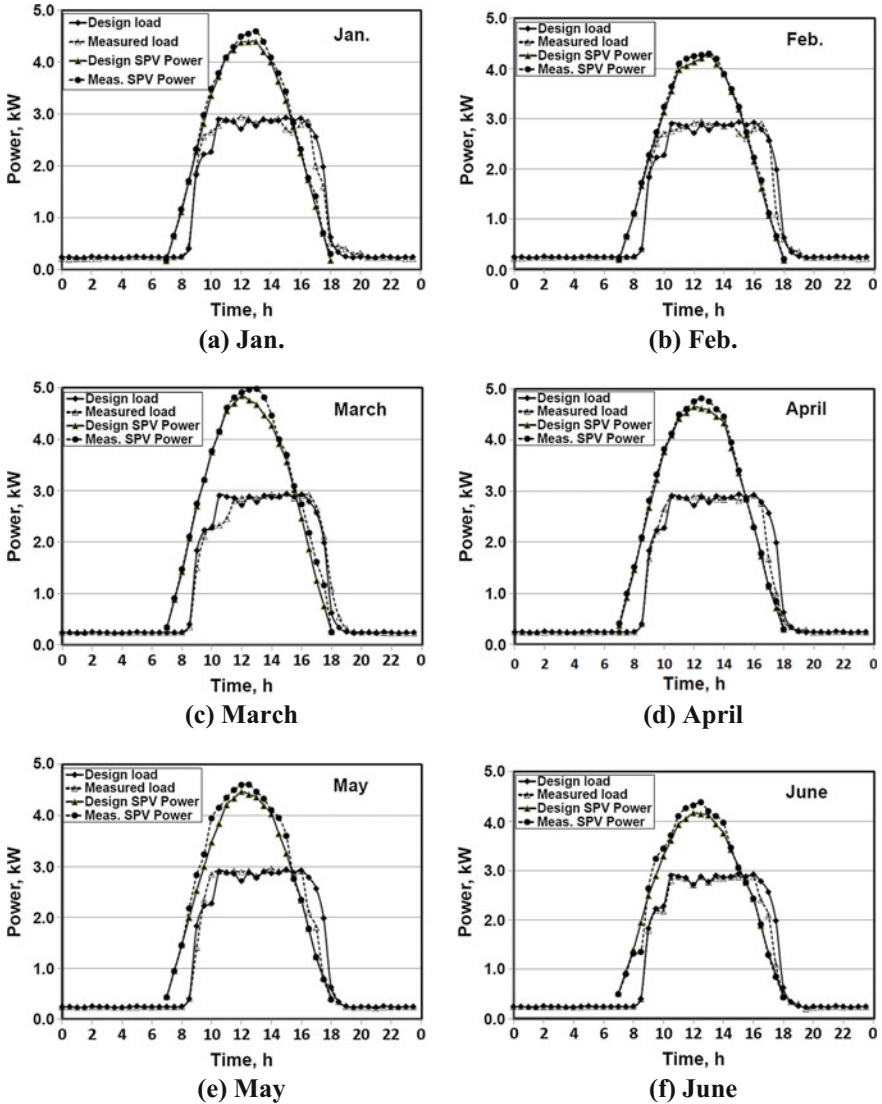


Fig. 11.26 a–f Variation of energy generation by SPV power plant and load

- (1) The design energy consumption by load is 27.5 kW, and the monthly average measured actual energy consumption by load is varying between 25.4 kWh/day (December) and 27.9 kWh/day (March). The deviation in monthly average daily energy consumption is in the range of -7.6 to $+1.4\%$ of design energy consumption.

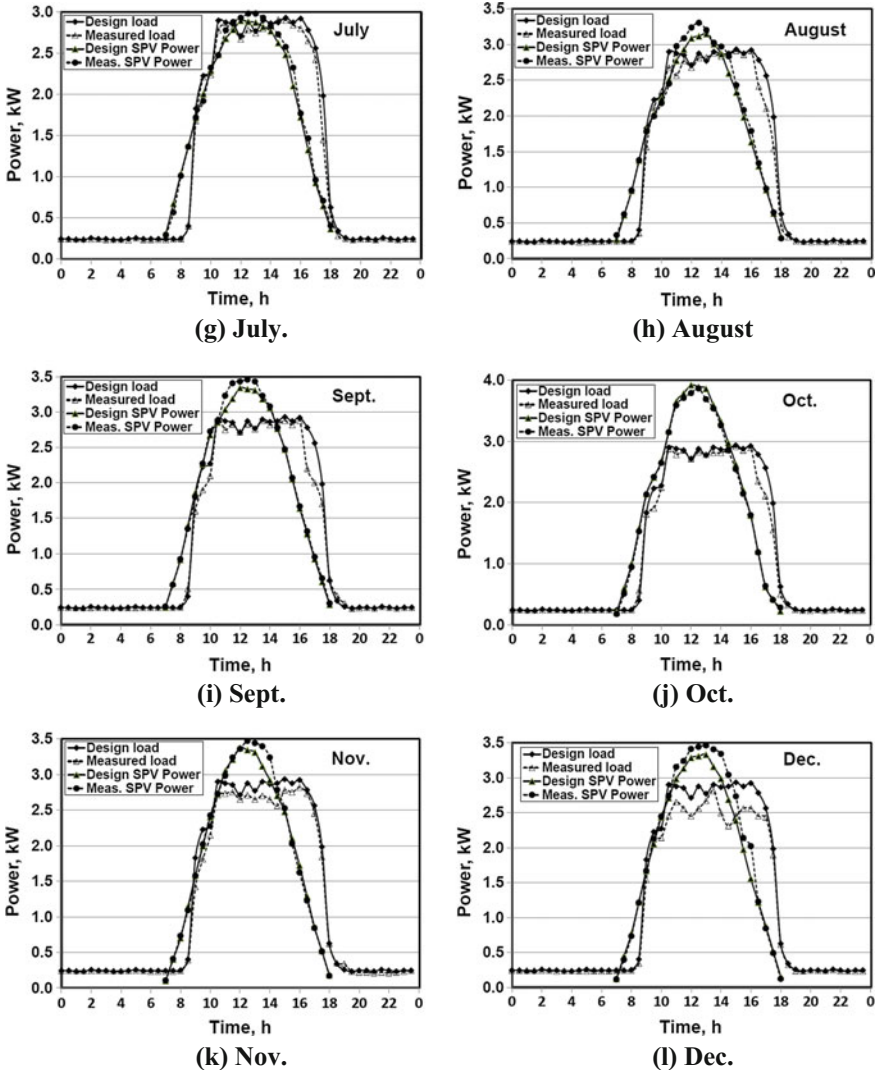


Fig. 11.26 (continued)

(2) The design energy generation by SPV power plant is varying between 22.1 kWh/day (July) and 34.1 kWh/day (March), and the excess energy generation export to grid is in the range of 7.2–23.9% of load during the sunny months of January to June. The design deficit in energy generation by SPV power plant to import from grid to meet the load requirement is in the range of –5.4 to –19.8% during the partial cloudy months of June to December.

Table 11.6 Power and energy parameters of SPV power plant

Month	Load energy (kWh/d) (increase in % of design)	Design SPV energy gen., kWh/d (excess energy, % of load)	Measured SPV energy gen., kWh/d (excess energy, % of load)	SPV energy directly met load measured, kWh/d (design, kWh/d)	Energy import from grid measured, kWh/d (design, kWh/d)	Net energy export to grid/import from grid measured, kWh/d (design, kWh/d)
January	27.8 (+1.2%)	30.7 (11.6%)	31.7 (13.9%)	23.0 (22.5)	4.8 (5.0)	+3.9 (3.2)
February	27.7 (+0.7%)	29.5 (7.2%)	30.1 (8.7%)	22.6 (22.2)	5.1 (5.3)	+2.4 (2.0)
March	27.9 (+1.4%)	34.1 (23.9%)	35.5 (27.2%)	22.8 (22.7)	5.1 (4.8)	+7.6 (6.6)
April	27.1 (-1.4%)	33.3 (21.2%)	34.1 (25.8%)	22.8 (22.5)	4.3 (5.0)	+7.0 (5.8)
May	26.9 (-2.2%)	32.2 (17.0%)	33.4 (24.2%)	23.0 (22.7)	3.9 (4.8)	+6.5 (4.7)
June	26.7 (-2.9%)	30.9 (12.5%)	31.3 (17.2%)	22.6 (22.9)	4.1 (4.6)	+4.6 (3.4)
July	27.1 (-1.4%)	22.1 (-19.8%)	22.5 (-17.0%)	21.0 (20.6)	4.6 (5.4)	-3.1 (-3.9)
August	26.6 (-3.3%)	22.4 (-18.6%)	22.9 (-13.9%)	20.5 (20.6)	6.1 (5.1)	-4.2 (-3.3)
September	26.8 (-2.5%)	23.8 (-13.5%)	24.2 (-9.7%)	20.9 (21.1)	5.9 (6.4)	-2.6 (-3.7)
October	26.9 (-2.2%)	26.0 (-5.4%)	25.4 (-5.6%)	21.4 (21.1)	5.5 (6.4)	-1.5 (-1.5)
November	26.3 (-4.4%)	22.7 (-17.5%)	23.0 (-12.5%)	19.8 (20.6)	6.5 (6.9)	-3.3 (-4.8)
December	25.4 (-7.6%)	22.6 (-18.0%)	23.8 (-6.3%)	19.6 (20.4)	5.8 (7.1)	-1.6 (-4.9)

- (3) The actual measured energy generation by SPV power plant is slightly higher than the design value and is varying between 22.5 kWh/day (July) and 35.5 kWh/day (March). The excess energy export to grid is in the range of 8.7–27.2% of load during the sunny months of January to June. The design deficit in energy generation by SPV power plant to import from the grid to meet the load requirement is in the range of –5.6 to –17.0% during the partial cloudy months of June to December.
- (4) The actual measured energy generation by solar PV power plant is increased compared to design value in the range of 1.5% (February) to 7.6% (December) except during the month of October decreased by –0.2% whereas the load is increased during January to March by 0.7–1.4% and decreased by 1.4–7.6% during the months from March to December.
- (5) The energy generation by SPV power plant directly met the load that is varying between 19.6 and 23.0 kWh/day.
- (6) The actual measured energy import from the grid is varying between 4.1 kWh/day (June) and 6.5 kWh/day (November) and is lower than the design value of 4.6 kWh/day (June) to 7.1 kWh/day (December).
- (7) The net monthly average daily energy export to grid during the sunny months of January to June is varying between +2.4 kWh/day (February) and +7.6 kWh/day (March), which is slightly higher than the design value in the range of 2.0–6.6 kWh/day.
- (8) The net monthly average energy import from grid during partial cloudy months of June to December is in the range of –1.5 kWh/day (October) to –4.2 kWh/day (August), which is slightly better than the design value in the range of –1.5 to –4.9%.

Figure 11.27 shows the variation in monthly energy consumption by the load. During the months of January, February, and March, the load is increased in the range of 0.7–1.4%, whereas in other months, the load is decreased in the range of 1.4–7.6% as compared to design value. The annual average load is decreased by 2.1%.

Fig. 11.27 Monthly energy consumption by load

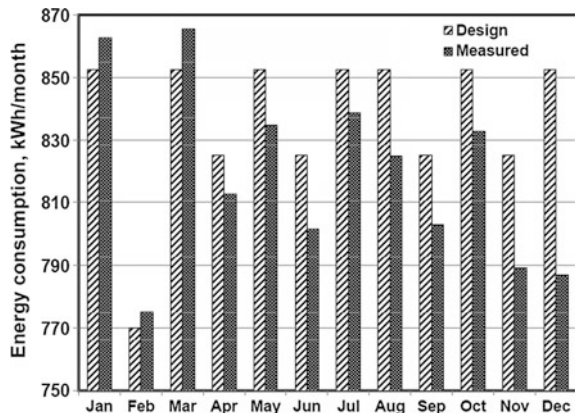


Figure 11.28 shows the variation in monthly energy generation by solar PV power plant. It is shown in the above figure that the actual measured energy generation by solar PV power plant is high compared to design value. The variation is in the range of 1.5–7.2%. The total energy generation by solar PV power plant is 10,267 kWh/y (increase of 2.3%).

Figure 11.29 shows the variation in monthly energy generation by solar PV power plant fed directly to meet the load requirement. The actual measured solar PV energy directly to the load is higher than the design value in all months except months of November and December, and the total annual energy is increased from 7766.2 to 7903.2 kWh/year (increase of 1.8%).

Figure 11.30 shows the variation in monthly excess energy generation by solar PV power plant which is exported to the grid. The actual measured excess energy generation by solar PV power plant is higher than the design value in all months except months of February, July, and October, and the total annual energy is increased from 2271.4 to 2363.4 kWh/year (increase of 4.0%).

Fig. 11.28 Monthly energy generation by SPV power plant

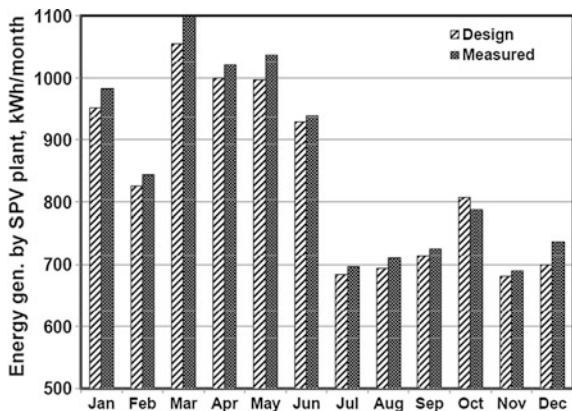


Fig. 11.29 Monthly energy generation by SPV power plant directly fed to grid

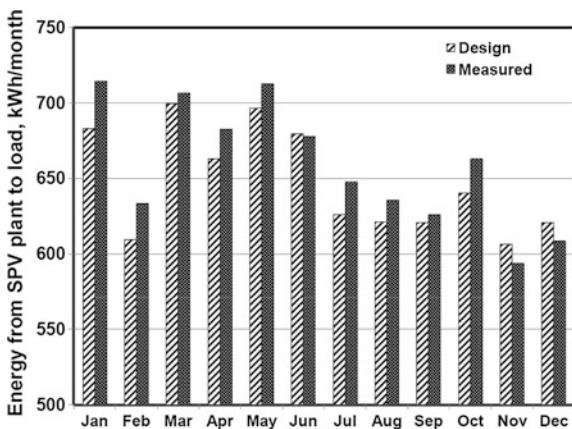


Fig. 11.30 Monthly excess energy generation by SPV power plant

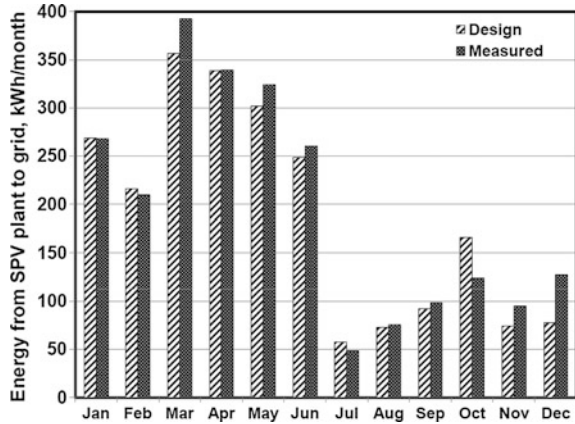


Fig. 11.31 Monthly energy import from grid

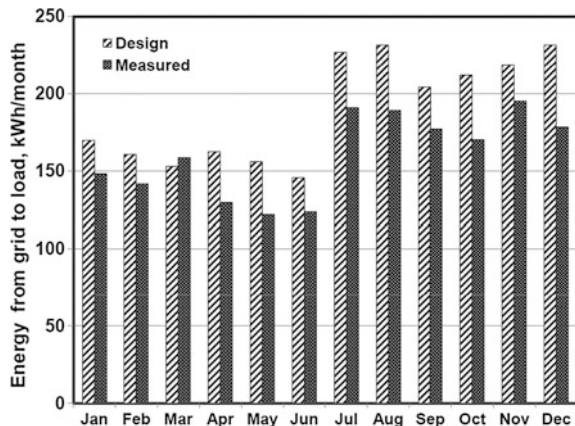
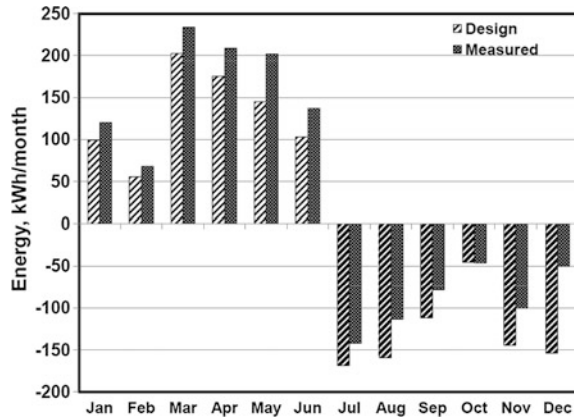


Figure 11.31 shows the variation in monthly average energy import from the grid during non-solar hours. The actual measured energy import from grid is less than the design value in all months, and the total energy import from grid is decreased from 2271.4 to 1924.4 kWh/year (decrease of 15.3%). This shows that the dependence on grid is minimized.

Figure 11.32 shows the variation in monthly net average energy export to the grid and energy import from the grid. The actual measured net energy export to the grid (during months between January and June) is increased compared to design value, and the net energy import from grid (during months between July and December) is reduced compared to design value. The net energy export to grid is increased from 781.7 to 970.2 kWh/y (increase of 24.1%), and the net energy import from grid is decreased from 781.7 to 531.2 kWh/y (decrease of 32.0%).

Fig. 11.32 Monthly net energy export to grid and net energy import from grid



11.8 Conclusions

The installation of solar PV power plant of 5.9 kW at one of the rural banks to meet the load requirement is working satisfactorily with good techno-economic viability. The total annual energy generation by solar PV power plant is 10,267 kWh/y that is higher compared to the design value of 10,035 kWh/y with an overall increase of 2.3%. The initial investment of \$7143 will provide the net saving of \$1292 per year after installation and operation of plant, and the anticipated payback period is 5.7 years. The estimated lifetime gain is about \$20,445 considering the replacement cost, operation and maintenance cost for the SPV power plant. The levelized cost of energy after implementation is \$0.081 per kWh, which is lower than the utility energy cost of \$0.10 per kWh and energy cost of DG set of \$0.32 per kWh.

References

1. Mandi RP, Kumar VS (2006) Integration of solar PV—diesel hybrid power system. *J Inst Eng (India)* 87:14–20
2. Lew DJ, Barley CD, Flowers LT (1997) Hybrid wind/photovoltaic systems for households in inner Mongolia. International conference on village electrification through renewable energy, New Delhi, 3–5 Mar 1997
3. Erge T, Hoffmann VU, Kiefer K (2001) The German experience with grid-connected PV-system. *Sol Energy* 70(6):479–487
4. Kim H-S, Okada N, Takigawa K (2001) Advanced grid connected PV system with functions to suppress disturbance by PV output variation and customer load change. *Sol Energy Mater Sol Cells* 67:559–569
5. Cooper PI (1974) Design philosophy and operating experience for Australian solar stills. *Sol Energy* 16:1–8
6. Christensen CB, Barker GM, Effect of tilt and azimuth on annual incident solar radiation for united states locations. In: Proceedings of solar forum 2001: solar energy: the power to choose, Washington, DC, Apr 21–25

7. Kamel F (1995) Perspectives on grid-connected photovoltaic solar generators. *Renew Energy* 6(5–6):515–520
8. Palomino GE (1997) Performance of a grid connected residential photovoltaic system with energy storage. 26th IEEE photovoltaic specialists conference, 29 Sept–3 Oct 1997
9. HOMER home page. <http://www.nrel.gov/international/tools/HOMER/homer.html>
10. Conti S, Raiti S, Tina G (2005) Simulink modelling of LV distributed generation. In: Proceedings of 18th international conference on electricity distribution, CIRED 2005, Turin, 6–9 June 2005

Chapter 12

Indirect Matrix Converter for Distributed Generation Application: An Experimental Study

Rahul Kumar Garg, Kavita Yadav, Vinod Kumar and Monika Vardia

12.1 Introduction

Because of increasing demand of electrical energy and environmental concerns, wind power has become the most promising renewable resource. In spite of its tremendous growth, the wind power industry keeps moving forward in order to increase the production, efficiency, and controllability of the wind turbines along with its easiness for the integration with power grid. Also, it is environment friendly in the sense that for every 1 kWh of electricity generated by wind, the emission of CO₂ is reduced by 1 kg, and operation of a wind turbine (WT) weighing 50 tons prevents burning of 500 tons of coal annually.

As per reports of REN21 Renewables report, 2015, and WWEA report, 2015, the wind power has grown very fast to a capacity of 428 GW in 2015 and it is expected to achieve 760 GW in 2020.

The wind power can be harnessed by a WECS which has components such as WT, an electric generator, a power electronic converter, and the corresponding control system. Based on the types of components used, different WECS topologies can be realized. However, the objective in all topologies is the same, i.e., the wind energy as the conversion of varying wind velocities into electric power at the grid frequency [1–3].

Variable speed operation of wind turbines is desirable for wind energy conversion system (WECS) as it yields 10–15% more output energy with less WT costs. Among various variable speed WECS configurations, the doubly fed

R.K. Garg · K. Yadav · V. Kumar (✉)
Department of Electrical Engineering, Maharana Pratap University
of Agriculture and Technology, Udaipur, India
e-mail: vinodcte@yahoo.co.in

M. Vardia
Faculty of Engineering, Pacific Academy of Higher Education
and Research University, Udaipur, India

induction generator (DFIG)-based topology has been the dominant technology in the market since late 1990s [4]. However, with the development in trends of WECS toward larger power capacity, increased power density, lower cost per kW, and the need for higher reliability, this situation has changed in the last few years. Moreover, DFIG requires gearbox to match the rotor and turbine, which many times suffers from faults and requires regular maintenance, making the system unreliable.

Therefore, nowadays, more attention has been paid to direct-drive gearless WECS concepts, for which the permanent magnet synchronous generator (PMSG) has been found to be superior owing to its various advantages such as self-excitation capability leading to a higher power factor (pf) and higher efficiency operation, lower maintenance costs, higher precision, higher power density, better grid compatibility, better voltage, and power capabilities with simple control method, except initial installation costs [5–7]. But due to the advanced research made in the field of permanent magnet materials fabrication, it has extended the PMSG lifetime with decreased production cost. Also, with the modern use of sensorless control will further enhance the robustness and reliability, while reducing the cost and complexity of the WECS. Many WT manufacturers such as Siemens Wind Power, Goldwind, GE Energy, and Vestas have adopted the direct-drive PMSG concept in their WECS production.

The power semiconductor devices being the backbone of power electronics converter used for WECS determine many critical performances such as reliability, cost, and efficiency. Module-packaged IGBT, press-pack-packaged IGBT, and the press-pack packaging integrated gate commutated thyristor (IGCT) are the potential high-power silicon-based semiconductor technologies for WECS application. Recently, there is a booming development of silicon carbide (SiC)-based devices, which are majorly in the form of MOSFET as well as diodes. The module packaging technology of IGBT has good applications with fewer mounting restrictions, but because of the soldering and bond wire connection of internal chips, it suffers from larger thermal resistance, lower power density, and higher failure rates [8].

During the last 25 years, trends in power electronic technologies for wind power application have changed dramatically. In early 1980s, the power electronics for wind turbines was just a soft starter for interconnection of squirrel cage induction generator with the grid, whereas in 1990s, the diode bridges with chopper were used to control wound rotor induction generator. In 2000, AC/DC/AC converters known as back-to-back converters were introduced in large scale which started to regulate the generated power from turbines [9].

Presently, power electronics plays an important and decisive role in delivering electrical power from WECS based on PMSG directly to the grid or load. Generally, full-scale power electronic converters are commonly used to control and regulate the frequency and voltage amplitude of the generated electricity to meet the grid code requirements. Various power processing topologies have been proposed and investigated from time to time by different researchers. Conventionally, the AC/DC/AC conversion system was adopted for wind power applications, where GSC may be a diode rectifier cascaded with a boost converter by [10], PWM rectifier called as voltage-sourced converter (VSC) by [6, 6, 11–13], or a multilevel

converter by [9]. However, the grid side converter is often a VSC unit. Though AC/DC/AC converter has high energy density and is relatively low in price, has serious concerns as mentioned in [14–16] with its large dc link electrolytic capacitor which is a common cause for its premature failure. The other main shortcomings of the above-mentioned AC/DC/AC conversion units are (i) large physical dimensions, high weight, and excessive volume/footprint of the DC link component, i.e., the DC capacitor or the inductor, (ii) the low reliability of DC capacitor, (iii) the poor line pf and harmonic distortion in line and machine currents, (iv) poor device utilization, and (v) poor pf operation.

It is therefore required to remove the dc capacitor, which after all is the main attractiveness of the all semiconductor matrix converters which have high merits over AC/DC/AC converter such as improved voltage gain with simplified control, free from commutation problems, compact in size, light weight, high reliability due to the absence of dc capacitor, and providing extremely fast transient response [14, 17, 18]. Also, it is considered as an emerging alternative as it provides a large number of control levers that allow for independent control on the voltage, frequency, input pf, and phase angle. Recently, some work has been reported in the literature on matrix converter (MC)-based WECS using simulation environment [14, 17–19]. Based on the state of the art in WECS research discussed above, this chapter aims to experimentally investigate the MC-interfaced PMSG for WECS under different conditions, e.g., grid/load unbalance/balance and varying wind conditions.

12.2 Topology of Wind Energy Conversion System Under Investigation

Figure 12.1 shows the block diagram of the proposed unidirectional MC-interfaced PMSG-based WECS under investigation.

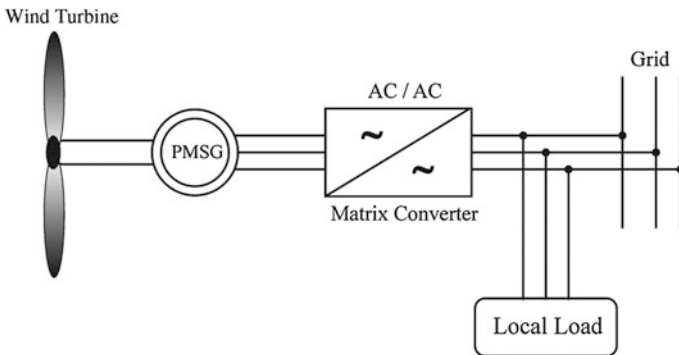


Fig. 12.1 Topology of wind energy conversion system under study

As it is shown in Fig. 12.1, MC is used for interfacing with the grid, and space vector PWM control is effectively used to achieve low-harmonic characteristics. It also performs pf control at grid interface and satisfies the reactive power demand. It implements the “perturbation and observation”-type MPPT scheme by controlling shaft speed to yield maximize energy output at varying wind speeds. A wind turbine emulator which drives the PMSG is developed for laboratory tests. Figure 12.2 presents the structure of the wind emulator. The wind speed changes, and load switching conditions are performed using the WT emulator, which consists of chopper dc drive, whose control is implemented using dSPACE DS1104 real time board.

It obtains the wind speed values, and by using the turbine characteristics and dc motor speed, it calculates the torque command of the WT. In this way, it is able to reproduce the steady and dynamic behavior of a real WT to the energy conversion system.

The schematic diagram of the unidirectional voltage-boosted MC with twelve switches (clamping circuit is not shown here) is shown in Fig. 12.3. It consists of

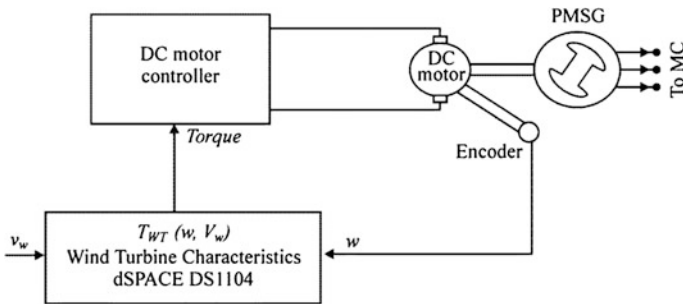


Fig. 12.2 Wind emulator system

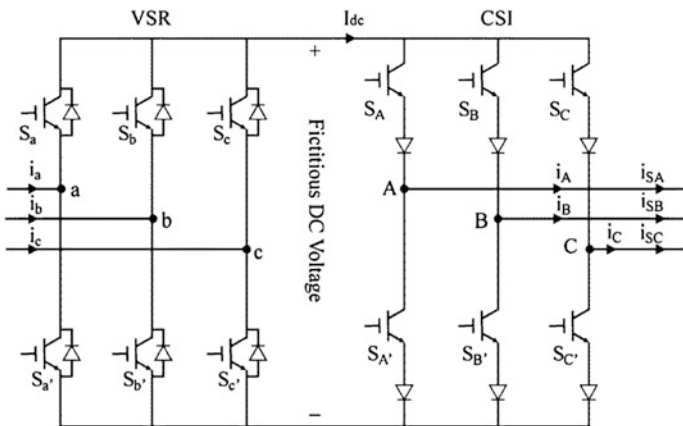


Fig. 12.3 Schematic diagram of the voltage-boosted MC topology

six switches with antiparallel diodes that are arranged as front-end voltage source rectifier (VSR), whereas other six switches with series diodes as rear-end current source inverter (CSI) as explained in [14].

12.3 Novel Control Scheme

As we know that, at any given wind velocity, maximum power can be captured from the wind, if the shaft speed is adjusted at the value corresponding to the peak power. The novel idea is to change the angular frequency of PMSG through SVPWM control of voltage-boosted MC to track the shaft speed corresponding to the maximum turbine power at all times. The proposed MC incorporates perturbation & observation-type MPPT, which is a part of the adaptive fuzzy control system, which through the MC manages to yield maximum wind power according to the current wind speed by regulating the angular frequency of the PMSG. The value of ω_{ref} is dynamically approached in real time from fuzzy controller, using P&O-type MPPT. The algorithm can be explained as below:

$$\text{Pertubtaion : } \omega_{\text{ref}}(t) = \omega_{\text{ref}}(t - 1) + s|\Delta\omega_{\text{ref}}| \quad (12.1)$$

$$\text{Observation : } \Delta P_0 = P_0(t) - P_0(t - 1) \quad (12.2)$$

where

$\omega_{\text{ref}}(t)$	actual angular frequency sampling
$\omega_{\text{ref}}(t - 1)$	previous angular frequency sampling
$ \Delta\omega_{\text{ref}} $	step of angular frequency disturbance
ΔP_0	difference of power
s	search direction

This method is achieved by changing the reference value of the frequency by $\Delta\omega_{\text{ref}}$ and then monitoring the corresponding change of the output power, ΔP_0 . With an increment (or decrement) of ω_{ref} , the corresponding increment (or decrement) of output power P_0 is estimated. If ΔP_0 is positive with last positive $\Delta\omega_{\text{ref}}$, in per-unit value by $L\Delta\omega_{\text{ref}} (pU)$, the search is continued in the same direction. If, on the other hand, *positive* $\Delta\omega_{\text{ref}}$ causes *negative* ΔP_0 , the direction of search is reversed. MC achieves maximum wind power acquisition from the WT by driving the angular frequency, ω_e , to its optimal reference value, ω_{ref} . This is accomplished by regulating the active power absorbed by MC, through modulation of phase angle of its SVPWM reference signal as explained in detail in [14, 20].

Figure 12.4 shows the control block diagram of the system that uses the power circuit of Fig. 12.1. The MC uses vector control in inner current control loop to permit fast transient response for system. For a particular wind velocity, there will be an optimum setting of generator speed. The speed loop will generate the torque

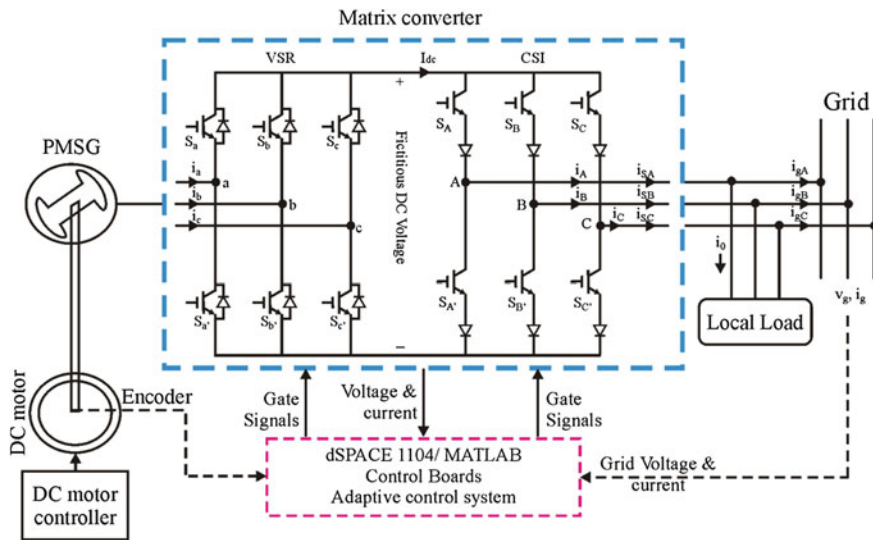


Fig. 12.4 Overall block diagram of the proposed matrix converter-interfaced PMSG for wind energy conversion system

component of machine current so as to balance the developed torque with the load torque [20].

12.4 Development of Hardware Laboratory Prototype

To verify the proposed adaptive control, a laboratory test is carried out on developed 1.2 kW prototype of MC-interfaced PMSG for WECS using dSPACE 1104 real-time control system, which is programmed in the MATLAB/Simulink environment. Figure 12.5 shows the picture of the test rig setup, which is the implementation of block diagram of the proposed system shown in Fig. 12.4. Here, three-phase programmable AC supply is used as a grid. To verify the wind simulator operation, the speed of the shaft is changed by implementing a speed loop control. At different speeds, the input power to the MC is measured. The measured power points are recorded, and the plot of the generator speed versus output power is generated as shown in Fig. 12.6.

Space vector pulse width modulation (SVPWM)-based switching signals given to the switches of MC and dc drive-based WT emulator are presented in Fig. 12.7. Figure 12.8 shows the implementation of space vector modulation (SVM) switching strategy as per explanations in previous section for MC of proposed system in dSPACE 1104 kit in MATLAB/Simulink environment. Three-phase variable resistive load, diode bridge rectifier inverter-fed induction motor, and diode bridge rectifier-fed dc motor are used as nonlinear inductive ac/dc loads.



Fig. 12.5 Schematic of the experimental setup of matrix converter interfaced PMSG for wind energy conversion system

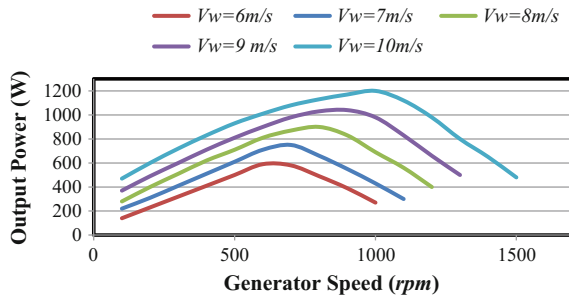


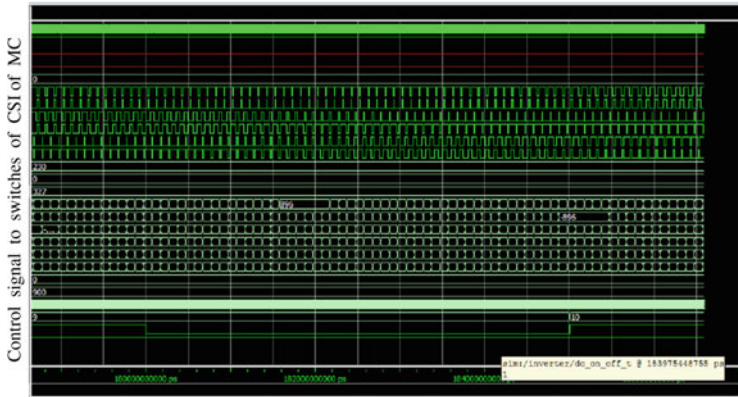
Fig. 12.6 Experimental plot of generator speed versus output power for different wind speeds

12.5 Experimental Investigation

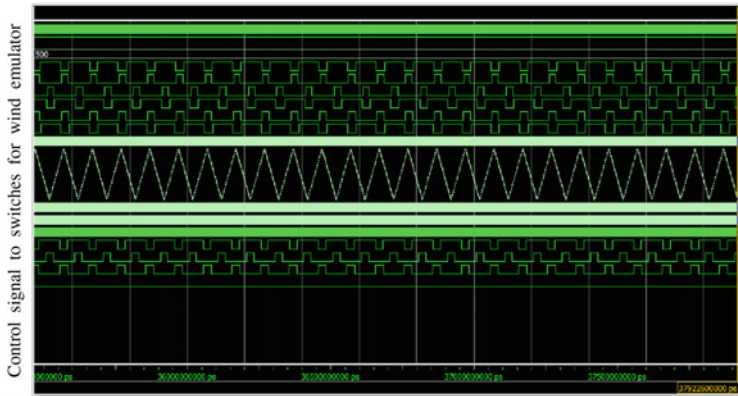
To verify the adaptive fuzzy control methods for developed laboratory 1.2 kW prototype of MC-based WECS, experimental investigation is carried out under both isolated and grid-connected modes for different balanced/unbalanced load and wind conditions.



(a) Control signal to VSR of MC



(b) Control signal to CSI of MC



(c) Control signal to dc drive based wind turbine emulator

Fig. 12.7 SVPWM switching signals to MC and dc drive-based wind turbine emulator

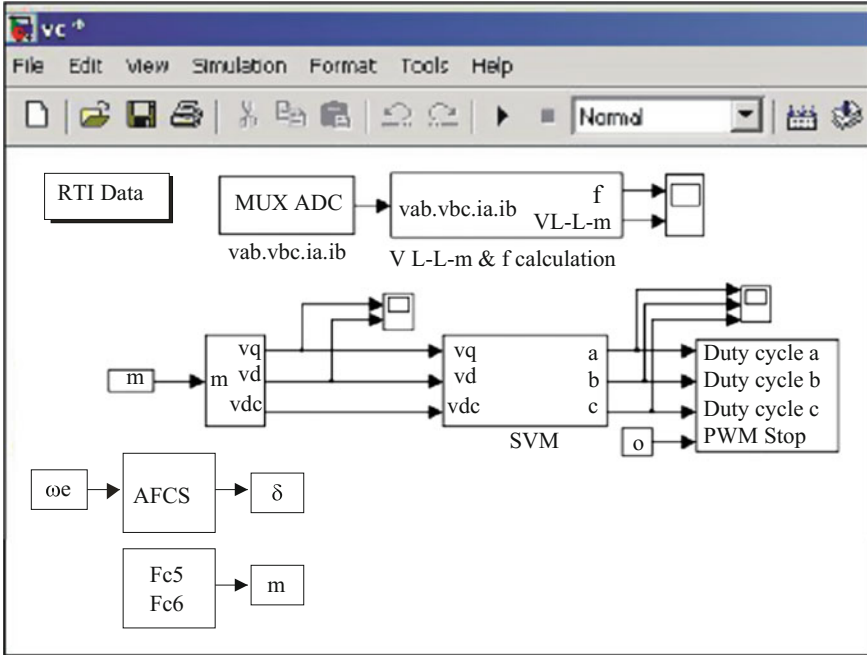


Fig. 12.8 SVPWM algorithm implemented in dSPACE 1104 for matrix converter of proposed WECS system in MATLAB/Simulink environment

12.5.1 Response Under Isolated Mode

In isolated mode, the main function of the proposed control is to keep the frequency at its set value and to regulate the load voltage at desired level. A certain amount of current corresponding to the rated voltage is fed to the load by the MC to achieve the desired voltage level at load terminals.

12.5.1.1 Response During Constant Resistive and Nonlinear Inductive Load

During isolated mode, WT is controlled to deliver power to an external load through unidirectional indirect MC. Here, the objective of the developed control is to keep regulated voltage across the load. Prototype has been tested experimentally under different resistive and nonlinear inductive load ranging from no load to 2.5 kW at different generator speeds.

From experimental waveforms of Fig. 12.9a, b, it can also be observed that three-phase load current and voltages are properly balanced and well regulated sinusoidally with unity pf for resistive load. Also, it can be seen that phase voltage

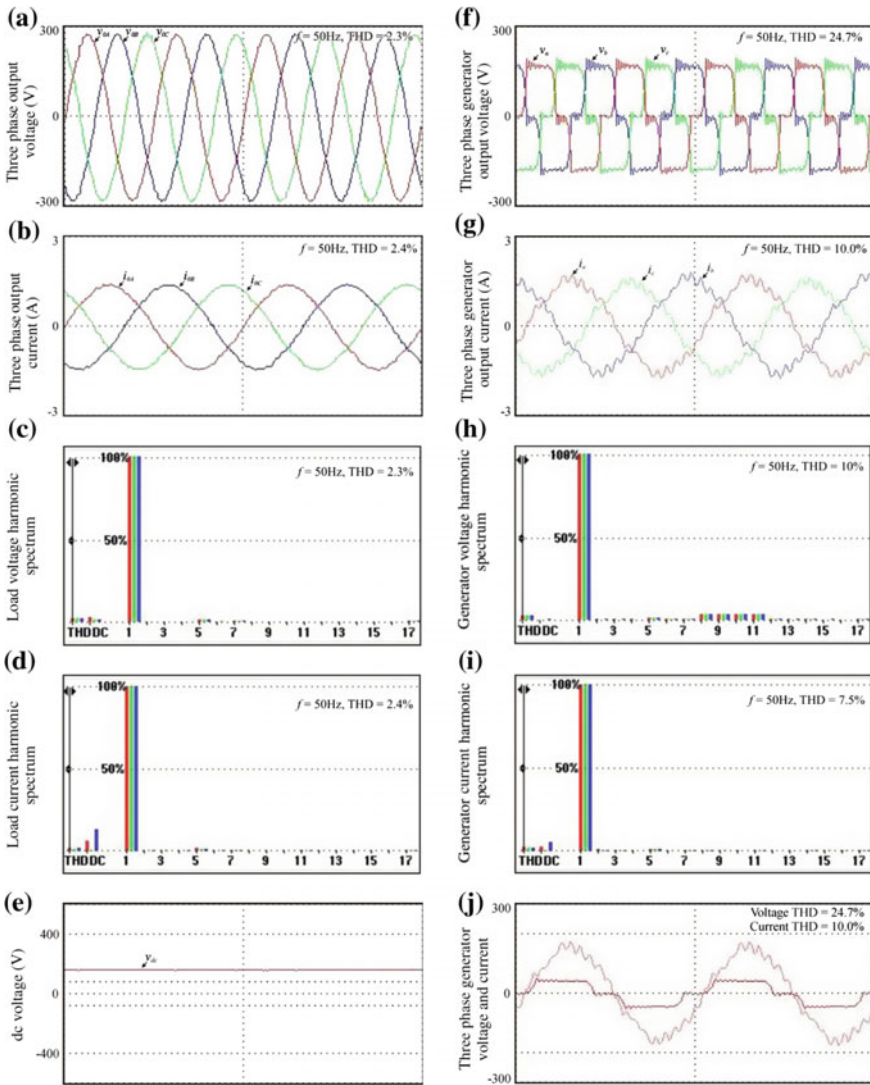


Fig. 12.9 Experimental waveforms during constant resistive load of 1 kW, 1200 rpm: **a** three-phase output voltage; **b** three-phase output current; **c** load voltage harmonic spectrum; **d** load current harmonic spectrum; **e** fictitious dc link voltage; **f** generator output voltage; **g** generator output current; **h** generator voltage harmonic spectrum; **i** generator current harmonic spectrum; and **j** generator phase voltage and current

and current of generator converter, fictitious dc link voltage, and the load voltage for resistive load are within safe limits. From load voltage and current harmonic spectrum of Fig. 12.9c, d, it is shown that total harmonic distortion (THD) of load voltage and load current is 2.3 and 2.4%, respectively, which is less than 5% and it

is in consent with the permissible limits of IEEE 1547, IEEE 519, and IEC 61727 standards and thus satisfies the general standards of produced power in terms of voltage and current inside 5% THD. Low THD is due to the use of SVPWM switching for the MC.

Unity pf operation with low THD satisfies the pf demand, and is far better as compare to pf and THD of about 0.94 and 4.25%, respectively, in case of converter topology proposed for wind power applications by Ref. [21]. It demonstrates the expected improvement when compared with similar works. Therefore, it is clear that the SVPWM-based MC-interfaced WECS succeeds in regulating the load voltage and frequency within satisfied limits of 220/400 V and 50 Hz, respectively, with low-harmonic characteristics.

12.5.1.2 Response During Nonlinear Inductive Dc Load

In order to validate the developed MC-interfaced WECS, experimental investigation using nonlinear inductive dc load is also carried out.

Here, diode rectifier-fed dc motor is used as a nonlinear inductive dc load. Figure 12.10 presents the experimental waveforms for constant nonlinear inductive dc load of 1 kW at generator speed of 1200 rpm.

12.5.1.3 Response During Varying Load Condition

Figure 12.11 demonstrates the effectiveness of the controls for laboratory prototype of WECS during dynamic conditions. The load is changed from 100 to 50% and then from 50 to 100% to simulate the transient load changing. It is observed that

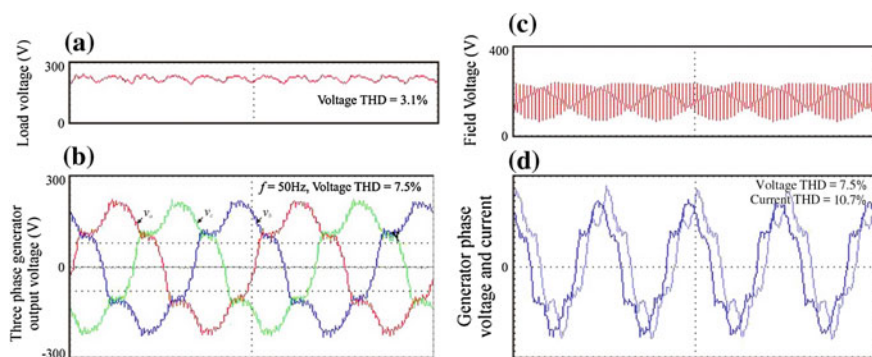
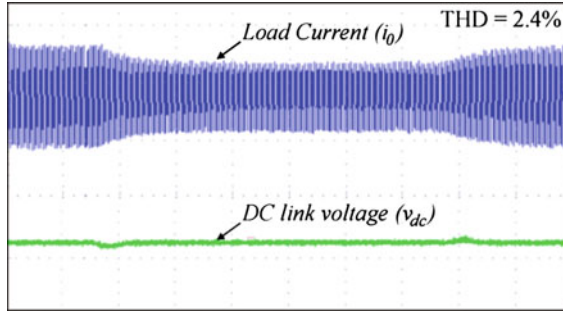
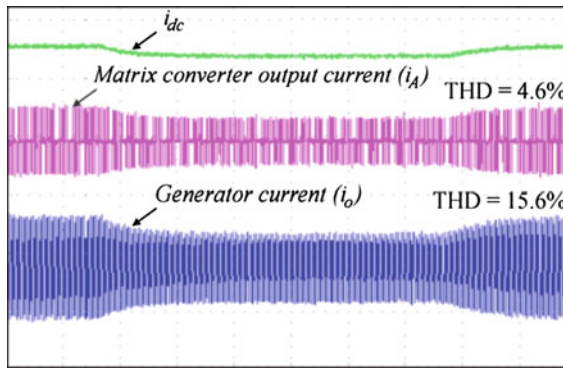


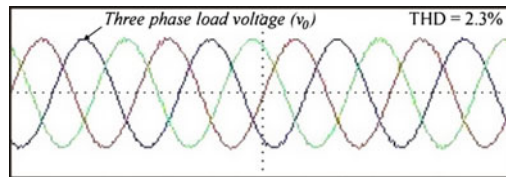
Fig. 12.10 Experimental waveforms during constant nonlinear dc load of 1 A, 1200 rpm: **a** output load voltage; **b** generator output voltage; **c** generator field voltage; and **d** generator phase voltage and current



(a) Instantaneous load current (i_θ), and fictitious dc link voltage (v_{dc})



(b) dc link current (i_{dc}), MC output current (i_A), and generator current (i_θ)



(c) Three phase load voltage (v_θ)

Fig. 12.11 Experimental waveform during varying load condition: **a** load voltage and fictitious dc link voltage; **b** dc link current, MC output current, and generator current; **c** three-phase load voltages response when the load changes from 100 to 50% and then from 50 to 100%

load voltage is well maintained despite the variation of loads. But, the load current is changing with load variation as expected.

It is seen that the controller can regulate the load voltage and frequency quite well under varying load conditions. When the load is changed, the load current varies and so closed loop control commands the necessary control action to maintain the constant voltage magnitude.

12.5.2 Response Under Grid-Connected Mode

In grid-connected mode, the main objective of the control algorithm is to track the dispatch power so as to yield maximum energy. Also, to achieve almost unity pf operation at the grid, the reactive power is controlled. Space vector PWM is effectively used to control the MC for interfacing the generator with the grid. Here, in this work, programmable AC supply available in the laboratory is used as a grid.

12.5.2.1 Under Steady-State Condition

The steady-state grid phase voltage and current waveforms for unity, lagging, and leading pf operations are shown in Fig. 12.12a–c.

This demonstrates the reactive power capability of the MC for wind power applications. The reactive power control capability of the proposed MC-based WECS is also illustrated in Fig. 12.12d for unity, lagging, and leading pf operation,

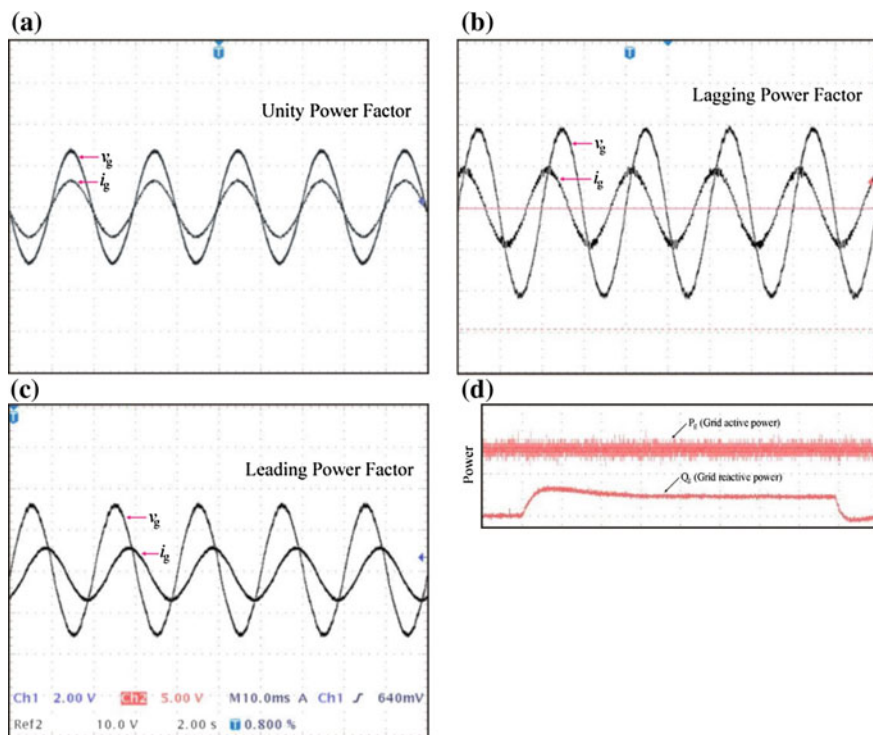


Fig. 12.12 Steady state grid phase voltage v_g and injected grid current i_g waveforms for **a** unity power factor operation; **b** lagging power factor operation; **c** leading power factor operation; and **d** injected grid active power P_g and reactive power Q_g

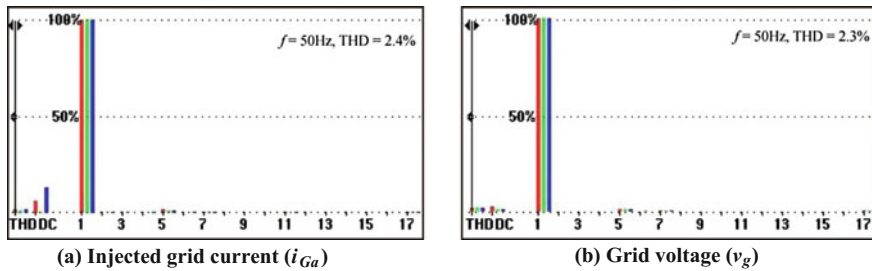


Fig. 12.13 Harmonic spectrum for injected grid current (i_{gA}) and grid voltage (v_g)

while keeping active power constant. Figure 12.12 shows the experimental results during steady-state condition. From experimental waveform of Fig. 12.12a, it is shown that grid phase voltage is regulated and sinusoidal, whereas that of dc link voltage is almost dc without any distortion. It can be observed from Fig. 12.12b that grid-injected phase current and voltages are well regulated sinusoidally with almost unity pf. A good equilibrium among the voltages can be seen. Also, the unfiltered MC current (i_A) is in phase with the grid phase voltage (v_g).

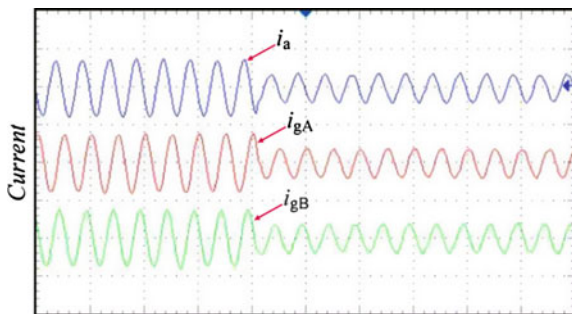
The grid current (i_g) has a slight phase lag induced by the filter capacitor, but this phase lag is negligible when the MC's current injection into the grid is increased. Figure 12.12c shows three-phase output grid currents illustrating the balanced nature. Figure 12.13 presents the harmonic spectrum for injected grid current and voltage, where it can be seen that THD is 2.4 and 2.3%, respectively. Also, pf is equal to 0.996 and THD is about 2.3%, which satisfies the pf demand, and is far better as compared to pf and THD of about 0.94 and 4.25%, respectively, in case of converter topology proposed for wind power applications in [21].

The THD measured for grid-injected current and voltage is quite low as per standard IEEE 1547, IEEE-519, and IEC 61727 and thus satisfies the general standards of produced power in terms of voltage and current THDs within the limits of 5%. This improvement in pf results in the reduction of about 13% generator conduction losses. This demonstrates the expected improvement when compared with similar works by [6, 21–23]. It is clear that this proposed optimal controller for MC interfaced WECS succeeds in regulating the load voltage and frequency within limits of 220/400 V and 50 Hz, respectively.

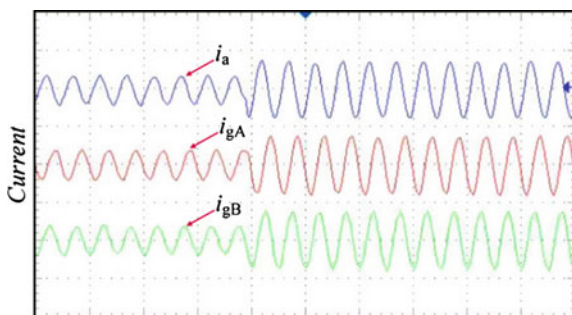
12.5.2.2 Dynamic Response Under Change in Current Command

To validate the robustness of voltage boost function of the MC, proposed system dynamic response is tested experimentally when current commands are increased and decreased. Figure 12.14 verifies the effectiveness of the proposed

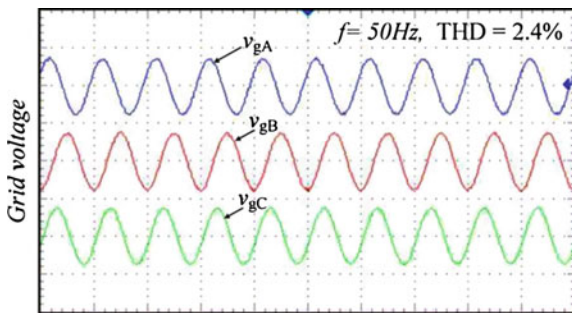
Fig. 12.14 Experimental waveforms during change in MC current command. **a** MC input current (i_a) and grid currents (i_{gA} and i_{gB}) response of current command decreasing; **b** MC input current (i_a) and grid currents (i_{gA} and i_{gB}) response of current command increasing; and **c** three-phase grid voltages (v_{gA} , v_{gB} , v_{gC}) during change in current command



(a) Current command decreasing



(b) Current command increasing



(c) Three phase grid voltages (v_{gA} , v_{gB} , v_{gC})

high-efficiency control system of the MC-interfaced WECS when input current amplitude commands are decreased from 3.5 to 1.5 A and increased from 1.5 to 3.5 A, respectively.

It can be noticed from the experimental waveforms that unity pf is maintained, despite of dynamic current command changing. Also, input current of MC can track effectively its current commands. The output current increases or decreases accordingly without deteriorating waveforms.

12.6 Conclusion

This chapter presents detailed explanation of the application and development of MC for DG. It also presents the experimental investigation of merits and demerits of use of MC for wind power application. From the experimental results, it can be verified that a good equilibrium among the load currents and voltages can be seen. Also, the load voltage and current waveforms are properly balanced and well regulated sinusoidally with unity pf operation for resistive load. Also, THD of load voltage and load current is 2.3 and 2.4%, respectively, which is less than 5% and it is in consent with the permissible limits of IEEE standard 1547, IEEE 519, and IEC 61727 and thus satisfies the general standards of produced power in terms of voltage and current inside 5%. Low THD is due to the use of SVPWM switching for the MC. This improvement in pf results in the reduction of about 13% in generator conduction losses.

References

1. Frerics LL (1990) Wind energy conversion systems. Prentice Hall, New York
2. Ackermann LST (2000) Wind Energy technology and current status: a review. *Renew Sustain Energy Rev* 4:315–375
3. Bansal RC, Zobaa AF, Saket RK (2005) Some issues related to power generation using wind energy conversion systems: an overview. *Int J Emerg Electr Power Syst* 3(2):1–19
4. Hansen AD, Iov F, Blaabjerg F, Hansen LH (2011) Review of contemporary wind turbine concepts and their market penetration. *J Wind Eng* 58(4):1081–1095
5. Liserre M, Cardenas M, Molinas M, Rodriguez J (2011) Overview of multi-MW wind turbines and wind parks. *IEEE Trans Ind Electron* 58(4):1081–1095
6. Chinchilla M, Arnaltes S, Burgos (2006) Control of permanent-magnet generators applied to variable-speed wind-energy systems connected to the grid. *IEEE Trans Energy Convers* 21(1):130–135
7. Kim KH, Jeung YC, Lee DC, Kim HG (2011) LVRT scheme of PMSG wind power systems based on feedback linearization. *IEEE Trans Power Electron* 27(5):2376–2384
8. Ma K, Blaabjerg M (2012) The impact of power switching devices on the thermal performance of a 10 MW wind power NPC converter. *Energies* 5(7):2559–2577
9. Blaabjerg F, Liserre M, Ma K (2012) Power electronics converters for wind turbine systems. *IEEE Trans Ind Appl* 48(2):708–719
10. Amei K, Takayasu Y, Ohji T, Sakui M (2002) A maximum power control of wind generator system using a permanent magnet synchronous generator and a boost chopper circuit. In: *Proceeding of PCC*, pp 1447–1452
11. Peña R, Cárdenas R, Reyes E, Clare J, Wheeler P (2009) A topology for multiple generation system with doubly fed induction machines and indirect matrix converter. *IEEE Trans Ind Electron* 56(10):4181–4193
12. Naidu M, Walters J (2003) A 4-kW 42-V induction-machine-based automotive power generation system with a diode bridge rectifier and a PWM inverter. *IEEE Trans Ind Appl* 39(5):1287–1293
13. Teodorescu R, Blaabjerg F (2004) Flexible control of small wind turbines with grid failure detection operating in stand-alone and grid connected mode. *IEEE Trans Power Electron* 19(5):1323–1332

14. Kumar V, Joshi RR, Bansal RC (2009) Optimal control of matrix converter based WECS for performance enhancement and efficiency optimization. *IEEE Trans Energy Convers* 24 (1):264–273
15. Tazil M, Kumar V, Bansal RC, Kong S, Dong ZY, Freitas W, Mathur HD (2010) Three-phase doubly-fed induction generators: an overview. *IET Electr Power Appl* 4(2):75–89
16. Liu X, Wang P, Loh PC, Blaabjerg F (2011) A Three-phase dual-input matrix converter for grid integration of two ac type energy resources. *IEEE Trans Ind Electron* 60(1):20–30
17. Barakati SM, Kazerani M, Aplevich JD (2009) Maximum power tracking control for a wind turbine system including a matrix converter. *IEEE Trans Energy Convers* 24(3):705–713
18. Ghedamsi K, Aouzellag D, Berkouk EM (2006) Application of matrix converter for variable speed wind turbine driving a doubly fed induction generator. In: *Proceedings of IEEE international symposium on power electronics, electrical drives, automation and motion*, pp 1201–1205
19. Cardenas R, Pena R, Tobar G, Clare J, Wheeler P, Asher G (2009) Stability analysis of a wind energy conversion system based on a doubly fed induction generator fed by a matrix converter. *IEEE Trans Ind Electron* 56(10):4194–4206
20. Kumar V, Joshi RR, Bansal RC (2015) Development of a novel control for matrix converter interfaced wind energy conversion system for dynamic performance enhancement. *Taylor Francis J Electr Compon Power Syst* 43(8–10):1062–1071
21. Oliveira DS, Reis JM, Silva CEA, Barreto LH, Fernando LM, Bruno LS (2010) A three-phase high-frequency semicontrolled rectifier for PM WECS. *IEEE Trans Power Electron* 25 (3):677–685
22. Haque ME, Negnevitsky M, Muttaqi KM (2010) A novel control strategy for a variable-speed wind turbine with a permanent-magnet synchronous generator. *IEEE Trans Ind Appl* 46 (1):331–339
23. Karaman E, Farasat M, Trzynadlowski AM (2013) Permanent-magnet synchronous-generator wind-energy systems with boost matrix converters. In: *Proceeding of IEEE energy conversion congress and exposition*, pp 2977–2981

Chapter 13

An Experimental Study on Zeta Buck–Boost Converter for Application in PV System

Neeraj Priyadarshi, Kavita Yadav, Vinod Kumar and Monika Vardia

13.1 Introduction

In the present times, as fossil fuels are depleted and exhausted on large scale, eco-friendly renewable energy sources are required as an alternate source of power. Wind, solar, fuel cells, geothermal, etc. are the primary renewable energy sources. Compared to other renewable sources, the PV system is considered as an emerging renewable technology since it requires less maintenance, possess low cost, and is eco-friendly in nature [1–5]. The recent PV system has very less tracked and conversion efficiency. Therefore, maximum power point tracking (MPPT) control algorithms are required to obtain the optimal power and highly tracked efficiency. The generation of PV power depends mainly on two parameters, i.e., insolation and surrounding temperature. The MPPT algorithm enhances the tracking efficiency as well as tries to make the operating point into maximum power point (MPP) [6–10].

Several control methods are employed to obtain the peak power from the PV panel. In this paper, perturb and observe (P and O), incremental conductance, and conventional fuzzy logic controller (FLC)-based MPPT have been discussed. The main disadvantage of the above-mentioned methods is that they fail to track maximum power under changing the weather conditions as well as oscillation around MPP [11–15]. The modified FLC-based MPPT presented in this research paper works under abrupt weather conditions which has low cost and high tracking efficiency and does not require any mathematical modeling analysis.

N. Priyadarshi (✉) · K. Yadav · V. Kumar
Department of Electrical Engineering,
College of Technology and Engineering, Udaipur, India
e-mail: neerajrjd@gmail.com

M. Vardia
Faculty of Engineering, Pacific Academy of Higher Education
and Research University, Udaipur, India

In recent times, different types of DC–DC converters have attracted much attention for their potential applications in the solar energy system as an efficient MPPT tracker. Normally, these converters function as buck or boost mode. The buck–boost converter has an added advantage that they can work for both step-up or step-down operation. The buck–boost converter is used as an interface between the PV system and the grid. Among these various topologies such as four switch type, cuk, sepic, and zeta converter [16], the zeta converter is best suited for the tracking purpose mainly because it provides output voltage, which has comparatively less ripple compared to other topologies. As these converters employ binary combinations of capacitors and inductors as dynamic storage elements, they are capable of intensifying and reducing the input signal without changing the polarities. Thus, they have high efficiency, high voltage conversion ratio, low cost, and reduced voltage stress compared to other topologies of buck–boost converter.

Several control methods, namely predictive current controller [17], hysteresis current controller [18], space vector pulse-width modulation (SVPWM) [19], and space vector modulation hysteresis current controller (SVMHCC), are employed for the generation of switching signals for voltage source inverter. Compared to other existing current controller, the SVMHCC provides an enhanced and modified controlling power of the overall tracking system. The MPPT and inverter controllers are first simulated in MATLAB/Simulink and then implemented in hardware using real-time dSPACE DS1104 control board.

13.2 Topology of Proposed Photovoltaic System

Figure 13.1 shows the proposed structure of the grid-connected PV system and its control. The zeta converter performs the MPPT functions. The FLC-based controller for MPPT and SVMHCC is used to generate the gating pulses of the inverter power switches. Zeta converter works as an interface between solar panel and three-phase VSI. The real-time dSPACE DS1104 control board is employed to control the inverter and the MPPT controllers.

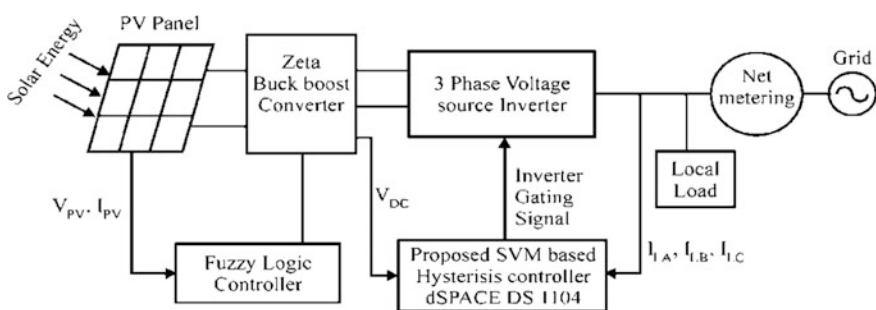


Fig. 13.1 Proposed grid PV system

13.3 Novel Control Scheme

A. Zeta Buck–Boost Converter

In the present work, the zeta converter with buck–boost characteristics has been selected, which is employed in MPPT system. The zeta converter is utilized for least output voltage ripple as a MPPT tracker. It is able to amplify and reduce the input voltage levels without inverting the polarities, as it includes two capacitors and two inductors as dynamic charge storage elements.

It has two operating modes: In the first mode, when switch is ON, the current flows through L and L_1 and diode is reversed biased, whereas the diode is forward biased in the second mode when switch is opened and inductor L_1 is fully discharged through R_L load, which is illustrated in Fig. 13.2.

B. Fuzzy Logic Controller-based MPPT

Compared to conventional MPPT algorithms, the intelligent fuzzy logic-based MPPT gives optimal tracking power, high convergence speed, and better dynamic response and there is no mathematical modeling required. It works effectively at abrupt weather condition. The block diagram of FLC, which comprises fuzzification, inference engine, and defuzzification blocks, is depicted in Fig. 13.3.

(i) Fuzzification:

Fuzzification is the method used to convert crisp value to fuzzy value. It combines the crisp input to the stored membership function which produces fuzzy inputs. The membership function is assigned for each input to convert the crisp values into fuzzy values. After assigning the membership function, it compares the stored membership function with real-time inputs to generate fuzzy inputs.

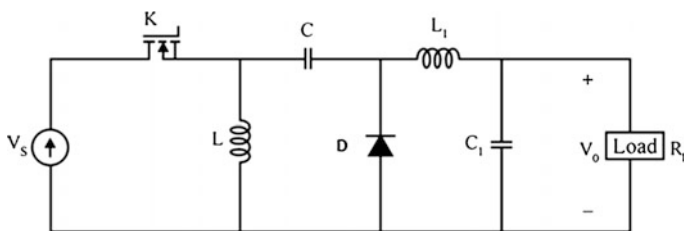


Fig. 13.2 Zeta converter

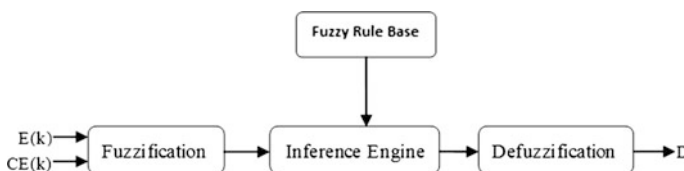


Fig. 13.3 Fuzzy logic controller

The error E and change of error CE of two fuzzy controller inputs are calculated as follows:

$$E(K) = \frac{P_{PV}(K) - P_{PV}(K - 1)}{V_{PV}(K) - V_{PV}(K - 1)} \tag{13.1}$$

$$CE(K) = E(K) - E(K - 1) \tag{13.2}$$

where $P_{PV}(K)$ and $V_{PV}(K)$ are the power and voltage of PV array, respectively. The 7 linguistic variables of input and output are shown in Fig. 13.4.

(ii) *Fuzzy inference engine (fuzzy rule base):*

The fuzzy rules are selected based on the complete behavior of the PV system. Fuzzy decisions are made on the basis of fuzzy rules to get optimal power point tracking of PV array at variable irradiance and ambient temperature. Mamdani’s method based on the max–min composition is used as a rule base, which is shown in Table 13.1.

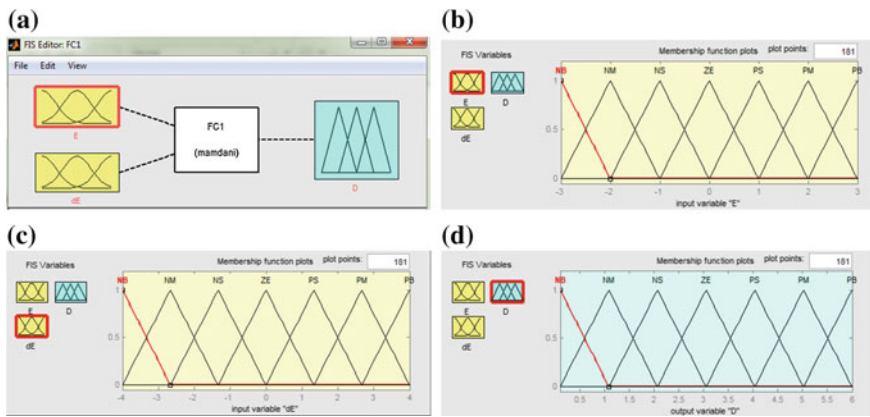
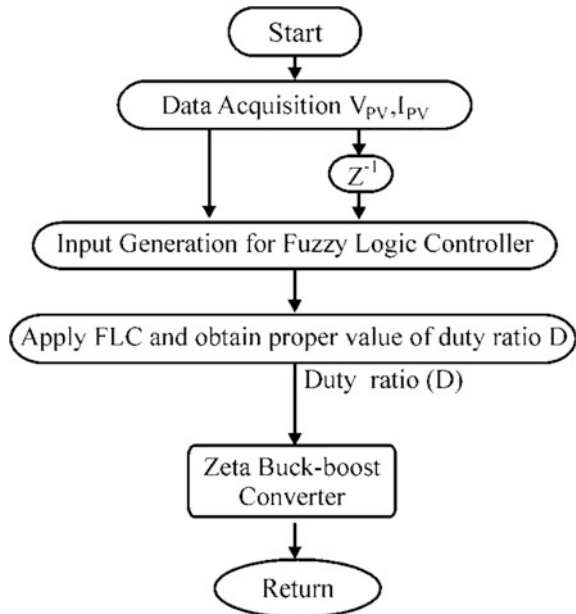


Fig. 13.4 a Picture of FLC FIS editor. b Membership function E . c Membership function dE . d Membership function output D

Table 13.1 Fuzzy rule base

dE	E						
	NB	NM	NS	ZE	PS	PM	PB
NB	ZE	ZE	ZE	PB	PB	PB	PB
NM	ZE	ZE	ZE	ZE	ZE	NM	PS
NS	ZE	ZE	PM	PS	PS	PS	PS
ZE	PS	PS	ZE	ZE	ZE	ZE	NS
PS	NS	NS	NS	NS	ZE	NS	ZE
PM	NS	NS	ZE	ZE	NS	NM	NS
PB	NB	NB	NB	NB	PM	NB	PM

Fig. 13.5 Flowchart of FLC-based MPPT algorithm



(iii) Defuzzification

Defuzzification method is used to get the numerical variable of the FLC output. The linguistic variables are converted into numerical values using this method. The defuzzification utilizes the centroid method for selecting the appropriate value of duty cycle for zeta converter. The optimum value of duty cycle is sent to the MOSFET of zeta buck–boost converter as a reference signal. The flowchart of the FLC-based MPPT is shown in Fig. 13.5.

C. Three-phase Inverter Control

Instantaneous reactive power (IRP) theory is employed to generate the reference current, which works in transient as well as in steady-state condition. Using park's transformation, the instantaneous real and reactive power is calculated. Figure 13.6 shows the complete block diagram for the generation of switching signal for three-phase voltage source inverter. This method of pulse generation is the combination of space vector modulation and hysteresis current controller. The error signal is generated by comparing the reference and actual compensating current, which works as an input to hysteresis controller. Using the switching function table, the upper and lower band errors are calculated as is shown in Fig. 13.7.

The output of upper band signal is calculated using six sectors [20] as follows:

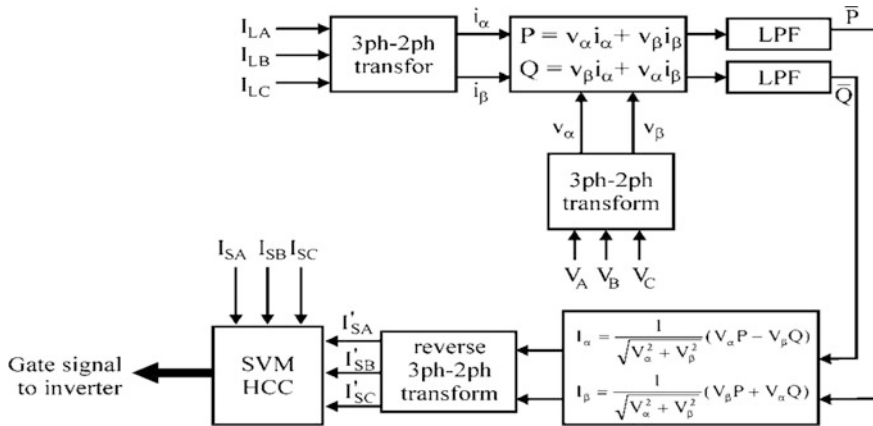


Fig. 13.6 Block diagram of three-phase VSI control

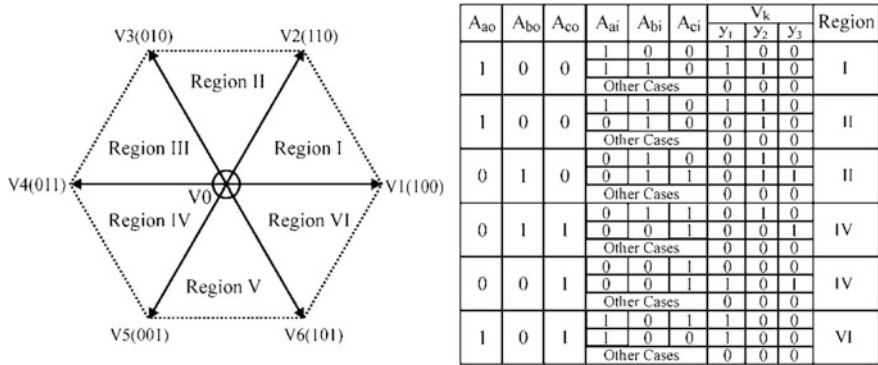


Fig. 13.7 Sectors and switching table of space vector

$$\begin{aligned}
 S_1 &= A_{ao}\bar{A}_{bo}\bar{A}_{co} \\
 S_2 &= A_{ao}A_{bo}\bar{A}_{co} \\
 S_3 &= \bar{A}_{ao}A_{bo}\bar{A}_{co} \\
 S_4 &= \bar{A}_{ao}\bar{A}_{bo}A_{co} \\
 S_5 &= \bar{A}_{ao}A_{bo}A_{co} \\
 S_6 &= A_{ao}\bar{A}_{bo}A_{co}
 \end{aligned}
 \tag{13.3}$$

where A_{ao} , A_{bo} , and A_{co} and A_{ai} , A_{bi} , and A_{ci} are upper band and lower band output hysteresis comparator signals [20].

The output of lower band signal is calculated using six sectors as follows:

$$\begin{aligned}
 y_1 &= S_1[A_{ai}\bar{A}_{bi}\bar{A}_{ci} + A_{ai}A_{bi}\bar{A}_{ci}] + S_2A_{ai}A_{bi}\bar{A}_{ci} \\
 &\quad + S_5A_{ai}\bar{A}_{bi}A_{ci} + S_6[A_{ai}\bar{A}_{bi}A_{ci} + A_{ai}\bar{A}_{bi}\bar{A}_{ci}] \\
 y_2 &= S_1A_{ai}A_{bi}\bar{A}_{ci} + S_2[A_{ai}A_{bi}\bar{A}_{ci} + \bar{A}_{ai}A_{bi}A_{ci}] \\
 &\quad + S_3[\bar{A}_{ai}A_{bi}\bar{A}_{ci} + \bar{A}_{ai}A_{bi}A_{ci}] + S_4\bar{A}_{ai}A_{bi}A_{ci} \\
 y_3 &= S_4\bar{A}_{ai}A_{bi}A_{ci} + S_4[\bar{A}_{ai}A_{bi}A_{ci} + \bar{A}_{ai}\bar{A}_{bi}A_{ci}] \\
 &\quad + S_5[\bar{A}_{ai}\bar{A}_{bi}A_{ci} + A_{ai}\bar{A}_{bi}A_{ci}] + S_6A_{ai}\bar{A}_{bi}A_{ci}
 \end{aligned}
 \tag{13.4}$$

where y_1 , y_2 , and y_3 are output signals of the inner band hysteresis comparators.

13.4 Development of Hardware Laboratory Prototype

Figure 13.8 shows the experimental setup of the proposed grid-connected PV system for performance verification. The dSPACE DS1104 kit is interfaced with Simulink-based simulation model. The voltmeter, ammeter, power quality analyzer Fluke 434, and digital oscilloscope have been used as measuring components for practical implementation. The three-phase ACs are measured using Fluke i400S. The three-phase inverter, IGBT driver, DC power supply, and pc with dSPACE DS1104 have been employed as major elements for experimental setup. Using the proposed controller, instantaneous active and reactive power, total harmonic distortion (THD), and power factor have been well maintained with better performance.



Fig. 13.8 Hardware structure of proposed grid PV system

13.5 Experimental Study Under Different Conditions

The dSPACE DS1104 kit is employed to interface with Simulink simulation model. The simulation model implemented in Simulink run on dSPACE DS1104. The PV current and voltage values are supplied to the dSPACE analog-to-digital converter and are utilized by the Simulink MPPT control block as depicted in Fig. 13.9. The generated gating pulses for three-phase VSI using dSPACE is shown in Fig. 13.10.

Figure 13.11 depicts the practical responses of grid voltage and current at unity power factor operation effectively.

By means of FLC and SVMHCC, the active and reactive power is well maintained and optimal power has been extracted through PV panel. Figure 13.12 depicts the practical responses of inverter voltage and current with fewer fluctuations.

Figure 13.13 describes the practical results of PV power, PV voltage, and PV current at steady-state condition. The PV current has low steady-state oscillation and attained MPP at relatively small time.

Figure 13.14a, b shows the THD spectrum of inverter voltage and current. The inverter voltage and current have 2.3 and 2.5% THD percentage, respectively, which follows standard IEEE 519. Figure 13.15 depicts the practical responses of PV power, PV voltage, and PV current during variable weather condition. The

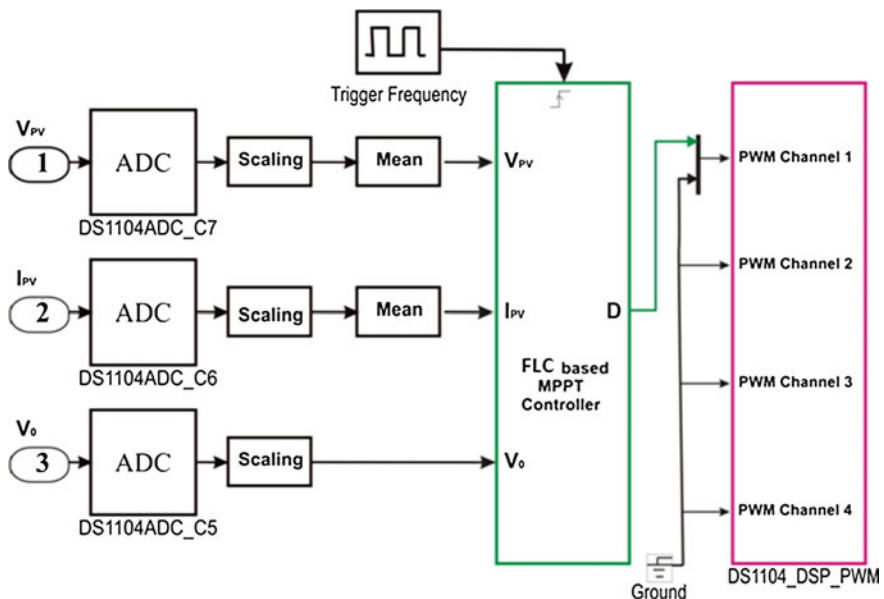


Fig. 13.9 FLC-based MPPT Simulink model for implementation in dSPACE

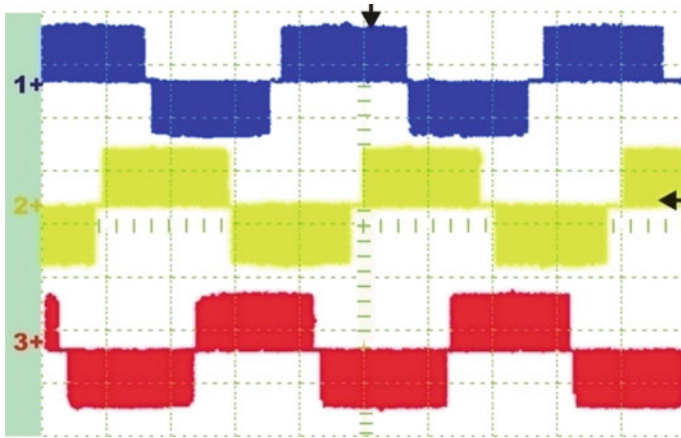


Fig. 13.10 Generated gate pulses for three-phase VSI using dSPACE

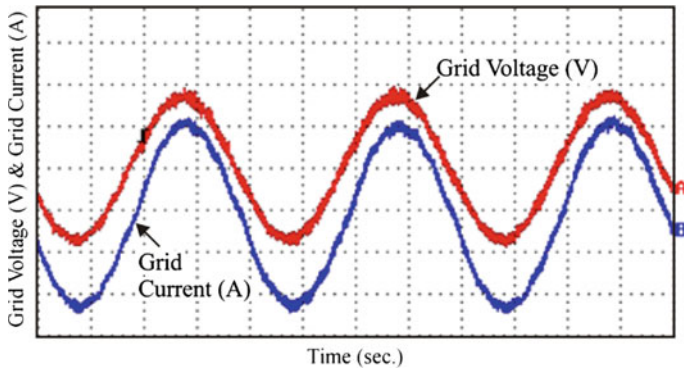


Fig. 13.11 Practical responses at unity power factor operation

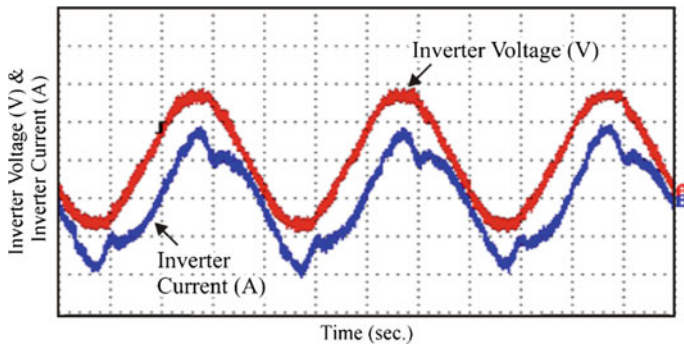


Fig. 13.12 Experimental results of inverter voltage and current

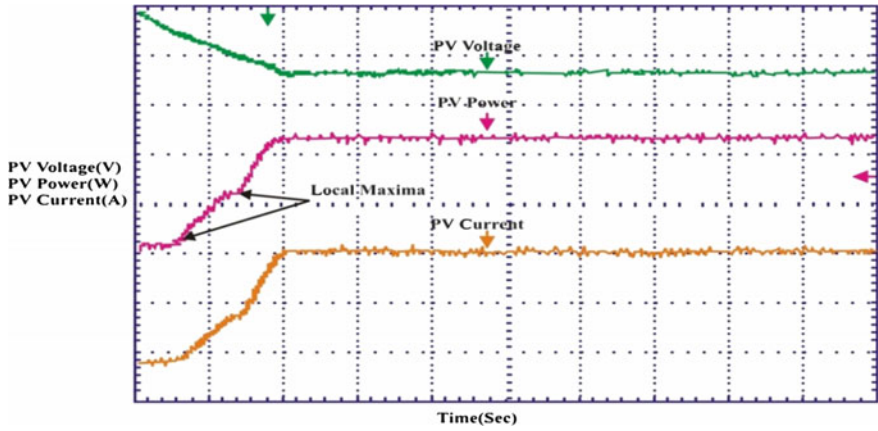
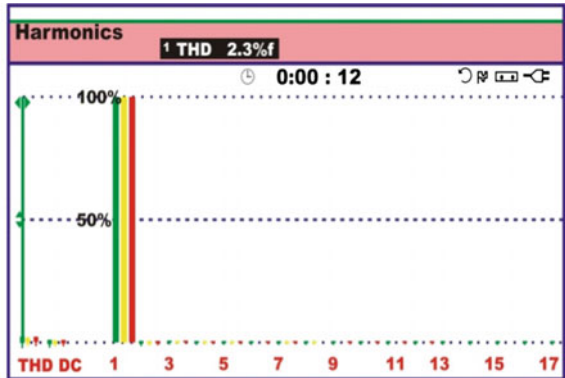
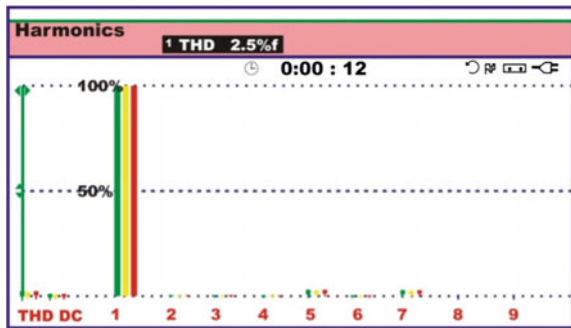


Fig. 13.13 Proposed MPPT under steady-state condition

Fig. 13.14 Total harmonic distortion spectrum



(a) Inverter voltage



(b) Inverter current

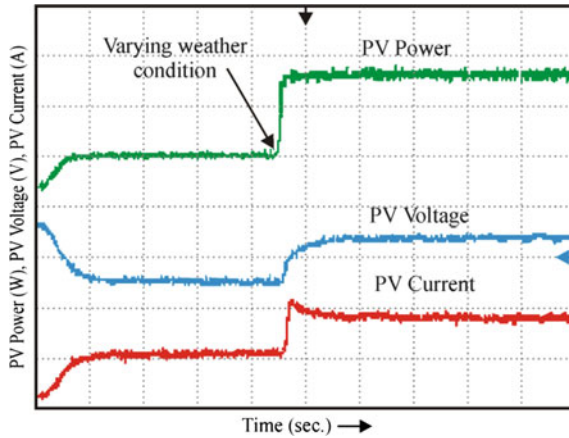


Fig. 13.15 Practical response of PV power, voltage, and current during abrupt weather condition

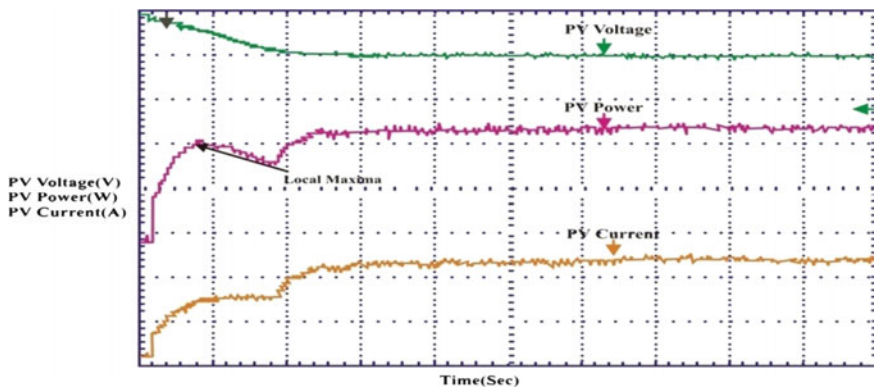
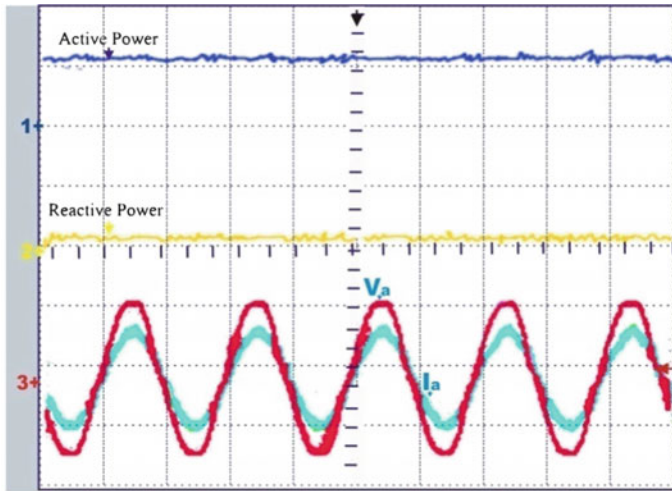


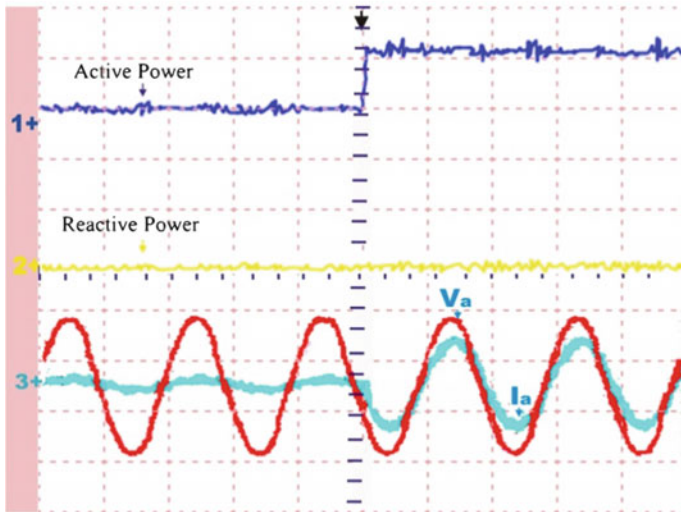
Fig. 13.16 Experimental results of the proposed MPPT under partial shading condition

proposed controller always tries to force the power to move new operating point directly under varying weather conditions. Hence, the MPP is attained in very small time and has negligible oscillation around MPP for every operating condition. To test the proposed control effectively, the PV source simulator is used to program I–V curves under partial shadow conditions. The experimental result in Fig. 13.16 shows that global MPP is achieved with small oscillation in relatively small time, which does not prevent the local maxima in the P–V curve.

Figure 13.17 shows the active and reactive power capability of the proposed grid-connected PV system. Active power is maintained constant, while the reactive power is controlled for leading, lagging, and unity power factor operation.



(a) unity power factor operation



(b) dynamic operation

Fig. 13.17 Experimental responses of active and reactive power

13.6 Conclusion

In this research work, the effectiveness of a zeta converter-based two-stage grid-integrated PV system has been investigated. The efficient control system of FLC-based MPPT and SVMHCC-based inverter control for grid-connected PV system has been implemented. For maximum power tracking and low output

voltage ripple, a zeta buck–boost converter is employed. The proposed controllers for grid-connected PV system are able to track maximum power from PV system, and it provides sinusoidal injected current to the grid in abrupt weather conditions. The hardware interface was implemented with dSPACE DS1104 real-time control board. The practical responses validate the maximum power tracking ability and stable grid requirements successfully.

References

1. Arora A, Gaur P (2015) AI based MPPT methods for grid connected PV systems under non linear changing solar irradiation. IEEE international conference on computer engineering and applications (ICACEA)-2015, pp 542–547
2. Mahmdi T, Lassad S (2015) A fuzzy controlled scheme for hybrid photovoltaic diesel AC pumping system. IEEE international conference on renewable energy congress (IREC), pp 1–6
3. Roy S (2006) Optimal planning for utility generation by photovoltaic sources spread across multiple sites. IEEE Trans Energy Convers 21(1):181–186
4. Woyte A, Van Thong V, Belmans R, Nijs J (2006) Voltage fluctuations on distribution level introduced by photovoltaic systems. IEEE Trans Energy Convers 21(1):202–209
5. Valenciaga F, Puleston PF (2005) Supervisor control for a stand-alone hybrid generation system using wind and photovoltaic energy. IEEE Trans Energy Convers 20(2):398–405
6. Billinton R (2005) Evaluation of different operating strategies in small stand-alone power systems. IEEE Transactions on energy conversion, vol 20, no 3, pp 654–660
7. Park M, Yu IK (2004) A novel real-time simulation technique of photovoltaic generation systems using RTDS. IEEE Trans Energy Convers 19(1):164–169
8. AbdulHadi M, Al-Ibrahim AM, Virk GS (2004) Neuro-fuzzy-based solar cell model. IEEE Trans Energy Convers 19(3):619–624
9. Agbossou K, Kolhe M, Hamelin J, Bose TK (2004) Performance of a stand-alone renewable energy system based on energy storage as hydrogen. IEEE Trans Energy Convers 19(3):633–640
10. Mohanty P (2014) Role of power converters in distributed solar power generation. J Autom Control Eng 2(1):38–42
11. Safari A, Mekhilef S (2011) Simulation and hardware implementation of incremental conductance MPPT with direct control method using cuk converter. IEEE Trans Ind Electron 58(4):1154–1161
12. Priyadarshi N, Kumar V, Joshi RR (2015) Zeta converter fed integrated inverter for grid connected PV system with optimal power point tracking. Int J Innov Res Sci Eng Technol 4(2):427–433
13. El-Sayed MA, Leeb S (2015) Fuzzy logic based maximum power point tracking using boost converter for solar photovoltaic system in Kuwait. International conference on renewable energies and power quality, Spain, vol 14, no 13, April 2015
14. Reisi AR, Moradi MH (2013) Classification and comparison of maximum power point tracking techniques of photovoltaic system: Review. Renew Sustain Energy Rev 19:433–443
15. Uddin MN, Rebeiro RS (2011) Online efficiency optimization of a fuzzy-logic-controller-based IPMSM drive. IEEE Trans Ind Electron 47(2):1043–1050
16. Shiau J-K, Lee M-Y, Wei Y-C, Chen B-C (2014) Circuit simulation for solar power maximum power point tracking with different buck-boost converter topologies. Ist international e-conference on energies, pp 1–17

17. Bouafia J, Gaubert, Krim F (2010) Design and implementation of predictive current control of three-phase PWM rectifier using space-vector modulation (SVM). *Energy Convers Manag* 51:2473–2481
18. Ibrahim Z, Hasim AS, Talib N, Mustafa R (2013) Performance investigation of photovoltaic grid connection for shunt active power filter with different PWM generation. *J Theor Appl Inf Technol* 57(2):305–311
19. Chitra A, Giridharan K, Chellamuthu C (2011) Grid connected inverter with SVPWM technique for photovoltaic application. *Elixir Int J* 38:4438–4442
20. Ling LP (2004) SVM based hysteresis current controller for a three phase active power filter. University Technology, Malaysia

Part IV
DG Modelling, Operation,
Control, Protection

Chapter 14

Modelling, Design, and Control of Smart DC Microgrid for Integration of Various Non-conventional Distributed Generators

Mahesh Kumar and S.N. Singh

14.1 Introduction

Electricity is one of the most convenient forms of energy, which has become a necessity of daily life for majority of the population across the globe. The electrical power is primarily generated from the conventional energy sources using fossil fuels such as coal, oil, and natural gas, which have been posing the environmental problems. In addition, the safety hazards are also attributed to the power generation from the fossil and nuclear power plants. Therefore, during the past few years, the non-conventional distributed energy resources (DERs) are being increasingly deployed and have witnessed fast development and attracted the attention of the utilities and researchers due to continuously growing energy demand, fast depletion of fossil fuels along with environmental concerns related to the global warming, reduction in ozone layer, greenhouse effect, and coupled with the emergence of electricity market [1–3]. The renewable and non-renewable DERs constitute various distributed generators (DGs) with capacity ranging from few kW to 10 MW [2], which are, generally, placed near the load centres, thus reducing the transmission and distribution losses and preventing the network congestion. The renewable-type DGs include wind turbine (WT), solar photovoltaic (SPV), fuel cells (FCs), solar thermal (ST), geothermal energy (GE), tidal energy (TE), low head (small) hydro, and biomass and biogas. The non-renewable energy DGs include microturbine (MT), gas turbine, internal combustion engine, and combustion turbine. Due to intermittent nature and uncertainty of the renewable energy sources (RESs), the

M. Kumar (✉) · S.N. Singh
Department of Electrical and Instrumentation Engineering,
Thapar University, Patiala, Punjab, India
e-mail: singhrmkumar@gmail.com

S.N. Singh
Department of Electrical Engineering, Indian Institute of Technology Kanpur,
Kanpur, India

direct connection of various DGs to the utility grid causes the problems of voltage rise, frequency variation, network contingency, more stress on electrical network, reduced power quality of the utility grid, stability, and protection issues [1, 3–5]. The capacity of the existing transmission lines is generally limited, and there are also difficulties in constructing new transmission lines.

Therefore, a new concept of the microgrid is a most promising solution, which has been conceptualized as a low-voltage (LV) or medium-voltage (MV) distribution network for the integration of various DGs and loads. The size of a microgrid can be of few MVA/MW. The microgrid can be classified as AC microgrid (ACMG) and DC microgrid (DCMG), which can operate in islanded mode as well as in grid-connected mode. A microgrid has the following main components [1, 6]: (1) renewable and non-renewable DGs; (2) energy storage systems (ESSs); (3) various DC and AC loads; (4) distribution network; and (5) power electronic converters and their respective controllers. The microgrid offers certain advantages such as accelerated use of the RESs, reduced transmission losses resulting in higher efficiency, higher flexibility, and better controllability due to the use of power electronic converters for interfacing. This also ensures higher power quality and independent operation from the utility grid in islanded mode, and allows bidirectional power flow between the microgrid and utility grid in a grid-connected mode.

Several power electronic converters are being used for interfacing various DGs, ESSs, and loads to the microgrids, which have been classified as voltage source converters (VSCs) and current source converters (CSCs). The VSCs are preferred over the CSCs because of their several advantages [1, 7], such as effective parallel operation, no DC filter required due to the presence of DC link capacitor, reduced AC filter requirement for higher order harmonics elimination, no need of separate reactive power source as VSC can operate in any of the four quadrants, no need of external circuit for commutation purpose, no risk of commutation failure, fast response due to high switching frequency, controlling of active and reactive power independently, and ability to supply the dump load. In addition, the power can be reversed either by current or by voltage reversal on DC side, and it requires only unidirectional voltage blocking. Thus, the pulse width modulation (PWM)-based VSCs are being widely used for integration of various DGs, ESSs, and loads to the microgrid [2, 8]. The VSCs allow effective voltage and power flow control, better quality of power conversion, power factor correction, system balancing, fault protection, and maximum power point tracking (MPPT) of the DG sources.

A DCMG has been preferred over an ACMG because of its certain advantages [1, 8, 9], which are as follows: (1) better current carrying capacity due to the absence of skin effect; (2) no need of controlling of frequency, phase, and reactive power resulting into better controllability; (3) reduced total losses due to the absence of corona and reactive power, resulting in higher efficiency; (4) easy control achieved by only controlling the DCMG voltage; (5) higher quality of power supply; (6) frequency synchronization is not required for interconnecting multiple DGs; (7) ACMG faces the problems of charging currents, while no issue in the DCMG; and (8) no signal and data communication required among the existing DG units in the DCMG. For a given size of cable, DC system can deliver $\sqrt{2}$ times

more power than the AC system, and during a blackout or voltage sag in the utility grid, it has no adverse impact on the DCMG voltage directly due to the stored energy of the DC capacitor and the voltage control of three-phase VSC. In addition, a DCMG has the fault-ride-through capability of its own.

Thus, the DCMG is one of the most promising options for the integration of various DGs and their interconnection to the utility grid. A ring-type architecture of the smart DCMG with autonomous controls has been presented and discussed in this chapter. The proposed DCMG has a different architecture than the various available architectures of the DCMGs in the literature. The regulation of the voltage is the most important requirement for the DCMG. The issues of voltage regulation, power balance, power quality, and coordinated control of the DCMG are related to the appropriate modelling and design of the DCMG under different operating scenarios. The dynamic modelling is relevant to the analysis of the small-signal stability of the DCMG system. The design of a DCMG system is the main issue, which has the impact upon technical and economical behaviour of the DCMG.

The objective of this chapter is to describe the DCMG architecture, modelling, and design of various components, such as DGs, ESSs, and the associated converters, and control strategies for the satisfactorily operation of the proposed DCMG under autonomous coordinated controlled (ACC) mode. A control strategy of the bidirectional three-phase VSC for integrating the WT generator (WTG) has been developed in this chapter. The performance analyses of the proposed DCMG with the developed control strategies are also carried out under different operating scenarios in islanded mode with and without ESS.

14.2 Proposed Architecture of a Smart DC Microgrid

The proposed ring-type architecture of a smart DC microgrid with autonomous controls, based on DC energy pool, is shown in Fig. 14.1. The objective of constructing a smart DCMG is to provide reliable, high-quality electric power in an environmental friendly and sustainable way. One of the most important features of a smart DCMG is its advanced structure which can facilitate the connections of various DG systems with AC and DC outputs, ESSs, and loads, as shown in Fig. 14.1.

Here, the proposed smart DCMG consists of the WT, SPV, solid oxide fuel cells (SOFCs) DGs, battery energy storage system (BESS), and various DC and three-phase as well as single-phase AC loads. The proposed DCMG can supply both DC and AC power to the various loads, simultaneously. The DCMG may also be interconnected to the utility grid for bidirectional power flow to balance power in the DCMG.

Generally, the DCMG can be controlled either in centralized or in decentralized manner [9]. In the centralized control, each DG source is to be controlled from a single point with a central controller and the communication link, which degrades the reliability of the DCMG system. However, in the decentralized control, each

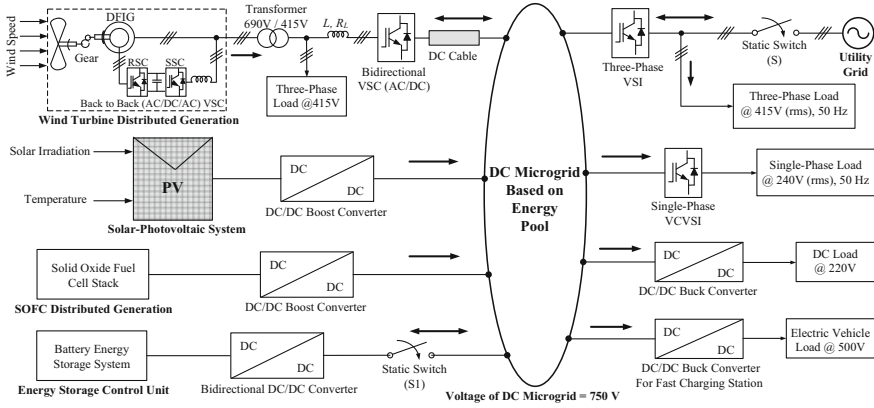


Fig. 14.1 Proposed architecture of a smart DC microgrid for the integration of various DGs

DG is controlled independently by using terminal quantities without any communication link. Thus, the decentralized control method maintains the reliability of the DCMG system by using the local information such as DC voltage of the microgrid for controlling each DGs integrated with the DCMG [10]. The DC microgrid/grid has been controlled by using DC bus signal as a decentralized control. The main problem in a DCMG is the circulating current among the DG units connected to the DCMG, which is mainly due to a voltage difference among them. These circulating currents can be minimized or eliminated by using the decentralized control, i.e. autonomous coordinated control [1, 8], which has been achieved by using only the DC voltage of the DCMG as common reference signal for all DG units. Each DG unit, connected to the DCMG, has been controlled autonomously without communicating with each other. From the review of various literatures, a DC voltage of 750 V for the proposed microgrid has been considered. The need of the transformers on the load side converters in the proposed DCMG has also been eliminated by selecting the proper DCMG voltage (750 V in the present study).

In the proposed DCMG, a variable speed WT comprising of doubly fed induction generator (DFIG) with back-to-back (AC-DC-AC) VSC, containing rotor side converter (RSC) and stator side converter (SSC), has been integrated with the DCMG through a bidirectional three-phase VSC. The RSC is used for MPPT and stator flux control, and to provide reactive power to the DFIG through the rotor circuit. The SSC is used to maintain active power balance in the WTG system and constant DC link voltage of the back-to-back converter used in the DFIG. The DFIG is being widely used with the WT DG because of its following advantages: high efficiency, better controllability, improved power quality, reduced mechanical stresses, independent control of active and reactive power, and low cost of the back-to-back VSC due to its lower rating typically between 20 and 30% of rated power of the DFIG [1, 11]. A part of the power generated by the WTG is consumed by the three-phase load connected in the local area of the WTG, and the

remaining generated power is being transmitted to the DCMG through the bidirectional three-phase VSC and DC cable. The SPV system, comprising of an MPPT controller to track the maximum output power, has been integrated with the DCMG through a DC-DC boost converter. The SOFC as controllable DG, with peak power capacity (PPC) of 1.8 times of its rated power capacity, has been integrated with the DCMG through a DC-DC boost converter. When the power generation from the WT and SPV DGs is unable to meet the load demand, the SOFC DG is turned-on to meet the load demand. The output of the SOFC DG varies according to the load changes. Beyond the PPC of the SOFC DG, the BESS has a major role in the operation of the DCMG under islanded mode, while the power balance has been fulfilled by the utility grid if the DCMG is operating in grid-connected mode. Therefore, in the islanded mode, a BESS has been considered and integrated with the DCMG through a bidirectional DC-DC converter to maintain the system power balance.

Under islanded mode of operation of the DCMG, if the surplus power is generated by the WTG, while the BESS is already fully charged, it is necessary to reduce the power generation of the WTG equal to the value of the surplus power for balancing the power in the DCMG. The power reduction can be achieved in a following ways depending on the WT technology and the availability of the fast communication systems [1, 12]:

- (1) The WT generation can be reduced through the control of the WT DFIG back-to-back VSC. This option is widely being used in the WTG with power converters for controlling the DFIG torque. Fast communication systems are needed for this purpose.
- (2) The WTG output power can be reduced by modifying the pitch angle of the WT. This option is applicable to all the WT technologies that use variable pitch blade control systems.
- (3) The WT generation can be reduced by controlling the three-phase rectifier, which is used to integrate the WTG to the DC system. This option is applicable only for the WT with squirrel-cage induction generator.

The DC loads operating at the voltages lower than the DCMG voltage have been integrated with the DCMG through the DC-DC buck converters. The three-phase and single-phase AC loads are connected to the DCMG through the three-phase voltage source inverter (VSI) and single-phase voltage-controlled voltage source inverter (VCVSI), respectively.

The key point of the power management in the DCMGs is to maintain the power balance between the DGs, BESSs, and the loads at any time, which is represented by the stable DC voltage of the microgrid. The stable DCMG voltage should be maintained within the permissible voltage range of $\pm 6\%$ of the rated voltage.

14.3 Modelling of DC Microgrid Components

The modelling of each components of the DC microgrid is very important part for the designing of the smart DCMG. Each DG unit with its associated converter is considered as a subsystem of the microgrid, and the dynamic model of each subsystem is derived as follows.

14.3.1 Distributed Generators

The modelling of the various DGs, which can be renewable or non-renewable, is the most important part of the smart DC microgrid. The modelling of the various types of renewable and non-renewable DGs is described in this section.

14.3.1.1 Wind Turbine DG

The WT DG converts the kinetic energy of the wind into the electrical energy. The kinetic energy available in the wind is converted into mechanical power by the rotor blades and prime mover of the WT DG. The mechanical power extracted from the available wind is given as follows [1, 4, 6, 8, 11, 13]:

$$P_{\text{mech}} = \frac{\partial(KE_{\text{wind}})}{\partial t} C_P(\lambda, \theta) = \frac{1}{2} C_P(\lambda, \theta) \rho_{\text{air}} A_b v_{\text{wind}}^3 \quad (14.1)$$

where P_{mech} is the mechanical power generated by the wind turbine (W), KE_{wind} is the kinetic energy of the wind (Joule), v_{wind} is the available wind speed (m/s), ρ_{air} ($=1.225 \text{ kg/m}^3$) is the air density, A_b ($=\pi R_b^2$) is the swept area of the rotor blades (m^2), R_b is the radius of rotor blade (m), and $C_P(\lambda, \theta)$ is the power performance coefficient or aerodynamic efficiency of the turbine which depends on the blade pitch angle θ and tip-speed ratio λ .

The power coefficient, tip-speed ratio (λ), and its parameter (λ_i) are defined by a generic equation as follows [1, 4, 8]:

$$\left. \begin{aligned} C_P(\lambda, \theta) &= C_1 \left(\frac{C_2}{\lambda_i} - C_3 \theta - C_4 \right) e^{-C_5/\lambda_i} + C_6 \lambda \\ \text{where, } \lambda &= \frac{\omega_t R_b}{v_{\text{wind}}} \quad \text{and} \quad \frac{1}{\lambda_i} = \frac{1}{\lambda + 0.08\theta} - \frac{0.035}{\theta^3 + 1} \end{aligned} \right\} \quad (14.2)$$

where C_1 to C_6 are the coefficients taken as follows: $C_1 = 0.5176$, $C_2 = 116$, $C_3 = 0.4$, $C_4 = 5$, $C_5 = 21$, and $C_6 = 0.0068$, ω_t ($=0.5p\omega_m$) is the electrical speed (elec. rad/s), p is the number of poles of the DFIG, and ω_m is the mechanical speed

of the rotor (mech. rad/s). The maximum power coefficient for a typical wind turbine varies between 0.48 and 0.50, and the theoretical maximum of C_p is called Betz limit, which is equal to 0.59.

The mathematical equations of the DFIG for both the stator and the rotor voltages and for electromechanical torque are expressed in per unit in rotating d - q synchronous reference frame (SRF) by the following Eqs. (14.3) and (14.4), respectively, as [1, 8, 11].

$$\left. \begin{aligned} v_{ds} &= -R_s i_{ds} - \omega_s \psi_{qs} + \frac{d\psi_{ds}}{dt}, \\ v_{qs} &= -R_s i_{qs} + \omega_s \psi_{ds} + \frac{d\psi_{qs}}{dt}, \\ v_{dr} &= -R_r i_{dr} - (\omega_s - \omega_r) \psi_{qr} + \frac{d\psi_{dr}}{dt}, \\ v_{qr} &= -R_r i_{qr} + (\omega_s - \omega_r) \psi_{dr} + \frac{d\psi_{qr}}{dt} \end{aligned} \right\} \quad (14.3)$$

$$T_e = \psi_{qr} i_{dr} - \psi_{dr} i_{qr} \quad (14.4)$$

where T_e is the electromechanical torque generated by the DFIG, v_{ds} and v_{qs} are the d - and q -axis stator voltages, v_{dr} and v_{qr} are the d - and q -axis rotor voltages, i_{ds} and i_{qs} are the d - and q -axis stator currents, i_{dr} and i_{qr} are the d - and q -axis rotor currents, R_s and R_r are the resistance of the stator and rotor windings, ω_s and ω_r are the stator and rotor electrical frequencies, ψ_{ds} and ψ_{qs} are the d - and q -axis stator flux linkages, and ψ_{dr} and ψ_{qr} are the d - and q -axis rotor flux linkages, respectively. The flux linkages are expressed as:

$$\left. \begin{aligned} \psi_{ds} &= -(L_s + L_m) i_{ds} - L_m i_{dr}, & \psi_{qs} &= -(L_s + L_m) i_{qs} - L_m i_{qr} \\ \psi_{dr} &= -(L_r + L_m) i_{dr} - L_m i_{ds}, & \psi_{qr} &= -(L_r + L_m) i_{qr} - L_m i_{qs} \end{aligned} \right\} \quad (14.5)$$

where L_m is the mutual inductance, and L_s and L_r are the stator and rotor leakage inductances, respectively.

The rotor variables, referred to the stator side by the appropriate turn ratio N , are determined as follows:

$$\left. \begin{aligned} i'_r &= \frac{N_r}{N_s} i_r, & v'_r &= \frac{N_s}{N_r} v_r, & \lambda'_r &= \frac{N_s}{N_r} \lambda_r, & R'_r &= \left(\frac{N_s}{N_r} \right)^2 R_r \\ L_{ms} &= \frac{N_s}{N_r} L_{sr}, & L'_r &= \left(\frac{N_s}{N_r} \right)^2 L_r, & L'_{lr} &= \left(\frac{N_s}{N_r} \right)^2 L_{lr} \end{aligned} \right\} \quad (14.6)$$

The active power (P) and reactive power (Q) generated by the DFIG are expressed as follows:

$$P = v_{ds}i_{ds} + v_{qs}i_{qs} + v_{dr}i_{dr} + v_{qr}i_{qr}, \quad \text{and} \quad Q = v_{qs}i_{ds} - v_{ds}i_{qs} + v_{qr}i_{dr} - v_{dr}i_{qr} \tag{14.7}$$

The wind speed model is described by a probability density function (pdf), the Weibull function, expressed as follows [1, 14]:

$$\left. \begin{aligned} f(v_{wind,l}) &= \frac{k}{c} \left(\frac{v_{wind,l}}{c}\right)^{k-1} e^{-(v_{wind,l}/c)^k}, \quad \text{and} \\ \bar{v}_{wind} &= \frac{1}{n} \sum_{l=1}^n v_{wind,l}, \\ \sigma^2 &= \frac{1}{n-1} \sum_{l=1}^n (v_{wind,l} - \bar{v}_{wind})^2 \end{aligned} \right\} \tag{14.8}$$

where $f(v_{wind,l})$ is the probability of wind speed, c is the Weibull scale parameter, k ($1 \leq k \leq 10$) is the dimensionless Weibull shape parameter, \bar{v}_{wind} is the average wind speed (m/s), and σ^2 is the variance in wind speed.

The Rayleigh probability density function is a special case of Weibull function in which Weibull shape parameter, k , is equal to 2 and can be expressed as follows [15]:

$$f(v_{wind,l}) = 2 \left(\frac{v_{wind,l}}{c}\right) e^{-(v_{wind,l}/c)^2} \tag{14.9}$$

The power generation by the wind turbine generator is a function of wind speed and is determined by Eq. (14.10) as follows [14, 15]:

$$\left. \begin{aligned} P_{WTG} &= P_{WTG,rated} \left(\frac{v_{wind}^k - v_{wind,cut-in}^k}{v_{wind,rated}^k - v_{wind,cut-in}^k} \right); \quad \text{for } v_{wind,cut-in} < v_{wind} < v_{wind,rated} \\ P_{WTG} &= P_{WTG,rated}; \quad \text{for } v_{wind,rated} \leq v_{wind} \leq v_{wind,cut-off} \\ P_{WTG} &= 0; \quad \text{for } v_{wind} \leq v_{wind,cut-in} \quad \text{and} \quad v_{wind} > v_{wind,cut-off} \end{aligned} \right\} \tag{14.10}$$

where P_{WTG} is the power generation by the WTG (W), $P_{WTG,rated}$ is the maximum rated power capacity of the WTG (W), v_{wind} is the available wind speed (m/s), $v_{wind,cut-in}$ is the cut-in wind speed (m/s), and $v_{wind,cut-off}$ is the cut-off wind speed (m/s).

The power generation from the WTG, between the range of cut-in wind speed and the rated wind speed ($v_{wind,cut-in} < v_{wind} < v_{wind,rated}$), has been determined as given in Eq. (14.10) and is less than the rated maximum power generation by the WTG. From above Eq. (14.10), it has been observed that the power generation from the WTG, at the rated wind speed and above-rated wind speed ($v_{wind} \geq v_{wind,rated}$) up to the cut-off wind speed ($v_{wind} \leq v_{wind,cut-off}$), is equal to the maximum rated power generation. The power generation from the WTG at the wind speed

equal to or less than the cut-in wind speed ($v_{wind} \leq v_{wind,cut-in}$) and above the cut-off wind speed ($v_{wind} > v_{wind,cut-off}$), is equal to zero.

14.3.1.2 Solar Photovoltaic System

Solar cell (or PV cell), which is a p-n junction semiconductor device that converts light energy into electricity, is a basic building block of the SPV system. The output of a SPV cell is about 2–3 W at 0.5–0.7 V. Several SPV cells have to be connected in series to produce a useful voltage. Such strings are connected in series and parallel combination, which forms a SPV module. Based on the power requirement, several such modules are connected in series and parallel combination to form a SPV array [1, 16]. The simplified equivalent circuit of an ideal SPV cell (i.e. $R_{se} = 0$ and $R_{sh} = \infty$) can be determined by a current source in parallel with a diode, as shown in Fig. 14.2a. Its series and parallel internal resistances have been considered in the model of a practical SPV cell. A general equivalent circuit model of the SPV array system is shown in Fig. 14.2b.

The current–voltage characteristic of a single SPV cell is described mathematically by the following basic equation [8, 16, 17]:

$$\left. \begin{aligned} I_{PV} &= I_{ph} - I_d - I_{sh}, \quad \text{and} \\ I_{PV} &= I_{ph} - I_{sat} \left[\exp\left(\frac{q}{KT_{cell}A}(V_{PV} + I_{PV}R_{se})\right) - 1 \right] - \left(\frac{V_{PV} + I_{PV}R_{se}}{R_{sh}}\right) \end{aligned} \right\} \quad (14.11)$$

where I_{PV} is the output current of the SPV cell (A), I_{ph} is the photocurrent (A), I_{sh} is the leakage current (A), V_{PV} is the output voltage across the terminal of the SPV cell (V), I_{sat} is the diode saturation current (A), q ($=1.6021 \times 10^{-19}$ °C) is the charge of an electron, K ($=1.38 \times 10^{-23}$ J/K) is the Boltzmann constant, T_{cell} is the cell’s operating temperature (K), A is the diode ideality factor which depends on PV

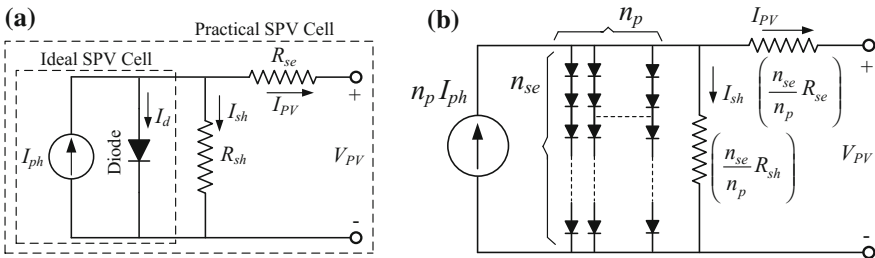


Fig. 14.2 **a** Simplified equivalent circuit of an ideal SPV cell and a practical SPV cell. **b** Equivalent model of the SPV array

technology, R_{se} and R_{sh} are the internal series and parallel resistances of the SPV cell (Ω), respectively, I_{max} and V_{max} is the current (A) and voltage at the maximum power (V), respectively, and I_d is the diode current (A).

The photocurrent depends on the SPV cell's operating temperature and solar irradiance (SI) and is expressed as

$$I_{ph} = [I_{sc} + \sigma_{I_{sc}}(T_{cell} - T_{ref})] \cdot \left(\frac{S}{1000} \right) \quad (14.12)$$

where S is the solar irradiation (kW/m^2), T_{ref} ($=25^\circ\text{C}$) is the reference cell temperature, $\sigma_{I_{sc}}$ is the temperature coefficient of short-circuit current ($\text{A}/^\circ\text{C}$), I_{sc} is the short-circuit current at Standard Test Condition (STC), i.e. 25°C temperature and 1 kW/m^2 solar irradiation (SI).

The SPV cell's saturation current varies with the cell's operating temperature and is expressed as:

$$I_{sat} = I_{rs}(T_{cell}/T_{ref})^3 \exp[qE_G(1/T_{ref} - 1/T_{cell})/KA] \quad (14.13)$$

where I_{rs} is the reverse saturation current of the diode (A), E_G ($=1.12 \text{ eV}$) is the band-gap energy of the semiconductor used in the SPV cell.

The reverse saturation current at the reference temperature is given as:

$$I_{rs} = I_{sc}/[\exp(qV_{oc}/n_{se}KAT_{ref}) - 1] \quad (14.14)$$

where V_{oc} is the open-circuit voltage (V), which can be determined assuming zero output current at STC and ignoring the shunt leakage current, and n_{se} is the number of series SPV cells in the SPV array system.

The current–voltage (I-V) characteristic of the SPV array system is expressed mathematically as [8, 17]:

$$I_{PV} = n_p I_{ph} - n_p I_{sat} \left[\exp\left\{ q(V_{PV} + I_{PV}(n_{se}R_{se}/n_p)) / n_{se}KT_{cell}A \right\} - 1 \right] - \left[\left\{ (n_p V_{PV} / n_{se}) + I_{PV}R_{se} \right\} / R_{sh} \right] \quad (14.15)$$

where n_p is the number of stacks in parallel with the SPV array system.

Since normally $I_{ph} \gg I_{sat}$, and ignoring the small diode and ground leakage currents under zero-terminal voltage, short-circuit current (I_{sc}) is approximately equal to the photocurrent, i.e. $I_{sc} \approx I_{ph}$. The power generation from the SPV system at STC is equal to the maximum rated generation capacity. The output of the SPV system increases with increasing SI and decreasing temperature and/or vice versa.

14.3.1.3 Solid Oxide Fuel Cell DG

The SOFCs are static conversion devices that convert the chemical energy of fuel directly into DC electrical energy through an electrochemical process at a high

temperature (600–1000 °C). High temperature helps to improve the efficiency (65%) of the SOFC, which is the highest efficiency among the various FCs. Its overall efficiency with combined heat and power applications can reach up to 85%. The output power generation from the SOFC DG is DC power. The output voltage of the FC varies when load changes. The peak power capacity of the SOFC DG is, generally, considered in the range of 130–180% of its rated power capacity [18]. The schematic diagram of an SOFC [1, 8, 19] is shown in Fig. 14.3.

The overall effective gas partial pressures in the channels (as in Fig. 14.3) are expressed as:

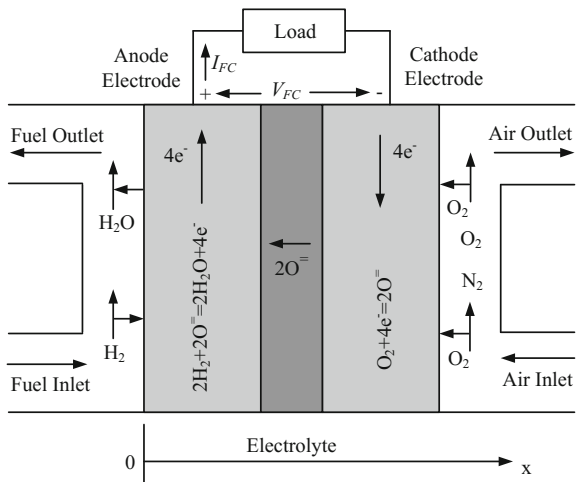
$$p_{H_2}^{ch} = \frac{p_{H_2}^{in} + p_{H_2}^{out}}{2}, \quad p_{H_2O}^{ch} = \frac{p_{H_2O}^{in} + p_{H_2O}^{out}}{2}, \quad \text{and} \quad p_{O_2}^{ch} = \frac{p_{O_2}^{in} + p_{O_2}^{out}}{2} \quad (14.16)$$

The instantaneous change in the effective partial pressures of H₂ and H₂O vapour anode gas flow channel can be determined using the ideal gas equations and is given by Eq. (14.17):

$$\left. \begin{aligned} \frac{V_a}{RT} \frac{dp_{H_2}^{ch}}{dt} &= M_{H_2}^{in} - M_{H_2}^{out} - \frac{I_{FC}}{2F}, \\ \frac{V_a}{RT} \frac{dp_{H_2O}^{ch}}{dt} &= M_{H_2O}^{in} - M_{H_2O}^{out} + \frac{I_{FC}}{2F} \quad \text{and,} \\ \frac{V_c}{RT} \frac{dp_{O_2}^{ch}}{dt} &= M_{O_2}^{in} - M_{O_2}^{out} - \frac{I_{FC}}{4F} \end{aligned} \right\} \quad (14.17)$$

The mass flow rate for H₂, H₂O, and O₂, at the inlet and outlet of the flow channels, has been expressed as:

Fig. 14.3 Schematic diagram of an SOFC



$$\left. \begin{aligned} M_{\text{H}_2}^{\text{in}} &= M_a * \frac{P_{\text{H}_2}^{\text{in}}}{P_a^{\text{ch}}}, & M_{\text{H}_2}^{\text{out}} &= M_a * \frac{P_{\text{H}_2}^{\text{out}}}{P_a^{\text{ch}}}, & M_{\text{H}_2\text{O}}^{\text{in}} &= M_a * \frac{P_{\text{H}_2\text{O}}^{\text{in}}}{P_a^{\text{ch}}}, \\ M_{\text{H}_2\text{O}}^{\text{out}} &= M_a * \frac{P_{\text{H}_2\text{O}}^{\text{out}}}{P_a^{\text{ch}}}, & M_{\text{O}_2}^{\text{in}} &= M_c * \frac{P_{\text{O}_2}^{\text{in}}}{P_c^{\text{ch}}}, & \text{and } M_{\text{O}_2}^{\text{out}} &= M_a * \frac{P_{\text{O}_2}^{\text{out}}}{P_c^{\text{ch}}} \end{aligned} \right\} \quad (14.18)$$

Thus, by using Eqs. (14.17) and (14.18), has been expressed as:

$$\left. \begin{aligned} \frac{dp_{\text{H}_2}^{\text{ch}}}{dt} &= \frac{2M_a RT}{V_a P_a^{\text{ch}}} p_{\text{H}_2}^{\text{in}} - \frac{2M_a RT}{V_a P_a^{\text{ch}}} p_{\text{H}_2}^{\text{ch}} - \frac{RT}{2FV_a} I_{\text{FC}} \\ \frac{dp_{\text{H}_2\text{O}}^{\text{ch}}}{dt} &= \frac{2M_a RT}{V_a P_a^{\text{ch}}} p_{\text{H}_2\text{O}}^{\text{in}} - \frac{2M_a RT}{V_a P_a^{\text{ch}}} p_{\text{H}_2\text{O}}^{\text{ch}} + \frac{RT}{2FV_a} I_{\text{FC}} \\ \frac{dp_{\text{O}_2}^{\text{ch}}}{dt} &= \frac{2M_c RT}{V_c P_c^{\text{ch}}} p_{\text{O}_2}^{\text{in}} - \frac{2M_c RT}{V_c P_c^{\text{ch}}} p_{\text{O}_2}^{\text{ch}} - \frac{RT}{4FV_c} I_{\text{FC}} \end{aligned} \right\} \quad (14.19)$$

Equation (14.19) in Laplace domain can be expressed as:

$$\left. \begin{aligned} P_{\text{H}_2}^{\text{ch}}(s) &= \frac{1}{(1 + \tau_a s)} \left[P_{\text{H}_2}^{\text{in}}(s) + \tau_a P_{\text{H}_2}^{\text{ch}}(0) - \frac{P_a^{\text{ch}}}{4FM_a} I_{\text{FC}}(s) \right] \\ P_{\text{H}_2\text{O}}^{\text{ch}}(s) &= \frac{1}{(1 + \tau_a s)} \left[P_{\text{H}_2\text{O}}^{\text{in}}(s) + \tau_a P_{\text{H}_2\text{O}}^{\text{ch}}(0) + \frac{P_a^{\text{ch}}}{4FM_a} I_{\text{FC}}(s) \right] \\ P_{\text{O}_2}^{\text{ch}}(s) &= \frac{1}{(1 + \tau_c s)} \left[P_{\text{O}_2}^{\text{in}}(s) + \tau_c P_{\text{O}_2}^{\text{ch}}(0) - \frac{P_c^{\text{ch}}}{8FM_c} I_{\text{FC}}(s) \right] \end{aligned} \right\} \quad (14.20)$$

where $\tau_a = \frac{V_a P_a^{\text{ch}}}{2M_a RT}$ and $\tau_c = \frac{V_c P_c^{\text{ch}}}{2M_c RT}$ are time constants associated with the pressure at anode and cathode, respectively; $M_{\text{H}_2}^{\text{in}}$ and $M_{\text{H}_2}^{\text{out}}$ are the mass flow rate of H_2 for inlet and outlet channels, respectively; $M_{\text{H}_2\text{O}}^{\text{in}}$ and $M_{\text{H}_2\text{O}}^{\text{out}}$ are the mass flow rate of H_2O for inlet and outlet channels, respectively; $M_{\text{O}_2}^{\text{in}}$ and $M_{\text{O}_2}^{\text{out}}$ are the mass flow rate of O_2 for inlet and outlet channels, respectively; V_a and V_c are the volume of the anode and cathode channel, respectively; M_a and M_c are the mass flow rate of gas inside anode channel and cathode channel, respectively; P_a and P_c are the pressures at anode and cathode channel, respectively; R ($=8.314 \text{ J/mol K}$) is the universal gas constant; F ($=96,486 \text{ C/mol}$) is the Faraday's constant; T is the operating temperature of the SOFC (K); and I_{FC} is the SOFC stack current (A). The physical meaning of the time constant τ_a is that it will take τ_a seconds to fill a tank of volume $V_a/2$ at pressure P_a^{ch} and same for τ_c .

The fuel utilization is the ratio between the fuel flow that reacts and the input fuel flow [18], and has been expressed by Eq. (14.21). The typical range of the fuel utilization is considered as 80–90%. The optimal fuel utilization has been considered as 85%. For a certain input H_2 flow, the demand current of the SOFC system is restricted in the given range and expressed by Eq. (14.22).

$$U_F = \frac{q_{H_2}^r}{q_{H_2}^{in}}, \quad \text{where} \quad q_{H_2}^r = \frac{N_{FC} I_{FC}^r}{2F} = 2K_r I_{FC}^r \quad \text{and} \quad K_r = \frac{N_{FC}}{4F} \quad (14.21)$$

$$\frac{0.8q_{H_2}^{in}}{2K_r} \leq I_{FC} \leq \frac{0.9q_{H_2}^{in}}{2K_r}, \quad \text{where} \quad q_{H_2}^{in} = \frac{2K_r I_{FC}}{0.85} \quad (14.22)$$

The SOFC stack output voltage is being determined by Nernst's equation [8, 18, 19], as described by Eq. (14.23).

$$V_{FC,stack} = N_{FC} \left(V_{0,FC} + \frac{RT}{2F} \left[\ln \left(\frac{p_{H_2} p_{O_2}^{0.5}}{p_{H_2O}} \right) \right] - r_{FC} I_{FC} \right) \quad (14.23)$$

where $q_{H_2}^r$ is the hydrogen flow that reacts (kmol/s), $q_{H_2}^{in}$ is the input hydrogen flow (kmol/s), K_r is a constant dependent on Faraday's constant, I_{FC}^r is the rated current of the SOFC (A), N_{FC} is the number of fuel cells connected in series in the SOFC stack, $V_{FC,stack}$ is the output voltage of the SOFC stack (V), $V_{0,FC}$ (=1.18 V) is the ideal standard potential of the SOFC, and r_{FC} is ohmic loss of a single SOFC (Ω). The p_{H_2} , p_{H_2O} , and p_{O_2} are the partial pressures of H_2 , H_2O , and O_2 , respectively, and are described as:

$$p_{H_2} = \frac{(q_{H_2}^{in} - 2K_r I_{FC})}{[K_{H_2}(1 + \tau_{H_2}s)]}, \quad p_{H_2O} = \frac{2K_r I_{FC}}{[K_{H_2O}(1 + \tau_{H_2O}s)]}, \quad p_{O_2} = \frac{(q_{O_2}^{in} - K_r I_{FC})}{[K_{O_2}(1 + \tau_{O_2}s)]} \quad (14.24)$$

where K_{H_2} , K_{H_2O} , and K_{O_2} are the valve molar constants (kmol s^{-1}/atm) for hydrogen, water, and oxygen, respectively, and τ_{H_2} , τ_{H_2O} , and τ_{O_2} are the response time constants (s) for the flow of hydrogen, water, and oxygen, respectively.

The dynamic model of the SOFC DG is shown, as given in [18], in Fig. 14.4.

14.3.2 Battery Energy Storage System

In order to solve the uncertainty problem of the RESs, the ESS units are commonly adopted in a microgrid under islanded mode. The various types of energy storage system technologies are batteries, super-capacitors, and flywheels. Generally, a battery is preferred among various ESSs for long-term power output. The BESS is a fast-responding device, which improves the reliability and provides higher flexibility in the control of the DCMG. The BESS can also mitigate the frequent and rapid power changes of the DGs and, therefore, solve the problems associated with intermittency of the RESs. The valve-regulated lead-acid (VRLA) batteries are being widely used with the integration of the RESs to maintain the power balance in

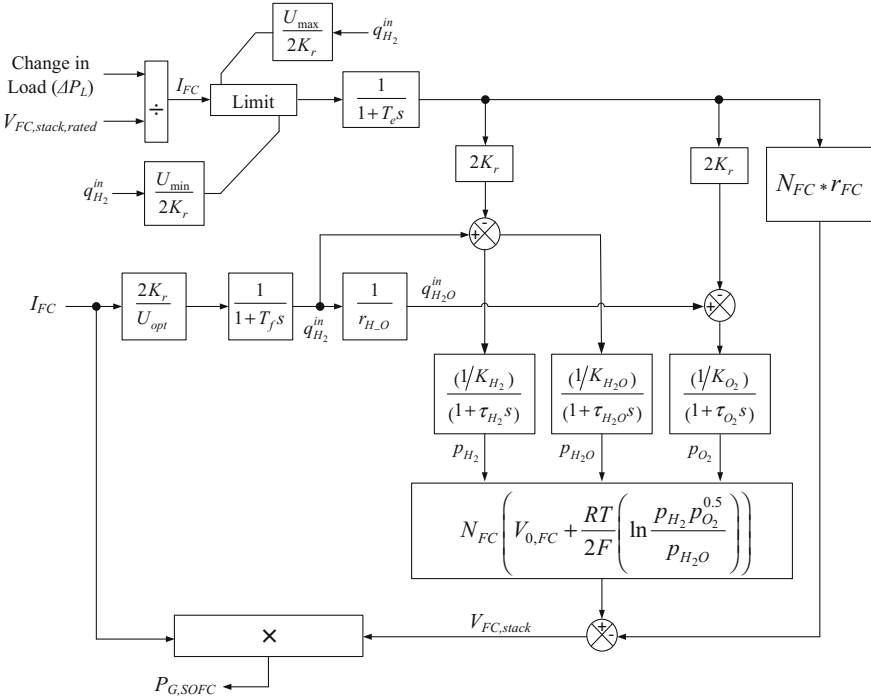
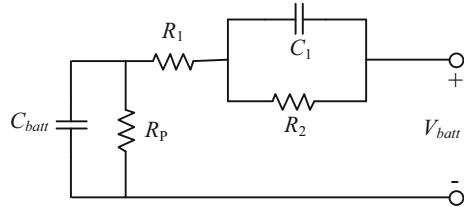


Fig. 14.4 Dynamic model of the SOFC DG system [18]

Fig. 14.5 Dynamic model of a lead-acid battery



the system. The VRLA battery is the least expensive storage device that exhibits reasonable performance and life characteristics. The dynamic model of a VRLA battery, neglecting the difference between the charge and the discharge resistance, is presented by Thevenin’s equivalent circuit [20, 21], as shown in Fig. 14.5. Since, the battery is an electrical energy storage device, which has been considered as an equivalent to a capacitor (C_{batt}). The capacitance C_{batt} is modelled as a controlled voltage source in the MATLAB/Simulink, which is controlled relative to the state of charge of the battery.

In Fig. 14.5, R_1 is the internal resistance of the battery, R_2 is the over-voltage resistance or impedance characteristic of C_1 that represents the charge transfer polarization, C_1 is the double-layer capacitance behaviour of the battery during

charge and discharge, R_p is the self-discharge resistance, and V_{batt} is the battery terminal voltage.

The charge and discharge voltage expressions used in the dynamic model of the VRLA battery [8] are given by Eq. (14.25):

$$\left. \begin{aligned} V_{\text{batt,ch}} &= V_{\text{batt},0} - R_1 i - k \frac{Q_{\text{batt}}}{it - 0.1 Q_{\text{batt}}} \cdot i^* - k \frac{Q_{\text{batt}}}{Q_{\text{batt}} - it} \cdot it + \text{Exp}(t) \\ V_{\text{batt,dch}} &= V_{\text{batt},0} - R_1 i - \underbrace{k \frac{Q_{\text{batt}}}{Q_{\text{batt}} - it} \cdot it}_{\text{Polarization Voltage}} - \underbrace{k \frac{Q_{\text{batt}}}{Q_{\text{batt}} - it} \cdot i^*}_{\text{Polarization Resistance}} + \text{Exp}(t) \end{aligned} \right\} \quad (14.25)$$

where $V_{\text{batt,ch}}$ and $V_{\text{batt,dch}}$ are the charging and discharging voltage of the battery (V), $V_{\text{batt},0}$ is the battery constant voltage (V), k is the polarization constant (V/Ah), Q_{batt} is the battery capacity (Ah), it ($=\int idt$) is the actual battery charge (Ah), i is the battery current (A), i^* is the filtered current (A), and $\text{Exp}(t)$ is exponential zone voltage (V).

To increase the life cycle of the battery and to protect the battery from zero charge state, a limit needs to be put on the maximum discharge current of the battery. Therefore, a minimum level of energy in a battery (specially in VRLA batteries and in lithium-ion batteries) during the discharge has been maintained at 5% of rated capacity of the battery; i.e., the depth of discharge of a battery is limited up to 95%. The size of the BESS is being considered as 20–50% of the WTG rated capacity [1]. Nowadays, the commercially available VRLA battery bank consists of cells of 12 V and the nominal capacity of each cell as 150 Ah.

14.3.3 DC and AC Loads

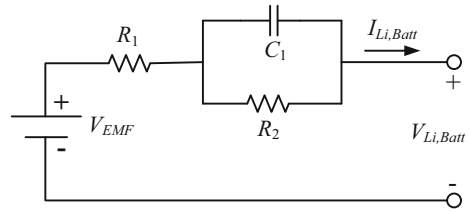
The loads are generally modelled as constant-resistance (CR), constant-current (CC), or constant-power (CP) type, depending on their characteristics. The steady-state characteristic of the loads, as a function of the voltage [1], is expressed as follows:

$$P_L(V_L) = K_{\text{CR}} V_L^2 + K_{\text{CC}} V_L + K_{\text{CP}} \quad (14.26)$$

The new model for resistive load, which takes the resistance as a function of the load current, has been expressed as follows:

$$\begin{aligned} V_L &= (R_0 + R_1 I_L) I_L = R_0 I_L + R_1 I_L^2, \quad \text{and} \\ P_L &= V_L I_L = V_L \left(-\frac{R_0}{2R_1} + \sqrt{\frac{V_L}{R_1} + \frac{R_0^2}{4R_1^2}} \right) \end{aligned} \quad (14.27)$$

Fig. 14.6 Dynamic model of a lithium-ion battery



where K_{CR} is the coefficient of the constant-resistance load, K_{CC} is the coefficient of the constant-current load, K_{PC} is the coefficient of the constant-power load, V_L is the load voltage, I_L is the load current, and P_L is the load power.

The various loads connected to the DCMG, as shown in Fig. 14.1, are mostly considered as constant-power loads (CPLs). A theoretical CPL is modelled as $P_L = V_L \cdot I_L = \text{constant}$. For a CPL, the instantaneous value of the impedance is always positive and the incremental impedance is always negative. The negative incremental impedance would cause the current to increase when the voltage decreases, and the current to decrease when the voltage increases. The negative incremental impedance causes the problem of instability in the system.

The lithium-ion battery is being widely used for the electric vehicle (EV) load, and its charging has been approximated as linear. The efficiency of the lithium-ion battery is higher (95%) than the other batteries. The EV batteries have been modelled as CPLs [22]. The analytical model of a lithium-ion battery has been expressed [22, 23], as shown in Fig. 14.6.

where V_{EMF} is the equilibrium voltage of the battery (V), $V_{Li,Batt}$ is the terminal voltage of lithium-ion battery (V), and $I_{Li,Batt}$ is the output current of lithium-ion battery (A).

14.3.4 PWM-Based Voltage Source Converters

The power electronic technology plays an important role in the DGs and in the integration of various DGs, ESSs, various loads, and utility grid to a microgrid.

14.3.4.1 Three-Phase Voltage Source Converters

Among various three-phase VSC configurations, the 2-level (conventional) VSC and the 3-level neutral point diode clamped VSC are the most widely used configurations for high-power applications. Although the switch arrangements, DC link structures, and the PWM modulation schemes of the 2-level VSC and the 3-level VSC are different, they adhere to the same principles in terms of the dynamics and control schemes.

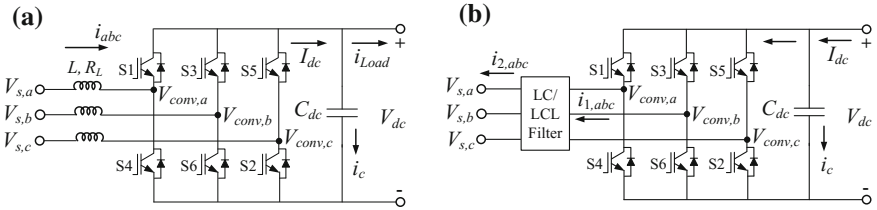
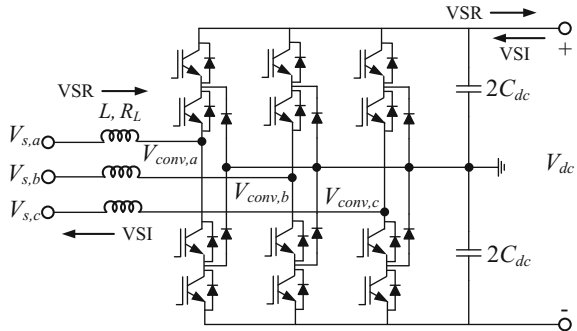


Fig. 14.7 a Three-phase, 2-level, VSR. b Three-phase, 2-level, VSI

Fig. 14.8 Three-phase, 3-level, VSR/VSI



The configurations of the 2-level voltage source rectifier (VSR) and 2-level VSI are shown in Fig. 14.7a, b, respectively. The configuration of 3-level VSR/VSI is shown in Fig. 14.8.

A 3-level VSC provides a significant better performance with respect to the total harmonic distortion in the output voltage. However, the more complex converter layout resulting in larger footprint and higher investment costs makes the 2-level converter technology the preferred solution. Hence, three-phase, 2-level VSCs have been considered for the integration of various AC -type DGs, AC loads, and the utility grid to the proposed DCMG.

Three-Phase Voltage Source Rectifier

From Fig. 14.7a, the voltage and current equations of a three-phase VSR in three-phase stationary reference frame can be written as follows [8, 24]:

$$v_{s,abc} = R_L \cdot i_{abc} + L \frac{di_{abc}}{dt} + v_{conv,abc} \quad \text{and} \quad C_{dc} \frac{dv_{dc}}{dt} = I_{dc} - i_{Load} \quad (14.28)$$

where $v_{s,abc}$ is the three-phase source voltage, i_{abc} is the three-phase input current to the VSR, $v_{conv,abc}$ is the input AC voltage of the VSR, L is the inductance of the phase reactors of the three-phase VSR, R_L is the resistance of the phase-inductor,

C_{dc} is the DC link capacitor of three-phase VSR, I_{dc} is the output DC current of the three-phase VSR, i_{Load} is the load current, and V_{dc} is the output DC voltage of the VSR or DCMG voltage.

Eq. (14.28) of three-phase VSR can be written into two-phase (α - β) stationary reference frame using Clark transformation as

$$v_{s,\alpha} = R_L \cdot i_\alpha + L \frac{di_\alpha}{dt} + v_{conv,\alpha} \quad \text{and} \quad v_{s,\beta} = R_L \cdot i_\beta + L \frac{di_\beta}{dt} + v_{conv,\beta} \quad (14.29)$$

where $v_{s,\alpha}$ and $v_{s,\beta}$ are the α -axis and β -axis voltage components of the source voltage, respectively; i_α and i_β are the α -axis and β -axis current components of the supply source, respectively; and $v_{conv,\alpha}$ and $v_{conv,\beta}$ are the α -axis and β -axis voltage components the AC input voltage to the VSR, respectively.

The voltage and current equations of the three-phase VSR into two-phase (d - q) rotating synchronous reference frame using Park transformation can be expressed as [24]

$$\left. \begin{aligned} v_{s,d} &= R_L i_d + L \frac{di_d}{dt} + v_{conv,d} - \omega L i_q \\ v_{s,q} &= R_L i_q + L \frac{di_q}{dt} + v_{conv,q} + \omega L i_d \end{aligned} \right\} \quad \text{and} \quad (14.30)$$

$$C_{dc} \frac{dv_{dc}}{dt} = \frac{3}{2} \left(\frac{v_{s,d} i_d + v_{s,q} i_q}{v_{dc}} \right) - i_{Load}$$

The power balance relationship between the AC input and DC output of a three-phase VSR is expressed as

$$P_{ac} = 1.5(v_{s,d} i_d + v_{s,q} i_q) = V_{dc} \cdot I_{dc} = P_{dc} \quad (14.31)$$

where $v_{s,d}$ and $v_{s,q}$ are the d -axis and q -axis voltage components of the source voltage, respectively; i_d and i_q are the d -axis and q -axis current components of the supply source, respectively; $v_{conv,d}$ and $v_{conv,q}$ are the d -axis and q -axis voltage components the AC input voltage to the VSR, respectively; ω ($=2\pi f_s$) is the angular frequency; f_s is the supply frequency; P_{ac} is the AC power of the VSC; and P_{dc} is the DC power of the VSC.

Three-Phase Voltage Source Inverter

From Fig. 14.7b, the voltage and current equations of the three-phase VSI with an LC output filter in three-phase stationary reference frame are given as [25]

$$v_{conv,abc} = R_{Lf} \cdot i_{abc} + L_f \frac{di_{1,abc}}{dt} + v_{s,abc}, \quad \text{and} \quad C_f \frac{dv_{s,abc}}{dt} = i_{1,abc} - i_{2,abc} \quad (14.32)$$

where $v_{s,abc}$ is the three-phase load voltage, $i_{1,abc}$ is the three-phase output AC current of the VSI, $i_{2,abc}$ is the three-phase load current connected across the VSI,

$v_{\text{conv},abc}$ is the three-phase output AC voltage of the VSI, L_f is the inductor of the LC filter, R_{L_f} is the resistance of the filter inductor, and C_f is the capacitor of the LC filter.

Eq. (14.32) can be written into two-phase (α - β) stationary reference frame using Clark transformation as follows:

$$\left. \begin{aligned} v_{\text{conv},\alpha} &= R_{L_f} \cdot i_\alpha + L_f \frac{di_\alpha}{dt} + v_{s,\alpha} \\ v_{\text{conv},\beta} &= R_{L_f} \cdot i_\beta + L_f \frac{di_\beta}{dt} + v_{s,\beta} \end{aligned} \right\} \text{ and } C_f \frac{dv_{s,\alpha\beta}}{dt} = i_{1,\alpha\beta} - i_{2,\alpha\beta} \quad (14.33)$$

where $v_{s,\alpha}$ and $v_{s,\beta}$ are the α -axis and β -axis voltage components of the load side voltage, respectively; $i_{1,\alpha}$ and $i_{1,\beta}$ are the α -axis and β -axis current components of the output AC current of the VSI, respectively; $v_{\text{conv},\alpha}$ and $v_{\text{conv},\beta}$ are the α -axis and β -axis voltage components of the VSI output AC voltage, respectively; and $i_{2,\alpha}$ and $i_{2,\beta}$ are the α -axis and β -axis current components of the load current, respectively.

Eq. (14.33) can be expressed into two-phase (d - q) rotating SRF by using Park transformation as follows:

$$\left. \begin{aligned} v_{\text{conv},d} &= R_{L_f} \cdot i_d + L_f \frac{di_d}{dt} + v_{s,d} + \omega L_f i_q \\ v_{\text{conv},q} &= R_{L_f} \cdot i_q + L_f \frac{di_q}{dt} + v_{s,q} - \omega L_f i_d \end{aligned} \right\} \text{ and } C_f \frac{dv_{s,dq}}{dt} = i_{dq} - i_{L,dq} \quad (14.34)$$

where $v_{s,d}$ and $v_{s,q}$ are the d -axis and q -axis voltage components of the load side voltage, respectively; $i_{1,d}$ and $i_{1,q}$ are the d -axis and q -axis current components of the output AC current of the VSI, respectively; $v_{\text{conv},d}$ and $v_{\text{conv},q}$ are the d -axis and q -axis voltage components the VSI output AC voltage, respectively; and $i_{2,d}$ and $i_{2,q}$ are the d -axis and q -axis current components of the load current, respectively.

From Fig. 14.7b, the voltage and current equations of the three-phase VSI with an LCL output filter in three-phase stationary reference frame can be expressed as follows [26]:

$$\left. \begin{aligned} v_{\text{conv},abc} &= R_{L_{f1}} i_{1,abc} + L_{f1} \frac{di_{1,abc}}{dt} + v_{C_f,abc} \\ v_{C_f,abc} &= L_{f2} \frac{di_{2,abc}}{dt} + R_{L_{f2}} i_{2,abc} + v_{s,abc} \end{aligned} \right\} \text{ and } C_f \frac{dv_{C_f,abc}}{dt} = i_{1,abc} - i_{2,abc} \quad (14.35)$$

where L_{f1} and L_{f2} are the inductors of the LCL filter, $R_{L_{f1}}$ and $R_{L_{f2}}$ are the resistances of the inductors (L_{f1}) and (L_{f2}), respectively, $i_{1,abc}$ and $i_{2,abc}$ are the output currents of three-phase VSI through the inductors L_{f1} and L_{f2} of the LCL filter, respectively, and $v_{C_f,abc}$ is the three-phase voltage across the filter capacitor (C_f).

Eq. (14.35) can be converted into two-phase (α - β) stationary reference frame using Clark transformation as follows:

$$\left. \begin{aligned} v_{\text{conv},\alpha\beta} &= R_{L_{f1}} i_{1,\alpha\beta} + L_{f1} \frac{di_{1,\alpha\beta}}{dt} + v_{C_f,\alpha\beta} \\ v_{C_f,\alpha\beta} &= L_{f2} \frac{di_{2,\alpha\beta}}{dt} + R_{L_{f2}} i_{2,\alpha\beta} + v_{s,\alpha\beta} \end{aligned} \right\} \text{ and } C_f \frac{dv_{C_f,\alpha\beta}}{dt} = i_{1,\alpha\beta} - i_{2,\alpha\beta} \quad (14.36)$$

where $v_{C_f,\alpha}$ and $v_{C_f,\beta}$ are the α -axis and β -axis voltage components of the filter capacitor voltage, respectively.

The voltage and current equations of the three-phase VSI with LCL filter into two-phase (d - q) rotating SRF using Park's transformation can be expressed as follows:

$$\left(\begin{aligned} v_{\text{conv},d} &= R_{L_{f1}} i_{1,d} + L_{f1} \frac{di_{1,d}}{dt} + v_{C_f,d} - \omega L_{f1} i_{1,q} \\ v_{\text{conv},q} &= R_{L_{f1}} i_{1,q} + L_{f1} \frac{di_{1,q}}{dt} + v_{C_f,q} + \omega L_{f1} i_{1,d} \\ v_{C_f,d} &= R_{L_{f2}} i_{2,d} + L_{f2} \frac{di_{2,d}}{dt} + v_{s,d} - \omega L_{f2} i_{2,q} \\ v_{C_f,q} &= R_{L_{f2}} i_{2,q} + L_{f2} \frac{di_{2,q}}{dt} + v_{s,q} + \omega L_{f2} i_{2,d} \end{aligned} \right), \text{ and} \quad (14.37)$$

$$\left(\begin{aligned} C_f \frac{dv_{C_f,d}}{dt} &= i_{1,d} - i_{2,d} + \omega C_f v_{C_f,q} \\ C_f \frac{dv_{C_f,q}}{dt} &= i_{1,q} - i_{2,q} - \omega C_f v_{C_f,d} \end{aligned} \right)$$

where $v_{C_f,d}$ and $v_{C_f,q}$ are the d -axis and q -axis voltage components of the filter capacitor voltage, respectively; V_{conv} ($=\delta V_{dc}$) is the AC output voltage of the three-phase VSC; and δ is the continuous duty ratio $\in [0, 1]$.

Modelling of Three-Phase VSR Under Unbalanced Loads

During the unbalanced operation, the expressions for the voltage drop over the phase reactors of the three-phase VSR hold for the positive-sequence as well as the negative-sequence voltages and currents. An unbalanced three-phase variable, with no zero sequence, has been decomposed into the positive- and negative-sequence components by using the delayed signal cancellation (DSC) method [27]. The DSC method is being widely used for the decomposition of the positive and the negative sequences into two-phase (α - β) stationary reference frame, as shown in Fig. 14.9.

The time required by the DSC method to calculate the symmetrical components is very small, which is a time delay of one-quarter of a period, i.e. $T/4$ (where $T = 1/f_s$ is the period of one cycle and f_s is the supply frequency), after the beginning of any transient. Thus, the time required for the DSC method is 5 ms at 50 Hz. It is also

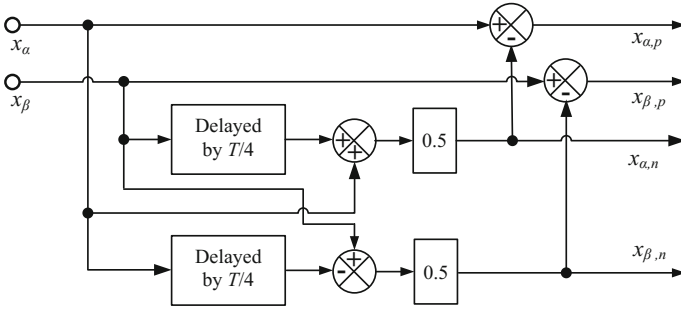


Fig. 14.9 Delayed signal cancellation method for decomposition of the positive- and the negative-sequence components of three-phase voltage/current

included within the sampling time ($T_s = 200 \mu\text{s}$ for 5 kHz switching frequency) of the controller. This technique allows achieving the accurate information on the sequence components.

The equations implemented in the block diagram of the DSC method for obtaining the positive- and the negative-sequence α - β components of the three-phase voltage/currents are expressed as follows:

$$x_{\alpha,n}(t) = 0.5 \left[x_{\alpha}(t) + x_{\beta} \left(t - \frac{T}{4T_s} \right) \right] \quad (14.38)$$

$$x_{\beta,n}(t) = 0.5 \left[x_{\beta}(t) - x_{\alpha} \left(t - \frac{T}{4T_s} \right) \right] \quad (14.39)$$

$$x_{\alpha,p}(t) = x_{\alpha}(t) - x_{\alpha,n}(t) = 0.5 \left[x_{\alpha}(t) - x_{\beta} \left(t - \frac{T}{4T_s} \right) \right] \quad (14.40)$$

$$x_{\beta,p}(t) = x_{\beta}(t) - x_{\beta,n}(t) = 0.5 \left[x_{\beta}(t) + x_{\alpha} \left(t - \frac{T}{4T_s} \right) \right] \quad (14.41)$$

where x_{α} and x_{β} are the α -axis and β -axis components of three-phase quantities (voltage/current), respectively; $x_{\alpha,p}$ and $x_{\alpha,n}$ are the α -axis positive- and negative-sequence components of three-phase quantities, respectively; and $x_{\beta,p}$ and $x_{\beta,n}$ are the β -axis positive- and negative-sequence components of three-phase quantities, respectively.

The voltage equations of the three-phase VSR into two d - q rotating synchronous reference frames (SRFs), viz. positive SRF and negative SRF, have been derived from Eq. (14.29) as follows [8, 28, 29]:

$$v_{s,d}^{p/n} = R L_d^{p/n} i_d^{p/n} + L \frac{d i_d^{p/n}}{dt} + v_{\text{conv},d}^{p/n} \mp \omega L i_q^{p/n} \quad (14.42)$$

$$v_{s,q}^{p/n} = R_L i_{dq}^{p/n} + L \frac{di_{dq}^{p/n}}{dt} + v_{\text{conv},q}^{p/n} \pm \omega L i_d^{p/n} \quad (14.43)$$

The minus sign in the last term of Eq. (14.42) and the plus sign in the last term of Eq. (14.43) stand for the positive (p)-sequence voltage equations in rotating d - q positive SRF. Similarly, the plus sign in the last term of Eq. (14.42) and the minus sign in the last term of Eq. (14.43) stand for the negative (n)-sequence voltage equations in rotating d - q negative SRF.

Under unbalanced condition, the apparent power is defined as follows [28, 29]:

$$S = P + jQ = \frac{3}{2} V_{s,dq} I_{dq}^* = \frac{3}{2} \left(e^{j\omega t} V_{s,dq}^p + e^{-j\omega t} V_{s,dq}^n \right) \cdot \left(e^{j\omega t} I_{dq}^p + e^{-j\omega t} I_{dq}^n \right)^* \quad (14.44)$$

where, $V_{s,dq}^p = V_{s,d}^p + jV_{s,q}^p$, $V_{s,dq}^n = V_{s,d}^n + jV_{s,q}^n$, $I_{dq}^p = I_d^p + jI_q^p$, and $I_{dq}^n = I_d^n + jI_q^n$.

By solving Eq. (14.44), the instantaneous active and reactive powers have been determined as follows:

$$\left. \begin{aligned} P(t) &= \text{Real}(S) = P_0 + P_{\cos 2} \cos(2\omega t) + P_{\sin 2} \sin(2\omega t) \\ Q(t) &= \text{Img}(S) = Q_0 + Q_{\cos 2} \cos(2\omega t) + Q_{\sin 2} \sin(2\omega t) \end{aligned} \right\} \quad (14.45)$$

where

$$\left\{ \begin{aligned} P_0 &= 1.5 \left(V_{s,d}^p I_d^p + V_{s,q}^p I_q^p + V_{s,d}^n I_d^n + V_{s,q}^n I_q^n \right) \\ P_{\cos 2} &= 1.5 \left(V_{s,d}^p I_d^n + V_{s,q}^p I_q^n + V_{s,d}^n I_d^p + V_{s,q}^n I_q^p \right) \\ P_{\sin 2} &= 1.5 \left(V_{s,q}^p I_d^p - V_{s,d}^p I_q^p - V_{s,q}^n I_d^n + V_{s,d}^n I_q^n \right) \end{aligned} \right\}, \quad \text{and}$$

$$\left\{ \begin{aligned} Q_0 &= 1.5 \left(V_{s,q}^p I_d^p - V_{s,d}^p I_q^p + V_{s,q}^n I_d^n - V_{s,d}^n I_q^n \right) \\ Q_{\cos 2} &= 1.5 \left(V_{s,q}^p I_d^n - V_{s,d}^p I_q^n + V_{s,q}^n I_d^p - V_{s,d}^n I_q^p \right) \\ Q_{\sin 2} &= 1.5 \left(V_{s,d}^p I_d^n + V_{s,q}^p I_q^n - V_{s,d}^n I_d^p - V_{s,q}^n I_q^p \right) \end{aligned} \right\}$$

where $V_{s,d}^p$ and $V_{s,q}^p$ are the positive-sequence components of the supply voltage along the d -axis and q -axis, respectively; I_d^p and I_q^p are the positive-sequence components of the input current to the VSR along the d -axis and q -axis, respectively; $V_{s,d}^n$ and $V_{s,q}^n$ are the negative-sequence components of the supply voltage along the d -axis and q -axis, respectively; I_d^n and I_q^n are the negative-sequence components of the input current to the VSR along the d -axis and q -axis, respectively; ω is the angular frequency; and $P_{\cos 2}$, $P_{\sin 2}$, $Q_{\cos 2}$, and $Q_{\sin 2}$ are the higher order power coefficients caused by unbalanced voltage.

From Eq. (14.45), the power coefficients in matrix form can be expressed as follows [11]:

$$\begin{bmatrix} P_0 \\ Q_0 \\ P_{\sin 2} \\ P_{\cos 2} \end{bmatrix} = \frac{3}{2} \begin{bmatrix} V_{s,d}^p & V_{s,q}^p & V_{s,d}^n & V_{s,q}^n \\ V_{s,q}^p & -V_{s,d}^p & V_{s,q}^n & -V_{s,d}^n \\ V_{s,q}^n & -V_{s,d}^n & -V_{s,q}^p & V_{s,d}^p \\ V_{s,d}^n & V_{s,q}^n & V_{s,d}^p & V_{s,q}^p \end{bmatrix} \begin{bmatrix} I_d^p \\ I_q^p \\ I_d^n \\ I_q^n \end{bmatrix} \quad (14.46)$$

From Eq. (14.16), the positive- and negative-sequence reference current components into rotating d - q SRF can be derived as follows:

$$\begin{bmatrix} I_d^p \\ I_q^p \\ I_d^n \\ I_q^n \end{bmatrix} = \frac{2}{3} \begin{bmatrix} V_{s,d}^p & V_{s,q}^p & V_{s,d}^n & V_{s,q}^n \\ V_{s,q}^p & -V_{s,d}^p & V_{s,q}^n & -V_{s,d}^n \\ V_{s,q}^n & -V_{s,d}^n & -V_{s,q}^p & V_{s,d}^p \\ V_{s,d}^n & V_{s,q}^n & V_{s,d}^p & V_{s,q}^p \end{bmatrix}^{-1} \begin{bmatrix} P_0 \\ Q_0 \\ P_{\sin 2} \\ P_{\cos 2} \end{bmatrix} \quad (14.47)$$

To remove DC link voltage ripple and to obtain the average zero reactive power coefficients, it is necessary to make $P_{\cos 2} = 0$, $P_{\sin 2} = 0$, and $Q_0 = 0$. From Eq. (14.47) and considering these conditions, the positive- and negative-sequence reference current components for the inner current controller of the three-phase/single-phase VSC are derived as follows [28, 29]:

$$\begin{bmatrix} I_{d,\text{ref}}^p \\ I_{q,\text{ref}}^p \\ I_{d,\text{ref}}^n \\ I_{q,\text{ref}}^n \end{bmatrix} = \frac{2}{3} \begin{bmatrix} V_{s,d}^p & V_{s,q}^p & V_{s,d}^n & V_{s,q}^n \\ V_{s,q}^p & -V_{s,d}^p & V_{s,q}^n & -V_{s,d}^n \\ V_{s,q}^n & -V_{s,d}^n & -V_{s,q}^p & V_{s,d}^p \\ V_{s,d}^n & V_{s,q}^n & V_{s,d}^p & V_{s,q}^p \end{bmatrix}^{-1} \begin{bmatrix} P_0 \\ 0 \\ 0 \\ 0 \end{bmatrix} = \frac{2P_0}{3\Delta} \begin{bmatrix} V_{s,d}^p \\ V_{s,q}^p \\ -V_{s,d}^n \\ -V_{s,q}^n \end{bmatrix} \left. \begin{array}{l} \text{where, } \Delta = \left[\left(V_{s,d}^p \right)^2 + \left(V_{s,q}^p \right)^2 \right] - \left[\left(V_{s,d}^n \right)^2 + \left(V_{s,q}^n \right)^2 \right], \text{ and } \Delta \neq 0 \end{array} \right\} \quad (14.48)$$

The power, P_0 , in Eq. (14.48) has been obtained from the DC voltage controller of the three-phase/single-phase VSC and is expressed as follows:

$$P_0 = V_{\text{dc,ref}} \cdot I_{\text{ref}} \quad (14.49)$$

where $V_{\text{dc,ref}}$ is the reference DC voltage of the VSC or DC microgrid, and I_{ref} is the reference current signal generated by the DC voltage PI controller of the VSC.

Modelling of Three-Phase VSI Under Unbalanced Loads

From Fig. 14.7b, the voltage drop equations of the three-phase VSI across LC output filter, under unbalanced load, for the positive- and negative-sequence components are expressed in rotating d - q SRFs as [29],

$$\left. \begin{aligned} \frac{di_d^p}{dt} &= -\frac{R_{L_f}}{L_f} i_d^p + \frac{1}{L_f} v_{\text{conv},d}^p - \frac{1}{L_f} v_{s,d}^p - \omega i_q^p, \\ \frac{di_q^p}{dt} &= -\frac{R_{L_f}}{L_f} i_q^p + \frac{1}{L_f} v_{\text{conv},q}^p - \frac{1}{L_f} v_{s,q}^p + \omega i_d^p \end{aligned} \right\} \quad (14.50)$$

$$\left. \begin{aligned} \frac{di_d^n}{dt} &= -\frac{R_{L_f}}{L_f} i_d^n + \frac{1}{L_f} v_{\text{conv},d}^n - \frac{1}{L_f} v_{s,d}^n + \omega i_q^n, \\ \frac{di_q^n}{dt} &= -\frac{R_{L_f}}{L_f} i_q^n + \frac{1}{L_f} v_{\text{conv},q}^n - \frac{1}{L_f} v_{s,q}^n - \omega i_d^n \end{aligned} \right\} \quad (14.51)$$

From Fig. 14.7b, the expressions of three-phase VSI for the voltage drop across the LCL filter inductor (L_{f1}) and current through the filter capacitor (C_f), for the positive- and negative-sequence components in rotating d - q SRFs, are expressed as follows:

$$\left. \begin{aligned} \frac{di_{1,d}^p}{dt} &= -\frac{R_{L_{f1}}}{L_{f1}} i_{1,d}^p + \frac{1}{L_{f1}} v_{\text{conv},d}^p - \frac{1}{L_{f1}} v_{C_f,d}^p + \omega i_{1,q}^p, \\ \frac{di_{1,q}^p}{dt} &= -\frac{R_{L_{f1}}}{L_{f1}} i_{1,q}^p + \frac{1}{L_{f1}} v_{\text{conv},q}^p - \frac{1}{L_{f1}} v_{C_f,q}^p - \omega i_{1,d}^p \end{aligned} \right\} \quad (14.52)$$

$$\frac{dv_{C_f,d}^p}{dt} = \frac{i_{1,d}^p}{C_f} - \frac{i_{2,d}^p}{C_f} + \omega v_{C_f,q}^p, \quad \text{and} \quad \frac{dv_{C_f,q}^p}{dt} = \frac{i_{1,q}^p}{C_f} - \frac{i_{2,q}^p}{C_f} - \omega v_{C_f,d}^p \quad (14.53)$$

$$\left. \begin{aligned} \frac{di_{1,d}^n}{dt} &= -\frac{R_{L_{f1}}}{L_{f1}} i_{1,d}^n + \frac{1}{L_{f1}} v_{\text{conv},d}^n - \frac{1}{L_{f1}} v_{C_f,d}^n - \omega i_{1,q}^n, \\ \frac{di_{1,q}^n}{dt} &= -\frac{R_{L_{f1}}}{L_{f1}} i_{1,q}^n + \frac{1}{L_{f1}} v_{\text{conv},q}^n - \frac{1}{L_{f1}} v_{C_f,q}^n + \omega i_{1,d}^n \end{aligned} \right\} \quad (14.54)$$

$$\frac{dv_{C_f,d}^n}{dt} = \frac{i_{1,d}^n}{C_f} - \frac{i_{2,d}^n}{C_f} - \omega v_{C_f,q}^n, \quad \text{and} \quad \frac{dv_{C_f,q}^n}{dt} = \frac{i_{1,q}^n}{C_f} - \frac{i_{2,q}^n}{C_f} + \omega v_{C_f,d}^n \quad (14.55)$$

The expressions of three-phase VSI for the voltage drop across the LCL filter inductor (L_{f2}), for the positive-sequence and the negative-sequence components into rotating d - q SRFs, are expressed as follows:

$$\left. \begin{aligned} \frac{di_{2,d}^p}{dt} &= -\frac{R_{L_{f2}}}{L_{f2}} i_{2,d}^p + \frac{1}{L_{f2}} v_{C_{f,d}}^p - \frac{1}{L_{f2}} v_{s,d}^p + \omega i_{2,q}^p \\ \frac{di_{2,q}^p}{dt} &= -\frac{R_{L_{f2}}}{L_{f2}} i_{2,q}^p + \frac{1}{L_{f2}} v_{C_{f,q}}^p - \frac{1}{L_{f2}} v_{s,q}^p - \omega i_{2,d}^p \end{aligned} \right\} \quad (14.56)$$

$$\left. \begin{aligned} \frac{di_{2,d}^n}{dt} &= -\frac{R_{L_{f2}}}{L_{f2}} i_{2,d}^n + \frac{1}{L_{f2}} v_{C_{f,d}}^n - \frac{1}{L_{f2}} v_{s,d}^n - \omega i_{2,q}^n \\ \frac{di_{2,q}^n}{dt} &= -\frac{R_{L_{f2}}}{L_{f2}} i_{2,q}^n + \frac{1}{L_{f2}} v_{C_{f,q}}^n - \frac{1}{L_{f2}} v_{s,q}^n + \omega i_{2,d}^n \end{aligned} \right\} \quad (14.57)$$

where $i_{1,d}^p$ and $i_{1,q}^p$ are the d - and q -axis positive-sequence components of the output current (i_1) of three-phase VSI through the filter inductor (L_{f1}), respectively; $i_{1,d}^n$ and $i_{1,q}^n$ are the d - and q -axis negative-sequence components of the output current (i_1), respectively; $i_{2,d}^p$ and $i_{2,q}^p$ are the d - and q -axis positive-sequence components of the output current (i_2) through the filter inductor (L_{f2}), respectively; $i_{2,d}^n$ and $i_{2,q}^n$ are the d - and q -axis negative-sequence components of the output current (i_2), respectively; $v_{conv,d}^p$ and $v_{conv,q}^p$ are the d - and q -axis positive-sequence components of the three-phase VSI AC voltage, respectively; $v_{conv,d}^n$ and $v_{conv,q}^n$ are the d - and q -axis negative-sequence components of the VSI AC voltage, respectively; $v_{C_{f,d}}^p$ and $v_{C_{f,q}}^p$ are the d - and q -axis positive-sequence components of the filter capacitor voltage, respectively; $v_{C_{f,d}}^n$ and $v_{C_{f,q}}^n$ are the d - and q -axis negative-sequence components of the filter capacitor voltage, respectively; $v_{s,d}^p$ and $v_{s,q}^p$ the d - and q -axis positive-sequence components of three-phase load voltage, respectively; and $v_{s,d}^n$ and $v_{s,q}^n$ the d - and q -axis negative-sequence components of three-phase load voltage, respectively.

Three-Phase Back-to-Back (AC-DC-AC) VSC

A three-phase back-to-back (AC-DC-AC) VSC has been used for controlling the DFIG in the WT DG. The back-to-back converter consists of two VSCs, viz. the stator side VSC and rotor side VSC, as shown in Fig. 14.10. Between these two VSCs, a DC link capacitor is placed as an energy storage, in order to minimize the ripple in the DC link voltage.

In Fig. 14.10, V_{sabc} and V_{rabc} are the three-phase voltage of the stator and rotor of the DFIG, respectively; i_{sabc} and i_{rabc} are the three-phase current of the stator and rotor of the DFIG, respectively; $V_{conv,sabc}$ and $V_{conv,rabc}$ are the three-phase AC voltages of the stator side VSC and rotor side VSC, respectively; P_s , Q_s and P_r , Q_r are the real and reactive power on the stator side and rotor side, respectively; $C_{dc,link}$ is the DC link capacitor of the back-to-back VSC; $i_{c,link}$ is the current flowing in the DC link capacitor; and $V_{dc,link}$ is the DC link voltage of the back-to-back VSC.

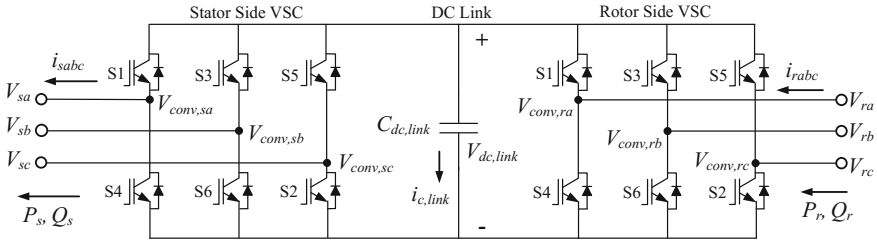


Fig. 14.10 Three-phase back-to-back (AC-DC-AC) VSC

14.3.4.2 Single-Phase Voltage-Controlled Voltage Source Inverter

The single-phase full-bridge VCVSI with an output second-order LC output filter, as shown in Fig. 14.11, has been used to interconnect all single-phase AC loads to the DCMG.

The dynamic equations for the voltage and current of the single-phase full-bridge VCVSI are given by Eq. (14.58):

$$v_{inv} = R_{L_f} i_L + L_f \frac{di_L}{dt} + v_a \quad \text{and} \quad 0 = i_L - i_o - C_f \frac{dv_a}{dt} \tag{14.58}$$

The small-signal state-space model of the single-phase VCVSI is expressed as follows:

$$\frac{d}{dt} \begin{bmatrix} i_L \\ v_a \end{bmatrix} = \begin{bmatrix} -R_{L_f}/L_f & -1/L_f \\ 1/C_f & 0 \end{bmatrix} \begin{bmatrix} i_L \\ v_a \end{bmatrix} + \begin{bmatrix} 1/L_f \\ 0 \end{bmatrix} v_{inv} + \begin{bmatrix} 0 \\ -1/C_f \end{bmatrix} i_o \tag{14.59}$$

where v_{inv} is the output AC voltage of the single-phase VCVSI, v_a is the single-phase load voltage, i_L is the current through the inductor (L_f) of the LC filter, i_o is the load current, R_{L_f} is the resistance of the filter inductor, C_f is the capacitance of the LC filter, $V_{inv} (= \delta V_{dc})$ is the output voltage of inverter, and $\delta (=1, 0, \text{ or } -1)$ is

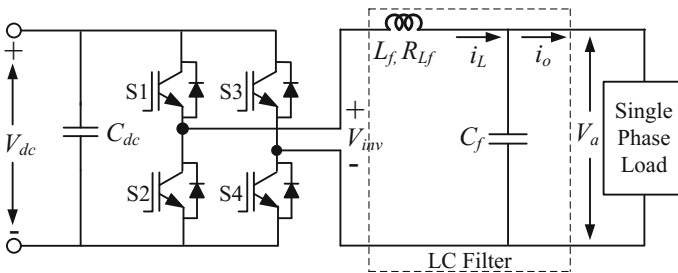


Fig. 14.11 Single-phase full-bridge VCVSI with an LC output filter

the control variable depending on the state of the switches in the single-phase full-bridge VCVSI.

The dynamic equations for the voltage and current of the single-phase full-bridge VCVSI with an output LC filter, into two-phase (α - β) stationary reference frame and into rotating d - q SRF, are expressed by Eqs. (14.60) and (14.61), respectively,

$$\left. \begin{aligned} v_{\text{inv},\alpha} &= R_{L_f} i_{L,\alpha} + L_f \frac{di_{L,\alpha}}{dt} + v_{a,\alpha}, \\ v_{\text{inv},\beta} &= R_{L_f} i_{L,\beta} + L_f \frac{di_{L,\beta}}{dt} + v_{a,\beta} \\ 0 &= i_{L,\alpha} - i_{o,\alpha} - C_f \frac{dv_{a,\alpha}}{dt}, \\ 0 &= i_{L,\beta} - i_{o,\beta} - C_f \frac{dv_{a,\beta}}{dt} \end{aligned} \right\} \quad (14.60)$$

$$\left. \begin{aligned} v_{\text{inv},d} &= R_{L_f} i_{L,d} + L_f \frac{di_{L,d}}{dt} - \omega L_f i_{L,q} + v_{a,d} \\ v_{\text{inv},q} &= R_{L_f} i_{L,q} + L_f \frac{di_{L,q}}{dt} + \omega L_f i_{L,d} + v_{a,q} \\ 0 &= i_{L,d} - C_f \frac{dv_{a,d}}{dt} - i_{o,d} - \omega C_f v_{a,q}, \quad \text{and} \\ 0 &= i_{L,q} - C_f \frac{dv_{a,q}}{dt} - i_{o,q} + \omega C_f v_{a,d} \end{aligned} \right\} \quad (14.61)$$

where $v_{\text{inv},\alpha}$ and $v_{\text{inv},\beta}$ are the α -axis and β -axis components of the single-phase VCVSI output AC voltage, respectively; $v_{a,\alpha}$ and $v_{a,\beta}$ are the α -axis and β -axis components of the load voltage, respectively; $i_{L,\alpha}$ and $i_{L,\beta}$ are the α -axis and β -axis components of the VCVSI output AC current components through the filter inductor, respectively; $i_{o,\alpha}$ and $i_{o,\beta}$ are the load current components along the α -axis and β -axis, respectively; $v_{\text{inv},d}$ and $v_{\text{inv},q}$ are the d -axis and q -axis components of the VCVSI output AC voltage, respectively; $v_{a,d}$ and $v_{a,q}$ are the d -axis and q -axis components of the load voltage, respectively; $i_{L,d}$ and $i_{L,q}$ are the d -axis and q -axis components of the VCVSI output AC current through the filter inductor, respectively; $i_{o,d}$ and $i_{o,q}$ are the d -axis and q -axis components of the load current, respectively; $i_o (=V_a/Z)$ is the load current; and Z is the load impedance.

14.3.4.3 DC-DC Buck Converter

The main purpose of the DC-DC buck converters, in this work, is to integrate the various DC loads into the DCMG, which are operating at the different DC voltages lower than the DCMG voltage, as shown in Fig. 14.1. A topology of the DC-DC buck converter is shown in Fig. 14.12a. The inductor voltage and inductor current waveforms for a DC-DC buck converter are shown in Fig. 14.13. In steady state, the average inductor voltage and average capacitor current, over one time period,

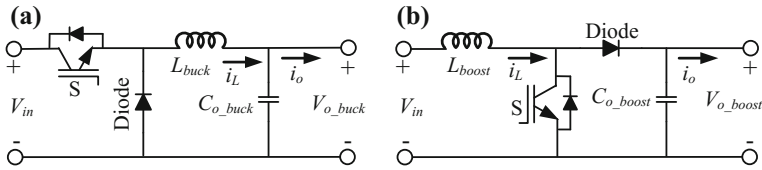


Fig. 14.12 a DC-DC buck converter. b DC-DC boost converter

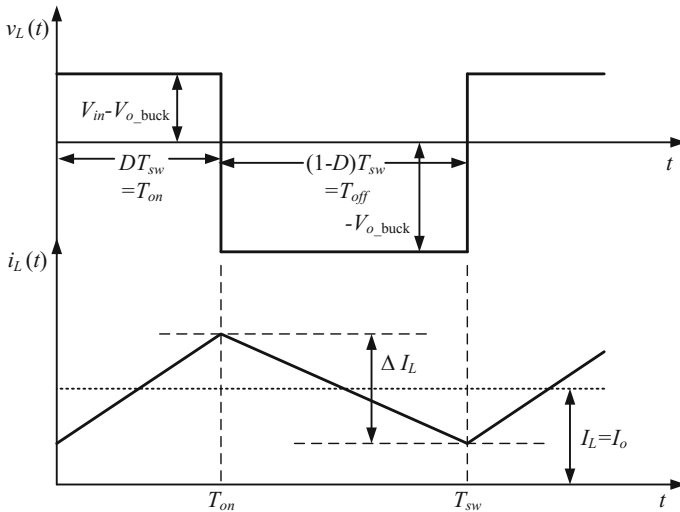


Fig. 14.13 Inductor voltage and inductor current waveforms of a DC-DC buck converter

must be zero. The relation between input–output voltage/current has been derived as follows:

$$V_{O_{buck}} = DV_{in} \quad \text{and} \quad I_o = I_L, \quad \text{where} \quad D = (T_{on}/T_{sw}) \quad (14.62)$$

where V_{in} ($=V_{dc}$) and $V_{O_{buck}}$ are the input DC voltage and average output DC voltage of the DC-DC buck converter, respectively; D is the average duty cycle; T_{on} is the turn on time of the switch (S); T_{sw} ($=1/F_{sw}$) is the switching time period of the converter; F_{sw} is the switching frequency of the converter; L_{buck} and $C_{O_{buck}}$ are the inductor and output capacitor of the DC-DC buck converter, respectively; I_o is the average output current; I_L is the current through the inductor; and $R_{L,dc}$ is the DC load connected across the output terminals of the DC-DC converter.

The average inductor voltage and average capacitor current expressions have been determined as follows:

$$\frac{d}{dt} \langle i_L \rangle = \frac{\langle v_{in} d \rangle}{L_{buck}} - \frac{\langle v_{O_{buck}} \rangle}{L_{buck}} \quad \text{and} \quad \frac{d}{dt} \langle v_{O_{buck}} \rangle = \frac{\langle \dot{i}_L \rangle}{C_{O_{buck}}} - \frac{\langle v_{O_{buck}} \rangle}{R_{L,dc} C_{O_{buck}}} \quad (14.63)$$

$$\text{or} \quad \frac{d}{dt} I_L = \frac{D V_{in}}{L_{buck}} - \frac{V_{O_{buck}}}{L_{buck}} \quad \text{and} \quad \frac{d}{dt} V_{O_{buck}} = \frac{I_L}{C_{O_{buck}}} - \frac{V_{O_{buck}}}{R_{L,dc} C_{O_{buck}}} \quad (14.64)$$

Considering the small perturbations in the various quantities as, $v_{in} = V_{in} + \tilde{v}_{in}$, $v_{O_{buck}} = V_{O_{buck}} + \tilde{v}_{O_{buck}}$, $i_L = I_L + \tilde{i}_L$, $i_o = I_o + \tilde{i}_o$, and $d = D + \tilde{d}$, Eq. (14.63) can be expressed as follows:

$$\left. \begin{aligned} \frac{d}{dt} \langle I_L + \tilde{i}_L \rangle &= \frac{\langle (V_{in} + \tilde{v}_{in})(D + \tilde{d}) \rangle}{L_{buck}} - \frac{\langle V_{O_{buck}} + \tilde{v}_{O_{buck}} \rangle}{L_{buck}} \\ \frac{d}{dt} \langle V_{O_{buck}} + \tilde{v}_{O_{buck}} \rangle &= \frac{\langle I_L + \tilde{i}_L \rangle}{C_{O_{buck}}} - \frac{\langle V_{O_{buck}} + \tilde{v}_{O_{buck}} \rangle}{R_{L,dc} C_{O_{buck}}} \end{aligned} \right\} \quad (14.65)$$

In the above equation, the quantities in capital letters, V_{in} , $V_{O_{buck}}$, I_L , I_o , and D are the average values. The quantities with tilde, \tilde{v}_{in} , $\tilde{v}_{O_{buck}}$, \tilde{i}_L , \tilde{i}_o , and \tilde{d} are the perturbations in the respective quantities.

The small-signal state-space model of the DC-DC buck converter can be derived from Eqs. (14.64) and (14.65) as follows:

$$\left. \begin{aligned} \frac{d}{dt} \begin{bmatrix} \tilde{i}_L \\ \tilde{v}_{O_{buck}} \end{bmatrix} &= \begin{bmatrix} 0 & -1/L_{buck} \\ \frac{1}{C_{O_{buck}}} & \frac{-1}{R_{L,dc} C_{O_{buck}}} \end{bmatrix} \begin{bmatrix} \tilde{i}_L \\ \tilde{v}_{O_{buck}} \end{bmatrix} + \begin{bmatrix} \frac{D}{L_{buck}} \\ 0 \end{bmatrix} \tilde{v}_{in} + \begin{bmatrix} \frac{V_{in}}{L_{buck}} \\ 0 \end{bmatrix} \tilde{d} \\ \text{and, output } (Y) &= [\tilde{v}_{O_{buck}}] = \begin{bmatrix} 0 & 1 \end{bmatrix} \begin{bmatrix} \tilde{i}_L \\ \tilde{v}_{O_{buck}} \end{bmatrix} \end{aligned} \right\} \quad (14.66)$$

The control transfer function, $G_{C_{buck}}(s)$, and disturbance transfer function, $G_{D_{ibuck}}(s)$, of the DC-DC buck converter have been derived from Eq. (14.66) as follows:

$$G_{C_{buck}}(s) = \left. \frac{\tilde{v}_{O_{buck}}(s)}{\tilde{d}(s)} \right|_{\tilde{v}_{in}=0} = \frac{V_{in}}{L_{buck} C_{O_{buck}} s^2 + (L_{buck}/R_{L,dc})s + 1} \quad (14.67)$$

$$G_{D_{ibuck}}(s) = \left. \frac{\tilde{v}_{O_{buck}}(s)}{\tilde{v}_{in}(s)} \right|_{\tilde{d}=0} = \frac{D}{L_{buck} C_{O_{buck}} s^2 + (L_{buck}/R_{L,dc})s + 1} \quad (14.68)$$

14.3.4.4 DC-DC Boost Converter

The voltage generated by the SPV system varies with the weather conditions, which is lower than the DCMG voltage. The output voltage of the SOFC DG varies with the load variation. Therefore, DC-DC boost converters have been used to integrate

the SPV and SOFC DGs to the DCMG, as shown in Fig. 14.1. The DC-DC boost converter is aimed to (1) boost the low generated voltage of the DG up to a constant DC voltage equal to the DCMG voltage and (2) maintain the power balance in the DCMG by controlling the load current, depending on the capacity of the SOFC DG. The topology of a DC-DC boost converter is shown in Fig. 14.12b. The inductor voltage and current waveforms for a DC-DC boost converter are shown in Fig. 14.14. Under steady state, the average inductor voltage and average capacitor current over one time period must be zero.

The relation between input voltage/current and output voltage/current has been derived as follows:

$$V_{\text{boost}} = V_{\text{in}} / (1 - D) \quad \text{and} \quad I_o = I_L (1 - D) \tag{14.69}$$

where V_{in} ($=V_{\text{PV}}$ or $V_{\text{FC,stack}}$) is the input DC voltage of the DC-DC boost converter, V_{boost} is the average output voltage of the DC-DC boost converter, and L_{boost} and C_{boost} are the inductor and output capacitor of the DC-DC boost converter, respectively.

The expressions for the average inductor voltage and capacitor current have been determined as follows:

$$\left. \begin{aligned} \frac{d}{dt} \langle i_L \rangle &= \frac{\langle v_{\text{in}} \rangle}{L_{\text{boost}}} - \frac{\langle v_{\text{boost}} (1 - d) \rangle}{L_{\text{boost}}} \quad \text{and} \\ \frac{d}{dt} \langle v_{\text{boost}} \rangle &= \frac{\langle i_L (1 - d) \rangle}{C_{\text{boost}}} - \frac{\langle v_{\text{boost}} \rangle}{R_{\text{L,dc}} C_{\text{boost}}} \end{aligned} \right\} \tag{14.70}$$

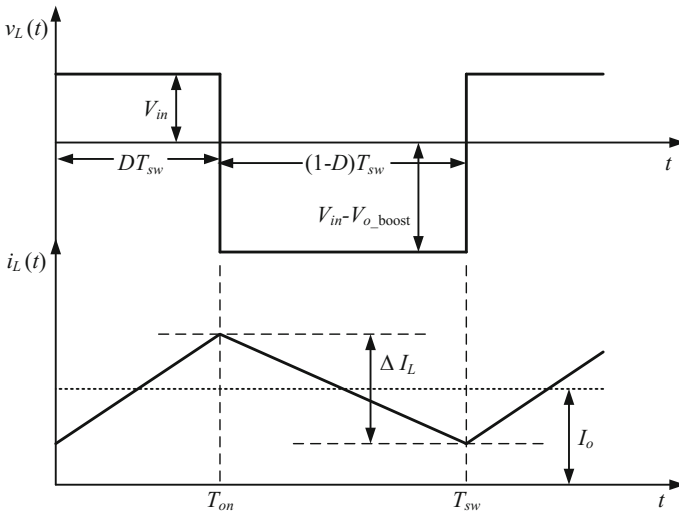


Fig. 14.14 Inductor voltage and inductor current waveforms of a DC-DC boost converter

$$\text{or } \frac{d}{dt} I_L = \frac{V_{in}}{L_{boost}} - \frac{V_{Oboost}(1-D)}{L_{boost}} \quad \text{and} \quad \frac{d}{dt} V_{Oboost} = \frac{I_L(1-D)}{C_{Oboost}} - \frac{V_{Oboost}}{R_{L,dc}C_{Oboost}} \quad (14.71)$$

Considering small perturbations in the various quantities, Eq. (14.70) can be expressed as follows:

$$\left. \begin{aligned} \frac{d}{dt} \langle I_L + \tilde{i}_L \rangle &= \frac{\langle V_{in} + \tilde{v}_{in} \rangle}{L_{boost}} - \frac{\langle (V_{Oboost} + \tilde{v}_{Oboost})(1 - (D + d)) \rangle}{L_{boost}} \\ \frac{d}{dt} \langle V_{Oboost} + \tilde{v}_{Oboost} \rangle &= \frac{\langle (I_L + \tilde{i}_L)(1 - (D + d)) \rangle}{C_{Oboost}} - \frac{\langle V_{Oboost} + \tilde{v}_{Oboost} \rangle}{R_{L,dc}C_{Oboost}} \end{aligned} \right\} \quad (14.72)$$

In the above equation, the quantities in capital letters, V_{in} , V_{Oboost} , I_L , I_o , and D , are the average values. The quantities with tilde, \tilde{v}_{in} , \tilde{v}_{Oboost} , \tilde{i}_L , \tilde{i}_o , and \tilde{d} , are the perturbations in the respective quantities.

The small-signal state-space model of the DC-DC boost converter can be derived from Eqs. (14.71) and (14.72) as follows:

$$\left. \begin{aligned} \frac{d}{dt} \begin{bmatrix} \tilde{i}_L \\ \tilde{v}_{Oboost} \end{bmatrix} &= \begin{bmatrix} 0 & \frac{-(1-D)}{L_{boost}} \\ \frac{(1-D)}{C_{Oboost}} & \frac{-1}{R_{L,dc}C_{Oboost}} \end{bmatrix} \begin{bmatrix} \tilde{i}_L \\ \tilde{v}_{Oboost} \end{bmatrix} + \begin{bmatrix} \frac{1}{L_{boost}} \\ 0 \end{bmatrix} \tilde{v}_{in} + \begin{bmatrix} \frac{V_{Oboost}}{L_{boost}} \\ \frac{-I_L}{C_{Oboost}} \end{bmatrix} \tilde{d} \\ \text{and, output } (Y) &= [\tilde{v}_{Oboost}] = [0 \quad 1] \begin{bmatrix} \tilde{i}_L \\ \tilde{v}_{Oboost} \end{bmatrix} \end{aligned} \right\} \quad (14.73)$$

The control transfer function, $G_{C_{boost}}(s)$, and disturbance transfer function, $G_{D_{i_{boost}}}(s)$, of the DC-DC boost converter can be derived from Eq. (14.73) as follows:

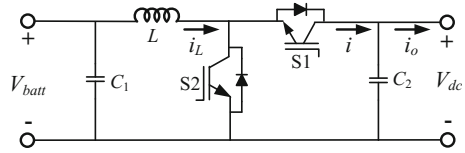
$$G_{C_{boost}}(s) = \left. \frac{\tilde{v}_{Oboost}(s)}{\tilde{d}(s)} \right|_{\tilde{v}_{in}=0} = \frac{(1-D)V_{Oboost} - sL_{boost}I_L}{L_{boost}C_{Oboost}s^2 + (L_{boost}/R_{L,dc})s + (1-D)^2} \quad (14.74)$$

$$G_{D_{i_{boost}}}(s) = \left. \frac{\tilde{v}_{Oboost}(s)}{\tilde{v}_{in}(s)} \right|_{\tilde{d}=0} = \frac{(1-D)}{L_{boost}C_{Oboost}s^2 + (L_{boost}/R_{L,dc})s + (1-D)^2} \quad (14.75)$$

14.3.4.5 Bidirectional DC-DC Converter

The bidirectional DC-DC converter (BDC) is aimed at controlling the bidirectional power flow between the two DC systems. The BDC has been used to integrate the BESS to the DCMG for controlling the charging and discharging of the BESS during the power mismatch at the DCMG. The topology of the BDC is shown in Fig. 14.15.

Fig. 14.15 Topology of bidirectional DC-DC converter



The BDC charges the BESS in the buck mode and discharges it in the boost mode operation. The terminal voltage (V_{batt}) of the battery (with internal resistance R_1) has been considered less than the DCMG voltage. The expressions for the average inductor voltage and average capacitor current of the BDC (for buck mode, i.e. charging mode of the BESS) are derived as follows:

$$\frac{d}{dt} \langle i_L \rangle = -\frac{R_1 \langle i_L \rangle}{L} + \frac{\langle v_{\text{dc}} d \rangle}{L} - \frac{\langle v_{\text{batt}} \rangle}{L} \quad \text{and} \quad \frac{d}{dt} \langle v_{\text{batt}} \rangle = \frac{\langle i_L \rangle}{C_1} - \frac{\langle i_o \rangle}{C_1} \quad (14.76)$$

The expressions for the average inductor voltage and average capacitor current of the BDC (for boost mode, i.e. discharging of the BESS) have been derived as follows:

$$\frac{d}{dt} \langle i_L \rangle = -\frac{R_1 \langle i_L \rangle}{L} - \frac{\langle v_{\text{dc}} (1-d) \rangle}{L} + \frac{\langle v_{\text{batt}} \rangle}{L} \quad \text{and} \quad \frac{d}{dt} \langle v_{\text{dc}} \rangle = \frac{\langle i_L (1-d) \rangle}{C_2} - \frac{\langle i_o \rangle}{C_2} \quad (14.77)$$

Considering small perturbations in various quantities as $v_{\text{batt}} = V_{\text{batt}} + \tilde{v}_{\text{batt}}$, $v_{\text{dc}} = V_{\text{dc}} + \tilde{v}_{\text{dc}}$, $i_L = I_L + \tilde{i}_L$, $i_o = I_o + \tilde{i}_o$, and $d = D + \tilde{d}$, the small-signal state-space model of the BDC for the both buck and the boost mode can be derived as given by Eqs. (14.78) and (14.79), respectively:

$$\left. \begin{aligned} \frac{d}{dt} \begin{bmatrix} \tilde{i}_L \\ \tilde{v}_{\text{batt}} \end{bmatrix} &= \begin{bmatrix} -R_1/L & -1/L \\ 1/C_1 & 0 \end{bmatrix} \begin{bmatrix} \tilde{i}_L \\ \tilde{v}_{\text{batt}} \end{bmatrix} + \begin{bmatrix} V_{\text{dc}}/L \\ 0 \end{bmatrix} \tilde{d} + \begin{bmatrix} D/L \\ 0 \end{bmatrix} \tilde{v}_{\text{dc}} + \begin{bmatrix} 0 \\ -1/C_1 \end{bmatrix} \tilde{i}_o \\ \text{and, output } (Y) &= \begin{bmatrix} \tilde{i}_L \\ \tilde{v}_{\text{batt}} \\ \tilde{i}_o \end{bmatrix} = \begin{bmatrix} 1 & 0 \\ 0 & 1 \\ 1 & 0 \end{bmatrix} \begin{bmatrix} \tilde{i}_L \\ \tilde{v}_{\text{batt}} \end{bmatrix} \end{aligned} \right\} \quad (14.78)$$

$$\left. \begin{aligned} \frac{d}{dt} \begin{bmatrix} \tilde{i}_L \\ \tilde{v}_{\text{dc}} \end{bmatrix} &= \begin{bmatrix} -R_1/L & \frac{-(1-D)}{L} \\ \frac{(1-D)}{C_2} & 0 \end{bmatrix} \begin{bmatrix} \tilde{i}_L \\ \tilde{v}_{\text{dc}} \end{bmatrix} + \begin{bmatrix} \frac{-V_{\text{dc}}}{L} \\ \frac{-I_L}{C_2} \end{bmatrix} \tilde{d} + \begin{bmatrix} 1/L \\ 0 \end{bmatrix} \tilde{v}_{\text{batt}} + \begin{bmatrix} 0 \\ \frac{-1}{C_2} \end{bmatrix} \tilde{i}_o \\ \text{and, output } (Y) &= \begin{bmatrix} \tilde{i}_L \\ \tilde{v}_{\text{dc}} \\ \tilde{i}_o \end{bmatrix} = \begin{bmatrix} 1 & 0 \\ 0 & 1 \\ (1-D) & 0 \end{bmatrix} \begin{bmatrix} \tilde{i}_L \\ \tilde{v}_{\text{dc}} \end{bmatrix} + \begin{bmatrix} 0 \\ 0 \\ -I_L \end{bmatrix} \tilde{d} \end{aligned} \right\} \quad (14.79)$$

14.4 Design of VSC Components

Nowadays, the PWM-based voltage source converters (VSCs) are being widely used for interfacing various DGs, ESSs, and loads to the microgrids, because of their several benefits offered by them [1, 7]. The design of various components of the PWM VSCs is presented in the following subsections.

14.4.1 DC Link Capacitor for VSC

A DC link capacitor is usually connected across the DC terminal of the VSC in order to achieve a stiff DC voltage source and a reduced voltage ripple on the DC side. The size of the DC side capacitor depends on the DC voltage of the VSC. The design of the DC side capacitor is an important part for the design of a DCMG system.

For proper operation of the PWM VSC, a minimum DC link voltage is required. The relation between the voltage at DC terminals and AC terminals of the three-phase VSC can be determined as follows [1, 30]:

$$V_{dc} = \left(2\sqrt{2}/\sqrt{3}\right) \cdot \frac{V_{ll,rms}}{m} \quad (14.80)$$

where V_{dc} is the voltage at the DC terminal of the three-phase VSC (V), $V_{ll,rms}$ is the rms value of the line–line voltage at AC terminals of the three-phase VSC (V), and m is the modulation index.

The magnitude of the ripple in the DC voltage depends on the DC link capacitor size and switching frequency. The transient voltage variation constraint should be considered, when the size of the DC capacitor is to be selected. The DC link capacitor is expressed as follows:

$$C_{dc} \geq \left(P_{n,conv} / \left(2\sqrt{3} \cdot \omega_1 \cdot V_{dc} \cdot \Delta V_{dc} \right) \right) \quad (14.81)$$

where $P_{n,conv}$ is the nominal power rating of the three-phase VSC (W), ΔV_{dc} ($\approx 5\%$ of V_{dc}) is the maximum DC voltage variation/ripple due to load change during a period of the AC supply (V), ω_1 ($=2\pi f_1$) is the fundamental angular frequency (rad/s), and f_1 is the fundamental frequency of AC supply (Hz).

14.4.2 Phase Reactors for Three-Phase VSR

The phase reactor is connected between the three-phase VSR and AC system. The phase reactors have been used for controlling both the active power and the reactive power flow by regulating the currents through them. The phase reactors work also

as AC filters to reduce the high-frequency harmonic contents of AC currents, which are caused by switching operation of the VSR. The phase reactors usually have about 0.15 pu impedance. The 0.15 pu phase reactor permits the VSC output voltage to shift in phase and amplitude with respect to the AC system point of common coupling [1, 31]. The phase reactors and the resistance of the phase reactors can be designed as follows:

$$X_{Ph} = 0.15 \frac{V_n^2}{P_{n,conv}}, \quad L_{Ph} = \frac{X_{Ph}}{\omega}, \quad \text{and} \quad R_{L_{Ph}} = 1\% \text{ of Phase-Reactance} = \frac{X_{Ph}}{100} \quad (14.82)$$

where V_n is the nominal line-to-line rms voltage of three-phase VSC (V), X_{Ph} is the reactance of the phase reactors (Ω), L_{Ph} is the inductance of the phase reactors (H), and $R_{L_{Ph}}$ is the resistance of the phase-inductors (Ω).

14.4.3 LC and LCL Filters for VSI

The line filter reduces the high-frequency harmonic contents from the output of the three-phase as well as single-phase inverters caused by the switching operation of the inverters. Hence, the sinusoidal line currents are obtained. Usually, the line filter consists of L filter, LC filter, and LCL filter. The filtering stage is included between the inverter and the load.

The LC filter of second order is a better choice, which has higher attenuation at any given frequency as compared to the first-order filter (L filter) of the same bandwidth. The single-phase LC filter is shown in Fig. 14.11, and its transfer function can be derived as follows:

$$G(s) = \frac{V_a(s)}{V_{inv}(s)} = \frac{1}{L_f C_f s^2 + R_{L_f} C_f s + 1} \quad (14.83)$$

By comparing this typical second-order transfer function with the standard second-order transfer function, one obtains the following:

$$\left. \begin{array}{l} \text{the corner frequency, } \omega_o = 1/\sqrt{L_f C_f} \quad \text{or} \quad f_o = 1/(2\pi\sqrt{L_f C_f}) \\ \text{and, the resonant peak magnitude, } Q = (1/R_{L_f})\sqrt{L_f/C_f} \end{array} \right\} \quad (14.84)$$

Sufficient attenuation has to be provided for switching frequency components and for higher frequencies. For this purpose, the filter is designed to provide a minimum attenuation of 30 dB or more for frequencies above switching frequency. From the transfer function of the LC filter, it is observed that the gain of the LC filter starts decreasing from the corner frequency at the rate of 40 dB/decade, and it is required to maintain the minimum gain of -30 dB at switching frequency. This

sets the criteria for the selection of the corner frequency, according to the attenuation requirement.

The LC filter is tuned below the switching frequency as follows:

$$(1/\omega_o) \geq (1/2\pi F_{sw}) \quad \text{or} \quad \sqrt{L_f C_f} \geq (1/2\pi F_{sw}) \quad (14.85)$$

For the switching frequency, $F_{sw} = 5$ kHz, considering the attenuation of 30 dB, the LC filter has been designed as follows:

$$30 = 40 \log\left(\frac{2\pi F_{sw}}{\omega_o}\right) \quad (14.86)$$

To avoid the low power factor, the reactive power caused by the filter capacitor for both the LC and the LCL filter should be less than 5% of the rated active power [26] and is expressed as follows:

$$C_f < \left(0.05 P_{n,Ph} / 2\pi f_1 V_{n,Ph}^2\right) \quad (14.87)$$

where $V_{n,Ph}$ is the nominal output phase voltage of the VSI and $P_{n,Ph}$ is the nominal rated power per phase of the VSI.

From Eqs. (14.84) to (14.87), the parameters of the LC filter have been designed for three-phase and single-phase VSI.

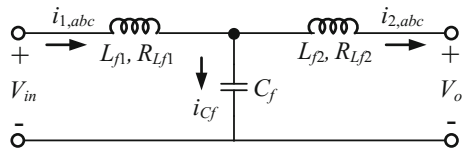
A third-order LCL filter for single-phase is shown in Fig. 14.16, which has certain advantages such as low output current distortion and reactive power production, and attenuation of 60 dB/decade for frequencies over the resonance frequency. For the given LCL filter, the resonance frequency (ω_{res}) has been derived within a specified range as follows [1, 26]:

$$\left. \begin{aligned} \omega_{res} &= \sqrt{(L_{f1} + L_{f2}) / L_{f1} L_{f2} C_f}, \quad f_{res} = 1 / (2\pi \omega_{res}) \\ \text{and, } 10f_s &< f_{res} < 0.5F_{sw} \end{aligned} \right\} \quad (14.88)$$

Several characteristics must be considered in the design of an LCL filter, such as current ripple, filter size, and switching ripple attenuation. The maximum current ripple at the output of the VSI is derived as follows:

$$\Delta I_1 = \frac{2V_{dc}}{3F_{sw}L_{f1}}(1 - m) \cdot m \quad (14.89)$$

Fig. 14.16 Configuration of single-phase LCL filter for the VSI



For a typical SPWM VSI, the maximum peak-to-peak ripple current can be obtained at $m = 0.5$, and then

$$\Delta I_{1,\max} = \frac{V_{dc}}{6F_{sw}L_{f1}}, \quad \text{where} \quad \Delta I_{1,\max} = 0.1I_{1,\max} \quad \text{and} \quad L_{f2} + L_g = 2L_{f1} \quad (14.90)$$

where $\Delta I_{1,\max}$ is the maximum peak-to-peak ripple current, L_g is the utility grid inductor under grid-connected mode, and R_{L_f} the resistance of the filter inductor, which is taken as 1% of the filter reactance.

14.4.4 Components of DC-DC Buck Converter

The continuous conduction mode (CCM) has been considered to design the parameters of various components of the DC-DC converters.

The relation between the peak-to-peak ripple inductor current and the inductor of the DC-DC buck converter, as shown in Fig. 14.12a, can be written as follows:

$$\left. \begin{aligned} \Delta I_L &= \frac{(V_{in} - V_{obuck})D}{F_{sw}L_{buck}} = \frac{V_{in}D(1-D)}{F_{sw}L_{buck}}, \quad \text{where} \quad \Delta I_L \leq 0.1I_L \\ \text{and, } L_{buck} &\geq \frac{10V_{in}D(1-D)}{F_{sw}I_L} \quad \text{or} \quad L_{buck} \geq \frac{10(1-D)V_{obuck}}{F_{sw}I_o}, \quad \frac{V_{obuck}}{I_o} = R_{L,dc} \end{aligned} \right\} \quad (14.91)$$

For the CCM operation of the DC-DC buck converter, the critical inductance ($L_{buck,crit}$) is expressed as follows:

$$\left. \begin{aligned} (1-D) &\leq \frac{2L_{buck}F_{sw}}{R_{L,dc}} \quad \text{or} \quad L_{buck} \geq \frac{(1-D)V_{obuck}}{2F_{sw}I_o} \\ L_{buck,crit} &= \frac{D(1-D)V_{in}}{2F_{sw}I_{L,\max}}, \quad \text{where} \quad I_{L,\max} = I_{o,\max} \quad \text{and} \quad L_{buck} < L_{buck,crit} \end{aligned} \right\} \quad (14.92)$$

The expression for output capacitor and input capacitor of the DC-DC buck converter can be derived as follows:

$$\left. \begin{aligned} C_{obuck} &= \frac{DV_{obuck}}{\Delta V_{obuck}F_{sw}R_{L,dc}}, \quad \text{For} \quad \frac{\Delta V_{obuck}}{V_{obuck}} \leq 1\% \quad \text{and} \quad \frac{\Delta V_{in}}{V_{in}} \leq 1\% \\ \text{Therefore, } C_{obuck} &\geq \frac{100D}{F_{sw}R_{L,dc}} \quad \text{and} \quad C_{inbuck} \geq \frac{1}{8} \left(\frac{\Delta I_L}{\Delta V_{in}F_{sw}} \right) \end{aligned} \right\} \quad (14.93)$$

14.4.5 Components of DC-DC Boost Converter

The parameters for various components of the DC-DC boost converter, as shown in Fig. 14.12b, are designed in CCM. The relation between the peak-to-peak ripple inductor current and the inductor can be written as follows:

$$\left. \begin{aligned} \Delta I_L &= \frac{DV_{in}}{F_{sw}L_{boost}} = \frac{D(1-D)^2 I_L V_{boost}}{F_{sw}L_{boost}I_o}, \quad \text{where } \Delta I_L \leq 0.1I_L \\ \text{Therefore, } L_{boost} &\geq \frac{10D(1-D)^2 V_{boost}}{F_{sw}I_o} \quad \text{and} \quad \frac{V_{boost}}{I_o} = R_{L,dc} \end{aligned} \right\} \quad (14.94)$$

For the CCM operation of the DC-DC boost converter, it can be derived as follows:

$$(1-D) \leq \sqrt{2L_{boost}F_{sw}/DR_{L,dc}} \quad \text{or} \quad L_{boost} \geq \left(D(1-D)^2 V_{O_{buck}} / 2F_{sw}I_o \right) \quad (14.95)$$

The expressions for the output capacitor and input capacitor of the DC-DC boost converter are given as follows:

$$\left. \begin{aligned} C_{O_{boost}} &= \frac{DI_o}{\Delta V_{O_{boost}} F_{sw}} = \frac{DV_{O_{boost}}}{\Delta V_{O_{boost}} F_{sw} R_{L,dc}}, \quad \text{where } \frac{\Delta V_{O_{buck}}}{V_{O_{buck}}} \leq 1\% \\ \text{Therefore, } C_{O_{boost}} &\geq \frac{100D}{F_{sw}R_{L,dc}} \quad \text{and} \quad C_{in_{boost}} \geq \frac{1}{8} \left(\frac{\Delta I_L}{\Delta V_{in} F_{sw}} \right), \quad \frac{\Delta V_{in}}{V_{in}} \leq 1\% \end{aligned} \right\} \quad (14.96)$$

14.5 Proposed Control Strategy of Bidirectional Three-Phase VSC for WT DG Integration

Various control strategies of three-phase VSR for integration of the wind turbine generator (WTG) to the DCMG/DC grid system are proposed in the literature [28, 29, 32, 33], which are mainly aimed at controlling and transferring the power only from the WT DG to the DCMG/DC grid system and not in the reverse direction. In the proposed DCMG, the WTG is integrated with the DCMG through the bidirectional three-phase VSC, since a three-phase load in the local area of the WTG has been considered, as shown in Fig. 14.1. The WTG supplies the power to the load, and the excess power generation by WTG is transmitted to DCMG through bidirectional three-phase VSC and DC cable.

A control strategy of the bidirectional three-phase VSC has been proposed, as shown in Fig. 14.17, which allows to control the power flow from the WTG to the DCMG and from the DCMG to the load in the local area of the WTG, to meet this

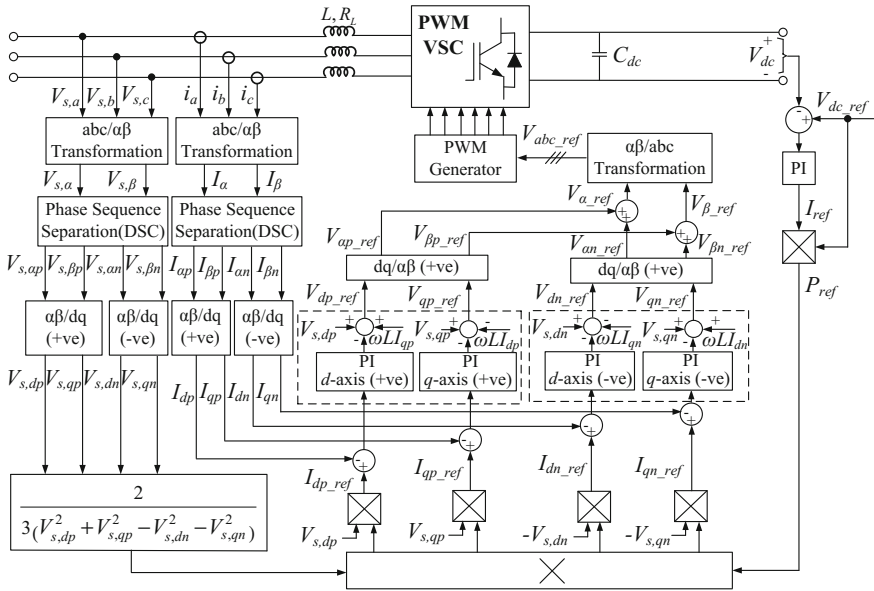


Fig. 14.17 Proposed control strategy of a bidirectional three-phase VSC

load demand under zero power generation or less power generation by the WTG. The proposed control strategy of the three-phase bidirectional VSC is also designed to maintain the constant DC voltage of the microgrid and mitigate the effects on the voltage under unbalanced condition.

The proposed control strategy, using a combination of feedback and two feed-forward (both AC voltage and current loops) control loops, with dual PI controllers, has been implemented into two rotating d - q SRFs, viz. positive SRF and negative SRF, for controlling the positive- and negative-sequence current components in its own SRF, independently, as shown in Fig. 14.17. In this control scheme, the three-phase voltages and currents are sensed and transformed from three-phase (abc) stationary reference frame into two-phase (α - β) stationary reference frame using Clark transformation. A delayed signal cancellation method has been used for the separation of the positive- and negative-sequence components of the voltage/current in two-phase (α - β) stationary reference frame. The positive and negative sequences of the voltages and currents are transformed from two-phase (α - β) stationary reference frame into two-phase (d - q) rotating SRF using Park’s transformation.

The voltage on the DC side terminals of the bidirectional three-phase VSC is measured and compared with its reference value, i.e. 750 V DCMG voltage. This voltage error is sent to the PI controller, which generates a reference current (I_{ref}) or a reference power signal (P_{ref}). This controlled reference power signal has been used as a feedback control signal in rectifier mode and as a feed-forward control signal in inverter mode in the proposed control strategy, as shown in Fig. 14.17.

With the help of the positive- and negative-sequence d - q components of the voltages and the controlled reference power signal, generated by the DC voltage controller, the positive- and negative-sequence reference currents ($I_{dq,pn,ref}$) have been determined for both positive- and negative-sequence current controllers. The positive- and negative-sequence d - q components of the measured three-phase currents have been compared with these generated reference currents, and the errors are controlled by the PI controllers, independently, in its own SRF. The PI current controllers provide the controlled reference positive- and negative-sequence voltages ($V_{dq,pn,ref}$), which have been transformed into two-phase (α - β) stationary reference frame by using inverse Park's transformation. By adding the α -axis positive- and negative-sequence reference voltage components, the α -axis controlled reference voltage ($V_{\alpha,ref}$) has been obtained. Similarly, the β -axis controlled reference voltage ($V_{\beta,ref}$) has been obtained by adding the β -axis positive- and negative-sequence reference voltage components. These α -axis and β -axis controlled reference voltages ($V_{\alpha,ref}$ and $V_{\beta,ref}$) have been transformed into three-phase (abc) stationary reference frame by using inverse Clark transformation, which provides three-phase controlled reference voltage ($V_{abc,ref}$). The three-phase controlled reference voltage is sent to the PWM generator to provide the controlled gate pulses for the three-phase VSC, as shown in Fig. 14.17. By using the feed-forward control loop signals, the effect of cross-coupling is cancelled, and hence, two independent controllers have been used to control the d -axis and the q -axis current components of each sequence, separately.

The modelling of the three-phase VSC under unbalanced conditions is given by Eqs. (14.42) and (14.43). Based on the model of the VSC, dynamics of the VSC can be visualized as two decoupled subsystems: the positive- and the negative-sequence subsystems. Each subsystem has been controlled independently, in its own SRF, in the proposed control strategy. The equations of the controlled reference positive- and negative-sequence voltages for the inner current controllers with cross-coupling between two (d and q) axes are derived as follows:

$$\left. \begin{aligned} V_{dp,ref} &= V_{s,dp} - (I_{dp,ref} - I_{dp}) \left(K_{PcVSC}^+ + \frac{K_{IcVSC}^+}{s} \right) + \omega LI_{qp} \\ V_{qp,ref} &= V_{s,qp} - (I_{qp,ref} - I_{qp}) \left(K_{PcVSC}^+ + \frac{K_{IcVSC}^+}{s} \right) - \omega LI_{dp} \\ V_{dn,ref} &= V_{s,dn} - (I_{dn,ref} - I_{dn}) \left(K_{PcVSC}^- + \frac{K_{IcVSC}^-}{s} \right) - \omega LI_{qn} \\ V_{qn,ref} &= V_{s,qn} - (I_{qn,ref} - I_{qn}) \left(K_{PcVSC}^- + \frac{K_{IcVSC}^-}{s} \right) + \omega LI_{dn} \end{aligned} \right\} \quad (14.97)$$

where K_{PcVSC}^+ and K_{IcVSC}^+ are the proportional and integral gains of the PI controllers for the positive-sequence current components, and K_{PcVSC}^- and K_{IcVSC}^- are the

Table 14.1 Parameters of dual PI controllers for bidirectional three-phase VSC

PI controllers	Proportional gain (K_P)	Integral gain (K_I)
Inner current controllers	$K_{P_{cvsc}}^+ = 1.5,$ $K_{P_{cvsc}}^- = 1.328$	$K_{I_{cvsc}}^+ = 9.4 \text{ s}^{-1},$ $K_{I_{cvsc}}^- = 8.83 \text{ s}^{-1}$
DC voltage controller	$K_{P_{Vdc}} = 0.0293$	$K_{I_{Vdc}} = 1.63 \text{ s}^{-1}$

proportional and integral gains of the PI controllers for the negative-sequence current components.

The closed-loop transfer function of the current controller and the closed-loop transfer function of the DC voltage controller are expressed as follows [34]:

$$\left. \begin{aligned}
 G_I(s) &= \frac{(K_{P_{cvsc}}/\tau R_L T_a)}{s^2 + (1/T_a)s + (K_{P_{cvsc}}/\tau R_L T_a)}, \quad \text{where } T_a = \frac{1}{2F_{sw}} \quad \text{and } \tau = \frac{L}{R_L} \\
 G_V(s) &= \frac{(1 + \ell^2 T_{sw} s)}{(\ell T_{sw} s + 1)(\ell^2 T_{sw}^2 s^2 + \ell(\ell - 1)T_{sw} s + 1)}, \quad \text{where } T_{sw} = \frac{1}{F_{sw}} = 2T_a
 \end{aligned} \right\} \quad (14.98)$$

where the output voltage of the VSC has been assumed to follow a voltage reference signal with an average delay time (T_a) equal to the half of a switching cycle, ℓ is considered between 2 and 4 in symmetric optimum tuning, F_{sw} ($=5 \text{ kHz}$) is the switching frequency, and T_{sw} ($=200 \text{ }\mu\text{s}$) is the switching cycle.

The parameters of the PI controllers for inner current as well as DC voltage control for the stable closed-loop system of the bidirectional three-phase VSC have been determined by using Bode plot-based technique, which is given in Table 14.1.

14.6 Control Strategies of DC-DC Boost Converters

The control strategy of the DC-DC boost converter, used for the integration of the SPV DG to the DCMG, is shown in Fig. 14.18a. In this control strategy, the measured output voltage of the DC-DC boost converter has been compared with the reference DCMG voltage (V_{dcref}), and this voltage error is sent to the PI voltage controller. The PI controller provides a controlled reference signal, which is compared with the carrier triangular waveform. The compared signal is sent to the PWM generator to provide the controlled duty cycle for the DC-DC boost converter. If the controller of the bidirectional three-phase VSC fails due to any technical reason, DC-DC boost converter controller establishes constant DCMG voltage. The parameters of the PI voltage controller, for the stable closed-loop system of the DC-DC boost converter, are determined by using the controllable transfer function of the DC-DC boost converter as described by Eq. (14.74). The parameters of the PI controller are determined by using Bode plot-based technique and found as $K_{P_{pv}} = 0.00226$ and $K_{I_{pv}} = 0.03627 \text{ s}^{-1}$.

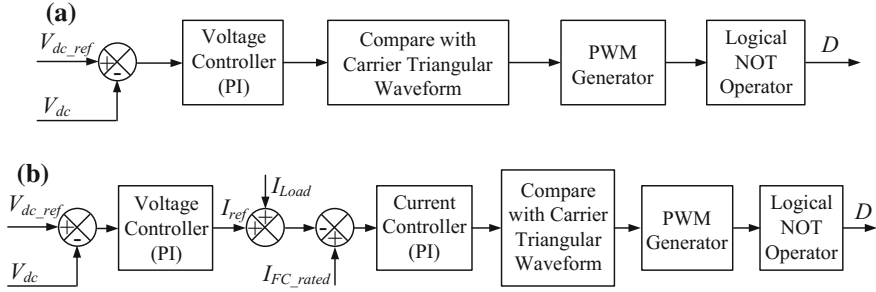


Fig. 14.18 Control strategies of DC-DC boost converter for **a** SPV system and **b** SOFC DG system

The control strategy of the DC-DC boost converter, used for integrating the SOFC DG to the DCMG, is shown in Fig. 14.18b. In this control strategy, the measured output voltage has been compared with the reference DCMG voltage (V_{dc_ref}), and this voltage error is sent to the PI voltage controller, which provides a reference current signal for the PI current controller. The output of the current controller is compared with the carrier triangular waveform. The compared signal is sent to the PWM generator to provide the controlled duty cycle for the DC-DC boost converter. The parameters of the PI controllers for both the voltage and current regulation for the stable closed-loop system are determined by using Bode plot-based technique, which are given as $K_{P_{V_{SOFC}}} = 0.001$, $K_{I_{V_{SOFC}}} = 0.015 \text{ s}^{-1}$, $K_{P_{C_{SOFC}}} = 10$, and $K_{I_{C_{SOFC}}} = 25 \text{ s}^{-1}$.

14.7 Simulation Results Under Islanded Mode

The performance analysis of the proposed DCMG as given in Fig. 14.1, along with the proposed control strategy for integrating the DGs, has been carried out under various operating scenario in islanded mode with and without BESS. Two case studies have been conducted to show the effectiveness of the proposed smart DCMG and the proposed control strategy in MATLAB/Simulink environment. In the simulation, the ratings of the WT, SPV, and SOFC DGs are considered as 600, 100, and 100 kW (with 1.8 times PPC of rated capacity of SOFC), respectively. The parameters used for the various components of the DCMG are taken from [1, 11, 13, 16–18]. The BESS, using VRLA battery, has the ability to supply the load of 250 kW for 4 h, and storage capacity of the BESS is 2.7 kWh with the voltage as 375 V.

14.7.1 Case 1: Variable Power Generation and Constant Load Without BESS

In this mode, the power generations by the WTG at varying wind speed, by SPV following SI and temperature, are variable, as shown in Figs. 14.19 and 14.20. Various individual loads connected to the DCMG are as follows: (1) 100 kW three-phase load in the local area of the WTG, (2) 100 kW across the three-phase VSI, (3) 200 kW across the single-phase VCVSI, (4) 150 kW DC load operating at 220 V across DC-DC buck converter, and (5) 150 kW EV load. The total load demand in the DCMG is constant at 700 kW, as given in Fig. 14.21.

Since it is well known that at the wind speed from rated wind speed up to cut-off wind speed, the power generation by the WT DG remains the same as maximum rated power. So, for the wind speed (\geq rated wind speed up to cut-off speed), the

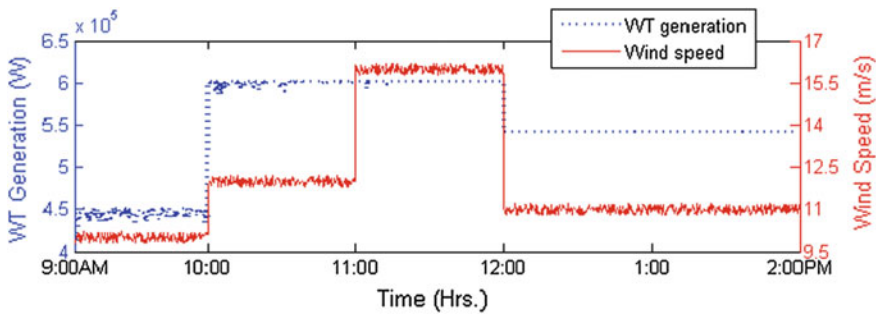


Fig. 14.19 Power generation by WTG with varying wind speed (case 1)

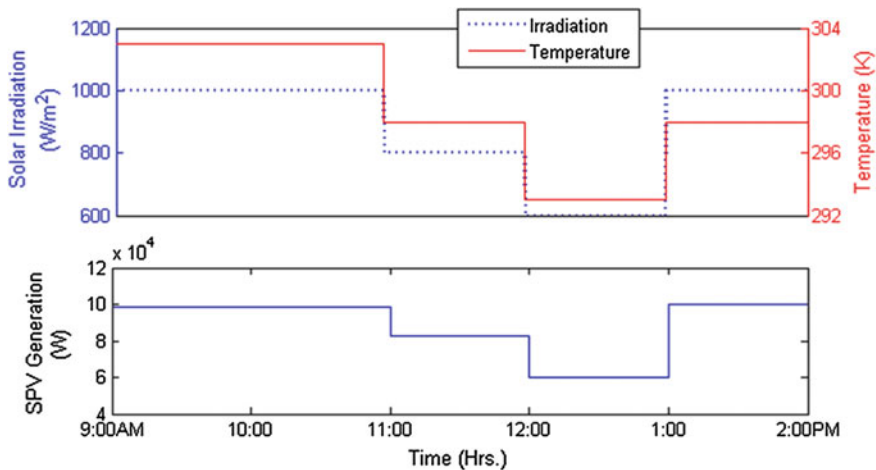


Fig. 14.20 Power generation by SPV with varying SI and temperature (case 1)

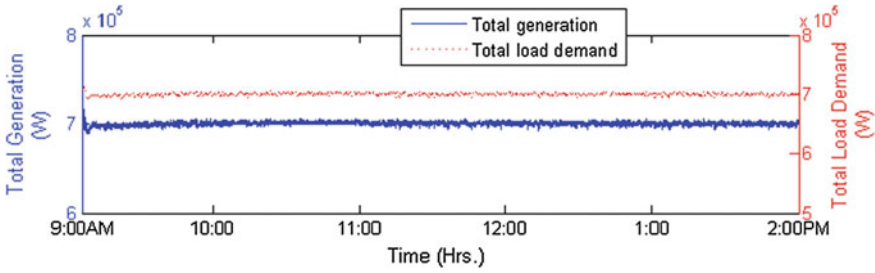


Fig. 14.21 Total power generation and total load demand (case 1)

power generation by WT DG would not be changed, and it will be constant and equal to maximum rated power. Therefore, in Fig. 14.19, at 10:00 h, the power generation by the WT DG at rated wind speed (i.e. 12 m/s) is maximum rated power (i.e. 600 kW). Since, power generation by the WT DG, at the wind speed from rated speed (i.e. 12 m/s) to cut-off speed (i.e. 25 m/s), will be maximum same as rated power (i.e. 600 kW). Therefore, during 10:00–12:00 h, the power generation by WT DG is same and maximum (i.e. 600 kW); however, the wind speed is increasing.

In the simulation, it is assumed that the solar irradiation and temperature are constant for next few hours. Therefore, power generation by SPV is shown constant for next one/two hours, as shown in Fig. 14.20. During 12:00–1:00 PM, solar irradiation is considered lower, and therefore, the SPV output power is less than during other hours. Here, it is considered, because it has also been assumed that solar irradiation may be decreased/increased at any time due to cloudy weather conditions.

The deficit power between the outputs of the WT and SPV DGs and total load demand is fulfilled by the SOFC DG, as shown in Fig. 14.22. The power generation by the SOFC DG varies according to the variation in the outputs of the WT and SPV DGs. As shown in Figs. 14.19, 14.20, 14.21 and 14.22, initially, WTG output

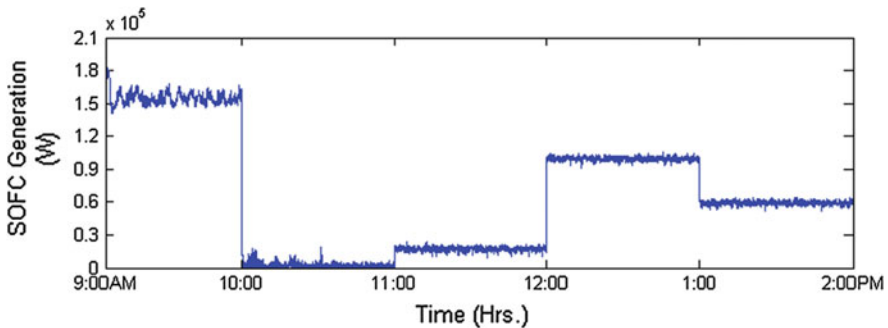


Fig. 14.22 Power generation by SOFC to meet the load demand (case 1)

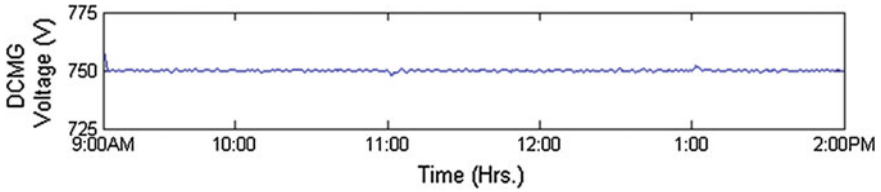


Fig. 14.23 DC voltage of the microgrid (case 1)

is 450 kW, SPV generation is 100 kW, and SOFC DG generates 150 kW to meet the load demand. At 10:00AM, the WT generation increases from 450 to 600 kW, SPV output remains the same, and then, SOFC generation is reduced to zero. From rated wind speed (12 m/s) to cut-off speed (25 m/s), the WT generation remains the same and maximum (600 kW), as given in Fig. 14.19, during 10:00AM–12:00Noon. At 11:00AM, the SPV output reduces from 100 to 83 kW, and then, SOFC generation is increased from zero to 17 kW, and so on. Thus, the deficit power between the total load demand and the outputs of WT and SPV DGs has been fulfilled by varying the generation of the SOFC DG, as in Fig. 14.22, within the PPC limit of the SOFC DG, as shown in Fig. 14.21. The DCMG voltage has also been established constant, as shown in Fig. 14.23.

14.7.2 Case 2: Variable Generation and Variable Load with BESS

In this case, the BESS is connected to the DCMG through a bidirectional DC-DC converter for controlling its charging and discharging during the power mismatch at the DCMG. The power generations by the WTG at varying wind speed and by the SPV system following the SI and temperature are variable, during 24 h in a day, as shown in Figs. 14.24 and 14.25. The total rated load of the DCMG has been considered as 500 kW. All individual loads are connected to the DCMG, and the total load is varied according to the residential load curve [35] for 24 h in a day, as given in Table 14.2.

The rated individual loads are considered as follows: 50 kW three-phase load in the local area of the WTG, 100 kW load across the three-phase VSI, 150 kW load across the single-phase VCVSI, and 100 kW of DC load and EV load each. The power generation by the SOFC DG is also varied according to the load demand variation and the output of the WT and SPV DGs, as shown in Fig. 14.26. Beyond the generation capacity of the SOFC DG, in case of the deficit power in the DCMG, the BESS discharges to meet the load demand. While, in case of surplus power generation by the WT and SPV DGs, the SOFC DG is turned off, and the surplus power is being used to charge the BESS, as shown in Figs. 14.24, 14.25 14.26 and 14.27.

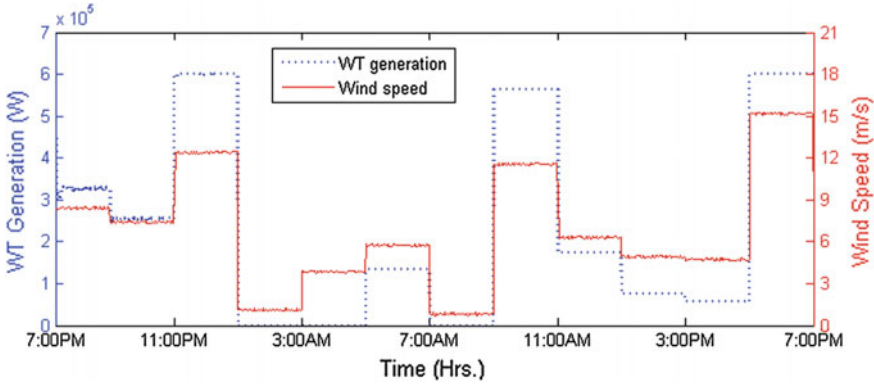


Fig. 14.24 Power generation by WTG according to variable wind speed (case 2)

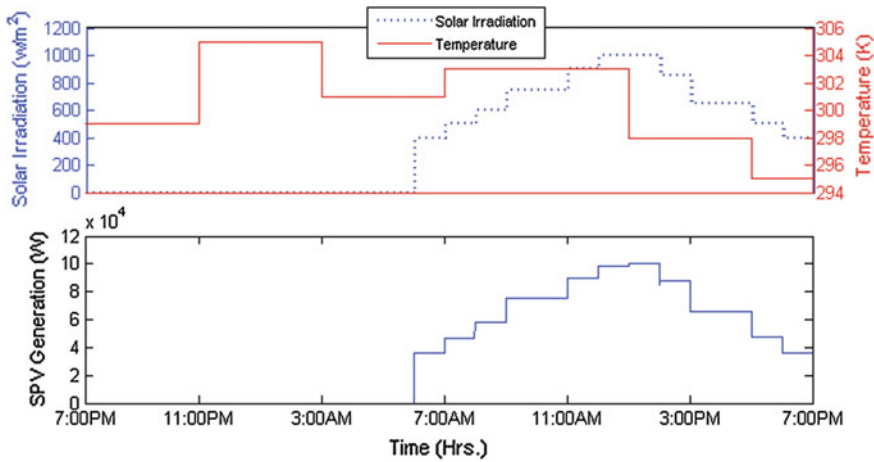


Fig. 14.25 Power generation by SPV following the SI and temperature (case 2)

Table 14.2 Variation of individual loads and total load connected to the DCMG

Time (h)	7:00PM	9:00PM	11:00PM	1:00AM	3:00AM	5:00AM
Load (pu)	1.0	0.85	0.7	0.55	0.47	0.4
Time (h)	7:00AM	9:00AM	11:00AM	1:00PM	3:00PM	5:00PM
Load (pu)	0.6	0.7	0.8	0.85	1.05	1.0

During 7:00PM–11:00PM, 5:00AM–7:00AM, and 11:00AM–1:00PM, the total load demand is more than the power generations by the WT and SPV DGs (as in Figs. 14.24, 14.25 and 14.27); the deficit power is fulfilled by only the SOFC DG generation; no output power from the BESS is used, as shown in Figs. 14.26 and

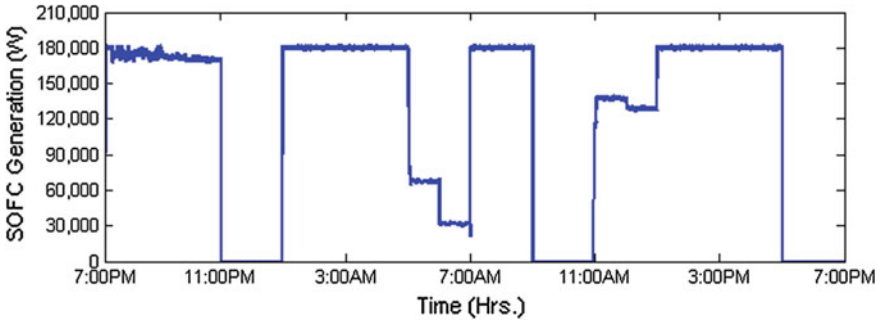


Fig. 14.26 Variable power generation by SOFC DG to meet load demand (case 2)

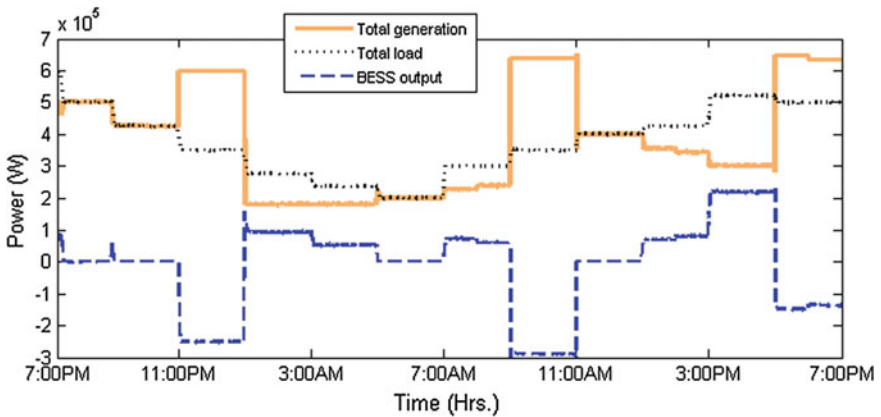


Fig. 14.27 Total generation, total load demand, and BESS output power (case 2)

14.27. During 11:00PM–1:00AM, 9:00AM–11:00AM, and 5:00PM–7:00PM, the power generations by WT and SPV DGs are more than the total load demand in the DCMG, and the surplus power during these periods is being used to charge the BESS, as shown in Figs. 14.24, 14.25 and 14.27. During these periods, no power is generated from the SOFC DG, as shown in Fig. 14.26.

During 1:00AM–5:00AM and 7:00AM–9:00AM, the power generation by WT DG is zero because the wind speed is less than the cut-in speed (i.e. ≤ 4 m/s), as shown in Fig. 14.24. Thus, during 1:00AM–5:00AM, 7:00AM–9:00AM, and 1:00PM–5:00PM, the total power generation by all three DGs connected to the DCMG is less than the total load demand, as shown in Figs. 14.24, 14.25, 14.26 and 14.27. During these periods, the deficit power is fulfilled by discharging the BESS, as shown in Fig. 14.27. The voltage of the DCMG has also been established as almost constant, as shown in Fig. 14.28. The spikes in the DCMG voltage are due to the transients under changing of the power generation as well as the load in each case.

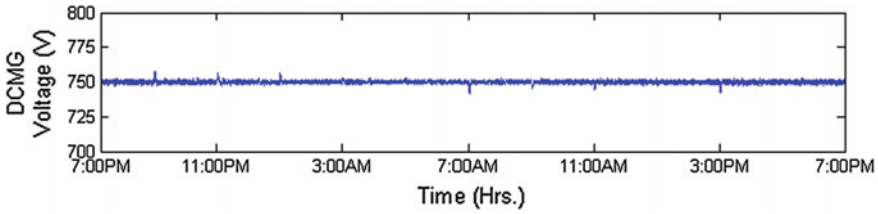


Fig. 14.28 DC voltage of the microgrid (case 2)

During 1:00AM–5:00AM and 7:00AM–9:00AM, the power generation by the WTG is zero, as shown in Fig. 14.24. Three-phase load in the local area of the WTG has been supplied by the power available from other DGs and BESS connected to the DCMG through the bidirectional three-phase VSC, as shown in Figs. 14.24, 14.27 and 14.29. Thus, the proposed control strategy of the bidirectional three-phase VSC gives satisfactory performance under both the rectifier mode and the inverter mode of operation. The current-controlled waveform for the proposed control strategy of the bidirectional three-phase VSC under variable generation and variable load has been obtained from the simulation test for both the rectifier and the inverter modes, as shown in Fig. 14.29.

Thus, from the simulation results, it is observed that the proposed DCMG with autonomous coordinated control maintains its reliability and eliminates the circulating current among the DGs. The proposed DCMG provides the supply to both DC and AC loads simultaneously. The BESS balances the power at DCMG in islanded mode for each case to ensure stability of the DCMG. The proposed DCMG eliminates the need of transformers on load side converters, which results in improving the efficiency of the DCMG system and reducing the cost of the proposed system.

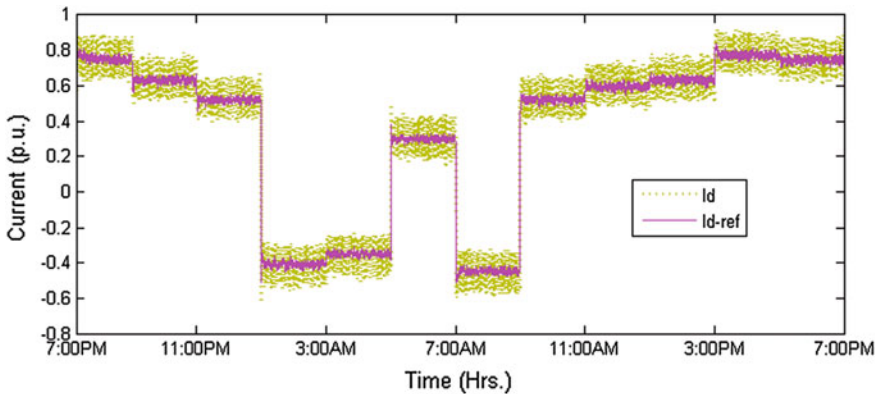


Fig. 14.29 Controlled current signals of bidirectional 3-phase VSC for WTG (case 2)

14.8 Conclusions

The detailed dynamic modelling and design of the various components, such as various DGs, BESS, loads, and their associated converters, of the DCMG has been presented in this chapter. In this chapter, a ring-type DCMG with autonomous coordinated controls has been proposed. A control strategy of the bidirectional three-phase VSC for the integration of the WT DG to the DCMG has also been developed in this chapter. The performance analyses of the proposed DCMG, with the proposed control strategy of the bidirectional three-phase VSC, have been carried out by considering the intermittent nature of the wind speed, solar irradiation, and temperature, under various operating scenarios in islanded mode, with and without BESS. In the proposed DCMG, the power mismatch between the outputs of the WT and SPV DGs and load demand has been fulfilled initially by the SOFC DG by controlling the load current within its PPC limit. Beyond the generation capacity of all the three DGs, the power mismatch in the DCMG is fulfilled by the BESS.

The simulation results demonstrate the effectiveness and robustness of the proposed DCMG with the proposed control strategy of the bidirectional three-phase VSC under different operating conditions, in islanded mode, with and without BESS. It is also observed that the proposed control strategy of the bidirectional three-phase VSC is able to control the bidirectional power flow through the three-phase VSC satisfactorily. The proposed control strategy also maintains constant DCMG voltage under various operating scenarios. The proposed DCMG, with autonomous coordinated control scheme, is found to provide reliable power supply at desired constant DC voltage. The circulating current among the DG units has been suppressed by controlling each DG unit autonomously without communicating with each other, by using only the DCMG voltage as a common reference signal for all the DG units. The DCMG operates satisfactorily for any variable load profile, under the both transient and steady-state conditions. The proposed DCMG is able to supply both the AC and the DC power to the loads simultaneously.

Thus, the proposed DCMG with autonomous coordinated control scheme can offer the opportunity of electrification in the remote rural areas.

References

1. Kumar M (2015) Development of control schemes for power management and operation of DC microgrids. Ph.D. thesis, Electrical Engineering Department, Indian Institute of Technology Kanpur, India
2. Kroposki B, Pink C, DeBlasio R, Thomas H, Simoes M, Sen PK (2010) Benefits of power electronic interfaces for distributed energy systems. *IEEE Trans Energy Convers* 25(3):901–908
3. Wang B, Sechilariu M, Locment F (2012) Intelligent dc microgrid with smart grid communications: control strategy consideration and design. *IEEE Trans Smart Grid* 3(4): 2148–2156

4. Xia Y, Ahmed KH, Williams BW (2013) Wind turbine power coefficient analysis of a new maximum power point tracking technique. *IEEE Trans Ind Electron* 60(3):1122–1132
5. Zhou T, François B (2011) Energy management and power control of a hybrid active wind generator for distributed power generation and grid integration. *IEEE Trans Ind Electron* 58(1):95–104
6. Liu X, Wang P, Loh PC (2011) A hybrid ac/dc microgrid and its coordination control. *IEEE Trans Smart Grid* 2(2):278–286
7. Sood VK (2004) HVDC and FACTS controllers, applications of static converters in power systems. Kluwer Academic Publishers, New York
8. Kumar M, Singh SN, Srivastava SC (2012) Design and control of smart DC microgrid for integration of renewable energy sources. In: Proceedings of IEEE power and energy society general meeting, San Diego, CA, USA, 2012, pp 1–7
9. Khorsandi A, Ashourloo M, Mokhtari H (2014) A decentralized control method for a low-voltage dc microgrid. *IEEE Trans Energy Convers* 29(4):793–801
10. Balog RS, Weaver WW, Krein PT (2012) The load as an energy asset in a distributed dc smart grid architecture. *IEEE Trans Smart Grid* 3(1):253–260
11. Nunes MVA, Lopes JAP, Züim HH, Bezerra UH, Almeida RG (2004) Influence of the variable-speed wind generators in transient stability margin of the conventional generators integrated in electrical grids. *IEEE Trans Energy Convers* 19(4):692–701
12. Bellmunta OG, Liang J, Ekanayake J, Jenkins N (2011) Voltage–current characteristics of multiterminal HVDC-VSC for offshore wind farms. *J Electric Power Syst Res* 81(2):440–450
13. Tapia A, Tapia G, Ostolaza JX, Sáenz JR (2003) Modelling and control of a wind turbine driven doubly fed induction generator. *IEEE Trans Energy Convers* 18(2):194–204
14. Prasad AR, Natarajan E (2006) Optimization of integrated photovoltaic–wind power generation systems with battery storage. *J Energy* 31(12):1943–1954
15. Atwa YM, El-Saadany EF (2011) Probabilistic approach for optimal allocation of wind-based distributed generation in distribution systems. *IET Renew Power Gener* 5(1):79–88
16. Villalva MG, Gazoli JR, Filho ER (2009) Comprehensive approach to modelling and simulation of photovoltaic arrays. *IEEE Trans Power Electron* 24(5):1198–1208
17. Mahmoud YA, Xiao W, Zeineldin HH (2013) A parameterization approach for enhancing PV model accuracy. *IEEE Trans Ind Electron* 60(12):5708–5716
18. Zhu Y, Tomsovic K (2002) Development of models for analyzing the load-following performance of microturbines and fuel cells. *J Electric Power Syst Res* 62(1):1–11
19. Gebregergis A, Pillay P, Bhattacharyya D, Rengaswamy R (2009) Solid oxide fuel cell modelling. *IEEE Trans Ind Electron* 56(1):139–148
20. Durr M, Cruden A, Gair S, McDonald JR (2006) Dynamic model of a lead acid battery for use in a domestic fuel cell system. *J Power Sour* 161(2):1400–1411
21. Shahriari M, Farrokhi M (2013) Online state-of-health estimation of VRLA batteries using state of charge. *IEEE Trans Ind Electron* 60(1):191–202
22. Richardson P, Flynn D, Keane A (2012) Local versus centralized charging strategies for electric vehicles in low voltage distribution systems. *IEEE Trans Smart Grid* 3(2):1020–1028
23. Tani A, Camara MB, Dakyo B (2012) Energy management based on frequency approach for hybrid electric vehicle applications: fuel-cell/lithium-battery and ultracapacitors. *IEEE Trans Veh Technol* 61(8):3375–3386
24. Wan C, Huang M, Tse CK, Wong SC, Ruan X (2013) Nonlinear behavior and instability in a three-phase boost rectifier connected to a nonideal power grid with an interacting load. *IEEE Trans Power Electron* 28(7):3225–3265
25. Houari A, Renaudineau H, Martin JP, Pierfederici S, Tabar FM (2012) Flatness-based control of three-phase inverter with output LC filter. *IEEE Trans Ind Electron* 59(7):2890–2897
26. Reznik A, Simões MG, Al-Durra A, Mueeen SM (2014) LCL filter design and performance analysis for grid interconnected systems. *IEEE Trans Ind Appl* 50(2):1225–1232
27. Svensson J, Bongiorno M, Sannino A (2007) Practical implementation of delayed signal cancellation method for phase-sequence separation. *IEEE Trans Power Del* 22(1):18–26

28. Song H, Nam K (1999) Dual current control scheme for PWM converter under unbalanced input voltage conditions. *IEEE Trans Ind Electron* 46(5):953–959
29. Hu J, He Y (2008) Modelling and control of grid-connected voltage-sourced converters under generalized unbalanced operation conditions. *IEEE Trans Energy Convers* 23(3):903–913
30. Karlsson P, Svensson J (2003) DC bus voltage control for a distributed power system. *IEEE Trans Power Electron* 18(6):1405–1412
31. Khatir M, Zidi SA, Hadjeri S, Fellah MK (2010) Dynamic performance of a back-to-back HVDC station based on voltage source converters. *J Electr Eng* 61(1):29–36
32. Lee DC, Lee GM, Lee KD (2000) DC-bus voltage control of three-phase ac/dc PWM converters using feedback linearization. *IEEE Trans Ind Appl* 36(3):826–833
33. Suh Y, Lipo TA (2006) Control scheme in hybrid synchronous stationary frame for PWM ac/dc converter under generalized unbalanced operating conditions. *IEEE Trans Ind Appl* 42(3):825–835
34. Bajracharya C (2008) Control of VSC-HVDC for wind power. M.S. thesis, Department of Electrical Power Engineering, Norwegian University of Science and Technology, Norway
35. Short TA (2004) *Electric power distribution handbook*. CRC Press, Boca Raton, p 47

Chapter 15

Effects of DG Operating Power Factor on Its Location and Size by Using GA in Distribution Systems

Bindeshwar Singh, R.P. Payasi and Janmejy Sharma

Abbreviations

DG	Distributed generation
DLMs	Different load models
DC	Direct current
AC	Alternating current
DPSN	Distribution power system network
AI	Artificial intelligence
GA	Genetic algorithm
PSO	Particle swarm optimization
PSI	Power stability index
EWG	Embedded wind generation
IEEE	Institute of Electrical and Electronics Engineers
EG	Embedded generation
AIS	Artificial immune system
DE	Differential evolution
CIT	Computational intelligence techniques
ICA	Imperialist competitive algorithm
MW	Megawatt
PV	Photovoltaic
DOE	Department of Energy
PL_Index	Real power index
QL_Index	Reactive power index
VD_Index	Voltage deviation index

B. Singh · R.P. Payasi · J. Sharma (✉)
Kamla Nehru Institute of Technology, Sultanpur 228118, UP, India
e-mail: imjanmejy@gmail.com

B. Singh
e-mail: bindeshwar.singh2025@gmail.com

R.P. Payasi
e-mail: payasirp@rediffmail.com

DG_P(P)_Index	Real power penetration of DG index
DG_Q(P)_Index	Reactive power penetration of DG index
WODG	Without DG
WDG	With DG
CONT.	Constant power load model
INSL.	Industrial load model
RESL.	Residential load model
COML.	Commercial load model
REFS.	Reference load model
P_{DG}	Real power of DG
Q_{DG}	Reactive power of DG
MVA_{DG}	Megavolt-ampere capacity of DG
PF_{DG}	Power factor of DG
LOC_{DG}	Location of DG
V_{max}	Maximum voltage limit
V_{min}	Minimum voltage limit
PURPA	Public Utilities Regulatory Policy Act
DER	Distributed energy resources
CIGRE	International Council Large Electric Systems
T&D	Transmission and distribution
GEN	Generation of population of size and location pair of DG
MAXGEN	Maximum generation of population of size and location pair of DG
DGP	DG planning
Min. RPL	Minimum real power loss
Min. QPL	Minimum reactive power loss
S_{PF}	System power factor

15.1 Introduction

15.1.1 A Brief History of DG

Distributed generation (DG) penetration in distribution system is not a new phenomenon. Prior to the advent of alternating current and large-scale steam turbines—during the initial phase of the electric power industry in the early twentieth century—all energy requirements, including heating, cooling, lighting, and motive power, were supplied in or near their point of use. Technical advances, economies of scale in power production and delivery, the expanding role of electricity in American life, and its concomitant regulation as a public utility, all gradually converged to enable the network of gigawatt-scale thermal power plants located far from urban centers that we know today, with high-voltage transmission and lower

voltage distribution lines carrying electricity to virtually every business, facility, and home in the country [1]. At the same time, this system of central generation was evolving, some customers found it economically advantageous to install and operate their own electric power and thermal energy systems, particularly in the industrial sector. Moreover, facilities with needs for highly reliable power, such as hospitals and telecommunications centers, frequently installed their own electric generation units to use for emergency power during outages. These “traditional” forms of DG, while not assets under the control of electric utilities, produced benefits to the overall electric system by providing services to consumers that the utility did not need to provide, thus freeing up assets to extend the reach of utility services and promote more extensive electrification.

Over the years, the technologies for both central generation and DG have improved by becoming more efficient and less costly. Implementation of Section 210 under the Public Utilities Regulatory Policy Act of 1978 (PURPA) sparked a new era of highly energy efficient and renewable DG for electric system applications [2]. Section 210 established a new class of non-utility generators called “qualifying facilities” (QFs) and provided financial incentives to encourage development of cogeneration and small power production. Many QFs have since provided energy to consumers on-site, but some have sold power at rates and under terms and conditions that have been either negotiated or set by state regulatory authorities or non-regulated utilities. Today, advances in new materials and designs for photovoltaic panels, microturbines, reciprocating engines, thermally activated devices, fuel cells, digital controls, and remote monitoring equipment among other components and technologies have expanded the range of opportunities and applications for “modern” DG and have made it possible to tailor energy systems that meet the specific needs of consumers. These technical advances, combined with changing consumer needs, and the restructuring of wholesale and retail markets for electric power, have opened even more opportunities for consumers to use DG to meet their own energy needs, as well as for electric utilities to explore possibilities to meet electric system needs with DG [3].

15.1.2 Definition of DG

DG definition has not been unified yet. The term “distributed generation” or DG refers to the small-scale generation of electric power by a unit sited close to the load being served. DG technologies range in size from 5 kW to 30 MW and include both fully commercial systems, such as reciprocating engines, and others that are primarily in the laboratory, such as fuel cells. This report provides a comprehensive assessment of the strengths and weaknesses of commercial and near-commercial DG technologies in the 5 kW–5 MW size range. The technologies profiled are reciprocating engines, microturbines, industrial combustion turbines, phosphoric acid and proton exchange membrane fuel cells, photovoltaic, and wind turbine systems [1, 2, 4, 5].

In general, DG may be defined as small-scale electric generator located locally at customer's site. However, there is no official agreement on defining what exactly DG is? Many literatures/countries/organizations defined DG more specifically depending on their own basis. Mostly they use generation capacity (MW), voltage level, or generation technology as criteria. Following are some sample definitions of DG.

Definition of DG as defined by reference (Ann, 2001) refers to the small generation units with capacity rating less than 30 MW. Those units are located close to consumers in order to save operating cost of the distribution network and to support the other specific need.

CIGRE defined DG by using capacity rating and location. DG refers to generating units which have 50 to 100 MW maximum capacities and normally connect to the distribution network. Therefore, according to this definition, any generation units installed on a transmission network cannot be considered as DG.

The US Department of Energy (DOE) defined DG as the module of electric generation located near the point of use. Distributed resources (DER or DR) can be either grid-connected or isolated. Those grid-connected DGs are typically installed on the distribution side.

IEEE states that "DER (Distributed Resources, or DR, can be referred to DG) is the generation of electricity from facilities sufficiently smaller than central generating plants, usually 10 MW or less, so as to allow interconnection at nearly any point in a power system, as Distributed Resources."

Furthermore, there are variations in the definitions proposed by different organizations (*IEEE*, *CIGRE*) that may cause confusion. Therefore, in this chapter, the following definition is used [6]:

DG is considered as an electrical source connected to the power system, in a point very close to/or at consumer's site, which is small enough compared with the centralized power plants.

15.1.3 DG Technologies

DG Technologies such as wind power, thermal power, solar power, photovoltaic, wave energy, geothermal energy, tidal energy, ocean energy, fuel cell, microturbines, synchronous and induction generators in Refs. [2, 3, 7, 8].

15.1.4 Types of DG

The different types of traditional and non-traditional DGs are classified and described from the constructional, technological, size, and power time duration point of view. The DGs may also be grouped into four major types based on

Table 15.1 Types of DG and their features [16]

Type of DG	Its features
Type 1 DG	This type of DG is capable of delivering only real power, and it operates at unity power factor, such as photovoltaic, microturbines, fuel cells, which are integrated into the main grid with the help of converters/inverters. However, according to the current status and grid codes, the photovoltaic sometimes is required to provide reactive power as well
Type 2 DG	This type of DG is capable of delivering both active and reactive power, and it operates in the range of (0.80–0.99) leading power factor. DG units based on synchronous machines (cogeneration, gas turbine, etc.) come under this type
Type 3 DG	This type of DG is capable of delivering only reactive power, and it operates at zero power factors. Synchronous compensators such as gas turbines are the example
Type 4 DG	This type of DG is capable of delivering active power, but consuming reactive power, and it operates in the range of (0.80–0.99) lagging power factor. Mainly induction generators, which are used in wind farms, come under this category. However, double-fed induction generator (DFIG) systems may consume or produce reactive power, i.e., operates similar to synchronous generator

terminal characteristics in terms of real and reactive power delivering capability. Mainly four types are considered for comparative studies which are described as follows in Table 15.1.

15.1.5 Benefits and Drawbacks of DG

Benefits: The following benefits of DG such as support of RPS Goals, mitigation of market power, airborne or outdoor emissions, reduced security risk to grid, reliability and power quality (distribution system), voltage support to electric grid, enhanced electricity price elasticity, NIMBY opposition to central power plants and transmission lines, land use effects, avoided T&D capacity, system losses, combined heat and power/efficiency improvement, consumer control, lower cost of electricity, consumer electricity price protection, reliability and power quality (DG owner), and ancillary services [2, 6, 9, 10].

Drawbacks: The following drawbacks of DG such as low efficiency when compared to traditional, high installation costs, high integration costs, and many DG technologies have low capacity, when power is bigger than load line losses are higher, and weather dependent.

15.1.6 Applications of DG

Applications of DG such as continuous power-based load, CHP, uninterrupted power supply (UPS), backup, backup with islanding, renewable, peak shavings, demand response, regulation, reserves, supply capacity and T&D deferral in Refs. [3, 6, 11, 12].

15.1.7 Advances in DG

The following advances are implemented presently such as the comparisons of the different types of DGs such as DG1, DG2, DG3, and DG4 from different power system performance points of view presented in open literatures. In the various open literatures, the hybrid techniques are presented such as GA + fuzzy, GA + ANN, GA + PSO, GA + TS, and GA + ABC for DG planning in distribution power system network from better power system performance point of view. In the open literatures regarding DG planning, only consider static load models, but in some references consider realistic model such as three-phase induction motors in open literatures in Refs. [6, 13, 14, 15].

15.2 Mathematical Modeling of DG

15.2.1 DG Modeling

To calibrate the effects of different types of DGs on DG planning for different load scenarios, a 38-bus distribution test system is adopted. In this chapter, the line impedances, load data, and line power limits are expressed in per unit at the base voltage of 12.66 kV and base MVA of 10 MVA. In traditional load flow analysis, the active and reactive power loads are assumed as constant power loads whereas in practice the loads may be voltage-dependent, i.e., industrial, residential, and commercial loads which may be represented by models as described in (IEEE Task Force, 1993). The voltage-dependent load model is a static load model that represents the power relationship to the voltage as exponential equation and represented in following form as Eqs. (15.1)–(15.2) in Refs. [16, 17, 18].

$$P_{i_bus} = P_{0i_bus} \left(\frac{|V_{i_bus}|}{|V_{0i_bus}|} \right)^{\alpha} \quad (15.1)$$

$$Q_{i_bus} = Q_{0i_bus} \left(\frac{|V_{i_bus}|}{|V_{0i_bus}|} \right)^{\beta} \quad (15.2)$$

where P_{i_bus} , Q_{i_bus} , P_{0i_bus} , Q_{0i_bus} , V_{i_bus} , and V_{0i_bus} are in per unit. Above Eqs. (15.1) and (15.2) neglect the frequency dependence of distribution system load, due to the fact that it is pan-system phenomenon which cannot be controlled locally and remains same for the whole of the system. In practice, the load on each bus may be the composition of industrial, residential, and commercial which may vary with seasonal day and night. Therefore, in this chapter the different load models at each bus are considered as described in [16, 19] and represented in the following form in Eqs. (15.3)–(15.4).

$$P_{i_bus} = w_{i_pi_bus} * P_{0i_bus} \left(\frac{|V_{i_bus}|}{|V_{0i_bus}|} \right)^{alpha_i} + w_{r_pi_bus} * P_{0i_bus} \left(\frac{|V_{i_bus}|}{|V_{0i_bus}|} \right)^{alpha_r} + w_{c_pi_bus} * P_{0i_bus} \left(\frac{|V_{i_bus}|}{|V_{0i_bus}|} \right)^{alpha_c} \quad (15.3)$$

$$Q_{i_bus} = w_{i_qi_bus} * Q_{0i_bus} \left(\frac{|V_{i_bus}|}{|V_{0i_bus}|} \right)^{beta_i} + w_{r_qi_bus} * Q_{0i_bus} \left(\frac{|V_{i_bus}|}{|V_{0i_bus}|} \right)^{beta_r} + w_{c_qi_bus} * P_{0i_bus} \left(\frac{|V_{i_bus}|}{|V_{0i_bus}|} \right)^{beta_c} \quad (15.4)$$

where $alpha$ and $beta$ are active and reactive exponents for industrial load models; $alpha_r$ and $beta_r$ are active and reactive exponents for residential load models; $alpha_c$ and $beta_c$ are active and reactive exponents for the commercial load model. $w_{i_pi_bus}$, $w_{r_pi_bus}$, and $w_{c_pi_bus}$ are the relevant factors for active industrial, residential, and commercial load models at bus i . $w_{i_qi_bus}$, $w_{r_qi_bus}$, and $w_{c_qi_bus}$ are the relevant factors for reactive industrial, residential, and commercial load models at i th bus in Refs. [20, 21, 22].

The following condition must be satisfied for all buses except *buses without load* (BWL) (Bus 1 is slack bus, and buses 34–38 are not having load) in Eqs. (15.5)–(15.6).

$$w_{i_pi_bus} + w_{r_pi_bus} + w_{c_pi_bus} = 1, \quad \text{for } i = 1 \text{ to } N_B, \text{ but } i_bus \neq \text{BWL} \quad (15.5)$$

$$w_{i_qi_bus} + w_{r_qi_bus} + w_{c_qi_bus} = 1, \quad \text{for } i = 1 \text{ to } N_B, \text{ but } i_bus \neq \text{BWL} \quad (15.6)$$

Apart from these situations, T1, T2, T3, and T4 are considered for comparative study. A 38-bus test system is assumed to be supplying power to the combination of industrial, residential, and commercial load without violating bus voltage and line capacity limits [22, 23]. The following test cases are developed for optimal size and location of DG for constant power and seasonal mixed load models for two

objectives: (1) real power loss (P_L) minimization; and (2) apparent power intake (S_{int}) minimization.

- Type 1 DG,
- Type 2 DG,
- Type 3 DG, and
- Type 4 DG.

15.2.2 Distribution Power System Performance Indices

The following distribution power system performance indices are as follows:

15.2.2.1 Real Power Loss Index (PL_Index)

The real power loss index is defined as in Eq. (15.7):

$$PL_Index = \frac{PL_Index_{WDG}}{PL_Index_{WODG}} \times 100 \quad (15.7)$$

As the lower value of this index indicates better benefits in terms of real power loss reduction accrued due to DG location and size in Refs. [24–27, 28].

15.2.2.2 Reactive Power Loss Index (QL_Index)

The reactive power loss index is defined as in Eq. (15.8):

$$QL_Index = \frac{QL_Index_{WDG}}{QL_Index_{WODG}} \times 100 \quad (15.8)$$

As the lower values of this index indicate better benefits in terms of reactive power loss reduction accrued due to DG location and size in Refs. [29–31, 32].

15.2.2.3 Voltage Deviation Index (VD_Index)

The voltage deviation index is defined as in Eq. (15.9):

$$VD_Index = \frac{|V_1| - |V_{i_bus}|}{|V_1|} \times 100 \quad (15.9)$$

It is interlinked to maximum voltage drop between each node and root node. The lower values of this index indicate the best performance of the network in Refs. [33, 34, 35].

15.2.2.4 Real Power Penetration of DG (DG_P (P)_Index)

DG_P penetration index: The ratio of the amount of DG active power injected into the network to the summation of active power with DG and without DG is given in Eq. (15.10) in Refs. [36–38, 39].

$$\text{DG_P(P)_Index} = \frac{P_{\text{WDG}}}{P_{\text{WODG}} + P_{\text{WDG}}} \quad (15.10)$$

15.2.2.5 Reactive Power Penetration of DG (DG_Q(P)_Index)

DG_Q penetration index: The ratio of the amount of DG reactive power injected into the network to the summation of reactive power with DG and without DG is given in Eq. (15.11) in Refs. [40–42, 43].

$$\text{DG_Q(P)_Index} = \frac{Q_{\text{WDG}}}{Q_{\text{WODG}} + Q_{\text{WDG}}} \quad (15.11)$$

where $P_{\text{WDG}} = 3.3990$ and $Q_{\text{WDG}} = 2.3634$ are in p.u.

15.2.2.6 System Power Factor

It is the ratio of real power (kW) to the apparent power (kVA) [44] is given in Eqs. (15.12)–(15.13).

$$\text{Without DG, } \cos \vartheta_{\text{WODGSystem}} = \frac{P_{\text{WODG}}}{\sqrt{P_{\text{WODG}}^2 + Q_{\text{WODG}}^2}} \quad (15.12)$$

$$\text{With DG, } \cos \vartheta_{\text{WDGSystem}} = \frac{P_{\text{WODG}} + P_{\text{WDG}}}{\sqrt{(P_{\text{WODG}} + P_{\text{WDG}})^2 + (Q_{\text{WODG}} + Q_{\text{WDG}})^2}} \quad (15.13)$$

15.3 Proposed Methodology for Optimal Placement and Size of DG

15.3.1 Fundamentals of GA

Genetic algorithms (GAs) are adaptive heuristic search algorithms based on the evolutionary ideas of natural selection and genetics. As such, they represent an intelligent exploitation of a random search used to solve optimization problems. Although randomized, GAs is by no means random; instead, they exploit historical information to direct the search into the region of better performance within the search space in Refs. [45–47]. The basic techniques of the GAs are designed to simulate processes in natural systems necessary for evolution, especially those follow the principles first laid down by Charles Darwin of “survival of the fittest.” Since in nature, competition among individuals for scanty resources results in the fittest individuals dominating over the weaker ones in Refs. [48–50, 51].

15.3.2 Reason for GA Used for Optimization of Problem

It is better than conventional AI in the sense that it is more robust. Unlike older AI systems, they do not break easily, even if the inputs are changed slightly, or in the presence of reasonable noise. Also, in searching a large state space, multimodal state space, or n-dimensional surface, a genetic algorithm may offer significant benefits over the more typical search of optimization techniques (linear programming, heuristic, depth first, breath first, and praxis) in Refs. [52–54, 55].

15.3.3 GA Overview

GA simulates the survival of the fittest among individuals over consecutive generation for solving a problem. Each generation consists of a population of character strings that are analogous to the chromosome that we see in our DNA. Each individual represents a point in a search space and a possible solution. The individuals in the population are then made to go through a process of evolution in Refs. [56–59].

15.3.3.1 Selection Operator

Key idea: Give preference to better individuals, allowing them to pass on their genes to the next generation. The goodness of each individual depends on its fitness. Fitness may be determined by an objective function or by a subjective judgment in Refs. [60, 61, 62].

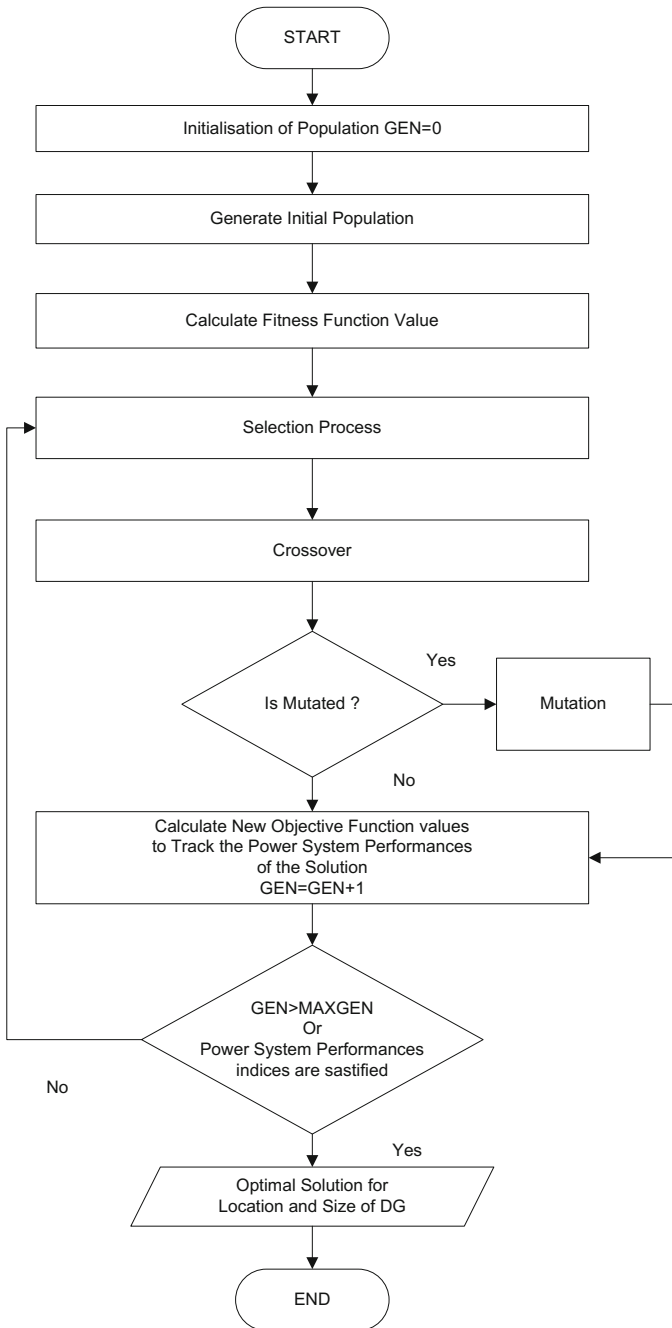


Fig. 15.1 Flowchart for optimal placement and size of DG by GA

15.3.3.2 Crossover Operator

Prime distinguished factor of GA from other optimization techniques. Two individuals are chosen from the population using the selection operator. A crossover site along the bit strings is randomly chosen. The values of the two strings are exchanged up to this point. If $S1 = 000000$, $s2 = 111111$, and the crossover point is 2, then $S1' = 110000$ and $s2' = 001111$. The two new offspring created from this mating is put into the next generation of the population. By recombining portions of good individuals, this process is likely to create even better individuals in Refs. [63–65].

15.3.3.3 Mutation

With some low probability, a portion of the new individuals will have some of their bits flipped. Its purpose is to maintain diversity within the population and inhibit premature convergence. Mutation alone induces a random walk through the search space mutation, and selection (without crossover) creates a parallel, noise-tolerant, hill climbing algorithm in Refs. [66, 67, 68].

15.3.4 *Effects of Genetic Operators*

Using selection alone will tend to fill the population with copies of the best individual from the population. Using selection and crossover operators will tend to cause the algorithms to converge on a good but suboptimal solution. Using mutation alone induces a random walk through the search space in Refs. [69, 70, 71]. Using selection and mutation creates a parallel, noise-tolerant, hill climbing algorithm. The flowchart for optimal placement of size of DG by GA is given in Fig. 15.1.

15.4 Simulation Results and Discussions

The IEEE 38-bus test system and its data are given below:

15.4.1 *IEEE 38-Bus Test System and Its Data*

The IEEE 38-bus test system and its data are given in figure and table, respectively [16, 72, 73] (Fig. 15.2).

The line parameters and load data for IEEE 38 bus are given in Table 15.2.

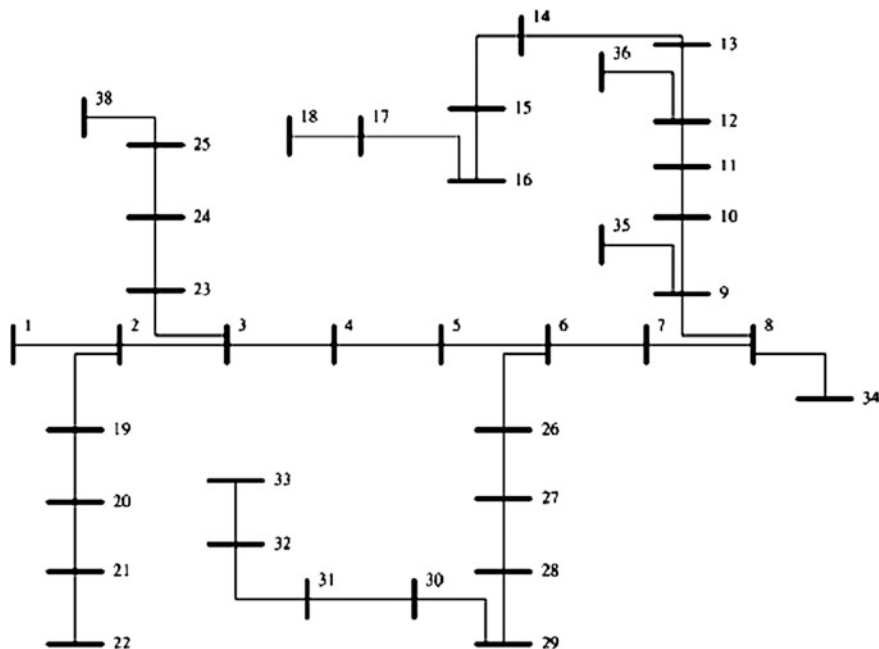


Fig. 15.2 IEEE 38-bus test system [16, 72, 73]

15.4.2 Real and Reactive Power Exponential Indices for DLMs [16, 72, 73]

The real and reactive power exponential indices for different load models are given in Table 15.3.

15.4.3 Analysis of DG Operating at 0.82 Leading Power Factor with DLMs

Table 15.4 shows the simulation results for DG-T2 type operating at 0.82 leading power factor with DLMs. The power system performance parameters such as PL_Index, QL_Index, VD_Index, DG_P (P)_Index, DG_Q (P)_Index, and system power factor are shown in Figs. 15.3, 15.4, 15.5, 15.6, 15.7 and 15.8, respectively.

Table 15.2 Line parameter and load data for 38-bus test system [72]

F	T	Line impedance (p. u.)		L	S_L (p.u.)	Load on the bus (p.u.)	
		R	X			P	Q
1	2	0.000574	0.000293	1	4.60	0.10	0.06
2	3	0.003070	0.001564	6	4.10	0.09	0.04
3	4	0.002279	0.001161	11	2.90	0.12	0.08
4	5	0.002373	0.001209	12	2.90	0.06	0.03
5	6	0.005100	0.004402	13	2.90	0.06	0.02
6	7	0.001166	0.003853	22	1.50	0.20	0.10
7	8	0.004430	0.001464	23	1.05	0.20	0.10
8	9	0.006413	0.004608	25	1.05	0.06	0.02
9	10	0.006501	0.004608	27	1.05	0.06	0.02
10	11	0.001224	0.000405	28	1.05	0.045	0.03
11	12	0.002331	0.000771	29	1.05	0.06	0.035
12	13	0.009141	0.007192	31	0.50	0.06	0.035
13	14	0.003372	0.004439	32	0.45	0.12	0.08
14	15	0.003680	0.003275	33	0.30	0.06	0.01
15	16	0.004647	0.003394	34	0.25	0.06	0.02
16	17	0.008026	0.010716	35	0.25	0.06	0.02
17	18	0.004538	0.003574	36	0.10	0.09	0.04
2	19	0.001021	0.000974	2	0.50	0.09	0.04
19	20	0.009366	0.008440	3	0.50	0.09	0.04
20	21	0.002550	0.002979	4	0.21	0.09	0.04
21	22	0.004414	0.005836	5	0.11	0.09	0.04
3	23	0.002809	0.001920	7	1.05	0.09	0.05
23	24	0.005592	0.004415	8	1.05	0.42	0.20
24	25	0.005579	0.004366	9	0.50	0.42	0.20
6	26	0.001264	0.000644	14	1.50	0.06	0.025
26	27	0.001770	0.000901	15	1.50	0.06	0.025
27	28	0.006594	0.005814	16	1.50	0.06	0.02
28	29	0.005007	0.004362	17	1.50	0.12	0.07
29	30	0.003160	0.001610	18	1.50	0.20	0.60
30	31	0.006067	0.005996	19	0.50	0.15	0.07
31	32	0.001933	0.002253	20	0.50	0.21	0.10
32	33	0.002123	0.003301	21	0.10	0.06	0.04
8	34	0.012453	0.012453	24	0.50	0.00	0.00
9	35	0.012453	0.012453	26	0.50	0.00	0.00
12	36	0.012453	0.012453	30	0.50	0.00	0.00
18	37	0.003113	0.003113	37	0.50	0.00	0.00
25	38	0.003113	0.002513	10	0.10	0.00	0.00

F = From bus, T = To bus, L = line number, S_L = Line apparent power limit, P = Real power load, Q = Reactive power load

Table 15.3 Exponential indexes of DLMs

Different load models	Alpha	Beta
CONT.	0	0
INSL.	0.18	6.0
RESL.	0.92	4.04
COML.	1.51	3.40
REFS.	0.91	1.0

15.4.3.1 PL_Index

Figure 15.3 shows that the values of PL_Index with respect to DLMs such as constant power, industrial, residential, commercial, and reference load models are 56.37, 49.17, 39.96, 33.19, and 57.17 in %, respectively, for DG-T2 type operating at 0.82 leading power factor. It shows that the minimum and maximum values of PL_Index are for commercial and reference load models, respectively.

15.4.3.2 QL_Index

Figure 15.4 shows that the values of QL_Index with respect to different load models such as constant power, industrial, residential, commercial, and reference load models are 36.53, 28.51, 32.48, 28.43, and 43.20 in %, respectively, for DG-T2 type operating at 0.82 leading power factor. It shows that the minimum and maximum values of QL_Index are for commercial and reference load models, respectively.

15.4.3.3 VD_Index

Figure 15.5 shows that the values of VD_Index with respect to DLMs such as constant power, industrial, residential, commercial and reference load models are 6.79, 5.82, 4.85, 7.76 and 6.79 in p.u., respectively, for DG-T2 type operating at 0.82 leading power factor. It shows that the minimum and maximum values of VD_Index are for residential and commercial load model, respectively.

15.4.3.4 DG_P (P)_Index

Figure 15.6 shows that the values of DG_P (P)_Index with respect to DLMs such as constant power, industrial, residential, commercial, and reference load models are 29.19, 26.58, 31.72, 30.80, and 29.23 in %, respectively, for DG-T2 type operating at 0.82 leading power factor. It shows that the minimum and maximum values of DG_P (P)_Index are for industrial and residential load model, respectively.

Table 15.4 Simulation result for DG-T2 type operating at 0.82 leading power factor with DLMS

Load Models	WODG/ WDG	Min. RPL	Min. QPL	P _{DG}	Q _{DG}	MVA _{DG}	PF _{DG}	LOC _{DG}	PL_Index	QL_Index	VD_Index	DG_P(P) _Index	DG_Q(P) _Index	S _{PF}	V _{min}	V _{max}
CONT.	WODG	0.1889	0.1259	–	–	–	–	–	100	100	8.13	100	–	0.8200	0.95	1.03
	WDG	0.0824	0.0799	1.3960	0.9746	1.7208	0.82	6	56.37	36.53	6.79	29.19	29.11	0.8303	0.96	1.03
	WODG	0.1889	0.1259	–	–	–	–	–	100	100	8.13	100	–	0.8200	0.95	1.03
INSL.	WODG	0.0960	0.0900	0.6756	0.4716	0.8240	0.82	30	49.17	28.51	5.82	26.58	25.63	0.8285	0.97	1.03
	WDG	0.1889	0.1259	–	–	–	–	–	100	100	8.13	100	–	0.8200	0.95	1.03
	WODG	0.1134	0.0850	0.4515	0.3152	0.5507	0.82	31	39.96	32.48	4.85	31.72	30.76	0.8236	0.98	1.03
COML.	WODG	0.1889	0.1259	–	–	–	–	–	100	100	8.13	100	–	0.8200	0.95	1.03
	WDG	0.1262	0.0901	1.5133	1.0563	1.8456	0.82	24	33.19	28.43	7.76	30.80	26.90	0.8228	0.95	1.03
	WODG	0.1889	0.1259	–	–	–	–	–	100	100	8.13	100	–	0.8200	0.95	1.03
REFS.	WODG	0.0809	0.0715	1.3371	0.9333	1.6307	0.82	26	57.17	43.20	6.79	29.23	28.31	0.8325	0.96	1.03

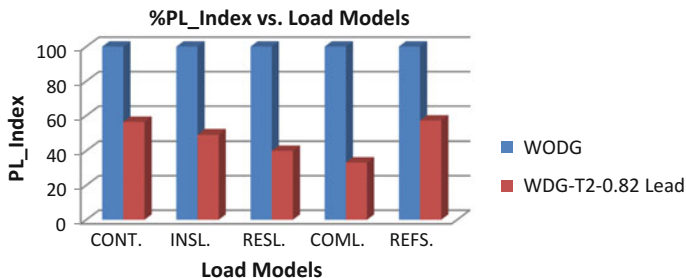


Fig. 15.3 PL_Index for DG-T2 type operating at 0.82 leading power factor with DLMs

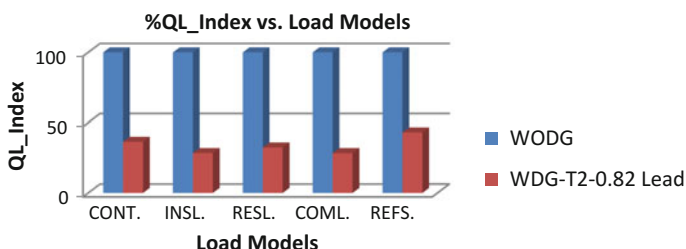


Fig. 15.4 QL_Index for DG-T2 type operating at 0.82 leading power factor with DLMs

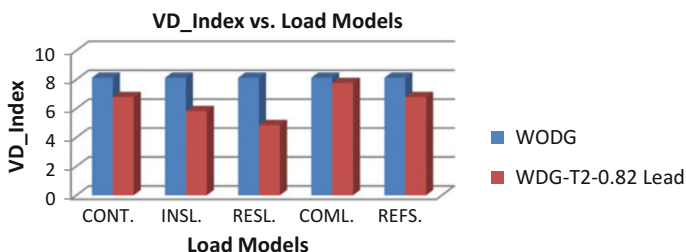


Fig. 15.5 VD_Index for DG-T2 type operating at 0.82 leading power factor with DLMs

15.4.3.5 DG_Q (P)_Index

Figure 15.7 shows that the values of DG_Q (P)_Index with respect to DLMs such as constant power, industrial, residential, commercial, and reference load models are 29.11, 25.63, 30.76, 26.90, and 28.31 in %, respectively, for DG-T2 type operating at 0.82 leading power factor. It shows that the minimum and maximum values of DG_Q (P)_Index are for industrial and residential load model, respectively.

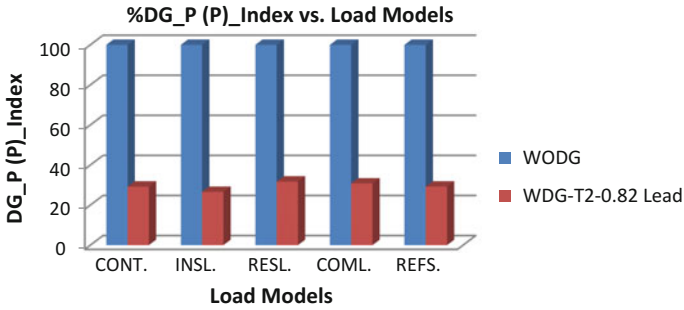


Fig. 15.6 DG_P (P)_Index for DG-T2 type operating at 0.82 leading power factor with DLMs

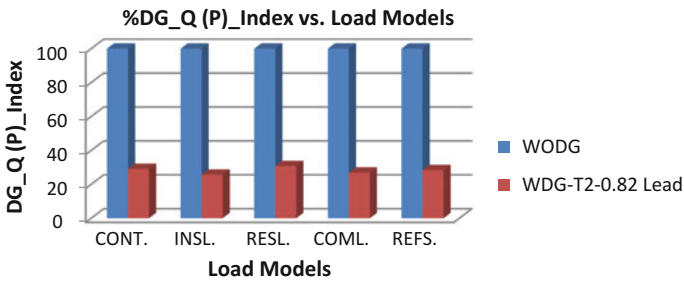


Fig. 15.7 DG_Q (P)_Index for DG-T2 type operating at 0.82 leading power factor with DLMs

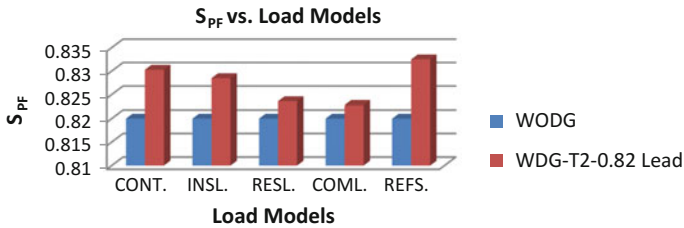


Fig. 15.8 S_{PF} for DG-T2 type operating at 0.82 leading power factor with DLMs

15.4.3.6 System Power Factor

Figure 15.8 shows that the values of system power factor with respect to DLMs such as constant power, industrial, residential, commercial, and reference load models are 0.8303, 0.8285, 0.8236, 0.8228, and 0.8325, respectively, for DG-T2 type operating at 0.82 leading power factor. The figure shows that the minimum and maximum values of system power factor are for commercial and reference load models, respectively.

15.4.4 Analysis of DG Operating at 0.86 Leading Power Factor with Different Load Models

Table 15.5 shows the simulation results for DG-T2 type operating at 0.86 leading power factor with DLMs. The power system performance parameters such as PL_Index, QL_Index, VD_Index, DG_P (P)_Index, DG_Q (P)_Index, and system power factor are shown in Figs. 15.9, 15.10, 15.11, 15.12, 15.13 and 15.14, respectively.

15.4.4.1 PL_Index

Figure 15.9 shows that the values of PL_Index with respect to DLMs such as constant power, industrial, residential, commercial, and reference load models are 56.32, 48.96, 39.70, 34.03, and 55.69 in %, respectively, for DG-T2 type operating at 0.86 leading power factor. It shows that the minimum and maximum values of PL_Index are for commercial and constant power load model, respectively.

15.4.4.2 QL_Index

Figure 15.10 shows that the values of QL_Index with respect to different load models such as constant power, industrial, residential, commercial, and reference load models are 36.61, 35.89, 32.36, 30.54, and 44.55 in %, respectively, for DG-T2 type operating at 0.86 leading power factor. It shows that the minimum and maximum values of QL_Index are for commercial and reference load models, respectively.

15.4.4.3 VD_Index

Figure 15.11 shows that the values of VD_Index with respect to different load models such as constant power, industrial, residential, commercial, and reference load models are 5.79, 6.82, 5.85, 6.76, and 5.79 in p.u., respectively, for DG-T2 type operating at 0.86 leading p.f. The figure shows that the minimum and maximum values of VD_Index are for residential and commercial load model, respectively.

15.4.4.4 DG_P (P)_Index

Figure 14.12 shows that the values of DG_P (P)_Index with respect to DLMs such as constant power, industrial, residential, commercial, and reference load models are 30.16, 27.32, 28.22, 34.89, and 29.03 in %, respectively, for DG-T2 type

Table 15.5 Simulation result for DG-T2 type operating at 0.86 leading power factor with DLMS

Load models	WODG/ WDG	Min. RPL	Min. QPL	P _{DG}	Q _{DG}	MVA _{DG}	PF _{DG}	LOC _{DG}	PL_Index	QL_Index	VD_Index	DG_P(P) _Index	DG_Q(P) _Index	S _{pf}	V _{min}	V _{max}
CONT.	WODG	0.1889	0.1259	–	–	–	–	–	100	100	8.13	100	–	0.8600	0.95	1.03
	WDG	0.0825	0.0798	1.4682	0.8712	1.7073	0.86	6	56.32	36.61	5.79	30.16	26.93	0.8712	0.96	1.03
	WODG	0.1889	0.1259	–	–	–	–	–	100	100	8.13	100	–	0.8600	0.95	1.03
INSL.	WDG	0.0964	0.0870	0.7123	0.4226	0.8283	0.86	30	48.96	35.89	6.82	27.32	25.16	0.8695	0.97	1.03
	WODG	0.1889	0.1259	–	–	–	–	–	100	100	8.13	100	–	0.8600	0.95	1.03
	WDG	0.1139	0.0990	0.4736	0.2810	0.5507	0.86	31	39.70	32.36	5.85	28.22	24.62	0.8615	0.98	1.03
COML.	WODG	0.1889	0.1259	–	–	–	–	–	100	100	8.13	100	–	0.8600	0.95	1.03
	WDG	0.1246	0.0950	1.8214	1.0808	2.1180	0.86	23	34.03	30.54	6.76	34.89	31.38	0.8602	0.95	1.03
	WODG	0.1889	0.1259	–	–	–	–	–	100	100	8.13	100	–	0.8600	0.95	1.03
REFS.	WODG	0.0837	0.0698	1.3910	0.8254	1.6175	0.86	6	55.69	44.55	5.79	29.03	25.88	0.8701	0.96	1.03

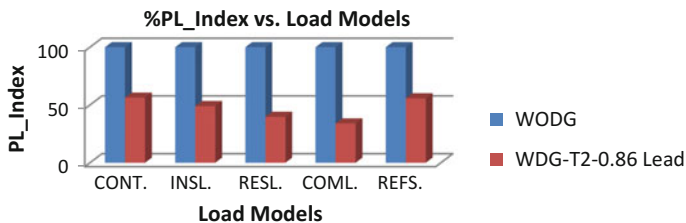


Fig. 15.9 PL_Index for DG-T2 type operating at 0.86 leading power factor with DLMs

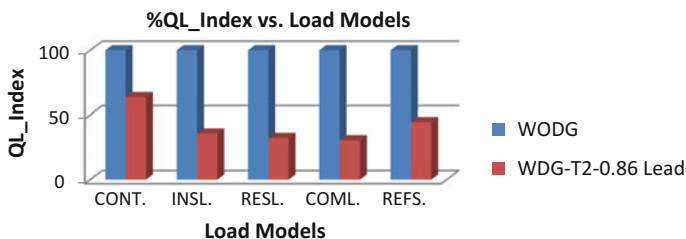


Fig. 15.10 QL_Index for DG-T2 type operating at 0.86 leading power factor with DLMs

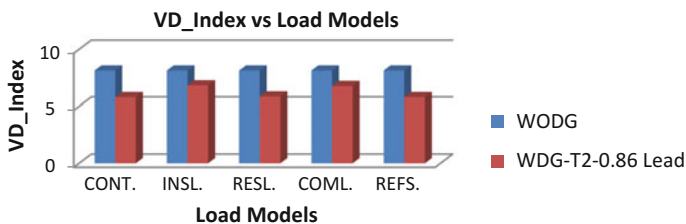


Fig. 15.11 VD_Index for DG-T2 type operating at 0.86 leading power factor with DLMs

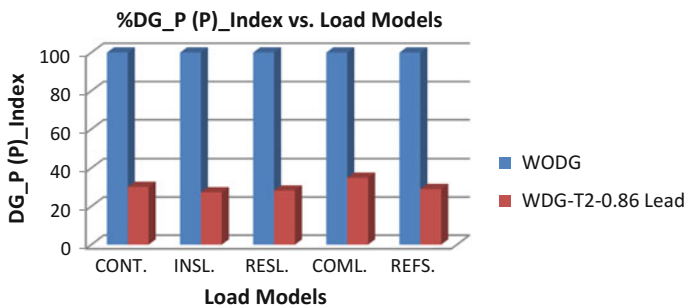


Fig. 15.12 DG_P (P)_Index for DG-T2 Type operating at 0.86 power factor with DLMs

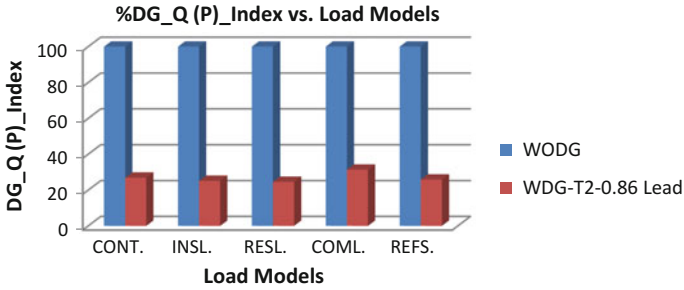


Fig. 15.13 DG_Q (P)_Index for DG-T2 Type operating at 0.86 power factor with DLMs

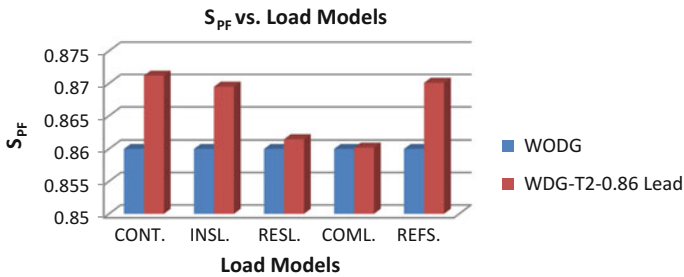


Fig. 15.14 S_{PF} for DG-T2 Type operating at 0.86 power factor with DLMs

operating at 0.86 leading p.f. It shows that the minimum and maximum values of DG_P (P)_Index are for industrial and commercial load models, respectively.

15.4.4.5 DG_Q (P)_Index

Figure 15.13 shows that the values of DG_Q (P)_Index with respect to DLMs such as constant power, industrial, residential, commercial, and reference load models are 26.93, 25.16, 24.62, 31.38, and 25.88 in %, respectively, for DG-T2 type operating at 0.86 leading power factor. It shows that the minimum and maximum values of DG_Q (P)_Index are for residential and commercial load models, respectively.

15.4.4.6 S_{PF}

Figure 15.14 shows that the values of system power factor with respect to DLMs such as constant power, industrial, residential, commercial, and reference load models are 0.8712, 0.8695, 0.8615, 0.8602, and 0.8701 are, respectively, for

DG-T2 type operating at 0.86 leading power factor. It shows that the minimum and maximum values of system power factor are for residential and commercial load models, respectively.

15.4.5 Analysis of DG Operating at 0.92 Leading Power Factor with DLMs

Table 15.6 shows the simulation results for DG-T2 type operating at 0.92 leading power factor with DLMs. The power system performance parameters such as PL_Index, QL_Index, VD_Index, DG_P (P)_Index, DG_Q (P)_Index, and system power factor are shown in Figs. 15.15, 15.16, 15.17, 15.18, 15.19 and 15.20, respectively.

15.4.5.1 PL_Index

Figure 15.15 shows that the values of PL_Index with respect to DLMs such as constant power, industrial, residential, commercial, and reference load models are 55.26, 47.69, 38.85, 33.03, and 55.21 in %, respectively, for DG-T2 type operating at 0.92 leading power factor. It shows that the minimum and maximum values of PL_Index are for commercial and constant power load model, respectively.

15.4.5.2 QL_Index

Figure 15.16 shows that the values of QL_Index with respect to DLMs such as constant power, industrial, residential, commercial, and reference load models are 37.64, 37.72, 32.54, 30.54, and 33.67 in %, respectively, for DG-T2 type operating at 0.92 leading power factor. It shows that the minimum and maximum values of QL_Index are for commercial and constant power load model, respectively.

15.4.5.3 VD_Index

Figure 15.17 shows that the values of VD_Index with respect to DLMs such as constant power, industrial, residential, commercial, and reference load models are 4.79, 4.82, 6.85, 5.76, and 4.79 in p.u., respectively, for DG-T2 type operating at 0.92 leading power factor. It shows that the minimum and maximum values of VD_Index are for reference and residential load models, respectively.

Table 15.6 Simulation result for DG-T2 type operating at 0.92 leading power factor with DLMs

Load models	WODG/ WDG	Min. RPL	Min. QPL	P _{DG}	Q _{DG}	MVA _{DG}	PF _{DG}	LOC _{DG}	PL_Index	QL_Index	VD_Index	DG_P(P) _Index	DG_Q(P) _Index	S _{PF}	V _{min}	V _{max}
CONT.	WODG	0.1889	0.1259	–	–	–	–	–	100	100	8.13	100	–	0.9200	0.95	1.03
	WDG	0.0845	0.0785	1.5831	0.6744	1.7208	0.92	6	55.26	37.64	4.79	31.77	25.20	0.9362	0.96	1.03
	WODG	0.1889	0.1259	–	–	–	–	–	100	100	8.13	100	–	0.9200	0.95	1.03
INSL.	WDG	0.0988	0.0910	0.7620	0.3246	0.8283	0.92	30	47.69	37.72	4.82	28.31	25.07	0.9289	0.97	1.03
	WODG	0.1889	0.1259	–	–	–	–	–	100	100	8.13	100	–	0.9200	0.95	1.03
	WDG	0.1155	0.0950	0.5066	0.2158	0.5507	0.92	31	38.85	32.54	6.85	28.97	25.36	0.9265	0.98	1.03
COML.	WODG	0.1889	0.1259	–	–	–	–	–	100	100	8.13	100	–	0.9200	0.95	1.03
	WDG	0.1265	0.0950	1.7218	0.7335	1.8716	0.92	24	33.03	30.54	5.76	33.62	28.68	0.9251	0.95	1.03
	WODG	0.1889	0.1259	–	–	–	–	–	100	100	8.13	100	–	0.9200	0.95	1.03
REFS.	WDG	0.0846	0.0835	1.4232	0.6062	1.5470	0.92	27	55.21	33.67	4.79	29.51	25.41	0.9300	0.96	1.03

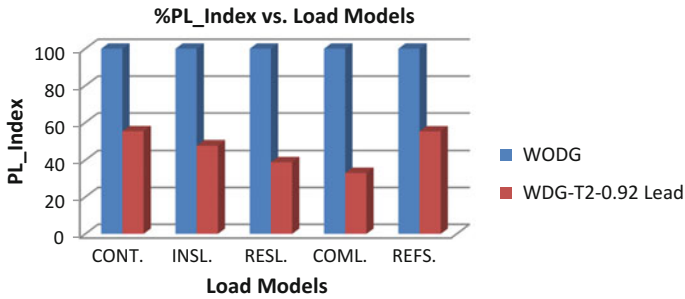


Fig. 15.15 PL_Index for DG-T2 type operating at 0.92 leading power factor with DLMs

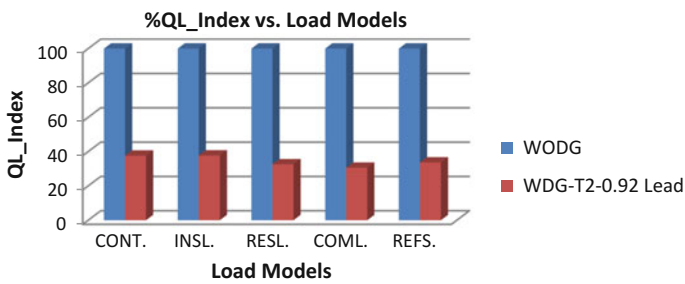


Fig. 15.16 QL_Index for DG-T2 type operating at 0.92 leading power factor with DLMs

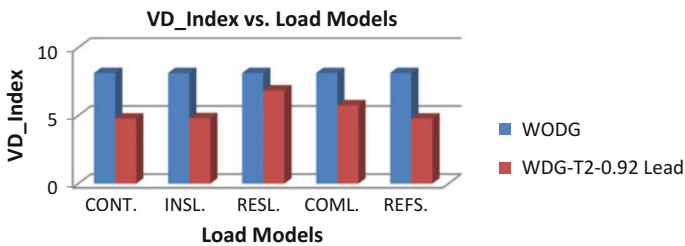


Fig. 15.17 VD_Index for DG-T2 type operating at 0.92 leading power factor with DLMs

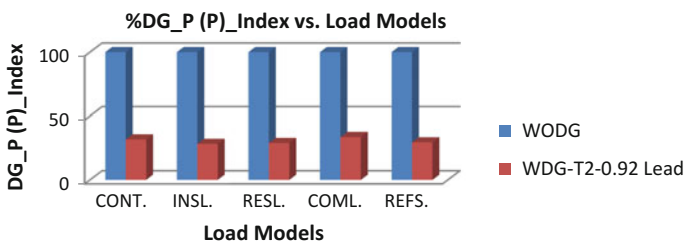


Fig. 15.18 DG_P (P)_Index for DG-T2 type operating at 0.92 leading power factor with DLMs

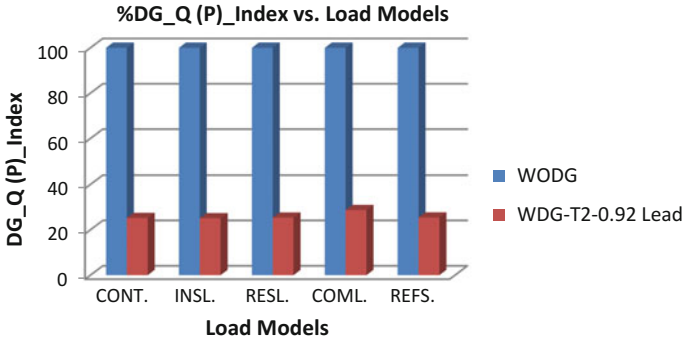


Fig. 15.19 DG_Q (P)_Index for DG-T2 type operating at 0.92 leading power factor with DLMs

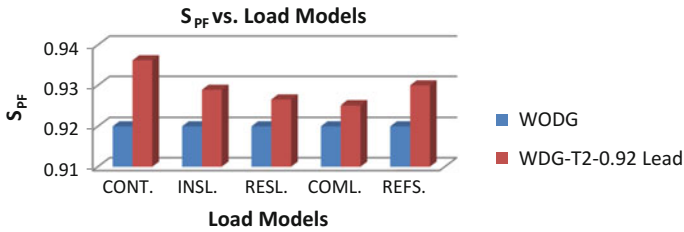


Fig. 15.20 S_{PF} for DG-T2 type operating at 0.92 leading power factor with DLMs

15.4.5.4 DG_P (P)_Index

Figure 15.18 shows that the values of DG_P (P)_Index with respect to DLMs such as constant power, industrial, residential, commercial, and reference load models are 31.77, 28.31, 28.97, 33.62, and 29.51 in %, respectively, for DG-T2 type operating at 0.92 leading power factor. It shows that the minimum and maximum values of DG_P (P)_Index are for industrial and commercial load model, respectively.

15.4.5.5 DG_Q (P)_Index

Figure 15.19 shows that DG_Q (P)_Index with respect to DLMs such as constant power, industrial, residential, commercial, and reference load models are 25.20, 25.07, 25.36, 28.68, and 25.41 in %, respectively, for DG-T2 type operating at 0.92 leading power factor. It shows that the minimum and maximum values of DG_Q (P)_Index are for industrial and commercial load model, respectively.

15.4.5.6 S_{PF}

Figure 15.20 shows that the values of system power factor with respect to DLMS such as constant power, industrial, residential, commercial, and reference load models are 0.9362, 0.9289, 0.9265, 0.9251, and 0.9300, respectively, for DG-T2 type operating at 0.92 leading power factor. It shows that the minimum and maximum values of system power factor are for industrial and commercial load models, respectively.

15.4.6 *Analysis of DG Operating at 0.96 Leading Power Factor with DLMS*

Table 15.7 shows the simulation results for DG-T2 type operating at 0.92 leading power factor with different load models. The power system performance parameters such as PL_Index, QL_Index, VD_Index, DG_P (P)_Index, DG_Q (P)_Index, and system power factor are shown in Figs. 15.21, 15.22, 15.23, 15.24, 15.25 and 15.26, respectively.

15.4.6.1 PL_Index

Figure 15.21 shows that the values of PL_Index with respect to DLMS such as constant power, industrial, residential, commercial, and reference load models are 53.89, 45.79, 37.63, 33.71, and 53.67 are in %, respectively, for DG-T2 type operating at 0.96 leading power factor. It shows that the minimum and maximum values of PL_Index are for commercial and constant power load model, respectively.

15.4.6.2 QL_Index

Figure 15.22 shows that the values of QL_Index with respect to DLMS such as constant power, industrial, residential, commercial, and reference load models are 44.47, 33.54, 31.14, 30.08, and 50.35 are in %, respectively, for DG-T2 type operating at 0.96 leading power factor. It shows that the minimum and maximum values of QL_Index are for commercial and reference load models, respectively.

15.4.6.3 VD_Index

Figure 15.23 shows that the values of VD_Index with respect to DLMS such as constant power, industrial, residential, commercial, and reference load models are 6.79, 5.82, 4.85, 7.76, and 6.79 are in p.u., respectively, for DG-T2 type operating

Table 15.7 Simulation result for DG-T2 type operating at 0.96 leading power factor with DLMs

Load models	WODG/ WDG	Min. RPL	Min. QPL	P _{DG}	Q _{DG}	MVA _{DG}	PF _{DG}	LOC _{DG}	PL_Index	QL_Index	VD_Index	DG_P(P) _Index	DG_Q(P) _Index	S _{PF}	V _{min}	V _{max}
CONT.	WODG	0.1889	0.1259	–	–	–	–	–	100	100	8.13	100	–	0.9600	0.95	1.03
	WDG	0.0871	0.0825	1.7037	0.4969	1.7747	0.96	6	53.89	44.47	6.79	33.43	27.37	0.9789	0.96	1.03
	WODG	0.1889	0.1259	–	–	–	–	–	100	100	8.13	100	–	0.9600	0.95	1.03
INSL.	WDG	0.1024	0.0950	0.7951	0.2319	0.8283	0.96	30	45.79	33.54	5.82	28.95	28.93	0.9698	0.97	1.03
	WODG	0.1889	0.1259	–	–	–	–	–	100	100	8.13	100	–	0.9600	0.95	1.03
	WDG	0.1178	0.0955	0.5286	0.1541	0.5507	0.96	13	37.63	31.14	4.85	29.45	26.12	0.9689	0.98	1.03
COML.	WODG	0.1889	0.1259	–	–	–	–	–	100	100	8.13	100	–	0.9600	0.95	1.03
	WDG	0.1271	0.0855	1.9875	0.5797	2.0704	0.96	23	33.71	30.08	7.76	36.89	29.69	0.9645	0.95	1.03
	WODG	0.1889	0.1259	–	–	–	–	–	100	100	8.13	100	–	0.9600	0.95	1.03
REFS.	WODG	0.0875	0.0625	1.5823	0.4615	1.6483	0.96	26	53.67	50.35	6.79	31.76	26.33	0.9754	0.96	1.03

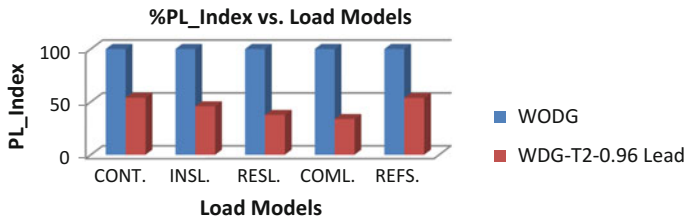


Fig. 15.21 PL_Index for DG-T2 type operating at 0.96 leading power factor with DLMs

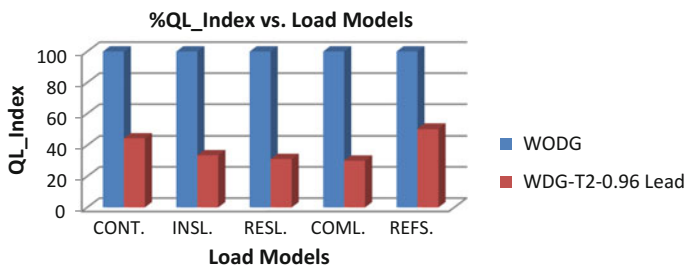


Fig. 15.22 QL_Index for DG-T2 type operating at 0.96 leading power factor with DLMs

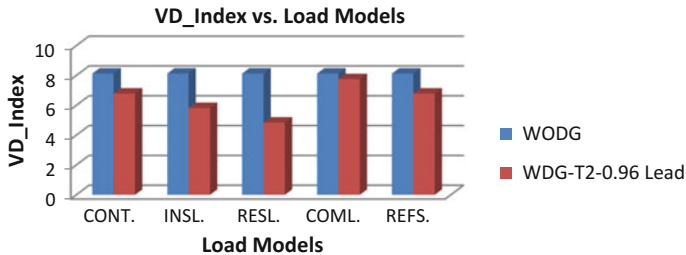


Fig. 15.23 VD_Index for DG-T2 type operating at 0.96 leading power factor with DLMs

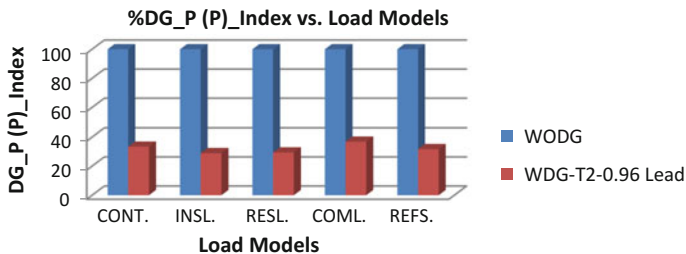


Fig. 15.24 DG_P (P)_Index for DG-T2 type operating at 0.96 leading power factor with DLMs

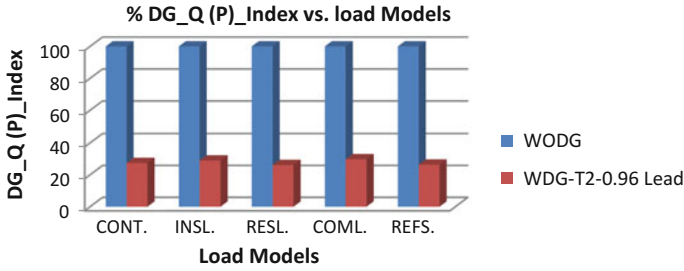


Fig. 15.25 DG_Q (P)_Index for DG-T2 type operating at 0.96 leading power factor with DLMs

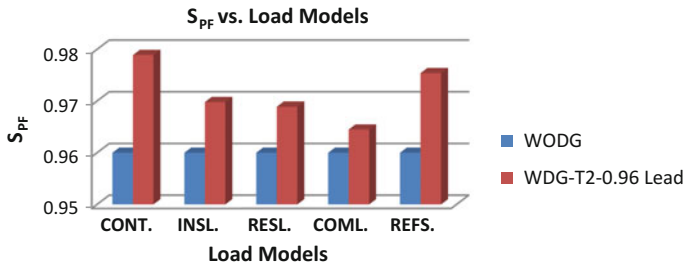


Fig. 15.26 S_{PF} for DG-T2 type operating at 0.96 leading power factor with DLMs

at 0.96 leading power factor. It shows that the minimum and maximum values of VD_Index are for residential and commercial load model, respectively.

15.4.6.4 DG_P (P)_Index

Figure 15.24 shows that the values of DG_P (P)_Index with respect to DLMs such as constant power, industrial, residential, commercial, and reference load models are 33.43, 28.95, 29.45, 36.89, and 31.76 are in %, respectively, for DG-T2 type operating at 0.96 leading power factor. It shows that the minimum and maximum values of DG_P (P)_Index are for industrial and commercial load model, respectively.

15.4.6.5 DG_Q (P)_Index

Figure 15.25 shows that the values of DG_Q (P)_Index with respect to DLMs such as constant power, industrial, residential, commercial, and reference load models are 27.37, 28.93, 26.12, 29.69, and 26.33 are in %, respectively, for DG-T2 type operating at 0.96 leading power factor. It shows that the minimum and maximum values of DG_Q (P)_Index are for industrial and commercial load model, respectively.

15.4.6.6 S_{PF}

Figure 15.26 shows that the values of system power factor with respect to DLMS such as constant power, industrial, residential, commercial, and reference load models are 0.9789, 0.9698, 0.9689, 0.9645, and 0.9754, respectively, for DG-T2 type operating at 0.96 leading power factor. It shows that the minimum and maximum values of system power factor are for commercial and constant power load model, respectively.

15.4.7 Analysis of DG Operating at 0.98 Leading Power Factor with DLMS

Table 15.8 shows the simulation results for DG-T2 type operating at 0.92 leading power factor with DLMS. The power system performance parameters such as PL_Index, QL_Index, VD_Index, DG_P (P)_Index, DG_Q (P)_Index, and system power factor are shown in Figs. 15.27, 15.28, 15.29, 15.30, 15.31 and 15.32, respectively.

15.4.7.1 PL_Index

Figure 15.27 shows that the values of PL_Index with respect to DLMS such as constant power, industrial, residential, commercial, and reference load models are 50.76, 44.15, 37.10, 37.23, and 52.19 are in %, respectively, for DG-T2 type operating at 0.98 leading power factor. It shows that the minimum and maximum values of PL_Index are for residential and reference load model, respectively.

15.4.7.2 QL_Index

Figure 15.28 shows that the values of QL_Index with respect to DLMS such as constant power, industrial, residential, commercial, and reference load models are 41.46, 30.81, 34.94, 30.54, and 43.05 are in %, respectively, for DG-T2 type operating at 0.98 leading power factor. It shows that the minimum and maximum values of QL_Index are for commercial and reference load models, respectively.

15.4.7.3 VD_Index

Figure 15.29 shows that VD_Index with respect to DLMS such as constant power, industrial, residential, commercial, and reference load models are 6.79, 5.82, 4.85, 6.79, and 6.79 are in p.u., respectively, for DG-T2 type operating at 0.98 leading

Table 15.8 Simulation result for DG-T2 type operating at 0.98 leading power factor with DLMs

Load models	WO DG/WDG	Min. RPL	Min. QPL	P _{DG}	Q _{BG}	MVA _{DG}	PF _{DG}	LOC _{DG}	PL_Index	QL_Index	VD_Index	DG_P(P)_Index	DG_Q(P)_Index	S _{PF}	V _{min}	V _{max}
CONT.	WODG	0.1889	0.1259	-	-	-	-	-	100	100	8.13	100	-	0.9800	0.95	1.03
	WDG	0.0930	0.0737	1.6863	0.3424	1.7208	0.98	6	50.76	41.46	6.79	33.16	30.65	0.9928	0.96	1.03
	WODG	0.1889	0.1259	-	-	-	-	-	100	100	8.13	100	-	0.9800	0.95	1.03
INSL.	WODG	0.1055	0.0871	0.8117	0.1648	0.8283	0.98	30	44.15	30.81	5.82	29.27	26.51	0.9844	0.97	1.03
	WDG	0.1889	0.1259	-	-	-	-	-	100	100	8.13	100	-	0.9800	0.95	1.03
	WODG	0.1188	0.0819	0.5396	0.1095	0.5507	0.98	14	37.10	34.94	4.85	28.70	24.42	0.9830	0.98	1.03
COML.	WODG	0.1889	0.1259	-	-	-	-	-	100	100	8.13	100	-	0.9800	0.95	1.03
	WDG	0.1299	0.0950	1.7198	0.3492	1.7549	0.98	24	37.23	30.54	6.79	33.59	30.87	0.9802	0.96	1.03
	WODG	0.1889	0.1259	-	-	-	-	-	100	100	8.13	100	-	0.9800	0.95	1.03
REFS.	WODG	0.0903	0.0717	1.6499	0.3350	1.6836	0.98	7	52.19	43.05	6.79	32.67	32.41	0.9876	0.96	1.03

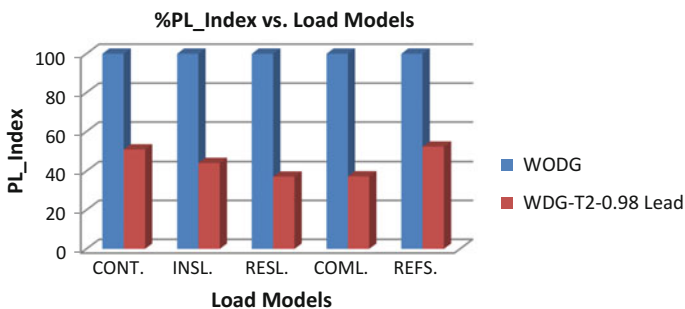


Fig. 15.27 PL_Index for DG-T2 type operating at 0.98 leading power factor with DLMs

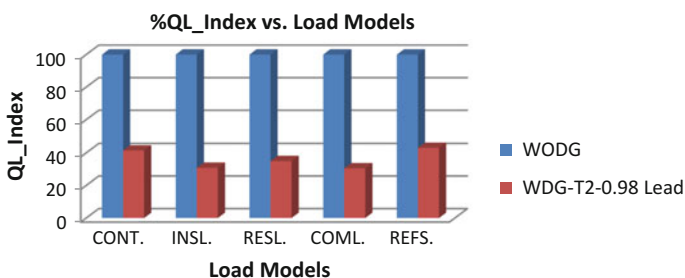


Fig. 15.28 QL_Index for DG-T2 type operating at 0.98 leading power factor with DLMs

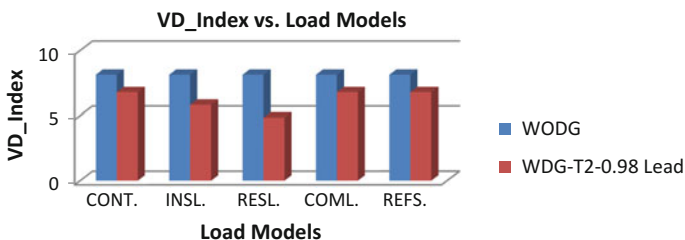


Fig. 15.29 VD_Index for DG-T2 type operating at 0.98 leading power factor with DLMs

power factor. It shows that the minimum and maximum values of VD_Index are for residential and reference load models, respectively.

15.4.7.4 DG_P (P)_Index

Figure 15.30 shows that the values of DG_P(P)_Index with respect to DLMs such as constant power, industrial, residential, commercial, and reference load models are 33.16, 29.27, 28.70, 33.59, and 32.67 are in %, respectively, for DG-T2 type

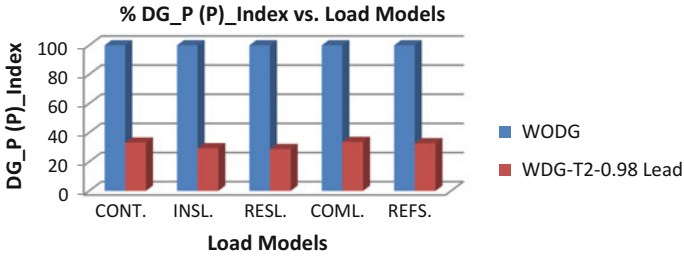


Fig. 15.30 DG_P (P)_Index for DG-T2 type operating at 0.98 leading power factor with DLMs

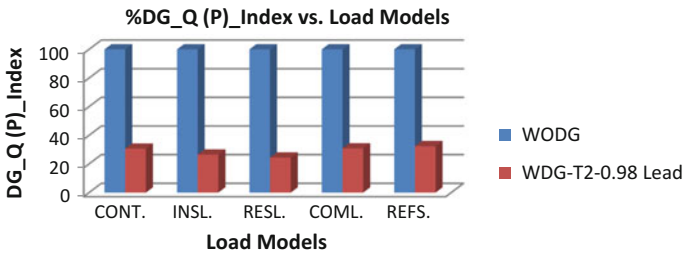


Fig. 15.31 DG_Q (P)_Index for DG-T2 type operating at 0.98 leading power factor with DLMs

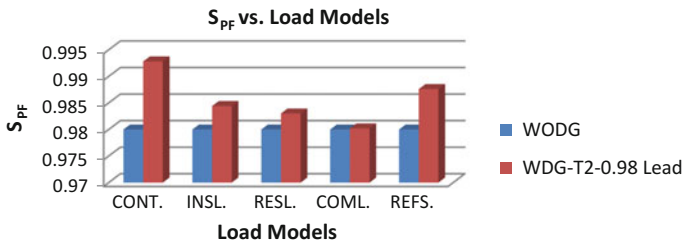


Fig. 15.32 S_{PF} for DG-T2 type operating at 0.98 leading power factor with DLMs

operating at 0.98 leading power factor. It shows that the minimum and maximum values of DG_P (P)_Index are for residential and commercial load models, respectively.

15.4.7.5 DG_Q (P)_Index

Figure 15.31 shows that the values of DG_Q (P) with respect to DLMs such as constant power, industrial, residential, commercial, and reference load models are 30.65, 26.51, 24.42, 30.87, and 32.41 are in %, respectively, for DG-T2 type

operating at 0.98 leading power factor. It shows that the minimum and maximum values of DG_Q (P)_Index are for industrial and reference load models, respectively.

15.4.7.6 S_{PF}

Figure 15.32 shows that the values of system power factor with respect to DLMs such as constant power, industrial, residential, commercial, and reference load models are 0.9928, 0.9844, 0.9830, 9802, and 0.9876, respectively, for DG-T2 type operating at 0.98 leading power factor. It shows that the minimum and maximum values of system power factor are for commercial and constant power load models, respectively.

15.4.8 Analysis of Comparisons of DG Operating at Different Power Factors Such as 0.82, 0.86, 0.92, 0.96, and 0.98 Leading Power Factors

Comparisons of power system performance parameters such as real power loss, reactive power loss, PL_Index, QL_Index, VD_Index, DG_P (P)_Index, DG_Q (P)_Index, and system power factor are shown in Figs. 15.33, 15.34, 15.35, 15.36, 15.37, 15.38, 15.39 and 15.40, respectively.

15.4.8.1 Real Power Loss

Figure 14.33 shows that the values of real power loss with respect to DLMs such as constant power, industrial, residential, commercial, and reference load models for DG-T2 type operating at different power factors such as 0.82, 0.86, 0.92, 0.96, and 0.98 leading power factors are increasing, respectively. It shows the minimum and

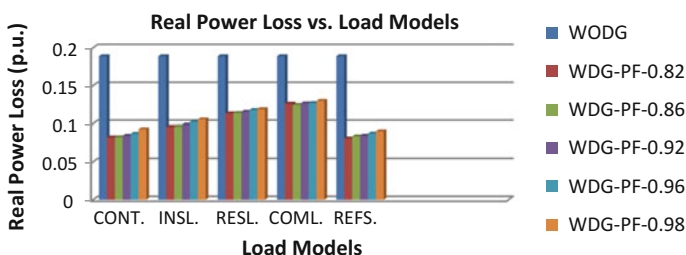


Fig. 15.33 Real power loss for DG-T2 type operating at 0.82, 0.86, 0.92, 0.96, and 0.98 leading power factors with DLMs

maximum values of real power loss at 0.82 and 0.98 leading power factors, respectively.

15.4.8.2 Reactive Power Loss

Figure 15.34 shows that the values of reactive power loss with respect to DLMs such as constant power, industrial, residential, commercial, and reference load models for DG-T2 type operating at different power factors such as 0.82, 0.86, 0.92, 0.96, and 0.98 leading power factors are increasing, respectively. It shows the minimum and maximum values of reactive power loss at 0.82 and 0.98 leading power factors, respectively.

15.4.8.3 PL_Index

Figure 15.35 shows that the values of PL_Index with respect to DLMs such as constant power, industrial, residential, commercial and reference load models for

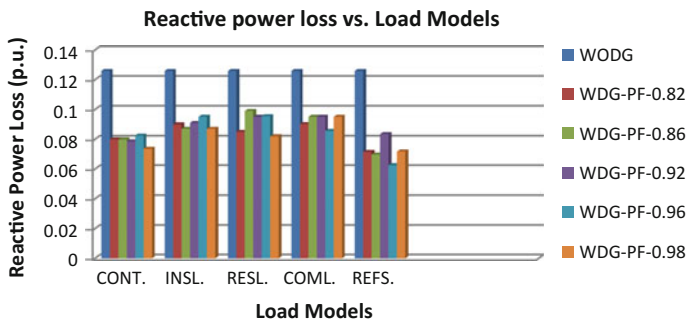


Fig. 15.34 Reactive power loss for DG-T2 type operating at 0.82, 0.86, 0.92, 0.96, and 0.98 leading power factors with DLMs

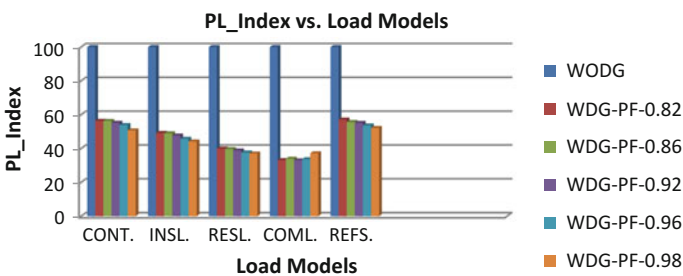


Fig. 15.35 PL_Index for DG-T2 type operating at 0.82, 0.86, 0.92, 0.96, and 0.98 leading power factors with DLMs

DG-T2 type operating at different power factors such as 0.82, 0.86, 0.92, 0.96, and 0.98 leading power factors are decreasing, respectively. It shows the minimum and maximum values of PL_Index at 0.98 and 0.82 leading power factors, respectively.

15.4.8.4 QL_Index

Figure 15.36 shows that the values of QL_Index with respect to DLMs such as constant power, industrial, residential, commercial, and reference load models for DG-T2 type operating at different power factors such as 0.82, 0.86, 0.92, 0.96, and 0.98 leading power factors are increasing, respectively. It shows the minimum and maximum values of QL_Index at 0.82 and 0.98 leading power factors, respectively.

15.4.8.5 VD_Index

Figure 15.37 shows that the values of VD_Index with respect to DLMs such as constant power, industrial, residential, commercial, and reference load models for DG-T2 type operating at different power factors such as 0.82, 0.86, 0.92, 0.96, and 0.98 leading power factors are increasing, respectively. It shows the minimum and maximum values of VD_Index at 0.82 and 0.98 leading power factors, respectively.

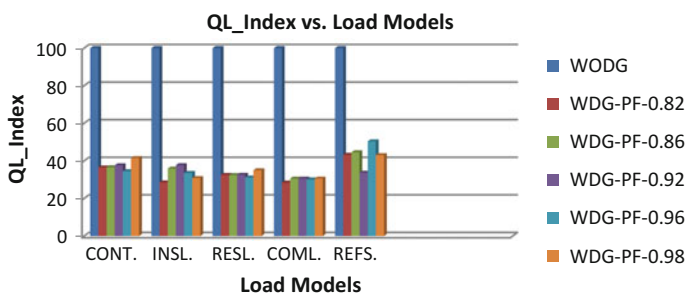


Fig. 15.36 QL_Index for DG-T2 type operating at 0.82, 0.86, 0.92, 0.96, and 0.98 leading power factors with DLMs

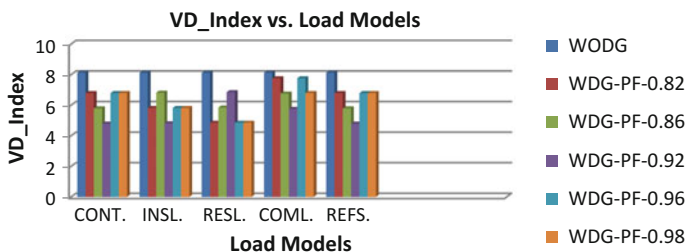


Fig. 15.37 VD_Index for DG-T2 type operating at 0.82, 0.86, 0.92, 0.96, and 0.98 leading power factors with DLMs

0.98 leading power factors are varying, respectively. It shows the minimum and maximum values of VD_Index at 0.92 and 0.98 leading power factors, respectively.

15.4.8.6 DG_P (P)_Index

Figure 15.38 shows that DG_P(P)_Index with respect to DLMs such as constant power, industrial, residential, commercial, and reference load models for DG-T2 type operating at different power factors such as 0.82, 0.86, 0.92, 0.96, and 0.98 leading power factors are increasing, respectively. It shows the minimum and maximum values of DG_P (P)_Index at 0.82 and 0.98 leading power factors, respectively.

15.4.8.7 DG_Q (P)_Index

Figure 15.39 shows that the values of DG_Q (P)_Index with respect to DLMs such as constant power, industrial, residential, commercial and reference load models for

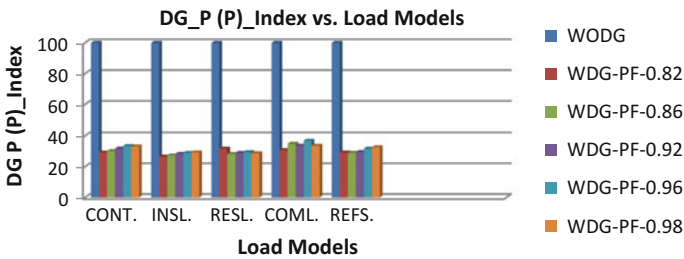


Fig. 15.38 DG_P (P)_Index for DG-T2 type operating at 0.82, 0.86, 0.92, 0.96, and 0.98 leading power factors with DLMs

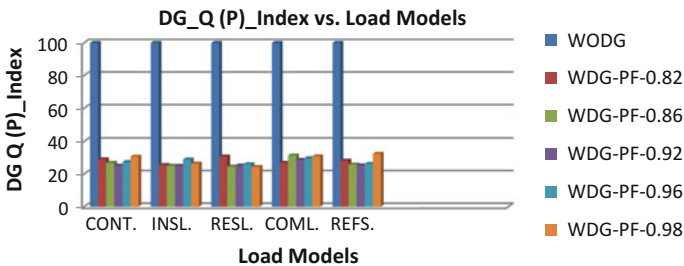


Fig. 15.39 DG_Q (P)_Index for DG-T2 type operating at 0.82, 0.86, 0.92, 0.96, and 0.98 leading power factors with DLMs

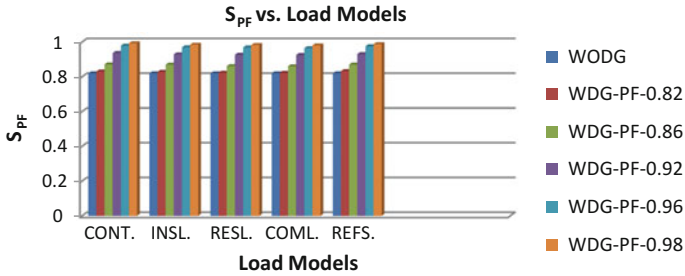


Fig. 15.40 S_{PF} for DG-T2 type operating at 0.82, 0.86, 0.92, 0.96, and 0.98 leading power factors with DLMs

DG-T2 type operating at different power factors such as 0.82, 0.86, 0.92, 0.96, and 0.98 leading power factors are increasing, respectively. It shows the minimum and maximum values of DG_Q (P)_{Index} at 0.82 and 0.98 leading power factors, respectively.

15.4.8.8 S_{PF}

Figure 15.40 shows that the values of system power factor with respect to DLMs such as constant power, industrial, residential, commercial, and reference load models are for DG-T2 type operating at different power factors such as 0.82, 0.86, 0.92, 0.96, and 0.98 leading power factors are increases. It show that the minimum and maximum values of system power factor at 0.82 and 0.98 leading power factors, respectively.

15.5 Conclusions and Future Scope of Research Work

15.5.1 Conclusions

In this chapter, different load models at every bus for DG-T2 type are considered such as constant power, industrial, residential, commercial, and reference load models. The DG planning based on different load models gives appropriate results. It is desirable to keep the DG planning indices, i.e., real power loss index (PL_{Index}), reactive power loss index (QL_{Index}), voltage deviation index (VD_{Index}) below the limits which are defined without DG conditions. By the application of DG, the MVA intake power is reduced. The conclusions are as follows:

- Proper siting and sizing can reduce losses.
- Size and location pair is different under different load model conditions.
- For DG implementation, load models should be taken into account.

15.5.2 Future Scope of Research Work

- System of higher number of buses can be taken.
- Multiple DG planning.
- For any practical system, it can be implemented.
- Comparison of different types of DG planning with static as well as realistic load models by hybrid AI techniques.
- Comparison of different types of DG and FACTS controller planning with static as well as realistic load models by AI techniques.
- Comparison of different types of DG and FACTS controller planning with static as well as realistic load models by hybrid AI techniques.
- Comparison of different types of DG planning with static as well as realistic load models by AI techniques.

Acknowledgements The author would like to thank technical and moral support given to this work by Prof. Raghuraj Singh, Director, Kamla Nehru Institute of Technology, Sultanpur (U.P.), India, and Prof. S.K. Sinha, Department of Electrical Engineering Kamla Nehru Institute of Technology, Sultanpur (U.P.), India. The authors also gratefully acknowledge the helpful comments and suggestions of the Prof. Deependra Singh, Department of Electrical Engineering Kamla Nehru Institute of Technology, Sultanpur (U.P.), India, which have improved the technical issues as well as qualities throughout this chapter.

References

1. Singh D, Singh D, Verma KS (2007) GA based optimal sizing and placement of distributed generation for loss minimization. *Int J Electr Comput Eng* 2:8
2. Singh D, Misra RK, Singh D (2007) Effect of load models in distributed generation planning. *IEEE transaction on power systems*, vol 22, no 4, Nov 2007
3. Hung DQ, Mithulananthan N, Bansal RC (2010) Analytical expressions for DG allocation in primary distribution networks. *IEEE transaction on energy conversion*, vol 25, no 3, Sep 2010
4. Chowdhury AA, Agarwal SK, Koval DO (2003) Reliability modeling of distributed generation in conventional distribution systems planning and analysis. *IEEE Trans Indus Appl* 39(5):1493–1498
5. Gupta V, Pahwa A (2004) A voltage drop-based approach to include cold load pickup in design of distribution systems. *IEEE Trans Power Syst* 19(2):957–963
6. Ochoa LF, Padilha-Feltrin A, Harrison GP (2006) Evaluating distributed generation impacts with a multiobjective index. *IEEE transaction on power delivery*, vol 21
7. Mao Y, Miu KN (2003) Switch placement to improve system reliability for radial distribution systems with distributed generation. *IEEE Trans Power Syst* 18(4):1346–1352
8. Chiradeja P, Ramakumar R (2004) An approach to quantify the technical benefits of distributed generation. *IEEE Trans Energy Conv* 19(4):764–773
9. Popovic DS, Popovic ZN (2004) A risk management procedure for supply restoration in distribution networks. *IEEE Trans Power Syst* 19(1):221–228
10. Mutale J, Strbac G, Curcic S, Jenkins N (2000) Allocation of losses in distribution systems with embedded generation. *IEE Proc Gener Transm Distrib* 147(1):7–14
11. Wang C, Nehrir MH (2004) Analytical approaches for optimal placement of distributed generation sources in power systems. *IEEE Trans Power Syst* 19(4):2068–2076

12. Costa PM, Matos MA (2004) Loss allocation in distribution networks with embedded generation. *IEEE Trans Power Syst* 19(1):384–389
13. Brahma SM, Girgis AA (2004) Development of adaptive protection scheme for distribution systems with high penetration of distributed generation. *IEEE Trans Power Deliv* 19(1):56–63
14. El-Khattam W, Hegazy YG, Salama MMA (2005) An integrated distributed generation optimization model for distribution system planning. *IEEE Trans Power Syst* 20(2):1158–1165
15. Carpinelli G, Celli G, Mocci S, Pilo F, Russo A (2005) Optimisation of embedded generation sizing and siting by using a double trade-off method. *IEE Proc-Gener Transm Distrib* 152(4):503–513
16. Payasi RP, Singh AK, Singh D (2011) Review of distributed generation planning: objectives, constraints, and algorithms. *Int J Eng Sci Technol* 3(3)
17. Coelho CAC, Pulido GT, Lechuga MS (2004) Handling multiple objectives with particle swarm optimization. *IEEE Trans Evolut Comput* 8(3):256–259
18. Keane A, Malley MO (2005) Optimal allocation of embedded generation on distribution networks. *IEEE Trans Power Syst* 20(3):1640–1646
19. Lalitha MP, Veera Reddy VC, Usha V (2005) Optimal DG placement for minimum real power loss in radial distribution systems using PSO. *J Theor Appl Inf Technol* 13:107–116
20. Bansal RC (2005) Optimization methods for electric power systems: an overview. *Int J Emerg Electr Power Syst* 2(1), Art. 1021
21. Celli G, Ghiani E, Mocci S, Pilo F (2005) A multiobjective evolutionary algorithm for the sizing and siting of distributed generation. *IEEE Trans Power Syst* 20(2):750–757
22. Popovic DH, Greatbanks JA, Begovic M, Pregelj A (2005) Placement of distributed generators and reclosers for distribution network security and reliability. *Electr Power Energy Syst* 27:398–408
23. Biswas Soma, Goswami SK (2011) Genetic algorithm based optimal placement of distributed generation reducing loss and improving voltage sag performance. *ACEEE Int J Electr Power Eng* 02(01):21–23
24. Haghifam M-R, Falaghi H, Malik OP (2008) Risk-based distributed generation placement. *IET Gener Transm Distrib* 2:252–260
25. Jabr RA, Pal BC (2009) Ordinal optimisation approach for locating and sizing of distributed generation. *IET Gener Transm Distrib* 3:713–723
26. Atwa YM, El-Saadany EF, Salama MMA, Seethapathy R (2010) Optimal renewable resources mix for distribution system energy loss minimization. *IEEE Trans Power Syst* 25(1):360–370
27. Ochoa LF, Dent CJ, Harrison GP (2010) Distribution network capacity assessment: variable DG and active networks. *IEEE Trans Power Syst* 25(1):87–95
28. Xiao J, Zhang Z, Bai L, Liang H (2016) Determination of optimal installation site and capacity of battery energy storage system in distribution network integrated with distributed generation. *IET Gener Transm Distrib* 10(3):601–607
29. Ochoa LF, Padilha-Feltrin A, Harrison GP (2008) Evaluating distributed time-varying generation through a multiobjective index. *IEEE Trans Power Deliv* 23:1132–1138
30. Porkar S, Poure P, Abbaspour-Tehrani-Fard A, Saadate S (2010) A novel optimal distribution system planning framework implementing distributed generation in a deregulated electricity market. *Electr Power Syst Res* 80:828–837
31. Singh RK, Goswami SK (2010) Optimum allocation of distributed generations based on nodal pricing for profit, loss reduction, and voltage improvement including voltage rise issue. *Electr Power Energy Syst* 32:637–644
32. Khod HM, Silva MR, Vale Z, Ramos C (2010) A probabilistic methodology for distributed generation location in isolated electrical service area. *Electr Power Syst Res* 80:390–399
33. Zhu D, Broadwater RP, Tam K-S, Seguin R, Asgerirsson H (2006) Impact of DG placement on reliability and efficiency with time-varying loads. *IEEE Trans Power Syst* 21(1):419–427
34. El-Khattam W, Hegazy YG, Salama MMA (2006) Investigating distributed generation systems performance using Monte Carlo simulation. *IEEE Trans Power Syst* 21(2):524–532

35. Haesen E, Driesen J, Belmans R (2007) Robust planning methodology for integration of stochastic generators in distribution grids. *IET Renew Power Gener* 1:25–32
36. Khalesi N, Rezaei N, Haghifam MR (2011) DG allocation with application of dynamic programming for loss reduction and reliability improvement. *Electr Power Energy Syst* 33:288–295
37. Harrison GP, Piccolo A, Siano P, Wallace AR (2008) Hybrid GA and OPF evaluation of network capacity for distributed generation connections. *Electr Power Syst Res* 78:392–398
38. Wang DTC, Ochoa LF, Harrison GP (2010) DG impact on investment deferral: network planning and security of supply. *IEEE Trans Power Syst* 25(2):1134–1141
39. Hashemi-Dezaki H, Akarian-Abyaneh H, Haeri-Khiavi H (2016) Impacts of direct cyber—power interdependencies on smart grid reliability under various penetration levels of microturbine/wind/solar distributed generations. *IET Gener Transm Distrib* 10(4):928–937
40. Harrison GP, Piccolo A, Siano P, Wallace AR (2007) Exploring the tradeoffs between incentives for distributed generation developers and DNOs. *IEEE Trans Power Syst* 22(2):821–828
41. Al Abri RS, Ehab El-Saadany F, Yasser Atwa M (2013) Optimal placement and sizing method to improve the voltage stability margin in a distribution system using distributed generation. *IEEE Trans Power Syst* 28(1):326–334
42. Ochoa LF, Padilha-Feltrin A, Harrison GP (2008) Time-series-based maximization of distributed wind power generation integration. *IEEE Trans Energy Convers* 23(3):968–974
43. Chen H, Wang Z, Yan H, Zou H, Luo B (2015) Integrated planning of distribution systems with distributed generation and demand side response. *Energy Procedia* 75:981–986
44. Dent CJ, Ochoa LF, Harrison GP (2010) Network distributed generation capacity analysis using OPF with voltage step constraints. *IEEE Trans Power Syst* 25(1):296–304
45. Momoh JA, Ma XW, Tomsovic K (1995) Overview and literature survey of fuzzy set theory in power systems. *IEEE Trans Power Syst* 10(3):1676–1690
46. IEEE Task Force on Load Representation for Dynamic Performance, Standard load models for power flow and dynamic performance simulation. *IEEE Trans Power Syst* 10(3):1302–1313
47. Sebastian B, Albert C, Bernhard S (2015) Capacity of low-voltage grids for distributed generation: classification by means of stochastic simulations. *IEEE Trans Power Syst* 30(2):689–700
48. Mendez Quezada VH, Abbad JR, San Román TG (2006) Assessment of energy distribution losses for increasing penetration of distributed generation. *IEEE Trans Power Syst* 21(2):533–540
49. Moradi MH, Abedini M (2012) A combination of genetic algorithm and particle swarm optimization for optimal DG location and sizing in distribution systems. *Electr Power Energy Syst* 34:66–74
50. Rao NS, Wan Y-H (1994) Optimum location of resources in distributed planning. *IEEE Trans Power Syst* 9(4):2014–2020
51. Othman MM, Elk Walid, Yasser GH, Almoataz YA (2015) Optimal placement and sizing of distributed generators in unbalanced distribution systems using supervised big bang-big crunch method. *IEEE Trans Power Syst* 30(2):911–919
52. Soroudi A, Ehsana M, Zareipour H (2011) A practical eco-environmental distribution network planning model including fuel cells and non-renewable distributed energy resources. *Renew Energy* 36(1):179–188
53. Georgilakis PS, Hatzigrygiou ND (2013) Optimal distributed generation placement in power distribution networks: models, methods, and future research. *IEEE Trans Power Syst* 28(3):3420–3428
54. Olivieri MMDA, Rocha MS, de Castro MRV, de Souza SM, Klaus W, Medeiros JC, Visconti IF, Galdino MAE, de Borges ELP, da Silva IWF, Lima AAN, de Carvalho CM, Soares YMS, Vieira JJ (2014) Distributed generation in the smart grid—case study of Parintins. *Energy Procedia* 57:197–206

55. Dent CJ, Ortiz A, Blake SR, Miller D, Roberts D (2015) Defining and evaluating the capacity value of distributed generation. *IEEE Trans Power Syst* 30(5):2329–2337
56. Akorede MF, Hizam H, Aris I, Ab Kadir MZA (2011) Effective method for optimal allocation of distributed generation units in meshed electric power systems. *IET Gener Transm Distrib* 5 (2):276–287
57. Aman MM, Jasmon GB, Mokhlis H, Bakar AHA (2012) Optimal placement and sizing of a DG based on a new power stability index and line losses. *Electrical Power Energy Syst* 43:1296–1304
58. Akram E, Mohammed E, Mohammed E, Zhe C (2015) A fuzzy-multiagent self-healing scheme for a distribution system with distributed generations. *IEEE Trans Power Syst* 30 (5):2612–2622
59. Gregorio MD, Javier C, Jose MA (2015) Joint expansion planning of distributed generation and distribution networks. *IEEE Trans Power Syst* 30(5):2579–2590
60. Gil HA, Joos G (2006) On the quantification of the network capacity deferral value of distributed generation. *IEEE Trans Power Syst* 21(4):1592–1599
61. Ghofrani-Jahromi Z, Mahmoodzadeh Z, Ehsan M (2014) Distribution loss allocation for radial systems including DGs. *IEEE Trans Power Deliv* 29(1):72–80
62. Krishnan M (2015) Intelligent energy control center for distributed generators using multi-agent system. *IEEE Trans Power Syst* 30(5):2442–2449
63. Shi R, Cui C, Su K, Zain Z (2011) Comparison study of two meta-heuristic algorithms with their applications to distributed generation planning. *Energy Procedia* 12:245–252
64. Mingrui Z, Jie C (2015) Islanding and scheduling of power distribution systems with distributed generation. *IEEE Trans Power Syst* 30(5):3120–3129
65. Vito C, Gaspare C, Vincenzo G, Giovanni M, Antonio P (2014) Optimal decentralized voltage control for distribution systems with inverter-based distributed generators. *IEEE Trans Power Syst* 29(1):230–241
66. Chad A, Yves B, Philippe V (2014) An autoground system for anti-Islanding protection of distributed generation. *IEEE Trans Power Syst* 29(2):873–880
67. James DF, Adam MB, Natashia B, Hamish W (2014) Comparison of mixed-integer programming and genetic algorithm methods for distributed generation planning. *IEEE Trans Power Syst* 29(2):833–843
68. Al SSK, Zeineldin HH, Vinod K (2014) Planning active distribution networks considering multi-DG configurations. *IEEE Trans Power Syst* 29(2):785–793
69. Piccolo A, Siano P (2009) Evaluating the impact of network investment deferral on distributed generation expansion. *IEEE Trans Power Syst* 24(3):1559–1567
70. Hugo MA, Diogo S, Waldir F (2014) A practical second-order based method for power losses estimation in distribution systems with distributed generation. *IEEE Trans Power Syst* 29(2):666–674
71. Payasi RP, Singh AK, Singh D (2013) Optimal location and size of different type of distributed generations with voltage step constraint and mixed load models. *Quality, reliability, security, and robustness in heterogenous network*. Springer, pp 341–357, Jan 2013. ISBN No: 978-3-642-37948-2 (Print), 978-3-642-37948-2 (Online). ISSN No: 1867-8211 (Print) 1867-822X
72. Payasi RP, Asheesh Singh K, Singh D, Navneet Singh K (2015) Multi-objective optimization of distributed generation with voltage step constraint. *Int J Sci Eng Technol* 7(3):33–41
73. Payasi RP, Asheesh Singh K, Singh D (2012) Effect of load models and voltage step constraint on distributed generation operated at unity and variable power factors. *Int Rev Electr Eng (IREE)* 7(6):6296–6305
74. Singh D, Misra RK (2010) Multi-objective feeder reconfiguration in different tariff structures. *IET Gener Transm Distrib* 4(8):974–988

Chapter 16

Protection Issues in Microgrids and Multi-microgrids

Sachit Gopalan, Victor Sreeram, Yateendra Mishra and Herbert Iu

16.1 Introduction

The traditional power system is facing major challenges such as the need for drastic reduction in greenhouse gas emissions to combat climate change, low energy efficiency, and increased load demand [1]. These challenges can be partly addressed by integrating distributed generators (DGs) that use alternative energy sources such as wind, fuel cells, photovoltaic (PV), and biomass with the distribution system. The benefits of using renewable energy sources in DGs are that they reduce carbon emissions and pollution while improving the power quality and reliability in meeting the rising load demand. However, the direct interconnection of a large number of DGs with the distribution system becomes difficult to manage due to the intermittent nature of their generation. An emerging method for integrating larger numbers of DGs with the distribution system is to organise them as a microgrid (MG). MGs have been introduced at the low-voltage (LV) or medium-voltage (MV) level to supply electrical and heat loads within small communities in

S. Gopalan (✉) · V. Sreeram · H. Iu
The University of Western Australia, Perth, Australia
e-mail: sachit.gopalan@research.uwa.edu.au

V. Sreeram
e-mail: victor.sreeram@uwa.edu.au

H. Iu
e-mail: herbert.iu@uwa.edu.au

Y. Mishra
Queensland University of Technology, Brisbane, Australia
e-mail: yateendra.mishra@qut.edu.au

industrial and residential areas. The advantages of MGs to end-users and utilities are higher power quality and reliability, higher energy efficiency, reduced costs, and reduced carbon emissions. However, the MG has a limited load capacity of 10 MVA. Multi-microgrids (MMGs) were proposed by the EU More Microgrids research project [2–4] as a way to supply electric power from renewable energy sources to larger load pockets.

The presence of DGs in a distribution system poses some additional challenges to the design of protection systems [5, 6]. Bidirectional power flows within the distribution system can cause the loss of coordination between the overcurrent protection devices during faulted conditions. The conventional practice is to use an islanding detection method to disconnect all DGs based on IEEE Standard 1547 when faults occur in active distribution systems. Though this approach is suitable when there is a small number of DGs, the system reliability will be significantly affected with higher penetrations of DGs. The conventional overcurrent protection scheme for the distribution system assumes high fault currents [7–11]. When a fault occurs within a grid-connected MG, the fault currents are high enough to enable the overcurrent relays to function. However, when a MG is separated from the distribution system, the significantly lower fault currents contributed by the inverter-connected DG sources cannot trigger the operation of overcurrent relays. This chapter will first review several proposed coordination strategies and protection schemes that address these issues. An adaptive overcurrent protection scheme for MMGs is then proposed that extends the existing MG adaptive protection schemes. The central controller (CC) in the proposed scheme has more advanced functionality as it monitors the variations in generation and load in each MG for automatically adjusting the relay characteristics.

When fault conditions occur in MMGs, the existing strategy disconnects all the DG sources which prevents its continued operation following fault clearance [12]. MMGs also experience varying fault current levels due to contributions from DGs and MGs. The DG protection issues of blinding of protection, failed reclosing, and false tripping also occur in MMGs. An adaptive overcurrent protection scheme is proposed in this chapter to address these challenges. It uses a number of controllers to monitor the dynamic variations in generation and load in the MGs and to adjust the overcurrent relay characteristics as required. This scheme disconnects faulted grid sections while allowing the remaining healthy sections to continue operation as well as addresses the different protection problems due to the presence of DGs.

The rest of this chapter is organised as follows: Sect. 16.2 briefly describes the background related to MGs and MMGs as well as protection issues associated with DGs. The various protection schemes and coordination strategies for MGs are reviewed in Sect. 16.3. An adaptive overcurrent protection scheme for MMGs is proposed in Sect. 16.4. Section 16.5 concludes this chapter.

16.2 Background

16.2.1 Microgrids

Microgrids (MGs) are low-voltage (LV) or medium-voltage (MV) networks that can interconnect various DG microsources and storage devices with loads [11]. MGs can be either DC or AC grids. DG microsources use resources such as wind, photovoltaic (PV), biomass, hydro-, and combined heat and power (CHP) plants. Flywheels, batteries, and super-capacitors can be used as storage devices. DG sources that can either be AC or DC, storage devices, and loads are connected via power electronic interfaces to the MG. An individual MG has a maximum load capacity of around 10 MVA. A MG can operate when connected to the MV distribution grid or in stand-alone mode. MGs can be deployed in rural and urban communities, industrial sites, and commercial areas.

The generation–load balance within the grid-connected MG changes dynamically due to intermittent generation from renewable energy sources and variable load demand [10]. Variations in generation and load demand can also occur due to seasonal changes in the intensity of sunlight, wind, and temperature. A grid-connected MG can either import power from or export power to the MV distribution grid. A MG that exports excess generated power to the MV distribution grid is a net generator (NG). Conversely, a net load (NL) MG imports power from the MV distribution grid to supply the excess load within the MG.

The architecture of a MG control structure proposed in [2] is shown in Fig. 16.1. It consists of components which include a Distribution Management System (DMS), a Microgrid Central Controller (MGCC), Load Controllers (LCs), and Microsource Controllers (MCs). The DMS manages the overall MG network operation. A MGCC is used to control the operation of the loads and microsources in the MG. The load (LC) and microsource (MC) controllers communicate data to the MGCC, and the MGCC sends commands to these controllers to balance generation and load.

MGs provide several benefits over conventional distribution systems [7–11]. MGs have been employed to reduce transmission losses, prevent network congestion, and allow the end-customers at the LV network to continuously receive power during network outages. The advantages of MGs to end-users, society, and

Fig. 16.1 Control structure for a MG that contains LCs and MCs [2]

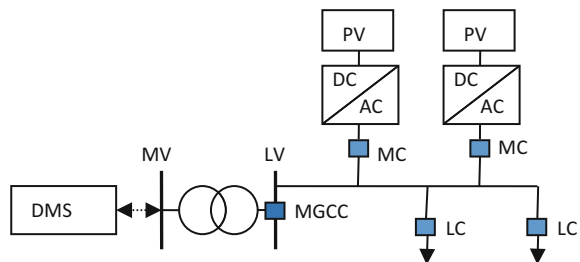


Table 16.1 Advantages and disadvantages of MGs

Advantages	Disadvantages
Reduces global warming and climate change	Has limited load capacity of 10 MVA
Supplies power to remote areas that cannot be easily reached from the main grid	Renewable energy sources are intermittent in nature
Can continue operation as single aggregated unit in islanded mode whenever power outages occur within distribution system	
CHP units directly meet heat and electricity requirements of customers	

utilities include higher power supply quality and reliability, higher energy efficiency, reduced costs of replacing electricity infrastructure, and reduced carbon emissions. Table 16.1 summarises the advantages and disadvantages of MGs.

16.2.2 Multi-microgrids

A multi-microgrid (MMG) consists of several individual MGs and other DGs connected to a MV distribution grid [2, 4]. It can be divided into smaller load pockets supplied by individual MGs. The MMG operates when either connected to the high-voltage (HV) transmission grid or islanded from it.

Figure 16.2 shows the proposed hierarchical frequency control scheme for MMGs in [13]. Microsource controllers (MCs) and MG central controllers (MGCCs) are present as agents that control the operation of DGs and MGs. The operation of the HV/MV substations is controlled by the remote telemetry units (RTUs). A Central Autonomous Management Controller (CAMC) is interfaced with a Distribution Management System (DMS) in a similar way to the scheme in Sect. 16.2.1. The CAMC performs the following tasks: reading active and reactive power measurement data from the MGCCs, DGs, and RTUs, and receiving commands from the DMS to balance generation and load by scheduling the operation of the MGCCs, DGs, and RTUs. This scheme operates in a similar way to that of the Automatic Generation Control (AGC) [14].

The presence of several MGs in a MMG enables it to provide improved reliability [2, 4]. It can also achieve higher stability and controllability by using a hierarchical control structure. These advantages are briefly outlined in Table 16.2.

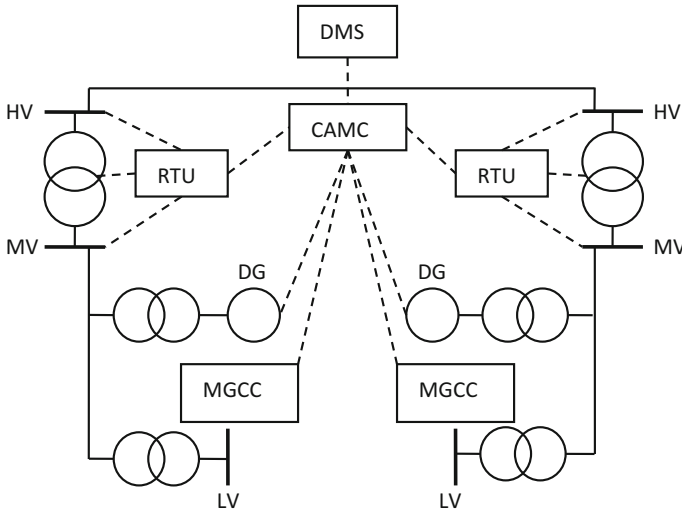


Fig. 16.2 Hierarchical frequency control structure for a MMG consisting of several LV-MGs connected to the MV grid [12]

Table 16.2 Advantages and disadvantages of MMGs

Advantages	Disadvantages
Supplies power to larger load pockets compared to single grid-connected MGs	Control and protection schemes are more complex compared to single grid-connected MGs
Presence of several MGs enables MMGs to provides improved reliability	
Hierarchical control structure ensures greater stability and controllability	

16.2.3 Protection Issues Associated with the Integration of Distributed Generation with the Distribution System

The protection of distribution systems and MGs containing DGs experiences a number of different problems [15]. These include the blinding of protection, false tripping, loss of coordination between fuses and reclosers, and failed reclosing. The following subsections describe these problems and review the possible solutions that have been proposed.

16.2.3.1 Blinding of Protection

The utility grid contribution to the fault current seen by the conventional over-current relays is reduced by the contributions from the DG sources [15]. This could

result in the relays not detecting the fault conditions since their thresholds have not been reached. Therefore, the reclosers, fuses, and relays may experience misoperation during fault conditions.

One possible solution for this problem proposed in [16] is to set overcurrent relay thresholds at a lower value so that faults can be detected despite reduced current levels due to the presence of DGs. However, this solution compromises the sensitivity and security of the protection system and may lead to false tripping when a fault occurs on an adjacent feeder. An adaptive overcurrent scheme proposed in [17] for a distribution feeder containing DGs decreases the overcurrent relay thresholds as the generation output increases. Another adaptive scheme in [18] uses the relationship between the overcurrent relay thresholds and the generator output to prevent the unnecessary disconnection of the distribution feeder.

16.2.3.2 False Tripping

False tripping occurs when DGs located on the healthy feeder section contribute to the fault on an adjacent feeder section connected to the same substation [15]. This results in the fault current seen by the conventional overcurrent relay on the healthy feeder section exceeding its threshold which then leads to the tripping of the healthy feeder section.

Directional overcurrent relays can be used to solve the problem of false tripping by detecting the direction of the currents from DG sources on the healthy feeder section [15]. If this relay on the healthy feeder section detects the fault on an adjacent feeder section, a transfer trip signal is sent to the CB on the adjacent feeder section to isolate the fault. This would enable the healthy feeder to remain connected to the grid. Another possible solution proposed in [19] is to use relays with a longer time delay that enables feeder sections containing DG sources to have longer fault clearing times.

16.2.3.3 Loss of Fuse–Recloser Coordination

The connection of DGs to the distribution system results in problems related to the loss of coordination between fuses and reclosers [15]. One problem is that the recloser is not able to detect the fault current levels correctly when DGs contribute towards it. The coordination between reclosers or between fuses and reclosers is also lost which can result in the fuse operating before the reclosers in clearing the fault. This leads to unnecessary interruptions when temporary faults are being cleared.

Brahma and Girgis [20] proposed a microprocessor-based recloser to restore the coordination between fuses and reclosers. Both the fast and slow trip curves are programmed in the microprocessor. The fast curve used during the first reclosing cycle should be programmed to be selective with the lateral fuses whenever DGs are connected to the distribution grid. The slow curve is used in the second

reclosing cycle to select the appropriate lateral fuses after DGs are disconnected from the distribution grid.

Another method of solving the fuse–recloser coordination problem proposed by Funmilayo and Butler-Purry [21] is by limiting the amount of fault current fed by the DG into the fault. The DG is connected to the main feeder via a lateral recloser and overcurrent relay. The lateral recloser is coordinated to operate before the recloser on the main feeder. When a fault occurs on the main feeder, its own recloser operates to clear the fault and then the lateral recloser operates to limit the fault current fed by the DG. These reclosers are reconnected after the temporary fault is cleared. If the temporary fault cannot be cleared by the reclosers, then the overcurrent relay disconnects the DG from the feeder. The fault can be cleared by the reclosers in a similar way to that of the conventional distribution grid. If the fault cannot be cleared by the reclosers, a permanent fault exists and the fault current will blow the fuse to remove the fault. If the fuse cannot clear the fault, the overcurrent relay will disconnect all the DGs in the distribution system and the recloser at the main feeder will lock out.

In the solution proposed by Tailor and Osman [22], the DGs are rapidly disconnected from the distribution grid whenever fault conditions occur. This is done to preserve the radial nature of the distribution grid and enable the fuses and reclosers to operate. A semiconductor switch containing two anti-parallel Gate Turn Off (GTO) thyristors and a microprocessor-based current sensing unit is used to perform the disconnection of the DGs during fault conditions.

16.2.3.4 Failed Reclosing

When a faulted feeder section is reclosed to clear the fault, one end of the feeder is left disconnected to extinguish the arc [15]. The DG connected to the feeder maintains the arc at the disconnected feeder end. This turns the temporary fault into a permanent one. DGs will also move away from synchronism with the main grid due to the load and generation becoming unbalanced. Therefore, the reconnection of the faulted section without synchronisation would lead to serious damage to DGs and high voltages and currents throughout the grid.

The problem of failed reclosing can be most effectively addressed by rapidly disconnecting the DG sources from the faulted feeder section before performing the reclosing operation [15]. The DGs are disconnected by the voltage or frequency protection relays based on the standard tolerances.

16.3 Review of the Existing Protection Schemes and Coordination Strategies for Microgrids

The protection of islanded MGs needs to consider the protection of the MV side of the MG, microsources, and distribution transformers as well as neutral grounding. In this section, various protection schemes and coordination strategies for MGs that address the protection challenges in both the grid-connected and islanded modes are reviewed.

16.3.1 Protection Coordination Strategies

Primary protection provides the initial action against the damaging impact of faults, whereas backup protection acts if the primary protection fails. Strategies are needed for coordinating the operation of primary and backup protection schemes. The following subsections will review the protection coordination strategies based on the optimisation methods, time grading, communication, and other techniques.

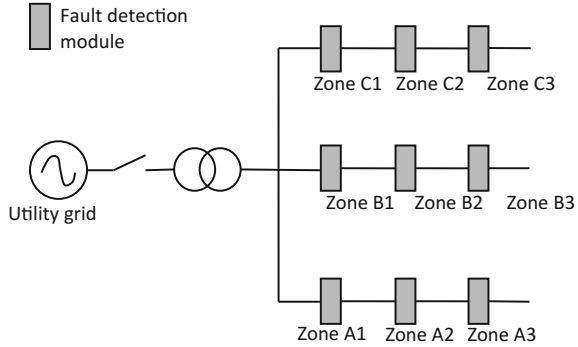
16.3.1.1 Optimisation Methods

Optimisation methods are used to solve the directional overcurrent protection coordination problem throughout the MG. The objective is to minimise the operating times of all the relays subject to different constraints. These constraints include backing up all relay and setting bounds on time dial settings (TDS) and pickup currents for each relay. Zeineldin et al. [23] solve the directional overcurrent protection coordination problem using the particle swarm optimisation (PSO) technique. This technique produces more accurate values than linear programming. Each relay in this approach has different settings for grid-connected and islanded modes of the MG. Najy et al. [24] employ a genetic algorithm (GA) to optimally coordinate the directional overcurrent relays. The GA technique is better able to exit local minima and converge to a better solution in faster time than the PSO technique. This method does not consider the fault ride-through of the synchronous generators nor the presence of inverter-interfaced DGs and energy storage devices.

16.3.1.2 Time Grading

Time-grading strategies determine the time delays in the operation of backup relays after the primary protection fails. Loix et al. [25] proposed a strategy for detecting and clearing faults within radial MGs that contain large numbers of inverter-interfaced DG microsources. In Fig. 16.3, each protection zone in a MG is

Fig. 16.3 MG containing multiple protection zones and corresponding fault detection modules [25]



covered by fault detection modules. When a fault occurs in a grid-connected MG, the traditional overcurrent protection is applied within a given time delay to detect the fault. Once this time delay is exceeded, the MG is disconnected from the grid and voltage measurements are used to detect the fault. Voltage and current measurements from the fault detection module are used to determine the direction for each fault type. Each module will selectively apply the time delays to clear the fault once the fault direction is known. The speed of the protection system operation can be improved when a communication network is included in the system. However, communication networks may also experience failures. The effectiveness of this scheme has not been evaluated.

A microprocessor-based protection strategy for both islanded and grid-connected MG operating modes was proposed in [26]. Each microprocessor relay in the MG consists of tripping, negative-sequence directional, three-phase protection, and interface modules as well as modules for phases A, B, and C. Each phase of the secondary mains feeder is protected by its corresponding phase module. The three-phase protection module uses zero/negative-sequence detection to provide redundant protection. Once a fault is detected by the primary protection relay, a time-grading technique containing directional elements is used to identify forward and reverse faults. If the primary protection relays fail, then different time delays will be applied selectively to each downstream relay until the fault is cleared. This scheme is able to adapt to different fault levels and types without using communication or adaptive protection devices. However, using the time-grading technique for protection coordination results in relatively long fault clearance times.

A control and protection scheme for the MG in both operating modes was proposed in [27]. The protection scheme coordinates the feeder and DG islanding protection within the MG. Differential protection is provided for each feeder, whereas each DG is protected by over/under-voltage and over/under-frequency relays. When a three-phase fault occurs on one of the feeders, the differential relays are activated. After a time delay, the islanding detection algorithms send the CB status and the DG interface control mode to the central control unit. If either the DG frequency or the voltage does not fall within their permissible ranges after a time delay, then the DGs are disconnected from the MG. The coordination between the

control and protection scheme prevents nuisance tripping of DGs and non-critical loads during islanded operation. This operation of this scheme is slower due to the absence of communication. Other fault conditions were not considered in this scheme.

16.3.1.3 Communication-Based

In communication-based, protection schemes, communication networks enable the interconnection of a central control unit with measurement devices and CBs. The central control unit determines the fault location by analysing the measured voltages and currents and sends trip signals to the nearby CBs.

Sortomme et al. [28] proposed a protection scheme using digital relays and communication for phase-A-to-ground faults. The primary protection uses the differential scheme for each feeder section to trip the switching device at each end of a faulted feeder. If the primary protection fails to operate for a feeder, a backup trip signal is sent after a time delay to the neighbouring relay on the same bus. Should either backup protection or the communication link fail, the relays employ tertiary protection in the form of comparative voltage protection until the system operation is restored. This scheme also detects high impedance faults (HIFs) from the measured differential current for faults that occur in islanded MGs. The looped configuration and ability to cope with communication failures increases the reliability of this scheme. However, placing relays and switching devices at each end of the feeder sections is costly. This protection scheme has not considered as errors and mismatches of the current transformers (CTs). It also assumes more advanced features in protective switchgear such as faster tripping times than currently available.

A scheme that uses an integrated protection and control (IPC) unit was proposed in [29] for radial grid-connected MG configurations. An optical Ethernet communication network is used to connect the IPC unit to the measurement devices, CBs, and control units at each bus. The IPC unit uses measurements such as currents, voltages, and other electrical quantities for making protection and control decisions that are to be sent to CBs and control units. The local feeder and remote busbar are protected using a pilot instantaneous overcurrent protection scheme. Communication networks enable this protection scheme to provide faster fault clearance times. However, this scheme has not considered the possibility of communication failures. The availability of communication channels is also limited.

A communication-based protection strategy has been proposed for different MG components which include feeders, buses, and DG sources by Dewadasa et al. [30]. Both the feeders and buses are protected by the primary differential scheme along with the backup overcurrent and under-voltage schemes. The differential scheme uses a characteristic containing user-defined slopes that define the operating and restrain regions. The backup protection schemes are only activated whenever communication failures are detected by the relays. On the other hand, DG sources are protected using under-voltage, overvoltage, reverse power flow, and

synchronism check relays. This protection strategy shows high levels of selectivity and sensitivity when detecting internal faults in both grid-connected and islanded MGs. It also ensures safe and reliable operation of the MG. However, this scheme does not consider the time synchronisation of the measured current phasors.

Nthontho et al. [31] proposed a wide-area differential scheme that protects a MG containing household PV systems against three-phase faults. The wireless mobile broadband connects the intelligent electronic devices (IEDs) and CBs located at each bus to the control centre. The real-time current measurements are monitored by the embedded sensors in the IEDs and these measurements are transmitted to the control centre. Advanced differential protection for each feeder is carried out by the control centre to determine the faulted location, send trip signals to the CBs at the faulted location, and apply auto-reclosing. Should the primary protection fail, backup protection will locate and isolate the fault using the current measurements and time-stamped Global Positioning System (GPS) coordinates. This scheme is simple to implement, provides effective operation, and can adapt to dynamic variations in generation and load in the MG. However, its operation has only been tested for small grid-connected MGs. This scheme has not considered the possibility of communication failures and the optimisation of the networking technologies.

Li et al. [32] investigated the communication-based differential and voltage-based schemes for islanded MGs. The differential scheme was deployed at every connection point in the MG. This scheme protects against both internal and external faults, can operate accurately, and works when there are changes in the MG topology. However, it can neither detect HIFs nor provide backup protection for adjacent feeders. Placing the relays at every connection point would make this scheme costly to implement. In the voltage-based scheme, the control centre uses the indicator voltage waveforms measured at each connection point to determine the fault type and location and sends trip signals to CBs at the faulted location. This method can accurately determine the faulted zone for large MGs when there is sufficient gradient voltage dip along the feeders. However, it does not work for shorter feeder distances due to the low gradient voltage dip. This method experiences a high computational burden.

A microprocessor-based communication-assisted protection strategy was proposed in [33] for MV-MGs. Directional, grid-connected, islanded, tripping, and interface modules are present in each microprocessor-based relay. The proposed strategy uses a communication network to connect a MG protection commander (MGPC) with the individual relays at each MG subsection. The MGPC uses the fault detection and directional signals from each relay to identify the faulted MG subsection. Primary protection trip signals are then sent by the MGPC to the CBs near the faulted MG subsection. Backup trip signals are sent to adjacent CBs after a time delay should the primary protection fails. If either the backup protection or communication fails, then time grading is applied to all CBs surrounding the faulted MG subsection. This strategy works effectively for different fault levels and types, MG operating modes, as well as different types, sizes, and locations of DGs. The use of communication links in this strategy gives it a faster fault clearing time than

the scheme in [26]. This scheme is improved further in [34] by adding a looped configuration to the MG to increase the reliability. These loop-forming lines are protected by an instantaneous differential scheme. However, the scheme in [34] does not consider the dynamic changes in generation and load.

Fletcher et al. [35] proposed a protection system design framework that combines both unit and non-unit protection for direct current (DC) MGs. The position of the feeder and its surrounding elements within the MG network determines the appropriate protection approach. If the coordination between the feeder and downstream protection devices cannot be achieved within the acceptable operating times, unit protection is adopted. Otherwise, non-unit protection is used for the feeder. This framework ensures accurate fault detection for internal zone faults. It also ensures that there is sufficient time for the protective devices at the load connection points to operate. The implementation of this framework minimises the system operating costs. The scheme only considers a MG with a single source power supply and no DG sources.

A fault protection and location method was proposed for a DC ring-bus MG in [36]. The MG is broken down into a number of protection zones which cover links and nodes. IEDs control CBs, probe power unit, and communication links in each protection zone. The currents flowing in each CB are monitored by the IEDs. If the currents exceed a threshold, then the overcurrent relays trip the CBs. For HIFs, the local and remote current measurements are used by the differential relays to trip the CBs around the faulted zone. If one of the CBs for the faulted link is not tripped, then the link IEDs will trip all of its CBs. The adjacent IEDs will trip the CBs on the faulted nodes. The faulted zones become locked out in this case. The probe power unit performs the reclosing function for the zones with temporary faults. If the fault is cleared within a fixed number of reclosing attempts, then the IEDs send closing signals to the CBs for the previously faulted zones. Otherwise, the fault is considered to be permanent and the faulted zone becomes locked out. The fault location scheme improves the system reliability and the mean time between the failures of protective switchgear. The fault location estimation is affected by the accuracy of parameters and measurements.

Ustun and Khan [37] proposed a multi-terminal hybrid protection strategy for MGs consisting of both traditional differential and adaptive protection schemes. The traditional differential scheme is used in high-sensitive areas which include transformers and sensitive loads in the MG. The adaptive protection scheme based on [38, 39] is used as the default. It is also the backup strategy when the differential scheme fails in high-sensitive areas of the MG. In high-sensitive areas, MGs have higher fault current levels compared to the less sensitive areas. Dynamic switching between the adaptive and differential schemes addresses the issue of communication failures. The relays monitor the signal-to-noise ratio (SNR) of the communication links to the MG Central Protection Unit (MCPU). If the SNR falls below the switching threshold when the adaptive scheme is active, then the differential scheme is activated. The protection scheme switches from the differential to the adaptive scheme once the switching threshold is exceeded by the SNR. This hybrid protection strategy is robust against communication failures and can protect its

expensive and sensitive equipment. However, the performance of this strategy is yet to be tested experimentally. It has also not been implemented on a real-life communication system.

16.3.1.4 Other Coordination Strategies

Primary and backup protection strategies that do not use communication links or time grading were proposed by Nikkhajoei and Lasseter [40] for both grid-connected and islanded MGs. For single-line-to-ground faults, primary protection uses differential current detection for zones upstream of the fault and zero-sequence detection for downstream zones. Line-to-line faults are detected using the negative-sequence current. Both single-line-to-ground and line-to-line faults are protected using I^2t and under-voltage backup protection. This scheme has not covered three-phase faults and does not enable single-phase tripping. It also lacks systematic coordination due to the absence of communication links and time grading.

Salomonsson et al. [41] proposed a protection system that uses primary protection schemes for the converter, battery, and feeder to protect against pole-to-pole and pole-to-ground faults that occur in a radial LV DC MG. Converter protection requires the measured current derivative to be compared against a threshold. On the other hand, the battery is protected by overcurrent relays and the DC link capacitor is protected using under-voltage relays. Ground faults are detected for feeders by comparing the measured ground currents of the converter and battery against their predefined settings. The CBs near the converter and battery would only be opened if the primary protection for the feeder fails. Backup protection is provided to the converter using fuses on the AC side. This strategy can easily detect and clear low-impedance ground faults. Using the converter current derivative and DC link under-voltage schemes enables the converter to be effectively protected. However, the low ground fault currents make the detection of HIFs within the MG difficult. The protection methods also lack systematic coordination.

A coordination strategy with directional overcurrent and earth fault protection relays for a biomass MG in Malaysia has been proposed in [42]. Non-directional phase and earth fault overcurrent relays are used for branches that do not link the power sources. Directional phase and earth fault overcurrent relays protect the branches that link to power sources and the main grid. The under-voltage relay is adopted for earth fault protection on the delta side of transformers since there is no grounded neutral. The three-phase fault was used to grade the phase overcurrent relays. The earth fault relays were graded by the single-phase-to-ground fault. This coordination strategy provides protection for all components in the MG. There is no systematic coordination between the protection relays.

16.3.2 Protection Schemes

Protection schemes enable relays to compare the measured data such as voltages and currents against their predefined thresholds. When these thresholds are exceeded, the relays send trip signals to the CBs. The protection schemes vary according to the operating characteristics defining the trip thresholds. The various schemes that have been proposed in the literature are discussed in the following subsections.

16.3.2.1 Voltage-Based

Voltage-based protection schemes are proposed by Al-Nasseri et al. [43–45] for islanded MGs containing inverter-interfaced microsources for different fault conditions. The measured utility voltages undergo multiple computations before being used to determine the fault type and zone. In [43], once the disturbance voltage exceeds the threshold for a particular fault type, the faulted zone is tripped. In [44], the mean average value of any two relays within the MG is compared against the measured voltage transmitted between these two relays to identify the faulted zone in the network. In [45], the trip signals are activated once the average voltages that are determined from the disturbance voltages for each generator exceed their thresholds. These schemes protect against internal and external faults that are relative to any zone. However, it does not cover HIF protection and does not provide single-phase tripping.

16.3.2.2 Harmonics Content-Based

Al-Nasseri and Redfern [46] proposed a protection scheme that uses the harmonics content of the inverter output voltage to detect fault conditions in the grid-connected MG containing solid-state power converter-interfaced DGs. The measured inverter phase voltages are converted to the frequency domain via discrete Fourier transforms (DFT). The windowing function extracts the fundamental frequency and the Total Harmonic Distortion (THD) of each phase voltage which are then used to determine the fault type. The fault location is determined by computing the THD sum for each generator and comparing them with each other. This scheme works for any fault condition and impedance. It does not accommodate additional DGs and several dynamic loads.

16.3.2.3 Admittance Relaying

The feeder segments inside a radial MG that is connected by back-to-back converters to the utility network are protected against the three-phase fault by

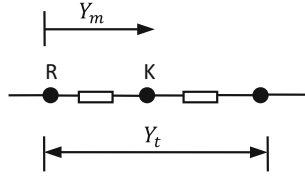


Fig. 16.4 Feeder segment consists of the measured admittance Y_m between arbitrary points R and K and admittance across entire feeder Y_t [47]

admittance relays proposed in [47]. Figure 16.4 shows the measured admittance Y_m between the relay and a point K on the feeder section and the total admittance Y_t across the feeder. The normalised admittance Y_r is determined by the following equation:

$$Y_r = \left| \frac{Y_m}{Y_t} \right| \quad (16.1)$$

The tripping time is determined from the inverse-time characteristic using the value of Y_r by the following equation:

$$t_p = \frac{A}{Y_r^\rho - 1} + k \quad (16.2)$$

where A , ρ , and k are known constants. The admittance relay detects a fault once Y_r exceeds 1 and sends trip signals to CBs after a time delay t_p near the faulted location. Backup protection is provided by each upstream admittance relay to its adjacent downstream relay. Safety margins are not required in this scheme since the inverse-time characteristic of each admittance relay can adequately cover their protection zones. However, this scheme has only been tested for small MG configurations.

16.3.2.4 Adaptive

In each adaptive protection scheme, different topologies are to be protected against all the possible short-circuit fault conditions. The relay database stores the calculated short-circuit fault currents. For any changes in grid topology, the relay database updates the new short-circuit current settings to the relays.

In the adaptive protection scheme proposed in [3], communication links were used to connect a MGCC to directional overcurrent relays at each bus. Offline calculations were performed by constructing event and action tables corresponding to the CB statuses and relay settings for the different MG topologies. The online operation of this scheme requires the MGCC to continually monitor the operating state of the MG and configure the relays with the extracted information from the

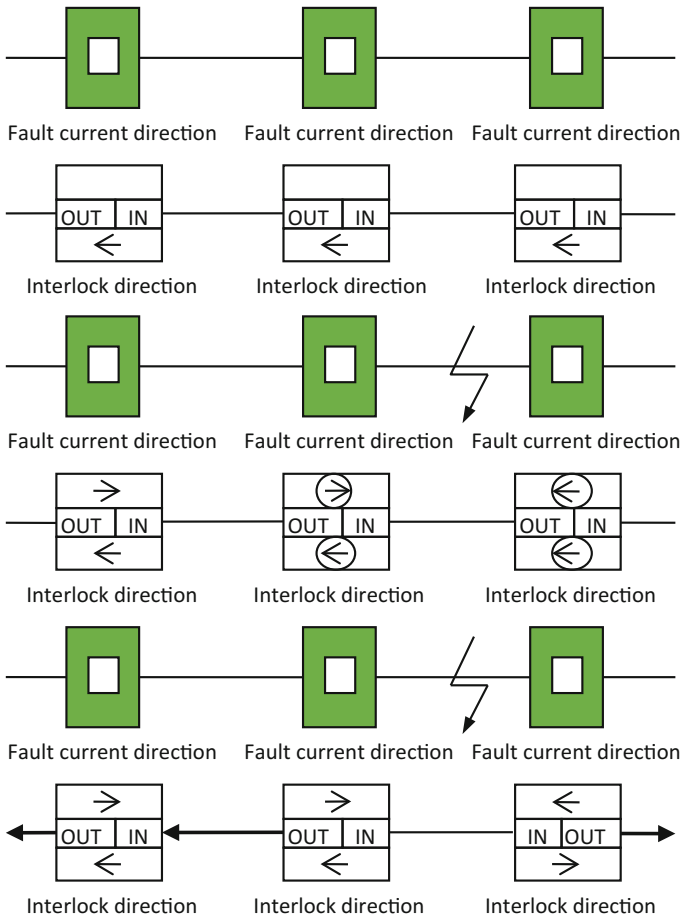


Fig. 16.5 Directional interlock for the adaptive protection scheme [3]

event and action tables. For the real-time operation of this scheme, the relays detect the fault incidence by comparing the current measurements against the relay settings. The fault location is then determined by comparing the fault current direction against the present interlock direction shown in Fig. 16.5. This scheme works effectively for different MG topologies and all fault types. The use of communication links provides improved speed of operation. However, this scheme uses excessive memory to store large amounts of offline calculations for larger MG topologies. This scheme does not protect against HIFs nor enables new loads and DGs to be connected to the MG.

Laaksonen [48] proposed a protection scheme for a LV-MG that enables a communication network to be connected between the MG Management System (MGMS) and different MG components. Protection strategies for both the MG

operating modes were developed for the Point of Common Coupling (PCC), LV feeders, loads, and DG units. The MGMS continually detects changes in the MG operating mode and sends appropriate settings and thresholds to the relays for each component. This scheme is able to withstand double-phase faults. The protection is fast, selective, and reliable due to the high-speed communication links. However, this scheme has not considered communication failures and does not support the plug-and-play of DGs.

An adaptive scheme that uses a central controller to protect a MG has been proposed by Ustun et al. [38]. The TCP/IP-based Ethernet communication system is used to connect a MG central protection unit (MGCPU) with all relays located at each bus and the DG. The MGCPU receives interrupts for calculating and updating the fault current thresholds in the relays whenever there are any changes to the MG configuration. Once the relays detect that their thresholds are exceeded by the measured currents, they send signals to set their fault detection statuses to the MGCPU and trip their corresponding CBs to isolate the fault. The universal models that use IEC 61850 and IEC 61850-7-420 enable the plug-and-play of DGs in this scheme. However, it is unable to cope with changing relay connections and does not calculate the fault current coefficient. The dynamic behaviour of the communication network has not been tested for this scheme. This scheme is extended in [39] to assign operating parameters which include the fault current coefficient and time-delay assignment for automating the calculation process. It adapts to dynamic changes within the MG and deals with new deployments of loads and DGs. However, the scheme needs to be extended to larger and more complex MGs.

16.3.2.5 Differential

Sortomme et al. [49] proposed a differential zone protection scheme to use an optimal number of relays and sensors in each protection zone. Current sensors are placed on the secondary side of the transformers for each load, and the relays are placed at the DG source locations. Faults are detected by the zone relays when the DG source currents exceed the sum of the load currents within the zone. The relays send trip signals to the DGs at the faulted zone as soon as a fault is detected. The optimal allocation of sensors, relays, and CBs was made by a genetic algorithm to minimise the total cost. This scheme is less expensive than the differential protection scheme in [28]. However, experimental validation of this scheme's operation has not been carried out.

A distributed statistical classifier relaying scheme has been proposed for islanded MGs containing inverter-interfaced DGs by Casagrande et al. [50]. The relay consists of the feature extraction, statistical classifier, communication channel, and differencing operator modules. The feature extraction module retrieves relevant features from the measured voltage and current time series. These features include the root mean square (RMS), THDs, and symmetrical components of voltage and currents as well as the power factor angles. Each relay transmits their feature vectors to other relays via the communication channel. The differential operator

subtracts the difference between the local and remote features to form the differential feature vector. The statistical classifier uses the differential and local feature vectors to make a decision on the occurrence of a fault within the network. This scheme protects against all the fault conditions. It is more effective than traditional differential relays based on the magnitude of fault current and shows high classification accuracy. However, the presence of communication infrastructure throughout the MG makes this scheme expensive to implement. It cannot adapt to dynamic changes in load and generation in the MG.

Kar and Samantaray [51] proposed a differential energy-based protection scheme for MGs using the S-transform technique. The measured currents at both ends of each feeder are converted to frequency domain using the S-transform technique. The resulting time–frequency contours are subsequently used to compute the differential energy for detecting the fault patterns. This value is compared against different thresholds for grid-connected and islanded modes of the MG as well as HIF conditions. The S-transform technique for computing the differential energy effectively detects faults within the MG. The differential energy technique is less sensitive to synchronisation error than the conventional differential current scheme. This scheme reliably protects against all the shunt faults and HIFs and works for both the grid-connected and islanded modes of the MG compared to the conventional differential current scheme. However, the thresholds are not adaptive to different MG topologies.

A differential protection scheme has been proposed for smart DC MGs in [52]. The central microcontroller sums all the sampled current measurements stored in memory and compares them with the trip threshold. Trip signals are sent to the CBs near the faulted sections when the threshold is exceeded. This scheme operates with a faster speed on the order of a few microseconds when implemented on a hardware prototype compared to traditional current differential protection schemes. However, this scheme is yet to be implemented on a larger scale DC network. The stability and reliability of this scheme has not been tested rigorously. This scheme also has measurement synchronisation issues.

16.3.2.6 WPT-Based

Saleh et al. [53] proposed a digital protection technique that utilises WPTs to detect and classify transient disturbances that occur in MGs. The vector of current samples is formed using the d-q components of the measured phase current samples. The high-frequency subband WPT coefficients are calculated by performing the circular convolution operation on both the vector of current samples and the half-band digital high-pass filter. A fault is detected when the high-frequency subband WPT coefficients are non-zero. Trip signals are subsequently sent to the faulted location. This technique is independent of the type, rating, and parameters of the protected equipment as well as the different fault current levels. Different types of transient disturbances have been accurately detected, classified, and isolated by the proposed technique. The technique is accurate, fast, simple, and reliable when evaluated by

simulation software and a hardware prototype. This technique is extended in [54] by using an index to coordinate the operation of multiple relays within the MG. This index uses signature information which includes the low-frequency approximations and high-frequency details from the d-q components of the measured currents. A fault is detected when the coordination index is zero and the first-level WPT details are non-zero at the fault location. The technique in [54] has improved coordination between the relays through the use of the coordination index. However, the technique in [54] has not been tested for larger MG networks.

16.3.2.7 Travelling Wave-Based

A travelling wave-based protection scheme for MGs containing inverter-based DG sources has been proposed in [55]. Each bus in the MG has a local IED that monitors the wavefronts. If they exceed a threshold, the local IED at each bus sends data which include the instrument transformer number, circuit number, time of the first waveform arrival, and its polarity to the central IED. The central IED uses the information from all the bus IEDs to identify and isolate the faulted line. The fault location and isolation is carried out by the central IED logic. If there are more than two lines at any bus, then the line with a different polarity to the other lines will get tripped. The line with the same polarities at both ends will get tripped when there are only two lines connected to the bus. For an instrument transformer at a single end of a bus, the trip signal should only be sent to the bus when the two wavefronts at the same end have the same polarity. This scheme works effectively under noisy conditions. It is also stable during non-fault disturbances such as the initialisation of the motor, dynamic changes between grid-connected and islanded modes, as well as changes in the MG topology. However, this scheme has not been implemented on a hardware prototype. It has not considered switch-on fault conditions, multiple fault locations, and system earthing.

16.3.3 Discussion of Coordination Strategies and Protection Schemes

Several coordination strategies and protection schemes have been proposed for MGs to address the challenges of bidirectional power flows from DGs and lower fault current levels within islanded MGs. The advantages and disadvantages of the coordination strategies and protection schemes are given in Tables 16.3 and 16.4, respectively.

Primary and backup protection are included in the protection coordination strategies. The optimisation techniques are suitable for grading directional over-current relays since it minimises the operating times of the relays and enables them to be backed up [23, 24]. However, they do not consider the different MG operating

Table 16.3 Advantages and disadvantages of several coordination strategies

Coordination strategy	Advantages	Disadvantages
Particle swarm optimisation [23]	More accurate than linear programming	Each relay has different settings for grid-connected and islanded modes of the MG
Genetic algorithm [24]	Better able to exit local minima and converge to a better solution in faster time compared to PSO	Directional overcurrent protection coordination does not consider the fault ride-through of the synchronous generators nor the presence of inverter-interfaced DGs and energy storage devices
Time grading [25]	Absence of communication increases the reliability of the scheme	Speed of operation could be slower due to the absence of communication network No experiments have been carried out to evaluate the scheme
Microprocessor-based strategy for LV-MGs [26]	Can protect against different fault current levels	Fault clearing times are slower due to the absence of communication network
DG and line protection for MG [27]	Coordination between the control and protection scheme prevents nuisance tripping of DGs and non-critical loads during islanded operation	Operation is slower due to the absence of communication Protection against other fault conditions not covered
Communication-assisted digital relays [28]	Scheme has increased reliability due to looped configurations and ability to address communication failures	Placing relays and switching devices at each end of all feeders is costly Scheme does not consider CT errors and mismatches Requires technical features not available in state-of-the-art equipment

(continued)

Table 16.3 (continued)

Coordination strategy	Advantages	Disadvantages
Integrated protection and control scheme [29]	Experiences rapid fault clearance	Does not consider possibility of communication failures or lack of availability of communication network
Communication-based protection strategy [30]	Highly selective and sensitive when detecting internal faults in both MG operating modes Provides safe and reliable operation	Time synchronisation of measured current phasors not considered in strategy
Wide-area differential protection [31]	Adapts to dynamic behaviour of generation and load in MGs Simple and effective technique	Only tested for MG containing small grid-connected PV systems Communication failures and optimisation of communication technologies not considered
Communication-based protection schemes [32]	Differential protection works for internal and external faults and can operate accurately for different MG configurations Voltage measurement method accurately determines faulted location provided that MG is large and sufficient gradient voltage dip exists along faulted feeder sections	Differential protection cannot detect HIFs, provide backup protection to neighbouring feeders, and is costly to implement Insufficient gradient voltage dip in voltage measurement method makes it unable to cope with reduced feeder distances Voltage measurement method has increased computational burden
Communication-assisted microprocessor-based strategy for MV-MGs [33]	Robust for different fault current levels, MG operating modes, and type, size, and location of DG units Experiences fast fault clearance times	Looped configuration of MG not considered
Communication-based strategy for looped MGs [34]	System reliability improved by using looped feeders	Does not consider the dynamic changes in generation and load (continued)

Table 16.3 (continued)

Coordination strategy	Advantages	Disadvantages
Unit and non-unit protection of DC MGs [35]	Framework enables accurate fault detection for internal zone faults Ensures sufficient time for the protective devices at the load connection points to operate. Minimises system operating costs	Only considers a single source power supply MG does not contain any DG sources
Fault protection method for DC MG [36]	Improves system reliability and mean time between failures of protective switchgear	Fault location estimation affected by the accuracy of parameters and measurements
Multi-terminal hybrid protection strategy of MGs [37]	Robust against communication failures Able to protect its expensive and sensitive equipment	Performance of this strategy is yet to be tested experimentally Strategy has also not been implemented on a real-life communication system
MG protection coordination strategy [40]	Provides primary and backup protection	Strategy does not consider three-phase faults Coordination of primary and backup modules not systematic Single-phase tripping not enabled
LV DC MG protection [41]	Easily detects and clears low-impedance ground faults. Combination of DC link voltage and converter current derivative makes converter protection more effective	HIFs difficult to detect due to low ground currents Protection methods do not have systematic coordination
Directional overcurrent and earth fault protection for MG [42]	Provides adequate protection for all the components in the MG	No systematic coordination between the protection relays Does not cover other fault types

Table 16.4 Advantages and disadvantages of various protection schemes

Protection scheme	Advantages	Disadvantages
Voltage-based [43–45]	Protects against faults that are internal and external to zones	Single-phase tripping and HIFs not considered
Harmonics content-based [46]	Works for any fault impedance. Detects any fault condition	Does not accommodate dynamic changes of the DG and load. Islanded mode of the MG not considered
Admittance relaying [47]	Each upstream relay provides backup to their downstream relay Safety margins not used for inverse-time characteristic of relay	Assumes the MG to be a small system
Novel adaptive protection scheme [3]	Can adapt to different MG configurations Communication makes speed of operation faster	Large amounts of computational memory would be used by offline calculation data HIFs not considered in scheme. Does not enable new loads and DGs to be connected to MG
Adaptive protection for future MGs [48]	Fast, selective, and reliable operation	Communication network failures not considered in scheme New deployments of plug-and-play DGs not present in MG
Centralised protection scheme based on IEC 61850-7-420 [38]	Plug-and-play DGs present in MG uses universal models based on IEC 61850 and IEC 61850-7-420	Fault current coefficient not calculated in scheme Unable to adapt to complex systems with changing relay connections. Dynamic behaviour of communication network not considered in scheme
Centralised protection scheme based on assignment of two parameters [39]	Adapts to dynamic changes within the MG and accommodate new deployments of loads and DGs	Does not consider larger and more complex MGs
Differential zone [49]	Deployment of switchgear in scheme reduces costs and is more effective	No experiments have been performed to evaluate the proposed scheme
Distributed statistical classifier relaying scheme [50]		Expensive to implement due to the presence of communication infrastructure throughout the MG. (continued)

Table 16.4 (continued)

Protection scheme	Advantages	Disadvantages
	<p>Protects against all fault conditions. More effective than traditional differential relays based on the magnitude of fault current</p> <p>High classification accuracy</p>	<p>Not adaptable to the dynamic changes in load and generation in the MG</p> <p>Only works for islanded MGs</p>
<p>Differential energy protection scheme [51]</p>	<p>Effectively detect faults within MG. Less sensitive to synchronisation error compared to conventional differential current scheme</p> <p>Reliably protects against all the shunt faults and HIFs</p> <p>Works for both grid-connected and islanded modes compared to conventional differential protection schemes</p>	<p>Thresholds not adaptive to the MG topology</p>
<p>High-speed differential protection scheme for smart DC MGs [52]</p>	<p>Operates faster than traditional current differential protection schemes</p>	<p>Not implemented on a larger scale DC network</p> <p>Stability and reliability of this scheme has not been tested rigorously</p> <p>Scheme contains measurement synchronisation issues</p>
<p>WPT-based digital protection scheme [53]</p>	<p>Independent of type, rating, and parameters of the protected equipment as well as different fault current levels</p> <p>Accurately detects, classifies, and isolates different transient disturbances</p> <p>Accurate, fast, simple, and reliable scheme</p>	<p>Lacks systematic coordination between the relays</p>
<p>Signature-coordinated digital multirelay protection scheme [54]</p> <p>Travelling wave-based protection scheme [55]</p>	<p>Improved coordination between the relays</p> <p>Works effectively under noisy conditions</p> <p>Achieves stability during non-fault disturbances such as the initialisation of the motor, dynamic changes between grid-connected and islanded modes, as well as changes in MG topology</p>	<p>Has not been tested for larger MG networks</p> <p>Yet to be implemented on a hardware prototype</p> <p>Does not consider switch-on fault conditions, multiple fault locations, and system earthing</p>

modes and the dynamic changes in generation and load. In most communication-based coordination strategies, a central controller is connected to individual relays in the MG. Communication links enable high speed of operation in these coordination strategies. However, only some of these schemes consider communication failures [28, 33, 37]. Coordination strategies that use time grading have slower fault clearing times [25, 26]. The coordination strategies that neither use communication nor time-grading techniques do not systematically coordinate both primary and backup protection [40, 41].

The protection schemes vary based on operating characteristics used for fault detection. Voltage-based schemes in [43, 44] are most effective for grounded faults within islanded radial MGs. The harmonic content-based protection scheme in [46] works for small MGs containing few DG sources. The admittance relaying scheme in [47] protects radial MGs consisting of different feeder sections. Adaptive protection schemes in [38, 39, 48, 56] are able to protect different radial MG topologies. The differential protection scheme for smart DC MGs in [52] only works for a small-scale hardware prototype. The differential zone protection scheme can effectively protect multiple zones in the MG [49]. The distributed statistical classifier relaying scheme in [50] only works for small islanded MGs containing fewer inverter-interfaced DGs. The differential energy protection scheme in [51] can be extended to larger MG topologies. The WPT-based schemes in [53, 54] effectively detect and isolate transient disturbances for a hardware prototype of a MG. The travelling wave-based protection scheme deals with both grid-connected and islanded MGs as well as different MG topologies [55].

16.4 Adaptive Overcurrent Protection Scheme for Multi-microgrids

There are a number of protection challenges in MMGs due to the presence of DGs and MGs in them [57]. The fault current levels vary in the MMG due to power flows from several MGs and DGs. The protection scheme for MMGs needs to deal with the intermittency in generation and the variable load demand. The presence of DGs can also cause problems such as blinding of protection, false tripping, and failed reclosing [58]. In the existing MMG protection scheme, all the DGs are disconnected whenever a fault occurs in any part of the MMG, making it impossible to continue operation under fault conditions.

As discussed in Sect. 16.3.2.4, several protection schemes have been proposed for single grid-connected MGs to deal with different fault current levels when there are dynamic changes in the MG topology, generation, and load. The protection scheme for MMGs proposed in this chapter builds on these MG protection schemes.

A new adaptive overcurrent protection scheme for MMGs is proposed in this chapter to isolate a faulted section from the rest of the MMG while allowing continued operation of the healthy sections. It also addresses the protection

problems caused by the presence of DGs including the blinding of protection, failed reclosing, and false tripping. The proposed scheme has a central controller (CC) to enable the communication between the MG central controllers (MGCCs) to monitor the dynamic changes in each MG and update the relay characteristics. The proposed scheme is designed to achieve faster tripping times for the most severe fault conditions compared to existing adaptive MG protection schemes in [3, 38, 39]. The effectiveness of the proposed protection scheme is evaluated for typical MMG scenarios containing different combinations of NL- and NG-MGs by simulation.

16.4.1 Multi-microgrid Network Configuration

The MMG models in this chapter consist of two individual MGs interconnected via transformers and long feeders to a HV transmission grid as shown in Fig. 16.6. The MG scenarios considered in this study include NL-MGs and NG-MGs for which the load capacities and power flow directions are indicated in Fig. 16.6. The different MMG components in the model are described below.

The HV transmission grid modelled as an infinite bus has voltage of 138 kV and frequency 60 Hz. The HV/MV transformers (25 MVA) have a grounded wye-connected HV side (138 kV) and a wye-connected MV side (25 kV). The transformers are connected to the HV transmission grid via feeders of length 60 km.

Figure 16.7 (adopted from [33, 34]) shows one of the MGs used in the MMG model with 19 buses and voltage rating of 25 kV. The Point of Common Coupling (PCC) is between the HV/MV transformer and the MG. The power ratings of DG sources inside the MG are also indicated in Fig. 16.7.

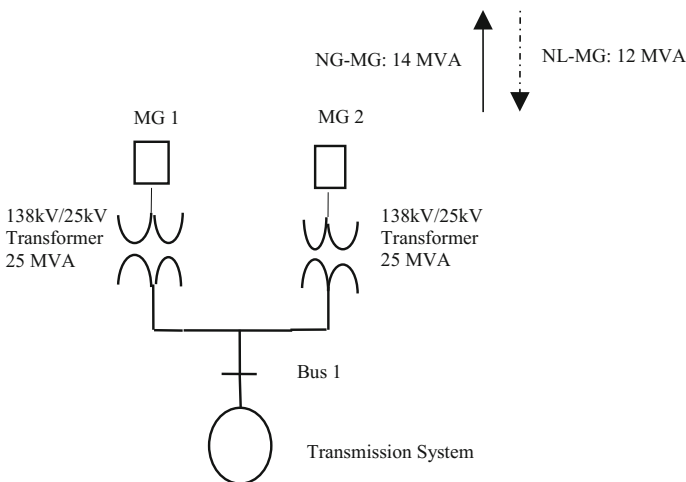


Fig. 16.6 Single-line diagram of the MMG configuration containing two MGs

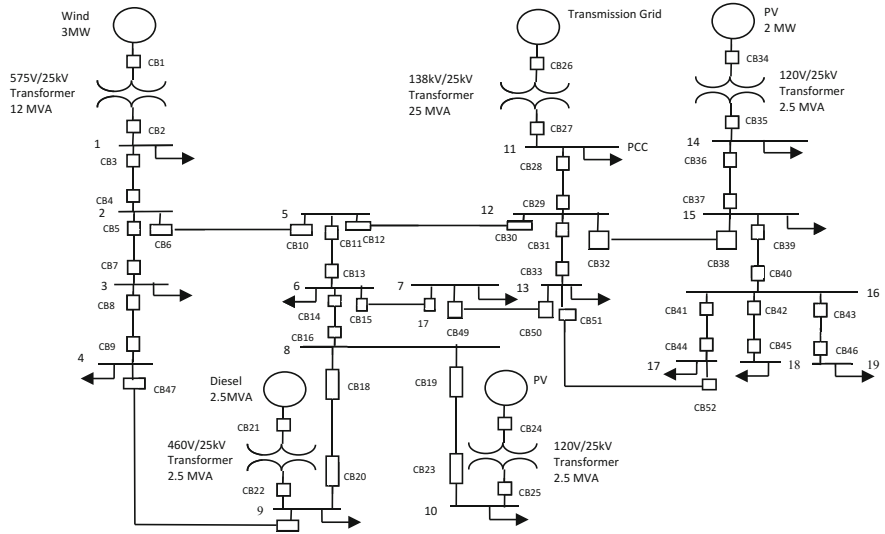


Fig. 16.7 Single-line diagram of a MG

Table 16.5 Balanced bus loads for MGs

Bus	P (MW)	Q (kvar)
1	0.5	2
3	0.5	2
6	0.5	2
7	0.5	2
9	0.5	2
10	0.5	2
13	2.5	2
14	2.5	2
15	0.5	2
17	0.5	2
18	0.5	2
19	0.5	2

The radial feeders in the MGs have a line length of 25 km. Looped feeders of the same length are included in the MGs to improve the reliability by maintaining the generation–load balance during fault conditions. These feeders are located between buses 4 and 9, 7 and 13, and 13 and 17 in each MG configuration.

The static loads are modelled as three-phase balanced delta-connected impedances with ungrounded neutrals. Table 16.5 shows the active and reactive powers of the static loads in each MG. The dynamic load connected on bus 5 has initial active and reactive powers of 2 MW and 5 kvar, respectively. The static loads on

bus 11 for the NL-MGs and NG-MGs have active and reactive powers of (2.5 kW, 0.5 kvar) and (2 MW, 2 kvar), respectively.

Fixed-speed squirrel-cage induction generators (575 V, 3 MW) have been used to model wind turbines. A compensation capacitor (-1.2 Mvar) is connected in parallel with each induction generator. A 12 MVA transformer connects a wind turbine to the MG. The PV sources (120 V, 2 MW) are connected to the MG via 2.5 MVA transformers. The diesel generator (460 V, 2.5 MVA) is modelled as a diesel engine connected to a synchronous generator. A stabilising resistor (10 kW) is present in parallel with the synchronous generator. A 2.5 MVA transformer connects the diesel generator to the MG.

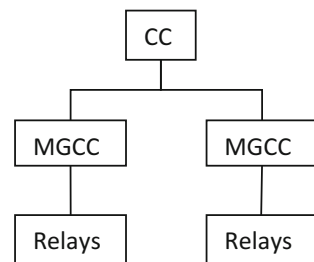
16.4.2 Description of Scheme

This scheme modifies the relay characteristics in the MMG based on variations in generation and load. Each bus is protected by an inverse definite minimum time (IDMT) overcurrent relay. This scheme also includes backup protection. The structure and operation of the proposed scheme is described below.

The proposed protection scheme consists of a CC, MG controllers (MGCCs), measurement devices, relays, circuit breakers (CBs), and communication links. The hierarchical control structure that indicates the communication links between the different controllers in the MMG is shown in Fig. 16.8. The CC is located near the HV/MV transformer and is connected to the MGCCs. Each MGCC is also in turn connected to the relays. This structure enables the continuous coordination of the controllers and relays to monitor the variations in generation and load and to update the relay operating characteristics. The relays, measurement devices, and CBs are located at each bus in the MMG. Each bus is protected by an inverse definite minimum time (IDMT) overcurrent relay.

The CC monitors any changes in the generation and load and updates the operating characteristics of all the relays based on these changes. The MGCCs continually measure the current levels at the point of common coupling (PCC) points of the MGs and transmit this information to the central controllers. If the CC detects any gradual variations to the current level, it calculates the operating parameters of the inverse overcurrent characteristic curves for each relay and sends

Fig. 16.8 Hierarchical control structure for the MMG as part of the adaptive overcurrent protection scheme



them to the respective MGCC. The equation for the IEEE standard inverse over-current characteristic curve is given as

$$t_p = \left(\frac{A}{M_I^p - 1} + B \right) \times \text{TMS} \quad (16.3)$$

where A , B , and p are the constants of the characteristic curve, TMS is the time multiplier setting, M_I is the ratio between the measured fault current and the relay threshold current, and t_p is the calculated time delay [58]. The equation for M_I is given as

$$M_I = \frac{I_x}{I_p} \quad (16.4)$$

where I_x is the measured fault current and I_p is the relay threshold current. The relay threshold current has to be greater than 1.25 times the measured maximum load current and less than the minimum fault current for both the primary and backup feeders. The TMS is determined by the equation,

$$\text{TMS} = \frac{T}{T_{\text{TMS}=1}} \quad (16.5)$$

where T is the desired time delay of the relay and $T_{\text{TMS}=1}$ is the largest time delay obtained from the characteristic curve for a TMS value of 1. These characteristic operating curves are updated in each relay by the MGCC.

The design of the adaptive overcurrent protection scheme needs to address the various DG protection problems mentioned in Sect. 16.2.3. As discussed in Sect. 16.2.3.1, the blinding of protection is avoided by setting the appropriate thresholds to take into account the reduced utility grid contribution to the fault current due to the contribution of DGs. The measured currents at each DG source are sent to the CC via the MGCCs and are used to calculate the thresholds for each relay. The relays will then correctly detect and isolate the faults that occur near DG sources.

In order to deal with the false tripping problem, the current thresholds are set at a high enough value to prevent tripping of the healthy feeder sections. As mentioned before, the current thresholds are set by the CC to lie between the minimum fault current levels and the maximum load current. It will also allow the DGs near the healthy feeder sections to ride through the fault located on the adjacent feeder section. This approach is similar to the adaptive overcurrent relays discussed in Sect. 16.2.3.2.

The bidirectional power flows from DGs are addressed by varying the thresholds based on the DG contributions to the fault current at any given time. The CC sets the thresholds for each relay by adding the individual contributions from each DG source. The power flow directions from different DGs are used by the CC to determine which DGs are contributing to the total fault current on each feeder

section. The methods described in Sect. 16.2.3.3 either disconnect or limit the infeed of DGs during fault conditions so that the fuses and reclosers operate in the conventional radial distribution system. The solution proposed in this thesis improves on these methods by enabling the DGs in the healthy sections to remain connected to the MMG and maintain their infeed undiminished during fault conditions.

To prevent failed reclosing, the DGs connected to the isolated faulted sections are rapidly separated in a similar way to the solution discussed in Sect. 16.2.3.4. This prevents the DGs from feeding the isolated faulted sections and turning the temporary fault condition into a permanent one.

The backup protection module at the feeder section ensures that the faulted feeder is isolated from the MG if the primary protection fails. This module checks the status of the CBs near the faulted feeder section after trip signals are sent to them. If these CBs fail to open, the backup protection module sends trip signals to the CBs located closest to the failed CBs. This ensures that the smallest portion of the MG near the faulted feeder section is isolated.

The flow chart in Fig. 16.9 describes the online operation of the proposed adaptive overcurrent protection scheme and backup protection. The current measurements at each bus are continuously monitored and compared against their thresholds. If the thresholds are exceeded, the current measurements corresponding to the time delay are calculated from the characteristic curve defined in Sect. 16.4.1. The relay sends trip signals to the CB at the same bus after the time delay and closing trip signals to CBs near the looped feeders. The looped feeders ensure generation-load balance throughout the entire MMG following the fault clearance. The backup protection module continuously checks the status of the CBs after trip signals are sent by the adaptive overcurrent relays. If it detects failure of the adaptive overcurrent scheme, then it sends trip signals to the CBs located closest to the failed CBs.

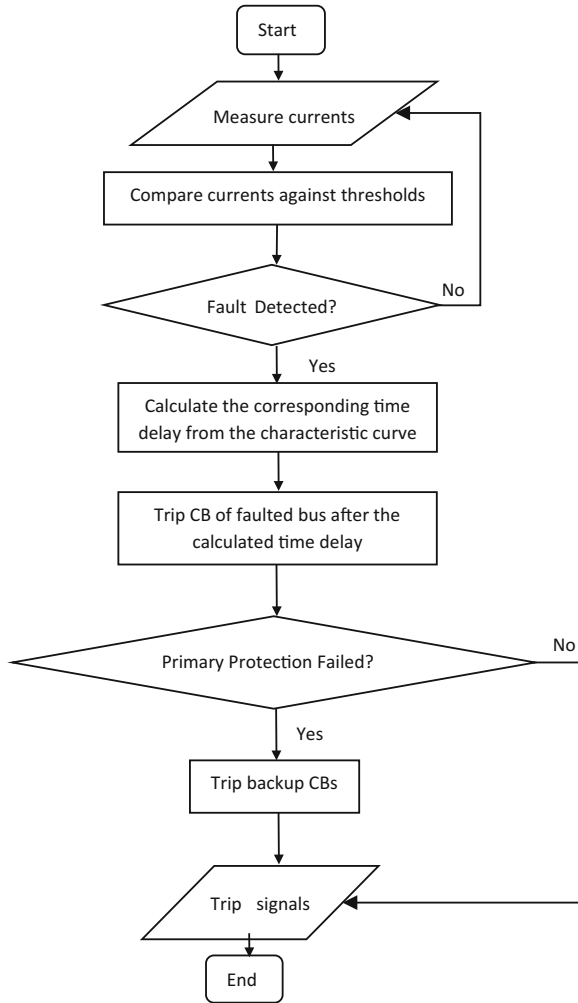
16.4.3 Simulation Results and Discussion

The effectiveness of the proposed adaptive overcurrent protection scheme in addressing the different protection challenges of MMGs was evaluated by simulation. The MMG scenarios considered in the simulations consisted of different combinations of NL-MGs and NG-MGs. The most severe fault conditions were simulated to study the robustness of the proposed scheme.

Simulations were carried out using MATLAB Simulink's SimPowerSystem toolbox with solver ode1 and a fixed time step of 1 microsecond. The 3-ph fault with impedance 1 m Ω was studied since it is the most severe fault condition that could occur in the network.

Figure 16.10 shows a single-line diagram of a MG where the fault locations used in the simulations are indicated. They are on the feeder sections between buses 5 and 6, 5 and 12, and 2 and 3. It also shows in red the CBs that are likely to be

Fig. 16.9 Flow chart for the online operation of the adaptive overcurrent protection scheme



activated on these feeder sections. The fault was introduced at 0.1 s after the voltages and currents reach steady state.

Simulations were carried out for the following cases: (i) MMG operation after isolating the faulted section, (ii) faulted feeder section close to one DG, and (iii) faulted feeder section close to two DGs. Case (i) studies the continued operation of the healthy section in the MMG following fault clearance of a feeder section as well as the effectiveness of primary and backup protection. In case (ii), the effectiveness of the proposed scheme in addressing the false tripping problem is evaluated. Case (iii) is to study the efficacy of the proposed scheme in addressing the problems of blinding of protection and failed reclosing.

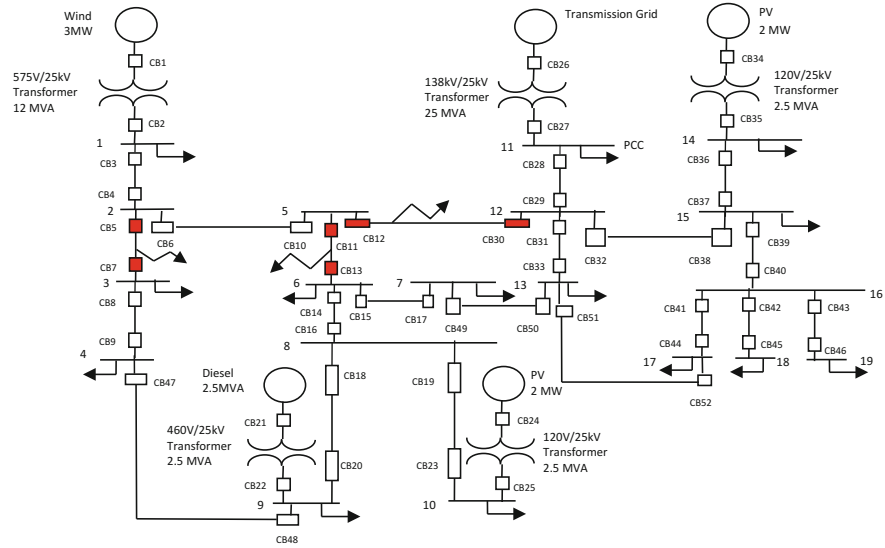


Fig. 16.10 Single-line diagram of MG showing the faults and CBs to open the faults

The following MMG scenarios were considered for each of the above cases: (a) two identical NL-MGs, (b) two identical NG-MGs, and (c) a combination of both the NL-MGs and NG-MGs. These scenarios correspond to the different operating states that could occur due to the variations of generation and load. Identical MGs are used in cases (a) and (b) to simplify MMG models consisting of two NL-MGs and NG-MGs, respectively. For these two cases, simulation results are given only for one of the two identical MGs. NL1 (NG1) refers to MG1 in the MMG containing two identical NL- (NG-) MGs.

16.4.3.1 MMG Operation After Isolating the Faulted Section

Primary Protection

For the MMG containing only NG-MGs, a 3-ph fault was introduced on the feeder section between buses 5 and 12 in NG1. Voltages and currents were measured on bus 5 which is one end of a faulted feeder section and on bus 18 which represents a healthy section. These measurements are shown in Figs. 16.11 and 16.12, respectively. Figure 16.13 shows the adaptive current thresholds for bus 5 in NG1. The fault occurred at 0.1 s and was cleared after 44.7 ms as indicated by the large ratio of the measured fault current to the current threshold. The currents from feeder section 5–12 at bus 5 going to zero after the fault is cleared imply that the faulted feeder section was effectively separated from the remaining MMG. The proposed scheme set the adaptive relay characteristics as shown in Fig. 16.13 following

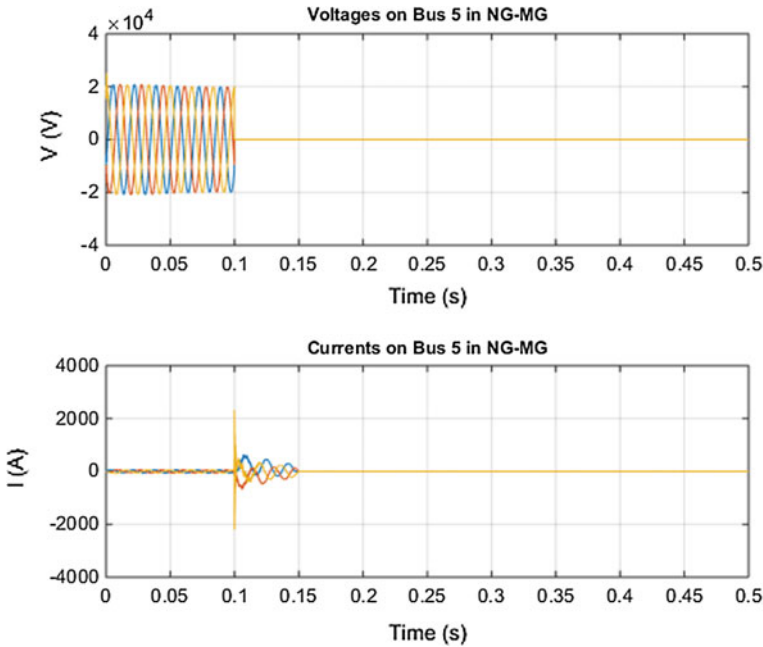


Fig. 16.11 Voltage and current waveforms on bus 5 in NG-MG when a 3-ph fault occurs on bus 5 in the same MG

changes in generation or load in the MG. This enabled the relays at each end of the feeder section to correctly detect and isolate the fault as indicated by the currents on bus 5 going to zero. After the 3-ph fault is cleared, the voltage and current waveforms on bus 18 had lower steady-state values indicating that the healthy MMG sections can continue operation. Similar results were obtained for MMG scenarios of only two NL-MGs and a combination of NL-MGs and NG-MGs.

Backup Protection

Simulations were carried out to study the effectiveness of the backup protection on a MMG containing only NG-MGs. The 3-ph bolted fault and HIF were introduced separately on the feeder section between buses 5 and 12 in NG1. Voltage and current measurements are shown in Fig. 16.14 for bus 5. The primary protection on bus 5 fails at 0.1447 s. The voltages and currents go to zero after the fault is cleared at 0.2 s when the CBs at buses 5 and 12 are opened. Hence, the backup protection can effectively isolate the faulted feeder section from the remaining MMG containing two NG-MGs after the primary protection fails. Similar results were obtained for MMGs containing two NL-MGs only and a combination of NL- and NG-MGs.

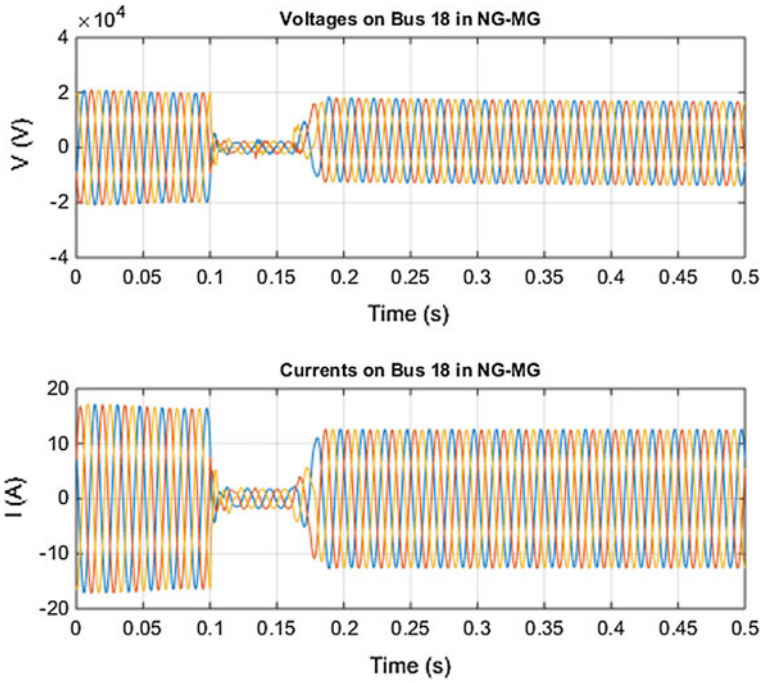


Fig. 16.12 Voltage and current waveforms on bus 18 in NG-MG when a 3-ph fault occurs on bus 5 in the same MG

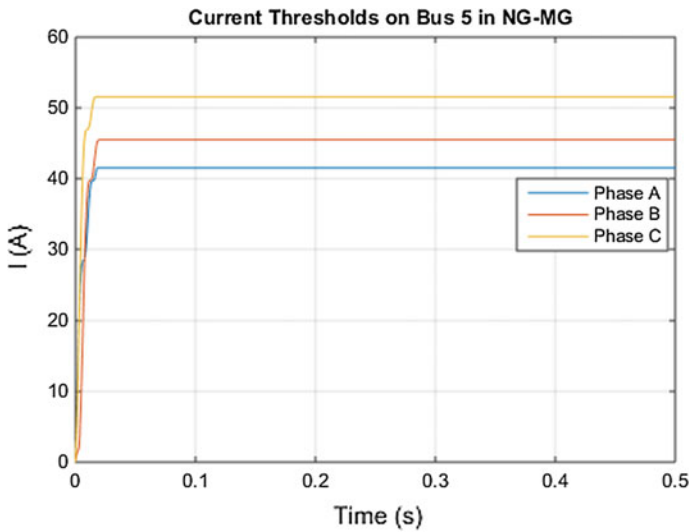
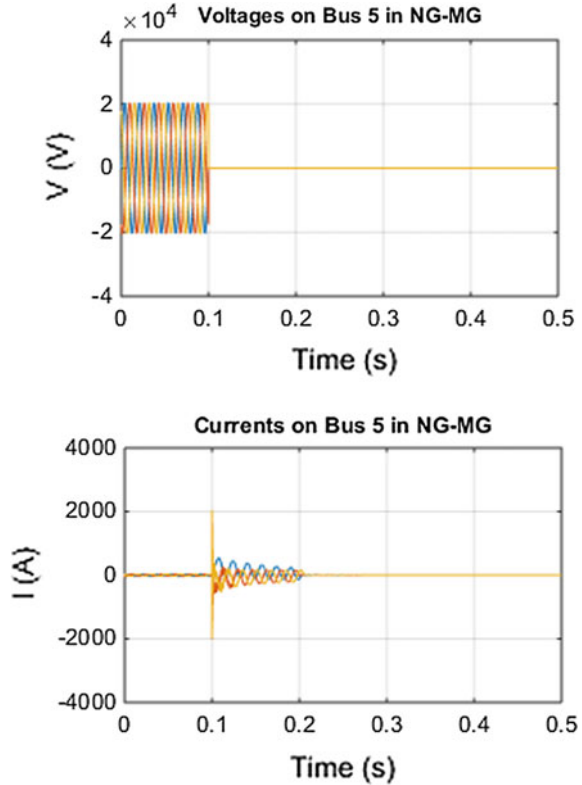


Fig. 16.13 Adaptive current thresholds on bus 5 in NG-MG

Fig. 16.14 Voltage and current waveforms on bus 5 in NG-MG when a 3-ph fault occurs at the same location to illustrate backup protection operation



16.4.3.2 Feeder Section Connected to One DG Source

The simulation was performed on a faulted feeder section near a DG source to study the effectiveness of the proposed scheme in avoiding the false tripping of a downstream healthy feeder section. A 3-ph fault was simulated between buses 2 and 3 in each MG of a MMG containing NL-MGs and NG-MGs since wind generators are located near bus 2. The nearby feeder section on bus 5 was checked to see whether false tripping had occurred. The measured voltages and currents on buses 2 and 5 in both MGs are shown in Figs. 16.15, 16.16, 16.17 and 16.18, respectively. The voltages on bus 2 and the feeder section 2–3 current at bus 2 are zero for both MGs since the CBs at these buses are opened after 34.2 ms to clear the fault. The relay on bus 2 was operated correctly because of its adaptive characteristics. After the fault was cleared, the voltage and current waveforms on bus 5

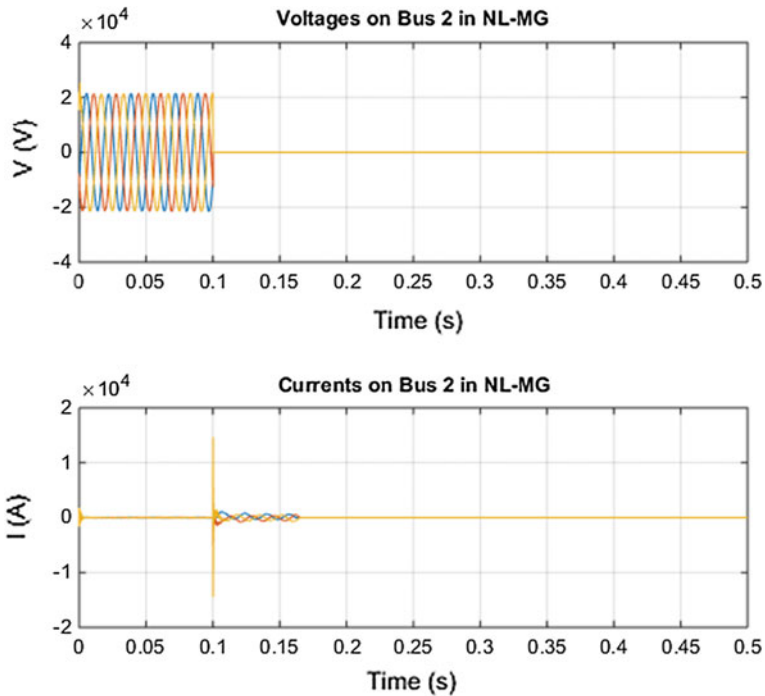


Fig. 16.15 Voltage and current waveforms on bus 2 in NL-MG when a 3-ph fault occurs on bus 2 in the same MG

are different from their pre-fault values which indicate that the CB at that bus remained closed, and therefore, there was no false tripping on bus 5. Similar results were obtained for MMG scenarios consisting of NL-MGs only and NG-MGs only.

16.4.3.3 Feeder Section Connected to Two DG Sources

Simulations were carried out to study the efficacy of the protection scheme in addressing the problems of blinding of protection and failed reclosing in a MMG containing only two NL-MGs. A 3-ph fault was simulated on a feeder section between buses 5 and 6 in NL1 near two DG sources which included a diesel generator and a PV source. The voltage and current waveforms on bus 5 are shown in Fig. 16.19. The voltages and currents on bus 5 go to zero after the fault was cleared in 27.6 ms by opening the CBs near the faulted feeder. The blinding of

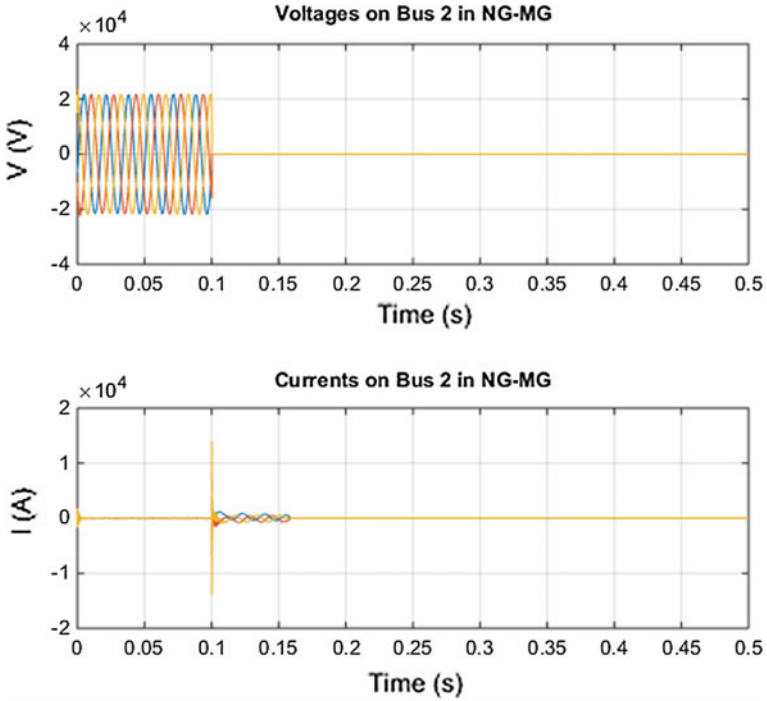


Fig. 16.16 Voltage and current waveforms on bus 2 in NG-MG when a 3-ph fault occurs on bus 2 in the same MG

protection did not occur as the relays trip the CBs on buses 5 and 6 when the utility grid contribution to the fault current was lowered by the diesel generator and PV source contributions.

Figure 16.20 shows the voltages and currents on bus 5 when the breaker on bus 5 in NL1 is reclosed. The voltages and currents on bus 5 between 0.1 and 0.1667 s all went to zero indicating that the relays at buses 5 and 6 prevented failed reclosing by tripping both sides of the faulted feeder section and the DG sources that are connected to it. Therefore, the CB on bus 5 was able to reclose one end of the faulted feeder section without the DG sources feeding into it. This is shown by the currents on bus 5 returning to steady state after the reclosing action. Other MMG scenarios consisting of only NG-MGs and a combination of NL-MGs and NG-MGs showed similar results.

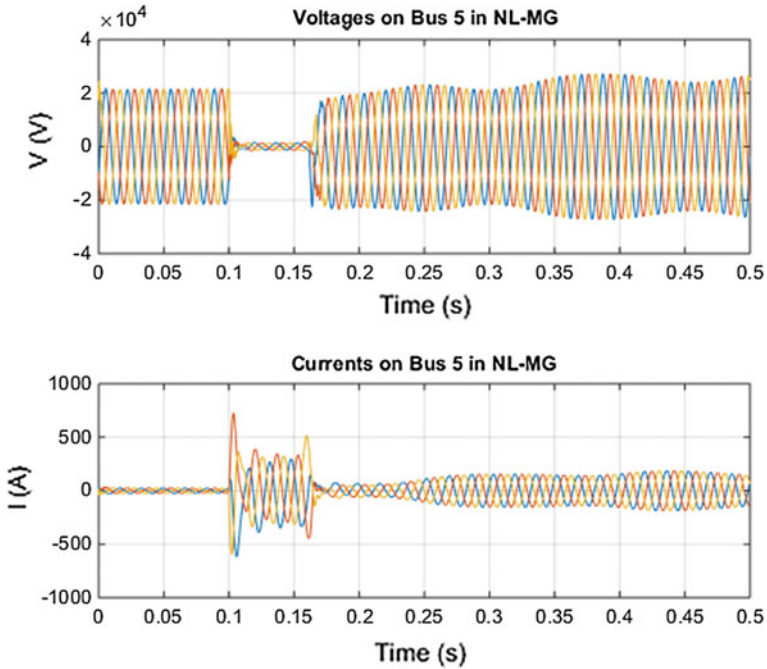


Fig. 16.17 Voltage and current waveforms on bus 5 in NL-MG when a 3-ph fault occurs on bus 2 in the same MG

16.4.3.4 Discussion of the Simulation Results

The proposed protection scheme which includes both primary and backup protection effectively detects and clears bolted 3-ph faults occurring on a feeder section in each of the MGs within the different MMG scenarios. After isolating the fault, the remaining healthy sections are able to continue operation. The looped feeders restore the generation-load balance in each MG after the fault is cleared.

Simulations showed that the proposed scheme can protect the different MMG scenarios against the problems of false tripping, blinding of protection, and failed reclosing. The problem of false tripping was prevented by isolating a faulted feeder section near a DG source and enabling the nearby healthy sections to continue operation. The blinding of protection was addressed by isolating the faulted feeder section when the utility grid contribution to the fault current is reduced by the contributions from two DG sources. The failed reclosing problem has been addressed by ensuring that DGs do not feed into the faulted section that has been isolated.

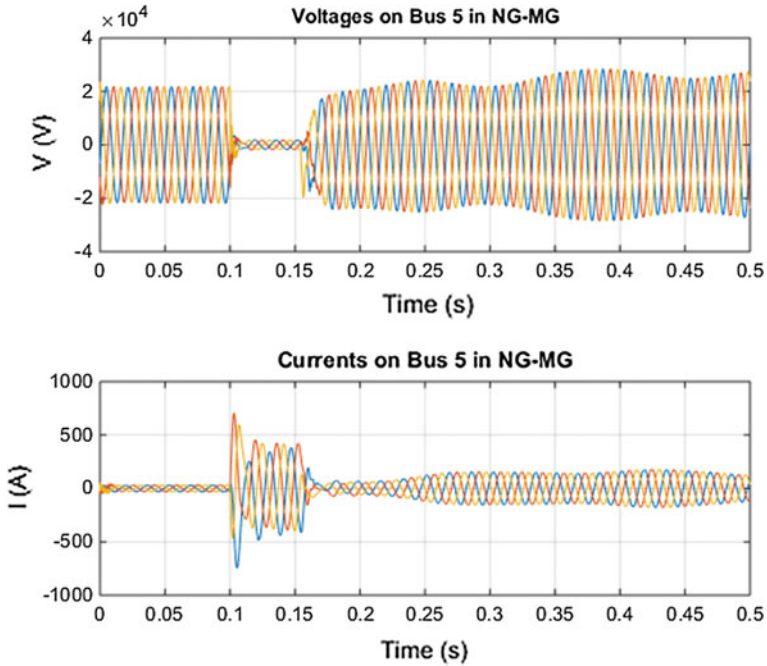


Fig. 16.18 Voltage and current waveforms on bus 5 in NG-MG when a 3-ph fault occurs on bus 2 in the same MG

16.4.4 Comparison with Existing Adaptive Schemes for MGs

The adaptive protection scheme in Oudalov and Fidigatti [3] uses event and action tables to store the CB statuses and relay settings, respectively, for all possible scenarios of the MG. The proposed scheme on the other hand calculates the relay settings on the fly instead of using lookup tables. The scheme in [3] incurs high computational overhead as it needs to frequently poll the individual relays to monitor the changes in generation and load and also uses the lookup tables to obtain the correct relay settings. Inverse-time overcurrent relays with maximum time delay of 44.7 ms in the proposed scheme enable faster tripping times than the directional

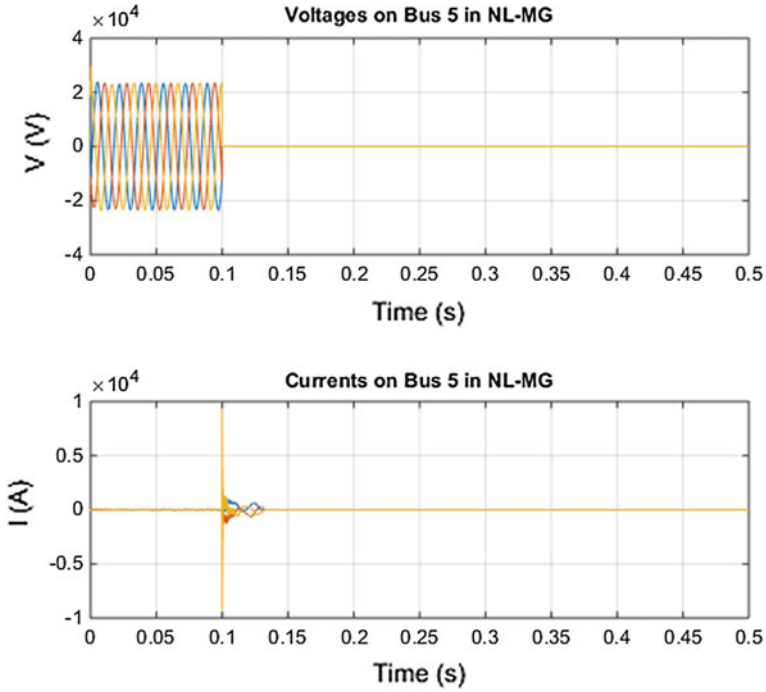


Fig. 16.19 Voltage and current waveforms on bus 5 in NL-MG when a 3-ph fault occurs on bus 5 in the same MG

overcurrent relays used in [3] which have a minimum time delay of 100 ms for the most severe fault conditions.

In the centralised MG protection scheme of Ustun et al. [38, 39], a MG central protection unit (MCPU) records the status of the MG operating condition and of DGs as well as calculate the operating currents for all the relays. The CC proposed in this chapter has more advanced functionality compared to [38, 39] since it continually monitors the variations in the generation and load by detecting changes in the PCC currents for each MG. The maximum tripping time delay of 44.7 ms for the proposed scheme is faster than the delay of 200 ms in [38, 39] for the most severe fault conditions.

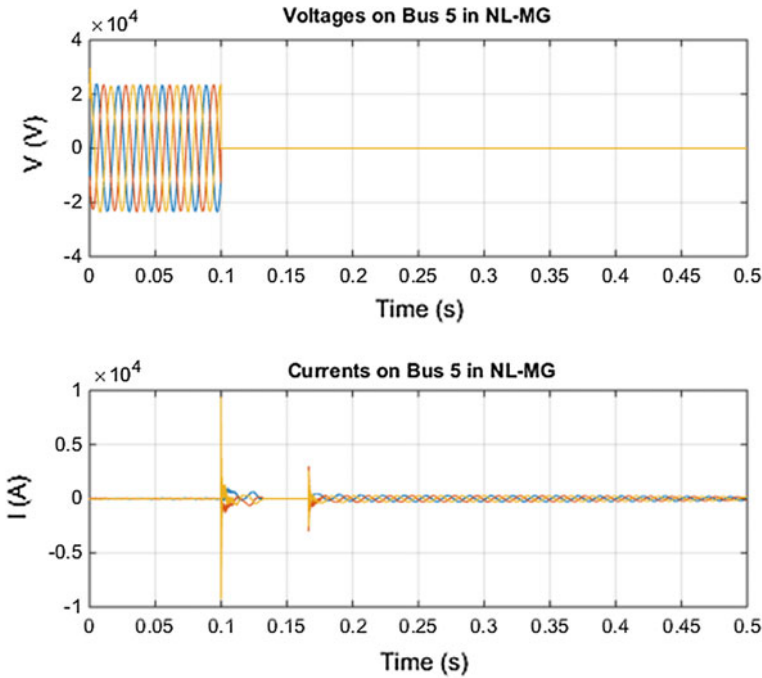


Fig. 16.20 Voltage and current waveforms on bus 5 in NL-MG when a 3-ph fault occurs on bus 5 in the same MG

16.5 Conclusion

The protection of MGs presents challenges similar to that of distribution systems with distributed generation. Bidirectional power flows from DGs adversely affect the coordination of conventional overcurrent protection devices which are also unable to detect the low fault currents from inverter-interfaced microsources in islanded MGs. This chapter reviewed the existing coordination strategies and protection schemes that address these challenges. A new adaptive overcurrent protection scheme was then proposed for MMGs that builds on the adaptive protection schemes previously proposed for MGs.

The fault current levels in the MMG vary due to power flows from DGs and the variations in the generation–load balance of MGs. The presence of DGs can also cause problems which include the blinding of protection, false tripping, and failed reclosing. With the existing protection scheme that disconnects all the DGs during a fault, the continued operation of the MMG is not feasible after fault clearance. The adaptive overcurrent protection scheme proposed in this chapter addresses these challenges. It automates the setting of relay characteristics according to the changing fault current levels caused by the intermittency in generation and variations in load demand. It uses a CC to monitor the dynamic variations in generation

and load from current measurements at the PCC points of each MG as well as to coordinate between the MGCCs. By using the inverse-time characteristics of overcurrent relays, the most severe fault conditions are isolated in a shorter time than by existing adaptive MG protection schemes. The effectiveness of the proposed scheme was evaluated by simulation. The simulation results show that the primary and backup protection effectively isolates the faulted sections and enables continued operation of the healthy sections for the different MMG scenarios. It also prevents blinding of protection, failed reclosing, and false tripping. Compared with existing adaptive MG protection schemes, this scheme has less computational overhead since it calculates the relay settings on the fly instead of polling relays and using lookup tables. As future work, the adaptive overcurrent scheme would be extended to deal with dynamic variations in generation by wind and PV sources as well as unbalanced static, synchronous, and induction motor loads. The impact of communication failures on the performance of the proposed scheme would also be studied.

References

1. Chowdhury SP, Chowdhury S, Crossley PA (2009) Microgrids and active distribution networks
2. Pecas Lopes JA (2007) Coordinated voltage support. Advanced architectures and control concepts for more microgrids. Available: www.microgrids.eu
3. Oudalov A, Fidigatti A (2009) Adaptive network protection in microgrids. *Int J Distrib Energy Res* 5:201–225
4. Pecas Lopes JA (2007) Algorithms for state estimation for MV multi-microgrids. Advanced architectures and control concepts for more microgrids. Available: www.microgrids.eu
5. Dewadasa M, Majumder R, Ghosh A, Ledwich G (2009) Control and protection of a microgrid with converter interfaced micro sources. In: Proceedings of 3rd international conference on power systems, Kharagpur, pp 1–6
6. Brahma SM, Girgis AA (2004) Development of adaptive protection scheme for distribution systems with high penetration of distributed generation. *IEEE Trans Power Deliv* 19:56–63
7. Basak P, Chowdhury S, Halder nee Dey S, Chowdhury SP (2012) A literature review on integration of distributed energy resources in the perspective of control, protection and stability of microgrid. *Renew Sustain Energy Rev* 16:5545–5556
8. Justo JJ, Mwasilu F, Lee J, Jung JW (2013) AC-microgrids versus DC-microgrids with distributed energy resources: a review. *Renew Sustain Energy Rev* 24:387–405
9. Planas E, Gil-de-Muro A, Andreu J, Kortabarria I, Martinez de Alegria I (2013) General aspects, hierarchical controls and droop methods in microgrids: a review. *Renew Sustain Energy Rev* 17:147–159
10. Ustun TS, Ozansoy C, Zayegh A (2011) Recent developments in microgrids and example cases around the world—a review. *Renew Sustain Energy Rev* 15:4030–4041
11. Jiayi H, Chuanwen J, Rong X (2008) A review on distributed energy resources and MicroGrid. *Renew Sustain Energy Rev* 12:2472–2483
12. Pecas Lopes JA, Gil NJ (2007) Hierarchical frequency control scheme for islanded multi-microgrids operation. In: Proceedings of IEEE Lausanne Power Tech, Lausanne, pp 473–478
13. Pecas Lopes JA, Gil NJ (2007) Hierarchical frequency control scheme for islanded multi-microgrids operation. In: Presented at the IEEE Lausanne Power Tech, Lausanne

14. Saadat H (1999) Power system analysis. McGraw Hill, New York
15. Coster E, Myrzik J, Kling W (2010) Effect of DG on distribution system protection. In: Gaeonkar DN (ed) Distributed generation, 2010 edn, pp 93–118
16. Maki K, Repo S, Jarventausta P. Effect of wind power based distributed generation on protection of distribution networks. In: Proceedings of 8th IEEE international conference on developments in power system protection, Amsterdam, pp 327–330
17. Baran M, El-Markabi I (2004) Adaptive overcurrent protection for distribution feeder with distributed generation. In: Proceedings of IEEE power systems conference and exposition, New York, pp 715–719
18. Vermeyen P (2008) Effect of distributed generation on fault detection and ripple control. Ph. D. thesis, Katholieke Universiteit Leuven
19. Deuse J, Grenard S, Bollen M, Hager M, Sollerkvist F (200) Effective impact of DER on distribution system protection. In: Proceedings of CIRED 19th international conference on electricity distribution, Vienna
20. Brahma SM, Girgis AA (2002) Microprocessor-based reclosing to coordinate fuse and recloser in a system with high penetration of distributed generation. In: Proceedings of IEEE power engineering society winter meeting, New York, pp 453–458
21. Funmilayo HB, Butler-Purpy KL (2009) An approach to mitigate the impact of distributed generation on the overcurrent protection scheme for radial feeders. In: Proceedings of IEEE power systems conference and exposition, Seattle, pp 1–11
22. Tailor J, Osman A (2008) Restoration of fuse-recloser coordination in distribution system with high dg penetration. In: Proceedings of IEEE power and energy society general meeting, Pittsburg
23. Zeineldin HH, El-Saadany EF, Salama MMA (2006) Protective relay coordination for micro-grid operation using particle swarm optimization. In: Proceedings of large engineering systems conference on power engineering, Halifax, pp 152–157
24. Najy WKA, Zeineldin HH, Woon WL (2013) Optimal protection coordination for microgrids with grid-connected. *IEEE Trans Industr Electron* 60:1668–1677
25. Loix T, Wijnhoven T, Deconinck G (2009) Protection of microgrids with a high penetration of inverter-coupled energy sources. In: Proceedings of IEEE power and energy society/CIGRE joint symposium, Calgary, pp 1–6
26. Zamani MA, Sidhu TS, Yazdani A (2011) A protection strategy and microprocessor-based relay for low-voltage microgrids. *IEEE Trans Power Deliv* 26:1873–1883
27. Zeineldin HH, El-Saadany EF, Salama MMA (2006) Distributed generation micro-grid operation: control and protection. In: Proceedings of power systems conference: advanced metering, protection, control, communication, and distributed resources, Clemson, pp 105–111
28. Sortomme E, Venkata SS, Mitra J (2009) Microgrid protection using communication-assisted digital relays. *IEEE Trans Power Deliv* 25:2789–2796
29. Li B, Li Y, Bo Z, Klimek A (2009) Design of protection and control scheme for microgrid systems. In: Proceedings of the 44th international universities power engineering conference (UPEC), Glasgow, pp 1–5
30. Dewadasa M, Ghosh A, Ledwich G (2011) Protection of microgrids using differential relays. In: Proceedings of Australasian universities power engineering conference (AUPEC), Brisbane, pp 1–6
31. Nthontho MP, Chowdhury SP, Winberg S, Chowdhury S (2012) Protection of domestic solar photovoltaic based microgrid. In: Proceedings of IET 11th international conference on developments in power systems protection, Birmingham, pp 1–6
32. Li X, Dysko A, Burt GM (2010) Application of communication based distribution protection schemes in islanded systems. In: Proceedings of 14th international universities power engineering conference (UPEC), Cardiff, pp 1–6
33. Zamani MA, Yazdani A, Sidhu TS (2012) A communication-assisted protection strategy for inverter-based medium-voltage microgrids. *IEEE Trans Smart Grid* 3:2088–2099

34. Zamani MA, Sidhu TS, Yazdani A (2013) A communication-based strategy for protection of microgrids with looped configuration. *Electr Power Syst Res* 104:52–61
35. Fletcher SDA, Norman PJ, Galloway SJ, Crolla P, Burt GM (2012) Optimizing the roles of unit and non-unit protection methods within DC microgrids. *IEEE Trans Smart Grid* 3:2079–2087
36. Park JD, Candelaria J, Ma L, Dunn K (2013) DC ring-bus microgrid fault protection and identification of fault location. *IEEE Trans Power Deliv* 28:2574–2584
37. Ustun TS, Khan RH (2015) Multiterminal hybrid protection of microgrids over wireless communications network. *IEEE Trans Smart Grid* 6:2493–2500
38. Ustun TS, Ozansoy C, Zayegh A (2012) Modeling of a centralized microgrid protection system and distributed energy resources according to IEC 61850-70420. *IEEE Trans Power Syst* 27:1560–1567
39. Ustun TS, Ozansoy C, Zayegh A (2013) Fault current coefficient and time delay assignment for microgrid protection system with central protection unit. *IEEE Trans Power Syst* 28:598–606
40. Nikkhajoei H, Lasseter RH (2007) Microgrid protection. In: *Proceedings of IEEE power engineering society general meeting, Tampa*, pp 1–6
41. Salomonsson D, Soder L, Sannino A (2009) Protection of low-voltage DC microgrids. *IEEE Trans Power Deliv* 24:1045–1053
42. Bakar AHA, Ooi B, Govindasamy P, Tan CK, Illias HA, Mokhlis H (2014) Directional overcurrent and earth-fault protections for a biomass microgrid system in Malaysia. *Int J Electr Power Energy Syst* 55:581–591
43. Al-Nasser H, Redfern MA, O’Gorman R (2005) Protecting micro-grid systems containing solid-state converter generation. In: *Proceedings of international conference on future power systems, Amsterdam*, pp 1–5
44. Al-Nasser H, Redfern MA, Li F (2006) A voltage based protection for micro-grids containing power electronic converters. In: *Proceedings of IEEE power engineering society general meeting, Montreal*, pp 1–7
45. Redfern MA, Al-Nasser H (2008) Protection of micro-grids dominated by distributed generation using solid state converters. In: *Proceedings of IET 9th international conference on developments in power system protection, Glasgow*
46. Al-Nasser H, Redfern MA (2008) Harmonics content based protection scheme for micro-grids dominated by solid state converters. In: *Proceedings of 12th international middle-east power system conference, Aswan*
47. Majumder R, Dewadasa M, Ghosh A, Ledwich G, Zare F (2011) Control and protection of a microgrid connected to utility through back-to-back converters. *Electr Power Syst Res* 81:1424–1435
48. Laaksonen HJ (2010) Protection principles for future microgrids. *IEEE Trans Power Electron* 25:2910–2918
49. Sortomme E, Ren J, Venkata SS (2013) A differential zone protection scheme for microgrids. In: *Proceedings of IEEE power and energy society general meeting, Vancouver*, pp 1–5
50. Casagrande E, Woon WL, Zeineldin HH, Svetinovic D (2014) A differential sequence component protection scheme for microgrids with inverter-based distributed generators. *IEEE Trans Smart Grid* 5:29–37
51. Kar S, Samantaray SR (2014) Time-frequency transform-based differential scheme for microgrid protection. *IET Gener Transm Distrib* 8:310–320
52. Fletcher SDA, Norman PJ, Fong K, Galloway SJ, Burt GM (2014) High-speed differential protection for smart dc distribution systems. *IEEE Trans Smart Grid* 5:2610–2617
53. Saleh SA, Ahshan R, Abu-Khaizaran MS, Alsaid B, Rahman MA (2014) Implementing and testing d-q WPT-based digital protection for microgrid systems. *IEEE Trans Ind Appl* 50:2173–2185
54. Saleh SA (2014) Signature-coordinated digital multirelay protection for microgrid systems. *IEEE Trans Power Electron* 29:4614–4623

55. Li X, Dysko A, Burt GM (2014) Traveling wave-based protection scheme for inverter-dominated microgrid using mathematical morphology. *IEEE Trans Smart Grid* 5:2211–2218
56. Oudalov A (2009) Novel protection systems for microgrids. Advanced architectures and control concepts for more microgrids. Available: www.microgrids.eu
57. Gopalan SA, Sreeram V, Iu HHC (2014) Review of coordination strategies and protection schemes for microgrids. *Renew Sustain Energy Rev* 32:222–228
58. Dewadasa M, Ghosh A, Ledwich G, Wishart M (2011) Fault isolation in distributed generation connected distribution networks. *IET Gener Transm Distrib* 5:1053–1061

Chapter 17

Power Management and Protection of Distribution Systems with Distributed Generations

Yuan Liao

17.1 Introduction

Electric distribution systems have recently witnessed a surge in the deployment of distributed generations (DG). The driving forces include economic considerations, energy independence, system reliability, environmental considerations, and technological advances. Traditional power distribution systems operate as a radial network and utilities plan and operate their systems based on forecast consumption. With increasing DGs, the network becomes multisourced and the power consumption and power flow pattern become more unpredictable, especially with intermittent renewable energy sources such as solar and wind generation being integrated [1]. Voltage and var control, system operation, optimization, and protection become more complicated [2, 3]. On the other hand, DGs may be exploited to achieve improved operation and control. In general, DGs provide both challenges and opportunities in modeling, operation, control, and protection.

This chapter first describes a power management system for distribution systems with DGs and microgrids [3–5]. The need for system modeling is discussed. Pricing signals are used to schedule available resources. The optimization target could be for an individual load or microgrid based on pricing signals from the outside grid to which they are connected. The target could also be to optimize resource scheduling for the entire distributions system based on a market bidding mechanism. To counter intermittency of DG outputs, a voltage and var optimization scheme is described, by taking advantage of the flexible reactive power controlling ability of smart inverters of DGs. References [6, 7] discuss some methods for protecting microgrid systems. This chapter presents a protection method for future distribution system by efficiently detecting fault occurrence, identifying fault section, and

Y. Liao (✉)

Department of Electrical and Computer Engineering, University of Kentucky,
Lexington, KY 40506, USA
e-mail: yliao@enr.uky.edu

locating the fault. A versatile fault location method is described to accurately pinpoint single or multiple, simultaneous faults that may occur on the network for better protecting the distribution system [8–14].

17.2 Power Management System

17.2.1 *Modeling and Simulation of Future Distribution Systems*

To understand the behavior and better design and operate distribution systems, modeling and simulation of different components and the system as a whole plays a pivotal role. This section presents an overview and development need of modeling and simulation.

Major components include generators and its control systems, power electronics components, transformers, lines, loads, voltage and var regulating devices, and storage devices. Storage devices may include dedicated battery systems, supercapacitors, or electric vehicles, etc.

Simulation can be classified into phasor-based simulation and time domain simulation. Simulation produces voltage, current, power, frequency, or other interested quantities versus time. Phasor-based simulation uses voltage and current phasors during simulation and is mainly used for steady state including power flow, dynamic analysis, and fault analysis. Time domain simulation uses voltage and current instantaneous values and is mainly used for analyzing faults, switching events, lightning events, and other transient phenomena. Time domain simulation yields voltage and current waveforms versus time. It is usually more time consuming than phasor-based simulation.

Examples of software packages for simulating distribution systems include Milsoft, OpenDSS, Matlab Simpowersystem, Electromagnetic Transients Program (EMTP), and ETAP. Another important aspect of energy study is thermal simulation software for buildings that estimates energy consumption and building space temperature based on building characteristics and ambient conditions; examples of software packages include EnergyPlus and SAM [15]. These different software packages have their own capabilities. Interfacing electrical simulation software with thermal simulation software will be necessary for performing a full range of studies, as explained below.

Consider interconnected residential, or commercial, or industrial buildings with certain thermal and operational loads and constraints. A building may have different types of electrical loads with varying schedules and different heating and cooling characteristics. A building is usually powered through an area electrical power system (AEP) but may also have its own generation systems such as PV, wind or CHP generation, or backup generators. It may also have its own energy storage systems with electrical storage such as a battery, or thermal storage such as mass

walls or water heating which may operate in charging or discharging mode. Certain loads may be under direct load control and/or other demand side management programs. A group of buildings may form a microgrid and operate in grid-connected or islanded mode.

Accurate modeling and simulation of the building load, storage system, generation and external power grid will be important to understand the interaction between different components, control and protect the system, and optimize system operation. Simulation will need to be performed at different timescales to study resource scheduling (long timescale, i.e., day, month, year), thermal loads (medium timescale, i.e., minutes), and transients, power quality issues, voltage and frequency control (short timescales, i.e., second or sub-second). Existing public domain software such as DOE’s EnergyPlus and SAM is not capable performing the full range of simulation studies. Therefore, it is necessary to integrate electrical software and thermal simulation software in future software development. It is useful to develop new methods and tools to model, simulate, and optimize the electrical system for multiple buildings.

Figure 17.1 shows the electrical components for microgrid-interconnected buildings. Electrical loads may include lighting loads, HVAC, water heaters,

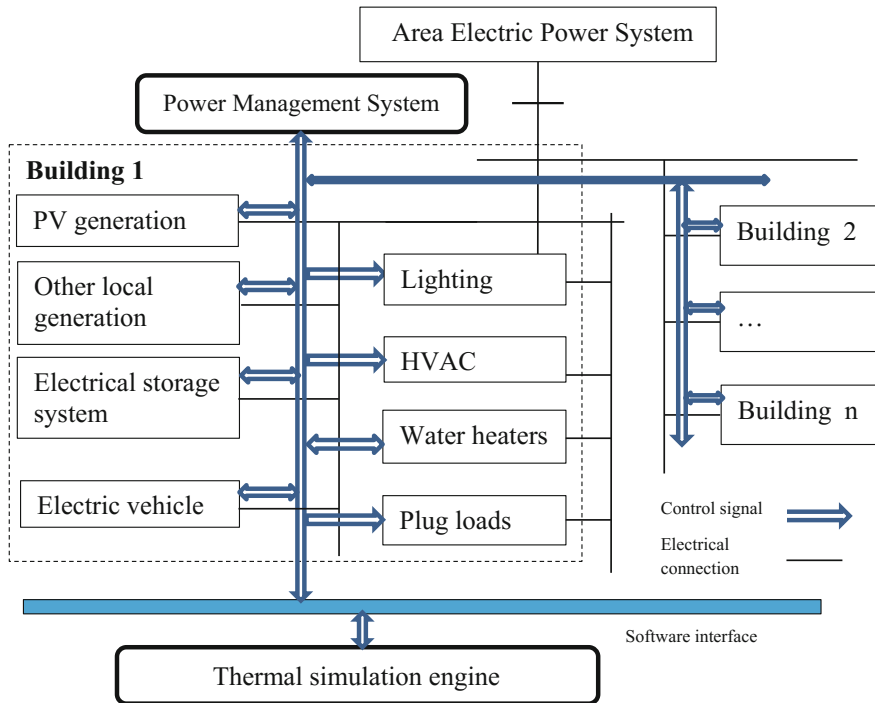


Fig. 17.1 Microgrid consisting of interconnected buildings

electric vehicle, and plug loads. Plug loads may include all sorts of electrical appliances: computers, printers, refrigerator, dishwasher, television, electric oven, and clothes washer and dryer. For general discussion, it is assumed that the power consumed by these electrical loads at a specified time interval is programmable as a function of control variables such as electricity price or demand response control signal. The thermal effects of these electrical loads will be modeled by another software module “Thermal simulation engine,” e.g., the EnergyPlus.

The thermal loads represent the heating or cooling loads, i.e., the amount of energy needed to be added to or be removed from the building to maintain the specified temperature or range within the building. The energy may be provided by electricity or fuel. However, this discussion focuses on electrical system portion of the building, so the “thermal loads” refers to only the electrical energy needed to meet the heating or cooling demands. The amount of thermal loads may be determined by another software module “Thermal simulation engine.”

The electrical controller takes the thermal loads as inputs and performs the simulation and optimization of the electrical system. The thermal simulation engine takes the electrical loads as inputs to perform thermal simulation to obtain the value of thermal loads. Appropriate methods will be needed to interface the thermal simulation engine and electrical simulation engine.

Useful research for the future may include the following:

- Develop appropriate methods and tools to simulate the electrical system and interface to thermal simulation software such as EnergyPlus
- Design a power management controller for the microgrid that coordinates the operation of all resources and loads in the microgrid (resource scheduling, load forecasting, PV generation forecasting, voltage and frequency control, battery system sizing)

17.2.2 Modeling and Simulation

To perform simulation with a time resolution of second or sub-second level, use of software package EMTP and Matlab Simpowersystem environment may be appropriate. Methods and modules can be developed to interface electrical simulation with other software such as EnergyPlus and SAM. This type of simulation is needed to study the voltage and frequency characteristics of the microgrid and protection of the microgrid. Power management system of microgrid needs to make sure to achieve required voltage and frequency specification. The effect of changing irradiation, wind speed and direction, etc. on the system operation can be studied. Algorithms for controlling DG inverters and battery storage system to mitigate voltage fluctuation and balance real power can be designed. Islanding detection method based on wavelet transform and phase angle shift and total harmonic distortion quantities can be developed to detect islanding of building electrical systems.

Another modeling capability is to model the smart appliances whose power consumption is controllable based on electricity price or other demand response

signal. Suppose the power consumption schedule of each smart appliance is provided at the desired simulation time resolution. Also assume that the schedule of charging and discharging of storage systems and local generation dispatch schedule is known. For each schedule scenario, the simulation can be carried out to study energy consumption, emission, energy cost, etc. of the microgrid during a studied time horizon. By changing the schedule and performing sensitivity studies, the deciding factors that affect a specific objective function may be determined. These studies may help determine the optimal settings of controllable parameters (e.g., electrical storage operation schedule, local generation dispatch schedule, electrical load schedule) to achieve a specific objective function (e.g., minimizing energy consumption, emission output, energy cost, or power quality specification violation). The simulation studies can also decide needed electrical storage size to achieve an objective. A more detailed discussion on the optimization formulation is presented in later sections.

17.2.3 Design of Microgrid Controller

A microgrid controller or power management system coordinates the planning and operations of all resources and loads in the microgrid to ensure reliable and economical operation of the microgrid subject to constraints such as environmental impacts, policy requirements, physical network limitation, and other resource constraints.

The microgrid will be modeled including the network model comprising topology, network impedance, generation, energy storage, and loads. Generator characteristics including maximum and minimum capacity, heat rate curve, fuel cost (e.g., gas tariff), minimum down/up time, maximum ramp up/down rate, start-up cost, shutdown cost, and any additional operating cost will be obtained. Characteristics of energy storage devices including capacity, charging/discharging rate, and roundtrip efficiency will be acquired. Loads will be classified into critical and noncritical loads, and the design will ensure service to the critical loads during islanded state. The electricity price/tariff of the grid (AEP) is assumed to be known. A security-constrained unit commitment and economic dispatch algorithm will be developed that optimizes the operation of the microgrid. The objective function is to minimize the total operating cost of the microgrid, which includes the fuel cost and any additional operating cost of the local generators and storage devices within the microgrid, and the cost of importing energy from AEP (which will be negative cost when exporting energy to AEP) for a studied period of time, say 24 h. The constraints will include all the relevant generator and energy device characteristics and spinning reserve requirements. Another critical constraint that ensures resilience and survivability of the grid will be made. Based on the specified critical loads in the microgrid, and generator characteristics such as ramp rate and capacity in the microgrid, the total generation dispatch including storage within the microgrid must be sufficient such that sufficient resources are operating when the microgrid is

grid-connected and the microgrid is able to operate in islanded mode while meeting the needs of all critical loads. Depending on the ramp rate and capacity of the resources, energy, frequency regulation, spinning reserve, and black start support can be provided by the microgrid to the AEP. The associated revenue, treated as negative cost, calculated based on the price of the provided services can be incorporated in the objective function. The controller will also allow unscheduled requests of such services depending on the operating conditions of the microgrid. In addition to directly exporting relevant services to the AEP, demand response within the microgrid can also be implemented to provide energy support to AEP when needed. Moreover, the microgrid will also be able to provide Volt/VAR support through voltage and VAR control as explained below.

In addition to meeting the energy demand of the microgrid, the design will also consider other requirements such as voltage and reactive power (VAR) regulation. Suppose the microgrid has different types of voltage and VAR control devices such as voltage regulators, capacitor banks, and possible power electronics-based inverters (e.g., renewable energy sources integrated into the system through inverters). In the design, the voltages of each bus, the load, and generation will be linked through power flow equations. The voltage limit will be subject to the range prescribed by regulations. The power factor at certain locations can also be treated as a constraint to the aforementioned optimization problem. Due to the mechanical nature of traditional regulating devices such as voltage regulators and capacitor banks, these devices are too slow to counter against fast changing voltage variations due to real output variations of renewable sources such as solar power caused by fast cloud movement. This design will take full advantage of the inverters through which the renewable energy sources are integrated into the grid. The power electronics inverters can be operated in four-quadrant, either supplying or absorbing reactive power depending on the need. They are fast and can reduce or eliminate fast voltage variations of any bus within the microgrid as well as the connection point of the microgrid and the AEP, and also reduce the wear and tear on the mechanical controlling devices.

The operation of the microgrid may also be subject to environmental constraints. For example, there may be an emission constraint. Based on the emission rates of generators in the microgrid, the emissions due to meeting the energy consumption in the microgrid can be calculated, which will be treated as a constraint in the optimization problem. Based on average generation emission rates of AEP, emission savings of using local generation instead of importing energy from AEP can also be calculated.

The formulated problem will be solved using appropriate techniques such as Lagrangian relaxation methods and commercially available optimization solvers such as IBM ILOG CPLEX package.

Consequently, the presented management system will coordinate the operation of the microgrid resources based on the considerations of reliability, survivability, economic operation, and environmental performance, including interactions with external entities when needed.

The optimal resource scheduling for the building can be performed from one day to several years. So the results will provide both short-term and long-term optimal energy scheduling schemes. To enhance the modeling and optimization accuracy, future research may develop building load forecasting and PV/wind generation forecast algorithms. The forecast results will provide inputs to the modeling and optimization algorithms.

Interconnected buildings are treated as a microgrid example in the above discussion, and the discussion is applicable to other types of microgrids. Simulation for different applications may require different levels of details in the models for the components.

17.2.4 Voltage and Var Control

This section presents the optimal voltage and var optimization and control method with participation of traditional voltage and var regulating devices (namely load tap changer transformers, voltage regulators, and capacitor banks) and power electronics-based inverters of DGs (i.e., smart controllers). The method mitigates voltage fluctuation due to DG output variability and optimizes controller settings, reduces the operation of traditional mechanical controllers, and thus reduces their tear and wear by exploiting the fast operation of smart controllers.

Figure 17.2 depicts a sample distribution system with DGs and the supervisory control and data acquisition (SCADA) and distribution management system (DMS). Traditional SCADA system collects real-time data (voltage and current magnitude, real and reactive power, sequence of events, status value) from field devices, i.e., remote terminal units (RTU) and transfers the data to a central office, where the data are processed and analyzed by DMS applications. Data could be acquired through report by exception or polling method, handled by data acquisition server (DAS). The SCADA applications usually include topology processing, and some straightforward calculations such as integration and addition operations on the obtained data. Example communication technologies include fiber optic, broadband over the power line, cellular, microwave systems, radio systems, and satellite. Choice of communication technology depends on an application's specific requirement on speed, bandwidth, and reliability for the communication system.

An operator or application can issue commands through the SCADA system to controllers, which control breakers, switches, voltage regulators, generator controllers, inverters, and tap changers.

Newer generation sensing, measurement and control devices that become available for deployment include advanced metering infrastructure (AMI), phasor measurement units (PMU), and digital fault recorders (DFR). AMI collects real-time load data from consumers and sends data to the utility and provides energy pricing data to consumers. It can also provide load control functions for utilities to control consumer load. PMU measures voltage and current phasors (magnitude and angle). DFR records voltage and current waveforms and status

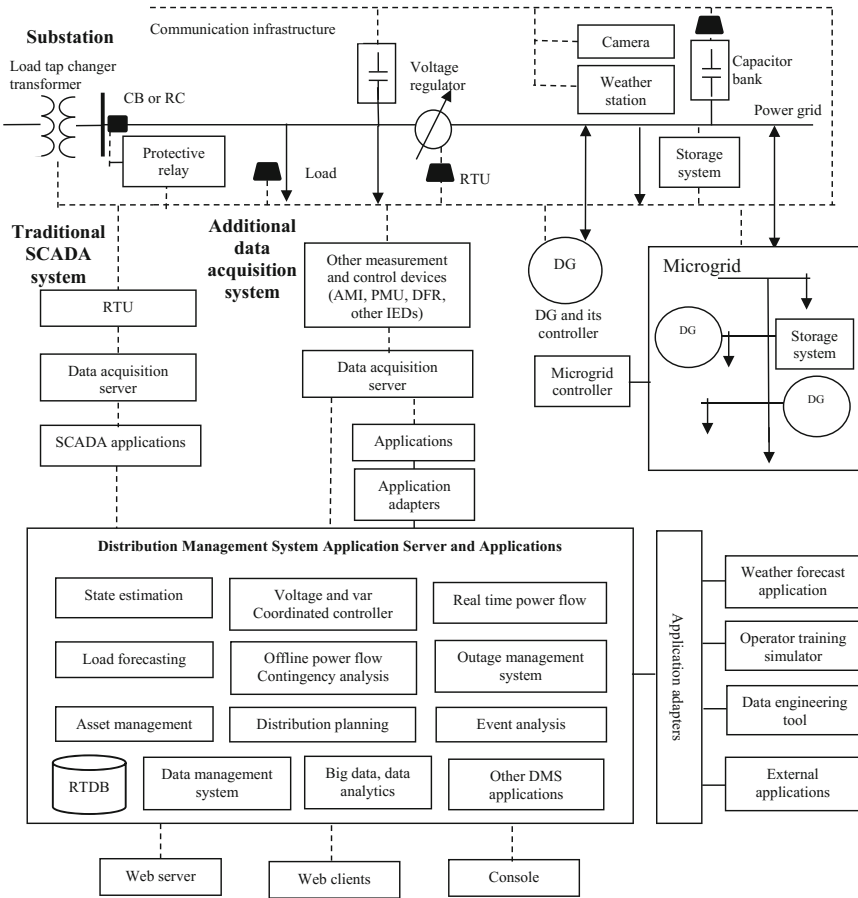


Fig. 17.2 Distribution system with DG, SCADA, and DMS

information preceding, during and after a fault. These different types of devices are usually termed as intelligent electronic devices (IED). Other types of IED may include power quality meters that capture power quality disturbance data, digital protective relays that provide voltage and current waveforms during a fault, and dynamic disturbance recorders that capture voltage, current, and frequency data during a dynamic event.

A weather station may capture temperature, wind speed, and direction. A camera may capture the cloud image and the cloud cover information. Based on these data, it may be possible to predict the near-term PV and wind generation for a better control.

With increasing DG deployment, more microgrids emerge. A microgrid consists of DGs and loads with a rough balance. A microgrid can be operated in grid-connected or off-grid mode. A microgrid controller is a system that consists of software and hardware for managing the operation of the microgrid.

Distribution management system (DMS) includes a suite set of applications for operating and managing the power distribution system. Common applications include state estimation, voltage and var control and optimization, real-time power flow, load forecasting, offline power flow and contingency analysis, outage management system, asset management, distribution system planning, event analysis, data management system, big data applications. The real-time database (RTDB) handles real-time data saving and retrieving. Real-time power flow calculates and predicts current and near-future system voltage, current and power flow, and thus provides pivotal data to operators for real-time operation.

A DMS system usually includes tools like operator training simulator and data engineering tool.

Various external applications can be integrated into the DMS system. Examples include weather forecast system, fault location system, outage prediction system, and any other third-party applications.

Consoles host the human machine interface (HMI). Through Web servers, the HMI is also accessible through Web clients.

A DG is interfaced to the AC power grid through a controller that can adjust the real power and reactive power injection to the grid. For example, a PV system can be connected to an AC power grid through an inverter that converts DC to AC power. The inverter has a four-quadrant operating range, which means that the PV can supply or consume real and reactive power. This ability provides great flexibility of using DG systems for reactive power and voltage regulation and optimization. By exploiting this ability, a two-layer integrated voltage and reactive power (var) control scheme, consisting of a fast control layer and a slower control layer, is described in the following section.

Mathematically, system voltages are a function of power injections, loads, and grid topology and grid parameters:

$$\mathbf{E} = \mathbf{f}(\mathbf{P}_1, \mathbf{Q}_1, \mathbf{P}_{dg}, \mathbf{Q}_{dg}, \mathbf{u}) \quad (17.1)$$

where \mathbf{E} represents the vector of system voltages, \mathbf{P}_1 and \mathbf{Q}_1 are the real and reactive power consumption of system loads, \mathbf{P}_{dg} , and \mathbf{Q}_{dg} are the real and reactive power supply of distributed generations, and \mathbf{u} symbolizes the control variables that consist of the settings of controllers. \mathbf{f} denotes the governing equations relying on the grid topology and grid parameters. If the grid topology changes, the SCADA system will capture this change, and \mathbf{f} will be updated accordingly. The current loads and generations can be obtained by the AMI system.

In the fast control level, the PV controller adjusts its reactive power output according to its real power output to counter the fast voltage fluctuation. At a certain operating point, the sensitivity of system voltages with respect to \mathbf{P}_{dg} and \mathbf{Q}_{dg} can be calculated. The amount of reactive power to counter the voltage change can also be computed. Then, the reactive power change supplied by the DG can be calculated according to the changes in the real power.

Another scheme for the fast control to counter fast voltage fluctuation is to perform a coordinated control of all the PV controllers. The objective is to maximize a voltage quality index, calculated based on the voltage of all the nodes in the system. Suppose that there are N nodes. The voltage quality index can be defined as the negative of the maximum voltage violation among all nodes. Or, the index is defined as the negative of the sum of the voltage deviation from nominal value of all nodes.

At the slower control level, the objective is to decide the settings of all voltage and var regulators while minimizing the power loss or power demand from the substation. The problem can be formulated as an optimization problem

Minimize P_{loss} or P_{demand}

Subject to:

$$\begin{aligned} \mathbf{g}(\mathbf{P}_1, \mathbf{Q}_1, \mathbf{P}_{\text{dg}}, \mathbf{Q}_{\text{dg}}, \mathbf{u}, \mathbf{E}) &= 0 \\ \mathbf{h}_1(\mathbf{P}_1, \mathbf{Q}_1, \mathbf{P}_{\text{dg}}, \mathbf{Q}_{\text{dg}}, \mathbf{u}, \mathbf{E}) &\geq 0 \\ \mathbf{h}_2(\mathbf{P}_{\text{dg}}, \mathbf{Q}_{\text{dg}}) &\geq 0 \end{aligned} \quad (17.2)$$

where \mathbf{g} stands for the general power flow equations, and \mathbf{h}_1 denotes the general form of constraints such as voltage limits, cable ratings, power factor limits, harmonic limits, and controller setting limits. \mathbf{h}_2 designates the DG power limits, where the real power is upper bounded by the forecasted DG real power, and the real and reactive power are together limited by the inverter rating. P_{loss} is the resistive loss dissipated in the grid and is calculated as the sum of product of the square of the current multiplied by the resistance of each branch of the grid. The branch current is a function of the node voltages and the branch impedance, and thus the branch current is a function of the node voltage. P_{demand} is the power drawn by the distribution grid from the substation and is calculated as the sum of the product of the voltage, current, and power factor at the substation. The unknown variables to be determined include \mathbf{P}_{dg} , \mathbf{Q}_{dg} , and \mathbf{u} . If maximum power from solar determined by solar irradiance is used, then \mathbf{P}_{dg} is assumed to be known. The DG outputs are continuous variables. The controller settings \mathbf{u} are integer variables that represent the tap positions of regulators and tap changer transformers, or the number of capacitive units of switchable capacitor banks that are switched into the grid. The solution is also applicable to mesh networks with multiple sources and substations.

One possible application scenario is described as follows: Every 15 min, the problem formulated in (17.2) is solved to obtain all the control settings, based on given load and PV real power output. Then, based on actual, changing PV real power output in real time (sub-second), the fast control layer is executed to mitigate voltage fluctuations. In practical applications, the number of operations for a controller during a specified period of time can also be a constraint.

Example results of the described two-layer voltage and var control and optimization method are shown below. The method is applied to a 12.47 kV feeder, with voltage regulated to 118–126 V, referred to the secondary side. Figure 17.3

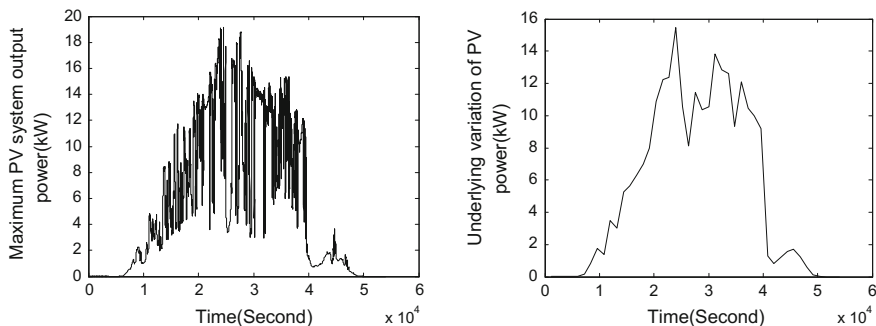


Fig. 17.3 Example instantaneous PV system output (*left*) and its average (*right*)

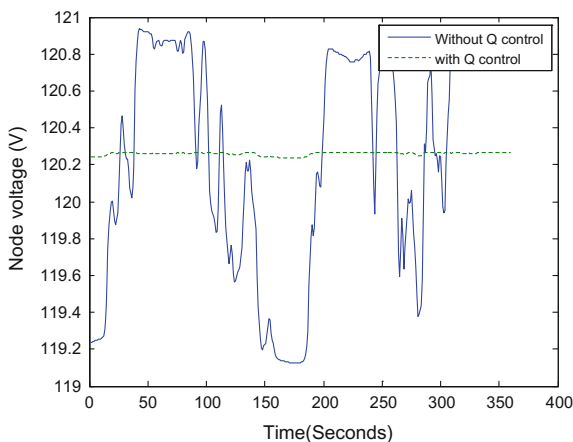
depicts sample PV system real power output every second and average value. The fast power fluctuation will cause fast voltage fluctuation and will be dealt with by the local fast control. The average value will be used by the global, slower control.

Figure 17.4 shows the voltage of a selected node with and without local reactive control. It can be seen that the fast fluctuations have been significantly mitigated and the voltage is kept within the required range of 118–126 V, with the presented control method.

Furthermore, a single-layer control scheme that decides all the control parameters is discussed below. The objective can be to minimize the loss, demand, or minimize a voltage violation index. Or, a multiobjective problem can be defined by combining the above objective functions. For example, to minimize the power loss and to minimize the sum of the voltage deviation can be the two objectives.

In this single-layer control, the problem defined in (17.2) is modified to include constraints on controllers. For example, for traditional mechanical controllers, their time constant of operation can be added; in other words, the controller settings

Fig. 17.4 Voltage profile for case with and without local reactive power control



cannot be changed within this time constant after one operation. This problem can be solved every one second. It is expected that most of the time, the parameters that change are the reactive power outputs of DGs, and most control parameters remain the same due to long time constant of control operation. The advantage of this formulation is that a better solution may be achieved. The shortfall is that it entails more frequent solution to (17.2) and thus more computational resources. However, solution to (17.2) may be greatly simplified since most control parameters change infrequently and thus are likely to be kept the same as in previous time interval.

In the previous discussions, no storage system is considered. Suppose that storage systems are provided by utilities at certain locations for mitigating the impacts of intermittent renewable energy sources. The storage system has a maximum charging power rate and drawing power rate, maximum energy capacity, charging efficiency, and drawing efficiency. Suppose that the energy price profile is provided for the studied time horizon. Storage system can provide real power output to compensate intermittent energy when needed and be charged during low-price energy period. Then, it may be feasible to formulate the voltage and var optimization problem considering economic factors. Depending on the need, this problem can be formulated with a focused scope on voltage and var control, or with a bigger scope regarded as part of the power management problem as discussed in next sections.

17.2.5 Microgrid Controller Design

This section focuses designing a microgrid controller of a microgrid that consists of local generations, storage systems, and loads. The microgrid needs to satisfy its own power balance (frequency regulation requirement) and voltage regulation requirement. The discussion is focused on the microgrid itself, and the AEP is considered as an external entity. The operation and optimization of the entire distribution system will be discussed in the next section.

The known data include energy purchase price profile for the studied time horizon for the energy purchased from the AEP, energy purchase upper cap from the AEP, energy sale price for energy sold to AEP, load profile in the microgrid, generation characteristics (minimum up/down time, maximum ramp rate, capacity, minimum output, energy cost curve, start-up cost, shutdown cost), storage system characteristics, load characteristics (total amount, curtailable amount), cost for unserved load (or penalty for unserved load). The microgrid may also operate in off-grid mode. The curtailable load is assumed to automatically respond to the demand response program of the utility based on pricing or demand response signal. For those loads such as washing machines, which do not require to be turned on during a specific interval, their operation schedule will also be determined. For each interval, the load will be specified as: firm load—the load that must be served and penalty will be imposed if not served; curtailable load—the load that can be shed automatically by demand response program; flexible operation time load,

whose operating schedule can be automatically decided by demand response program. For flexible operation time load, the load has a flexible operation time and specified power and energy consumption. For example, between 1 and 24 h, the washing machine will operate with a power of 700 W and a total energy consumption of 1400 Wh.

Other possible inputs include the emission constraints and emission characteristics of generations. Furthermore, the storage system has a maximum charging power rate and drawing power rate, maximum energy capacity, charging efficiency, and drawing efficiency.

The problem is to minimize the total operating cost for the microgrid to meet all the loads in the microgrid for the studied time horizon T such as 24 h. Suppose the simulation time resolution is ΔT . The control variables for each time interval include generation commitment status and output, storage system charging or drawing status, and charging or drawing rate, energy purchased from the utility, energy sale to the utility, voltage/var regulating device settings, and load served/unserved. Suppose initial statuses are known. The optimization problem will find out these control variables for each time interval. If the network of the microgrid needs to be modeled, then the power flow equations involving each node of the network need to be developed. For those loads such as washing machines, which do not require to be turned on during a specific interval, their operation schedules will also be determined.

Renewable generations such as PV generation may be assumed to be always on and generate the maximum possible power according to solar irradiance. The renewable generation profile is assumed to be known for the simulation horizon.

A formulation is presented as follows: Without losing generality, the simulation resolution is assumed to be one hour; a finer time interval will follow similar formulation. The generation cost is assumed to be a constant value; in more accurate modeling, quadratic cost function can be used, if any, or can be approximated by piece-wise step or linear functions. Reserve refers to spinning reserve. In more generic formulation, reserve may be expanded to include non-spinning reserve as well. Load or demand is based on forecast. Further consideration of any uncertainty may use techniques such as stochastic programming. The formulation can be applied to a microgrid, a single residential house, commercial, or industrial building. It is assumed that the microgrid will receive pricing information in advance

In the following formulation, generation units refer to thermal units unless otherwise stated. Renewable generations are considered as negative load.

a. Inputs

- C_{gsui} start-up cost of generation unit i
- C_{gsdi} shutdown cost of generation unit i
- C_{gei} energy rate of generation unit i
- P_{gmaxi} maximum capacity of generation unit i
- P_{gmini} minimum capacity of generation unit i ;

N_g	the number of generation units;
S_g	set $\{1, \dots, N_g\}$;
N_h	the number of hours;
S_h	set $\{1, \dots, N_h\}$;
U_{gi0}	the unit status preceding hour 1 (1 for on line, 0 for off line);
P_{gi0}	the initial dispatch of unit i preceding hour 1;
M_{guti}	minimum up time of unit i ;
M_{gdti}	minimum down time of unit i ;
L_{gui}	maximum ramp up dispatch increment of unit i ;
L_{gdi}	maximum ramp down dispatch decrement of unit i ;
R_k	reserve requirement in hour k ;
C_{epurk}	rate of electricity purchase from AEP in hour k ; a negative value indicates AEP encourages energy consumption by microgrid due to unwanted surplus;
C_{esalek}	rate of electricity sale to AEP in hour k ;
C_{donk}	payment to the microgrid by the AEP in hour k for each MWh load switched on under demand response signal;
C_{doffk}	payment to the microgrid by the AEP in hour k for each MWh load switched off under demand response signal;

The energy purchase upper cap from AEP is not included here for simplicity, but can be added if needed;

N_{fl}	the number of firm loads;
S_{fl}	set $\{1, \dots, N_{fl}\}$;
D_{flik}	firm load i in hour k ;
C_{flpi}	penalty for unserved firm load i ;
N_{al}	the number of adjustable loads, whose power consumption can be adjusted;
S_{al}	set $\{1, \dots, N_{al}\}$;
D_{almaxi}	maximum capacity of adjustable load i ;
D_{almini}	minimum capacity of adjustable load i ;
D_{ali0}	initial power of adjustable load i ;
U_{ali0}	initial on or off status of adjustable load i ;

Adjustable load is a more general term than curtailable load in that adjustable load will increase or decrease according to a pricing signal. Sometimes increasing the load will result in profit if an unwanted surplus of generation exists in the system.

N_{il}	the number of interruptible loads, which can be turned on or off in its entirety;
S_{il}	set $\{1, \dots, N_{il}\}$;
D_{ili}	interruptible load capacity i ;

Turning on or off interruptible loads may result in profit depending on pricing signal. It is assumed here that changing status does not incur any operating cost;

otherwise, a start-up and shutdown cost may be assigned similarly to a generator, and the situation can be dealt with accordingly.

- N_{fol} the number of flexible operation time loads;
- S_{fol} set $\{1, \dots, N_{fol}\}$;
- D_{foli} flexible operation time load power i ;
- D_{folei} total energy consumption of flexible operation time load i ;

The operation of loads can be of real-time decision to be made by the owner, or be automatically decided by a program. However, for a day-ahead schedule, the owner can decide which plan a load will follow.

- N_s the number of storage devices;
- S_s set $\{1, \dots, N_s\}$;
- Q_{smaxi} maximum energy capacity of storage i ;
- Q_{si0} initial energy of storage i ;
- e_{sci} charging efficiency of storage i ;
- e_{sdi} drawing efficiency of storage i ;
- $P_{scrmaxi}$ maximum charging rate of storage i ;
- $P_{sdrmaxi}$ maximum drawing rate of storage i ;

From the owner's point of view, keeping the curtailable or interruptible load off will save electricity consumption and thus money. However, if the curtailable/interruptible load is turned on and then turned off, the owner may receive incentive from AEP, which may be more profitable. Under demand response signal, microgrid may choose to switch on or off the interruptible loads and adjustable curtailable loads and also charge or draw the storage devices as well.

In a nutshell, the adjustable load, interruptible load, flexible operation time load, and the storage device are treated as resources that can be dispatched. There is no specific requirement on how much of these loads should be met. If there are such requirements, appropriate constraints and penalty for not fulfilling the requirements can be added.

b. Variables

Unknown variables are listed as follows:

- p_{gik} dispatch of generation unit i in hour k , continuous variable;
- u_{gik} commitment status of generation unit i in hour k , binary variable, 1 for on, 0 for off;
- s_{gik} start-up action of generation unit i in hour k , binary variable, 1 for start-up, 0 for no action;
- d_{gik} shutdown action of generation unit i in hour k , binary variable, 1 for start-up, 0 for no action;
- p_{ufik} unserved load for firm load i in hour k , continuous variable;
- p_{purk} purchased power from AEP in hour k , continuous variable;
- p_{salek} sale power to AEP in hour k , continuous variable;
- u_{alik} status of adjustable load i in hour k , binary variable, 1 for on, 0 for off;

- p_{alik} actual power of adjustable load i in hour k , continuous variable;
 s_{alik} start-up action of adjustable load i in hour k , binary variable, 1 for start-up, 0 for no action;
 d_{alik} shutdown action of adjustable load i in hour k , binary variable, 1 for shutdown, 0 for no action;
 u_{ilik} status of interruptible load i in hour k , binary variable, 1 for on, 0 for off;
 s_{ilik} start-up action of interruptible load i in hour k , binary variable, 1 for start-up, 0 for no action;
 d_{ilik} shutdown action of interruptible load i in hour k , binary variable, 1 for shutdown, 0 for no action;
 u_{fik} status of flexible operation time load i in hour k , binary variable, 1 for on, 0 for off;
 q_{sik} energy of storage i at the end of hour k , or at the beginning of hour $(k + 1)$, continuous variable;
 p_{scrik} charging rate of storage i in hour k , continuous variable;
 p_{sdrik} drawing rate of storage i in hour k , continuous variable;
 s_{scik} charging action of storage i in hour k , binary variable, 1 for charging, 0 for no charging;
 d_{sdik} drawing (discharging) action of storage i in hour k , binary variable, 1 for drawing, 0 for no drawing;

c. Constraints

The constraints of the formulated optimization problem are presented as follows:

Constraints for generations

The power dispatch of generator i in hour k is p_{gik} .

Generation unit capacity constraints

$$P_{g\min i} u_{gik} - p_{gik} \leq 0, \quad \forall k \in S_h, \quad \forall i \in S_g \quad (17.3.a)$$

$$p_{gik} - P_{g\max i} u_{gik} \leq 0, \quad \forall k \in S_h, \quad \forall i \in S_g \quad (17.3.b)$$

Generation start-up and shutdown relationship

$$s_{gik} - d_{gik} - u_{gik} + u_{gi(k-1)} = 0, \quad \forall k \in S_h, \quad \forall i \in S_g \quad (17.4.a)$$

$$s_{gik} + d_{gik} \leq 1, \quad \forall k \in S_h, \quad \forall i \in S_g \quad (17.4.b)$$

Generation initial unit status and output

$$u_{gi0} = U_{gi0}, \quad \forall i \in S_g \quad (17.5.a)$$

$$p_{gi0} = P_{pi0}, \quad \forall i \in S_g \quad (17.5.b)$$

Generation ramp up constraints

$$P_{gi(k+1)} - P_{gik} \leq L_{gui}, \quad k = 0, \dots, N_h - 1, \quad \forall i \in S_g \quad (17.6)$$

Generation ramp down constraints

$$P_{gik} - P_{gi(k+1)} \leq L_{gdi}, \quad k = 0, \dots, N_h - 1, \quad \forall i \in S_g \quad (17.7)$$

Generation minimum up time constraints

$$\sum_{m=k}^{M_{guti} + k - 1} u_{gim} \geq M_{guti} s_{gik}, \quad k = 1, \dots, N_h + 1 - M_{guti}, \quad \forall i \in S_g \quad (17.8)$$

$$\sum_{m=k}^K u_{gim} \geq (K - k + 1) s_{gik}, \quad k = N_h + 2 - M_{guti}, \dots, N_h - 1, \quad \forall i \in S_g \quad (17.9)$$

Generation minimum down time constraints

$$M_{gdti} - \sum_{m=k}^{M_{gdti} + k - 1} u_{gim} \geq M_{gdti} d_{gik}, \quad k = 1, \dots, N_h + 1 - M_{gdti}, \quad \forall i \in S_g \quad (17.10.a)$$

$$(K - k + 1) - \sum_{m=k}^K u_{gim} \geq (K - k + 1) d_{gik}, \quad (17.10.b)$$

$$k = N_h + 2 - M_{gdti}, \dots, N_h - 1, \quad \forall i \in S_g$$

Constraints for storage devices

The power consumption of storage i in hour k is

$$p_{sik} = s_{scik} p_{scrik} - d_{scik} p_{sdrik} \quad (17.11)$$

A positive value means charging, negative value means drawing, and zero means doing nothing.

Storage capacity constraints

$$0 \leq q_{sik} \leq Q_{s\max i}, \quad \forall k \in S_h, \quad \forall i \in S_s \quad (17.12)$$

Storage charging and drawing relationship

$$s_{sik} + d_{sik} \leq 1, \quad \forall k \in S_h, \quad \forall i \in S_s \quad (17.13)$$

Storage initial output

$$q_{si0} = Q_{si0}, \quad \forall i \in S_s \quad (17.14)$$

Storage charging and drawing power and energy constraints

$$p_{scrik} \leq P_{scrmaxi} \quad (17.15.a)$$

$$p_{sdrik} \leq P_{sdrmaxi} \quad (17.15.b)$$

$$q_{sik} - q_{si(k-1)} = s_{scik}p_{scrik}\epsilon_{sci} - d_{scik}p_{sdrik}/\epsilon_{sdi}, \quad \forall k \in S_h, \forall i \in S_s \quad (17.15.c)$$

Constraints for adjustable loads

The power consumption of adjustable load i in hour k is p_{alik} .

Adjustable loads capacity constraints

$$D_{almini}u_{alik} - p_{alik} \leq 0, \quad \forall k \in S_h, \forall i \in S_{al} \quad (17.16.a)$$

$$p_{alik} - D_{almaxi}u_{alik} \leq 0, \quad \forall k \in S_h, \forall i \in S_{al} \quad (17.16.b)$$

Adjustable loads start-up and shutdown relationship

$$s_{alik} - d_{alik} - u_{alik} + u_{ali(k-1)} = 0, \quad \forall k \in S_h, \forall i \in S_{al} \quad (17.17.a)$$

$$s_{alik} + d_{alik} \leq 1, \quad \forall k \in S_h, \forall i \in S_{al} \quad (17.17.b)$$

Adjustable loads initial conditions

$$p_{ali0} = D_{ali0}, \quad \forall i \in S_{al} \quad (17.18.a)$$

$$u_{ali0} = U_{ali0}, \quad \forall i \in S_{al} \quad (17.18.a)$$

The payment from AEP to adjustable load i in hour k is

$$C_{alk} = \begin{cases} C_{donk}(p_{alik} - p_{ali(k-1)}), & p_{alik} \geq p_{ali(k-1)} \\ C_{doffk}(p_{ali(k-1)} - p_{alik}), & p_{ali(k-1)} \geq p_{alik} \end{cases} \quad (17.19)$$

For a demand response command of increasing load, the first equation is reward and the second equation is penalty with a positive C_{donk} and negative C_{doffk} .

For a demand response command of reducing load, the first equation is penalty and the second equation is reward with a negative C_{donk} and positive C_{doffk} .

Constraints for interruptible loads

The power consumption of interruptible load i in hour k is

$$p_{ilik} = u_{ilik}D_{ili} \quad (17.20)$$

Interruptible loads start-up and shutdown relationship

$$s_{ilik} - d_{ilik} - u_{ilik} + u_{il(k-1)} = 0, \quad \forall k \in S_h, \quad \forall i \in S_{il} \quad (17.21.a)$$

$$s_{ilik} + d_{ilik} \leq 1, \quad \forall k \in S_h, \quad \forall i \in S_{il} \quad (17.21.b)$$

Interruptible loads initial status and output

$$u_{il0} = U_{il0}, \quad \forall i \in S_{il} \quad (17.22)$$

The on and off status is useful for responding to demand response signal. For example, if turning off the load receives credits in an hour, only those online loads have a chance to participate in this program.

The payment from AEP to interruptible load i in hour k is $s_{ilik}C_{donk}D_{ili} + d_{ilik}C_{doffk}D_{ili}$. If AEP encourages turning off load in hour k , it can set a high positive value of C_{doffk} and negative value of C_{donk} to reward turning off load and punish turning on load.

Constraints for flexible operation time loads

The power consumption for flexible operation time load i in hour k is

$$p_{folik} = u_{folik}D_{foli} \quad (17.23)$$

Energy constraints

$$\sum_k (u_{folik}D_{foli}) = D_{folei}, \quad \forall k \in S_h, \quad \forall i \in S_{fol} \quad (17.24)$$

Initial conditions

$$u_{fol0} = U_{fol0}, \quad \forall k \in S_h, \quad \forall i \in S_{fol} \quad (17.25)$$

If the load needs to run for a certain number of consecutive hours once started, then this constraint can be treated as minimum up time similar to the formulation for a generator. A start-up action variable and related constraints can be written similar to those for generators.

System power balance constraints

$$\begin{aligned} \sum_{i_1} p_{gi_1k} + p_{purk} - p_{salek} &= \sum_{i_2} p_{si_2k} + \sum_{i_3} p_{ali_3k} + \sum_{i_4} p_{ili_4k} \\ &+ \sum_{i_5} p_{foli_5k} + \sum_{i_6} D_{fli_6k} + \sum_{i_7} p_{ufi_7k}, \quad \forall k \in S_h \end{aligned} \quad (17.26)$$

The left side is the power supply including the generation, purchased power, and sale power. The right side represents the power consumption including power for storage, adjustable load, interruptible load, flexible operation time load, firm load, and unserved firm load.

Note that system loss is not considered in this formulation.

System reserve requirements

$$\sum_i (P_{g\max i} u_{gik} - p_{gik}) + R_{loadk} \geq R_k, \quad \forall i \in S_g, \quad \forall k \in S_h \quad (17.27)$$

The term R_{loadk} represents the reserve provided by load reduction and storage. Here, it is assumed reserve requirement is a positive value. If the reserve value is negative to model the ability of the microgrid to absorb surplus of generation, the formulation will need to be modified.

$$R_{loadk} = \sum_{i_1} p_{sri_1k} + \sum_{i_2} p_{ali_2k} + \sum_{i_3} p_{ili_3k} + \sum_{i_4} p_{fili_4k} \quad (17.28)$$

For reserve provided by storage, it will include the reduction in any charging consumption and additional drawing capacity. Since the power consumption of storage i in hour k is $p_{sik} = s_{scik}p_{scrik} - d_{scik}p_{sdrik}$, its reserve will be

$$p_{srik} = (s_{scik}p_{scrik} - d_{scik}p_{sdrik}) + P_{sdr\max i} \quad (17.29)$$

To help obtaining a solution, a variable, unmet reserve, may be introduced.

System emission constraints

Suppose that the microgrid is provided with a certain amount of emission allowance within a period of time, say a month, a season or a year. Emission types may include SO_2 , CO_2 , and NO_x . Additional emission allowance may be purchased from an open emission allowance market at the market credit price. From the perspective of the microgrid, it may produce its energy using cheap, dirty generators and purchase emission allowance, or produce energy using clean, expensive generators without purchasing or purchasing less emission allowance. Or the microgrid will purchase energy from AEP to save emission. Intuitively, there is trade-off between generating energy using different types of generators, purchasing energy, and purchasing emission allowance.

The following inputs are provided:

E_{grj}	emission rate (lb/MWh) for generator unit i for emission type j
e_{gij}	total emission output (lbs) for unit i for emission type j for the entire simulation horizon
e_{gjk}	total emission output (lbs) in hour k for emission type j for all units
E_{allowj}	emission allowance (lbs) for emission type j
E_{pricej}	emission allowance market price (\$/lbs) for emission type j

Unknown variables include the following:

e_{purj} emission allowance purchase from emission market lbs for emission type j

e_{salej} emission allowance sale to emission market lbs for emission type j

The emission output for unit i for emission type j for the entire optimization horizon is obtained by summing emission output in each hour as

$$e_{gij} = \sum_k (p_{gik} E_{grij}) \quad (17.30)$$

The emission output for all units for emission type j is calculated by summing output for each unit as

$$e_{gj} = \sum_i e_{gij} \quad (17.31)$$

Alternatively, the emission output for all units for emission type j in hour k is

$$e_{gjk} = \sum_i (p_{gik} E_{grij}) \quad (17.32)$$

Then, the emission output for all units for emission type j for the entire time horizon is

$$e_{gj} = \sum_k e_{gjk} \quad (17.33)$$

So, the emission constraints are obtained as follows:

$$0 \leq e_{gj} \leq E_{allowj} + e_{purj} - e_{salej} \quad (17.34)$$

$$e_{purj} \geq 0 \quad (17.35)$$

$$0 \leq e_{salej} \leq E_{allowj} \quad (17.36)$$

It is noted that other constraints may include voltage constraints, transmission constraints, contingency constraints, and fuel constraints.

d. Objective

The objective is to minimize the total operational cost for the microgrid defined as follows. It is apparent that this formulation is applicable to individual load where applicable.

$$\begin{aligned} \text{Minimize } & \sum_k (C_{gek} + C_{gsk} + C_{gdk} + C_{purk} + C_{unsk} - C_{salek} - C_{alk} - C_{ilk}) \\ & + C_{emp} - C_{ems} \end{aligned} \quad (17.37)$$

- C_{gek} generation energy cost, $C_{gek} = \sum_i (C_{gei}P_{gik})$
 C_{gsk} generation start-up cost, $C_{gsk} = \sum_i (C_{gsui}S_{gik})$
 C_{gdk} generation shutdown cost, $C_{gdk} = \sum_i (C_{gsdi}d_{gik})$
 C_{purk} cost for purchasing energy from AEP, $C_{purk} = C_{epurk}P_{purk}$
 C_{unsk} penalty for unserved firm load, $C_{unsk} = \sum_i (C_{\text{flpi}}P_{ufik})$
 C_{salek} revenue for energy sale to AEP, $C_{salek} = C_{esalek}P_{salek}$ and C_{alk} and C_{ilk} are referred to previous sections
 C_{emp} cost of purchasing additional emission allowance from market,
 $C_{emp} = \sum_j (e_{purj}E_{pricej})$
 C_{ems} revenue from selling emission allowed to market, $C_{ems} = \sum_j (e_{salej}E_{pricej})$

Without losing generality, unserved load is only considered for firm load.

If the AEP provides an offer to purchase reserve from the microgrid at certain price for each hour, then the microgrid will sell part of its reserve to the AEP. The objective function will include the profit from selling reserve, and the reserve requirement constraint will be modified accordingly. A new variable, the amount of reserve sold to AEP in each hour, will be introduced.

When network is considered, for each time interval, power flow equations need to be developed based on load and generation data for that time interval. Including optimization of voltage and var regulating device settings in the formulation will increase complexity. One way to simplify formulation is to ignore voltage and var regulating device optimization in this formulation. Then, these devices will be considered in the economic dispatch problem after the unit commitment problem is obtained.

If the microgrid is very small, the network model may be reduced to a node to simplify the formulation of the problem. With proper simplification (using DC power flow and piece-wise cost function), the problem can be formulated as a mixed integer linear programming (MILP) problem. For a real-time balancing market operation, the microgrid will re-optimize the scheduling of its resources based on real-time information.

In the following section, a market-based resource scheduling optimization approach to minimize the cost for satisfying the load and ancillary services for the entire distribution system is presented, which clears energy market and ancillary market simultaneously.

17.3 Market-Based Resource Scheduling for the Distribution System

This section presents a method for resource scheduling for the entire distribution system based on power market mechanism by simultaneously clearing energy market and ancillary service markets. Each resource can bid its contribution to the energy market and ancillary service (e.g., reserve) market with a bidding price. The

operator will determine the actual allocation of resource to each market based on an optimization procedure. Without losing generality, only spinning reserve is considered here, and only certain constraints for generators are included. Formulation for clearing the energy market and spinning reserve market is presented below.

Supply side data

- P_{gBEik} bidding energy of generator i in hour k ;
- B_{gEik} bidding price for energy of generator i in hour k ;
- P_{gBSRik} bidding spinning reserve of generator i in hour k ;
- B_{gSRik} bidding price for spinning reserve of generator i in hour k ;
- P_{gmini} minimum energy output of generator i ;
- P_{gmaxi} maximum energy output of generator i ;

The generator includes the substation and each DG as well.

- D_{ilik} capacity of interruptible load i in hour k , which can be interrupted and hence serve as reserve;
- $D_{ilBSRik}$ bidding interruptible load i in hour k to spinning reserve market;
- B_{ilSRik} bidding price for interruptible load i in hour k for spinning reserve;

Inputs related to storage device are as follows:

- P_{sBEik} bidding energy of storage i in hour k ;
- B_{sEik} bidding price for energy of storage i in hour k ;
- P_{sBSRik} bidding spinning reserve of storage i in hour k ;
- B_{sSRik} bidding price for spinning reserve of storage i in hour k ;

When storage device operates in drawing mode, storage device can supply energy like a generator. It can provide spinning reserve as well.

Demand side data

- D_{flik} firm load i in hour k ;
- R_k spinning reserve requirement in hour k ;

Variables to be determined

- p_{gEik} allocated energy of generator i in hour k to the energy market;
- p_{gSRik} allocated capacity of generator i in hour k to spinning reserve market;
- p_{ilSRik} allocated interruptible load i in hour k to spinning reserve market;
- p_{sEik} allocated energy for storage i in hour k to the energy market, i.e., drawing power;
- p_{sSRik} allocated capacity for storage i in hour k to the spinning reserve market;

Objective function

For each hour k , the cost to satisfy the load and spinning reserve is

$$\begin{aligned}
C_{\text{total}k} = & \sum_i B_{gEik} p_{gEik} + \sum_i B_{gSRik} p_{gSRik} + \sum_i B_{ilSRik} p_{ilSRik} \\
& + \sum_i B_{sEik} p_{sEik} + \sum_i B_{sSRik} p_{sSRik}
\end{aligned} \tag{17.38}$$

Then, the objective function will be to minimize the sum of the cost in each hour.

$$\text{Minimize } C_{\text{total}} = \sum_k C_{\text{total}k} \tag{17.39}$$

Constraints

Some constraints are given below: $\forall k \in S_h$.

For generator i :

$$p_{gEik} \leq P_{gBEik} \tag{17.40}$$

$$p_{gEik} + p_{gSRik} \leq P_{g\text{max}i} \tag{17.41}$$

$$u_{gik} P_{g\text{min}i} \leq p_{gEik} \leq \max(P_{gBEik}, P_{g\text{max}i}) \tag{17.42}$$

$$0 \leq p_{gSRik} \leq \min(P_{gBSRi}, P_{g\text{max}i} - P_{g\text{min}i}) \tag{17.43}$$

$\min(.,.)$ returns the smaller value of the two arguments.

For interruptible load i :

$$0 \leq p_{ilSRik} \leq \min(D_{ilik}, D_{ilBSRik}) \tag{17.44}$$

For storage i :

The rationale for storage device to provide reserve is that it can stop charging and begin drawing, or increase drawing power if already drawing. If no allocation for energy market is made for a storage device, that device can be in charging mode like a load, or do nothing.

$$0 \leq p_{sEik} \leq \min(P_{sBEik}, P_{s\text{drmax}i}) \tag{17.45}$$

$$0 \leq p_{sSRik} \leq P_{sBSRik} \tag{17.46}$$

$$0 \leq p_{sSRik} \leq P_{s\text{drmax}i} + p_{sik} \tag{17.47}$$

$$0 \leq q_{sik} \leq Q_{s\text{max}i} \tag{17.48}$$

$$s_{sik} + d_{sik} \leq 1 \tag{17.49}$$

$$q_{si0} = Q_{si0} \quad (17.50)$$

$$q_{sik} - q_{si(k-1)} = s_{scik}p_{scrik}\varepsilon_{sci} - d_{scik}p_{sEik}/\varepsilon_{sdi} \quad (17.51)$$

$$0 \leq p_{scrik} \leq P_{scrmaxi} \quad (17.52)$$

Energy consumed by storage device is

$$p_{sik} = s_{scik}p_{scrik} - d_{scik}p_{sEik} \quad (17.53)$$

Energy and reserve constraint:

$$\sum_{\text{generator } i} p_{gEik} = \sum_{\text{firmload } i} D_{fik} + \sum_{\text{int.load } i} D_{ilik} + \sum_{\text{storage } i} p_{sik} \quad (17.54)$$

$$\sum_{\text{generator } i} p_{gSRik} + \sum_{\text{int.load } i} p_{iISRik} + \sum_{\text{storage } i} p_{sSRik} \geq R_k \quad (17.55)$$

Additional constraints can be added similar to what are described in earlier sections. Notations not defined here are the same as those defined in earlier sections.

With regard to voltage and var optimization, consumers' inverters may participate in a reactive power market by bidding how much reactive power to provide to the system and the price. An appropriate pricing policy needs to be developed in the future.

17.4 Protection of Distribution System with Distributed Generations

Distribution system fault detection and location has been an important, yet challenging research topic due to network unbalance and lack of measurements. Increasing deployment of distributed generations (DG) in the system poses more challenges for fault detection and location. Recent developments and deployment of smart grid technologies including enhanced communication infrastructure and sensing instrument such as phasor measurement units (PMU) provide new opportunities to find novel solutions for fault detection and location. This section presents an online fault detection and location solution for distribution systems with DGs. The method will be applicable to both radial and non-radial, unbalanced systems, be applicable to simultaneous faults and make the most of available measurements.

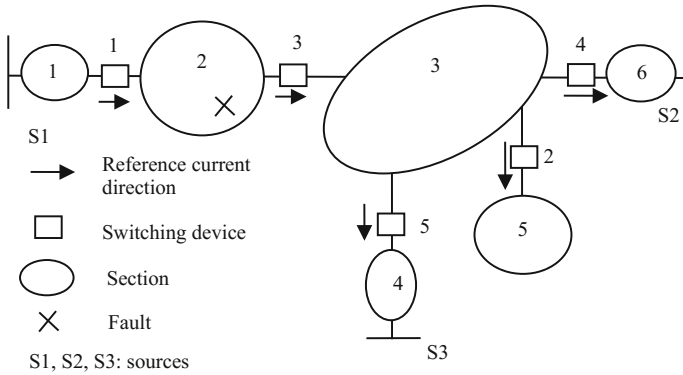


Fig. 17.5 Three-source network with a fault in section two

17.4.1 Overall Approach

The presented solution is illustrated by using a sample distribution network as depicted in Fig. 17.5. There are three sources including DGs. The network is partitioned into sections or subnetworks, which are connected through switching devices. PMUs are assumed to be installed at the switching device locations to capture the voltage and current phasors at a minimum rate of 30 measurements per second according to PMU standard. These real-time measurements are transferred to a central location for processing. When a fault is detected in a section, that section will be promptly isolated by surrounding switching devices such as circuit breakers, so that the remaining network can continue operation. If a switching device does not have fault current interrupting capability, then a bigger portion of the network would have to be isolated; so it is preferred to have circuit breaker type switching devices for minimized power outage.

Once the faulted section is identified, the voltage and current measurements obtained from different locations will be exploited to pinpoint the fault location. Note that the method allows for simultaneous faults occurring in either the same subnetwork or different networks.

17.4.2 Fault Section Identification Method

Switching devices are named nodes. A section or subnetwork connection matrix N is defined based on the connection of sections through nodes and the reference current direction. Note that the reference current direction can be arbitrary. Let element N_{kl} denote the k th row and l th column of N . $N_{kl} = 1$, if node l has a reference current direction into the k th section. $N_{kl} = -1$, if node l has a reference current direction out of the k th section. $N_{kl} = 0$, if node l is not connected to the k th section. The connection matrix of the network depicted in Fig. 17.5 is obtained as

$$N = \begin{bmatrix} -1 & 0 & 0 & 0 & 0 \\ 1 & 0 & -1 & 0 & 0 \\ 0 & -1 & 1 & -1 & -1 \\ 0 & 0 & 0 & 0 & 1 \\ 0 & 1 & 0 & 0 & 0 \\ 0 & 0 & 0 & 1 & 0 \end{bmatrix} \quad (17.56)$$

A current vector I is defined to consist of the current phasors flowing through each node.

$$I = [I_1 \quad I_2 \quad I_3 \quad I_4 \quad I_5]^T \quad (17.57)$$

where the superscript T denotes matrix or vector transpose.

The faulted section identification vector F_S is calculated as the product of N and I :

$$F_S = NI \quad (17.58)$$

The value of each element of F_S indicates whether a fault occurs in the corresponding section. Suppose high-speed communication is available, F_S will be calculated online and a fault will thus be identified in real time. Load currents will be appropriately considered.

17.4.3 Fault Location Method

The presented method is applicable to single faults or simultaneous, multiple faults. A prominent feature is that no fault type information is needed. The following discussion illustrates the method assuming that two faults occur simultaneously, at point r or d , respectively. It will become evident that the method is applicable to locate any number of simultaneous faults.

Bus r or d may comprise multiple nodes depending on the number of phases of the faulted line segment; there will be one node added for a single-phase line, two nodes for a two-phase line and three nodes for a three-phase line. The fault currents at the nodes of buses r and d are denoted as I_f and I_g , respectively. Now assume that measurements from two buses k and l are available. Then, the superimposed voltage quantities for the nodes of the buses are obtained as

$$\begin{bmatrix} \Delta E_k \\ \Delta E_l \end{bmatrix} = - \begin{bmatrix} Z_{kr} & Z_{kd} \\ Z_{lr} & Z_{ld} \end{bmatrix} \begin{bmatrix} I_f \\ I_g \end{bmatrix} \quad (17.59)$$

where the Z terms are the transfer impedances between related nodes and are functions of the unknown fault locations.

Equation (17.59) can be rewritten as

$$\Delta \mathbf{E}_{kl} = -\mathbf{Z}_{klrd} \mathbf{I}_{fg} \quad (17.60)$$

For measurements from another two buses i and j ,

$$\Delta \mathbf{E}_{ij} = -\mathbf{Z}_{ijrd} \mathbf{I}_{fg} \quad (17.61)$$

Eliminating the fault current \mathbf{I}_{fg} from (17.60) and (17.61) yields

$$(\mathbf{Z}_{klrd}^T \mathbf{Z}_{klrd})^{-1} (\mathbf{Z}_{klrd}^T \Delta \mathbf{E}_{kl}) = (\mathbf{Z}_{ijrd}^T \mathbf{Z}_{ijrd})^{-1} (\mathbf{Z}_{ijrd}^T \Delta \mathbf{E}_{ij}) \quad (17.62)$$

Then, the two unknown fault locations can be derived by separating the above equations into real and imaginary parts and solving them.

If the measurements from only two buses k and l are available, the fault location method is discussed below. It follows from (17.60) that

$$\mathbf{I}_{fg} = -(\mathbf{Z}_{klrd}^T \mathbf{Z}_{klrd})^{-1} (\mathbf{Z}_{klrd}^T \Delta \mathbf{E}_{kl}) \quad (17.63)$$

The voltages at the fault nodes during the fault are

$$\begin{bmatrix} \mathbf{E}_r \\ \mathbf{E}_d \end{bmatrix} = \begin{bmatrix} \mathbf{E}_{r0} \\ \mathbf{E}_{d0} \end{bmatrix} - \begin{bmatrix} \mathbf{Z}_{rr} & \mathbf{Z}_{rd} \\ \mathbf{Z}_{rd} & \mathbf{Z}_{dd} \end{bmatrix} \begin{bmatrix} \mathbf{I}_f \\ \mathbf{I}_g \end{bmatrix} \quad (17.64)$$

The complex powers consumed by the fault resistances at the two fault locations are

$$S_r = \mathbf{E}_r^T \mathbf{I}_f^* \quad (17.65)$$

$$S_d = \mathbf{E}_d^T \mathbf{I}_g^* \quad (17.66)$$

Fault resistances only consume real power, so the imaginary part of (17.65)–(17.66) is zero, solving which will lead to the unknown fault locations.

When measurements from multiple sites are available, optimal estimation theory may be applied to obtain an optimal estimate. The general idea is that multiple equations will be written based on available measurements. The measurement vector (consisting of measurements) and the function vector (consisting of equations involving fault locations) are related by

$$\mathbf{S} = \mathbf{F}(\mathbf{X}) + \boldsymbol{\mu} \quad (17.67)$$

where $\boldsymbol{\mu}$ reflects meter accuracy; a corresponding weighting matrix \mathbf{R} is defined. The optimal estimate of \mathbf{X} is obtained by minimizing the cost function defined as

$$J = (S - F(X))^T R^{-1} (S - F(X)) \quad (17.68)$$

The solution can be derived following an iterative procedure. State estimation-based techniques that are capable of detecting and removing bad measurement may be utilized to enhance fault location accuracy. By taking advantage of optimization theory, the algorithm will be capable of utilizing all available data and at the same time picking up potential bad data and thus providing the optimal fault location estimate.

It is clear from the derivation that the method is applicable to cases where more than two faults occur simultaneously.

17.4.4 Evaluation Studies

The method has been tested using a sample 18-bus distribution system with three DGs as shown in Fig. 17.6 and has achieved highly accurate results. Different types of faults have been studied including single line to ground (LG), double line to ground (LLG), double line (LL), three phase (LLL), three phase to ground faults (LLL_G). For simultaneous faults, various combinations have been investigated. For example, a LG and a LLG fault may occur at different locations. Specific fault types include AG (phase A to ground), BG, CG, AB (phase A to phase B), BC, AC, ABG (phase A to phase B to ground), BCG, ACG, ABC (three phase), and ABCG (three-phase grounded fault).

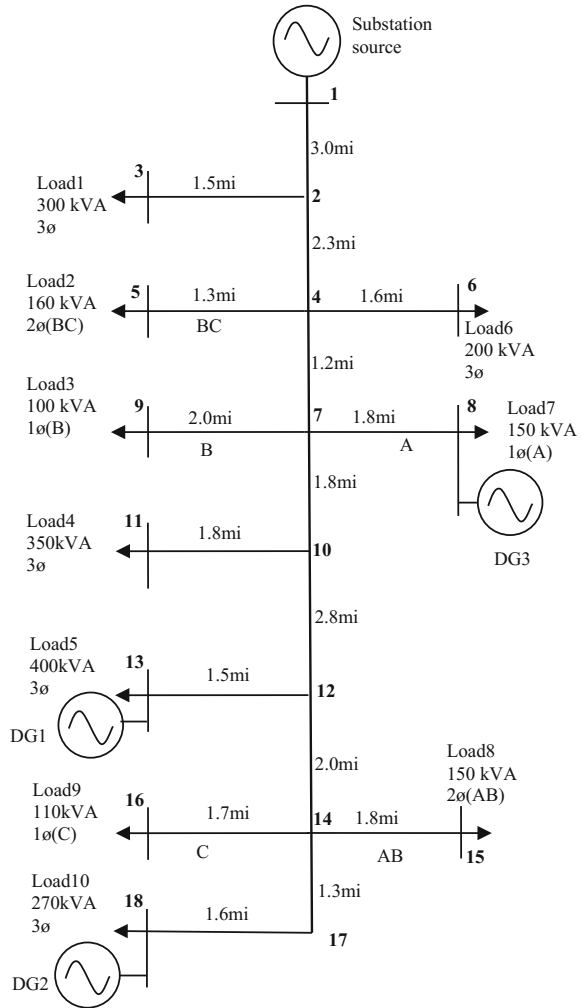
Table 17.1 shows the fault location estimates for single and multiple faults using measurements at bus 1 and bus 10. Case 1 represents a single fault case, where (1–2, AG) means the fault is of type AG and falls on feeder section 1–2. The fault is 0.3 p.u. from bus 1 with a fault resistance of 20 Ω. The last column gives the estimation error in percentage. The sixth case includes two simultaneous faults: fault 1 and fault 2, whose characteristics are provided in respective row. The results evince that the fault location algorithm has yielded highly accurate estimates for single and multiple faults.

Table 17.2 lists fault location results for single and multiple faults using measurements from bus 1 and bus 13. Again, highly accurate results have been achieved by the presented method.

Table 17.3 shows fault location results for cases where three simultaneous faults occur by using measurements from bus 1, bus 13, and bus 18. It is again manifested that the presented method has produced highly accurate estimates.

It is not always possible to estimate the fault location for all three simultaneous faults based on measurements from bus 1, 13, and 18. For example, simultaneous faults occurring on (1–2), (4–7), and (10–12) cannot be located by measurements from bus 1, 13, and 18, due to meter measurement dependence (meter at bus 13 and 18), but can be located with measurements at bus 1, 13, and 6. Note that measurement dependence is relative to fault location; in other words, two measurements

Fig. 17.6 Power distribution system with DGs



may be dependent, or has a linear relationship based on network parameters for a fault, but may be independent for another fault depending on where the fault is. Adding more measurements certainly may help improve accuracy. Generally speaking, the number of meters should equal or exceed the number of simultaneous faults in order to locate the faults. More detailed meter placement for fault location observability may be performed.

Table 17.1 Fault location results using measurements at bus 1 and bus 10

Case type	Fault number	Fault section, and fault type	FL (p.u.)	Fault res. (ohm)	FL Esti. err. (%)
Single fault	Fault 1	(1–2, AG)	0.3	20	0.01
Single fault	Fault 1	(1–2, AB)	0.5	1	0.01
Single fault	Fault 1	(1–2, ABG)	0.7	[1, 1, 50]	0.03
Single fault	Fault 1	(1–2, ABC)	0.7	[1, 2, 2]	0.03
Single fault	Fault 1	(1–2, ABCG)	0.6	[1, 1, 1, 20]	0.01
Multiple faults	Fault 1	(1–2, AG)	0.2	5	0.08
	Fault 2	(4–7, AG)	0.5	1	0.01
Multiple faults	Fault 1	(1–2, AG)	0.6	20	0.20
	Fault 2	(4–7, AB)	0.8	2	0.05
Multiple faults	Fault 1	(2–4, AG)	0.3	10	0.08
	Fault 2	(7–9, BG)	0.5	10	0.04
Multiple faults	Fault 1	(1–2, AG)	0.6	5	0.06
	Fault 2	(10–12, ABG)	0.2	[1, 5, 5]	0.05
Multiple faults	Fault 1	(1–2, AG)	0.8	5	0.23
	Fault 2	(10–12, ABC)	0.6	[1, 1, 3]	0.09

Table 17.2 Fault location results using measurements at bus 1 and bus 13

Case type	Fault number	Fault section, and fault type	FL (p.u.)	Fault res. (ohm)	FL Esti. err. (%)
Single fault		(1–2, AG)	0.3	20	0.01
Single fault		(1–2, AB)	0.5	1	0.01
Single fault		(1–2, ABG)	0.7	[1, 1, 50]	0.04
Single fault		(1–2, ABC)	0.7	[1, 2, 2]	0.04
Single fault		(1–2, ABCG)	0.6	[1, 1, 1, 20]	0.02
Multiple faults	Fault 1	(1–2, AG)	0.2	5	0.08
	Fault 2	(4–7, AG)	0.5	1	0.01
Multiple faults	Fault 1	(1–2, AG)	0.6	20	0.20
	Fault 2	(4–7, AB)	0.8	2	0.05
Multiple faults	Fault 1	(2–4, AG)	0.3	10	0.08
	Fault 2	(7–9, BG)	0.5	10	0.05
Multiple faults	Fault 1	(1–2, AG)	0.6	5	0.05
	Fault 2	(12–14, ABG)	0.2	[1, 1, 5]	0.02
Multiple faults	Fault 1	(4–7, AG)	0.8	1	0.08
	Fault 2	(17–18, ABC)	0.6	[1, 1, 3]	0.17

Table 17.3 Fault location results using measurements at bus 1, bus 13, and bus 18

Case type	Fault number	Fault section, and fault type	FL (p.u.)	Fault res. (ohm)	FL Esti. err. (%)
Multiple faults	Fault 1	(1–2, AG)	0.5	5	0.03
	Fault 2	(4–7, AG)	0.7	5	0.02
	Fault 3	(12–14, BG)	0.9	10	0.07
Multiple faults	Fault 1	(1–2, AB)	0.3	1	0.01
	Fault 2	(7–9, BG)	0.3	5	0.03
	Fault 3	(17–18, AG)	0.5	1	0.03

17.5 Conclusions

Future distribution systems will host more distributed generations, and more microgrids will emerge. Optimal operation, control and protection of the system is more challenging. This chapter discusses new methods to optimize the operation of future distribution systems, considering real power balance and also voltage regulation. Possible simulation method is presented. New protection methods considering distributed generations are also presented. It also discusses the need to develop new methods and tools to model, simulate, and optimize the operation and control of electrical system for microgrids consisting of multiple, interconnected residential, commercial, or industrial buildings, considering thermal and operational loads and constraints.

References

1. The smart grid: An introduction, department of energy (2009). [https://energy.gov/sites/prod/files/oeprod/DocumentsandMedia/DOE_SG_Book_Single_Pages\(1\).pdf](https://energy.gov/sites/prod/files/oeprod/DocumentsandMedia/DOE_SG_Book_Single_Pages(1).pdf)
2. Bansal RC, Bhatti TS, Kothari DP (2003) Artificial intelligence techniques for reactive power/voltage control in power systems: a review. *Int J Power Energy Syst* 23(2):81–89
3. Paaso EA, Liao Y, Cramer AM (2015) Dual-layer voltage and VAR control approach with active participation from distributed solar generations. *Electr Power Compon Syst* 43(8–10):854–865
4. Liao Y, Feng X, Pan J (2004) Analysis of interaction between ancillary service markets and energy market using power market simulator. International conference on electric utility deregulation, restructuring and power technologies, Hong Kong, 5–8 2004
5. Feng X, Liao Y (2010) Unit commitment by structure based solution and efficient Lagrangian relaxation. *Int J Emerg Electr Power Syst* 11(1) (Article 9)
6. Zamani MA, Yazdani A, Sidhu TS (2012) A communication-assisted protection strategy for inverter-based medium-voltage microgrids. *IEEE Trans Smart Grid* 3:2088–2099
7. Gopalan SA, Sreeram V, Iu HHC (2014) A Review of coordination strategies and protection schemes for microgrids. *Renew Sustain Energy Rev* 32:222–228
8. Liao Y (2011) Generalized fault location methods for overhead electric distribution systems. *IEEE Trans Power Delivery* 26(1):53–64

9. Liao Y (2014) Identification of faulted feeder section in distribution systems using overcurrent information from switching devices. *Int J Emerg Electr Power Syst* 15(2)
10. Liao Y (2013) Electric distribution system fault location considering shunt capacitances. *Electr Power Compon Syst* 41(5):519–536
11. Liao Y (2014) A novel method for locating faults on distribution systems. *Electr Power Syst Res J* 117:21–26
12. Xiu W, Liao Y (2014) Novel fault location methods for ungrounded radial distribution systems using measurements at substation. *Electr Power Syst Res* 106:95–100
13. Liao Y (2009) Fault location observability analysis and optimal meter placement based on voltage measurements. *Electr Power Syst Res* 79(7):1062–1068
14. Xiu W, Liao Y (2014) Fault location observability analysis on power distribution systems. *Electr Power Compon Syst* 42(16):1862–1871
15. EnergyPlus Engineering Reference. Website: <https://energyplus.net/>

Chapter 18

Protection of Distribution Systems Integrated with Distributed Generation

Adeyemi Charles Adewole, Raynitchka Tzoneva
and Alexander Apostolov

18.1 Introduction

The conventional electric power system (EPS) is made up of the generation, transmission, and distribution systems. The generating stations serve as the point where the electric power is produced. The electric power produced is wheeled to the distribution system through the transmission system. The primary distribution system serves as the link connecting the electric power produced at the generating station to the various load centres via the secondary distribution system. Large industrial customers are usually connected directly to the primary distribution system. The electric distribution system is made up of substation power transformers, distribution transformers, three-phase feeders, single- or two-phase laterals, protective devices, switching devices, capacitor banks, and service conductors.

Generally, protection in the EPS is aimed at ensuring the reliable supply of affordable electric power, the protection of equipment and the public, the maintenance of acceptable power quality, and the preservation of the integrity of the system. Thus, protective devices are applied in the EPS to reliably isolate the faulty components of the EPS as quickly as possible and restore power to the healthy sections in the shortest possible time.

In the past, distribution systems were radial in nature and the feeders were protected using overcurrent protective relays. This is typically implemented using phase- and ground-overcurrent relays. For distribution bus protection, an overcurrent relay sited at the transformers connected to the distribution system was commonly used. The above-mentioned protection are relatively simple and cheaper to

A.C. Adewole (✉) · R. Tzoneva · A. Apostolov
Centre for Substation Automation and Energy Management Systems (CSAEMS),
Cape Peninsula University of Technology, Cape Town, South Africa
e-mail: adewolea@cput.ac.za

implement and do not require transmission-level protective devices, or communication-assisted schemes. Thus, the use of complicated protection schemes such as the directional protection, distance protection, transfer tripping, and permissive schemes are unnecessary. Also, the requirements for fault clearance and auto-reclosing sequence are minimal.

In recent times, distribution generation (DG) is being integrated in the EPS mainly because of the ever increasing load demand and the lack of new generation and transmission infrastructures to support this growing demand. DG is related to the use of small generating units installed as close as possible to the load centres at the distribution or subtransmission systems.

The advantages associated with the use of DG units include the following:

- increase in system security and reliability of supply;
- reduction in transmission losses and congestion;
- efficient use of primary energy resources and waste heat (in combined heat and power (CHP) plants);
- reduction in greenhouse emissions (for DG-based renewable energy resources); and
- the possible stimulation of competition in the electricity market through the decentralisation of electric power generation.

However, there are issues associated with the integration of DG units in the EPS. Some of these include the following:

- changes in system conditions and parameters as a result of the changes in power flow, voltage profile, and fault current levels;
- the interconnection of DG units transforms the structure of the EPS. This implies that the operator must learn to simultaneously manage the central- and local-generated power;
- the power electronics technology used in connecting some DG units to the distribution system may cause harmonics, power quality issues, and low fault current contribution compared to synchronous or induction machine DG units; and
- changes in the system parameters may require a review of the equipment ratings and protection philosophy previously implemented in the conventional EPS.

This chapter provides an introduction to protection in conventional distribution systems, followed by some requirements for the integration of DG units in distribution systems. The influence of DG units on distribution system protection is discussed afterwards. Case studies are presented for a typical distribution system and for a distribution system integrated with DG units. Lastly, the application of emerging technologies in the protection of distribution systems integrated with DGs is discussed.

18.2 Introduction to Distribution Systems

Distribution systems belong to the portion of the EPS that is made up of distribution substations and feeders connecting the customers to the EPS. Distribution substations are commonly fed by subtransmission lines or directly by transmission lines (in some countries). Generally, distribution systems are in the medium voltage (MV) range and operate within the voltage range of about 6.6–66 kV. In some countries, distribution systems may extend to the 132 kV voltage level. Distribution feeders usually consist of three-phase overhead lines and/or underground cables with a mix of three-phase, two-phase, or single-phase laterals (tap-offs) to the various customer premises. The servitude to the secondary customers terminates at a lower secondary voltage of about 400 V (three-phase circuits) or 230 V \pm 10% (single-phase circuits) in Europe, Africa, most of Asia, most of South America and Australia, while 240 V (three-phase circuits) 120 V \pm 5% (single-phase circuits) is used in North America.

The loads at the customer premises can be grouped into industrial, commercial, and residential loads. Industrial loads are composed of mainly induction motor loads, while the commercial loads comprise of air conditioning, space heating, and discharge lighting loads (mercury vapour, sodium vapour, and fluorescent lamps). Residential loads are made up of household appliances typically comprising of heating, lighting, oven, and other domestic loads. The composition of these loads would depend on the time of the day (peak or base loads), weather (hot or cold), and the season of the year (summer or winter). Also, the characteristics of these loads play an important role in the ability of the power system to withstand contingencies and maintain an acceptable level of system security and stability [1–3].

18.2.1 Protection in Distribution Systems

Short circuit faults are abnormal system conditions which can occur as a result of equipment failures caused by insulation failure, malfunction, or ageing. Also, lightning, animal/bird contact, environmental conditions, and human errors can cause the interruption of the normal electric power flow which could result in equipment damages, fatal injuries, or death to humans or animals.

There are two types of short circuit faults in power systems. These are the symmetrical and the unsymmetrical faults. Symmetrical faults are balanced three-phase faults, while unsymmetrical faults comprise of single-phase-to-ground, phase-to-phase, and phase-to-phase-to-ground faults. A three-phase fault occurs when all the three phases of the circuit come into contact with each other. A single-phase-to-ground fault is the most common type of short circuit, and it occurs when one of the phases of the electric circuit comes into contact with an alternative current path or ground. Phase-to-phase faults occur when two phases come in contact with each other, while phase-to-phase-to-ground faults occur when

two phases come in contact with each other with a conductive path to ground. About 75–90% of short circuit faults are temporary in nature, while the rest are permanent and would require corrective maintenance to clear the fault [4, 5].

In order to protect distribution systems against short circuit faults, protective devices are usually applied to timely isolate the faulty section of the distribution system. Four requirements for protection in power systems are as follows: (i) the timely operation (speed) of the protective devices; (ii) sensitivity; (iii) selectivity; and (iv) reliability. That is, the implemented protection should be designed to operate timely within the shortest possible time and detect severe and less severe fault conditions (sensitivity). Selectivity is related to the ability of the protective scheme to operate sequentially as designed for the primary and backup zones, thereby maintaining maximum continuity of services with little disconnection. The reliability of a protective relaying scheme can be divided into its dependability and security of operation. Dependability refers to the ability of the protective relaying scheme to operate correctly when required to, while the security of operation is the ability of the protective device not to operate when not required.

Distribution systems are usually divided into zones of protection which are protected individually and with some overlap in order to ensure total coverage such that in the event of a fault, the faulted zone is isolated reliably without causing disruptions in the healthy zones. These protection zones can be based on the individual equipment in the distribution system. This would typically comprise of the bus, transformer, feeder, and load/motor zones.

A description of the various types of protection commonly used at these protection zones in distribution systems is given below:

- Bus zone: overcurrent (ANSI 50/51) protection and differential (87) protection;
- Transformer zone: primary fuses, phase- or ground-fault overcurrent (50/51) protection, and differential (87) protection;
- Feeder zone: fuses, phase- or ground-fault overcurrent (50/51) protection, directional (67) protection (for looped distribution system), line differential (87L), and distance (21) protection (not common);
- Loads: fuses, overload protection, phase- or ground-fault overcurrent (50/51) protection;
- Motors: fuses, phase- or ground-fault overcurrent (50/51) protection, under-voltage (27) protection, negative phase-sequence current (46) protection, negative phase-sequence voltage (47) protection, and thermal/locked rotor (49) protection.

These protection zones can be designed to have primary and backup (secondary) protections. The primary protection is the closest protection device to the fault, and it is designed to operate for permanent faults within its protection zone, while the backup protection is designed to operate in the event that the primary protection fails. The backup protection can be co-located with the primary protection, or it can be located at the remote end. It is usually configured with a delay sufficient to allow

the primary protection to act first [6]. Commonly used protective devices in distribution systems are presented in the proceeding subsection.

18.2.2 Protection Devices in Distribution Systems

In order to design and implement the appropriate protection against short circuit faults, it is necessary to know the impact of the various types of faults on the currents in the distribution system. The information required for this can be obtained through the calculation of the maximum short circuit current and the minimum short circuit current. The magnitude of the short circuit current is dependent on the fault current contribution from the source, the transformer impedance, the motor contribution, and the location of the fault.

The most common type of distribution feeder protection is the non-directional phase- and ground-overcurrent (50/51) protective relays for phase and ground faults, respectively. These overcurrent protective relays are used in combination with fuses, line reclosers, and sectionalisers located in the downstream of the distribution system. Fuses serve as the primary protection for the laterals and small-sized transformers, while line reclosers and the overcurrent protective relays can serve as the backup protection for lateral circuits. Other types of protection that can be found in distribution system include directional protection, differential protection, thermal protection, and overvoltage protection.

Figure 18.1 illustrates a section of a typical distribution system comprising of the main intake substation (Intake S/S) connected to the grid (distribution infeed), main feeder line, transformer (T1), and loads (loads 1–4 and a motor load). The various protection zones are highlighted as shown in Fig. 18.1. Typically, an overcurrent protective relay or recloser can be used at the Intake S/S, while fuses could be used in the protection of the loads. Additional protection is required in the protection of transformer T1 and the motor load. Typical protection in distribution systems are further discussed in this subsection.

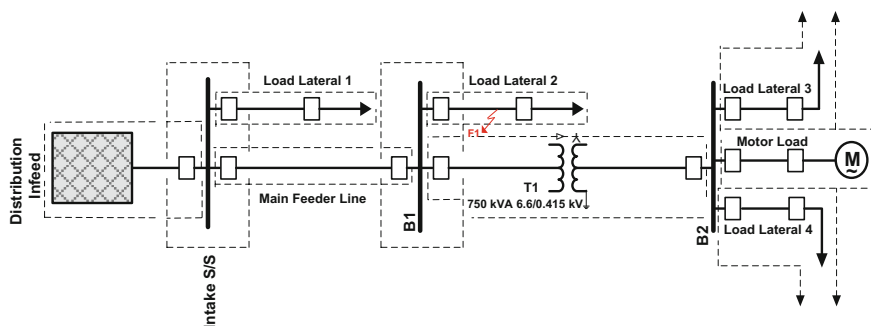


Fig. 18.1 Typical distribution system with various protection zones

1. Fuses

Fuses are a type of overcurrent device with fuse elements designed to heat up and melt during overload or overcurrent conditions. Generally, fuses can be classified into two types based on their mode of operation: the expulsion type and the current-limiting type fuses. The expulsion fuse is an open type of fuse with a fusible element made of silver or tin. It melts during an overcurrent condition and produces an arc on melting. The fault is cleared at the first or second zero-current crossing. Expulsion fuses can be further subdivided into two classes based on their operating speed: the ANSI K-type and T-type classes. K-type fuses are generally faster and have a lower speed ratio, while the T-type fuses are slower with a higher speed ratio compared to the K-type.

Another type is the N-type fuse with the same speed ratio as the K-type and is made from tin. The speed ratio is obtained as the ratio of the melting current at 0.1 s to the melting current at 300 or 600 s depending on the fuse current rating [7]. K-type fuses are commonly applied where fast time–current characteristics are required, for example, in transformer, capacitor, and lateral protection. T-type fuses are mainly used where coordination is required with protective relays and reclosers.

The current-limiting fuse is a type of fuse made from silicon sand. An overcurrent condition causes the silicon sand to melt and create a narrow glass tube (fulgurite) in the process, thereby forcing the current to zero. This fast operating action makes the current-limiting fuses to be faster than the expulsion type, and they typically have an operating time of about half a cycle. A common application for the current-limiting fuse is in areas where high fault clearing capability is required. They can interrupt faults up to 50 kA, while the expulsion fuses are generally limited to about 13 kA [7]. In the sizing of a fuse, the continuous current rating of the fuse must be equal to or greater than the maximum short-time load that will pass through it. Typically, fuses have four stages of operation: current sensing, arc initiation, arc interruption, and current interruption stages.

The operating principle of fuses is based on the minimum melting (MM) curve which gives the minimum melt time and the total clearing (TC) curve which defines the time required for the fuse element to completely melt. Figure 18.2 shows the time–current characteristics of a fuse comprising of the MM and the TC curves. These operating times are dependent on the magnitude of the current, the duration of the overcurrent, and the electrical properties of the fuse. The minimum melt time (T_{mm}) is the time between an overcurrent condition large enough to cause the element to melt and the instant when arcing occurs. The arcing time (T_{arc}) is the time required to interrupt the current after the fuse melts. The total clearing time (T_{tc}) indicates the total time from the beginning of an overcurrent condition to the final interruption of the circuit.

The total clearing time is mathematically given as:

$$T_{tc} = T_{mm} + T_{arc} \quad (18.1)$$

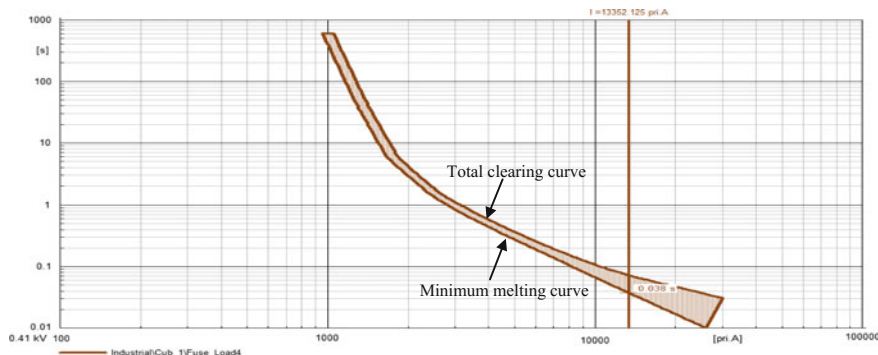


Fig. 18.2 Time–current characteristics of the minimum melting and total clearing times of a fuse

The type of fuse rating to use in a distribution system will depend on the continuous current carrying capacity of the fuse, the nominal voltage, the maximum design voltage, and the interrupting capacity of the fuse. For instance, the fuse at load 3 is a 250 A SMU-40 fuse from S&C Electric Company with a short circuit current of 13.352 kA (indicated by the brown vertical line) for a three-phase short circuit fault and would have a minimum melt time of 0.038 s and a total clearing time of 0.073 s which are indicated by the point where the vertical line strikes the time–current characteristics (TCC) curve as shown in Fig. 18.2.

2. Overcurrent Protective Relaying

Although the protection based on fuses is cheap and simple to implement, it is difficult to control the operating time of fuses. Also, a physical replacement is required once a fuse element melts. Overcurrent (50/51) protective relays provide protection against excessive overcurrent that can occur due to overload or fault current conditions. Usually, the overcurrent relay requires only current inputs from current transformers (CTs) for its operation. However, some protection schemes such as the directional overcurrent (67) protection (for meshed or looped systems) and the voltage supervised-overcurrent (51 V) protection (commonly for industrial generator backup protection) require voltage inputs from voltage transformers (VTs). The CTs and VTs transform the measured currents and voltages from the lines/buses typically to 1 A or 5 A current supply and 110–115 V voltage supply, and serve as the inputs to the analogue input module of the protective relays.

Overcurrent protection can be divided into three: instantaneous overcurrent (50), definite time overcurrent (50TD), and inverse time overcurrent (51) relays. The instantaneous overcurrent relay is designed to operate immediately the current magnitude exceeds a pre-determined (pickup current) level. The pickup setting should be as sensitive as possible and must not trip for non-fault conditions such as transformer inrush, cold-load pickup, motor starting, power swings, and for external faults outside its protection zone. Instantaneous overcurrent is mainly used for close-in faults on long feeders and is meant to operate by issuing a trip signal within

a few milliseconds to the relevant circuit breaker. The definite-time overcurrent relay operates when the pickup current level is reached and after an intentional time delay elapses. It is used for short length feeders where the fault current does not change with the location of the fault across the feeder. The inverse time overcurrent relay has an operate time that is inversely proportional to the fault current based on some mathematically derived characteristic curves. This implies that severe faults are cleared faster compared to less severe faults. They are commonly applied in distribution feeder protection/load areas. The time–current characteristics of the inverse time overcurrent relay are defined by the IEC 60255 and the North American standards. These characteristics and their mathematical equations are given in Tables 18.1 and 18.2. Figures 18.3 and 18.4 show the plots of these various characteristics using the equations defined in Tables 18.1 and 18.2.

Overcurrent protective relays are required to provide protection against phase and ground faults. These relays can be directional or non-directional depending on the system topology and protection requirements. For radial distribution systems, non-directional overcurrent relays would suffice, while for looped distribution systems, directional overcurrent relays are more appropriate. Three conditions are required for the directional overcurrent relays to operate: the current magnitude, intentional time delay, and the direction of the current flow. The pickup of the phase-overcurrent relay is usually set at k times the maximum short-time load or greater, where k is taken as 1.25–1.5 [4, 8]. The pickup threshold of the

Table 18.1 IEC 60255 overcurrent relay characteristics [9]

Overcurrent relay characteristics	Equation (IEC 60255 definitions)
Standard inverse	$t = (\text{TMS}) \times \frac{0.14}{(\text{PSM})^{0.02} - 1}$
Very inverse	$t = (\text{TMS}) \times \frac{13.5}{(\text{PSM}) - 1}$
Extremely inverse	$t = (\text{TMS}) \times \frac{80}{(\text{PSM})^2 - 1}$
Long-time standby earth fault	$t = (\text{TMS}) \times \frac{120}{(\text{PSM}) - 1}$

Table 18.2 US and IEEE overcurrent relay characteristics [9]

Overcurrent relay characteristics	Equation (North American definitions)
IEEE moderately inverse	$t = \frac{\text{TD}}{7} \left[\left(\frac{0.0515}{(\text{PSM})^{0.02} - 1} \right) + 0.114 \right]$
IEEE very inverse	$t = \frac{\text{TD}}{7} \left[\left(\frac{19.61}{(\text{PSM})^2 - 1} \right) + 0.491 \right]$
IEEE extremely inverse	$t = \frac{\text{TD}}{7} \left[\left(\frac{28.2}{(\text{PSM})^2 - 1} \right) + 0.1217 \right]$
US C08 inverse	$t = \frac{\text{TD}}{7} \left[\left(\frac{5.95}{(\text{PSM})^2 - 1} \right) + 0.18 \right]$
US CO2 short time inverse	$t = \frac{\text{TD}}{7} \left[\left(\frac{0.02394}{(\text{PSM})^{0.02} - 1} \right) + 0.01694 \right]$

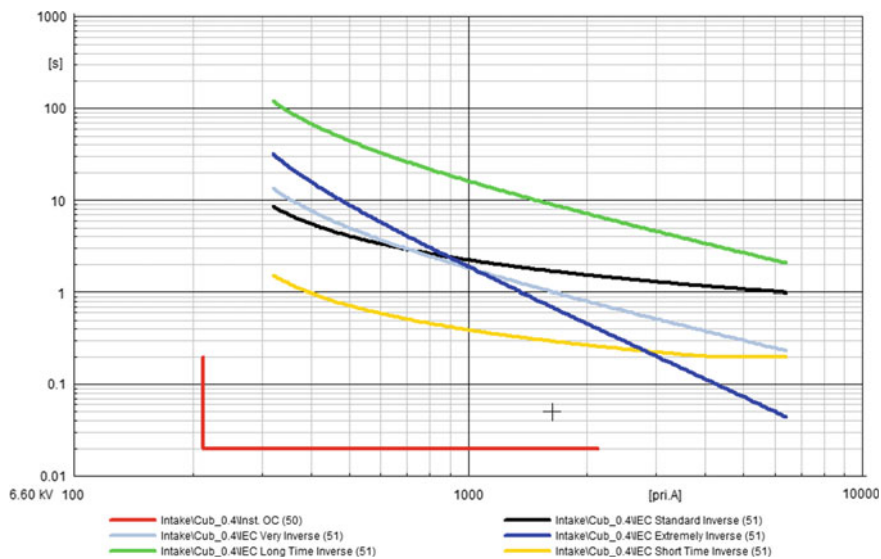


Fig. 18.3 IEC 60255 time–current characteristics for instantaneous and inverse time overcurrent protection characteristics

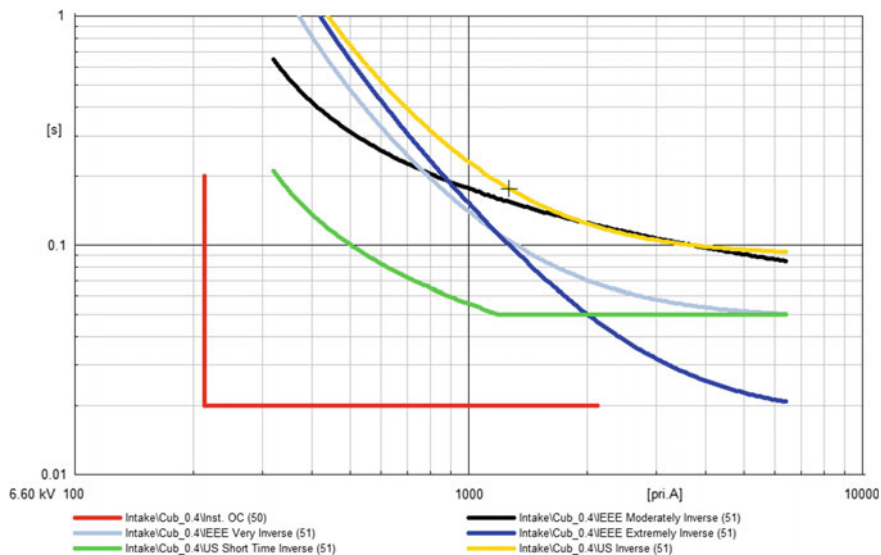


Fig. 18.4 North American time–current characteristics for instantaneous and inverse time overcurrent protection characteristics

ground-overcurrent relay must be set above the maximum zero-sequence current in the system and should be set as low as possible in order to provide acceptable sensitivity. k is usually taken as 0.1–0.2 of the maximum short-time load current or twice the maximum load unbalance [4, 8].

Negative sequence overcurrent protection can be applied for feeder remote end faults which are usually accompanied by low levels of short circuit fault currents. These low-level fault current limits the sensitivity of the phase-overcurrent relay and also causes an increase in the fault clearing time. The suitability of the negative sequence overcurrent element is due to the production of negative sequence current during unbalanced fault conditions. Thus, it will operate for both phase and ground faults.

where $PSM = \frac{\text{Fault current}}{\text{Pickup current}}$, TMS is the time multiplier setting, and TD is the time dial setting.

3. Reclosers

Reclosers are a type of overcurrent protective device integrated with fault sensing, relaying, fault interruption, and reclosing functionalities in distribution systems with overhead lines (OHL). They are designed to operate instantaneously or with intentional time delays. When circuit breakers are tripped as a result of faults, reclosers automatically... reclosers automatically attempt to close the tripped circuit breakers by using a pre-determined number of shots (attempts) to clear the faults before lockout. They can be installed at the substation or along a line, and use either oil or vacuum as the interrupting medium within an interrupting chamber. The self-contained controls of reclosers can be hydraulic or electronic-based. Reclosers with hydraulic controls sense overcurrent conditions using a trip coil connected in series with the line. The recloser contacts are tripped open during overcurrent conditions by the action of a plunger which is attracted onto the coil. Electronically-controlled reclosers have a separate electronic cabinet that is used in the programming of the recloser operations. This comes with the pre-selected time–current tripping characteristics and the reclosing times. They are easily customisable, flexible, facilitates substation automation, and more accurate compared to the hydraulically-controlled reclosers. Most modern microprocessor-based protective relays have recloser functionality incorporated in them and can be used in substations or at higher voltage levels where reclosers are not available.

The time–current characteristics of reclosers are shown in Fig. 18.5. This comprises of the fast characteristic curve (FCC) and the slow characteristic curves (SCC). Curve A indicates the FCC, while curves B and C indicate the SCC. The FCC is used for instantaneous tripping, typically in fuse-saving protection schemes. The SCC delays the recloser operation such that if the fault condition still persists after the operation of the fast characteristic of the recloser, then the fuses will be allowed to clear such permanent faults. Reclosers are commonly configured for one fast operation using the fast characteristic, followed by two time-delayed operations using the slow characteristic.

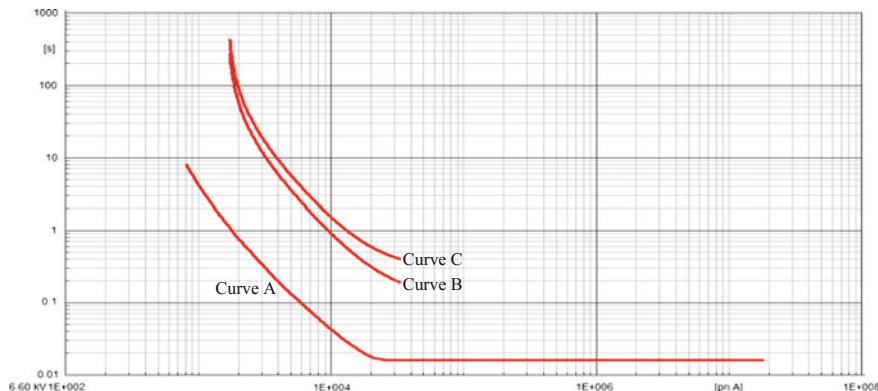


Fig. 18.5 Recloser time–current characteristics for 1-fast (instantaneous) operation and 2-slow (time-delayed) operations

4. Sectionalisers

Sectionalisers are a class of pole-mounted switching devices that are capable of operating and isolating the faulted section of the distribution feeder during the dead (de-energised) circuit time. They are used in conjunction with reclosers or breakers and are designed to count the number of reclosing or breaker operations during faults. After a predetermined number of reclosing/breaker operations (attempts), a sectionaliser will operate to isolate the faulty section of the system.

Sectionalisers can be single phase or three phase. They have no time–current characteristics since they are only designed to detect or count current interruption and operate. They can easily be coordinated with the other protection devices in the distribution system.

18.2.3 Protection Coordination and Strategies in Electric Distribution Systems

Typical protection in a distribution system will comprise of transformer overcurrent protective relay, feeder overcurrent protective relays, and bus protective relays. The transformer overcurrent protection is commonly used in the protection of the bus zone in some utilities. Differential protection is also used in the protection of large transformers, while fuses are used for small-sized transformers. Fuses are also applied in the protection of the lateral sections of distribution feeders.

The operation of the various protective devices in the distribution system involves the coordination of the time–current characteristics of the protective devices such that the sequence of operation of the devices will occur in a pre-planned specified order. This is done in order to allow the primary protection to operate first well before the backup protection is required to operate. Relay

coordination can be achieved by using time, current, or a combination of time and current [8, 9]. Protection coordination and two commonly used protection coordination philosophies are presented below:

1. Protection Coordination

Protective device coordination using time assigns time setting to the protective devices in the system such that the device closest to the fault would be the first to operate. Conversely, device coordination using current is based on the principle that the fault current resulting from a short circuit varies with the location of the fault due to the difference in the impedance between the source and the fault location. Thus, the device with the highest fault current is required to operate first. A combination of time and current can be used to achieve a protection scheme in which the operating time of the protective device is inversely proportional to the fault current. This implies that the operating time for large fault currents will be faster compared to lesser fault currents. Thus, the limitations associated with protection coordination using time or current are overcome.

A coordinating time interval (CTI) is used in the coordination of the protective devices in the distribution system. The CTI is the interval between the operation of the protective devices at the substation end and at the remote downstream end. The various protective devices are configured such that remote faults are cleared by the downstream protective devices, while the upstream protective device acts as the backup protection. This implies that for remote faults, the upstream protective device should have an operating time greater than the sum of the operating times for the remote downstream protective devices and the CTI. In practice, this would allow the rest of the distribution system upstream to remain energised, while the faulty section of the distribution system is disconnected by the operation of the downstream protective device.

2. Fuse-Saving Scheme

The fuse-saving scheme is designed to intentionally allow the upstream protective devices, such as the substation breaker or recloser, to operate for temporary downstream faults for a predetermined number of attempts before the downstream fuse melts to clear the permanent fault. This approach minimises the number of customers that are impacted by the outages that would have been caused by the melting of the fuse element.

However, the number of momentarily interruptions increases and would affect the reliability indices of the distribution system. For example, a fuse-saving scheme for the main feeder line and Load Lateral 2 can be implemented as shown in Fig. 18.1 for fault F1 using a recloser at the intake bus configured for 1 fast trip and 2 slow trips, respectively. The recloser is coordinated with the fuse at the load lateral such that the recloser (fast trips) operates faster than the fuse for faults on the lateral. Thus, the lateral fuse is prevented from operating (melting) to clear temporary faults.

3. Fuse-Blowing Scheme

The fuse-blowing scheme is designed to clear downstream faults without waiting for the upstream protective devices to operate. The characteristic curves of the overcurrent protective relay or recloser are set above the fuse curves such that the fuses operate first to clear the faulted section of the distribution system, while the substation protective relay or recloser acts as the backup protection.

This type of protection scheme prevents the momentary outages associated with the fuse-saving scheme where the recloser operation isolates a large number of customers. However, the fuse-blowing scheme causes outages for an extended amount of time and is cleared only when the damaged fuses have been physically replaced. In Fig. 18.1, a fuse-blowing scheme for the main feeder line and Load Lateral 2 implies that the fuse at the lateral will operate and clear faults faster than the recloser, or the recloser could be configured not to trip for faults on that lateral.

The fuse-saving scheme is suitable for rural distribution feeders or residential feeders that are not sensitive to momentary outages, while the fuse-blowing scheme is suitable for feeders serving critical loads that must not be momentarily interrupted.

4. Relay–Recloser–Sectionalizer Coordination

Relay–recloser–sectionalizer coordination is a combinational scheme involving relay–recloser and recloser–sectionalizer coordination. For relay–recloser coordination, the relay operation should be time-delayed such that downstream faults are cleared by the reclosers. The relay can also be set for instantaneous trip for fault locations short of the recloser's protection zone. For recloser–sectionalizer coordination, the sectionalizer counts the number of operation of the upstream recloser and is configured for one shot less than the total number of recloser operations such that the recloser can energise the healthy segment of the system after the sectionalizer must have operated to isolate the faulty segment.

Another possible combination is the recloser–sectionalizer–fuse coordination in which the sequence of operation of the fuse and the sectionalizer is adjusted to coordinate with the recloser fast and slow curves. The particular coordination scheme to adopt will generally depend on the utility philosophy and experience, system requirements, and the preference of the planning/protection engineer.

18.3 Distribution Systems Integrated with Distributed Generation

Distribution generation refers to a class of small-scale, distributed, and decentralised power plants that are located as close as possible to the customer end or at the distribution and subtransmission networks [10]. The goal of these power plants also referred to as embedded/dispersed generation can be the supply of the local loads or as backup supply during emergency or utility outages.

Distributed generation sources can be renewable energy sources or non-renewable energy sources. Renewable energy sources are influenced by geographical and meteorological conditions. Examples are photovoltaic generation, wind power plants, tidal, wave, and micro-hydro generation. The distributed generation from non-renewable energy sources is not restricted by geographical or meteorological constraints and can be connected at any point in the distribution system. Examples of non-renewable energy sources include fuel cells, microturbines, combustion engines, steam turbines, Stirling engines, reciprocating engines, and diesel or gas combustion turbines. Table 18.3 shows the various types of distributed generation prime movers, various types of distributed generation technology, and their characteristics. Distributed generation can be classified into four categories based on their capacity [10]. This classification is presented in Table 18.4.

The technical, environmental, and economic benefits of the integration of the distributed generation in the EPS include the supply of real and reactive power, improved voltage control, improvement of the system’s voltage profile, reduction in electric losses, increased transmission and distribution capacities, reduction in environmental pollution (with renewable sources), and improved system reliability. DG units are commonly integrated to the distribution system via synchronous or induction generators, or via power electronic converters.

Figure 18.6 shows a section of the distribution system in Fig. 18.1 when it is integrated with a DG unit at load 2 lateral. The DG unit supplies part of the load demand at load 2. For a short circuit fault along load 2 lateral or along the main feeder, the DG unit will contribute to the total short circuit fault current I_f .

Table 18.3 Types of prime movers and distributed generation technologies

Type of prime mover	Type of technology	Characteristics
Rotating	Reciprocating engines, combustion turbines, steam turbines, wind turbines, water turbines, and microturbines	Rotating prime movers directly/indirectly drive rotating generators through a shaft, reduction gearbox, or power electronics converter
Non-rotating	Photovoltaic, fuel cells	Non-rotating prime movers directly produce DC power

Table 18.4 Classification of DG units according to capacity

Type of DG	Capacity (kW)
Micro	0.001–5
Small	5–5000
Medium	5000–50,000
Large	50,000–300,000

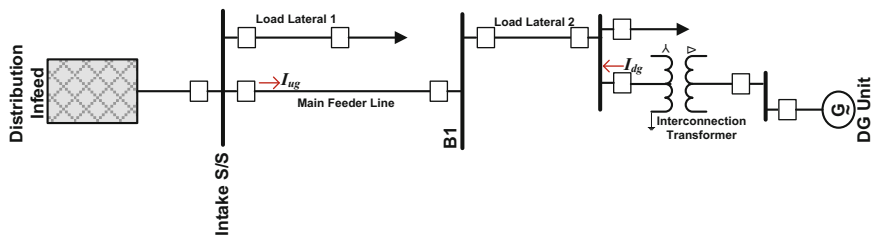


Fig. 18.6 Section of a distribution system integrated with distributed generation

This is given as:

$$I_f = I_{ug} + I_{dg} \tag{18.2}$$

where I_{ug} is the fault current from the utility (grid side), and I_{dg} is the fault current contribution from the integrated DG unit.

From Eq. (18.2), it can be seen that the fault current in a distribution system integrated with DG units will increase due to the additional fault current contributed by the integrated DG unit(s). This will depend on the fault location and the type of DG technology used. This section presents the technical impact of the integration of distributed generation and the general considerations prior to the integration of DG units in the EPS.

18.3.1 Impact of the Integration of Distributed Generation on Electric Distribution Systems

The integration of distributed generation would result in a change in the direction of the power flow in distribution systems from the previously radial distribution systems to bidirectional meshed/looped distribution systems. Impact studies are necessary prior to the integration of distributed generation to the distribution system in order to avoid any negative effect that could arise from such interconnection. The extent of the impact of the integration will depend on the size of the distributed generation, the type of technology used, the point of interconnection, and the prevailing characteristics of the existing utility [11, 12].

The impact studies can be carried out using computer-based packages capable of electromagnetic time domain simulation. It should be noted that the accuracy of these impact studies will depend on the differential-algebraic equations (DAE) implemented in the models of the power system package used. The impact studies should generally cover the following:

1. Mode of Operation

DG units can be operated in three different modes: the grid-connected mode, the islanded mode, and the standby mode. The grid-connected mode of operation involves the parallel operation of the DG units alongside the utility supply. This is the most commonly implemented mode of operation. In this mode, the DG units must be capable of automatically shutting down during faults. In the islanded mode of operation, the DG units operate in isolation from the utility grid and may continue to fully or partially supply local loads at the DG side of the system. Thus, there is no power flow to and from the grid. The stand-by mode is designed to supply the essential loads during a major supply disruption. In most cases, the DG units are emergency (backup) systems powered by diesel or gas engines that are started when there is an outage of the utility supply. They are usually operated after the loads are disconnected from the utility network with a change-over switch.

The DG penetration level for a distribution system may be defined as:

$$\text{Penetration level} = \frac{\text{Rated DG output power}}{\text{Distribution peak load}} \quad (18.3)$$

2. Type of DG Technology

Distributed generation is integrated to the distribution system using synchronous generator, induction generator, or power electronics-based technology. Synchronous generators produce fault currents that are six times the generated full load current. The fault currents produced will decay within seconds as the generator field collapses. Unlike the synchronous generators, the fault currents produced by induction generators are less.

Power electronics-based technology does not produce significant fault currents. Typically, the fault current contribution is about 1.2–1.5 times the inverter's rated load current [12]. The commonly applied fault detection algorithms in protective relaying based on fault current magnitude might fail for a distribution system integrated with power electronics-based distributed generation. Other types of detection algorithm based on voltage supervision or frequency sensing can be used to supplement the traditional overcurrent protective relaying.

3. Short Circuit Current Level

Fault currents are induced in power systems as a result of abnormal conditions (disturbances). The presence of distributed generation would affect the short circuit contribution from all the sources in the distribution system. The additional short circuit current contribution from the DG units will depend on the type of technology used, the penetration level, and the location of the DG units with respect to the fault location.

The increase in the short circuit current in the distribution system integrated with distribution generation will affect the continuous current carrying capacity, short circuit ratings of the equipment, protection settings, protection coordination, and the

short circuit interrupting capacity of the protective devices. For example, power electronics-based DG have the least fault current contribution compared to synchronous or induction generator-based DG units. This implies that equipment ratings will be different depending on the type of technology used (though fault current limiters can be used). Also, the size of the DG units and the penetration level add to the total short circuit current obtained in an interconnected distribution system. However, the lack of sustained short circuit current could affect the ability of the protective devices to accurately detect and discriminate against short circuit faults. A fault current source (FCS) device was proposed in [13] to increase the fault current contribution of power electronics-based DG units during faults. The FCS will be activated by the voltage sag that ensues during a fault condition. Upon activation, the FCS will attempt to restore the voltage to the pre-fault condition thereby injecting some fault current into the network. This will consequently facilitate the operation of the protective device in the system.

FCS would typically consist of the following:

- an energy storage device that can supply for a specific duration the active power required for the fault current;
- a power electronic circuit or switch for releasing the active power from the FCS into the low voltage network;
- a circuit for monitoring the system, detection of fault conditions, and triggering of the FCS; and
- a recharging system for restoring the charge of the energy storage device after the delivery of the fault current.

4. Protective Relaying

The integration of distributed generation in the distribution system will affect the existing protection schemes. This is because the normally radial distribution system is transformed into a bidirectional loop system with current flow from the grid to the distribution system and from the DG units to the distribution system. Hence, the review of the existing protection settings/schemes is necessary. The reviewed protection will typically comprise the utility-side protection, DG-side protection, interconnection transformer protection, and the protection at the point of common coupling (PCC). Generally, the type of protection to use in an interconnected system will depend on the size of the DG, the DG technology, and the point of connection in the grid (subtransmission/distribution systems or at the customer end of the meter). Also, the type of interconnection (interface) transformer used in connecting the DG unit to the utility will determine whether ground faults are detectable in the system. If the DG interconnection transformer does not provide ground fault current, the protection might fail to detect ground faults. Furthermore, some transformers with on-load tap changers are not designed with reverse power flow considerations, and this might affect the transformer operation or its associated protection.

Some common protection issues that occur as a result of the integration of distributed generation include the following:

- failure of the utility protection schemes;
- sympathetic tripping whereby the protective device on an unfaulted feeder trips for faults on adjacent feeders;
- protection blinding due to the increase or reduction in the fault current seen by the protective device thereby causing the protective device to overreach or underreach its zone of protection;
- unintended islanding of the interconnected system;
- unsynchronised reclosing; and
- loss of protection coordination.

The DG mode of operation may also impact the protection settings and coordination of the implemented protection scheme. For example, if the DG unit is in a parallel grid-connected mode, a different configuration setting may be required compared to that needed for islanded or standby modes of operation.

18.3.2 Requirements for the Integration of Distributed Generation in Distribution Systems

Most utilities have a list of requirements that must be satisfied by the DG owner or independent power producer (IPP) before, during, and after the interconnection of distributed generation to the utility's network. These requirements are put in place in order to address issues relating to safety, power quality, protection, and other technical or financial issues.

The IEEE 1547 [12, 14] categorised the technical requirements for the interconnection of distributed generation into the general requirements, requirements for operation under abnormal conditions, power quality, and islanding. These requirements are summarised below.

1. General Requirements

The general requirements that must be satisfied prior to the interconnection of distributed generation to the distribution system are broadly discussed here under the equipment capacity ratings and interconnection grounding. The integration of the DG units would result in an increase in the power flow, improvement in the voltage profile, and an increase in the fault current level in the system. Therefore, it will be necessary to carry out equipment upgrades and ensure that the continuous current-carrying capacity and the short circuit capacity ratings of the equipment can withstand the new system conditions. Also, the type of interconnection transformer used is important. Interconnection grounding depends on the type of transformer at the PCC. The interconnected system can be solidly grounded, ungrounded, or

grounded through a grounding impedance. Five types of transformer connection can be implemented: delta-delta (Δ - Δ), grounded wye-delta (Y_g - Δ), delta-wye (Δ - Y), delta-grounded wye (Δ - Y_g), and grounded wye-grounded wye (Y_g - Y_g) connections [15]. These various transformer connection types have their advantages and disadvantages. An incompatible transformer connection or grounding can result in overvoltage conditions (phase-to-neutral voltage on the unfaulted phases becomes equal to the phase-to-phase voltage), unwanted ground currents, and equipment damage. The particular type of grounding or transformer to use will also depend on the practice at the connecting utility.

Delta-delta, delta-grounded wye, and ungrounded wye-delta do not have zero-sequence currents for ground faults at the feeder. That is, the DG units will not contribute any fault currents for ground faults at the primary of the interconnection transformer. However, overvoltages are likely to occur if the DG unit continues to supply the feeder from an ungrounded source after the feeder breaker has been tripped open. For the grounded wye-delta transformer, no zero sequence current is obtained for faults at the interconnection transformer end. However, a zero sequence current is provided for feeder faults. The grounded wye-grounded wye transformer does not result in overvoltages for ground faults at the feeder. However, it causes the feeder protection device to overreach for ground faults at the transformer end and for ground faults on adjacent feeders connected to the same substation bus.

2. Abnormal Condition Requirements

Synchronous- and induction generator-based distributed generation will contribute more fault current compared to inverter-based distributed generation. Inverter-based DG units have little or no inertia and are capable of quickly limiting their output compared to synchronous and induction generator-based DG. Under abnormal fault conditions, the DG units are required to be disconnected from the system for faults at the utility side of the interconnected distribution system. This is required so that the DG units do not continue to energise the fault after the disconnection of the utility.

Some utility regulations and national standards require that the DG units should have a voltage/frequency fault ride through capability, such that the DG units stay connected to the grid during temporary fault conditions. However, the ability of the DG units to detect an abnormal condition and comply with these standards would depend mainly on the type of DG technology and the type of fault.

3. Power Quality Requirements

The IEEE 1547 standard specifies that the presence of DG units must not cause the voltage and system frequency to deviate from the prescribed limits. Five voltage ranges are specified as shown in Table 18.5. The interconnected DG units are required to cease supplying the distribution system within the clearing time specified in Table 18.5. Similarly, Table 18.6 gives the frequency ranges in the system and their required clearing time. Also, it is required that the integration of DG units in distribution networks does not adversely impact the capacitor/voltage

Table 18.5 Interconnection system default response to abnormal voltages [14]

Voltage range (% of the base voltage ^a)	Clearing time (s)	Clearing time: adjustable up to and including (s)
$V < 45$	0.16	0.16
$45 \leq V < 60$	1	11
$60 \leq V < 88$	2	21
$110 < V < 120$	1	13
$V \geq 120$	0.16	0.16

^aBase voltages are the nominal system voltages stated in ANSI C84.1: Table 1

Table 18.6 Interconnection system default response to abnormal frequencies [14]

Function	Default settings		Ranges of adjustability	
	Frequency range (Hz)	Clearing time (s)	Frequency range (Hz)	Clearing time (s) adjustable up to and including
Underfrequency 1	<57	0.16	56–60	10
Underfrequency 2	<59.5	2	56–60	300
Overfrequency 1	>60.5	2	60–64	300
Overfrequency 2	>62	0.16	60–64	10

regulator controls or affect power quality by introducing harmonics or flicker in the system. Furthermore, it is important that a generator-load balance is maintained during the operation of the DG units in the islanded mode in order not to cause power quality problems due to over/under frequency.

4. Protection Requirements

As previously mentioned, the conventional distribution system is usually planned as a passive network with power flowing unidirectional from the central generating stations to the distribution system via the transmission network. With a distribution network integrated with DG unit, the erstwhile passive network becomes an active one. Therefore, the existing protection philosophy for the conventional distribution system would need to be reviewed prior to the integration of DG units. Aside the review of the utility protection, it is necessary to incorporate protection at the DG units and at the PCC.

Therefore, the protection of a distribution system integrated with distributed generation can be categorised into three: (i) utility-side protection; (ii) DG unit protection; and (iii) interconnection protection. Some of the protection requirements are summarised below:

Pre-integration requirements:

- the protection at the DG units and the PCC must utilise utility-grade protective relays;
- requirements relating to the type of interconnection transformer, instrument transformers, protection operating speed, and other associated functions may be imposed on the DG operator before the interconnection is approved by the connecting utility;
- the overcurrent protection should be upgraded with directional supervision in order to prevent sympathetic tripping for faults on adjacent lines;
- a protection must be provided at the PCC to protect the utility from the damage that can be caused by the additional short circuit fault currents contribution from the DG units;
- the interconnection protection is also required to protect the DG units from the possible damage that can be caused by the reclosing actions occurring at the utility side;
- generator protection is required to protect the DG units from internal short circuit faults and any other abnormal conditions that can be caused by the loss of field, over-excitation, and reversed power conditions;
- anti-islanding detection and protection schemes must be in place to prevent unintentional islanding in the interconnected power system; and
- the protection implemented in a distribution system integrated with DG units must satisfy the fault ride through (FRT) requirements specified in the grid code for that network. The FRT characteristics define the operation limits (e.g. terminal voltage at the PCC) for which the DG units must still operate without disconnection. The FRT capability of DG units is very important especially in systems with a high penetration level of DG (like the European grid). This is because the disconnection of the DG units could lead to widespread instability in the system.

Operational requirements:

- the integration of DG units must not result in overvoltages in the electric power system and must be within acceptable limits as stated in the relevant utility grid code;
- the integration of DG units must not cause overfrequency and must be within the specified limits;
- the DG must not feedback and energise the utility system when the utility is de-energised;
- reclosers must be coordinated with the interconnected system and should take place only after the distribution system has been resynchronised to the DG. Thus, it is required that automatic reclosing should not be used. Also, the distribution system must not reclose when the island is out of phase. Furthermore, the reconnection or resynchronisation should only be carried out when the utility line has been restored [8].

18.4 Protection in Distribution Systems Integrated with Distributed Generation

18.4.1 Types of Protection in DG Integrated Distribution System

The protection zones and the various types of commonly applied protection in the distribution system were highlighted in Sect. 18.2. With the integration of DG units, the utility-side protection may need to be upgraded to include other protective relay elements such as the directional power (32), phase-balance current (46), phase-balance voltage (47), and overvoltage (59) relays. The protection required at the PCC and the DG unit is discussed below.

1. DG Unit Protection

The protective relays at DG units are for protection against internal short circuit faults and other abnormal fault conditions such as loss-of-field, overexcitation, unbalanced currents and reverse power that the DG units may be subjected to. The type of protection at the DG unit would typically depend on the size of the generator. Figure 18.7 shows a typical protective relaying scheme for a medium-sized DG unit as recommended in [16]. The functions of these protective relaying elements are presented in Table 18.7. These protective elements are commonly connected at the terminals of the DG units and can be obtained from a single multifunctional protective intelligent electronic device (PIED).

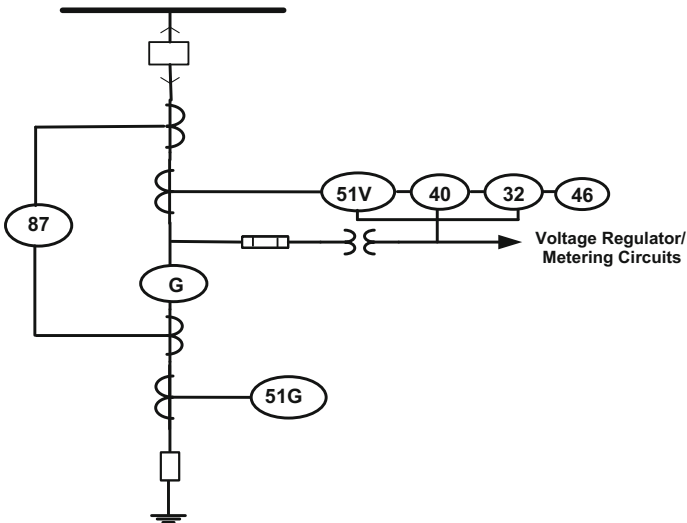


Fig. 18.7 Protective relaying elements for medium-sized DG units

Table 18.7 Types of generator protection and their functionality

Functionality	Protection device
Fault backfeed protection	Voltage-constrained inverse time overcurrent (51 V)
Abnormal flow of power	Directional power (32)
System restoration	Synchronism check (25)
Unbalanced current and phase reversal conditions	Negative sequence current/voltage (46/47)
Overcurrent condition	Differential (87)
Loss of field protection	Offset mho impedance (40) relay
Field faults	Generator field ground (64 F) relay

2. Interconnection Protection

The interconnection protection is located at the PCC and at the interconnection transformer. It is required to prevent the operation of the DG units in an islanded mode after the main feeder is disconnected following a fault condition. This is needed in order to ensure that the DG units do not continue to supply the fault current in the distribution system after the main feeder has been disconnected. Also, when the distribution system is in the islanded mode, the fault current seen by protection devices is less compared to when the main feeder is connected to the distribution system. Thus, the protection scheme in the distribution system might lose its coordination or completely fail. In addition, such islanded mode of operation might lead to a frequency instability (over/under frequency) problem due to the generator-load imbalance, or voltage instability especially in a distribution system with induction motor loads. Induction motors are known to stall at low voltages and draw up very high current during restarting. Consequently, such induction motor loads could get disconnected by their protective devices. In an industrial system with a considerable amount of induction motor loads, the disconnection of the motor loads could lead to an overvoltage problem in the rest of the interconnected system.

The particular type of protection to use will mainly depend on the utility standard practices, type of DG technology, type of interconnection transformer, mode of operation, and system topology. Typically, the PCC protection should comprise of utility-grade protective relays. Table 18.8 presents the various types of protective relays that can be applied and their corresponding functionality.

Figure 18.8 shows the typical types of PCC protection that can be found in a distribution system integrated with distributed generation. The location of the PCC protection can be at the primary or secondary sides of the interconnection transformer [15].

Table 18.8 Types of interconnection protection and their functionality

Functionality	Protection device(s)
Loss of parallel operation (loss of mains)	Over/under voltage (59/27), Over/under frequency (81 O/U), ROCOF (81R), Loss of Mains (LOM)
Fault backfeed protection	Voltage-constrained inverse time overcurrent (51 V), directional overcurrent (67), distance (21)
Abnormal power flow protection	Directional power (32)
System restoration	Synchronism check (25)
Preventing the reconnection of the DG to a de-energised utility	Voltage check (27)
Unbalanced current/phase reversal conditions	Negative sequence current/voltage (46/47)

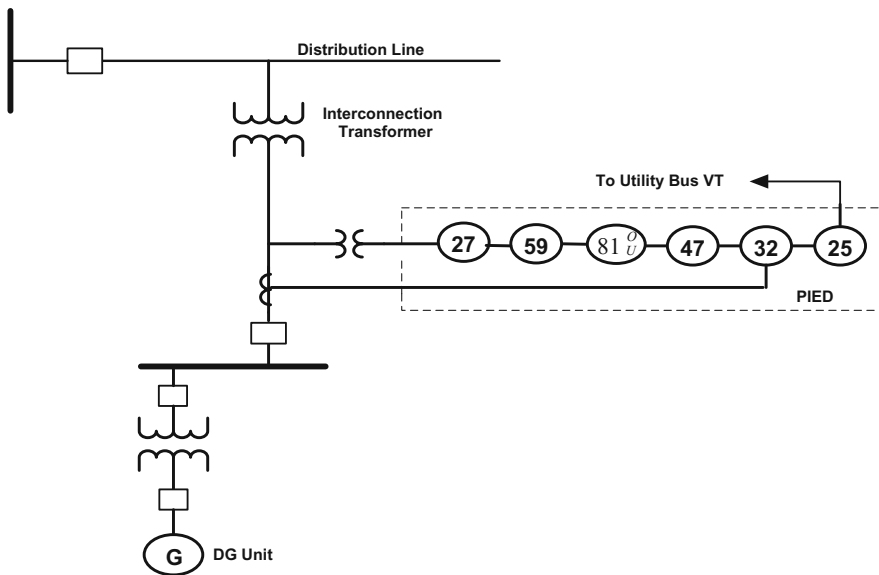


Fig. 18.8 Typical connection at a generator interconnection PCC

18.4.2 Protection Considerations in DG-Integrated Distribution System

For the distribution feeder shown in Fig. 18.1, non-directional overcurrent protective relays would suffice in the protection against phase and ground faults. With the integration of DG units as shown in Fig. 18.6, it would be necessary to upgrade the overcurrent feeder protection with directional supervision in order to avoid sympathetic tripping. For a distribution system shown in Fig. 18.9 with two transformers supplying a single bus with a sectionalising breaker, the bus will typically be protected with the backup time-delayed transformer overcurrent

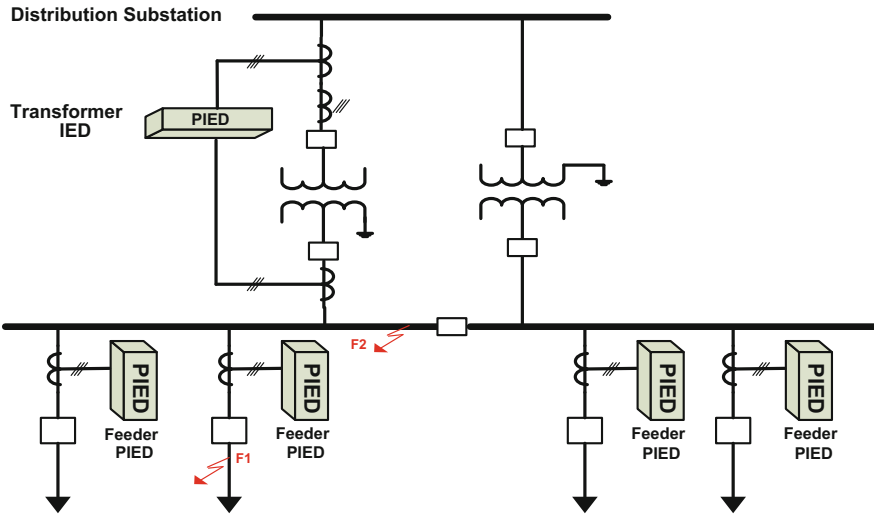


Fig. 18.9 Distribution network feeder and bus protection

protection. If the distribution system has DG units, the fault clearing time of this overcurrent protection is slow and would result in the loss of the DG units during faults. Coordination of the feeder and bus protection devices would need to be implemented such that for a fault on any of the protected feeders shown in Fig. 18.1 (without DG units), even though the transformer overcurrent PIED also sees the fault current alongside the feeder protection, only the feeder protection must trip for the fault. Similarly, for a fault on the bus, only the transformer protection should detect the fault and operate.

For the feeder and bus protection coordination for a distribution system with DG units, if a fault F1 occurs on the feeder shown in Fig. 18.9, the PIED of the faulted feeder will see the fault in the forward direction, while the transformer PIED and the PIEDs on the other feeders will see a fault in the reverse direction. For fault F2, the PIEDs on the feeders with DG units will see a reverse fault, while no fault will be seen by the feeder protection if no DG unit exists on that feeder. Advanced protection schemes based on some emerging technologies are discussed in Sect. 18.5.

18.5 Case Studies

Load flow, short circuit, and protection coordination studies were carried out in this section using a typical distribution system. A conventional distribution system is first studied. Afterwards, a distribution system integrated with distributed generation is considered.

18.5.1 Test System Model

The distribution system shown in Fig. 18.1 is modelled in DIgSILENT PowerFactory version 15.2.6, and it is used in this section to study the coordination of the various protection devices in distribution system. The distribution system has 2 loads (loads 1 and 2) modelled as constant power (PQ) loads at the 6.6 kV section (Intake S/S and bus B1) and 2 PQ loads (loads 3 and 4) at the 0.415 kV section. Load 5 is an induction motor load, and it is also connected to bus B2. The loads on the 0.415 kV section of the distribution system are connected to the intake incomer via a 750 kVA 6.6/0.415 kV step-down transformer. The parameters used in the modelling of this system are given in Tables 18.15, 18.16, 18.17 and 18.18 of the Appendix.

18.5.2 Protection of a Conventional Distribution System

The main feeder is protected using a recloser (Cooper Form 6) configured for overcurrent (50/51) protection. The load laterals (loads 1–4) are protected with fuses (SMU-40 fuses from S&C Electric Company). The 6.6/0.415 kV transformer is protected by an Alstom MCCG63 protective relay, while the motor load is protected by a Siemens 7SJ70 protective relay. The configuration settings are determined through load flow study and short circuit calculations. The short circuit studies used close-in three-phase faults to calculate the maximum short circuit currents at the respective line section, while the minimum short circuit current at each section is calculated using a single-phase-to-ground fault at the remote end of the line section.

The maximum short circuit calculations are used in the determination of the equipment ratings, while the minimum short circuit currents are applied in the configuration settings of the protection devices in order to make them as sensitive as possible. The superposition fault calculation method is used in this section in the calculation of the maximum and minimum short circuit fault currents in the distribution system.

The fuses at loads 1–4 are sized using the load flow results. An over-load factor (OLF) of 1.3 was applied, and the nearest fuse ratings available were chosen. The protection settings of the relays are calculated to cater for the temporary inrush currents that could occur during motor starting. Typically, during the first half cycle, the inrush current could be higher than 20 times the normal full load current. After this half-cycle, the motor starts and the starting current subsides to 4–8 times the nominal steady-state current for some seconds. Thus, as a motor reaches its running speed, the currents subside to its normal running level. A pickup setting greater than 8 times the nominal current was selected to allow for possible motor inrush currents. This enables the protection settings to be correctly located in between the starting inrush current level and the motor damage curve. The same applies to the transformer protection implemented. A pickup value greater than

12 times the nominal value of the current at the high voltage (HV) side of transformer T1 was selected. The extremely inverse overcurrent characteristics of protective relays are best suitable for the fuse time–current characteristics and motor starting curves better than the other inverse overcurrent characteristics. Thus, it was used as the preferred characteristic for the transformer protection relay. The recloser sited at the main feeder was configured for 3 reclosing shots comprising of 1-fast and 2-slow operations before lockout. The fast recloser operation is an instantaneous trip, while the slow operation is a time-delayed trip. Simulations and experimental results for the case studies conducted are presented below.

1. Case Study 1: Recloser–Fuse Coordination

The first case study carried out for the conventional distribution system is a recloser–fuse protection coordination which is commonly implemented in fuse-saving schemes. In this case, the recloser at the intake end is configured to clear temporary faults along the intake feeder and the lateral lines of loads 1–2. The information required for the recloser–fuse coordination is obtained from the fault calculation studies carried out. The recloser–fuse coordination is successful if the operating time of the recloser is less than the minimum melting time of the fuse on the load lateral. A *K* factor of 1.25 was used as the grading margin between the recloser’s operating time and the fuses’ minimum melting time. The time–current characteristics obtained for the recloser–fuse coordination is shown in Fig. 18.10.

From Fig. 18.10, it can be seen that the fuse TCC are located between the FCC and SCC of the recloser. For a temporary fault at load 2, the recloser fast curve will operate first as shown on the time–current plot given in Fig. 18.11. However, for a

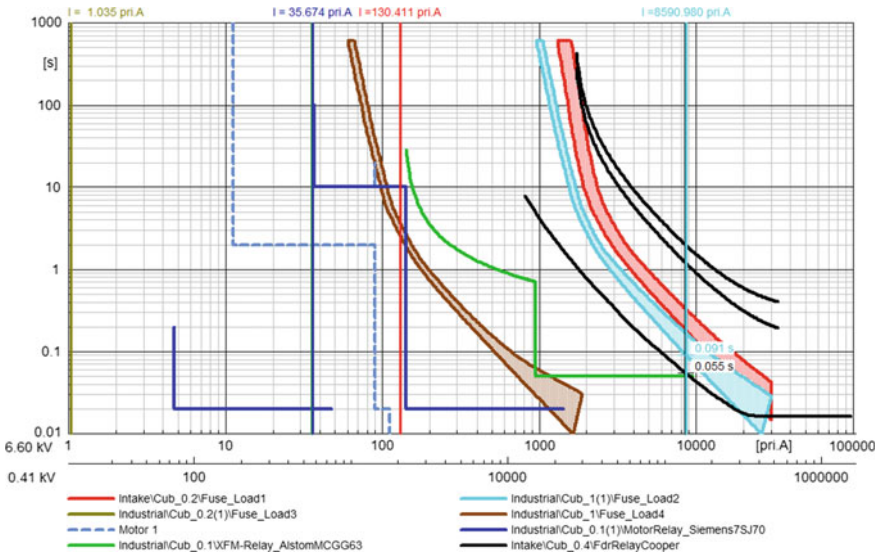


Fig. 18.10 Time–current characteristics for recloser–fuse coordination (3-phase fault)

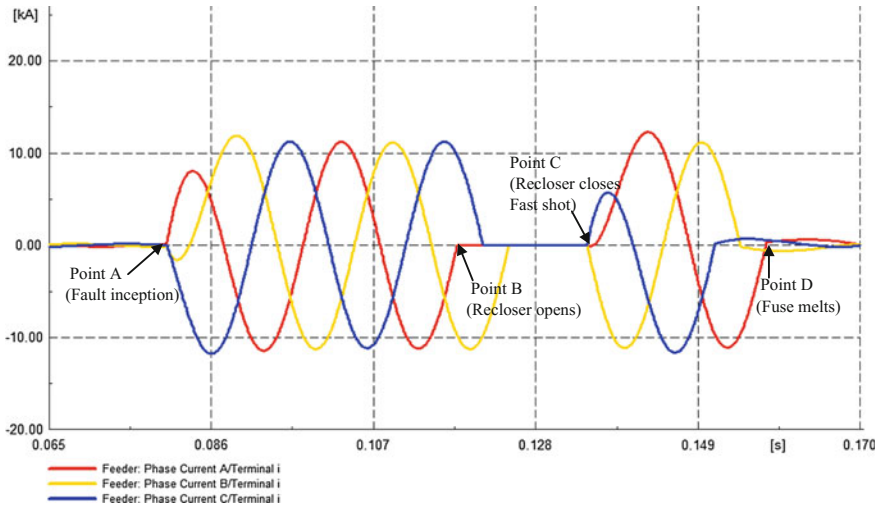


Fig. 18.11 Three-phase current plots at the main feeder showing the recloser–fuse coordination for a three-phase fault at load 2

permanent fault, the fuse at the loads will begin to melt to clear the fault. The relay operate time for a three-phase short circuit fault with a fault current of 8.591 kA was obtained to be 0.065 s, while the fuse had a minimum melting time of 0.091 s. In the event of a failure of the fuse, the recloser SCC will attempt to clear the fault before the recloser locks out. In Fig. 18.11, Point A is the fault inception point, while Point B is the point where the recloser operates in order to clear the fault. The recloser’s fast characteristic operates at Point C. Since the fault is a permanent one, the fuse at the load lateral melts at Point D and successfully clears the fault.

For a fault on any of the load laterals, the fast characteristic of the recloser would operate in response by tripping its breaker. If the fault is a permanent one, then the fuse on the faulted load lateral would melt in order to clear the fault. In the event of the fuse on the load lateral failing, the slow characteristic of the recloser would operate to clear the fault before the recloser locks out. This implies that the total clearing time of the fuse must be less than the operating time of the recloser’s slow characteristics.

2. Case Study 2: Primary Backup Protective Coordination

Primary backup protection coordination is considered in Case Study 2. For the low voltage (LV) section of the distribution system comprising of a motor load and 2 loads (loads 3 and 4), the backup protection is provided sequentially by the transformer overcurrent (50/51) relay located at the HV side of the transformer T1 and the recloser at the Intake S/S bus. This implies that if the overcurrent protection devices (OCPDs) at these loads fail, the overcurrent relay at transformer T1 will operate to clear the fault. If the fuses and the transformer relay all fail, then the recloser at the incomer bus should operate and trip its breaker in order to clear the

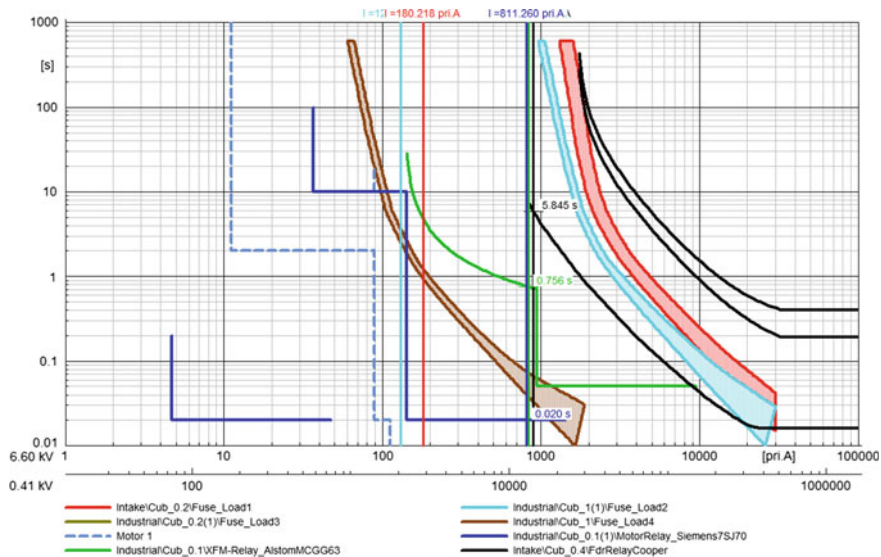


Fig. 18.12 Coordination of primary backup protection in the electric distribution system

fault. Similarly, the transformer relay and the Intake S/S recloser serve as the main and backup protection for the transformer T1.

The primary and backup protection for the motor load is illustrated in the time–current characteristics curve as shown in Fig. 18.12 for a three-phase fault at Motor 1 feeder. From Fig. 18.12, it can be seen that the primary protection for the motor (Siemens 7SJ70 relay) trips instantaneously within a cycle (20 ms), while the first backup protection (transformer relay–Alstom MCGG63) has a trip time of 0.756 s. The second backup protection (at the Intake S/S) has a trip time of 5.845 s. The coordination is done with a CTI of 0.3 s. For the second backup protection, the trip time can be made faster by changing the overcurrent characteristic and calculating the appropriate time dial setting required for a faster recloser operate time.

18.5.3 Protection of a Distribution System Integrated with Distributed Generation

The distribution system shown in Fig. 18.1 is modified with the integration of DG units at the locations indicated in Fig. 18.13. Firstly, two locations (DG units 1 and 2) are individually considered for DG placement. Afterwards, both locations are simultaneously integrated with DG units. DG unit 3 was considered separately at the LV section of the distribution system. The DG units used at locations 1 and 2 are interconnected to the distribution system via a 750 kVA 6.6/0.48 kV step-up interconnection transformer. The parameters of the interconnection transformer are

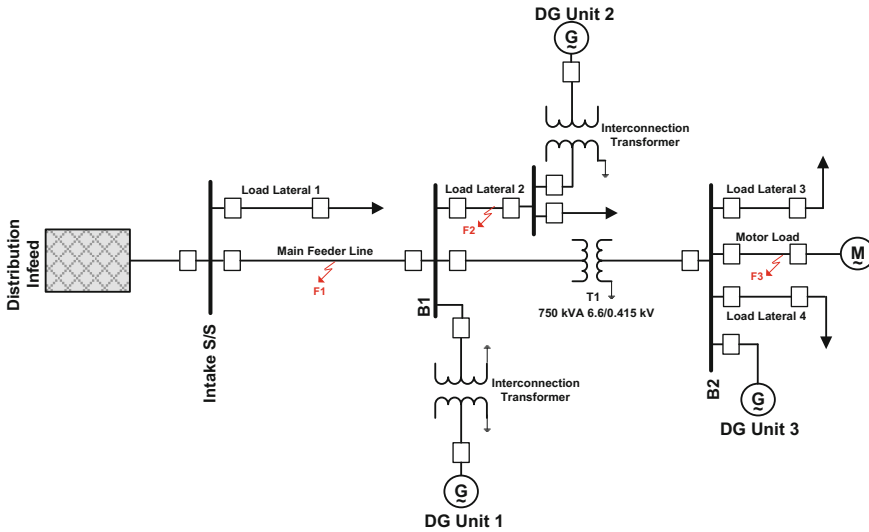


Fig. 18.13 Electric distribution system integrated with a DG units

the same as that of the transformer between buses B1 and B2. Thus, only a maximum of about 18% penetration level can be achieved with this transformer rating without exceeding its defined limits. The parameters of the DG units and the interconnection transformer are given in the Appendix. The base case has a total connected load of 3.8 MVA. The DG penetration levels were calculated using Eq. 18.3. Six case studies were initially considered as shown in Table 18.9.

The minimum short circuit fault currents for single-phase-to-ground faults obtained at the farthest end of each of the segments are given in Table 18.10. From Table 18.10, it was observed that the impact of the integration of the DG on short circuit current is more at the feeder line, loads 1–2, and the HV side of transformer T1. This additional fault current contribution by the DG units will have an effect on the equipment short-time ratings and the settings of the protective devices in the distribution system. The highest percentage increase in short circuit current was obtained for a single-phase-to-ground short circuit fault at load 2.

Table 18.9 Case studies carried out based on the penetration level and interconnection transformer windings

Case study	Penetration level (%)	Transformer connection
1	5.0	Delta-delta (Δ - Δ)
2	5.0	Grounded wye-grounded wye (Yg-Yg)
3	10.0	Delta-delta (Δ - Δ)
4	10.0	Grounded wye-grounded wye (Yg-Yg)
5	18.0	Delta-delta (Δ - Δ)
6	18.0	Grounded wye-grounded wye (Yg-Yg)

Table 18.10 Minimum short circuit fault currents from single line-to-ground faults

Fault location	Base case (no DG)	5% (Δ - Δ)		5% (Yg-Yg)		10% (Δ - Δ)		10% (Yg-Yg)		18% (Δ - Δ)		18% (Yg-Yg)	
		Min fault (kA)	Min fault (kA)	Min fault (kA)	Min fault (kA)	Min fault (kA)	Min fault (kA)	Min fault (kA)	Min fault (kA)	Min fault (kA)	Min fault (kA)	Min fault (kA)	Min fault (kA)
Main feeder	13.733	13.911	14.091	13.912	14.092	13.914	14.093	13.914	14.093	13.914	14.093	13.914	14.093
Load lateral 1	13.732	13.866	14.000	13.866	14.090	13.865	14.090	13.865	14.090	13.865	14.090	13.865	14.090
Load lateral 2	6.577	6.757	6.941	6.763	7.000	6.722	7.009	6.722	7.009	6.722	7.009	6.722	7.009
Load lateral 3	2.285	2.428	2.428	2.430	2.430	2.433	2.433	2.433	2.433	2.433	2.433	2.433	2.433
Load lateral 4	2.285	2.428	2.428	2.430	2.430	2.433	2.433	2.433	2.433	2.433	2.433	2.433	2.433
XFM-HV cable	6.940	7.141	7.346	7.155	7.352	7.164	7.370	7.164	7.370	7.164	7.370	7.164	7.370
XFM-LV cable	2.333	2.338	2.338	2.621	2.621	2.624	2.624	2.624	2.624	2.624	2.624	2.624	2.624
Motor	2.293	2.297	2.297	2.299	2.299	2.302	2.302	2.302	2.299	2.302	2.302	2.302	2.302
PCC XFM-LV cable	-	2.714	2.713	2.715	2.714	2.715	2.715	2.715	2.714	2.715	2.715	2.715	2.715
PCC XFM-HV cable	-	5.606	5.817	5.613	5.825	5.624	5.836	5.624	5.825	5.624	5.836	5.624	5.836
PCC cable	-	6.956	7.163	6.962	7.169	6.972	7.179	6.972	7.169	6.972	7.179	6.972	7.179

From Table 18.10, it can be seen that a higher level of fault current was obtained for ground faults when the transformer at the PCC is a wye-grounded type. For an 18% DG penetration level, a 25% increase in fault current was observed for single-phase-to-ground faults on the main feeder, while about 2% increase in short circuit current was observed when the delta-delta transformer was used. Also, the short circuit fault current obtained was dependent on the DG size and the location of the DG unit.

The case studies, simulations, and experimental results obtained when the distribution system was integrated with distributed generation are presented below.

1. Case Study 1: Recloser–Fuse Coordination

Similar to the simulations carried out in Sect. 18.5.2, a recloser–fuse coordination study was carried out for temporary single-phase-to-ground short circuit faults at load 2 lateral; the recloser is configured to operate instantaneously for temporary faults. If the fault persists, the fuse is meant to clear the fault by melting. Tables 18.11 and 18.12 give the operate time of the recloser and the fuse at load 2 without DG units, with DG units at load 2 lateral, and with DG units simultaneously located at bus B1 and Load Lateral 2.

Generally, it was observed that the operate time of the fuse (T_{tc}) decreased as the DG penetration level increased. It was also observed that the operate time of the recloser increased when the DG units were connected in the system. This is caused by the reduction in the fault current contribution from the utility, while the proximity of the DG unit to the load 2 lateral resulted in an increase in the fault current flowing through the lateral. Thus, in a fuse-saving scheme, this could cause the fuse to begin to melt even before the recloser operates. This would lead to the loss of the recloser–fuse coordination previously obtained in Sect. 18.4.2. Similar result was also obtained for DG3.

2. Case Study 2: Primary Backup Protective Coordination

Case Study 2 investigates the impact of DG integration on the coordination of the primary and backup protective devices. From the simulations carried out, it was

Table 18.11 Recloser–fuse operate times for short circuit faults at load 2 with DG unit at load 2 lateral

Protective device	No DG unit	Yg-Δ transformer	Yg-Yg transformer
	Operating time (s)		
Load 2 fuse	0.126	0.124	0.125
Recloser	0.032	0.034	0.033

Table 18.12 Recloser–fuse operate times for short circuit faults at load 2 with DG units 1 and 2

Protective device	No DG unit	Yg-Δ transformer	Yg-Yg transformer
	Operating time (s)		
Load 2 fuse	0.126	0.122	0.111
Recloser	0.032	0.036	0.034

Table 18.13 Motor relay transformer relay coordination for three-phase short circuit faults at motor end with DG unit at bus B1

Protective device	No DG unit	Yg- Δ transformer	Yg-Yg transformer
	Operating time (s)		
Motor relay	0.020	0.020	0.020
Transformer relay	0.756	0.746	0.746

Table 18.14 Motor relay–transformer relay coordination for three-phase short circuit faults at motor end with DG units at bus B1 bus and load 2 lateral

Protective device	No DG unit	Yg- Δ transformer	Yg-Yg transformer
	Operating time (s)		
Motor relay	0.020	0.020	0.020
Transformer relay	0.756	0.738	0.738

seen that the primary backup protection coordination previously obtained for the case without the integration of DG still served until the DG penetration level was 18% at the two DG locations. The operate time of the backup protection (transformer relay) for the motor load decreased as the DG units were integrated (Tables 18.13 and 18.14). This operate time would continue to decrease as the penetration level of the DG units increased. This is because the increase in short circuit current will result in shorter operate time since an inverse definite overcurrent relay was used. However, no difference in the operate time was obtained when the type of interconnection transformer is changed. When a DG unit was placed at the LV side only (DG Unit 3), the transformer protective relay at bus B1 was seen to operate for fault (F1) on the main feeder (reverse fault). This is due to the fault current contribution from DG Unit 3 flowing in the reverse direction towards the fault F1. Thus, the protection at transformer T1 will need to be replaced by a directional overcurrent (67) protective relay.

18.6 Application of Emerging Technologies

Some protective relaying methods for application in distribution systems integrated with DG units were proposed in [17–22]. However, the application of these methods are limited to distribution systems with low penetration level of DG units, and they were directed at specific problems such as protection blinding, sympathetic tripping, and loss of protection coordination that are associated with the integration of DG units. Advanced protection schemes that are suitable as solutions to these problems would require communication between the protective devices at the utility, DG units, and the PCC protection. Two emerging technologies that can be applied are discussed in the following subsection.

18.6.1 IEC 61850-Based Protection Schemes

Fundamentals of IEC 61850

The IEC 61850 standard is an international non-proprietary standard for communication networks and systems in power systems. It provides a single suite of protocols and services to address communications within and outside the substation through the integration of protection, control, and metering functions. It also provides the means for interlocking and intertripping and other associated advantages of the Ethernet communication. The new functionalities supported by the application of IEC 61850 logical nodes (LN) and logical devices (LD) result in a significant improvement in the protection, automation, and control functions in power systems. The IEC 61850-8-1 [23] presents data interchange process across the Ethernet communication network using the Abstract Communication Service Interface (ACSI). The ACSI maps multimedia messaging (multimedia messaging service, MMS) over the ISO/IEC 8802-3 frames. Similarly, the IEC 61850-9-2 [24] discusses the specific communication service mapping (SCSM) for the transmission of sampled values (SVs) according to the IEC 61850-7-2 using the ISO/IEC 8802-3.

Typically, the communication in substations takes place over three distinct levels: the process level, bay level, and the station level. Data acquisition using CTs and VTs takes place at the process level. The output of these CTs and VTs is sampled, converted to digital representations (SVs), and formatted for subsequent transmission through the process bus local area network (LAN). The sampling rate to use will depend on the application. Eighty samples per cycle (4000 samples per second for 50 Hz/4800 samples per second for 60 Hz) are specified for protection application, while 256 samples per cycle (12,800 samples per second for 50 Hz/15,360 samples per second for 60 Hz) are used for measurement-related application. The sampling rates have been standardised in the new IEC 61869-9 standard [25] to 4800 samples per second (protection application) and 14,400 samples per second (measurement application) (IEC 2016). The process-level information from merging units is communicated over the LAN to the protection and control devices that are located at the bay level. Protection, control, and metering functions are performed at the bay level by the bay devices. The bay devices receive their current and voltage input from the process level. Examples of bay devices include PIEDs, fault recorders, and phasor measurement units (PMUs). The station-level functions represent the overall substation wide coordination, substation Human Machine Interface (HMI), and the Supervisory Control and Data Acquisition (SCADA) system interfaces.

The communication required for the advanced protection/control schemes in distribution systems integrated with DG units will typically take place between the PIEDs in multiple bays over the logical interface (number 8) as shown in Fig. 18.14, while the communication required between the process bus and the bay level devices is via the logical interfaces denoted with numbers 4 and 5.

Physical PIEDs are implemented with LDs and LNs using the concept of data modelling. IEC 61850 data modelling decomposes the devices' functionalities into

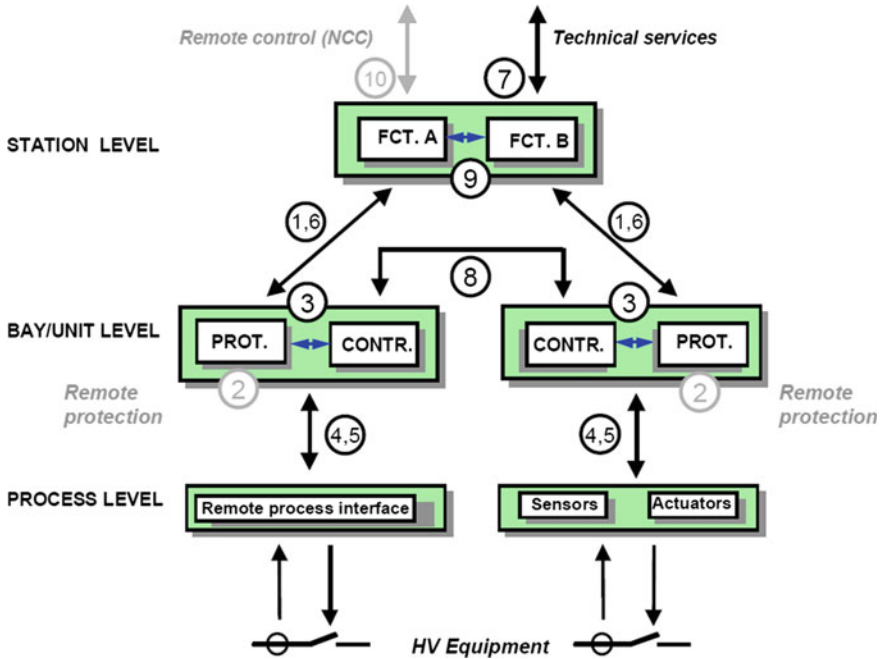


Fig. 18.14 Levels in power system automation and logical interfaces

smaller entities that can be used in the exchange of information between different devices. A LN contains a list of data with dedicated data attributes. The information in the data and data attributes is exchanged by the communication services according to defined rules. This concept makes it easier to have multiple LDs containing multiple instances of LNs, each of which contains a predefined set of data classes. Every data class contains many data attributes (status value—stVal, quality flag—q, time stamp—t). The recent revision of the IEC 61850 (IEC 61850 Ed. 2) allows for the inter-substation communication typically required between the dispersed DG units and the utility grid. This is based on the communication of generic object oriented substation event (GOOSE) messages using the user datagram protocol (UDP). Also, the application of IEC 61850 has been extended to cover distributed energy resources (DERs) in the IEC 61850-7-420 technical report (TR). This would allow for the functional modelling of DERs, communication architecture, protection, control, and metering based on the IEC 61850 concept.

Advanced Protection Schemes using the IEC 61850

Advanced protection based on the exchange of information between the utility and the DG units would require communication equipment and availability of communication channel. The communication medium for IEC 61850 GOOSE messages can be microwave link, spread spectrum radio, fibre, pilot wire, and

Internet-based network. Some advanced protection schemes that can be implemented with IEC 61850 GOOSE messages are discussed below:

1. Adaptive Protection using Multiple Setting Groups

A commonly proposed adaptive protective relaying method in distribution systems integrated with DG units is the use of multiple setting groups available in most microprocessor-based PIEDs. For this, programmable scheme logic (PSL) can be used in monitoring certain breakers in the distribution system. These breakers are used in signifying the system operating condition or topology. The statuses of these breakers are then communicated to the relevant protection devices, station computer or programmable logic controller (PLC) in order to activate an alternate setting group. For example, setting group 1 can be applied when the system is operating without distributed generation, while setting group 2 is applied for grid-connected mode of operation with the DG unit online. Similarly, setting group 3 can be applied for an islanded mode of operation. Such schemes were presented in [26, 27].

However, this would require offline fault studies and coordination because the settings of all the protective relays in the system will need to be updated. One problem that can affect the use of multiple setting groups is the intermittent nature of PV systems and wind turbine generators. An extension proposed in [27] is to change the characteristic curves of the overcurrent protection. Other possible solutions include changing the protective pickup settings or the trip settings in order to adjust to the changes in the system conditions [26, 27]. For an adaptive protection scheme based on the use of multiple setting groups, IEC 61850 GOOSE messages can be published from a station computer to the PIEDs within the multicast group to change their setting group as the system operating mode changes.

2. Directional Comparison Distribution Bus Protection Scheme

Bus protection at the transmission level is commonly provided using low- or high-impedance bus differential protective relays. However, bus differential protection is not usually used in most distribution systems because of the high cost associated with the installation and the maintenance of some of the required auxiliary equipment. Thus, transformer backup protection is commonly implemented for the protection of distribution bus zones. This often results in a slow fault clearing time and the consequent loss of the DG units in the system. Faster fault clearing time can be obtained using protection schemes based on the exchange of signals between the feeder PIEDs, the transformer PIED, and the IED protecting the sectionalising breaker [28]. Typically, the transformer PIED will be configured to subscribe to the GOOSE messages published by the feeder directional overcurrent protection IED.

If a fault (F1) occurs on any of the distribution feeders of the system as shown in Fig. 18.15, the fault will be seen by the PIED on that particular feeder as a fault in the forward direction. The PIED protecting the feeder(s) with DG units, the transformer or the sectionalising breaker connected to the protected bus will send a GOOSE message indicating the detection of a fault, combined with the fault

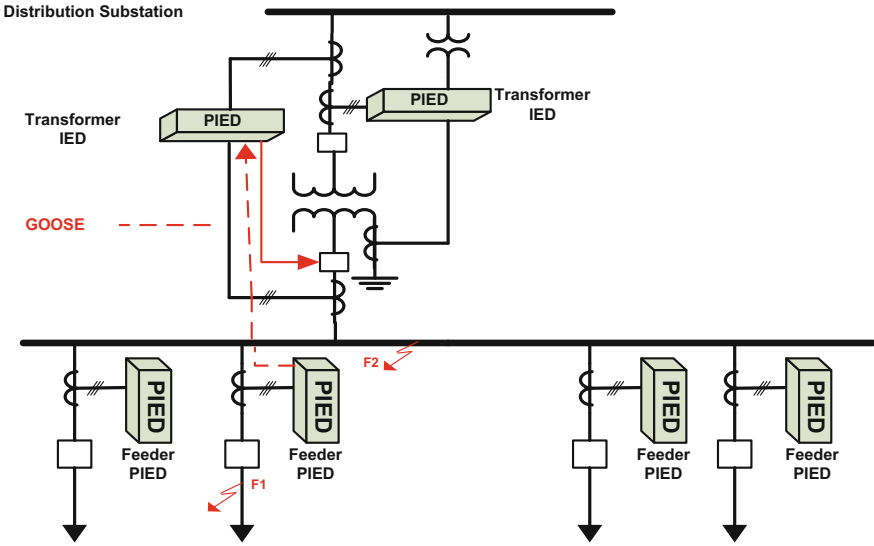


Fig. 18.15 Directional comparison distribution bus protection scheme

direction determined by the PIED. In this case, the faulted feeder PIED will detect a forward fault and the other PIEDs will see a reverse fault or no fault (if there is no DG on that particular feeder), indicating to the PIED performing the directional comparison scheme that an external fault to the bus has occurred.

If the fault is on the bus (F2), all PIEDs will see a reverse fault or no fault (if the feeder does not have a DG unit connected). That is, no PIED will see a forward fault. The bus protection function of the central unit or the subscribing PIED detects a bus fault and publishes a message to trip all breakers connected to the bus. Therefore, a fast fault clearance that supports the ride through capability of DGs is easily obtained compared to the traditional backup transformer protection scheme with its associated long time delay.

3. Selective Backup Tripping for Feeder Protection

The operate time for the backup transformer protection for faults on the feeders have a long fault clearing time that may affect DG units connected to the distribution system. A selective backup protection can be applied for feeders with DG units using GOOSE messages. This can be implemented in two ways:

- In the first method, the absence of a blocking message from any of the feeder PIEDs for a fault F1 (Fig. 18.15), for a fault condition detected by the transformer protection would result in two questions. That is, is the fault located on any of the feeders or is the fault on the distribution bus? Since feeder faults occur more frequently compared to distribution bus faults, the transformer PIED will first attempt to clear the fault by tripping the breaker of the failed PIEDs

with a GOOSE message. If the fault persist, then the source breakers are tripped in order to clear the fault on the bus; and

- The second method uses the GOOSE repetition mechanism to activate the selective backup tripping PSL of the transformer PIED. Healthy feeder PIEDs are required to publish GOOSE messages to the transformer PIED within the pre-defined maximum repetition time. When the feeder PIED fails, the ‘GOOSE absent’ information would activate the selective backup logic of the transformer PIED. The two methods highlighted above will in effect accelerate the operation of the backup transformer protection.

4. Direct Transfer Trip

It is often required that DG units should be disconnected before autoreclosing actions take place. This is because the DG unit might continue to feed the short circuit fault currents that will prevent the extinction of the developed arc. When a fault occurs on the feeder with DG unit, a direct transfer trip (DTT) scheme can be implemented in which GOOSE messages are published from the feeder PIED to the DG interconnection PIED [29]. A central PLC can be configured to subscribe to breaker statuses from the DG-interconnected system and execute a pre-programmed protection logic. DTTs can then be published to the appropriate breaker in order to clear a fault condition. Thus, GOOSE messages are used as fast intertrip commands for disconnecting the DG units within the time frame specified for reclosing.

5. Break Failure Protection

Breaker failure protection (BFP) can easily be implemented in DG-interconnected distribution networks. The breaker failure protection function in the feeder PIEDs could be configured to publish GOOSE messages if the feeder PIED operates but fails to trip its breaker. The published breaker failure GOOSE messages will be subscribed to by the transformer protection PIED which will in turn trip the necessary breakers in order to clear the fault.

A similar design is the use of the breaker failure function of the transformer PIED. When a fault occurs on the feeder and is rightly detected by the feeder PIED, it publishes GOOSE messages to indicate the operation of its protection trip elements. The published GOOSE message is subscribed to by the transformer PIED, which then initiates its breaker failure function. If the fault still persists after the timer of the breaker failure function times out, then the transformer PIED will operate to trip the breakers required to clear the fault. The total clearing time of the BFP should be within the tolerable system stability limit and should only operate when desired.

The total clearing time of the BFP is given as:

$$T_{tc} = T_{pu} + T_{bft} + T_{at} + T_{bub} + T_{tt} \quad (18.4)$$

where

T_{tc}	BFP total clearing time
T_{pu}	BFP pickup time
T_{bft}	Breaker failure timer
T_{at}	Auxiliary trip relay time
T_{bub}	Local backup breaker time
T_{tt}	Transfer trip time.

6. Anti-Islanding

Anti-Islanding (A-I) protection schemes are designed to prevent the formation of islands in the distribution network. This is because the isolation of a section of the network from the rest of the distribution network would likely result in a myriad of power quality problems, out of phase reclosing, and is a threat to system stability. The IEEE 1547 standard specifies an islanding detection time equal or less than 2 s. Thus, reliable and fast methods for the identification of islands are needed. A-I schemes can be generally classified into passive, active, and communication-based schemes.

An IEC 61850-based A-I protection scheme can be implemented with GOOSE messages. In such a scheme, a utility PIED publishes GOOSE messages to the feeder PIEDs at the DG locations. A DG unit is considered to be islanded from the grid if the feeder PIED cannot subscribe to the GOOSE messages from the utility PIED. An A-I scheme based on the Rate-of-Change of Frequency df/dt protection elements of the utility and DG PIEDs can also be implemented. If an islanding event occurs by the opening of the substation breaker, the df/dt element of the DG PIED will operate and disconnect the DG unit but the df/dt element at the substation will not. Thus, the utility PIED is required to publish a GOOSE message to block the operation of the df/dt element of the DG IED. The DG PIED will trip the DG unit only after the pickup timer of the df/dt element times out and in the absence of the df/dt element operate message from the utility. In addition to the methods discussed above, a direct transfer trip from the utility PIED to the DG feeder PIED can be used to achieve a simple and reliable A-I scheme which is not affected by the prevailing DG penetration level.

18.6.2 Synchronphasor-Based Protection Schemes

Fundamentals of Synchronphasor Measurements

Synchronphasor measurements are phasors from PMUs time-synchronised to an accurate time source such as the global positioning system (GPS). The processing steps performed by a PMU are defined in the IEEE Std. C37.118.1TM-2011 reference model [30] as shown in Fig. 18.16. In the reference model, a fixed frequency sampling synchronised to an absolute time base is used. This is followed by the

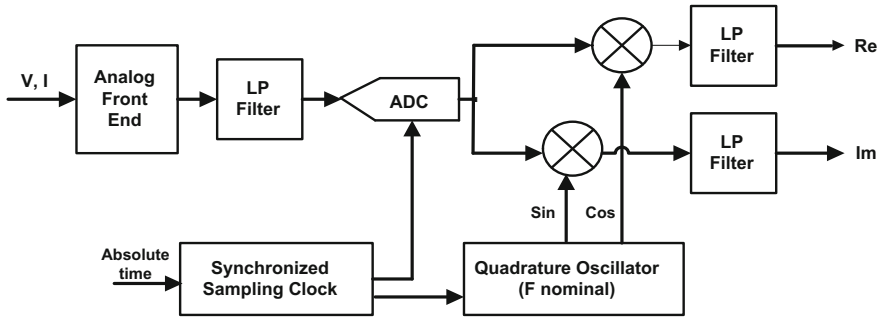


Fig. 18.16 Signal processing steps of the PMU reference model

complex multiplication of the sampled input with the nominal frequency carrier. Low-pass filters are then applied to the real and imaginary outputs of the complex demodulator. The outputs from the low-pass filters are the real and imaginary parts of the synchrophasor estimates, respectively.

Typically, the synchrophasor measurements are synchronised with a 1- μ s time source. These phasors of currents and voltages can be streamed in their polar or rectangular formats using serial or Ethernet communication platforms to other PMUs or to phasor data concentrators (PDCs) in the substation or control centres. The PDCs collect and time align the measurements from the widely dispersed PMUs in the power system and makes these measurements available to other applications in the substation or control centre.

Unlike conventional Supervisory Control and Data Acquisition (SCADA) with 1 measurement every 2–10 s, synchrophasor measurements can have up to 240 measurements every second for a 60 Hz system or 200 measurements every second for a 50 Hz system. Thus, synchrophasors allow for high-speed time-stamped wide area measurements suitable for the real-time monitoring, protection, and control applications required in systems integrated with distributed generation. A typical synchrophasor-based scheme would require PMUs (at the utility, PCC, and DG units), PDCs, time synchronisation sources (e.g. GPS satellite clock), data archiver/historian (optional), and a communication network infrastructure.

Advanced Protection Schemes using PMU Measurements

Synchrophasor-based protection schemes in distribution systems integrated with DG units are few and have not been extensively investigated. Some synchrophasor-based protection applications in the existing literature and some envisaged future applications are discussed below.

1. Anti-Islanding Detection

The IEEE 1547 specifies an islanding detection time equal or less than 2 s. Thus, reliable and fast methods for the identification of islands are needed. The high-speed reporting rates of wide area synchrophasor measurements from various parts of the

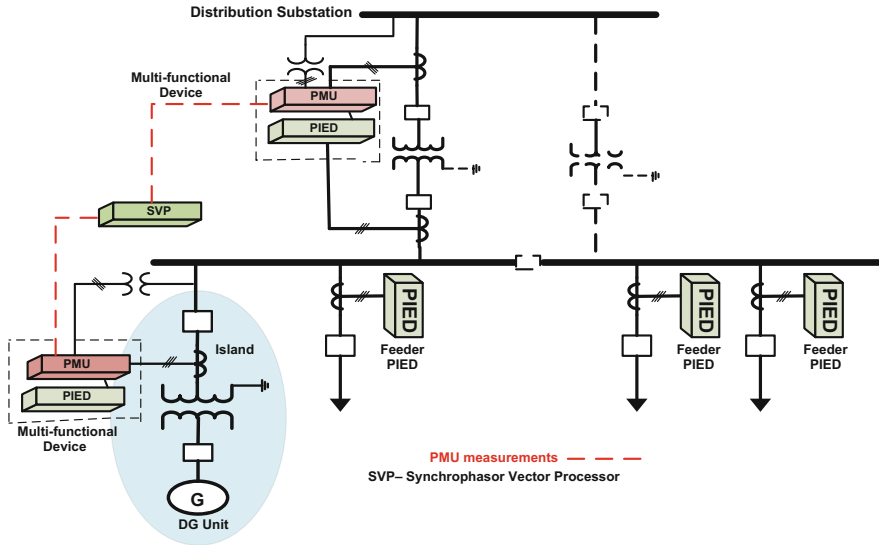


Fig. 18.17 Anti-islanding protection scheme using synchrophasor measurements

power system are capable of satisfying the IEEE 1547 requirement for anti-islanding. A typical implementation of an anti-islanding scheme based on synchrophasor measurements would have PMUs located at the DG units and also at the utility side of the distribution system. A synchrophasor-based A-I detection algorithm based on the combination of phase angle difference and acceleration-slip was proposed in [31]. The algorithm also included a blocking logic designed to avoid nuisance trips. The performance tests conducted gave a maximum total operating time of 500 ms. Figure 18.17 shows an anti-islanding scheme implemented on a centralised PLC running an algorithm based on the phase angle difference computed from the PMU measurements obtained at the DG side and the utility grid [32].

2. Line Differential Protection

Synchrophasor measurements can be applied in the design of a backup differential protection in distribution systems integrated with distributed generation. Line differential protection is based on the calculation of the differential current using the respective current measurements from the local and remote ends of the protected line. The time stamps on the synchrophasor measurements allows for the ease of comparison of the current samples at all the ends of the line [33]. Also, the estimation algorithm of the P-class synchrophasor measurements is adequate for this purpose. A line differential protection scheme whereby a differential PIED issues a synchrophasor-based intertrip signal to the remote PIED whenever the differential PIED operates for an internal fault condition was described in [28, 34]. The tripping of the local breaker by the differential element would result in an intertrip signal to

the PIED at the remote end. This will effectively ensure that the breakers at both ends of the line are tripped.

3. Post-Islanding Grid Resynchronisation

After the formation of an island (controlled or otherwise), the event that caused the islanding condition is cleared and an attempt is made to reconnect the islanded DG to the rest of the interconnected distribution system. However, reconnection must be carried out only when the island and the utility are synchronised. Synchrophasor measurements obtained from the PMU installed at the utility grid and the islanded DG section can be applied to aid the resynchronisation of the interconnected system. The voltage phase angle difference between the utility grid and the islanded DG can be monitored, and the reconnection at the PCC can be carried out when the phase angle of the island closely matches with that of the main grid (phase angle difference = 0). Other PMU measurements that could be monitored are the frequency and the rate of change of frequency (ROCOF) measurements.

18.7 Conclusion

This chapter presents the protection of electric power distribution systems without and with integrated distributed generation. The most commonly used protective devices in distribution systems are presented and discussed. The coordination of these various protective devices is further elucidated. Also, the integration of distributed generation, their impact, and the requirements for integration is described. Furthermore, case studies using a typical distribution system are presented. These are aimed at exploring and illustrating the protection principles for conventional distribution systems and distribution systems integrated with DG units. In addition, the application of emerging technologies in the protection of DG integrated distribution systems is presented. The emerging technologies considered include the technologies based on the IEC 61850 standard and the IEEE C37.118 synchrophasor standard respectively.

In the planning and operation studies for conventional distribution systems, it is necessary to carry out load flow studies, short circuit studies, protection studies, protection settings configuration, and coordination. The same applies to distribution systems integrated with distributed generation. Studies must be carried out on the system and the existing protection should be modified or upgraded with the inclusion of utility-grade protection at the PCC and at the DG units. Also, the DG owner must satisfy all the requirements of the connecting utility. In the nearest future, the traditional protection (especially in DG interconnected systems) would be replaced by centralised setting-less protective relaying implemented on a station computer in a completely digital substation having IEC 61850 GOOSE and SV messages, and also synchrophasor measurements. Such protective relaying would

have novel adaptive algorithms that are fast, accurate, and reliable irrespective of the DG penetration level or type.

Appendix

Power system modelling parameters

See Tables 18.15, 18.16, 18.17 and 18.18.

Table 18.15 Substation grid parameters

Substation Grid	
Parameter	Value
Bus type	PV
Voltage set point	1 p.u.
Active power	0 MW
Max short circuit power	300 MVA
Max short circuit current	26.24 kA
Min short circuit power	200 MVA
Min short circuit current	17.49 kA
Nominal frequency	50 Hz

Table 18.16 Transformer parameters

Transformer	
Parameter	Value
<i>Transformer T1</i>	
Power	750 kVA
Voltage	6.6/0.415 kV
No. of phases/vector group	3-phase DYN
<i>DG interconnection transformer</i>	
Power	3.75 MVA
Voltage	6.6/0.415 kV
No. of phases/vector group	3-phase YND

Table 18.17 DG parameters

DGs (synchronous machines)	
Parameter	Value
Power (5% penetration level)	1.335 MVA
Synchronous reactance	1.76 p.u. (xd), 1.66 p.u. (xq)
Subtransient reactance	0.13 p.u. (x'')
Transient reactance	0.21 p.u. (x')
Stator resistance	0 p.u.

Table 18.18 Line and load parameters

Line segments	
Parameter	Value
<i>Main feeder/loads 1–2 lateral</i>	
Rated voltage	6.6 kV
Rated current in air	1 kA
Positive and negative sequence impedance per length	AC resistance (R') 0.1 Ω /km
	Reactance (X') 0.1 Ω /km
<i>Loads 3–4 laterals</i>	
Rated voltage	0.415 kV
Rated current in air	1 kA
Positive and negative sequence impedance per length	AC resistance (R') 0.1 Ω /km
	Reactance (X') 0.1 Ω /km
Positive and negative sequence impedance per length	AC resistance (R_0') 0.2 Ω /km
	Reactance (X_0') 0.15 Ω /km

References

1. Kundur P (1994) Power system stability and control. McGraw-Hill, New York, USA
2. Taylor CW (1994) Power system voltage stability. McGraw-Hill, New York, USA
3. Adewole AC, Tzoneva R (2016) Impact of customer load characteristics on voltage stability assessment in smart grids using synchrophasor measurements. In: Domestic use of energy conference, Cape Town, 29–31 Mar 2016, p 1–7
4. Gers JM, Holmes EH (2004) Protection of distribution networks, 2nd edn. IEEE power and energy series
5. Gonen T (2008) Electric power distribution system engineering. CRC Press LLC, Boca Raton, USA
6. Horowitz SH, Phadke AG (2008) Power system relaying, 3rd edn. Wiley
7. Short TA (2004) Electric power distribution handbook. CRC Press LLC, Boca Raton, USA
8. Blackburn JL, Domin TJ (2007) Protective relaying: principles and applications, 3rd edn. CRC Press LLC, Boca Raton, USA
9. Network protection and automation guide NPAG (2011) Alstom Grid Publishers, UK
10. Ackermann T, Andersson G, Soder L (2001) Distribution generation: a definition. Electr Power Syst Res 57:195–204
11. Girgis A, Brahma S (2001) Effect of distributed generation on protective device coordination in distribution networks. In: Large engineering system conference, pp 115–119
12. IEEE Std 1547.2™ (2008) IEEE standard for interconnecting distributed resources with electric power systems
13. Van Overbeeke F (2009) Fault current source to ensure the fault level in inverter-dominated networks. In: CIRED 20th international conference and exhibition on electricity distribution-part 1, pp 1–4
14. IEEE Std 1547a™ (2014) IEEE standard for interconnecting distributed resources with electric power systems
15. Mozina C (2001) Interconnection protection of IPP generator at commercial/industrial facilities. IEEE Trans Ind Appl 37(3):681–688
16. IEEE Std. 242 (2001) IEEE Recommended Practice for Protection and Coordination of Industrial and Commercial Power Systems

17. Hadjsaid N, Canard J, Dumas F (1999) Dispersed generation impact on distribution networks. *IEEE Comput Appl Power* 12:22–28
18. Brahma SM, Girgis AA (2004) Development of adaptive protection scheme for distribution systems with high penetration of distributed generation. *IEEE Trans Power Delivery* 19(1):56–63
19. Chaitusaney S, Yokoyama A (2008) Prevention of reliability degradation from recloser-fuse miscoordination due to distributed generation. *IEEE Trans Power Delivery* 23(4):2545–2554
20. Oudalov A, Fidigatti A (2009) Adaptive network protection in microgrids. *Int J Distrib Energy Sources* 5(3): 201–225
21. Zamani A, Sidhu T, Yazdani A (2010) A strategy for protection coordination in radial distribution networks with distributed generators. In: *Proceeding of the IEEE power energy society general meeting*, pp 1–8
22. Hussain B, Sharkh SM, Hussain S, Abusara MA (2013) An adaptive relaying scheme for fuse saving in distribution networks with distributed generation. *IEEE Trans Power Delivery* 28(2):669–677
23. IEC 61850-8-1 (2011) Communication networks and systems for power utility automation-specific communication service mapping (SCSM)-mappings to MMS (ISO 9506-1 and ISO 9506-2) and to ISO/IEC 8802-3. International Electrotechnical Commission (IEC)
24. IEC 61850-9-2 (2011) Communication networks and systems for power utility automation-specific communication service mapping (SCSM)-sampled values over ISO/IEC 802-3. International Electrotechnical Commission (IEC)
25. IEC 61869 (2016) Instrument transformers-part 9: digital interface for instrument transformers. IEC 61869-Part 9
26. Coffele F, Booth C, Dysko A, Burt G (2012) Quantitative analysis of network protection blinding for systems incorporating distributed generation. *IET Gener Transm Distrib* 6(12): 1218–1224
27. Jennett KI, Booth CD, Coffele F, Roscoe AJ (2015) Investigation of the sympathetic tripping problem in power systems with large penetrations of distributed generations. *IET Gener Transm Distrib* 9(4):379–385
28. Apostolov A (2015) Improving the protection of distribution systems with DERs. *PAC World Magazine*, 1–6, Mar 2015
29. Antonova G, Nardi M, Scott A, Pesin M (2012) Distributed generation and its impact on power grids and microgrids. In: *65th annual conference for protective relaying*, pp 152–161
30. IEEE Standard C37.118.1 (2011) IEEE standard for synchrophasor measurements for power systems
31. Pena P, Etxegarai A, Valverde L, Zamora I, Cimadevilla I (2013) Synchrophasor-based anti-islanding detection. In: *IEEE grenoble PowerTech conference*, pp 1–6
32. Schweitzer EO, Whitehead DE (2009) Real-world synchrophasor solutions. In: *63rd annual Georgia tech protective relaying conference*, Georgia, USA, Apr 2009, pp 1–12
33. Phadke AG, Thorp JS (2008) *Synchronized phasor measurements and their applications*, Springer
34. IEEE power system relaying committee report on use of synchrophasor measurements in protective relaying applications, 2013

Part V
**Miscellaneous: Power Electronics,
Reliability, Economic Aspects,
Energy Storage and Management**

Chapter 19

Power Electronic Applications, Grid Codes, Power Quality Issues, and Electricity Markets for Distributed Generation

Akshay Kumar Rathore and Prasanna Udupi Rajagopal

19.1 Distributed Generation

Renewable energy sources and microgrids are seen as effective alternative options to encourage clean environment, reduce emission, and offer more choices to the users against utility monopoly, continuous electricity supply, local generation, own backup, and use of renewable energy sources against conventional fuel depletion threat, climate change, and global warming. Distributed generation (DG) is a partial solution to this concern in addition to transportation electrification. DG, also known as on-site generation, generally refers to small-scale electric power generators that produce electricity at a site close to customers or that are tied to an electric distribution system. Distributed generators include, but are not limited to, synchronous generators, induction generators, reciprocating engines, microturbine fuel cells, solar photovoltaics, and wind turbines. Conventional power stations, such as coal-fired power station, gas and nuclear powered plants, as well as hydroelectric dams and large-scale solar power stations, are centralized and often require electricity to be transmitted over long distances. On the contrary, distributed energy resource (DER) systems are decentralized, modular, and more flexible technologies that are located close to the load or consumers. DER systems typically use renewable energy sources, including small hydro, biomass, biogas, solar power, wind power, and geothermal power, and increasingly play an important role for the electric power distribution system. A grid-connected device for electricity storage can also be classified as a DER system and is often called a distributed energy storage system (DESS). By means of an interface, DER systems can be managed

A.K. Rathore (✉)

Electrical and Computer Engineering, Concordia University, Montreal, Canada
e-mail: arathore@encs.concordia.ca

P.U. Rajagopal

Texas Instruments Incorporated, Dallas, TX, USA

and coordinated within a smart grid. Distributed generation and storage enable collection of energy from many sources and may lower environmental impacts and improve security of supply. There are many reasons a customer may choose to install a distributed generator. DG can be used to generate a customer's entire electricity supply, for peak shaving, for standby or emergency generation, as a green power source (using renewable technology), or for increased reliability. In some remote locations, DG can be less costly as it eliminates the need for expensive construction of distribution and/or transmission lines.

The benefits of DG are as follows:

1. Lowers the capital cost because of the small size of the DG,
2. Reduces the need for large infrastructure construction or upgrades because the DG can be constructed at the load location,
3. Reduces pressure on distribution and transmission lines,
4. Produces zero or nearzero pollutant emissions with renewable technologies,
5. Increases reliability acting as a backup or standby power available to the customers,
6. Offers customers a choice in meeting their energy needs, and
7. Reduced electricity bill with renewable-to-grid integration.

With recent focus and high interest of various countries in the concepts of zero energy buildings, smart grids, microgrids, smart homes, and smart city have raised the need of renewable technologies and their integration to the conventional grid. Significant growth in renewable energy market is also a reason behind this focus.

However, with growing global energy demand and lack of power generating capacity, electrical power industries are facing serious challenges and working toward a solution to overcome. Integrating DG output to the grid improves grid reliability. Overall, it enhances the grid capacity and is noted as a prime component of a smart grid. At distribution side, DG avoids major investments in transmission and distribution system by sitting near to the customer. It opens business markets in remote areas inaccessible by power lines.

The harvested power from renewable energy sources is available mostly in variable DC or variable ac form. In addition, alternative energy source output (solar cells and fuel cells) is low voltage and the same is true for energy storage and needs voltage gain to interface with grid or microgrid. The energy harvested from alternative energy sources, i.e., solar photovoltaic, wind, fuel cells, can be delivered to the grid directly or firstly used by the local load, and the surplus is supplied to the grid or can be stored in DC form. Power electronic converters are enabling technologies to perform these important tasks and promote such technologies to match the source and load profiles. The major challenge is to maintain high efficiency with intermittent variability, load profile, and usage. The converters used for interfacing renewable sources with grid are supposed to perform complicated tasks like grid synchronization while maintaining the safety requirements and standards of the utility grid. High-frequency power electronic conversion units are preferred to realize low cost, compact, and lightweight systems.

Reliable, high-density, and efficient power electronic systems are required for grid integration. Grid integration can be implemented in several ways based on selected power conversion configuration and control. Higher installation cost and the connection issues that may impact the grid power quality are the major concerns of DG to grid integration.

This section compares and evaluates interfacing schemes for integrating renewable energy sources to grid using multistage high-frequency (HF) transformer-isolated power electronic system. Various features such as grid power factor, grid current THD, density of power converters, easiness of connection and simplicity of control, risk of high-frequency transformer saturation, losses and component ratings, and volume and cost of electrolytic capacitor are compared. Based on their competitive merits and characteristics of energy source(s), a suitable scheme is justified.

19.2 DG to Grid Interface and Power Control Schemes

Power electronics is an enabling technology in renewable energy conversion to convert variable solar/fuel cell DC voltage into regulated output DC voltage or ac voltage of desired voltage and frequency as shown in Fig. 19.1. Renewable energy

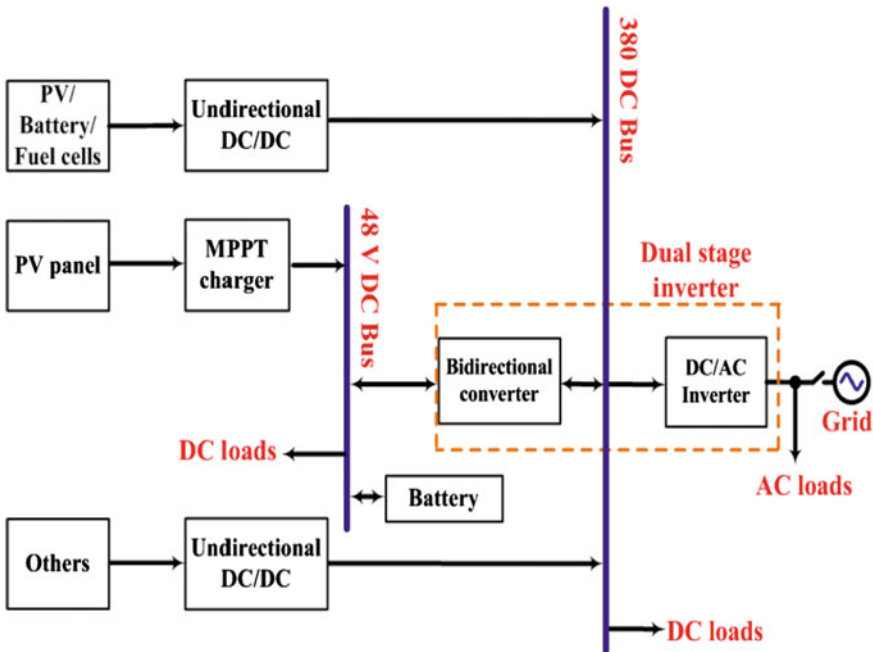


Fig. 19.1 Renewable integration and microgrid architecture

source voltage must be first boosted above the peak of the grid voltage. This DC/AC power conversion is possible using single-stage or multistage power conversion.

A single-stage DC/AC power conversion system using a transformer-isolated inverter is shown in Fig. 19.2 that uses line frequency transformer to scale the voltage before connecting to the utility line. Figure 19.3 shows a two-stage power conversion system using a front-stage non-isolated DC/DC boost converter to boost the input voltage partially followed by an inverter connected to the utility line using a line frequency transformer to offer the rest of the voltage gain. This configuration needs lower transformer turns ratio than former due to additional stage of boost converter. Similarly, several other options are also available using line frequency transformer isolation. Line frequency transformer scales the fuel cell stack voltage up to the utility line peak voltage. Such configurations show high efficiency but require line frequency transformer, which is heavy, bulky, and costly. Therefore, multistage power conversion with high-frequency (HF) transformer isolation as shown in Fig. 19.4 is desired to realize a small size, economical, and lightweight system design. Voltage gain is obtained by HF transformer-isolated DC/DC converter. Input DC voltage is first inverted to HF AC, which is elevated by HF transformer and then converted into DC voltage by rectifier. The first two HF stages

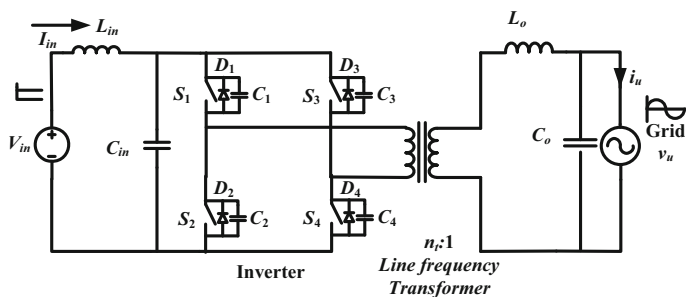


Fig. 19.2 Single-stage DC/AC inversion using line frequency transformer isolation

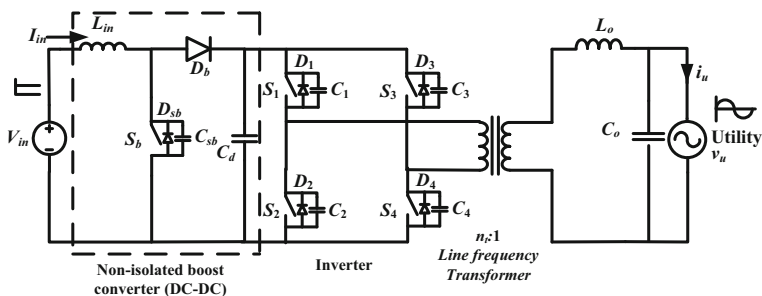


Fig. 19.3 Two-stage DC/AC conversion using line frequency transformer isolation

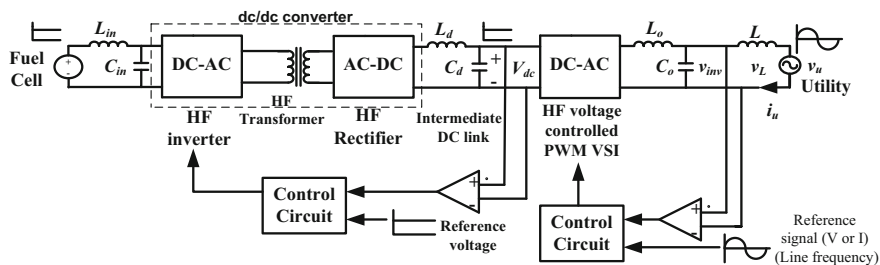


Fig. 19.4 Multistage DC/AC conversion using high-frequency transformer

form a DC/DC converter to form an intermediate high-voltage DC bus. Elevated voltage of DC bus is inverted to utility line or load voltage through an inverter at desired frequency. However, increasing the number of stages of power conversion increases the number of components and reduces the efficiency of the system.

Voltage control, usually, sine pulse width modulation (SPWM), is implemented for stand-alone applications, and current control is adopted for grid-tied applications. Voltage-fed or current-fed and resonant or PWM converter topologies have been reported in the literature for power conditioning of a fuel cell system. In all configurations, front-end converter is expected to track maximum power point (MPP) based on current fuel flow rate and temperature conditions in case of fuel cells and irradiance and temperature in case of solar. A maximum power point tracking (MPPT) algorithm needs to be implemented to operate the front-end converter to operate the fuel cell at MPP under all operating conditions for the best utilization of the source energy.

Solar panel and fuel panel stack voltages are low for domestic 4–5 kW system and are usually within the range of 20–60 V. Voltage gain requirement is very high (above 8 for North American voltage standards and 16 as per European and Asian voltage standards) for minimum input voltage at nominal power. It cannot be obtained with a non-isolated single boost converter. Interleaved boost converter and cascaded boost converter offer higher gain on the cost of higher components' count and footprint size on printed circuit board (PCB). Therefore, power conditioning system with transformer isolation is desired for such application. Isolation offers added benefit of safety.

Single-stage DC/AC power conditioning system using an inverter uses a line frequency transformer before connecting to the utility grid. A two-stage power conversion system using a front-stage non-isolated DC/DC boost converter followed by an inverter connected to the utility grid uses line frequency transformer. Similarly, several other options are also available using line frequency transformer isolation. All these configurations require line frequency transformer (with first scheme requiring high turns ratio), which is large in size, heavy, and costly. Therefore, the line frequency transformer-isolated schemes are eliminated from the choices, and one has to go with multistage power conversion with high-frequency (HF) transformer isolation to achieve and realize a compact and lightweight design.

Although such systems have lower efficiency compared to single-stage inverters owing to higher number of power conversion stages and increase in number of power semiconductor devices and components, efficiency can be improved by using higher current rating devices, interleaving or connecting devices in parallel. Therefore, multistage inverter-based scheme is desired.

Renewable-to-grid interfacing schemes can be classified into several categories using isolated power converter configurations available in the literature. A classification is shown in Fig. 19.5.

Grid integration scheme using single-ended converters (forward and flyback circuits) is preferred for low power generations (<300 W). Such a scheme is the best fit for microinverter (photovoltaic AC module) and is widely covered recently [1, 2].

At high power, such as microgrid or DG grid or in centralized configuration, integration scheme with double-ended converters (multilevel, full-bridge, push-pull, and half-bridge) is suitable. Therefore, in this section, only double-ended high-frequency power conditioning system-based approach has been described. Renewable-to-grid integration schemes can be classified into two categories based on the type of control of power conditioning system:

1. *Voltage control*
2. *Current control*

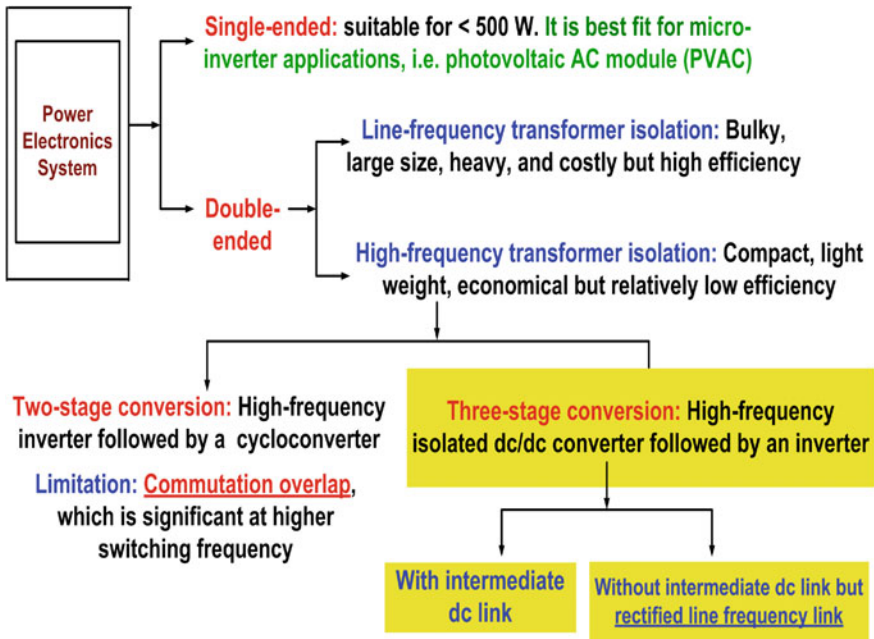


Fig. 19.5 Power conversion systems for renewable-to-utility interfacing schemes

Voltage control interface is shown in Fig. 19.4. Front-end HF DC/DC converter with step-up HF transformer scales the low voltage from solar/fuel cells to a voltage above the peak of the utility grid voltage. Electrolytic capacitor at the output of DC/DC converter forms a stiff interface DC link. A PWM voltage source inverter (VSI) converts the input DC voltage into modulated ac voltage using standard sine pulse width modulation (SPWM). The modulated ac output is filtered to develop sine waveform. An extra inductor of large value is connected between the power conditioning system and the grid to control the current injected into the grid. The current is dependent on the MPPT command. Because of voltage control, additional large inductor is required because two voltage sources cannot be connected in parallel for obvious reasons. Voltage control interface is usually implemented and employed for off-grid applications. If designed and implemented for grid-connected mode, it requires a tedious control to adjust the reactive power to minimum while injecting active power to the grid to maintain high power factor. Additionally, it requires an extra inductor in series with grid for phase adjustment between the inverter and grid voltage to feed power into the grid at unity power factor. Also, the power factor is unstable with load current and source voltage variations [3–5]. These issues limit its implementation for grid-tied application. However, sine voltage waveform generation at the inverter output makes it suitable for stand-alone application.

Current control interface is usually implemented and employed for grid-tied operation. Current control is simpler than voltage control grid interface. Stable unity power factor operation has been demonstrated with varying voltage and current owing to intermittent nature of renewable energy sources. In addition, no extra large inductor is required.

Current control scheme for grid integration can be implemented in the following two ways:

1. *Intermediate fixed DC link* and
2. *Intermediate rectified sine link*

These two current-controlled interfaces are discussed next.

19.2.1 Three-Stage Current-Controlled Conversion with Intermediate Fixed DC Link [6–9]

A three-stage power conversion system with intermediate DC link is shown in Fig. 19.6. The front-end topology is modulated to invert input DC into HF ac, which is rectified and filtered to deliver a constant voltage V_{DC} at the DC link. The DC link forms the input DC voltage for the next-stage current-controlled VSI. The current-controlled inverter is modulated to generate sinusoidal current that is injected into the grid to feed desired power based on reference signal. Average current control, peak current control, or hysteresis band current (HBCC) control can be adopted. The operating waveforms with HBCC are shown in Fig. 19.7.

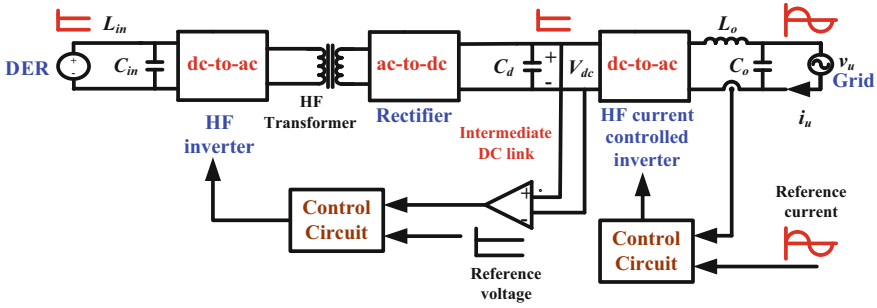


Fig. 19.6 Three-stage unit with last-stage HF current-controlled inverter (Scheme A)

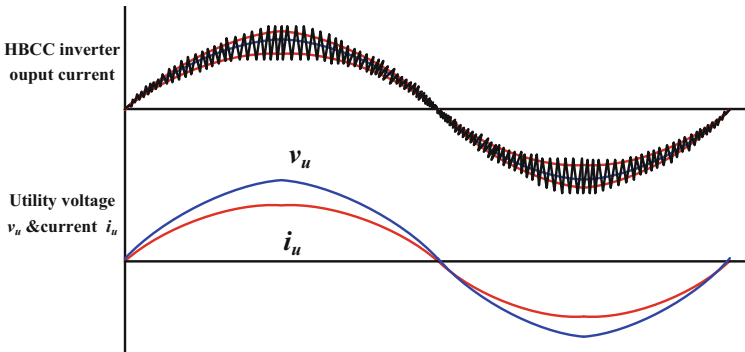


Fig. 19.7 Operating waveforms for the scheme shown in Fig. 19.6 with HBCC technique

To supply power into the grid at unity power factor, the reference current is maintained in phase with the grid voltage v_u . Second harmonic current pulsation is absorbed at DC link by capacitor C_o . Key features of this scheme are described as follow:

Benefits: (1) Components of front-end HF inverter and rectifier stages are designed for average power, and only the components of III stage HF current-controlled inverter are designed for peak power. (2) Second harmonic current component is absorbed at DC link by the large electrolytic capacitor reducing the risk of low-frequency current ripple to reach the source. (3) Control is simpler and makes the grid interface easy. (4) Grid power factor is stable with source voltage and load current variations.

Issues: All the three power conversion stages are HF switched. It is possible to achieve soft switching for front-end two stages; however, it is difficult to attain soft switching for third-stage current-controlled VSI. Therefore, switching losses in the system are higher.

19.2.2 Three-Stage Current-Controlled Conversion with Intermediate Rectified Sine Link [10–17]

A three-stage power conversion system with rectified sine link is shown in Fig. 19.8. Front-end HF inverter is line-current-modulated followed by an unfolding line frequency inverter. It is a highly adopted and implemented scheme [10–17].

Front-end HF inverter is modulated with line current reference to develop HF AC current of varying amplitude that is rectified and filtered to generate rectified sinusoidal current waveform of $2\times$ the line frequency forming a rectified sine DC link. The rectified sine current is unfolded after every half line cycle by a line frequency inverter to generate line frequency sine current to inject into the grid in synchronism with grid voltage. The sample operating waveforms are shown in Fig. 19.9. Second harmonic current is reflected and absorbed at the source by C_{in} . Key features are discussed next:

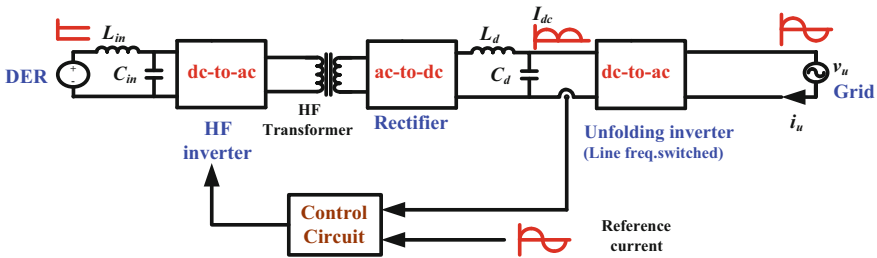


Fig. 19.8 Three-stage unit with line current modulation and III stage unfolding inverter (Scheme B)

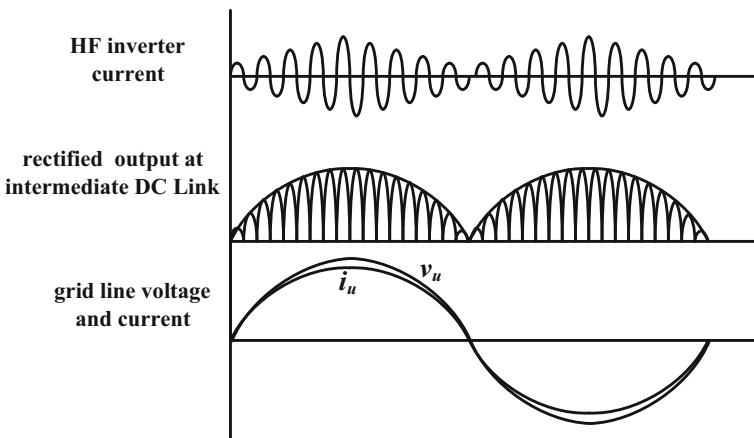


Fig. 19.9 Operating waveforms for the scheme shown in Fig. 1.8 when a resonant inverter is used

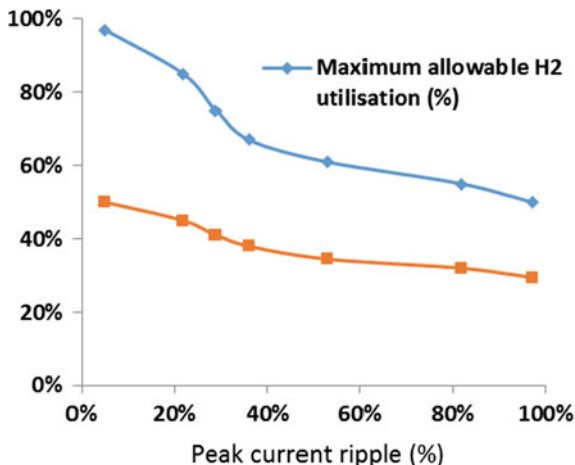
Benefits: (1) Grid connection is easy and simple. (2) Only front-end HF inverter has to be controlled. (3) Grid power factor is stable with source voltage and load current variations. (4) Third-stage unfolding inverter is line frequency (50/60 Hz) switched.

Issues: (1) Components of all power conversion stages are designed at peak power. (2) Risk of HF transformer saturation is more because of front-stage control. Therefore, flux sensing or series capacitor is usually placed to avoid transformer saturation.

The comparison between the discussed two current control schemes is discussed next:

1. **Switching losses:** Grid-connected inverter stage in scheme B is line frequency controlled, while in scheme A, it is HF switched, and therefore, scheme B has much lower switching losses.
2. **Transformer saturation:** Line frequency current reference control applied to front-stage conversion in scheme B subjects HF transformer to a risk of saturation, while scheme A employs square wave modulation, thus freeing from this risk.
3. **Components rating:** Components of all three power conversion stages in scheme B must be designed for peak power rating resulting in derating and poor utilization of components compared to scheme A.
4. **High power density/Transformer leakage inductance:** In an isolated power conversion system, power transfer capacity depends upon the value of series or leakage inductance and the switching frequency. An attempt to increase the leakage or series inductance and/or switching frequency reduces the power transfer capacity of the circuit. For a given value of switching frequency and power rating, design of scheme A realizes higher value of leakage inductance compared to scheme B. Therefore, single cell of scheme A can handle higher power compared to single cell of scheme B. Scheme B may need interleaving of converter cells to match power rating of scheme A at one point of power rating. Interleaving requires $2\times$ the components increasing the volume and cost. It is also added to the control complexity to maintain equal current sharing between the converter cells. Therefore, scheme A is entitled for higher power rating design compared to scheme B.
5. **Risk of low-frequency harmonics at input:** The low-frequency ripple is seen at the input in scheme B. Decoupling capacitor across the source absorbs the second harmonic pulsation. But, there is still a possibility of second harmonic ripple reaching the source, i.e., solar panel/fuel cell stack. Ripple can perturb and then adjust the operating point below the maximum power point resulting in a system shut down. The second harmonic current component is absorbed at the DC link in scheme B, and the source is not subjected to low-frequency ripple. It supports scheme A to be a better choice.

Fig. 19.10 Effect of current ripple on fuel utilization in fuel cells



Fuel utilization is critical and important in fuel cell system in order to result in low-cost energy and high overall system efficiency. It requires fuel cell stack current ripple to be minimized. The same holds good for solar to get faster return on investment.

Effect of current ripple on fuel cell utilization is demonstrated in Fig. 19.10. It affects overall fuel-to-load efficiency. Therefore, low current ripple is expected to achieve high efficiency.

6. **Electrolytic capacitor:** In a power electronic system, electrolytic capacitor is considered to be the most unreliable component. This component has large footprint size and limited life based on thermal operating conditions. It also covers a major fraction of the total converter cost and volume. For fuel cell/solar applications, input voltage is usually low and varies from 30 to 60 V based on external conditions. The intermediate DC link voltage for 1-phase system is set at 350 V for scheme A.

Details of the decoupling capacitors selected for these two schemes are shown in Table 19.1. Input capacitor C_{in} used in scheme B has higher energy storage capacity as compared to C_o in scheme A. Alternative energy sources like solar and fuel cells have wide voltage variation (>1:2). Therefore, decoupling capacitor in

Table 19.1 Details of decoupling capacitors for second harmonic absorption for the two schemes

Energy storage/decoupling capacitor	Scheme A	Scheme B
Value/rating	$C_o = 2.2$ mF, 450 V electrolytic	$C_{in} = 100$ mF, 80 V electrolytic
Cost	24 \$ US	37 \$ US
Volume	Dia = 2.5", height = 4.13"	Dia = 3", height = 5.63"
Life	2000 h @ 85 °C	2000 h @ 85 °C

scheme B should be of higher voltage rating than the maximum possible source voltage. For a given operating voltage range of 30–60 V, an 80 V capacitor is selected. Similarly, DC link voltage in scheme A is fixed at 350 V, and therefore, a 450 V capacitor is selected.

Although C_{in} has more energy storage capacity in scheme B than C_{DC} in scheme A, the effective energy storage capacity of C_{in} becomes lower at lower input voltage ($V_{in} = 30$ V). Effective energy storage capacity, in scheme A, is $\frac{1}{2} C_{DC} V^2$ ($=\frac{1}{2} 0.0022 \times 350^2$) = 134.75 J. However, effective energy storage capacity at full load at low input voltage is $\frac{1}{2} C_{in} V^2$ ($\frac{1}{2} 0.1 \times 30^2$) = 45 J for 100 mF value capacitor. If low decoupling capacitor value is used, then the input current ripple and RMS current through the devices will have high value and reduce efficiency. Therefore, to achieve the comparable performance of the two schemes, scheme B requires decoupling capacitor of higher energy capacity and that is large in volume and cost. For the same lifetime of the decoupling capacitor, scheme A claims stable operation, comparable efficiency, small size, and low cost.

19.3 DC/DC Converters for Non-conventional Energy Sources

Alternative energy sources such as fuel cells, solar PV, and energy storage offer low variable DC voltage and need DC/DC converter to interface with high-voltage DC bus and DC/AC inversion into utility/load interactive AC voltage as shown in Fig. 19.11.

High-frequency power electronic conversion units are preferred to realize low cost, compact, and lightweight systems. However, to improve the efficiency for

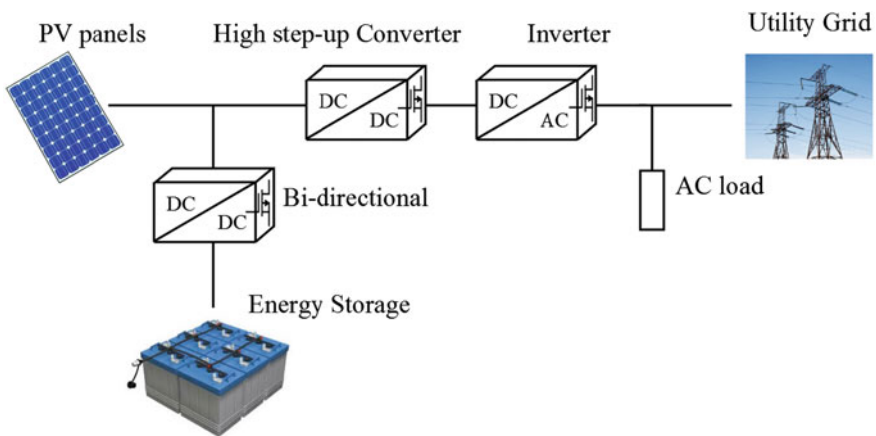


Fig. 19.11 Power electronic system to interface alternate energy sources and storage to grid/load

effective utilization of renewable energy and reduce cooling/thermal requirements, soft switching of semiconductor devices needs to be implemented.

The criterion to be satisfied by interfacing DC/DC converters is as follows:

- (a) High gain: Voltage from fuel cell stacks or PV arrays is generally less than 100 V, while the DC bus voltage of a microgrid or distributed energy system is about 380–400 V. The interfacing converters are expected to provide the required gain.
- (b) Accommodate source variability: The fuel cell and PV voltages vary with fuel inflow and temperature, respectively. Hence, the interfacing DC/DC converter should be able to operate satisfactorily for wide input voltage variations.
- (c) Low input current ripple: The lifetime of the fuel cell stack and the maximum power point tracking in PV is highly dependent on the magnitude of the input current ripple. The ripple in the input current is to be maintained less than 5% to ensure minimum impact on the fuel cell conditions and to allow accurate power tracking in case of PVs.
- (d) Galvanic isolation: In front-end DC/DC converters, galvanic isolation is preferred to ensure high voltage gain and also to provide electrical isolation between the source and the utility DC bus for safety reasons.
- (e) Reduced circuit complexity: The front-end DC/DC converter should be a cost-effective and efficient solution with lower device count and should provide the flexibility of easy control.
- (f) Modularity and scalability: Modularity in the circuit design is preferred as it reduces the manufacturing costs, required maintenance, and increases the converter reliability. Modular topologies can also be scaled up to meet high-power requirements.
- (g) Compact and lightweight design: Soft switching permits high operating frequencies with depreciation in the circuit magnetics and volume. The device voltages and the electromagnetic interference (EMI) are mitigated with soft-switching operation. Hence, high power density, compact, lightweight, and highly efficient systems can be easily realized.
- (h) Range of soft switching: Soft switching is generally preferred over a wide range of source voltage and load variations to ensure satisfactory performance under all operating conditions.

To mitigate the switching losses and achieve high efficiency, soft switching is necessary. Soft switching can be implemented in several ways: (1) PWM technique, (2) resonant tank leading to the development of resonant converters, and (3) auxiliary transition circuit. To obtain and maintain soft switching and to maintain load regulation, duty cycle modulation and variable frequency modulation are usually employed. The classification is shown in Fig. 19.12. These types have their own merits and demerits based on the applications and specifications. Major challenge is to maintain soft switching with variations in source voltage and load current. To maintain soft switching and high efficiency over such large variations without compromise on circuit complexity and rated load performance (circulating currents

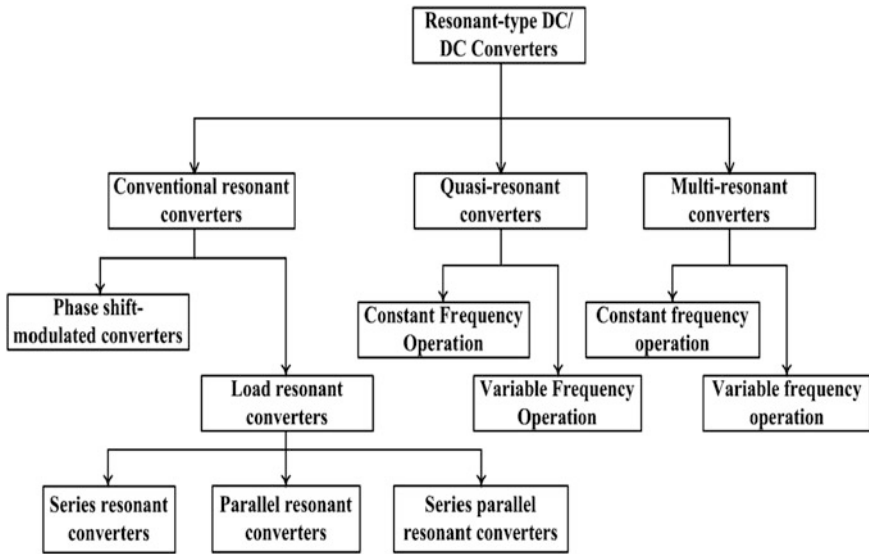


Fig. 19.12 Classification of soft-switching resonant converters

and components' ratings) is a real challenge. There are two major types of DC–DC converters, viz. voltage-fed and current-fed converters. Resonant converters can be operated in either variable frequency mode or fixed-frequency mode, but the operation in variable frequency mode makes the design of filters and control circuit difficult. In the present application, variation in switching frequency required is very large due to wide variations in the input voltage and load conditions. Therefore, fixed-frequency operation is considered.

From the above discussions, following eight soft-switching DC–DC converter configurations are possible.

1. Fixed-frequency series resonant DC/DC converter (SRC) [18],
2. Fixed-frequency parallel resonant DC/DC converter (PRC) [19],
3. Fixed-frequency series–parallel or LCC-type resonant DC/DC converter (SPRC) [20],
4. Fixed-frequency LCL SRC with capacitive filter [21, 22],
5. Fixed-frequency LCL SRC with inductive filter [23],
6. Fixed-frequency phase-shifted PWM full-bridge DC/DC converter [24–26],
7. Fixed-frequency dual-active-bridge (DAB) DC/DC converter [27, 28], and
8. Fixed-frequency current-sharing half-bridge DC/DC converter [29, 30].

The major drawbacks of the resonant converters are listed below:

1. The performance of the resonant converters can be optimized only over a single point. This degrades the converter performance over wide input and load ranges.

2. The resonance develops circulating currents that flow through the circuit components including the power semiconductor devices. It leads to poor efficiency at light load and at voltage variation.
3. The circulating current due to resonance results in higher peak current through the devices and magnetics leading to the requirement of overrated VA rating components.
4. For variation in input voltage, voltage regulation is maintained by variable frequency modulation to maintain soft switching of the semiconductor devices. With variable frequency operation, the range of switching frequency variation can be very high at large voltage variation of PV/fuel cells. It causes complexity in magnetics and filter design as well as optimizes the operating points.

Owing to these drawbacks, resonant converters are not ideal choices for low-voltage high-current applications with high source variability.

Among the above-mentioned power converters, the SRC and SPRC can operate with ZVS only for very narrow variations in input voltage and load current. In the case of PRC, the inverter peak current does not reduce enough with reduction in load current. Therefore, first three circuit topologies are not considered for further study. Hence, only the later five topologies are discussed next.

19.3.1 Fixed-Frequency LCL SRC with Capacitive Output Filter (Topology A)

Figure 19.13 shows LCL-type modified SRC topology with capacitive output filter. It employs LCL resonance circuit for soft switching of the power semiconductor devices. The converter has been analyzed using Fourier series approach [21] and approximate analysis [22]. It has been demonstrated that the converter operates in lagging power factor mode ensuring ZVS of all primary switches. The peak current and RMS current through the semiconductor devices decrease with load current.

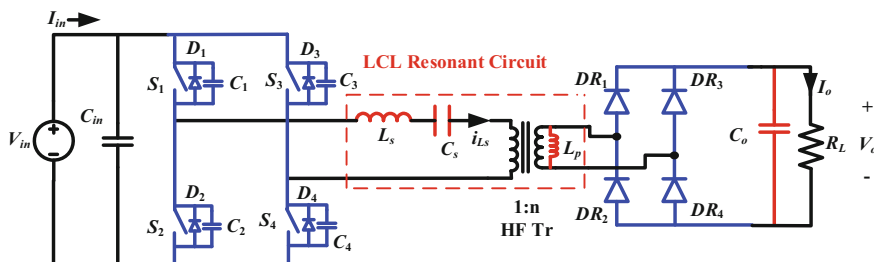


Fig. 19.13 LCL series resonant converter with capacitive output filter

The analysis and design procedure of the converter are given in [21] and shown in Appendix 19.1. The calculated values of the component are $n = 18$, $L_s = 0.17 \mu\text{H}$, $L_p = 550 \mu\text{H}$, $C_s = 17.56 \mu\text{F}$, $C_1 - C_4 = 47 \text{ nF}$, and $C_o = 25 \mu\text{F}$.

19.3.2 Fixed-Frequency LCL SRC with Inductive Output Filter (Topology B)

Figure 19.14 shows LCL-type SRC topology with inductive output filter. This converter has been analyzed using approximate analysis [23]. It has been illustrated that the converter also operates in lagging power factor mode ensuring ZVS of all primary-side semiconductor devices. The peak current through the devices decreases with load current.

The analysis and design of the converter is reported in [23]. The design equations are given in Appendix 19.2. The component values calculated for the present application are $n = 22$, $L_s = 0.13 \mu\text{H}$, $L_p = 844 \mu\text{H}$, $C_s = 23.5 \mu\text{F}$, $C_1 - C_4 = 80 \text{ nF}$, $L_o = 700 \mu\text{H}$, and $C_o = 1 \mu\text{F}$.

19.3.3 Fixed-Frequency Phase-Shifted PWM Full-Bridge Converter with Inductive Output Filter (Topology C)

The phase-shifted full-bridge PWM converter with inductive output filter is shown in Fig. 19.15. It attains ZVS of the primary devices with comparatively low circulating current compared to resonant converters. ZVS is achieved by filter inductance, transformer leakage inductance, snubber capacitance, and parasitic junction capacitance of semiconductor devices.

Analysis and design is highlighted in [24–26] and given in Appendix 19.3. The calculated values of the components are $n = 20.3$, $L_s = 70 \text{ nH}$, $C_1 = C_2 = 65 \text{ nF}$, $C_3 = C_4 = 58 \text{ nF}$, $L_o = 500 \mu\text{H}$, and $C_o = 1 \mu\text{F}$.

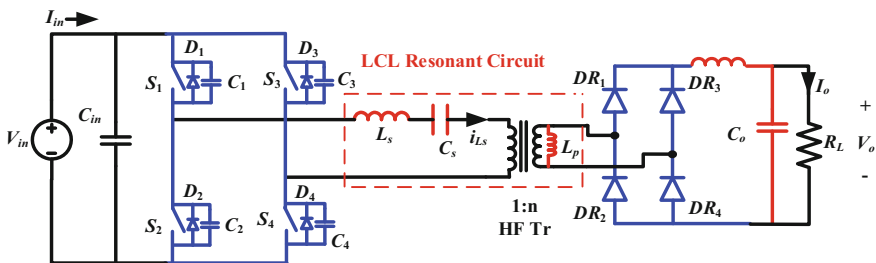


Fig. 19.14 LCL resonant converter with inductive output filter

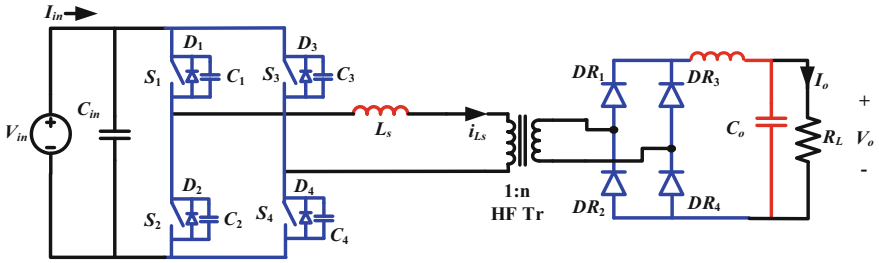


Fig. 19.15 Full-bridge phase-shifted PWM converter with inductive output filter

19.3.4 Fixed-Frequency Dual-Active-Bridge (DAB) Converter (Topology D)

Figure 19.16 shows dual-active-bridge converter having two active full bridges with bidirectional ability. One bridge is modulated by a fixed switching pattern. The second bridge is operated with fixed-frequency fixed duty cycle but phase-shifted with first bridge gating signals to produce a phase difference between primary voltage (v_p) and secondary voltage (v_s) across transformer to adjust the load voltage with any variability. All primary-side semiconductor devices operate with ZVS for all input voltage and load conditions if $v_p > V_o/n$. If the primary current lags primary voltage, the primary-side devices undergo ZVS, and if the secondary current leads secondary voltage, the secondary side undergoes ZVS. The converter is analyzed and designed in [27, 28], and the equations are reported in Appendix 19.4. The calculated values of the components are $n_t = 17.3$, $L_s = 0.3 \mu\text{H}$, $C_1 - C_4 = 68 \text{ nF}$, $C_5 - C_8 = 0.2 \text{ nF}$, and $C_o = 25 \mu\text{F}$.

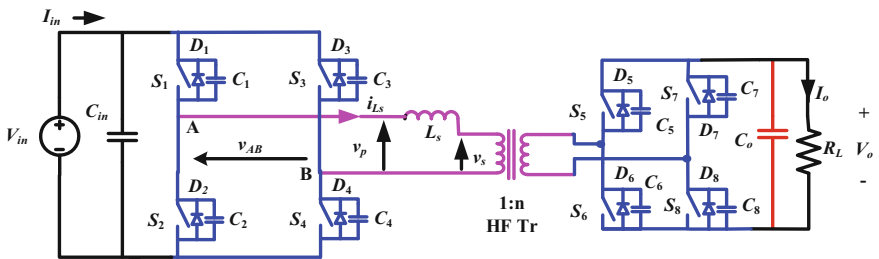


Fig. 19.16 Dual-active-bridge converter

19.3.5 Fixed-Frequency Current-Fed Half-Bridge Converter (Topology E)

Topologies A–D are voltage-fed converter, which are buck-derived isolated converters. However, the specifications and applications mentioned need voltage gain (boost). Therefore, boost-derived converters may be more suitable for such specifications and applications. Current-fed half-bridge isolated converter is current-sharing circuit and is suitable for such applications. Turn-off voltage spike, hard switching, and need of auxiliary snubber circuit to limit or clamp device voltage are the major limitations of such converters. A topology with active-clamping ZVS is shown in Fig. 19.17. It has been analyzed and designed in [29, 30].

The device turn-off voltage spike is absorbed by active-clamping circuit, resulting in reduced snubber capacitor value across the main switches and reduced switching losses. The configuration is able to maintain ZVS for wide input range. Switch peak and RMS current decrease with decrease in load current and increase in input voltage, and ZVS is maintained, thereby increasing the efficiency at high input and reduced load. The design equations [29, 30] are given in Appendix 19.5. The calculated values of the components are $n = 3.5$, $L_1 = L_2 = 100 \mu\text{H}$, $L_s = 0.75 \mu\text{H}$; $C_1 = C_2 = C_{\text{oss}}$, $C_a = 10 \mu\text{F}$, $C_{a1} = C_{a2} = 11.72 \text{ nF}$, and $C_o = 25 \mu\text{F}$.

Table 19.2 demonstrates the merits, demerits, and the problems associated with these converter topologies. Based on the comparison of attributes, key features, and the performance, i.e., efficiency and ZVS range, a suitable circuit topology for the present application can be selected.

Table 19.3 shows a comparison of various components' ratings in the above-mentioned converter topologies for the given single-cell specifications. The values shown in Table 19.3 are normalized using the following base values, and

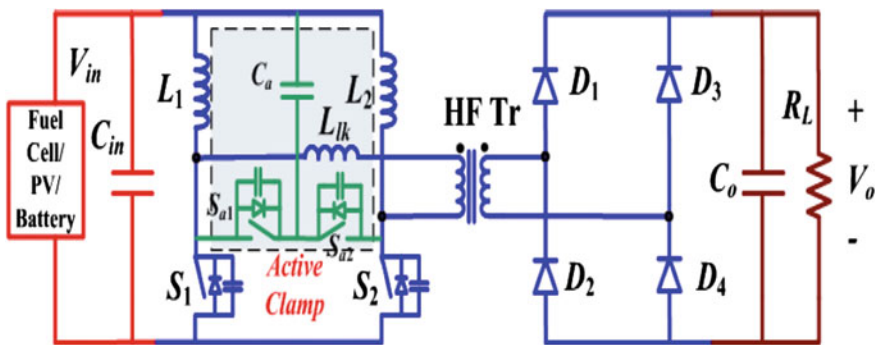


Fig. 19.17 Current-fed half-bridge converter with capacitive output filter

Table 19.2 Drawbacks/problems associated with DC–DC converters

Parameters	Topology A	Topology B	Topology C	Topology D	Topology E
Switch peak current with increasing input voltage	Increases	Increases	Increases but relatively low	Increases	Decreases
RMS current with increasing input voltage	Increases	Decreases	Increases	Increases	Decreases
Duty cycle loss	No	Yes	Yes	No	No
Rectifier diode voltage ringing	No	Yes, needs snubber	Yes, needs snubber	No	No
ZVS range	ZVS is lost at light load and higher input voltage ^a	ZVS is lost at light load and higher input voltage ^a	ZVS is lost at light load and higher input voltage	ZVS is lost at light load and higher input voltage ^a	ZVS is lost at light load and higher input voltage ^b
Diode turn-off	ZCS	Hard	Hard	ZCS	ZCS

^aBetter at light load^bBetter at input voltage**Table 19.3** Comparison of various parameters for various topologies for $V_{in} = 22$ V at full load and in brackets for $V_{in} = 41$ V at full load (2 kW)

Parameters	Topology A	Topology B	Topology C	Topology D	Topology E
Peak current through L_s (A)	149 (284.6)	141.2 (153.8)	114 (129)	132 (247.4)	92 (49.5)
Peak main switch current (A)	149 (284.6)	141.2 (153.8)	114 (129)	132 (247.4)	138 (74)
Main switch RMS current (A)	77 (103.7)	80 (78.6)	72.2 (75.7)	41.8 (47.1)	58.6 (36.2)
Aux. switch RMS current (A)	–	–	–	–	11.7 (9.5)
Peak aux. switch current (A)	–	–	–	–	45.5 (24.5)
$n = N_s/N_p$	18	22	20.3	17.3	3.5

the per-unit (p.u.) values obtained are given in Table 19.4. Base values on the primary side of the HF transformer are base voltage $V_B = V_{in,min} = 22$ V, base power (for both active and apparent) $P_B = P_o = 2$ kW (nominal or full-load output power), and base current $I_B = P_B/V_B = 91$ A.

Base values for the secondary side of the HF transformer are $V_B = V_o = 380$ V, $P_B = P_o = 2$ kW (full-load power), and $I_B = P_B/V_B = 5.27$ A. VA rating of transformer/switch/tank is normalized by dividing it by base power or nominal power.

Table 19.4 Normalized per-unit (p.u.) values of Table 1.3

Parameters	Topology A	Topology B	Topology C	Topology D	Topology E
Peak current through L_s	1.64 (3.13)	1.55 (1.69)	1.25 (1.42)	1.45 (2.72)	1.01 (0.54)
Peak current through L_p	0.33 (0.29)	0.27 (0.27)	–	–	–
Peak voltage across C_s	0.64 (0.69)	0.54 (0.26)	–	–	–
Switch RMS current	0.85 (1.14)	0.88 (0.87)	0.79 (0.83)	0.92 (1.04)	0.64 (0.4)
Peak HF switch voltage	1 (1.86)	1 (1.86)	1 (1.86)	1 (1.86)	5 (4.18)
Peak switch current	1.64 (3.13)	1.55 (1.69)	1.25 (1.42)	1.45 (2.72)	1.5 (0.81)
Peak rectifier diode/switch voltage	1 (1)	1.71 (2.66)	1.2 (2.23)	1 (1)	1 (1)
Transformer VA rating	1.2 (1.7)	1.25 (1.58)	1.13 (1.6)	1.3 (2.72)	1.40 (1.24)
Switch VA rating	0.85 (2.13)	0.88 (1.61)	0.79 (1.55)	0.93 (1.86)	3.22 (1.76)
Tank VA rating	1.35 (2.14)	1.15 (1.23)	0.26 (0.28)	1.15 (1.38)	0.34 (0.18)

Table 19.2 demonstrates that for the given application and specifications, none of the voltage-fed converters (topologies A–D) maintain ZVS for the entire operating range of load current and source voltage. Converters with inductive output filter (topologies B–C) suffer from the problem of duty cycle loss and voltage ringing across rectifier diodes and need lossy RCD snubber circuit to limit the voltage across the rectifier diodes.

Capacitive output filter topologies (A, D–E) are better suited because they are free from such drawbacks, and rectifier diode voltage is clamped at load voltage. Topology C cannot maintain ZVS at light load conditions even at fixed source voltage. For a narrow variation of source voltage, topology A can demonstrate ZVS for wide load variation (up to 10% load), but the peak current and RMS current through the switches increase with increase in input voltage as shown in Tables 19.3 and 19.4. It results in higher conduction losses at high input voltage and reduces the converter efficiency. ZVS is also lost at upper value of input voltage range. Topology D employs more number of sets of switches and driving circuits. The key drawback of this converter is large circulating current at higher value of source voltage. Peak current and RMS current through the switches increase with increase in source voltage, thereby causing higher conduction losses in primary-side switches and decreasing the converter efficiency. If the source voltage variation and input currents are higher (as in the present application due to low input voltage specifications), then only current-fed circuit topology E maintains ZVS at higher source voltage. Also as shown in Tables 19.3 and 19.4, RMS and peak currents through the switches in topology E reduce with increase in source voltage that increases the converter efficiency at upper range of input voltage. Capacitive output filter offers this converter to be free from the problems of duty cycle loss and rectifier diode ringing. Voltage across rectifier diode is clamped at the output voltage, and the rectifier diodes achieve ZCS. Series tank inductor value can be realized. Along with these merits, higher efficiency and wider ZVS range than

voltage-fed converters make this converter suitable for this application. Therefore, active-clamped current-fed half-bridge converter (topology E) is a preferred choice for the present specifications and application.

19.4 Energy Storage

Energy storage has several applications like peak load shaving during peak demand hours, energy storage during off-peak hours, handling load transients in applications by acting as buffer unit, etc. Based on application and sizing, various energy storage systems are possible. For large-sized distributed generation, pumped hydrosystem is quite popular and needs large infrastructure and initial investment cost. For medium-sized generation system and application, flywheel has been a popular option too.

For small- and medium-sized applications and generation systems, two emerging choices are batteries and ultracapacitors. Batteries have higher energy density, while the ultracapacitors have higher power density. These two choices are quite popular in handling load transients in generation systems and vehicles, in particular fuel cell powered-applications.

For efficient operation of the fuel cell, the fuel cell operating point should be adjusted as a function of the electrical load. Since this adjustment for reactant utilization involves mechanical systems, the response time of the fuel cell to varying electrical loads can be slow. For the same reason, the fuel cells cannot respond to the electrical load transients as fast as desired.

The mismatch between the fuel cell time constant and the typical electrical load time constant requires secondary source of energy, also called power/energy buffer or energy storage device in the system.

The solution is to combine the fuel cells with secondary source of energy to provide the difference between the load demand and the output power generated by the fuel cells during the transient duration. This secondary source of energy with fast dynamics compensates for the slow dynamics of the fuel cells, responds to the fast-changing electrical load during transients, and supports the increase or decrease in power demand until the fuel cell output can be adjusted to meet the new demand value at steady state.

Between the two mentioned solutions, ultracapacitor is a good option due to several advantages such as better power density, long life cycle, and very good charge/discharge efficiency and can be constructed in modular or stackable format power density. Ultracapacitors can also provide large transient power instantly and thus are capable of providing energy for the increased load demand. Ultracapacitors have more cycles of charging and discharging during their lifetime, providing high cycling capability and maintenance-free operation, and can effectively serve as cost-effective alternative to batteries for residential or utility applications especially during short peak demand or transient periods.

19.4.1 Bidirectional DC/DC Converters for Energy Storage Application

This section presents a comparison of two potential soft-switching bidirectional voltage-fed and current-fed dual-active converters for energy storage application. The comparison and evaluation are done from the perspective of the circulating and peak currents, RMS currents through the devices, components' ratings, size, losses, and efficiency.

The design of the two bidirectional voltage-fed and current-fed converters is done for the following specifications: input voltage $V_{in} = 48$ V, output voltage $V_o = 380$ V, power rating $P_o = 5$ kW, and switching frequency $f_s = 100$ kHz.

19.4.1.1 Voltage-Fed Dual-Active-Bridge Converter (VFDAB)

Figure 19.18 shows voltage-fed dual-active-bridge (VFDAB) converter. All the switches are operated by fixed-frequency fixed duty cycle gating patterns. The high-voltage side bridge is controlled to produce phase difference between primary voltage (v_p) and secondary voltage (v_s) of transformer to regulate the output voltage with variations in load and input voltage [27, 28].

All primary switches are expected to operate with ZVS for all input voltage and load conditions if $v_p > V_o/n$. If the primary current lags primary voltage, the primary-side switches undergo ZVS, and if the secondary current leads secondary voltage, secondary side switches undergo ZVS. The converter has been analyzed in [27, 28]. The design equations are given in Appendix 19.4. The calculated values of the components for the given specifications are $n = 8$, $L_s = 0.57$ μ H, and $C_o = 10$ μ F.

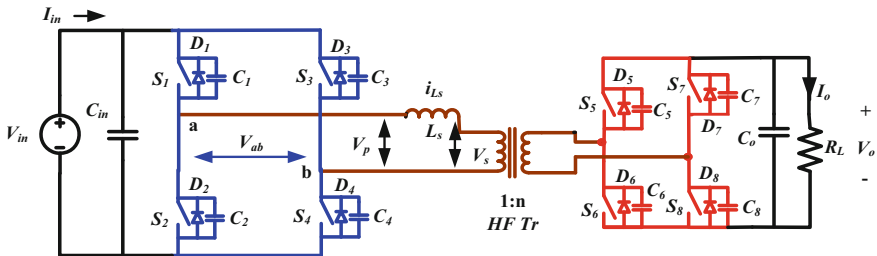


Fig. 19.18 Secondary-side-controlled voltage-fed dual-active full-bridge DC/DC converter

19.4.1.2 Current-Fed Dual-Active-Bridge Converter (CFDAB)

Naturally clamped soft-switching bidirectional current-fed dual-active-bridge (CFDAB) converter is shown in Fig. 19.19. The converter achieves zero-current switching (ZCS) of primary switches and ZVS of secondary switches. This topology shows better part-load efficiency than hard-switching and active-clamped current-fed converter owing to reduced circulating current and switching losses. The converter has been analyzed in [31]. The design is reported in Appendix 19.5. Calculated values of the components are $n = 3.2$, $L_s = 1.7 \mu\text{H}$, and $C_o = 10 \mu\text{F}$.

Table 19.5 shows a comparison of various parameters of these two converters for the given specifications. All the values given in Table 19.5 are normalized using the following base values, and the obtained per-unit (p.u.) values are given in Table 19.6. The base values on the primary side of the HF transformer are base voltage $V_B = V_{in,min} = 48 \text{ V}$, base power $P_B = P_o = 5 \text{ kW}$ (nominal or full-load output power), and base current $I_B = P_B/V_B = 104.17 \text{ A}$. Base values for the secondary side of the HF transformer are $V_B = V_o = 380 \text{ V}$, $P_B = P_o = 5 \text{ kW}$ (full-load power), and $I_B = P_B/V_B = 13.16 \text{ A}$. VA rating of transformer/switch is normalized by dividing base power or nominal power.

It is clear from Table 19.5 that CFDAB is clearly observed to have lower peak current through the components and results in lower circulating currents. Table 19.6 shows that VFDAB has almost double-peak current value and the value is much higher than average input current. It indicates high circulating currents in VFDAB. Lower circulating current results in lower conduction losses into the semiconductor devices. As demonstrated in Table 19.5, peak HF switch voltages of both VFDAB and CFDAB are both rather low. For VFDAB, the voltage is clamped at battery voltage by input capacitor, making it possible to utilize low-voltage-rating semiconductor device with low on-state resistance (80 V devices). For CFDAB, the voltage across primary switch is rather clamped at reflected output voltage, making it possible to utilize low-voltage-rating semiconductor device with low on-state resistance (100 V devices). Although on-state resistance of primary device of

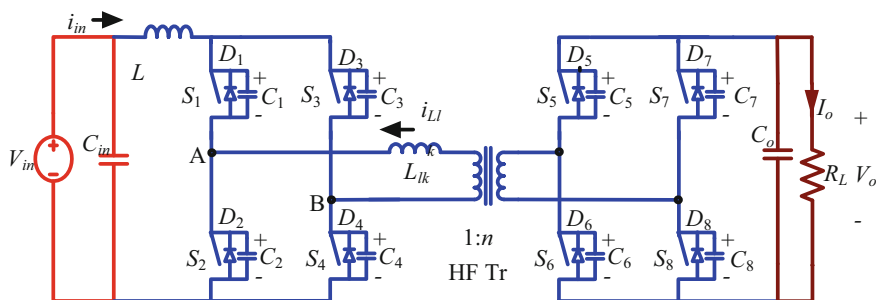


Fig. 19.19 Current-fed dual-active full-bridge DC/DC converter

Table 19.5 Comparison of parameters for the two converter topologies at $V_{in} = 48$ V and full load (5 kW)

Parameters	VFDAB	CFDAB
Peak current through L_{lk} (A)	218.75	113.25
Primary switch RMS current (A)	123.25	65.63
Secondary switch RMS current (A)	5	5.64
Peak primary switch voltage (V)	48	60
Peak primary switch current (A)	218.75	113.25
Peak secondary switch voltage (V)	380	380
Transformer VA rating (VA)	9325	6220
n	8	3.2

Table 19.6 Normalized values of Table 1.5

Parameters	VFDAB	CFDAB
Peak current through L_{lk} (p.u.)	2.1	1.08
Primary switch RMS current (p.u.)	1.2	0.63
Peak primary switch voltage (p.u.)	1	1.25
Peak primary switch current (p.u.)	2.08	1.03
Peak secondary switch voltage (p.u.)	1	1
Transformer VA rating (p.u.)	1.86	1.24
n	8	3.2

VFDAB is lower than that of CFDAB due to low voltage rating, the conduction loss in primary devices is still much higher than the loss of CFDAB owing to higher switch RMS current of VFDAB as clearly shown in Table 19.5.

Large peak currents in the VFDAB result in higher turn-off switching losses compared to CFDAB, which has relatively low device peak currents.

Saving in conduction losses and switching losses in devices results in higher efficiency of the CFDAB for the given specifications of low voltage higher current.

For the present application, once the battery is charged to a higher voltage than its nominal value, both switch peak and RMS current go higher and the efficiency falls. However, for the CFDAB, in that case, it maintains higher efficiency when the battery voltage fluctuates and load current reduces.

Also, CFDAB requires transformer of lower kVA rating and smaller turns ratio. Thus, the transformer of CFDAB, if properly designed, can achieve smaller volume and less loss than VFDAB. As illustrated in Table 19.5, the turns ratio of VFDAB is much higher than CFDAB for the same specifications. With high transformer turns ratio, it is difficult to realize the low transformer leakage inductance in VFDAB. Power transfer capacity of an isolated power electronic system also depends on the leakage inductance of the transformer and the switching frequency. Increase in switching frequency as well as leakage inductance limits the power transfer capacity. It should be noted that transformer turns ratio is very high in VFDAB compared CFDAB. For a given switching frequency and rated power, CFDAB design attains higher value of leakage inductance than VFDAB. Therefore,

for higher power design, CFDAB can handle with single cell, while VFDAB will need two or more cells with interleaving. Thus, CFDAB is entitled for higher power capacity and density design compared to VFDAB.

Due to DC current drawn from the battery, CFDAB has better battery utilization than VFDAB. High-power single-cell design, better battery utilization, lower peak currents, lower transformer kVA ratings, reduced circulating currents, and better part-load efficiency make CFDAB more promising for energy storage application.

19.5 Grid Codes for DG

The increased concern about energy security, operating flexibility, and the cost has resulted in the emergence of advanced development of small, modular decentralized generation technologies such as wind turbines, fuel cells, photovoltaics, and microturbines [32]. This has restructured the energy market and the utility grid. Incentives and initiatives for the installation of renewable energy sources globally have increased exponentially over the last decade. Currently, most of the countries are going toward net metering system with accompanying interconnection rules, allowing small-scale renewable sources to pump power to the grid. The increased penetration of decentralized generation may provoke several technical issues in the functioning of the grid like power quality issues such as under- or overvoltages at the point of connection, malfunctioning of protection, and injection of distortion to the grid [33]. In addition, the operation, control, and protection of the microgrid as an autonomous system present challenging problems. Issues include voltage profile, reliability, safety, protection, electromagnetic compatibility (EMC), security, stray voltages and currents, and transition between grid-connected mode to islanding and vice versa. Integration issues also depend on the type of the sources used; for example, PV and wind are intermittent and uncertain in nature, whereas fuel cell or battery storage can be controlled to provide necessary power. Sudden loss of power generation from solar or wind generators may cause stability issues in the grid or has adverse effect on the power quality [34].

19.5.1 Grid Regulations and Standards

In order to have a safe and reliable operation of DG and grid, it is necessary to have a common standards mutually agreed by both the supplier and the grid operator [35]. Generally, there are local regulations imposed by the grid operators in many of the places. However, lots of efforts have been put up by few of the international bodies to develop standards for grid interconnection of distributed resources. Institute of Electrical and Electronics Engineers (IEEE), International Electrotechnical commission (IEC), and German Commission for Electrical,

Electronic and Information Technologies of DIN and VDE are the leading commissions to propose standards and regulations to interconnect DERs to the utility grid [36].

Since enactment of the Public Utilities Regulatory Policy Act in 1978, several standards have been proposed in USA, IEEE 929-2000, *Recommended Practice for Utility Interface of Photovoltaic (PV) Systems* [37], which applies to residential scale and other small-scale interconnected PV. UL 1741, *Standard for Inverters, Converters, and Controllers for Use in Independent Power Systems* [38] by Underwriters Laboratories Inc., became an important safety listing in 1999, which is derived from IEEE 929. UL 1741 addresses issues related to construction, electrical safety, and principles derived from the National Electric Code and related to UL standards for converters, charge controllers, and interconnection system equipment (ISE) intended for use in stand-alone (not grid-connected) or utility-interactive (grid-connected) power systems. In May 2007, UL1741 acknowledges using of IEEE 1547 and IEEE 1547.1 in conjunction with the UL standard for the utility interactive equipment.

IEEE 1547-2003, *Standard for Interconnecting Distributed Resources with Electric Power Systems* [39], is the most commonly referred standard which addresses all types of interconnected generation up to 10 MVA and establishes mandatory requirements. This sets it apart from the several previous IEEE guides or recommended practices on DG, which convey only suggestions and recommendations. A series of standards derived from IEEE 1547 will address testing, performance, application, and communication, as well as design of islanded systems:

- IEEE Standard 1547.1-2005 (1547.1a-2015) “*IEEE Standard Conformance Test Procedures for Equipment Interconnecting Distributed Resources with Electric Power Systems*” [40, 41].
- IEEE Standard 1547.2-2008 “*IEEE Application Guide for IEEE Std 1547™, IEEE Standard for Interconnecting Distributed Resources with Electric Power Systems.*”
- IEEE Standard 1547.3-2007 “*IEEE Guide for Monitoring, Information Exchange, and Control of Distributed Resources Interconnected with Electric Power Systems.*”
- IEEE Standard 1547.4-2011 “*IEEE Guide for Design, Operation, and Integration of Distributed Resource Island Systems with Electric Power Systems.*”
- IEEE Standard 1547.5 has not been issued, yet. Its intended scope is to address issues when interconnecting electric power sources of more than 10 MVA to the power grid.
- IEEE Standard 1547.6-2011 “*IEEE Recommended Practice for Interconnecting Distributed Resources with Electric Power Systems Distribution Secondary Networks.*”
- IEEE Standard 1547.7-2013 “*IEEE Guide for Conducting Distribution Impact Studies for Distributed Resource Interconnection.*”

The TC-82 committee on solar photovoltaic energy systems has developed the standard IEC 61727, *Photovoltaic (PV) Systems—Characteristics of the Utility Interface*. IEC-62116, *Testing procedure of Islanding Prevention Measures for Utility Interactive Photovoltaic Inverters*, describes requirements for testing of the inverter. Similarly, there are multiple standards and recommendations related to the interconnection of DERs. This chapter focuses mainly on the IEEE standards, describing important parameters to consider while designing of the inverter and connecting to the grid.

19.5.2 Response to Abnormal Grid Conditions

The grid requirements play crucial role in the design and performance of the DG inverter. In this section, most significant standard requirements for the distributed generation and its interface to the grid have been explained focusing mainly on the IEEE 1547 standards.

19.5.2.1 Abnormal Voltage and Frequency

During abnormal grid conditions, the DGs need to be disconnected from the utility grid. The disconnection time denotes the time between the occurrence of abnormal condition, and the inverter stops energizing the grid. Table 19.7 shows the clearing time for the IEEE 1547 standard, which has been amended in 2014 including both default clearing time and the adjustable range for clearing time [42]. For DG greater than 300 W (which was 30 kW in the earlier version of standard), the voltage and the clearing times have to be field adjustable. Depending on the mutual agreement between electrical power system (EPS), DG operator, and the type of source connected to the grid, the inverters can continue to be connected to the grid after default

Table 19.7 Interconnection system response to abnormal voltage conditions according to IEEE 1547a-2014

Default settings ^a		
Voltage range (% of base value ^b)	Clearing time (s)	Clearing time: adjustable up to and including (s)
$V < 45$	0.16	0.16
$45 \leq V < 60$	1	11
$60 \leq V < 88$	2	21
$110 < V < 120$	1	13
$120 \leq V$	0.16	0.16

^aUnder mutual agreement between the EPS and DER operators, other static or dynamic voltage and clearing time trip settings shall be permitted

^bBase voltage is the nominal system voltages as stated in ANSI C84.1-2011

Table 19.8 Interconnection system response to abnormal grid frequencies as per IEEE 1547a-2014

	Default settings		Ranges of adjustability	
	Frequency (Hz)	Clearing time (s)	Frequency (Hz)	Clearing time adjustable up to and including (s)
UF1	<57	0.16	56–60	10
UF2	<59.5	2	56–60	300
OF1	>60.5	2	60–64	300
OF2	>62	0.16	60–64	10

clearing time in order to ride through short-term disturbances in the grid. Similar disconnection time for different voltage ranges can be found in other standards such as IEC 61727 and VDE 0126-1-1. Germany has a smaller clearing time of 0.2 s requiring fast monitoring of voltage and quicker response to abnormal voltages. Root-mean-square (RMS) or fundamental of the voltage at the point of common coupling (PCC) is considered for the detection of abnormal voltage conditions.

Similar to abnormal voltage, the DERs need to cease to energize the grid when the system frequency is in the range given in Table 19.8 according to IEEE 1547 standards. Clearing time can be fixed or dynamic under the mutual agreement between the EPS and the DG operators. With the revised standard, DERs shall be permitted to supply reduced power output to the grid as a function of frequency in coordination with functions UF1, UF2, OF1, and OF2 to ride-through and support grid stability during temporary fault conditions.

19.5.3 *Islanding*

Islanding is a condition in which distributed generators continue to supply power to the local load even if the power from the utility grid is not available. There are two types of islanding, namely scheduled islanding and unscheduled islanding, based on the circumstances under which islanding is formed [43].

19.5.3.1 **Scheduled Islanding**

As the name suggests, this is a planned islanding in which local EPS is disconnected from the main EPS as shown in Fig. 19.20. These transitions are intentional events for which the time and duration of the island formation are preplanned, agreed by all the involved parties. DER island formed is also referred to as microgrid which refers to all intentional island systems which includes local EPS or area EPS. Basic requirements for an EPS to qualify as DER island is that it should have local generation and load, ability to disconnect from and parallel with the EPS, and be able to supply power to local load regulating voltage and frequency. Since it

is planned islanding, knowledge of operating conditions of the system prior to island formation assists in smooth transition from the grid-connected mode.

Key merits of DER island systems are as follows:

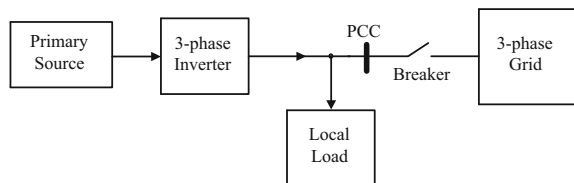
- i. Improve reliability of the supply by providing quality voltage to the local loads in case of outage or disturbance. Power quality issues such as voltage distortion, flicker, harmonics, voltage sag, and lightening transients can be avoided. By islanding, damaging of the customer equipment is eliminated,
- ii. Continue to supply power to loads disconnecting from the grid in anticipation of a power outage on the main grid side caused by an event that can be anticipated, such as an incoming hurricane, storm, or wildfires,
- iii. Allow for maintenance on the EPS while powering the loads connected in the islanded system, and
- iv. Instead of waiting for the outage in the main grid to occur, intentional islanding provides smooth and controlled transition avoiding quality issues in the microgrid.

IEEE 1547.4 provides detailed design considerations and operation requirements for the intentional island. During transition to island, enough DER needs to be present to support the local load by providing stable voltage and frequency. Controller needs to be tested to verify smooth transition to quickly dampen the transients without tripping any protection schemes. When the DER is isolated from the grid, it is important that the microgrid has sufficient local power generation and energy storage in order to confirm that local loads are powered with the specified power quality. In AC microgrids, it is important to supply both real and reactive powers to the specified load range. In case of inverter-based DG, controller needs to transit from grid-synchronized current control mode to fixed-frequency voltage control mode. During the reconnection back to the EPS, voltage, frequency, and phase angle have to be within the range and in phase sequence, as shown in Fig. 19.20.

19.5.3.2 Unscheduled or Unintentional Islanding

Unscheduled transitions are unplanned events that are typically triggered by unforeseen circumstances such as loss of area EPS or equipment failure, and the DER island system may be automatically sectionalized from the area EPS by

Fig. 19.20 DG island system connected to the utility grid through breaker



protective equipment. Unintentional islanding can be dangerous to utility workers who are working on either maintenance or to clear fault if it is still powered. Hence, it is necessary to detect loss of the utility grid as soon as possible and stop powering the island which is referred to as anti-islanding. This also prevents automatic reconnection of DGs to the grid. According to various standards, DGs need to be designed to disconnect from the grid in case of consequences of an uncontrolled islanding, which have generally variation in grid voltage and frequency in order to protect the equipment connected to the grid from any disturbances. Hence, it is essential to choose the right anti-islanding technique to ensure safe, reliable, and robust islanding. It should be able to detect the island condition under all possible grid conditions distinguishing between islanding condition and small perturbations in the grid parameters. Before discussing various anti-islanding techniques, reliability measure of detection technique associated with anti-islanding is discussed, i.e., non-detection zone (NDZ).

19.5.3.3 Non-detection Zone (NDZ)

Reliability and performance of the islanding detection technique is measured by the non-detective zone (NDZ), which is the range of loads connected locally to form an island for which the islanding detection method fails to detect islanding. This zone can be defined in terms of active and reactive power mismatch between DG and local load at the PCC where the islanding is not demonstrable.

Typical configuration of inverter connected to the utility grid and local load is as shown in Fig. 19.21a presenting power flow. P_{DG} and Q_{DG} are the active and reactive powers from the DG, respectively. Active and reactive powers drawn from the grid are represented as ΔP and ΔQ . Real power, P_L , and reactive power supplied to the local load, Q_L , are obtained as

$$\begin{aligned} P_L &= P_{DG} + \Delta P \\ Q_L &= Q_{DG} + \Delta Q \end{aligned} \tag{19.1}$$

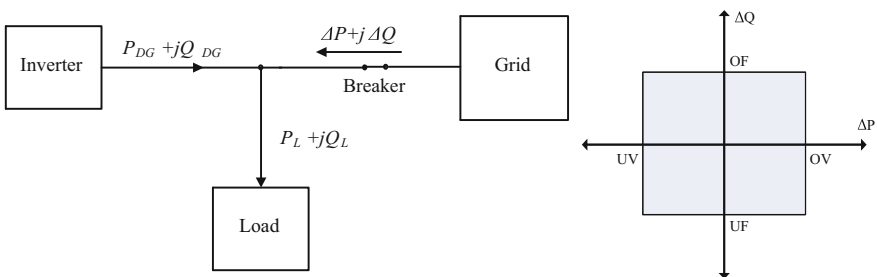


Fig. 19.21 a Integration of DG to the utility grid and b non-detection zone (NDZ)

If power generated by the DG, P_{DG} , is equal to load power, P_L , then the effective active power drawn from the grid ΔP becomes zero. Similarly, there is no mismatch between reactive power generated by DG and the reactive power by the load if ΔQ is zero. If the DG operates in unity power factor (that means $Q_L = 0$), then $\Delta Q = Q_L$. When the utility breaker is opened, the behavior of the system depends on the ΔP and ΔQ at the time of disconnection. If the resonant frequency of the local load matches with the grid voltage, then the reactive power drawn will be zero. If $\Delta P \neq 0$ and $\Delta Q = 0$, then the amplitude of voltage at PCC will change, and the overvoltage protection (OVP) or under-voltage protection (UVP) can detect the change. Change in voltage, ΔV , during disconnection can be derived as

$$\Delta V = KV \quad (19.2)$$

where K is given by

$$K = \sqrt{\left(\frac{P_{DG}}{P_L}\right)} - 1 \quad (19.3)$$

If P_{DG} is greater than P_L during the disconnection, then K is positive that means there is an increase in the voltage. Similarly, if P_{DG} is smaller than P_L , then K is negative implying decrease in the voltage at the PCC. Reactive power is the function of both frequency as well as voltage amplitude. When $\Delta Q \neq 0$, there will be change in both voltage and frequency. Depending on the reactive power, Q_{DG} supplied from the DG at the time of interruption, new values of voltage V' , and frequency ω' can be related to (19.4). Due to disconnection of the grid, $\Delta Q = 0$ resulting in new value of reactive power of the local load, Q'_L , same as the reactive power generated by the DG, i.e., Q_{DG} .

$$Q'_L = Q_{DG} = \left(\frac{1}{\omega'L} - \omega'C\right)(V')^2 \quad (19.4)$$

Islanding detection becomes complicated when the load matches the power generated. When ΔP and ΔQ are zero, there will not be any change in the frequency and voltage amplitude. Even for small values of ΔP and ΔQ , change in voltage and frequency will be insignificant for the over-/under-voltage (OUV)/over-/under-frequency (OUF) to detect islanding. Hence, it is possible to derive the NDZ based on the threshold values of active and reactive powers as shown in Fig. 19.21b. Incapability of OUV/OUF method leads to various other techniques of islanding detection, which would result in either smaller or no NDZ.

19.5.4 *Anti-islanding Techniques [44]*

Islanding detection techniques can be classified into several types, and they are discussed individually next:

19.5.4.1 *Passive Inverter-Resident Method [45]*

These techniques are implemented at the inverter levels which are based on the detection of an abnormality in power quality parameters such as voltage, frequency, phase angle, or harmonics at PCC between the PV inverter and the utility. These methods have nonzero NDZ and generally combined with active methods to shrink the NDZ.

A. *Under-/Over-Frequency (UOF) and Under-/OverVoltage (UOV) Islanding Detection:*

All interconnected DGs are required to cease its operation and stop energizing the PCC when the frequency and voltage go beyond a specified range by having an OUV and OUF protection. This method is implemented by sensing the voltage at PCC and frequency. As discussed in earlier section, amplitude of voltage changes if $\Delta P \neq 0$ and it can be detected by OUV protection. There will be change in frequency during grid interruption if grid is supplying reactive power prior to the disconnection, which can be sensed by OUF detection. However, minimum value of ΔP and ΔQ is necessary in order to detect the islanding successfully, which can be very significant value. Hence, this method has very large NDZ. For this reason, this method is alone insufficient for islanding detection and therefore combined with other active methods.

B. *Voltage Phase Jump Detection*

In case of grid-connected inverter, its output current is synchronized with the grid voltage during normal operation of unity power factor by utilizing phase-locked loop (PLL). During the interruption of the grid, phase difference between the voltage and the output current is seen due to mismatch in reactive power. Same principle has been used in techniques with other names such as power factor detection and transient phase detection. For an inverter regulating its output current, reference value is obtained from PLL. When the grid is disconnected, there will be jump in the voltage at PCC as shown in Fig. 19.22. This method can detect faster than the frequency in case of OUF technique. In case of zero-crossing detection-based PLL, this method can be easily implemented. However, with the advanced PLLs with quick response, phase jump can be difficult to detect. It is also difficult to choose the threshold value of the phase jump in order to obtain reliable islanding detection isolating the phase jumps due to switching of reactive loads in the grid. There will not be any phase change without power mismatch; hence, NDZ cannot be zero.

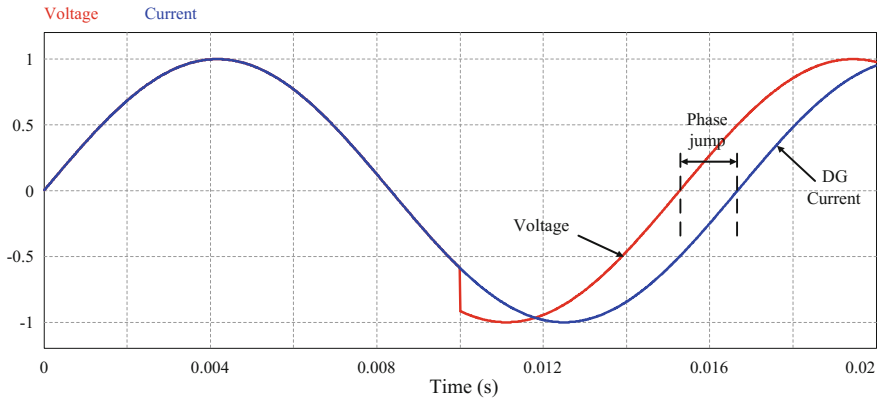


Fig. 19.22 Waveforms showing phase jump detection method

C. Harmonics Detection (State estimators, Voltage harmonic monitoring)

Basic principle behind this method is to utilize the change in the impedance as seen by the inverter at higher frequencies at the time of islanding. In this method, the grid-connected inverter monitors the total harmonic distortion of the voltage at the PCC and shuts down if THD crosses its threshold value. During the presence of the utility grid, voltage THD is lower since the grid voltage is stiff and sinusoidal. Harmonic current generated from the inverter goes through grid, which generally has lower impedance as compared to local load.

When grid is disconnected, impedance of the system changes to only loads connected locally. Voltage THD increases due to the injection of harmonic current from the inverter. As soon as the grid is removed, current starts flowing through the local load resulting in higher THD. In an alternate method, it is possible to detect islanding by estimating change in the output impedance at a specific higher order frequency.

Since this method does not depend on the power mismatch like earlier methods, the NDZ can be reduced to zero. This can also be used when multiple inverters are connected. However, it is very difficult to select the threshold value, which ensures reliable detection. Sometimes, the grid voltage THD can be quite high due to highly polluted or weak grid resulting in nuisance tripping of the inverter. This method may also fail when the quality of the output is high with lower harmonic distortion. In order to overcome false tripping, more advanced techniques have been derived based on similar principle. Kalman filters are used to estimate change in 3rd, 5th, and 7th harmonics in the voltage to analyze greater spectrum of frequency to increase the robustness in detection.

19.5.4.2 Active Inverter-Resident Method [46]

Unlike passive methods, these methods inject a disturbance at the PCC and try to force a change of power quality parameter causing an abnormal condition. Active methods effectively reduce the NDZ. The basic idea behind the active detection methods is to observe change in the power system parameters by adding small perturbation at the output of the interconnected inverter. It is possible to control the current that is being generated by the DG inverter as given by

$$i_{DG,ref} = I_{peak} \sin(\omega t + \phi) \quad (19.5)$$

Disturbance can be injected by varying any of the three parameters, amplitude of current, I_{peak} , frequency ω , and phase angle, ϕ . Response of the system can be observed by measuring the output voltage, and change in its response is used to detect islanding. Another active method can be implemented by injecting current of specific harmonic frequency to measure the output impedance at that frequency. Few of the active methods based on the above-mentioned principles have been discussed.

A. Grid Impedance Measurement

Change in output impedance of the inverter due to islanding is utilized in this method by changing the current reference as given in (19.5). Usually, a small disturbance is added to the I_{peak} value which gets reflected on the output voltage. During grid-connected mode, the output impedance is low and impedance changes to higher value at the instant of disconnection. A small perturbation in the inverter current results in perturbation in power leading to change in the output voltage given by

$$\Delta V = \frac{\Delta P}{2} \sqrt{\frac{R}{P}} \quad (19.6)$$

There will be a detectable change in the voltage during the event of disconnection. Since the inverter is measuring change in dV/dI , this method is known as impedance measurement method. As compared to passive method, this could reduce NDZ to a very small value. However, quality of the grid voltage is affected due to the injected disturbance. Selection of threshold impedance value is very critical in this method. For higher impedance grids, the threshold value has to be set at higher value. This method is effective for single inverter connected in a potential island and has lower reliability in multiple inverter system.

B. Harmonic Injection/Harmonic Impedance Measurement

Harmonic injection method is an extension of harmonic detection method explained in passive methods. This differentiates from the passive method by injecting a current harmonic of a specific frequency in order to detect islanding. This harmonic frequency is selected different from the frequencies that are normally

present in the grid voltage and generated from the inverter. During grid-connected mode, grid impedance is much lower than the local load impedance at the harmonic frequency leading to the absence of harmonic voltage. While DG is in islanded condition, the harmonic current flows through the load resulting in harmonic voltage. Hence, change in impedance at harmonic frequency is utilized to detect islanding.

In another method called as double harmonic injection, harmonic current of two different frequencies are being injected at different time instants. Different pairs of frequencies are proposed in literature such as (40, 60 Hz), (400, 500 Hz), and (400 and 600 Hz). Injection of harmonics at the instant of zero crossing of fundamental reference leads to reduced disturbance on the grid. Impedances Z_1 and Z_2 are measured for two different frequencies ω_1 and ω_2 , respectively. Grid impedance parameters can be calculated from Z_1 and Z_2 using the following equations.

$$L_g = \sqrt{\left(\frac{Z_1^2 - Z_2^2}{\omega_1^2 - \omega_2^2}\right)}; \quad \omega_1 > \omega_2 \quad (19.7)$$

$$R_g = \sqrt{\left(\frac{\omega_1^2 Z_1^2 - \omega_2^2 Z_2^2}{\omega_1^2 - \omega_2^2}\right)}; \quad \omega_1 > \omega_2 \quad (19.8)$$

$$Z_g = \sqrt{\left(R_g^2 + (\omega_g L_g)^2\right)} \quad (19.9)$$

NDZ can be very low in this method, and it can be eliminated by using sub-harmonic injection at the cost of power quality. Multiple inverters injecting the same harmonics may result in false tripping of the inverter due to the increase in the amplitude of the voltage. On the other hand, reducing the amplitude of the current injection may weaken the detection.

C. Slide-Mode Frequency Shift (SFS)

From (19.5), there are three parameters which can be varied: current amplitude, phase angle, and frequency. In this method, positive feedback is applied to the phase angle of the voltage in order to destabilize the inverter operation during islanded condition.

During normal operation, DG inverters are generally operated in unity power factor injecting only active power to the grid. Phase angle between the grid voltage and the inverter output current are maintained zero. In this method, phase angle between the voltage and the current reference is changed as a function of frequency of the PCC voltage as shown in Fig. 19.23. This characteristic curve is designed in such a way that the phase angle of inverter increases faster compared with the phase of local load with a unity power factor near the grid frequency. While connected to the utility grid, output voltage is stabilized at the grid voltage and frequency, and hence, the operating point is brought back to the grid frequency, i.e., point B in

Fig. 19.23 Relation between phase angle and current versus frequency for slide-mode frequency shift detection method

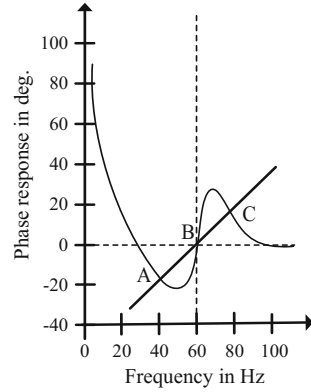


Fig. 19.23. After the island formation, operating point of phase frequency depends on the intersection of load characteristic and the inverter phase response characteristic. If load is considered unity power factor, then its characteristic is linear as shown. At the instant of grid disconnection, new operating point moves to either point A or point C depending on the perturbation. In case of small perturbation in the frequency away from the grid frequency, then it causes the phase error to increase due to positive feedback. Positive feedback of the system can be realized by PLL function. If the frequency is disturbed by reduction in its value, then it will result in positive phase error and PLL tries to decrease the frequency. Similar positive feedback can be analyzed for increase in perturbation of the frequency. Hence, this perturbation drives the system to new operating point of either A or C during the islanded condition. Inverter phase curve is designed in such a way that it results in point A and point C which are outside the over-frequency protection (OFP)/under-frequency protection (UFP) range leading to inverter shut down. Similar principle has been adopted in another method known as phase-locked loop slip method. In this technique, existing PLL is utilized to detect the islanding.

This is a very effective and robust method with very small NDZ, and it can be used while multiple inverters are connected. Power quality has been affected due to this method, which could cause system-level instability and issues related to transient response.

D. Voltage Shift Method

This method is also known as Sandia voltage shift (SVS) technique or positive feedback on voltage. It is based on a positive feedback of the PCC voltage amplitude, which is similar to active power variation method. The DG inverter reduces its current output and its active power if there is reduction in the amplitude of voltage. When the grid is connected, reduction in output power has very insignificant or negligible effect. However, in the absence of grid, there will be further reduction in the voltage due to the load characteristic, which is RLC load response. Relation between active power variation and the voltage variation is given by

$$\Delta P_{DG} = \frac{2 \times \Delta V \times V}{R} \tag{19.10}$$

Decrease in the amplitude of voltage leads to further reduction in the inverter output current resulting in positive feedback in the voltage loop, ultimately detected by the under-voltage protection (UVP). Similar to frequency shift method, it is possible to implement using both increase and decrease in voltage leading to OVP or UVP, respectively. However, UVP is preferred keeping safety of equipment into consideration. It is possible to increase the response time of detection by using accelerated voltage shift algorithm. Generally, this method is implemented along with SFS method to obtain effective detection with negligible NDZ. In case of PV inverter, decrease in voltage amplitude leads the PV to operate off the maximum power point.

E. Frequency Shift (Active Frequency Drift or Frequency Bias or Sandia Frequency Shift)

In the frequency bias method, current waveform injected by the DG is being distorted to force the frequency of the voltage at PCC to change. Since the grid frequency is fixed, it is not possible to drift the frequency of the voltage during grid-connected condition, whereas the injected disturbance is able to change the frequency during islanded condition until it reaches OUF limit.

The output current waveform is distorted by increasing the frequency and adding a zero segment for the remaining time of the half cycle as shown in Fig. 19.24. Frequency of the current is increased to be 0.5–1.5 Hz higher than the frequency of voltage in the previous cycle. During the positive half cycle, output current is a sinusoidal with frequency $f + \Delta f$. Once it reaches zero, it is maintained at that value till zero crossing of the voltage. Similar current reference is obtained for the negative half cycle. The ratio of the zero time interval ($T_B - T_A$) to half of the line

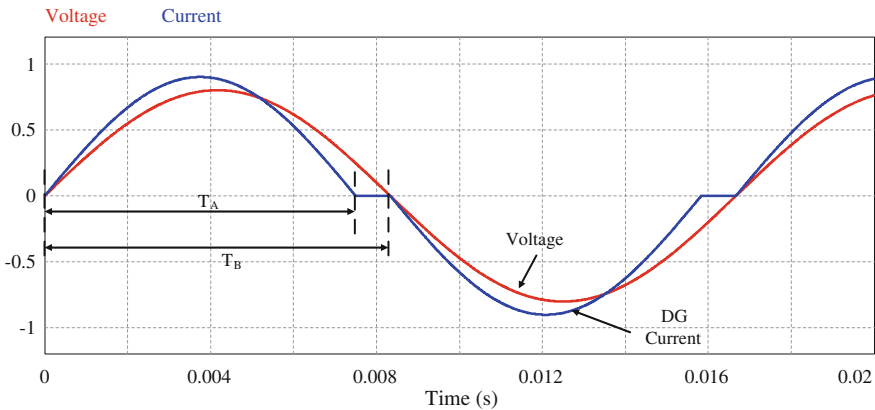


Fig. 19.24 Voltage and current waveform for implementation of frequency drift detection method

frequency cycle of the voltage, T_B , is represented as the chopping fraction, “ cf ,” given by

$$cf = \frac{T_B - T_A}{T_B} = \frac{\Delta f}{f + \Delta f} \quad (19.11)$$

$$i_{\text{ref}} = I_{\text{peak}} \sin(2\pi(f + \Delta f)t) \quad (19.12)$$

During grid-connected mode, the distortion in current does not have any impact on the voltage at PCC. However, while in islanded mode, the injected current flowing through the local load drifts the frequency of the voltage. The phase error between voltage and current is sensed by the PLL, which leads to increase in the frequency in order to compensate for the phase difference. In the subsequent cycles, the frequency of the current is further increased from the grid frequency. This process is continued till the frequency drifts toward the frequency limit that is detected by OFP. This method is very easy to implement but at the cost of distorted current injection to the grid compromising the power quality. Another demerit of this method is that discontinuous current waveform may cause radiated and conducted radio frequency interference.

Frequency bias detection technique is extended in Sandia frequency shift technique where chopping frequency is chosen depending on the error in the line frequency as given in the equation.

$$cf = cf_o + K(f_v - f_{\text{inv}}) \quad (19.13)$$

Where cf_o is the chopping frequency when there is no frequency error and K is the acceleration gain. f_v represents the frequency of the voltage at PCC, and f_{inv} is the line frequency. While connected to the grid, cf remains small due to stable frequency of the grid voltage. As soon as the grid is disconnected, chopping fraction starts increasing due to positive feedback in the frequency loop until it is detected by the OFP. This method is an effective method as compared with the frequency bias method. By this method, it is possible to keep the distortion in injected current at a lower value during grid-connected mode and it amplifies the current distortion once the grid is isolated. For $cf_o = 0.05$, the total harmonic distortion (THD) in the inverter current is equal to approximately 5% at the rated line frequency. NDZ can be reduced to zero for loads with $Q_f < 4.8$, when $K = 0.1$ for the given cf_o of 0.05 [55].

19.5.4.3 Grid-Resident Method

This method, also known as utility level technique, is based on the utility grid-side detection technique. Communication-based methods involve transmission of data over power line using power line carrier communication (PLCC) between grid and

PCC. One more method is based on switched impedance technique where external impedance is used to force an abnormal PCC voltage or phase angle in order to detect islanding.

These methods are not resident in the local inverter. Additional devices like impedance, communication systems need to be installed at the utility level in order to detect the islanding. These techniques are used when utility has the responsibility to protect local loads and hardware from over-/under-voltage and frequency. Techniques such as impedance insertion, power line carrier communication (PLCC), and supervisory control and data acquisition (SCADA) have been discussed.

A. Impedance Insertion Technique

Impedance insertion method is implemented by installing an impedance of low value at the utility system within the potential island. Impedance, which is usually capacitor bank, is connected to the utility at point A through a switch S_2 as shown in Fig. 19.25. Normally, when the breaker is closed, the switch S_2 is in open condition. When the breaker switch opens during interrupt in the utility grid, the impedance is connected to point A by closing S_2 after a short delay. This addition of capacitance to the PCC would disrupt the balance between load and generation resulting in sudden change in phase angle and step change in frequency which would be detected by the under-frequency (UF) or over-frequency (OF) detection.

It is possible to connect resistor bank instead of capacitor bank which would result in detectable change in the voltage amplitude at the PCC. However, capacitor banks are preferred over resistors due to the reason that it can be used to support reactive power to the grid. If local load is highly inductive, this addition of capacitance would compensate resulting in balanced load. This might lead to failure of islanding detection. Hence, short delay between opening of breaker and closing of S_2 is provided. As soon as the breaker opens, the local load would be highly inductive and closing of S_2 results in large frequency deviation which triggers the island detection. Minimum size of capacitor bank is decided based on the minimum phase jump needed to be detected by the OUF detector.

This method is very effective in preventing islanding with the help of small delay between switching to ensure that it works without fail for any type of local load. And it is very well known and practiced technique to add capacitor bank to the grid for reactive power compensation. Major disadvantage of this method is additional expense of installation of capacitor bank. Response time is slower compared to active techniques due to the delay between switching.

Fig. 19.25 Islanding detection method using external switched capacitor

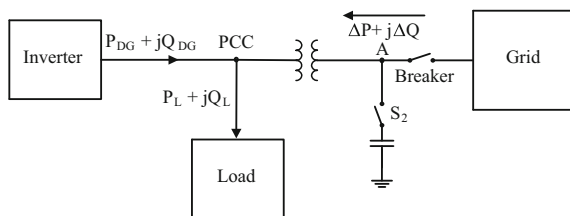
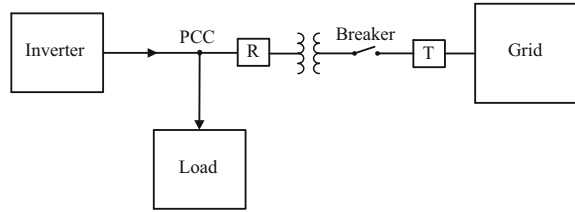


Fig. 19.26 Islanding detection technique using PLCC-based communication showing transmitter (T) and receiver (R) units



B. Power Line Carrier Communication (PLCC) Technique

Another grid-resident method of islanding detection is based on the communication between the grid and the DG system. Power line carrier communication (PLCC) has been used to address the islanding detection by sending signal along the power line. PLCC is a communication protocol that uses power line to send data along with the electric power transmission. Typical system configuration is shown in Fig. 19.26, which includes transmitter (T) and receiver (R) placed on either side of the breaker. A PLCC transmitter which is located on the grid side sends signal over the power line to the receiver which is located on the DG side. Receiver can also be part of the inverter. During normal operation when grid is connected, R receives the signal sent over power line. If the signal is disrupted, this indicates the discontinuity in the line. As soon as the PLCC signal is lost, the receiver can trigger DG to cease operation and stop energizing the PCC (Fig. 19.26).

This method can effectively be used when multiple DGs are connected, and it does not have NDZ. This method can be easily implemented if PLCC exists in the utility system. Compared to other methods, this is not interfering power quality. Performance of this technique is independent of DG and type of load. It is essential to have a fail-safe and fool-proof PLCC to make sure failure of communication is only due to loss of continuity rather than communication failure. One of the shortcomings is being installation of additional PLCC transmitter on the grid taking into consideration safety and isolation which could be expensive.

C. Supervisory Control And Data Acquisition (SCADA)

Supervisor control and data acquisition (SCADA) is a remote monitoring and control system generally used for larger control plants whose components are physically located in distinct places. Application of this type of systems includes power generation, power transmission, and industrial control systems. With the advancements in communication and smart metering in microgrid, SCADA has become very popular. It uses an extensive dedicated communication and sensing network to monitor and control grid activities and respond during emergency situation. In order to implement SCADA for islanding detection, additional sensors like voltage and current sensors should be installed. All the DGs connected to the grid need to have a communication link to receive signals from SCADA during interruption of the utility grid.

19.5.5 Unintentional Islanding Test

This section presents procedure and steps involved in testing the inverter performance during islanding condition. Objective of the test is to make sure the inverter stops energizing the system when an islanding condition is present and to determine the trip time. These test procedures ensure safe and reliable operation of DG systems connected to the grid following the grid standard requirements.

Main objective of this test is to detect the unintentional islanding and cease to energize the area within the specified time. Typical test setup as recommended by the IEEE 1547 standard is as shown in Fig. 19.27. EUT represents the equipment under test, i.e., the DG inverter that is being verified for conformance. RLC load is connected in parallel with the inverter, which acts as a local load. Resonance frequency of the load is selected as the grid frequency, and the quality factor, Q_f , is adjusted to 1 as given by

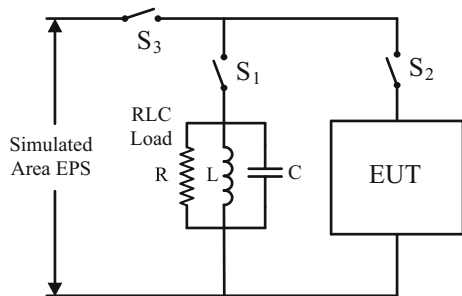
$$Q_f = R\sqrt{\frac{C}{L}} \quad \text{or} \quad Q_f = \frac{\sqrt{P_{qL} \cdot P_{qC}}}{P} \tag{19.14}$$

where Q_f is the quality factor of the parallel RLC resonant load, R is the effective load resistance, C is the effective load capacitance, L is the effective inductance, P_{qL} is the reactive power per phase consumed by the inductive load, P_{qC} is the reactive power per phase consumed by the capacitive load, P is the real output power per phase, and f is the frequency. When $Q_f = 1$, reactive power generated by C should be equal to reactive power absorbed by L , i.e., $P_{qL} = P_{qC} = P$. EUT is set to provide 100% of its rated output power during the test at the nominal voltage and frequency. Values of R , L , and C are calculated from the following equations.

$$R = \frac{V^2}{P} \tag{19.15}$$

$$L = \frac{V^2}{2\pi \times f \times P \times Q_f} \tag{19.16}$$

Fig. 19.27 Test setup requirement for unintentional islanding (IEEE 1547.1)



$$C = \frac{P \times Q_f}{2\pi \times f \times V^2} \quad (19.17)$$

These values are fine-tuned until the fundamental component of the current flowing through the switch S_3 is less than 2% of the rated current of the EUT under steady-state condition. Switch S_3 is opened, and the time between opening of S_3 and instant at which EUT ceases to energize has to be less than 2 s. Similar process is followed at different power levels of EUT (33 and 66%) and also at various load reactive power values (95–105%) noting down the response time. If any of these tests results in longer than the specified time, then the unit fails the test. Hence, it is very critical to select the anti-islanding technique which is robust and reliable under all possible conditions. IEEE 929-2000 provides standards for interfacing of PV systems with the utility grid that has requirement of Q_f to be 2.5.

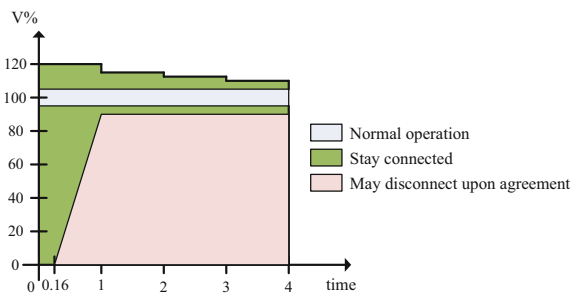
There is wide variety of approaches adopted in different standards to validate the anti-islanding detection. In Japan, Japanese Industrial Standard, JIS C 8962 (Testing Procedure of Power Conditioners for Small Photovoltaic Power Generating Systems), is followed. Germany (DIN VDE 0126), Dutch (NEN1010), and UK (G77) follow different standards, codes, and test procedures for the safe interconnection of PV inverter to the grid.

19.5.6 Fault Ride-Through (FRT) Capability

The size of RES interconnected to the grid has been increasing rapidly. Power generated from these sources is variable, therefore, referred to as variable energy resources (VERs), connect at the utility scale along with the interconnection to the bulk power systems. With the increased renewable penetration, VERs could be a significant share as compared to bulk power generators resulting in variability and uncertainty of power generation. Under these circumstances, it is possible for large portion of DGs to trip on voltage or frequency disturbances in the grid due to a transmission contingency, which could potentially affect the main power grid stability. Tripping of DGs could further affect the grid voltage or frequency resulting in a chain reaction causing to cease energy from nearby power generators.

In order to increase the tolerance to the utility grid disturbances, fault ride-through capabilities have been proposed for grid-connected power converters which can actively control active and reactive powers during transient conditions. During disturbances in the grid, voltage ride-through (VRT) and frequency ride-through (FRT) of the grid-tied converter assist in power system stability during momentary system disturbances. Even though ride-through requirements are not stipulated in IEEE 1547, VRT and FRT are permitted [47]. In earlier version of IEEE 1547-2003, maximum trip time was mentioned for DERs of less than 30 kW during abnormal voltage and frequency conditions. In the latest amendment in 2015, clearing times can be field adjustable for DERs greater than 300 W under

Fig. 19.28 Typical voltage ride-through requirement (WECC-0060) [49]



mutual agreement between the EPS and DER. However, FRT requirements are very stringent in Europe (such as Germany, UK, Spain, and Italy [48]), which has higher penetration of renewables.

Under fault ride-through scheme, grid-tied converters are not disconnected from the grid supporting the voltage recovery even if the voltage goes down to zero for a specified time. This is performed by injecting necessary reactive power to the grid and reducing the active power. Once the fault is cleared, the active power is restored back to the rated value.

Figure 19.28 shows typical boundaries for voltage ride-through. Region marked in green color shows the circumstances under which the converter operates in VRT where top area is high voltage ride-through (HVRT) and lower part is low voltage ride-through (LVRT). The converter stays connected to the grid and supplies reactive current for voltage support to recover from fault. Active power during this time is limited to prevent current flow. Inverters used for PV or wind can supply reactive power at partial output, but reactive power capability at full power means that the converter needs to be oversized to handle full active and reactive powers. Moreover, PV inverter can be utilized at night for reactive power compensation without additional burden and reduction in active power.

19.6 Power Quality

Due to increased penetration of DGs, it is very crucial to maintain the power quality that is being injected into the grid in order to uphold the grid stability and quality. Hence, there are standards and practices to govern power quality in terms of parameters such as harmonics in current, DC injection, flicker, frequency, and power factor.

Table 19.9 Maximum harmonics distortion in the current

Individual harmonic order h (odd harmonics ^a)	$h < 11$	$11 \leq h < 17$	$17 \leq h < 23$	$23 \leq h < 35$	$35 \leq h$	Total demand distortion (TDD)
Percent (%)	4.0	2.0	1.5	0.6	0.3	5.0

^aEven harmonics are limited to 25% of the odd harmonic limits given in the table

19.6.1 Current Harmonics

Managing harmonics in the power system is the responsibility of both end users and system operators/owners which is applicable to both voltage and current harmonics. The amount of harmonic voltage distortion supplied to other users depends on the aggregate effects of the harmonic current injected by all the users and characteristics of the grid impedance. Harmonic voltage distortion limits are provided to maintain voltage quality and to reduce potential negative effects on the equipment connected to the grid. Voltage harmonics in grid also increases the losses in transmission, line transformers, capacitor banks, and end equipment. This necessitates all the users to limit the harmonic current emission at a reasonable value specified in the standards. Table 19.9 shows harmonic distortion limit for the current injected into the grid according to IEEE 1547 standard. Limits for both individual harmonics and total harmonics are itemized. Total demand distortion (TDD) is calculated as the ratio of the root-mean-square (RMS) of the harmonic current considering up to 50th order excluding interharmonics expressed as a percent of the maximum demand current. System owners or operators need to limit the voltage distortion at the PCC as per the IEEE 519-2014 standards [50, 51]. Also, DG should not create any objectionable flicker in the voltage which may affect other customers connected on the same EPS.

19.6.2 DC Current Injection

Injection of DC current into the utility grid can lead to the saturation of the transformers resulting in trips or overheating. Hence, it is necessary to limit the DC component of the current injected into the grid, which is 0.5% of the full-rated output current at the point of DER connection as per IEEE 1547 standard. This is one of the interconnection tests, which the DER needs to satisfy. For interconnection with galvanic isolation, this issue is minimized. However, for the design of transformerless topology, additional precaution needs to be taken care of limiting the DC current. In standards like VDE 0126-1-1, maximum trip time has been specified, and hence, special sensing for measuring DC current and tripping mechanism has to be implemented. PV panels are installed with backplane framed

by a metallic casing, which is connected to the ground. Capacitance between the panel and ground creates path for leakage current leading to DC current injection. Hence, selection of inverter topology plays an important role in limiting the DC current injection.

19.6.3 Power Factor

Grid-connected inverters, which are fed by renewable energy sources, can be operated to deliver reactive power to support grid voltage. Participation of DGs in grid voltage control has been implemented at higher power levels where DERs are connected directly at the distribution level. However, this has not been considered at lower power levels. IEC61727 has requirement in terms of power factor that needs to be limited to more than 0.9 when the output is more than 50%. However, IEEE 1547 does not have any limitation on the power factor allowing the DGs to supply reactive power to the utility grid.

19.6.4 Reconnection to the Grid

Accurate and reliable synchronization of AC signals from external energy sources to the grid is very critical. IEEE 1547.1 discusses the standards for accurate and reliable synchronization of the DG sources to the utility grid. It is very critical to connect the source in parallel to the grid with minimal effect on the voltage waveform at the PCC to ensure negligible disturbance to the loads connected to the grid.

There are two basic test procedures: First one is to verify the synchronization algorithm that connects external source to the grid when the key synchronization parameters are within the given range, and second is to verify the start-up current after synchronization. These tests should demonstrate that at the moment the paralleling device closes, all three parameters in Table 19.10 are within the given range. This test should also demonstrate that if any of the parameters are outside of the ranges given in Table 19.10, the paralleling device should not close. The DER unit should be able to parallel with the area EPS without causing a voltage fluctuation at the PCC greater than $\pm 5\%$ of the prevailing voltage level of the area EPS at the PCC and meet the flicker requirements of 4.3.2.

Table 19.10 Synchronization parameter limits for interconnection to an EPS

Aggregate rating of DR (kVA)	Frequency difference (Δf , Hz)	Voltage difference (ΔV , %)	Phase angle difference ($\Delta \phi$, °)
0–500	0.3	10	20
>500–1500	0.2	5	15
>1500–10,000	0.1	3	10

19.7 DG in Electricity Market

Integration of DG has modernized the energy market and the utility grid. Even though higher capital cost has pulled renewable sources initially, incentives and initiatives for installation of clean energy sources globally have increased exponentially over the last decade.

19.7.1 Demand Response

In traditional power grid, changes in energy demand are handled by either operating reserves or spinning reserve which throttles the power generation and tries to match supply and demand. With the increased renewable generation in grid, which is intermittent and has high fluctuations, mismatch between supply and demand is increased. Instead of load-following method, utility grid is moving toward load-shaping strategy by realizing demand response. Demand response provides a prospect for consumers to play crucial role in the operation of the grid by reducing the peak demand by scheduling or shifting their usage to nonpeak hours. Time-based pricing methods such as time-of-use pricing, critical peak pricing, variable peak pricing, real-time pricing, and critical peak rebates motivate consumers to lower their cost of electricity by engaging in demand response efforts by prioritizing their loads and shifting lower priority loads to the time when grid price is lower. This could be considered as a win-win situation for both consumers and grid operators. Consumers are invited to participate indirectly in the grid stability program by diverting the power flow to prevent overloading of the system. This also saves money to the operator through reduction in peak power generation capability by avoiding construction of new power plants [52].

Another way of handling supply–demand mismatch is by installing peak power shaving systems in the grid. Conventionally, gas turbines based on natural gas are used as peak shaving plants which are run only when the demand is high. One of the largest grid storage available is pumped storage hydroelectric plants. Water at lower elevation is pumped back to the higher elevation reservoir or dam during low grid price and used to generate electricity during peak power demand. Another option is to install energy storage systems based on battery or ultracapacitors to store energy during excess power in the grid and feed it back during higher load requirement. Secondary batteries which are used in electric or hybrid electric vehicles can be used for peak shaving application. According to California Independent System Operator (CAISO), 350 MW of additional regulation capacity and 800 MW of ramping capacity are required to support variations in 9000 MW installed wind generation plant. Sophisticated models for consumer behavior, power flow, and availability of renewable sources on hourly or subhourly forecasting are essential to handle DGs. Researchers are also looking for utilizing

plug-in hybrid vehicles (PHEVs) that are connected to the grid for load shaping or peak shaving by operating in V2G and G2V modes.

19.7.2 Energy Economics

Electricity produced by large central power generators is sold in wholesale market for much lesser price than the retail price paid by the consumers. This increase is driven by the added cost of transmission and distribution service to bring the electricity from the point of generation to utilization. Higher cost is also the result of transmission losses, customer service, and compensation for the variations in the load demand. Even though renewable sources have higher capital cost, with the incentives from policy makers and government, payback time can be reduced drastically. For example, European energy policy has been liberalized energy markets to promote development of low-cost future energy systems focusing on cutting greenhouse gases emphasizing on global climate change policy [53]. Currently, most of the countries are going toward net metering system with accompanying interconnection rules allowing small-scale renewable sources to pump power to the grid. Price-anticipated consumers as a result of dynamic retail pricing system have improved the penetration to higher extent. This ensures grid independence and reduces the burden of adding new central power plants and extending transmission lines. With the stringent grid interconnection, overall reliability of the grid can be improved without additional cost. Governmental agencies like the US Department of Energy (DOE) have taken up initiatives to enable participation of consumer in generation and storage, operating resiliency, optimizing energy resources, and conceptualizing smart grid on distributed generation [54].

19.8 Conclusion

This chapter discussed the merits and need of DG and importance of power electronics an enabling technology to promote DG for utility and load interactive power conversion and control for grid integration. Power electronic systems for storage, DC bus interface in microgrid, and utility interface have been discussed, compared, and evaluated. This chapter also discusses overview of the most commonly used standards for interconnection of DGs to the utility grid. It is necessary to have a unified grid standards around the world; however, there are multiple standards followed by different countries. In this chapter, IEEE 1547 is being taken up for study, which has standards and guidelines for interfacing of distributed resources up to 10MVA to the grid. Even though standards followed in different countries may slightly differ in terms of numerical specifications and few additional features, considerations needed to be taken while designing the DG inverter remains almost the same. The standards and practices to govern quality in terms of parameters such

as harmonics in current, DC injection, flicker, frequency, and power factor are discussed. Monitoring and detection of unintentional islanding is critical considering safety of the workers. Various commonly used anti-islanding techniques have been discussed with their pros and cons. Another feature of DGs that is expected to play a crucial role in bringing higher stability of the grid is fault ride-through capability.

This document cannot be considered as replacement for the standards for the design of grid-connected inverters. Readers are suggested to go through the detailed documentation of suitable standards.

Appendix 1: Design Equations for LCL SRC with C Filter

Base values are $V_B = V_{in,min}$, $Z_B = (L_s/C_s)^{1/2}$, and $I_B = V_B/Z_B$. Converter gain is $M = V_o'/V_B$, $V_o' = V_o/n$. Normalized load current is $J = n \cdot I_o/I_B$. Normalized switching frequency $F = \omega_s/\omega_r = f_s/f_r$, $\omega_s = 2\pi f_s$; $\omega_r = 1/(L_s C_s)^{1/2}$. The values of L_s and C_s are calculated by following equations [21]:

$$L_s = \left[\frac{M \cdot J \cdot V_B^2}{P_o} \right] \left[\frac{F}{2 \cdot \pi \cdot f_s} \right] \quad (19.18)$$

$$C_s = \left[\frac{F \cdot P_o}{2 \cdot \pi \cdot f_s \cdot M \cdot J \cdot V_B^2} \right] \quad (19.19)$$

Selecting suitable ratio of series resonant inductor to parallel inductor L_s/L_p' , the value of L_p' or $L_p = n^2 L_p'$ can be calculated [6]. The values at optimum point are as follows:

$$J = 0.427, \quad M = 0.965, \quad F = 1.1, \quad L_s/L_p' = 0.1, \quad \text{and } n = 18.$$

$$J = 0.427, \quad M = 0.965, \quad F = 1.1, \quad L_s/L_p' = 0.1, \quad n = 18.$$

Appendix 2: Design Equations for LCL SRC with L-Filter

The base quantities used are $V_B = V_{in,min}$, $Z_B = R_L'$, and $I_B = V_B/Z_B$. The reflected output voltage is $V_o' = V_o/n$. Normalized reflected output voltage is given by

$$V'_{opu} = \frac{V_o'}{V_B} = \frac{\sin(\delta/2)}{\sqrt{D_1^2 + D_2^2}} \quad (19.20)$$

where

$$D_1 = \frac{\pi^2}{8} \left[\frac{X_{L_{\text{spsu}}} - X_{C_{\text{spsu}}}}{X_{L_{\text{ppu}}}} + 1 \right]; \quad D_2 = [X_{L_{\text{spsu}}} - X_{C_{\text{spsu}}}] \quad (19.21)$$

$$X_{L_{\text{spsu}}} = (Q_{\text{SF}})(F), \quad X_{C_{\text{spsu}}} = Q_{\text{SF}}/F, \quad X_{L_{\text{ppu}}} = (F)(Q_{\text{SF}}) \left(L'_p / L_s \right) \quad (19.22)$$

Normalized switching frequency, $F = \omega_s / \omega_r = f_s / f_r$, $\omega_r = 1 / (L_s C_s)^{1/2}$; $\omega_s = 2\pi f_s$, δ is the inverter output pulse width; full-load quality factor $Q_{\text{SF}} = (L_s / C_s)^{1/2} / R'_L$; $R'_L = R_L / n^2$.

The values at optimum point are as follows [9]: V_o' (gain) = 0.795, $F = 1.1$, $Q_{\text{SF}} = 0.5$, $L_s / L'_p = 0.075$, and $n = 22$. The values of C_s and L_s are calculated using the following equations [23]:

$$C_s = F / [2\pi f_s (Q_{\text{SF}})(R'_L)], \quad L_s = [Q_{\text{SF}} \cdot R'_L]^2 (C_s) \quad (19.23)$$

$$L'_p = L_p / n^2 = L_s / 0.075 \text{ (optimum point).}$$

Appendix 3: Design Equations for Phase-Shifted Full-Bridge PWM Converter

Assume a peak-to-peak ripple current of $\Delta I_o = 0.3$ A (10% of full-load current) in the output at minimum input voltage and full load. Taking the effect of duty cycle loss and dead gaps, effective duty ratio is assumed to be $D_{\text{eff}} = 0.85$. Then, the transformer turns ratio is given by [24–26]

$$n = \frac{V_{\text{in}}}{D_{\text{eff}} \cdot V_o} \quad (19.24)$$

The value of series resonant inductor L_s is given by

$$L_s = \frac{V_{\text{in}}(1 - D_{\text{eff}})}{4 \cdot n \cdot I_o \cdot f_s} \quad (19.25)$$

The value of output filter inductor is given by

$$L_o = \frac{(n \cdot V_{\text{in}} - V_o) \cdot D_{\text{eff}}}{2 \cdot \Delta I_o \cdot f_s} \quad (19.26)$$

Appendix 4: Design Equations for Secondary Controlled Full-Bridge Converter

ZVS condition for the primary switches can be given as

$$\delta > \left(1 - \frac{1}{M}\right) \cdot \frac{\pi}{2} \quad (19.27)$$

ZVS condition for the secondary-side switches can be given as

$$\delta > (1 - M) \cdot \frac{\pi}{2} \quad (19.28)$$

where $M = \frac{V_o}{n \cdot V_{in}}$; $n = \frac{N_s}{N_p}$

Series tank inductance can be calculated by [27, 28]

$$L_s = \frac{V_o \cdot V_{in} \cdot \delta \cdot (\pi - \delta)}{n \cdot \omega_s \cdot \pi \cdot P_o} \quad (19.29)$$

P_o = output power, ω_s = angular switching frequency (rad/s), and δ = phase shift between primary- and secondary-side voltage across the transformer leakage inductance.

Appendix 5: Design Equations for Current-Fed Converter

Boost inductor values can be calculated as follows [29, 30]:

$$L_1 = L_2 = \frac{V_{in} \cdot D}{\Delta I_{in} \cdot f_s} \quad (19.30)$$

Transformer turns ratio is given by [16]

$$D = 1 - \frac{n \cdot V_{in}}{V_o} \quad (19.31)$$

where D = duty ratio of main switches = T_{on}/T_s , T_{on} = ON time of the main switches and T_s = switching time period, V_{in} = input voltage, f_s = switching frequency, ΔI_{in} = permissible input current ripple, and n = secondary to primary turns ratio of the HF transformer.

The series tank inductance is given by

$$L_s = \frac{(1-D) \cdot V_{in} \cdot V_o}{n \cdot f_s \cdot P_o} \left[\frac{n \cdot V_{in}}{V_o \cdot (1-D)} - 1 \right] \quad (19.32)$$

P_o = full-load output power.

Appendix 6: Design Equations for CFDAB Converter [31]

1. Maximum voltage across the primary switches is

$$V_{P,SW} = \frac{V_o}{n} \quad (19.33)$$

2. Input and output voltages are related as

$$V_o = \frac{n \cdot V_{in}}{2 \cdot (1-d)} \quad (19.34)$$

3. Leakage inductance of the transformer or series inductance L_{lk} is calculated using

$$L_{lk} = \frac{V_o \cdot (d-0.5)}{2 \cdot n \cdot I_{in} \cdot f_s} \quad (19.35)$$

4. RMS current through the primary switches is given by

$$I_{P,sw,rms} = I_{in} \sqrt{\frac{2-d}{3}} \quad (19.36)$$

5. Values of boost inductors are given by

$$L = \frac{V_{in} \cdot (d-0.5)}{\Delta I_{in} \cdot f_s} \quad (19.37)$$

6. Output rectifier devices: Average rectifier secondary switch current is given by

$$I_{S,sw,av} = P_o / (2V_o) \quad (19.38)$$

References

1. Schlecht MF (1980) A line interfaced inverter with active control of the output current waveform. In: Proceedings IEEE PESC 1980, pp 234–241
2. Nagao M, Harada K (1997) Power flow of photovoltaic system using buck-boost PWM power inverter. In: Proceedings PEDS'97, vol 1, pp 144–149
3. Bhat AKS, Dewan SB (1988) Resonant inverters for photo voltaic array to utility interface. IEEE Trans Aerosp Electron Syst AES-24(4):377–386
4. Rathore AK, Bhat AKS, Oruganti R (2011) Classification and comparison of interfacing schemes for connecting fuel cells to a single-phase utility line. Int J Power Electron
5. Fox DA, Shuey KC, Stechschulte DL (1979) Peak power tracking technique for photovoltaic arrays. In: IEEE power electronics specialists conference record, pp 219–227
6. Anderson M, Alvesten B (1995) 200 W low cost module integrated utility interactive for modular photovoltaic energy systems. In: Proceedings IEEE IECON'95, vol 1, Nov 1995, pp 572–577
7. Lohner A, Meyer T, Nagel A (1996) A new panel-integratable inverter concept for grid-connected photovoltaic systems. In: Proceedings IEEE ISIE'96, vol 2, pp 827–831
8. Martins DC, Demonti R (2000) Interconnection of photovoltaic panels array to a single-phase utility line from a static conversion system. In: Proceedings of IEEE PESC'00, vol 3, June 2000, pp 1207–1211
9. Martins DC, Demonti R, Ruther R (2000) Analysis of utility interactive photovoltaic generation system using a single power static inverter. In: Proceedings of IEEE photovoltaic specialists conference, 15–22 Sept 2000, pp 1719–1722
10. Bonte L, Baert D (1982) A low distortion PWM DC-AC inverter with active current and voltage control, allowing line-interfaced and stand-alone photovoltaic applications. In: IEEE INTELEC'82, 3–6 Oct 1982, pp 90–95
11. Steigerwald RL, Tompkins RE (1982) A comparison of high-frequency link schemes for interfacing a DC source to a utility grid. In: Proceedings IEEE IAS'82, vol 17, pp 759–766
12. Steigerwald RL, Ferraro A, Turnbull FG (1982) Application of power transistors to residential and intermediate rating photovoltaic array power conditioners. In: IEEE international semiconductor power converter conference record, IEEE-IAS record, pp 84–96
13. Cocconi A, Cuk S, Middlebrook R (1983) High-frequency isolated 4 kW photovoltaic inverter for utility interface. In: Proceedings of 7th PCI conference, 13–15 Sept 1983, pp 325–345
14. Bose BK, Szczesny PM, Steigerwald RL (1985) Microcomputer control of a residential photovoltaic power conditioning system. IEEE Trans Ind Appl IA-21(5):1182–1191
15. Pitel IJ (1986) Phase-modulated resonant power conversion techniques for high-frequency link inverters. IEEE Trans Ind Appl IA-22(6):1044–1051
16. Bhat AKS, Dewan SB (1988) DC-to-utility interface using sinewave resonant inverter. In: IEEE Proceedings, vol 135, Part B, No. 5, Sept 1988, pp 193–201
17. Rajagopalan V, Haddad KA, Charette A, Rajashekara KS (1990) Analysis and design of a dual series resonant converter for utility interface. IEEE Trans Ind Appl 26(1):80–87
18. Sabate JA, Lee FC (1991) Off-line application of the fixed-frequency clamped-mode series resonant converter. IEEE Trans Power Electron 6(1):39–47
19. Tsai FS, Sabate J, Lee FC (1989) Constant-frequency, zero-voltage-switched, clamped-mode parallel-resonant converter. In: IEEE international telecommunication energy conference, paper # 16.4, pp 1–7
20. Bhat AKS (1989) Fixed frequency PWM series-parallel resonant converter. IEEE industry applications society annual meeting, vol 1, pp 1115–1121
21. Bhat AKS (1994) Analysis and design of LCL-type resonant converter. IEEE Trans Ind Electron 41(1):118–124

22. Min KJ et al (1995) Design considerations based on AC complex circuit analysis for LCL type series resonant converter with phase shift control. in: IEEE international conference on control & instrumentation (IECON), pp 323–328
23. Bhat AKS (1995) Analysis and design of a fixed frequency LCL-type series resonant converter. IEEE Trans Aerosp Electron Syst 31(1):125–137
24. Mweene LH, Wright CA, Schlecht MF (1989) A 1 kW, 500 kHz front-end converter for a distributed power supply system. In: IEEE applied power electronics conference, pp 423–432
25. Dalal DB (1990) A 500 kHz multi-output converter with zero voltage switching. In: IEEE applied power electronics conference, pp 265–274
26. Sabate JA, Vlatkovic V, Ridley RB, Lee FC, Cho BH (1990) Design considerations for high voltage, high power, full-bridge ZVS PWM converters. IEEE applied power electronics conference, pp 275–284
27. Peng F et al (2004) Low cost fuel cell converter system for residential power generation. IEEE Trans Power Electron 19(5):1315–1322
28. Divan DM et al (1991) A three-phase soft switched high power density dc/dc converter for high power applications. IEEE Trans Ind Appl 27(1):63–73
29. Han S, Yoon H, Moon G, Youn M, Kim Y, Lee K (2005) A new active clamping zero-voltage switching PWM current-fed half bridge converter. IEEE Trans Power Electron 20(6):1271–1279
30. Rathore AK, Bhat AKS, Oruganti R (2012) Analysis, design and experimental results of wide range ZVS active-clamped L-L type current-fed dc-dc converter for fuel cell to utility interface application. IEEE Trans Industr Electron 59(1):473–485
31. Xuwei P, Rathore AK (2014) Novel bidirectional snubberless naturally commutated soft-switching current-fed full-bridge isolated DC/DC converter for fuel cell vehicles. IEEE Trans Ind Electron 61(5):2307–2315
32. Dugan RC, Key TS, Ball GJ (2006) Distributed resources standards. IEEE Ind Appl Mag 12(1):27–34
33. Teodorescu R, Liserre M, Rodriguez P (2011) Grid converters for photovoltaic and wind power systems. Wiley publishers, New York
34. Blaabjerg F, Teodorescu R, Liserre M, Timbus AV (2006) Overview of control and grid synchronization for distributed power generation systems. IEEE Trans Ind Electron 53(5):1398–1409
35. NERC (2012) Special assessment report (IVGTF 1-3) Interconnection requirements for variable generation, Sept 2012
36. Gaonkar DN (ed) (2010) Distributed generation. ISBN 978-953-307-046-9
37. IEEE Std. 929-2000 (2000) IEEE recommended practice for utility interface of photovoltaic (PV) systems. Sponsored by IEEE standards coordinating committee 21 on photovoltaics. Published by the IEEE, New York
38. UL1741 (1999) UL Standard for safety for static converters and charge controllers for use in photovoltaic power systems. Underwriters laboratories, 1st edn, 7 May 1999 (Revised Jan 2001)
39. IEEE Std 1547-2003 (2003) IEEE standard for interconnecting distributed resources with electric power systems. IEEE, , July 2003
40. IEEE Std 1547.1-2005 (2005) IEEE standard conformance test procedure for equipment interconnecting distributed resources with electric power systems. IEEE, July 2005
41. IEEE Std 1547.1a-2015 (2015) IEEE standard conformance test procedure for equipment interconnecting distributed resources with electric power systems-amendment 1. IEEE, Mar 2015
42. IEEE Std 1547a-2014 (2014) IEEE standard for interconnecting distributed resources with electric power systems-amendment 1. IEEE, May 2014
43. IEEE Std 1547.4-2011 (2011) IEEE guide for design, operation, and integration of distributed resource island systems with electric power systems. IEEE, July 2011

44. Bower W, Ropp M (2002) Evaluation of islanding detection methods for utility-interactive inverters in photovoltaic systems. SANDIA Report SAND2002-3591, Albuquerque, NM: Sandia National Labs, Nov 2002. Online ordering: <http://www.doe.gov/bridge>
45. De Mango F, Liserre M, Dell'Aquila A, Pigazo A (2006) Overview of anti-islanding algorithms for PV systems. Part I: passive methods. In: Proceedings of the 12th international power electronics and motion conference, Aug 2006, pp 1878–1883
46. De Mango F, Liserre M, Dell'Aquila A (2006) Overview of anti-islanding algorithms for PV systems. Part II: active methods. In: Proceedings of the 12th international power electronics and motion conference, Aug 2006, pp 1884–1889
47. NERC Integration of Variable Generation Task Force (IVFTF1-7) Report (2013) Performance of distributed energy resources during and after system disturbance voltage and frequency ride-through requirements, Dec 2013
48. Moreno-Munoz S, de la Rosa JJG, Lopez MA, Gil de Castro AR (2009) Distributed resources standards: the case of Spain. IEEE ISIE
49. WECC-0060—PRC-024-WECC-1-CR (2009) Generator low voltage ride-through criterion—regional criterion (draft). www.wecc.biz
50. IEEE Std 519-1992 (1992) IEEE recommended practice and requirements for harmonic control in electric power systems. IEEE, June 1992
51. IEEE Std 519-2014 (2014) IEEE recommended practice and requirements for harmonic control in electric power systems. IEEE, Mar 2014
52. Ipakchi A, Albuyeh F (2009) Grid of the future. IEEE Power Energy Mag 52–62
53. Marnay C, Asano H, Papathanassiou S, Strbac G (2008) Policymaking for microgrids. IEEE Power Energy Mag 66–77
54. Kezunovic M, Vittal V, Meliopoulos S, Mount T (2012) The big picture. IEEE Power Energy Mag 22–34
55. Luiz A, Lopes C, Sun H (2006) Performance assessment of active frequency drifting islanding detection methods. IEEE Trans Energy Convers 21(1):171–180

Chapter 20

Reliability Evaluation and Enhancement of Microgrid Incorporating the Effect of Distributed Generation

Debomita Ghosh, Sanchari Deb and Dushmantha Kumar Mohanta

20.1 Introduction

One of the major challenges of twenty-first century is the growing energy crisis. The unsustainable nature of fossil fuels and the emissions from conventional units have led scientists and researchers to delve into the alternate energy resources. This led to the emergence of microgeneration constituting low-voltage end user and producer with the ability to tackle the energy crisis, maintaining an eco-friendly approach. Microgrid is single-controlled units in power system that may or may not be connected to the grid [1]. Different small scale generation sources (distributed generation) used in microgrid are diesel generator (DG), solid oxide fuel cell (SOFC), wind turbine, solar PV cell, biomass, etc. The reliability analysis of microgrid is still one of the major concerns for engineers and researchers because of the sporadic nature of renewable energy resources involved, different operating modes, operational complexity and large number of intermediate states involved in microgrid [2]. The reliability analysis of microgrid by traditional methods involves a lot of computational burden. Moreover, the random behavior of complex system like microgrid is difficult to model by the traditional methods. The two-state binary model of reliability analysis cannot be applied in case of renewable resources. This is because of the possibility of state to reside in intermediate state depending upon wind velocity and solar irradiation respectively. Monte Carlo simulation (MCS),

D. Ghosh (✉) · D.K. Mohanta
Department of Electrical and Electronics Engineering,
Birla Institute of Technology, Mesra, Ranchi 835215, India
e-mail: debomita.ghosh@bitmesra.ac.in

D.K. Mohanta
e-mail: dkmohanta@bitmesra.ac.in

S. Deb
Centre for Energy, Indian Institute of Technology, Guwahati 781039, India
e-mail: sancharideb@yahoo.co.in

fault tree analysis (FTA) and Bayesian network (BN) are some of the popular methods which can be utilized for reliability and adequacy assessment of microgrid [3–8].

In [3], Anthony et al. used state duration sampling-based Monte Carlo simulation for evaluating different adequacy indices such as loss of load expectation (LOLE) and loss of energy expectation (LOEE) of a hybrid microgrid having high penetration of renewable resources. In [4], Wang and Singh used Monte Carlo simulation and population-based search methods such as genetic algorithm and particle swarm optimization for evaluating typical adequacy indices of a wind power-based power system. In [5], Youli and Nagasaka explored the scope of Monte Carlo Simulation for well-being analysis of a laboratory-based microgrid. In [6], Li et al. used fault tree analysis for evaluating the reliability indices of an islanded microgrid. In [7], Shi and Bazzi used Monte Carlo simulation and fault tree analysis for evaluating reliability and component importance indices of a hybrid microgrid. In [8], Deb et al. used Bayesian network for reliability evaluation of different components such as solar PV cell, wind turbine, and diesel generator used in microgrid.

Wind turbine and solar PV cell being outdoor equipment are affected by extreme weather condition [8]. The performance of wind turbine and solar PV cell is enervated by high wind speed and low solar irradiation, respectively. The system reliability of solar PV cell decreases for high ambient temperature as well as high relative humidity [8]. In this chapter, the different techniques for reliability analysis of microgrid such as Monte Carlo simulation, fault tree analysis, Bayesian network, the effect of extreme weather on reliability, and adequacy of microgrid, and different ways for improvement of reliability of microgrid are presented. Further, a comparative analysis of different techniques of reliability and adequacy analysis of microgrid is also included in this chapter.

The arrangement of this chapter is as follows. Section 20.2 illustrates the different unit sources used in microgrid. Section 20.3 exemplifies the techniques for reliability analysis. Section 20.4 illustrates the reliability analysis of different components used. Section 20.5 illustrates the principles of uncertainty analysis of different renewable energy resources involved. Section 20.6 depicts the different approaches for the evaluation of different adequacy indices. Section 20.7 demonstrates the effect of extreme weather condition on different reliability indices of microgrid. Section 20.8 demonstrates the procedure for reliability and adequacy evaluation of microgrid by taking typical case studies. Section 20.9 illustrates the reliability improvement techniques by incorporating redundancies. Section 20.10 concludes the chapter.

20.2 Unit Source Combinations Used in Microgrid

Microgrids are the combination of renewable energy resources with non-renewable units. The reliability analysis and the improvement of microgrid are a major challenge as it has the potential to work in islanded mode as well as feed the utility

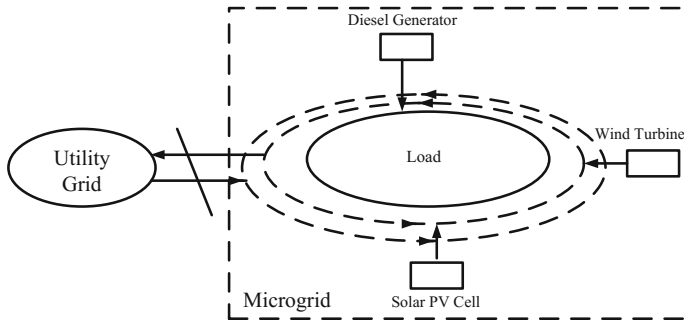


Fig. 20.1 Layout of microgrid

grid during energy crisis as in Fig. 20.1 [1–8]. This prevents complete blackout of the grid system. Wind and solar energy are popular renewable sources of energy used in microgrids. Diesel generator and solid oxide fuel cells are some of the non-renewable units used in microgrid. A brief description of the different unit sources used in microgrid is presented in this section.

20.2.1 Diesel Generator

Diesel generator (DG) is one of the oldest sources of energy which is developed around 100 years ago. It is becoming popular nowadays because of its low installation cost and high reliability. But the major drawback of DG is the high cost of fuel associated with it and the emissions which causes environmental degradation. Diesel generator is a multi-component system [9, 10]. But for reliability analysis, only some of the major components are considered such as

- i. Fuel pump
- ii. Cooling radiator
- iii. Alternator
- iv. Automatic voltage regulator (AVR)

For the DG to be in ON state, all the components must be in upstate considering series connection of components. Failure of even a single component means failure of the entire system. As the name indicates, fuel pump or injection pump is the equipment that pumps diesel into the diesel engine. The sufficient storage capacity of the fuel pump is sufficient to keep the generator in operating state. The different elements of the generator are heated up due to its continuous and uninterrupted use. So in order to withdraw the excess heat and increase the life cycle of the DG, it is necessary to have a cooling and ventilation system. Sometimes, raw water is used for the cooling purpose of the generator. Hydrogen is superior to other coolants because of its inherent capacity of absorbing heat of large and oversized generator

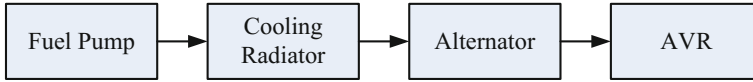


Fig. 20.2 Reliability block diagram of diesel generator

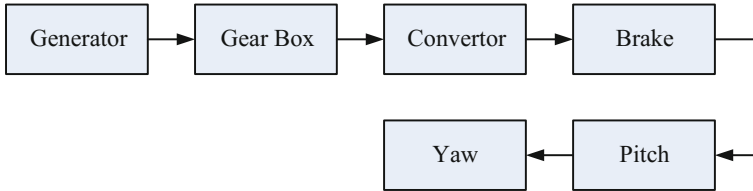


Fig. 20.3 Reliability block diagram of wind turbine

units. The alternator is the integral component of the generator which is responsible for generating electrical output from the mechanical input delivered by the engine. An amalgamation of stationary and moving parts is encased in the housing of alternator. A relative motion between the magnetic and electric field is produced, which in turn generates electricity. AVRs are used to control the output voltage to avoid voltage fluctuations and damage to DG. The primary functions of AVR are as follows [11]:

- To regulate the generator terminal voltage,
- To adjust the reactive power,
- To improve transient as well as dynamic stability, and
- To suppress overvoltage on load rejection.

Figure 20.2 shows the reliability block diagram of the DG. The DG can reside in two states, ON state and OFF state. The binary two-state model of reliability analysis can be directly applied for reliability analysis of DG.

20.2.2 Wind Turbine

The popularity of wind power as a source of microgrid is increasing day by day. Wind power is becoming trendy because of the sophisticated construction of modern wind turbines which are less prone to failures as well as low operational cost of wind turbine. Though the installment cost and maintenance cost of wind turbine are high, still it is gaining popularity because of its almost negligible operating cost. Wind turbine is an intricate system consisting of several mechanisms as shown in Fig. 20.3. The different major components of wind turbine are [12] as follows:

- i. Generator
- ii. Gearbox
- iii. Converter
- iv. Brake
- v. Pitch
- vi. Yaw

Wind turbines usually possess an AC generator that transforms wind turbine's mechanical energy into electrical energy. Gearbox facilitates the generator in facing the wind speeds more than tolerable range of wind speed. The DC power is converted to AC by using converter. The converter also performs reactive power compensation. The yaw constantly adjusts the rotor in the track of wind. The brake is used to obstruct the rotor during disasters. Considering the security of the system, the wind turbine is shut down completely until the damaged part of the brake is repaired. The pitch is used to regulate the output of the turbine [13, 14].

20.2.3 Solar PV Cell

The low cost and easy availability of solar power have led scientists and researchers to explore this alternate source of energy. The main components of solar photovoltaic cell are [15] as follows:

- i. Solar panel
- ii. Automatic charge controller
- iii. Battery bank
- iv. Converter

Solar panels are positioned on outdoor, and the solar cell is charged during daylight hours. Automatic charge controller controls the charging of battery. This logic-based controller guarantees that when the battery is fully charged the charging current is restricted from flowing. Similarly, when the battery voltage falls below a certain threshold value, the flow of current is again restarted [15]. The battery bank serves as the primary energy storage device to guarantee uninterrupted availability of power. A DC/AC converter is used for driving AC loads. Figure 20.4 shows the corresponding reliability block diagram of solar PV cell.

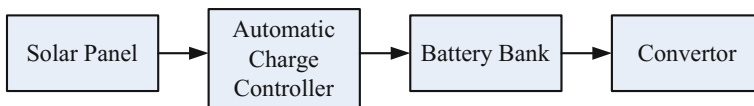


Fig. 20.4 Reliability block diagram of solar photovoltaic cell

20.3 Reliability Analysis Techniques of Microgrid

Reliability and adequacy analysis of microgrid is an important challenge for microgrid planners. To assess the reliability of microgrid including renewable resources such as solar and wind, stochastic models have to be developed. Some of the well-known techniques used for reliability analysis of microgrids are Monte Carlo simulation, fault tree analysis, and Bayesian network which are majorly discussed in this section.

20.3.1 Monte Carlo Simulation

Monte Carlo simulation is used for stochastic as well as deterministic simulation based on generation of random numbers. This approach is frequently utilized if the system is complicated or possesses many uncertain factors and nonlinearities. Due to the unpredicted nature of the failures in any system, Monte Carlo simulation can be utilized to simulate these failures. Time sequential simulation or state duration sampling is one of the types of Monte Carlo simulation which is used when the system behavior and performance depend on precedent events. A simulated history is required in time sequential simulation, and this can be acquired by generating the uptime and downtime for the system components in a random manner [16]. The equations for time to failure (*TTF*) and time to repair (*TTR*) are (20.1) and (20.2), respectively.

$$TTF = -\frac{1}{\lambda} \ln(u) \quad (20.1)$$

$$TTR = -\frac{1}{\mu} \ln(u) \quad (20.2)$$

where λ and μ are failure rate and repair rate of the system, respectively. u is a random number generated between 0 and 1.

i. Series System:

For further exemplification of reliability analysis by Monte Carlo simulation, a series system is shown as in Fig. 20.5.

Fig. 20.5 Series system

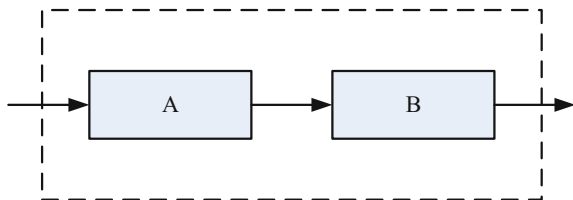
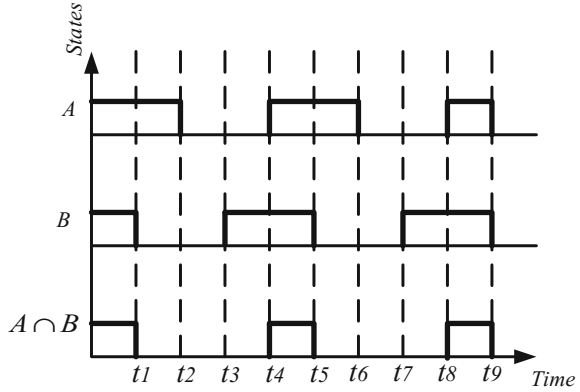


Fig. 20.6 Randomly generated *TTF* and *TTR* of *A* and *B* with superimposed states of the series system



For the system to be in ON state, both the components must be in ON state. The *TTF* (failure/year) and *TTR* (repair/hour) for the probability of components *A* and *B* are generated randomly based on Monte Carlo simulation for a certain simulation time, and the superimposed states of the series system are shown in the Fig. 20.6.

Reliability of the series system is given as in (20.3)

$$R_s = \frac{T_{ON}}{T} = \frac{T_{A \cap B}}{T} \tag{20.3}$$

Similarly, for a system having X_i components, where $i = 1 \dots n$ in series, reliability is given by (20.4)

$$R_s = \frac{T_{(X_1 \cap X_2 \dots X_n)}}{T} \tag{20.4}$$

ii. *Parallel System:*

Figure 20.7 shows a parallel combination of two elements, and Fig. 20.8 shows the randomly generated *TTF* and *TTR* of *A* and *B* and superimposed states of the system.

Reliability of the parallel system is given as in (20.5)

$$R_p = \frac{T_{A \cup B}}{T} \tag{20.5}$$

Similarly, for X_i components, where $i = 1 \dots n$, reliability is given as in (20.6)

$$R_p = \frac{T_{X_1 \cup X_2 \dots X_n}}{T} \tag{20.6}$$

Fig. 20.7 Parallel system

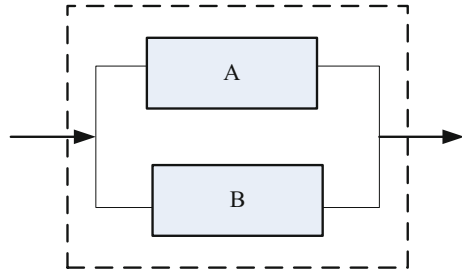


Fig. 20.8 Randomly generated *TTF* and *TTR* of *A* and *B* with superimposed states of the parallel system

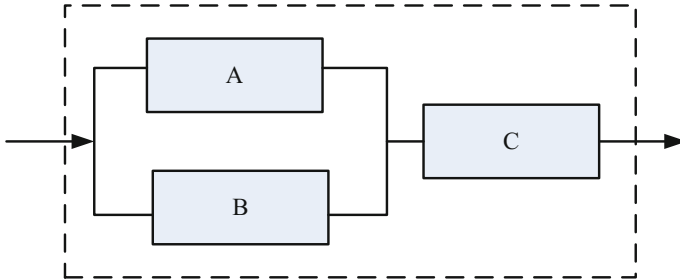
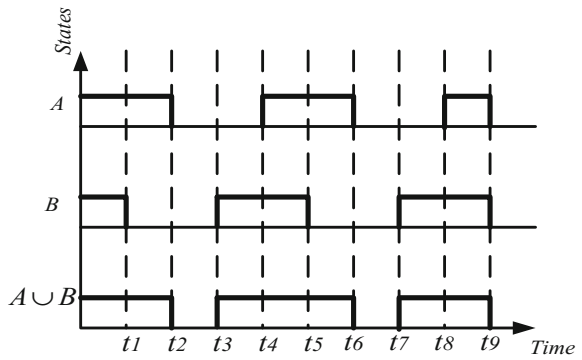


Fig. 20.9 A complex system with series and parallel combinations

iii. *Complex System:*

Figure 20.9 shows a complex system having parallel and series combinations of components *A*, *B*, and *C*. Further, Fig. 20.10 shows the randomly generated *TTF* and *TTR* of *A*, *B*, *C*, and superimposed states of the system.

Reliability of the complex system is given as in (20.7)

$$R_c = \frac{T_{(A \cup B) \cap C}}{T} \tag{20.7}$$

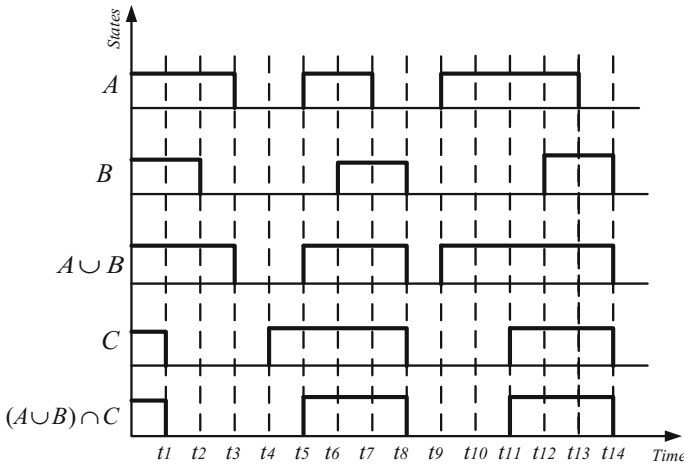


Fig. 20.10 Randomly generated *TTF* and *TTR* of *A*, *B*, and *C* with superimposed states of the system

Similarly, for a system having X_i components, where $i = 1 \dots n$, in parallel, and Y_j components, where $j = 1 \dots m$, in series, the expression for system reliability is given as in (20.8)

$$R_c = \frac{T_{((X_1 \cup X_1 \cup \dots \cup X_n) \cap Y_1 \cap Y_2 \cap \dots \cap Y_m)}}{T} \tag{20.8}$$

20.3.2 Fault Tree Analysis

Fault tree analysis is a simple deductive process where an unfavorable or unwanted event called the top event is proposed and the probable means for this event to occur are analytically deduced. The different series and parallel events that led to the occurrence of top event are represented graphically and logically with the help of majorly AND and OR gate [17]. The different symbols and gates used in fault tree analysis are given in Tables 20.1 and 20.2, respectively.

In case of an inhibit gate, the occurrence of output event depends on the occurrence of all the input events as well as an additional conditional event. It is nothing but an AND gate with a supplementary event. In reality, an inhibit gate is incapable of providing any additional modeling capabilities, but it only involves the occurrence of an additional event. As an example, consider the case where events *A* and *B* must occur as well as a third event *C* (the so-called conditional event) in order for the system to fail.

To analyze the method, series system, parallel system, and complex system are presented.

Table 20.1 Different symbols used in fault tree analysis [17–20]




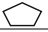
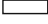







Symbol	Representation	Definition
	Basic event	Event which requires no further development
	Conditional event	Event involving specific terms or condition
	Undeveloped event	An event which cannot be further developed due to lack of information
	External event	An event which is normally expected to occur
	Intermediate event	An event which occurs due to one or more antecedent causes acting through logic gates
	Transfer symbol	This is used to subdivide a complete event into number of sub-event

Table 20.2 Different gates used in fault tree analysis [17–20]

Symbol	Name	Representation	Truth table		
			Input1	Input2	Output
	AND gate	The output will arise only if all inputs will occur	Input1	Input2	Output
			0	0	0
			0	1	0
			1	0	0
			1	1	1
	OR gate	The output occurs if any input occurs	Input1	Input2	Output
			0	0	0
			0	1	1
			1	0	1
			1	1	1
	Exclusive OR	The output occurs if exactly one input occurs	Input1	Input2	Output
			0	0	0
			0	1	1
			1	0	1
			1	1	0
	NOT gate	The output event occurs if the input event does not occur	Input	Output	
			0	1	
			1	0	
	NOR gate	The output is false, if there is at least one true input	Input1	Input2	Output
			0	0	1
			0	1	0
			1	0	0
			1	1	0
	NAND gate	The output is true, if there is at least one false input event	Input1	Input2	Output
			0	0	1
			0	1	1
			1	0	1
			1	1	0

(continued)

Table 20.2 (continued)

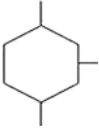
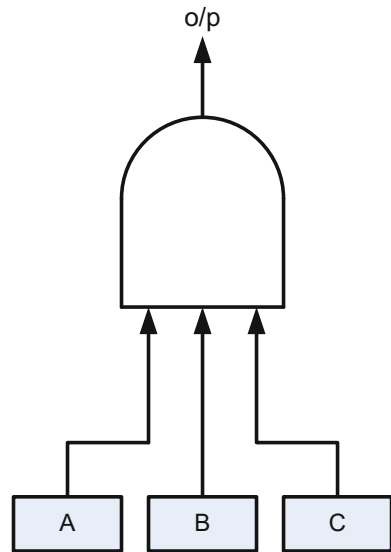
Symbol	Name	Representation	Truth table			
			Input1	Input2	Input3	Output
	Inhibit gate	If the input occurs under an enabling condition specified by a conditioning event, the output occurs	0	0	0	0
			0	0	1	0
			0	1	0	0
			0	1	1	0
			1	0	0	0
			1	0	1	0
			1	1	0	0
			1	1	1	1

Fig. 20.11 Fault tree of a series system



i. *Series System:*

For a series system with three components *A*, *B*, and *C*, the fault tree model is shown in Fig. 20.11.

Since it is a series system, for the system to be in ON state, all the three components must be in ON state. Hence, its fault tree is represented by an AND gate as shown in Fig. 20.11 with its corresponding truth table as given in Table 20.3.

After the construction of the fault tree, it is necessary to compute the probability of the top event. One of the approaches for doing that is Boolean algebra approach [21]. This method initiates with the topmost event, and the topmost event is logically expressed in terms of events: basic, incomplete, and intermediate.

Table 20.3 Truth table for a series system

A	B	C	State of system
0	0	0	0
0	0	1	0
0	1	0	0
0	1	1	0
1	0	0	0
1	0	1	0
1	1	0	0
1	1	1	1

Any intermediate events in the resulting logic statement are themselves substituted logically by the events in the subsequent hierarchical level. This continues until the logical statements signifying the top event are in terms of basic and incomplete events only.

The Boolean logic expression for the series system is $A.B.C$

The probability of top event is given by:

$$P(\text{top}) = P(A)P(B)P(C) \tag{20.9}$$

where $P(A)$, $P(B)$, and $P(C)$ represent the probability of being in ON state of individual component.

Similarly, for a system having X_i components, where $i = 1 \dots n$, in series, the equation for system reliability is

$$P(\text{top}) = P(X_1)P(X_2) \dots P(X_n) \tag{20.10}$$

ii. *Parallel System:*

The FTA of a parallel system is represented by OR gate as shown in the Fig. 20.12, and the corresponding truth table is given in Table 20.4.

The expression for the reliability of this parallel system is given by (20.11):

$$P(\text{top}) = P(A) + P(B) + P(C) - P(A)P(B) - P(B)P(C) - P(C)P(A) + P(A)P(B)P(C) \tag{20.11}$$

where $P(A)$, $P(B)$, and $P(C)$ represent the probability of being in ON state of individual components.

iii. *Complex System:*

The complex system with both series and parallel combinations and its fault tree is shown in Figs. 20.13 and 20.14, respectively.

For such a complex system, the reliability analysis by Boolean algebra approach is very much time-consuming and involves a lot of computational burden as the truth table will have five inputs and thirty-two combinations of different cases.

Fig. 20.12 Fault tree of parallel system

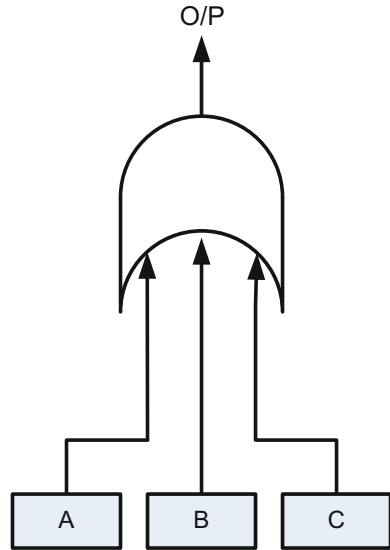


Table 20.4 Truth table for a parallel system

A	B	C	State of system
0	0	0	0
0	0	1	1
0	1	0	1
0	1	1	1
1	0	0	1
1	0	1	1
1	1	0	1
1	1	1	1

So another method for evaluation of reliability is by minimal cut set methodology which can be used for such complex system [22]. In this method, minimal cut sets are formulated to locate the weak points of the system. A minimal cut set is defined as the smallest combination of primary failures in which if they all occur, will cause the top event to occur.

The method of deducing minimal cut set is illustrated below. The process uses a top-down approach beginning with the top event and then proceeds as follows:

- i. The inputs are written in terms of basic event and input gates as separate items in a list if the top event is an OR gate.
- ii. The inputs are written in terms of basic events and input gates as one single item of a list if the top event is an AND gate.
- iii. Each gate in the new list is considered and replaced as in step (1) if it is an OR gate or as in step (2) if it is an AND gate.

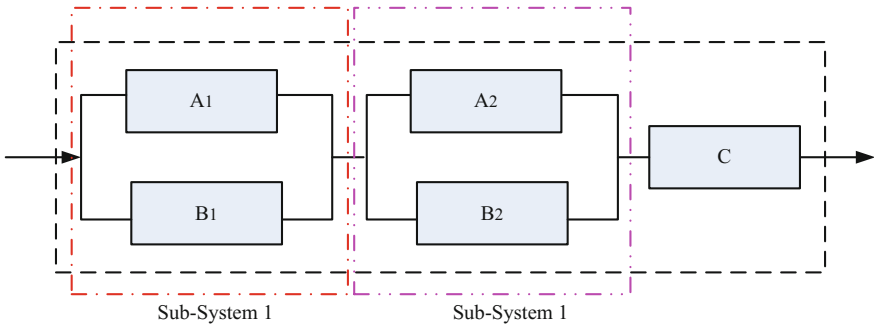
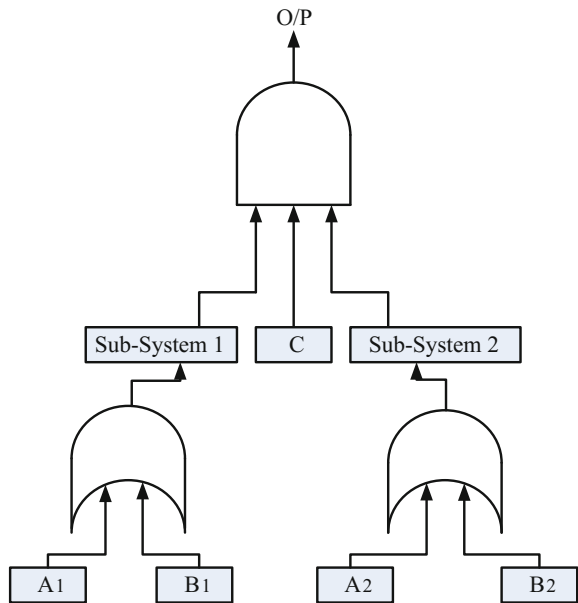


Fig. 20.13 Complex system

Fig. 20.14 Fault tree of complex system



iv. Step (3) is continuously repeated for each new list, and the resultant list after completion of all the aforementioned steps is the minimal cut set list.

In the fault tree shown in Fig. 20.14, since the top event is an AND gate so the inputs as single item in the list.

Sub-system 1, Sub-system 2, C

Sub-system 1 and Sub-system 2 are the resultant of OR gate so the inputs are written separately.

A₁, Sub-system 2, C

B_1 , Sub-system 2, C

And further, the final list of minimal cut sets is

$A_1A_2C, A_1B_2C, B_1A_2C, B_1B_2C$

The probability of top event is given by:

$$P(\text{top}) = P((A_1A_2C)U(A_1B_2C)U(B_1A_2C)U(B_1B_2C)) \tag{20.12}$$

20.3.3 Bayesian Network

Bayes’ theorem developed in 1760 which updates probabilities based on new information is the fundamental of Bayesian network. A Bayesian network (BN) is a directed acyclic graph (DAG) constructed by the variables (nodes) along with the directed edges [23, 24]. In a Bayesian network the nodes that have no arrows directed into them are called root nodes or parent nodes, and they possess prior probability table (PPT). The nodes that have arrows directed into them are called child nodes, and they possess conditional probability table (CPT).

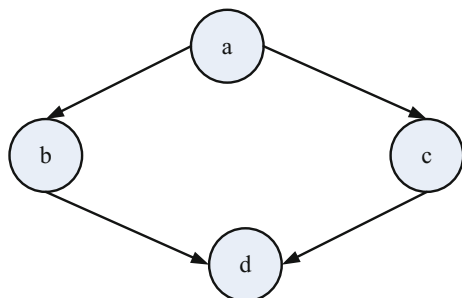
Figure 20.15 shows a simple Bayesian network comprising of four nodes $a, b, c,$ and d . Here, a is the parent node, b and c are child nodes of a , and d is the child node of b and c , respectively.

Any complex system can be modeled by Bayesian network, and the different reliability indices can be evaluated by bucket elimination algorithm. The algorithm will produce accurate answer for any arrangement. However, the time required to produce the result will be much longer for some ordering versus others.

The algorithm associated with bucket elimination is as follows [8, 25]:

- i. Each node of the Bayesian network is arranged in some order.
- ii. Each conditional probability table associated with each node is put in one bucket.
- iii. Processing of a bucket is performed backward with respect to the node order. Processing a bucket eliminates the variable in the bucket from subsequent computation.

Fig. 20.15 Bayesian network



- iv. The bucket function is created by multiplying all the functions containing the current node.
- v. Variable elimination is performed by using summation over the current node.

The newly created function table is placed in the appropriate bucket.

For the Bayesian network shown as in Fig. 20.15, $P(d = 1)$ is as given in (20.13)

$$P(d = 1) = \sum_{a=0,1} P(a) \sum_{b=0,1} P(b|a) \sum_{c=0,1} P(c|a) \quad (20.13)$$

The buckets in the reverse order are d , c , b , and a .

$$\text{Bucket 1} = \lambda(d|b, c) = \sum_{d=1} P(d|b, c) \quad (20.14)$$

$$\text{Bucket 2} = \lambda(c|a) = \sum_{c=0,1} P(c|a) \lambda(d|b, c) \quad (20.15)$$

$$\text{Bucket 3} = \lambda(b|a) = \sum_{b=0,1} P(b|a) \lambda(c|a) \quad (20.16)$$

$$\text{Bucket 4} = \lambda(a) = \sum_{a=0,1} P(a) \lambda(b|a) \quad (20.17)$$

So, node d is considered first. After that, node c will be taken into account for processing. The results are obtained by multiplication and summation. The entire procedure is repeated up to bucket 4. Bucket 4 will contain the desired probability of $P(d = 1)$. Now, the probability of 'a' when $d = 1$ which is the posterior probability is given by:

$$P((a|d) = 1) = \frac{P(a, d = 1)}{P(d = 1)} \quad (20.18)$$

Based on Eqs. (20.13)–(20.18), system reliability and posterior probability calculation can be made. Diagnostic importance factor (DIF) which is utilized for critical component ranking is computed based on posterior probabilities. DIF gives the fraction of system unreliability that involves the component failure [26–31]. The component with higher DIF is more critical compared to others with a lower value of DIF. For DIF computation, let S denote the failure event of the system, and e_k denotes the failure event of the k th component of this system. Thus, DIF is as given in (20.19).

$$(\text{DIF}) = P(e_k = 0|S = 0) \quad (20.19)$$

For further illustration of Bayesian network, series, parallel, and complex systems are considered.

Fig. 20.16 Bayesian network for series system

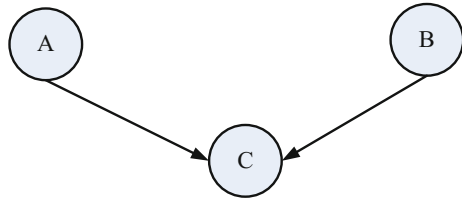


Table 20.5 Prior probability table of nodes *A* and *B*

Nodes	State	Probability
<i>A</i>	0	0.4
	1	0.6
<i>B</i>	0	0.3
	1	0.7

Table 20.6 Conditional probability table of node *C*

State of output	<i>A</i>	State 0		State 1	
	<i>B</i>	State 0	State 1	State 0	State 1
State 0	1		1	1	0
State 1	0		0	0	1

i. *Series System:*

Figure 20.16 shows the Bayesian network of a series system having elements *A* and *B*. Node *C* represents the event of success of the system whose conditional probability table is as given in Table 20.6 with prior probability in Table 20.5.

The expression of system reliability is given by (20.20) with the results in Table 20.7:

$$P(C = 1) = P(C|A, B) * P(A) * P(B) \tag{20.20}$$

For the model as in Fig. 20.16, it is considered that both *A* and *B* are independent of each other. If *B* is dependent on *A*, then the Bayesian network is as shown in Fig. 20.17.

The system reliability is given by (20.21)

$$P(C = 1) = P(C|A, B) * P(B|A) * P(A) \tag{20.21}$$

ii. *Parallel System:*

For two components *A* and *B* to be in parallel, the PPT is same as given in Table 20.5, but the CPT of the node *C* is as given in Table 20.8.

The expression for system reliability is given by (20.22):

$$P(C = 1) = P(C|A, B) * P(A) * P(B) \tag{20.22}$$

Thus, the overall reliability is 0.88 as per the third bucket of Table 20.9 unlike for series system which is 0.42 as in Table 20.7.

Table 20.7 Bucket no. 1, 2, and 3

Bucket no. 1	A	B	$\lambda(C A,B)$
	0	0	0
	0	1	0
	1	0	0
	1	1	1
Bucket no. 2	A	$\lambda(C A,B) * P(B)$	
	0	$0 * 0.3 + 0 * 0.7 = 0$	
	1	$0 * 0.3 + 1 * 0.7 = 0.7$	
Bucket no. 3	C	$\lambda(C A,B) * P(B) * P(A)$	$P(C)$
	0	$0 * 0.4$	$0 + 0.42 = 0.42$
	1	$0.7 * 0.6$	

Fig. 20.17 Bayesian network for dependent series system

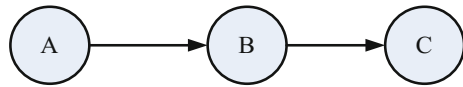


Table 20.8 Conditional probability table of node C

State of output	A	State 0		State 1	
	B	State 0	State 1	State 0	State 1
State 0	1		0	0	0
State 1	0		1	1	1

Table 20.9 Bucket no. 1, 2, and 3

Bucket no. 1	A	B	$\lambda(C A,B)$
	0	0	0
	0	1	1
	1	0	1
	1	1	1
Bucket no. 2	A	$\lambda(C A,B) * P(B)$	
	0	$0 * 0.3 + 1 * 0.7 = 0.7$	
	1	$1 * 0.3 + 1 * 0.7 = 1$	
Bucket no. 3	C	$\lambda(C A,B) * P(B) * P(A)$	$P(C)$
	0	$0.7 * 0.4$	$0.28 + 0.6 = 0.88$
	1	$1 * 0.6$	

Fig. 20.18 Bayesian network for complex system

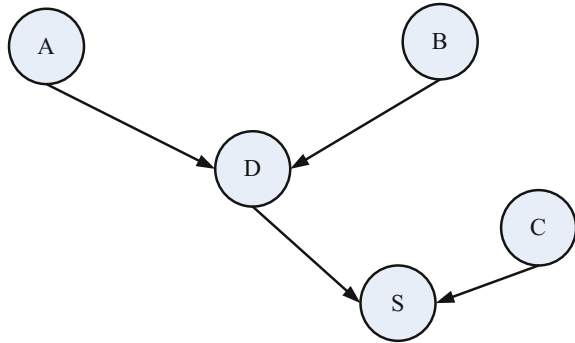


Table 20.10 Prior probability table of nodes *A*, *B*, and *C*

Nodes	State	Probability
<i>A</i>	0	0.4
	1	0.6
<i>B</i>	0	0.3
	1	0.7
<i>C</i>	0	0.37
	1	0.63

Table 20.11 Conditional probability table of nodes *D* and *S*

Nodes	State of output	<i>A</i>		<i>B</i>	
		0	1	0	1
<i>D</i>					
	0	1	0	0	0
	1	0	1	1	1
<i>S</i>	State of output	<i>D</i>	0	1	
		<i>C</i>	0	1	0
	0	1	1	1	0
	1	0	0	0	1

ii. *Complex System:*

Figure 20.18 shows the Bayesian network of the complex system. Here, *D* is an intermediate node representing the event of success of the parallel sub-system having *A* and *B* as components. *S* represents the success of the entire system. The prior probability table of nodes *A*, *B*, and *C*, CPT of nodes *D* and *S* are given in (Table 20.10) and (Table 20.11) respectively.

The expression of system reliability of the complex is given by (20.23) with the results as given in (Table 20.12):

$$P(S = 1) = P(S|D, C) * P(C) * P(D|A, B) * P(A) * P(B) \tag{20.23}$$

The major advantages of Bayesian networks over the other two methods are as follows:

Table 20.12 Bucket no. 1, 2, 3, 4, and 5

Bucket no. 1	<i>D</i>	<i>C</i>	$\lambda(S D,C)$
	0	0	0
	0	1	0
	1	0	0
	1	1	1
Bucket no. 2	<i>D</i>	$\lambda(S D,C) * P(C)$	
	0	$0 * 0.37 + 0 * 0.63 = 0$	
	1	$0 * 0.37 + 1 * 0.63 = 0.63$	
Bucket no. 3	<i>A</i>	<i>B</i>	$\lambda(S D,C) * P(C) * P(D A,B)$
	0	0	$0 * 1 + 0 * 0.63 = 0$
	0	1	$0 * 0 + 1 * 0.63 = 0.63$
	1	0	$0 * 0 + 1 * 0.63 = 0.63$
	1	1	$0 * 0 + 1 * 0.63 = 0.63$
Bucket no. 4	<i>A</i>	$\lambda(S D,C) * P(C) * P(D A,B) * P(A)$	
	0	$0 * 0.3 + 0.63 * 0.7 = 0.441$	
	1	$0.63 * 0.3 + 0.63 * 0.7 = 0.63$	
Bucket no. 5	<i>S</i>	$\lambda(S D,C) * P(C) * P(D A,B) * P(A) * P(B)$	<i>P(S)</i>
	0	$0.441 * 0.4 = 0.1764$	0.5544
	1	$0.63 * 0.6 = 0.378$	

- i. Posterior probability calculation is possible by only Bayesian networks. Diagnostic importance factor which is calculated based on posterior probabilities can be computed by only Bayesian network and not by other methods such as fault tree and Monte Carlo simulation.
- ii. Risk achievement worth and risk reduction worth which are used for determining optimum maintenance policy can only be computed by Bayesian network.
- iii. Bayesian network involves less computational complexity compared to fault tree and Monte Carlo simulation.

There are many softwares available for Bayesian network. Some of the well-known software for Bayesian network is Bayes Server, Hugin, GeNiE, and Smile.

GeNiE software is used extensively for reliability modeling by Bayesian network in this chapter. GeNiE is a flexible and accessible platform for reliability assessment by Bayesian networks. This software is developed by University of Pittsburgh and has been made available to the research community in July 1998.

The main features of this software are as follows:

- i. graphical editor to make and amend network models,
- ii. support different types of nodes with general, Noisy MAX distributions,
- iii. open multiple networks in single window and cut and paste sub-parts of models in multiple networks,

- iv. completely integrated with MS Excel, and
- v. calculation of posterior probabilities and sensitivity analysis.

20.4 Reliability Evaluation of Different Components of Microgrid

Diesel generator, solar PV cell, and wind turbine are the major unit sources used in microgrid. All the three aforementioned sources are multi-component complicated system. System reliability of these unit sources can be evaluated by any of the techniques discussed in the preceding section.

20.4.1 Reliability Evaluation of Different Unit Sources of Microgrid by Monte Carlo Simulation

In this method, the time to failure and time to repair of all the components of the unit source are generated randomly for a certain time period based on the probabilistic approach for DG, solar PV, and wind turbine. Since the components of the unit sources are connected in series, for the probability of source to be in upstate, all the probability of components must be in upstate. *TTF* (failure/year) and *TTR* (repair/hour) of all the components are superimposed. System reliability is calculated as explained in Sect. 20.3.1.

The simulated *TTF* and *TTR* for different components of DG are as shown in Fig. 20.19. The mathematical expression for system reliability is given by (20.24):

$$P(\text{DG} = 1) = t_1 + (t_{14} - t_{13}) + (t_{21} - t_{20})/T \quad (20.24)$$

where T is the total simulation time.

The simulated *TTF* and *TTR* for different components of solar PV cell are as shown in Fig. 20.20. The mathematical expression for system reliability is given by (20.25):

$$P(\text{PVcell} = 1) = t_2 + (t_{14} - t_{13}) + (t_{21} - t_{20})/T \quad (20.25)$$

The simulated *TTF* and *TTR* for different components of wind turbine are as shown in Fig. 20.21. The mathematical expression for system reliability is given by (20.26):

$$P(\text{WTG} = 1) = t_1 + (t_{20} - t_{18})/T \quad (20.26)$$

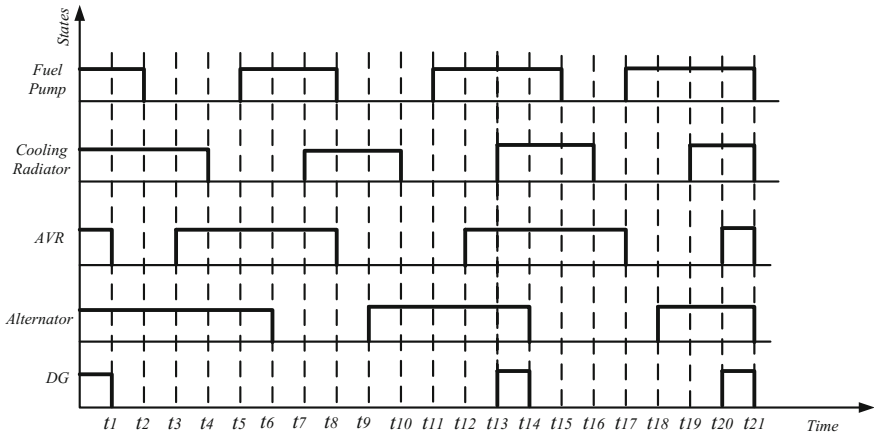


Fig. 20.19 TTF and TTR of different components of DG generated by Monte Carlo simulation

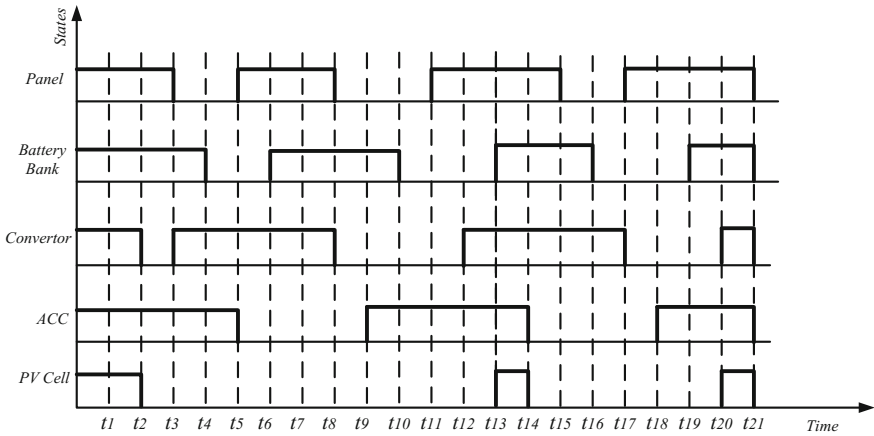


Fig. 20.20 TTF and TTR of different components of solar PV cell generated by Monte Carlo simulation

Thus, the reliability analysis from the three resources may be obtained for the generated TTF and TTR.

20.4.2 Reliability Evaluation of Different Unit Sources of Microgrid by Fault Tree Analysis

Reliability of different unit sources of microgrid can be evaluated by fault tree analysis by considering the top event as system reliability [7]. System modeling is

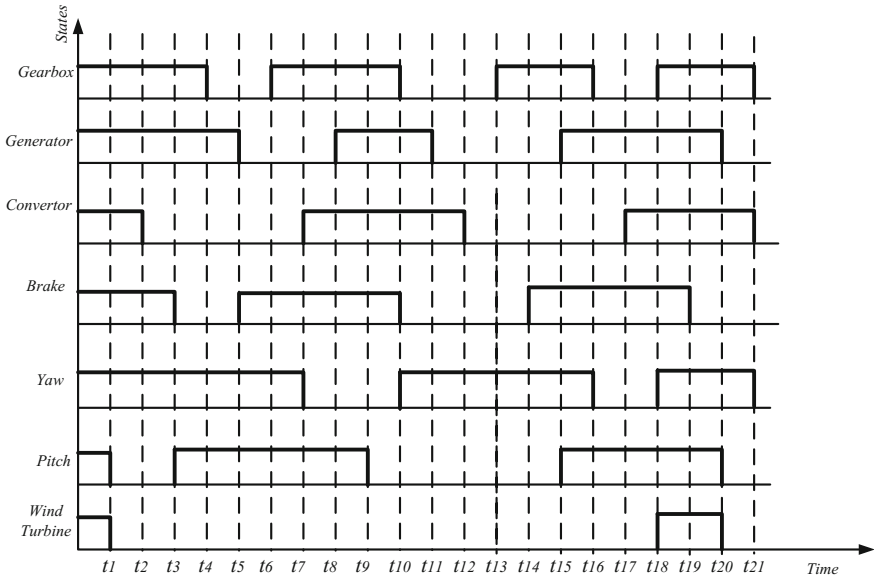
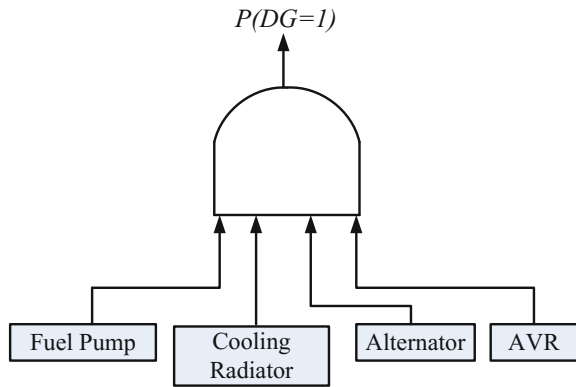


Fig. 20.21 TTF and TTR of different components of wind turbine generated by Monte Carlo simulation

Fig. 20.22 Fault tree of diesel generator



accomplished with AND and OR gates. For further illustration, let us take the example of diesel generator. The major components of DG are fuel pump, cooling radiator, alternator, and AVR. As it is a series combination of all the components, the fault tree representation of this unit source is as shown in Fig. 20.22.

The truth table for this fault tree is similar to that of four-input AND gate as given in Table 20.13.

The expression of system reliability is given by (20.26):

Table 20.13 Truth table for computation of LOLP

State of power output from DG	State of power output from wind turbine	State of power output from solar PV Cell	State of load	State of LOLP
0	0	0	0	0
0	0	0	1	1
0	0	1	0	0
0	0	1	1	1
0	1	0	0	0
0	1	0	1	1
0	1	1	0	0
0	1	1	1	0
1	0	0	0	0
1	0	0	1	1
1	0	1	0	0
1	0	1	1	0
1	1	0	0	0
1	1	0	1	0
1	1	1	0	0
1	1	1	1	0

$$P(\text{DG} = 1) = P(\text{fuel pump}) * P(\text{cooling radiator}) * P(\text{alternator}) * P(\text{AVR}) \quad (20.27)$$

Similarly, solar PV cell is a series combination of panel, battery bank, convertor, and ACC, and the expression of system reliability is given by (20.28):

$$P(S = 1) = P(\text{solar panel}) * P(\text{battery bank}) * P(\text{convertor}) * P(\text{ACC}) \quad (20.28)$$

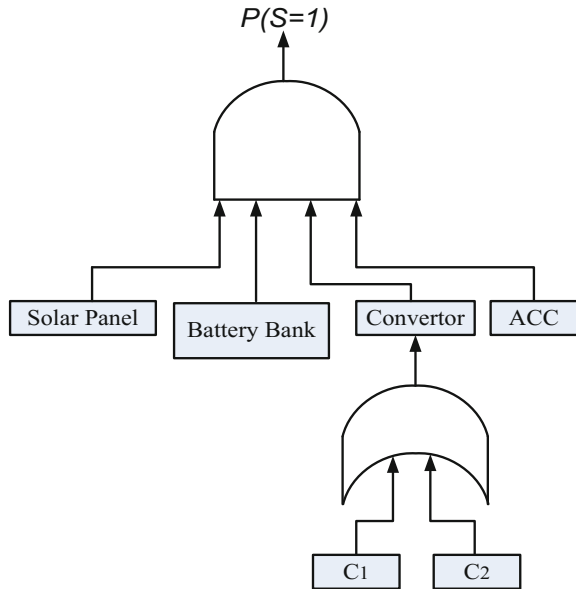
Figure 20.23 shows the fault tree of a solar PV cell having redundant convertors. The expression for system reliability is given by (20.29):

$$P(S = 1) = P(\text{panel}) * P(\text{Battery bank}) * (P(C1) * (1 - P(C2))) + (P(C2) * (1 - P(C1))) \quad (20.29)$$

Further wind turbine is also a series combination of components as illustrated in Sect. 20.3.2. Thus, the expression for system reliability is given by (20.30):

$$P(\text{WTG} = 1) = P(\text{generator}) * P(\text{gearbox}) * P(\text{convertor}) * P(\text{brake}) * P(\text{yaw}) * P(\text{pitch}) \quad (20.30)$$

Fig. 20.23 Fault tree of solar PV cell with redundant convertors



20.4.3 Reliability Analysis of Different Unit Sources of Microgrid by Bayesian Network

The system reliability of different unit sources of microgrid can also be evaluated by Bayesian network. The system modeling is done by Bayesian network, and system reliability is evaluated by bucket elimination algorithm [8]. Moreover, one of the important features of this Bayesian network is that the critical component ranking of the unit sources can be performed with the help of posterior probabilities obtained.

For further illustration, let us take the example of solar PV cell, DG, and wind turbine. The Bayesian network of solar PV cell in GeNiE is shown below as in Fig. 20.24.

The expression of system reliability is given by

$$\begin{aligned}
 P(S = 1) &= P(S = 1 | \text{solar panel, Battery bank, Converter, ACC}) \\
 &\quad * P(\text{solar panel}) * P(\text{Battery bank}) \\
 &\quad * P(\text{Converter}) * P(\text{ACC})
 \end{aligned}
 \tag{20.31}$$

Here, the nodes are eliminated, and ultimately, system reliability is evaluated by bucket elimination algorithm as illustrated in Sect. 20.3.3.

Similarly, the expression of system reliability for DG and wind turbine is given in Eqs. (20.32) and (20.33):

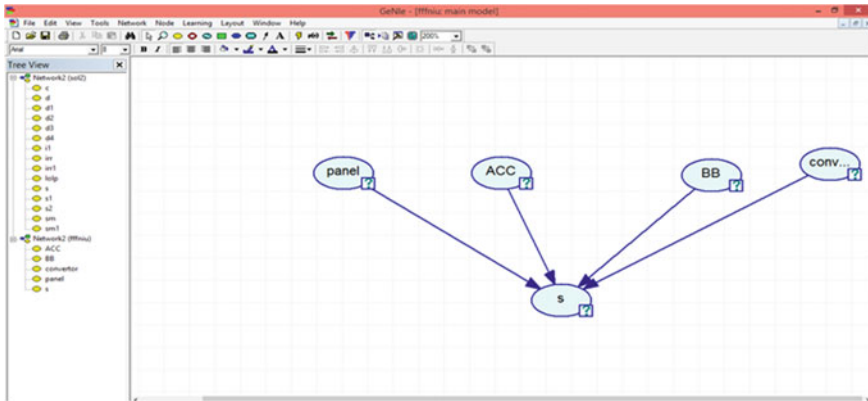


Fig. 20.24 Bayesian network of solar PV cell in GeNIe

$$\begin{aligned}
 P(S = 1) &= P(S = 1 | \text{fuel pump, AVR, Cooling radiator, Alternator}) \\
 &\quad * P(\text{fuel pump}) * P(\text{AVR}) * P(\text{cooling radiator}) \\
 &\quad * P(\text{Alternator})
 \end{aligned}
 \tag{20.32}$$

$$\begin{aligned}
 P(S = 1) &= P(S = 1 | \text{generator, gearbox, Brake, yaw, convertor, pitch}) \\
 &\quad * P(\text{generator}) * P(\text{gearbox}) * P(\text{Brake}) \\
 &\quad * P(\text{yaw}) * P(\text{convertor}) * P(\text{pitch})
 \end{aligned}
 \tag{20.33}$$

20.5 Uncertainty Analysis of Renewable Resources

The renewable sources of energy such as wind turbine and solar PV cell associated with microgrid are stochastic in nature. As a result of which the power output from these sources are random. The power output from wind turbine depends on wind speed and the power output from solar PV cell depends on solar irradiation. Solar irradiation and wind speed vary throughout the year. Monte Carlo simulation-based Weibull distribution is used for uncertainty analysis of the renewable energy resources associated with microgrid [32–35].

For wind turbine, the wind velocity is simulated for a certain period by using Monte Carlo simulation-based Weibull distribution. To simulate the wind speed, the Eqs. (20.34), (20.35), and (20.36) are used [32–35].

$$v = \alpha(-\ln U)^{1/\beta}
 \tag{20.34}$$

$$\alpha = \bar{v}\Gamma\left(1 + \frac{1}{\beta}\right) \tag{20.35}$$

$$\beta = \left(\frac{\delta}{\bar{v}}\right)^{-1.086} \tag{20.36}$$

where v is the velocity of wind speed, α is the scale parameter of Weibull distribution, β is the shape parameter of Weibull distribution, U is a randomly generated number, \bar{v} is the mean wind speed, δ is the standard deviation, and Γ is gamma function.

The relation between output power of wind turbine and wind velocity is given by Eq. (20.37) [32–35]:

$$\left. \begin{aligned} P_{\text{WTG}} &= 0 && \forall 0 < v < v_{\text{cut in}} \\ &= av^k + bP_{\text{rated}} && \forall v_{\text{cut in}} < v < v_{\text{rated}} \\ &= P_{\text{rated}} && \forall v_{\text{rated}} < v < v_{\text{cut out}} \end{aligned} \right\} \tag{20.37}$$

where

$$a = \frac{P_{\text{rated}}}{(v_{\text{rated}}^3 - v_{\text{cut in}}^3)}, \quad b = \frac{P_{\text{rated}}}{(v_{\text{cut out}}^3 - v_{\text{rated}}^3)}$$

where P_{WTG} is the power output from wind turbine, P_{rated} is rated power output from wind turbine, $v_{\text{cut in}}$ is cut-in wind velocity, v_{rated} is rated wind velocity, $v_{\text{cut out}}$ is cutout wind velocity, and k is a constant. The cut-in wind velocity is 3 m/s, rated wind velocity is 12 m/s, and cutout wind velocity is 25 m/s, respectively [32–35].

The power output from solar PV cell is dependent on solar irradiation [32–35]. The variation of mean value of solar irradiation from summer to winter affects the power output from solar PV cell. The power output can be zero because of PV cell internal fault as well as low solar irradiation. The solar irradiation is simulated for one-year period by the same procedure as described in case of wind turbine. The equation for power output of solar PV cell is given by (20.38) [32–35].

$$\begin{aligned} P_{\text{out}} &= \eta_c \times p_{\text{rated}} \times S^2 && \text{for } S > S_{\text{threshold}} \quad \text{and} \quad S < S_{\text{rated}} \\ &= \eta_c \times p_{\text{rated}} && \text{for } S > S_{\text{rated}} \end{aligned} \tag{20.38}$$

where S is solar irradiation, η_c is efficiency of solar PV cell, p_{rated} is rated power output, $S_{\text{threshold}}$ is threshold value of solar irradiation, P_{out} is power output from PV cell, S_{rated} is rated solar irradiation, $S_{\text{threshold}}$ is considered to be 600 kW/m², and S_{rated} is considered to be 1000 kW/m². Here, it is assumed that the solar PV cell is 100% efficient.

After the calculation of the speed of wind and the corresponding power output, clustering technique is utilized to divide the power output and wind speed into a number of clusters and the probability of occurrence of a particular cluster is also evaluated. Similarly, the solar irradiation and corresponding power output are also divided into a number of clusters.

20.6 Adequacy Analysis of Microgrid

The power supply from microgrid must be reliable and adequate in order to meet the ever-increasing energy demand. There are different adequacy indices for generating system adequacy assessment. They are as follows:

- Loss of load probability (LOLP)
- Loss of load expectation (LOLE)
- Loss of load frequency (LOLF)
- Loss of load duration (LOLD)

When the load demand exceeds, the available generating capacity loss of load occurs. LOLP gives the probability that the load demand is greater than available generating capacity [16]. LOLE is the average number of days or hours in a given period in which the daily peak load or hourly load is expected to exceed the available generating capacity [16]. Mathematically, LOLE is given as in (20.39)

$$\text{LOLE} = \sum_{i \in S} p_i T \quad (20.39)$$

where p_i is the probability of system state i , and S is the set of all system states associated with loss of load.

LOLF identifies the expected frequency of encountering a deficiency [16]. Mathematically, LOLF is given as in (20.40)

$$\text{LOLF} = \sum_{i \in S} F_i - f_i \quad (20.40)$$

where F_i is the frequency of departing system state i , and f_i is the portion of F_i which corresponds to not going through the boundary between loss of load and no loss of load state.

LOLD is the ratio of LOLE and LOLF. LOLD signifies the expected duration for which load demand exceeds the available generating capacity.

LOLF and LOLD provide physical characteristics and additional parameters of the system which are helpful to power system planners.

For further illustration, let us consider a generating system having 2 generating units of capacity 10 MW, each of forced outage rate 0.02. The load model is

considered to be a constant load of 15 MW. The generating system which is a combination of 2 generating units can be in 3 states. These 3 states are as follows:

- i. State 1 in which it delivers zero output. In this state, both the generating units are in downstate. The probability of occurrence of this state is $0.02 * 0.02 = 0.0004$.
- ii. State 2 in which it delivers 10 MW. In this, only one of the generating units is in upstate and other is in downstate. The probability of occurrence of this state is $2 * 0.02 * 0.98 = 0.0392$.
- iii. State 3 in which it delivers 20 MW. In this state, both the generating units are in upstate. The probability of occurrence of this state is $0.98 * 0.98 = 0.9604$.

Since the peak load considered here is 15 MW, loss of load will occur in state 1 and state 2. LOLP is the summation of the probability of occurrence of state 1 and state 2. Further, LOLE is $365 * \text{LOLP}$ day/year.

For the aforementioned generating system, let 'a' be the frequency of occurrence of state for which there is no loss of load and 'b' is the frequency of occurrence of state for which there is loss of load. Mathematically, LOLF is the subtraction of these two frequencies.

20.6.1 Adequacy Analysis by Monte Carlo Simulation

A typical deterministic method cannot be used to evaluate microgrid reliability because of the random behavior of renewable sources involved in microgrid. Monte Carlo simulation which is a probabilistic method can be used to determine the adequacy indices of a microgrid. The basic steps involved for the evaluation of adequacy indices of microgrid are as follows [32]:

- i. First, the generation model of the unit sources used in microgrid is constructed. For conventional units like DG, a binary two-state model is constructed, and for renewable sources such as wind turbine and solar PV cell, the generation model is constructed considering the uncertainty in wind speed and solar irradiation, respectively, as illustrated in the previous section.
- ii. The time versus power output curve of all the unit sources is superimposed to obtain the net power output of the microgrid.
- iii. The power output curve and load curve are compared to obtain the different adequacy indices.

Figure 20.25 shows the LOLP evaluation for hybrid microgrid sources where total generation is compared with load demand in KW to evaluate LOLP. *TTF* and *TTR* are being in failure/year and repair/hour, respectively. The total generation is an aggregation of generation from DG, wind turbine, and solar PV cell, respectively.

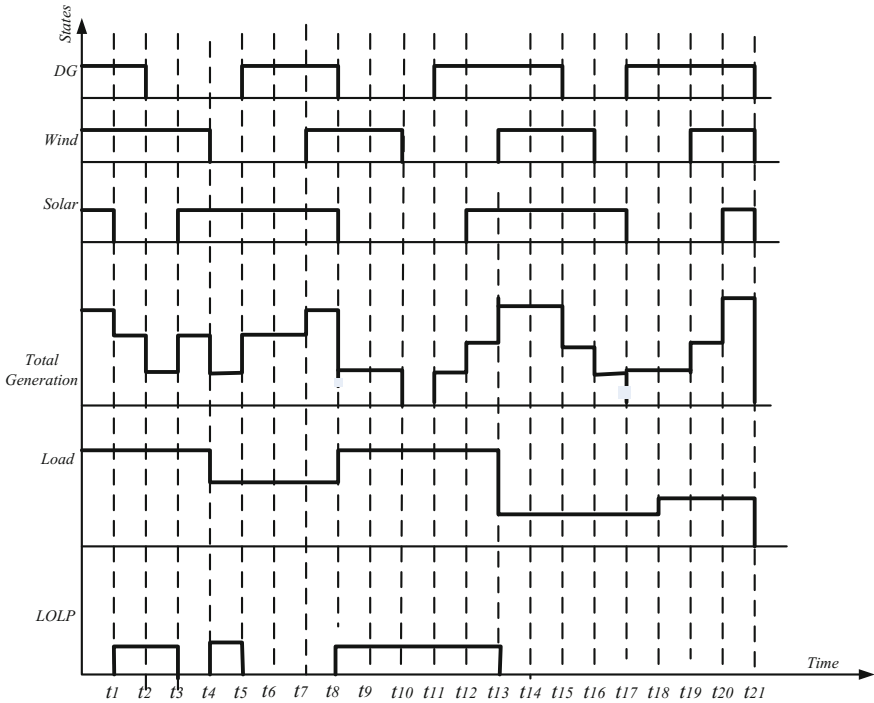


Fig. 20.25 TTF and TTR graphs for the evaluation of LOLP for hybrid microgrid sources

20.6.2 Adequacy Analysis by Fault Tree

Fault tree analysis is good at signifying the logical relation among system failure, structure of the complex system, and the failures of components of the system. The fault tree for the evaluation of adequacy indices of microgrid is illustrated in Fig. 20.26.

Here, it is considered that the wind turbine and solar PV cell can give either rated output or no output. For computational simplicity, the intermediate states of wind turbine are not considered. The capacity of all the unit sources is considered to be 50 KW, and peak load is 100 KW.

Based on this truth table developed, the expression of LOLP is given by (20.41):

$$\begin{aligned}
 P(\text{LOLP} = 1) = & \{ \{ (1 - P(\text{DG})) * (1 - P(\text{WTG})) * (1 - P(\text{solar})) * P(\text{load}) \} \\
 & + \{ (1 - P(\text{DG})) * (1 - P(\text{WTG})) * P(\text{solar}) * P(\text{load}) \} \\
 & + \{ (1 - P(\text{DG})) * P(\text{WTG}) * (1 - P(\text{solar})) * P(\text{load}) \} \\
 & + \{ P(\text{DG}) * (1 - P(\text{WTG})) * (1 - P(\text{solar})) * P(\text{load}) \} \}
 \end{aligned}
 \tag{20.41}$$

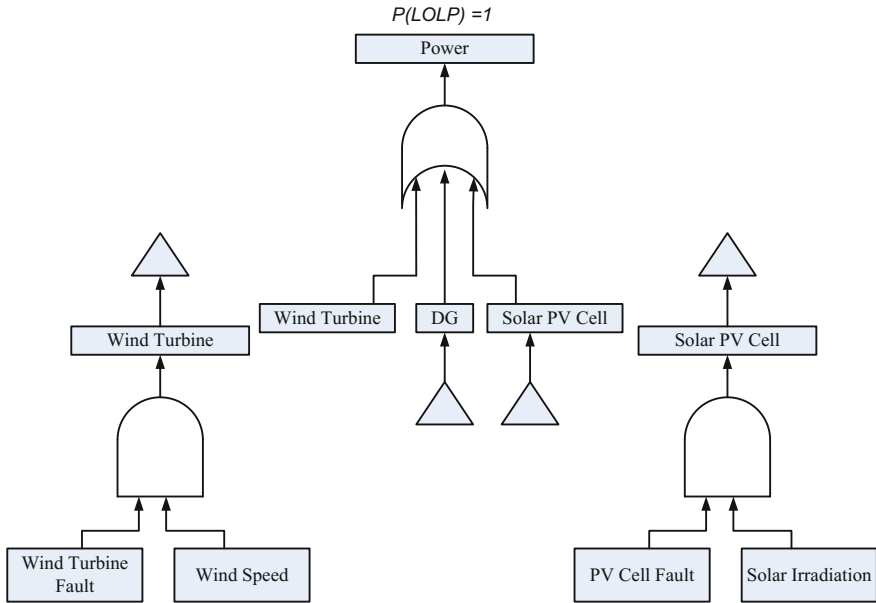


Fig. 20.26 Fault tree of microgrid for the evaluation of adequacy indices

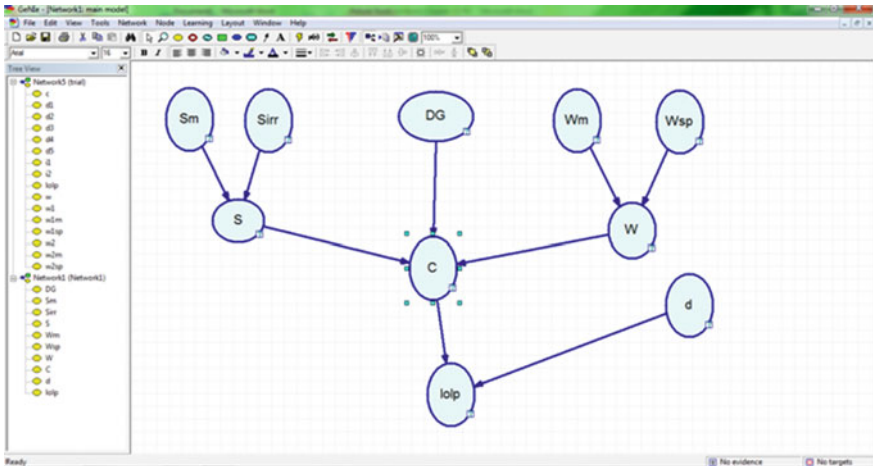


Fig. 20.27 Bayesian model of microgrid for the evaluation of adequacy indices

20.6.3 Adequacy Analysis by Bayesian Network

Bayesian network has the capacity to deal with uncertainties involved in case of microgrid. The Bayesian network of microgrid is illustrated below in Fig. 20.27.

Here, S_m represents the event of solar PV cell in downstate due to internal fault, S_i represents no power output from PV cell due to low solar irradiation, S is the net power output from PV cell, DG represents power output from diesel generator, W_m represents the event of wind turbine in downstate due to internal fault, W_s represents no power output from wind turbine due to inadequate wind speed, W represents net power output from wind turbine, c represents net power output from the microgrid, and d represents the load model.

The expression for LOLP is given by Eq. (20.42)

$$\begin{aligned}
 P(\text{LOLP} = 1) &= P(\text{LOLP}|c, d) * P(l) * P(t|\text{DG}, W, S) * P(\text{DG}) \\
 &* P(W|W_m, W_s) * P(W_m) * P(W_s) \\
 &* P(S|S_m, S_{\text{irr}}) * P(S_m) * P(S_{\text{irr}})
 \end{aligned} \tag{20.42}$$

20.7 Effect of Extreme Weather Condition on Reliability of Microgrid

Wind turbine and solar PV cell being outdoor equipment are affected by extreme weather condition. The system reliability of wind turbine as well as solar PV cell decreases for extreme weather condition. The system reliability of wind turbine and solar PV cell is enervated by inadequate wind speed and low solar irradiation, respectively. The failure rate of solar PV cell is very much affected by temperature and relative humidity. Repair rate is considered independent of weather. The relationship between failure rate and temperature is as given in (20.43) [36]:

$$\text{Failure rate, } f_{\text{temp}} = f_0 * \exp^{-a} \tag{20.43}$$

where $a = E/K * (1/T - 1/T_0)$, $T_0 = 298$ K, K is Boltzmann constant, $E = 0.8$ eV, T is the temperature at which failure rate is to be evaluated, and f_0 is the failure rate for normal temperature.

The relationship between relative humidity and failure rate is as given in (20.44) [36]:

$$\text{Failure rate, } f_{\text{RH}} = f_0 \left(\frac{\text{RH}_1}{\text{RH}_0} \right)^n \tag{20.44}$$

where $n = 2.6$, $\text{RH}_0 = 65\%$, and RH_1 is the relative humidity at which failure rate is to be evaluated.

The wind turbine also being outdoor equipment is very much vulnerable to atmospheric condition. The failure rate of wind turbine is majorly like wind speed. The relationship between wind speed and failure rate of different components is analyzed by Mamdani fuzzy inference [37].

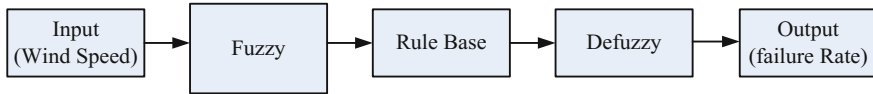


Fig. 20.28 Mamdani fuzzy inference

Figure 20.28 shows the Mamdani fuzzy inference for exploring the effect of wind speed on failure rate of different components of wind turbine. The input speed is categorized into three categories: low (3–5) m/sec, medium (5–12) m/sec, and high (12–25) m/sec. Similarly, the output failure rate is categorized into three categories: low, medium, and high. The range selected for the failure rate varies for different components. Since system reliability and power output from renewable sources are affected by extreme weather condition, the adequacy indices deteriorate.

20.8 Reliability Improvement of Microgrid

One of the approaches of improving reliability is to use superior components with less failure rates, but that will increase the cost involved in the production of components [38]. Due to the limitations imposed in terms of cost nowadays, the reliability of a system is increased by incorporating redundancy. Redundancy involves the creation of new parallel paths in the system. There are many methods for the introduction of redundancy. Some of the methods are discussed below.

20.8.1 Element Redundancy

Let C_1 be an element with reliability r_1 . Another element C_2 with reliability r_2 is connected with C_1 in parallel as shown in Fig. 20.29.

The system reliability of the resulting system after the addition of elemental redundancy is given by (20.45):

$$r_{\text{sys_ER}} = r_1 + r_2 - r_1 r_2 \quad (20.45)$$

which is greater than r_1 .

20.8.2 Component Redundancy

In component redundancy, a redundant path is provided for each component as shown in Fig. 20.30.

Fig. 20.29 Elemental redundancy

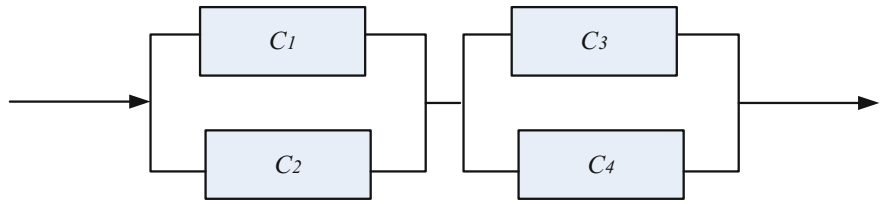
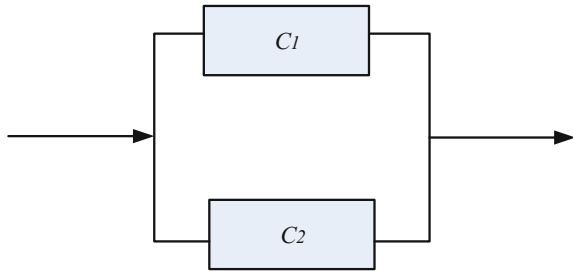


Fig. 20.30 Component redundancy

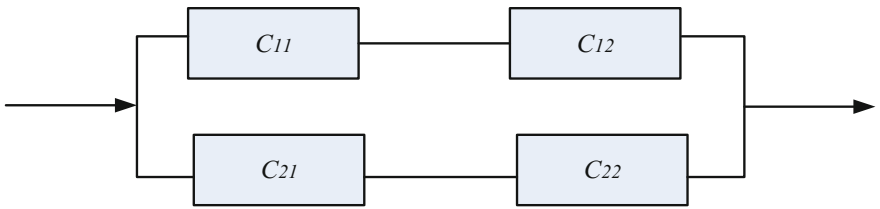


Fig. 20.31 Unit redundancy

The reliability of C_1 and C_2 is r_1 and that of C_3 and C_4 is r_2 , respectively. And system reliability of the system after adding redundancy is as follows:

$$r_{\text{sys_CR}} = \{1 - (1 - r_1)^2\} * \{1 - (1 - r_2)^2\} \tag{20.46}$$

20.8.3 Unit Redundancy

Duplication at unit level is called unit redundancy. Incorporation of unit redundancy is easier than component redundancy, but component redundancy gives better reliability compared to unit redundancy. Unit redundancy is as shown in Fig. 20.31 [38].

The reliability of C_{11} and C_{21} is r_1 and that of C_{12} and C_{22} is r_2 , respectively. And system reliability of the system after adding redundancy is as given in (20.47)

$$r_{\text{sys_UR}} = 1 - (1 - r_1 r_2) * (1 - r_1 r_2) \tag{20.47}$$

20.8.4 Standby Redundancy

In all the redundancies discussed above, all the components operate simultaneously and as a result face wear and tear during the operation of the system. But in case of standby redundancy, only one redundant component is operating at a time and one or more than one component is considered as standby to take over the operation when the first one fails. Standby redundancy is as shown in Fig. 20.32 [38].

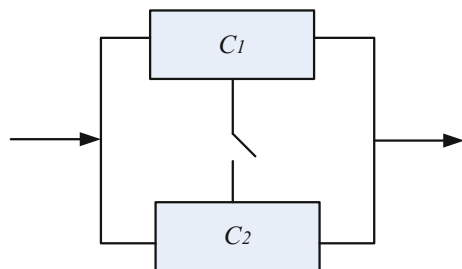
The system reliability as well as adequacy indices of microgrid is affected by extreme weather condition. In order to improve the adequacy indices during extreme weather, redundant units can be added. In order to bolster the performance of microgrid during extreme weather, DGs can be added to the microgrid in the form of standby redundancy.

20.9 Case Study

The case study considered as shown in Fig. 20.33 is a combination of utility grid with microgrid. When the contact S_1 is opened, the microgrid operates in islanded mode. On the other hand, when the contact S_1 is closed, the system operates in grid-fed microgrid mode. The reliability analysis is tested firstly with stand-alone microgrid followed by grid-fed microgrid system. The comparative analysis will help to identify the impact of distributed generation system for reliable and uninterrupted power supply.

The following cases are considered for reliability analysis of stand-alone microgrid:

Fig. 20.32 Standby redundancy



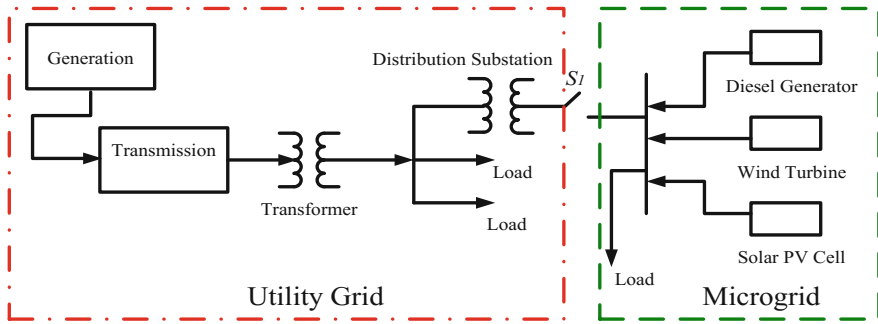


Fig. 20.33 Microgrid considered for analysis

Table 20.14 Failure rate data of different unit sources used in microgrid

Type	Component	Failure rate (occ/year)
Solar PV cell	Solar panel	0.004
	Automatic charge controller	4
	Battery bank	1497
	Convertor	0.5
Wind turbine	Generator	0.021
	Gearbox	0.045
	Convertor	0.067
	Brake	0.005
	Pitch	0.052
	Yaw	0.026
DG	Fuel pump	0.24
	Cooling radiator	0.01
	Generator	0.09
	AVR	0.07

- Case 1:6 diesel generators
- Case 2:4 diesel generators +2 wind turbines
- Case 3:4 diesel generator +2 solar PV cell
- Case 4:4 diesel generator +1 wind turbine +1 solar PV cell

The capacity of DG, wind turbine, and solar PV cell is 1500 KW. The peak load considered is 2250 KW, which can be met easily by 2 DGs. But since the reliability of the DGs cannot be unity, more than 3 DGs are utilized. The failure rates required for reliability evaluation of different components are given as in Table 20.14 [1, 23]. Based on these failure rates, the probability of being in upstate and downstate is evaluated considering an exponential distribution.

Table 20.15 gives the system reliability of different unit sources used in microgrid computed by Monte Carlo simulation, fault tree analysis, and Bayesian network as illustrated in Sect. 20.4. If we compare the system reliability obtained by the three

Table 20.15 System reliability calculation of different unit sources of microgrid for normal weather condition

Type	System reliability by Monte Carlo	System reliability by fault tree	System reliability by Bayesian network
Solar PV cell	0.75	0.812	0.81
Wind turbine	0.945	0.979	0.98
DG	0.987	0.992	0.992

Table 20.16 System reliability and DIF for different unit sources of microgrid by Bayesian network for normal weather condition

Type	Component	DIF	Ranking
Solar PV cell	Panel	9.48×10^{-5}	4
	Automatic charge controller	0.208	2
	Battery bank	0.78	1
	Convertor	0.052	3
Wind turbine	Generator	0.02	5
	Gearbox	0.377	1
	Convertor	0.224	2
	Pitch	0.149	4
	Brake	0.02	5
	Yaw	0.212	3
DG	Fuel pump	0.152	2
	Cooling radiator	0.011	4
	Generator	0.144	3
	AVR	0.714	1

methods, it is seen that the system reliability values are almost same for all three methods. The system reliability of wind turbine obtained by Monte Carlo simulation, fault tree analysis, and Bayesian network are 0.945, 0.979, and 0.98, respectively. The value of system reliability obtained by Monte Carlo simulation is slightly different from the value obtained by other two methods because of the randomly generated *TTF* and *TTR*. The system reliability of DG is 0.992. Similarly, for solar PV cell, the system reliability is 0.81. The system reliability of DG is 0.992 which is the highest compared to the other two. Table 20.16 gives the DIF and component ranking of all the three elements used in the hybrid microgrid for normal weather condition.

It is seen that in case of wind turbine, the DIF of gearbox is 0.377 which is highest, as a result of which it is considered as the most critical component of the wind turbine. Similarly, for solar PV cell, the battery bank is the most critical component with DIF of 0.78. And for DG, AVR is the most critical component with a DIF of 0.714.

Based on these values of system reliability, adequacy indices of the microgrid for all the cases considered can be evaluated for normal weather by taking IEEE RTS load model as given in Table 20.17. The DG can either give full output

Table 20.17 Different clusters of solar irradiation, wind velocity, and power output [40]

Wind velocity (m/sec)	Power output (MW)	Solar irradiation (kW/m ²)	Power output (MW)
(0–5)	(0–300)	(0–250)	(0–500)
(5–10)	(300–600)	(250–500)	(500–1000)
(10–15)	(600–900)	(500–750)	(1000–1500)
(15–20)	(900–1200)	(750–1000)	1500
(20–25)	(1200–1500)		

Table 20.18 IEEE RTS load model [39]

Percentage of peak load	Probability
0.9900	0.0006
0.9505	0.0034
0.9210	0.0061
0.8896	0.0171
0.8612	0.0236
0.8348	0.0371
0.8068	0.0482
0.7782	0.0499
0.7467	0.0517
0.7126	0.0590
0.6792	0.0711
0.6481	0.0738
0.6179	0.0754
0.5866	0.0630
0.5519	0.0695
0.5184	0.0805
0.4864	0.0949
0.4512	0.0769
0.4149	0.0690
0.3733	0.0292

or zero output. But the renewable energy resources such as solar PV cell and wind turbine can be in some intermediate states depending on atmospheric condition. The different possible states of these renewable sources considering their random behavior are obtained by proper clustering technique and are given as in Table 20.18.

Tables 20.19 and 20.20 report the adequacy indices obtained by Monte Carlo simulation, fault tree analysis, and Bayesian network, respectively. From the results obtained, it is clear that the adequacy indices obtained by all three methods tally with each other. The LOLP for case 1 is 0.0029456 which signifies that the probability of load demand exceeding available capacity is 0.0029456, and LOLE is 1.07 day/year which signifies that in one year, the generating capacity is less than load demand for approximately 1 day. LOLF and LOLD for case 1 are 0.0558

Table 20.19 Adequacy index calculation of stand-alone microgrid for normal weather condition by Monte Carlo simulation and fault tree analysis

Case	Monte Carlo				Fault tree	
	LOLP	LOLE (day/year)	LOLF (occ/year)	LOLD (day/occ)	LOLP	LOLE (day/year)
1	0.0022456	0.819644	0.0528	15.52	0.0029456	1.07
2	0.003578	1.30597	0.0817	16.25	0.004558	1.6636
3	0.0044177	1.61	0.0826	19.49	0.0064175	2.3423875
4	0.003135	1.14427	0.0551	19.29	0.003425	1.250

Table 20.20 Adequacy indices of stand-alone microgrid for normal weather condition by Bayesian network [40]

Case	LOLP	LOLE (day/year)	LOLF (occ/year)	LOLD (day/occ)
1	0.0029456	1.07	0.0558	19.16
2	0.004578	1.67097	0.0837	19.96
3	0.0064177	2.342	0.0846	27.688
4	0.003435	1.253775	0.0651	19.254

Table 20.21 Severity ranking of stand-alone microgrid by Bayesian network

Case 2			Case 3			Case 4		
Unit	DIF	Rank	Unit	DIF	Rank	Unit	DIF	Rank
DG	0.65	1	DG	0.71	1	DG	0.765	1
Wind turbine	0.043	2	Solar PV Cell	0.058	2	Wind turbine	0.071	2
						Solar PV cell	0.0460	3

occ/year and 19.16 day/occ, respectively. These two indices indicate the expected frequency and duration of the deficiencies: the LOLP of case 2, i.e., the combination of DG and wind turbine is 0.004578 and the LOLP of case 3, i.e., the combination of DG and solar PV is 0.0064177, respectively. Though the LOLP is higher compared to case 1, they are preferred because of their renewable form and environmentally friendly behavior. Moreover, the operating cost of case 1 is high compared to the other combinations considered in the case study. The LOLP, LOLE, LOLF, and LOLD for case 4 are least compared to case 2 and case 3, thereby providing the advantage of hybrid combination. The lesser the values of the reliability indices, the more reliable the system is. Case 4 utilizes two forms of energy resources from the nature with zero emission, leading to a pollution-free environment.

The severity ranking of different combinations of the hybrid microgrid is given as in Table 20.21. For case 2, the DIF of DG is 0.65 and that of wind turbine is 0.043. So DG is more crucial compared to that of wind turbine. But the DIF of DG

Table 20.22 Adequacy indices for IEEE RTS load with supply from power utility grid

Reserve power (KW)	LOLP	LOLE (day/year)
100	1	365
300	1	365
600	1	365
750	1	365
850	0.987	360.255

for case 3 is more compared to that of case 2. This signifies that in a DG solar-based microgrid, DG must be given more maintenance compared to that of DG wind-based microgrid. DG is the most critical followed by wind turbine and solar PV cell for case 4 which is a hybrid combination of all three sources. This analysis is significant for meeting the maintenance policy of the microgrid resources for uninterrupted and quality power. The entire analysis is done for stand-alone microgrid when there is complete unavailability of supply from utility grid.

If the supply is taken just from utility grid, considering the availability of utility grid of reliability 0.998 with reserve power of 100 KW after meeting its own load requirements [41]. It is observed that the LOLP of the IEEE RTS load is 1 with LOLE of 365 days/year. This signifies that the total load will be in complete blackout even when the reliability of utility grid is 0.998. The same condition will persist with the increase of reserve to 750 KW. With 850 KW reserve, the utility grid will be able to meet only 1.3% of the requirement for just around 5 days as given in Table 20.22.

Thus, increasing the reserve to meet the additional load requirement is completely uneconomical. Moreover, the development of new generating stations with conventional resources will be an additional burden on the gradual depleting fossil fuel. Thus, with the geographical sprawl and ever-increasing demand of uninterrupted power, the distributed generation is gaining importance.

Further, the analysis is extended considering a combination of utility grid of reliability 0.998 with reserve power of 100 KW and microgrid. In such case, the results improve compared to the stand-alone microgrid as given in Tables 20.19 and 20.20. The adequacy indices for microgrid with supply from power utility grid are tabulated in Table 20.23.

In real time, bidirectional power flow occurs in case of grid-connected microgrid as shown in Fig. 20.33. The microgrid has the property to not only meet its own load requirement but also can serve the utility grid, thus participating in energy bidding and gaining revenues. The utility grid and microgrid share their power only after meeting their own load requirements.

The entire reliability analysis for stand-alone microgrid is further extended and tested with extreme weather condition. This is because two major renewable sources such as wind turbine and solar PV cell are affected by extreme weather conditions.

Failure rate range and the defuzzified values of different components of wind turbine which are used as input of Mamdani fuzzy inference are shown in Table 20.24.

Table 20.23 Adequacy indices for microgrid with supply from power utility grid and microgrid

Case	LOLP	LOLE (day/year)	LOLF (occ/year)	LOLD (day/occ)
1	0.0021458	0.783217	0.0526	14.9
2	0.004187	1.528255	0.0811	18.84
3	0.0059180	2.16007	0.0829	26.5
4	0.003122	1.139	0.051	22.7

Table 20.24 Failure rate for different components of wind turbine [8]

Component	Failure rate (occ/year)					
	Low		Medium		High	
	Fuzzified	Defuzzified	Fuzzified	Defuzzified	Fuzzified	Defuzzified
Generator	(0.021–0.03421)	0.0270	(0.0342–0.093)	0.0551	(0.093–0.105)	0.0990
Gearbox	(0.045–0.075)	0.0616	(0.075–0.16)	0.1072	(0.16–0.18)	0.1723
Convertor	(0.67–0.09)	0.0789	(0.09–0.165)	0.1251	(0.165–0.268)	0.2144
Pitch	(0.052–0.092)	0.0720	(0.092–0.157)	0.1153	(0.157–0.208)	0.1843
Brake	(0.005–0.007)	0.0060	(0.007–0.01)	0.0100	(0.01–0.02)	0.0182
Yaw	(0.026–0.05)	0.0376	(0.05–0.09)	0.0700	(0.09–0.104)	0.0980

Table 20.25 Failure rate of different components of solar PV cell for extreme weather

Solar PV cell				
Component	Failure rate at 308 K	Failure rate at 310 K	Failure rate at 75% relative humidity	Failure rate at 85% relative humidity
Panel	0.010992	0.0112	0.00588	0.00824
Automatic charge controller	10.992	11.2	5.88	8.24
Battery bank	4113.756	4191.6	2200.59	3083.82
Convertor	1.375	1.4	0.735	1.03

Table 20.26 System reliability of wind turbine and PV cell for extreme weather [8]

Type	Cause	System reliability
Solar PV cell	Temperature 308 K	0.586
	Temperature 310 K	0.583
	Relative humidity 75%	0.738
	Relative humidity 85%	0.662
Wind turbine	Low wind speed	0.967
	Medium wind speed	0.94
	High wind speed	0.927

The failure rates of different components of PV cell for extreme weather conditions as analyzed by Mamdani fuzzy inference are reported in Table 20.25. Based on these failure rates of different components obtained for extreme weather, the system reliability of wind turbine and solar PV cell is computed as in Table 20.26.

For solar PV cell, the system reliability is 0.586 at 308 K and is 0.583 at 310 K, respectively. Both the values are quite less compared to the normal weather condition. Again, the system reliability of PV cell is 0.738 for relative humidity of 75% and is 0.662 at relative humidity of 85%, respectively. Thus, it is observed that there is a decreasing trend in system reliability with increasing values of both temperature and relative humidity. Similarly, for wind turbine, system reliability for low, medium, and high wind speed is 0.967, 0.94, and 0.927, respectively. These values also indicate that system reliability decreases for increasing wind speed. But the effect of atmospheric condition on wind turbine is less than that of a PV cell. This is because of the constructional efficiency and the use of safety sub-system in wind turbine.

Similarly, the adequacy indices are also deteriorated because of extreme weather condition. On analyzing case 2 which is an amalgamation of diesel generator and wind turbines, wind turbine being outdoor equipment is affected by extreme weather condition. Two criteria of extreme weather condition are considered for analysis. First criterion is with the wind velocity exceeding 25 m/sec, and the second criterion is with wind velocity exceeding 20 m/sec. For criterion 1, there is no power output from wind turbine as wind turbine stops working. For criterion 2, both system reliability and power output from wind turbine are affected as given in Table 20.26. Similarly, case 3 which is a combination of diesel generator and solar PV cell is affected by extreme weather condition. The only criterion considered for analysis of solar PV cell is high ambient temperature. Case 4 is a combination of all the 3 sources. The two criteria of extreme weather condition are firstly wind velocity >25 m/sec and ambient temperature normal and secondly high ambient temperature and wind velocity within range. For criterion 1, both power output and system reliability of solar PV cell are not affected by no power output from wind turbine. This is because of the sophisticated design conditions which automatically stops working for high wind velocity. For criterion 2, wind turbine is not affected and the system reliability of solar PV cell decreases.

Table 20.27 gives the adequacy indices for extreme weather condition. The LOLP of case 2 for extreme weather condition is 0.0082289 which is high as compared to normal weather as shown in Table 20.19. The LOLE, LOLF, and LORD of case 2 for extreme weather condition are 3.0035, 0.0959, and 20.51, respectively, which also follow similar trend when compared to that of normal

Table 20.27 Adequacy indices for stand-alone microgrid in extreme weather condition

Case	Extreme weather							
	Criterion 1				Criterion 2			
	LOLP	LOLE (day/year)	LOLF (occ/year)	LORD (day/occ)	LOLP	LOLE (day/year)	LOLF (occ/year)	LORD (day/occ)
2	0.0082289	3.0035	0.0959	31.96	0.005176	1.8892	0.0929	20.38
3	0.00811655	2.96015	0.09419	31.29				
4	0.00818	2.98	0.0946	31.50	0.00505	1.82	0.0905	20.16

Table 20.28 Adequacy indices for stand-alone microgrid with addition of standby DG

Case	Extreme weather							
	Criterion 1				Criterion 2			
	LOLP	LOLE (day/year)	LOLF (occ/year)	LOLD (day/occ)	LOLP	LOLE (day/year)	LOLF (occ/year)	LOLD (day/occ)
2	0.00511	1.86515	0.0867	20.51	0.004976	1.81624	0.0919	20.18
3	0.0050	1.824	0.08599	20.21				
4	0.0049	1.79	0.084	21.30	0.003635	1.32	0.0671	19.78

weather condition as given in Table 20.19. The LOLP of case 3 for extreme weather condition is 0.00811655 which is also high compared to that of normal weather condition. Other cases and other adequacy indices also follow similar pattern.

Table 20.28 gives the adequacy indices of hybrid microgrid after addition of standby DG. The improvement of adequacy indices is clear from the results obtained.

The system reliability of different unit sources used in microgrid is evaluated in this section. The system reliability of DG is high compared to the renewable resources. But it is seen that DG unlike other renewable resources is unaffected by environmental factors such as wind speed, temperature, and relative humidity. But the use of DG is becoming less popular nowadays because of its high operating cost and environmental degradation associated with it. On the other hand, renewable energy resources are gaining popularity because of its easy availability and environmentally friendly nature. Thus, the future works possible are as follows:

- i. Optimal planning of microgrid considering cost, reliability, and environmental factors
- ii. Location-based planning of microgrid
- iii. Evaluation of risk indices of microgrid
- iv. Determination of optimal maintenance policy of microgrid

20.10 Conclusion

The applications of microgrid which is an amalgamation of conventional units with renewable sources are increasing day by day. Microgrids are mostly used for rural electrification as construction of transmission lines is always not possible for villages located in remote areas due to geographical constraints. In such cases, microgrid is an excellent option for providing power supply at cheap rates. Industrial and mining units are mostly established in remote and isolated areas where connection with the utility grid is always not possible. In countries with limited power generation capacity, grid integration is always a chief concern. In such cases, the development of islanded microgrid by utilizing the available renewable resources for meeting the power demand is the only viable option.

Solar- or wind energy-based microgrids are set up nowadays in order to relieve the utility grid from excessive power demand.

Higher penetration of renewable resources has increased energy efficiency and reduced pollution as well as congestion of conventional units, as a consequence of which microgrids have emerged as combination of renewable units with conventional units. But reliability and adequacy analysis of microgrids is a major challenge. The different techniques of reliability analysis of microgrid, the advantages of Bayesian network over the other existing traditional methods, and the adequacy analysis of a hybrid microgrid are performed. The effect of extreme weather conditions on different adequacy indices is also analyzed. Further, different techniques for improving reliability are also discussed.

References

1. Banerji A, Sen D, Bera AK, Ray D, Paul D, Bhakat A, Biswas SK (2013) Microgrid: a review. In: Global humanitarian technology conference: South Asia satellite (GHTC-SAS), Trivandrum, India, 23–24 Aug 2013. IEEE, pp 27–35
2. Zhang J, Yang Z, Zhou Q (2014) Reliability assessment for microgrid with multi-energy demand. In: 2014 China international conference on electricity distribution (CICED), Shenzhen, China, 23–25 Sept 2014. IEEE, pp 1163–1167
3. Giacomoni AM, Goldsmith SY, Amin SM, Wollenberg BF (2012) Analysis, modeling, and simulation of autonomous microgrids with a high penetration of renewables. In: IEEE power and energy society general meeting, San Diego, California USA, 22–26 July 2012. IEEE, pp 1–6
4. Wang L, Singh C (2008) Population-based intelligent search in reliability evaluation of generation systems with wind power penetration. *IEEE Trans Power Syst* 23(3):1336–1345
5. Youli S, Nagasaka K (2010) Monte Carlo simulation method used in reliability evaluation of a laboratory-based micro grid. In: Proceedings of the international multi conference of engineers and computer scientists, vol 2. Kowloon, Hong Kong, 17–19 Mar 2010
6. Li Z, Yuan Y, Li F (2010) Evaluating the reliability of islanded microgrid in an emergency mode. In: 45th International conference on universities power engineering (UPEC), Cardiff, Wales, 1–3 Sept 2010. IEEE, pp 1–5
7. Shi X, Bazzi AM (2015) Fault tree reliability analysis of a microgrid using Monte Carlo simulations. In: 2015 IEEE power and energy conference at Illinois (PECI), Illinois, 20–21 Feb 2015. IEEE, pp 1–5
8. Deb S, Ghosh Mohanta DK (2016) Reliability analysis of PV cell, wind turbine and diesel generator by using Bayesian network. In: International conference on electrical, electronics and optimization, ICEEOT, Chennai, India, 3–5 Mar 2016. IEEE, pp 2714–2719
9. Kale SA, Jagtap PP, Helonde JB (2011) Role of micro sources within micro grid. In: 4th international conference on emerging trends in engineering and technology, Port Louis, Mauritius, 18–20 Nov 2011. IEEE, pp 174–179
10. Smith CA, Donovan MD, Bartos MJ (1990) Reliability survey of 600 to 1800 kW diesel and gas-turbine generating units. *IEEE Trans Ind Appl* 26(4):741–755
11. Htay M, Win KS (2008) Design and construction of automatic voltage regulator for diesel engine type stand-alone synchronous generator. *World Acad Sci Eng Technol* 42:652–658
12. Su C, Fu YQ (2014) Reliability assessment for wind turbines considering the influence of wind speed using Bayesian network. *Eksplotacjai Niezawodność* 16:1–8

13. Ghaedi A, Abbaspour A, Fotuhi-Firuzabad M, Moeini-Aghtaie M (2014) Toward a comprehensive model of large-scale DFIG-based wind farms in adequacy assessment of power systems. *IEEE Trans Sustain Energy* 5(1):55–63
14. Blaabjerg F, Liserre M, Ma K (2012) Power electronics converters for wind turbine systems. *IEEE Trans Ind Appl* 48(2):708–719
15. Sharma D, Rana JK, Gupta S (2010) Measurement of reliability parameters for solar (PV) system by employing Boolean function technique. *Res J Math Stat* 2(2):81–85
16. Li W (2013) Reliability assessment of electric power systems. Springer Science and Business Media
17. Baig AA, Ruzli R, Buang AB (2013) Reliability analysis using fault tree analysis: a review. *Int J Chem Eng Appl* 4(3):1–5
18. Volkanovski A, Čepin M, Mavko B (2009) Application of the fault tree analysis for assessment of power system reliability. *Reliab Eng Syst Saf* 94(6):1116–1127
19. Song G, Chen H, Guo B (2014) A layered fault tree model for reliability evaluation of smart grids. *Energies* 7(8):4835–4857
20. Javadi MS, Nobakht A, Meskarbashee A (2011) Fault tree analysis approach in reliability assessment of power system. *Int J Multidisc Sci Eng* 2(6):46–50
21. Saxena A, Manglani T (2013) Enhancing computer system reliability using fault tree analysis. *Int J Recent Res Rev* 6:12–17
22. Kohda T (2006) A simple method to derive minimal cut sets for a non-coherent fault tree. *Int J Autom Comput* 3(2):151–156
23. Mahadevan S, Zhang R, Smith N (2001) Bayesian networks for system reliability reassessment. *Struct Saf* 23(3):231–251
24. Limin H, Yongli Z, Gaofeng F (2002) Reliability assessment of power systems by Bayesian networks. In: International conference on power system technology, PowerCon, vol 2, Kuming, China, 13–17 Oct 2002. IEEE, pp 876–879
25. Santana P, Williams B (2012) A bucket elimination approach for determining strong controllability of temporal plans with uncontrollable choices. In: 26th conference on artificial intelligence. Ontario, Canada, July 2012, pp 2453–2454
26. Daemi T, Ebrahimi A, Fotuhi-Firuzabad M (2012) Constructing the Bayesian network for components reliability importance ranking in composite power systems. *Int J Electr Power Energy Syst* 43(1):474–480
27. Daemi T, Ebrahimi A (2012) Evaluation of components reliability importance measures of electric transmission systems using the Bayesian network. *Electric Power Compon Syst* 40(12):1377–1389
28. Hilber P, Bertling L (2007) Component reliability importance indices for electrical networks. In: International power engineering conference (IPEC). Singapore, 3–6 Dec 2007. IEEE, pp 257–263
29. Meng FC (1996) Comparing the importance of system components by some structural characteristics. *IEEE Trans Reliab* 45(1):59–65
30. Wang W, Loman J, Vassiliou P (2004) Reliability importance of components in a complex system. In: Reliability and maintainability, annual symposium-RAMS. Los Angeles, CA, USA. IEEE, pp 6–11
31. Espiritu JF, Coit DW, Prakash U (2007) Component criticality importance measures for the power industry. *Electric Power Syst Res* 77(5):407–420
32. Ghahderijani MM, Barakati SM, Jamshidi A (2012) Application of stochastic simulation method in reliability assessment of a PV-Wind-Diesel-SOFC hybrid microgrid. *Int J Eng Technol* 4(5):586–589
33. Ghahderijani MM, Barakati SM, Tavakoli S (2012) Reliability evaluation of stand-alone hybrid microgrid using Sequential Monte Carlo simulation. In: 2nd Iranian conference on renewable energy and distributed generation. Tehran, Iran, 1–3 Mar 2012. IEEE, pp 33–38
34. Fang LB, Cai JD (2011) Reliability assessment of microgrid using sequential Monte Carlo simulation. *J Electron Sci Technol* 9(1):31–34

35. Wei H, Zijun H, Li F, Hongliang T, Li Z (2011) Reliability evaluation of microgrid with PV-WG hybrid system. In: 4th international conference on electric utility deregulation and restructuring and power technologies (DRPT). Weihai, Shandong, 6–9 July 2011. IEEE, pp 1629–1632
36. Mishra PR, Joshi JC (1996) Reliability estimation for components of photovoltaic systems. *Energy Convers Manag* 37(9):1371–1382
37. Fotuhi M, Ghafouri A (2007) Uncertainty consideration in power system reliability indices assessment using fuzzy logic method. In: Conference on power engineering, 2007 large engineering systems. Montreal, Que, 10–12 Oct 2007. IEEE, pp 305–309
38. Srinath LS Concepts in reliability. Affiliated East West Press, New Delhi
39. Li W (2013) Reliability assessment of electric power systems using Monte Carlo methods. Springer Science and Business Media
40. Deb S, Ghosh D, Mohanta DK (2016) Adequacy analysis of stand alone hybrid microgrid by using Bayesian network. In: 5th international conference on computation of power, energy, information and communication (ICCPEIC), Melmaruvathur, India, 20–21 Apr 2016. IEEE, pp 331–336.
41. Hammons Thomas J, Nikolai V (2010) Power industry reliability coordination in Asia in a market environment. *Int J Eng Bus Manag* 2(1):009–022

Chapter 21

Economic Aspects of Distributed Generation

Ponnaganti Pavani and Sri Niwas Singh

21.1 Introduction

Planners of distribution companies (DisCos) continually take measures for developing new planning strategies to meet the load growth and provide a reliable electricity supply at minimum life cycle cost. In the past, the capacity investment planning studies for serving the forecasted load demand in the distribution systems are carried out by considering the addition of new substations or expanding the existing substation capacity and associated new feeder requirements involving huge capital. In the present days, competitive electricity market forces the DisCo planners to investigate the economical and technical feasibilities of new capacity expansion alternatives such as distributed generation (DG) [1]. DG can be defined as a small-scale generating unit located close to the load being served. A wide variety of DG technologies exists such as wind turbines, photovoltaic, biomass, micro-turbines, fuel cells, batteries, etc. Both the DisCos and/or the customers can invest in and operate DG units. The integration of DG as a generating source at the distribution level made the network an active (generating power) network. The DG in the distribution network plays a significant role in the DisCos operation, structure, design and expansion issues. DG technologies, their benefits and concepts, and their beneficial effect on the electricity market make credible alternatives in the DisCo planning problem. Investment in DG is a very attractive distribution planning option in the case where the cost of un-served load is very costly or availability of power is for limited period.

The opening of electricity markets in many countries has led to a clear separation between generation, transmission and distribution activities in order to find the

P. Pavani (✉)
Aalborg University, Aalborg, Denmark
e-mail: pap@et.aau.dk

S.N. Singh
IIT Kanpur, Kanpur, India

operational range which is more secure, reliable and economic [2]. DG is one of the new system planning options [3] which should be investigated in combination with the traditional distribution system planning options. Traditionally, distribution companies were purchasing energy from wholesale electricity markets to distribute the power to the final customers. Nevertheless, the restructuring process of the electricity sector has stimulated the introduction of new agents and the unbundling of traditional DisCo into technical and commercial tasks, including the provision of ancillary services with the help of DG [4]. The distribution system planning problem determines the type, capacity, and siting of new distribution equipment, taking capacity restrictions on feeders, voltage drop, demand forecasts, etc. [5]. The economic benefits of the DisCo investing in the DG capacity are evaluated using cost benefit analysis in [6]. In deregulated electricity markets, there is an incentive for DisCo to reduce the loss of distribution systems which can be achieved by distributed generation present in the system [7]. In a deregulated power system, DisCos may wish to determine the costs and benefits of DG from different points of view. It is difficult to find a single configuration and a particular planning method that satisfies each company.

In this chapter, a cost-benefit analysis based on profit maximization is carried out to show the benefits of the DGs allocation and network reconfiguration. Various constraints such as power balance equations, voltage limits, feeder thermal limit and DG generation limits are considered in the problem formulation. It is assumed that the DGs are owned and maintained by distribution utility. The DG minimum capacity limit is varied and its effect on the DisCos profit is evaluated. In this work, the profit margin is also taken into account. The DG types considered in this work are diesel generator (DT), micro-turbine (MT). It is assumed four DGs are present in the system, out of which, two DGs are DT and two DGs are MT. The proposed method is evaluated on standard IEEE 33-node and 69-node test distribution systems.

21.2 DG Cost Evaluation

Cost is one of the important elements in nearly all the distributed generation project evaluations. However, it alone is insufficient for complete analysis. Both reliability and power quality are also essential elements of the decision along with the type of DG selected. But cost is more often not taken in the primary consideration in most of the planning situations, since selecting the lowest cost option may not viable to achieve target reliability and power quality levels. Thus, evaluation of cost is usually the critical element in a DG planning evaluation. Inclusion of all costs is much more important than in traditional transmission and distribution (T&D) planning studies, because DG options often differ significantly among themselves. The operation and maintenance (O&M) costs are rarely included in typical T&D studies, because they usually do not vary significantly. However, O&M differs substantially among various DG options, and differs a great deal from O&M for

T&D, thus it must be considered. In DG studies, energy cost (fuel) often varies a great deal, that this cost must also be included in studies of distribution level generation. Various costs involved in the DG planning are described as below:

- Fixed costs: These costs do not vary as function of output power. The cost of the basic DG unit, itself, is usually a fixed cost. The annual costs of taxes, insurance, inspection, scheduled maintenance, testing, re-certification of a DG unit in service do not depend on run time.
- Variable costs: DG unit's fuel costs do vary with usage i.e., the more it runs, the higher the fuel costs. These are a function of load served. Some types of maintenance and service costs are variable too. High run of DG units needs to be inspected for stress-caused wear and tear (ageing).
- Continuing costs: These are required to keep the facility in operation and include inspection and maintenance, fuel supplies, replacement parts, taxes, insurance, electrical losses, and perhaps other expenditures. They persist as long as the facility is in use. Usually continuing costs are studied on periodic basis such as daily, monthly, or annually.

21.3 Problem Formulation

The DGs type, and number is fixed and the DGs size is the variable in the optimization problem.

- Monte Carlo simulations are carried out to find the network reconfiguration (NR) of the system and optimal DG locations for power loss reduction and reliability improvement.
- The hourly varying distribution network load is considered and it is assumed that electricity price is varying hourly.
- The DG penetration level is considered to be 15% of the total load.
- Two loading conditions—considered are i.e., normal load (no load growth) and 5% load growth.

The DGs planning period (T) is considered to be 15 years.

21.3.1 *Optimal DG Sizing and Siting*

Monte Carlo simulations are carried out to find the optimal DGs (ODGs) location and optimal Network Reconfiguration (NR). The formulation for the ODGs placement and their sizing and optimal NR [8] are given in the following subsection:

- There are four DG variables for any ODGs optimization problem, i.e., type, location, size and number. The fixed variables are type, number and design variables are taken as size, location. The DGs number is fixed to four and types are fixed to diesel generator (DT), micro-turbine (MT).
- All possible DGs combination as a set of four are considered and the optimal DGs sizing is found for real power loss reduction and reliability improvement. Backward/forward sweep load flow algorithm is used for power loss calculation and minimal cut set are used for finding the reliability [9]. The formulation for the sizing of k th DGs combination is given by,

$$\text{Min } w_1 P_{\text{loss}}^k + w_2 Q_{\text{as}}^k \quad (21.1)$$

$$\text{sub.to } P_i^k = \sum_{q=1}^n V_i V_q Y_{iq} \cos(\delta_i - \delta_q - \theta_{iq}) \quad (21.2)$$

$$Q_i^k = \sum_{q=1}^n V_i V_q Y_{iq} \sin(\delta_i - \delta_q - \theta_{iq}) \quad (21.3)$$

$$\sum_{i=1}^n P_{\text{DG}i}^k \leq 0.2 P_{\text{D}} \quad (21.4)$$

$$P_{\text{DG}i}^{\text{min}} \leq P_{\text{DG}i}^k \leq P_{\text{DG}i}^{\text{max}} \quad (21.5)$$

$$V_{\text{min}} \leq V_i^k \leq V_{\text{max}} \quad (21.6)$$

$$S_i^k \leq S_i^{\text{rated}} \quad (21.7)$$

where

$$\sum_{j=1}^2 w_j = 1 \quad (21.8)$$

$$P_{\text{loss}} = \sum_{j=1}^l r_j \frac{P_j^2 + Q_j^2}{\|V_j^2\|} \quad (21.9)$$

$$Q_{\text{as}} = \frac{1}{L} \sum_{s=1}^L Q_s \quad (21.10)$$

where P_{loss}^k , Q_{as}^k are the system real power loss and the average system unreliability for k th DG combination, respectively. P_i^k , Q_i^k are the real and reactive power injections at i th bus for k th DG combination, respectively. r_j is the resistance of the

j th line. V_i, V_q are the voltage at i th and q th buses, respectively. Y_{iq} is the bus admittance matrix iq th element. δ_i, δ_q are the phase angles of i th and q th buses, respectively. θ_{iq} is the phase angle of the bus admittance matrix iq th element. P_{DGi}^k is the real power generation at i th bus for k th DG combination. P_D is the total system demand, $P_{DGi}^{\min}, P_{DGi}^{\max}$ are the lower and upper limits on real power generation of DG at i th bus. V_{\min}, V_{\max} are the lower and limits of voltage. S_l^k and S_l^{rated} are the thermal limit of l th feeder and maximum thermal limit, respectively. L is the number of loads connected at a bus.

21.3.2 Network Reconfiguration

Different binary combinations of tie-switches are considered and preserving system radial nature as primal objective, reconfiguration algorithm is carried for power loss reduction and reliability improvement with the ODGs. The formulation for NR is given by,

$$\text{Min } w_1 P_{\text{loss}} + w_2 Q_{\text{as}} \quad (21.11)$$

$$\text{sub.to } P_i^k = \sum_{q=1}^n V_i V_q Y_{iq} \cos(\delta_i - \delta_q - \theta_{iq}) \quad (21.12)$$

$$Q_i^k = \sum_{q=1}^n V_i V_q Y_{iq} \sin(\delta_i - \delta_q - \theta_{iq}) \quad (21.13)$$

$$P_i = P_{Gi} - P_{Di} \quad (21.14)$$

$$Q_i = Q_{Gi} - Q_{Di} \quad (21.15)$$

$$V_{\min} \leq V_i^k \leq V_{\max} \quad (21.16)$$

$$S_l^k \leq S_l^{\text{rated}} \quad (21.17)$$

21.3.3 Cost/Benefit Analysis

For economic analysis, the costs of the DGs are modelled. The distribution companies are responsible for meeting the committed demand and operation & management of DG installations. The main focus of distribution companies will be on cost reduction along with improving the reliability and power quality of customer service. Cost/benefit analysis is generally applied as a ranking method, to prioritize project. Usually, the cost analysis of a large capital asset is done in a discounted

manner, because some of the costs and much of the production will occur in the future. Present Worth (PW) analysis is a method of measuring and comparing costs and savings that occur at different times on a consistent and equitable basis for decision-making. The utilities do include inflation in their planning and their PW analysis. In such cases, an increment to account for the Inflation Rate (IF) is added to the discount Interest Rate (IR). A relatively low PW factor means that the planning process will more likely select the project and plans that spend today in order to reduce costs tomorrow. The formula for calculating the PW factor [10] is:

$$PWF = \sum_{t=1}^T \left(\frac{1 + IF}{1 + IR} \right)^t \quad (21.18)$$

Use of discounted economic analysis is reasonable for the inclusion of uncertainty in the exact value of future costs and future needs. Expenditure of money that will be spent many years from now is more important. An evaluation method that recognizes this by weighing today's expenses more than tomorrows is simple. Discounting of future costs in this manner is almost universal in regulated utility planning. The PW analysis essentially discounts the value of future costs and savings just because they lie in the future.

Here, a cost evaluation approach is explained for the utility-owned DGs in the distribution system. The objective function is the maximizing profit of the distribution utility with the introduction of DG. The DG locations are chosen to be four. DG cost is composed of the installation cost, emission cost, fuel cost, operation and maintenance cost. DG benefits are composed of loss reduction revenue and power purchase saving due to application of DG. The costs and revenue incomes are expressed as follows.

- (a) **Installation cost:** The cost associated with the capital investment for given DG capacity given by,

$$C_{INS} = \sum_{i=1}^{N_{DG}} P_{DGi} IC_i \quad (21.19)$$

- (b) **Operation cost:** The cost for operating the DG with pre-determined capacity during a time period T_{DGi} . PWF is involved in operation cost, as the money will be spend in the future.

$$C_O = \sum_{i=1}^{N_{DG}} P_{DGi} O_i T_{DGi} \quad (21.20)$$

$$PWF(C_O) = PWF * C_O$$

- (c) **Maintenance cost:** For maintenance cost, the money will be spend in the future, so the PWF is involved. The cost associated for maintaining the installed DG in the network and is given as,

$$C_M = \sum_{i=1}^{N_{DG}} P_{DGi} M_i \quad (21.21)$$

$$PWF(C_M) = PWF * C_M$$

- (d) **Emission cost:** The emission cost of each DG is given by,

$$C_{EM} = \sum_{i=1}^{N_{DG}} P_{DGi} E_{\text{penalty}} E_{\text{factor}_i} T_{DG} \quad (21.22)$$

$$PWF(C_{EM}) = PWF * C_{EM}$$

- (e) **Fuel cost:** The fuel cost of the DG during time period T_{DG} is given as below,

$$C_{FC} = \sum_{i=1}^{N_{DG}} C_{FCi} T_{DG} \quad (21.23)$$

$$C_{FCi} = a_{DGi} P_{DGi}^2 + b_{DGi} P_{DGi} + c_{DGi} PWF(C_{FC}) = PWF * C_{FC}$$

- (f) **Power Purchase Reduction Revenue**

In restructured power system, DisCo purchases its power from electricity market in order to meet the power demand of the customer. The DGs installed by distribution utility are utilized in fulfilling the power demand of its customer and can also be used to sell the generated power and/or charge the batteries during low demand period. The DGs generation sold to the market (grid) during time period T_{DG} ,

$$R_{ES} = \sum_{i=1}^{N_{DG}} P_{DGi} E_{\text{price}} T_{DG} \quad (21.24)$$

$$PWF(R_{ES}) = PWF * R_{ES}$$

(g) Loss Reduction Revenue

Introduction of the DGs in the distribution network reduces the real power loss if properly placed and sized, which is a major concern of distribution utility. The loss reduction revenue in the presence of DGs can be evaluated as:

$$\begin{aligned} R_{LR} &= \Delta P_{\text{loss}} E_{\text{price}} T_{\text{DG}} \\ \text{PWF}(R_{LR}) &= \text{PWF} * R_{LR} \end{aligned} \quad (21.25)$$

where, PWF is the present worth factor, IR is the discount interest rate, IF is the inflation rate and t is the number of years over which payments are made. N_{DG} is the number of DGs in the system; E_{price} is the grid electricity price; E_{penalty} is the pollutant emission penalty of i th DG; E_{factor} is the emission factor of i th DG; T is the total number of hours DG is operating, ΔP_{loss} is change in the system real power loss with DG at i th node; C_{INS} is the installation cost. C_O, C_M are the operation and maintenance costs of the DG, respectively; $C_{\text{FC}i}$ is the fuel cost of i th DG; $a_{\text{DG}i}, b_{\text{DG}i}, c_{\text{DG}i}$ are the cost coefficients of i th DG. R_{ES} is the revenue obtained by selling the DG energy in the market, R_{LR} is the revenue obtained by reduction of loss by the DG, IC_i, O_i, M_i are the initial installation cost and initial operation and maintenance costs of the i th DG, respectively.

The profit maximization problem with DG capacity as variable is carried out using *fmincon* tool in Matlab. *fmincon* solver uses a sequential quadratic programming (SQP) method. In this method, the function solves a quadratic programming (QP) sub-problem in every iteration. The solver updates an estimate of the hessian of the Lagrangian at each iteration using the BFGS formula [11]. The optimization model for the profit maximization is as follows.

$$\begin{aligned} \text{Max Profit} &= \{\text{PWF}(R_{\text{ES}}) + \text{PWF}(R_{\text{LR}})\} - \{C_{\text{INS}} + \text{PWF}(C_O) + \text{PWF}(C_M) \\ &\quad + \text{PWF}(C_{\text{EM}}) + \text{PWF}(C_{\text{FC}})\} \end{aligned} \quad (21.26)$$

$$\text{sub.to } P_i^k = \sum_{q=1}^n V_i V_q Y_{iq} \cos(\delta_i - \delta_q - \theta_{iq}) \quad (21.27)$$

$$Q_i^k = \sum_{q=1}^n V_i V_q Y_{iq} \sin(\delta_i - \delta_q - \theta_{iq}) \quad (21.28)$$

$$P_{\text{DG}i}^{\text{min}} \leq P_{\text{DG}i}^k \leq P_{\text{DG}i}^{\text{max}} \quad (21.29)$$

$$V_{\text{min}} \leq V_i^k \leq V_{\text{max}} \quad (21.30)$$

$$S_i^k \leq S_i^{\text{rated}} \quad (21.31)$$

21.3.4 Profit Margin

The profit margin (PM) is the percentage of revenue remaining after all operating expenses, interests, dividends, taxes and preferred stock dividends have been deducted from utilities revenue. The PM variation with respect to varying load is also considered. The formula for PM is given in Eq. (21.31) as:

$$PM = \frac{\text{Total revenues} - \text{Total expenses}}{\text{Total revenues}} \quad (21.32)$$

21.3.5 Constraint on DG Minimum Capacity

The benefits that can be obtained from the DGs are power loss reduction, voltage profile improvement. Proper sizing in either planning or operation times, is an important factor that is to be considered in planning which can have great impact on distribution system protection. Either a DisCo or any company investing money, it always tries to operate the system in an optimal manner and attain decent profit. Generally, DGs are having its own lower and upper limits which can be found from its capability curve. A wide range of DG operation, within the given operational limits can be chosen which fits to be more appropriate depending on the objective of the planner. The constraint on minimum DG capacity limit is varied and its effect on DisCo profit is evaluated.

$$P_{DGi}^{\min} \geq x \% \text{total DG penetration} \quad (21.33)$$

21.4 Proposed Approach

The steps involved in the proposed method are given below:

- Monte Carlo Simulations are carried out for finding the ODGs and NR based on power loss reduction and reliability improvement as objectives.
- Cost/benefit analysis of distributed generation based on profit maximization subjected to various operating constraints is carried out for two scenarios,
 - ODGs,
 - Both ODGs and NR.
- Effect of varying minimum DG capacity limit on profit, power loss and profit margin are also evaluated.

21.5 Simulation Studies

The performance of the proposed approach is demonstrated on standard two test systems, IEEE 33-node and 69-node radial distribution systems. Simulations are carried out on Matlab 2008a platform. Backward/forward sweep distribution load flow algorithm is used for the power loss calculation. The DGs are modeled as constant PQ load for simplicity. The objective is profit maximization (financial loss minimization) by optimally placing the DGs and sizing them along with optimal network reconfiguration. The optimization problem is carried out by considering various operating constraints and the DGs capacity being the variables.

The DGs planning period is considered as 15 years. The load curve with hourly variation is assumed to be constant and its Load Scaling Factor (LSF) [12] is shown in Fig. 21.1. It is assumed that the price of electricity is hourly variable all over the day with 10% standard deviation as shown in Fig. 21.2 [13].

- The pollutant emission costs and their emission factors that are considered in this work are given in Table 21.1 [14].
- The DGs cost data considered are given in Table 21.2 [15].

Fig. 21.1 Market price for a day

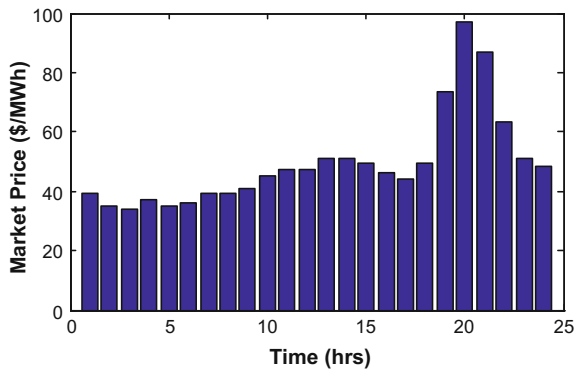


Fig. 21.2 Load scaling factor of a time variant distribution load

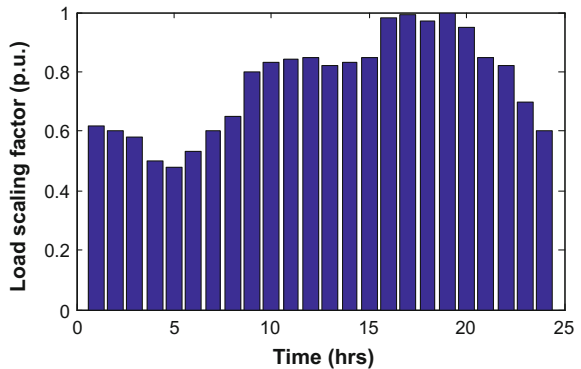


Table 21.1 Emission costs and factors for pollutants

Emission type	Penalty for pollution emission (\$/kg)	Emission factor for MT and DT (g/kWh)
NO _x	1.250	0.6188
SO ₂	0.875	0.000928
CO	0.145	0.1702
CO ₂	0.004125	184.829

Table 21.2 Cost data of the DGs

Cost type		Cost of MT	Cost of DT
Installation cost (Rs/MW)		25×10^6	35×10^6
Operation cost (Rs/MW)		25×10^3	35×10^3
Maintenance cost (Rs/MW)		MC	MC
Fuel cost coefficients	a_{DG}	0.01	0.003
	b_{DG}	40	43

Note $MC_i = (10^4 * 0.2 * IC_i)/\text{year}$

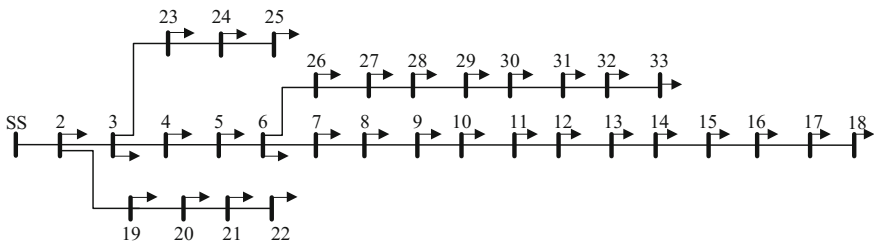
- It is assumed that the DGs are out of service for 10% over a year.
- Two scenarios are considered.
 - Case I: Yearly load growth is assumed to be zero.
 - Case II: Yearly load growth is considered to be 5% of the base year.
- For the ODGs problem, a set of four DG with all combinations are considered and their optimal sizing for 20% DGs penetration level is found. Equal weights given to both the objectives in both the ODGs and network reconfiguration problem. Using fuzzy tool, the ODGs location and sizing is determined for minimum power loss and improved reliability condition.
- In NR problem, with the obtained ODGs in the system, tie-switches are considered at 18–22 and 25–33 for test system-I and 27–35, 50–52, 46–67 and 65–69 for test system-II. All possible binary combinations of tie-switches are considered for which the reconfiguration algorithm is carried out.
- The results obtained from Monte Carlo simulations for the ODGs location & sizing and optimal NR with the ODGs are given in Tables 21.3 and 21.4, respectively.

Table 21.3 ODGs results

	ODGs location	Power loss (kW)
Test system I	12, 14, 20, 25	90
Test system II	24, 27, 61, 64	58

Table 21.4 Output of network reconfiguration with the ODGs

Data	Test system I		Test system II	
	Base case	After NR	Base case	After NR
Open switches	18–22, 25–33	6–7, 29–30	27–35, 50–52, 46–67, 65–69	19–20, 51–52, 45–46, 59–60
Unreliability (%)	0.0018	0.0008268	0.0025	0.0011
Down time (hr/year)	15.3961	7.2436	22.2704	9.8853
Power loss (kW)	211	26	256	22

**Fig. 21.3** Single line diagram of IEEE 33-node distribution network

21.5.1 IEEE 33-Node Distribution Network

The single line diagram of the test system is shown in Fig. 21.3 [16]. The base system voltage is 12.66 kV and the total load in the system is 3.715 MW and 2.3 MVar. In base case condition, the total real and reactive power losses in the system are 211 kW and 110 kVar, respectively. From the Monte Carlo simulations, the ODG locations obtained are buses 12, 14, 20 and 25 and NR results are open switches 6–7, 29–30 with closed tie-switches 18–22, 25–33.

21.5.2 Restriction on DG Minimum Capacity Limit

The minimum penetration limits of the DGs at 12, 14, 20 and 25 are 3, 2.5, 3 and 4% respectively. The constraint as given in Eq. (21.33) is included in the optimization formulation and the corresponding profit, power loss and profit margin, respectively, for Case I and Case II, are shown in Figs. 21.4 and 21.5. The DG penetration level is taken as 15% of load. The ODGs sizes with and without

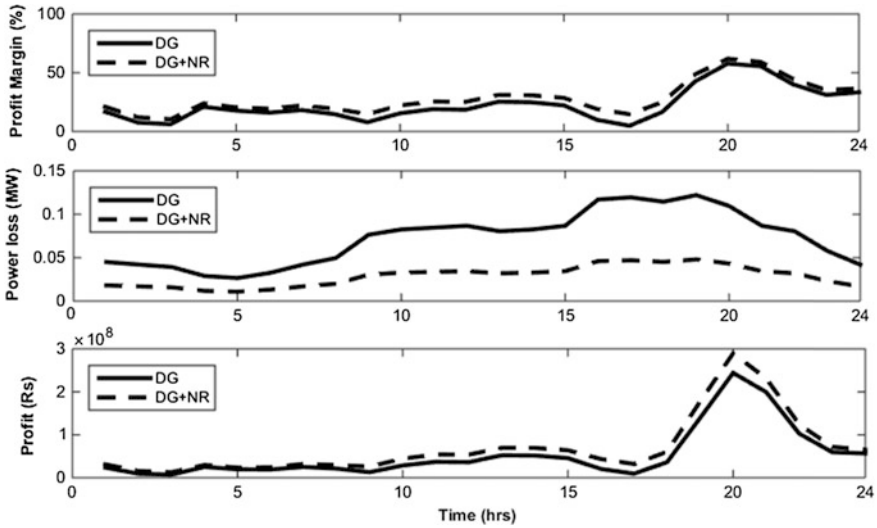


Fig. 21.4 Test system I: profit margin, power loss and profit in case I

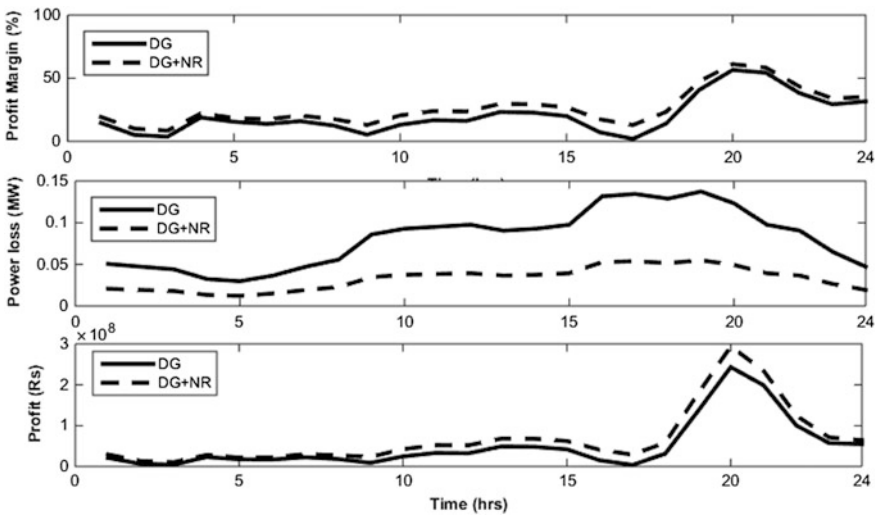


Fig. 21.5 Test system I: profit margin, power loss and profit in case II

restriction on each DG minimum capacity limit is given in Table 21.5. The costs/benefits output results of the test system-I corresponding to peak load hour of the day in the system is given in Table 21.6.

Table 21.5 Test system I-ODG sizing with and without restriction on minimum capacity limit on each DG for peak load hour

	ODG size with restriction on each DG minimum capacity (kW)	ODG size without restriction on each DG minimum capacity (kW)
Case I	273, 210, 111, 149	459, 210, 37, 37
Case II	298, 210, 117, 156	493, 209, 39, 39

Table 21.6 Test system I-output results of costs/benefits for peak load hour of a day

Costs/Benefits (INR)	Case I		Case II	
	ODGs	ODGs and N R	ODGs	ODGs and NR
Installment cost	1.556×10^7		1.6332×10^7	
Operation cost	1.5867×10^8		1.6654×10^8	
Maintenance cost	2.4435×10^6		2.5647×10^6	
Emission cost	4.1820×10^5		4.3895×10^5	
Fuel cost	1.1151×10^6		1.1704×10^6	
Revenue from DG power sold to market	3.527×10^8		3.7027×10^8	
Loss reduction revenue	0.6940×10^8	1.147×10^8	0.6×10^8	1.1015×10^8
Profit	2.4397×10^8	2.8932×10^8	2.4322×10^8	2.9377×10^8
Real power loss (kW)	110	43	123	49
Min. voltage (p.u.)	0.9623	0.9771	0.9588	0.9745

21.5.3 IEEE 69-Node Distribution Network

The IEEE 69-node system is shown in Fig. 21.6 [17]. The total real and reactive power load on the system are 3.8089 MW and 2.6914 MVAR, respectively. In base case condition without DG, the total real power loss in the system is 247.5 kW and reliability indices SAIFI and SAIDI are 1.6369 per customer and

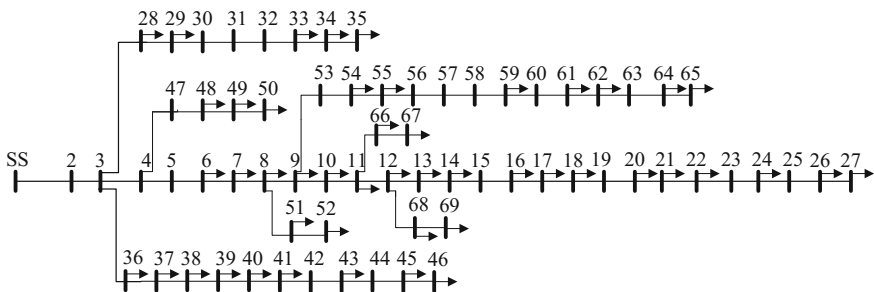


Fig. 21.6 Single line diagram of IEEE 69-node distribution network

17.5294 h/customer, respectively. The maximum and the minimum bus voltage magnitudes, at base case condition, are 1.0 and 0.951 p.u., respectively, where the substation voltage (bus 1) is assumed to be 1.0 p.u. The DG locations considered at buses 24, 27, 61 and 64 and network reconfiguration results after Monte Carlo simulations are open switches 19–20, 51–52, 45–46 and 59–60 with closed tie-switches 27–35, 50–52, 46–67 and 65–67.

21.5.4 Restriction on DG Minimum Capacity Limit

The minimum penetration limits of the DGs at 24, 27, 61 and 64 are 5, 2.5, 3, and 4%, respectively. The constraint as given in Eq. (21.33) is included in the optimization formulation and the corresponding profit, power loss and profit margin, respectively, for Case I and Case II, are shown in Figs. 21.7 and 21.8. The DG penetration level is taken as 15% of load. The ODGs sizes for locations 24, 27, 61 and 65, with and without restriction on each DG minimum capacity limit is given in Table 21.7 The costs/benefits output results of the test system-2 corresponding to peak load hour of the day in the system is given in Table 21.8.

It is clear with the considered DG penetration level and the ODGs and NR obtained from the Monte Carlo simulations, there is huge reduction in the power loss and improvement in the voltage profile of the system. For both the test systems, with base case and load growth condition, there will be no change in the installment cost, operation cost, maintenance cost, emission cost and fuel cost. With both the ODGs and NR, there is increased loss reduction revenue to the Disco thereby

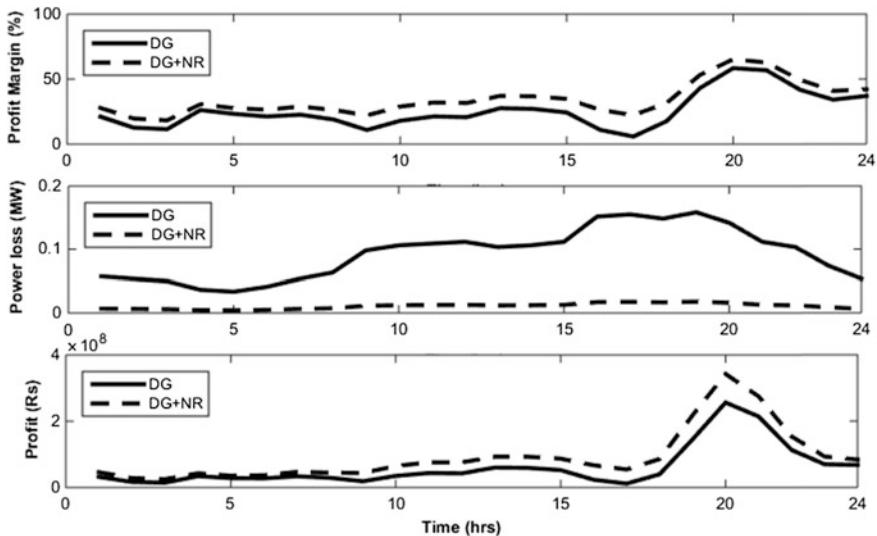


Fig. 21.7 Test system II-profit margin, power loss and profit in case I

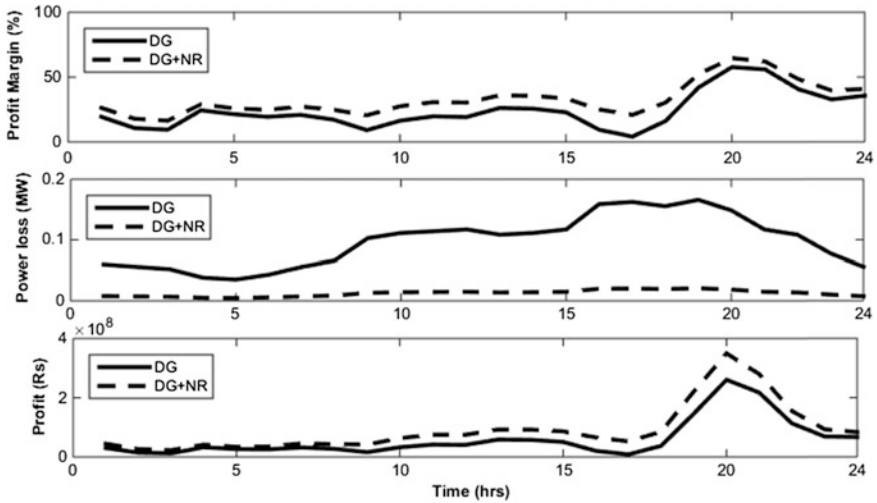


Fig. 21.8 Test system II-profit margin, power loss and profit in case II

Table 21.7 Test system I-ODG sizing with and without restriction on minimum capacity limit on each DG for peak load hour

	ODG size with restriction on each DG minimum capacity (kW)	ODG size without restriction on each DG minimum capacity (kW)
Case I	386, 108, 114, 152	559, 38, 38, 126
Case II	405, 114, 120, 160	580, 40, 40, 138

Table 21.8 Test system II-output results of costs/benefits for peak load hour of a day

Costs/Benefits (INR)	Case I		Case II	
	ODGs	ODGs and N R	ODGs	ODGs and NR
Installment cost	1.5922×10^7		1.6713×10^7	
Operation cost	1.6236×10^8		1.7042×10^8	
Maintenance cost	2.500×10^6		2.6244×10^6	
Emission cost	4.2793×10^5		4.4916×10^5	
Fuel cost	1.1410×10^6		1.1976×10^6	
Revenue from DG power sold to market	3.6097×10^8		3.7889×10^8	
Loss reduction revenue	0.779×10^8	1.6391×10^8	0.733×10^8	1.6215×10^8
Profit	2.5654×10^8	3.4253×10^8	2.6086×10^8	3.4964×10^8
Real power loss (kW)	142	16	149	19
Min. voltage (p.u.)	0.9531	0.9875	0.9523	0.9864

Table 21.9 Test system II-cost/benefit ratio for both test systems

Costs/benefits ratio (%)	Case I		Case II	
	ODGs	ODGs and NR	ODGs	ODGs and NR
Test System I	57.79	61.88	56.53	61.10
Test System II	58.45	65.26	57.68	64.62

overall profit obtained has got increased. This is due to the reason that with the network reconfiguration there is huge reduction in the losses which increased the revenue that is obtained from the loss reduction which helped DisCo in achieving more profit and high profit margin, especially during high demand period. With relaxing this constraint in-order to meet the system requirements, only two DGs are participating more for both the test systems, which is clear from Tables 21.5 and 21.7. Most importantly, it can be observed that for both the test systems, the profit margin with DG + NR is high than with only DG condition. The costs/benefits ratio for both the test systems is given in Table 21.9.

With load growth of 5%, the costs along with revenues are increased than compared to base load profile, so the ODGs dispatch also changed to meet the system operating constraints. The DG minimum capacity is placing a restriction on each DG on its minimum generation.

21.6 Conclusions

This chapter aims at maximizing the DisCo profit with the DGs, using cost benefit analysis by finding the optimal DG capacity corresponding to each hour. The DGs location and network reconfiguration information is obtained from the Monte Carlo simulations which are carried out prior to the cost/benefit analysis. Time varying load under base case and 5% load growth conditions are taken and their effect on profit, power loss and profit margin is evaluated. The proposed optimization model minimizes the total system cost, DG investment and operating costs, cost of purchasing power by distribution utility, and the payments toward compensating for system losses. The restriction on DG minimum capacity and its effect on profit margin is evaluated. The DisCo obtained high profit margin with the proposed algorithm and also with the considered locations of DG and their optimal sizes, the test systems voltage profile are well within prescribed limits and also power loss reduction is significant. This is repeated for both the ODGs and NR and can be observed from results that with both the ODGs and NR case, the DisCo is getting high profit margin than in the case where only the ODGs are considered. By applying the proposed cost/benefit analysis of the distributed generation, the DisCos/DG owners can get significant insight in choosing the projects that can maximize the profit under various scenarios. It can be recommended that this work if implemented in a micro-grid system brings huge profit to both the DG owners and technical benefits to the electric utilities.

References

1. Dugan R, McDermott T, Ball G (2001) Planning for distributed generation. *IEEE Trans Ind Appl* 7(2):80–88
2. Shahidehpour M, Yamin H, Li Z (2002) Market operations in electric power systems: forecasting, scheduling, and risk management. Wiley-IEEE Press, New York
3. Brown R, Pan J, Feng X, Koutlev K (2001) Siting distributed generation to defer T&D expansion In: *IEEE/PES transmission & distribution conference and exposition*, pp 622–627
4. Palma-Behnke R, José Luis Cerda A, Vargas L, Jofré A (2005) A distribution company energy acquisition market model with integration of distributed generation and load curtailment options. *IEEE Trans Power Syst* 20(4):1718–1727
5. Haffner S, Pereira L, Barreto L (2008) Multistage model for distribution expansion planning with distributed generation Part I problem formulation. *IEEE Trans Power Del* 23(2):915–923
6. El-Khattam W, Bhattacharya K, Hegazy Y, Salama M (2004) Optimal investment planning for distributed generation in a competitive electricity market. *IEEE Trans Power Syst* 19(3):1674–1684
7. Borges CL, Falco DM (2006) Optimal distributed generation allocation for reliability, losses, and voltage improvement. *Int J Electr Power Energy Syst* 28(6):413–420
8. Pavani P, Singh SN (2014) Placement of DG for reliability improvement and loss minimization with reconfiguration of radial distribution systems. *Int J Energy Sect Manage* 8(3):312–329
9. Amanulla B, Chakrabarti S, Singh S (2012) Reconfiguration of power distribution systems considering reliability and power loss. *IEEE Trans on Power Del* 27(2):918–926
10. Willis HL (2004) Power distribution planning reference book. Dekker, Abingdon
11. Byrd RH, Gilbert JC, Nocedal J (2000) A trust region method based on interior point techniques for nonlinear programming. *Math Program* 89(1):149–185
12. Chen C, Duan S, Cai T, Liu B, Hu G (2011) Optimal allocation and economic analysis of energy storage system in microgrids. *IEEE Trans Power Electron* 26(10):2762–2773
13. Ramachandran B, Srivastava S, Edrington C, Cartes D (2011) An intelligent auction scheme for smart grid market using a hybrid immune algorithm. *IEEE Trans Ind Electron* 58(10):4603–4612
14. California Energy Commission (2000) Emissions from distributed generation. Siting Committee Workshop, Evaluating Distributed Generation CEQA and Permit Streamlining, Apr 2000
15. Siah M, Porkar S, Abbaspour-tehrani-fard A, Poure P, Saadate S (2010) Competitive distribution system planning model integration of dg, interruptible load and voltage regulator devices. *Iran J Sci Technol, Trans B: Eng* 34(B6):619–635
16. Eminoglu U, Hocaoglu MH (2009) Distribution systems forward/backward sweep based power flow algorithms: a review and comparison study. *Electr Power Compon Syst* 37(1):91–110
17. Ghosh S, Das D (1999) Method for load-ow solution of radial distribution networks. *IEE Proc Gener Transm Distrib* 146(6):641–648

Chapter 22

Solar PV System with Energy Storage and Diesel Generator

Rajashekar P. Mandi

22.1 Introduction

The renewable energy systems (RES) play an important role for the growth of Indian power sector because they produce the energy without environmental pollution and are infinite energy sources. The growth of renewable energy systems is slow due to unstable power output and intermittent availability. Use of individual renewable energy system alone will have low capacity factor. Therefore, integration or hybridization of renewable energy systems with conventional energy system will enhance the utilization factor and energetic and exergetic efficiencies of renewable energy conversion systems. Integration involves hybrid energy sources such as, solar photovoltaic, wind, and micro-hydel with conventional systems (diesel generator sets or grid) for supply to consumer loads.

The design of a hybrid power system (HPS) must provide a reliable and cost-effective power supply to the load. The control of HPS is more complicated due to diversity in power generation characteristic of different renewable energy sources. The prediction of energy generation from these energy sources is difficult because these energy systems are seasonal and intermittent [1].

There are two types of HPS that can be adopted based on the level of penetration of renewable energy systems: (a) fraction of the total load is supplied by the renewable energy systems, i.e., a conventional generator (diesel) working continuously. In this system, the reliability and availability of power is good; the control is simple; the fuel savings are modest; and a minimum of supervision is needed. (b) Another option is renewable energy as the main source of energy and conventional generator as a standby power. In this case, a complicated controller is essential; reliability and availability factors are modest; fuel savings are good.

R.P. Mandi (✉)

School of Electrical & Electronics Engineering, REVA University, Bangalore, India
e-mail: rajashekarmandi@yahoo.com

The solar PV systems are popular because of the following reasons [2]:

- PV energy production is free from emissions,
- Decreasing prices for PV components in recent years, and
- High reliability and good efficiencies of PV systems.

The conventional solar PV system has non-steady output power characteristic that depends on weather conditions in a short period, although PV array output power average shows nearly regular characteristics to have a peak output power nearly at noon [3]. Therefore, integration of this solar PV with other renewable energy sources or conventional power is an important way of increasing utilization and energetic and exergetic efficiencies of energy conversion systems.

Such integration encounters complexities arising from the diverse nature of the solar energy sources, low energy densities, intermittent availability, and stochastic elements. Recent developments in processing, control, and management of power are enabling stable operation of solar PV-diesel support-integrated systems [4].

22.2 Energy Sources

22.2.1 Solar PV System

Solar PV energy is the energy converted from solar radiation into electricity by using photovoltaic (PV) cells or solar cells which use the photoelectric effect to produce electricity. The PV cells are the most important building blocks of the solar PV power system. The production of electrical energy from solar PV system is very simple, but the overall efficiency in converting the total solar radiation into electricity is less.

The hourly power generation by solar PV power plant (kW) is estimated by using the following equation:

$$P_h(t) = \frac{\text{OSCA} \times H_T(t) \times \eta_{\text{cell}}(t) \times \eta_{\text{inv}}(t) \times \eta_{\text{TR}}(t)}{10^3} \quad (22.1)$$

where OSCA is the optimum solar cell area (m^2), $H_T(t)$ is the hourly solar radiation on the panel tilted surface (W/m^2), η_{inv} is the inverter efficiency (%) that varies with the solar PV power output, η_{TR} is the transformer efficiency (%) if transformer is used to step-up the inverter output voltage for high voltage applications, and $\eta_{\text{cell}}(t)$ is the PV cell efficiency in the field (%) and is given by

$$\eta_{\text{cell}}(t) = \eta_{\text{cr}} \times [1 - 0.0062 \times (T_{\text{cell}}(t) - T_{\text{cr}})] \quad (22.2)$$

where η_{cr} is the PV cell efficiency (%) at standard test condition (STC), T_{cr} is the PV cell temperature ($^{\circ}\text{C}$) at test condition, STC and is given by

$$T_{\text{cell}}(t) = T_a(t) + q \times H_T(t) \quad (22.3)$$

where T_a is the ambient temperature ($^{\circ}\text{C}$) and q is the solar cell temperature coefficient, which will be in the range $0.003\text{--}0.006 \text{ }^{\circ}\text{C}/\text{W m}^2$.

The monthly output energy of PV system (kWh/month) is computed as follows:

$$\text{TPV}_m = \sum_{d=1}^n \left(\sum_{i=t_1}^{i=t_2} P_h(t) \right)_d \quad (22.4)$$

where d is the day in a month, n is the total number of days in a month that varies from 28 or 29 days for February, 30 days for April, June, September and November, 31 days for remaining months, t_1 is the sunrise time (h) and t_2 is sunset time (h).

The yearly output energy of PV system (kWh/year) is computed as follows:

$$\text{TPV}_y = \sum_{m=1}^{m=12} (\text{TPV}_m)_m \quad (22.5)$$

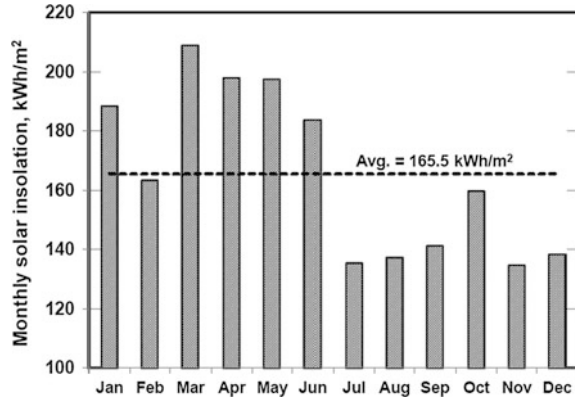
The tilt of the solar panel also plays an important role in energy generation. The module installation angle in relation to the Sun affects the module energy output. The module produces more power when the sunlight source is directly perpendicular to the surface of the module. A typical optimum tilt angle for average module power production over the year in a fixed system will be latitude of the particular site. The optimal tilt angle of the PV array (degree) for a given month is given by

$$S = \phi - \delta \quad (22.6)$$

where ϕ is the latitude of the site in degree, δ is the sun's declination angle, and declination angle lies between $\pm 23.45^{\circ}$.

The optimum fixed tilt angle for the selected site is 12.97° (latitude of the site) which will reduce the average energy output by about 3% for the whole year compared to the tracking system. As the tilt angle increases up to the latitude of the site, the output increases and, beyond the latitude, the output decreases [5]. The solar tracking system gives the maximum power output but needs more control and cost [6]. The total monthly solar insolation is presented in Fig. 22.1. The solar insolation is high of about 209 kWh/m^2 month during the month of March and is low of 134.7 kWh/m^2 month during the month of November. The annual average solar insolation is 165.5 kWh/m^2 month. During the months January, March, April, May, and June, the solar insolation is higher than the annual average value whereas during other months it is less than the annual average value. The solar energy is generally available from 07:00 to 18:00 h and will not be there during evening and night hours from 18:00 to 07:00 h.

Fig. 22.1 Monthly solar insolation at particular site



22.2.2 Diesel Generator

Diesel generator (DG) set is planned to support the power during non-availability of solar power. Diesel generators are being used as a common source of power for standby power during power cut from utility, isolated towns and islands. The generation cost for DG set is on higher side and also produce more air pollution. However, to meet the power demand for remote applications make them a necessity. They are able to supply constant and stable power supply to the load and are reliable in the providing long-term power supply. Diesel generators also need controlling devices to allow the matching of load requirements and power output. The performance of DG set depends on the loading of DG set. The specific energy generation (SEG) of DG set is the energy generated by DG set for one liter of diesel consumption. The excess energy after meeting the load will be used to charge the energy storage devices, i.e., batteries in this case.

22.2.3 Batteries

Since the energy generation by solar PV power plant is intermittent in nature and seasonal, to provide the firm power to the load, energy storage components are essential in stand-alone mode of operation. The excess power generation from solar PV power plant after meeting the load will be used to charge the batteries. During low-load requirement, i.e., during the night hours, the load will be met by batteries. Batteries will not be allowed to deep discharge, i.e., depth of discharge (DOD) is considered as 30% to maintain the life span of batteries [7].

22.3 Integration of Energy Systems

The solar power is optimized based on the load requirement and accordingly the size of DG set and battery banks are designed. The solar PV with DG set can be integrated in three different configurations, i.e., series, switched, and parallel [8–10]. In series configuration, the overall efficiency is low and large capacity of energy storage system is required. The switched and parallel configurations are more suitable for low-load, medium-load, and high-load operations [11]. The three modes are as follows [12, 13]:

- Solar PV with inverter only—low-load operation,
- DG set and charging battery by DG set power—medium-load operation, and
- Solar PV with inverter and DG set in parallel—high-load operation.

The proposed controller is developed using MATLAB Simulink tool and also HOMER software using the modular concept [14]. The modularity of the controller integrates various types of generators with different priority options, loads, knowledge base system, and database. One of the key points of modular concept is to use the high-level abstraction models of HPS. The high-level models shall contain information about their behavior and interaction that are essential to the expert controller functions such as scheduling of generators, protection of components against overload/underload, and ensuring power balance [15].

The controller will control the operation of inverter, power conditioner, battery charger, and DG set operation. During start-up the controller chooses inverter-only operation, if the notional battery state of charge is above minimum level. When the load increases above the set value, the DG set will be started and introduced in parallel with the inverter. In order to get more efficiency of DG set, it is economical to operate the DG set near to its full load capacity. Depending on the actual site load, the resulting system operation could involve either load sharing or battery charging. When the load on DG set falls below a set value, the system will revert to inverter-only operation [16].

Figure 22.2 gives the schematic of the integration of solar photovoltaic (SPV) with DG set. Figure 22.3 gives the flow diagram of the integrated energy system under consideration. The inputs to the controller are solar (SPV) power, DG set power, battery power, and load. The controller senses the load if solar power is available (i.e., between 07:00 and 18:00 h), the SPV supply the power to load. If the SPV power is not there and load is less than battery charge, the battery provides the power supply to load. If the battery charge is lower than the load, the DG set will start and supply the power to the load. The surplus power of DG set is used to charge the battery. If the battery is fully charged, the DG set will operate under partial loading. If the load is more than the sum of SPV power and battery charge, the DG set will start and supply the power to load [17].

Fig. 22.2 Schematic of integration of SPV with DG set and battery bank

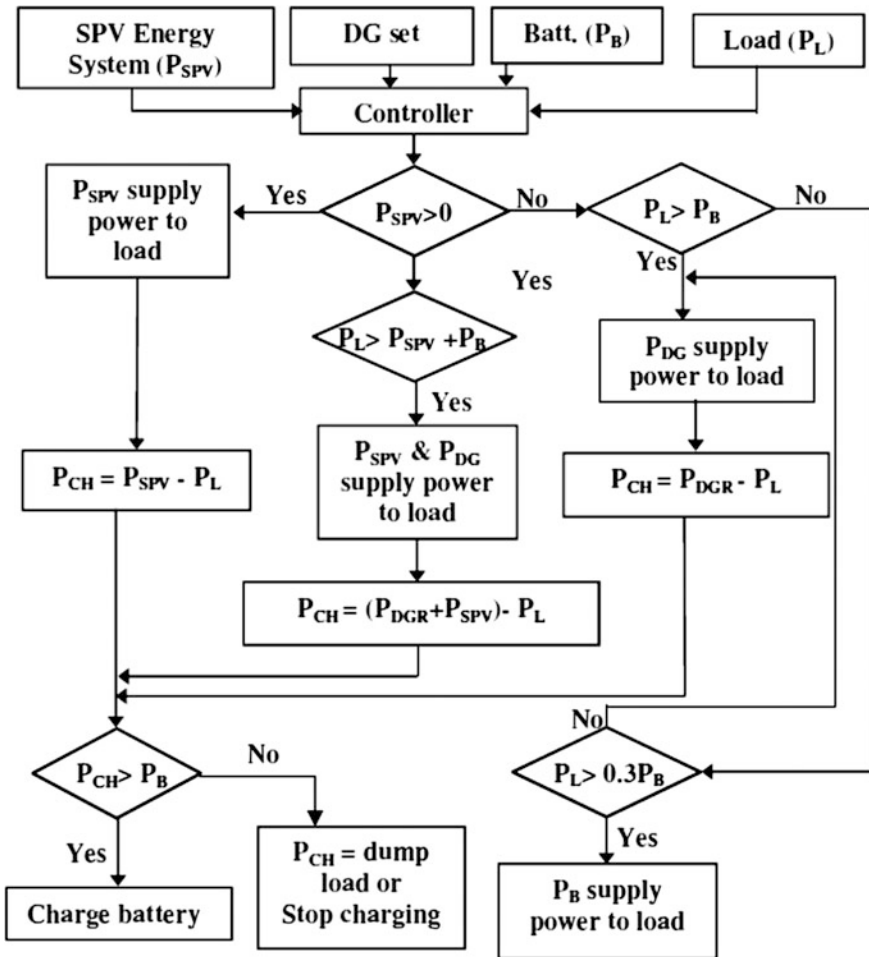
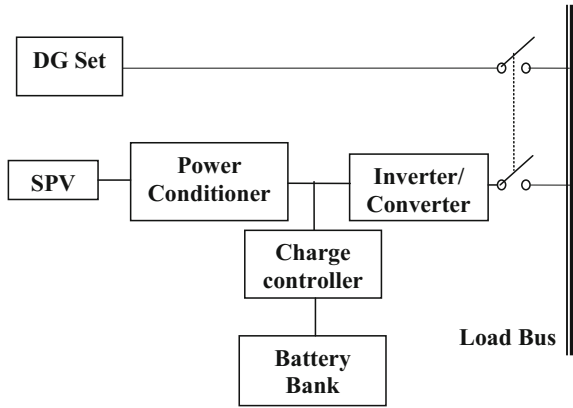


Fig. 22.3 Flow diagram of hybrid system of SPV with DG set and battery bank

22.4 Load Pattern

A typical remote hamlet in Karnataka, India, is selected for analysis and its load data are given in Table 22.1. The load pattern of a typical day for the selected site is presented in Fig. 22.4. The daily average energy requirement is 206.08 kWh/day and the peak power is 13.15 kW for a typical day. The morning peak is between 07:00 and 10:00 h, and the evening peak is between 16:00 and 22:00 h. The energy ratio between peak hour and non-peak hour is 56%, which is normal.

22.5 Mathematical Modeling

22.5.1 Power Generated by Solar PV

(a) Solar power (kW) is computed as follows:

$$P_{SPV}(t) = A \times H_T(t) \times \eta_{cell}(t) \times \eta_{inv}(t) \times 10^{-7} \quad (22.7)$$

where A is the area of solar PV panel area (m^2), $H_T(t)$ is the measured hourly solar irradiance (W/m^2), $\eta_{cell}(t)$ is the instantaneous PV cell efficiency (%) computed from Eq. (22.2), $\eta_{inv}(t)$ is the instantaneous inverter efficiency (%) based on the loading of inverter.

(b) The solar power (kW) supplied to load is calculated as follows:

$$P_{SPV}(t) = P_L(t) \quad (22.8)$$

(c) The solar power (kW) used for battery charging is calculated as follows:

$$C_{SPV}(t) = P_{SPV}(t) - P_L(t) \quad (P_{SPV}(t) > P_L(t) \text{ and } P_{batt} < P_{r-batt}) \quad (22.9)$$

$$P_{batt}(t) = P_{batt} + C_{SPV}(t) \quad (22.10)$$

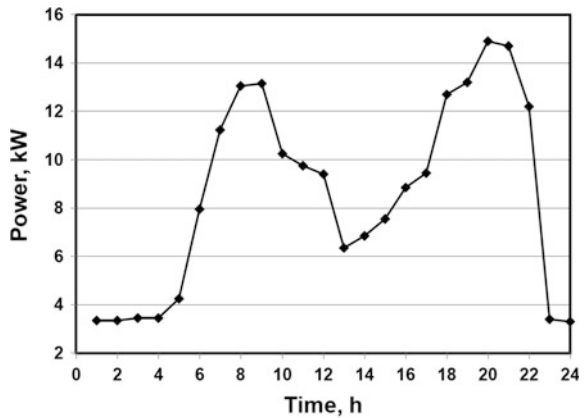
where P_{batt} is power available in battery (kW) and P_{r-batt} is the rating of battery (kW).

(d) The total energy supplied (kWh/day) by solar PV to load is given by

Table 22.1 Load details

Sl. No.	Particulars of load	Power (W)	Quantity (Nos.)	Average operation (h/day)	Energy (kWh/day)
01	Household lighting	50	209	7	73.15
02	Community center lighting	50	29	5	7.25
03	Street lighting	60	12	12	8.64
04	Health center lighting and heating	1510	1	4	6.04
05	Water pumps	3700	3	4	44.4
06	Small-scale industries such as flour mills and chilling plant	3700	3	6	66.60
	Total	8764			206.08

Fig. 22.4 Load pattern of a typical day



$$E_{SPVd} = \sum_{t=7}^{18} (P_{SPV}(t) - C_{SPV}(t)) \tag{22.11}$$

where ‘t’ is hour and varies from 07:00 to 18:00 h.

(e) The total energy supplied (kWh/day) by solar PV for battery charging is given by

$$EC_{SPVd} = \sum_{t=7}^{18} C_{SPV}(t) \tag{22.12}$$

(f) The total energy supplied (kWh/day) by solar PV for both load and battery charging is given by

$$TE_{SPVd} = E_{SPVd} + EC_{SPVd} \quad (22.13)$$

22.5.2 Power Supplied by DG Set

(a) The DG set power (kW) supplied to load is calculated as follows:

$$P_{DG}(t) = P_L(t) \quad (P_{SPV}(t) = 0 \text{ and } P_{batt} < 0.3P_{r-batt}) \quad (22.14)$$

$$P_{DG}(t) = P_L(t) - P_{batt} \quad (P_{SPV}(t) = 0 \text{ and } 0.3P_{r-batt} < P_{batt} < P_L) \quad (22.15)$$

$$P_{DG}(t) = P_L(t) - P_{SPV} \quad (0 < P_{SPV}(t) < P_L(t) \text{ and } P_{batt} < 0.3P_{r-batt}) \quad (22.16)$$

(b) The DG set power (kW) used for battery charge is calculated as follows:

$$C_{DG}(t) = P_{DG}(t) - P_L(t) \quad (P_{r-DG} > P_{DG}(t) > P_L \text{ and } P_{batt} < P_{r-batt}) \quad (22.17)$$

$$P_{batt}(t) = P_{batt} + C_{DG}(t) \quad (22.18)$$

(c) The total energy supplied (kWh/day) by DG set to load is given by

$$E_{DGd} = \sum_{t=1}^{24} (P_{DG}(t) - C_{DG}(t)) \quad (22.19)$$

where 't' is time (h) and varies from 01:00 to 24:00 h.

(d) The total energy supplied (kWh/day) by DG set for battery charging is given by

$$EC_{DGd} = \sum_{t=1}^{24} C_{DG}(t) \quad (22.20)$$

(e) The total energy supplied (kWh/day) by DG set for both load and battery charging is given by

$$TE_{DGd} = E_{DGd} + EC_{DGd} \quad (22.21)$$

22.5.3 Power Supplied by Battery Bank

(a) The battery power (kW) supplied to load is calculated as follows:

$$P_{\text{batt}}(t) = P_L(t) \quad (P_{\text{SPV}}(t) = 0 \text{ and } P_{\text{batt}} > 0.4P_{r-\text{batt}}) \quad (22.22)$$

$$P_{\text{batt}}(t) = P_L(t) - P_{\text{SPV}}(t) \quad (0 > P_{\text{SPV}}(t) < P_L(t)) \quad (22.23)$$

(b) The total energy supplied (kWh/day) by Battery to load is given by

$$E_{\text{batt-d}} = \sum_{t=1}^{24} (P_{\text{batt}}(t)) \quad (22.24)$$

22.6 Optimization of Energy Sources

To optimize the use of solar photovoltaic and conventional power (DG set) along with energy storage (battery bank) system, three different configurations (low SPV, medium SPV, and high SPV) of solar PV, DG set, and battery banks are sized to meet the load requirement by using a simulation tool. The optimization is discussed with respect to important criteria such as energy system availability; dependence on conventional energy source such as DG set and energy storage; overall cost of the system; and life cycle cost of energy, reliability, and pollution [18].

22.6.1 Energy System Availability

The peak power requirement to meet the load is 13.15 kW and the energy requirement is 206.08 kWh/day. The power ratings chosen to meet the load requirement are given in Table 22.2. The peak power requirement of load is occurring at 09:00 h whereas the peak solar power availability is between 12:00 and 13:00 h (load of 6.35–9.40 kW). Therefore, the power generation of solar PV power plant will not match with peak power of load. In order to optimize the use of solar PV power generation to meet the load, three different configurations are simulated.

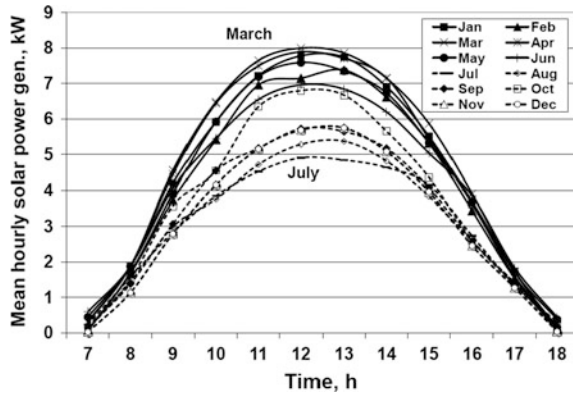
22.6.1.1 Low Solar Photovoltaic (LSPV) Power Plant

In this simulation, the total solar PV power plant capacity is considered as 8.0 kW, i.e., designed power output will be peak at 12:00 noon, i.e., at a solar irradiance of 1000 W/m² at STP. The rating of solar PV power plant chosen is 60.8% of peak

Table 22.2 Power system sizing

Sl. No.	Particulars	Low SPV	Medium SPV	High SPV
01	Peak power rating of SPV (kW)	8.0	16.0	32.0
02	Rating of DG set (kVA)	12.0	8.0	5.0
03	Battery bank capacity, peak power (kW)/energy (kWh/day)	5.0/36	8.0/54	20.0/120

Fig. 22.5 Hourly solar power generation by SPV power plant for LSPV (monthly mean)



power. The load is peak of 13.15 kW happening at 09:00 h whereas the solar power availability is varying between 2.84 and 4.56 kW (35.5–57.0%) for the design value of 8 kW SPV power plant. The DG set rating is considered as 12 kVA to meet the power requirement during peak hours. The battery bank size of 36 kWh (17.5% of total load energy) is selected with peak battery power of 5.0 kW.

Figure 22.5 gives the variation of hourly solar power generation (monthly mean) by solar PV power plant for 12 months for LSPV. The solar PV peak power generation is high during the month of March, i.e., 8.0 kW at 12:00 noon and the low peak is during the month of July at 12:00 noon, i.e., 4.91 kW (61.4% of rating). The solar PV power generation during other months lies between these two values due to variation in global solar irradiance.

Figure 22.6 shows the power supplied by SPV power plant, DG set, and battery bank during the month of March (high solar month) for LSPV. During the night hours, the power is met by battery bank till 05:00 h. At 05:00 h, DG set starts feeding power to load because the battery bank charge reduces to below 30% and also load increases. The excess power generation by DG set after meeting load is used to charge the battery bank. DG set will be operated till 11:00 h. The solar PV power plant starts generating power at 07:00 h and its power is less than the load requirement. Between 07:00 and 11:00 h, both DG set and SPV power plant will be operating in parallel to meet the load power requirement. After 11:00 h, solar PV power generation is more than the load requirement, the SPV power plant supplies the total load, and excess power generation is used to charge the battery bank.

Fig. 22.6 Monthly average power generation by SPV power plant during March month for LSPV

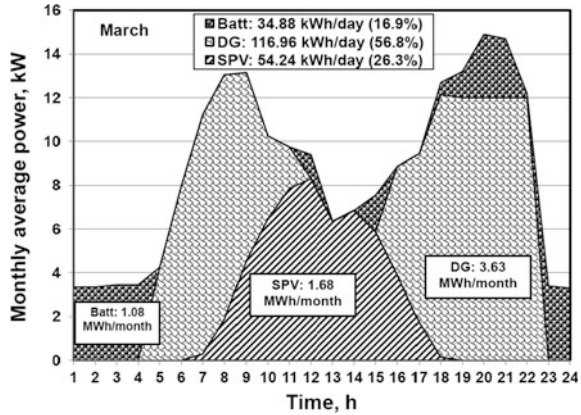
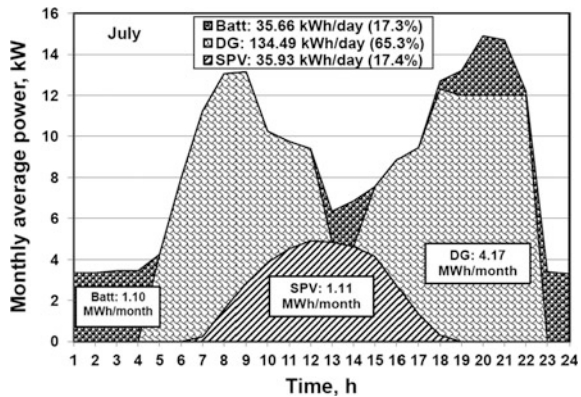


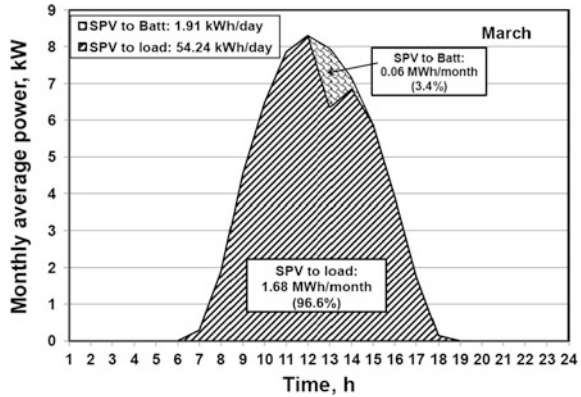
Fig. 22.7 Monthly average power generation by SPV power plant during July month for LSPV



Again at 16:00 h, the load power requirement is more than the SPV power, the DG set starts providing the power till 22:00 h. The excess power generation by DG set is fed to the battery bank for charging. The charging power to battery bank is cut-off at 5.0 kW. Between 22:00 and 5:00 h, the power is supplied from battery bank. The energy supplied by SPV power plant to load is 54.24 kWh/day (1.68 MWh/month) that forms about 26.3% of load requirement. The energy supplied by DG set to load is 116.96 kWh/day (3.63 MWh/month) that forms about 56.8% of load requirement. The energy supplied by DG set is more i.e., twice (2.15 times) than that of the energy supplied by SPV. The energy supplied to load by battery banks is 34.88 kWh/month (1.08 MWh/month) that forms about 16.9% of load requirement.

Figure 22.7 shows the power supplied by SPV power plant, DG set, and battery bank during the month of July (low solar month) for LSPV. During the night hours, the power is met by battery bank till 05:00 h. At 05:00 h, DG set starts feeding power to the load because the battery bank charge reduces to below 30% and also load increases. The excess power generation by DG set is used to charge the battery bank after meeting the load power requirement. DG set will be operated till 12:00 noon.

Fig. 22.8 SPV energy supplied to load and for battery charging during March month for LSPV



The solar PV power plant starts generating power at 07:00 h, and its power is less than the load requirement. Between 07:00 and 12:00 h, both DG set and SPV power plant will be operating in parallel to meet the load power requirement. After 12:00 h, solar PV power generation is more than the load requirement, the SPV power plant supplies the total load, and excess power generation is used to charge the battery bank. Again at 15:00 h, the load power requirement is more than the SPV power and the DG set starts providing the power till 17:00 h. The excess power generation by DG set is fed to battery bank for charging after meeting the load requirement. The charging power to battery bank is cut-off at 5.0 kW. Between 18:00 and 5:00 h, the power is supplied from the battery bank. The energy supplied by SPV power plant to load is 35.93 kWh/day (1.10 MWh/month) that forms about 17.4% of load requirement. The energy supplied by DG set to load is 134.49 kWh/day (4.17 MWh/month) that forms about 65.3% of load requirement. The energy supplied by DG set is nearly four times (3.74 times) than that of energy supplied by SPV. The energy supplied to load by battery banks is 35.66 kWh/month (1.11 MWh/month) that forms about 17.3% of load requirement. The energy supplied by SPV power plant is less by about 34% compared to energy generated during the month of March whereas the energy supplied by DG set is increased by 15% compared to March month. The energy supplied by battery bank to load is also increased by 3% compared to March month.

Figure 22.8 gives the energy generation by SPV power plant, energy supplied directly to the load and energy used for battery charging during the month of March for LSPV. The energy supplied by SPV power plant to load during March month is 54.24 kWh/day that forms about 96.6% of total energy generated by SPV power plant, and the energy used for battery charging is 3.4% of total energy whereas during the month of July the energy supplied by SPV power plant to load is zero due to low solar irradiance.

Figure 22.9 gives the energy generation by DG set, energy supplied directly to load and energy used for battery charging during the month of March for LSPV.

Fig. 22.9 DG set energy supplied to load and battery charging during March month for LSPV

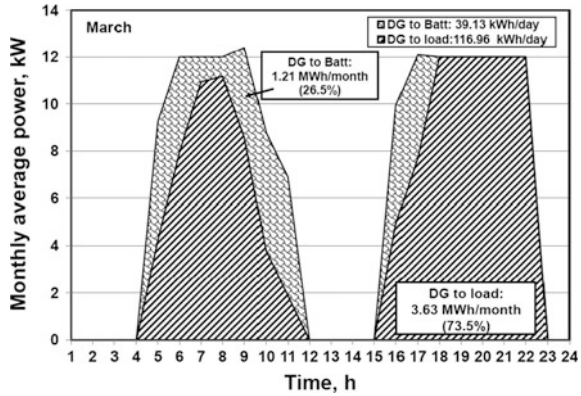
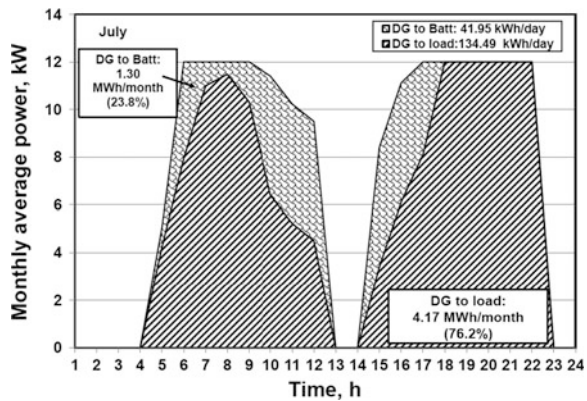


Fig. 22.10 DG set energy supplied to load and battery charging during July month for LSPV



The energy supplied by DG set to load is 116.96 kWh/day that forms about 73.5% of total energy generated by DG set. The energy used for battery charging is 26.5% of total energy. During the month of July, the energy supplied by DG set to load is 134.49 kWh/day that forms about 76.2% of total energy generated by DG set and the energy used for battery charging is 23.8% of total energy (refer Fig. 22.10). The dependence on DG set power is more during the month of July compared to March month.

Figure 22.11 presents the state of energy capacity of battery (i.e., battery charge availability), battery charging by SPV and DG set during the month of March for LSPV.

- 01:00–05:00 and 18:00–24:00 h, battery supplies power to the load.
- 06:00–11:00 and 16:00–17:00 h, DG set will supplies the power to load and excess power is used to charge the battery.
- 12:00 noon and 15:00 h, battery supplies power to the load partially.
- 13:00–14:00 h, SPV supplies power to the load and excess power is used to charge the battery.

Fig. 22.11 State of battery charge during March month for LSPV

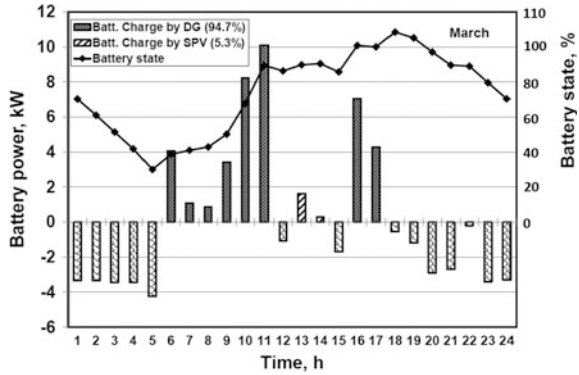


Fig. 22.12 State of battery charge during July month for LSPV

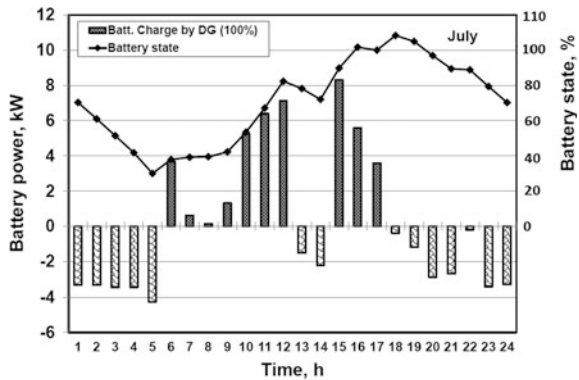
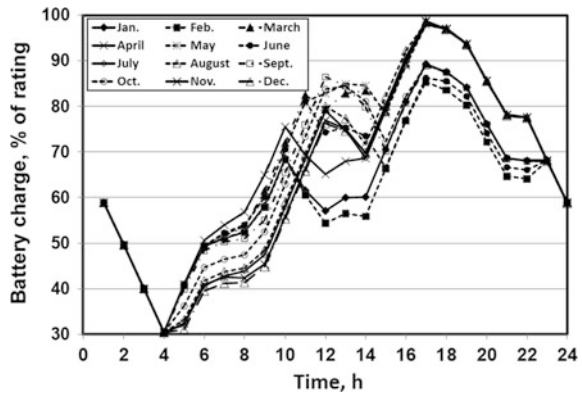


Fig. 22.13 State of battery charge throughout the year for LSPV



- The total energy supplied by DG set to charge battery bank is 97.4% of total battery capacity whereas 2.6% will be supplied by SPV.

During the month of July, the entire 100% battery charging is done by DG set due to low solar irradiance (refer Fig. 22.12).

Fig. 22.14 Energy supplied by SPV and DG set for one year for LSPV

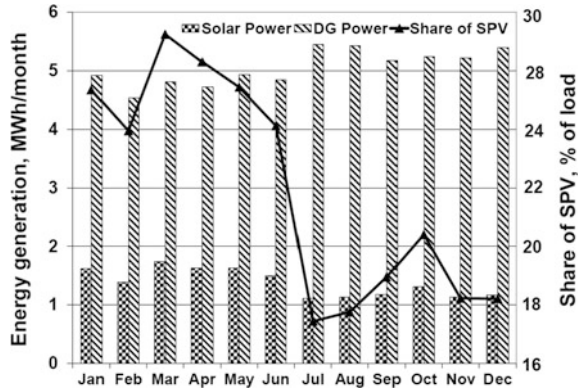


Fig. 22.15 Total energy share by SPV and DG set for one year for LSPV

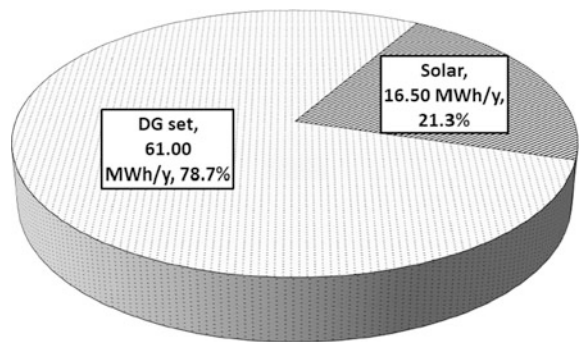


Figure 22.13 gives the variation of battery charge state throughout the year for LSPV. The battery charge state varies from 30.4 to 98.8%.

Figure 22.14 gives the variation of energy supplied by SPV power plant and DG set and share of SPV power plant. The major portion of the energy supply is from DG set in all months. The energy share by SPV power plant varies between 17.4% (during July) and 27.2% (during March). The major portion of the energy comes from DG set, i.e., 61.0 MWh/year that forms 78.7% total energy generation, and energy generation by SPV power plant is 16.5 MWh/year that forms 21.3% of total energy generation (refer Fig. 22.15) for LSPV.

The specific solar energy generation (SSEG) is the amount of monthly average of daily solar energy available with unit area of solar PV panel, or sometime, it is also referred as sun hour. The SSEG depends on the particular site condition and also vary with season. The SSEG varies between 4.3 and 6.7 kWh/m² day. The gap between the energy supplied by DG set and SPV plant is very high due to the use of less solar penetration. Figure 22.16 gives the variation of energy generated by SPV plant and DG set with SSEG. It is shown from the above figure that the energy generation by SPV power plant increases from 1.11 MWh/month (SSEG:

Fig. 22.16 Energy supplied by SPV and DG set with SSEG for LSPV

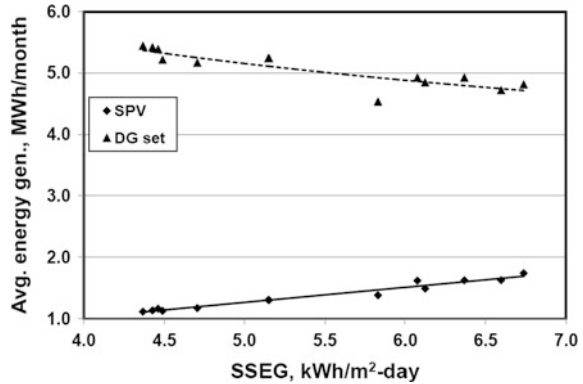
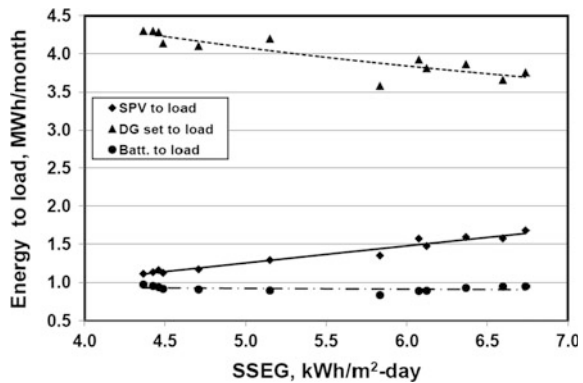


Fig. 22.17 Energy supplied by SPV, DG set, and battery to load with SSEG for LSPV

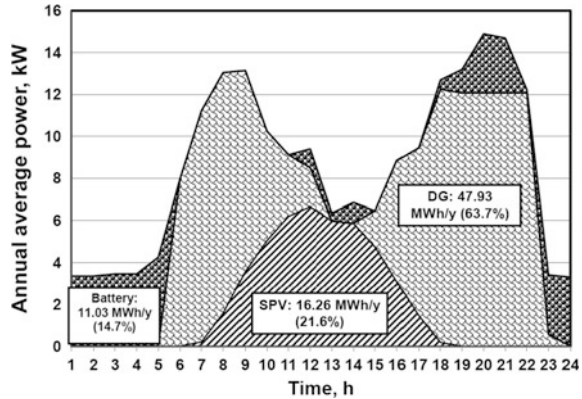


4.3 kWh/m² day) to 1.74 MWh/month (SSEG: 6.7 kWh/m² day). The energy generation by DG set decreases from 5.45 MWh/month (SSEG: 4.3 kWh/m² day) to 4.54 MWh/month (SSEG: 6.7 kWh/m² day).

Figure 22.17 shows the variation of energy supplied by SPV power plant, DG set, and battery bank to the load with SSEG. The energy supplied by SPV power plant directly to the load is increased from 1.11 MWh/month (SSEG: 4.3 kWh/m² day) to 1.68 MWh/month (SSEG: 6.7 kWh/m² day). The energy supplied by DG set directly to the load is decreased from 4.30 MWh/month (SSEG: 4.3 kWh/m² day) to 3.58 MWh/month (SSEG: 6.7 kWh/m² day). The energy supplied by battery bank directly to the load is almost same with a slight variation of 0.94–0.97 MWh/month.

Figure 22.18 gives the annual average energy share by SPV power plant, DG set, and battery to meet the load requirement for LSPV. The annual average energy supplied by SPV power plant to load is 16.26 MWh/year that forms 21.6%, by DG set to load is 47.93 MWh/year (2.95 times of energy shared by SPV power plant) that forms about 63.7%, and by battery bank to load is 11.03 MWh/year that forms about 21.0%. The total energy supplied by SPV power plant and DG set is

Fig. 22.18 Annual energy share by SPV power plant, DG set, and battery bank to load for LSPV



77.17 MWh/year and the total energy consumption by load is 75.22 MWh/year. The estimated energy loss in battery charging and other electronic controllers is 1.95 MWh/month that forms 2.53%.

22.6.1.2 Medium Solar Photovoltaic (MSPV) Power Plant

In this simulation, the design total solar PV power plant capacity is considered as 16.0 kW (power output) at peak sun hour, i.e., at a solar irradiance of 1000 W/m² at STP. The rating of solar PV power plant chosen is 121.7% of peak power requirement of load. The load is peak of 13.15 kW happening at 09:00 h whereas the solar power availability for the design value of 16 kW SPV power plant is varying between 5.61 and 9.08 kW (35.1–56.8%). The DG set rating is considered as 8 kVA to meet the power requirement during peak hours. The battery bank size of 54 kWh (26.2% of total load energy) is selected with peak battery power of 8.0 kW.

Figure 22.19 gives the variation of hourly solar power generation (monthly mean) by solar PV power plant for 12 months for MSPV. The solar PV peak power generation is high during the month of March, i.e., 16.0 kW at 12:00 noon and the low peak is during the month of July at 12:00 noon, i.e., 9.81 kW (61.3% of rating).

Figure 22.20 shows the power supplied by SPV power plant, DG set, and battery bank during the month of March (high solar month) for MSPV. During the night hours, the power is supplied by battery bank till 05:00 h. At 05:00 h, DG set starts feeding power to the load because the battery bank charge reduces to below 30% and also load increases. The excess power generation by DG set is used to charge the battery bank after meeting the load power requirement. DG set will be operated till 09:00 h. The solar PV power plant starts generating power at 07:00 h and its power is less than the load requirement. Between 07:00 and 09:00 h, both DG set and SPV power plant will be operating in parallel to meet the load power requirement. After 09:00 h, solar PV power generation is more than the load requirement, the SPV power plant supplies the total load, and excess power

Fig. 22.19 Hourly solar power generation by SPV power plant for MSPV (monthly mean)

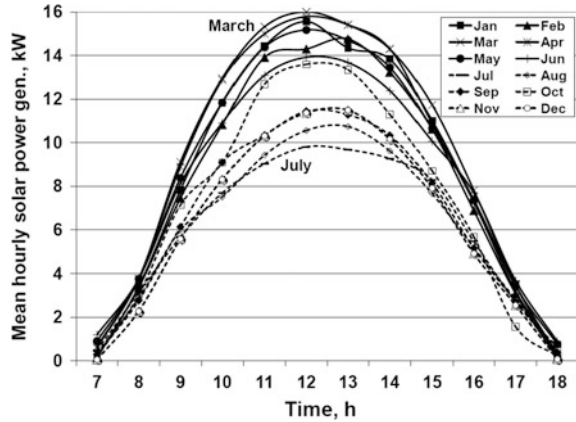
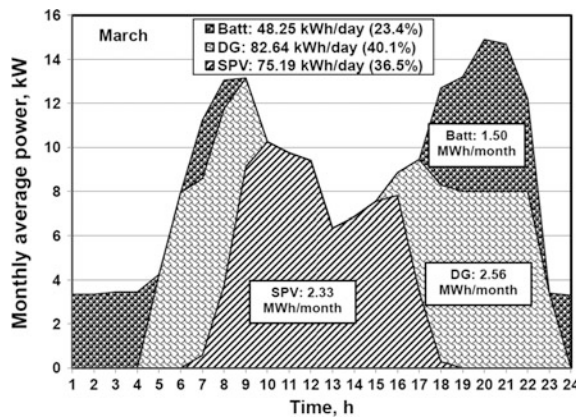


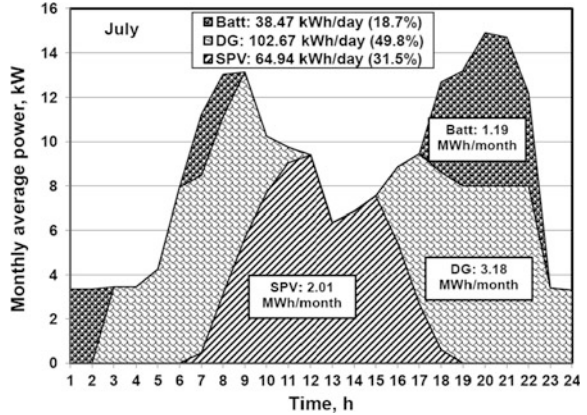
Fig. 22.20 Monthly average power generation by SPV power plant during March month for MSPV



generation is used to charge the battery bank till 15:00 h. Again at 15:00 h, the load power requirement is more than the SPV power, the DG set starts providing the power till 23:00 h. The excess power generation by DG set is fed to battery bank for charging. The charging power to battery bank is cut-off at 8.0 kW. Between 23:00 and 5:00 h, the power is supplied from the battery bank. The energy supplied to load by SPV power plant is 75.19 kWh/day (2.33 MWh/month) that forms about 36.5% of load requirement. The energy supplied by DG set to load is 82.64 kWh/day (2.56 MWh/month) that forms about 40.1% of load requirement. The energy supplied by DG set is slightly more than that of energy supplied by SPV (1.1 times). The energy supplied to load by battery banks is 48.25 kWh/month (1.50 MWh/month) that forms about 23.4% of load requirement.

Figure 22.21 shows the power supplied by SPV power plant, DG set, and battery bank during the month of July (low solar month) for MSPV. During the night hours, the power is supplied by battery bank till 03:00 h. At 03:00 h, DG set starts

Fig. 22.21 Monthly average power generation by SPV power plant during July month for MSPV



feeding power to load because the battery bank charge reduces to below 30% and also load increases. The excess power generation by DG set is used to charge the battery bank after meeting the load power requirement. DG set will be operated till 11:00 h. The solar PV power plant starts generating power at 07:00 h and its power is less than the load requirement. Between 07:00 and 11:00 h, both DG set and SPV power plant will be operating in parallel to meet the load power requirement. After 12:00 h, solar PV power generation is more than the load requirement, the SPV power plant supplies the total load, and excess power generation is used to charge the battery bank till 15 h. Again at 15:00 h, the load power requirement is more than the SPV power, the DG set starts providing the power till 24:00 h. The excess power generation by DG set is fed to battery bank for charging. The charging power to battery bank is cut-off at 8.0 kW. The energy supplied to load by SPV power plant is 64.94 kWh/day (2.01 MWh/month) that forms about 31.5% of load requirement. The energy supplied by DG set to load is 102.67 kWh/day (3.18 MWh/month) that forms about 49.8% of load requirement. The energy supplied by DG set is more than (1.58 times) that of energy supplied by SPV. The energy supplied to load by battery banks is 38.47 kWh/month (1.19 MWh/month) that forms about 18.7% of load requirement. The energy supplied by SPV power plant is less by about 13.6% compared to energy generated during March month whereas the energy supplied by DG set is increased by 24.2% compared to March month. The energy supplied by battery bank to load is decreased by 20.2% compared to March month.

Figure 22.22 gives the energy generation by SPV power plant, energy supplied directly to load and energy used for battery charging during the month of March for MSPV. The energy supplied by SPV power plant to load during March month is 75.19 kWh/day that forms about 67% of total energy generated by SPV power plant and the energy used for battery charging is 37.11 kWh/day (1.15 MWh/month) that forms about 33% of total energy whereas during the

Fig. 22.22 SPV energy supplied to load and for battery charging during March month for MSPV

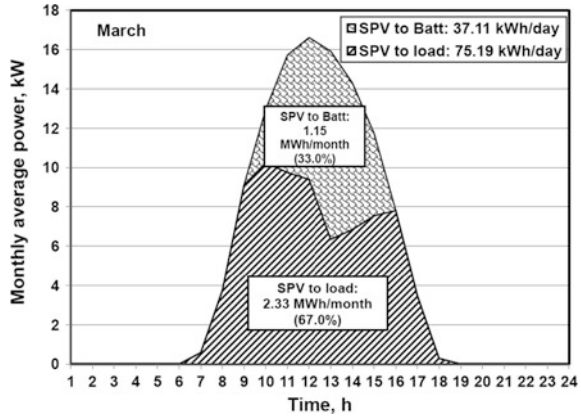
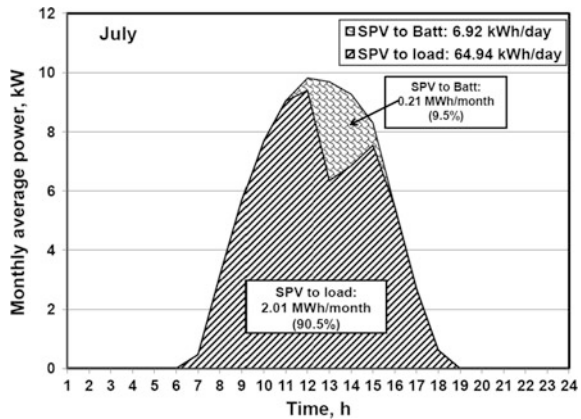


Fig. 22.23 SPV energy supplied to load and for battery charging during July month for MSPV



month of July the energy supplied by SPV power plant to load is 64.94 kWh/day that forms 90.5% of total energy generated by solar PV power plant and energy used for battery charging by SPV is 6.92 kWh/day (0.21 MWh/month) that forms 9.5% of total SPV energy (refer Fig. 22.23).

Figure 22.24 gives the energy generation by DG set, energy supplied directly to the load, and energy used for battery charging during March month for MSPV. The energy supplied by DG set to load is 82.64 kWh/day that forms about 80.8% of total energy generated by DG set. The energy used for battery charging is 19.66 kWh/day (0.61 MWh/month) that forms 19.2% of total energy. During the month of July, the energy supplied by DG set to load is 102.67 kWh/day that forms about 72.8% of total energy generated by DG set and the energy used for battery charging is 38.34 kWh/day (1.19 MWh/month) that forms about 27.2% of total energy (Refer Fig. 22.25). The dependence on DG set power is slightly more during the month of July compared to March month due to reduced solar irradiance.

Fig. 22.24 DG set energy supplied to load and for battery charging during March month for MSPV

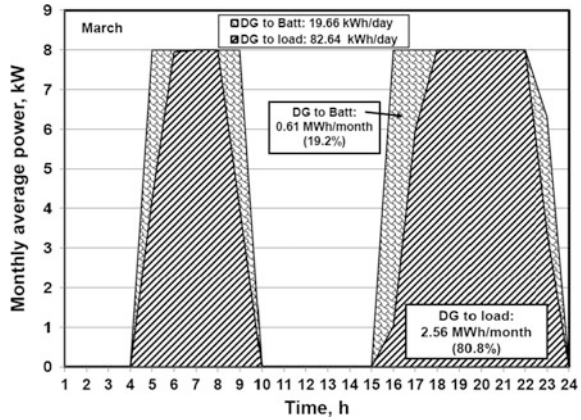


Fig. 22.25 DG set energy supplied to load and for battery charging during July month for MSPV

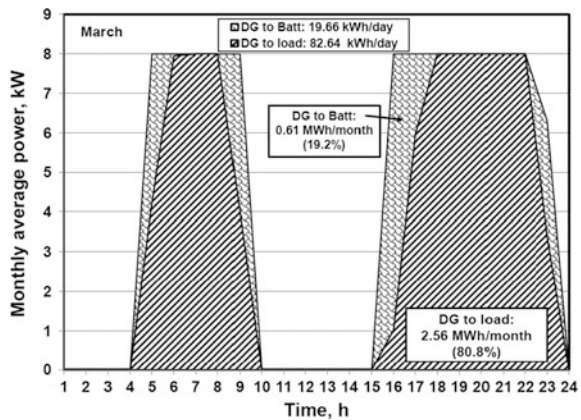


Figure 22.26 presents the state of energy capacity of battery (i.e., battery charge availability), battery charging by SPV, and DG set during the month of March for MSPV.

- 00:00–04:00, 07:00–08:00, and 18:00–22:00-h, battery supplies power to the load.
- 05:00–06:00, 09:00, 16:00–17:00, and 23:00 h, DG set supplies power to the load and excess power is being used to charge battery.
- 10:00–15:00 h, SPV supplies power to the load and excess power is used to charge the battery.
- The total energy supplied by SPV to charge battery is 65.4% of total battery capacity whereas 34.6% is supplied by DG set.

Figure 22.27 presents the state of energy capacity of battery (i.e., battery charge availability), battery charging by SPV, and DG set during the month of July for MSPV.

Fig. 22.26 State of battery charge during March month for MSPV

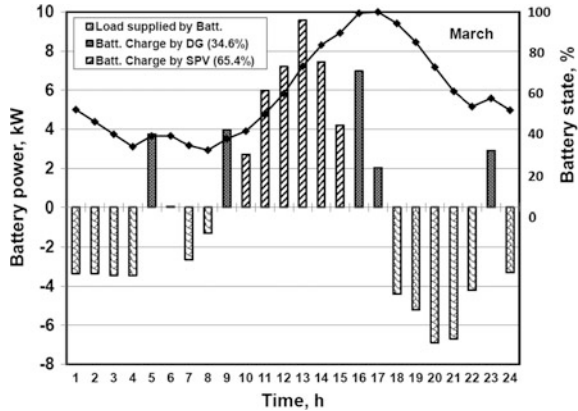
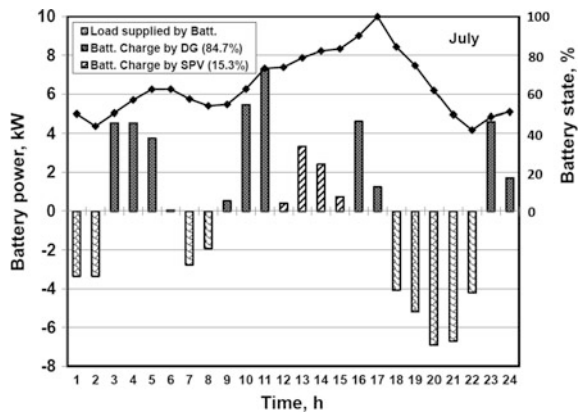


Fig. 22.27 State of battery charge during July month for MSPV



- 01:00–02:00, 07:00–08:00, and 18:00–22:00 h, battery supplies power to the load.
- 03:00–06:00, 09:00–11:00, 16:00–17:00, and 23:00–24:00 h, DG set supplies power to load and excess power is used to charge battery.
- 12:00–15:00 h, SPV supplies power to the load and excess power is used to charge the battery.
- The total energy supplied by SPV to charge battery is 15.3% of total battery capacity whereas 84.7% is supplied by DG set.

Figure 22.28 gives the variation of battery charge state throughout the year for MSPV. The battery charge state varies from 30.1 to 102.6%.

Figure 22.29 gives the variation of energy supplied by SPV power plant and DG set and share of SPV power plant. The energy supplied by SPV power plant varies between 2.23 MWh/month (July) and 3.48 MWh/month (March). The energy supplied by DG set varies between 3.05 MWh/month (March) and

Fig. 22.28 State of battery charge throughout the year for MSPV

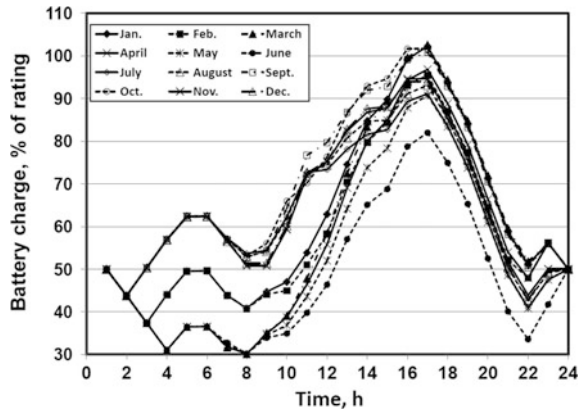
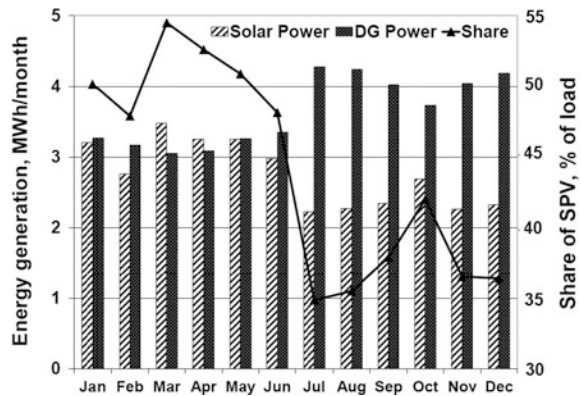


Fig. 22.29 Energy supplied by SPV and DG set for one year for MSPV



4.27 MWh/month (July). The energy share by SPV power plant varies between 34.9% (during July) and 54.5% (during March). The total energy supplied by SPV power plant is 33.04 MWh/year that forms 43.1% whereas the total energy supplied by DG set is 43.68 MWh/year which forms 56.9%. DG set energy generation is slightly higher by 13.8% that of SPV power plant (refer Fig. 22.30) for MSPV.

Figure 22.31 gives the variation of energy generated by SPV power plant and DG set with SSEG. It is shown from the figure that the energy generation by SPV power plant increases from 71.86 MWh/month (SSEG: 4.3 kWh/m² day) to 112.29 MWh/month (SSEG: 6.7 kWh/m² day). The energy generation by DG set decreases from 137.86 MWh/month (SSEG: 4.3 kWh/m² day) to 98.32 MWh/month (SSEG: 6.7 kWh/m² day).

Figure 22.32 shows the variation of energy supplied by SPV, DG set, and battery bank to load with SSEG. The energy supplied by SPV power plant directly to load is increased from 1.09 MWh/month (SSEG: 4.3 kWh/m² day) to 2.33 MWh/month (SSEG: 6.7 kWh/m² day). The energy supplied by DG set directly to load is

Fig. 22.30 Total energy share by SPV and DG set for one year for MSPV

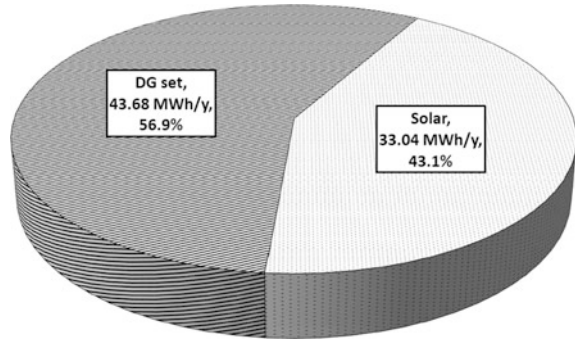


Fig. 22.31 Energy supplied by SPV and DG set with SSEG for MSPV

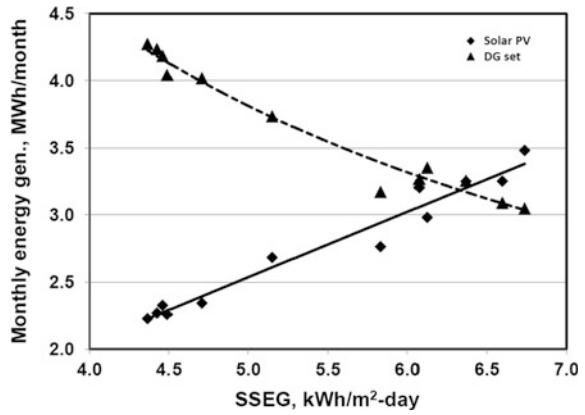
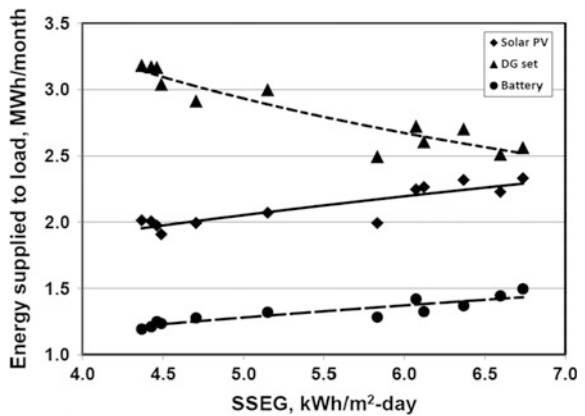


Fig. 22.32 Energy supplied by SPV, DG set, and battery to load with SSEG for MSPV



decreased from 3.18 MWh/month (SSEG: 4.3 kWh/m² day) to 2.49 MWh/month (SSEG: 6.7 kWh/m² day). The energy supplied by battery bank directly to load is almost same with slight variation between 1.19 and 1.50 MWh/month.

Fig. 22.33 Annual energy share by SPV power plant, DG set, and battery to load for MSPV

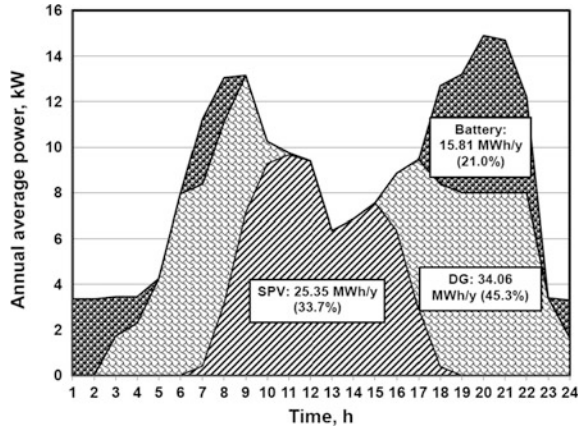


Figure 22.33 gives the annual average energy share by SPV power plant, DG set, and battery to meet the load requirement for MSPV. The annual average energy supplied by SPV power plant to load is 25.35 MWh/year that forms 33.7%, by DG set to load is 34.06 MWh/year (1.34 times of energy shared by SPV power plant) that forms about 45.3%, and by battery bank to load is 15.81 MWh/year that forms about 21.0%. The total energy supplied by SPV power plant and DG set is 76.72 MWh/year, and the total energy consumption by load is 75.22 MWh/year. The estimated energy loss in battery charging and other electronic controllers is 1.50 MWh/month that forms 1.96%.

22.6.1.3 High Solar Photovoltaic (HSPV) Power Plant

In this simulation, the design total solar PV power plant capacity is considered as 32.0 kW (power output) at 12:00 noon, i.e., at a solar irradiance of 1000 W/m² at STP. The rating of solar PV power plant chosen is 243.3% of peak power requirement of load. The load is peak of 13.15 kW happening at 09:00 h whereas the solar power availability for the design value of 32 kW SPV power plant is varying between 11.2 and 18.1 kW (35.0–56.6%). The DG set rating is considered as 5 kVA to meet the power requirement during non-solar hours. The battery bank size of 120 kWh (58.2% of total load energy) is selected with peak battery power of 20.0 kW.

Figure 22.34 gives the variation of hourly solar power generation (monthly mean) by solar PV power plant for 12 months for HSPV. The solar PV peak power generation is high during the month of March, i.e., 32.0 kW at 12:00 noon, and the low peak is during the month of July at 12:00 noon, i.e., 19.63 kW (61.3% of rating).

Figure 22.35 shows the power supplied by SPV power plant, DG set, and battery bank during the month of March (high solar month) for HSPV. During the night hours, the power is supplied by battery bank till 08:00 h. DG set will feed very less power between 07:00 and 08:00 h whereas solar power is less. The solar

Fig. 22.34 Monthly mean hourly solar power generation by SPV power plant for HSPV

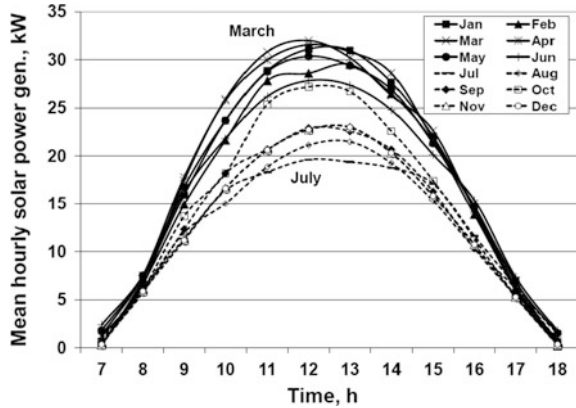
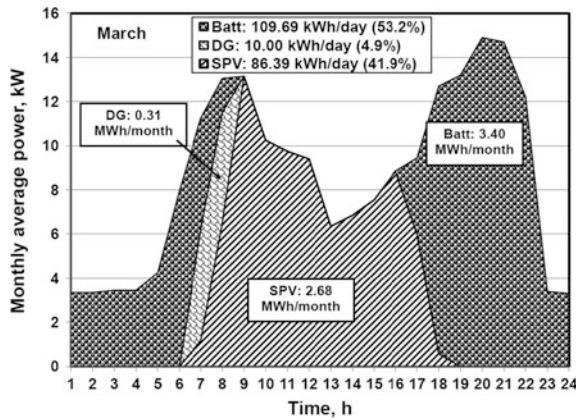


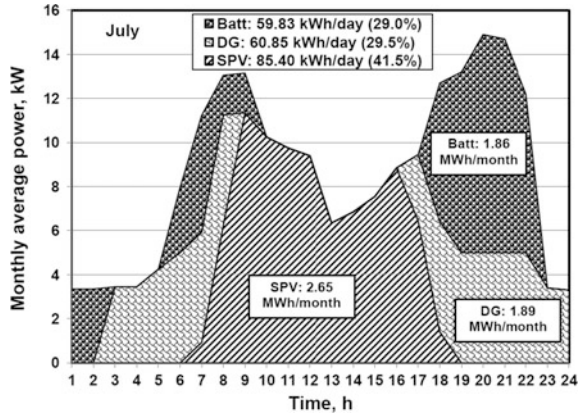
Fig. 22.35 Monthly average power generation by SPV power plant during March month for HSPV



PV power plant starts generating power at 07:00 h and starts feeding power to load in parallel with DG set till 08:00 h. Between 09:00 and 18:00 h, solar PV power plant feeds the power to load and excess power generation charges the battery bank. Between 18:00 and 24:00 h, the power is supplied from battery bank. The energy supplied to the load by SPV power plant is 86.39 kWh/day (2.68 MWh/month) that forms about 41.9% of load requirement. The energy supplied by DG set to load is less of about 4.9 kWh/day (0.31 MWh/month) that forms only about 4.9% of load requirement. The energy supplied to load by battery banks is 109.69 kWh/month (3.40 MWh/month) that forms about 53.2% of load requirement which is more than that of directly power fed from SPV power plant. The energy supplied by DG set is very less than that of energy supplied by SPV and battery bank. Therefore, the dependence on conventional power plant i.e., DG set is reduced, but the dependence on energy storage (battery bank) is increased.

Figure 22.36 shows the power supplied by SPV power plant, DG set, and battery bank during the month of July (low solar month) for HSPV. Battery bank will supply the power to load between 01:00–02:00, 06:00–09:00, and 18:00–22:00 h. At 03:00 h, DG set starts feeding power to load because the battery bank charge reduces

Fig. 22.36 Monthly average power generation by SPV power plant during July month for HSPV



to about 30% and also the load increases. The DG set will supply the power to load between 03:00–08:00 and 17:00–24:00 h. The excess power generation by DG set is used to charge the battery bank after meeting the load power requirement. The solar PV power plant starts generating power at 07:00 h, and its power is less than the load requirement. Between 07:00–08:00 and 17:00–18:00 h, both DG set and SPV power plant will be operating in parallel to meet the load power requirement. Between 10:00 and 12:00 h, solar PV power generation is more than the load requirement, the SPV power plant supplies the total load, and excess power generation is used to charge the battery bank. The energy supplied to the load by SPV power plant is 85.40 kWh/day (2.65 MWh/month) that forms about 41.5% of load requirement. The energy supplied by DG set to load is 60.85 kWh/day (1.89 MWh/month) that forms about 29.5% of load requirement. The energy supplied by DG set is less than that of energy supplied by SPV. The energy supplied to load by battery banks is 59.83 kWh/day (1.86 MWh/month) that forms about 29.0% of load requirement. The energy supplied by SPV power plant is less by about 1.1% compared to energy generated during the month of March whereas the energy supplied by DG set is increased by about 5 times compared to March month. The energy supplied by battery bank to load is decreased by 45.5% compared to March month.

Figure 22.37 gives the energy generation by SPV power plant, energy supplied directly to load and energy used for battery charging during the month of March for HSPV. The energy supplied by SPV power plant to load during March month is 86.39 kWh/day that forms about 44% of total energy generated by SPV power plant and the energy used for battery charging is 109.69 kWh/day (3.40 MWh/month) that forms about 56% of total energy which is very high due to the power share by SPV power plant is high that needs to be stored in battery. The battery bank is 100% charged by SPV power plant only. During the month of July, the energy supplied by SPV power plant to load is 85.40 kWh/day that forms 57.9% of total energy generated by solar PV power plant and energy used for battery charging by SPV is 62.23 kWh/day (1.93 MWh/month) that forms 42.1% of total SPV energy (refer Fig. 22.38).

Fig. 22.37 SPV energy supplied to load and for battery charging during March month for HSPV

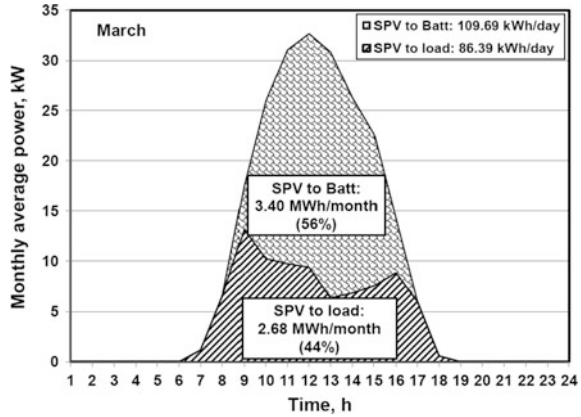
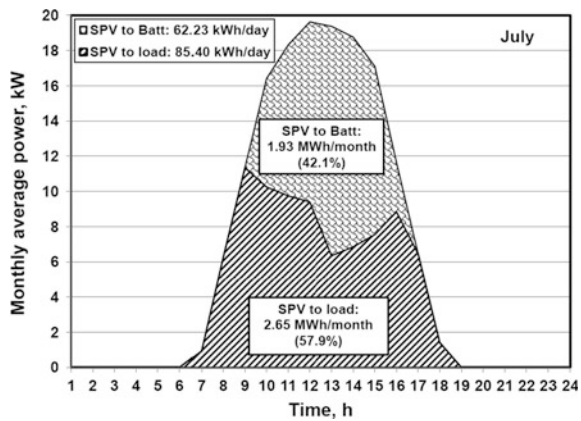


Fig. 22.38 SPV energy supplied to load and for battery charging during July month for HSPV



Since the major power is fed from SPV power plant, the energy supplied by DG set to load is only 10.0 kWh/day (0.31 MWh/month) that forms about 4.9% of total load energy and DG power is not used to charge battery. During the month of July, the energy supplied by DG set to load is 60.85 kWh/day that forms about 88.3% of total energy generated by DG set and the energy used for battery charging is 8.16 kWh/day (0.25 MWh/month) that forms about 11.7% of total energy (refer Fig. 22.39). The dependence on DG set power is slightly more during the month of July compared to March month due to reduced solar irradiance. But overall battery charging is less dependent on DG set.

Figure 22.40 presents the state of energy capacity of battery (i.e., battery charge availability), battery charging by SPV, and DG set during the month of March for HSPV.

- 01:00–08:00 and 17:00–24:00 h, battery supplies power to the load.
- 09:00–16:00 h, SPV supplies power to load and excess power is used to charge battery.

Fig. 22.39 DG set energy supplied to load and for battery charging during July month for HSPV

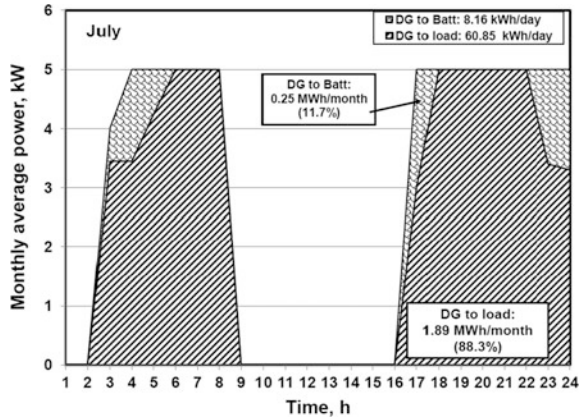
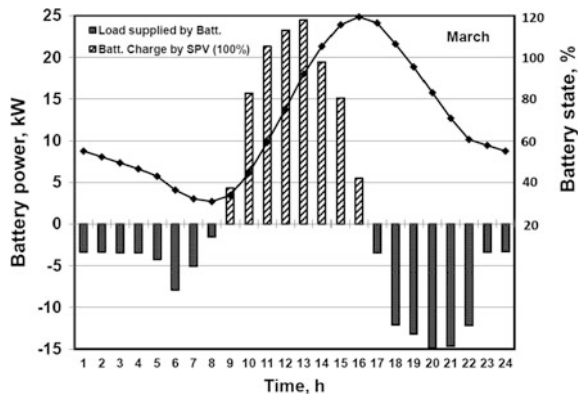


Fig. 22.40 State of battery charge during March month for HSPV



- The total energy supplied by SPV to charge battery is 100% of total battery capacity and no DG set power is used for battery charging.
- The battery state is varying between 30.8 and 119.4% and between 14:00 and 18:00 h the battery state is slightly higher than 100% during the month of March.

Figure 22.41 presents the state of energy capacity of battery (i.e., battery charge availability), battery charging by SPV, and DG set during the month of July for HSPV.

- 01:00–02:00, 06:00–09:00, and 18:00–22:00 h, battery supplies power to the load.
- 03:00–05:00, 17:00, and 23:00–24:00 h, DG set will supply the power to load and excess power is used to charge battery.
- 10:00–16:00 h, SPV supplies power to the load and excess power is used to charge the battery.

Fig. 22.41 State of battery charge during July month for HSPV

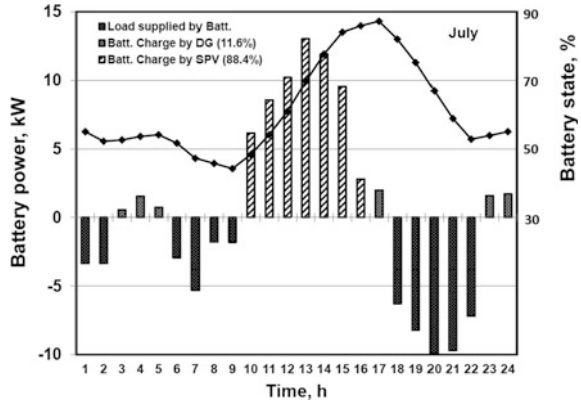
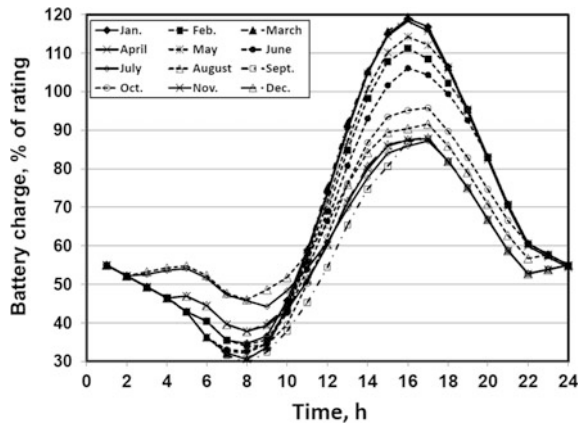


Fig. 22.42 State of battery charge throughout the year for HSPV



- The total energy supplied by SPV to charge battery is higher by about 88.4% of total battery capacity whereas the energy used by DG set to charge battery is 11.6% which is less.
- The battery state is varying between 44.3 and 87.2% and is normal.

Figure 22.42 gives the variation of battery charge state throughout the year for HSPV. The battery charge state varies from 29.7 to 119.4%.

Figure 22.43 gives the variation of energy supplied by SPV power plant and DG set and share of SPV power plant. The energy supplied by SPV power plant varies between 4.56 MWh/month (July) and 6.68 MWh/month (March). The energy supplied by DG set varies between 3.05 MWh/month (March) and 4.27 MWh/month (July). The energy share by SPV power plant varies between 70.8% (during July) and 96.2% (during March). The total energy supplied by SPV power plant is 66.24 MWh/year that forms 82.1% whereas the total energy supplied by DG set is 14.44 MWh/year which forms 17.9%. SPV power plant energy generation is higher compared to DG set by 64.2% (refer Figure 22.44) for HSPV.

Fig. 22.43 Energy supplied by SPV and DG set for one year for HSPV

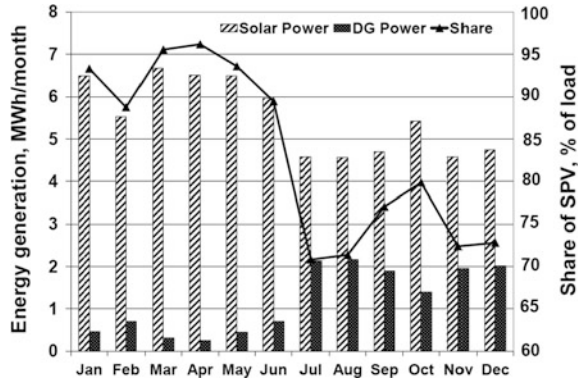


Fig. 22.44 Total energy share by SPV and DG set for one year for HSPV

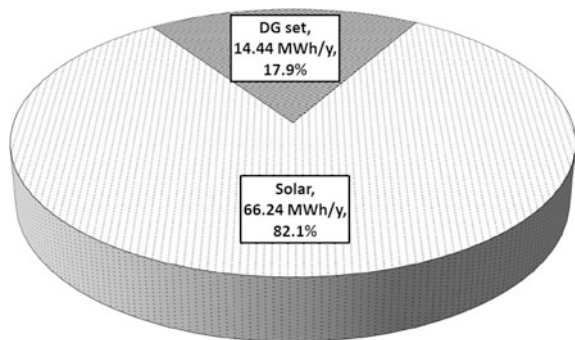


Figure 22.45 gives the variation of energy generated by SPV power plant and DG set with SSEG. It is shown from the figure that the energy generation by SPV power plant increases from 4.58 MWh/month (SSEG: 4.3 kWh/m² day) to 6.68 MWh/month (SSEG: 6.7 kWh/m² day) which is much higher than that of DG set energy. The energy generation by DG set decreases from 2.14 MWh/month (SSEG: 4.3 kWh/m² day) to 0.31 MWh/month (SSEG: 6.7 kWh/m² day).

Figure 22.46 shows the variation of energy supplied by SPV, DG set, and battery bank to load with SSEG. The energy supplied by SPV power plant directly to load is slightly increased from 2.44 MWh/month (SSEG: 4.3 kWh/m² day) to 2.79 MWh/month (SSEG: 6.7 kWh/m² day) because major portion of SPV energy is used for battery charging. The energy supplied by DG set directly to load is decreased from 1.86 MWh/month (SSEG: 4.3 kWh/m² day) to 0.31 MWh/month (SSEG: 6.7 kWh/m² day). The energy supplied by battery bank directly to load is increased from 1.85 to 3.40 MWh/month due to higher share of SPV.

Figure 22.47 gives the annual average energy share by SPV plant, DG set, and battery to meet the load requirement for HSPV. The annual average energy supplied by SPV plant to load is 31.3 MWh/year that forms 41.6%, by DG set to load is 12.88 MWh/year that forms 17.1%, and by battery bank to load is 31.04 MWh/year

Fig. 22.45 Energy supplied by SPV and DG set with SSEG for HSPV

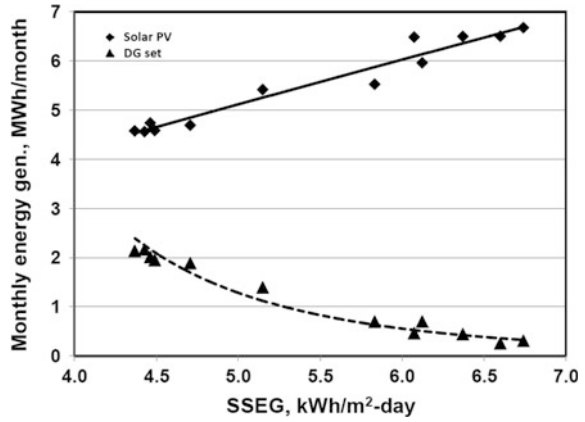


Fig. 22.46 Energy supplied by SPV, DG set, and battery to load with SSEG for HSPV

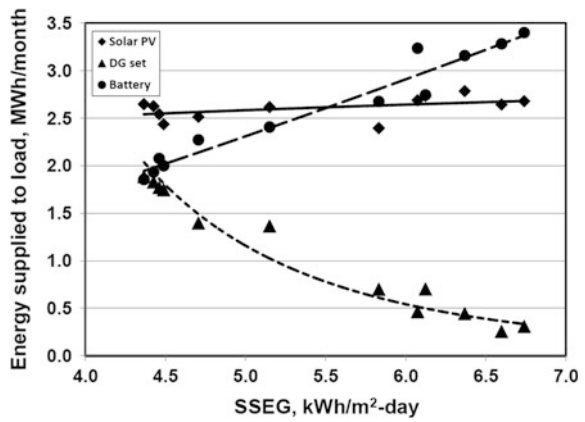
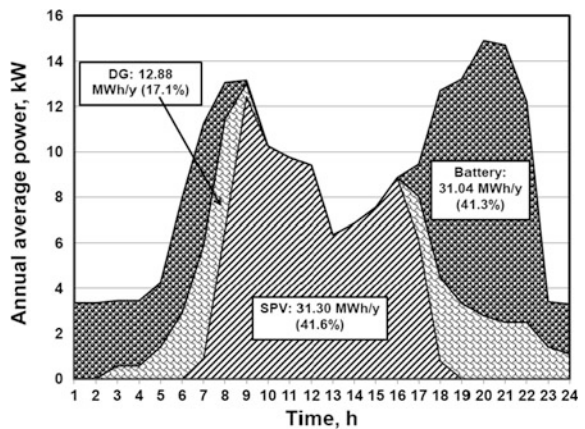


Fig. 22.47 Annual energy share by SPV power plant, DG set, and battery to load for MSPV



that forms about 41.3%. The total energy supplied by SPV power plant and DG set is 80.67 MWh/year, and the total energy consumption by load is 75.22 MWh/year. The estimated energy loss in battery charging and controllers is 5.45 MWh/month that forms 6.76% which is higher than other two configurations because the energy loss in battery charge and discharge cycle of battery bank is high.

22.6.2 Reliability of the System

Reliability is defined as the probability that a system will perform properly for a specified period of time under a given set of operating conditions [17]. The measure of reliability of the power system is how long the renewable energy system supplies power with what capacity factor. Generally, the reliability of the SPV power plant is better compared to other renewable energy system, but the environmental conditions like cloud cover (clearness index) will reduce the energy generation by SPV power plant. The ambient temperature also influences the energy generation by SPV power plant because at higher cell temperature, the efficiency of solar cell from converting solar radiation to electrical energy will reduce. The reliability of energy generation by DG set and battery bank will be higher compared to SPV power plant. As the share of SPV power plant increases, the reliability of the total hybrid energy system decreases. While designing the solar PV based hybrid energy system, the reliability factor may also be considered along with life cycle cost of energy. The clearness index values depend on the location and the time of year considered that varies between 0.3 (overcast climates) and 0.8 (sunny location).

22.7 Cost-Benefit Analysis

The optimization of hybrid energy system highly influenced by techno-economic feasibility of the hybrid energy system [18]. In order to calculate the simple life cycle cost of energy, it is considered capital cost, operation and maintenance (O&M) cost, fuel cost, and recovery cost for replacement of equipment at the end of life for each component of the hybrid energy system, i.e., life for PV panels is considered as 25 years, 3 years for battery banks, and 10 years for electronic components.

- (a) **Annualized capital cost:** The annualized capital cost (ACC) (\$/year) is computed by

$$ACC = CC \times CRF(i, L_{proj}) \quad (22.25)$$

where CC is initial capital cost (\$), CRF is capital recovery factor and is given by

$$\text{CRF}(i, L_{\text{proj}}) = \frac{i(1+i)^{L_{\text{proj}}}}{(1+i)^{L_{\text{proj}}}-1} \quad (22.26)$$

where i is interest rate (%) and L_{proj} is life of the project (y).

- (b) **Annualized replacement cost:** The annualized replacement cost (\$/year) is calculated by

$$\text{ARC} = \text{CRC} \times \left[f_{\text{rep}} \times \text{SFF}(i, L_{\text{comp}}) - \left(\frac{L_{\text{rem}}}{L_{\text{comp}}} \right) \times \text{SFF}(i, L_{\text{proj}}) \right] \quad (22.27)$$

where CRC is capital recovery cost at the end of life of component (\$), f_{rep} is replacement factor and is given by

$$f_{\text{rep}} = \begin{cases} \frac{\text{CRF}(i, L_{\text{proj}})}{\text{CRF}(i, L_{\text{rep}})} & \text{for } L_{\text{rep}} > 0 \\ 0 & \text{for } L_{\text{rep}} = 0 \end{cases} \quad (22.28)$$

where L_{rep} is replacement cost duration and is given by

$$L_{\text{rep}} = L_{\text{comp}} \times \text{INT} \left(\frac{L_{\text{proj}}}{L_{\text{comp}}} \right) \quad (22.29)$$

where L_{comp} is life time of the individual components (y), L_{rem} is remaining life of component (y) and SFF is sinking fund factor and is given by

$$\text{SFF}(i, L_{\text{proj}}) = \frac{i}{(1+i)^{L_{\text{proj}}}-1} \quad (22.30)$$

- (c) **Annual maintenance cost:** Operation and maintenance (O&M) cost for SPV power plant, i.e., for SPV panels and related DC components is considered as 0.5% of capital cost per year. The O&M cost for DG set is considered as 10% of the capital cost because it consists of moving parts which needs more maintenance compared to other components of hybrid energy system. The O&M cost for battery bank is considered as 5% of capital cost per year. The O&M cost for inverter system including power conditioner and battery charger is also considered as 5% of capital cost per year.
- (d) **Annual fuel cost:** It is the cost for running the DG set. The average present cost of generation by DG set is \$0.35 per kWh.

Total annualized cost of energy (\$/year) is given by

$$TAC = ACC + ARC + AMC + AFC \tag{22.31}$$

Life cycle cost of energy (LCCOE) (\$/kWh) is calculated by

$$LCCOE = \frac{TAC}{E} \tag{22.32}$$

Tables 22.3 22.4, and 22.5 give the economics of life cycle cost analysis for low, medium, and high SPV power plants, respectively.

Figure 22.48 shows the capital cost for SPV power plant and DG set for implementing the hybrid energy system. The SPV cost varies between \$7300 and \$26,353 (2.61 times) with the increase in SPV share from 21.3 to 82.1% whereas the capital cost for DG set decreases from \$570 to \$288 (49.5%). Figure 22.49 shows the capital cost for battery bank and inverter system including power conditioner and battery charger for implementing the hybrid energy system. The battery cost increases from \$1364 to \$3620 (1.65 times) whereas the capital cost for inverter system increases from \$610 to \$2090 (2.43 times). Figure 22.50 shows the total capital cost for installation of hybrid energy system and specific cost for SPV power plant for three configurations. The total capital cost increases from \$9844 to \$32,351 that increase the capital initial investment by 2.29 times whereas the share of SPV increases from 21.3 to 82.1%, i.e., change in share of SPV is 2.85 times. The specific capital cost (SCC) is computed as follows:

$$SCC = \frac{CC}{E_{SPV}} \tag{22.33}$$

where CC is capital cost (\$) and E_{SPV} is the energy generated by SPV power plant per year (kWh/year).

The specific cost for low SPV configuration is \$0.614 per kWh/year; for medium SPV, it is \$0.538 per kWh/year; and for high SPV, it is \$0.524 per kWh/year. As the size of SPV power plant increases, the specific cost for installation of SPV power plant decreases.

Table 22.3 Economics of life cycle cost analysis for LSPV power plant

Component	Capital cost (\$)	Annualized capital cost (\$/year)	Annualized replacement cost (\$/year)	Annual O&M cost (\$/year)	Annual fuel cost (\$/year)	Total Annualized cost (\$/year)
Solar PV	7300	684	0	37	0	721
DG set	570	54	81	57	21,258	21,450
Battery	1364	128	260	68	0	456
Inverter	610	57	13	31	0	101
Total	9844	923	354	193	21,258	22,728

Life cycle cost of energy: \$0.302 per kWh

Table 22.4 Economics of life cycle cost analysis for MSPV power plant

Component	Capital cost (\$)	Annualized capital cost (\$/year)	Annualized replacement cost (\$/year)	Annual O&M cost (\$/year)	Annual fuel cost (\$/year)	Total Annualized cost (\$/year)
Solar PV	13,870	1300	0	71	0	1371
DG set	418	39	60	42	15,222	15,363
Battery	2043	192	390	102	0	684
Inverter	1108	104	24	55	0	183
Total	17,439	1635	474	270	15,222	17,601

Life cycle cost of energy: \$0.234 per kWh

Table 22.5 Economics of life cycle cost analysis for HSPV power plant

Component	Capital cost (\$)	Annualized capital cost (\$/year)	Annualized replacement cost (\$/year)	Annual O&M cost (\$/year)	Annual fuel cost (\$/year)	Total Annualized cost (\$/year)
Solar PV	26,353	2469	0	135	0	2604
DG set	288	27	42	29	5032	5130
Battery	3620	339	682	181	0	1202
Inverter	2090	196	45	105	0	346
Total	32,351	3031	769	450	5032	9282

Life cycle cost of energy: \$0.123 per kWh

Fig. 22.48 SPV and DG set capital cost for hybrid energy system

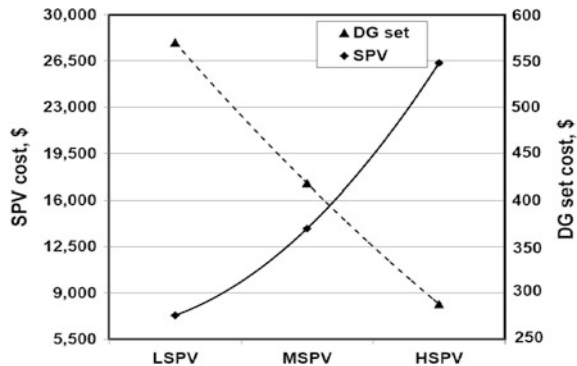


Figure 22.51 shows the split-up of capital cost components for hybrid energy systems for three configurations. The capital cost for SPV plant increases from 74.1 to 81.5% which shows that the capital cost for SPV power plant dominates almost 3/4th of the total capital cost. The capital cost share for DG set to provide firm power decreases from 5.8 to 0.9%. The capital cost share of battery system decreases from 13.9 to 11.2%. The capital cost for inverter and other electronic components increases from 6.2 to 6.5%.

Fig. 22.49 Battery and power controller and inverter capital cost for hybrid energy system

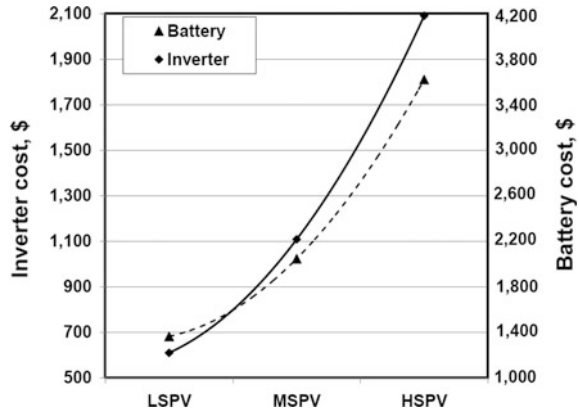


Fig. 22.50 Total capital cost for hybrid energy system

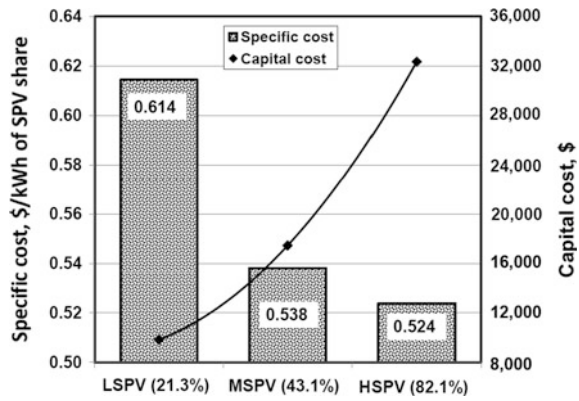


Fig. 22.51 Split-up of capital cost components for hybrid energy systems

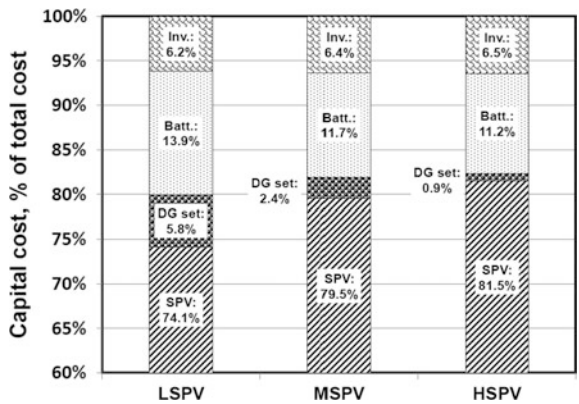


Fig. 22.52 Split-up of annualized cost for each component for hybrid energy systems

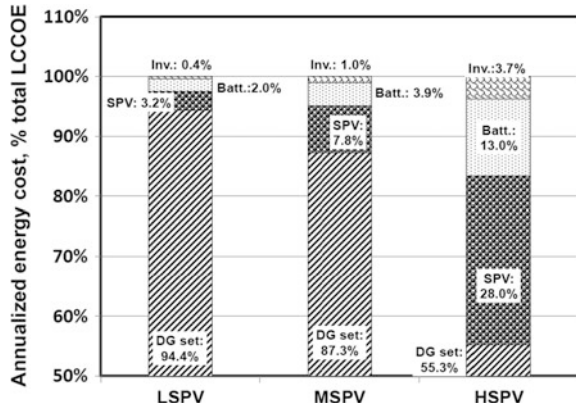


Fig. 22.53 Life cycle cost of energy for hybrid energy systems

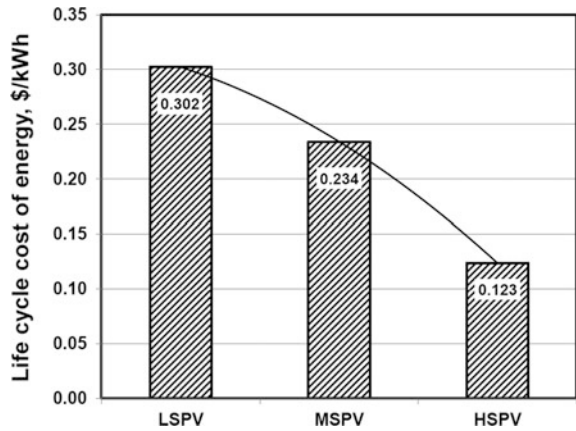


Figure 22.52 shows the split-up of annualized cost for each component for hybrid energy systems for three configurations. The annualized cost for DG set is higher in the range of 55.3–94.4% because the fuel cost is more for operating the DG set. This annualized cost for DG set decreases from 94.4 to 55.3% of total annualized cost because energy cost for of DG set is very high compared to other forms of energy. The annualized cost for SPV power plant increases from 3.2 to 28.0% due to increased share of SPV power plant. The annualized cost for battery bank increases from 2.0 to 13.0% and the annualized cost for inverter and other controller system also increases from 0.4 to 3.7% due to increased share of SPV power plant.

Figure 22.53 shows the life cycle cost of energy (LCCOE) for hybrid energy system. The life cycle cost is computed by considering the average life of project as 25 years, life of solar PV panels as 25 years, inverter and other electronic components as 10 years, and battery bank life as 3 years. The LCCOE is \$0.302 per kWh for LSPV power plant, \$0.234 per kWh for MSPV power plant, and \$0.123 per kWh for HSPV power plant. This LCCOE is less than the cost of energy

generation by DG set alone which is about \$0.35 per kWh. It is shown from the figure that as the share of SPV increases, the LCCOE decreases because the share of energy generation by DG set, i.e., share of fuel cost comes down.

22.8 Pollution

The major cause of CO₂ emission is mainly because of electrical power generation by conversion of fuels, especially fossil fuels like coal [19]. The world electrical energy generation through CO₂ emitting technology (fossil fuel based) is about 86.9% of total electrical energy generation and non-CO₂ emitting technology is 13.1% of total electrical energy generation (renewable: 1.93%, hydro: 6.68%, and nuclear: 4.49%) [20]. The Indian electrical energy generation through CO₂ emitting technology (fossil fuel based) is about 69.5% of total electrical energy generation and non-CO₂ emitting technology is 30.5% of total electrical energy generation (renewable: 12.5%, hydro: 16.1%, and nuclear: 1.9%). The energy generation in India through non-CO₂ emitting route is better than world's average.

The world's average specific CO₂ emission (emission of CO₂ in kg for generation of electrical energy of 1 kWh) is varying between 0.525 and 0.547 kg/kWh. The world's average specific CO₂ emission by coal-fired power plant is 0.920 kg/kWh, by oil plant is 0.583 kg/kWh, and by natural gas plant is 0.452 kg/kWh. The specific CO₂ emission in Indian power plant is varying between 0.81 and 1.05 kg/kWh.

Most of the electrical energy generation is through burning of fossil fuels which generate CO₂ emission that increases the global warming. The Indian average CO₂ emission liberated by energy generation by coal-fired power plants is 0.93 kg of CO₂ emission per kWh and by DG set is about 0.69 kg of CO₂ emission per kWh of energy generated [21]. The energy generation by solar PV power plant is free from pollution such as global warming and CO₂ emission.

The CO₂ emission by hybrid energy system (tonne/year) is computed by

$$\text{CO}_{2\text{-gen.}} = (E_{\text{DG}} \times \text{SCO}_{2\text{-DG}}) \times 10^{-3} \quad (22.34)$$

where E_{DG} is the energy supplied by DG set (kWh/year), and $\text{SCO}_{2\text{-DG}}$ is the specific CO₂ emission by DG set (kg/kWh).

The reduction of CO₂ emission by implementing hybrid energy system (tonne/year) is computed by

$$\text{CO}_{2\text{-red.}} = [(E_{\text{DG}} + E_{\text{SPV}}) \times \text{SCO}_{2\text{-coal}} \times 10^{-3}] - \text{CO}_{2\text{-gen.}} \quad (22.35)$$

where E_{SPV} is the energy supplied by SPV power plant (kWh/year) and $\text{SCO}_{2\text{-coal}}$ is the specific CO₂ emission by coal-fired power plant (kg/kWh).

The present CO₂ emission without implementation of hybrid solar PV power system is estimated as 73.0 tonne/year. The computed reduction in CO₂ emission

Table 22.6 Techno-economics of SPV—DG hybrid energy system

Sl. No.	Particulars	Low SPV	Medium SPV	High SPV
01	Peak power rating of SPV (kW)	8.0	12.0	16.0
02	Rating of DG set (kVA)	12.0	10.0	8.0
03	Battery bank capacity, peak power (kW)/energy (kWh/day)	5.0/36	6.0/44	8.0/54
04	Annual energy supplied by SPV power plant to load (MWh/year)	16.26	25.35	31.30
05	Annual energy supplied by SPV power plant for battery charging (MWh/year)	0.24	7.69	34.94
06	Total annual energy supplied by SPV power plant (MWh/year)	16.50 (21.3%)	33.04 (43.1%)	66.24 (82.1%)
07	Annual energy supplied by DG set to load (MWh/year)	47.93	34.06	12.88
08	Annual energy supplied by DG set for battery charging (MWh/year)	13.07	9.62	1.56
09	Total annual energy supplied by DG set (MWh/year)	61.00 (78.7%)	43.68 (56.9%)	14.44 (17.9%)
10	Annual energy supplied by battery bank to load (MWh/year)	11.03	15.81	31.04
11	Capital cost (\$)	9844	17,439	32,351
12	Annualized cost (\$/year)	22,728	17,601	9282
13	Life cycle cost of energy (\$/kWh)	0.302	0.234	0.123
14	Reduction in CO ₂ emission (tonne/year)	30.0	41.2	65.1

for LSPV configuration is 30.0 tonne/year (reduction of 41.1%), by MSPV is 41.2 tonne/year (56.4%), and by HSPV is 65.1 tonne/year (89.1%).

22.9 Conclusions

Table 22.6 gives the results of simulation of three different configurations of hybrid energy system. The use of solar PV power plant along with the conventional power generator (DG set) and energy storage battery bank reduces the life cycle cost of energy compared to operation of only DG set. The increase in share of SPV generation from 21.3 to 82.1% reduces the dependence on DG set from 78.7 to 17.9%, and the overall reduction in CO₂ emission is increased from 30.0 to 65.1 tonne/year. The capital cost increases from \$9844 to \$32,351 (increase of 69.6%), and the annualized cost decreases from \$22,728 to \$9282 (reduction of 59.3%). The increased share of SPV power generation reduces the life cycle cost of energy from \$0.302 to \$0.123 per kWh (decrease of 59.3%). However, the increased share of SPV reduces the reliability of the power system as more energy is generated by SPV power plant which is intermittent in nature and seasonal.

References

1. Mandi RP, Yaragatti UR (2011) Grid interacted solar photovoltaic power plant for rural banks. In: Proceedings of international conference on roadmap for smart grid, organized by CPRI, Bangalore, held on 3–4 Aug 2011, pp 131–136
2. Erge T, Hoffmann VU, Kiefer K (2001) The German experience with grid-connected PV-system. *Sol Energy* 70(6):479–487
3. Kim H-S, Okada N, Takigawa K (2001) Advanced grid connected PV system with functions to suppress disturbance by PV output variation and customer load change. *Sol Energy Mater Sol Cells* 67:559–569
4. Mandi RP, Yaragatti UR (2010) Solar PV-diesel hybrid energy system for rural applications. In: Proceedings of fifth international conference on industrial and information systems-2010, Published in IEEE Explorer, organized by National Institute of Technology Karnataka, Surathkal, during 29 July–1 Aug 2010, pp 555–560
5. Grid-tied photovoltaic system performance conversion efficiency factor, solar module tilt angle. Website: <http://www.solarexpert.com/grid-tie/system-performance-factors.html>
6. de Almeida AT, Martins A, Jesus H, Climaco J (1983) Source reliability in combined wind-solar-hydro system. *IEEE Trans Power Apparatus Syst* PAS-102(6)
7. Website: <http://www.energymatters.com.au/components/battery-voltage-discharge/>
8. Kamel Fouad (1995) Perspectives on grid-connected photovoltaic solar generators. *Renew Energy* 6(5–6):515–520
9. Langworthy A (1991) Intelligent power station control systems for remote area power supply. In: *Electric energy conference*, Darwin, pp 68–74
10. Ernest Palomino G, Performance of a grid connected residential photovoltaic system with energy storage. In: 26th IEEE photovoltaic specialists conference, 29 Sept–3 Oct 1997
11. Wichert B (1997) PV-diesel hybrid energy systems for remote area power generation—a review of current practice and future developments. *Renew Sustain Energy Rev* 1(3):209–228
12. Peippo K, Lund PD (1994) Optimal sizing of solar array and inverter in a grid-connected photovoltaic systems. *Sol Energy Mater Sol Cells* 32:95–114
13. Nayar CV (1995) Recent developments in decentralized mini-grid diesel power systems in Australia. *Appl Energy* 52:229–242
14. HOMER home page. <http://www.nrel.gov/international/tools/HOMER/homer.html>
15. Mandi RP, Yaragatti UR (2013) Optimal hybridization of renewable energy systems to improve energy efficiency. *J CPRI* 9(4):521–532
16. Rajan CCA (1997) Stand-alone wind-solar photovoltaic integrated power generation system for rural areas. In: Proceedings of national conference on application of solar energy—recent developments, at ERC, CPRI, Trivandrum, 20–21 Nov 1997, pp 18–21
17. Mandi RP, Yaragatti UR (2013) Integration of renewable energy system solar PV with diesel. *J CPRI* 9(4):533–542
18. Mandi RP (2015) Solar PV—LED rooftop systems for office lighting applications. *MGIRE J* 1(1):44–55. ISSN 2393-9605
19. Raghuvanshi SP, Chandra A, Raghav AK (2006) Carbon dioxide emissions from coal based power generation in India. *J Energy Convers Manage* 47(2006):427–441
20. IEA Statistics (2014) CO₂ emissions from fuel combustion, 2014 edn. International Energy Agency, Paris
21. International Energy Agency (2012) CO₂ emissions from fuel combustion: beyond 2020 documentation, 2012 edn

Chapter 23

Intelligent Energy Management Strategy Considering Power Distribution Networks with Nanogrids, Microgrids, and VPP Concepts

Jackson J. Justo

23.1 Introduction

Energy sector is undergoing a transformation by moving away from a few, centralized power plants to a decentralized with many small of low to high voltages bidirectionally networked production plants and consumers forming the so-called energy vectors [1–3]. Actually, as the world changes, urbanization also continues, whereby cities are playing a greater role as the new “units of change.” Cities have become the defining places where the cost, availability, and finite nature of natural resources; with emissions and compliance; and with climate change. This is a set of progressively developing and intrinsically linked challenges, toward which action must be accelerated. In particular, energy management algorithms (EMAs) are an integral part of the energy transformation process to achieve the expected performance benefits. The optimal performance of EMAs depends strongly on the ability to forecast the present and future energy demands and compare with the available generation capacity from the various interconnected sources. For instance, information available about the renewable energy (such as temperature, humidity, wind, and road grade) and mobile energy storage system (such as traffic density, traffic lights, and location of charging station) is very important in operating the power distribution networks with EMAs at optimal efficiency [4].

Historically, the concept of supervisory control and data acquisition (SCADA) system was introduced in the late 1960s. Afterward, the energy management system solution with set of functionalities that relied on SCADA data was introduced in the 1970s [5]. During that time, the EMA design was based on the notion that power system goes through the following distinct states: normal, alert, emergency, and restorative states and hence the EMS functionalities needed to assist operators’

J.J. Justo (✉)

Department of Electrical, Electronics, and Computer Systems Engineering,
University of Pretoria, Hatfield Campus, Pretoria 0028, South Africa
e-mail: jackjusto2009@gmail.com

ability to monitor the system behavior as it goes through any of these four operating states and make decisions to steer it back to the normal state [6]. As the time went by, many things have changed in the area of power systems such as (i) introduction of the electricity markets which accommodates competitive trading, (ii) growth of the power system infrastructure to meet demand for integration of renewable resources, and (iii) EMS technology to improve computations, communications, and visualization. As the “central nerve system” of the grid operations and open electricity market, the EMS design is undergoing tremendous changes to meet the needs of the evolving utility industry. Thus, the SCADA solutions based on proprietary computer hardware and software have made access to the third-party software providers difficult [7, 8].

Looking into the integration of renewable energy resources (RERs) such as wind, solar PV, and min-hydro-power, low-carbon and reasonably priced energy can be offered. On the other hand, they are inflexible and cannot respond to demand for electricity in the same way the conventional energy generating units like thermal energy resource can. In addition, when wind and solar PV systems reach certain levels of penetration on a grid system, levels that are different for every grid, there are technical and market effects that grid operators must contend with such as (i) including demand/supply curves, (ii) negative pricing, and (iii) voltage/frequency disruptions. Thus, energy storage systems have become the powerful and appealing alternative for upgrading grid infrastructure with high penetration of renewable energy resources to solve such challenges [9–11].

Focusing on the need of decarbonization of electricity infrastructures, the interest for alternative energy has shifted on integration of RERs into the power distribution networks in the form of nanogrid (n -grid), microgrid (μ -grid), and virtual power plants (VPPs). Based on the literature review, the following are typical definitions of the three concepts:

- **Nanogrid (i.e., n -grid)** is a local DC distribution system mainly installed for residential and commercial buildings applications [12, 13]. The n -grid uses low-voltage DC technology to provide various advantages such as easier integration with renewable energy sources and energy storage system such as battery banks, and increased savings. In the near future, power distribution systems would use n -grid with renewable energy sources and storage devices to become self-sufficient in generation with bare minimum consumption from the grid [14]. Then, multiple connections of such nanogrid can composite the so-called multi-nanogrid systems (MNS). The MNS are nothing but the interconnection of many single DC distribution networks which enhances the interactive use of energy available in neighboring RERs to increase the reliability of power supply of the neighboring buildings [15, 16].
- **Microgrid (i.e., μ -grid)** also named minigrid system is defined as a kind of technology which can control DER, controllable load, and energy storage system components to increase an acceptance ability of intermittent distributed power of local power system, and improve the reliability of the operation [17, 18]. While most of the present studies/researches focus on the application of

ESS and DER units on internal μ -grid operation, external μ -grid operation and configuration have been little exploited [19, 20]. Then, multiple configurations of such microgrid can composite multi-microgrid systems (MMS). The MMS can enhance the interactive use of clean energy and make full use of various μ -grid ESSs.

- **Virtual power plant (VPP)** can be defined as a power network integrating several types of power sources such as micro-combined heat and power (μ -CHP), wind turbines, small hydro-, solar photovoltaics, backup gensets, and energy storage systems. In general, the VPP operates in a coordinated manner, whereby controllable energy market through energy brokers (single energy pool) and VPP central control shares information to provide a reliable overall power generation/supply to/from the consumers [21, 22].

To this point, the chapter provides a current and future state of the art on the application of EMAs into power distribution networks (PDNs). More emphasize is directed to broaden its usage to a set of players in the global energy market. More attention is directed on utilization of IEMSSs in PDNs with n -grids, μ -grids, and VPPs. In fact, with the evolution of energy system on energy savings in manufacturing industries and smart cities with government buildings, intelligent energy management systems (IEMSSs) are expected to be the enabling technology for cost saving and decarbonization. Thus, this overview provides the details of application of IEMSSs in the PDNs with DER units. Technically, the IEMSSs represent a mechanism that can enable energy industry to improve energy efficiency and energy savings, and comply with various grid-operating standards such as fault ride through requirements. Until now, there is still significant loss of energy as most of these sectors have not seen the same penetration of IEMSSs as larger facilities due to the lower expenditures on energy management in the market. Though today, the market is expanding into adjacent functions, such as demand response and property management which broadens the capabilities of the next-generation IEMSSs.

Within that framework, the chapter is organized into the following sections: A brief introduction of integration of renewable energy resources in the form of n -grids and μ -grids into the power distribution networks is presented in Sect. 23.2. Next, Sect. 23.3 presents the operation of the next-generation power distribution while Sect. 23.4 is the heart of this chapter which discusses the details of the configuration of smart distribution networks with various intelligent energy management strategies. Finally, the conclusion and recommendations are summarized in Sect. 23.5.

23.2 Integration of Renewable Energy Resources into Power Distribution Networks

This section contemplates the possible future power distribution network (PDN) architectures with the integration of RERs in the form of nanogrids (n -grids), microgrids (μ -grids), and virtual power plants (VPP). These three components of

modern grid structure, i.e., n -grid, μ -grid, and VPP, can easily be achieved through hierarchical dynamic decoupling between generation, distribution, and consumption, whereby bidirectional power converters are the center of energy control. Considering the case of single commercial building, it is considered only as intelligent as the PDN when it connects several units such as n -grids or μ -grids with embedded EMAs. This is the reason why smart buildings are considered as an extension of the smart grid. Structurally, n -grid differs from μ -grid in terms of type of power supplied by the basic configuration. It means that n -grid system in most cases is an autonomous AC- or DC-based PDN which digitally connect individual devices to one another as well as to power generation and storage system within the building [23, 24]. Meanwhile, μ -grid system can be developed for single building and are mostly interfaced with the utility.

In order to provide a clear understanding of the operation of DER in distribution networks, consider Fig. 23.1, which shows the possible configurations of the future PDN in which several energy vectors (i.e., E_1 , E_2 , and E_3) are interconnected to provide reliable power supply to various load demands such as the electrified transportation sector and fast-growing urban areas. In other words, let the power generated from renewable energy sources be P_{RE} , that from energy storage sources be P_{ESS} and that from nonrenewable energy sources be P_{NRE} . Then, the power demanded by load be P_{LD1} for normal loads P_{LD2} for mobile energy storage systems. The following relationship shows the power balance between supply and demand:

$$P_{RE} + P_{NRE} = P_{LD1} + P_{LD2} \quad (23.1)$$

where P_{RE} stands for the total power generated by DER such as wind (P_W), solar PV (P_{SPV}), geothermal (P_{GTH}), and energy storage system (P_{ESS}) and be expressed as:

$$P_{RE} = P_W + P_{SPV} + P_{GTH} + P_{ESS} \quad (23.2)$$

P_{NRE} represents the power generated from gas power plant (P_G), biomass (P_B), min-hydro-power plant (P_{HD}) which is described by (23.3) as follows:

$$P_{NRE} = P_G + P_B + P_{HD} \quad (23.3)$$

23.2.1 Nanogrid Systems

As the introduction of smart-grid concepts aimed at improving the existing power grid networks with active smart devices and decentralized energy resources (DERs), the concept comes with new energy architects which are smaller scale power generation and distribution infrastructures called n -grid systems. They are seen smaller and technologically simpler than μ -grids which typically serve a single load or a single building. Starting from a small building powered by a single DG unit to a street or village powered by multiple DER units, these units can be connected to

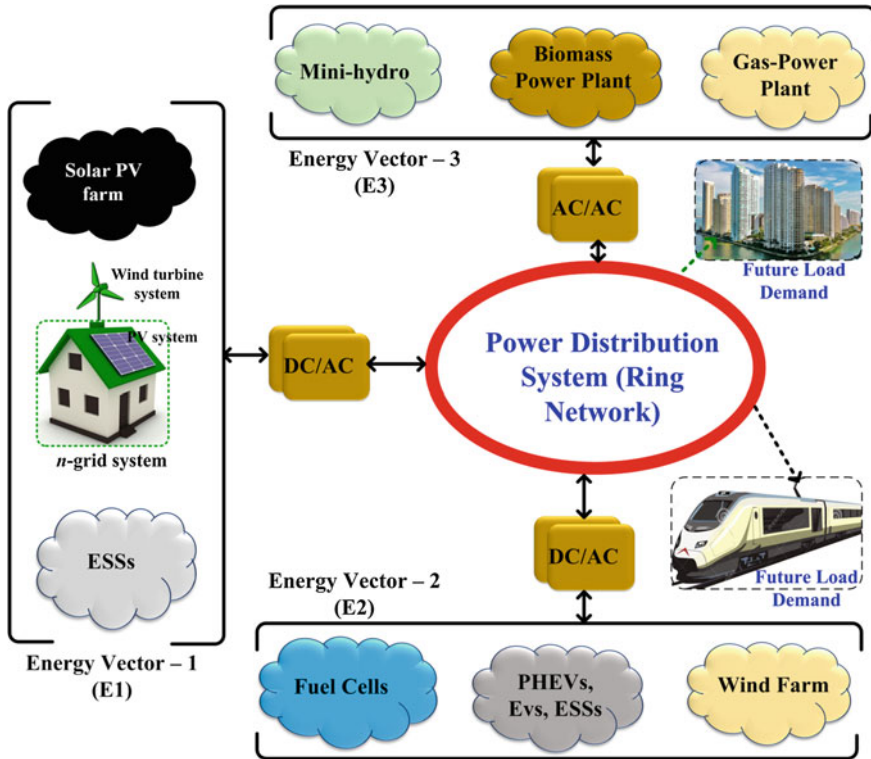


Fig. 23.1 Typical integration of renewable energy resources into power distribution systems in the form of energy vectors with future load demand

one another to create a complex power network comprising *n*-grids and μ -grids structures. In fact, *n*-grid systems face less technical and regulatory barriers than their microgrid counterparts; hence, their substantial deployment is already undergoing. Some of the benefits of the *n*-grid system are given as:

- Monitoring authorities discover other grids and generation system sharing strategy such as electricity price and quantity.
- Power can be easily exchanged with mutual beneficial.
- Controllers can track cumulative energy.
- Only data exchanged based on price and quantity.
- Visibility of the systems adjacent grids.
- Easy to bring individual devices into grid network.
- Facilitate the way for the adoption of μ -grid concept.
- The increase of μ -grid utility means enables local μ -grid prices.
- Reduces μ -grid cost and complexity.
- The concept of *n*-grid can easily scale-up/deploy much faster than μ -grid concept.

- With n -grid concept, mobile devices and mobile buildings can easily be integrated.
- It is the concept which is helpful in the electrification process in most developing countries as it easily utilizes the renewable energy resources.
- It is more secure than μ -grid or conventional power networks.

Figure 23.2 depicts the typical example of n -grid system configuration in several residential houses which are interconnected to support each other and improve the reliability of power supply. The structure consists of local power production, in which solar PV system and wind form the hybrid system. In such configuration, the n -grid could just as easily use a single RE source, or a nonrenewable source such as a diesel generator which is operated in: (i) grid-connected mode and (ii) islanded or autonomous mode. Although n -grids can be direct current (DC) or alternating current (AC), the majority of literature favors DC as it has higher efficiency. In the future, interconnection between multiple autonomous n -grids could be possible as indicated in Fig. 23.2a (which is a practical realization of the current state of the art in rural areas) with the help of advanced EMS algorithms. Moreover, grid-connected interconnection between multiple n -grids operations is also a possible configuration with mixed AC and DC distribution systems as shown in Fig. 23.2b. The challenges now remain on: (i) How to optimally operate? (ii) How to interconnect several n -grid structures to improve the reliability? and (iii) How to manage energy transactions in isolated and grid-connected modes? The n -grid structures are now common in most of the rural areas; therefore, it is important to look as important concept to facilitate the electrification process to the population without access to electricity.

23.2.2 *Microgrid Systems*

Considering the definition of μ -grid system, it is a discrete energy system consisting of DERs (i.e., DSM, ESSs, and generation) and loads capable of operating in parallel with or independently from the main power grid networks. Moreover, the concepts of μ -grid systems are modern, small-scale versions of the conventional electricity network. Usually, modern μ -grid systems are entitled to attain certain requirements such as power supply reliability, carbon emission reduction, exploitation of renewable energy sources, and electricity cost reduction. Like the bulk power system, intelligent μ -grid system locally generates, distributes, and regulates power flow to and from consumers. The μ -grid system is an ideal way to integrate various RERs and moving energy storage units such as the electrical vehicles (EVs) and hybrid electric vehicles (HEVs). Considering the intelligent μ -grid system at the community level, the structure allows customers to be involved with electricity enterprising [2].

In order to illustrate the conceptual framework of μ -grid system configuration, Fig. 23.3 depicts a typical example of a single building (i.e., residential houses) powered by isolated (i.e., islanded) μ -grid system. It consists of the various RERs,

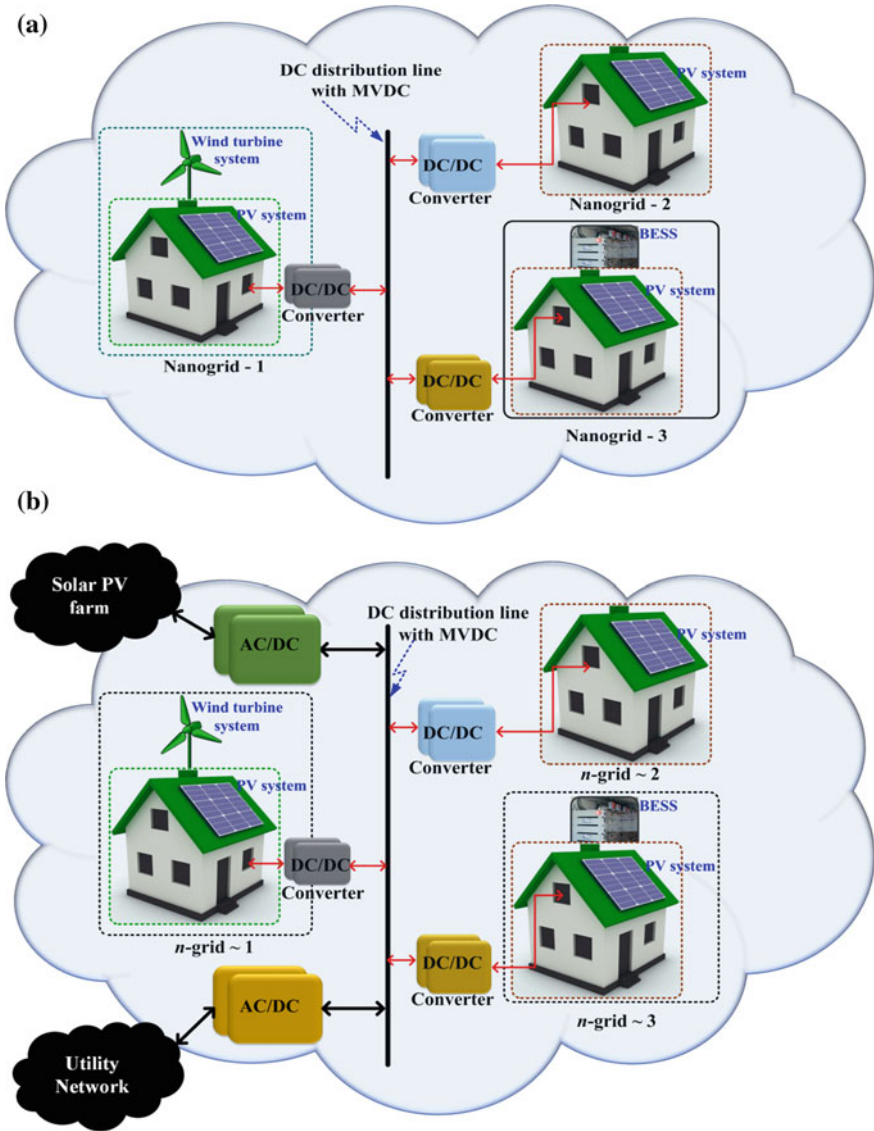


Fig. 23.2 Typical example of n -grid system configuration in **a** Interconnected multiple n -grids in isolated configuration. **b** Interconnected multiple n -grids in grid-connected configuration

EVs, ESS, and conventional distribution networks. The network can operate in either isolated or grid-connected mode with RERs units being the main power generators. Considering the case of grid-connected mode, when the RERs generate excess power, the excess power is transported into grid or stored into energy storage devices. On the other hand, when the RERs generate low power compared to load

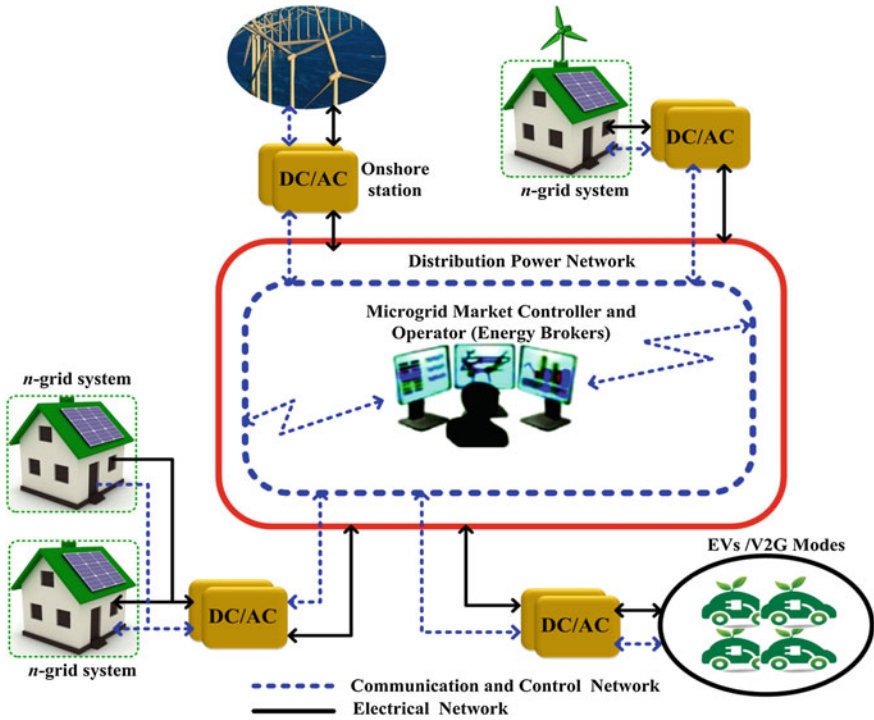


Fig. 23.3 A typical example of μ -grid system configuration

demand, the deficiency is covered by the power from the grid or the energy storage system discharge to compensate for the power deficiency. In the islanded mode of operation, it occurs when there is fault in the grid leading to the disconnection.

As μ -grid system comprises local low-voltage (LV) and even medium-voltage (MV) distribution networks with RERs and ESSs, the μ -grid controller or operator’s role is to manage power flow and real-time electricity pricing between the components within the network in order to meet objectives such as (i) minimize electricity cost, (ii) improve reliability, and (iii) reduce power plant emissions in the case of standby generators, subject to individual/unit operating constraints. In so doing, the interconnected RER units will satisfy the supply/demands of energy consumers. Next, larger μ -grid systems allow aggregation of consumers and RERs to form a concept known as a virtual power plant (VPP) which is discussed in the next subsection.

23.2.3 Virtual Power Plants

With distributed energy generation growing and increasing amounts of renewable power coming onto the grid, new technologies and business models are helping to

balance loads and smooth variability and integrate diverse energy resources. Along with the rising energy consumption in the world, these new technologies will in particular influence the way we generate, distribute, and consume electric energy. Moreover, one distributed generation technology with significant growth potential is the virtual power plant (VPP). In the VPP model, an energy aggregator gathers a portfolio of various small- to medium-sized generators and operates them as unified and flexible resources on the energy market (i.e., an energy pool) or sells their power as a system reserve. The negative aspects of increased uncoordinated RER penetration are the main motivations for the adopting VPP energy model. Earlier, various DERs were installed with a “fit-and-forget” approach and they were not visible to the system operators. This “fit-and-forget” approach is still being applied in most of the rural areas in developing countries such as those in the Southern African Development Communities (SADC).

Technically, the VPP aggregates all units including customers and small generating units into a single entity which are then controlled from a centralized unit. By applying the VPP concept which is envisioned to handle the RERs and to intensify their visibility within power markets, rural electrification process can finally be accomplished. As stated earlier, by combining various small- to medium-sized RERs a “single virtual generating unit” can be formed to act as a conventional power plant which is capable of being visible or manageable on an individual basis. In other words, the energy concept represents the Internet of energy (IoE). Figure 23.4 depicts an example of a typical VPP structure, whereby owners of the interconnected RERs send their power to an energy pool through a centralized control center. The main objective is to reduce operational cost of interconnected μ -grid units (such as fuel cost, utility bill, battery degradation, and cost of equipment maintenance) while improving the utilization of RERs in the VPP network.

Considering the architectural concept of VPP model, there is no real competition for the VPP as it is anticipated to use cheap and ubiquitous information and communication technologies, while other technology trends such as building energy storage systems incur comparatively heavy costs. Implementation of the VPPs on the other hand can also avoid expensive installation costs in, for example, a community with several houses. Self-consumption for home or industrial use is also hampered by having to produce “the right amount of power at the right time.” Such operating conditions of the VPPs enable it to deliver the needed energy at peak usage times, and store any surplus power to give the energy aggregator more options than would exist in a single power plant or conventional power distribution networks. Other advantages include improved power network efficiency and security, cost and risk savings in transmission systems, increased value from existing infrastructure assets, and reduced emissions from peaking power plants. And, importantly, VPPs can also enable more efficient integration of RERs into the grid by balancing their variability allowing customers to participate in power generation with their small capacities.

Moreover, the operation of a VPP relies on intelligent-based software systems to remotely and automatically dispatch and optimize generation, demand-side or energy

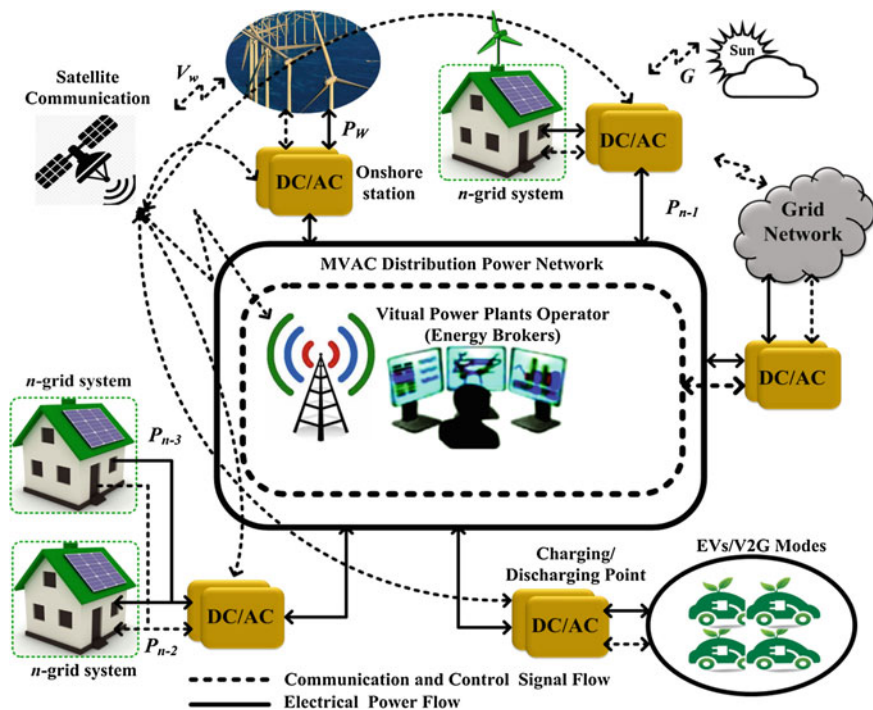


Fig. 23.4 Typical example of VPP configuration, i.e., “the Internet of energy” with centralized control and decentralized power plants

storage resources (e.g., EVs, PHEVs, BESS, and bidirectional inverters) in a single, secure Web-connected system. In order to bring diverse of independent resources into a unified network, complex planning and scheduling are required. In this case, the key ingredient that can make the VPP model workable is actually software. There must a server system installed in a control room, with communication channels such as mobile phone or DSL connections to link with the IEMS. The IEMS software with several advanced applications such as forecasting applications, scheduling applications, automatic generation control, real-time pricing, data transmitters and receivers, transducers, and all sorts of advanced instrumentations are all together interconnected to create an optimally operated energy system. For instance, with the forecasting applications, the VPP-IEMS uses for weather forecasting (i.e., solar insolation and wind speed) and predict the state of charge (SoC) on BESS to calculate the real-time electrical and thermal loads which have to be supplied as well as for forecast the generation from RER units. These forecasts are used in the scheduling applications similar to the normal short-term unit commitment and economic dispatch in large power systems. It calculates the schedule for the entire VPP and all the DER units before issuing a relevant command to each of the interconnected components. In so doing, the operator of the VPP uses the schedule to market the energy and power on the

energy exchange to generate the real-time pricing so that power consumers can buy through the e-energy market, or generate control signal as tertiary or secondary control reserve [9].

23.3 Next-Generation Power Distribution Networks with Energy Management Systems

As the attentions on smart grid continue to grow, interest in the enhancement of all parts of power systems with much efforts directed on distribution networks has been renowned. Focusing on the “power distribution network” refers to the lower voltage (e.g., 33 kV) system that is energized at the distribution substation, and delivers power to loads via a primary distribution system with MVAC (e.g., 132 kV ring network). Technically, the primary power distribution system has been a radial network with many feeders and then laterals are energized by these feeders which are distribution systems. Actually, the concept of distribution engineering is very complex, whereby [10–13] will be used as reference materials to create the classical concept.

Regarding the essence of the smart-grid philosophy, the following seven principles are to be implemented:

- Self-healing from power disturbance events,
- Enabling active participation by consumers in demand response using the available locally generated power from RERs,
- Operating resiliently against physical and cyber-attack,
- Providing power quality for the twenty-first-century needs, i.e., power with various qualities according to the customer demands (active and reactive powers),
- Integrating all possible generation units such as RERs and ESSs options and
- Enabling new products, services, and markets as new energy business models.

In the context of moving into smart grids, the next subsection discusses the intelligent energy management systems (IEMS) for the next-generation power distribution systems. The focus is based on the applications of IEMs in n -grid, μ -grid, and virtual power plants (VPPs).

23.3.1 IEMS for the Next-Generation Power Distribution Systems with DER

Since most RERs are weather dependent and may not follow the demand change through every hour, it is envisioned that the next-generation power distribution systems will be networked and interaction between several systems would improve

renewable energy harvesting as well as supply reliability. For instance, in case there is any other systems could answer the request by absorbing/supplying the additional power, the involved systems may exchange energy as long as it is allowed in the distribution network with security constraints. The most significant of these are the following:

- Local DC generation is readily feasible with PV solar.
- Local DC storage is becoming feasible with more efficient and less expensive battery technology.
- Devices powered by standard low-voltage DC are increasingly available and valued for convenience.
- Many loads are now natively DC (e.g., all electronics, LED lighting, and many motor drives) and most others could readily be converted to DC.
- Conversion between AC and DC requires relatively expensive hardware, adds losses, and reduces reliability.
- DC–DC conversion is now efficient and inexpensive.
- Mobility and flexibility are increasingly valued.
- Entangling devices in buildings with external controls as with the smart grid introduces security and privacy concerns and vulnerabilities.
- The utility grid is unreliable or nonexistent in some parts of the world; it is always unreliable to some degree everywhere.
- The desire for local reliability and resiliency is growing with concern about natural- or human-caused disasters
- It is increasingly likely that most buildings will have local generation, local fixed storage, or an electric vehicle if not all three.

The EMS represents the heart of the information and communication system technologies in the future power distribution networks. It manages the operation of other components using communication technologies in the bidirectional ways. The next subsection will highlight the applications of IEMS in nanogrid and microgrid systems with RERs.

23.3.2 Intelligent Energy Management System in Nanogrids and Microgrids

As stated earlier, the energy management algorithm in μ -grid system involves how to determine the most economic dispatch of the RERs that minimizes the total operating cost while satisfying the load demand and operating constraints. Many research findings have been reported on IEMS of hybrid systems using techniques such as genetic algorithm (GA), differential evolution (DE), neural network, fuzzy logic, and neuro-fuzzy, among others. These advanced intelligent algorithms are used by EMS algorithm for energy resource forecasting, scheduling, automatic generation control, and generating real-time energy pricing.

In particular, IEMS uses weather forecasts such as solar insolation and wind speed information to predict the state of charge on battery energy storage system and calculates the electrical and thermal loads which have to be supplied, as well as for forecasting the power generation from renewable units. The forecasted information is later used in the scheduling application, a process similar to a short-term unit commitment and economic dispatch in large conventional power systems. In the nature, the IEMS will be entitled to calculate the schedule for the entire microgrid systems which is integrated with several small generation units, i.e., n -grid systems and the entire μ -grid system.

For sound operation of μ -grid system in both grid-connected mode and stand-alone mode, proper EMAs are very important. These EMAs determine output powers and/or voltages of each RER unit, which are then fed to the control system of interfacing power converters as the control tracking references. Usually, EMAs are like a downsized version of the unit commitment problem that is traditionally applied to large central generators in the μ -grid system. In the grid-connected mode, the MG adjusts the power balance of power supply and demand by allowing power from the main grid and vice versa to maximize operational benefits through the EMAs [7]. In the stand-alone mode, the μ -grid system aims to keep a continuous power supply to customers using RER bids. One of the main constraints with RERs introduced is stability and reliability problems associated with their power scheduling [8]. The intermittent nature of some RERs, such as wind turbines and solar PV systems, leads to an output that often does not suit the load demand profile. It is difficult to produce accurate day-ahead schedules in μ -grid system using power generated from only RERs. Therefore, the energy storage systems (ESSs) play an important role in μ -grid system by allowing those operations with a more flexible and reliable management of energy [9]. The ESSs can save energy at low price hours and sell it at high price hours, which will help the network to work more efficiently and economically. Meanwhile, the operation and control in μ -grid systems become more complicated and challenging as several participants are evolved. Table 23.1 summarizes the operations of both n -grid and μ -grid systems with embedded IEMS algorithms to mimic the future power distribution networks.

23.3.3 Intelligent Energy Management System with Virtual Power Plant Concept

It is envisioned that many future distribution systems will be networked or looped with mixed AC and DC to create a very complex VPP structure. It is also anticipated that sensors will be used for direct control of system components, more than in contemporary distribution systems. The main points in the future distribution system designs are auto-configuration capability (e.g., electronic switch closures to reconfigure systems such as the use of electric ship technologies in reconfiguration);

Table 23.1 Typical pseudocode for implementation of advanced controller embedded with IEMS for n -grid and μ -grid operations

EMS strategy	Pseudocode for sequential operations
1. Nanogrid controller and EMS operation	<ul style="list-style-type: none"> • Initialization: $k \leftarrow 0$. The local controller (LC), i.e., n-grid controller sets the initial schedule randomly and returns them to the microgrid central controller (MGCC) • Repeat • The LC updates all relevant parameters and sends the appropriate control signals to local power converter for action ($k \leftarrow k$) • The LC installed at each DER unit and load calculates the new schedule by solving the corresponding local EMS algorithm • Update status then sends updated signals to central local controller (CLC) • The CLC communicates the new schedule to microgrid or grid controller • MGCC updates parameters to reflect the new schedule • $k \leftarrow k + 1$ • Until convergence
2. Microgrid central controller (MGCC) and EMS operation	<ul style="list-style-type: none"> • Initialization: $k \leftarrow 0$. The MGC sets the initial schedule randomly and returns them to the microgrid central controller (MGCC) • Repeat • The MGCC updates all relevant parameters and sends the appropriate control signals to local controllers ($k \leftarrow k$) • The MGCC oversees the operation of each DER unit dispatch power based on optimal power flow by solving the corresponding MG EMS • Update status then sends updated signals to central local controller (CLC) • The MGCC communicates the new schedule to all generating components within the μ-grid by commanding with an appropriate signal for the action to follow • MGCC updates parameters to reflect the new schedule • $k \leftarrow k + 1$ • Until convergence

more flexible and well managed integration of RERs into the distribution system; implementation of reliability management (e.g., increased reliability where needed, cost/benefit analysis to identify priority circuits operations, possible implementation of hyper-reliability philosophies where warranted); management of power quality, i.e., active/reactive power; improved customer average service reliability; accommodation of electric vehicle loads; and the development of strategies such as when/where to operate/connect network legacy radial systems.

Currently, power distribution networks (PDNs) supply electricity directly from transmission systems to end users, and hence, to cope with the decarbonization of electricity generation, transport, and heat, these PDNs will need to undergo significant developments. The PDN, which is historically designed only for unidirectional power flows with very limited observability, will need to accommodate several small- to medium-scale DG units such as solar PV, wind, and ESSs. As the demand for electrical energy is anticipated to continue rising whereby the electrification of transport and heating infrastructure are putting additional strains on the power networks. These are the challenges of adapting the PDNs to new and variable levels of demand and generation (i.e., new formed energy vectors) require forward thinking and technical innovation. By understanding the aging process of critical assets and evaluating the cost-effective integration of several technologies (e.g., RERs, IEMSs, and ICTs), possible configurations of multi energy vectors can be achieved.

In this way, some features of both energy and information systems become synergic: On the one hand, the forecast that could be provided by the cloud computer offers a confident image about the energy consumption demands. On the other hand, the power networks allow to spend during the low demand period the excess power generated to be stored by the ESSs allowing a better performance with low exploitation costs during peak demands. Table 23.2 presents a

Table 23.2 Typical pseudocode for implementation of advanced controller embedded with IEMS for VPP operations

EMS strategy	Pseudocode for sequential operations
Virtual power plants with embedded n -grid, μ -grid system	<ul style="list-style-type: none"> • Initialization: $k \leftarrow 0$. The local controller (LC), i.e., n-grid controller sets the initial schedule randomly and return them to the microgrid central controller (MGCC) • Repeat, for all interconnected n-grid • The LC updates all relevant parameters and sends the appropriate control signals to local power converter for action ($k \leftarrow k$) and to μ-grid central controller (MGCC) • The LC installed at each DER unit and load calculates the new schedule by solving the corresponding local EMS algorithm, and then updates MGCC-EMS which also updates VPP-EMS • Updated status sends to central controller of VPP (i.e., CC-VPP) and to energy market brokers through communication channels, e.g., broadband or wireless or satellite with 4G LTE or 5G technologies, ZigBee, and WiMax • The CC-VPP communicates the new schedule to μ-grid through MGCCs and μ-grid via LCs • MGCCs and LCs update their corresponding DER parameters by adjusting the control signals of each interfacing power converter to reflect the new schedule • $k \leftarrow k + 1$ • Until convergence

summarized basic implementation of the EMS strategy for a typical VPP unit with several interconnected μ -grid systems. Note that, the μ -grid system may also comprise several interconnected n -grid units which are also interlinked together to form a complex network.

23.3.4 Next-Generation Power Distribution Networks with Vehicle-to-Anything Concepts

With the participation of electrical vehicles (EVs) in grid operation, the concept of smart grid can become smarter. Figure 23.5 shows a comprehensive grid system, i.e., MVAC power distribution network that incorporates EV charging fleets and n -grid system. By smart scheduling for EV charging/discharging through the well-controlled charging points (charging fleets), it is likely to mitigate the fluctuations of electricity price and further flatten the supply/demand curve. Thus, intelligent scheduling algorithm needs to decide when to charge the EV battery, when to discharge the battery and where to discharge, and by how much should a given EV discharge, i.e., low limits of SoC to be discharged. The decision can be made by the consumers (i.e., owners of the EVs) based on the real-time pricing

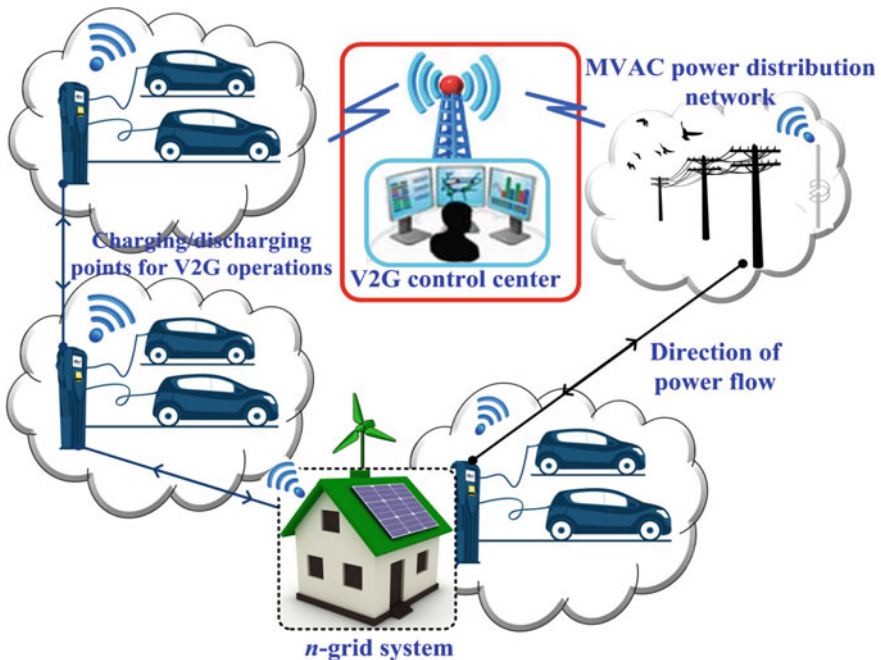


Fig. 23.5 Typical example of integrated charging/discharging points for EVs with power distribution networks

(RTP) and the sell-back market price, or made by utility based on the supply and demand curves. In other opinions, the value of intelligent scheduling is in realizing the EV battery's full potential as a tool for stabilizing the power grid in the future. In other words, the presence of EVs can function to mitigate the fluctuation of electricity price and further flatten the price curve as much as possible. As mentioned earlier, by utilizing the three EV operating modes which are, namely (i) vehicle to grid (V2G), (ii) vehicle to home (V2H), and (iii) vehicle to battery (V2B), their potentiality can finally be realized.

This section provides a review of the main approaches used in modeling and control of energy management of HEVs. For instance, considering a constant voltage mode (i.e., CV), energy can be dissipated in a number of ways including:

- **Brake utilization:** The EV brake is usually applied by the driver to decelerate the vehicle resulting in the loss of kinetic energy in the form of heat. The heat energy can be transformed to recharge the EV battery in order to save energy loss during braking operation.
- **Engine start/stop:** The engine often runs idle during the utilization of vehicle resulting in an unnecessary consumption of fuel. In this case, the EV-EMA can be designed to reduce the unnecessary SoC consumptions.
- **Uneconomic engine operating condition:** An engine often demonstrates non-linear fuel consumption behaviors in certain operating conditions that cause an excessive use of fuel.
- **Unscheduled load:** Certain mechanical and electrical loads get activated when economic operating point of engine increase with the fuel consumption.

23.3.5 *Next-Generation Power Distribution Networks with Energy Storage Systems*

Energy storage systems (ESSs) in combination with advanced high power converters application distribution network with RERs have a great technical role to play and will have a huge impact on future electrical supply systems leading to many financial benefits. So far, when ESSs are integrated into conventional electric grids, specially designed topologies and/or control for almost each particular case is required. This means costly design and debug time of individual component/control system every time the utility decides to add the ESS. However, our present and future power network situation requires extra flexibility in the integration more than ever. Mainly for small and medium storage systems in both (customers and suppliers) sides, the storage moves from central generation to distributed one (including intelligent control and advanced power electronics conversion systems). Nevertheless, storage devices, standardized architectures and techniques for distributed intelligence and smart power systems as well as planning tools and models to aid them are still lagging behind.

To summarize the discussion on ESSs, the following are their technical role and functions which include the following:

- Grid voltage and frequency support
- Grid angular (transient) stability
- Load levelling/peak shaving
- Spinning reserve
- Power quality and reliability improvement
- Ride through support
- Unbalanced load compensation

More ESSs are available nowadays with different technologies, capabilities, and applications. The design of versatile ESSs having capability to operate in wide ranges of power and energy density is required. Since no single energy storage technology has this capability, ESS combining different types of energy storage devices such as **pumped-hydro storage (PHS)**, **compressed air energy storage (CAES)**, **regenerative fuel cells**, supercapacitors, **batteries energy storage system (BESS)**, superconducting magnetic energy storage (SMES), kinetic energy storage in flywheels, and **thermal and hydrogen** will be the possible options. Even though detailed design procedures is required to determine the most suitable energy storage system for the microgrid, designers should always start with consideration of the relative characteristics of microsources and loads [7, 15].

Taking the BESS as an example to demonstrate the application of IEMS, bidirectional power converter control is entitled to maintain DC link voltage at a specified value. In the charging mode, the power converter operates as a buck converter and controls the input voltage, which is the DC link voltage. In the discharging mode, the converter operates as a boost converter and controls the output voltage, which is the DC link voltage. In both modes, the bidirectional power converter control objective is to keep the DC link voltage at a specified voltage and also to regulate the charging/discharging current. The bidirectional converter control is implemented as a dual-loop control with an external voltage control loop and an internal current control loop. The control command to operate in charging or discharging mode comes from the intelligent energy management system (IEMS) algorithm. The main signal for the charging/discharging control algorithm is the state-of-charge (SOC). In order to protect the battery from deep discharging and overcharging, the battery SOC will be regulated between say $SOC_{\min} = 30\%$ and $SOC_{\max} = 80\%$. Note that these threshold numbers can be easily changed based on design criterion and will not change the algorithmic framework.

The following actions may be implemented in the IEMS algorithm based on the detected operating scenario:

- **Scenario 1: BESS charging mode**

SOC is within 30–90% while $P_{DER} > P_L$ or
 SOC < 30% and $P_{DER} > P_L$

where P_{DER} is power generated by distributed energy resource, and P_{L} is the power demanded by load.

- **Scenario 2: BESS discharging mode**

SOC is within 30–90% while $P_{\text{DER}} < P_{\text{L}}$ or
SOC > 30% and $P_{\text{DER}} < P_{\text{L}}$

- **Scenario 3: Input power if there is another available source**

SOC < 30% while $P_{\text{DER}} < P_{\text{L}}$

- **Scenario 4: Export power if there is another available source**

SOC > 90% while $P_{\text{DER}} > P_{\text{L}}$

- **Scenario 5: Termination operating mode**

SOC < 30% and $P_{\text{DER}} < P_{\text{L}}$ and no other available source or
SOC > 90% while $P_{\text{DER}} > P_{\text{L}}$, and no other available loads.

23.4 Information and Communication Infrastructures in Power Distribution Networks

In order to achieve an intelligent grid, a succession of building subsystems must be realized. A solid foundation and functionality of each subsystem is necessary in the overall performance of the next-generation power distribution networks with various interconnected RERs. This is due to the fact that each subsystem serves as the feed for the next component leading to complex operational regimes of which makes conventional management approaches no longer adequate. Figure 23.6 indicates the typical structure in which the ICT infrastructure can be applied between the μ -grid control center with IEMS (i.e., MGCC-IEMS) and n -grid control center with IEMS (i.e., LC-IEMS) to realize the concept of demand-side management. The next subsection outlines the application details of ICT network in n -grids and μ -grids.

23.4.1 ICT in Nanogrid Systems

As many aspects of our electricity systems are rapidly changing, including the ability to locally generate power with DERs and integrate local energy storage, the key factors that led to our current grid architecture may no longer hold in the near future. A new approach to power distribution network within modern buildings in cities or rural areas is local power distribution (LPD). In LPD, individual devices or residential houses are organized into n -grids, i.e., a single domain of power.

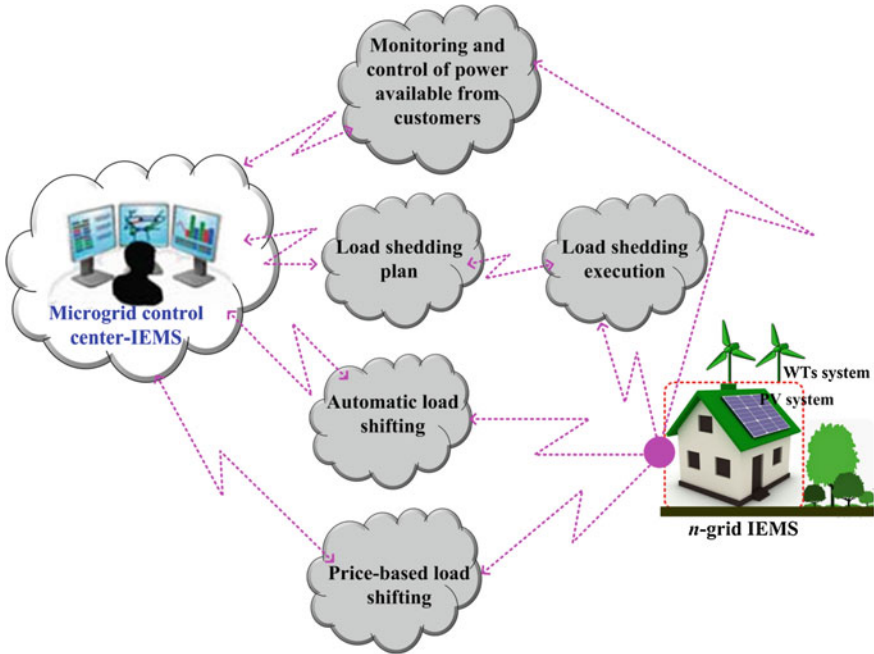


Fig. 23.6 Typical example of communication control signal for demand-side management between μ -grid IEMS (MGCC-IEMS) and customer (LC-IEMS)

However, in future, multiple n -grids networked to each other to form a local generation unit and to build wide μ -grid are possible. Traditionally, n -grids inherently incorporate DC power for higher power efficiency. This new model for electricity distribution in buildings is implemented with a layered model of power called “Network Power Integration” which isolates communication about power from communication for functional purposes.

23.4.2 ICT in Microgrid Systems

Figure 23.7 presents the typical architecture of a mixed AC and DC μ -grid systems. The PV systems and BESSs are interconnected to either AC bus or DC bus through the DC/DC/AC or just DC/DC converters while the offshore wind turbines are linked to the AC or DC bus through the AC/DC/AC converters or an HVDC link. On the other hand, the n -grids or residential house power systems with stable power networks, i.e., those houses with DERs are also engaged in the power generation at some point during peak power demand in order to improve the reliability of power supply and earn income through selling their excess power to the local certified

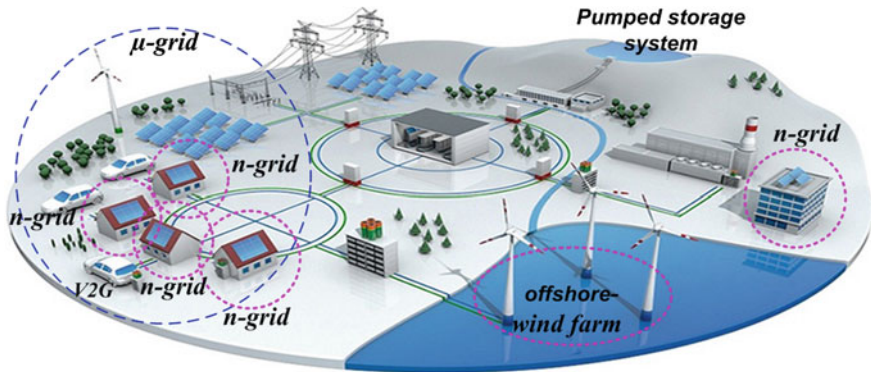


Fig. 23.7 Typical configuration of VPP system interconnected with μ -grid and n -grids systems

energy brokers. To sum-up the discussion, below are two cases which the μ -grid and n -grid systems operation may encounter:

Case 1: Islanding operation—Interconnected DERs mainly provide both AC and DC powers to the loads through the microgrid local control. In this mode of operation, to ensure stability and economical operation of the DER units, active and reactive powers should be shared simultaneously depending on the available energy resources from each unit. Traditionally, droop control strategies have been applied without communication lines and are being used to achieve power sharing by imitating steady-state characteristics of the synchronous generator in the islanded microgrid system [16].

Case 2: Grid-connected operation— AC and DC microgrids are connected to grid via the point of common coupling (PCC) with their AC and DC bus bars and power flow between microgrid systems and the grid is controlled through the energy market controller (i.e., energy broker). In that case, using the swing equation, method like virtual synchronous generator has been applied to imitate the steady-state and transient characteristics of the network. Moreover, the inertia of the RER units can be enhanced compared to the droop control strategy at the expense of oscillatory and dynamic power sharing among the units which could respond sluggishly due to the virtual inertia. Therefore, application of the more improved droop control method to share the active and reactive powers among the RER units in islanded microgrids is a favorite approach [17].

23.4.3 ICT in Virtual Power Plants

Evolution of energy market accelerates toward the direction of a greater reliance upon RERs, ICT technologies, and new frameworks necessary to manage this

increasing two-way complexity which remains unclear. Nevertheless, successful strategies deployed today all over the globe such as virtual power plant (VPP) require the application of ICTs to meet their operating constraints. Optimal operation of VPPs is faced with optimal bidding and identifying arbitrage opportunities in a market environment. This subsection therefore presents an arbitrage strategy for VPPs by participating in energy, ancillary service (i.e., spinning reserve and reactive power services), and markets using the ICT. Based on the security-constrained price-based unit commitment, the VPP model aims to maximize the profit (revenue and minimize costs) considering arbitrage opportunities [23–26].

23.4.4 ICT with Advanced Smart Meter Infrastructure

Advanced metering infrastructure (AMI) is an integrated system of smart meters, communications networks, and data management systems that enables a two-way communication between utilities and customers. Customer systems include in-home displays, home area networks, energy management systems, and other customer-side-of-the-meter equipment that enable smart-grid functions in residential, commercial, and industrial facilities. The AMI can be used with electricity or natural gas services. It records interval energy consumption and other data, and regularly communicates those data to a utility. Smart meters can also receive communications from a utility [27]. In fact, the AMI typically communicates through local data relays and at least one communication media (i.e., cellular, power line carrier, and Wi-fi network) with centralized control software and centralized data storage (e.g., meter data management system or MDM) on the utility's servers.

Generally, AMI provides the following:

- Timely and accurate billing data to minimize estimates, inquiries, and adjustments.
- Structure necessary for utilities to provide rate structures suited to the specific setting, e.g., time-of-use rates and load control.
- Data and tools to improve power quality, outage detection, and revenue protection.
- Foundation for smart-grid applications.
- Structure for customers to better understand their energy use and make more informed energy usage choices.
- Dispatch maintenance teams timeously.
- Load control and limiting.
- Network maintenance and extension information available.

To conclude the discussion, utilization of the AMI can eliminate or minimize the aforementioned issues. They are capable of recording zero readings and informing

the utility companies through AMI in which the infrastructures for smart meter assumes that the circuit is not closed and does not perform reading.

23.5 Conclusion and Recommendations

Given the evolution of energy market in manufacturing industries and smart cities with government buildings, intelligent energy management systems (IEMSs) are poised to be the tools that enable cost and carbon savings. The energy market is as diverse as it is large, consisting of buildings of all ages, sectors, and management regimes. Thus, the IEMSs represent a mechanism that can enable energy industry to improve performance, save energy, and comply with regional grid codes and laws. Until now, there are still significant losses of energy as most of these sectors have not seen the same penetration of IEMSs as larger facilities due to the lower expenditures on energy management in market. Moreover, low penetration of direct digital control IEMSs hardly make the extant of these sectors. Principally, these systems traditionally focus on two key functions: energy conception and energy analytics.

Although it has slowed considerably, consumption of electricity continues to grow in developed and developing economies. Further to this, there are some unknowns which might accelerate this growth, such as electrification of vehicle fleets using renewable energy resources and geothermal heat pump space and water heating. Most analysts anticipate that RER will provide a large share of the expanded generation capacity required to meet this seemingly inexorably increasing electricity demand. Furthermore, given the urgency of tackling the climate change problem, most of the added assets must be carbon-free renewables or nuclear, end-use efficiency improvements, or highly efficient fossil-fired technologies. In developed economies worldwide, the current power delivery paradigm has been in place for more than a century, i.e., since the emergence of polyphase AC systems around the turn of the last century. A key feature of this structure is that universal service is delivered at a consistent level of power quality and reliability (PQR) throughout large regions. A future possible structure for the electricity generation and service delivery leaves the existing high-voltage meshed grid paradigm in place relying on new configuration such as nanogrid, microgrid, and virtual power plants. These involve with radical reorganization of parts of the distribution network and customer sites. Managing a much more diverse dispersed system poses major challenges to the current centralized grid paradigm, particularly since many of these assets are small to tiny by macrogrid standards and they may ultimately number in the millions. They are also not ones that centralized control can rely upon to a function in traditionally dependable ways, e.g., renewable energy generation which can be highly variable and changes in output of generators are not independent. Although most involved in the industry agree that a paradigm shift is both necessary and desirable to manage the new energy system, the nature of the future system remains quite unclear.

With the possible structures described in this chapter, the traditional grid or macrogrid remains similar at the high-voltage meshed level. Four new entities can now be added in the power networks more locally:

- **Community grids or milligrids:** This operates a segment of the existing distribution system.
- **Microgrids:** These are akin to current customer sites but which have autonomous control.
- **Nanogrids:** Such as telecom or Ethernet networks that currently distribute power to many low-power devices. Although the concept has recently extended into residential houses particularly in rural areas, it has not reached its maximum utilization point. The latter exist currently in the local electrical systems but are not typically considered a part of the traditional electricity supply system.
- **Virtual power plants (VPPs):** This is the self-consumption model for home or industrial use which is also hampered by having to produce “the right amount of power at the right time.”

All these new entities exhibit some localized control with embedded IEMS, providing appropriate local heterogeneous PQR which becomes a possibility. These new grid concepts enable a more “bottom-up” approach making the next-generation electricity distribution networks smarter than the presence, in contrast to the historic “top-down” model of electricity.

References

1. Quiroz C, Mohmood A, Tari Z (2013) A probabilistic model to predict the survivability of SCADA systems. *IEEE Trans Industr Inf* 9(4):1975–1985
2. Justo JJ, Mwasilu F, Lee J, Jung JW (2013) AC-microgrid versus DC-microgrid with distributed energy resources: a review. *Renew Sustain Energy Rev* 24:387–405
3. Lund H, Munster E (2006) Integrated energy systems and local energy markets. *Energy Policy* 34:1152–1160
4. Infield D, Li F (2008) Integrating micro-generation into distribution systems: a review of recent research. In: *Proceedings of power and energy society general meeting-conversion and delivery of electrical energy in the 21st century*. July 2008
5. Yang Q, Barria JA, Green TC (2011) Communication infrastructure for distributed control of power distribution networks. *IEEE Trans Industr Inf* 7(2):316–327
6. Hammons TJ et al (2000) Renewable energy alternatives for developed countries. *IEEE Trans Energy Convers* 15(4):481–493
7. Nguyen A, Lauber J, Dambrine M (2014) Optimal control based algorithm for energy management of automotive power systems with battery/supercapacitor storage devices. *Energy Convers Manag* 87:410–420
8. Werth A, Kitamura N, Tanaka K (2015) Conceptual study for open energy systems: distributed energy network using interconnected DC nanogrids. *IEEE Trans Smart Grid* 6(4):621–630
9. Martinez Cesena EA, Capuder T, Mancarella P (2016) Flexible distributed multienergy generation system expansion planning under uncertainty. *IEEE Trans Smart Grid* 7(1):348–357

10. Chen C, Duan S, Cai T, Liu B, Hu G (2010) Smart energy management system for optimal microgrid economic operation. *IET Renew Power Gener* 5(3):258–267
11. Wu J, Guan X (2013) Coordinated multi-microgrid optimal control algorithm for smart distribution management system. *IEEE Trans Smart Grid* 4(4):2174–2181
12. Li X, Hui D, Lai X (2013) Battery energy storage station (BESS)-based smoothing control of photovoltaic (PV) and wind power generation fluctuations. *IEEE Trans Sustain Energy* 4(2):464–473
13. Sun C, Hu X, Moura SJ, Sun F (2015) Velocity predictors for predictive energy management in hybrid electrical vehicles. *IEEE Trans Control Syst Technol* 23(3):1197–1204
14. Li N, Uckun C, Constantinescu EM, Birge JR, Hedman KW, Botterud A (2016) Flexible operation of batteries in power system scheduling with renewable energy. *IEEE Trans Sustain Energy* 7(2):685–696
15. Black M, Strbac G (2007) Value of bulk energy storage for managing wind power fluctuations. *IEEE Trans Energy Convers* 1(1):197–205
16. Chaouachi A, Kamel RM, Andoulsi R, Nagasaka K (2013) Multiobjective intelligent energy management for a microgrid. *IEEE Trans Industr Electron* 60(4):1688–1699
17. Wu H, Liu X, Ding M (2014) Dynamic economic dispatch of a microgrid: mathematical models and solution algorithm. *Electr Power Energy Syst* 63:336–346
18. Sechilariu M, Wang BC, Locment F, Jouglet A (2014) DC microgrid power flow optimization by multi-layer supervision control. Design and experimental validation. *Energy Convers Manag* 82:1–10
19. Luo X, Wang J, Dooner M, Clarke J (2015) Overview of current development in electrical energy storage technologies and the application potential in power system operation. *Appl Energy* 137:511–536
20. Wu G, Boriboonsomsin K, Barth MJ (2014) Development and evaluation of intelligent energy management strategy for plug-in hybrid electric vehicles. *IEEE Trans Transp Syst* 15(3):1091–1100
21. Wang XF, Peng F, Mao BB, Chen WR (2011) On power following energy management strategy based on fuzzy optimization. In: *IEEE proceeding control conference (CCC), 2011 30th Chinese, Yantai China, 22–24 July 2011*, pp 5073–5077
22. Grillo S, Marinelli M, Massucco S, Silverstro F (2012) Optimal energy management strategy of battery-based storage system to improve renewable energy integration in distribution networks. *IEEE Trans Smart Grid* 3(2):950–958
23. Nezamabadi H, Nazar MS (2016) Arbitrage strategy of virtual power plants in energy, spinning reserve and reactive power markets. *IET Gener Transm Distrib* 10(3):750–763
24. Liu Y, Xin H, Wang Z, Gan D (2015) Control of virtual power plants in microgrids: a coordinated approach based on photovoltaic systems and controllable loads. *IET Gener Transm Distrib* 9(10):921–928
25. Marinelli M, Sossan F, Costanzo GT, Bindner HW (2014) Testing of a predictive control strategy for balancing renewable sources in a microgrid. *IEEE Trans Sustain Energy* 5(4):1426–1433
26. Arefifar SA, Mohamed YARI, El-Fouly THM (2012) Supply-adequacy based optimal construction of microgrids in smart distribution systems. *IEEE Trans Smart Grid* 3(3):1491–1502
27. Mohassel RR, Fung A, Raahemifar K (2014) A survey on advanced metering infrastructure. *Int J Electr Power Energy Syst* 63:473–484

Index

A

AC and DC Microgrids, 410, 810, 811
Active and reactive power control, 227, 229
Active and reactive power demand, 285
Active rectifier, 250, 251, 253, 258, 260,
262–266, 268, 274, 278, 279
Adaptive overcurrent protection, 504, 527, 531,
532, 543

B

Back-to-back converters (RSC and FEC), 171,
178
Biomass, 3, 28–31, 51, 64
Bus zone protection, 586, 618

C

Closed loop control scheme, 171, 178, 180,
181, 193, 201, 202
Combined Heat and Power (CHP), 31, 35, 37,
50
Contingency analysis, 150, 153, 557, 672
Cost-benefit analysis, 731, 732, 782

D

DC collection grid, 249, 250
DC Microgrid (DCMG), 409–411, 414
Diesel generator, 731, 732, 734, 749, 752
Distributed Generation (DG), 3, 4, 10, 12, 15,
38, 39, 42, 43, 49, 54, 64, 69–71, 73–75,
84, 89, 173, 285, 286, 292–296, 300, 302,
304, 307, 309, 312, 314, 315, 339, 375,
390, 460–464, 467, 489, 507, 543, 549,
557, 573, 580, 583, 596–602, 605, 614,
622–624, 631, 685, 719, 724, 794, 799, 805
Distributed Generation Planning, 464, 497, 498

Distributed generations (DGs), 409, 414, 731
Distributed renewable energy technologies, 3,
4
Distribution systems protection, 584–586, 593,
604, 616, 622, 623
Distribution companies (DisCos), 731, 732,
735
Distribution networks, 285, 287, 288, 294–296,
302, 312, 314, 315
Distribution Power Network, 462, 464
Distribution systems, 731, 732, 740
Doubly Fed Induction Machine (DFIM),
171–179, 188, 193, 195, 197, 201, 202
Dynamic stability, 109
Dynamic stability analysis, 688

E

Electro-technical commission, 206, 207
Energy demand, 685, 712
Energy storage system (ESS), 89, 247, 285,
313, 315, 332, 334, 348, 410, 421, 550,
651, 676, 749, 753, 791, 792, 798, 803
Environment degradation, 149, 687, 727

F

Fault-ride through, 411, 601, 603, 672, 673,
678, 793
Feeder zone protection, 586
Flickers, 227–229, 234–236, 243
Fossil fuels, 685
Fuel, 69–71, 73–80, 82–91, 93–96, 99–102
Future distribution systems, 549, 580
Future power distribution networks, 793, 802,
803
Fuzzy logic controller (FLC), 393

G

Gas turbines, 69, 89, 90
 Genetic Algorithms, 468
 Geothermal, 3, 50–60, 64
 Green-house gases, 70, 71, 75, 82, 84
 Grid code, 20, 227, 231, 240, 242, 243, 376, 463, 603, 655, 813
 Grid-connected microgrid, 551, 554, 556

H

Harmonics, 227–229, 234, 235, 243
 Hybrid power system (HPS), 749

I

IEA, 206
 IEC 61400, 205–210, 215, 218, 221, 223, 224
 Imbalance voltage fluctuations, 227–229, 234, 243
 Integration of renewable energy generation, 109
 Intelligent energy management system (IEMS), 791, 793, 801–803, 808, 813
 Interconnection requirements, 227, 243
 Islanding detection, 631, 660–662, 669, 670, 672

L

Large scale wind power systems, 150
 Load flow analysis (LFA), 149, 150, 152–154, 156–159, 161, 163–167, 169, 464

M

Matrix converter (MC), 375, 377–381, 385, 388, 390
 Maximum power point tracking (MPPT), 16, 24, 261, 279, 378, 379, 393, 410, 635, 643
 Microgrid, 685–687, 690, 705, 706, 709, 710, 712, 713, 715, 719–721, 724, 727, 791–793, 795, 796, 802, 804, 805, 808, 810, 813
 Micro-turbine, 90–94, 96, 98–102, 731, 732, 734
 Multi-microgrid (MMG), 506

N

Nanogrids (n-grids), 791–794, 802, 804, 809, 813
 Natural gas, 70, 71, 74, 76, 80, 81, 84–87, 93, 94, 101
 Newton-Raphson (NR) method, 150, 154, 165, 169
 NIWE, 205, 206, 217, 220, 221, 224
 Non-renewable distributed generation technology, 69

O

Offshore wind farm, 248–253, 258, 259, 262, 265, 270, 271, 274, 276, 279
 Open loop control scheme, 171, 180, 181, 201, 202
 Operation and maintenance cost, 373
 Optimal DG locations, 731, 733
 Optimal operation, 72, 78, 81, 82, 86–88, 580, 812

P

Partial shading conditions, 393
 Photovoltaic (PV), 285, 293
 Photovoltaic (PV) power system, 393
 Power electronics, 631, 633, 654, 677
 Power factor, 285, 293, 297, 299, 305–307, 309, 312, 314
 Power flow analysis, 464
 Power management systems, 549, 552, 553
 Power quality, 3, 19, 75, 206, 208, 210, 215, 221, 228, 232, 234, 235, 247, 279, 399, 410–412, 463, 503, 551, 553, 556, 583, 600, 601, 621, 631, 633, 655, 659, 662, 665, 666, 668, 670, 673, 801, 804, 812, 813
 Power system performance, 464, 466, 471, 477, 481, 485, 489, 493
 Protection coordination strategy, 524
 Protection schemes, 504, 507, 510, 512, 514, 516, 521, 523, 525–527, 543, 544
 Protective relays, 556, 583, 587–589, 592, 593, 603–606, 609, 618

R

Reactive power compensation, 332
 Reciprocating engine, 69–76, 79–82, 84–89, 94, 101, 102
 Reliability, 109, 112, 113
 Reliability analysis, 660, 663, 685–688, 690, 696, 706, 709, 719, 724, 728
 Reliability indices, 685, 686, 699, 723
 Renewable Energy Resources (RER), 50, 51, 53, 59, 60, 64, 83, 84, 228, 313, 375, 503, 584, 631–633, 637, 675, 685, 686, 710, 722, 727, 792, 793, 795, 796, 813
 Renewable energy sources (RES), 149, 150, 749
 Replacement cost, 373
 Reverse power flow, 285, 302, 304
 Rotor position and speed, 171, 179, 186, 201

S

Sensor-less estimation techniques, 171, 179, 181, 201

Short circuit current, 583, 587, 589, 598, 608, 612, 614, 615
 Smart DC Microgrid, 411, 412, 414
 Solar energy integration, 343
 Solar-PV, 317–321, 330, 332, 334–337, 339, 340
 Solar PV system, 3, 6, 7, 10, 12, 14, 16, 97, 346, 347, 349, 351, 417, 631, 632, 642, 657, 721, 750, 792, 796, 803
 Space vector pulse width modulation (SVPWM), 380, 390
 Standard and design specifications, 205
 Steam turbines, 73
 Sustainable development, 28, 149, 169
 System frequency performance, 110

T

TAPS-2000, 217, 223, 224
 TC-88, 206, 207
 Techno-economic analysis, 343
 Total annual energy generation, 373
 Total harmonic distortion (THD), 384, 388, 390

U

Un-interrupted power supply (UPS), 343, 349

V

Voltage control, 317, 325, 340
 Voltage profile, 110, 112, 123, 139, 285, 293, 295, 297, 298, 300, 301, 304, 305, 307, 314, 330, 331, 336, 340, 559, 584, 596, 600, 655
 Voltage regulation, 317, 318, 322, 324, 335, 340
 Voltage Source Converter(VSC), 248, 251, 253, 255–257, 266, 267, 409, 410, 441
 Voltage stability, 317, 318, 336, 337, 340, 341
 V-Q curve analysis, 337, 340

W

Wind energy conversion, 16
 Wind energy conversion system (WECS), 150, 375, 377, 380
 Wind energy conversion unit, 248–252, 258, 260, 262, 264–268, 271, 272, 274–276, 278
 Wind farms, 18–20, 22, 24, 27, 28, 109–111, 113, 122, 123, 125, 128, 133, 137–139, 144, 145, 150, 154, 206, 228–232, 234–237, 240, 243, 249, 250, 252, 463
 Wind turbines, 205–207, 209, 211, 212, 214–221, 223, 224, 409, 414–416, 445

Z

Zeta buck–boost converter, 393, 395, 397, 405